NASA/TM–2015-218675/Volume II
NESC-RP-12-00770

Check-Cases for Verification of 6-Degree-of-Freedom Flight Vehicle Simulations

Appendices

Daniel G. Murri/NESC
Langley Research Center, Hampton, Virginia

E. Bruce Jackson
Langley Research Center, Hampton, Virginia

Robert O. Shelton
Johnson Space Center, Houston, Texas

January 2015

NASA STI Program . . . in Profile

Since its founding, NASA has been dedicated to the advancement of aeronautics and space science. The NASA scientific and technical information (STI) program plays a key part in helping NASA maintain this important role.

The NASA STI program operates under the auspices of the Agency Chief Information Officer. It collects, organizes, provides for archiving, and disseminates NASA's STI. The NASA STI program provides access to the NTRS Registered and its public interface, the NASA Technical Reports Server, thus providing one of the largest collections of aeronautical and space science STI in the world. Results are published in both non-NASA channels and by NASA in the NASA STI Report Series, which includes the following report types:

- TECHNICAL PUBLICATION. Reports of completed research or a major significant phase of research that present the results of NASA Programs and include extensive data or theoretical analysis. Includes compilations of significant scientific and technical data and information deemed to be of continuing reference value. NASA counter-part of peer-reviewed formal professional papers but has less stringent limitations on manuscript length and extent of graphic presentations.

- TECHNICAL MEMORANDUM. Scientific and technical findings that are preliminary or of specialized interest, e.g., quick release reports, working papers, and bibliographies that contain minimal annotation. Does not contain extensive analysis.

- CONTRACTOR REPORT. Scientific and technical findings by NASA-sponsored contractors and grantees.

- CONFERENCE PUBLICATION. Collected papers from scientific and technical conferences, symposia, seminars, or other meetings sponsored or co-sponsored by NASA.

- SPECIAL PUBLICATION. Scientific, technical, or historical information from NASA programs, projects, and missions, often concerned with subjects having substantial public interest.

- TECHNICAL TRANSLATION. English-language translations of foreign scientific and technical material pertinent to NASA's mission.

Specialized services also include organizing and publishing research results, distributing specialized research announcements and feeds, providing information desk and personal search support, and enabling data exchange services.

For more information about the NASA STI program, see the following:

- Access the NASA STI program home page at *http://www.sti.nasa.gov*

- E-mail your question to help@sti.nasa.gov

- Phone the NASA STI Information Desk at 757-864-9658

- Write to:
  NASA STI Information Desk
  Mail Stop 148
  NASA Langley Research Center
  Hampton, VA 23681-2199

NASA/TM–2015-218675/Volume II
NESC-RP-12-00770

Check-Cases for Verification of 6-Degree-of-Freedom Flight Vehicle Simulations

Appendices

Daniel G. Murri/NESC
Langley Research Center, Hampton, Virginia

E. Bruce Jackson
Langley Research Center, Hampton, Virginia

Robert O. Shelton
Johnson Space Center, Houston, Texas

National Aeronautics and
Space Administration

Langley Research Center
Hampton, Virginia 23681-2199

January 2015

Acknowledgments

The assessment team is grateful to Mr. Edwin Crues for providing permission to reuse this orbital scenario description and would like to express appreciation to Mrs. Pamela Sparks for keeping us organized.

The use of trademarks or names of manufacturers in the report is for accurate reporting and does not constitute an official endorsement, either expressed or implied, of such products or manufacturers by the National Aeronautics and Space Administration.

Available from:

NASA STI Program / Mail Stop 148
NASA Langley Research Center
Hampton, VA 23681-2199
Fax: 757-864-6500

Check-cases for Verification of Six-Degree-of-Freedom Flight Vehicle Simulations – Volume II: Appendices

October 30, 2014

List of Appendices

A Nomenclature **7**
A.1 Symbology . . . 7
A.2 Acronyms . . . 9

B Models **10**
B.1 Vehicle models . . . 10
B.1.1 Spheroid - atmospheric check-cases . . . 12
B.1.2 Spheroid - orbital check-cases . . . 12
B.1.3 Brick . . . 13
B.1.4 Cylinder . . . 14
B.1.5 F-16 aircraft . . . 14
B.1.6 Two-stage rocket . . . 30
B.1.7 ISS . . . 37
B.2 Geodesy models . . . 37
B.2.1 Flat Earth . . . 38
B.2.2 Spheroidal Earth . . . 38
B.2.3 WGS-84 . . . 39
B.3 Coordinate systems . . . 40
B.3.1 Orbital flight coordinates . . . 41
B.3.2 Atmospheric flight coordinates . . . 42
B.4 Gravitation models . . . 44
B.4.1 Constant gravity . . . 44
B.4.2 Inverse square gravitation . . . 44
B.4.3 Spherical harmonic gravitation . . . 45
B.4.4 Gravitational effects on the vehicle . . . 46
B.5 Atmosphere models . . . 48
B.5.1 U.S. Standard Atmosphere 1976 Model . . . 48
B.5.2 Marshall Engineering Thermosphere Model (MET) . . . 48
B.6 Simulation Tools Description . . . 49
B.6.1 JEOD/Trick (JSC) . . . 49
B.6.2 LaSRS++ (LaRC) . . . 50
B.6.3 MAVERIC (MSFC) . . . 51
B.6.4 POST II (LaRC) . . . 51
B.6.5 VMSRTE (ARC) . . . 52
B.6.6 Core (AFRC) . . . 52
B.6.7 JSBSim (Open source) . . . 53

C Check-case scenario descriptions **53**

C.1 Atmospheric scenarios . . . 53

C.1.1 Check-case 1 – dragless sphere . . . 56

C.1.2 Check-case 2 – dragless tumbling brick . . . 57

C.1.3 Check-case 3 – dragless tumbling brick with aerodynamic damping . . . 58

C.1.4 Check-case 4 – sphere dropping over non-rotating, spherical Earth . . . 58

C.1.5 Check-case 5 – sphere dropping over rotating, spherical Earth . . . 59

C.1.6 Check-case 6 – sphere dropping over rotating, ellipsoidal Earth . . . 59

C.1.7 Check-case 7 – sphere dropping through a steady wind field . . . 60

C.1.8 Check-case 8 – sphere dropping through a varying wind field . . . 60

C.1.9 Check-case 9 – eastward ballistic flight of a sphere . . . 61

C.1.10 Check-case 10 – northward ballistic flight of a sphere . . . 61

C.1.11 Check-case 11 – steady flight of a subsonic aircraft . . . 62

C.1.12 Check-case 12 – steady flight of a supersonic aircraft . . . 63

C.1.13 Check-case 13.1 – altitude change of a subsonic aircraft . . . 63

C.1.14 Check-case 13.2 – velocity change of a subsonic aircraft . . . 64

C.1.15 Check-case 13.3 – course change of a subsonic aircraft . . . 64

C.1.16 Check-case 13.4 – lateral offset maneuver of a subsonic aircraft . . . 65

C.1.17 Check-case 14 – maneuvering flight of a supersonic aircraft. . . . 66

C.1.18 Check-case 15 – circumnavigation of the North pole . . . 66

C.1.19 Check-case 16 – circular flight around the Equator-IDL intersection . . . 67

C.1.20 Check-case 17 – flight of two-stage launch vehicle . . . 68

C.2 Orbital scenarios . . . 68

C.2.1 Check-case 2 – ISS in spherical gravity . . . 69

C.2.2 Check-case 3A – ISS in 4×4 harmonic gravity . . . 70

C.2.3 Check-case 3B – ISS in 8×8 harmonic gravity . . . 71

C.2.4 Check-case 4 – ISS with third-body disturbances . . . 72

C.2.5 Check-case 5A – ISS (minimal solar activity) . . . 73

C.2.6 Check-case 5B – ISS (mean solar activity) . . . 74

C.2.7 Check-case 5C – ISS (maximal solar activity) . . . 75

C.2.8 Check-case 6A – sphere with fixed drag . . . 76

C.2.9 Check-case 6B – sphere with dynamic drag . . . 77

C.2.10 Check-case 6C – cylinder undergoing plane change firing . . . 78

C.2.11 Check-case 6D – cylinder undergoing Earth departure firing . . . 79

C.2.12 Check-case 7A – sphere in 4×4 gravity and third-body perturbations . . . 80

C.2.13 Check-case 7B – sphere in 8×8 gravity and third-body perturbations . . . 81

C.2.14 Check-case 7C – sphere in 4 × 4 gravity with drag and third-body perturbations . . . 82
C.2.15 Check-case 7D – sphere in 8 × 8 gravity with drag and third-body perturbations . . . 83
C.2.16 Check-case 8A – ISS free rotation with zero rates . . . 84
C.2.17 Check-case 8B – ISS free rotation with a non-zero rates . . . 85
C.2.18 Check-case 9A – ISS being torqued with zero initial rates . . . 85
C.2.19 Check-case 9B – ISS being torqued with non-zero initial rates . . . 86
C.2.20 Check-case 9C – ISS under torque and force with zero initial rates . . . 86
C.2.21 Check-case 9D – ISS under torque and force with a non-zero initial rates . . . 87
C.2.22 Check-case 10A – cylinder in circular orbit with gravity gradient with zero initial rates 88
C.2.23 Check-case 10B – cylinder in circular orbit with gravity gradient with non-zero initial rates . . . 88
C.2.24 Check-case 10C – cylinder in elliptical orbit with gravity gradient with zero initial rates 89
C.2.25 Check-case 10D – cylinder in elliptical orbit with gravity gradient with a non-zero initial rates . . . 90
C.2.26 Check-case Full – ISS responding to all effects . . . 91
C.3 Geodetic parameters used for comparisons . . . 92

D Results **92**
D.1 Scenario comparisons – Atmospheric . . . 97
D.1.1 Check-case 1 – dragless sphere . . . 97
D.1.2 Check-case 2 – dragless tumbling brick . . . 110
D.1.3 Check-case 3 – dragless tumbling brick with aerodynamic damping . . . 123
D.1.4 Check-case 4 – sphere dropping over non-rotating, spherical Earth . . . 136
D.1.5 Check-case 5 – sphere dropping over rotating, spherical Earth . . . 149
D.1.6 Check-case 6 – sphere dropping over rotating, ellipsoidal Earth . . . 162
D.1.7 Check-case 7 – sphere dropping through a steady wind field . . . 175
D.1.8 Check-case 8 – sphere dropping through a varying wind field . . . 188
D.1.9 Check-case 9 – eastward ballistic flight of a sphere . . . 201
D.1.10 Check-case 10 – northward ballistic flight of a sphere . . . 215
D.1.11 Check-case 11 – steady flight of a subsonic aircraft . . . 228
D.1.12 Check-case 12 – steady flight of a supersonic aircraft . . . 242
D.1.13 Check-case 13.1 – altitude change of a subsonic aircraft . . . 255
D.1.14 Check-case 13.2 – velocity change of a subsonic aircraft . . . 269
D.1.15 Check-case 13.3 – course change of a subsonic aircraft . . . 282
D.1.16 Check-case 13.4 – lateral offset maneuver of a subsonic aircraft . . . 295
D.1.17 Check-case 15 – circumnavigation of the North Pole . . . 309
D.1.18 Check-case 16 – circular flight around the equator-IDL intersection . . . 324

D.1.19 Check-case 17 – flight of two-stage launch vehicle . . . 339
D.2 Scenario comparisons – Orbital . . . 352
D.2.1 Check-case 02 – ISS in spherical gravity . . . 352
D.2.2 Check-case 03A – ISS in 4×4 harmonic gravity . . . 361
D.2.3 Check-case 03B – ISS in 8×8 harmonic gravity . . . 371
D.2.4 Check-case 04 – ISS with third-body disturbances . . . 380
D.2.5 Check-case 05A – ISS (minimal solar activity) . . . 389
D.2.6 Check-case 05B – ISS (mean solar activity) . . . 398
D.2.7 Check-case 05C – ISS (maximal solar activity) . . . 407
D.2.8 Check-case 06A – sphere with fixed drag . . . 416
D.2.9 Check-case 06B – sphere with dynamic drag . . . 425
D.2.10 Check-case 06C – cylinder undergoing plane change firing . . . 434
D.2.11 Check-case 06D – cylinder undergoing Earth departure firing . . . 443
D.2.12 Check-case 07A – sphere in 4×4 gravity and third-body perturbations . . . 452
D.2.13 Check-case 07B – sphere in 8×8 gravity and third-body perturbations . . . 461
D.2.14 Check-case 07C – sphere in 4×4 gravity with drag and third-body perturbations . . . 470
D.2.15 Check-case 07D – sphere in 8×8 gravity with drag and third-body perturbations . . . 479
D.2.16 Check-case 08A – ISS free rotation with zero rates . . . 488
D.2.17 Check-case 08B – ISS free rotation with non-zero rates . . . 497
D.2.18 Check-case 09A – ISS being torqued with zero initial rates . . . 506
D.2.19 Check-case 09B – ISS being torqued with non-zero initial rates . . . 515
D.2.20 Check-case 09C – ISS under torque and force with zero initial rates . . . 524
D.2.21 Check-case 09D – ISS under torque and force with non-zero initial rates . . . 533
D.2.22 Check-case 10A – cylinder in circular orbit with gravity gradient with zero initial rates 542
D.2.23 Check-case 10B – cylinder in circular orbit with gravity gradient with non-zero initial rates . . . 551
D.2.24 Check-case 10C – cylinder in elliptical orbit with gravity gradient with zero initial rates 560
D.2.25 Check-case 10D – cylinder in elliptical orbit with gravity gradient with non-zero initial rates . . . 569
D.2.26 Check-case Full – ISS responding to all effects . . . 578

E Discussion of results **588**
E.1 Quality of matches . . . 588
E.1.1 Quantitative match of parameters . . . 588
E.1.2 Atmospheric scenarios . . . 588
E.1.3 Orbital scenarios . . . 596
E.2 Corrections to improve matching . . . 599

E.2.1 Simulation parameters 599
E.2.2 Simulation conventions 599
E.2.3 Initial conditions 601
E.2.4 Output data recording differences 604
E.2.5 Timing of external forces and torques 606
E.3 Suggestions for future work 606

A Nomenclature

A.1 Symbology

$\vec{A}$	Gravitational acceleration vector
a_p	Three-hour-interval geomagnetic activity index
$\mathbf{B}$	Inertial-to-body transformation matrix
b	Reference wingspan
C	Aerodynamic coefficient
$\bar{C}_{nm}$	Normalized, unit-less gravitation coefficient of degree n and order m
$\bar{c}$	Mean aerodynamic chord
D	Drag
d	Differential operator
F	Force
$F_{10.7}$	Daily 10.7 cm solar flux
$\bar{F}_{10.7}$	Six-solar-rotation mean 10.7 cm solar flux
$\mathbf{G}$	Gravity gradient matrix
G	Universal gravitational constant
$\mathbf{g}$	Unit of acceleration
$\mathbf{H}$	Second derivative of U with respect to ECEF coordinates
h	Geometric altitude
$\mathbf{I}$	Inertia tensor
I	Moment or product of inertia
I_{sp}	Specific fuel consumption
J_2	Second degree zonal harmonic coefficient of gravitation
$\mathbf{M}$	RNP matrix to transform ECI into ECEF coordinates
M	Mass of the Earth
m	Mass or gravitational model order
n	Gravitational model degree
O	"Order of" operator
P	Intersection of Prime Meridian and Equator, or arbitrary vehicle location
$\bar{P}_{n,m}$	Normalized associated Legendre function of degree n and order m
p	Roll rate
q	Pitch rate
$\vec{R}$	Inertial position vector
R	Radius
r	Yaw rate, or radius
r_2	Radius of spherical Earth of equal surface area as reference ellipsoid
r_e	Equatorial radius of the Earth
r_p	Polar radius of the Earth
S	Reference area
$\bar{S}_{nm}$	Normalized, unit-less gravitation coefficient of degree n and order m
s	Intersection of Earth's surface of radius vector to arbitrary point P
T	Torque
t	Time
U	Potential function
u_b	Atmosphere-relative velocity component along the body x-axis
v_b	Atmosphere-relative velocity component along the body y-axis

w_b Atmosphere-relative velocity component along the body z-axis
X Earth-centered inertial axis from Earth center through Equator/Prime Meridian (lat. 0, long. 0) intersection at $t = 0$ (for atmospheric check-cases); axis aligned with the mean equinox at epoch J2000 (for orbital check-cases)
X Earth-centered, Earth-fixed axis from Earth center through Equator/Prime Meridian (latitude 0, longitude 0) intersection
$\bar{x}$ Location of center of mass along body x-axis
x Inertial position coordinate along the inertial **X**-axis
x Body longitudinal axis, +forward
Y Earth-centered inertial axis from Earth center forming a right-hand-rule with **X** and **Z**
Y Earth-centered, Earth-fixed axis forming a right hand rule with X and Z
$\bar{y}$ Location of center of mass along body y-axis
y Inertial position coordinate along the inertial **Y**-axis
y Body lateral axis, +right to an observer facing in positive x direction
Z Earth-centered inertial axis from Earth center through North Pole
Z Earth-centered, Earth-fixed axis from Earth center through the North Pole, or geopotential height
$\bar{z}$ Location of center of mass along body z-axis
z Inertial position coordinate along the inertial **Z**-axis
z Body vertical axis, +down
α Angle of attack, projected into the body x-z plane
α_{total} Unconstrained angle of attack
β Ballistic coefficient or angle of sideslip
V Velocity
δ_{ij} Kronecker delta
ϵ Eccentricity figure of the Earth
θ Pitch attitude
λ Longitude
μ Gravitational parameter (product of GM)
$\vec{\nu}$ Normal vector to the surface of the Earth
$\bar{\nu}$ Projection of $\vec{\nu}$ on the Equatorial plane of the Earth
ρ Moment arm of differential element of mass
$\vec{\tau}$ Gravity gradient torque
ϕ Bank angle, or geodetic latitude
ψ Heading angle
ω Earth's mean rotation rate

Subscript
cm Center of mass
1 Body 1
2 Body 2
b body of vehicle
D Drag component
L Lift component
l Rolling component
m Pitching component
n Yawing component
s Surface of the Earth

T	True airspeed
xx	Moment of inertia around the body x-axis
yy	Moment of inertia around the body y-axis
Y	Sideforce component
zz	Moment of inertia around the z axis
xy	Cross-product of inertia in the body x-y plane
yz	Cross-product of inertia in the body y-z plane
zx	Cross-product of inertia in the body z-x plane

Math symbols

$\bar{o}$	Mean or average value of o
$\dot{o}$	Time rate-of-change of o
$\ddot{o}$	Time rate-of-acceleration of o
$\|E\|$	Absolute value of E or scalar magnitude of $\vec{E}$
$\vec{E}$	3-dimensional vector whose magnitude, $\|\vec{E}\|$, is E
ΔE	Change in E
∇E	Gradient of E

A.2 Acronyms

2D	Two-dimensional
AFRC	Armstrong Flight Research Center
ANL	Aircraft nose left
ANR	Aircraft nose right
ANU	Aircraft nose up
ARI	Aileron-to-rudder interconnect
CM	Center of Mass
CWFN	Clockwise from North
DAVE-ML	Dynamic Aerospace Vehicle Exchange Markup Language
DCM	Direction cosine matrix
DOF	Degrees-of-freedom
DUT1	Difference between Universal Time and Coordinated Universal Time, seconds
ECEF	Earth-centered, Earth-fixed (rotating coordinate frame)
ECI	Earth-centered Inertial (non-rotating coordinate frame)
EOM	Equations of Motion
FORTRAN	FORmula TRANslator
GEM-T1	Goddard Earth Model T1
GNC	Guidance, Navigation and Control
IC	Initial Condition
IDL	International Date Line
IERS	International Earth Rotation and Reference System Service
ITRF	International Terrestrial Reference Frame
ISS	International Space Station
J2000	Earth-centered Inertial Frame for Epoch 2000
JEOD	JSC Engineering Orbital Dynamics
JSBSim	Open-source, data-driven, simulation framework in C++
JSC	Johnson Space Center

KEAS	Knots Equivalent Airspeed
kt	knots (nautical miles per hour)
KTAS	Knots True Airspeed
LaRC	Langley Research Center
LaSRS++	Langley Standard Real-time Simulation in C++
LQR	Linear Quadratic Regulator
LRC	Local Reference Coordinates
LVLH	Local Vertical, Local Horizontal
LWD	Left Wing Down
MAC	Mean Aerodynamic Chord
MAVERIC	Marshall Aerospace Vehicle Representation in C
MAX	Maximum thrust level
MET	Marshall Engineering Thermosphere
MET95	Marshall Engineering Thermosphere, (1995 version)
MET99	Marshall Engineering Thermosphere, (1999 version)
MET07	Marshall Engineering Thermosphere (2007 version)
MIL	Military (maximum unaugmented, non-afterburning) thrust level
MRC	Moment Reference Center
MSFC	Marshall Space Flight Center
MSIS	Mass Spectrometer Incoherent Scatter
MSL	Mean Sea Level
N.A.	Not Applicable
NED	North-East-Down
NESC	NASA Engineering and Safety Center
PLA	Power Lever Angle
PM	Prime Meridian
POST II	Program to Optimize Simulated Trajectories II
RNP	Rotation-Nutation-Precession
RWD	Right Wing Down
S-119	ANSI/AIAA S-119-2011 Flight Dynamic Model Exchange Standard
SAS	Stability Augmentation System
SIM	Label used for comparison plots for anonymized simulation tool results
SRB	Solid Rocket Booster
TED	Trailing Edge Down
TEL	Trailing Edge Left
TFrames	Tools to Facilitate the Rapid Assembly of Missile Engagement Simulations
VMSRTE	Vertical Motion Simulator Real-Time Environment
WGS-84	World Geodetic System 1984
XML	eXtensible Markup Language

B Models

B.1 Vehicle models

A set of reference vehicles was proposed based mostly on existing non-proprietary vehicle models. An overview of each model is given below. These models are available from `http://nescacademy.nasa.gov/`

`flightsim/index.html`.

For the quiescent (non-maneuvering) orbital scenarios, we only need consider two characteristics of the orbiting vehicle: inertial properties and drag characteristics.

Inertial properties The mass of an orbiting vehicle determines its response to outside forces and torques. The mass properties of a satellite are captured by

- Total mass

$$m = \int_b dm \tag{1}$$

where m is the total mass, b is the body of the vehicle, and dm represents a differential unit of mass.

- Center of mass (CM)

$$\begin{pmatrix} \bar{x} \\ \bar{y} \\ \bar{z} \end{pmatrix} = \int_b \begin{pmatrix} x \\ y \\ z \end{pmatrix} dm \tag{2}$$

where dm represents a differential element of mass located at the point (x, y, z) and the integration is performed over the volume of the vehicle.

- Inertia tensor

$$I = \begin{bmatrix} I_{xx} & -I_{xy} & -I_{xz} \\ -I_{xy} & I_{yy} & -I_{yz} \\ -I_{xz} & -I_{yz} & I_{zz} \end{bmatrix} \tag{3}$$

and

$$\begin{aligned} I_{xx} &= \int_b (\rho_y^2 + \rho_z^2) dm \\ I_{yy} &= \int_b (\rho_x^2 + \rho_z^2) dm \\ I_{zz} &= \int_b (\rho_x^2 + \rho_y^2) dm \\ I_{xy} &= \int_b \rho_x \rho_y dm \\ I_{xz} &= \int_b \rho_x \rho_z dm \\ I_{yz} &= \int_b \rho_y \rho_z dm \end{aligned} \tag{4}$$

where

$$\rho = \begin{pmatrix} \rho_x \\ \rho_y \\ \rho_z \end{pmatrix} = \begin{pmatrix} x - \bar{x} \\ y - \bar{y} \\ z - \bar{z} \end{pmatrix} \tag{5}$$

Drag characteristics In general, the characterization of forces and moments exerted as the vehicle moves through a medium can be quite complex; however, for the purposes of comparing orbital trajectories, a simple ballistic coefficient model will suffice.

Given the definition of ballistic drag coefficient, β_D, as

$$\beta_D = \frac{m}{C_D S} \tag{6}$$

and substituting C_D into the equation for aerodynamic drag

$$D = \frac{1}{2}\rho {V_T}^2 S C_D \tag{7}$$

an equivalent expression, given the ballistic drag coefficient β_D, is

$$D = \frac{\rho {V_T}^2 \beta_D}{m} \tag{8}$$

For the atmospheric scenarios, the aerodynamic models are typically non-linear and table-based, and propulsion models (if included) are affected by vehicle airspeed. The same mass property definitions given previously still apply.

B.1.1 Spheroid - atmospheric check-cases

The simplest model used in generating a representative aerodynamic-flight reference trajectories was a sphere of fixed size, inertia, and a constant drag coefficient, as given in Tables 1 and 2. These are somewhat arbitrary values.

Table 1. Atmospheric Spheroid Mass and Inertial Characteristics

Parameter	Value[a]
I_{xx}	3.6 slug-ft^2
I_{yy}	3.6 slug-ft^2
I_{zz}	3.6 slug-ft^2
I_{xy}	0.0 slug-ft^2
I_{yz}	0.0 slug-ft^2
I_{zx}	0.0 slug-ft^2
m	1.0 slug
$\bar{x}$	0.0 ft
$\bar{y}$	0.0 ft
$\bar{z}$	0.0 ft

[a] measured from the CM

Table 2. Atmospheric Spheroid Aerodynamic Characteristics

Parameter	Value
S	0.1963495 ft^2
C_L	0.0
C_D	0.1
C_Y	0.0
C_l	0.0
C_m	0.0
C_n	0.0

B.1.2 Spheroid - orbital check-cases

A different spheroid with metric units was used in generating the orbital reference trajectories. It had fixed size and inertia as given in Table 3. This model was reused from the earlier orbital simulation comparison study [1] and had a radius of $1/\sqrt{\pi}$ m.

Table 3. Orbital Spheroid Mass and Inertial Characteristics

Parameter	Value
I_{xx}	$2/(5\pi)$ kg-m^2
I_{yy}	$2/(5\pi)$ kg-m^2
I_{zz}	$2/(5\pi)$ kg-m^2
I_{xy}	0.0 kg-m^2
I_{yz}	0.0 kg-m^2
I_{zx}	0.0 kg-m^2
m	1.0 kg
$\bar{x}$	0.0 m
$\bar{y}$	0.0 m
$\bar{z}$	0.0 m

B.1.3 Brick

The next-simplest model evaluated was a brick-shaped object with rotational aerodynamic damping, as given in Tables 4 and 5. No attempt was made to ascertain the actual parameters; these inertia properties were estimated assuming homogeneity while the assumed aerodynamic characteristics were completely arbitrary. The moments and products of inertia were given about axes that originate at the CM.

The brick was assumed to be standard size: 8 inches by 4 inches by 2.25 inches, corresponding to the x, y, and z body axes dimensions as shown in Figure 1.

Table 4. Estimated U.S. Standard Face Brick Mass and Inertial Characteristics

Parameter	Value
I_{xx}	0.001894220 slug-ft^2
I_{yy}	0.006211019 slug-ft^2
I_{zz}	0.007194665 slug-ft^2
I_{xy}	0.0 slug-ft^2
I_{yz}	0.0 slug-ft^2
I_{zx}	0.0 slug-ft^2
m	0.155404754 slug
$\bar{x}$	0.0 ft
$\bar{y}$	0.0 ft
$\bar{z}$	0.0 ft

Table 5. Fictitious U.S. Standard Face Brick Aerodynamic Characteristics

Parameter	Value
S	0.22222 ft^2
b	0.33333 ft
$\bar{c}$	0.66667 ft
C_L	0.0
C_D	0.01
C_Y	0.0
C_l	0.0
C_m	0.0
C_n	0.0
C_{l_p}	−1.0
C_{l_r}	0.0
C_{m_q}	−1.0
C_{n_p}	0.0
C_{n_r}	−1.0

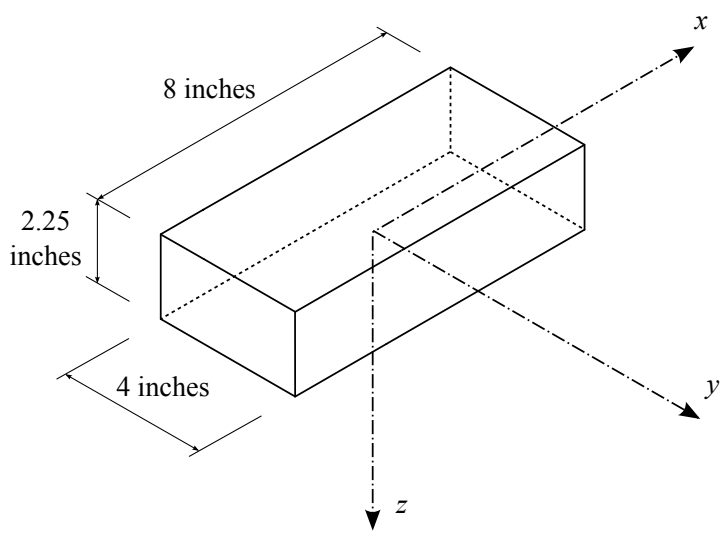

Figure 1. U.S. Standard Face Brick

B.1.4 Cylinder

A uniform-density cylinder of size 12 m x 1 m x 1 m, used for certain orbital check-cases, also was reused from the earlier orbital simulation comparison study [1]. Its mass properties are given in Table 6. The moments of inertia were about the CM.

B.1.5 F-16 aircraft

The single-engine fighter chosen for both subsonic and supersonic atmospheric flight scenarios was based on a fairly well-known example, the General Dynamics (now Lockheed Martin) F-16. Stevens and Lewis [2] provided a FORTRAN model of this aircraft for subsonic flight in their text. Garza and Morelli [3] expanded this model with additional wind-tunnel data from another NASA report [4].

This expanded model was converted from Matlab® scripts of Garza and Morelli into the ANSI/AIAA S-119-2011 format [5]. The expanded model set included aerodynamic, mass properties, and propulsion subsystem models that were implemented as function tables for most of the aero and propulsion force and moment contributions; the mass properties were fixed constants given in Table 7.

Two additional subsystem models were developed to provide a simple linear quadratic regulator (LQR) stability augmentation control law, allowing simple maneuvering with pre-programmed pilot inputs as in atmospheric cases 11 and 13, and an autopilot controller designed to perform the circumnavigations described

Table 6. Mass Properties for Cylinder

Parameter	Value
I_{xx}	500 kg-m^2
I_{yy}	12,250 kg-m^2
I_{zz}	12,250 kg-m^2
I_{xy}	0.0 kg-m^2
I_{yz}	0.0 kg-m^2
I_{zx}	0.0 kg-m^2
m	1,000 kg
$\bar{x}$	6.0 m
$\bar{y}$	0.0 m
$\bar{z}$	0.0 m

Table 7. Example F-16 Mass and Inertial Characteristics

Parameter	Value
S	300.0 ft ^{2}
b	30.0 ft
$\bar{c}$	11.32 ft
I_{xx}	9,496.0 slug-ft^2
I_{yy}	55,814.0 slug-ft^2
I_{zz}	63,100.0 slug-ft^2
I_{xy}	0.0 slug-ft^2
I_{yz}	0.0 slug-ft^2
I_{zx}	982.0 slug-ft^2
m	637.26 slug
$\bar{x}$	25% MAC
$\bar{y}$	0.0 ft
$\bar{z}$	0.0 ft

in atmospheric cases 15 and 16. These models, described below, are available in S-119 format from the Web repository found at `http://nescacademy.nasa.gov/flightsim/index.html`.

F-16 Autopilot with stability augmentation system – `F16_control.dml` The S-119-encoded model named `F16_control.dml` provided stability augmentation for subsonic piloted flight as well as a selectable three-axis autopilot with course capture-and-track capability. It was the basis for the more specialized maneuvering `F16_gnc.dml` autopilot described next, but was used as-is for the arbitrary maneuvering in check-case 13.

Inputs to the controller are given in Table 8; outputs are shown in Table 9.

Two discrete inputs controlled the behavior of the control system. If the stabilityAugmentationOn_disc input was 'true' (> 0.5), the vehicle's dynamics were stabilized through feedback. This was the mode used in this assessment.

If autopilotOn_disc was 'true,' stability augmentation was engaged and the vehicle responded to airspeed, altitude, and heading commands (equivalentAirspeedCommand, altitudeMslCommand and trueBaseCourseCommand, which acted as a desired heading input). If lateralDeviationError was non-zero, the vehicle attempted to intercept and track a desired course along the direction supplied in trueBaseCourseCommand.

Two simple LQR gain feedback matrices were used to provide stabilization of the longitudinal and lateral/directional axes. The choice of weighting to select the gains was somewhat arbitrary and non-optimal, and resulted in a fairly high-bandwidth closed-loop system. This controller is completely unsuitable for manned flight and probably piloted motion-based simulation, but served to exercise the F-16 model for atmospheric subsonic check-case 11.

Supplied LQR gain values were intended for flight at 10,000 ft and 287 kt equivalent airspeed (KEAS). Flight at other speed/altitude combinations was sub-optimal or even unstable.

No pilot inputs were used in any of the check-cases.

No actuator dynamics were modeled in an attempt to keep the implementation as simple as possible.

While trimming the F-16 model to an equilibrium state, stabilityAugmentationOn_disc and autopilotOn_disc were both set to 'false' (< 0.5). It was recommended that the simulation tool's trim feature should adjust the inputs trimmedPilotControl_throttle and trimmedPilotControl_long to trim the longitudinal state of the vehicle. If the simulation's trim feature instead manipulated pilotControl_throttle and pilotControl_long, then the simulation should have set trimmedPilotControl_throttle and trimmedPilotControl_long to zero. (The `F16_control.dml` file specifies a non-zero initial condition for these two trim variables that is close to their trim values for straight and level flight at 10,000 ft mean sea level (MSL) and Mach 0.5.)

The original model was encoded in the S-119 format. It has been converted into hierarchical system block diagrams for this report to better describe its operation; but the S-119 model `F16_control.dml` was the normative description of this model.

The top-level *F16_control* block is shown in Figure 2. The inputs and outputs are described in Tables 8 and 9 respectively.

Lateral autopilot block. This part of the *F16_control* system, shown in Figure 3, attempted to steer the vehicle through bank commands to acquire and track a given course. If lateral track error was available, the controller would attempt to reduce that error. Some logic was required to wrap the resulting ground track angle feedback signal to fall within ±180 deg. This error was multiplied by a gain, was limited to ±30 degrees, and was output as the commanded bank angle (autopilotCommandedBankAngle) (+RWD).

Table 8. Input Signals - `F16_control.dml`

Name	Units	Sign	Description
pilotControl_throttle	$0 \rightarrow +1$	+incr	Pilot throttle control position
pilotControl_long	$-1 \rightarrow +1$	+aft	Pilot longitudinal control position
pilotControl_lat	$-1 \rightarrow +1$	+right	Pilot lateral control position
pilotControl_yaw	$-1 \rightarrow +1$	+right	Pilot rudder pedal position
trimmedPilotControl_throttle	$0 \rightarrow +1$	+incr	Trimmed position of throttle
trimmedPilotControl_long	$-1 \rightarrow +1$	+aft	Trimmed position of pitch control
stabilityAugmentationOn_disc	$0, 1$	+true	Stability augmentation engage flag (discrete)
autopilotOn_disc	$0, 1$	+true	Autopilot engage flag (discrete)
equivalentAirspeedCommand	KEAS	> 0	Desired equivalent airspeed (autopilot input)
altitudeMslCommand	ft	> 0	Desired absolute altitude (autopilot input)
lateralDeviationError	ft	+right	Lateral deviation error from desired course for autopilot
trueBaseCourseCommand	deg	+CWFN	True heading of desired ground track (autopilot input)
altitudeMsl	ft	+up	Geometric altitude above mean sea level (SAS and autopilot feedback)
equivalentAirspeed	KEAS	+up	Equivalent airspeed (SAS and autopilot feedback)
angleOfAttack	deg	+ANU	Angle of attack (SAS feedback)
angleOfSideslip	deg	+ANL	Angle of sideslip (SAS feedback)
eulerAngle_Roll	deg	+RWD	Roll angle (SAS feedback)
eulerAngle_Pitch	deg	+ANU	Pitch angle (SAS feedback)
eulerAngle_Yaw	deg	+CWFN	Heading angle (autopilot feedback)
bodyAngularRate_Roll	rad/s	+RWD	Body roll rate (SAS feedback)
bodyAngularRate_Pitch	rad/s	+ANU	Body pitch rate (SAS feedback)
bodyAngularRate_Yaw	rad/s	+ANR	Body yaw rate (SAS feedback)

F16_control

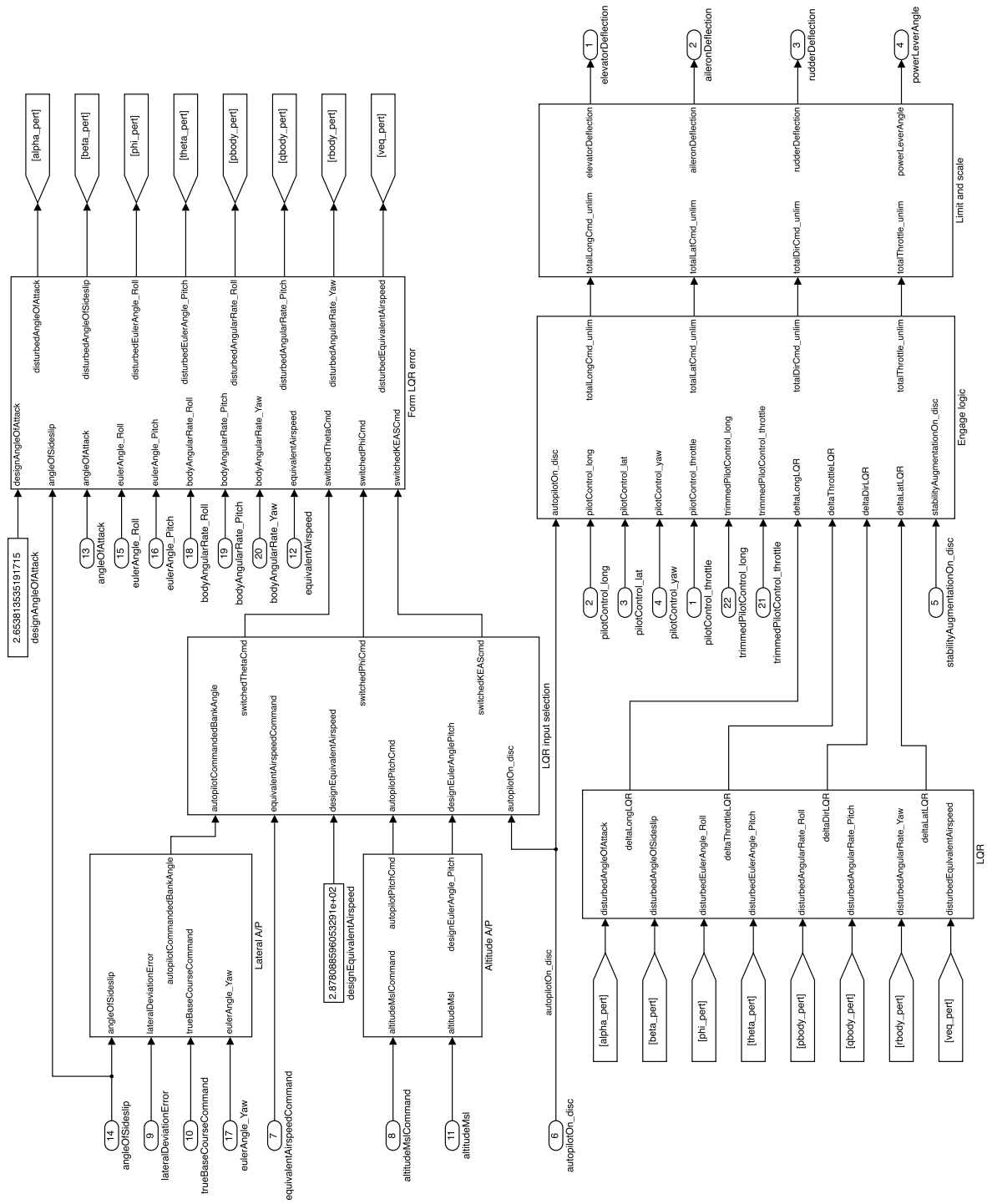

Figure 2. *F16_control*: Simple LQR-based Stability Augmentation and Autopilot for Example Simulations

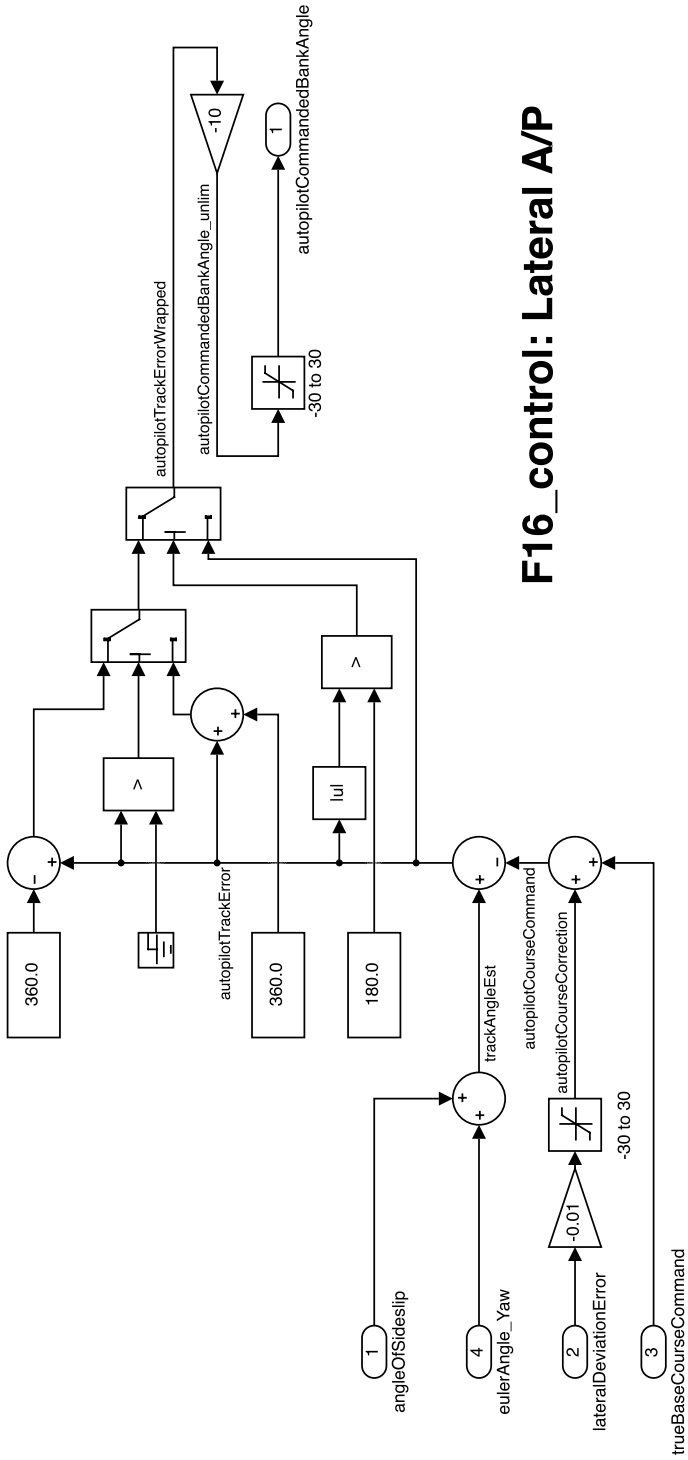

Figure 3. *Lateral autopilot*: Calculate Bank Angle Command to Track a Given Course or Ground Track

Table 9. Output Signals - `F16_control.dml`

Name	Units	Sign	Description
elevatorDeflection	deg	+TED	Elevator command
aileronDeflection	deg	+LWD	Aileron deflection (right - left)/2
rudderDeflection	deg	+TEL	Rudder deflection
powerLeverAngle	pct	$0 \rightarrow 100$	Throttle (power lever angle) 50 is MIL (max dry) thrust; 100 is MAX (burner)

Altitude autopilot block. This part of the *F16_control* system, shown in Figure 4, formed an error between the commanded altitude (altitudeMslCommand) and current altitude above sea level (altitudeMsl), multiplied by a gain of -0.05 deg/ft, limited the product to ± 5 and added this change in pitch to the designEulerAngle_pitch angle to form the autopilotPitchCmd output (+ANU).

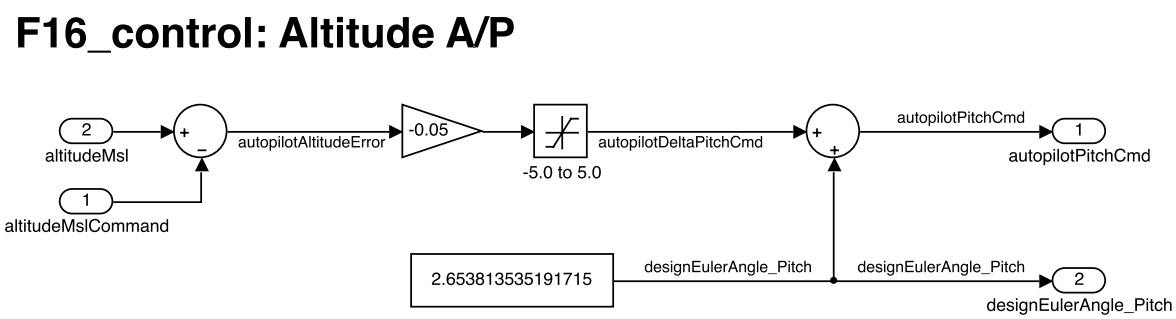

Figure 4. *Altitude autopilot*: Calculate Pitch Angle Delta Command to Hold an Assigned Altitude

LQR input selection block. This portion of the *F16_control* system, shown in Figure 5, selected the reference quantities for pitch attitude, bank attitude, and reference airspeed used to form the error for the LQR controller for these quantities. If autopilotOn_disc > 0.5, the previously calculated autopilotPitchCmd and autopilotCommandedBankAngle values, along with a user-provided equivalentAirspeedCommand, were fed to the downstream LQR controller; otherwise the trimmed designEulerAnglePitch and designEquivalent-Airspeed were used along with a value of 0.0 for bank angle reference.

Form LQR error block. As shown in Figure 6, this portion of the *F16_control* system compared (subtracted) the selected reference quantities for pitch attitude, bank attitude, and velocity from the current sensed values. It also formed an error between the trimmed angle of attack and current angle of attack. Quantities that are normally zero, including angle of sideslip, and body rates, were also fed back as errors.

These errors were then passed to the actual LQR gain blocks.

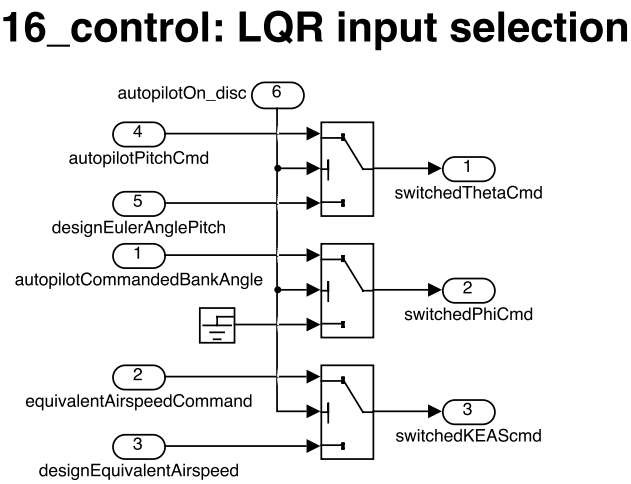

Figure 5. *LQR input selection*: Select Between Trimmed and Commanded Pitch, Roll, and Airspeed LQR Reference Inputs

LQR block. This portion of the *F16_control* system, shown in Figure 7, multiplied errors in the eight state variables (four longitudinal, four lateral/directional) to calcluate corrections to the longitudinal, lateral, directional control surface and throttle commands.

The gains were picked for the 10,000 ft, Mach 0.5 flight condition; operation at other flight conditions may not be satisfactory.

Engage logic block. This part of the *F16_control* system, shown in Figure 8, limited pilot inputs and, depending on the autopilot and stability augmentation engage settings, either passed those pilot inputs directly to the surfaces and engine power lever, augmented them with LQR-derived stability augmentation signals, or disregarded them entirely when the autopilot was engaged.

When the autopilot was engaged (autopilotOn_disc > 0.5) the stability augmentation signals were automatically included in the output signals.

Limit and scale block. This last piece of the *F16_control* system, shown in Figure 9, initially limited output commands to ± 1.0 (full-scale) and then scaled these outputs to the maximum deflection angle for the control surfaces and the power lever. An aileron-to-rudder interconnect (ARI) gain provided rudder commands to minimize sideslip while maneuvering the vehicle.

F-16 Guidance, autopilot and stability augmentation system – `F16_gnc.dml` A more capable control system was provided in the *F16_gnc* model, encoded in S-119 model as `F16_gnc.mdl`. This used the same autopilot and LQR control system as the *F16_control* control system model discussed previously, but added a guidance block upstream of the autopilot. This guidance block provided bank angle steering commands to the autopilot to guide the vehicle in a circular flight path around a designated latitude/longitude

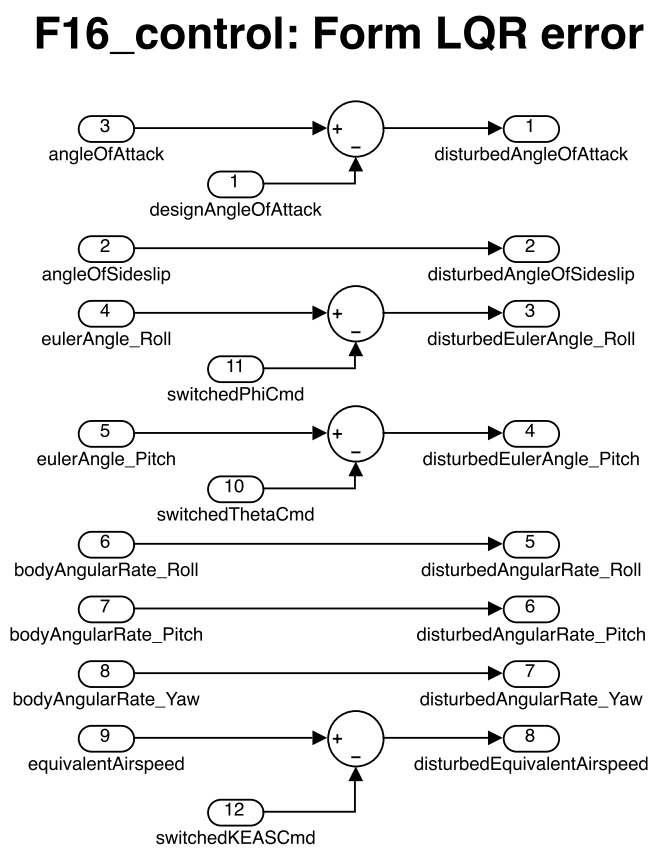

Figure 6. *Form LQR Error*: Select Between Trimmed and Commanded Pitch, Roll and Airspeed LQR Reference Inputs

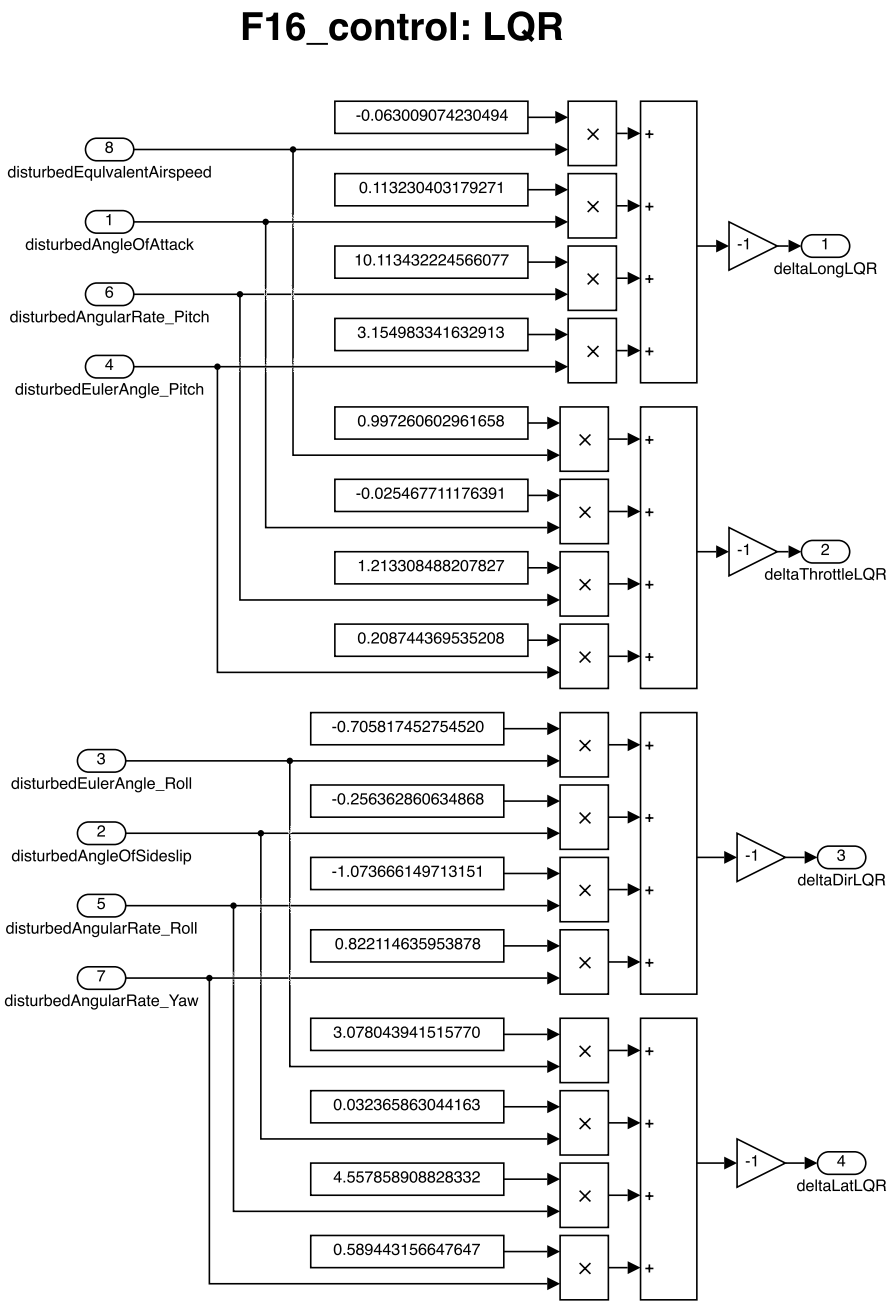

Figure 7. *LQR*: Linear Quadratic Regulator for Subsonic F-16 Model

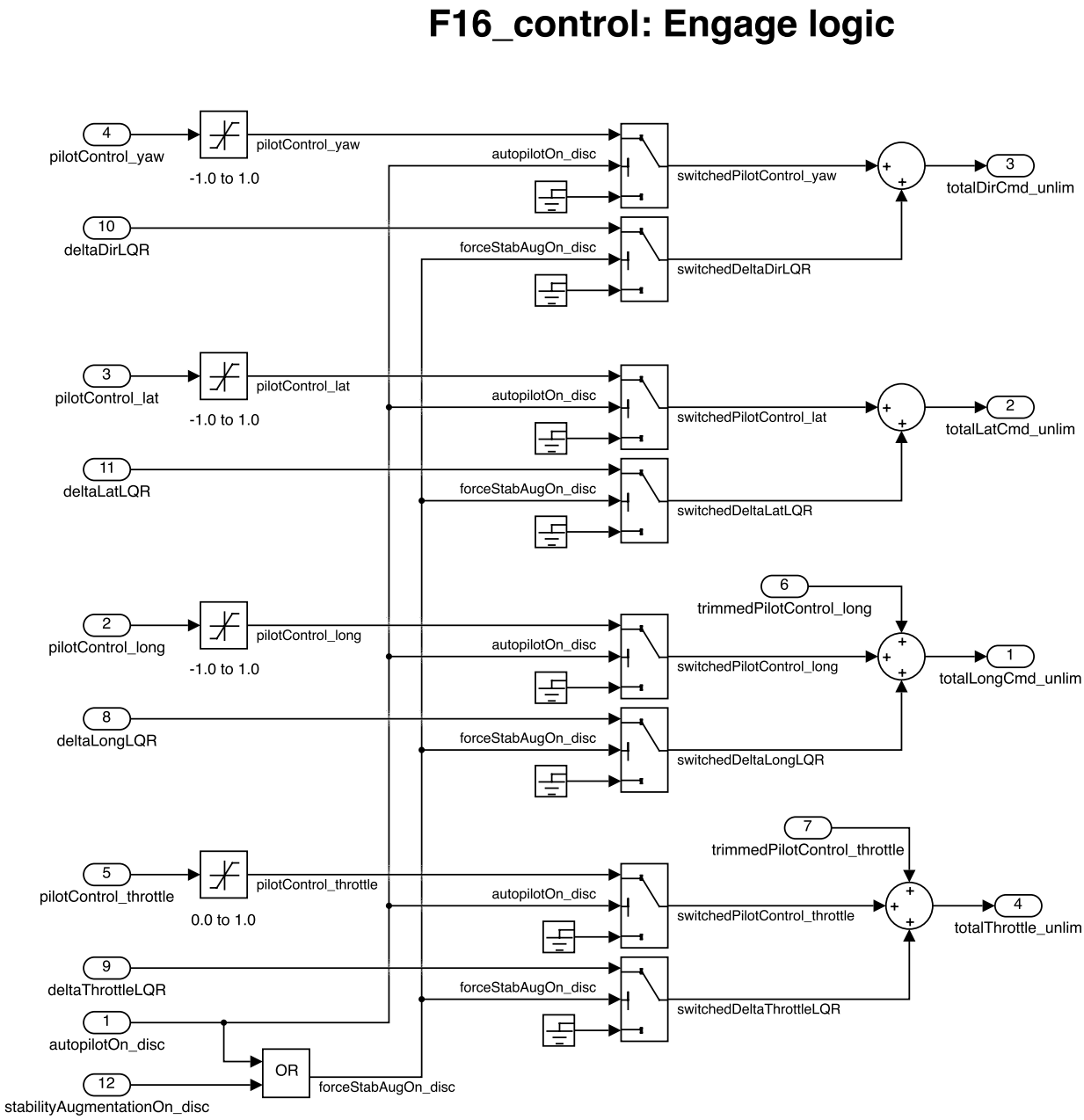

Figure 8. *Engage logic*: Select Sources to Drive Control Surfaces and Power Lever Angle

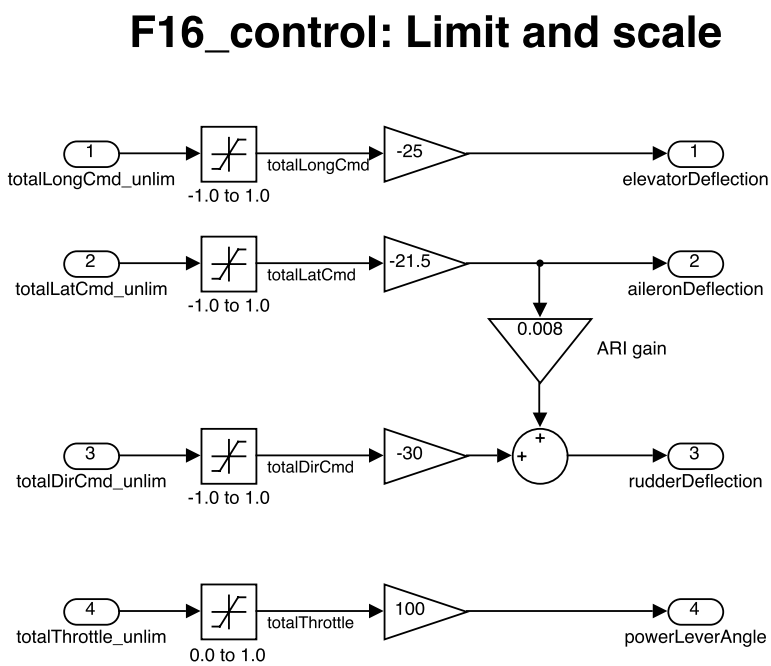

Figure 9. *Limit and scale*: Limit and Scale Output Commands

position. In particular, this system included a selection input that would circumnavigate either the North Pole or the Equator/International Date Line (IDL) intersection in a counter-clockwise direction. This control algorithm was used for atmospheric check-cases 15 and 16 instead of the *F16_control* used for check-case 13.

Inputs to the *F16_control* system are given in Table 10; outputs are shown in Table 11.

The primary difference between *F16_gnc* and *F16_control* was the GNC version had no trueBaseCourseCommand or lateralDeviationError input; the behavior of the vehicle when autopilotOn_disc was 'true' (> 0.5) depended on the value of selectCircumnavigator_disc: if 'false' (< 0.5), the vehicle would be commanded to fly toward and circle around the Equator/IDL intersection; if 'true' (> 0.5), the vehicle would be commanded to fly toward and circle the North Pole at a distance of 3 nautical miles at the specified altitude and speed. In addition to the new selectCircumnavigator_disc input were two new navigation feedback signal inputs, geLatitude and geLongitude, for the current vehicle geodetic latitude and longitude position coordinates, respectively.

The outputs were the same as for *F16_control*.

These circles took approximately 3.5 simulated minutes at 10,000 ft and 287 KEAS.

The *F16_gnc* model was encoded and made available to participants in the S-119 format. It was converted into the hierarchical system block diagrams shown in this report to better describe its operation; but the S-119 model file `F16_gnc.dml` is the normative description of this model.

The top-level *F16_gnc* block is shown in Figure 10. The inputs and outputs are described in Tables 10 and 11 respectively.

With the exception of the *Circumnavigator* block, the *F16_gnc* system had the same structure as the previously described *F16_control* system.

Circumnavigator. The block that was unique to the *F16_gnc* system was the *Circumnavigator* block, depicted in Figure 11. This block took current "ownship" position and generated both a heading angle (trueBaseCourseCommand) and a lateral offset value (lateralDeviationError), which the downstream autopilot structure (identical to the *F16_control* autopilot previously described) used to steer the vehicle in the horizontal plane through a varying bank angle command.

The value of the selectCircumnavigator_disc input chose whether the circumnavigator would steer toward a circle around the North Pole or a circle around the Equator/IDL intersection. In the case of the North Pole (selectCircumnavigator_disc > 0.5), the baseline heading angle was a constant 90° for a counterclockwise encirclement. The lateral offset was calculated by subtracting the current ownship geodetic latitude in degrees from 90°, converting that angular distance from the North Pole into feet, and then subtracting the desired circular radius (3 nm, converted to feet) to arrive at the distance outside (+ or right of desired course) or inside (− or left of desired course) the circle as the lateral offset value.

In the case of selecting the Equator/IDL intersection (selectCircumnavigator_disc $== 0$), the distance of the ownship from the intersection was the sum of the squares of latitude converted to feet, and $(180 - |\text{longitude}|)$ converted into feet. From this distance the radius of the 3 nm circle, converted to feet, was subtracted to form the distance outside (+ right) or inside (− left) of the desired circle. The heading command was the tangent angle of the circle heading counter-clockwise, which was simply the four-quadrant arc tangent of the ratio of north displacement to east displacement, converted to degrees.

Table 10. Input Signals - `F16_gnc.dml`

Name	Units	Sign	Description
pilotControl_throttle	$0 \rightarrow +1$	+incr	Pilot throttle control position
pilotControl_long	$-1 \rightarrow +1$	+aft	Pilot longitudinal control position
pilotControl_lat	$-1 \rightarrow +1$	+right	Pilot lateral control position
pilotControl_yaw	$-1 \rightarrow +1$	+right	Pilot rudder pedal position
trimmedPilotControl_throttle	$0 \rightarrow +1$	+incr	Trimmed position of throttle
trimmedPilotControl_long	$-1 \rightarrow +1$	+aft	Trimmed position of pitch control
stabilityAugmentationOn_disc	$0, 1$	+true	Stability augmentation engage flag (discrete)
autopilotOn_disc	$0, 1$	+true	Autopilot engage flag (discrete)
selectCircumnavigator_disc	$0, 1$	+Npole	Selects point to circle; 0 = Equator/IDL, 1 = North Pole
geLatitude	deg	+north	Geodetic latitude of vehicle's CM (nav feedback)
geLongitude	deg	+east	Geodetic longitude of vehicle's CM east of PM (nav feedback)
equivalentAirspeedCommand	KEAS	> 0	Desired equivalent airspeed (autopilot input)
altitudeMslCommand	ft	> 0	Desired absolute altitude (autopilot input)
altitudeMsl	ft	+up	Geometric altitude above mean sea level (SAS and autopilot feedback)
equivalentAirspeed	KEAS	+up	Equivalent airspeed (SAS and autopilot feedback)
angleOfAttack	deg	+ANU	Angle of attack (SAS feedback)
angleOfSideslip	deg	+ANL	Angle of sideslip (SAS feedback)
eulerAngle_Roll	deg	+RWD	Roll angle (SAS feedback)
eulerAngle_Pitch	deg	+ANU	Pitch angle (SAS feedback)
eulerAngle_Yaw	deg	+CWFN	Heading angle (autopilot feedback)
bodyAngularRate_Roll	rad/s	+RWD	Body roll rate (SAS feedback)
bodyAngularRate_Pitch	rad/s	+ANU	Body pitch rate (SAS feedback)
bodyAngularRate_Yaw	rad/s	+ANR	Body yaw rate (SAS feedback)

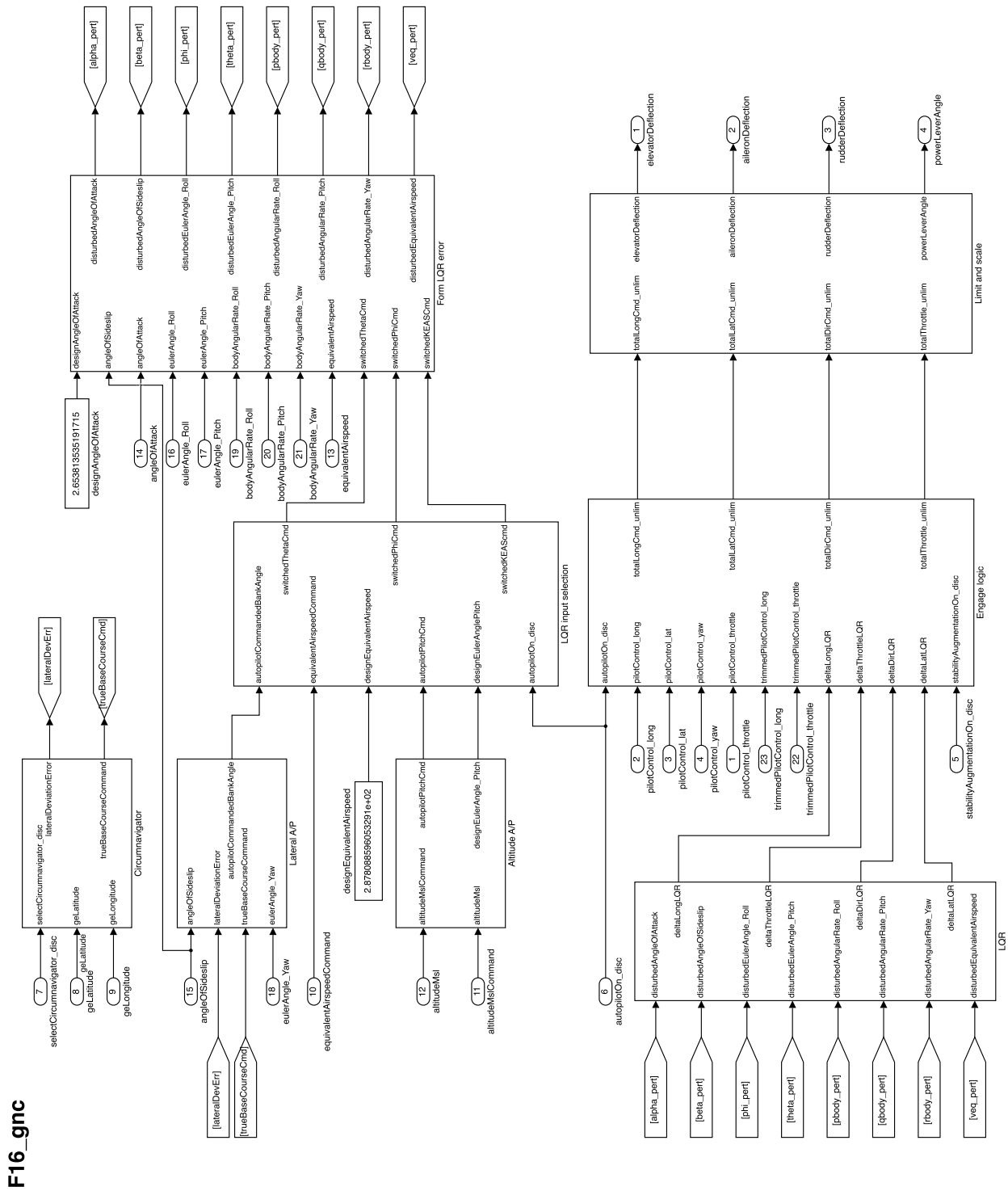

Figure 10. *F16_gnc*: Guidance and Control System for Check-cases 15 and 16

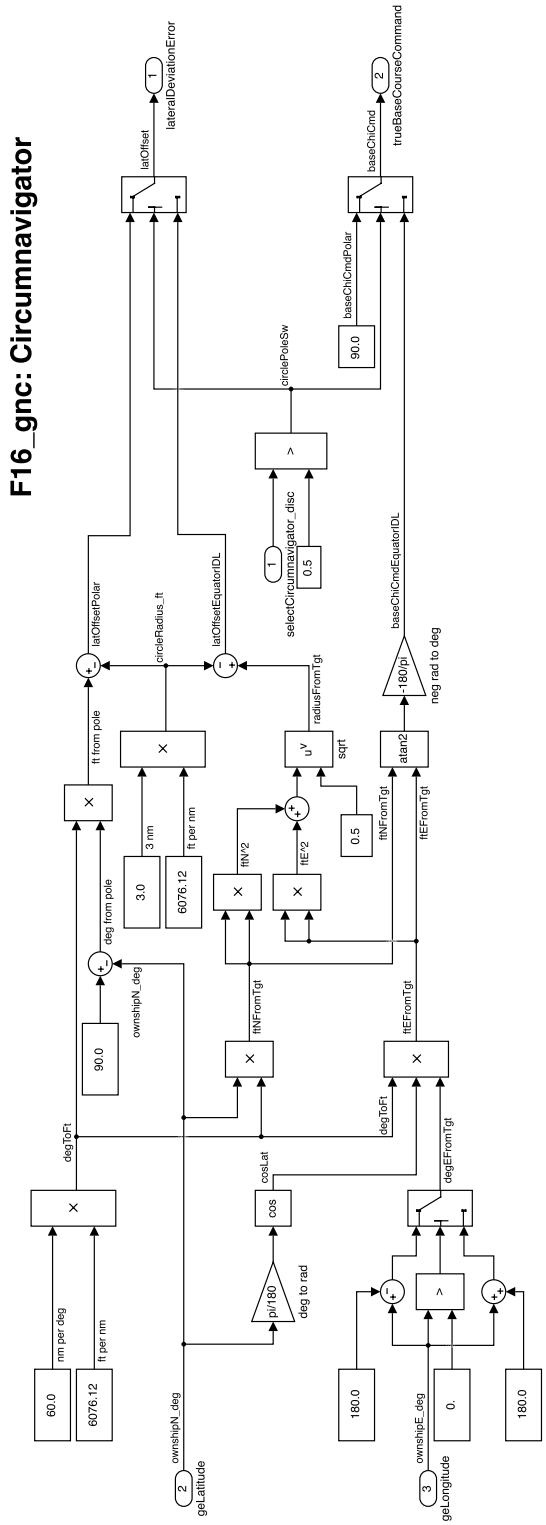

Figure 11. *Circumnavigator*: Guidance Algorithm for Check-cases 15 and 16

Table 11. Output Signals - `F16_gnc.dml`

Name	Units	Sign	Description
elevatorDeflection	deg	+TED	Elevator command
aileronDeflection	deg	+LWD	Aileron deflection (right - left)/2
rudderDeflection	deg	+TEL	Rudder deflection
powerLeverAngle	pct	$0 \rightarrow 100$	Throttle (power lever angle) 50 is MIL (max dry) thrust; 100 is MAX (burner)

B.1.6 Two-stage rocket

A two-stage rocket model was imagined by Dr. Eric Queen of NASA's Langley Research Center (LaRC) for this effort in an unpublished document. The scenario involved a two-stage rocket being fired from the Equator at an initial pitch attitude; during the boost, a short coast occurred after the first stage was expended, and then the second stage fired (which included a step change in the location and amount of mass) as the vehicle's flight path pitched over in response to gravity. At the end of the second-stage firing, the remaining vehicle mass was intended to be in a highly elliptical orbit.

A notation on one page of the original document indicates the aero data are based on "V2 at Mach 3"; another notation indicates the rockets are modeled after the Shuttle solid rocket boosters (SRB). No attribution of any other data appeared necessary.

The vehicle was envisioned to be two 3 m diameter solid rocket boosters stacked vertically; the first stage was 25 m long with a dry mass of 35,000 kg and 180,000 kg of propellant. The second stage was 10 m long with a dry mass of 15,000 kg carrying 80,000 kg of propellant, for a total booster length of 35 m. It was carrying a 4,000 kg payload to orbit.

The vehicle was stable and had no active guidance or control.

The vehicle model was provided in the following files:

- `twostage_aero.dml`, Rev A, dated 2014-03-27: simple aerodynamics model
- `twostage_prop.dml`, dated 2013-08-10: simple propulsion model
- `twostage_inertia.dml`, dated 2012-08-09: mass properties model

The inputs and outputs for each of these models are given in Tables 12 to 18 below.

Two-stage rocket aerodynamics model – `twostage_aero.dml`. The aero model for the two-stage rocket had two inputs – angle of attack, α and angle of sideslip, β – that were defined in an aircraft sense:

$$\tan\alpha = \frac{w_b}{u_b}$$

$$\sin\beta = \frac{v_b}{V}$$

These angles were used to form a "total angle of attack" (α_{total}) giving the angle of the velocity-vector to the rocket body centerline as

$$\alpha_{\text{total}} = \sqrt{\alpha^2 + \beta^2}$$

These three angles (α, α_{total}, β) were used as inputs into linearly interpolated one-dimensional (1D) function tables.

Outputs were the traditional aerodynamic force and moment coefficients measured about the reference point (the location of the reference point along the central body axis was an output of the inertia model, and changed depending on whether the vehicle had staged or not). Rolling moment was identically zero for convenience.

Table 12. Input Signals - `twostage_aero.dml`

Name	Units	Sign	Description
angleOfAttack	deg	+ANU	Angle of attack
angleOfSideslip	deg	+ANL	Angle of sideslip

Two-stage rocket propulsion model – `twostage_prop.dml`**.** The first stage was modeled as having 17,000,000 N thrust with an I_{sp} of 360 sec. The second stage had 5,000,000 N thrust with an I_{sp} of 390 sec. Both stages were to burn in turn until all the propellant in each stage was depleted.

It was an error to have both stages burning simultaneously.

Two-stage rocket mass properties model – `twostage_inertia.dml`**.** This model linearly interpolates mass properties, including center of mass location, during flight. Inputs were total fuel consumed in stages 1 and 2 and a flag to indicate if the vehicle had staged (dropped the first stage). Outputs were mass properties, fuel fraction consumed in both stages, and the location of the moment reference center (which moved when the vehicle staged).

The starting mass properties of each stage are given in Table 16.

Implementation. Inputs from the simulation framework were normal flight conditions: angle of attack, angle of sideslip, and dynamic pressure. These were used to obtain aerodynamic coefficients of forces and moments about the current moment reference center (MRC), which changed when the vehicle staged.

The specified ICs (see below) were assumed for the flight conditions, and the first stage was ignited by passing the appropriate flag to the propulsion model. The resulting thrust acted along the body x-axis and began to accelerate the vehicle. The amount of fuel consumed by each stage had to be calculated by external logic; the mass of fuel consumed was provided to the inertia model, which provided the current mass properties including the offset between the CM and the aerodynamic MRC.

This moment arm was used to transfer the aero forces and moments from the reference center to the current CM using an external cross-product operation of the two vector quantities; thus the actual moments and aerodynamic forces were summed with the thrust value from the propulsion model and accelerations were calculated at the CM.

The simulation framework integrated the accelerations twice to arrive at new flight conditions, and the simulation loop would then start over.

Table 13. Output Signals - `twostage_aero.dml`

Name	Units	Sign	Description
longitudinalReferenceLength	m	const.	Longitudinal reference length [3 m]
lateralReferenceLength	m	const.	Lateral reference length [3 m]
referenceArea	m^2	const.	Reference area [7 m^2]
liftCoefficient	–	+up	Total coefficient of force normal to flight path in body x-z plane
sideforceCoefficient	–	+right	Total coefficient of force parallel the body y-axis
dragCoefficient	–	+down	Total coefficient of force parallel to the flight path
rollingMomentCoefficient	–	+RWD	Total coefficient of moment around the body x-axis (rolling moment)
pitchingMomentCoefficient	–	+ANU	Total coefficient of moment around the body y-axis (pitching moment)
yawingMomentCoefficient	–	+ANR	Total coefficient of moment around the body z-axis (yawing moment)

Table 14. Input Signals - `twostage_prop.dml`

Name	Units	Sign	Description
stage1firing_flag	0, 1	+firing	Indicates if the first stage is firing
stage2firing_flag	0, 1	+firing	Indicates if the second stage is firing

External logic was also required to account for the angular momentum carried away by the rocket exhaust. This term is the product of a fractional gain, the rate of change of the mass tensor, and the rocket angular rate. For the check-cases, it was assumed that the exhaust would carry away half the angular moment change (i.e. fraction gain = 0.5) due to the mass tensor change.

Some internal logic was required to turn off the first stage when it was depleted (remaining fuel fraction reached 0), then the vehicle was allowed to coast for 96.79 sec before the first vehicle was dropped (or staged) and the second stage was ignited. The second stage continued to burn until fuel depletion.

At this point the vehicle was in an elliptical orbit with a perigee greater than 125 km for a circular, rotating, Earth.

The simulation framework was responsible for the appropriate atmospheric model, integrating both the equations of motion (EOM) and the fuel consumed values, providing the moment transfer to the center of mass, estimating the angular momentum lost to the engine exhaust, and providing the simple switching and timing logic for coasting and staging upon depletion of the propellant of the first stage.

Initial conditions The rocket was launched from sea level at the Equator heading eastward with an initial pitch attitude of 55.220 degrees (measured from horizontal). The initial velocity was +0.1 ft/s upwards for comparisons sake and to avoid singularities involving division by zero.

For simplicity's sake, the center-of-mass of the vehicle started at sea level (which would have physically placed the lower part of the rocket below sea level).

Initial angular rates were zero with respect to the launch site. The vehicle pitched over along the flight path in response to the effect of gravity as it accelerated away from the launch site (a so-called 'gravity turn').

Atmosphere model For comparison, the full U.S. Standard Atmosphere 1976 was specified for this check-case [6]. Many simulations that support the 1976 atmosphere do not include the portion in the thermosphere, which is a separate set of tables or equations. Therefore for comparison purposes, the atmospheric density was set to zero above 86 km. This zeroed the atmospheric forces and moments in the thermosphere.

Table 15. Output Signals - `twostage_prop.dml`

Name	Units	Sign	Description
bodyThrustForce_X	N	+fwd	Steady-state thrust of engine in body x-axis
bodyThrustForce_Y	N	+right	Steady-state thrust of engine in body y-axis (always 0)
bodyThrustForce_Z	N	+down	Steady-state thrust of engine in body z-axis (always 0)
bodyThrustMoment_Roll	N-m	+RWD	Steady-state moment of engine about the body x-axis (always 0)
bodyThrustMoment_Pitch	N-m	+RWD	Steady-state moment of engine about the body y-axis (always 0)
bodyThrustMoment_Roll	N-m	+RWD	Steady-state moment of engine about the body z-axis (always 0)
massDot	kg/s	+incr	Propellant consumption rate

Table 16. First-stage Mass and Inertial Characteristics

		Stage 1		Stage 1	
Parameter	Units	Full	Empty	Full	Empty
I_{xx}	kg-m^2	353,250	150,750	111,375	21,375
I_{yy}	kg-m^2	33,501,637.473 461	10,886,636.572 139	941,063.762 626	212,384.868 421
I_{zz}	kg-m^2	353,250	150,750	111,375	21,375
I_{xy}	kg-m^2	0.0	0.0	0.0	0.0
I_{yz}	kg-m^2	0.0	0.0	0.0	0.0
I_{zx}	kg-m^2	0.0	0.0	0.0	0.0
m	kg	314,000	134,000	99,000	19,000
$\bar{x}$	m	16.918 790	9.421 642	4.797 980	3.947 368
$\bar{y}$	m	0.0	0.0	0.0	0.0
$\bar{z}$	m	0.0	0.0	0.0	0.0

Table 17. Input Signals - `twostage_inertia.dml`

Name	Units	Sign	Description
rocketHasStaged	0, 1	+staged	If non-zero, indicates first stage is missing.
stage1fuelConsumed	kg	–	Amount of fuel burned in first stage
stage2fuelConsumed	kg	–	Amount of fuel burned in second stage

Table 18. Output Signals - `twostage_inertia.dml`

Name	Units	Sign	Description
stage1FuelRemainingFrac	frac	$0 \rightarrow 1$	Fraction of fuel remaining in first stage
stage2FuelRemainingFrac	frac	$0 \rightarrow 1$	Fraction of fuel remaining in second stage
bodyMomentOfInertia_Roll	kg-m^2	> 0	Rolling moment of inertia about the body x-axis
bodyMomentOfInertia_Pitch	kg-m^2	> 0	Pitching moment of inertia about the body y-axis
bodyMomentOfInertia_Yaw	kg-m^2	> 0	Yawing moment of inertia about the body x-axis
bodyProductOfInertia_ZX	kg-m^2	0	Cross-product of inertia in the body x-z plane (no sign reversal)
bodyProductOfInertia_XY	kg-m^2	0	Cross-product of inertia in the body x-y plane (no sign reversal)
bodyProductOfInertia_YZ	kg-m^2	0	Cross-product of inertia in the body y-z plane (no sign reversal)
totalMass	kg	> 0	Total mass of the vehicle
vrsPositionOfMrc	m	+aft	Longitudinal location of the MRC (+aft from nose)
bodyPositionOfCmWrtMrc_X	m	+fwd	Longitudinal location of the CM relative to MRC
bodyPositionOfCmWrtMrc_Y	m	+right	Lateral location of the CM relative to MRC
bodyPositionOfCmWrtMrc_Z	m	+down	Vertical location of the CM relative to MRC

B.1.7 ISS

A vehicle with a mass distribution representative of the International Space Station (ISS), used in certain orbital check-cases, was reused from the earlier orbital simulation comparison study [1]. Its mass properties are given in Table 19. The moments and products of inertia were given about axes that originate at the CM.

Table 19. Mass Properties for ISS-like Vehicle

Parameter	Value
I_{xx}	1.02×10^8 kg-m^2
I_{yy}	0.91×10^8 kg-m^2
I_{zz}	1.64×10^8 kg-m^2
I_{xy}	6.96×10^6 kg-m^2
I_{yz}	-5.90×10^5 kg-m^2
I_{zx}	5.48×10^6 kg-m^2
m	400,000 kg
$\bar{x}$	-3.0 m
$\bar{y}$	-1.5 m
$\bar{z}$	4.0 m

B.2 Geodesy models

This section describes the way in which most flight simulation tools model the surface of the Earth. We describe three simple models that are commonly used in the simulation of atmospheric and orbital vehicles.

There is a connection between models for gravitation and those for geodesy. Geodetic models include a reference surface to serve as an idealized sea level. By definition any such surface should also be a level surface for the gravity potential function (which is the sum of gravitation and the centrifugal acceleration due to the Earth's rotation), i.e. it should be normal to the local gravity vector.

The pairing of geodetic and gravitational models considered here is

- Flat Earth – constant gravitation assumed
- Spheroidal Earth – inverse square law gravitation model[1]
- Ellipsoidal Earth (World Geodetic System 1984 (WGS-84)) – spherical harmonic gravitation model

For the round and ellipsoidal models, we locate points using the familiar altitude h, latitude ϕ and longitude λ. The altitude should be measured along the normal vector $\vec{\nu}$ to the surface of the reference shape (sphere or ellipsoid). The latitude ϕ is defined to be the angle between $\vec{\nu}$ and the equatorial plane $z = 0$. If $\bar{\nu}$ is the projection of $\vec{\nu}$ on the equatorial plane, then the longitude λ is the angle between $\overrightarrow{(0, P)}$ and $\bar{\nu}$ where P is the intersection of the Prime Meridian and the Equator. We adopt the sign convention that east longitude is positive as is latitude north of Equator.

[1]The round Earth is commonly paired with the inverse square law gravitation model. However, the resulting gravity vector (gravitation plus centrifugal acceleration due to the Earth's rotation) is deflected from the surface normal because the inverse square law generates no northward component of gravitation to counteract the southward component of centrifugal acceleration due to the Earth's rotation that appears at locations away from the pole and Equator. This problem disappears if the round Earth is modeled without rotation, but the resultant gravity is then overestimated by a slight amount at many locations due to the missing centrifugal acceleration.

B.2.1 Flat Earth

The simplest way to model the surface of the Earth is as a plane. The coordinates for such a system are usually given in either runway-aligned coordinates (for terminal maneuvers) or in a three-dimensional framework oriented north, east and down. In at least one approximation the position of the vehicle is given as geodetic latitude, longitude and radius from the center of Earth, which are spherical coordinates, but the "translational rates" of these spherical positions are integrated as if they were translational rates across a flat surface.

These are valid approximations for the appropriate simulation application but generally lead to errors in line-of-sight calculations and/or high-speed flight.

B.2.2 Spheroidal Earth

The next step on the ladder of complexity is to model the Earth as a perfect sphere. To this end, we need only a single number r_2, the radius of a sphere with an equal surface area as the WGS-84 ellipsoidal Earth, to specify the model. The equation of the point s on the surface of a spherical Earth is simply

$$X^2 + Y^2 + Z^2 = r_2^2 \tag{9}$$

While coordinate systems are discussed in the next section, it is appropriate to state the method for moving between spherical coordinates (latitude, longitude and altitude) to frequently-used rectangular coordinates, as shown in Figure 12.

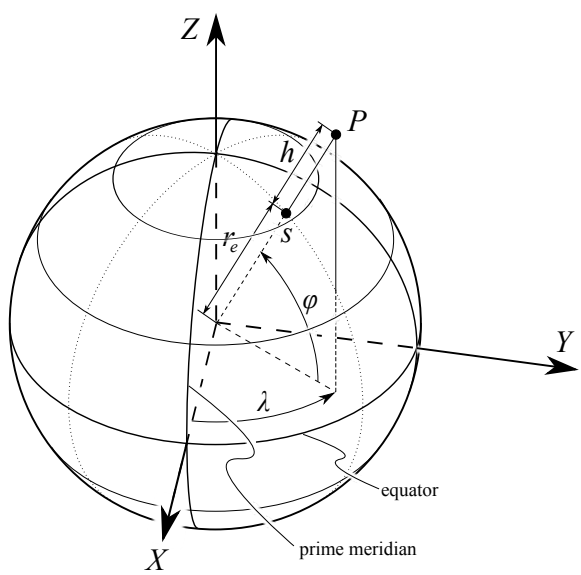

Figure 12. Relationship between Earth-fixed Cartesian Coordinates and Spherical (geocentric) Coordinates for Spherical Earth

The conversion from spherical altitude, latitude, and longitude coordinates to the normally rotating Earth-centered, Earth-fixed (ECEF) Cartesian coordinates is given by

$$\begin{pmatrix} X \\ Y \\ Z \end{pmatrix} = (h + r_2) \begin{pmatrix} \cos(\phi)\cos(\lambda) \\ \cos(\phi)\sin(\lambda) \\ \sin(\phi) \end{pmatrix} \tag{10}$$

The conversion in the other direction from ECEF to altitude, latitude, and longitude is described by

$$\begin{aligned} h &= \sqrt{X^2 + Y^2 + Z^2} - r_2 \\ \phi &= \sin^{-1}\left(\frac{Z}{\sqrt{X^2 + Y^2 + Z^2}}\right) \\ \lambda &= \text{atan2}(Y, X) \end{aligned} \tag{11}$$

where $\text{atan2}(Y, X)$ is a 4-quadrant arc-tangent function.

B.2.3 WGS-84

The World Geodetic System is a standard for use in cartography, geodesy, and navigation. It comprises a standard coordinate frame for the Earth, a standard ellipsoidal reference surface (the datum or reference ellipsoid) for raw altitude data, and a gravitational equipotential surface (the geoid) that defines the nominal sea level. The latest revision is WGS-84 (dating from 1984 and last revised in 2004 [7]).

Although WGS-84 is based on just four constants, we derive from them an additional parameter: r_p, the polar radius. Due to polar flattening of the Earth, r_p is slightly less than r_e, as shown in Figure 13.

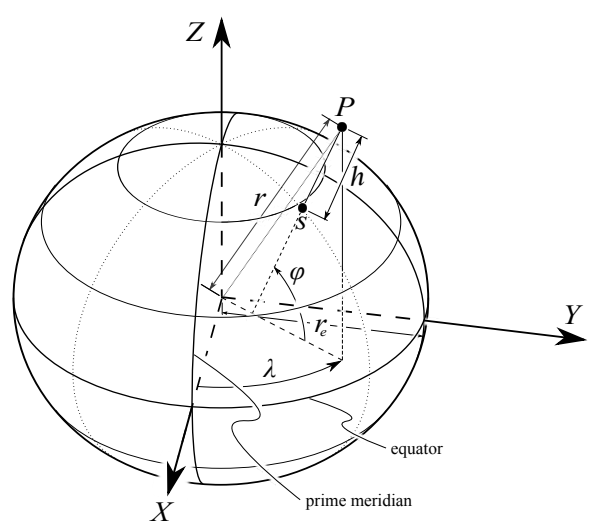

Figure 13. Relationship between Earth-fixed Cartesian Coordinates and Ellipsoidal (geodetic) Coordinates for Spherical Earth

The geodetic ellipsoid is then defined by the equation

$$\frac{X^2+Y^2}{r_e^2}+\frac{Z^2}{r_p^2}=1 \tag{12}$$

The transformations between altitude, latitude, longitude, and ECEF Cartesian are significantly more complicated in the ellipsoidal Earth case. Note that all meridians on the reference ellipsoid are congruent ellipses having semi-major axis r_e and semi-minor axis r_p. The eccentricity ϵ of the meridian ellipses is a convenient parameter for expressing these transformations.

$$\epsilon=\sqrt{1-\left(\frac{r_p}{r_e}\right)^2} \tag{13}$$

Then we can write the transformation from altitude, geodetic latitude, and longitude to ECEF as

$$\begin{pmatrix} X \\ Y \\ Z \end{pmatrix}=\begin{pmatrix} \left[h+\frac{r_e}{\sqrt{1-\epsilon^2\sin^2\phi}}\right]\cos\phi\cos\lambda \\ \left[h+\frac{r_e}{\sqrt{1-\epsilon^2\sin^2\phi}}\right]\cos\phi\sin\lambda \\ \left[h+(1-\epsilon^2)\frac{r_e}{\sqrt{1-\epsilon^2\sin^2\phi}}\right]\sin\phi \end{pmatrix} \tag{14}$$

Obtaining a concise transformation in the opposite direction (from ECEF Cartesian to h, ϕ, λ) is a challenging algebra problem that requires use of the quartic formula; often an iterative or approximation is used. For details on these solutions, see Borkowski [8] or the tutorial video by NASA Engineering and Safety Center's (NESC) Dr. James R. Beaty [9].

B.3 Coordinate systems

An important part of developing dynamic simulations is dealing with coordinate systems. There are a number of such systems involved in this study.

Of prime interest is the selection of the system that is considered to be inertial, or non-moving. While in real-life no such system actually exists, low Earth orbit simulation tools typically use a pseudo-inertial system whose origin translates with the planet center and whose axes are fixed with respect to the stars, such as the J2000 coordinate system described in section B.3.1 below. The Earth is considered to be a rotating object in the J2000 system, and its orientation with respect to the J2000 system is specified through a time-dependent transformation matrix containing three rotations.

Most aerodynamic vehicle simulations make a simplification by treating the Earth as an inertial system, or as a rotating object that is turning on its polar axis at a constant rate around a fixed, or inertial, coordinate system located at the Earth's center (the Earth-centered inertial (ECI) frame). Some aerodynamic simulations simplify this even further and treat a position on the Earth, such as a runway, as the origin of a non-moving inertial frame.

Selection of the inertial coordinate system is important to avoid introducing errors in the calculation of derivatives (linear velocities and accelerations), or equivalently, in performing numerical integration of rotational states, due to rotational effects.

B.3.1 Orbital flight coordinates

Coordinate systems are a fundamental consideration in the planning, simulation and execution of space missions. There are often multiple, related, coordinate systems for a single vehicle, and usually at least two for every celestial object. However, most of these systems result from application-specific requirements such as placement of sensors and other devices.

To keep matters as simple and consistent as possible, we specialize to the case of a single vehicle body-axis system with axes and origin fixed with respect to a rigid vehicle. The mass properties of the vehicle will be defined in terms of this system. Since our orbital cases all involve Earth-centric scenarios, we can eliminate all but three planetary systems – ECI, ECEF, and the local horizontal, local vertical (LVLH) for the vehicle.

The ECI system is not a truly inertial system because its origin is accelerating with the Earth as it makes its traversal around the sun. The key "inertial" feature is that the axes of the ECI frame do not rotate. This is critical because propagation of 6-degrees-of-freedom (DOF) dynamics in a rotating frame is extremely complex.

We need the ECEF frame in order to compute other environmental factors such as atmosphere and gravity that are linked to the planet.

There is a key transformation that links these two frames. This transformation is usually composed of four elements:

- Rotation – the rotation of Earth about its polar axis
- Nutation – a "wobble" of the polar axis with respect to some mean value
- Precession – the slow drift of the mean pole around a 23.5° cone
- Polar motion – approximated by a constant value in these comparisons

The ECI and ECEF systems used here were established by the International Earth Rotation and Reference System Service (IERS). The ECI system, known as J2000, is modeled on an equatorial system at the epoch of noon on 1 January 2000 in Greenwich, England. It is formally defined with respect to extra-galactic quasar sources.

The IERS publishes code and data to transform J2000 to an Earth-fixed system defined by its three coordinate axes X, Y and Z.

- The X axis points from the center of the Earth to the intersection of Equator and Prime Meridian.
- The Z axis points from the center of the Earth to the north pole.
- The Y axis is defined $Y = Z \times X$

The IERS publishes code and tabular data, which can be used to compute X, Y and Z in J2000 coordinates. The rotation-nutation-precession (RNP) matrix $\mathbf{M}$, which transforms from ECI to ECEF, is thus given by

$$\mathbf{M} = \begin{pmatrix} X \\ Y \\ Z \end{pmatrix} \tag{15}$$

where X, Y and Z comprise the rows of the matrix $\mathbf{M}$.

It is useful to describe vehicle attitude for guidance, navigation, control (GNC), and communications by means of standard Euler angles (roll, pitch, yaw) with respect to an LVLH coordinate system as in Figure 14.

The LVLH system is defined as follows.

- Z-axis: Defined to be a unit vector pointing from the vehicle CM to the CM of the central body
- Y-axis: Defined as a unit vector that is normal to the orbit plane, pointing in the direction opposite to the instantaneous orbit angular momentum vector.
- X-axis: Completes a standard, right-handed coordinate frame

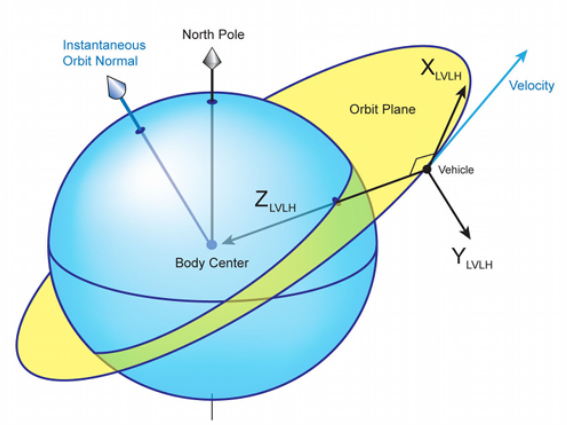

Figure 14. LVLH Frame

B.3.2 Atmospheric flight coordinates

As mentioned previously, a 6-DOF atmospheric flight simulation may treat the ECI coordinate system, located at the center of the Earth, as the inertial frame for state propagation.

Many simulations assume the X-axis is in the plane of the Prime Meridian, but the WGS-84 standard [7] actually uses the IERS Reference Meridian, located about 300 feet east of the Prime Meridian.

Unlike the more complex RNP rotations between ECEF and ECI systems in most orbital simulations, most atmospheric flight simulations assume these systems share the polar axis of rotation and are related through a single rotation, as shown in Figure 15, where the systems are coincident at some predefined time (typically, but not necessarily, $t = 0$) and then the ECEF X- and Y-axes rotate eastward around the Equator at the rotational rate of the Earth. Sometimes the period of this rotation is assumed to be 24.0 hours, but the WGS-84 standard specifies a mean Earth rotational rate $\omega = 7,292,115.0 \times 10^{-11}$ rad/s corresponding to the "inertial" or sidereal period of 23.9345 hours (slightly less than a day, since the Earth is orbiting around the sun: the Earth rotates approximately 361 degrees in a solar day between local noons).

Propagating the position of the vehicle and other items of interests in the ECI frame is normally done in rectilinear coordinates **X**, **Y**, and **Z**. Positions in the ECEF frame are usually specified in polar coordinates of geocentric latitude, geocentric longitude, and radius from the Earth's center. Conversion between these coordinate sets is straightforward and found in many textbooks. When performing navigation calculations,

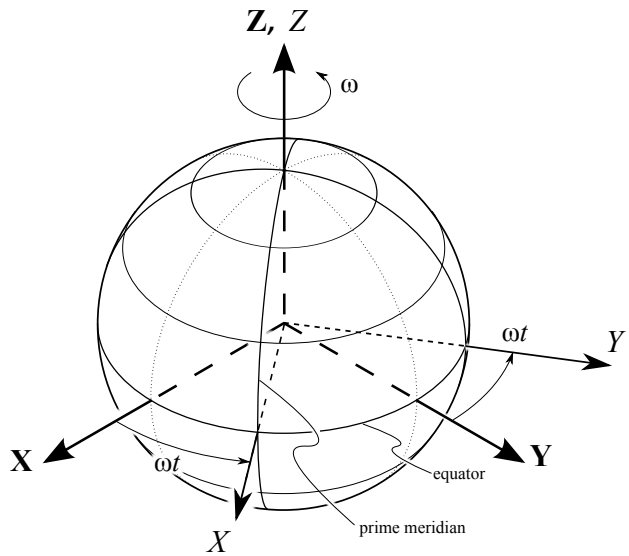

Figure 15. Rotation from ECI Frame to ECEF Frame

however, coordinates are often necessarily expressed in geodetic latitude, longitude and altitude coordinates, where altitude is normally relative to "sea level." Converting from ECEF spherical geocentric coordinates to geodetic coordinates is a bit more involved due to dealing with the WGS-84 reference ellipsoid. An exact solution exists to convert from geodetic to geocentric (and is given in Section B.2.3 above), but the exact closed-form solution for the geocentric to geodetic conversion problem involves solving a fourth-order polynomial. Simplified methods for dealing with this conversion vary between simulation tools, but involve either an iterative solution or a one- or two-pass approximation method. Refer to Section B.2.3 for more information.

The actual shape of the "sea-level" zero altitude reference is a further complication involving considerable calculations to arrive at a useful approximate, undulating geoid surface. Many atmospheric flight simulation tools treat the WGS-84 reference ellipsoid as the zero-altitude reference, but this can introduce vertical navigation errors on the order of hundreds of feet.

Another coordinate system often used is a local reference coordinates (LRC) frame whose orientation can be fixed at a location on the Earth, for example a runway. In this case, the origin of the runway coordinate system is usually located at the runway threshold with the x_{rwy} axis aligned with the centerline and pointed down the runway, the y_{rwy} axis to the right of centerline, and either an h_{rwy} axis pointing up or a z_{rwy} axis pointing into the ground. Another example of an LRC frame has its origin directly beneath the vehicle on the surface of the Earth and is oriented north, east and down (the NED frame). The vehicle's attitude is often expressed relative to this NED frame. Many other LRC orientations are possible and, aside from the runway and NED frames, will require full specification when models are shared.

The final common coordinate system, for both aircraft and spacecraft, is the body-axis system. In flight dynamics applications, the common convention is for the x-axis to point forward along the body of the vehicle, the z-axis to point down, and the y-axis completing the right-hand rule out the right side of the vehicle. For most aircraft, this is straightforward and vehicle subsystem models (aerodynamics, inertial properties, landing gear, propulsion systems) are defined in these body axes. Often, however, geometric

properties such as location of the CM, landing gear, and other vehicle geometries are defined in a vehicle reference system, used for mechanical layout, in which the x and z axes are reversed in direction and with an origin located off the vehicle (typically a point forward and below) but in the plane of symmetry (if one exists).

Aerodynamic models have a number of coordinate systems for measuring reaction forces and moments, stability, and other quantities; they are beyond the scope of this study as the conventional body axis has been used almost exclusively for these vehicle models.

B.4 Gravitation models

This section describes four types of gravitational models commonly used in aircraft and space vehicle simulations representing increasing fidelity in modeling the value of gravitation as a function of ECEF position.

In this report, we keep the same distinction as the WGS-84 document (reference [7]) where "gravitation" refers to the attraction (force per unit mass) between the vehicle and the Earth (and Sun and Moon, in orbital check-cases involving these effects); "gravity" is the net acceleration involving Earth's gravitation, summed with centrifugal acceleration due to rotation of the Earth, that yields the familiar, at rest, sea-level accelerations on the order of 32.2 ft/s^2 or 9.81 m/s^2.

B.4.1 Constant gravity

For the simplest gravity model (which combines gravitation and centrifugal accelerations), the standard unit of acceleration due to gravity at the Earth's surface ($\mathbf{g}$) is defined in SI units (9.80665 m/s^2); the English truncated approximation often cited is 32.174 ft/s^2. These values should be used as a constant where indicated.

B.4.2 Inverse square gravitation

The simplest gravitation model which could be considered for the propagation of a space vehicle is the model first proposed by Sir Isaac Newton in which the attractive force on each of two masses is given by

$$\begin{aligned}\vec{F}_1 &= \frac{G m_1 m_2 \left(\vec{R}_2 - \vec{R}_1\right)}{|\vec{R}_2 - \vec{R}_1|^3} \\ \vec{F}_2 &= \frac{G m_1 m_2 \left(\vec{R}_1 - \vec{R}_2\right)}{|\vec{R}_2 - \vec{R}_1|^3}\end{aligned} \tag{16}$$

where $\vec{R}_1$ and $\vec{R}_2$ are the positions of each of two point masses m_1 and m_2 respectively and G is the universal gravitational constant.

The force is directed so as to represent an equal and opposite attraction between the point masses, and its magnitude is proportional to the product of the masses divided by the square of the distance, hence the "inverse square" nomenclature.

In a two-mass system, it is possible to solve equation 16 exactly yielding the familiar Keplerian solutions. The differential equations

$$\ddot{\vec{R}}_1 = \frac{Gm_2\left(\vec{R}_2 - \vec{R}_1\right)}{|\vec{R}_2 - \vec{R}_1|^3}$$
$$\ddot{\vec{R}}_2 = \frac{Gm_1\left(\vec{R}_1 - \vec{R}_2\right)}{|\vec{R}_2 - \vec{R}_1|^3} \tag{17}$$

can be further simplified to the central force problem described by

$$\ddot{\vec{R}} = -\mu\frac{\vec{R}}{|\vec{R}|^3} \tag{18}$$

where $\vec{R}$ represents the position of m_2 with respect to their common center of mass, and $\mu = G\frac{m_1^3}{(m_1+m_2)^2}$. For the purposes of simulating a vehicle m_2 in the gravitational well of a planet m_1, the simplification $m_1 >>> m_2$ gives

$$\mu = Gm_1 \tag{19}$$

B.4.3 Spherical harmonic gravitation

The inverse-square gravitation model relies on the fact that the Earth is nearly spherical and assumes it is of constant density, and thus its gravitational potential is approximately the same as if the entire mass of the Earth were concentrated at its center. The mathematics of spherical harmonic expansions provides a convenient model for the gravitational potential of the Earth with its flattening at the poles and other non-spherical irregularities and, for higher-order models, captures localized differences in the Earth's density.

Gravitational fields are typically developed and expressed in spherical[2] coordinates.

The coordinate frames in which the fields are developed are typically planet-fixed, that is, fixed with respect to the planetary body and, therefore, are generally non-inertial.

The basic formulation of the spherical harmonic expansion of a potential function is given in references [10, 11]:

$$U(r,\lambda,\phi) = \frac{\mu}{r}\sum_{n=0}^{\infty}\sum_{m=0}^{n}\left(\frac{R}{r}\right)^n \bar{P}_{n,m}(sin\phi)(\bar{C}_{n,m}\cos m\lambda + \bar{S}_{n,m}\sin m\lambda) \tag{20}$$

where (r,λ,ϕ) are the geocentric coordinates radius, longitude, and latitude (Figure 13), μ is the gravitational parameter ($\mu = GM$); n and m are model degree and order; R is the mean equatorial radius of the gravitational body; $\bar{P}_{n,m}$ is the fully normalized associated Legendre function of degree n and order m; and $\bar{C}_{n,m}$ and $\bar{S}_{n,m}$ are fully normalized unit-less gravitation coefficients that are related to the mass distribution of the body [10, 12]. The overhead bar denotes a coefficient that is fully normalized using the relationship

$$\left\{\begin{array}{c}\bar{C}_{n,m}\\ \bar{S}_{n,m}\end{array}\right\} = \sqrt{\frac{(n+m)!}{(2-\delta_{0m})(2n+1)(n-m)!}}\left\{\begin{array}{c}C_{n,m}\\ S_{n,m}\end{array}\right\} \tag{21}$$

[2]Here the term *spherical* means coordinates based on a spherical body as opposed to an oblate elliptical body (i.e., geocentric vs. geodetic coordinates).

where $\delta_{0m} = 1$ when $m = 0$, and $\delta_{0m} = 0$ when $m \neq 0$.

The zero-degree term (C_{00}) represents the spherical surface upon which the higher degree terms are imposed. It is unity by definition ($C_{00} = 1$). All $\bar{S}_{n,m}$ terms vanish for $m = 0$ because the sine term in equation 20 vanishes when $m = 0$. It can be shown [10,13] that the location of the CM $(\bar{x}, \bar{y}, \bar{z})$ of the gravitational body is related to the un-normalized first-degree coefficients by

$$\begin{aligned} \bar{x} &= RC_{1,1} \\ \bar{y} &= RS_{1,1} \\ \bar{z} &= RC_{1,0} \end{aligned} \tag{22}$$

The normal practice is to define the spherical coordinate system such that the origin is located at the CM. Therefore, the first-degree terms C_{10}, C_{11}, and S_{11} all equal zero. With these definitions of the zero-degree and first-degree terms, the spherical harmonic potential model becomes

$$U(r, \lambda, \phi) = \frac{\mu}{r}\left[1 + \sum_{n=2}^{\infty}\sum_{m=0}^{n}\left(\frac{R}{r}\right)^n \bar{P}_{n,m}(sin\phi)(\bar{C}_{n,m}\cos m\lambda + \bar{S}_{n,m}\sin m\lambda)\right] \tag{23}$$

An important special case of the spherical harmonic gravitation model is the J_2 simplification. The coefficient $\bar{C}_{2,0}$ reflects the oblateness of the Earth and dominates the higher order terms. Many simulations only need the accuracy provided by these first two terms of the spherical harmonic expansion, and such implementations are often called the J_2 gravitation model. The name arises from the equivalence between the un-normalized $C_{2,0}$ and the previous historical harmonic parameter $J_2 = -C_{2,0}$.

With this substitution, equation 23 reduces to

$$U(r, \phi) = \frac{\mu}{r}\left[1 - \frac{J_2}{2}\left(3\sin^2\phi - 1\right)\right] \tag{24}$$

which shows that the gravitation potential varies only with latitude and radius from the Earth's center when using only the first non-zero harmonic term for an oblate spheroid.

B.4.4 Gravitational effects on the vehicle

The effect of gravitation has an important effect on any motion through the known universe. Given a gravitational potential function U, such as equation 23 for an ellipsoidal Earth, the corresponding gravitational acceleration field can be viewed as the gradient of U. In general, we write the equation for the gravitational acceleration $\vec{A}$ as

$$\vec{A} = \nabla U(\vec{R}) \tag{25}$$

Translational effects – inverse-square For the inverse-square approximation, calculating the gravitational acceleration components in the ECI frame is straightforward because we can write U simply in terms of the x, y, and z components of the inertial position $\vec{R}$ and arrive at the gravitational potential function for the inverse-square law model:

$$U(\mathsf{x}, \mathsf{y}, \mathsf{z}) = \frac{\mu}{\sqrt{\mathsf{x}^2 + \mathsf{y}^2 + \mathsf{z}^2}} \tag{26}$$

Differentiating equation 26 gives acceleration for the inverse-square gravitation approximation:

$$\vec{A} = \begin{pmatrix} \ddot{\mathsf{x}} \\ \ddot{\mathsf{y}} \\ \ddot{\mathsf{z}} \end{pmatrix} = \frac{-\mu}{(\mathsf{x}^2+\mathsf{y}^2+\mathsf{z}^2)^{\frac{3}{2}}} \begin{pmatrix} \mathsf{x} \\ \mathsf{y} \\ \mathsf{z} \end{pmatrix} \tag{27}$$

Translational effects – J_2 model Since most simulation tools perform integration in a rectangular inertial frame, equation 23 can transformed from geocentric spherical to rectangular ECI coordinates using the following conversions (similar to equations 11):

$$\begin{aligned} r &= \sqrt{(\mathsf{x}^2+\mathsf{y}^2+\mathsf{z}^2)} \\ \phi &= \sin^{-1}(\frac{\mathsf{z}}{r}) \end{aligned} \tag{28}$$

By substituting equations 28 into equation 24 and taking the derivatives of U with respect to x, y, and z (as in reference [14]) we obtain the scalar accelerations in the ECI frame:

$$\ddot{\mathsf{x}} = -\mu\frac{\mathsf{x}}{r^3}\left[1 - \frac{3J_2{r_e}^2(5\mathsf{z}^2 - r^2)}{2r^4}\right] \tag{29}$$

$$\ddot{\mathsf{y}} = -\mu\frac{\mathsf{y}}{r^3}\left[1 - \frac{3J_2{r_e}^2(5\mathsf{z}^2 - r^2)}{2r^4}\right] \tag{30}$$

$$\ddot{\mathsf{z}} = -\mu\frac{\mathsf{z}}{r^3}\left[1 - \frac{3J_2{r_e}^2(5\mathsf{z}^2 - 3r^2)}{2r^4}\right] \tag{31}$$

where r_e is the equatorial radius of the reference WGS-84 ellipsoid.

Note that when state propagation is performed in the ECI (or other inertial) frame, the centrifugal acceleration contribution to Earth's rotation is not explicitly included.

Translational effects – higher-order harmonics There is significantly more complexity required to compute the gradient of the harmonic version of the potential defined by equation 20. Since the potential is defined in terms of planet-fixed coordinates, and the derivatives must be taken with respect to inertial Cartesian coordinates, it is essential to have ready access to the time varying transformation $\mathbf{M}$ defined in equation 15. We can write the equation for inertial translational acceleration as

$$\vec{A} = \mathbf{M}^T \frac{\partial U}{\partial \vec{R}_{\text{pfixed}}}(\mathbf{M}\vec{R}_{\text{inertial}}) \tag{32}$$

and similarly,

$$\mathbf{H}_{\text{inertial}} = \mathbf{M}^T\mathbf{H}_{\text{pfixed}}\mathbf{M} \tag{33}$$

where $\vec{R}_{\text{pfixed}}$ is the Cartesian planet-fixed position, $\vec{R}_{\text{inertial}}$ is the inertial Cartesian position, H_{inertial} is the matrix of second derivatives of U with respect to inertial Cartesian coordinates and $\mathbf{H}_{\text{pfixed}}$ is the matrix of second derivatives of U computed with respect to Earth-fixed Cartesian coordinates.

Rotational effects of gravitation. The other important effect of gravity on orbiting vehicles is the torque exerted by the gravity gradient, which can be computed from $\mathbf{H}_{\text{inertial}}$ as defined in equation 33. This effect is usually omitted from atmospheric flight simulations but is important for orbital flight simulation. Orbital flight simulations are generally performed with higher-order harmonic models, so only that gravitational potential is considered here.

It is convenient to use the inertia tensor I as defined in equations 3 and 4 and a gradient approximation for gravity near the vehicle to provide an accurate estimate of torque due to gravity gradient.

Note that the inertia tensor is commonly expressed in the body-fixed frame, and we often wish to express torque in the body frame. To this end, we transform the gravity gradient matrix from the inertial frame to spacecraft body-fixed coordinates using a similarity transformation

$$\mathbf{G} = \mathbf{B}\mathbf{H}_{\text{inertial}}\mathbf{B}^T \tag{34}$$

where $\mathbf{B}$ is the inertial to body-fixed transformation matrix.

The gravitational torque acting on the spacecraft can then be expressed as

$$\vec{\tau} = \int \vec{\rho} \times \mathbf{G}\vec{\rho} dm \tag{35}$$

where the vector $\vec{\rho}$ is defined as in equation 5. The torque can be expressed in terms of elements of $\mathbf{I}$ and $\mathbf{G}$ as

$$\vec{\tau} = \begin{pmatrix} G_{2,3}(I_{zz} - I_{yy}) - G_{1,3}I_{xy} + G_{1,2}I_{xz} - I_{yz}(G_{3,3} - G_{2,2}) \\ G_{1,3}(I_{xx} - I_{zz}) + G_{2,3}I_{xy} - G_{1,2}I_{yz} - I_{xz}(G_{1,1} - G_{3,3}) \\ G_{1,2}(I_{yy} - I_{xx}) - G_{2,3}I_{xz} + G_{1,3}I_{yz} - I_{xy}(G_{2,2} - G_{1,1}) \end{pmatrix} \tag{36}$$

B.5 Atmosphere models

B.5.1 U.S. Standard Atmosphere 1976 Model

The U.S. Standard Atmosphere 1976 model [6] is used for the majority of the atmospheric check-case scenarios. This model can be implemented as linear interpolation of the 1D tables printed in the source document with ambient pressure, temperature and density as a function of either geometric altitude (h) or geopotential height (Z). A more accurate implementation is to realize, in software, the non-linear numerical equations from [6] used to generate the tables found in the report.

B.5.2 Marshall Engineering Thermosphere Model (MET)

The Marshall Engineering Thermosphere (MET) model is an empirical model whose coefficients were obtained from satellite drag analyses. It is a static diffusion model and is essentially the Smithsonian's Jacchia 1970 model (ref [15]) with two additions from the Jacchia 1971 model (ref [16]). In addition to thermospheric densities and temperatures, the well-documented code provides several often-used parameters like gravitational acceleration and specific heat. MET was developed at NASA's Marshall Space Flight Center (MSFC) in Huntsville primarily for engineering applications of low Earth orbiting spacecraft.

The MET model was developed to represent, in so far as practical for engineering applications, the variability of the ambient mass density at orbital altitudes. It is the standard neutral atmospheric density model used for control and lifetime studies involving all orbiting spacecraft projects.

Inputs to the model are time (year, month, day, hour, and minute), position (altitude and geographic latitude and longitude), the previous day's solar radio flux ($F_{10.7}$), the centered solar radio flux averaged over 6 solar rotations ($\bar{F}_{10.7}$) and the a_p index at 6 to 7 hours before the time in question (for some studies the daily planetary geomagnetic index, a_p, may be used instead of the 3–hourly a_p value).

With these inputs the exospheric temperature can be calculated. It should be stressed that in the original development of the model, the prime objective was to model the total neutral density of the thermosphere by adjusting temperature profiles until agreement between modeled and measured total densities was achieved. Thus, agreement between modeled and measured temperature is not always achieved. Thomson–scatter temperature measurements generally show that the temperature lags the density by a couple of hours, whereas in the MET model the temperature and density are in phase.

With the exospheric temperature specified, the temperature can be calculated for any altitude between the lower boundary (90 km) and the upper level (2500 km) of the model from an empirically determined temperature profile. The density for all points on the globe at 90 km altitude is assumed constant, and mixing prevails to 105 km. Between these two altitudes, the mean molecular mass varies as a result of the dissociation of molecular to atomic oxygen. At 120 km altitude, the ratio of atomic-to-molecular oxygen is assumed to be 1.5. Density between 90 and 105 km is calculated by integration of the barometric equation. For altitudes above 105 km the diffusion equation for each of the individual species (O_2, O, N_2, He and Ar) is integrated upwards from the 105-km level. For hydrogen, the integration of the diffusion equation proceeds upwards from 500 km altitude. The total mass density is calculated by summing the individual specie mass densities.

The total density is then further modified by the effects of the seasonal–latitudinal density variation of the lower thermosphere below 170 km altitude and seasonal–latitudinal variations of helium above 500 km. These two effects have been incorporated in the MET model using equations developed by Jacchia for his 1971 thermospheric model.

The final output of the MET model is total mass density, temperature, pressure, individual specie number densities, mean molecular weight, scale–height, specific heats, and the local gravitational acceleration.

The total mass density, the temperature, and the individual species all have the same phase variation in the MET model (i.e., they all maximize at the same local time). For some studies involving the effects of various species on an orbiting spacecraft, it may be required to use the MSIS (Mass Spectrometer Incoherent Scatter) model [17] if accurate phases of the various species are required.

In this study, several variants of the MET model were used (MET95, MET98, and MET07).

The models are described in references *NASA Marshall Engineering Thermosphere Model* [18], *An Improvement in the Numerical Integration Procedure used in the NASA Marshall Engineering Thermosphere Model* [19], and *NASA Marshall Engineering Thermosphere Model – Version 2.0* [20]. Availability of these models vary, but can be requested from the Natural Environments Branch (EV44) at NASA Marshall Space Flight Center.

B.6 Simulation Tools Description

A brief description of the participating simulation tools is given in this section.

B.6.1 JEOD/Trick (JSC)

The Johnson Space Center (JSC) Engineering Orbital Dynamics (JEOD) is a suite of models needed to propagate the 6-DOF states of one or more rigid vehicles in the orbital or interplanetary environment.

The software models vehicle dynamics, environment, and interactions and provides necessary math and software utilities to work with a simulation engine. "Trick" is a generic simulation tool which provides the infrastructure to define, initialize, and run the simulation model and log and display its output. JEOD and Trick leverage a common history, which enables an integrated simulation framework for orbital vehicles.

JEOD was employed for the orbital check-cases; it used a Runge-Kutta fourth-order integration method with a 1.0-sec time step. Dynamic Aerospace Vehicle Exchange Markup Language (DAVE-ML) models were translated into source code by hand.

B.6.2 LaSRS++ (LaRC)

The Langley Standard Real-Time Simulation in C++ (LaSRS++) is an object-oriented framework for construction of aerospace vehicle simulations [21]. LaSRS++ simulations support desktop analysis, hardware-in-the-loop simulations, and high-fidelity, human-in-the-loop simulators. Projects using LaSRS++ have modeled commercial transport aircraft, military fighters, advanced concept aircraft, launch vehicles, planetary landers, crewed spacecraft, planetary aircraft, and unmanned aerial vehicles.

DAVE-ML models of the F-16 and two-stage rocket were interrogated at run-time using a customized library developed at LaRC. The simpler models (ISS, brick, and spheroids) were built in C++ by hand.

LaSRS++ was employed for both the atmospheric and orbital check-cases. For all cases, the integration methods used were the same, but were customized depending upon which state was being propagated, as given in Table 20.

Frame rates varied depending on the check-case, as given in Table 21. Frame rates were selected to minimize integration error differences with other simulations using Runge-Kutta integration methods. (LaSRS++ simulations are normally operated with frame rates of 100 Hz or less.)

Table 20. Integration Method for LaSRS++ Check-case Implementations

States	Method
Translational velocity	Second-order Adams-Bashforth
Position	Second-order Taylor series
Angular velocity	Second-order Adams-Bashforth
Quaternion Attitude	Local linearization algorithm [22]

Table 21. Frame-rates Used in LaSRS++ Check-case Implementations

Check-case	Frame-rate (1/s)
Atmospheric Cases 1 – 10	500
Atmospheric Cases 11, 13 – 16	100
Atmospheric Case 12	200[a]
Atmospheric Case 17	1,000[b]
Orbital Cases 2 – 6B	500
Orbital Case 6C	10,000[c]
Orbital Case 6D	40,000[c]
Orbital Case 7A – 8B	500
Orbital Case 9A – 9D	2,000[c]
Orbital Case 10A – Full	500

[a] supersonic vehicle dynamics not stable at 100 Hz
[b] better matches POST II timing of engine cutoff
[c] higher frame-rate better handles square pulse inputs

B.6.3 MAVERIC (MSFC)

Marshall Aerospace Vehicle Representation in C (MAVERIC) is a low- to high-fidelity 3-DOF/6-DOF vehicle flight simulation program developed at MSFC, written primarily in the C and C++ programming languages. MAVERIC was designed to be generic and data-driven and can provide for the rapid development of an end-to-end vehicle flight simulation which starts at launch and ends at "wheel stop" after landing (or splashdown). The vehicle simulation models are layered upon a set of foundational software called TFrames. TFrames is a time-based differential equation solver environment and is public-domain software. TFrames provides an environment for developing a dynamic simulation that insulates the simulation developer from the tedious programming details associated with numerical integration, discrete data sampling, table look-ups, etc. High-level routines provide convenient interfaces between the simulation code and the numerical integration engine.

MAVERIC was used to exercise some but not all of the atmospheric and orbital check-cases; it used a Runge-Kutta fourth-order integration method with a 0.1-sec time step. DAVE-ML models were translated into source code by hand.

B.6.4 POST II (LaRC)

The Program to Optimize Simulated Trajectories II (POST II) is a generalized point mass, discrete parameter targeting, and optimization program. POST II provides the capability to target and optimize point mass trajectories for multiple powered or un-powered vehicles near an arbitrary rotating, oblate planet. POST II has been used successfully to solve a wide variety of atmospheric ascent and reentry problems, as well as exo-atmospheric orbital transfer problems. The generality of the program is evidenced by its multiple phase simulation capability which features generalized planet and vehicle models. This flexible simulation capability is augmented by an efficient discrete parameter optimization capability that includes equality and inequality constraints.

POST II increases the trajectory simulation capability of the original POST computer code and provides a state-of-the-art software tool. POST II contains many basic models (such as atmosphere, gravity, propulsion, and navigation system models) that are used to simulate a wide variety of launch, orbital, and entry missions.

As indicated above, POST II can support multiple vehicles in a single simulation, each with independently defined environments, vehicle, and attracting body characteristics. Thus, each vehicle can have its own GNC system for completely independent, on-board autonomy. Conversely, effects of multi-body and interaction forces that depend on the relationship of one vehicle to another can be included.

Additionally, POST II can support 3-DOF and 6-DOF trajectories within the same simulation; not only can each vehicle trajectory support different DOFs, but also each trajectory segment within a given simulation can be either 3-DOF or 6-DOF.

POST II was employed against most of the atmospheric and orbital check-cases; it used a Runge-Kutta fourth-order integration method for all of the cases but the frame-rate varied depending on the case as shown in Table 22

The DAVE-ML models were translated into source code by hand except for the F-16 GNC models, which were interrogated at run-time using a customized library developed at LaRC.

Table 22. Frame-rates Used in POST II Check-case Implementations

Check-case	Frame-rate (1/s)
Atmospheric Cases	100
Orbital Cases 2 – 6B, 7	10
Orbital Case 6C & 6D	10[a]
Orbital Case 8 – FULL	20

[a] 1,000 Hz during thruster burns

B.6.5 VMSRTE (ARC)

The Vertical Motion Simulator Real-Time Environment (VMSRTE) provides a flexible environment for man-machine research, capable of rapid prototyping and run-time reconfiguration of vehicle models, simulator hardware, and the surrounding laboratory, combined with efficient operation and data collection. It offers source-level debugging and the ability to alter simulation and facility variables during program execution. A standardized framework streamlines simulation development by providing elements that are common to most simulations. A wide variety of vehicles have been simulated on the Vertical Motion Simulaton (VMS) including rotorcraft, Vertical and/or Short Take-off and Landing (V/STOL) and conventional aircraft, spacecraft, and airships. Research topics have also spanned a wide range, including handling qualities, guidance and display development, flight control design, concept demonstration and evaluation, human-factors, and simulation fidelity requirements.

VMSRTE was employed for some of the atmospheric check-cases; it used an Adams-Bashforth second-order integration method [23] with a 0.01-sec time step. DAVE-ML models were translated into an Ames-unique function table processor input deck and FORTRAN code snippets for access using a customized Perl script.

B.6.6 Core (AFRC)

All current simulations at NASA Armstrong Flight Research Center (AFRC) are based on a common software framework, called "Core." Core is used for aircraft simulations ranging from gliders to suborbital vehicles and runs on platforms ranging from laptop computers to pilot-in-the-loop / aircraft-in-the-loop simulators. Core is composed of standard models, mathematical routines, a user interface, hardware interfaces, timing routines, data recording and data input subsystems, external application interfaces, and other sharable

modules. Core is predominately written in the C++ computer programming language but supports legacy FORTRAN models. Currently the simulators located at AFRC are used for engineering analysis more than for pilot training. Typical simulation tasks include evaluation of new vehicle concepts, control law development and validation, flight safety analysis, mission planning, flight envelope expansion, and post-flight data analysis.

Core was employed for some of the atmospheric check-cases; it used a Runge-Kutta fourth-order integration method with a 0.01-sec time step. DAVE-ML models were interpreted at run-time by use of the Janus [24] software library.

B.6.7 JSBSim (Open source)

JSBSim is an open source, high fidelity, flight dynamics and control software library written almost entirely in C++ in a collaborative, volunteer effort by a small team of developers. It has been in development since 1997 and has been incorporated into several larger simulation applications, including the FlightGear open source flight simulator, Outerra, and OpenEaagles, and has been used by engineers for studies at major aerospace organizations. It can be built and run both as an integral part of a larger simulation framework and as a stand-alone batch program on several platforms (Microsoft Windows, Apple Macintosh, Linux, Unix, etc.). JSBSim provides models of general classes of objects such as aerodynamic models, flight control system components, engines, mass properties, and so on, with vehicle-specific characteristics read from a set of configuration files in an XML format. Vehicles that have been modeled within JSBSim encompass the range from a simple ball to gliders, unmanned aerial vehicles, airships, airliners, launch vehicles, all the way to an orbital spacecraft with an extensive aerodynamic database, rocket propulsion systems, and guidance and control laws.

JSBSim was exercised for the atmospheric check-cases; it used a “higher-order” Adams-Bashforth integration method at 120 frames per simulated second.

The DAVE-ML files were converted into the JSBSim XML input format by hand.

C Check-case scenario descriptions

The check-case scenarios examined in this assessment are given in tables presented in Volume I and reproduced here. Atmospheric check-case 14 was not completed due to resource constraints.

C.1 Atmospheric scenarios

For atmospheric flight, a set of scenarios with increasingly complex models and initial conditions was agreed upon, as shown in Table 23. These models ranged from the obligatory dropped cannonball to a two-stage rocket launch.

Tables 25 through 44 show the initial conditions for each of the atmospheric check-cases.

In general, a 6-DOF simulation tool operated by iteratively using instantaneous flight conditions such as Mach number, angles-of-attack and sideslip, and control surface deflections (if any) to perform linear function interpolations of multidimensional aerodynamic coefficient data tables. These interpolated data typically consist of non-dimensional force and moment coefficients acting at or about some fixed reference point in the body-axis coordinate frame. These aerodynamic forces and moments were then scaled to full value, added to any propulsive forces and moments, and transferred to the current CM. The resulting linear and angular

Table 23. Atmospheric Check-case Scenarios

Number	Name	Verifies	Gravitation	Geodesy	Atmosphere	Winds
1	Dropped sphere with no drag	Gravitation, translational EOM	J_2	WGS-84	1976	N.A.
2	Tumbling brick with no damping, no drag	Rotational EOM	J_2	WGS-84	1976	N.A.
3	Tumbling brick with dynamic damping, no drag	Inertial coupling	J_2	WGS-84	1976	none
4	Dropped sphere with constant C_D, no wind	Gravitation, integration	$1/R^2$	Round fixed	1976	still air
5	Dropped sphere with constant C_D, no wind	Earth rotation	$1/R^2$	Round rotating	1976	still air
6	Dropped sphere with constant C_D, no wind	Ellipsoidal Earth	J_2	WGS-84	1976	still air
7	Dropped sphere with constant C_D + wind	Wind effects	J_2	WGS-84	1976	steady wind
8	Dropped sphere with constant C_D + wind shear	2D wind	J_2	WGS-84	1976	$f(h)$
9	Sphere launched eastward along Equator	Translational EOM	J_2	WGS-84	1976	still air
10	Sphere launched northward along Prime Meridian	Coriolis	J_2	WGS-84	1976	still air
11	Subsonic F-16 trimmed flight across planet	Atmosphere, air-data calculations	J_2	WGS-84	1976	still air
12	Supersonic F-16 trimmed flight across planet	Supersonic air-data calculations	J_2	WGS-84	1976	still air
13	Subsonic F-16 maneuvering flight	Multidimensional table look-up	J_2	WGS-84	1976	still air
14	Supersonic F-16 maneuvering flight (not completed)	Mach effects in tables	J_2	WGS-84	1976	still air
15	Circular F-16 flight around North pole	Propagation, geodetic transforms	J_2	WGS-84	1976	still air
16	Circular F-16 flight around Equator/dateline intersection	Sign changes in lat. & long.	J_2	WGS-84	1976	still air
17	Two-stage rocket to orbit	Staging, entire atmosphere	J_2	WGS-84	1976	$f(h)$

Table 24. Exo-atmospheric Check-case Scenarios

Number	Name	Verifies	Gravitation	Atmosphere	3rd body pert.	Body
1	Earth Modeling Parameters	Environmental constants	$1/R^2$	MET	none	ISS
2	Keplerian Propagation	Integration, RNP, orientation	$1/R^2$	MET	none	ISS
3A	Gravitation Modeling: 4×4	4×4 harmonic gravitation model	4×4	MET	none	ISS
3B	Gravitation Modeling: 8×8	8×8 harmonic gravitation model	8×8	MET	none	ISS
4	Planetary Ephemeris	Third body gravitational forces	$1/R^2$	MET	sun, moon	ISS
5A	Min. Solar Activity	Free molecular flow	$1/R^2$	MET	none	ISS
5B	Mean Solar Activity	Free molecular flow	$1/R^2$	MET	none	ISS
5C	Max. Solar Activity	Free molecular flow	$1/R^2$	MET	none	ISS
6A	Const Density Drag	Response to constant force	$1/R^2$	const	none	sphere
6B	Aero Drag with Dyn. Atmos.	Response to dynamic drag	$1/R^2$	MET	none	sphere
6C	Plane Change Maneuver	Response to propulsion firing	$1/R^2$	MET	none	cylinder
6D	Earth Departure Maneuver	Response to propulsion firing	$1/R^2$	MET	none	cylinder
7A	4×4 Gravitation	Translation response	4×4	MET	sun, moon	sphere
7B	8×8 Gravitation	Translation response	8×8	MET	sun, moon	sphere
7C	All Models with 4×4 Gravitation	Translation response	4×4	MET	sun, moon	sphere
7D	All Models with 8×8 Gravitation	Translation response	8×8	MET	sun, moon	sphere
8A	Zero Initial Attitude Rate	Integration methods for rotation	$1/R^2$	MET	none	ISS
8B	Non-Zero Initial Attitude Rate	Integration methods for rotation	$1/R^2$	MET	none	ISS
9A	Zero Initial Rate w/ Torque	Rotational response	$1/R^2$	MET	none	ISS
9B	Non-Zero Initial Rate w/ Torque	Rotational response	$1/R^2$	MET	none	ISS
9C	Zero Initial Rate w/ $T + F$	Rotational response	$1/R^2$	MET	none	ISS
9D	Non-Zero Initial Rate w/ $T + F$	Rotational response	$1/R^2$	MET	none	ISS
10A	Zero Initial Attitude Rate	Gravity gradient modeling	$1/R^2$	MET	none	cylinder
10B	Non-Zero Initial Rate	Gravity gradient modeling	$1/R^2$	MET	none	cylinder
10C	Zero Initial Rate; Elliptical Orbit	Gravity gradient modeling	$1/R^2$	MET	none	cylinder
10D	Non-Zero Initial Rate; Ellip. Orbit	Gravity gradient modeling	$1/R^2$	MET	none	cylinder
FULL	Integrated 6-DOF Orbital Motion	Combined effects response	8×8	MET	sun, moon	ISS

accelerations were then determined by inverting the current mass tensor. These accelerations, expressed in the body axes, were (usually) rotated into the inertial (ECI) reference system, gravitation was added, and the resulting six accelerations (three linear, three angular) were integrated twice to obtain rates/velocities and attitudes/positions in inertial space. These values were then transformed back into ECEF positions to calculate Earth-relative body-axis velocities, angles-of-attack and sideslip, velocity with respect to the atmosphere (for Mach number and dynamic pressure), and often the position of the vehicle relative to other Earth-fixed locations, e.g. a runway or launch site.

Key parameters that were compared in the resulting solutions were aerodynamic linear and angular forces and moments, velocity in local (NED) and inertial frames, angular body-axis rates relative to the local frame, vehicle center-of-mass position in geodetic spherical, ECEF rectangular, and inertial rectangular coordinates, vehicle attitude relative to the local frame (Euler angles), local gravity, atmospheric properties (density, ambient temperatures and pressures and speed of sound), climb rate, Mach number, dynamic pressure, and true airspeed (when recorded). These comparison plots can be found in Appendix D.1.

The specific scenarios for each of the atmospheric check-cases are described below, along with a table giving both initial state values and problem assumptions, including the vehicle being simulated, geodetic Earth model, atmosphere model, and gravitational model to be used.

Position is the initial position of the CM of the vehicle in geodetic (Earth-centered, Earth-fixed) latitude, longitude and height above the reference ellipsoid or sphere. Units are deg / deg / ft above reference ellipsoid or sphere.

Velocity is the initial Earth-relative velocity, given in local (NED) axes in ft/s, in the order x-y-z.

Attitude is the initial vehicle orientation, given in spherical Euler angles with a 3-2-1 rotation (yaw, pitch, roll) from the geodetic NED axes; they are listed in reverse order to match convention: roll angle, pitch angle, and yaw angle in degrees.

Rate is initial rotation rate presented in body-axis quantities relative to the inertial frame in order of roll, pitch and yaw rates in deg/s.

The duration of each scenario is also specified. Each simulation provider was encouraged to provide data at their chosen frame-rate and to include key atmospheric and aerodynamic parameters, as well as both Earth-fixed (geodetic) and inertial states (if applicable).

C.1.1 Check-case 1 – dragless sphere

The initial atmospheric check-case scenario called for the smaller spheroid (described in Section B.1.1) to be dropped from an initial position located 30,000 ft over the Equator/Prime Meridian intersection. As specified in Table 25, its initial linear velocity should have matched the Earth's eastward rotation rate at that altitude so that it was initially motionless (in a linear sense) with respect to the still atmosphere; however, it should have had zero inertial rotation; thus it had a small residual rotation relative to the Earth below and the atmosphere surrounding it.

The sphere's orientation was chosen such that the body x-axis was pointed north, the body z-axis was initially pointed down, with the body y-axis completing the orthogonal right-hand-rule by pointing east. Thus the vehicle would have had a small amount of 'roll rate' with respect to the rotating Earth.

The sphere is imagined to have no reaction with the atmosphere - no damping, and no drag; it will accelerate downward toward the ellipsoidal Earth in response to second-harmonic (J_2) gravitation as a function of its geometric height (described in Section B.4.3). This is achieved by setting the coefficient of drag (C_D) in Table 2 to zero for this scenario.

Table 25. Initial Conditions for Atmospheric Scenario 1

Scenario	1: Dragless sphere			
Vehicle	Dragless sphere			
Geodesy	WGS-84 rotating			
Atmosphere	US 1976 STD; no wind			
Gravitation	J_2		**Duration**	30 s
Initial states	**Position** (deg, deg, ft MSL)	**Velocity** ft/s	**Attitude** deg	**Rate** deg/s
Geodetic	[0, 0, 30000]			
Local-relative		[0, 0, 0]	[0, 0, 0]	
Body axes				[-0.004178073, 0, 0]
Notes	C_D set to zero			

C.1.2 Check-case 2 – dragless tumbling brick

The second atmospheric check-case scenario called for the brick 'vehicle' (described in Section B.1.3) to be dropped from the same initial position as as the sphere in atmospheric scenario 1 (30,000 ft over the Equator/Prime Meridian intersection). Its initial linear velocity should also have matched the Earth's eastward rotation rate at that altitude.

The brick's orientation was chosen such that the body x-axis (aligned with the longest dimension) was pointed north, the body z-axis (shortest dimension) was initially pointed down, with the body y-axis (medium dimension) completing the orthogonal right-hand-rule by pointing east.

The initial rotation rate of the brick about each axis, specified in Table 26, was such that the inertial rates were 10, 20, and 30 deg/s, respectively. Table 26 gives these rates relative to the rotating Earth, so a smaller value for 'roll rate' is specified.

The brick was imagined to have no reaction with the still atmosphere - no rotational damping, no lift, and no drag; it would accelerate downward toward the rotating ellipsoidal Earth in response to second-harmonic (J_2) gravitation as a function of its geometric height. This was achieved by setting all the aerodynamic coefficient values in Table 5 to zero for this scenario.

Table 26. Initial Conditions for Atmospheric Scenario 2

Scenario	2: Tumbling brick with no damping or drag			
Vehicle	Dragless rotating brick			
Geodesy	WGS-84 rotating			
Atmosphere	US 1976 STD; no wind			
Gravitation	J_2		**Duration**	30 s
Initial states	**Position** (deg, deg, ft MSL)	**Velocity** ft/s	**Attitude** deg	**Rate** deg/s
Geodetic Local-relative Body axes	[0, 0, 0]	[0, 0, 0]	[0, 0, 0]	[9.995821927, 20, 30]
Notes	C_{l_p}, C_{m_q}, C_{n_r} set to zero			

C.1.3 Check-case 3 – dragless tumbling brick with aerodynamic damping

This atmospheric scenario was a repeat of the previous one, except the brick's aerodynamic damping was turned on (still no lift, drag or sideforce was modeled).

The initial rotation rate should start to damp out as the velocity of the vehicle relative to the still atmosphere (airspeed) increased.

Table 27. Initial Conditions for Atmospheric Scenario 3

Scenario	3: Tumbling brick with damping but no drag			
Vehicle	Dragless rotating sphere with aero damping			
Geodesy	WGS-84 rotating			
Atmosphere	US 1976 STD; no wind			
Gravitation	J_2		**Duration**	30 s
Initial states	**Position** (deg, deg, ft MSL)	**Velocity** ft/s	**Attitude** deg	**Rate** deg/s
Geodetic Local-relative Body axes	[0, 0, 0]	[0, 0, 0]	[0, 0, 0]	[9.995821927, 20, 30]
Notes	C_D set to zero			

C.1.4 Check-case 4 – sphere dropping over non-rotating, spherical Earth

This scenario involved the sphere from atmospheric scenario 1 being dropped from the same altitude above the Earth. However, in this scenario, the sphere had drag (nominal value of C_D given in Table 2), was rotating about its body axes relative to the Earth at 10, 20, and 30 deg/s, respectively, and the Earth was modeled as a round, non-rotating, sphere. The gravitational model used should have been the inverse square

law given in Section B.4.2 rather than the J_2 harmonic gravity model used in the previous scenarios, as given in Table 28.

Table 28. Initial Conditions for Atmospheric Scenario 4

Scenario	4: Sphere with round non-rotating Earth			
Vehicle	Sphere with constant C_D			
Geodesy	Round non-rotating			
Atmosphere	US 1976 STD; no wind			
Gravitation	inverse square		**Duration**	30 s
Initial states	**Position** (deg, deg, ft MSL)	**Velocity** ft/s	**Attitude** deg	**Rate** deg/s
Geodetic	[0, 0, 30000]			
Local-relative		[0, 0, 0]	[0, 0, 0]	
Body axes				[10, 20, 30]

C.1.5 Check-case 5 – sphere dropping over rotating, spherical Earth

In this scenario, the same sphere with drag is dropped as in the previous scenario, but in this check-case, the round Earth was rotating. The spherical vehicle had the same initial rotation rate relative to inertial space, but with the Earth rotating, the Earth-relative rotation had the small bias in the roll axis, as given in Table 29.

Table 29. Initial Conditions for Atmospheric Scenario 5

Scenario	5: Sphere with round rotating Earth			
Vehicle	Sphere with constant C_D			
Geodesy	Round rotating			
Atmosphere	US 1976 STD; no wind			
Gravitation	inverse square		**Duration**	30 s
Initial states	**Position** (deg, deg, ft MSL)	**Velocity** ft/s	**Attitude** deg	**Rate** deg/s
Geodetic	[0, 0, 30000]			
Local-relative		[0, 0, 0]	[0, 0, 0]	
Body axes				[9.995821927, 20, 30]

C.1.6 Check-case 6 – sphere dropping over rotating, ellipsoidal Earth

This check-case (defined in Table 30) was a repeat of the first check-case ("Check-case 1 – dragless sphere" scenario), except the sphere in this case had a non-zero drag coefficient (given in Table 2).

Table 30. Initial Conditions for Atmospheric Scenario 6

Scenario	6: Sphere with ellipsoidal rotating Earth			
Vehicle	Sphere with constant C_D			
Geodesy	WGS-84 rotating			
Atmosphere	US 1976 STD; no wind			
Gravitation	J_2		**Duration**	30 s
Initial states	**Position** (deg, deg, ft MSL)	**Velocity** ft/s	**Attitude** deg	**Rate** deg/s
Geodetic	[0, 0, 30000]			
Local-relative		[0, 0, 0]	[0, 0, 0]	
Body axes				[-0.004178073, 0, 0]

C.1.7 Check-case 7 – sphere dropping through a steady wind field

This scenario (given in Table 31) was identical to the previous check-case except the addition of a constant 20 ft/s wind coming from the west, resulting in an additional eastward force on the sphere as it dropped. Aside from having a slight roll rate, the sphere had no initial motion with respect to the Earth's surface; thus at time $t = 0$ sec the sphere would encounter a sideways airspeed component due to the atmosphere moving eastward at a constant linear rate.

Table 31. Initial Conditions for Atmospheric Scenario 7

Scenario	7: Sphere with steady wind			
Vehicle	Sphere with constant C_D			
Geodesy	WGS-84 rotating			
Atmosphere	US 1976 STD; steady 20 ft/s wind from due west			
Gravitation	J_2		**Duration**	30 s
Initial states	**Position** (deg, deg, ft MSL)	**Velocity** ft/s	**Attitude** deg	**Rate** deg/s
Geodetic	[0, 0, 30000]			
Local-relative		[0, 0, 0]	[0, 0, 0]	
Body axes				[-0.004178073, 0, 0]

C.1.8 Check-case 8 – sphere dropping through a varying wind field

Atmospheric check-case 8 was similar to check-case 7 previously discussed, using the same sphere from Section B.1.1 except the wind velocity was a function of vehicle height above the ground, as given in Table 32. The initial wind was from the west at 70 ft/s at 30,000 ft, tapering to 20 ft/s from the east at the surface; however, the scenario ended before reaching the surface.

Table 32. Initial Conditions for Atmospheric Scenario 8

Scenario	8: Sphere with wind shear			
Vehicle	Sphere with constant C_D			
Geodesy	WGS-84 rotating			
Atmosphere	US 1976 STD; wind varies linearly with altitude			
Gravitation	J_2		**Duration**	30 s
Initial states	**Position** (deg, deg, ft MSL)	**Velocity** ft/s	**Attitude** deg	**Rate** deg/s
Geodetic	[0, 0, 30000]			
Local-relative		[0, 0, 0]	[0, 0, 0]	
Body axes				[-0.004178073, 0, 0]
Notes	$V_{\text{wind}} = (0.003h - 20)$ ft/s from west; h is height MSL in ft.			

C.1.9 Check-case 9 – eastward ballistic flight of a sphere

The same sphere was put to the test in this scenario when it was launched eastward from the Equator/Prime Meridian intersection, starting at sea level, with an initial 45° vertical flight path angle as specified in Table 33. The cannonball was oriented to point eastward with zero pitch and roll angles (with respect to the launch point) and with zero angular rate (again with respect to the launch point).

Table 33. Initial Conditions for Atmospheric Scenario 9

Scenario	9: Sphere launched ballistically eastward along Equator			
Vehicle	Sphere with constant C_D			
Geodesy	WGS-84 rotating			
Atmosphere	US 1976 STD; no wind			
Gravitation	J_2		**Duration**	30 s
Initial states	**Position** (deg, deg, ft MSL)	**Velocity** ft/s	**Attitude** deg	**Rate** deg/s
Geodetic	[0, 0, 0]			
Local-relative		[0, 1000, -1000]	[0, 0, 90]	
Body axes				[0, 0, 0]
Notes	Initial velocity is $\sqrt{2,000}$ ft/s aligned 45° from vertical, heading east; zero angular rate relative to launch platform			

C.1.10 Check-case 10 – northward ballistic flight of a sphere

In this case, the sphere was launched northward from the same spot as in check-case 9 with the same initial velocity and vertical flight path angle as specified in Table 34. In this case, the sphere's body x-axis was aligned northward (but still zero pitch or roll angle with respect to the launch point). As before, there was no relative rotation with respect to the launch point.

Table 34. Initial Conditions for Atmospheric Scenario 10

Scenario	10: Sphere launched ballistically northward along Prime Meridian			
Vehicle	Sphere with constant C_D			
Geodesy	WGS-84 rotating			
Atmosphere	US 1976 STD; no wind			
Gravitation	J_2		**Duration**	30 s
Initial states	**Position** (deg, deg, ft MSL)	**Velocity** ft/s	**Attitude** deg	**Rate** deg/s
Geodetic Local-relative Body axes	[0, 0, 0]	[1000, 0, -1000]	[0, 0, 0]	[0, 0, 0]
Notes	Initial velocity is $\sqrt{2,000}$ ft/s aligned 45° from vertical, heading north; zero angular rate relative to launch platform			

C.1.11 Check-case 11 – steady flight of a subsonic aircraft

This scenario utilized the F-16 model described in Section B.1.5 but the vehicle was to be uncontrolled, as this was a test of how well the vehicle was trimmed for straight and level flight for non-trivial initial conditions (given in Table 35): positioned 10,000 ft above First Flight airport in Kitty Hawk, NC on a heading of 45° true at 400 KTAS relative to the still atmosphere.

Each simulation's trim solver solved for zero linear and angular accelerations (1 g flight) at 400 KTAS at 10,013 ft MSL by varying pitch attitude, elevator position, and throttle setting.

Table 35. Initial Conditions for Atmospheric Scenario 11

Scenario	11: Subsonic winged flight (trimmed straight & level)			
Vehicle	Unaugmented F-16			
Geodesy	WGS-84 rotating			
Atmosphere	US 1976 STD; no wind			
Gravitation	J_2		**Duration**	180 s
Initial states	**Position** (deg, deg, ft MSL)	**Velocity** ft/s	**Attitude** deg	**Rate** deg/s
Geodetic Local-relative Body axes	[36.01916667, -75.67444444, 10013]	[400, 400, 0]	[0, 0, 45]	[0, 0, 0]
Notes	Initial position is 10,000 ft above KFFA airport on a 45° true course. 335.15 KTAS. Stability augmentation off. Test of trim solution.			

C.1.12 Check-case 12 – steady flight of a supersonic aircraft

This case mimicked the previous case, with the exception of altitude and airspeed (30,000 ft MSL and 2000 ft/s (Mach 20), as given in Table 36). The vehicle was trimmed for level, un-accelerated flight by varying pitch attitude, elevator position, and throttle setting before allowing the open-loop vehicle fly for 180 sec.

Table 36. Initial Conditions for Atmospheric Scenario 12

Scenario	12: Supersonic winged flight (trimmed straight & level)			
Vehicle	Unaugmented F-16			
Geodesy	WGS-84 rotating			
Atmosphere	US 1976 STD; no wind			
Gravitation	J_2		**Duration**	180 s
Initial states	**Position** (deg, deg, ft MSL)	**Velocity** ft/s	**Attitude** deg	**Rate** deg/s
Geodetic Local-relative Body axes	[36.01916667, -75.67444444, 30013]	[1414.213562, 1414.213562, 0]	[0, 0, 45]	[0, 0, 0]
Notes	Initial position is 30,000 ft above KFFA airport on a 45° true course. True airspeed 2,000 ft/s. Stability augmentation off. Test of trim solution.			

C.1.13 Check-case 13.1 – altitude change of a subsonic aircraft

This scenario started with the same initial conditions as atmospheric case 11 (Section C.1.11) but the *F16_control* autopilot was engaged (by setting autopilotOn_discrete and stabilityAugmentationOn_disc both > 0.5). At $t = +5.0$ sec, a 100-ft increase in commanded altitude was made (through control law input altitudeMslCommand), and the response of the vehicle to that command change was recorded.

Table 37. Initial Conditions for Atmospheric Scenario 13.1

Scenario	13.1: Maneuvering flight of 6-DOF rigid aircraft with non-linear aerodynamics (subsonic): Altitude change			
Vehicle	F-16 with simple autopilot			
Geodesy	WGS-84 rotating			
Atmosphere	US 1976 STD; no wind			
Gravitation	J_2		**Duration**	20 s
Initial states	**Position** (deg, deg, ft MSL)	**Velocity** ft/s	**Attitude** deg	**Rate** deg/s
Geodetic Local-relative Body axes	[36.01916667, -75.67444444, 10013]	[400, 400, 0]	[0, 0, 45]	[0, 0, 0]
Notes	Initially straight & level. $t = 5$ sec: command altitude 100-ft increase.			

C.1.14 Check-case 13.2 – velocity change of a subsonic aircraft

This scenario started with the same initial conditions as atmospheric case 11 (Section C.1.11) but the *F16_control* autopilot was engaged (by setting autopilotOn_discrete and stabilityAugmentationOn_disc both > 0.5). At $t = +5.0$ sec, a 5-kt decrease in commanded equivalent airspeed was made (through control law input equivalentAirspeedCommand), and the response of the vehicle to that command change was recorded.

Table 38. Initial Conditions for Atmospheric Scenario 13.2

Scenario	13.2: Maneuvering flight of 6-DOF rigid aircraft with non-linear aerodynamics (subsonic): Velocity change			
Vehicle	F-16 with simple autopilot			
Geodesy	WGS-84 rotating			
Atmosphere	US 1976 STD; no wind			
Gravitation	J_2		**Duration**	20 s
Initial states	**Position** (deg, deg, ft MSL)	**Velocity** ft/s	**Attitude** deg	**Rate** deg/s
Geodetic Local-relative Body axes	[36.01916667, -75.67444444, 10013]	[400, 400, 0]	[0, 0, 45]	[0, 0, 0]
Notes	Initially straight & level. $t = 5$ sec: decrease commanded 5 KEAS.			

C.1.15 Check-case 13.3 – course change of a subsonic aircraft

This scenario started at the same initial conditions as atmospheric case 11 (Section C.1.11) but the *F16_control* autopilot was engaged (by setting autopilotOn_discrete and stabilityAugmentationOn_disc both > 0.5). At $t = +15.0$ sec, a 15° change in commanded heading to the right was made (through control law input

trueBaseCourseCommand), and the response of the vehicle to that command change was recorded.

Table 39. Initial Conditions for Atmospheric Scenario 13.3

Scenario	13.3: Maneuvering flight of 6-DOF rigid aircraft with non-linear aerodynamics (subsonic): Heading change			
Vehicle	F-16 with simple autopilot			
Geodesy	WGS-84 rotating			
Atmosphere	US 1976 STD; no wind			
Gravitation	J_2		**Duration**	30 s
Initial states	**Position** (deg, deg, ft MSL)	**Velocity** ft/s	**Attitude** deg	**Rate** deg/s
Geodetic Local-relative Body axes	[36.01916667, -75.67444444, 10013]	[400, 400, 0]	[0, 0, 45]	[0, 0, 0]
Notes	Initially straight & level. $t = 15$ sec: command 15° right heading change.			

C.1.16 Check-case 13.4 – lateral offset maneuver of a subsonic aircraft

This scenario started at the same initial conditions as atmospheric case 11 (Section C.1.11) but the *F16_control* autopilot was engaged (by setting autopilotOn_discrete and stabilityAugmentationOn_disc both > 0.5). At $t = +20.0$ sec, a 2,000-ft lateral offset was commanded to the right (through control law input lateralDeviationError), and the response of the vehicle to that command change was recorded.

In order to exercise this maneuver correctly, updates for the input feedback signal lateralDeviationError had to be calculated for each time step by additional user-supplied logic, based on the aircraft's position relative to the new offset course. Otherwise, the vehicle would continue along the initial correction heading and not return to the base course heading.

Table 40. Initial Conditions for Atmospheric Scenario 13.4

Scenario	13.4: Maneuvering flight of 6-DOF rigid aircraft with non-linear aerodynamics (subsonic): Lateral course offset			
Vehicle	F-16 with simple autopilot			
Geodesy	WGS-84 rotating			
Atmosphere	US 1976 STD; no wind			
Gravitation	J_2		**Duration**	60 s
Initial states	**Position** (deg, deg, ft MSL)	**Velocity** ft/s	**Attitude** deg	**Rate** deg/s
Geodetic Local-relative Body axes	[36.01916667, -75.67444444, 10013]	[400, 400, 0]	[0, 0, 45]	[0, 0, 0]
Notes	Initially straight & level. $t = 20$ sec: 2,000-ft lateral course offset.			

C.1.17 Check-case 14 – maneuvering flight of a supersonic aircraft.

This set of maneuvers for a supersonic maneuvering aircraft was intended to mimic those of the subsonic aircraft described in check-cases 13.1 through 13.4 above. Due to resource constraints, a working autopilot was not completed and these check-cases were not performed.

Table 41. Initial Conditions for Atmospheric Scenario 14

Scenario	14: Maneuvering flight of 6-DOF rigid aircraft with non-linear aerodynamics (supersonic)			
Vehicle	F-16 with simple autopilot			
Geodesy	WGS-84 rotating			
Atmosphere	US 1976 STD; no wind			
Gravitation	J_2		**Duration**	60 s
Initial states	**Position** (deg, deg, ft MSL)	**Velocity** ft/s	**Attitude** deg	**Rate** deg/s
Geodetic Local-relative Body axes	[36.01916667, -75.67444444, 30013]	[1414.213562, 1414.213562, 0]	[0, 0, 45]	[0, 0, 0]
Notes	Initially straight & level. $t = 10$ sec: increment throttle 0.5 (fraction) for 5 sec. $t = 20$ sec: long. stick doublet amp 0.1 for 3 sec each way (starting aft). $t = 30$ sec: rudder pedal doublet, starting right. $t = 40$ sec: roll stick doublet, starting right.			

C.1.18 Check-case 15 – circumnavigation of the North pole

This scenario tested for state propagation difficulties near 90° latitude, as well as proper wrapping of the vehicle longitudinal position as the IDL is crossed at ±180 geodetic longitude.

For this scenario, the vehicle started at an initial position and heading near the north pole as given in Table 42. The *F16_gnc* control system was added to the vehicle to provide the appropriate steering guidance (as well as vehicle control and augmented stability). The selectCircumnavigator_disc input was set to 1.0 to indicate the north pole was the center of the 3-nm circular flight path, and both autopilotOn_discrete and stabilityAugmentationOn_disc were set to 1.0. Both geodetic latitude and longitude had to be calculated and provided to the control system through geLatitude and gnLongitude inputs, respectively.

The vehicle turned left from the original heading, flew to and intercepted the desired circular track, flying counter-clockwise around the north pole for the duration of the simulation.

Table 42. Initial Conditions for Atmospheric Scenario 15

Scenario	15: Circular flight around North Pole			
Vehicle	F-16 with circumnavigating autopilot			
Geodesy	WGS-84 rotating			
Atmosphere	US 1976 STD; no wind			
Gravitation	J_2		**Duration**	180 s
Initial states	**Position** (deg, deg, ft MSL)	**Velocity** ft/s	**Attitude** deg	**Rate** deg/s
Geodetic	[89.95, -45, 10000]			
Local-relative		[0, 563.643, 0]	[0, 0, 90]	
Body axes				[0, 0, 0]
Notes	Initial conditions trimmed straight and level; engage autopilot at first time step.			

C.1.19 Check-case 16 – circular flight around the Equator-IDL intersection

This scenario tested for proper change-of-sign in geodetic latitude as the Equator was crossed in both directions, as well as proper wrapping of the vehicle longitudinal position as the IDL was crossed in both directions at ±180 geodetic longitude.

For this scenario, the vehicle started at an initial position and heading near the intersection of the Equator and IDL as given in Table 43. The *F16_gnc* control system was included in the vehicle model to provide the appropriate steering guidance (as well as vehicle control and augmented stability). The selectCircumnavigator_disc input was set to 0 to indicate the Equator-IDL intersection was the center of the 3 nm circular flight path, and both autopilotOn_discrete and stabilityAugmentationOn_disc were set to 1.0. Both geodetic latitude and longitude had to be calculated and provided to the control system through geLatitude and gnLongitude inputs, respectively.

The vehicle turned left from the original heading, flew to and intercepted the desired circular track, flying counter-clockwise around the 0 latitude, ±180° longitude location for the duration of the simulation.

Table 43. Initial Conditions for Atmospheric Scenario 16

Scenario	16: Circular flight around Equator/IDL intersection			
Vehicle	F-16 with circumnavigating autopilot			
Geodesy	WGS-84 rotating			
Atmosphere	US 1976 STD; no wind			
Gravitation	J_2		**Duration**	180 s
Initial states	**Position** (deg, deg, ft MSL)	**Velocity** ft/s	**Attitude** deg	**Rate** deg/s
Geodetic	[0, -179.95, 10000]			
Local-relative		[563.643, 0, 0]	[0, 0, 0]	
Body axes				[0, 0, 0]
Notes	Initial conditions trimmed straight and level; engage autopilot at first time step.			

C.1.20 Check-case 17 – flight of two-stage launch vehicle

The final "atmospheric" check-case employed an idealized two-stage rocket that, when launched, achieved a highly elliptical orbit without guidance. Initial conditions are given in Table 44; the vehicle model is described in Section B.1.6.

Due to the lack of guidance and a strong dependence of the final position upon very small attitude changes and timing of engine burnout, this scenario was fairly sensitive to integration methods and simulation step size. It was recommended to use a time step of 0.001 sec (1,000 iterations per sec of simulation time), especially when using a lower-order integration method.

This case also required some external logic to calculate fuel burn, initiate staging, and detect burnout, as described in Section B.1.6.

Table 44. Initial Conditions for Atmospheric Scenario 17

Scenario	17: Two-stage rocket to orbit			
Vehicle	Two-stage unguided rocket			
Geodesy	WGS-84 rotating			
Atmosphere	US 1976 STD; no wind			
Gravitation	J_2		**Duration**	200 s
Initial states	**Position** (deg, deg, ft MSL)	**Velocity** ft/s	**Attitude** deg	**Rate** deg/s
Geodetic	[0, 0, 0]			
Local-relative		[0, 0, -0.32808399]	[0, 55.22, 90]	
Body axes				[0, 0, 0]

C.2 Orbital scenarios

The goal of the orbital check-case scenarios was to compare propagation of a 6-DOF vehicle in an orbital environment. These cases idealized the vehicle as a rigid body and compared time histories of position, velocity, attitude and attitude rate. The orbital environment is fundamentally different from the atmospheric domain because orbiting bodies are not subject to the strong damping effects of atmospheric flight. Therefore, even tiny perturbations such as higher-order gravitation terms and third-body effects will produce large differences in vehicle state over time.

The orbital scenarios (shown in Table 24) were designed to exercise various options ranging from spherical Earth/gravitation and no drag to full geopotential-gravitation, third-body perturbations and drag. The tests were organized in such a way as to build incrementally so that higher-order effects can be seen as they are introduced. These scenarios matched those developed for an earlier simulation comparison study. [1]

Tables 47 through 72 show the initial conditions for each of the atmospheric check-cases.

Key parameters that are commonly needed to support vehicle state propagation were also compared. For example, in order to compute non-spherical gravitational accelerations, they must be calculated in the ECEF frame. These accelerations must then be converted into a non-rotating inertial frame (ECI) for integration.

The RNP transformation matrix **M**, representing the rotation, nutation and precession angles between the ECEF and ECI frames, is required to convert the non-spherical gravitational accelerations into the ECI

frame; it is also needed in order to relate the inertial state of the vehicle to locations on the planet. In the same manner, we needed a model of the upper atmosphere in order to model drag. We compared RNP matrices (inferred from ECEF positions) and atmosphere models as a means of isolating sources of variation among the various simulations.

The orbital cases can be described according to the following outline:

Drag-Free Translation These were primarily designed to test the numerical integration and gravitation models. The complexity varied from pure spherical gravitation through higher-order gravitational harmonics and third-body effects.

Translation with Drag These cases were similar to their drag-free counterparts except that a simple drag model was introduced and exercised with constant and variable atmospheric density. In all orbital cases, the drag was modeled by a simple ballistic coefficient.

Rotational Propagation These cases compared the rotational propagation with various initial attitudes, attitude rates, and torques.

Maneuvers These cases involved application of thrust to change the trajectory in various ways.

Two example orbits were defined, reusing the orbits defined the draft DSES report [25]. One (given in Table 45) was a nearly circular representative of a low Earth orbit; the other (given in Table 46) was highly elliptical.

Table 45. Nearly Circular Example Orbit Definition in J2000 Coordinates

Parameter	Value
Time	2007/324:00:00:00 (UTC)
r_x	-4,292,653.41 m
r_y	955,168.47 m
r_z	5,139,356.57 m
v_x	109.649663 m/s
v_y	-7,527.726490 m/s
v_z	1,484.521489 m/s

The specific scenarios for each of the orbital check-cases are described below, along with a table giving both initial state values and problem assumptions, including the vehicle being simulated, geodetic Earth model, atmosphere model, and gravitational model to be used as well as test duration.

For each scenario, the duration was fixed at 28,800 sec; participants were encouraged to provide data recorded every 60 sec.

C.2.1 Check-case 2 – ISS in spherical gravity

This was the simplest orbital check-case in which all effects except for a pure inverse-square gravitation field were turned off. This case provided an opportunity to compare integration techniques (by comparing inertial position and velocity) and models for Earth rotation (by comparing planet-fixed position and velocity). The

Table 46. Highly Elliptical Example Orbit Definition in J2000 Coordinates

Parameter	Value
Time	2007/324:00:00:00 (UTC)
r_x	-4,315,967.74 m
r_y	960,356.20 m
r_z	5,167,269.53 m
v_x	129.091037 m/s
v_y	-7,491.513855 m/s
v_z	1,452.515654 m/s

vehicle was an idealization of the International Space Station described in Table 19, and the orbit is described in Table 45.

Table 47. Initial Conditions for Orbital Scenario 2

Scenario	2: Keplerian Propagation
Vehicle type	ISS
Orbit type	Nearly circular
Atmosphere model	$\bar{F}_{10.7} = 128.8\ 10^{-22}$ watt / m^2 / Hz, $A_p = 15.7$
Aerodynamic drag	Off
Gravitation model order	Inverse square
Gravity gradient effects	Off
Planetary ephemeris **Sun/Moon perturbations**	Off Off
Initial inertial rotation rate (body axes)	$[0.000000, -0.065000, 0.000000]$ deg/s
Initial LVLH attitude (3-2-1 Euler sequence)	$[0.000000, -11.600000, 0.000000]$ deg

C.2.2 Check-case 3A – ISS in 4×4 harmonic gravity

This check-case was identical to the previous check-case (Check-case 2 – ISS in spherical gravity) except that the terms of degree and order up to 4 were included in the spherical harmonics gravitation model. This case provided a comparison of spherical harmonics gravitation calculations and showed the effect of the first few non-spherical terms on the vehicle state.

Table 48. Initial Conditions for Orbital Scenario 3A

Scenario	3A: 4×4 Gravity Model
Vehicle type	ISS
Orbit type	Nearly circular
Atmosphere model	$\bar{F}_{10.7} = 128.8\ 10^{-22}$ watt / m^2 / Hz, $A_p = 15.7$
Aerodynamic drag	Off
Gravitation model order	4×4
Gravity gradient effects	Off
Planetary ephemeris **Sun/Moon perturbations**	Off Off
Initial inertial rotation rate (body axes)	$[0.000000, -0.065000, 0.000000]$ deg/s
Initial LVLH attitude (3-2-1 Euler sequence)	$[0.000000, -11.600000, 0.000000]$ deg

C.2.3 Check-case 3B – ISS in 8×8 harmonic gravity

This check-case was identical to "Check-case 2 – ISS in spherical gravity" except that the terms of degree and order up to 8 were included in the spherical harmonics gravitation model. This case provided a comparison of spherical harmonics gravitation calculations and showed the effect of higher order non-spherical terms on the vehicle state.

Table 49. Initial Conditions for Orbital Scenario 3B

Scenario	3B: 8×8 Gravity Model
Vehicle type	ISS
Orbit type	Nearly circular
Atmosphere model	$\bar{F}_{10.7} = 128.8\ 10^{-22}$ watt / m^2 / Hz, $A_p = 15.7$
Aerodynamic drag	Off
Gravitation model order	8×8
Gravity gradient effects	Off
Planetary ephemeris **Sun/Moon perturbations**	Off Off
Initial inertial rotation rate (body axes)	$[0.000000, -0.065000, 0.000000]$ deg/s
Initial LVLH attitude (3-2-1 Euler sequence)	$[0.000000, -11.600000, 0.000000]$ deg

C.2.4 Check-case 4 – ISS with third-body disturbances

This check-case was identical to "Check-case 2 – ISS in spherical gravity" except that the gravitational effects of Sun and Moon were included. This case required an ephemeris model (Jet Propulsion Laboratory's DE405 [26]) was used and demonstrated the effect of third-body perturbations.

Table 50. Initial Conditions for Orbital Scenario 4

Scenario	4: Planetary Ephemeris
Vehicle type	ISS
Orbit type	Nearly circular
Atmosphere model	$\bar{F}_{10.7} = 128.8\ 10^{-22}$ watt / m^2 / Hz, $A_p = 15.7$
Aerodynamic drag	Off
Gravitation model order	Inverse square
Gravity gradient effects	Off
Planetary ephemeris **Sun/Moon perturbations**	On On
Initial inertial rotation rate (body axes)	$[0.000000, -0.065000, 0.000000]$ deg/s
Initial LVLH attitude (3-2-1 Euler sequence)	$[0.000000, -11.600000, 0.000000]$ deg

C.2.5 Check-case 5A – ISS (minimal solar activity)

This check-case was designed to exercise the MET model of the outer atmosphere. The gravitation model was identical to that in the "Check-case 2 – ISS in spherical gravity" scenario; however, the initial conditions placed the vehicle in the highly elliptical orbit (described in Table 46) so that the model was tested over a great range of altitudes. Although the atmospheric model was included, we did not include any drag forces for this case, as the intent was to compare the atmospheric model implementations without introducing other factors. These cases varied the input parameter $F_{10.7}$ described in Section B.5.2 for the MET. This case used a relatively low value of this parameter.

Table 51. Initial Conditions for Orbital Scenario 5A

Scenario	5A: Minimum Solar Activity
Vehicle type	ISS
Orbit type	Highly elliptical
Atmosphere model	$\bar{F}_{10.7} = 70\ 10^{-22}$ watt / m^2 / Hz, $A_p = 0$
Aerodynamic drag	Off
Gravitation model order	Inverse square
Gravity gradient effects	Off
Planetary ephemeris **Sun/Moon perturbations**	Sun only Off
Initial inertial rotation rate (body axes)	$[0.000000, -0.065000, 0.000000]$ deg/s
Initial LVLH attitude (3-2-1 Euler sequence)	$[0.000000, -11.600000, 0.000000]$ deg

C.2.6 Check-case 5B – ISS (mean solar activity)

This check-case was designed to exercise the MET model of the outer atmosphere. The gravitation model was identical to that in the "Check-case 2 – ISS in spherical gravity" scenario; however, the initial conditions placed the vehicle in the highly elliptical orbit (described in Table 46) so that the model was tested over a great range of altitudes. Although the atmospheric model was included, we did not include any drag forces for this case, as the intent was to compare the atmospheric model implementations without introducing other factors. These cases varied the input parameter $F_{10.7}$ described in Section B.5.2 for the MET. This case used a nominal value of this parameter.

Table 52. Initial Conditions for Orbital Scenario 5B

Scenario	5B: Mean Solar Activity
Vehicle type	ISS
Orbit type	Highly elliptical
Atmosphere model	$\bar{F}_{10.7} = 128.8\ 10^{-22}$ watt / m^2 / Hz, $A_p = 15.7$
Aerodynamic drag	Off
Gravitation model order	Inverse square
Gravity gradient effects	Off
Planetary ephemeris **Sun/Moon perturbations**	Sun only Off
Initial inertial rotation rate (body axes)	$[0.000000, -0.065000, 0.000000]$ deg/s
Initial LVLH attitude (3-2-1 Euler sequence)	$[0.000000, -11.600000, 0.000000]$ deg

C.2.7 Check-case 5C – ISS (maximal solar activity)

This check-case was designed to exercise the MET model of the outer atmosphere. The gravitation model was identical to that in the "Check-case 2 – ISS in spherical gravity" scenario; however, the initial conditions placed the vehicle in the highly elliptical orbit (described in Table 46) so that the model was tested over a great range of altitudes. Although the atmospheric model was included, we did not include any drag forces for this case, as the intent is to compare the atmospheric model implementations without introducing other factors. These cases varied the input parameter $F_{10.7}$ described in Section B.5.2 for the MET. This case used a relatively high value of this parameter.

Table 53. Initial Conditions for Orbital Scenario 5C

Scenario	5C: Maximum Solar Activity
Vehicle type	ISS
Orbit type	Highly elliptical
Atmosphere model	$\bar{F}_{10.7} = 250\ 10^{-22}$ watt / m^2 / Hz, $A_p = 25$
Aerodynamic drag	Off
Gravitation model order	Inverse square
Gravity gradient effects	Off
Planetary ephemeris **Sun/Moon perturbations**	Sun only Off
Initial inertial rotation rate (body axes)	$[0.000000, -0.065000, 0.000000]$ deg/s
Initial LVLH attitude (3-2-1 Euler sequence)	$[0.000000, -11.600000, 0.000000]$ deg

C.2.8 Check-case 6A – sphere with fixed drag

This was the first check-case involving aerodynamic drag. In order to isolate the effects of drag from the atmosphere model, the density was fixed at a known, constant value. The vehicle used was the sphere described in Table 3, and drag was modeled by a simple ballistic coefficient. The initial conditions described in Table 46 placed the vehicle in the highly elliptical orbit we used for the atmospheric comparisons.

Table 54. Initial Conditions for Orbital Scenario 6A

Scenario	6A: Aerodynamic Drag with Constant Density
Vehicle type	Sphere
Orbit type	Highly elliptical
Atmosphere model	$\bar{F}_{10.7} = 128.8\ 10^{-22}$ watt / m^2 / Hz, $A_p = 15.7$
Aerodynamic drag	$C_D = 0.02$, $S_{\text{ref}} = 1$ m^2
Gravitation model order	Inverse square
Gravity gradient effects	Off
Planetary ephemeris **Sun/Moon perturbations**	Sun only Off
Initial inertial rotation rate (body axes)	$[0.000000, -0.065000, 0.000000]$ deg/s
Initial LVLH attitude (3-2-1 Euler sequence)	$[0.000000, -11.600000, 0.000000]$ deg

C.2.9 Check-case 6B – sphere with dynamic drag

This check-case is identical to the previous scenario (Check-case 6A – sphere with fixed drag) except that the constant density was replaced by the density computed by the MET model.

Table 55. Initial Conditions for Orbital Scenario 6B

Scenario	6B: Aerodynamic Drag with Dynamic Atmosphere
Vehicle type	Sphere
Orbit type	Highly elliptical
Atmosphere model	$\bar{F}_{10.7} = 128.8\ 10^{-22}$ watt / m^2 / Hz, $A_p = 15.7$
Aerodynamic drag	$C_D = 0.02$, $S_{\text{ref}} = 1$ m^2
Gravitation model order	Inverse square
Gravity gradient effects	Off
Planetary ephemeris **Sun/Moon perturbations**	Sun only Off
Initial inertial rotation rate (body axes)	$[0.000000, -0.065000, 0.000000]$ deg/s
Initial LVLH attitude (3-2-1 Euler sequence)	$[0.000000, -11.600000, 0.000000]$ deg

C.2.10 Check-case 6C – cylinder undergoing plane change firing

This check-case had the same gravitation, initial conditions and drag configuration as the "Check-case 2 – ISS in spherical gravity" scenario, except that the mass properties were those of the 1,000-kg cylinder described in Table 6, and the initial attitude was aligned with the LVLH frame.

After 1,000 sec, a force of $29,000$ N was applied along the $-y$ body axis (through the vehicle's CM). Due to the initial orientation and the fact that the vehicle maintained a fixed LVLH orientation, this thrust was directed perpendicular to the plane of the orbit. The duration of the maneuver was 93 sec.

Table 56. Initial Conditions for Orbital Scenario 6C

Scenario	6C: Plane Change Maneuver
Vehicle type	Cylinder
Orbit type	Nearly circular
Atmosphere model	$\bar{F}_{10.7} = 128.8\ 10^{-22}$ watt / m^2 / Hz, $A_p = 15.7$
Aerodynamic drag	Off
Gravitation model order	Inverse square
Gravity gradient effects	Off
Planetary ephemeris **Sun/Moon perturbations**	Sun only Off
Initial inertial rotation rate (body axes)	$[0.000000, -0.065000, 0.000000]$ deg/s
Initial LVLH attitude (3-2-1 Euler sequence)	$[0.000000, 0.000000, 0.000000]$ deg
Notes	$29,000$ N force in negative body y-axis direction, starting at $t = 1,000$ sec for 93 sec

C.2.11 Check-case 6D – cylinder undergoing Earth departure firing

This check-case was identical to the "Check-case 6C – cylinder undergoing plane change firing" scenario except that a force of $66,400$ N was applied along the $+x$ body axis direction (through the vehicle's CM) for 48 sec. Due to the direction and magnitude of the force, the effect was performance of an Earth departure maneuver.

Table 57. Initial Conditions for Orbital Scenario 6D

Scenario	6D: Earth Departure Maneuver
Vehicle type	Cylinder
Orbit type	Nearly circular
Atmosphere model	$\bar{F}_{10.7} = 128.8\ 10^{-22}$ watt / m^2 / Hz, $A_p = 15.7$
Aerodynamic drag	Off
Gravitation model order	Inverse square
Gravity gradient effects	Off
Planetary ephemeris **Sun/Moon perturbations**	Sun only Off
Initial inertial rotation rate (body axes)	$[0.000000, -0.065000, 0.000000]$ deg/s
Initial LVLH attitude (3-2-1 Euler sequence)	$[0.000000, 0.000000, 0.000000]$ deg
Notes	$66,400$ N force in positive body x-axis direction, starting at $t = 1,000$ sec for 48 sec

C.2.12 Check-case 7A – sphere in 4×4 gravity and third-body perturbations

This check-case showed the effects of low-order spherical harmonics along with third-body perturbations. It was similar to "Check-case 3A – ISS in 4×4 harmonic gravity" scenario with the following exceptions:

- The mass properties of the vehicle were those of the sphere described by Table 3 rather than those of the ISS.
- The orbit was highly elliptical which tended to demonstrate third-body effects.
- Gravitation from Sun and Moon were both included.

Table 58. Initial Conditions for Orbital Scenario 7A

Scenario	7A: No Drag with 4×4 Gravity
Vehicle type	Sphere
Orbit type	Highly Elliptical
Atmosphere model	$\bar{F}_{10.7} = 128.8\ 10^{-22}$ watt / m^2 / Hz, $A_p = 15.7$
Aerodynamic drag	Off
Gravitation model order	4×4
Gravity gradient effects	Off
Planetary ephemeris **Sun/Moon perturbations**	On On
Initial inertial rotation rate (body axes)	$[0.000000, -0.065000, 0.000000]$ deg/s
Initial LVLH attitude (3-2-1 Euler sequence)	$[0.000000, -11.600000, 0.000000]$ deg

C.2.13 Check-case 7B – sphere in 8×8 gravity and third-body perturbations

This check-case was identical to the previous scenario (Check-case 7A – sphere in 4×4 gravity and third-body perturbations) except that the degree and order of the Earth gravitation field was 8×8 rather than 4×4.

Table 59. Initial Conditions for Orbital Scenario 7B

Scenario	7B: No Drag with 8×8 Gravity
Vehicle type	Sphere
Orbit type	Highly elliptical
Atmosphere model	$\bar{F}_{10.7} = 128.8\ 10^{-22}$ watt / m^2 / Hz, $A_p = 15.7$
Aerodynamic drag	Off
Gravitation model order	8×8
Gravity gradient effects	Off
Planetary ephemeris **Sun/Moon perturbations**	On On
Initial inertial rotation rate (body axes)	$[0.000000, -0.065000, 0.000000]$ deg/s
Initial LVLH attitude (3-2-1 Euler sequence)	$[0.000000, -11.600000, 0.000000]$ deg

C.2.14 Check-case 7C – sphere in 4×4 gravity with drag and third-body perturbations

This check-case was identical to the "Check-case 7A – sphere in 4×4 gravity and third-body perturbations" scenario except that aerodynamic drag was enabled as in the "Check-case 6B – sphere with dynamic drag" scenario.

Table 60. Initial Conditions for Orbital Scenario 7C

Scenario	7C: All Models with 4×4 Gravity
Vehicle type	Sphere
Orbit type	Highly elliptical
Atmosphere model	$\bar{F}_{10.7} = 128.8\ 10^{-22}$ watt / m^2 / Hz, $A_p = 15.7$
Aerodynamic drag	$C_D = 0.02$, $S_{\text{ref}} = 1$ m^2
Gravitation model order	4×4
Gravity gradient effects	Off
Planetary ephemeris **Sun/Moon perturbations**	On On
Initial inertial rotation rate (body axes)	$[0.000000, -0.065000, 0.000000]$ deg/s
Initial LVLH attitude (3-2-1 Euler sequence)	$[0.000000, -11.600000, 0.000000]$ deg

C.2.15 Check-case 7D – sphere in 8×8 gravity with drag and third-body perturbations

This case was identical to "Check-case 7C – sphere in 4×4 gravity with drag and third-body perturbations" scenario except that the degree and order of the Earth gravitation field was 8×8 rather than 4×4.

Table 61. Initial Conditions for Orbital Scenario 7D

Scenario	7D: All Models with 8×8 Gravity
Vehicle type	Sphere
Orbit type	Highly elliptical
Atmosphere model	$\bar{F}_{10.7} = 128.8\ 10^{-22}$ watt / m^2 / Hz, $A_p = 15.7$
Aerodynamic drag	$C_D = 0.02$, $S_{\text{ref}} = 1$ m^2
Gravitation model order	8×8
Gravity gradient effects	Off
Planetary ephemeris **Sun/Moon perturbations**	On On
Initial inertial rotation rate (body axes)	$[0.000000, -0.065000, 0.000000]$ deg/s
Initial LVLH attitude (3-2-1 Euler sequence)	$[0.000000, -11.600000, 0.000000]$ deg

C.2.16 Check-case 8A – ISS free rotation with zero rates

This was the first check-case which compared rotational propagation. The configuration for gravitation, drag, mass properties and orbit were the same as original "Check-case 2 – ISS in spherical gravity" scenario. The difference was that the orientation and attitude rates were set with respect to the inertial as opposed to the local LVLH frame. The attitude rates were set to 0 with respect to the inertial frame.

Table 62. Initial Conditions for Orbital Scenario 8A

Scenario	8A: Zero Initial Attitude Rate
Vehicle type	ISS
Orbit type	Nearly circular
Atmosphere model	Off
Aerodynamic drag	Off
Gravitation model order	Inverse square
Gravity gradient effects	Off
Planetary ephemeris **Sun/Moon perturbations**	Off Off
Initial inertial rotation rate (body axes)	$[0.000000, 0.000000, 0.000000]$ deg/s
Initial LVLH attitude (3-2-1 Euler sequence)	$[0.000000, -11.600000, 0.000000]$ deg

C.2.17 Check-case 8B – ISS free rotation with a non-zero rates

The configuration of this check-case was identical to that for "Check-case 2 – ISS in spherical gravity." It was repeated here to highlight the effect of a non-zero inertial attitude rate.

Table 63. Initial Conditions for Orbital Scenario 8B

Scenario	8B: Non-zero Initial Attitude Rate
Vehicle type	ISS
Orbit type	Nearly circular
Atmosphere model	Off
Aerodynamic drag	Off
Gravitation model order	Inverse square
Gravity gradient effects	Off
Planetary ephemeris **Sun/Moon perturbations**	Off Off
Initial inertial rotation rate (body axes)	$[0.000000, -0.065000, 0.000000]$ deg/s
Initial LVLH attitude (3-2-1 Euler sequence)	$[0.000000, -11.600000, 0.000000]$ deg

C.2.18 Check-case 9A – ISS being torqued with zero initial rates

This check-case was identical to "Check-case 8A – ISS free rotation with zero rates" except that beginning at $t = 1,000$ sec, a torque of 10 N-m was applied about the positive body x-axis. The applied torque continued for an additional $1,000$ sec, then was set to zero for the duration of the run.

Table 64. Initial Conditions for Orbital Scenario 9A

Scenario	9A: Zero Initial Attitude Rate with Torque
Vehicle type	ISS
Orbit type	Nearly circular
Atmosphere model	Off
Aerodynamic drag	Off
Gravitation model order	Inverse square
Gravity gradient effects	Off
Planetary ephemeris **Sun/Moon perturbations**	Off Off
Initial inertial rotation rate (body axes)	$[0.000000, 0.000000, 0.000000]$ deg/s
Initial LVLH attitude (3-2-1 Euler sequence)	$[0.000000, -11.600000, 0.000000]$ deg

C.2.19 Check-case 9B – ISS being torqued with non-zero initial rates

This check-case was identical to C.2.17 except that beginning at $t = 1,000$ sec, a torque of 10 N-m was applied about the positive body x-axis. The applied torque continued for an additional $1,000$ sec, then was set to zero for the duration of the run.

Table 65. Initial Conditions for Orbital Scenario 9B

Scenario	9B: Non-zero Initial Attitude Rate with Torque
Vehicle type	ISS
Orbit type	Nearly circular
Atmosphere model	Off
Aerodynamic drag	Off
Gravitation model order	Inverse square
Gravity gradient effects	Off
Planetary ephemeris **Sun/Moon perturbations**	Off Off
Initial inertial rotation rate (body axes)	$[0.000000, -0.065000, 0.000000]$ deg/s
Initial LVLH attitude (3-2-1 Euler sequence)	$[0.000000, -11.600000, 0.000000]$ deg

C.2.20 Check-case 9C – ISS under torque and force with zero initial rates

This check-case was identical to "Check-case 8A – ISS free rotation with zero rates" except that beginning at $t = 1,000$ sec, a force of 10 N was applied in the positive body x-axis direction, through the vehicle's CM, and a torque of 10 N-m was applied about the positive body x-axis. The external force and torque were applied for an additional $1,000$ sec, then were set to zero for the duration of the run.

Table 66. Initial Conditions for Orbital Scenario 9C

Scenario	9C: Zero Initial Attitude Rate with Torque and Force
Vehicle type	ISS
Orbit type	Nearly circular
Atmosphere model	Off
Aerodynamic drag	Off
Gravitation model order	Inverse square
Gravity gradient effects	Off
Planetary ephemeris **Sun/Moon perturbations**	Off Off
Initial inertial rotation rate (body axes)	$[0.000000, 0.000000, 0.000000]$ deg/s
Initial LVLH attitude (3-2-1 Euler sequence)	$[0.000000, -11.600000, 0.000000]$ deg

C.2.21 Check-case 9D – ISS under torque and force with a non-zero initial rates

This check-case was identical to "Check-case 8B – ISS free rotation with a non-zero rates" except that beginning at $t = 1,000$ sec, a force of 10 N was applied in the positive body x-axis direction, through the vehicle's CM, and a torque of 10 N-m was applied about the positive body x-axis. The external force and torque were applied for an additional $1,000$ sec, then were set to zero for the duration of the run.

Table 67. Initial Conditions for Orbital Scenario 9D

Scenario	9D: Non-zero Initial Attitude Rate with Torque and Force
Vehicle type	ISS
Orbit type	Nearly circular
Atmosphere model	Off
Aerodynamic drag	Off
Gravitation model order	Inverse square
Gravity gradient effects	Off
Planetary ephemeris **Sun/Moon perturbations**	Off Off
Initial inertial rotation rate (body axes)	$[0.000000, -0.065000, 0.000000]$ deg/s
Initial LVLH attitude (3-2-1 Euler sequence)	$[0.000000, -11.600000, 0.000000]$ deg

C.2.22 Check-case 10A – cylinder in circular orbit with gravity gradient with zero initial rates

This was the first of the check-cases for the effects of gravity gradient torque. These cases all used the same cylindrical body described by Table 6. The initial attitude was defined with respect to the LVLH frame in such a way that the cylinder was pitched at an angle of 85 degrees from the local horizontal, and then yawed 1 degree out of the LVLH X-Z plane. For this case, we used the nearly circular orbit with initial conditions described in Table 45. This gave rise to a system that, in the limit of small angle approximations, acted like a simple harmonic oscillator with the pitch angle rocking through a 10-degree range about the local vertical and the yaw oscillating through a 2-degree range of the LVLH X-Z plane.

Table 68. Initial Conditions for Orbital Scenario 10A

Scenario	10A: Zero Initial Rotation Rate in Circular Orbit with Gravity Gradient
Vehicle type	Cylinder
Orbit type	Nearly circular
Atmosphere model	$\bar{F}_{10.7} = 128.8\ 10^{-22}$ watt / m^2 / Hz, $A_p = 15.7$
Aerodynamic drag	Off
Gravitation model order	Inverse square
Gravity gradient effects	On
Planetary ephemeris **Sun/Moon perturbations**	Off Off
Initial inertial rotation rate (body axes)	$[0.000000, 0.000000, 0.000000]$ deg/s
Initial LVLH attitude (3-2-1 Euler sequence)	$[0.000000, 85.000000, 1.000000]$ deg

C.2.23 Check-case 10B – cylinder in circular orbit with gravity gradient with non-zero initial rates

This case differed from "Check-case 10A – cylinder in circular orbit with gravity gradient with zero initial rates" only in that there was a small initial pitch rate of 0.01 deg/s. The effect was to slightly increase the amplitude and retard the phase of the pitch oscillation.

Table 69. Initial Conditions for Orbital Scenario 10B

Scenario	10B: Non-zero Initial Rotation Rate in Circular Orbit with Gravity Gradient
Vehicle type	Cylinder
Orbit type	Nearly circular
Atmosphere model	$\bar{F}_{10.7} = 128.8\ 10^{-22}$ watt / m^2 / Hz, $A_p = 15.7$
Aerodynamic drag	Off
Gravitation model order	Inverse square
Gravity gradient effects	On
Planetary ephemeris **Sun/Moon perturbations**	Off Off
Initial inertial rotation rate (body axes)	$[0.000000, -0.065000, 0.000000]$ deg/s
Initial LVLH attitude (3-2-1 Euler sequence)	$[0.000000, 85.000000, 1.000000]$ deg

C.2.24 Check-case 10C – cylinder in elliptical orbit with gravity gradient with zero initial rates

This check-case differed from "Check-case 10A – cylinder in circular orbit with gravity gradient with zero initial rates" only in that we used the highly elliptical orbit described in Table 46. This demonstrated that the frequency of the resulting oscillations was a function of the magnitude of the gravity gradient, which is a function of the altitude. The vehicle rocked more slowly at apoapsis, and more rapidly near periapsis.

Table 70. Initial Conditions for Orbital Scenario 10C

Scenario	10C: Zero Initial Rotation Rate in Elliptical Orbit with Gravity Gradient
Vehicle type	Cylinder
Orbit type	Highly elliptical
Atmosphere model	$\bar{F}_{10.7} = 128.8\ 10^{-22}$ watt / m^2 / Hz, $A_p = 15.7$
Aerodynamic drag	Off
Gravitation model order	Inverse square
Gravity gradient effects	On
Planetary ephemeris **Sun/Moon perturbations**	Off Off
Initial inertial rotation rate (body axes)	$[0.000000, 0.000000, 0.000000]$ deg/s
Initial LVLH attitude (3-2-1 Euler sequence)	$[0.000000, 85.000000, 1.000000]$ deg

C.2.25 Check-case 10D – cylinder in elliptical orbit with gravity gradient with a non-zero initial rates

This check-case differed from check-case 10C only in that there was a tiny initial pitch rate. The effect was to slightly increase the amplitude and retard the phase of the pitch oscillation.

Table 71. Initial Conditions for Orbital Scenario 10D

Scenario	10D: Non-zero Initial Rotation Rate in Elliptical Orbit with Gravity Gradient
Vehicle type	Cylinder
Orbit type	Highly elliptical
Atmosphere model	$\bar{F}_{10.7} = 128.8\ 10^{-22}$ watt / m^2 / Hz, $A_p = 15.7$
Aerodynamic drag	Off
Gravitation model order	Inverse square
Gravity gradient effects	On
Planetary ephemeris **Sun/Moon perturbations**	Off Off
Initial inertial rotation rate (body axes)	$[0.000000, -0.065000, 0.000000]$ deg/s
Initial LVLH attitude (3-2-1 Euler sequence)	$[0.000000, 85.000000, 1.000000]$ deg

C.2.26 Check-case Full – ISS responding to all effects

This was the culminating orbital check-case where we turned on all effects common to the available simulations. These were:

- 8×8 gravitation model
- Gravity gradient (spherical term only, with no gradient contribution from Sun or Moon).)
- Third-body effects from Sun and Moon (spherical model only).
- Constant aerodynamic drag as check-case 6B.
- Highly elliptical orbit described in Table 46

Table 72. Initial Conditions for Orbital Scenario Full

Scenario	Full: All Effects in Elliptical Orbit
Vehicle type	ISS
Orbit type	Highly elliptical
Atmosphere model	$\bar{F}_{10.7} = 128.8\ 10^{-22}$ watt / m^2 / Hz, $A_p = 15.7$
Aerodynamic drag	$C_D = 2$, $S_{\text{ref}} = 1,400$ m^2
Gravitation model order	8×8
Gravity gradient effects	On
Planetary ephemeris **Sun/Moon perturbations**	On On
Initial inertial rotation rate (body axes)	$[0.000000, -0.065000, 0.000000]$ deg/s
Initial LVLH attitude (3-2-1 Euler sequence)	$[0.000000, -11.600000, 0.000000]$ deg

C.3 Geodetic parameters used for comparisons

For historical reasons, the exact WGS-84 [7] geodetic and gravitational parameters were not used for the orbital check-cases. Instead, the parameters used in the original DSES study [25] were re-used. These parameters were cited to have come from the "Explanatory Supplement to the Astronomical Almanac" [27] which itself included the Goddard Earth Model T1 (GEM-T1) [28] geodesy model. However, in the DSES study, some of these parameters were truncated.

Table 73 contains parameter values and unit conversions, in SI and English units, that should be used in attempting to replicating the check-case results given in Section D. Table 74 contains the coefficients for the spherical harmonic geopotential model to be used for orbital check-cases that specify 4×4 or 8×8 harmonics; these were based on GEM-T1 [28].

D Results

One purpose of the check-cases is to assess the extent to which differences in implementation (such as selection of native coordinate systems) can affect results. Despite an attempt to define initial conditions (attitudes, positions, rates and velocities) as unambiguously as possible, some ambiguity remained (and the initial condition values continued to be refined throughout the assessment) which illustrated one of the challenges in communicating simulation models between different simulation frameworks.

In general, the atmospheric results are given in English units. This is believed to be common practice in the U.S. even as the orbital community has mostly adopted SI units; this paper reflects that difference between the U.S. aviation and space communities. (There are exceptions in both camps; several of these tools can handle either set of units.)

The identities of the various tools were masked to encourage participation in this voluntary effort. Also, the atmospheric cases used numerical designations (SIM 1, SIM 2, etc.) while the orbital cases used alpha

Table 73. Geodetic Model Parameters and Unit Conversions for Ellipsoidal Earth

Atmospheric check-cases		
Parameter	SI units	English units
Equatorial radius of the Earth	6378137.0 m	20925646.32546 ft
Radius of the sphere Earth model	6371007.1809 m	20902254.5305 ft
Gravitational constant for the Earth	$3.986004418 \times 10^{14}$ m^3/s^2	$1.407644175720511 \times 10^{16}$ ft^3/s^2
Rotation Rate of the Earth		7.292115×10^{-5} rad/s
Second degree zonal harmonic (J_2)		0.00108262982
Flattening of the WGS84 Earth ($1/f$)		298.257223563
Orbital check-cases		
Parameter	SI units	English units
Equatorial radius of the Earth	6378137.0 m	20925646.32546 ft
Gravitational constant for the Earth	$3.98600436 \times 10^{14}$ m^3/s^2	$1.407644155238004 \times 10^{16}$ ft^3/s^2
Gravitational constant for the Sun	1.3271244×10^{20} m^3/s^2	$4.686695588395551 \times 10^{21}$ ft^3/s^2
Gravitational constant for the Moon	4.90266×10^{12} m^3/s^2	$1.731358039487733 \times 10^{14}$ ft^3/s^2
Rotation Rate of the Earth		$7.29211514670638 \times 10^{-5}$ rad/s
Flattening of the Earth ($1/f$)		298.3
IERS Leap Seconds		32 s
DUT1 Time Correction		−0.469 s
Unit Conversions		
Units from/to	Exact	Approximate value
meter to foot	1/0.3048	3.28083989501312336
ft/s to knot conversion	1097.28/1852	0.59248380129589633
m/s to knot conversion	3600/1852	1.94384449244060475
kilogram to slug	0.3048/4.4482216152605	0.0685217658567917552
radians to degrees	$180/\pi$	57.2957795130823209

Table 74. Geopotential Harmonic Coefficients for Ellipsoidal Earth

Coefficient	Value	Coefficient	Value
$C_{2,0}$	$-4.8416499 \times 10^{-4}$	$S_{2,0}$	0
$C_{2,1}$	0	$S_{2,1}$	0
$C_{2,2}$	2.4389280×10^{-6}	$S_{2,2}$	$-1.3998397 \times 10^{-6}$
$C_{3,0}$	9.5723751×10^{-7}	$S_{3,0}$	0
$C_{3,1}$	2.0297737×10^{-6}	$S_{3,1}$	2.4959463×10^{-7}
$C_{3,2}$	9.0354910×10^{-7}	$S_{3,2}$	$-6.2041982 \times 10^{-7}$
$C_{3,3}$	7.2098662×10^{-7}	$S_{3,3}$	1.4131694×10^{-6}
$C_{4,0}$	5.3873219×10^{-7}	$S_{4,0}$	0
$C_{4,1}$	$-5.3342722 \times 10^{-7}$	$S_{4,1}$	$-4.7511891 \times 10^{-7}$
$C_{4,2}$	3.4700208×10^{-7}	$S_{4,2}$	6.6403042×10^{-7}
$C_{4,3}$	9.9097790×10^{-7}	$S_{4,3}$	$-2.0062149 \times 10^{-7}$
$C_{4,4}$	$-1.9003480 \times 10^{-7}$	$S_{4,4}$	3.0845955×10^{-7}
$C_{5,0}$	6.8780161×10^{-8}	$S_{5,0}$	0
$C_{5,1}$	$-5.8950310 \times 10^{-8}$	$S_{5,1}$	$-9.5543463 \times 10^{-8}$
$C_{5,2}$	6.5579025×10^{-7}	$S_{5,2}$	$-3.2340559 \times 10^{-7}$
$C_{5,3}$	$-4.4820358 \times 10^{-7}$	$S_{5,3}$	$-2.1513633 \times 10^{-7}$
$C_{5,4}$	$-2.9482361 \times 10^{-7}$	$S_{5,4}$	5.2408737×10^{-8}
$C_{5,5}$	1.7775628×10^{-7}	$S_{5,5}$	$-6.6602811 \times 10^{-7}$
$C_{6,0}$	$-1.4810038 \times 10^{-7}$	$S_{6,0}$	0
$C_{6,1}$	$-8.1375094 \times 10^{-8}$	$S_{6,1}$	2.3890050×10^{-8}
$C_{6,2}$	5.1609578×10^{-8}	$S_{6,2}$	$-3.7499560 \times 10^{-7}$
$C_{6,3}$	6.1970909×10^{-8}	$S_{6,3}$	4.6429830×10^{-9}
$C_{6,4}$	$-9.2797469 \times 10^{-8}$	$S_{6,4}$	$-4.7330695 \times 10^{-7}$
$C_{6,5}$	$-2.6576497 \times 10^{-7}$	$S_{6,5}$	$-5.3774724 \times 10^{-7}$
$C_{6,6}$	9.0593110×10^{-9}	$S_{6,6}$	$-2.3633442 \times 10^{-7}$
$C_{7,0}$	9.0533705×10^{-8}	$S_{7,0}$	0
$C_{7,1}$	2.7709714×10^{-7}	$S_{7,1}$	9.7817738×10^{-8}
$C_{7,2}$	3.1771079×10^{-7}	$S_{7,2}$	9.1608267×10^{-8}
$C_{7,3}$	2.5074289×10^{-7}	$S_{7,3}$	$-2.0916391 \times 10^{-7}$
$C_{7,4}$	$-2.7374044 \times 10^{-7}$	$S_{7,4}$	$-1.2202073 \times 10^{-7}$
$C_{7,5}$	3.4749784×10^{-9}	$S_{7,5}$	1.9651896×10^{-8}
$C_{7,6}$	$-3.5785266 \times 10^{-7}$	$S_{7,6}$	1.5091751×10^{-7}
$C_{7,7}$	1.5976040×10^{-9}	$S_{7,7}$	2.2001281×10^{-8}
$C_{8,0}$	4.5902321×10^{-8}	$S_{8,0}$	0
$C_{8,1}$	2.8856051×10^{-8}	$S_{8,1}$	5.4722278×10^{-8}
$C_{8,2}$	7.0380074×10^{-8}	$S_{8,2}$	6.8449357×10^{-8}
$C_{8,3}$	$-1.9966400 \times 10^{-8}$	$S_{8,3}$	$-8.6936688 \times 10^{-8}$
$C_{8,4}$	$-2.4606388 \times 10^{-7}$	$S_{8,4}$	6.7745274×10^{-8}
$C_{8,5}$	$-2.4933453 \times 10^{-8}$	$S_{8,5}$	8.5300324×10^{-8}
$C_{8,6}$	$-6.6417800 \times 10^{-8}$	$S_{8,6}$	3.1283228×10^{-7}
$C_{8,7}$	7.0424829×10^{-8}	$S_{8,7}$	7.4862572×10^{-8}
$C_{8,8}$	$-1.1888272 \times 10^{-7}$	$S_{8,8}$	1.2233200×10^{-7}

designations (SIM A, SIM B, etc.) to identify the various simulations. Two of these simulation tools are represented in both atmospheric and orbital results.

Simulation developers were free to pick the numerical integration time step sizes and integration methods that they felt gave the most accurate results. There was no requirement to run in real-time (e.g., pilot- or hardware-in-the-loop).

In plotting differences from average, a difficulty was encountered with angles restricted to fall within a range of values. For example, vehicle yaw angle ψ is kept within $-180 \leq \theta \leq +180$ degrees. When calculating a difference or an average on these values, as soon as one simulation tool performs the wrap limit, the numerical difference or average of the ensemble makes no sense. For this reason, the Euler angles and angles of latitude and longitude are not differenced against some average. Instead, the angle difference between two angles α and β is calculated using the trigonometric angle difference equation 37:

$$\alpha - \beta = \arctan \frac{\sin\alpha\cos\beta - \cos\alpha\sin\beta}{\cos\alpha\cos\beta + \sin\alpha\sin\beta} \tag{37}$$

In this report, the angles estimated by SIM 5 and SIM B are used as the somewhat arbitrary reference, since they are present in most check-cases and appear reasonable.

Table 75 provides a description of the output quantities that are compared in the ensuing trajectory plots. These variable names are based on the S-119 standard and often include units-of-measure as a suffix.

Table 75. Check-case Output Parameters

Parameter label	Units	Size	Description (sign convention)
aero_bodyForce	lbf	3-vector	Aerodynamic forces resolved into body x-y-z axes
aero_bodyMoment	ft-lbf	3-vector	Aerodynamic moments about the CM, resolved into body x-y-z axes
airDensity	$\frac{\text{kg}}{\text{m}^3}$ or $\frac{\text{slug}}{\text{ft}^3}$	scalar	Atmospheric density
altitudeMsl	ft or m	scalar	Geometric altitude above reference ellipsoid, sphere, or plane
altitudeRateWrtMsl	ft/min	scalar	Rate of climb relative to reference surface (+up)
ambientPressure	lbf/ft^2	scalar	Atmospheric (static) pressure
ambientTemperature	K or °R	scalar	Atmospheric (static) temperature
bodyAngularRateWrtEi	$\frac{rad}{s}$ or $\frac{deg}{s}$	3-vector	Pitch, roll and yaw rates around body x-y-z axes with respect to ECI frame
bodyLocalGravitation	m/s^2	3-vector	Gravitational acceleration resolved into body x-y-z axes
dynamicPressure	lbf/ft^2	scalar	Dynamic pressure due to relative motion between vehicle and the surrounding atmosphere
eiAccel	m/s^2	3-vector	Acceleration of the vehicle's CM with respect to the ECI frame, resolved in the ECI X-Y-Z axes
eiPosition	ft or m	3-vector	Position of the vehicle's CM with respect to the ECI frame, resolved in the ECI X-Y-Z axes
eiVelocityWrtEi or eiVelocity	ft/s or m/s	3-vector	Velocity of the vehicle's CM with respect to the ECI frame, resolved in the ECI X-Y-Z axes
eulerAngle	deg or rad	3-vector	Attitude of the vehicle with respect to the LVLH frame (orbital check-cases) or NED frame (atmospheric check-cases), resolved into pitch, roll and yaw angles using a 3-2-1 sequence
feVelocity	ft/s	3-vector	Velocity of the vehicle's CM with respect to the flat-Earth frame, resolved in the N-E-D axes
gast	rad	scalar	Rotation angle of Earth (Greenwich Apparent Sidereal Time)
gePosition	ft or m	3-vector	Position of the vehicle's CM with respect to the ECEF frame, resolved in the ECEF X-Y-Z axes
latitude	deg	scalar	Position of the vehicle's CM given as the geodetic latitude
localGravity	ft/s^2	scalar	Gravitational acceleration of the vehicle's CM in the local "down" direction
longitude	deg	scalar	Position of the vehicle's CM given as the geodetic longitudinal
mach	–	scalar	Mach number
speedOfSound	ft/s	scalar	Sonic velocity in the atmosphere at the current altitude
trueAirspeed	nmi/h (kt)	scalar	Velocity of the vehicle's CM with respect to the surrounding atmosphere

D.1 Scenario comparisons – Atmospheric

D.1.1 Check-case 1 – dragless sphere

This section shows cross-plots for six of the selected simulation tools in modeling the dynamics of a dragless spheroid, accelerating towards the surface of the Earth from 30,000 ft above the Equator. This scenario is described in Section C.1.1. Figures 16a through 16x compare results between the six simulation tools, as well as the deviances of the outputs from each tool from the ensemble average value.

In this check-case the atmospheric forces and moments acting on the vehicle were zero. The inertial rotational rate expressed in body coordinates (p, q, r) was also zero. Thus, the apparent rotation of the sphere with respect to the Earth was due to the Earth's rotation and, given the initial north-up orientation of the sphere, caused only the roll angle to change. All the simulations accurately produced these outcomes.

The translational motion of the sphere was governed only by gravitation and the centrifugal and Coriolis accelerations due to the Earth's rotation. The net effect of the stronger gravitation acting against the weaker centrifugal accelerations caused the sphere to descend and the Coriolis acceleration caused the sphere to travel slightly eastward. In general, the simulations agreed in the translational motion of the sphere. The differences shown were less than 0.01 inches in position and 0.01 in/s in velocity. The differences shown were assumed to reflect differences in numerical integration techniques used by the different simulation tools.

For atmospheric properties, there was close agreement among the simulations for temperature. However, for atmospheric density and pressure, only SIM 3, 4, 5, and 6 came to consensus. The difference between SIM 1, SIM 2, and the consensus group was the result of different approaches to implementing the U.S. Standard Atmosphere 1976 Model. The consensus group solved the actual mathematical equations for temperature, pressure, and density. On the other hand, SIM 1 and SIM 2 used lookup tables with linear interpolation between breakpoints. SIM 1 used a table with 1,000-meter breakpoints; SIM 2 used a table with 500-meter breakpoints. Because the temperature formula is a linear function, linear interpolation produced no temperature differences between SIM 1, SIM 2, and the consensus group. However, pressure and density are not linear functions; therefore, the difference in density and pressure between SIM 1, SIM 2, and the consensus group depicted a hill-and-valley pattern, in which each valley of near-zero difference was associated with a break-point in the lookup table. The hill pattern difference in density also caused the hill-and-valley pattern difference seen for SIM 1 in dynamic pressure.

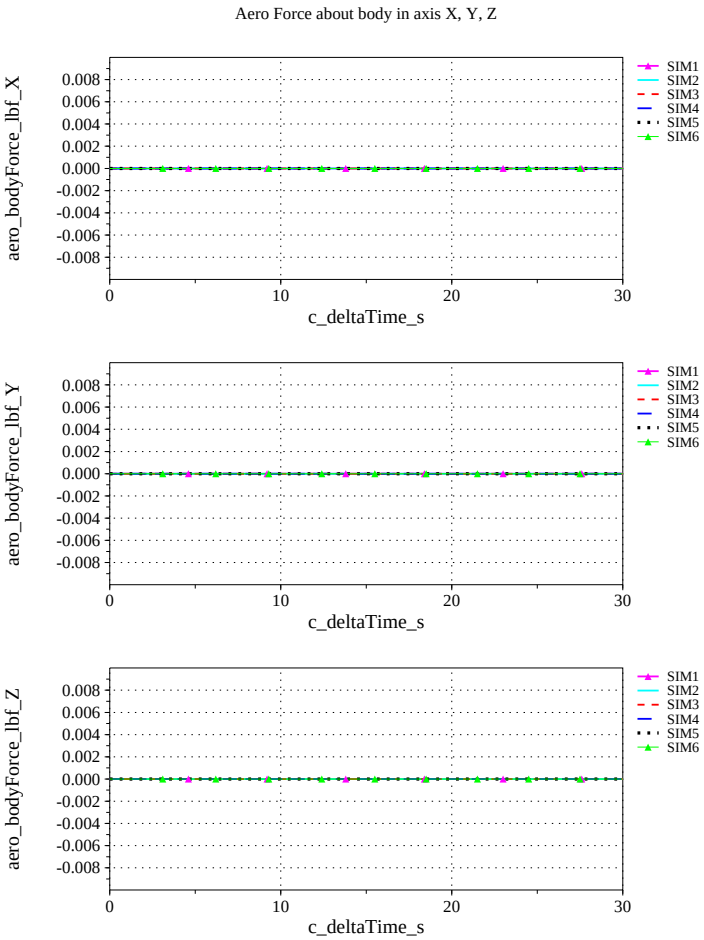

(a) Aerodynamic Forces Compared

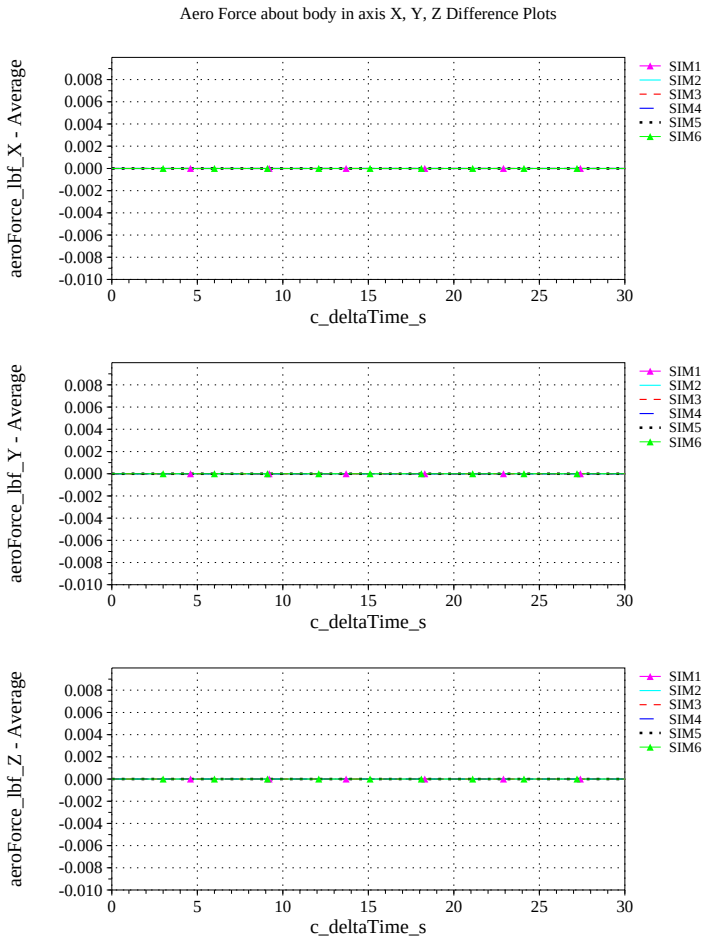

(b) Aerodynamic Forces Differenced

Figure 16. Check-case 1: Dragless Sphere; See Discussion in Section D.1.1

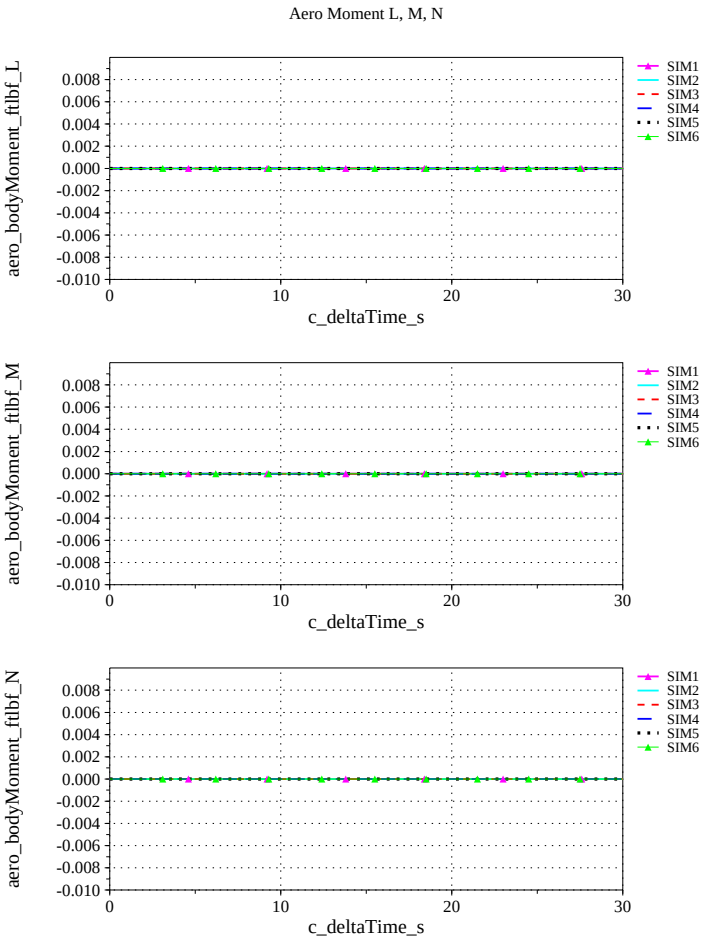

(c) Aerodynamic Moments Compared

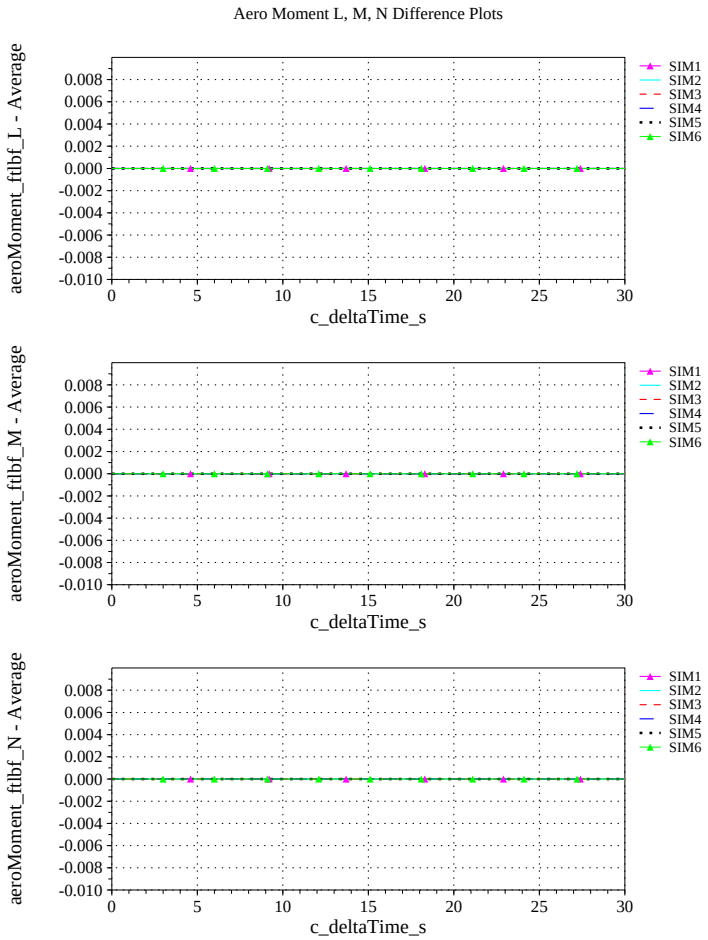

(d) Aerodynamic Moments Differenced

Figure 16. Check-case 1: Dragless Sphere; See Discussion in Section D.1.1 (Cont'd)

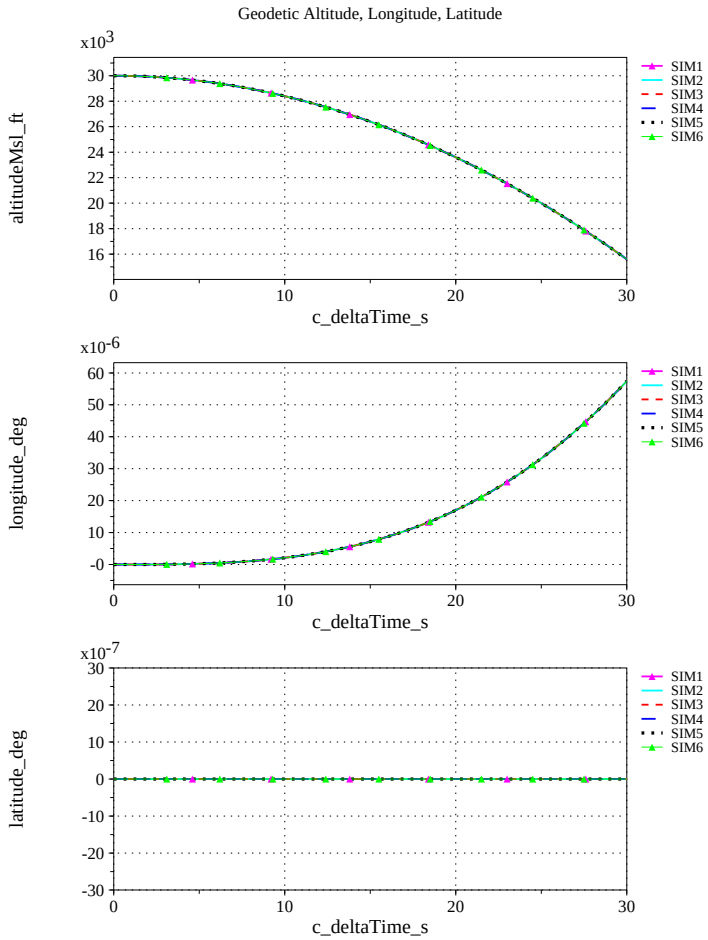

(e) Altitude, Geodetic Latitude and Longitude Compared

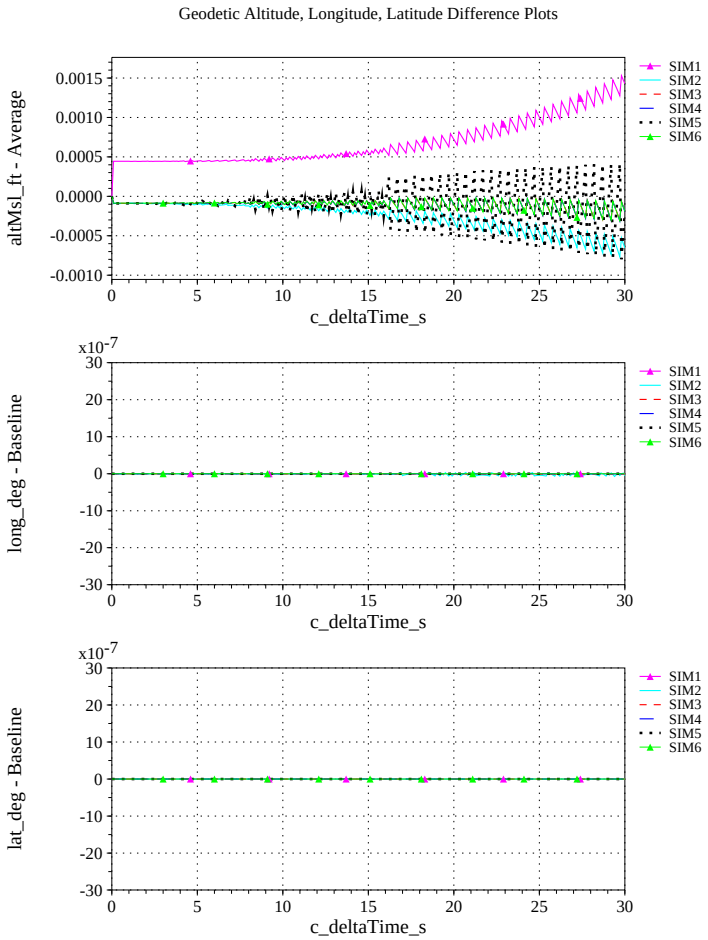

(f) Altitude, Geodetic Latitude and Longitude Differenced

Figure 16. Check-case 1: Dragless Sphere; See Discussion in Section D.1.1 (Cont'd)

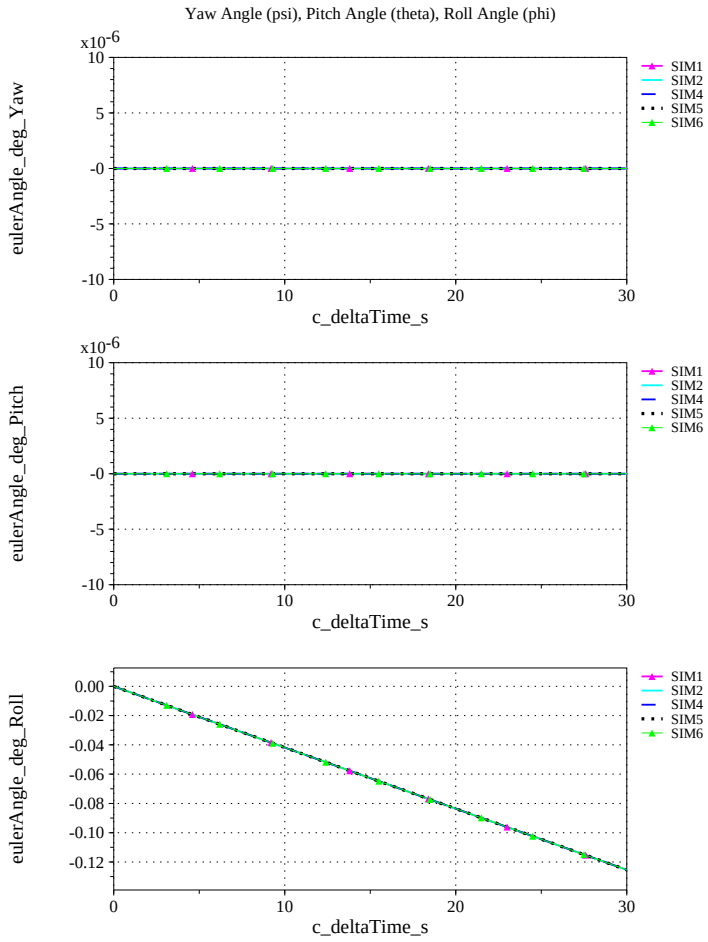

(g) Euler Angles (w.r.t. NED Frame) Compared

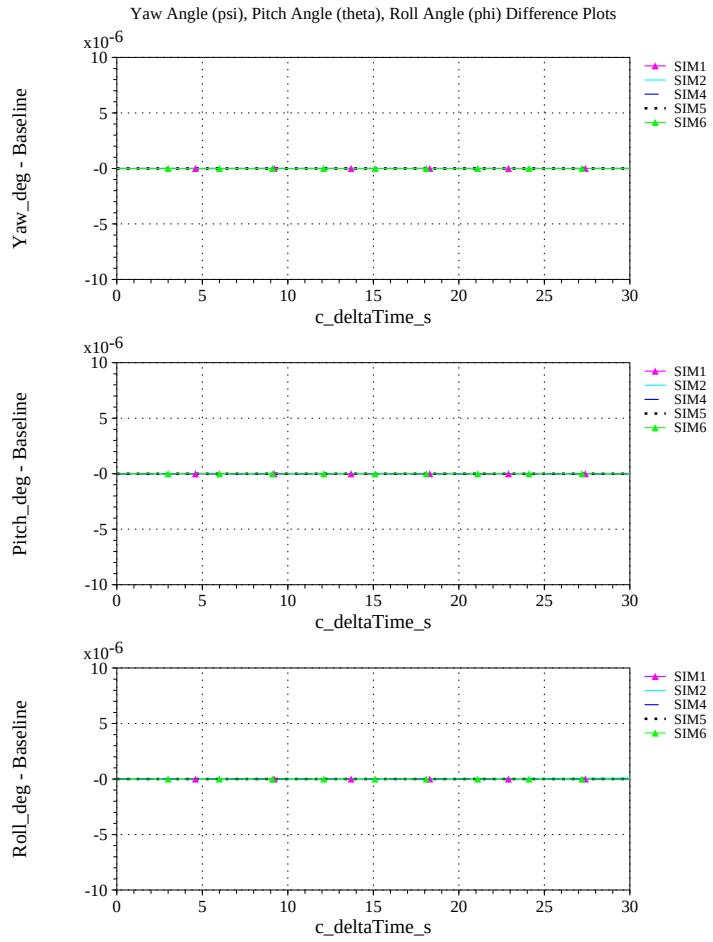

(h) Euler Angles (w.r.t. NED Frame) Differenced

Figure 16. Check-case 1: Dragless Sphere; See Discussion in Section D.1.1 (Cont'd)

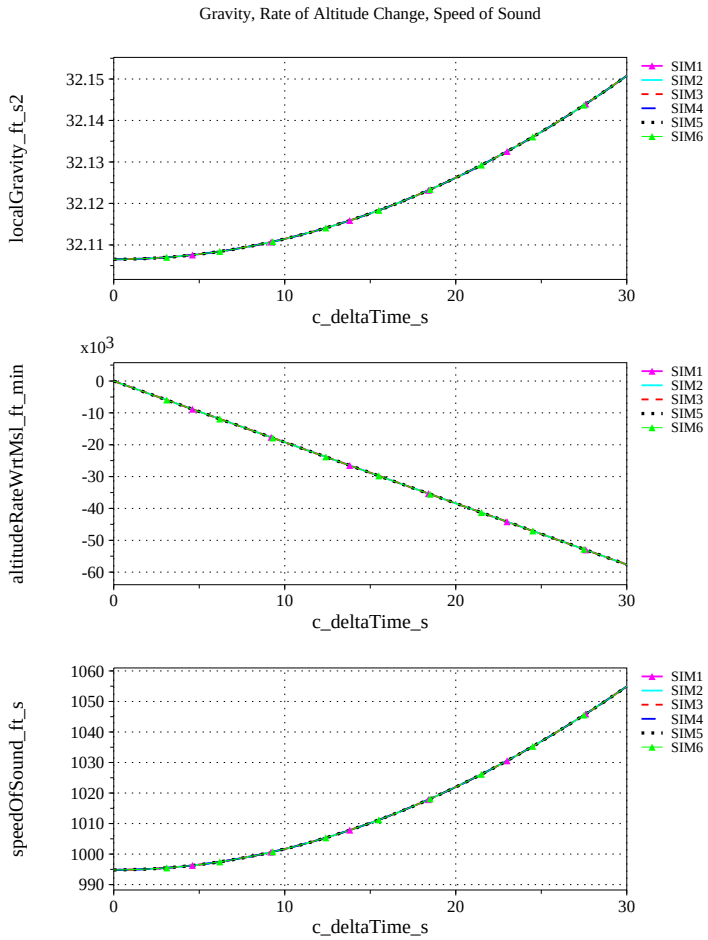

(i) Gravity, Climb Rate, and Speed-of-sound Compared

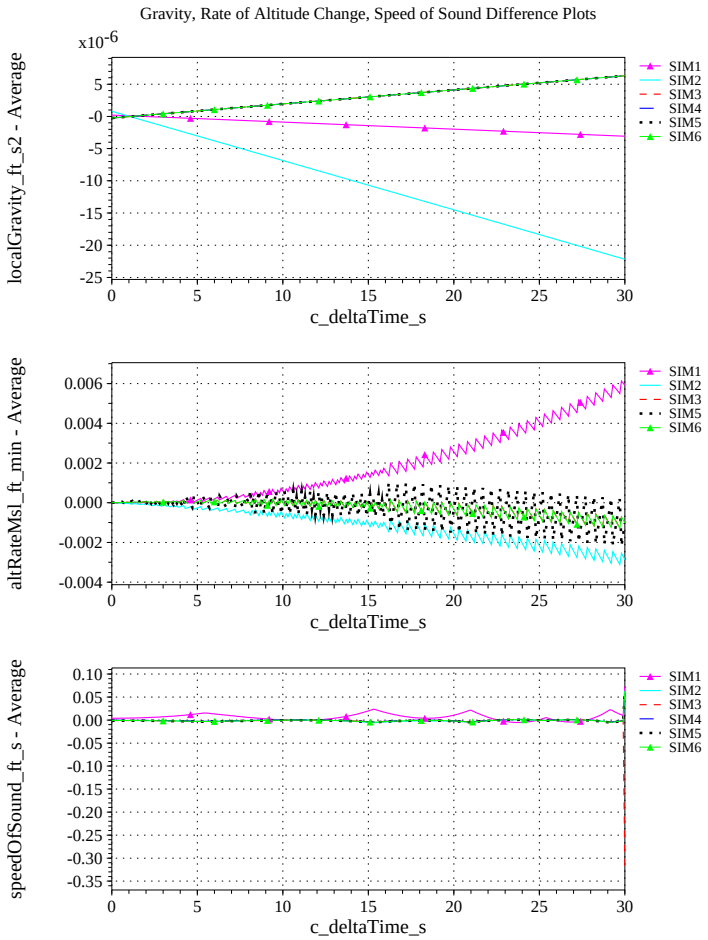

(j) Gravity, Climb Rate, and Speed-of-sound Differenced

Figure 16. Check-case 1: Dragless Sphere; See Discussion in Section D.1.1 (Cont'd)

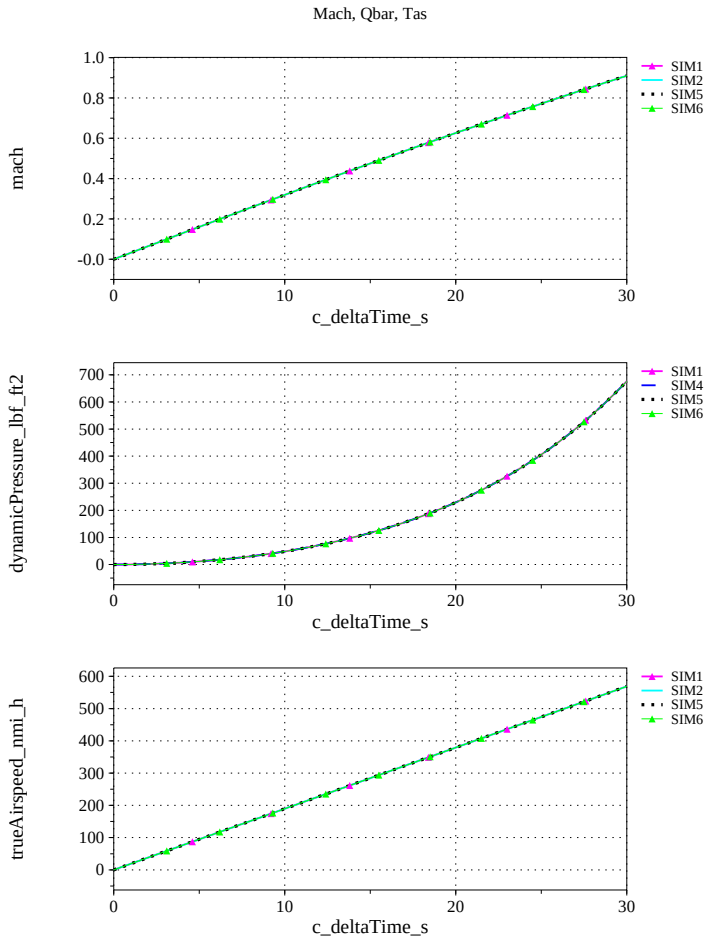

(k) Mach, Dynamic Pressure, and True Airspeed Compared

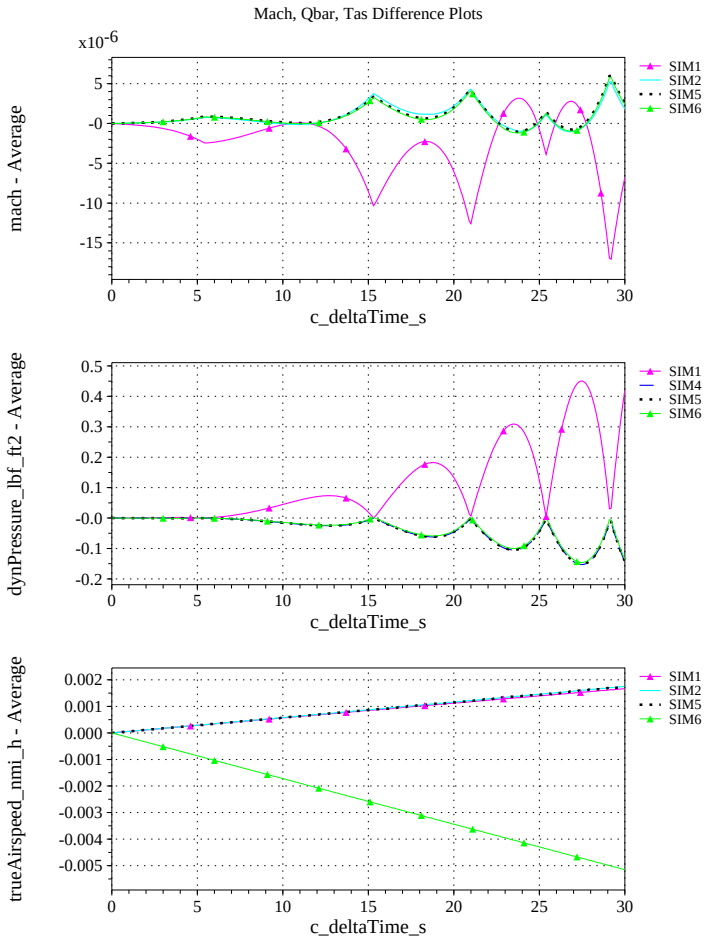

(l) Mach, Dynamic Pressure, and True Airspeed Differenced

Figure 16. Check-case 1: Dragless Sphere; See Discussion in Section D.1.1 (Cont'd)

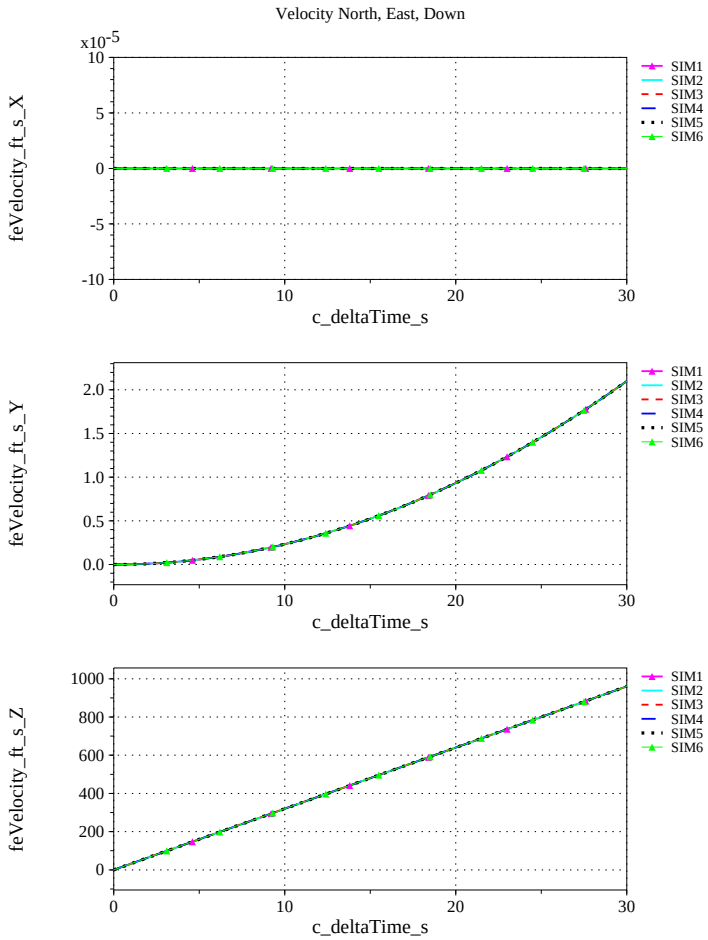

(m) NED Velocities Compared

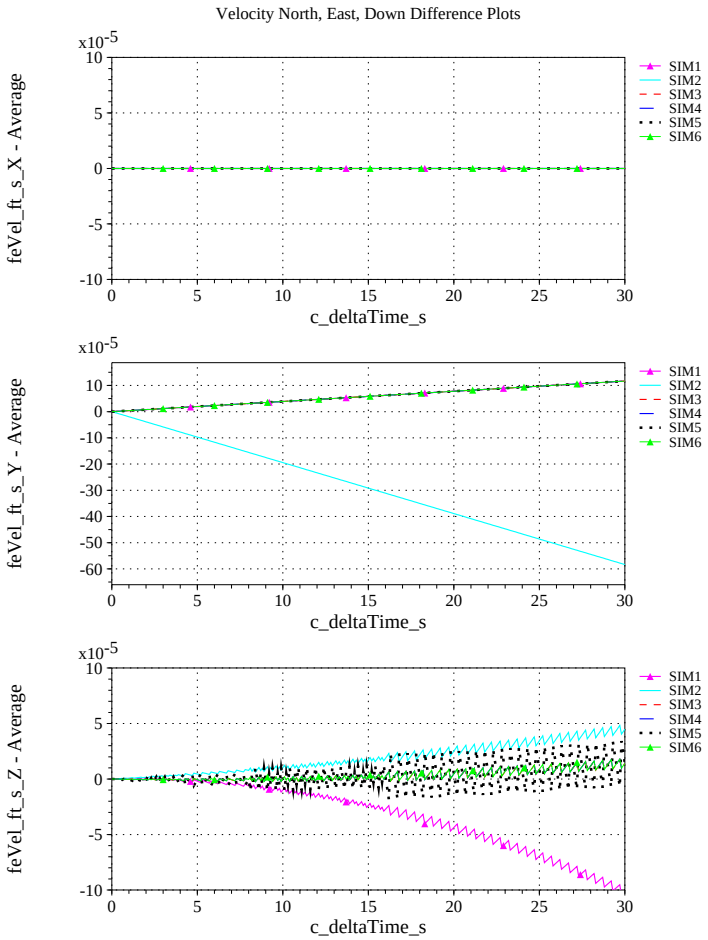

(n) NED Velocities Differenced

Figure 16. Check-case 1: Dragless Sphere; See Discussion in Section D.1.1 (Cont'd)

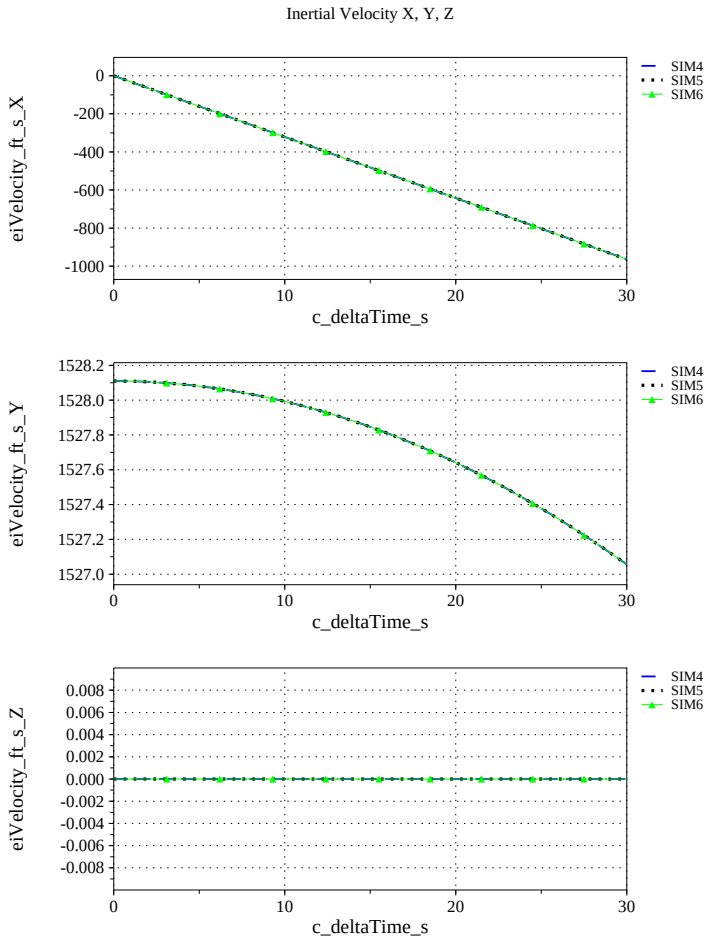

(o) Inertial Velocities Compared

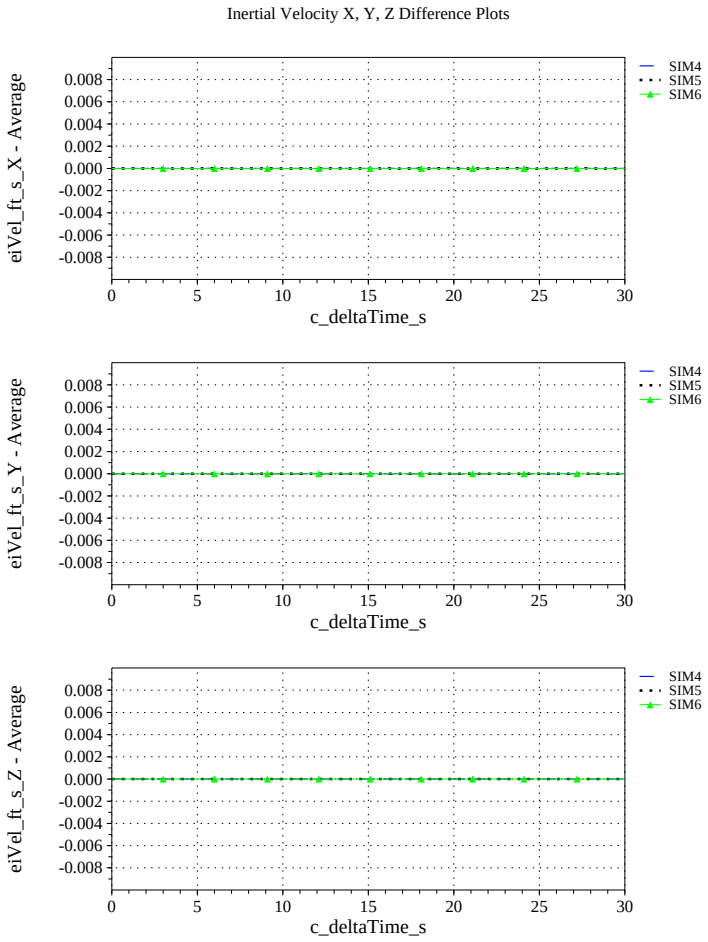

(p) Inertial Velocities Differenced

Figure 16. Check-case 1: Dragless Sphere; See Discussion in Section D.1.1 (Cont'd)

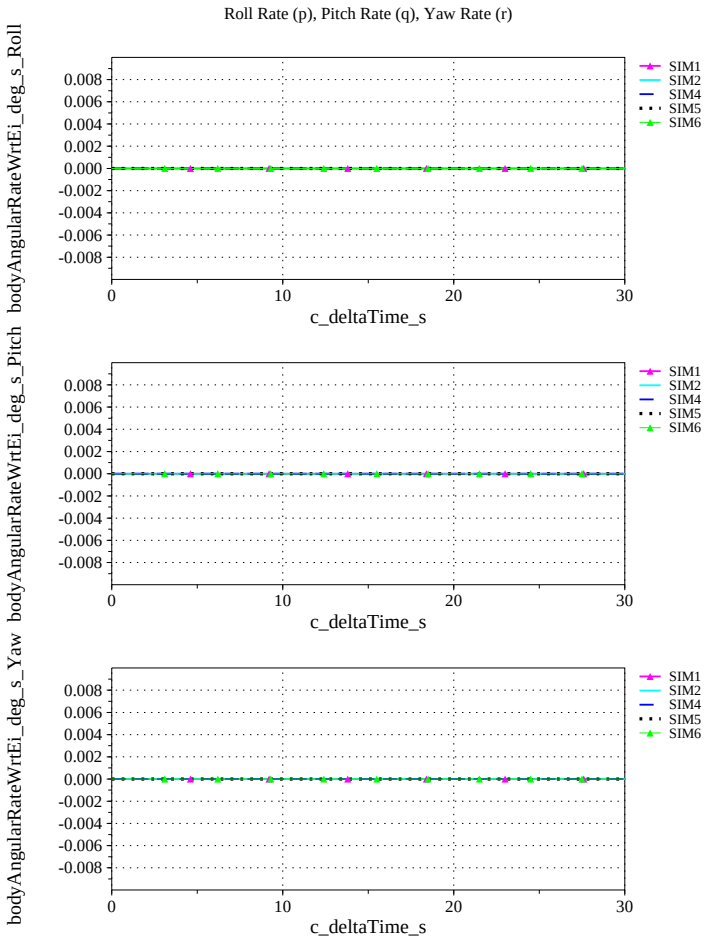

(q) Body-axis Angular Rates (w.r.t. NED Frame) Compared

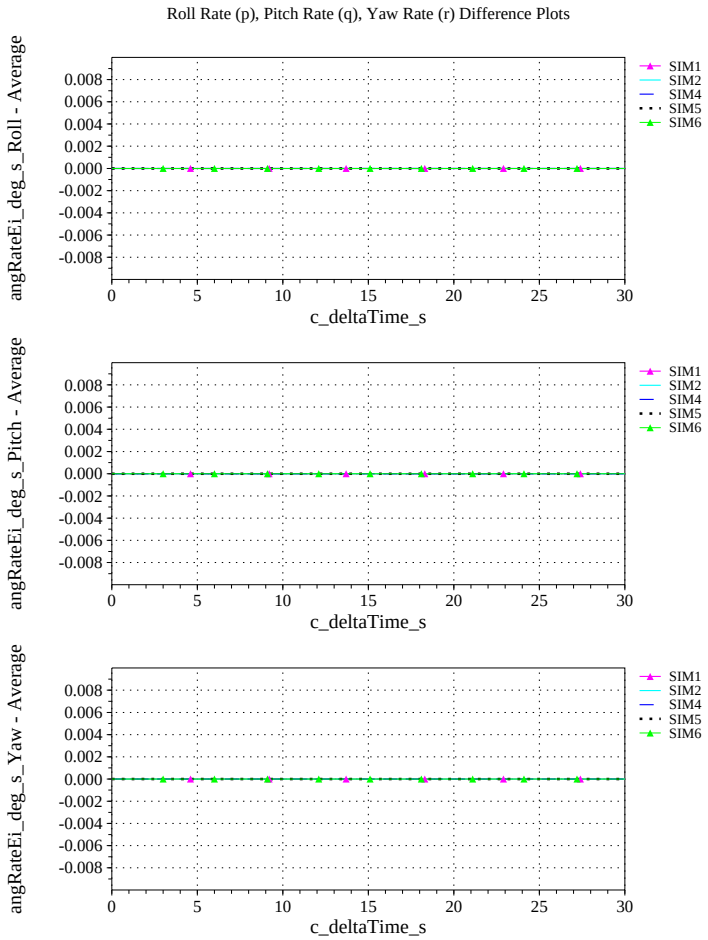

(r) Body-axis Angular Rates (w.r.t. NED Frame) Differenced

Figure 16. Check-case 1: Dragless Sphere; See Discussion in Section D.1.1 (Cont'd)

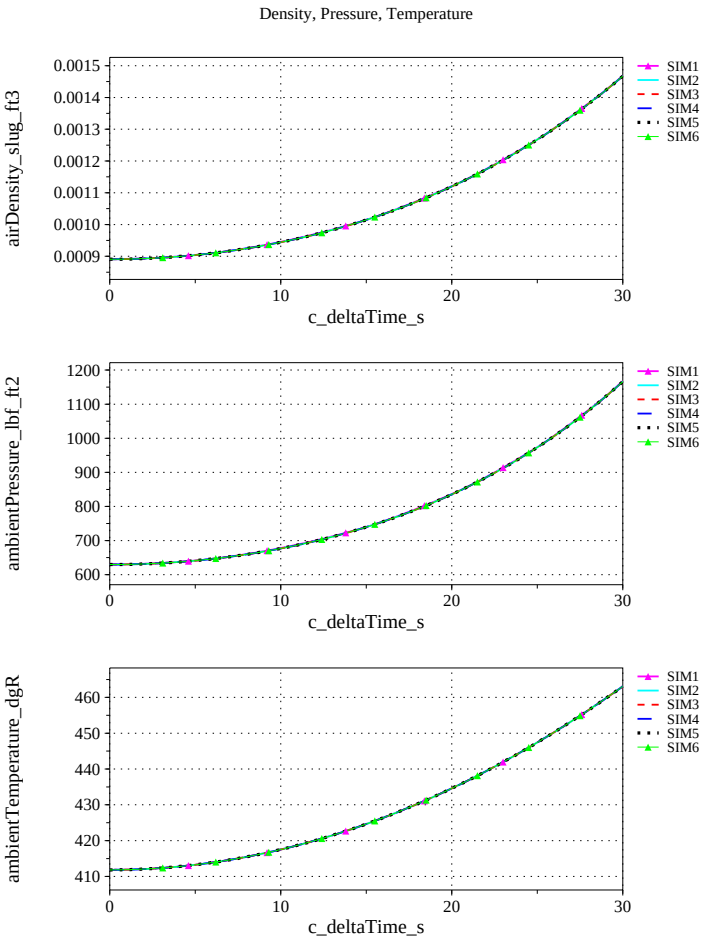

(s) Atmospheric Properties Compared

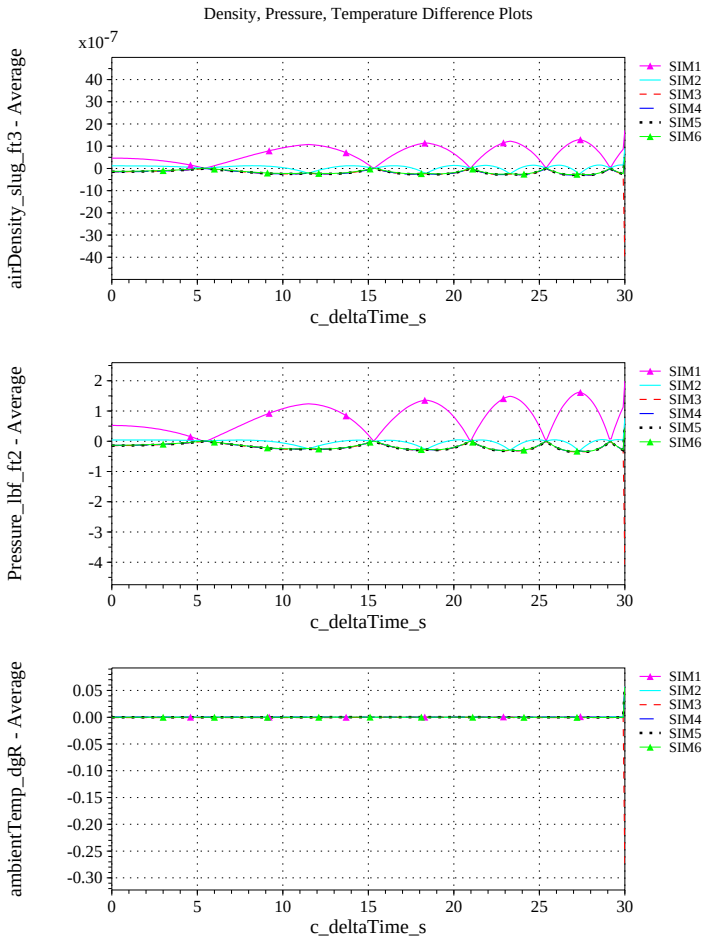

(t) Atmospheric Properties Differenced

Figure 16. Check-case 1: Dragless Sphere; See Discussion in Section D.1.1 (Cont'd)

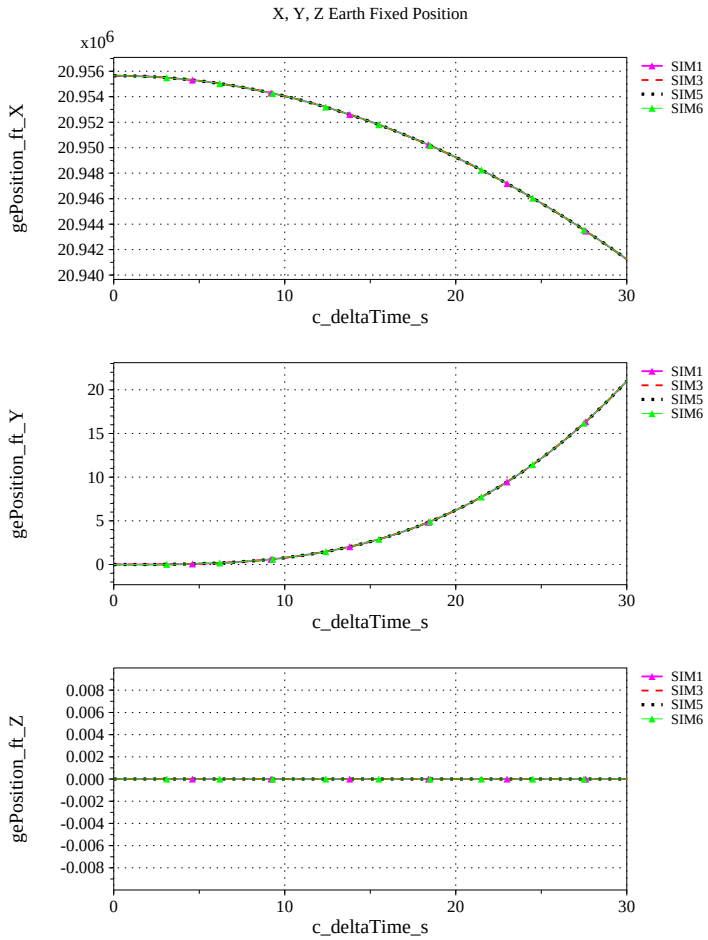

(u) Earth-centered, Earth-fixed Rectangular (X-Y-Z) Positions Compared

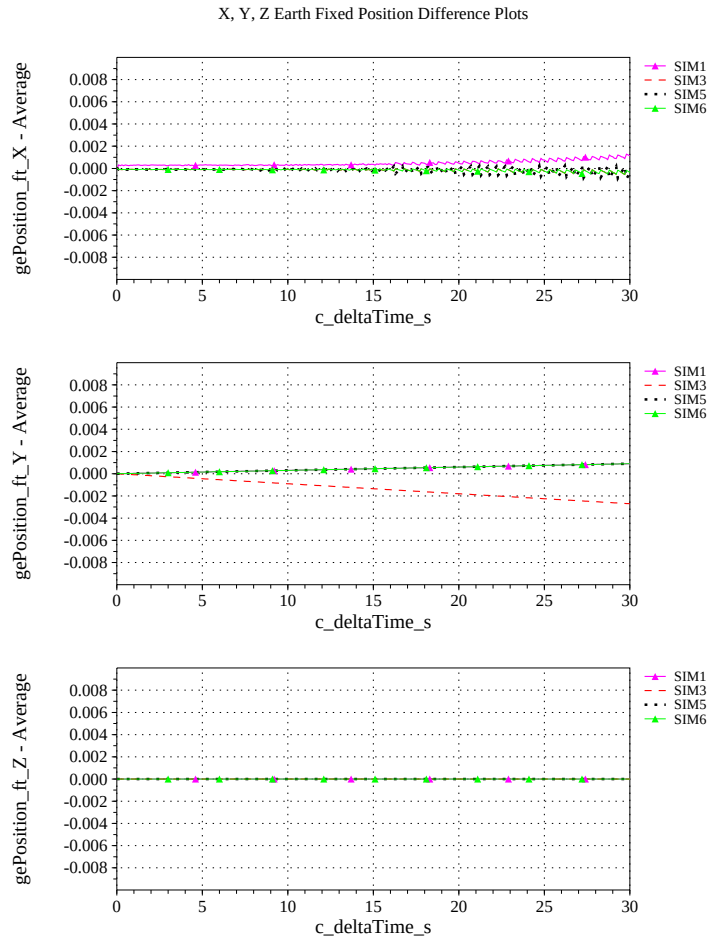

(v) Earth-centered, Earth-fixed Rectangular (X-Y-Z) Positions Differenced

Figure 16. Check-case 1: Dragless Sphere; See Discussion in Section D.1.1 (Cont'd)

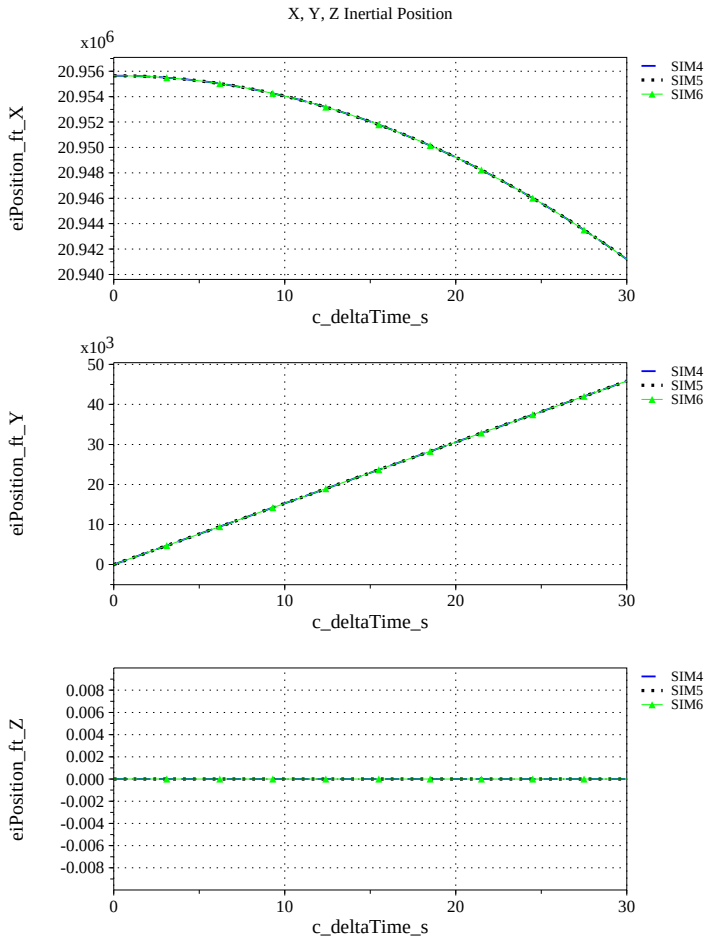

(w) Earth-centered Inertial Rectangular (x-y-z) Positions Compared

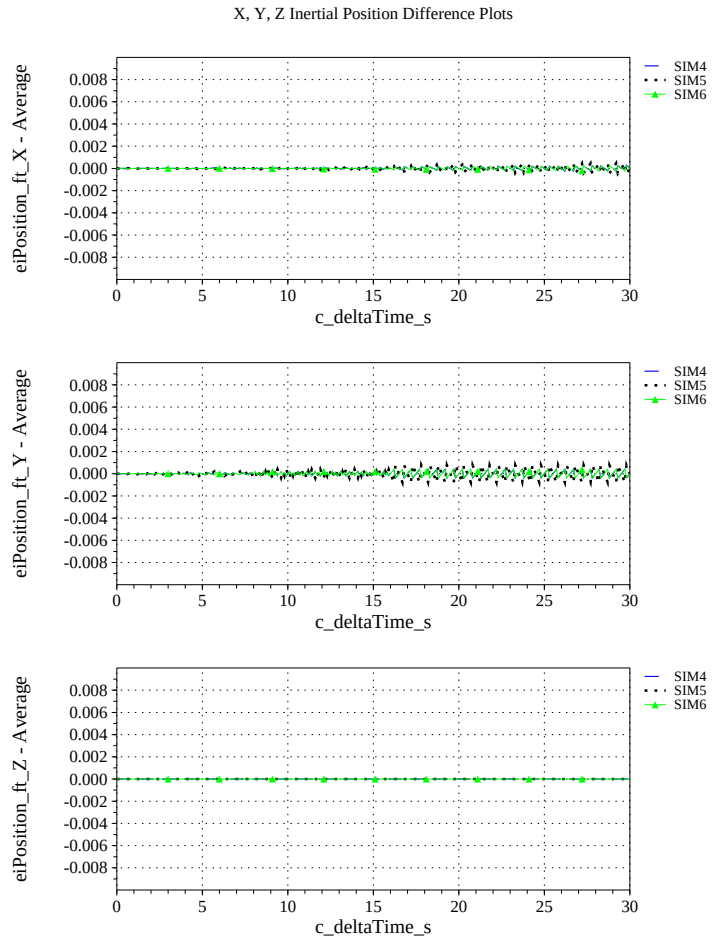

(x) Earth-centered Inertial Rectangular (x-y-z) Positions Differenced

Figure 16. Check-case 1: Dragless Sphere; See Discussion in Section D.1.1 (Concluded)

D.1.2 Check-case 2 – dragless tumbling brick

This section shows cross-plots for five of the selected simulation tools in modeling the dynamics of a dragless tumbling brick with no damping accelerating towards the surface of the Earth from 30,000 ft above the Equator and with an initial inertial angular rate (10, 20 and 30 deg/s, respectively, in the body axis system). This scenario is described in Section C.1.2. Figures 17a through 17x compare results between the five simulation tools, as well as the deviances of the outputs from each tool from the ensemble average value.

Although the simulated vehicle changed from a sphere to a brick, gravitation remains the only external force acting on the vehicle in this check-case. Therefore, the translational motion in this scenario was identical to the previous one (Check-case 1 – dragless sphere). As with check-case 1, all simulations agreed on translational states to better than 0.01 inches in position and 0.01 in/s in velocity. Likewise, the results for atmospheric properties, which were functions of position, are identical to those in case 1. The differences presented were due to the difference between algebraic and linear table interpolation implementations of the atmosphere model.

Rotational dynamics were the focus of this check-case. This scenario simulated a brick with a constant angular momentum. The resulting inertial angular rates expressed in body coordinates (i.e., p, q, and r) were sinusoids with a constant amplitude and frequency. The simulations generally agreed on the angular rates to within 0.004 deg/s. These differences are assumed to reflect differences in the numerical integration methods between the simulations when integrating angular accelerations into angular rates. For orientation, all simulations except SIM 2 were in close agreement. The Euler angle solution from SIM 2 slowly diverged from the other simulations over time with differences approaching ± 4 degrees after $t = 30$ sec. This difference appears to result from the difference in the integration method of SIM 2 for the integral that integrated orientation from the angular rates.

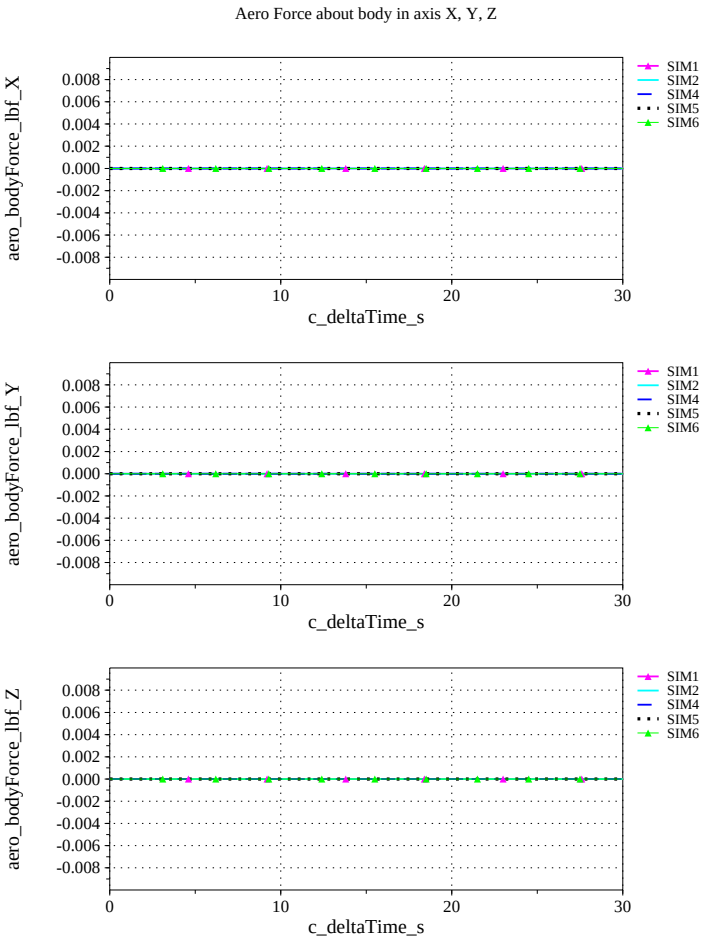

(a) Aerodynamic Forces Compared

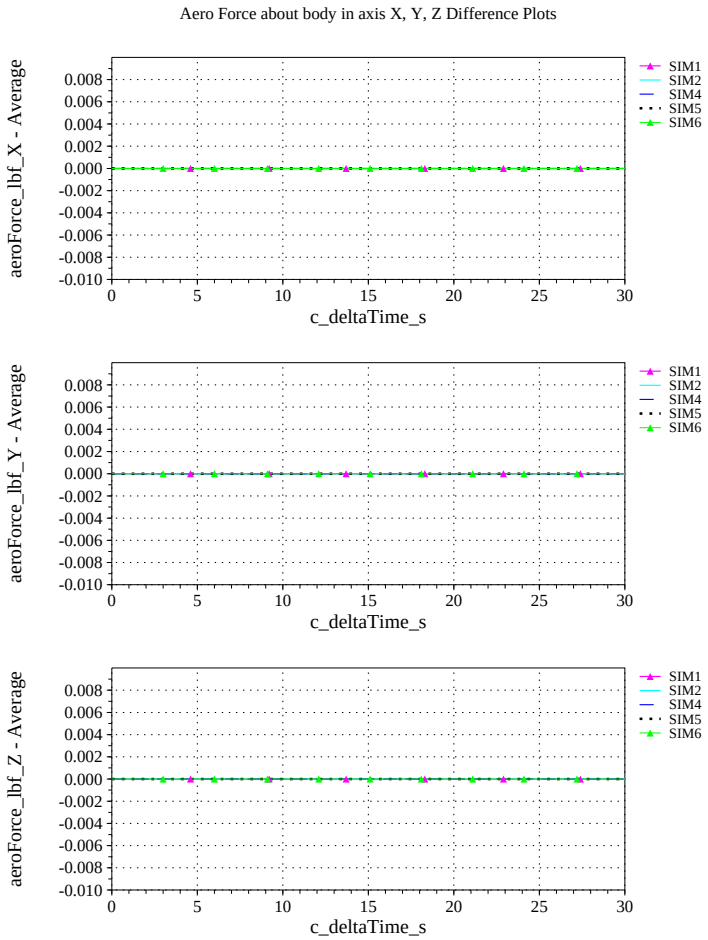

(b) Aerodynamic Forces Differenced

Figure 17. Check-case 2: Dragless Tumbling Brick; See Discussion in Section D.1.2

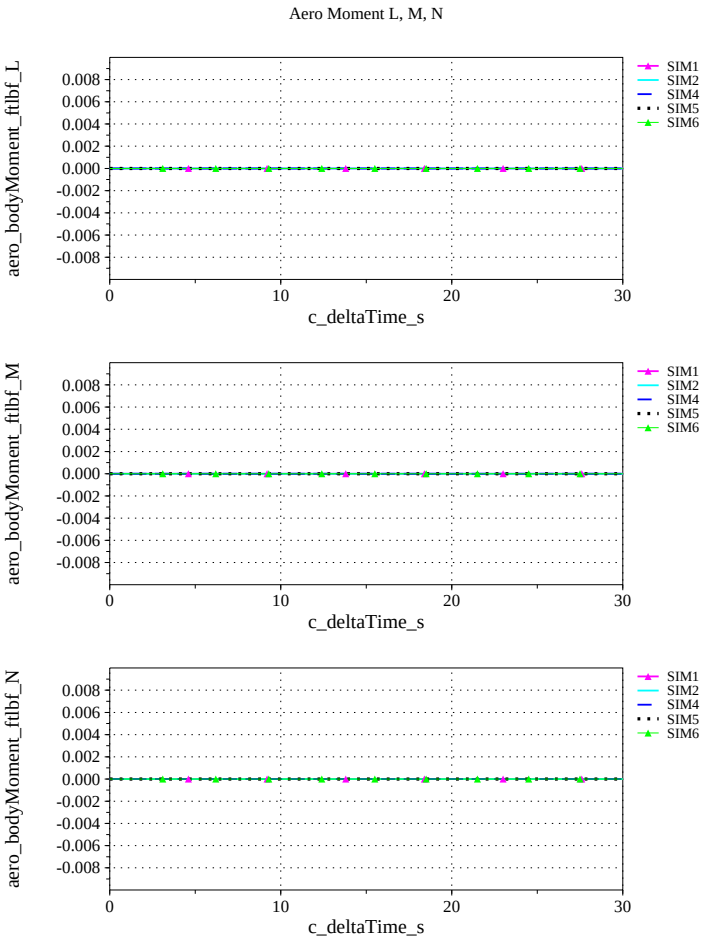

(c) Aerodynamic Moments Compared

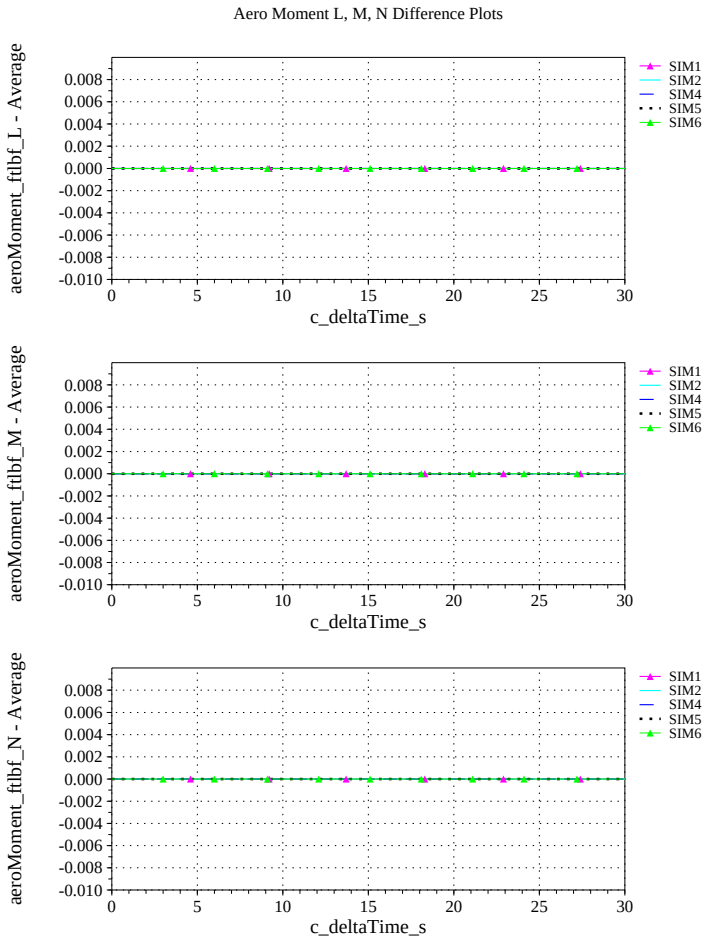

(d) Aerodynamic Moments Differenced

Figure 17. Check-case 2: Dragless Tumbling Brick; See Discussion in Section D.1.2 (Cont'd)

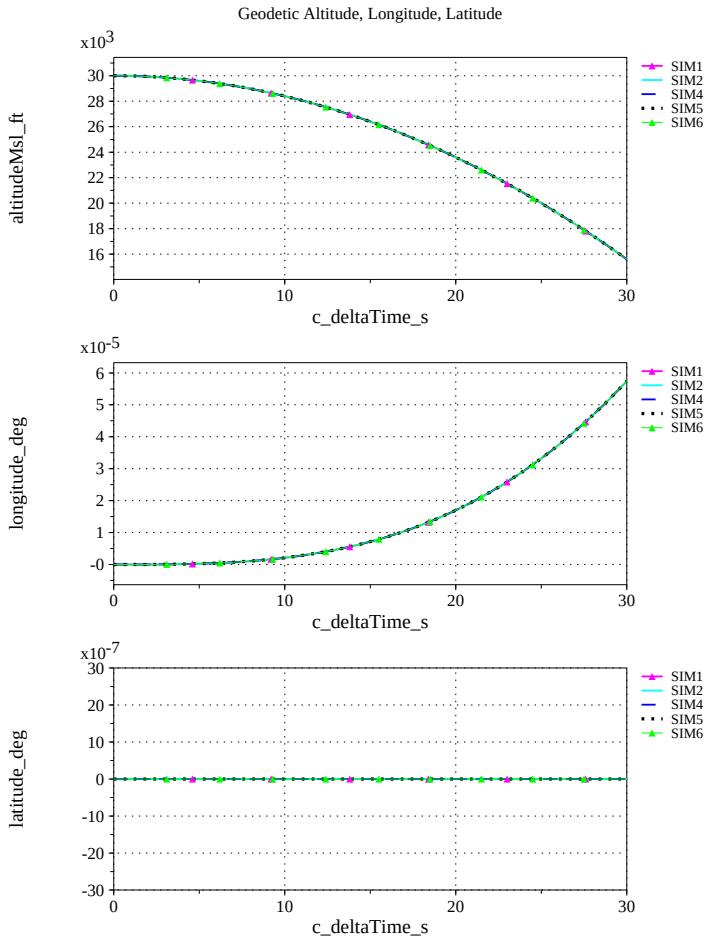

(e) Altitude, Geodetic Latitude and Longitude Compared

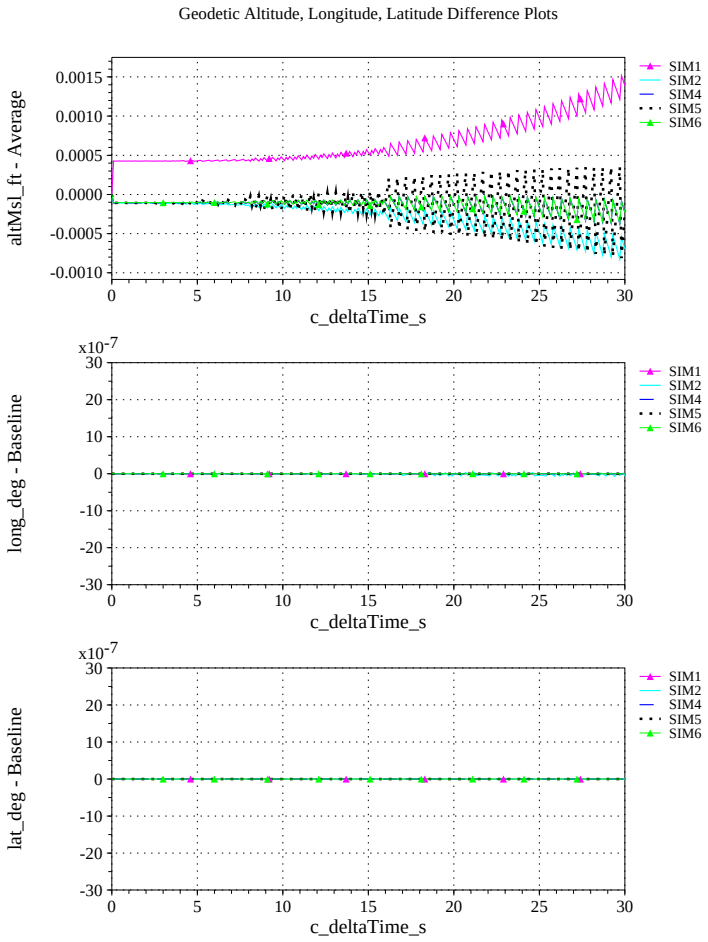

(f) Altitude, Geodetic Latitude and Longitude Differenced

Figure 17. Check-case 2: Dragless Tumbling Brick; See Discussion in Section D.1.2 (Cont'd)

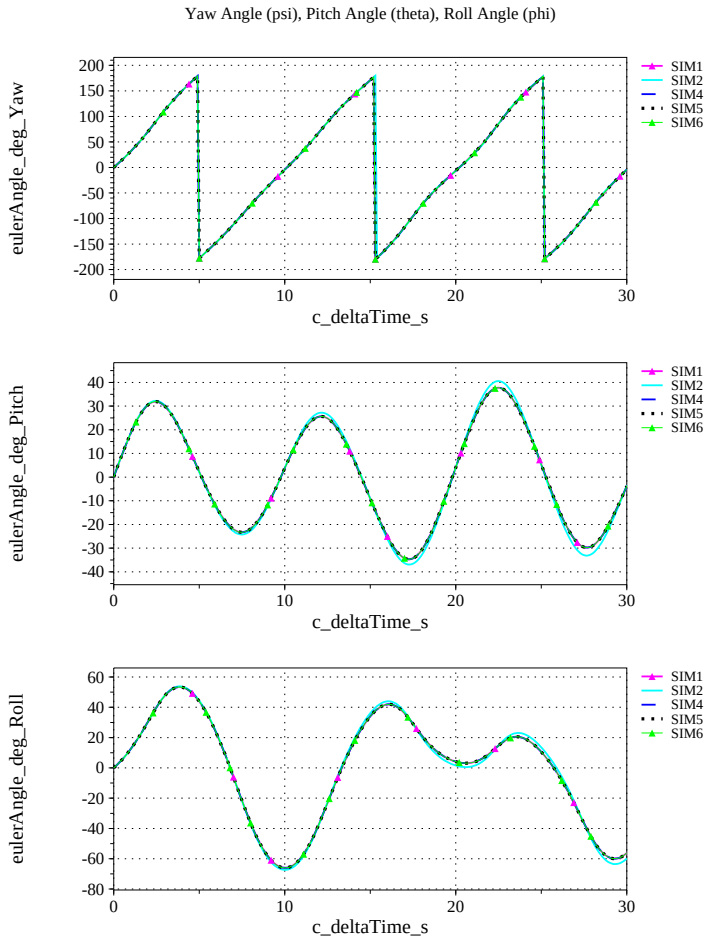

(g) Euler Angles (w.r.t. NED Frame) Compared

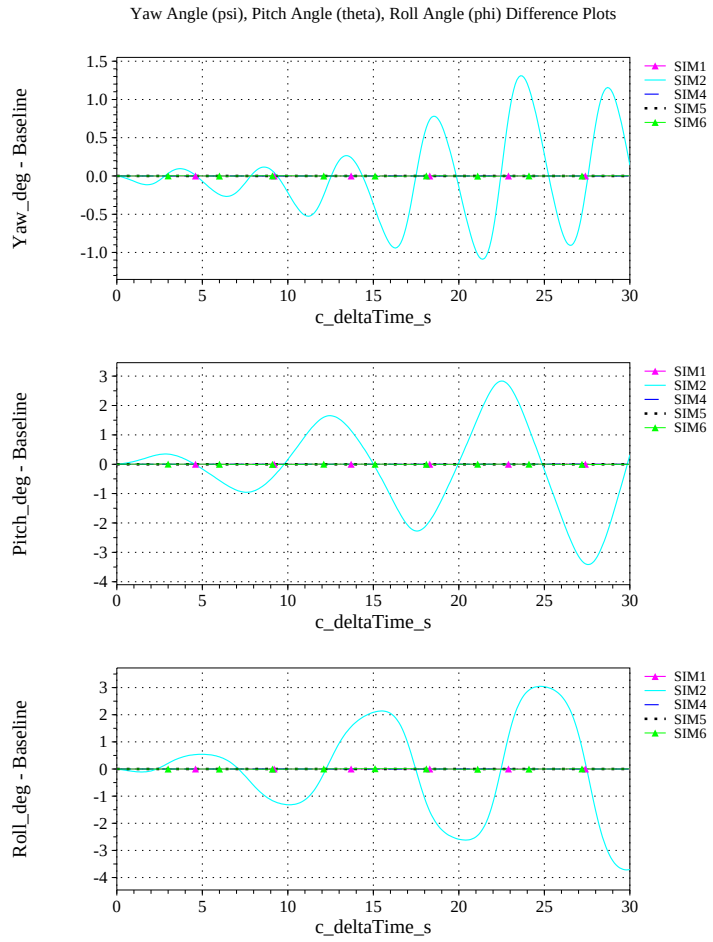

(h) Euler Angles (w.r.t. NED Frame) Differenced

Figure 17. Check-case 2: Dragless Tumbling Brick; See Discussion in Section D.1.2 (Cont'd)

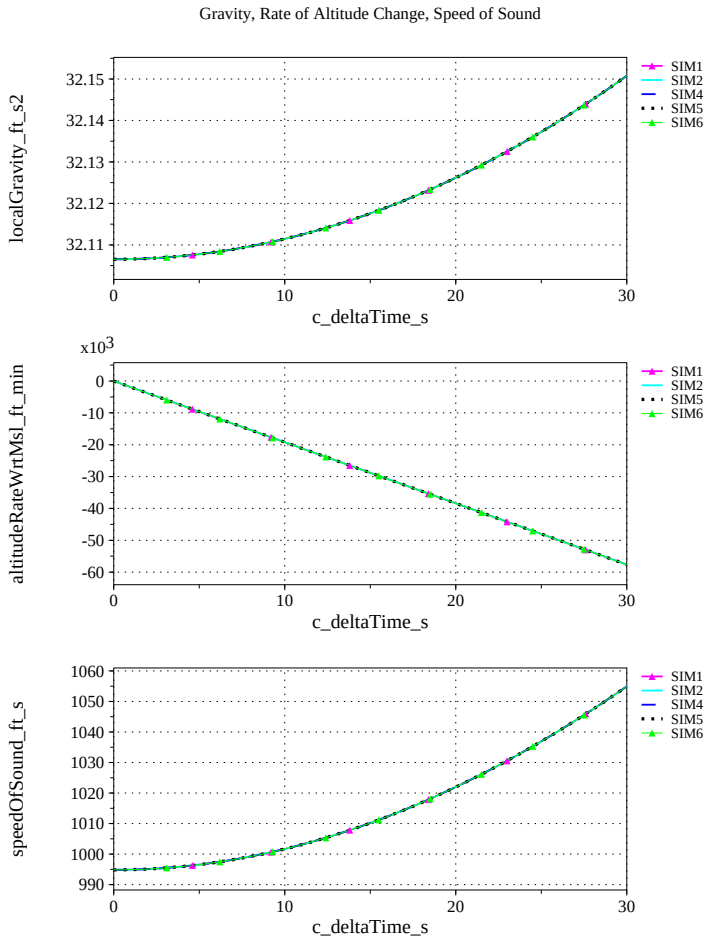

(i) Gravity, Climb Rate, and Speed-of-sound Compared

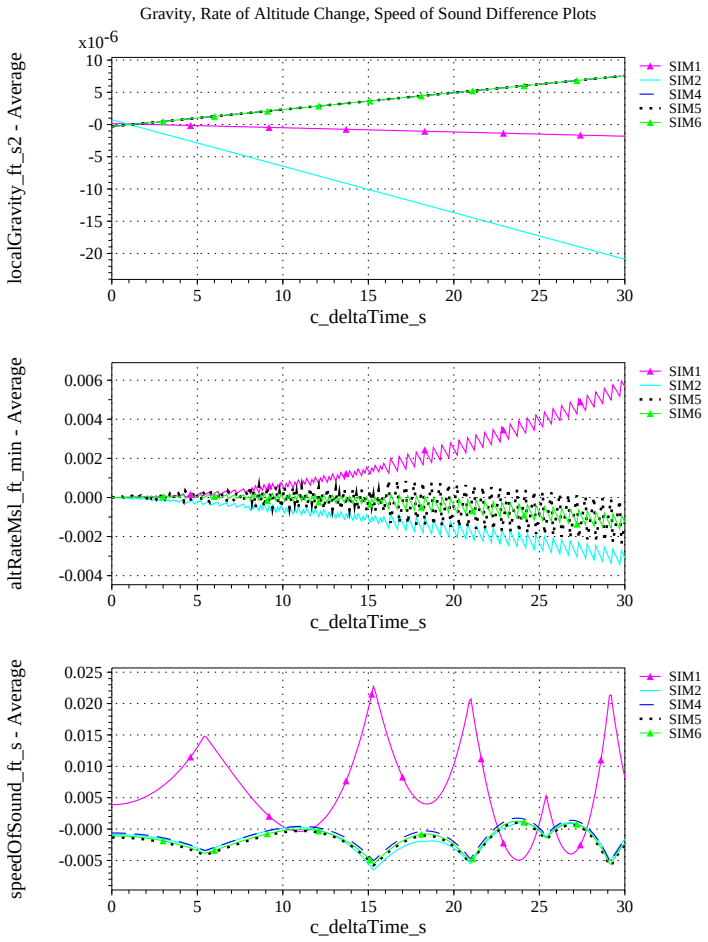

(j) Gravity, Climb Rate, and Speed-of-sound Differenced

Figure 17. Check-case 2: Dragless Tumbling Brick; See Discussion in Section D.1.2 (Cont'd)

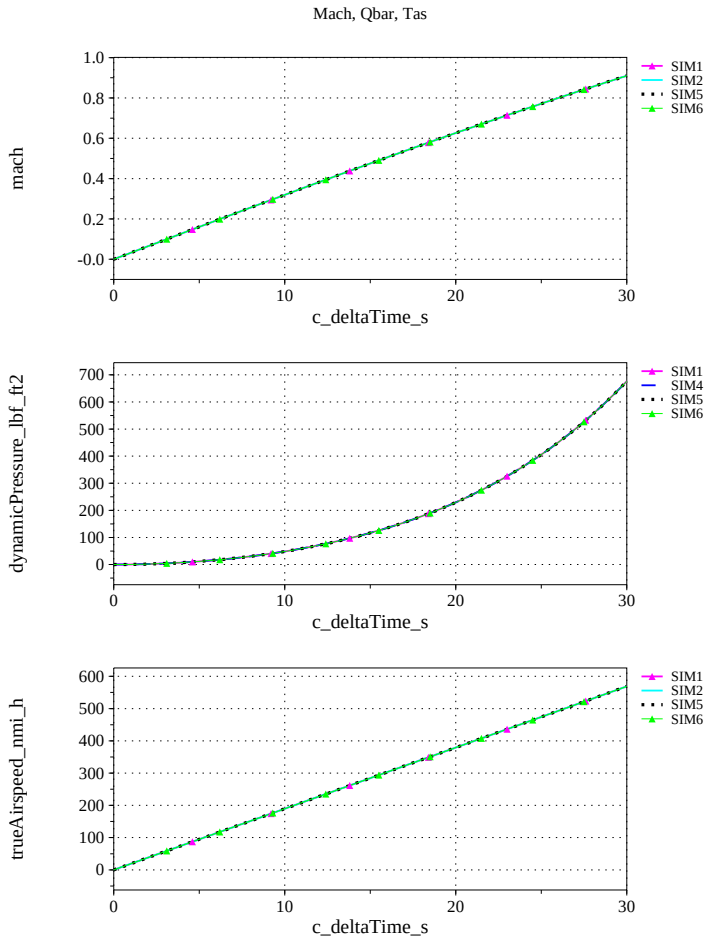

(k) Mach, Dynamic Pressure, and True Airspeed Compared

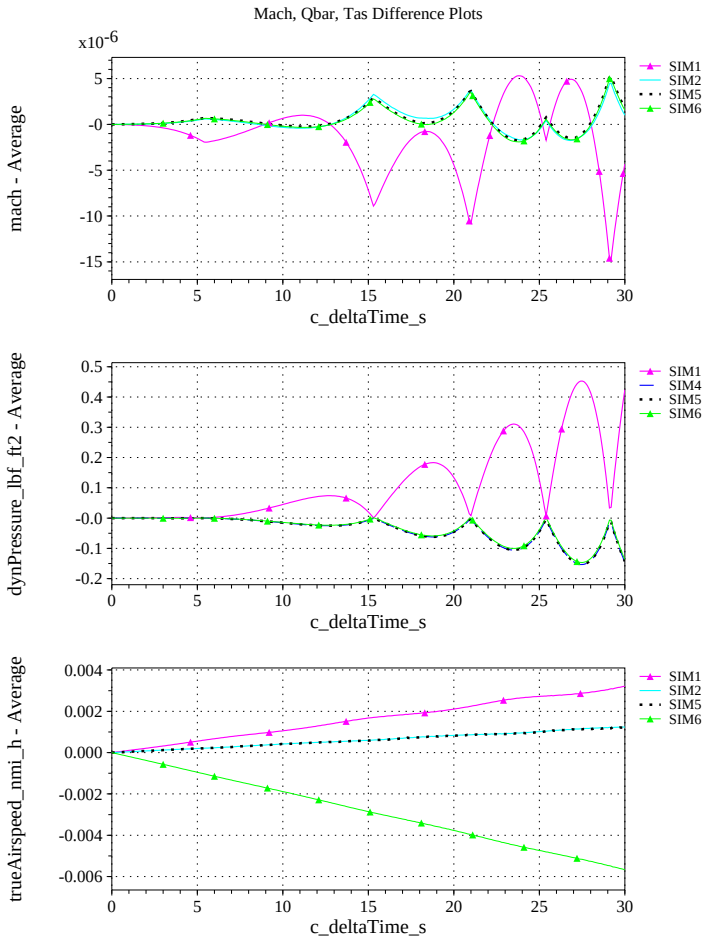

(l) Mach, Dynamic Pressure, and True Airspeed Differenced

Figure 17. Check-case 2: Dragless Tumbling Brick; See Discussion in Section D.1.2 (Cont'd)

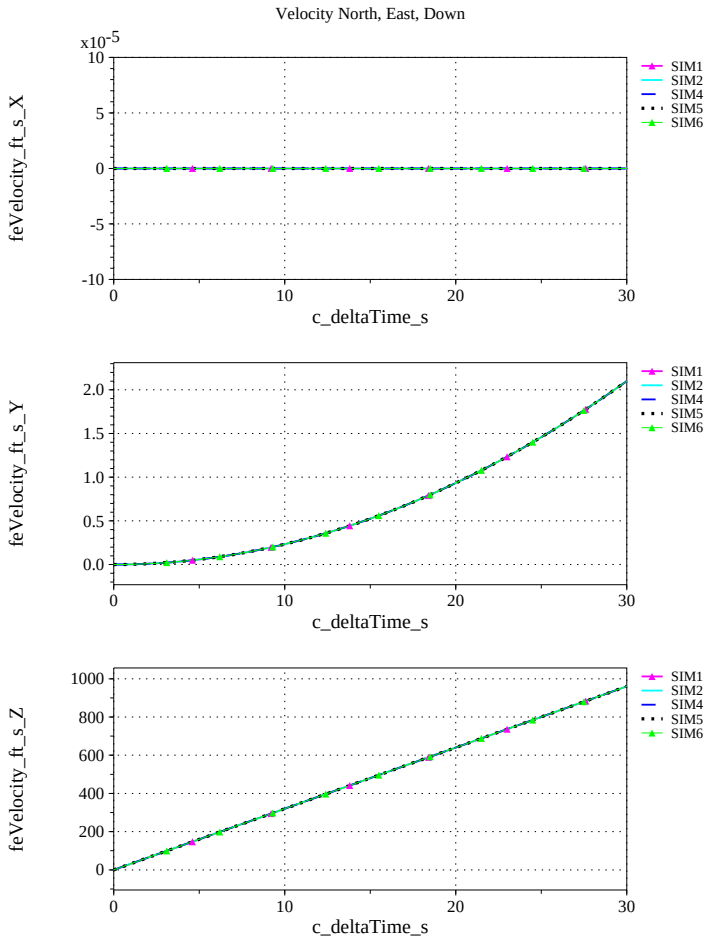

(m) NED Velocities Compared

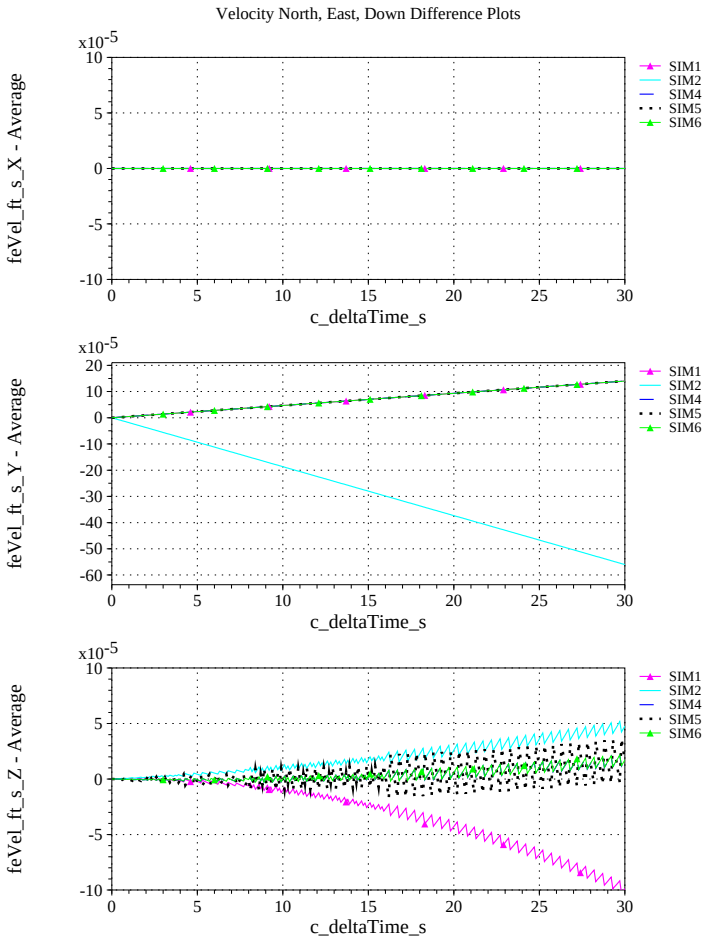

(n) NED Velocities Differenced

Figure 17. Check-case 2: Dragless Tumbling Brick; See Discussion in Section D.1.2 (Cont'd)

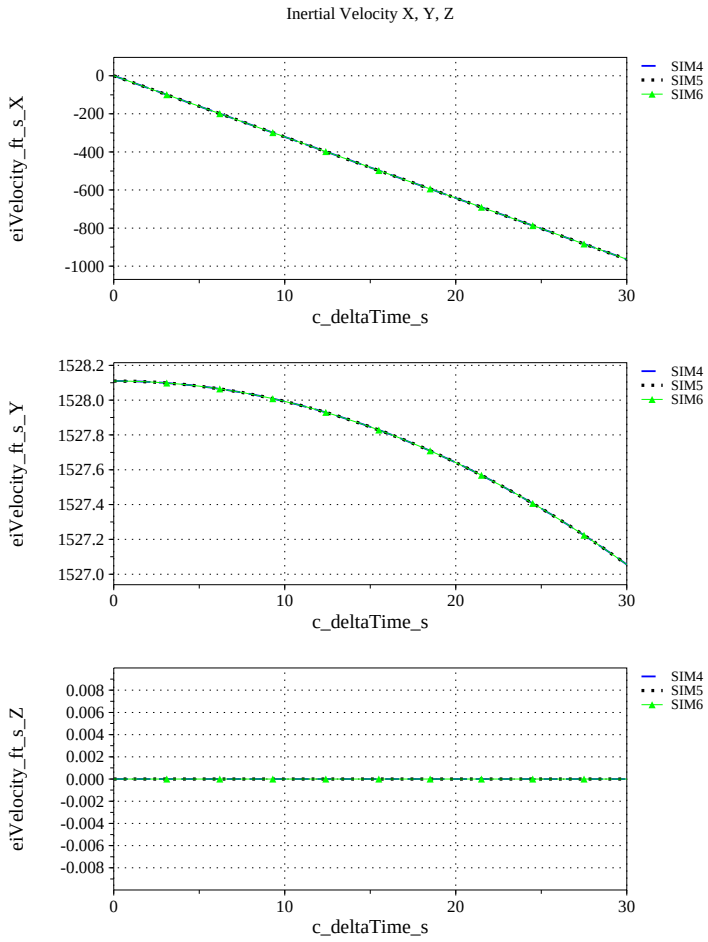

(o) Inertial Velocities Compared

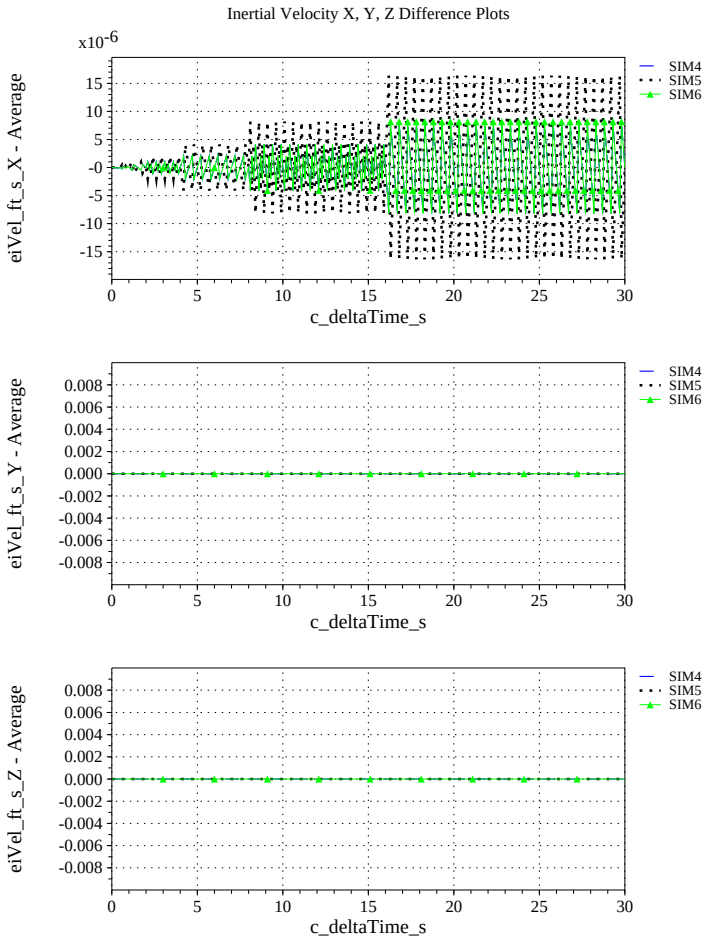

(p) Inertial Velocities Differenced

Figure 17. Check-case 2: Dragless Tumbling Brick; See Discussion in Section D.1.2 (Cont'd)

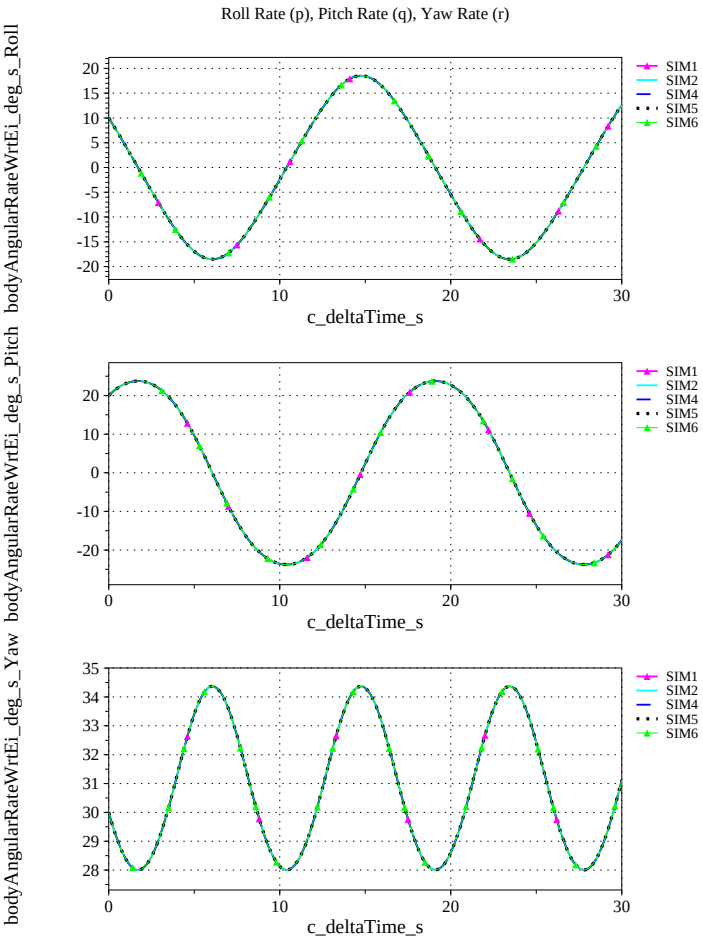

(q) Body-axis Angular Rates (w.r.t. NED Frame) Compared

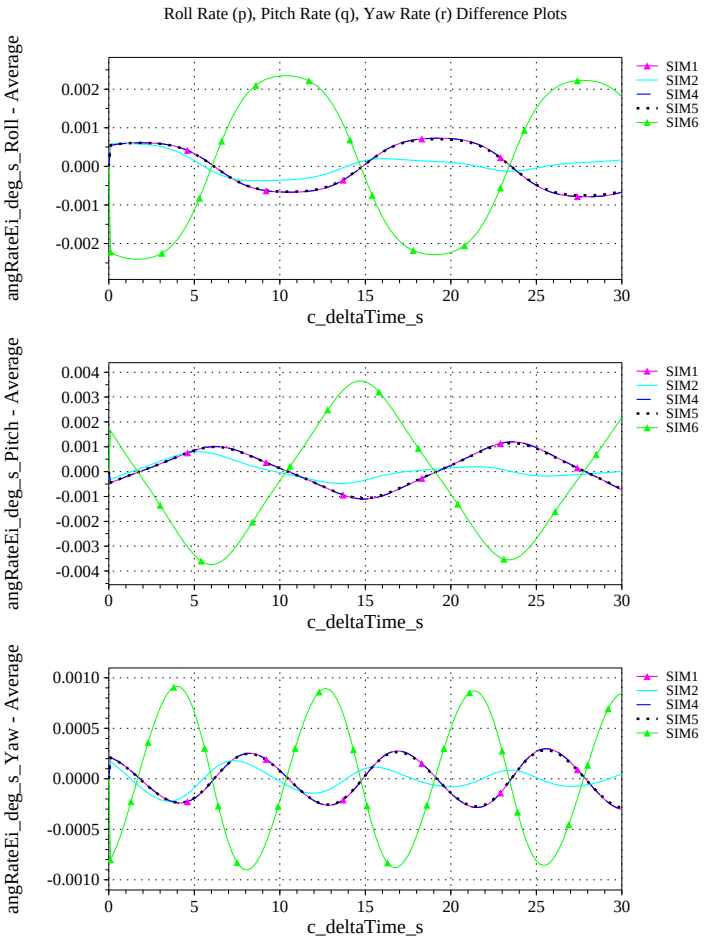

(r) Body-axis Angular Rates (w.r.t. NED Frame) Differenced

Figure 17. Check-case 2: Dragless Tumbling Brick; See Discussion in Section D.1.2 (Cont'd)

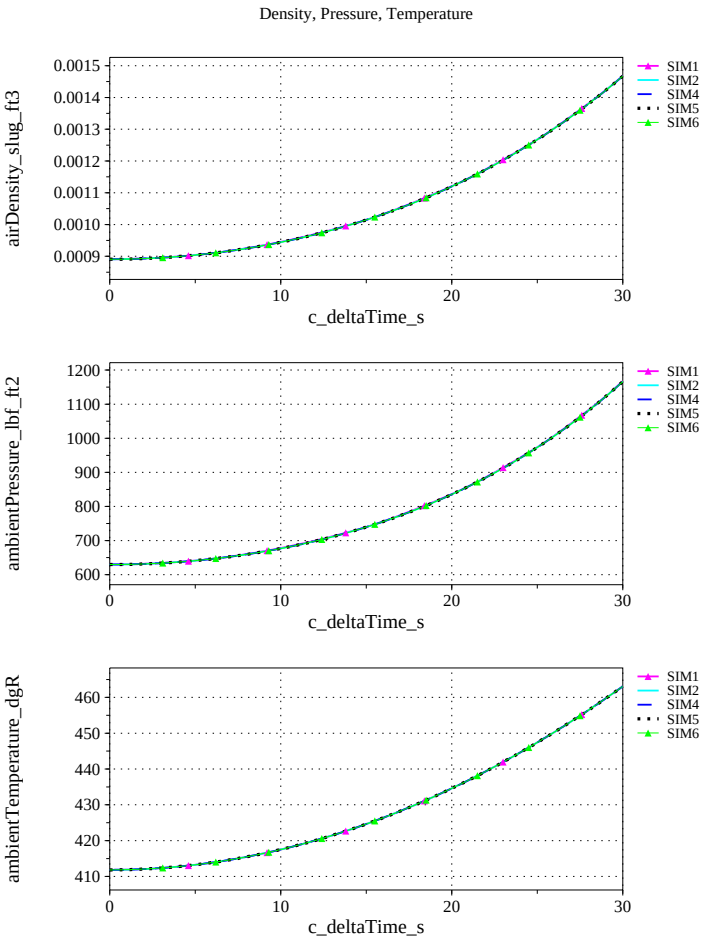

(s) Atmospheric Properties Compared

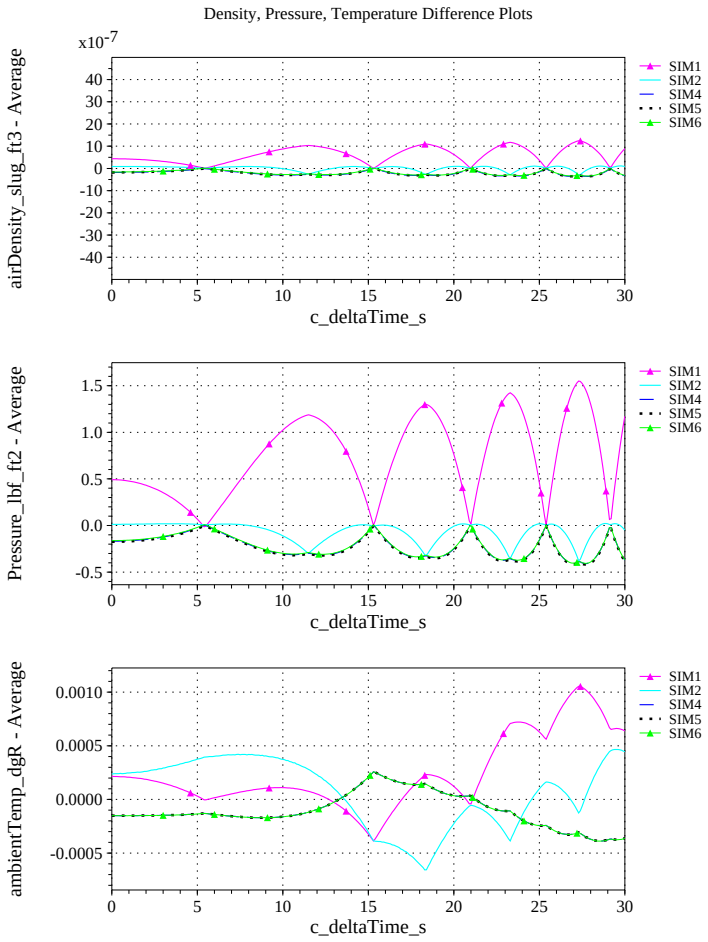

(t) Atmospheric Properties Differenced

Figure 17. Check-case 2: Dragless Tumbling Brick; See Discussion in Section D.1.2 (Cont'd)

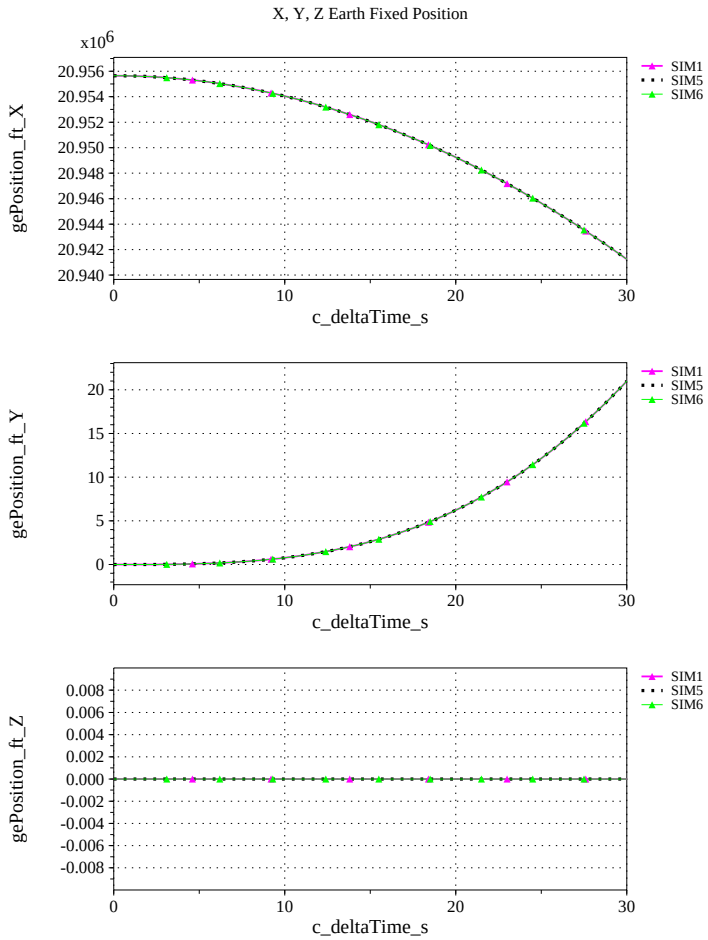

(u) Earth-centered, Earth-fixed Rectangular (X-Y-Z) Positions Compared

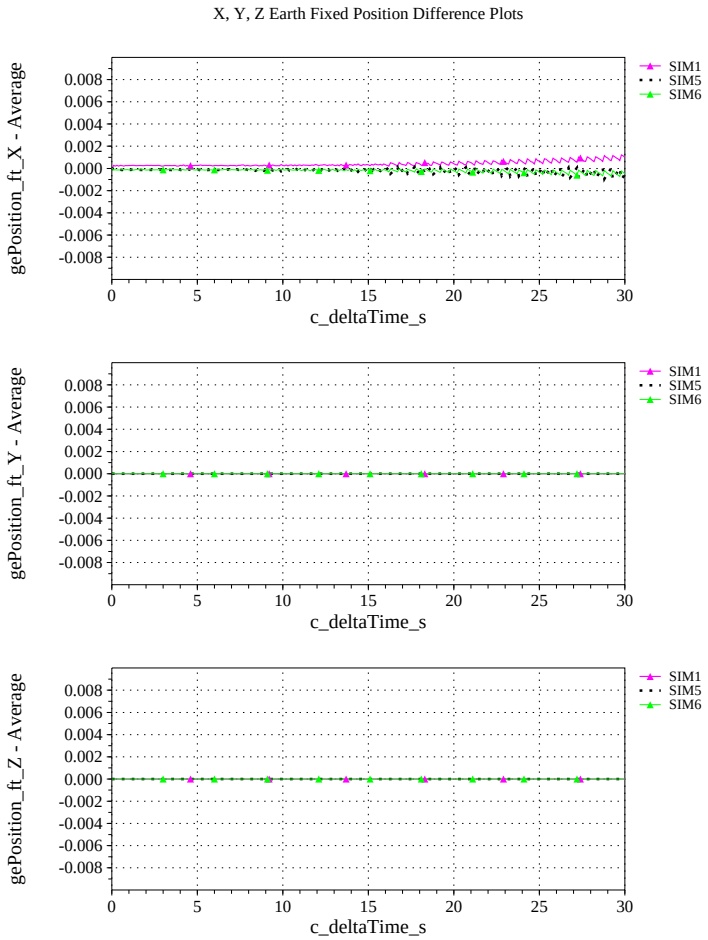

(v) Earth-centered, Earth-fixed Rectangular (X-Y-Z) Positions Differenced

Figure 17. Check-case 2: Dragless Tumbling Brick; See Discussion in Section D.1.2 (Cont'd)

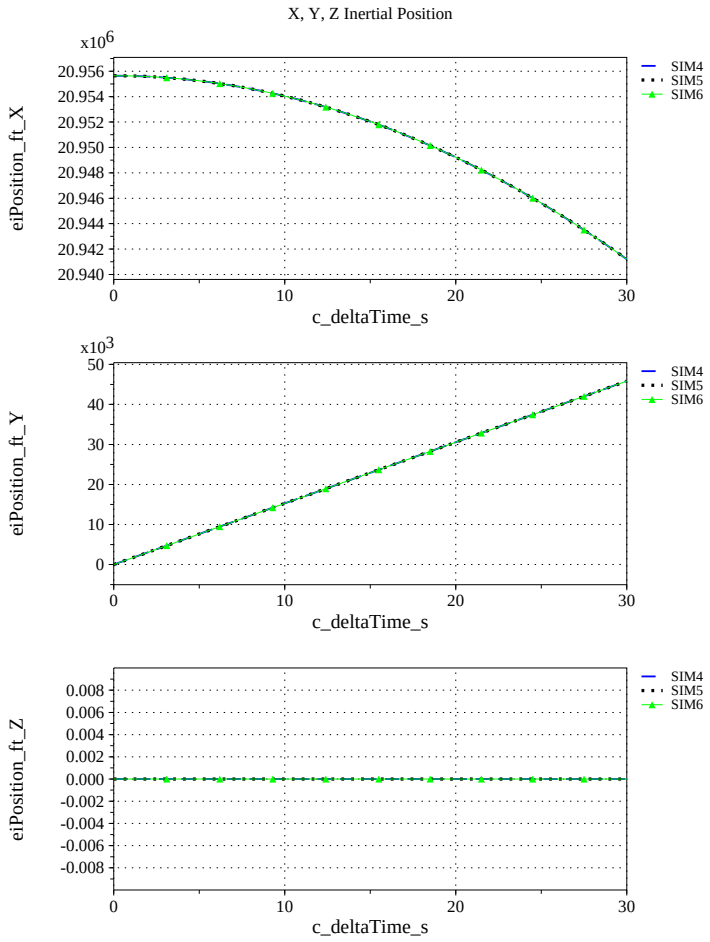

(w) Earth-centered Inertial Rectangular (x-y-z) Positions Compared

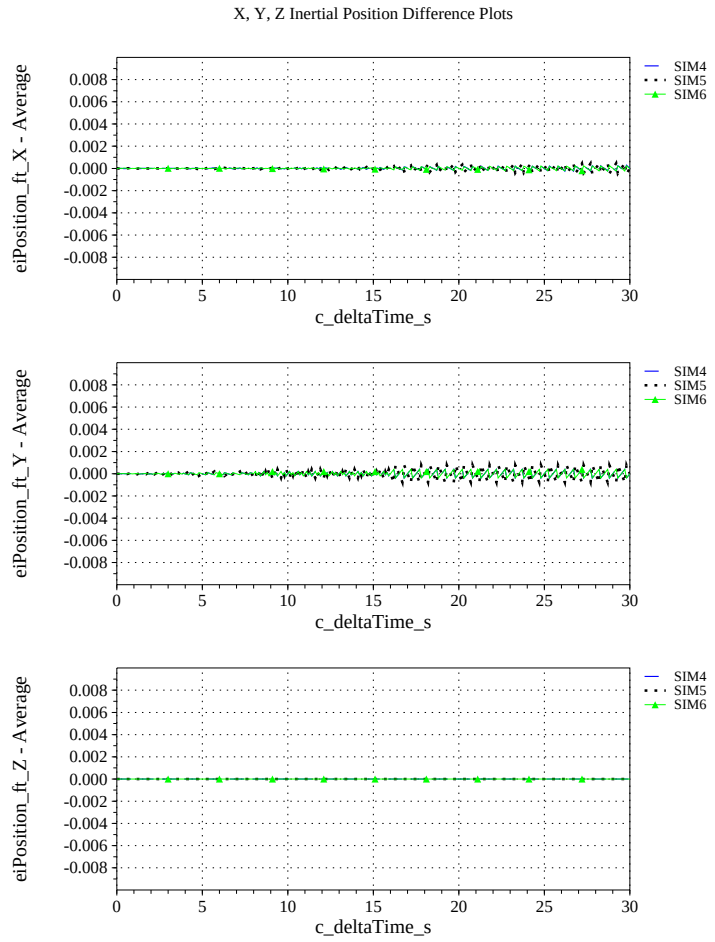

(x) Earth-centered Inertial Rectangular (x-y-z) Positions Differenced

Figure 17. Check-case 2: Dragless Tumbling Brick; See Discussion in Section D.1.2 (Concluded)

D.1.3 Check-case 3 – dragless tumbling brick with aerodynamic damping

This section shows cross-plots for five of the selected simulation tools in modeling the dynamics of a dragless tumbling brick with aerodynamic damping, accelerating as it falls through the atmosphere, after starting with an initial inertial angular rate (10, 20 and 30 deg/s, respectively, in the body axis system). This scenario is described in Section C.1.3. Figures 18a through 18x compare results between the five simulation tools, as well as the deviances of the outputs from each tool from the ensemble average value.

Results for translational states and atmospheric properties were identical to the two previous check-cases. This check-case expanded upon the previous scenario (Check-case 2 – dragless tumbling brick) by adding aerodynamic damping to the rotational motion of the brick. Due to the differences in atmospheric density, the aerodynamic moments for SIM 1 and SIM 2 differed slightly (less than $\pm 3.5 \times 10^{-6}$ lbf-ft) from the remaining simulations. In turn, the combination of aerodynamic differences and differences in integration methods produced differences in inertial angular rates smaller than ± 0.06 deg/s. However, the largest differences were confined to the first 20 sec before the aerodynamic damping reduced the angular momentum of the brick to near zero. These differences in angular rates combined with additional differences in integration error from the integration of the angular rates to produce differences in the predicted orientation of the brick between the simulations.

In yaw angle, SIM 4, 5, and 6 agreed on orientation to within 0.05 degrees. SIM 2 settled to a difference, from the ensemble average, of about -0.15 degrees from a peak difference of -0.35 degrees at around $t = 9$ sec. SIM 1 had an increasing difference that settled to around -0.32 degrees. In pitch angle, SIM 1, 4, 5, and 6 agree to within about 0.1 degree. After about six seconds, SIM 2 exhibited an increasing difference with the other simulations that decreased to less than -0.65 degrees at the end of the run. In roll angle, all simulations agreed to within 0.1 degrees by the end of the run although SIM 2 did exhibit an earlier departure from the other simulations that peaked near 0.5 degrees at around $t = 7.5$ sec.

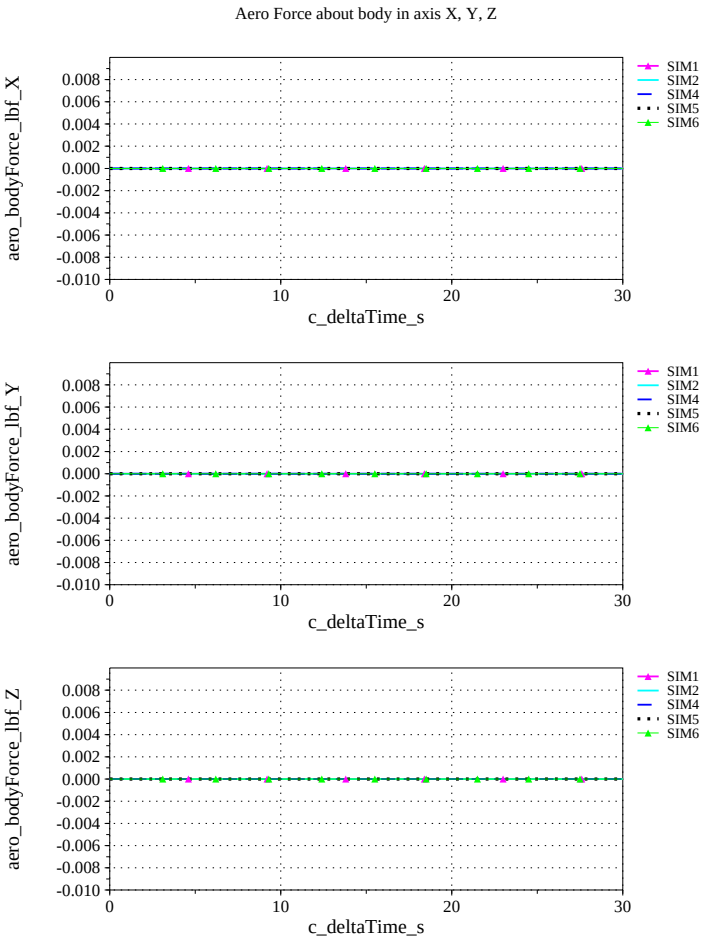

(a) Aerodynamic Forces Compared

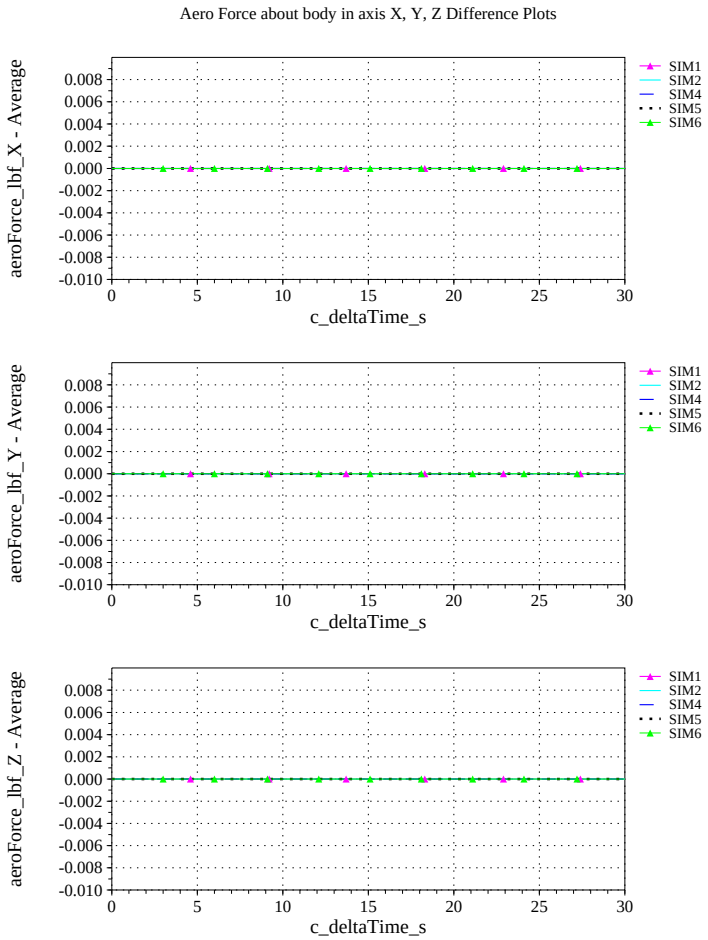

(b) Aerodynamic Forces Differenced

Figure 18. Check-case 3: Dragless Tumbling Brick with Aerodynamic Damping; See Discussion in Section D.1.3

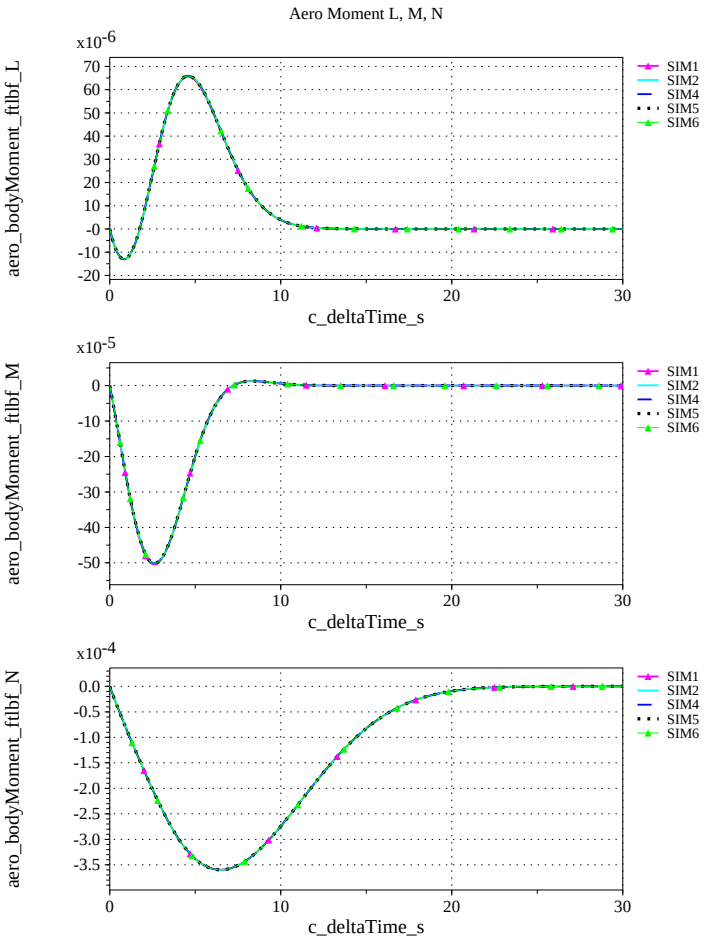

(c) Aerodynamic Moments Compared

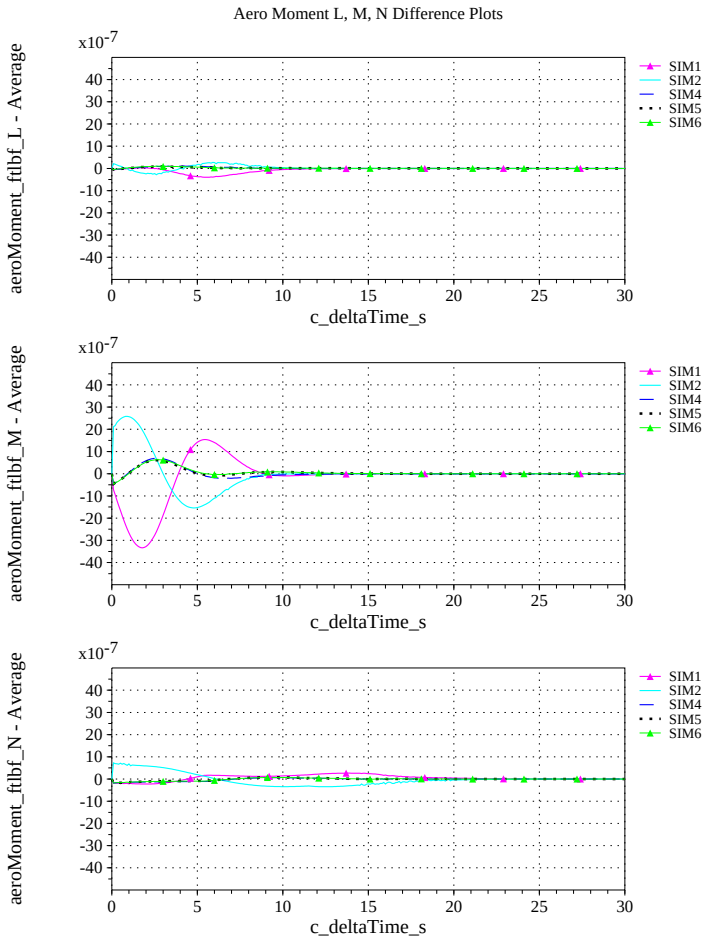

(d) Aerodynamic Moments Differenced

Figure 18. Check-case 3: Dragless Tumbling Brick with Aerodynamic Damping; See Discussion in Section D.1.3 (Cont'd)

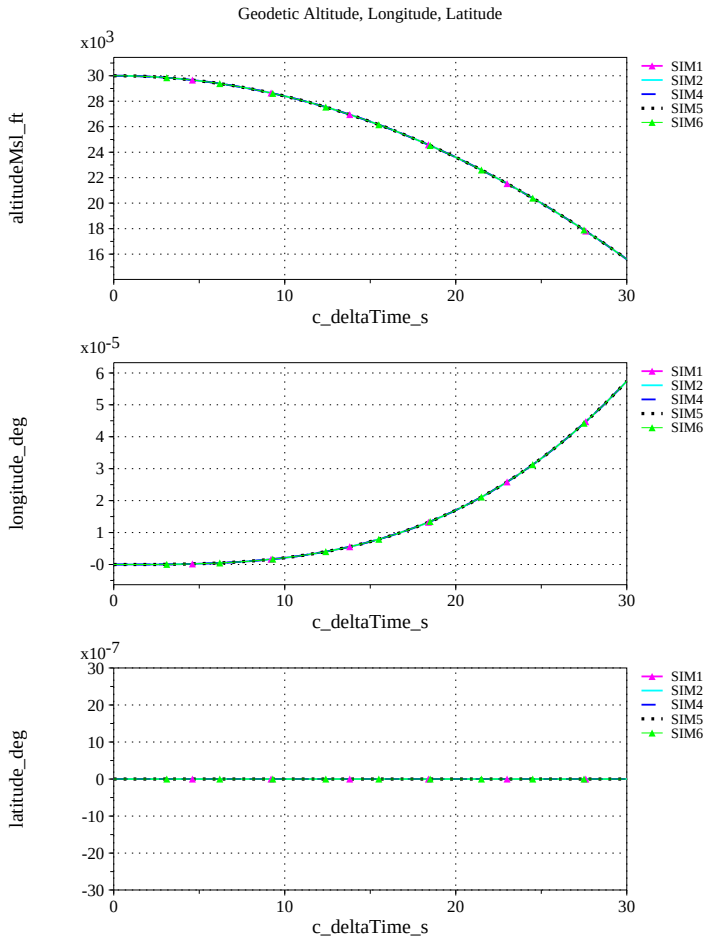

(e) Altitude, Geodetic Latitude and Longitude Compared

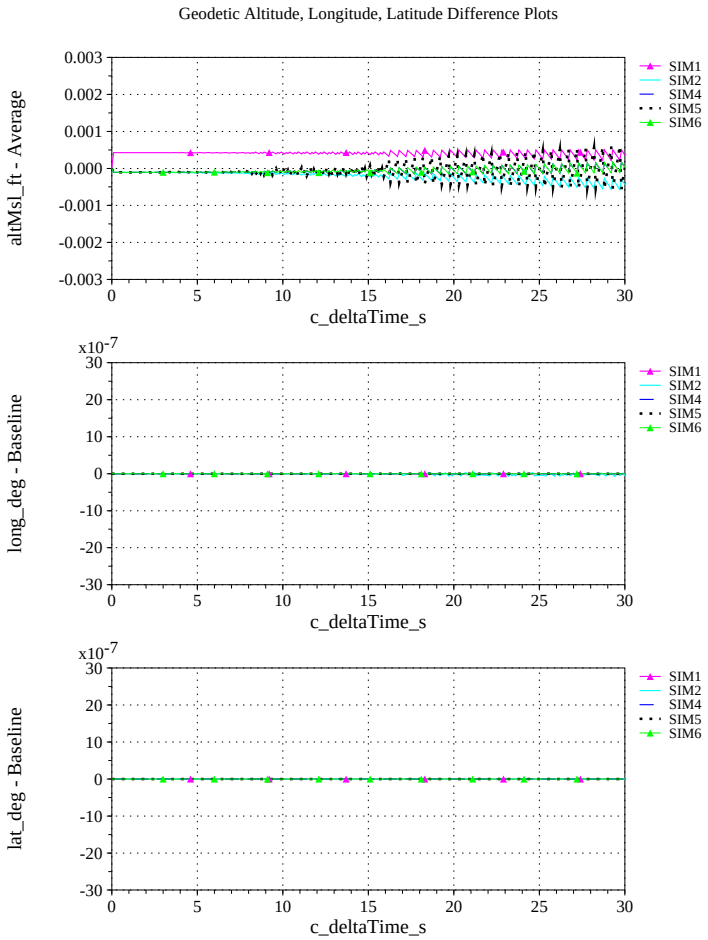

(f) Altitude, Geodetic Latitude and Longitude Differenced

Figure 18. Check-case 3: Dragless Tumbling Brick with Aerodynamic Damping; See Discussion in Section D.1.3 (Cont'd)

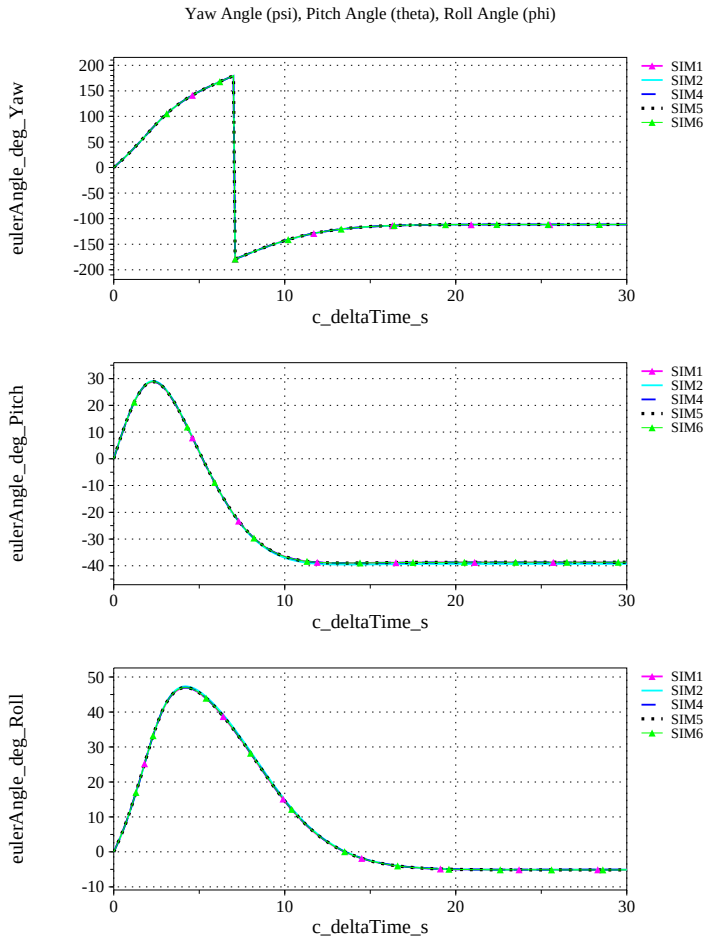

(g) Euler Angles (w.r.t. NED Frame) Compared

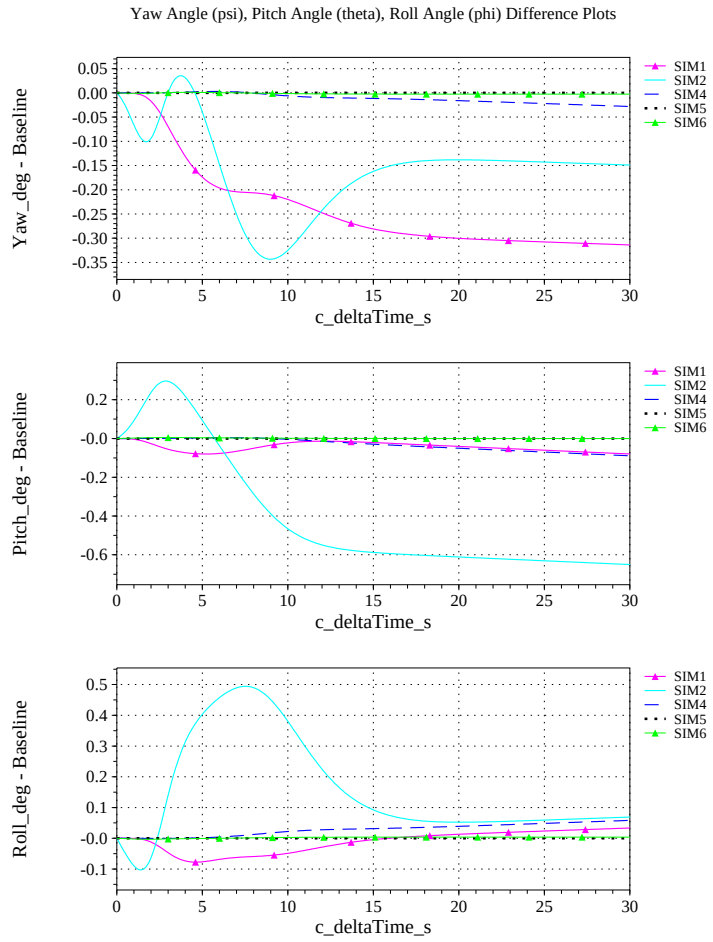

(h) Euler Angles (w.r.t. NED Frame) Differenced

Figure 18. Check-case 3: Dragless Tumbling Brick with Aerodynamic Damping; See Discussion in Section D.1.3 (Cont'd)

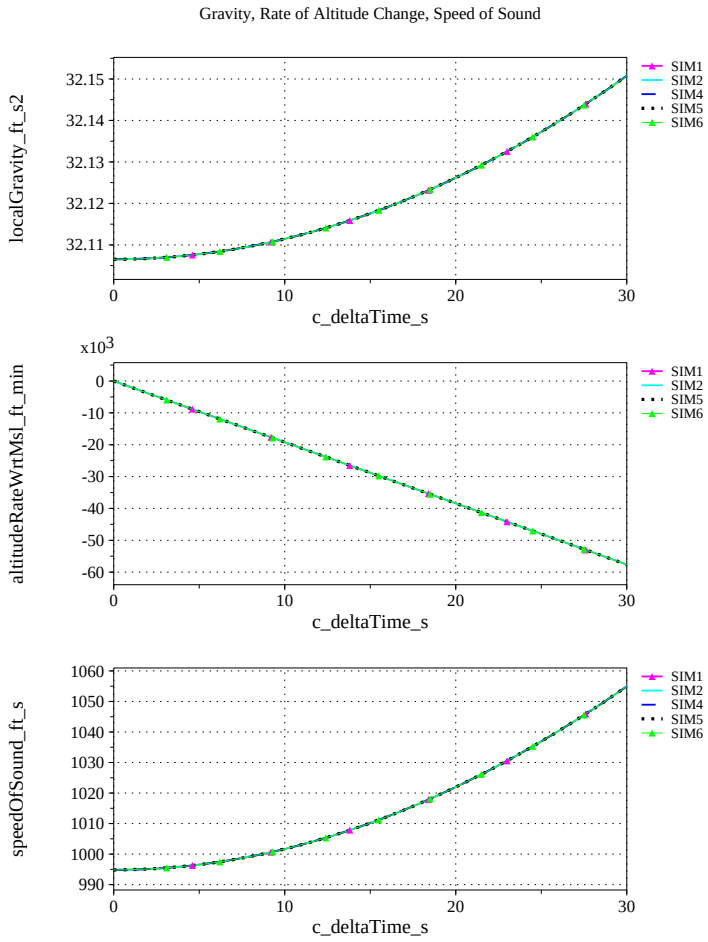

(i) Gravity, Climb Rate, and Speed-of-sound Compared

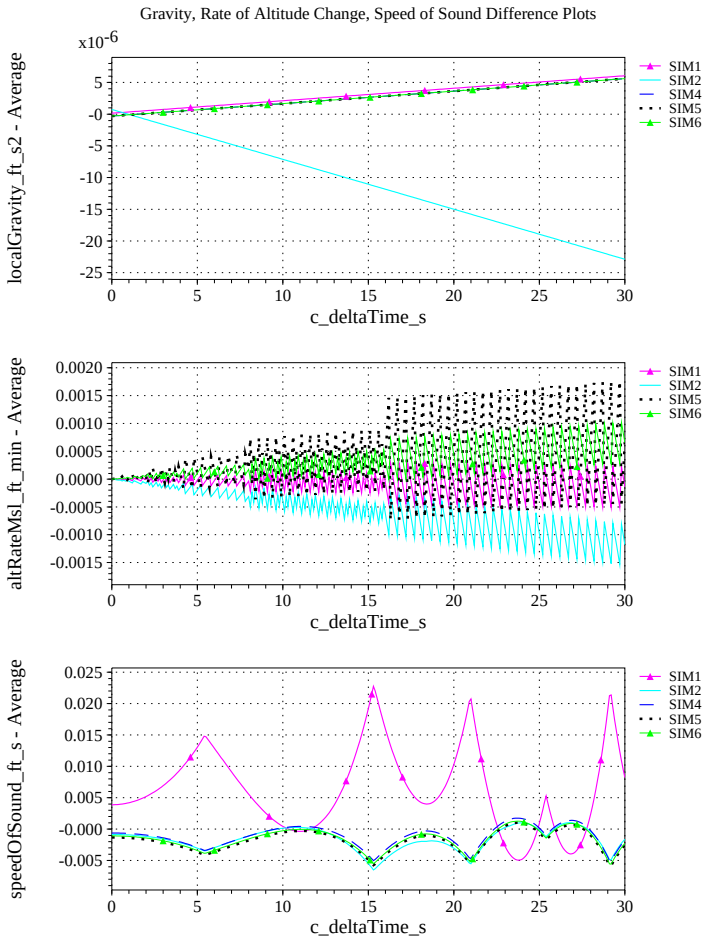

(j) Gravity, Climb Rate, and Speed-of-sound Differenced

Figure 18. Check-case 3: Dragless Tumbling Brick with Aerodynamic Damping; See Discussion in Section D.1.3 (Cont'd)

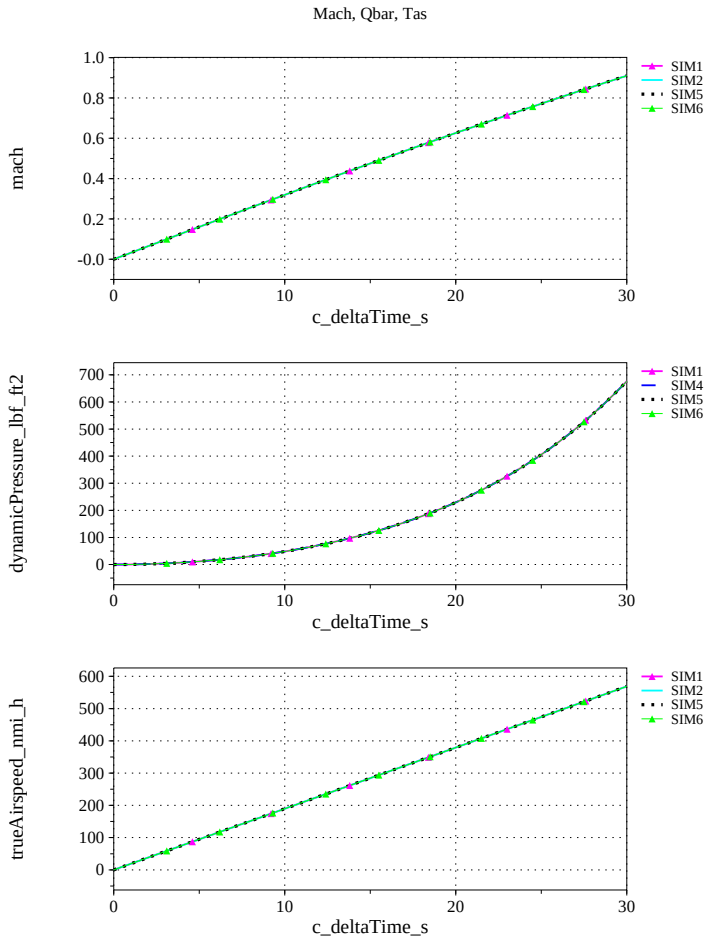

(k) Mach, Dynamic Pressure, and True Airspeed Compared

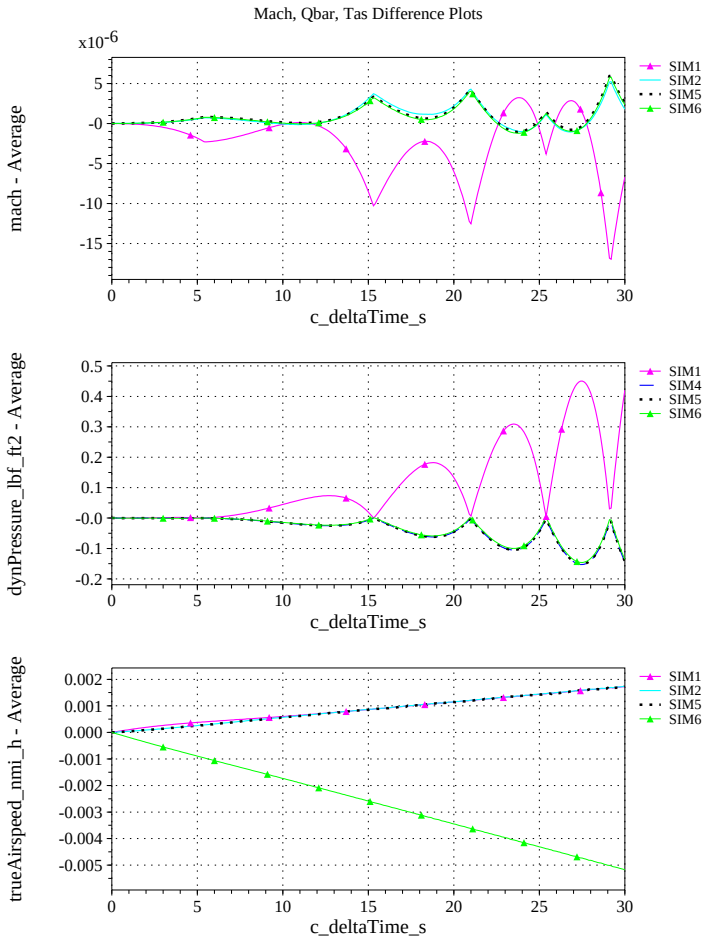

(l) Mach, Dynamic Pressure, and True Airspeed Differenced

Figure 18. Check-case 3: Dragless Tumbling Brick with Aerodynamic Damping; See Discussion in Section D.1.3 (Cont'd)

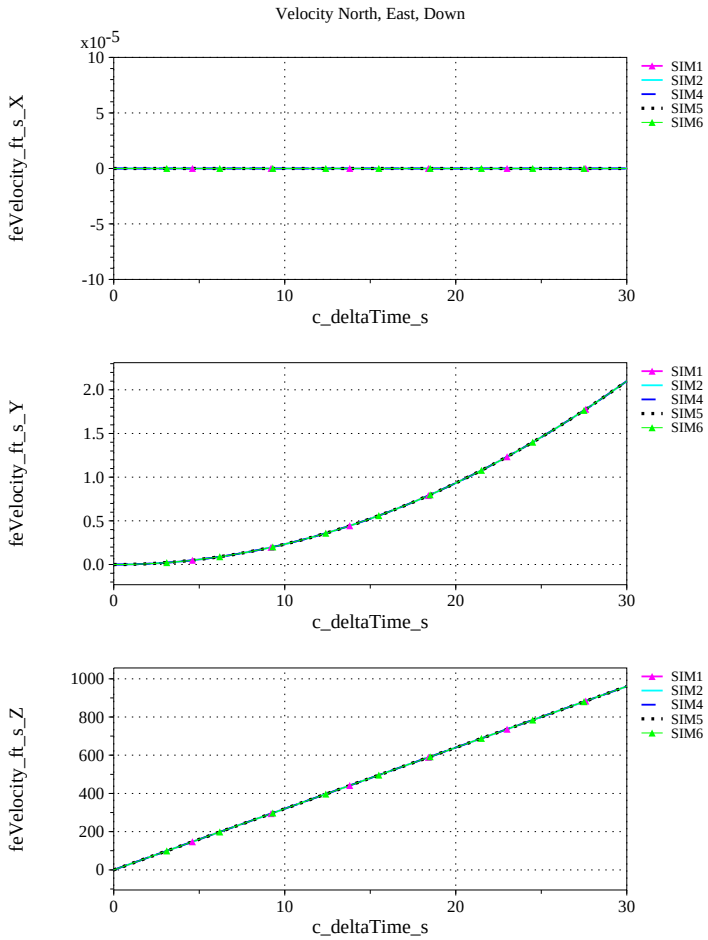

(m) NED Velocities Compared

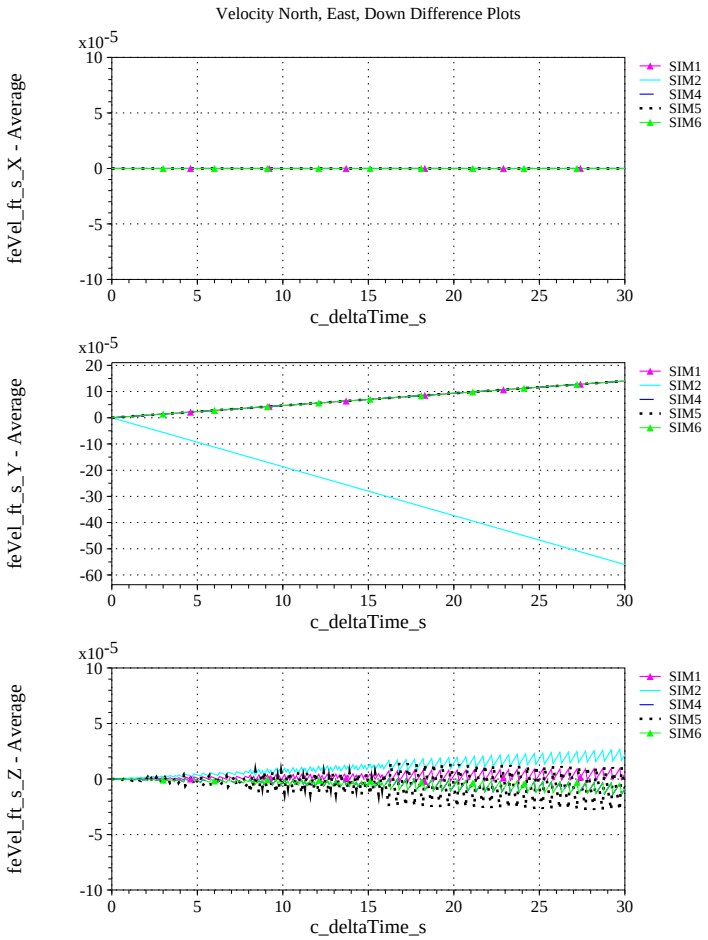

(n) NED Velocities Differenced

Figure 18. Check-case 3: Dragless Tumbling Brick with Aerodynamic Damping; See Discussion in Section D.1.3 (Cont'd)

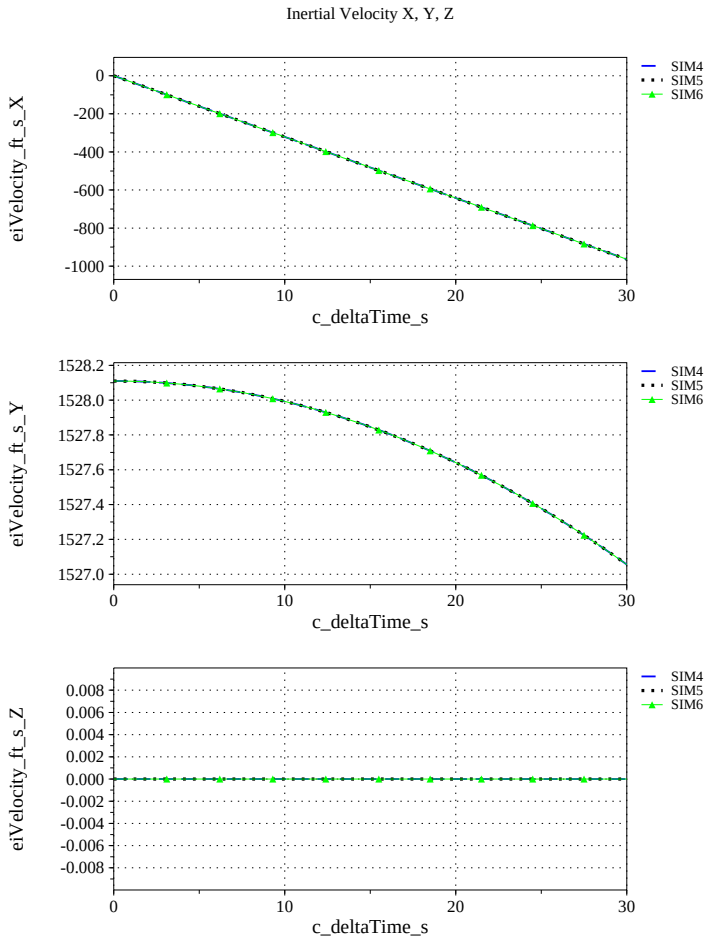

(o) Inertial Velocities Compared

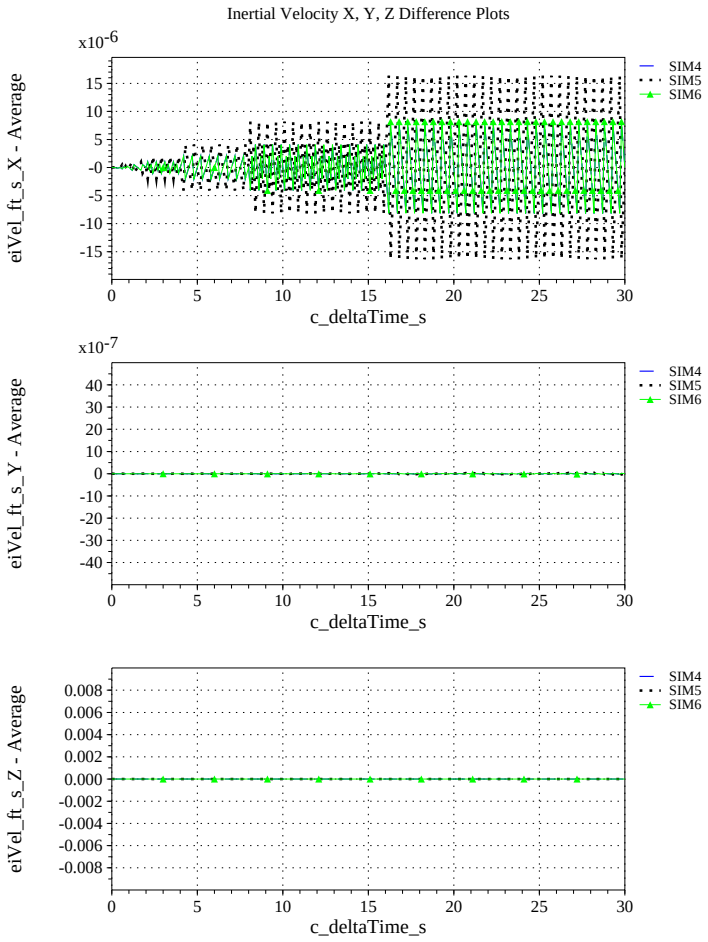

(p) Inertial Velocities Differenced

Figure 18. Check-case 3: Dragless Tumbling Brick with Aerodynamic Damping; See Discussion in Section D.1.3 (Cont'd)

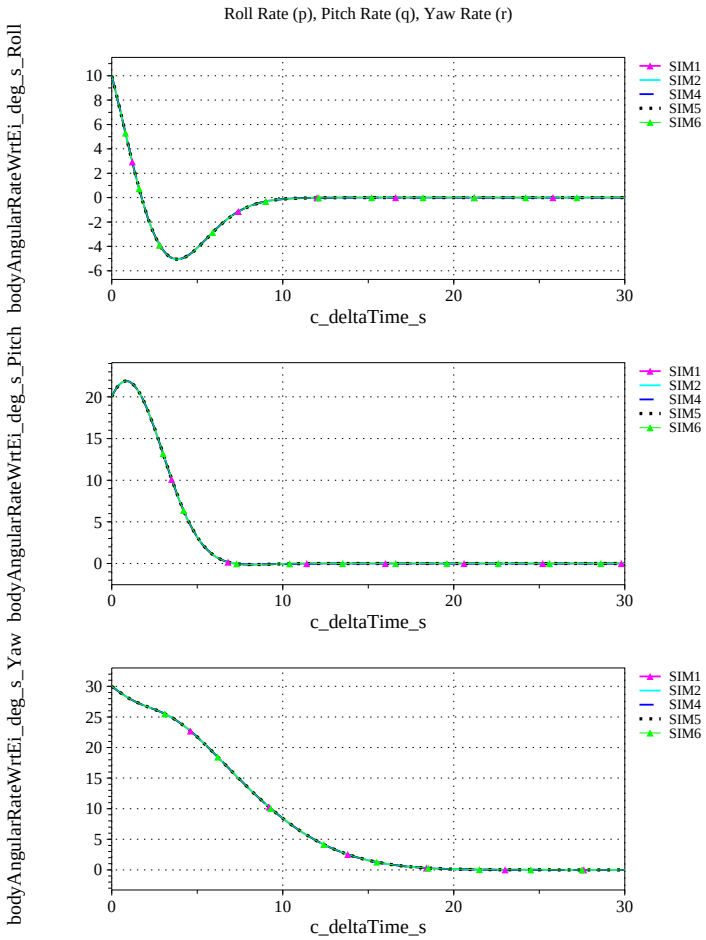

(q) Body-axis Angular Rates (w.r.t. NED Frame) Compared

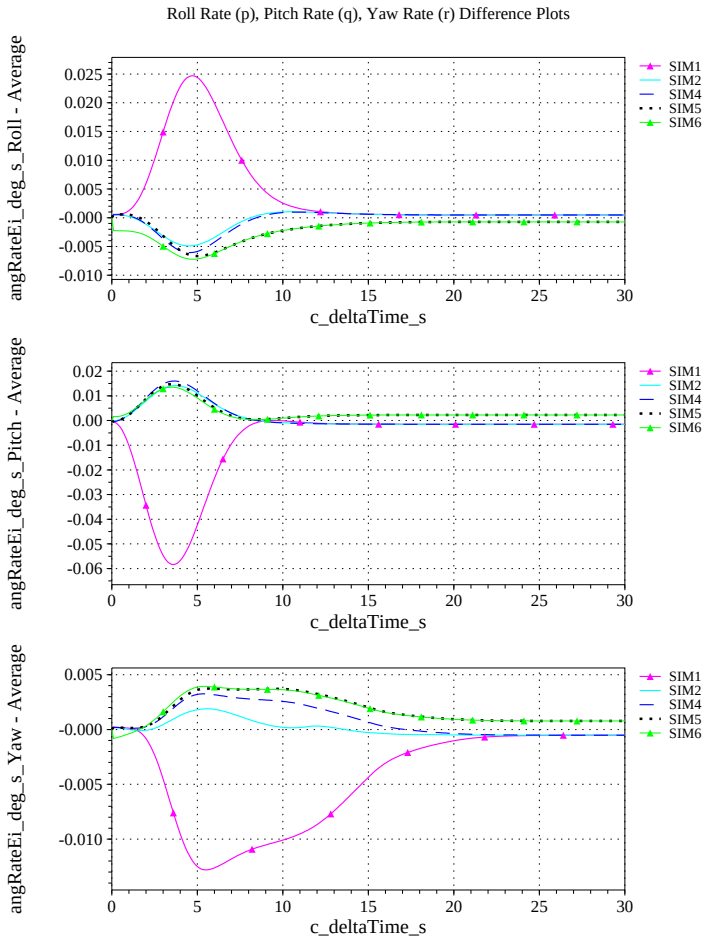

(r) Body-axis Angular Rates (w.r.t. NED Frame) Differenced

Figure 18. Check-case 3: Dragless Tumbling Brick with Aerodynamic Damping; See Discussion in Section D.1.3 (Cont'd)

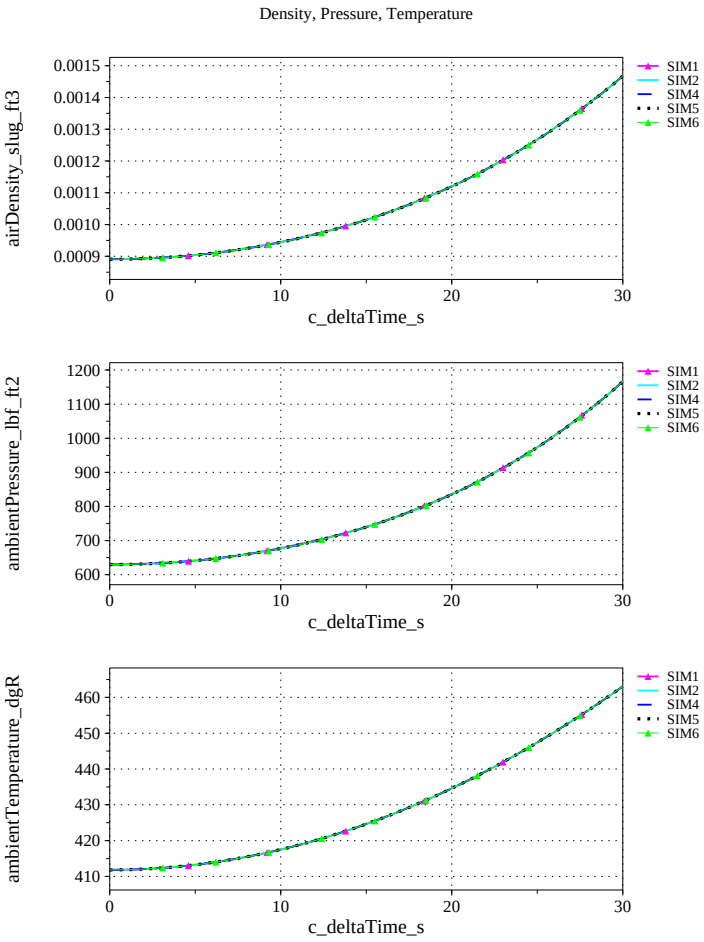

(s) Atmospheric Properties Compared

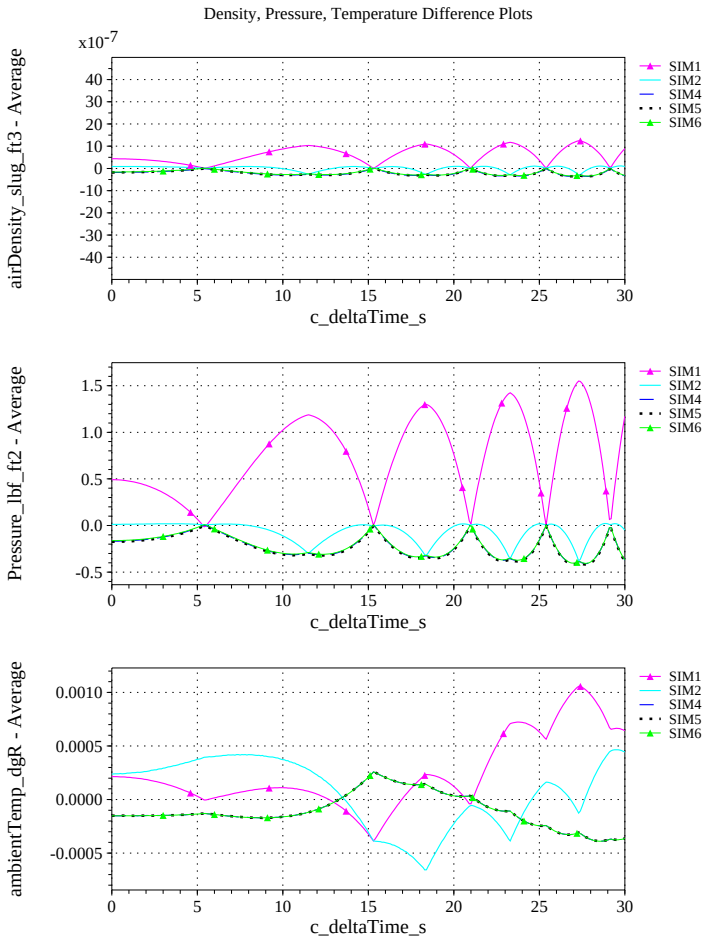

(t) Atmospheric Properties Differenced

Figure 18. Check-case 3: Dragless Tumbling Brick with Aerodynamic Damping; See Discussion in Section D.1.3 (Cont'd)

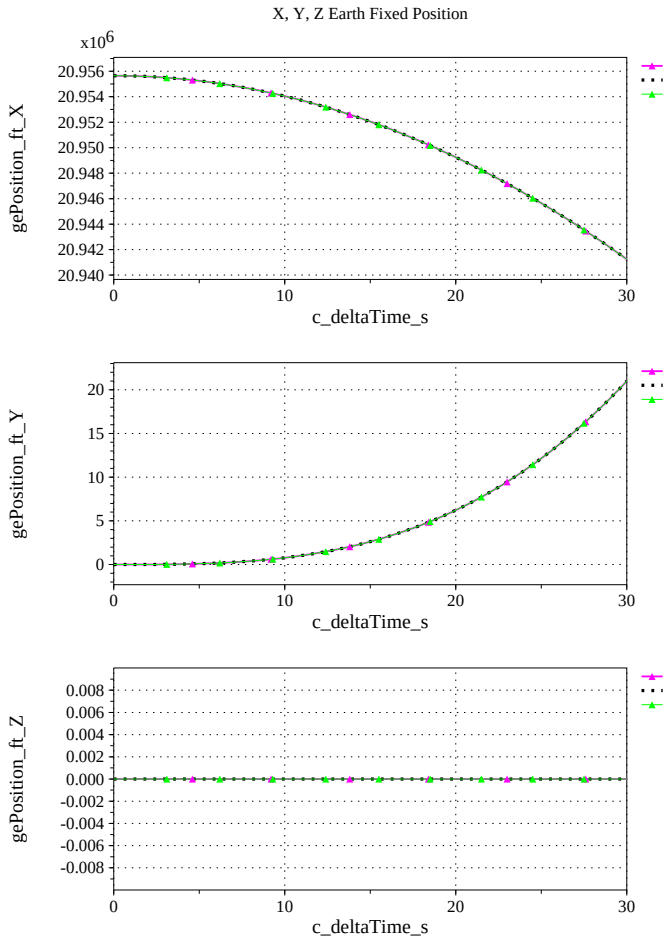

(u) Earth-centered, Earth-fixed Rectangular (X-Y-Z) Positions Compared

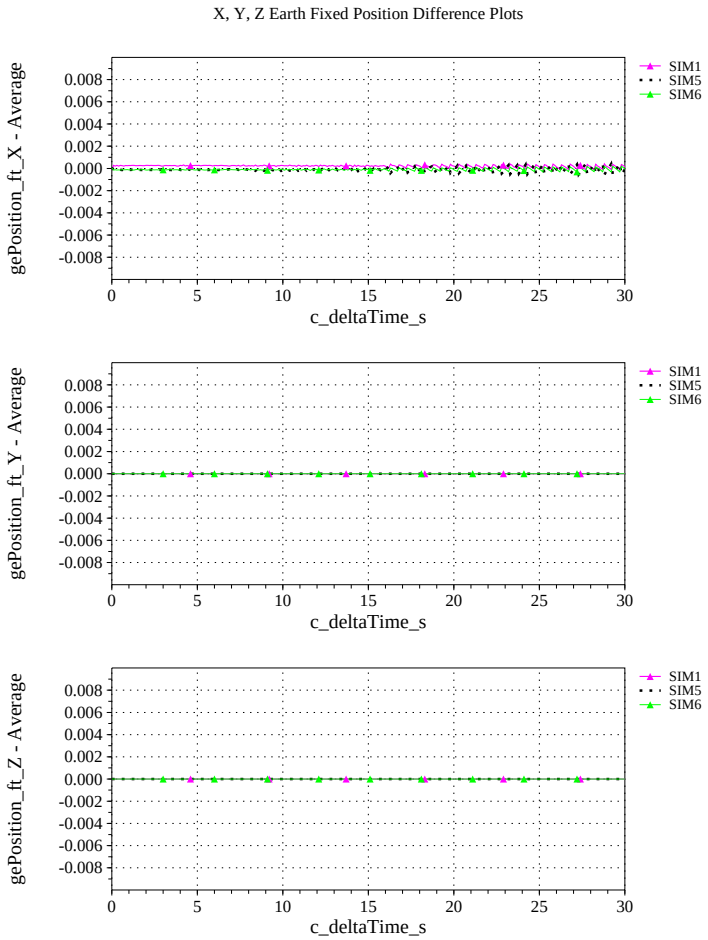

(v) Earth-centered, Earth-fixed Rectangular (X-Y-Z) Positions Differenced

Figure 18. Check-case 3: Dragless Tumbling Brick with Aerodynamic Damping; See Discussion in Section D.1.3 (Cont'd)

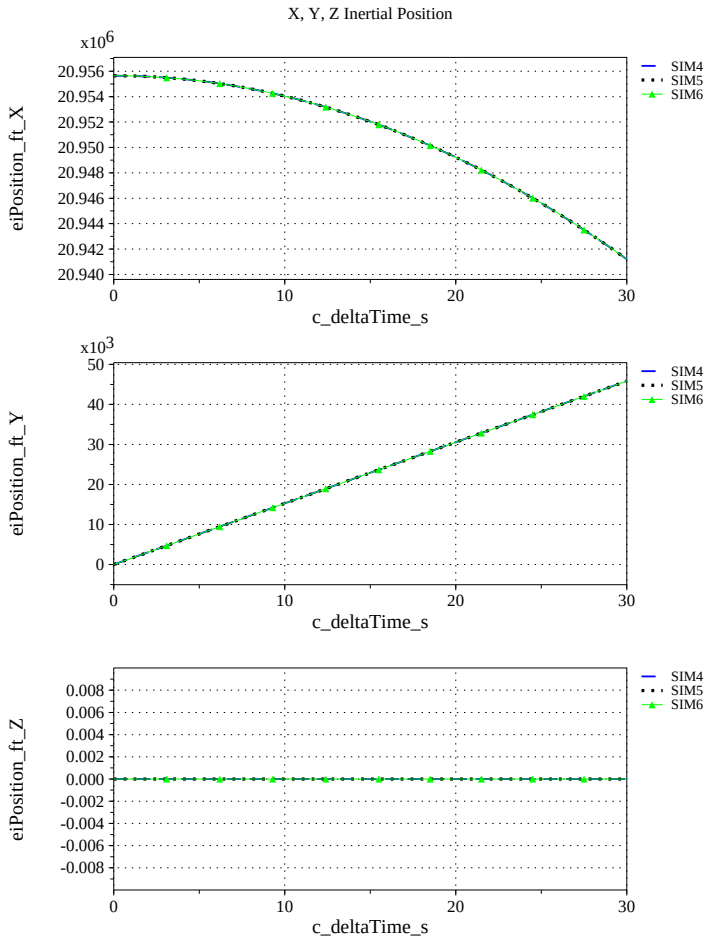

(w) Earth-centered Inertial Rectangular (x-y-z) Positions Compared

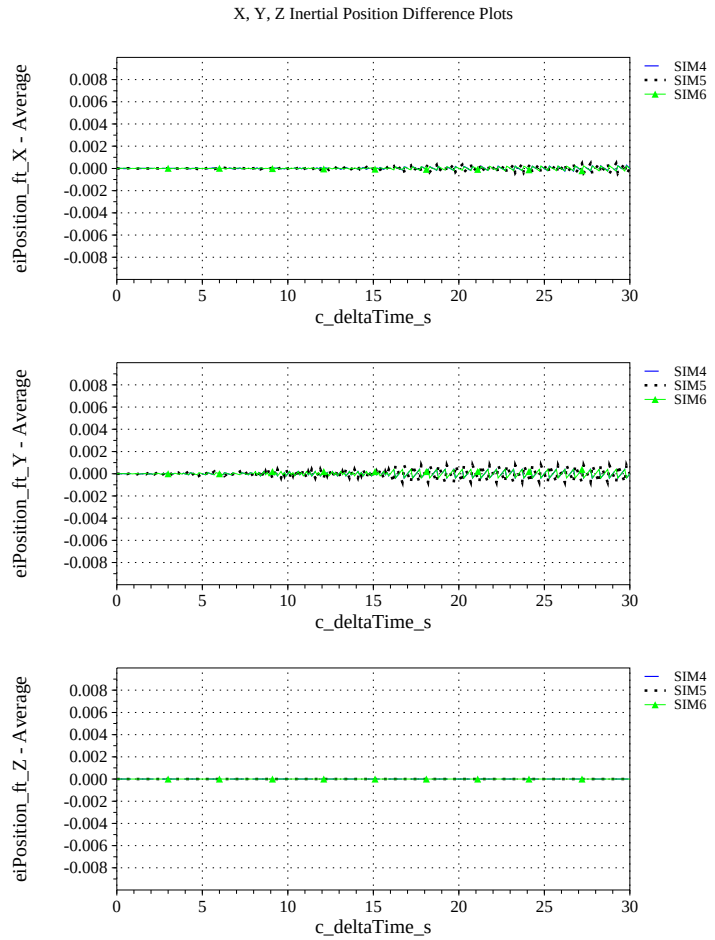

(x) Earth-centered Inertial Rectangular (x-y-z) Positions Differenced

Figure 18. Check-case 3: Dragless Tumbling Brick with Aerodynamic Damping; See Discussion in Section D.1.3 (Concluded)

D.1.4 Check-case 4 – sphere dropping over non-rotating, spherical Earth

This section shows cross-plots for four of the selected simulation tools in modeling the dynamics of a sphere dropped with a fixed drag coefficient through a still atmosphere in a non-rotating Earth with spherical gravity. This scenario is described in Section C.1.4. Figures 19a through 19x compare results between the four simulation tools, as well as the deviances of the outputs from each tool from the ensemble average value.

This check-case exercised both translational and rotational motion over a non-rotating, spherical Earth. In general SIM 4, 5, and 6 agreed on the predicted translational states of the sphere. There are a number of factors, however, that caused SIM 2 to produce a different trajectory. First, SIM 2 showed an initial north velocity of 0.01 ft/s while the other simulations have an initial north velocity of zero. The difference in initial north velocity led to a difference in latitude that steadily rose to about 8×10^{-7} degrees by the end of the run. Throughout the run, SIM 2 exhibited a gravitational acceleration that was approximately 0.05 ft/s^2 lower than the other simulations. The lower gravity appeared to be the primary cause of differences in downward velocity and altitude. The lower gravity started a feedback loop in which velocity and altitude differences cascaded into differences in atmospheric density, dynamic pressure, and aerodynamic drag. The difference in aerodynamic drag created further differences in velocity and altitude. In this feedback, a secondary cause of difference in atmospheric density, previously discussed in the "Check-case 1 – dragless sphere" scenario, was due to implementation of the U.S. Standard Atmosphere 1976 model using a look-up table. These root causes were verified by altering SIM 5 to use a look-up table for atmospheric density and to use an Earth gravitation constant that produced the lower gravity. The altered SIM 5 matched the altitude results of SIM 2 to within 0.006 ft.

The vehicle in this scenario had constant angular momentum with no external torques. Moreover, because the vehicle is a uniform sphere, the inertial angular rates in body coordinates (p, q, r) also remained constant. All simulations exhibited this constant angular rate. However, SIM 2 exhibited differences from the other simulations in predicted Euler angles. As first suggested in the "Check-case 2 – dragless tumbling brick" scenario, the SIM 2 differences were likely due to integration step sizes or order.

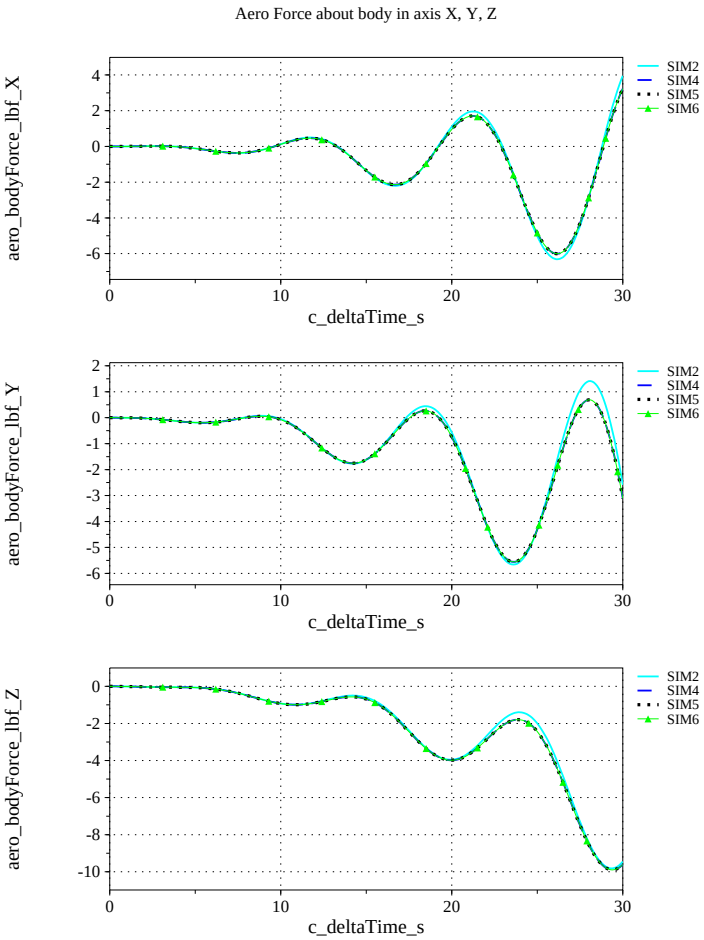

(a) Aerodynamic Forces Compared

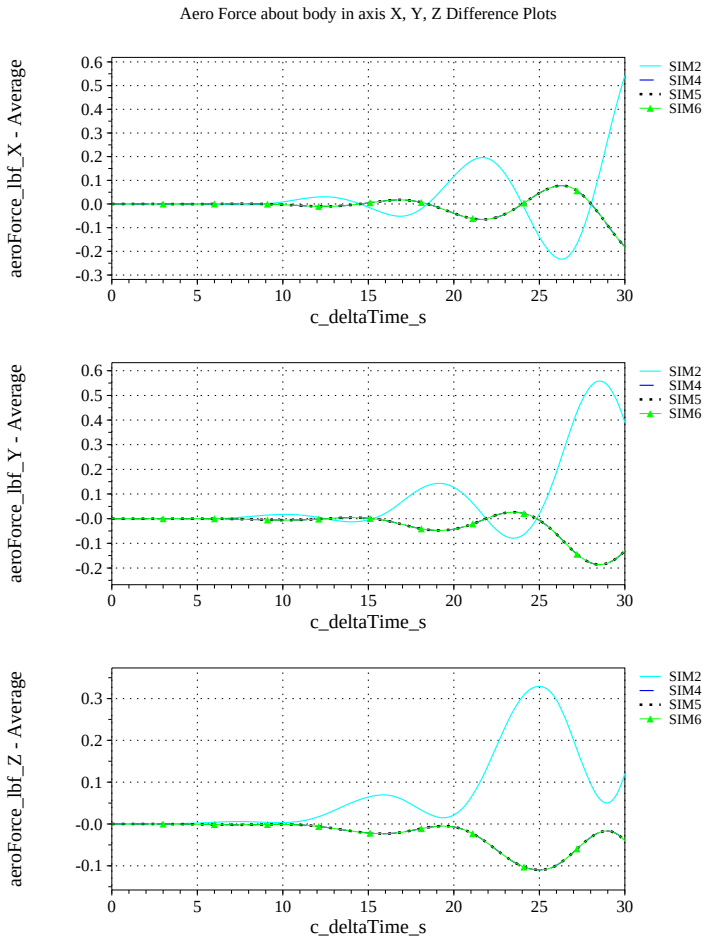

(b) Aerodynamic Forces Differenced

Figure 19. Check-case 4: Sphere Dropping over Non-rotating, Spherical Earth; See Discussion in Section D.1.4

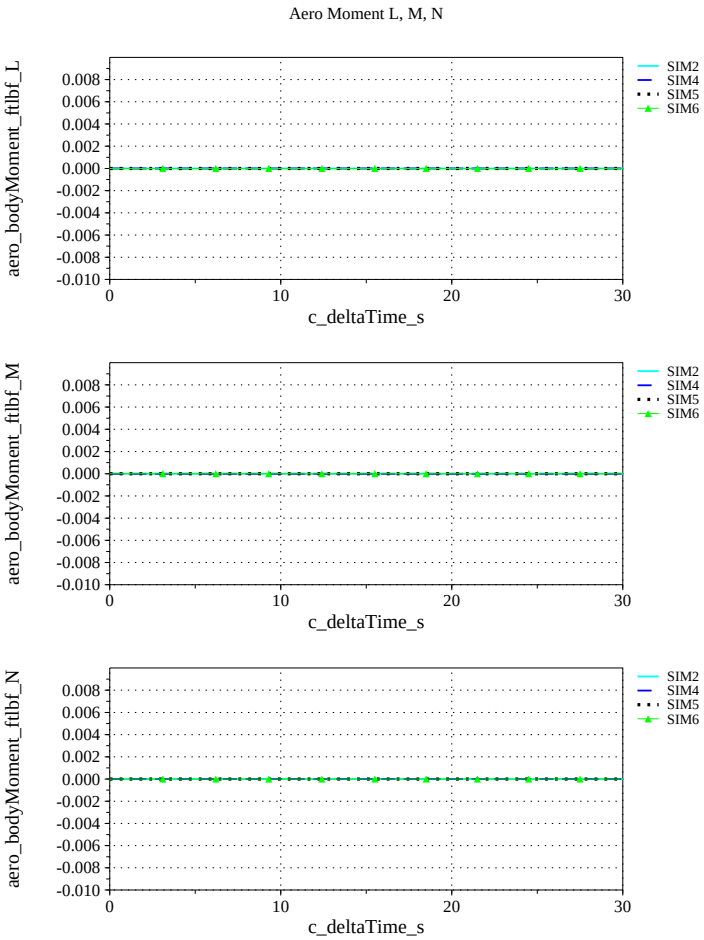

(c) Aerodynamic Moments Compared

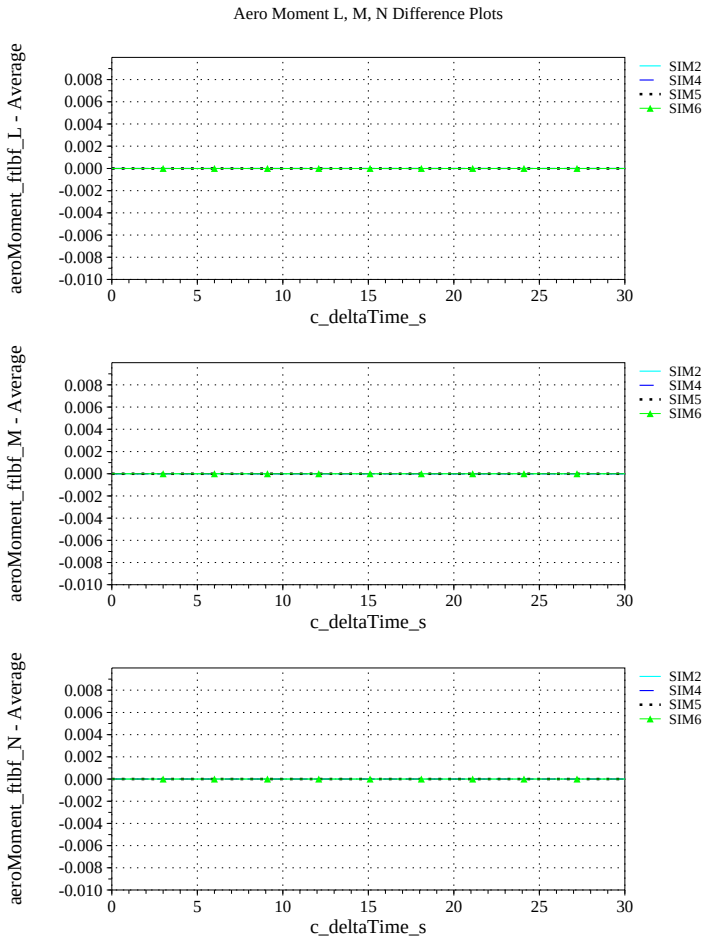

(d) Aerodynamic Moments Differenced

Figure 19. Check-case 4: Sphere Dropping over Non-rotating, Spherical Earth; See Discussion in Section D.1.4 (Cont'd)

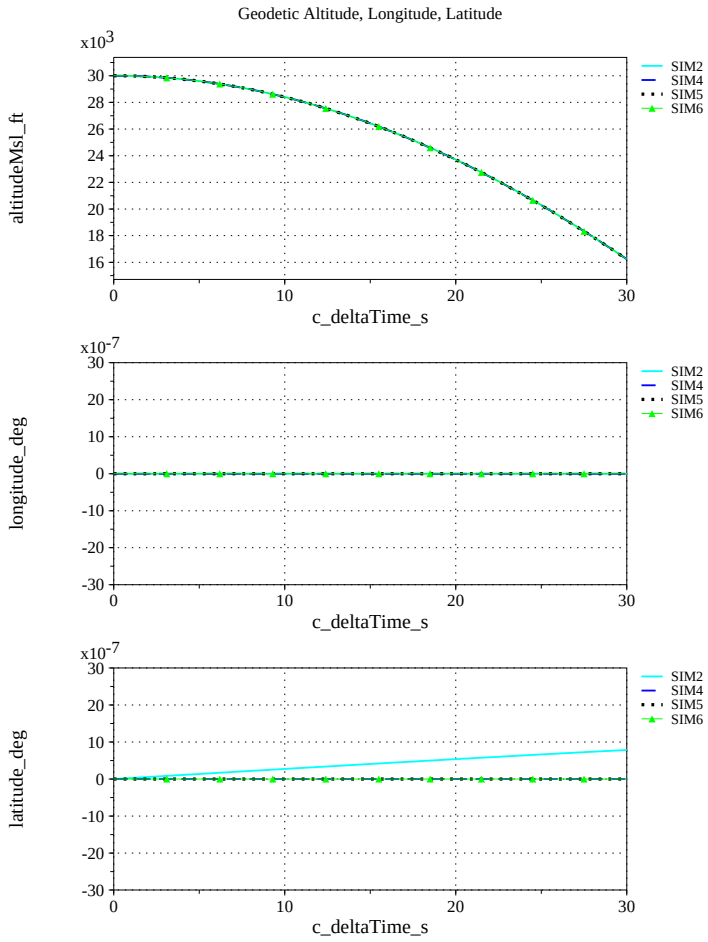

(e) Altitude, Geodetic Latitude and Longitude Compared

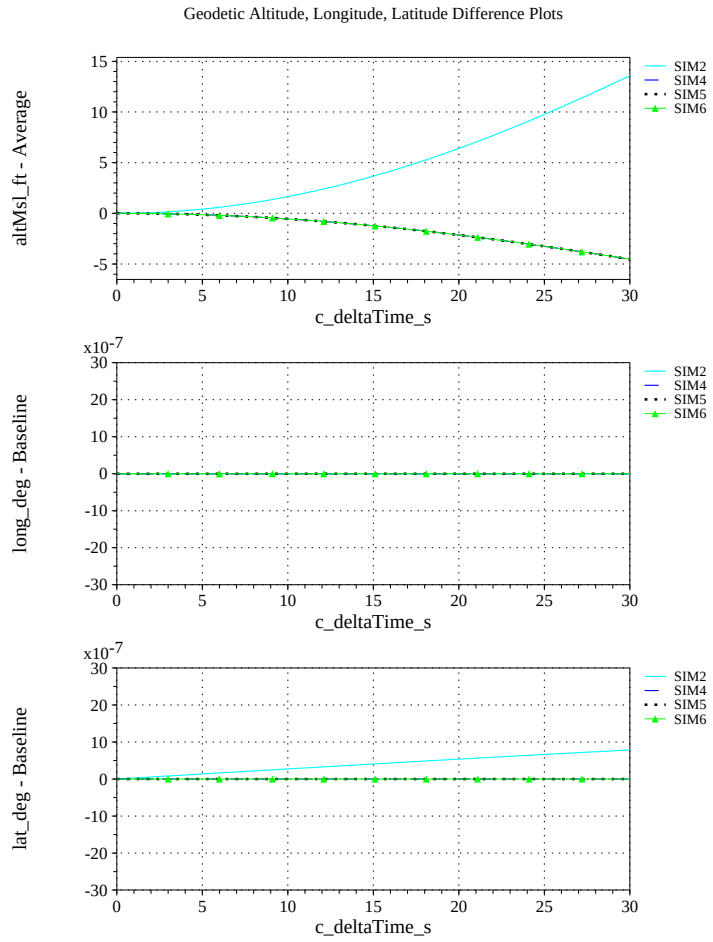

(f) Altitude, Geodetic Latitude and Longitude Differenced

Figure 19. Check-case 4: Sphere Dropping over Non-rotating, Spherical Earth; See Discussion in Section D.1.4 (Cont'd)

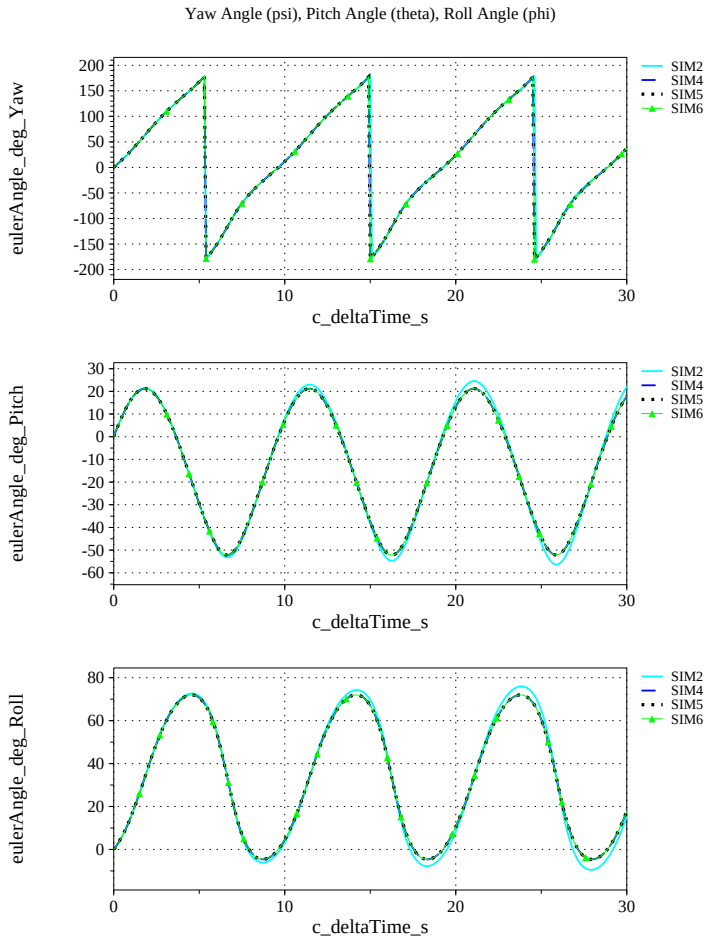

(g) Euler Angles (w.r.t. NED Frame) Compared

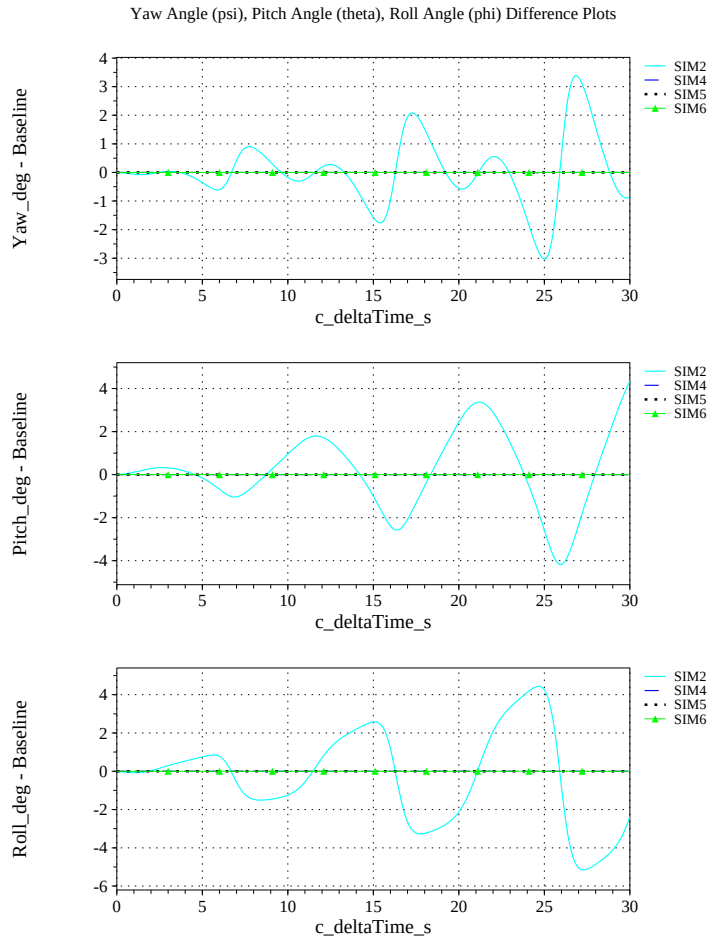

(h) Euler Angles (w.r.t. NED Frame) Differenced

Figure 19. Check-case 4: Sphere Dropping over Non-rotating, Spherical Earth; See Discussion in Section D.1.4 (Cont'd)

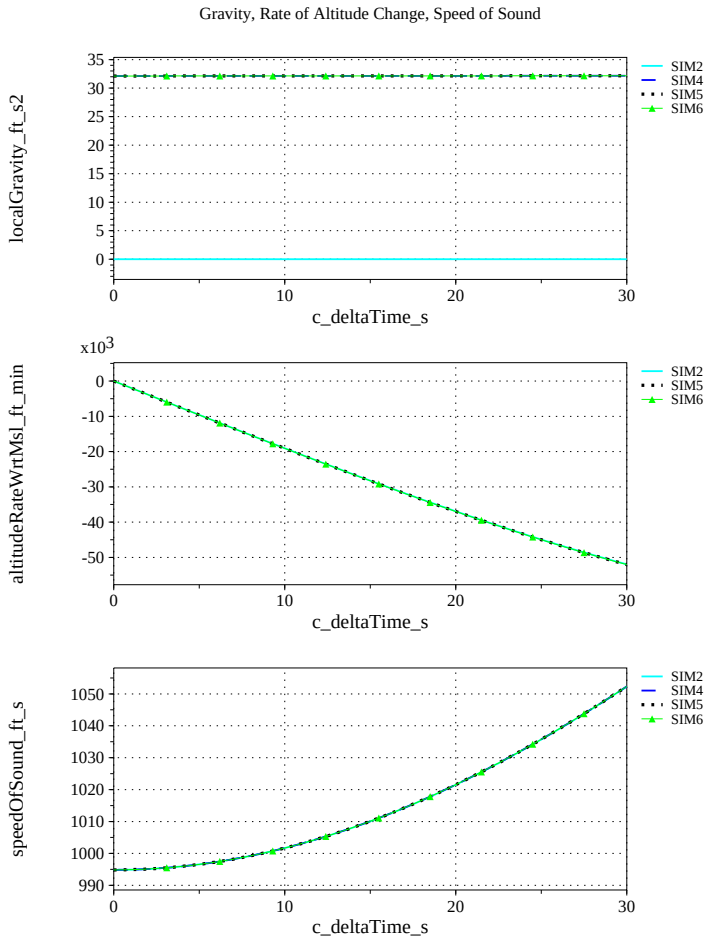

(i) Gravity, Climb Rate, and Speed-of-sound Compared

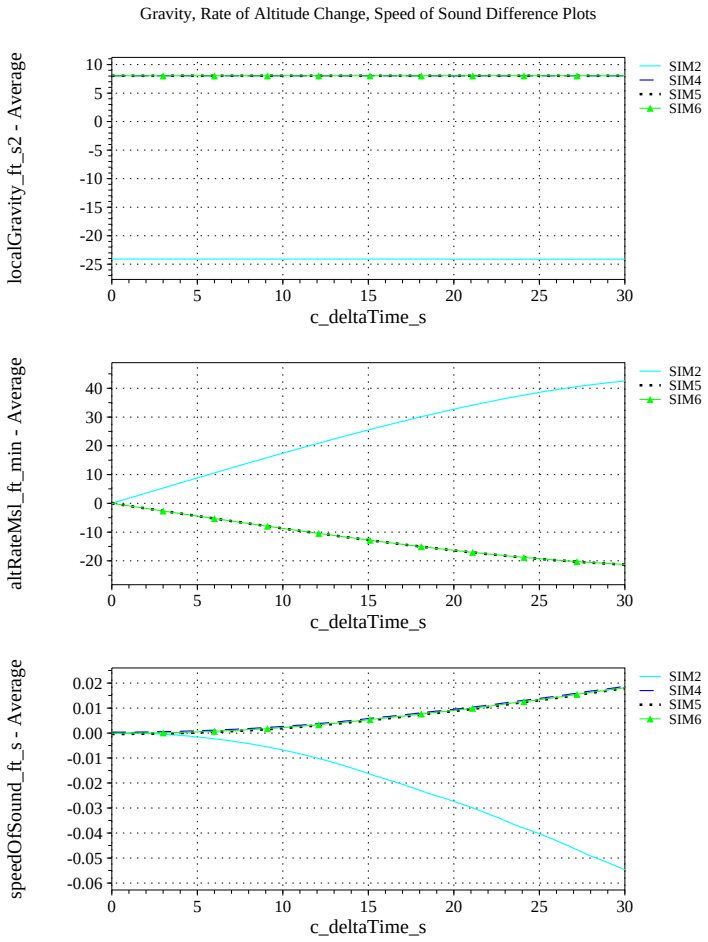

(j) Gravity, Climb Rate, and Speed-of-sound Differenced

Figure 19. Check-case 4: Sphere Dropping over Non-rotating, Spherical Earth; See Discussion in Section D.1.4 (Cont'd)

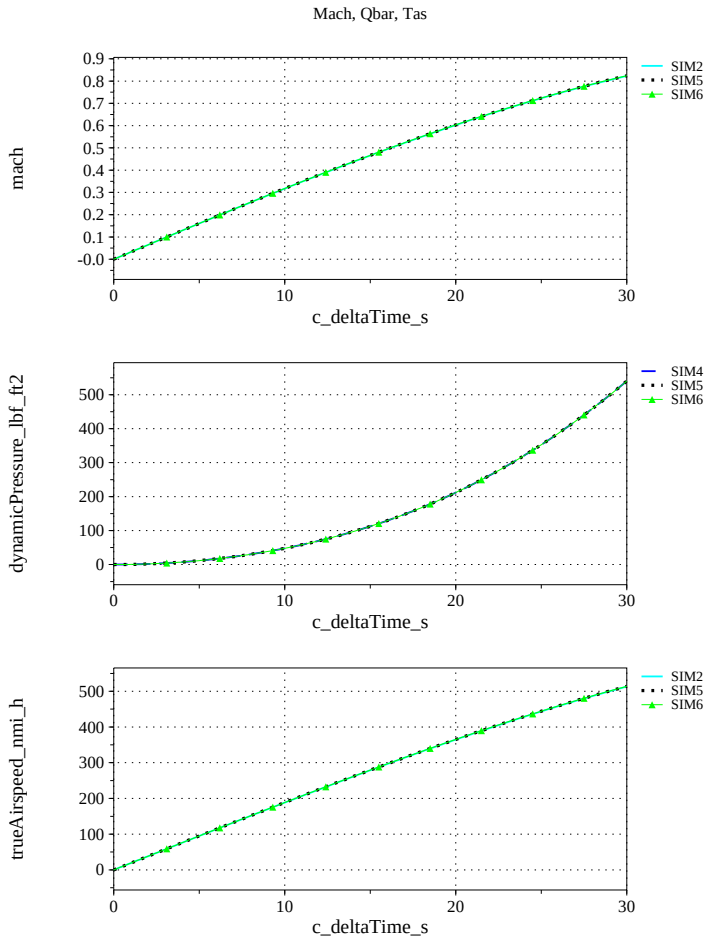

(k) Mach, Dynamic Pressure, and True Airspeed Compared

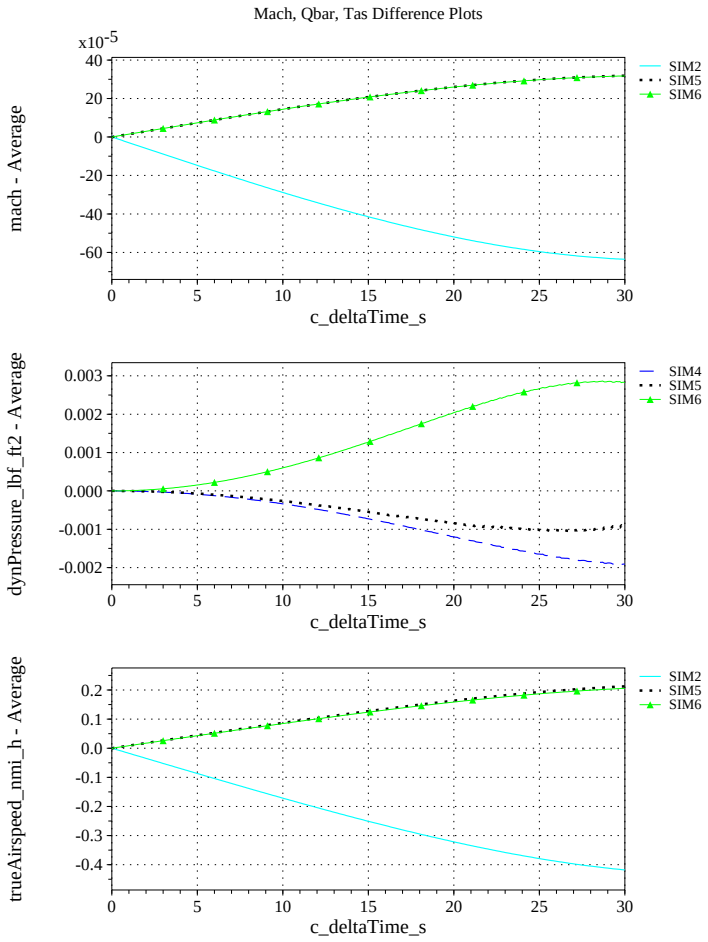

(l) Mach, Dynamic Pressure, and True Airspeed Differenced

Figure 19. Check-case 4: Sphere Dropping over Non-rotating, Spherical Earth; See Discussion in Section D.1.4 (Cont'd)

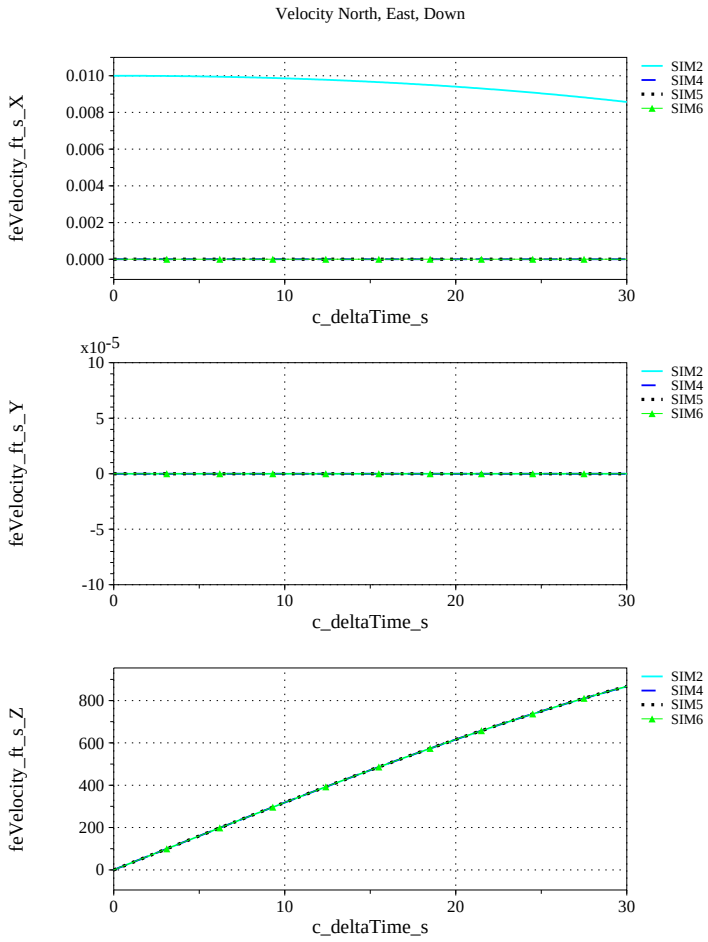

(m) NED Velocities Compared

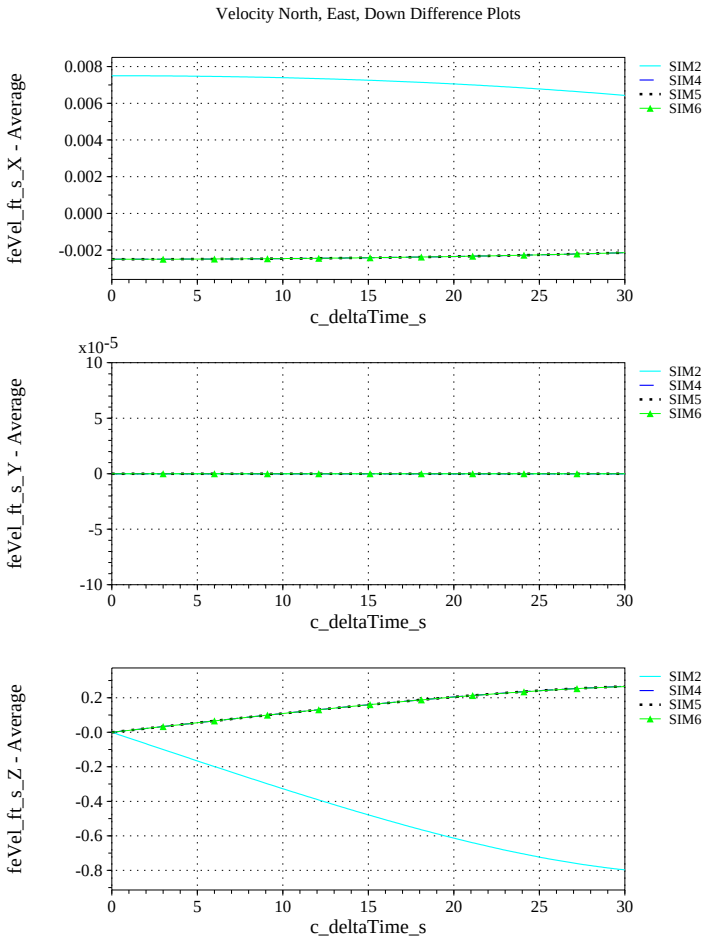

(n) NED Velocities Differenced

Figure 19. Check-case 4: Sphere Dropping over Non-rotating, Spherical Earth; See Discussion in Section D.1.4 (Cont'd)

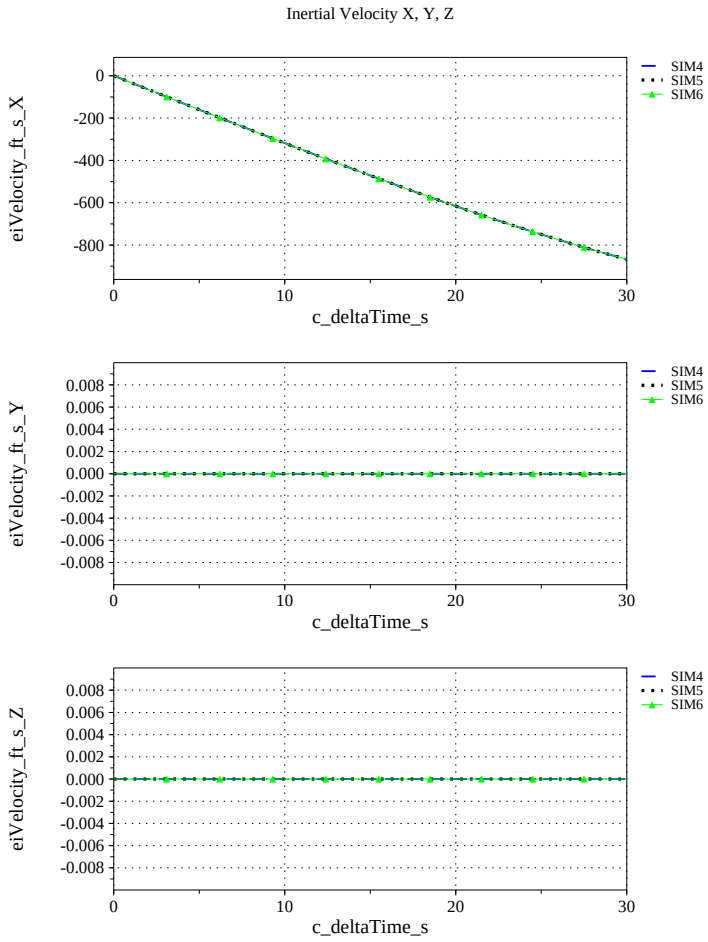

(o) Inertial Velocities Compared

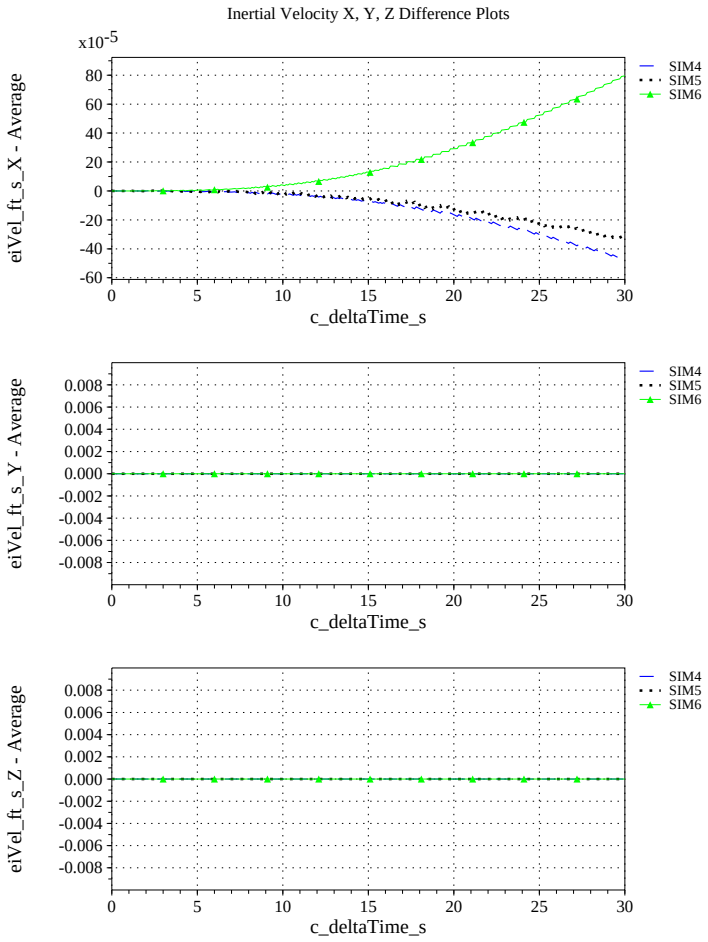

(p) Inertial Velocities Differenced

Figure 19. Check-case 4: Sphere Dropping over Non-rotating, Spherical Earth; See Discussion in Section D.1.4 (Cont'd)

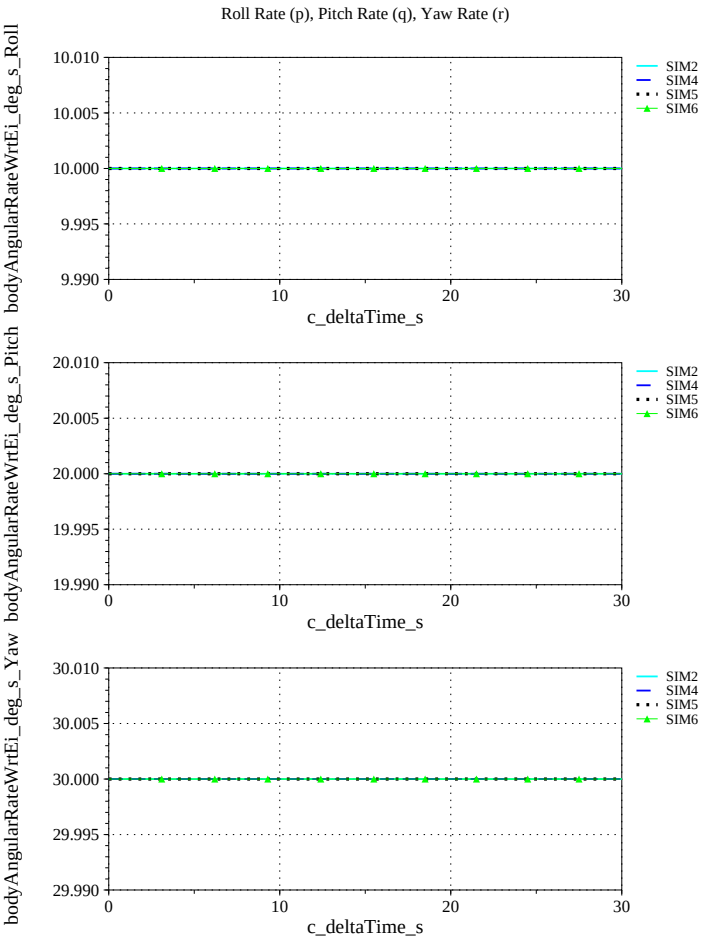

(q) Body-axis Angular Rates (w.r.t. NED Frame) Compared

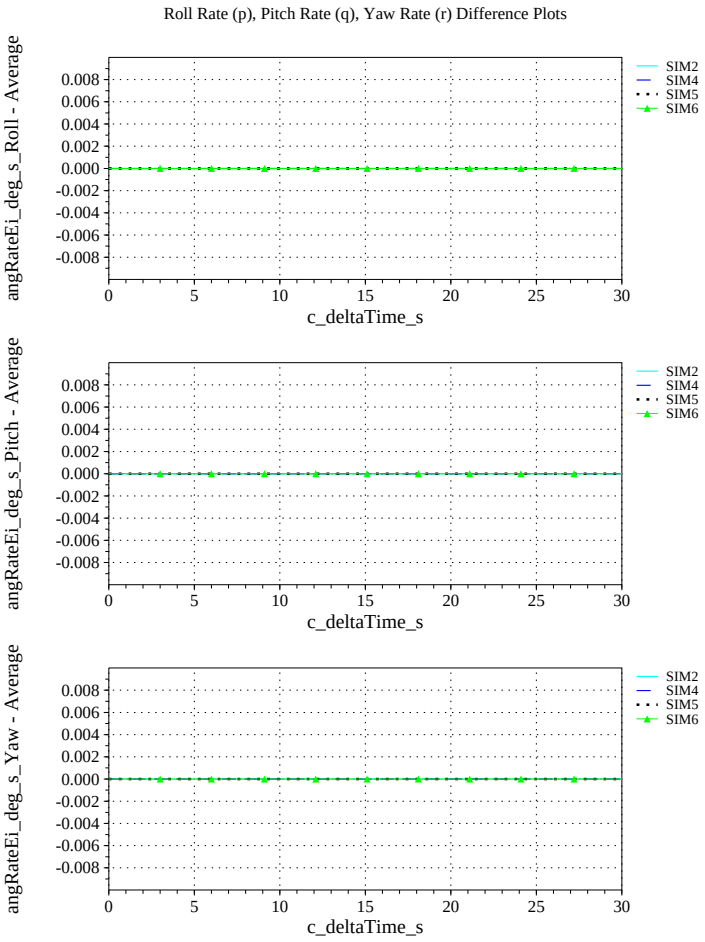

(r) Body-axis Angular Rates (w.r.t. NED Frame) Differenced

Figure 19. Check-case 4: Sphere Dropping over Non-rotating, Spherical Earth; See Discussion in Section D.1.4 (Cont'd)

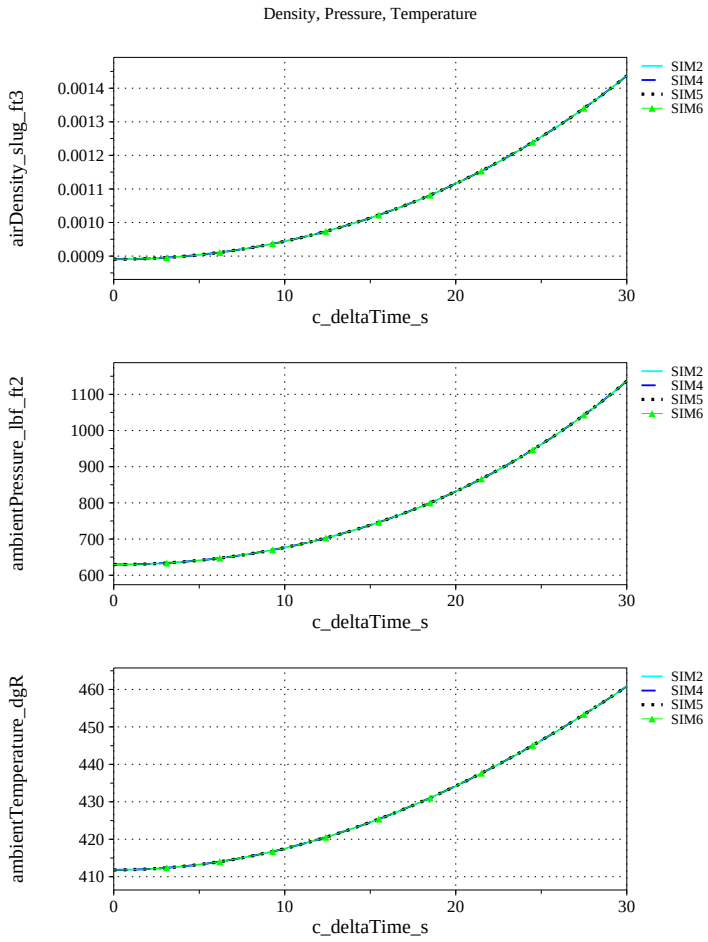

(s) Atmospheric Properties Compared

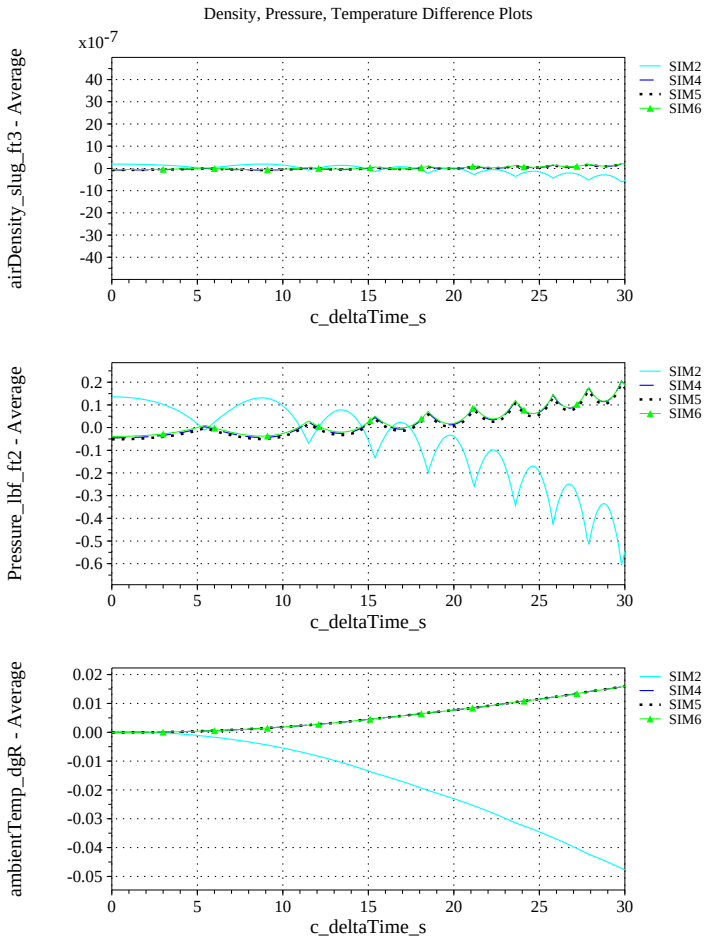

(t) Atmospheric Properties Differenced

Figure 19. Check-case 4: Sphere Dropping over Non-rotating, Spherical Earth; See Discussion in Section D.1.4 (Cont'd)

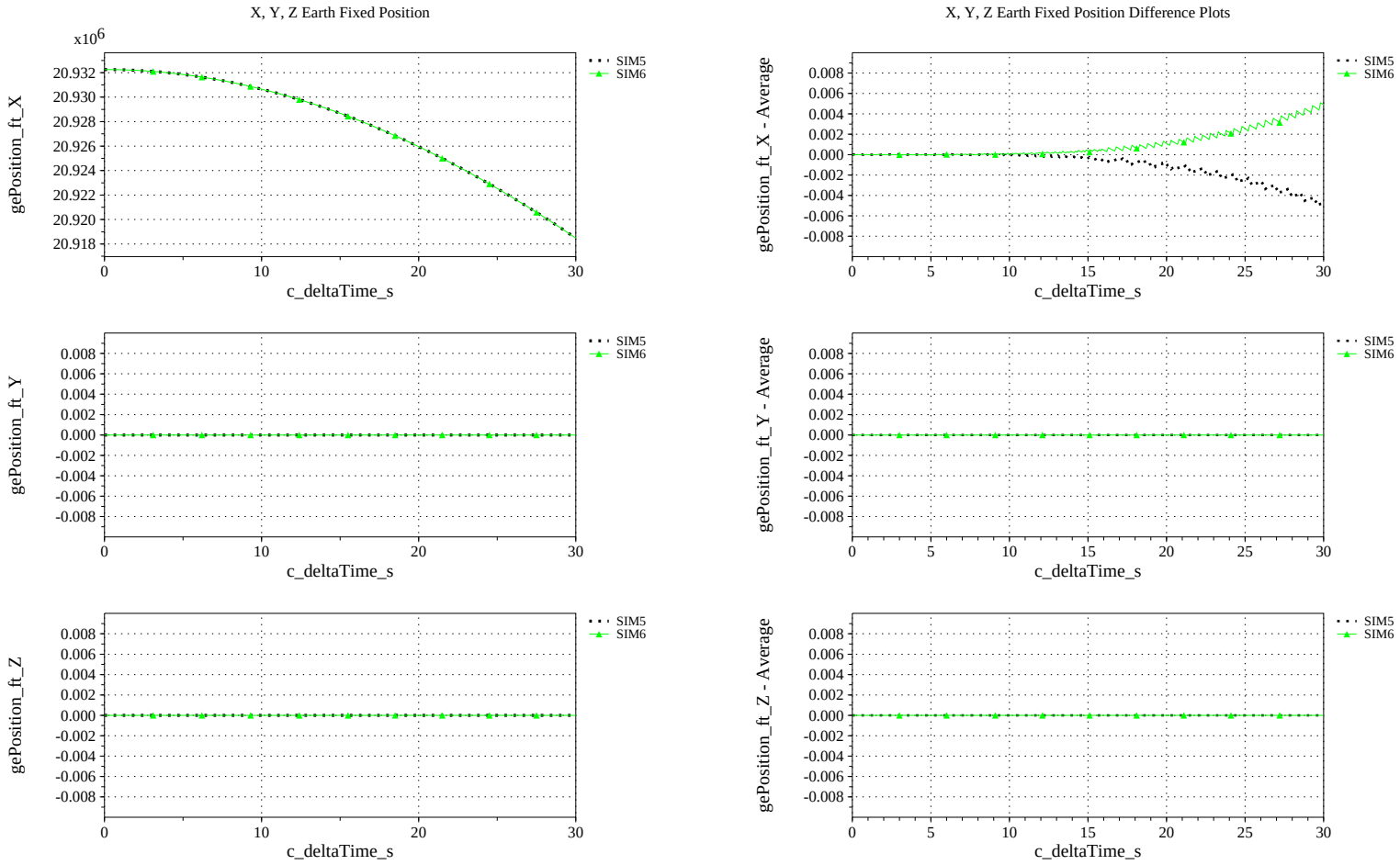

(u) Earth-centered, Earth-fixed Rectangular (X-Y-Z) Positions Compared (v) Earth-centered, Earth-fixed Rectangular (X-Y-Z) Positions Differenced

Figure 19. Check-case 4: Sphere Dropping over Non-rotating, Spherical Earth; See Discussion in Section D.1.4 (Cont'd)

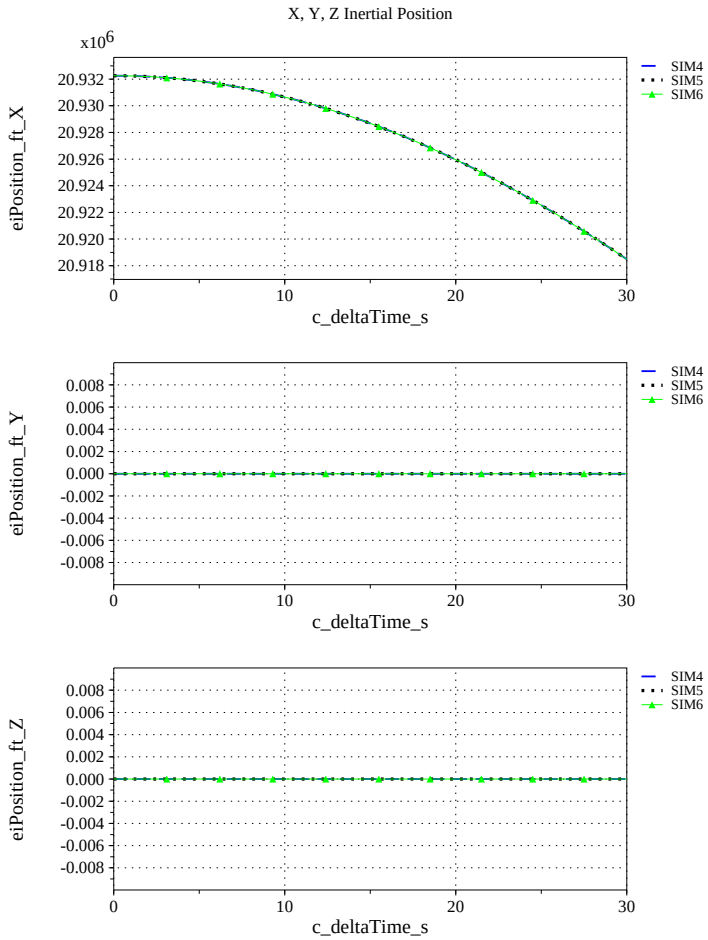

(w) Earth-centered Inertial Rectangular (x-y-z) Positions Compared

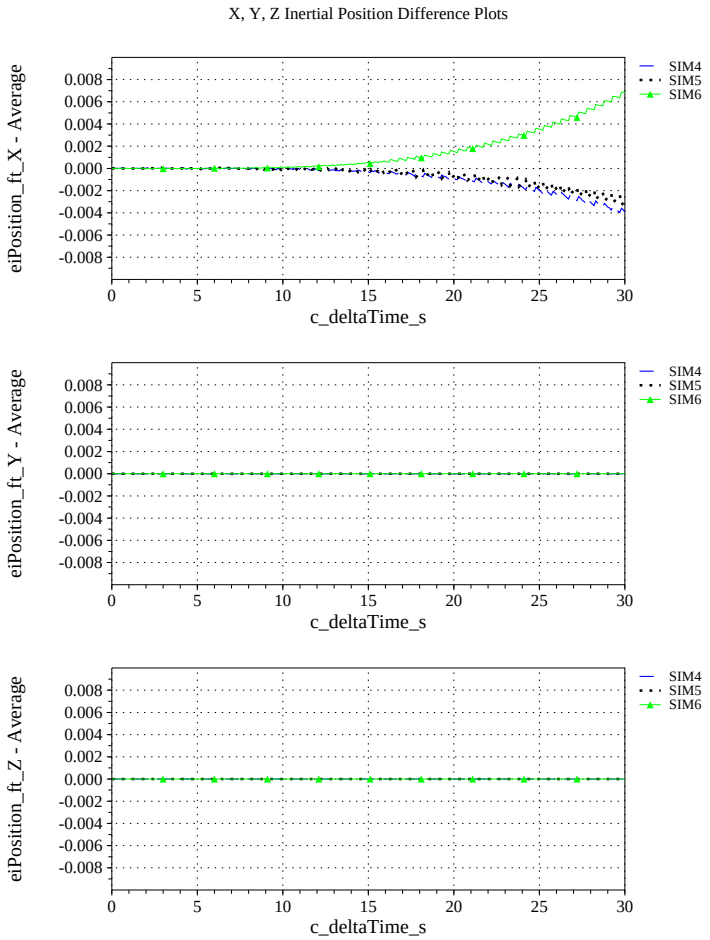

(x) Earth-centered Inertial Rectangular (x-y-z) Positions Differenced

Figure 19. Check-case 4: Sphere Dropping over Non-rotating, Spherical Earth; See Discussion in Section D.1.4 (Concluded)

D.1.5 Check-case 5 – sphere dropping over rotating, spherical Earth

This section shows cross-plots for four of the selected simulation tools in modeling the dynamics of a sphere dropped with a fixed drag coefficient through a still atmosphere in a round rotating Earth with spherical gravity. This scenario is described in Section C.1.5. Figures 20a through 20x compare results between the four simulation tools, as well as the deviances of the outputs from each tool from the ensemble average value.

This check-case scenario is identical to the "Check-case 4 – sphere dropping over non-rotating, spherical Earth" scenario but with the addition of Earth rotation. Likewise, the differences between the simulations were nearly the same as in the previous check-case. Again, SIM 2 exhibited a different trajectory from SIM 4, 5, and 6 due to an initial north velocity of 0.01 ft/s, a gravitation difference of approximately -0.05 ft/s^2, and the linear table interpolation implementation of the atmosphere model. With the addition of Earth's rotation, SIM 2 also exhibited a visible, though negligible, difference in longitude as the differences in downward velocity induced a difference in Coriolis acceleration. Adding the Earth's rotation did not visibly change differences in angular rates or orientation. All simulations agreed on angular rates. The predicted orientation in SIM 2 differed identically from the previous atmospheric case and appears to have been caused by a difference in integration method used to integrate the angular rates.

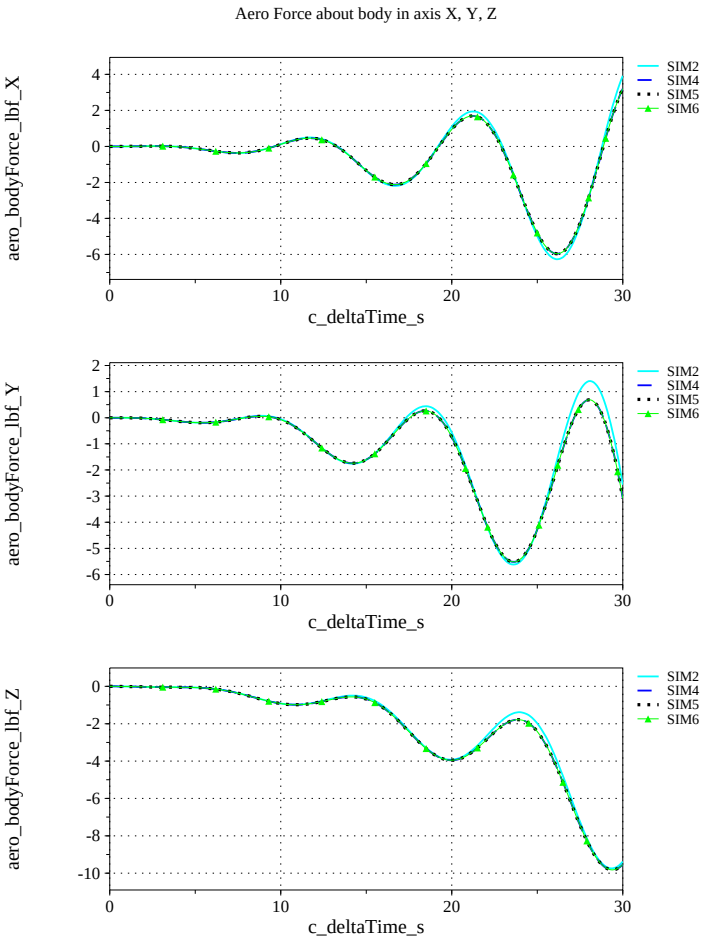

(a) Aerodynamic Forces Compared

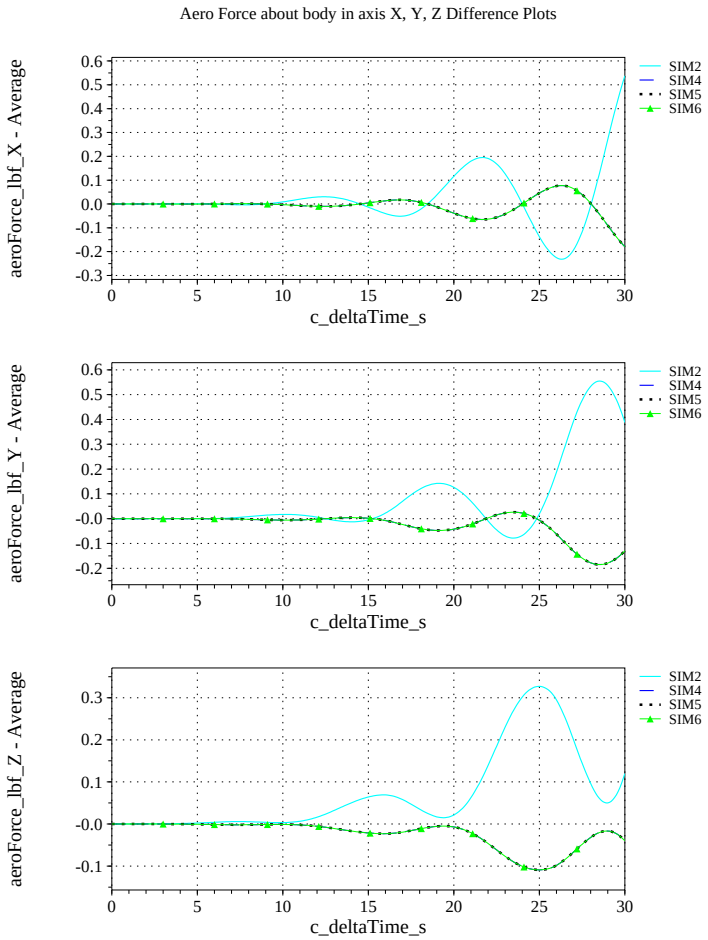

(b) Aerodynamic Forces Differenced

Figure 20. Check-case 5: Sphere Dropping over Rotating, Spherical Earth; See Discussion in Section D.1.5

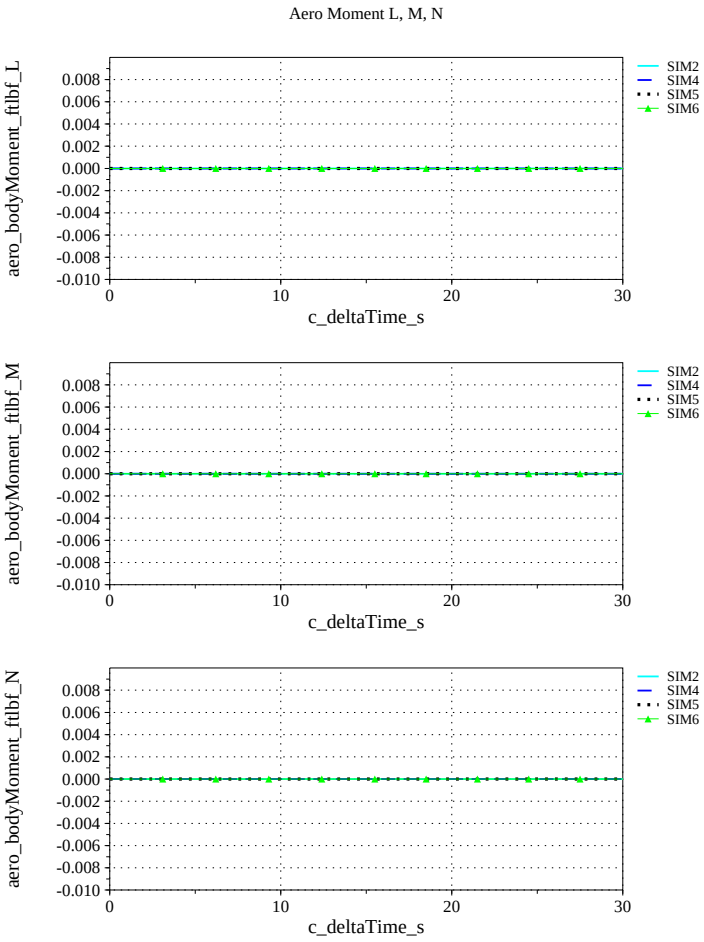

(c) Aerodynamic Moments Compared

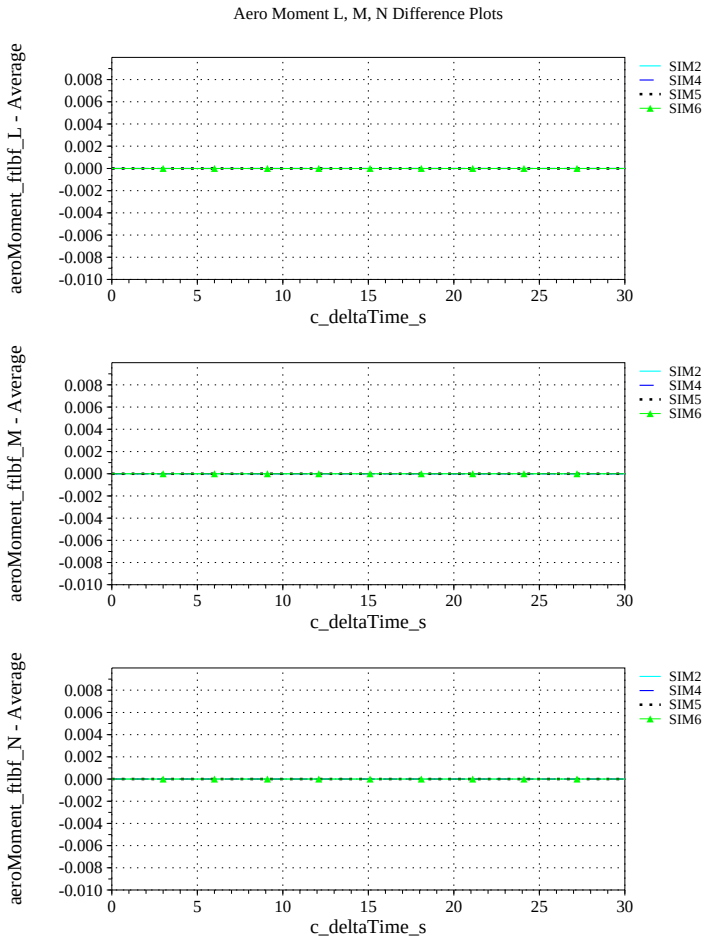

(d) Aerodynamic Moments Differenced

Figure 20. Check-case 5: Sphere Dropping over Rotating, Spherical Earth; See Discussion in Section D.1.5 (Cont'd)

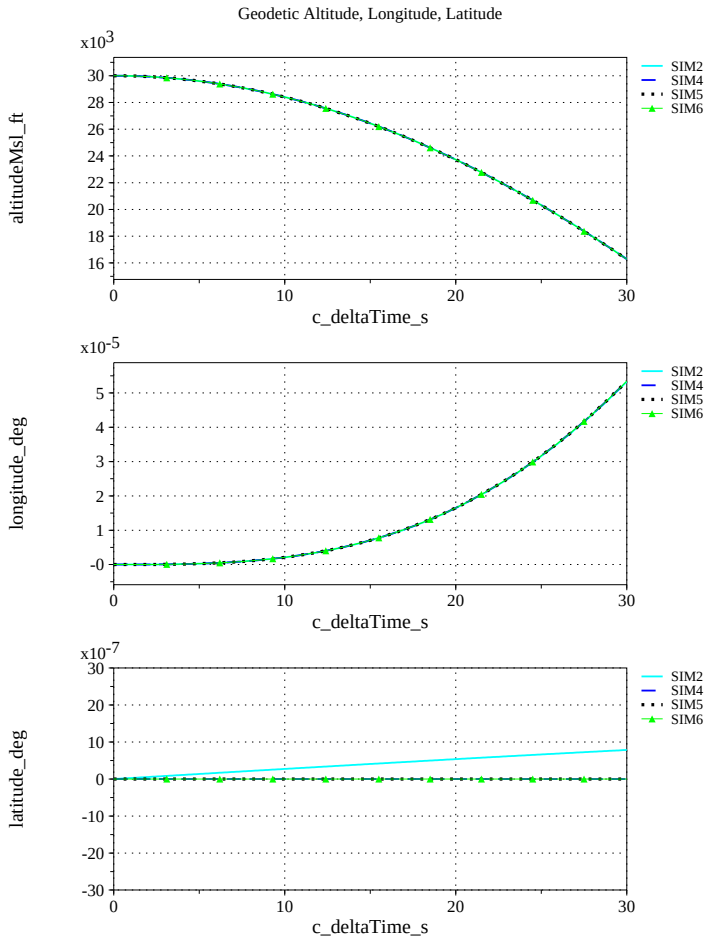

(e) Altitude, Geodetic Latitude and Longitude Compared

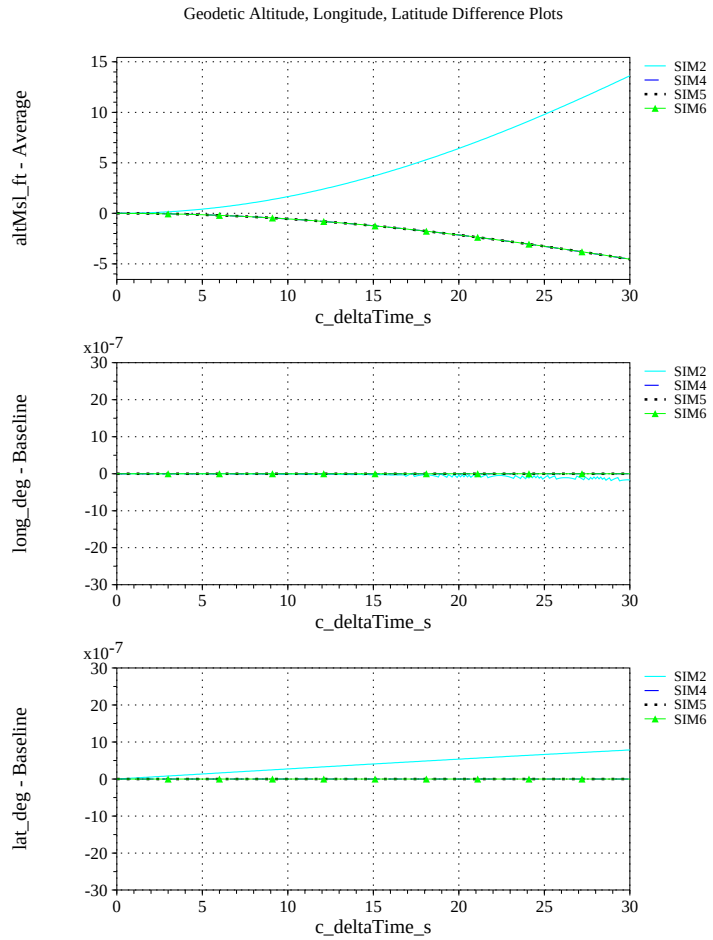

(f) Altitude, Geodetic Latitude and Longitude Differenced

Figure 20. Check-case 5: Sphere Dropping over Rotating, Spherical Earth; See Discussion in Section D.1.5 (Cont'd)

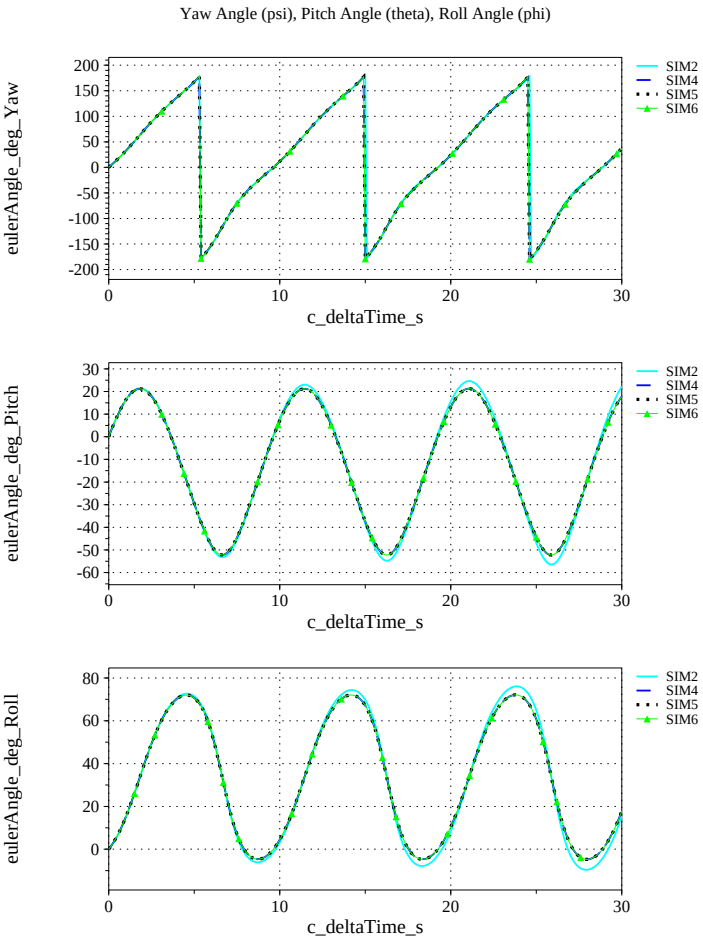

(g) Euler Angles (w.r.t. NED Frame) Compared

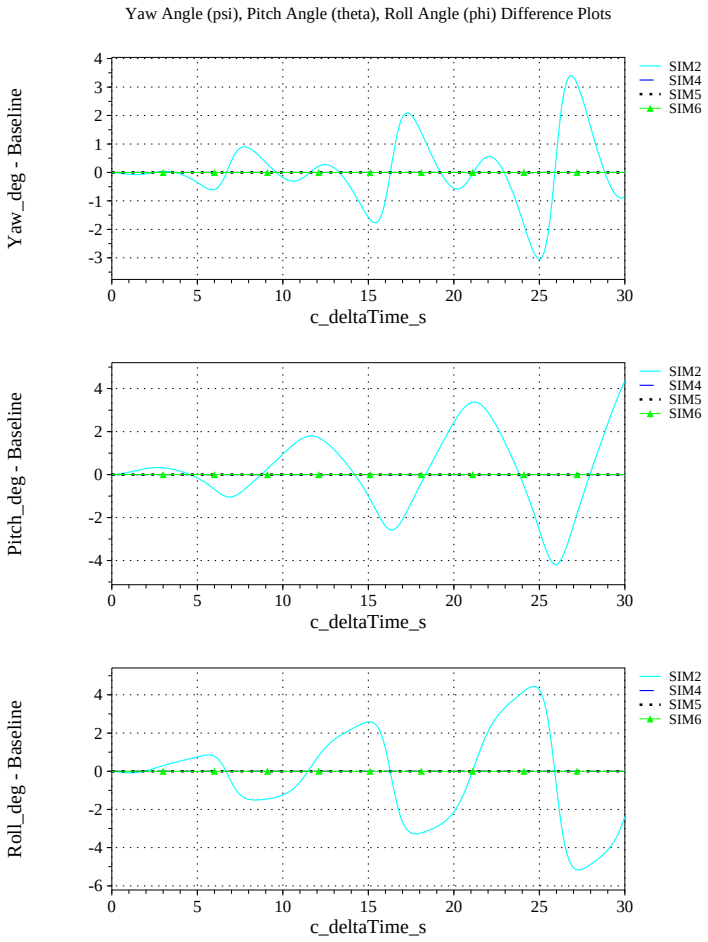

(h) Euler Angles (w.r.t. NED Frame) Differenced

Figure 20. Check-case 5: Sphere Dropping over Rotating, Spherical Earth; See Discussion in Section D.1.5 (Cont'd)

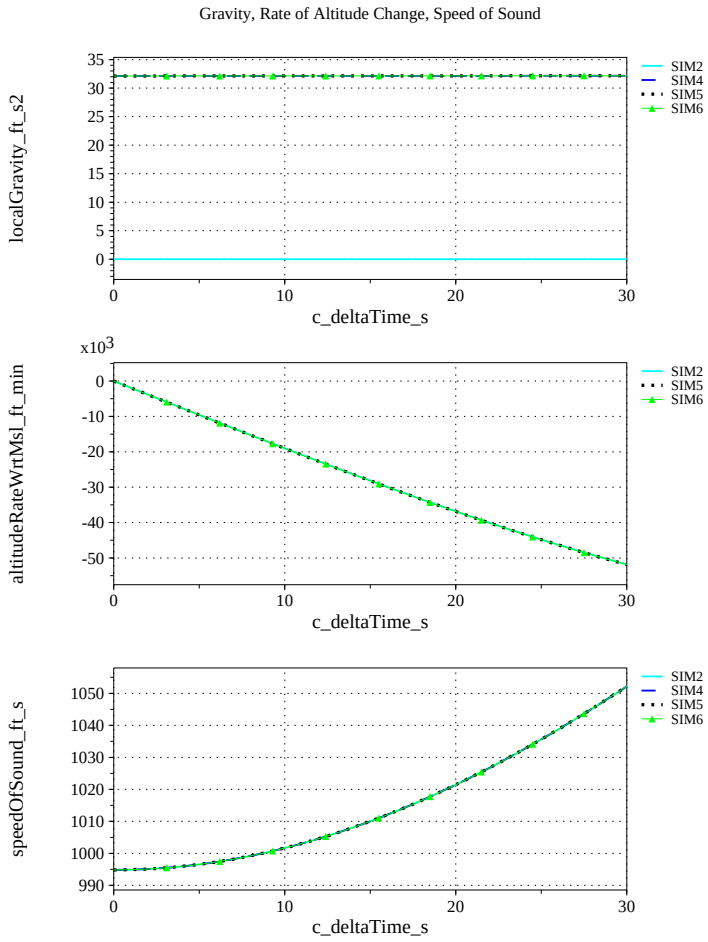

(i) Gravity, Climb Rate, and Speed-of-sound Compared

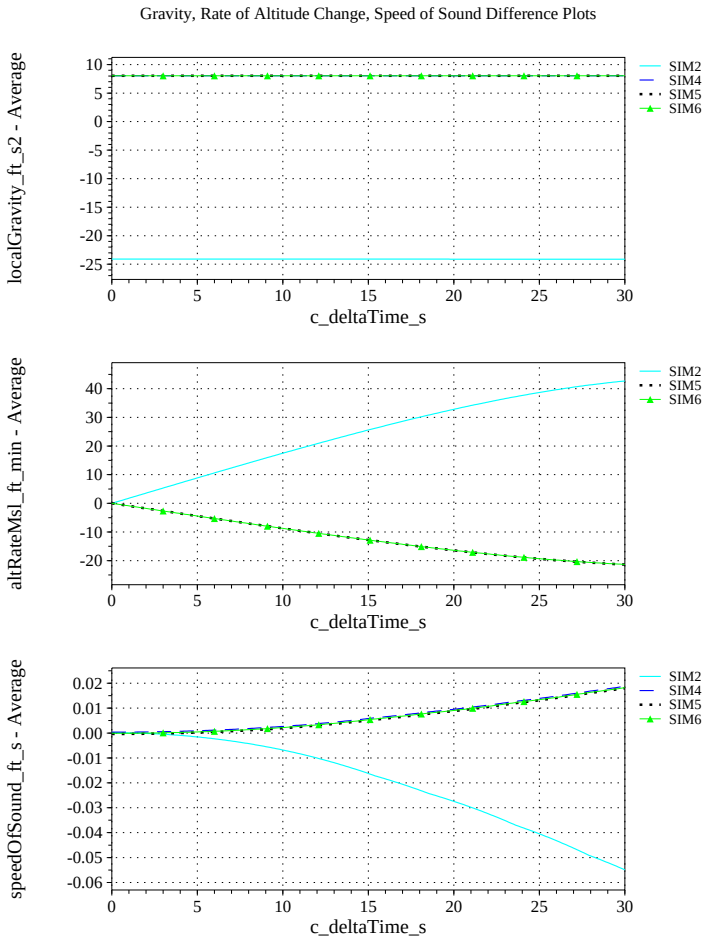

(j) Gravity, Climb Rate, and Speed-of-sound Differenced

Figure 20. Check-case 5: Sphere Dropping over Rotating, Spherical Earth; See Discussion in Section D.1.5 (Cont'd)

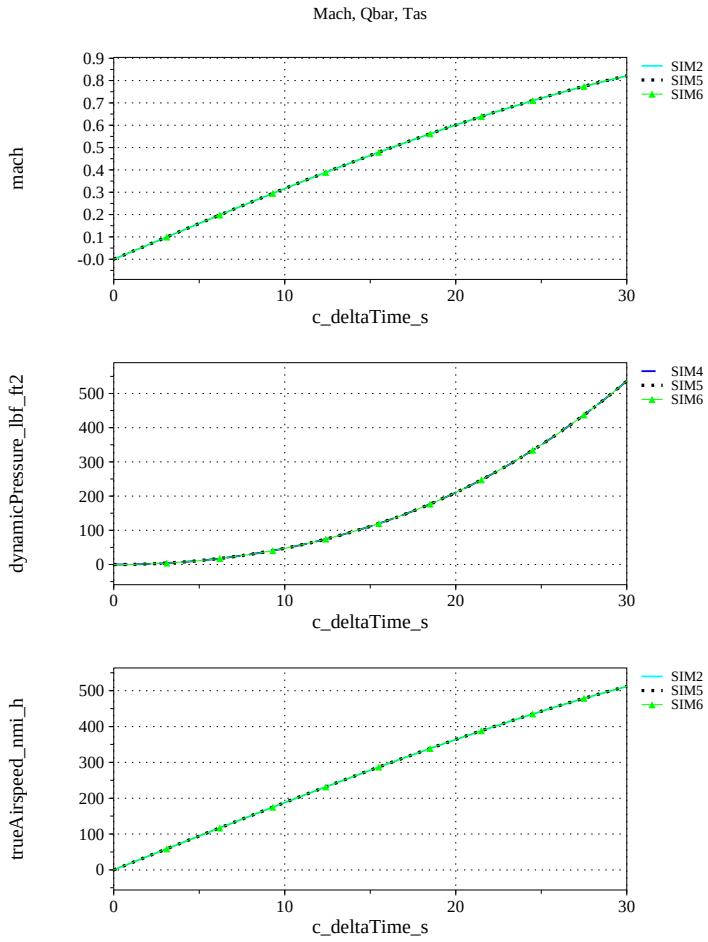

(k) Mach, Dynamic Pressure, and True Airspeed Compared

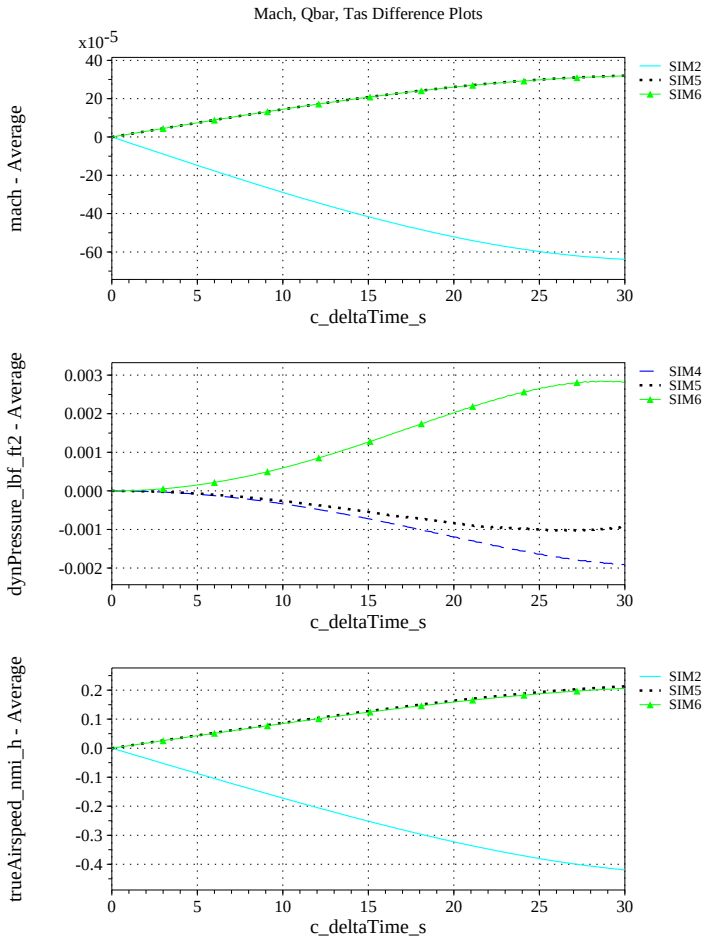

(l) Mach, Dynamic Pressure, and True Airspeed Differenced

Figure 20. Check-case 5: Sphere Dropping over Rotating, Spherical Earth; See Discussion in Section D.1.5 (Cont'd)

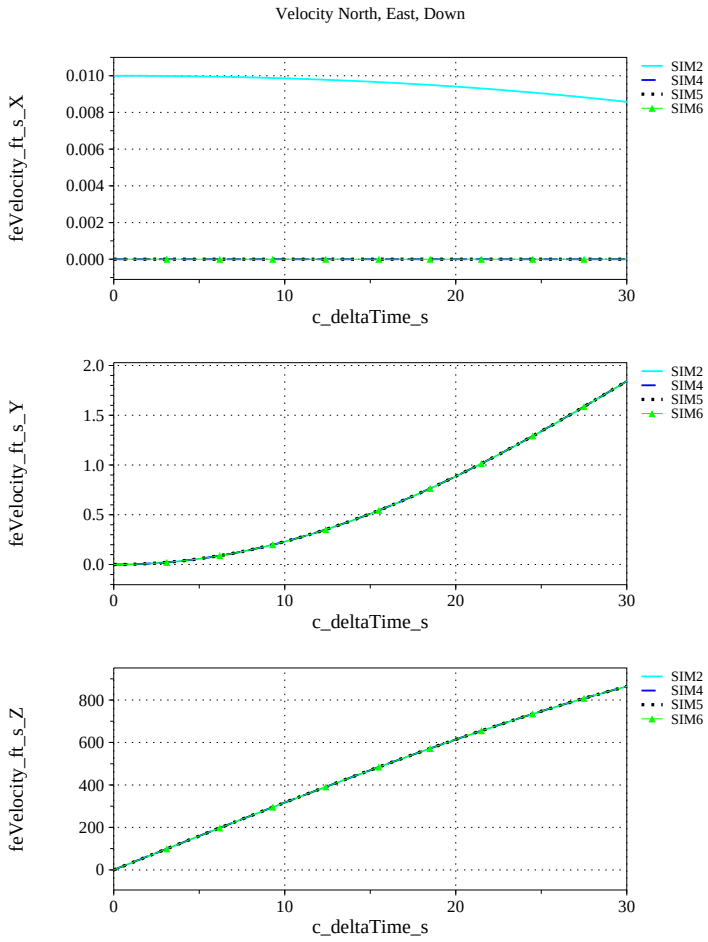

(m) NED Velocities Compared

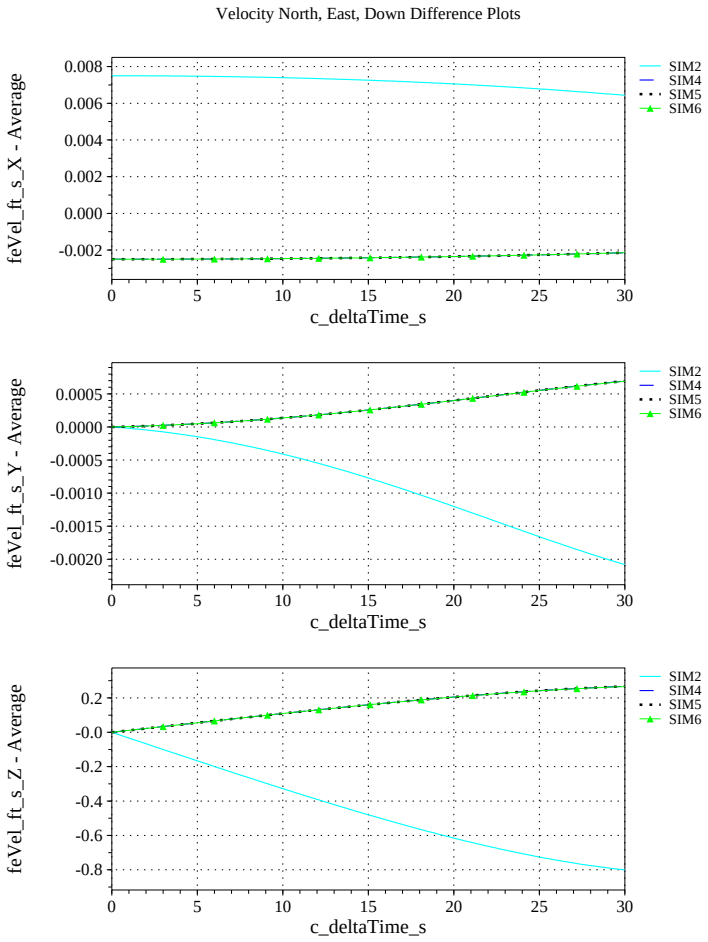

(n) NED Velocities Differenced

Figure 20. Check-case 5: Sphere Dropping over Rotating, Spherical Earth; See Discussion in Section D.1.5 (Cont'd)

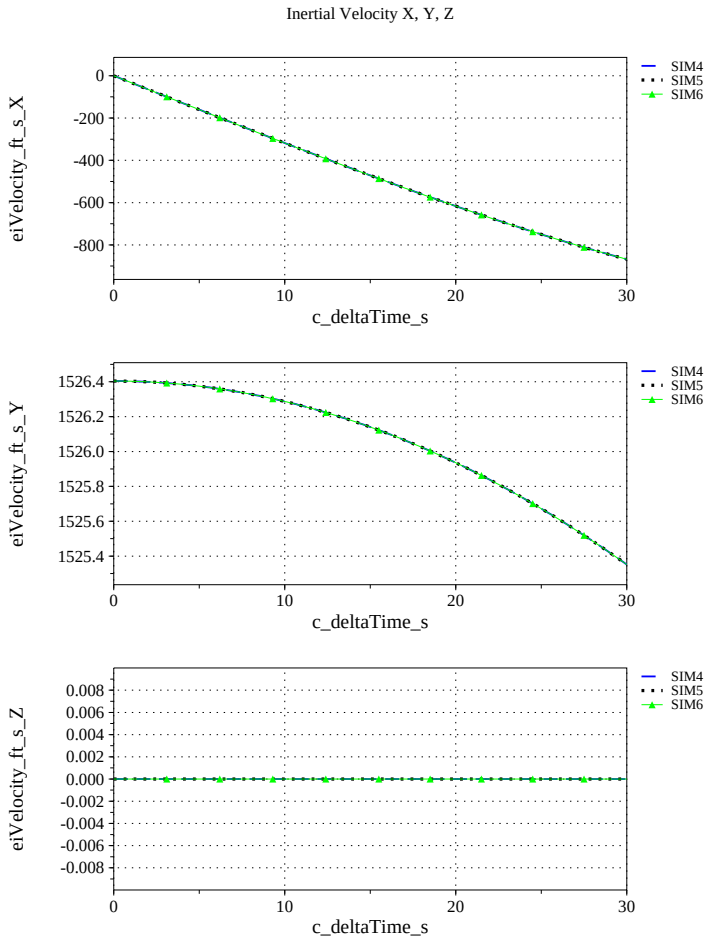

(o) Inertial Velocities Compared

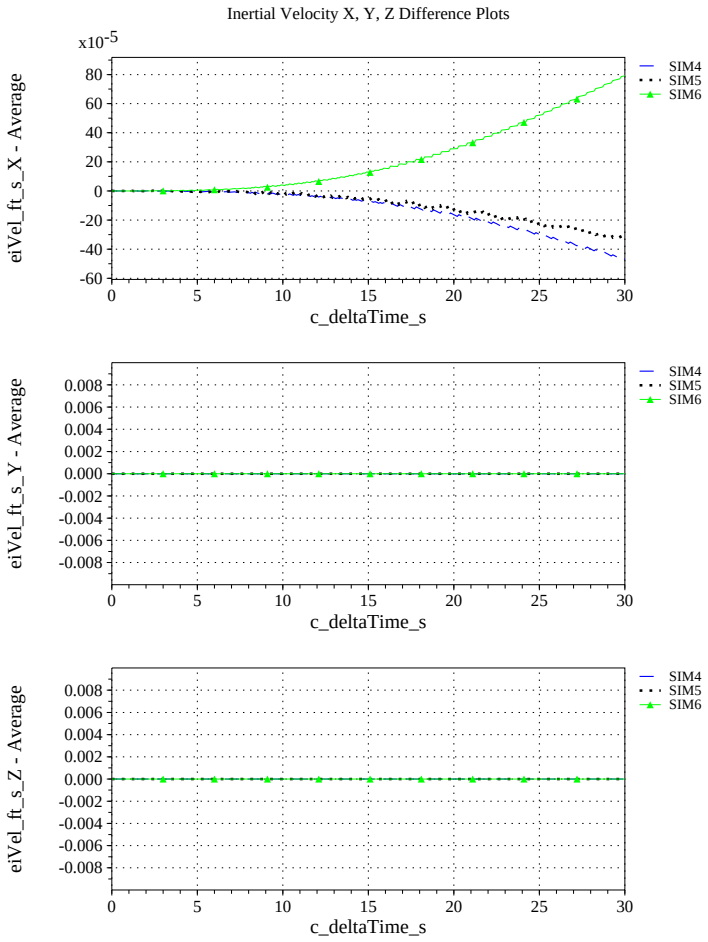

(p) Inertial Velocities Differenced

Figure 20. Check-case 5: Sphere Dropping over Rotating, Spherical Earth; See Discussion in Section D.1.5 (Cont'd)

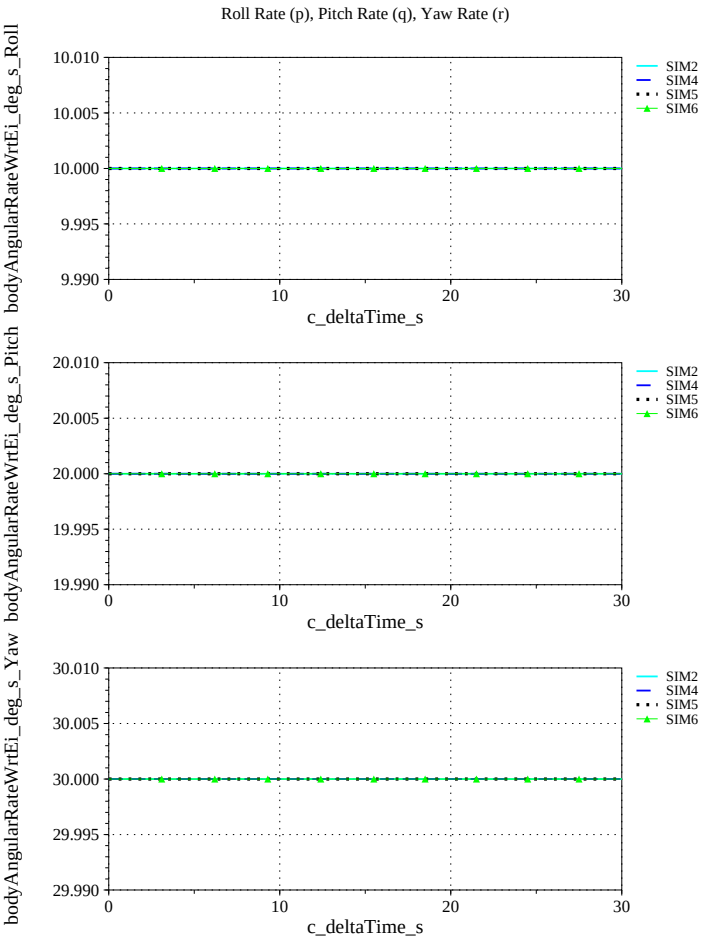

(q) Body-axis Angular Rates (w.r.t. NED Frame) Compared

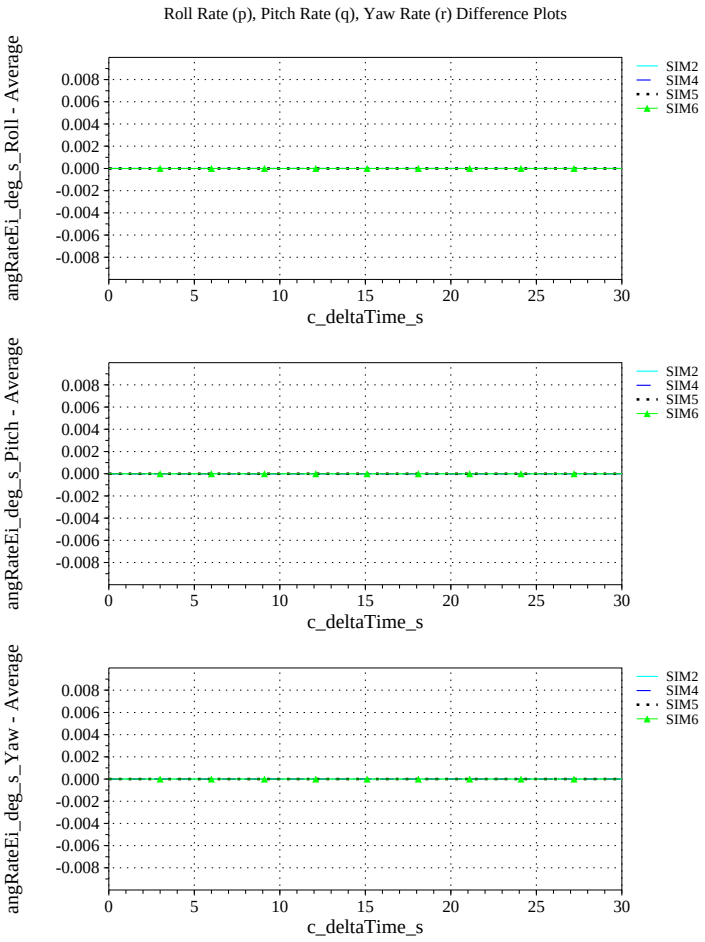

(r) Body-axis Angular Rates (w.r.t. NED Frame) Differenced

Figure 20. Check-case 5: Sphere Dropping over Rotating, Spherical Earth; See Discussion in Section D.1.5 (Cont'd)

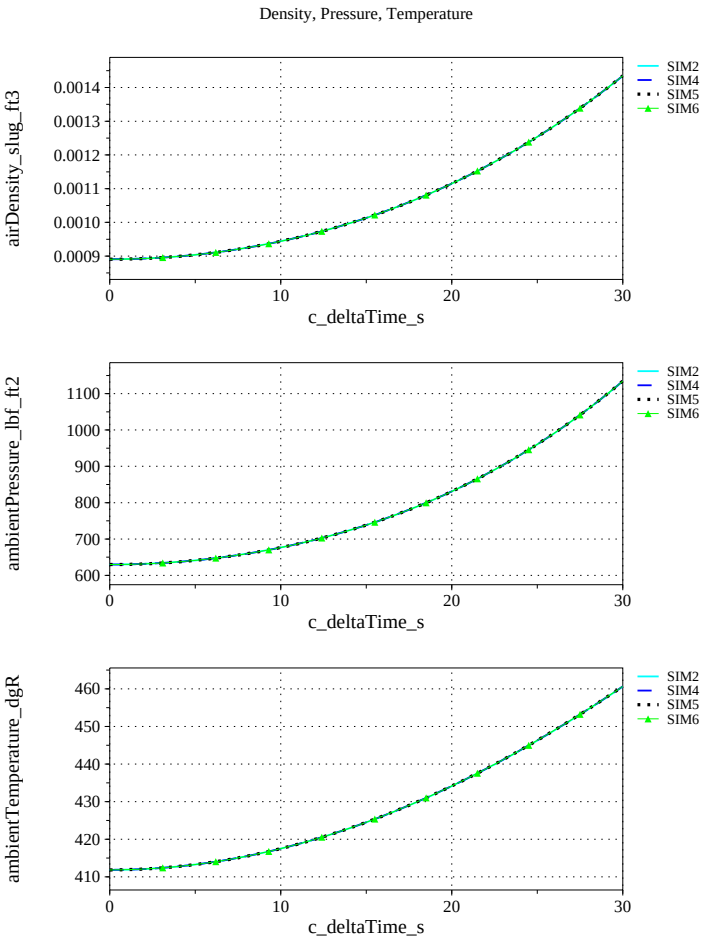

(s) Atmospheric Properties Compared

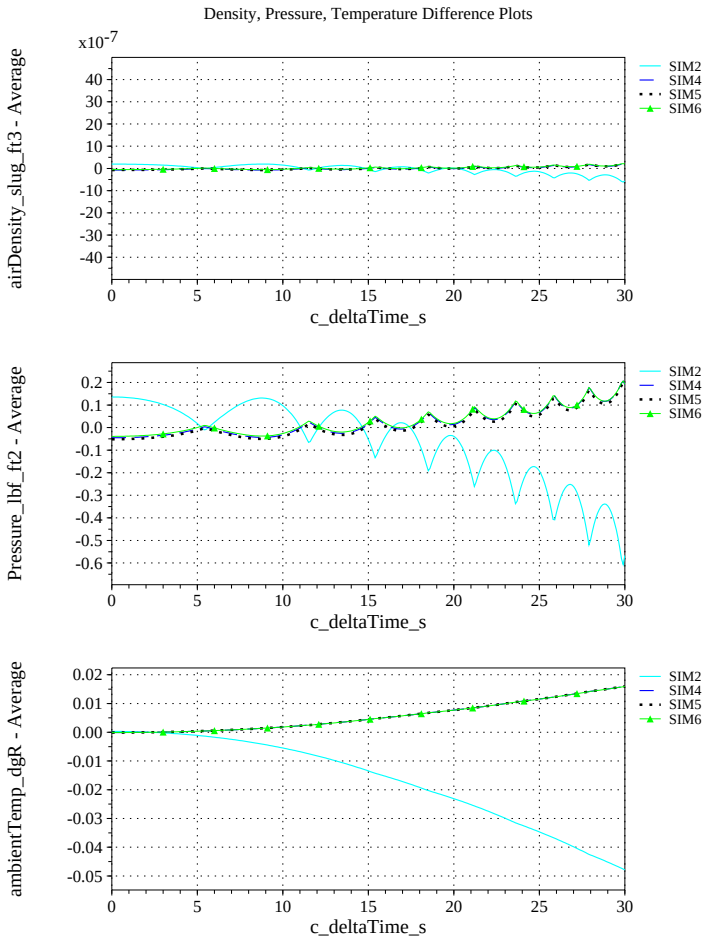

(t) Atmospheric Properties Differenced

Figure 20. Check-case 5: Sphere Dropping over Rotating, Spherical Earth; See Discussion in Section D.1.5 (Cont'd)

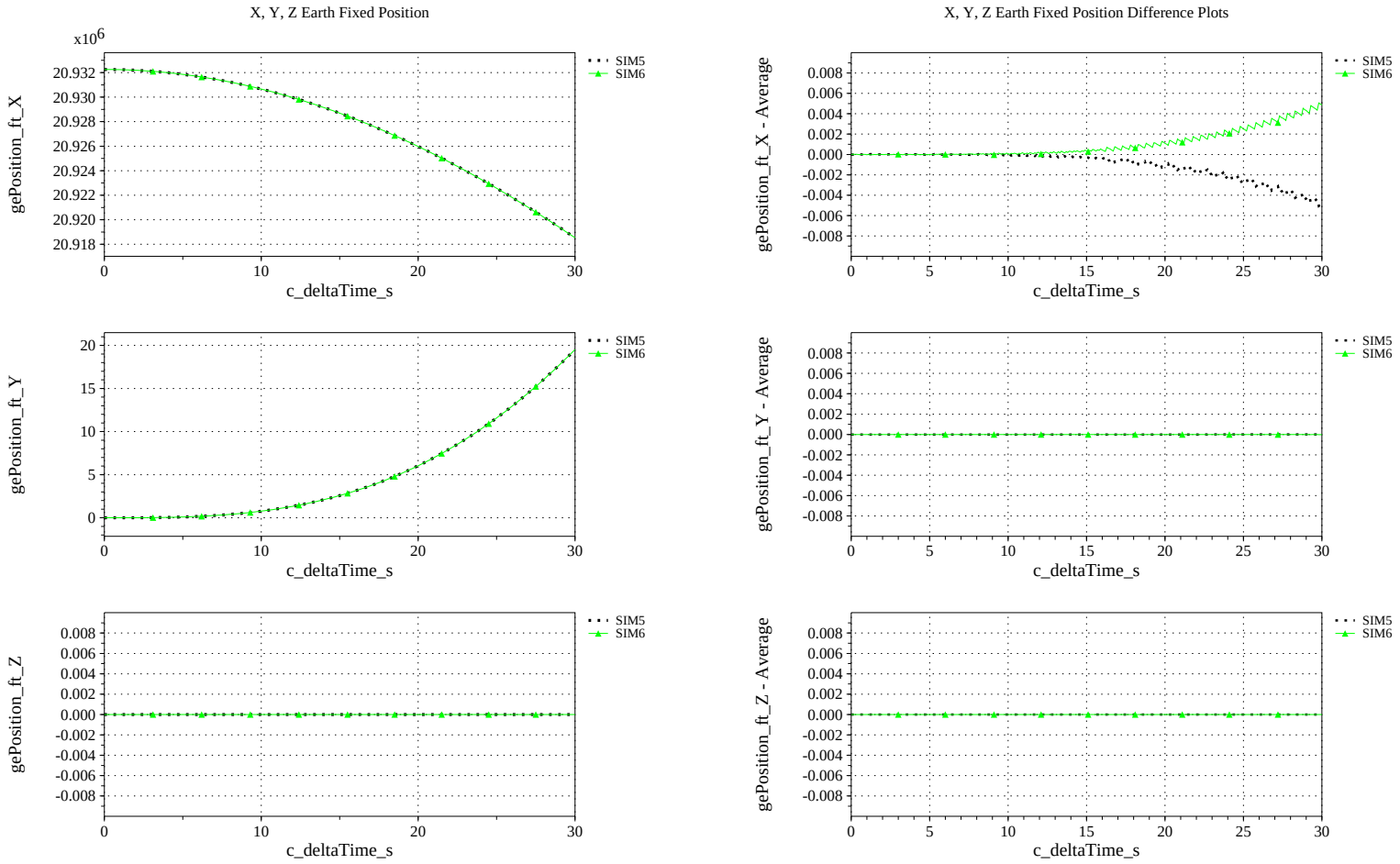

(u) Earth-centered, Earth-fixed Rectangular (X-Y-Z) Positions Compared (v) Earth-centered, Earth-fixed Rectangular (X-Y-Z) Positions Differenced

Figure 20. Check-case 5: Sphere Dropping over Rotating, Spherical Earth; See Discussion in Section D.1.5 (Cont'd)

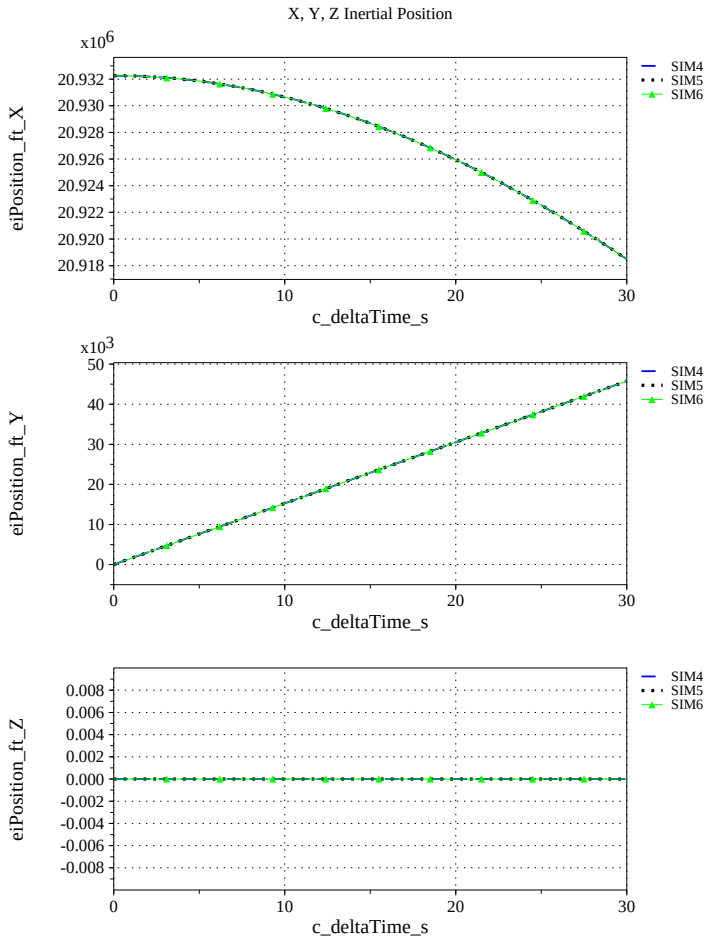

(w) Earth-centered Inertial Rectangular (x-y-z) Positions Compared

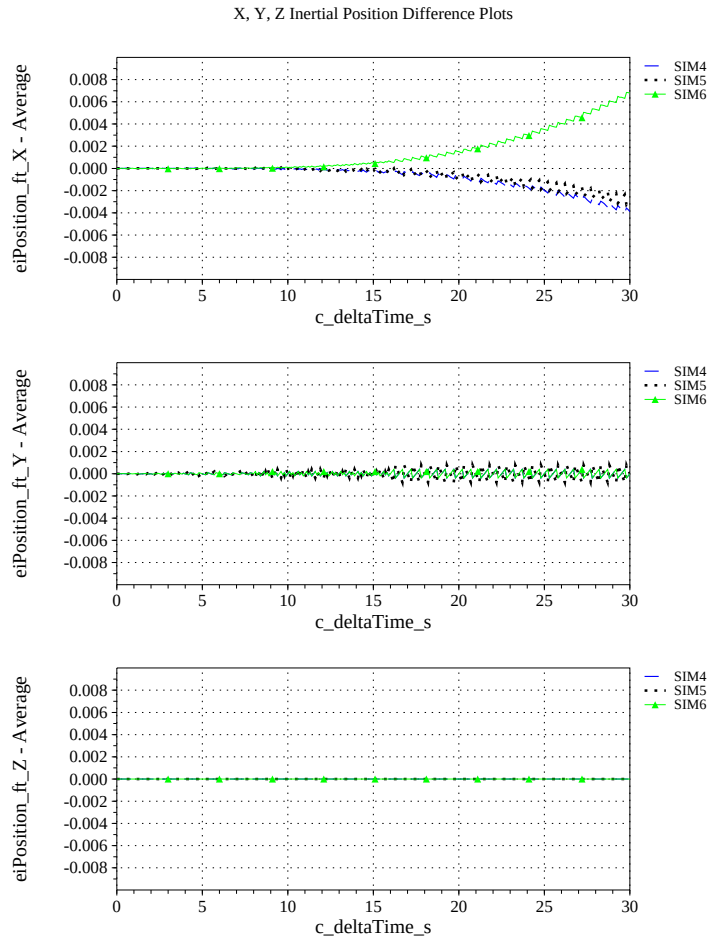

(x) Earth-centered Inertial Rectangular (x-y-z) Positions Differenced

Figure 20. Check-case 5: Sphere Dropping over Rotating, Spherical Earth; See Discussion in Section D.1.5 (Concluded)

D.1.6 Check-case 6 – sphere dropping over rotating, ellipsoidal Earth

This section shows cross-plots for six of the selected simulation tools in modeling the dynamics of a sphere dropped with a fixed drag coefficient through a still atmosphere in a ellipsoidal rotating Earth with J_2 gravitational harmonics. This scenario is described in Section C.1.6. Figures 21a through 21x compare results between the six simulation tools, as well as the deviances of the outputs from each tool from the ensemble average value.

This check-case was identical to "Check-case 1 – dragless sphere" scenario with the addition of aerodynamic drag. Since drag is a function of both velocity and atmospheric density (which, in turn, is a function of altitude), this scenario could amplify differences in predicted velocity and altitude that were visible in atmospheric case 1. Furthermore, the differences in atmospheric density among the simulations due to choices of atmospheric model implementation would now have an effect on translational dynamics through the aerodynamic forces.

As discussed in atmospheric check-case 1, small differences in atmospheric density arose because simulation SIM 3, 4, 5, and 6 implemented the atmosphere model using formulas and SIM 1 and SIM 2 used look-up tables. Differences in aerodynamic forces were consistent with differences in velocity and atmospheric density with the exception of SIM 2 and SIM 3.

SIM 2 and SIM 3 both had additional contributors to differences in aerodynamic forces. In the case of SIM 2, it appeared that the aerodynamic force lagged the other simulations by 0.01 sec, or one frame in a 100-Hz simulation. This finding was corroborated by reconstructing the aerodynamic force using the density and velocity reported by SIM 2. The aerodynamic forces reported by SIM 2 were best reconstructed using a linear interpolation of the velocity and density delayed by 0.01 sec. Though the reported aerodynamic forces lagged one frame, the differences in recorded velocity were smaller than would be expected if this lag also existed in the EOM. In the case of SIM 3, apparent differences in vehicle orientation caused differences in the recorded aerodynamic forces and moments in body coordinates. Though SIM 3 did not record angular rates or Euler angles, its differences in the aerodynamic y and z forces could be reproduced by assuming the sphere had an initial Earth relative rate of zero. The other simulations initialized to an inertial rate of zero.

Differences in the other external force, gravitation, were consistent with differences in altitude. The combined effect of differences in aerodynamic and gravitation forces on the translational states remained modest. All simulations agreed that there was no northward velocity. Likewise, differences in longitude and in eastward velocity (due to Coriolis effect) were negligible. In the downward axis, the simulations did show differences in the range $-0.07 to 0.010$ ft/s for downward velocity and in the range $-0.6 to 0.4$ ft for altitude.

Among the simulations that recorded rotational states, there were no visible differences.

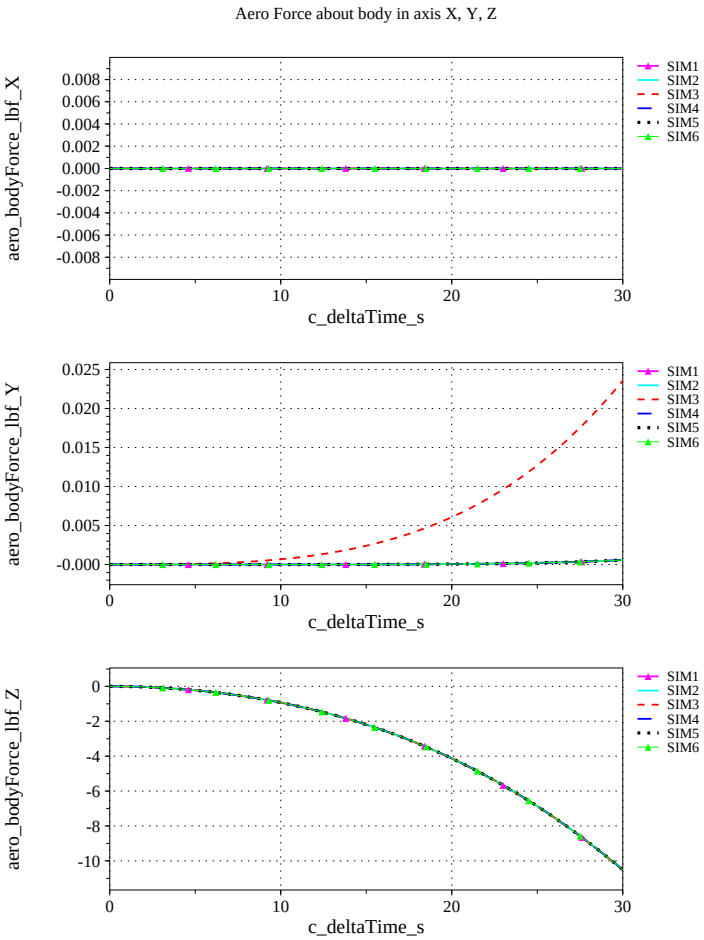

(a) Aerodynamic Forces Compared

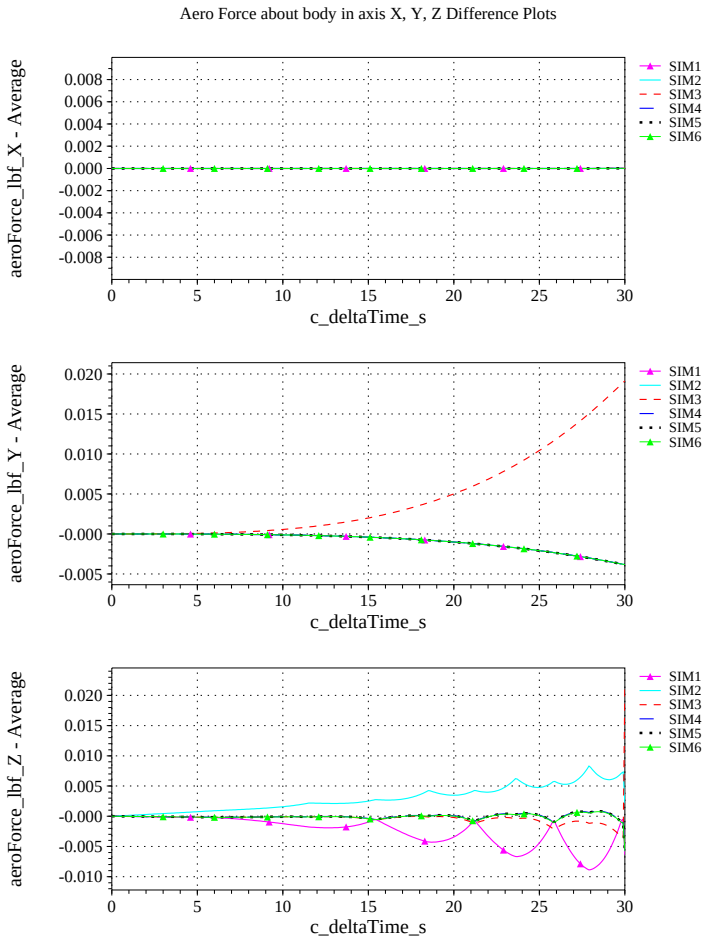

(b) Aerodynamic Forces Differenced

Figure 21. Check-case 6: Sphere Dropping over Rotating, Ellipsoidal Earth; See Discussion in Section D.1.6

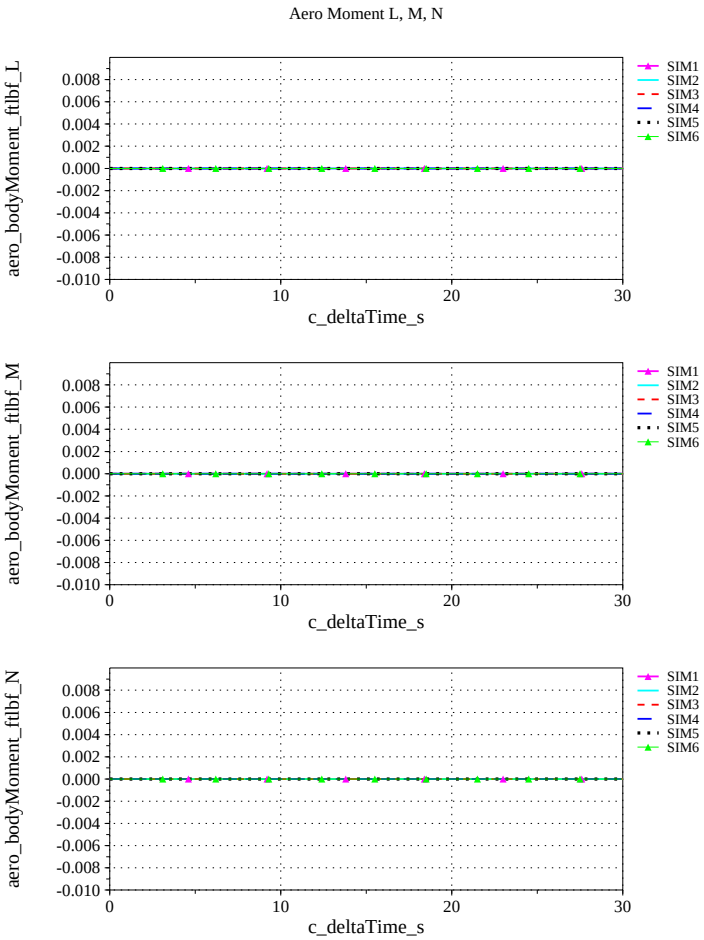

(c) Aerodynamic Moments Compared

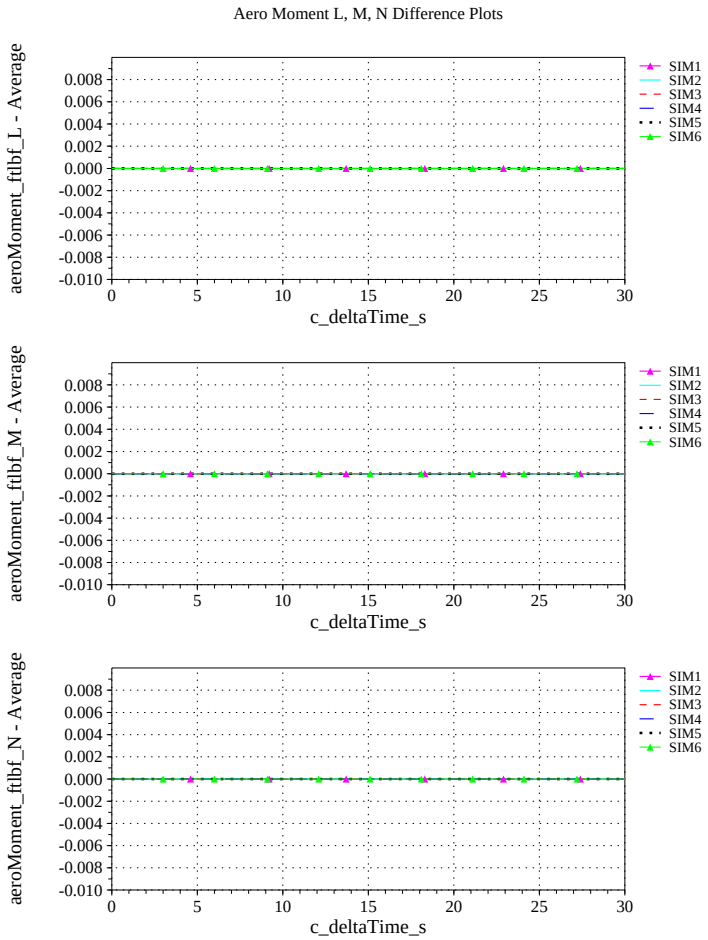

(d) Aerodynamic Moments Differenced

Figure 21. Check-case 6: Sphere Dropping over Rotating, Ellipsoidal Earth; See Discussion in Section D.1.6 (Cont'd)

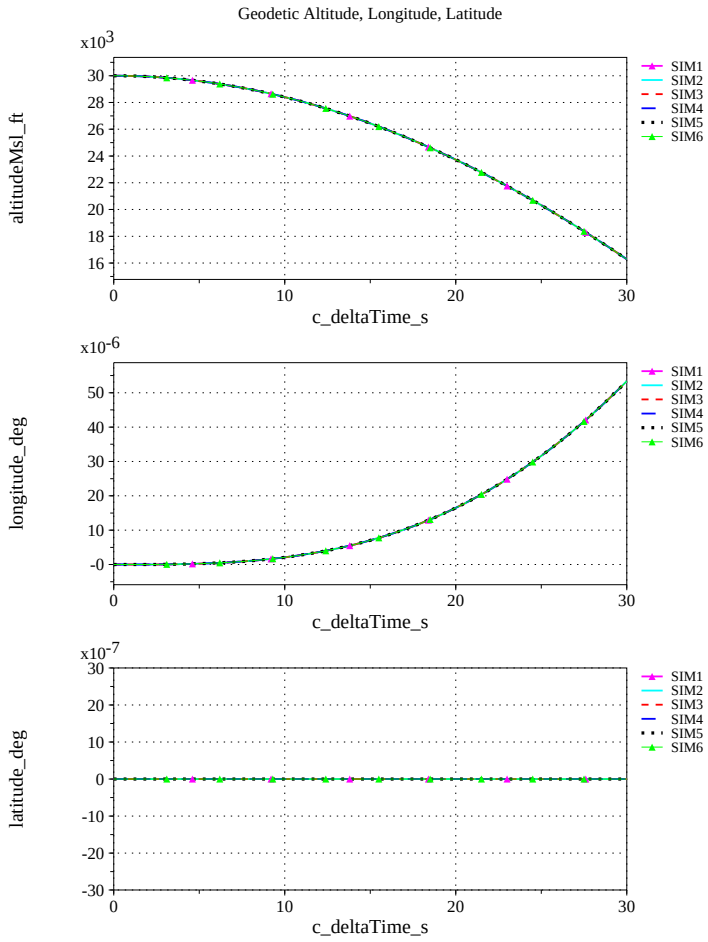

(e) Altitude, Geodetic Latitude and Longitude Compared

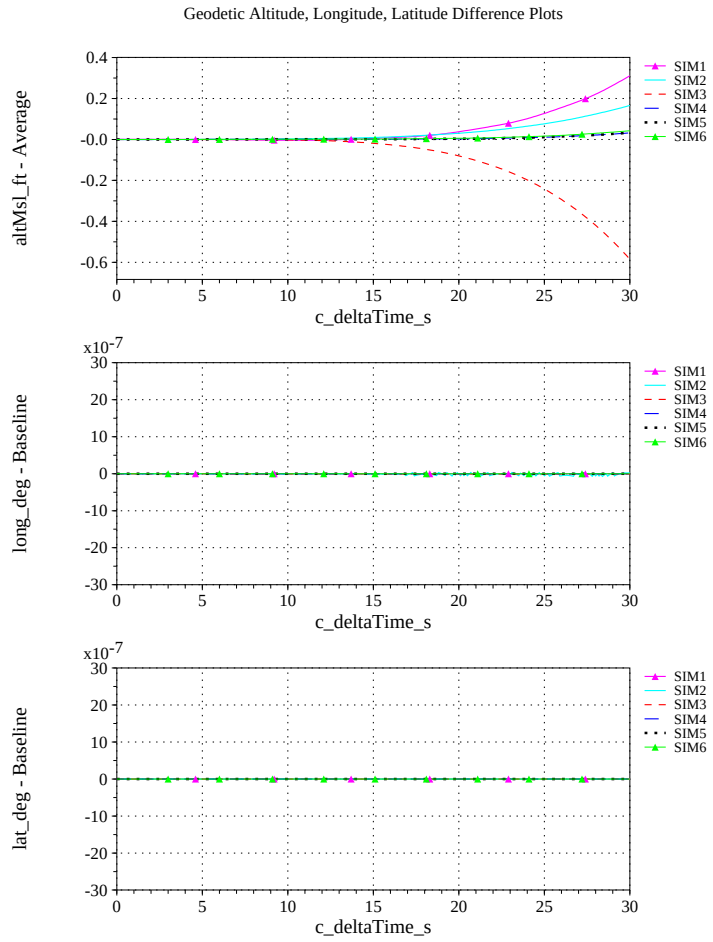

(f) Altitude, Geodetic Latitude and Longitude Differenced

Figure 21. Check-case 6: Sphere Dropping over Rotating, Ellipsoidal Earth; See Discussion in Section D.1.6 (Cont'd)

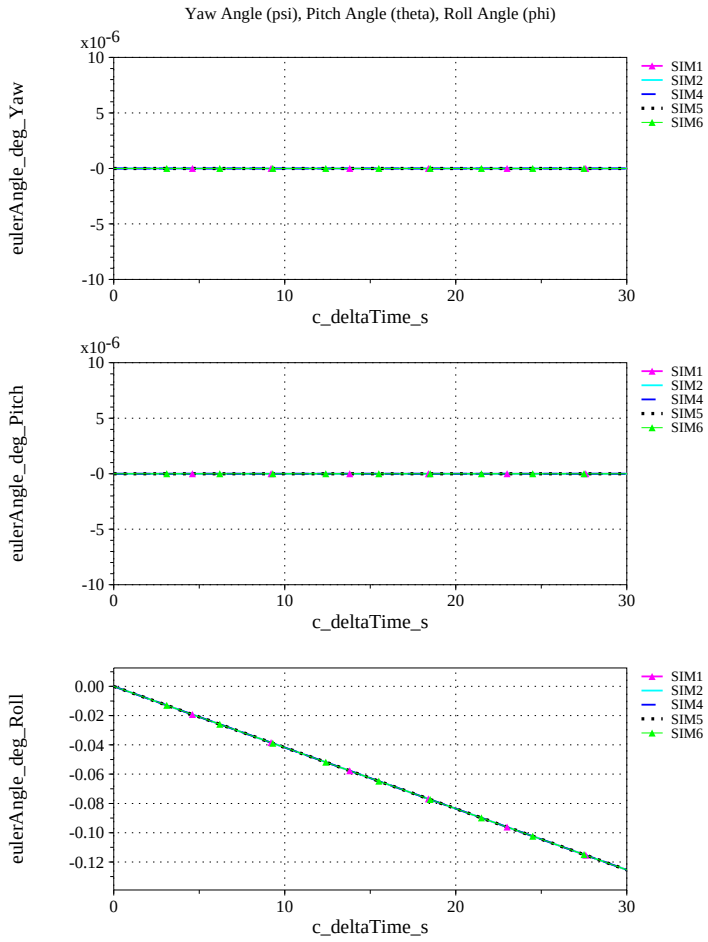

(g) Euler Angles (w.r.t. NED Frame) Compared

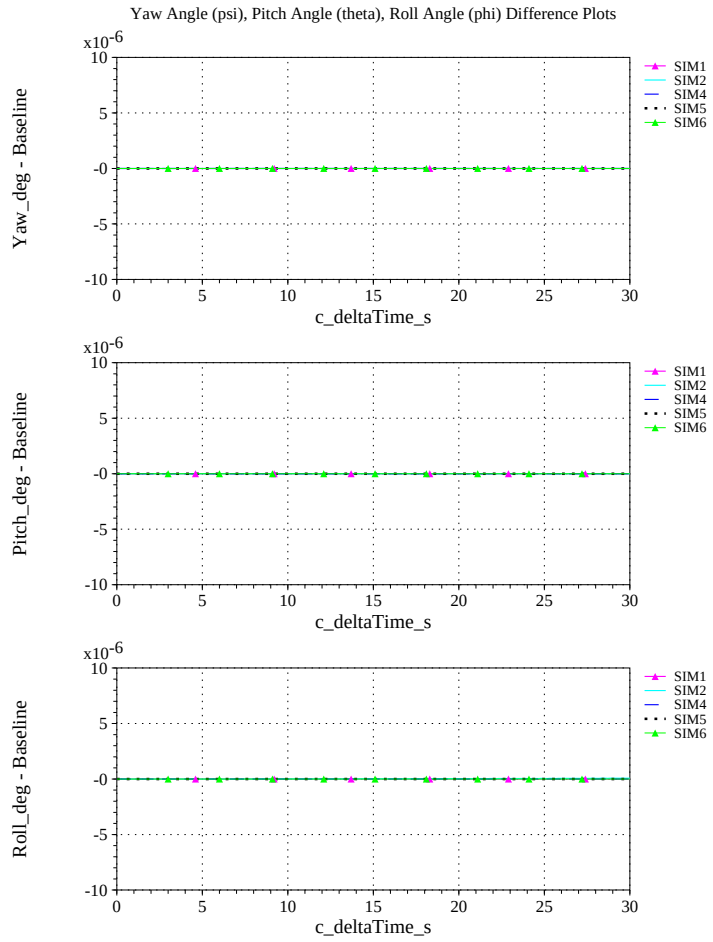

(h) Euler Angles (w.r.t. NED Frame) Differenced

Figure 21. Check-case 6: Sphere Dropping over Rotating, Ellipsoidal Earth; See Discussion in Section D.1.6 (Cont'd)

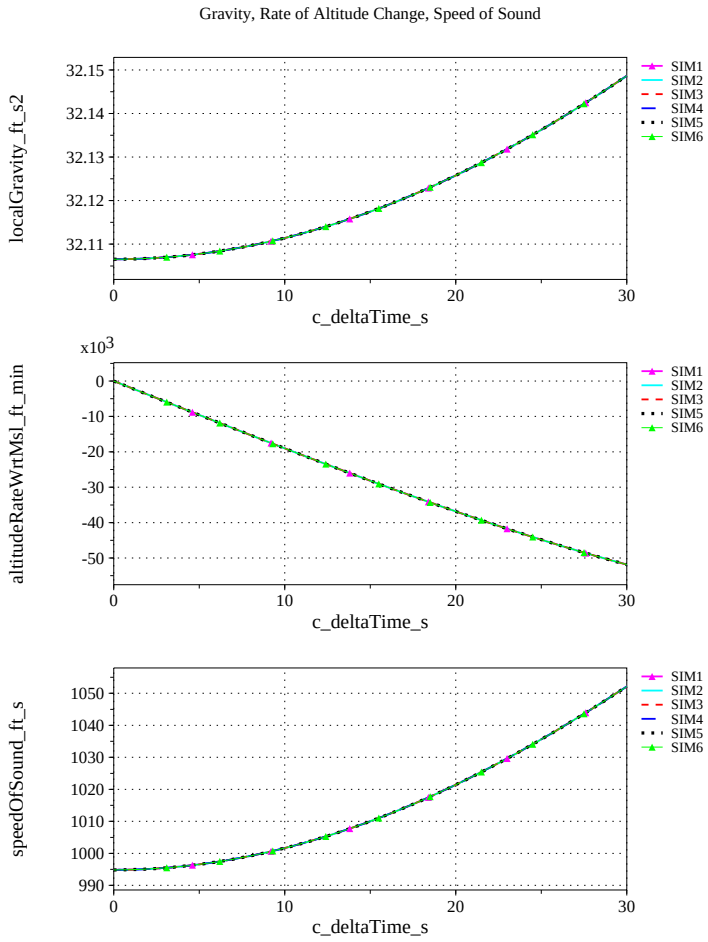

(i) Gravity, Climb Rate, and Speed-of-sound Compared

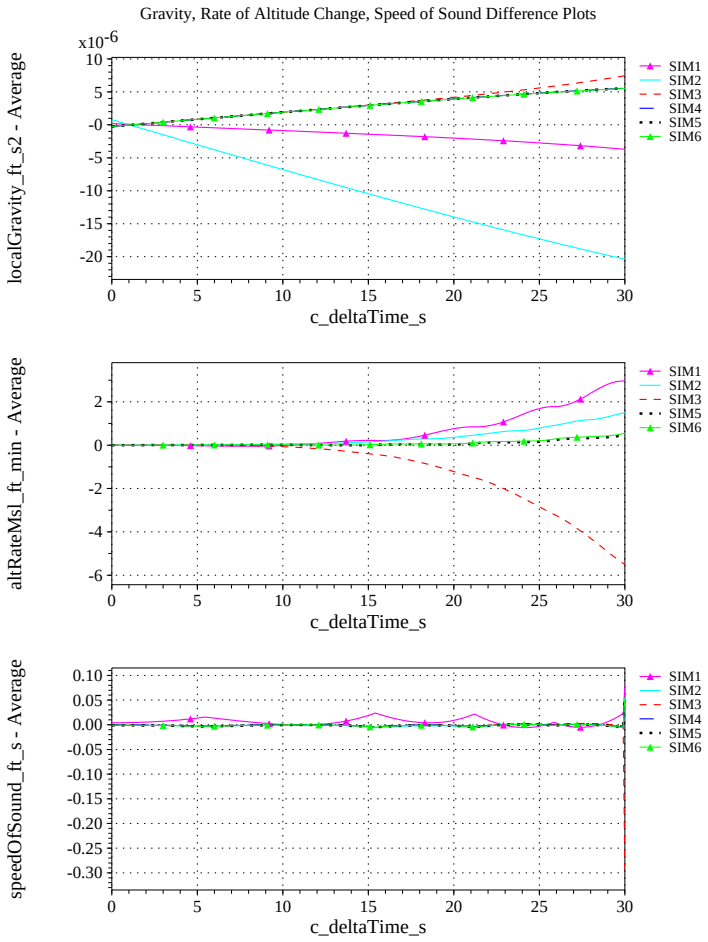

(j) Gravity, Climb Rate, and Speed-of-sound Differenced

Figure 21. Check-case 6: Sphere Dropping over Rotating, Ellipsoidal Earth; See Discussion in Section D.1.6 (Cont'd)

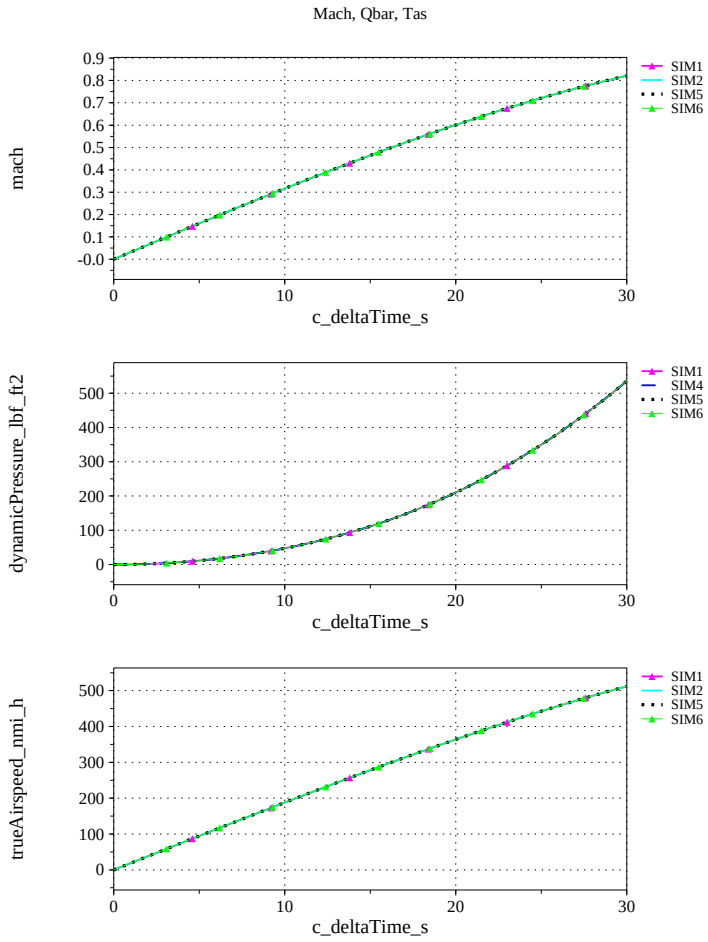

(k) Mach, Dynamic Pressure, and True Airspeed Compared

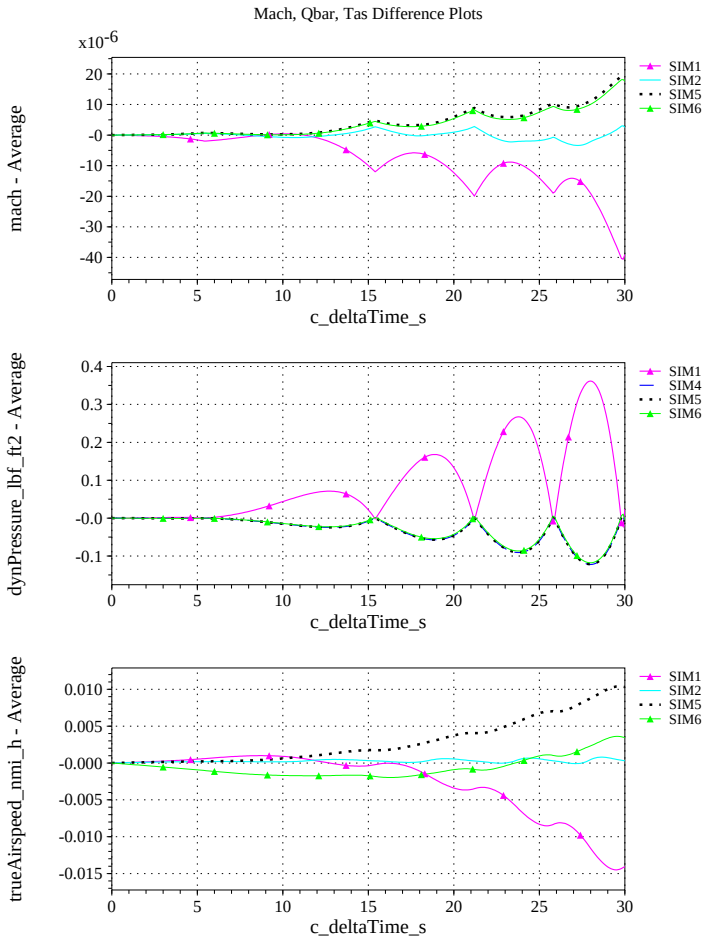

(l) Mach, Dynamic Pressure, and True Airspeed Differenced

Figure 21. Check-case 6: Sphere Dropping over Rotating, Ellipsoidal Earth; See Discussion in Section D.1.6 (Cont'd)

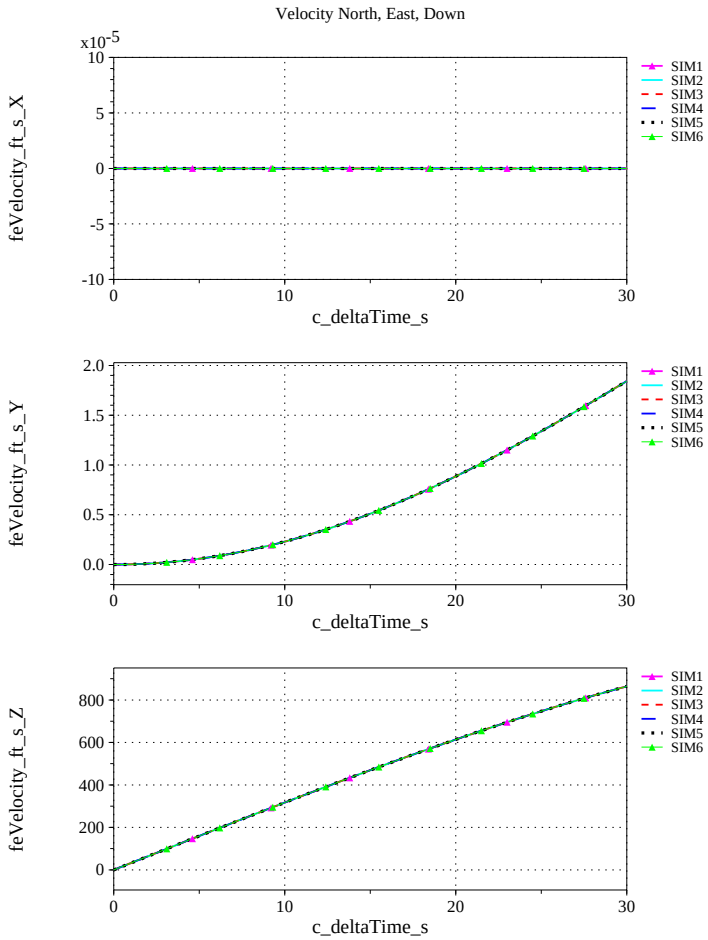

(m) NED Velocities Compared

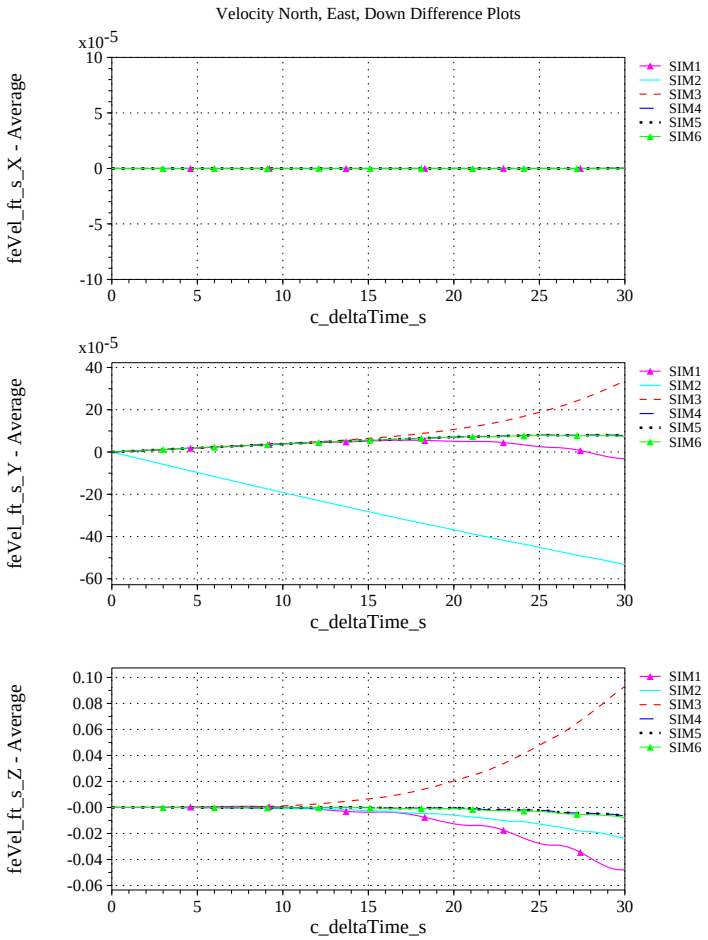

(n) NED Velocities Differenced

Figure 21. Check-case 6: Sphere Dropping over Rotating, Ellipsoidal Earth; See Discussion in Section D.1.6 (Cont'd)

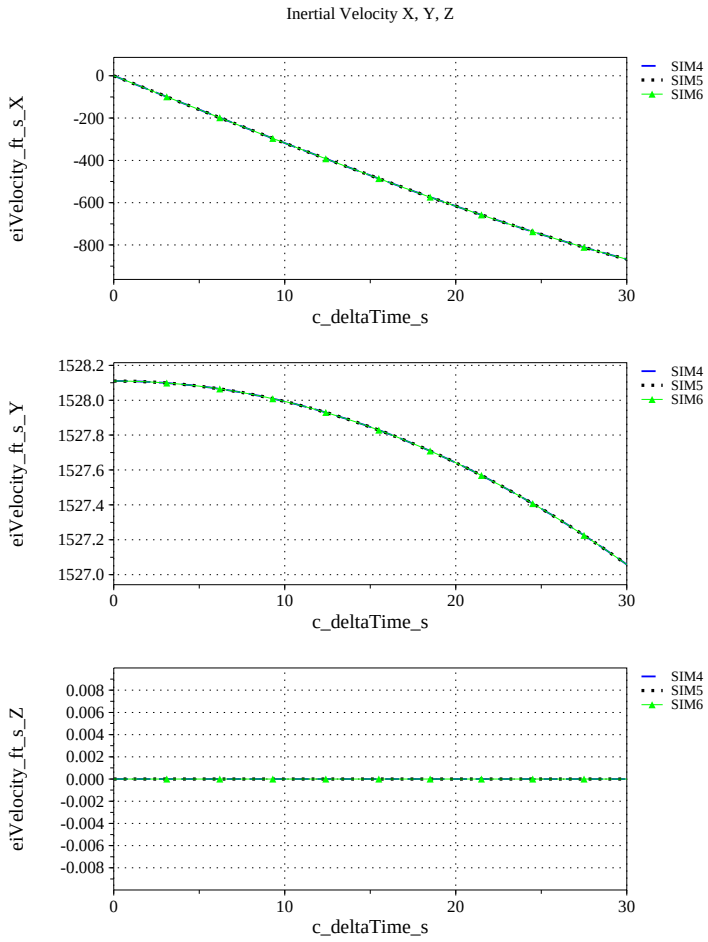

(o) Inertial Velocities Compared

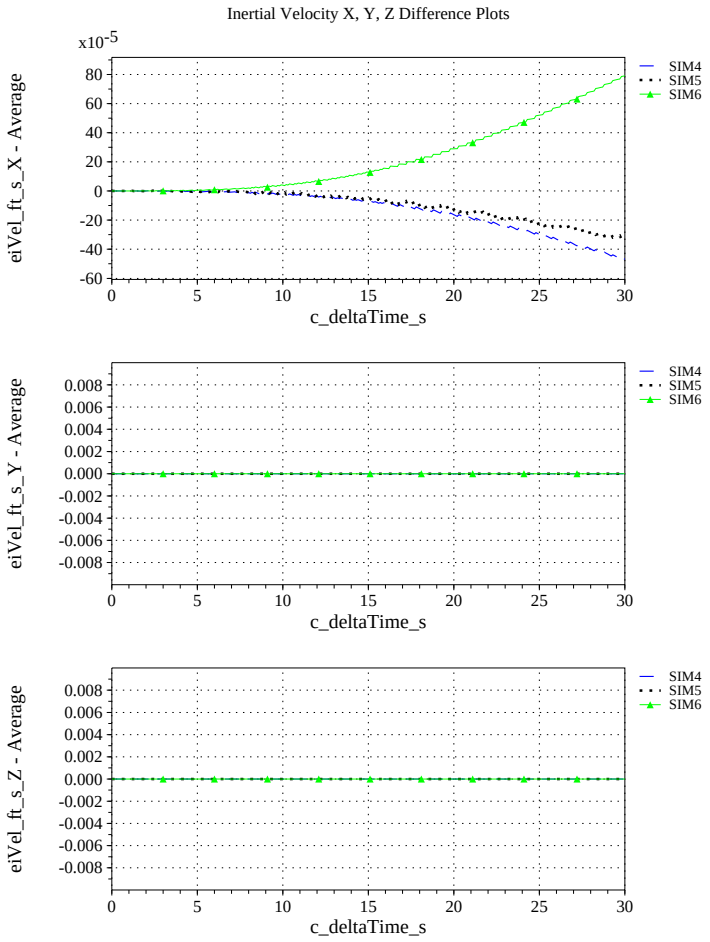

(p) Inertial Velocities Differenced

Figure 21. Check-case 6: Sphere Dropping over Rotating, Ellipsoidal Earth; See Discussion in Section D.1.6 (Cont'd)

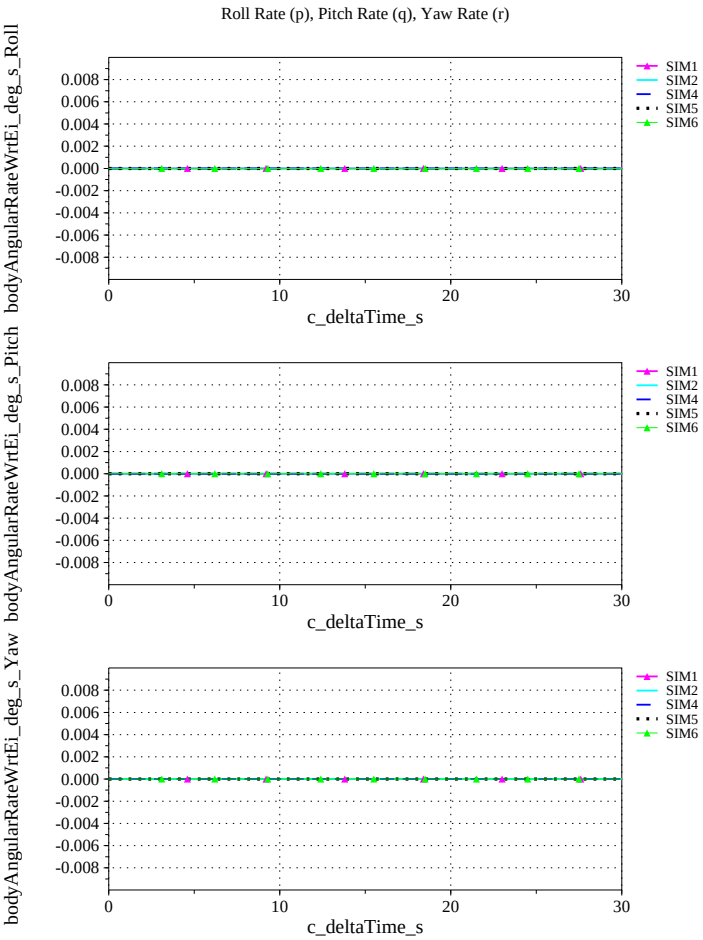

(q) Body-axis Angular Rates (w.r.t. NED Frame) Compared

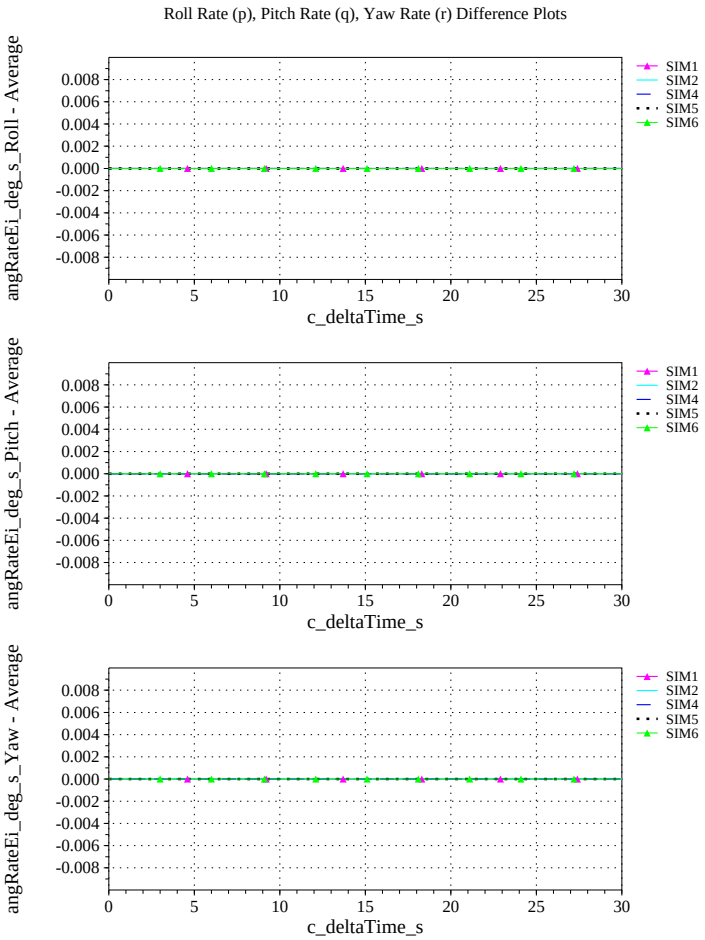

(r) Body-axis Angular Rates (w.r.t. NED Frame) Differenced

Figure 21. Check-case 6: Sphere Dropping over Rotating, Ellipsoidal Earth; See Discussion in Section D.1.6 (Cont'd)

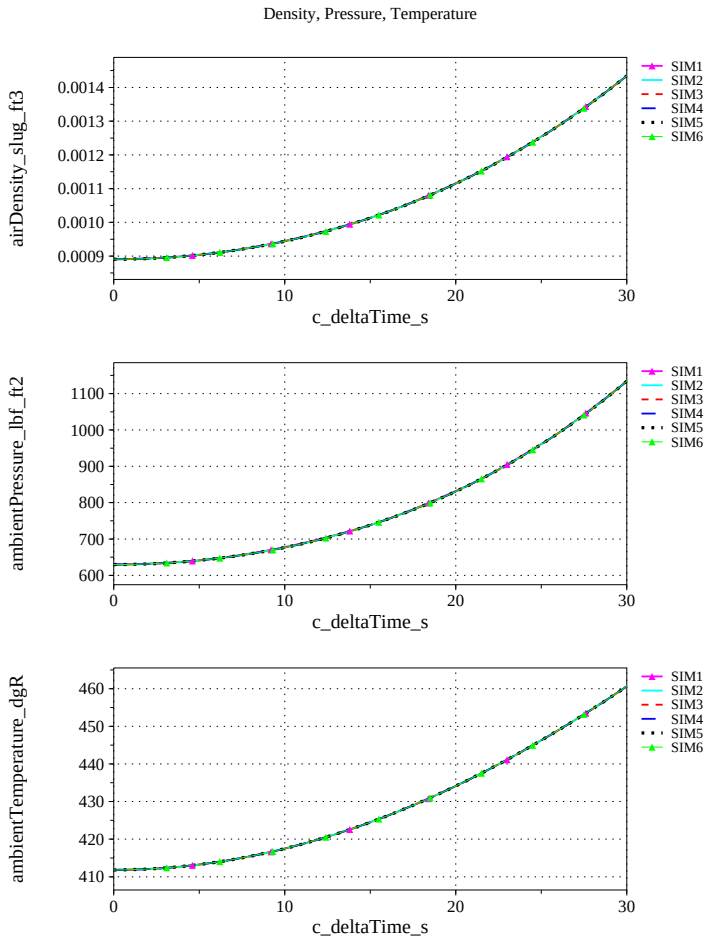

(s) Atmospheric Properties Compared

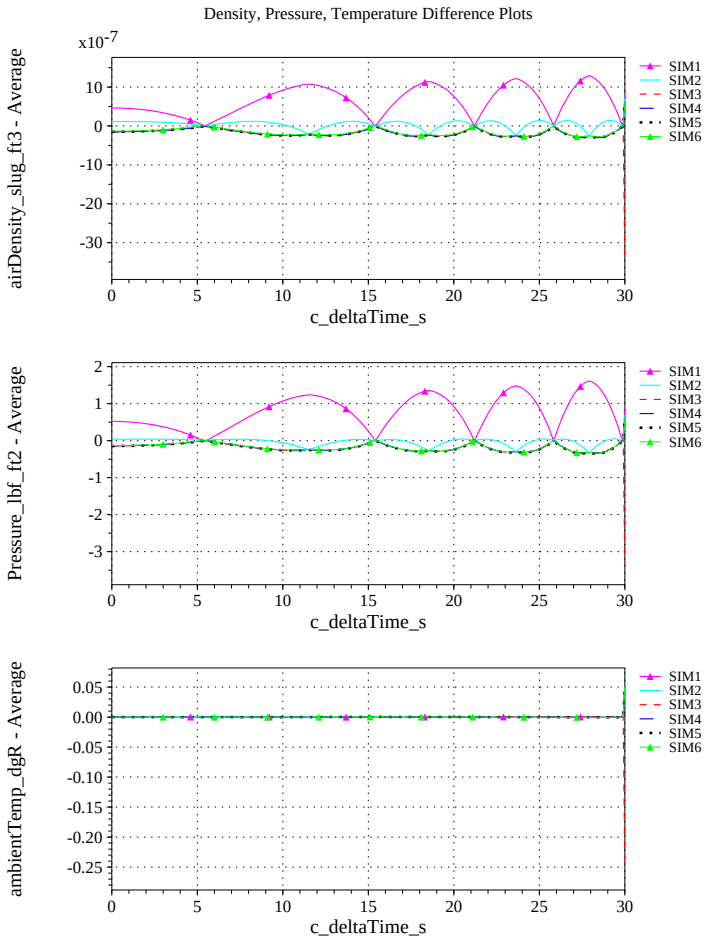

(t) Atmospheric Properties Differenced

Figure 21. Check-case 6: Sphere Dropping over Rotating, Ellipsoidal Earth; See Discussion in Section D.1.6 (Cont'd)

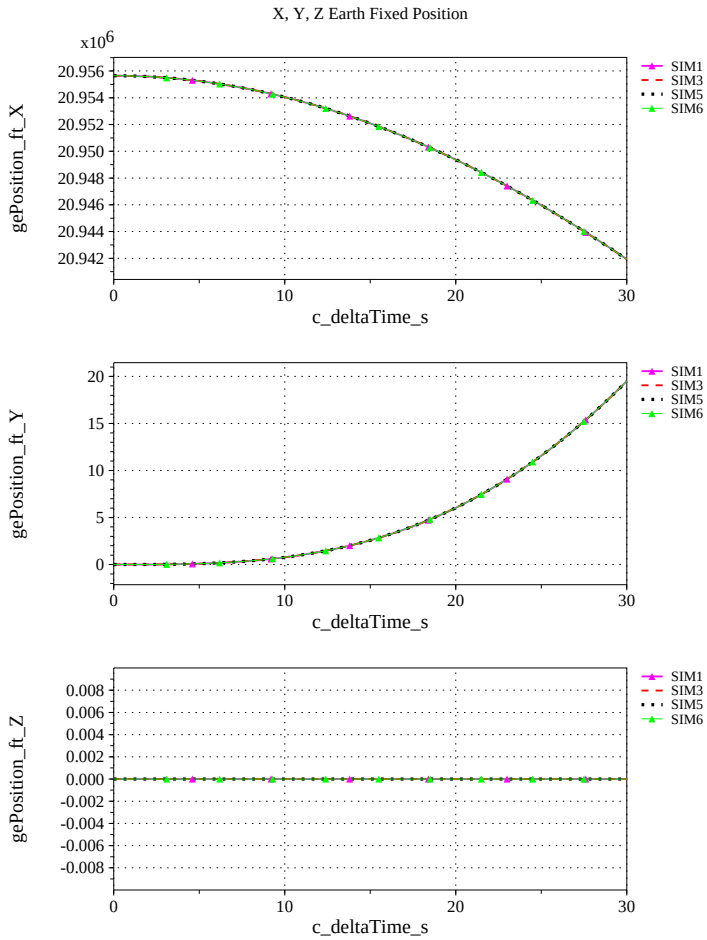

(u) Earth-centered, Earth-fixed Rectangular (X-Y-Z) Positions Compared

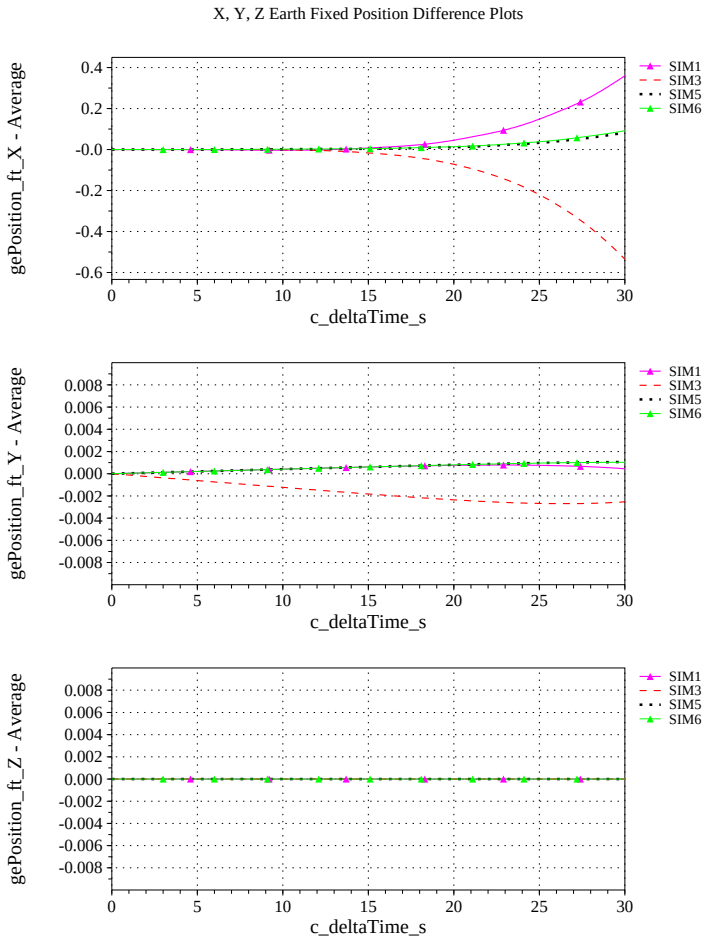

(v) Earth-centered, Earth-fixed Rectangular (X-Y-Z) Positions Differenced

Figure 21. Check-case 6: Sphere Dropping over Rotating, Ellipsoidal Earth; See Discussion in Section D.1.6 (Cont'd)

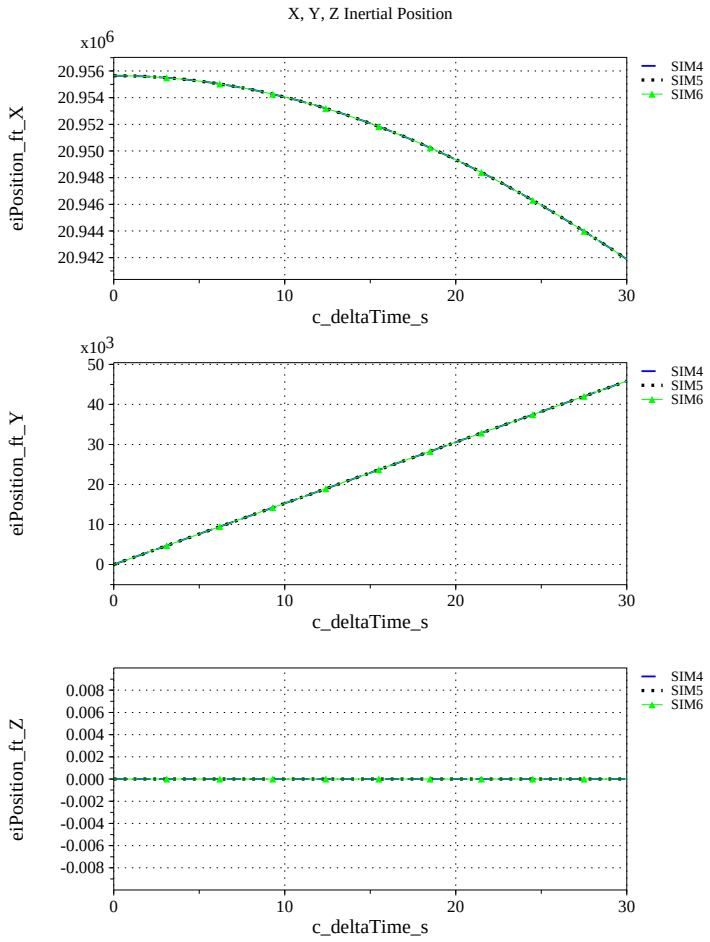

(w) Earth-centered Inertial Rectangular (x-y-z) Positions Compared

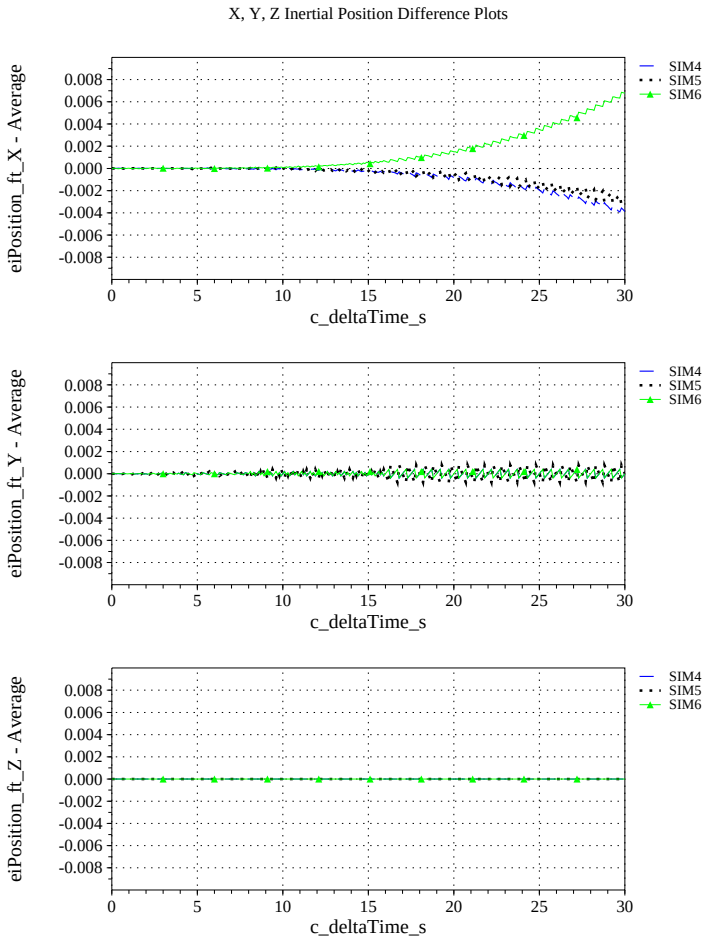

(x) Earth-centered Inertial Rectangular (x-y-z) Positions Differenced

Figure 21. Check-case 6: Sphere Dropping over Rotating, Ellipsoidal Earth; See Discussion in Section D.1.6 (Concluded)

D.1.7 Check-case 7 – sphere dropping through a steady wind field

This section shows cross-plots for six of the selected simulation tools in modeling the dynamics of a sphere dropped with a fixed drag coefficient through an steadily moving atmosphere in an ellipsoidal rotating Earth with J_2 gravitational harmonics. This scenario is described in Section C.1.7. Figures 22a through 22x compare results between the six simulation tools, as well as the deviances of the outputs from each tool from the ensemble average value.

This atmospheric check-case added a constant wind from the west to the previous scenarios. The addition of winds did not introduce new contributors to differences among the simulations. Differences visible for this case are nearly identical to the prior case:

- SIM 3, 4, 5, and 6 implemented their atmosphere models using formulas. SIM 1 and 2 used lookup tables with linear interpolation. Since atmospheric pressure and density are non-linear functions, these atmospheric properties differed slightly between the formulaic and lookup tables results in-between altitude breakpoints.
- The simulations used different numerical integration methods and exhibited differences in integrated and other numerical values
- The aerodynamic forces recorded by SIM 2 appeared to lag the other simulations by 0.01 sec. However, this appeared to be an error only in the recording process; translational states exhibited smaller differences than would be expected if this lag also existed in SIM 2's EOM.
- The aerodynamic force differences for SIM 3 were indicative of a difference in initial rotational rate. Though SIM 3 did not record rotational states, the differences in the aerodynamic forces could be matched if one assumed that SIM 3 was initialized to a zero angular rate relative to the Earth. The other simulations are initialized to an inertial angular rate of zero.

All differences visible between the simulations appear to have been caused by these contributing factors.

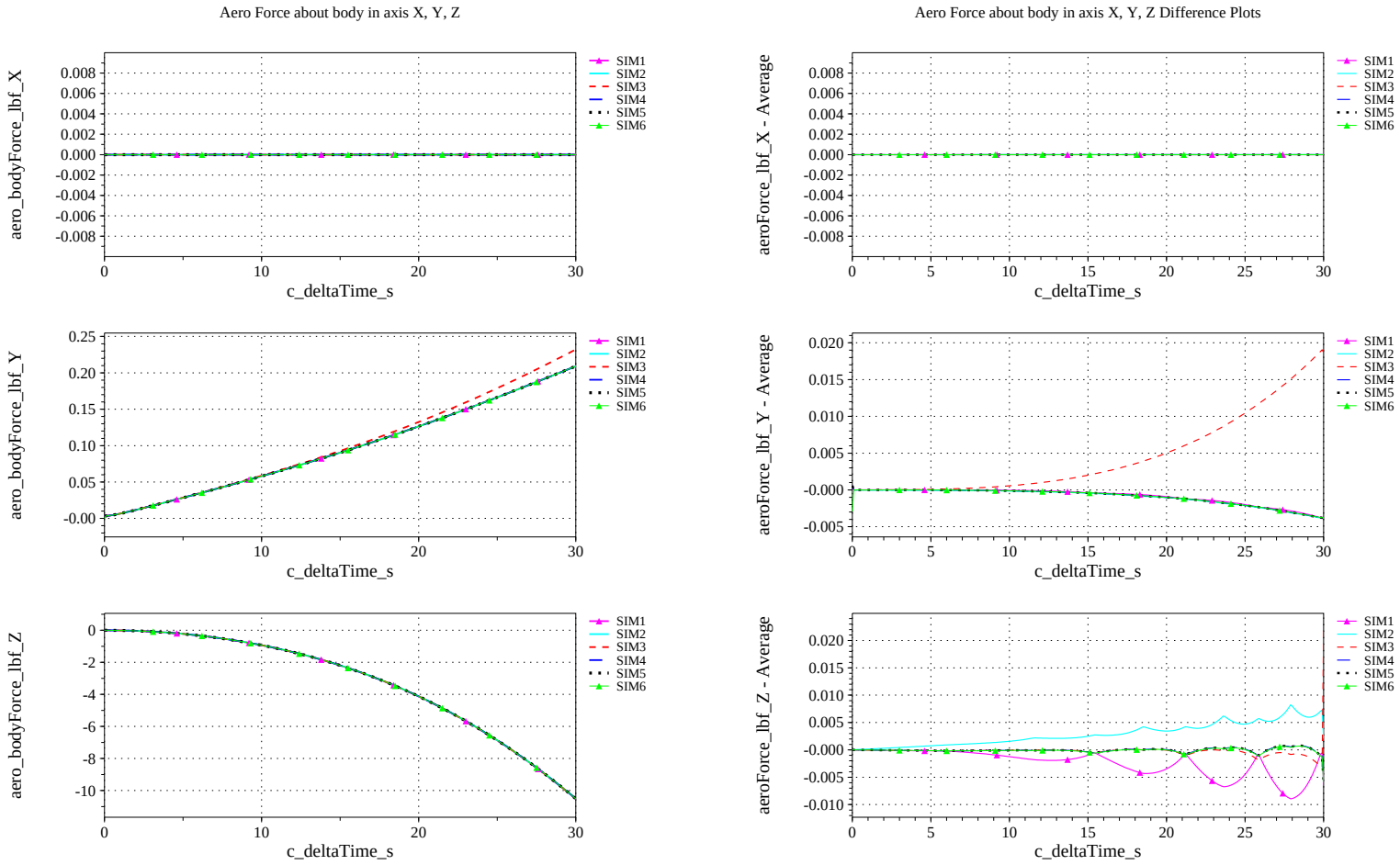

(a) Aerodynamic Forces Compared

(b) Aerodynamic Forces Differenced

Figure 22. Check-case 7: Sphere Dropping through a Steady Wind Field; See Discussion in Section D.1.7

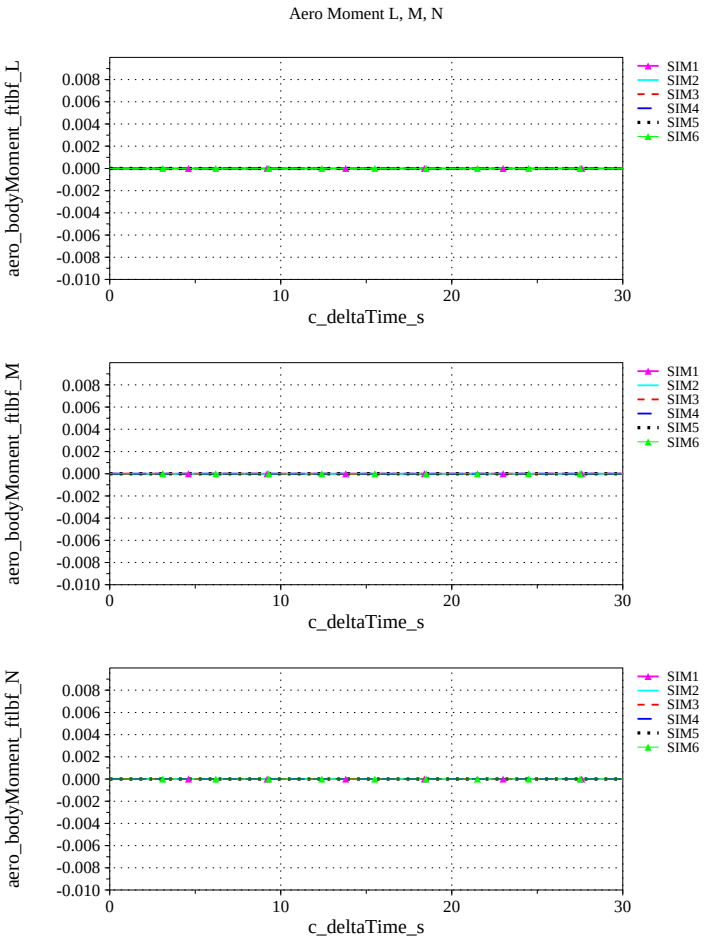

(c) Aerodynamic Moments Compared

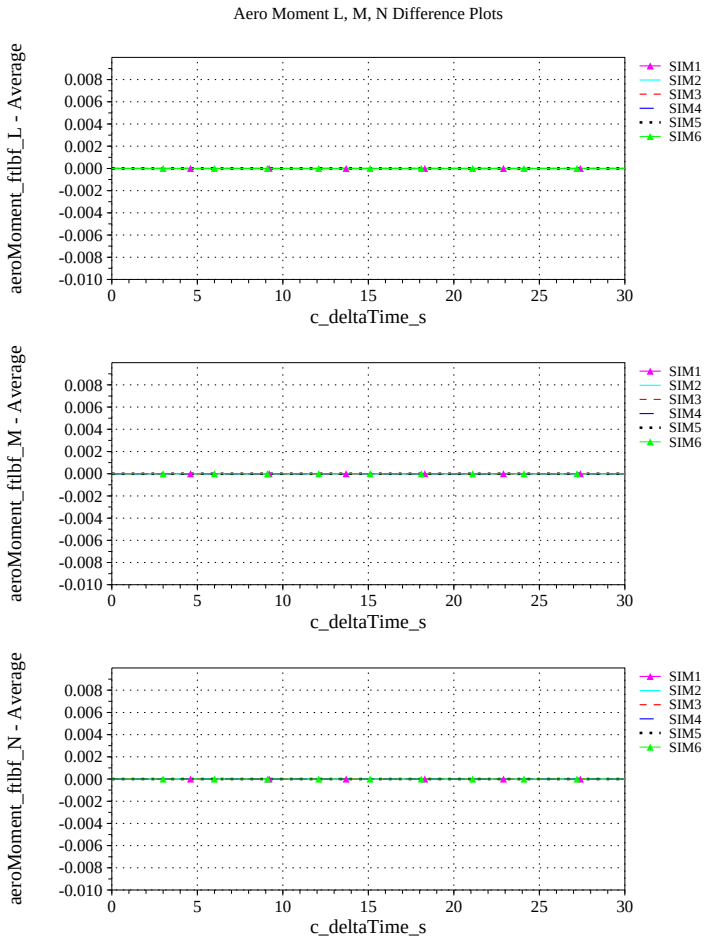

(d) Aerodynamic Moments Differenced

Figure 22. Check-case 7: Sphere Dropping through a Steady Wind Field; See Discussion in Section D.1.7 (Cont'd)

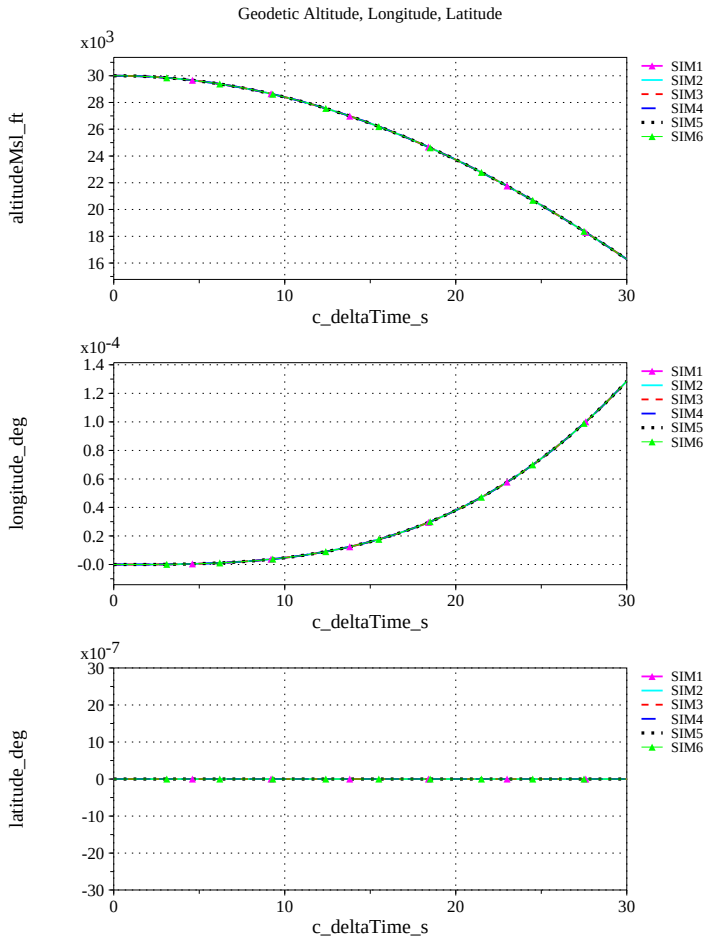

(e) Altitude, Geodetic Latitude and Longitude Compared

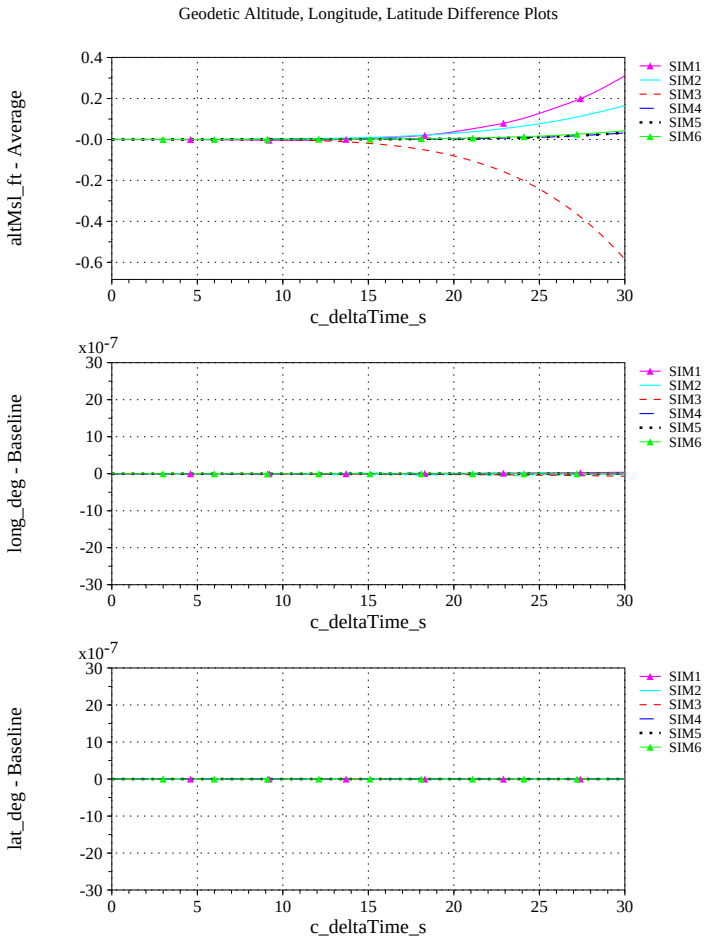

(f) Altitude, Geodetic Latitude and Longitude Differenced

Figure 22. Check-case 7: Sphere Dropping through a Steady Wind Field; See Discussion in Section D.1.7 (Cont'd)

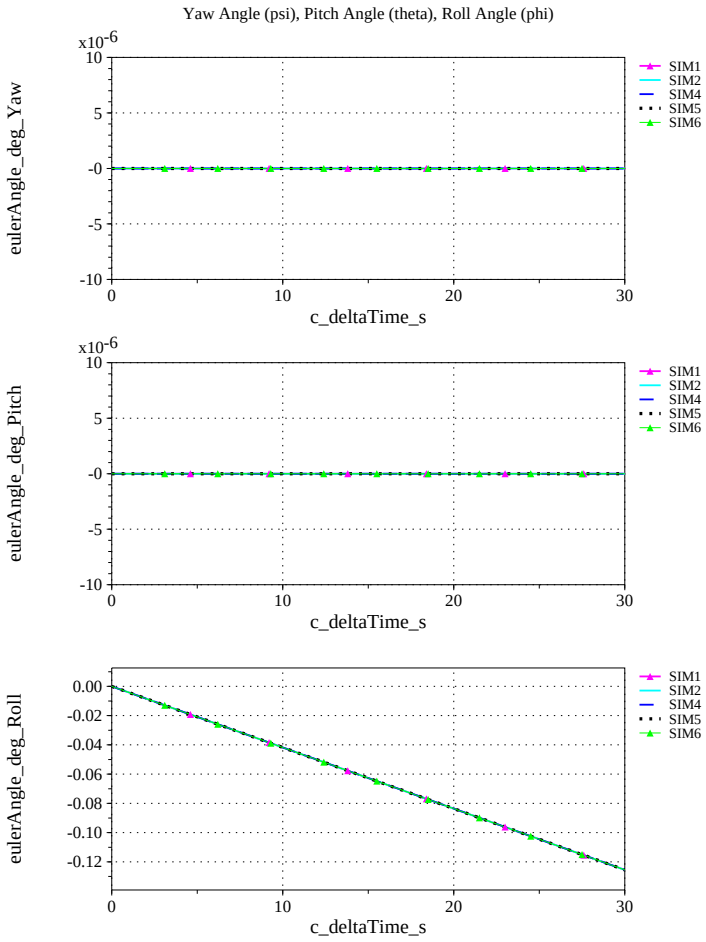

(g) Euler Angles (w.r.t. NED Frame) Compared

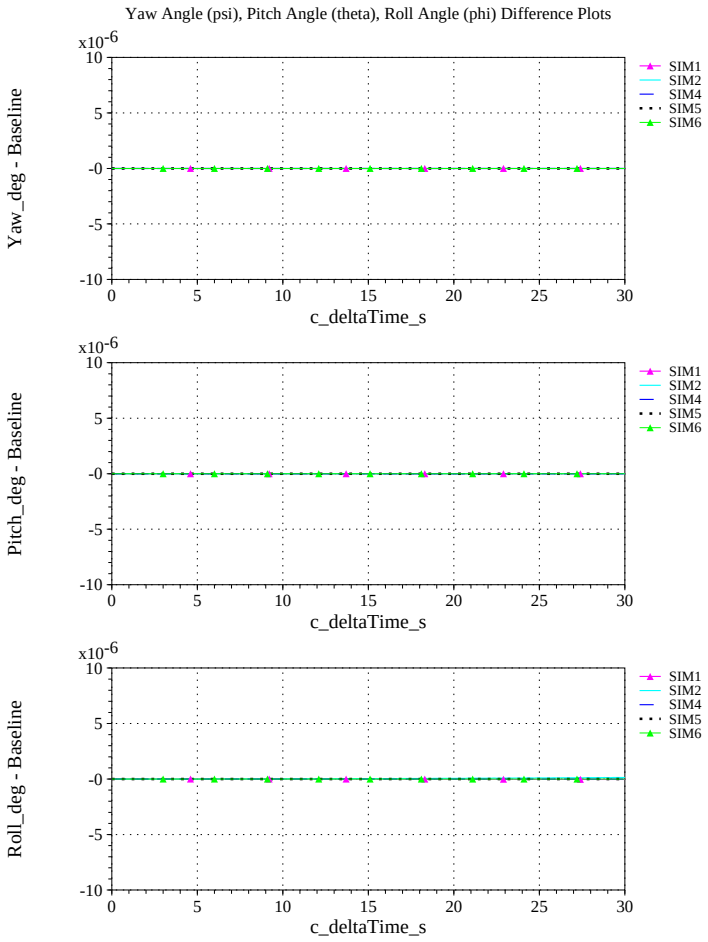

(h) Euler Angles (w.r.t. NED Frame) Differenced

Figure 22. Check-case 7: Sphere Dropping through a Steady Wind Field; See Discussion in Section D.1.7 (Cont'd)

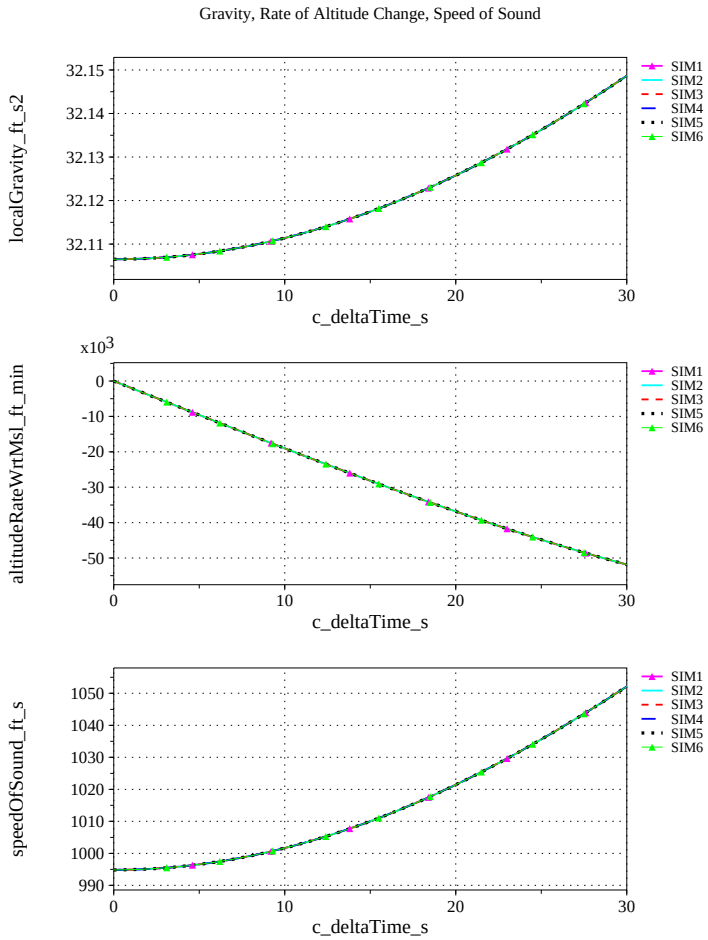

(i) Gravity, Climb Rate, and Speed-of-sound Compared

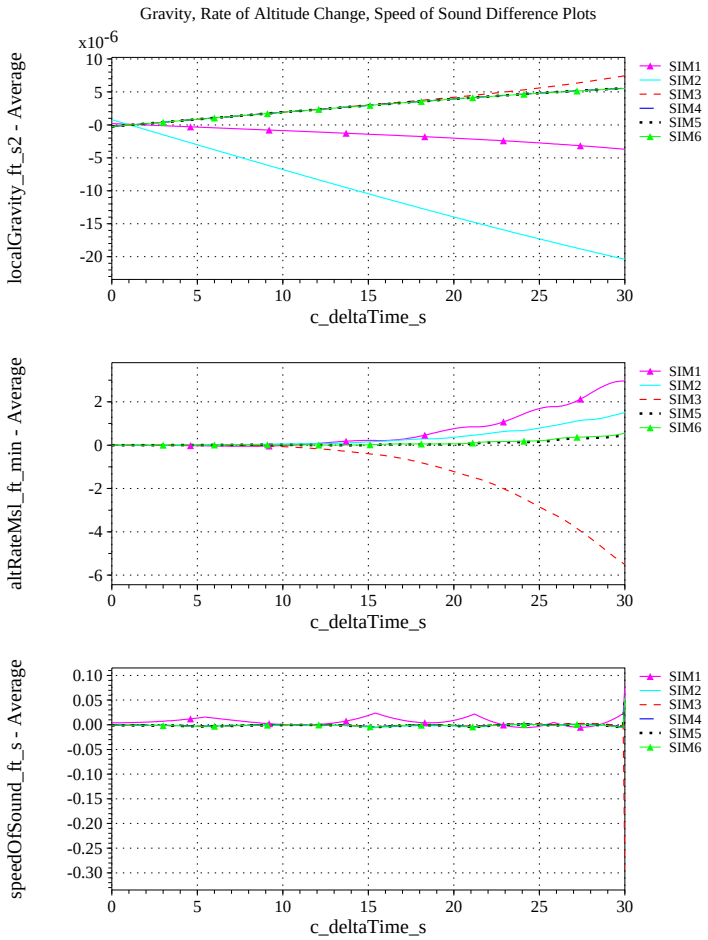

(j) Gravity, Climb Rate, and Speed-of-sound Differenced

Figure 22. Check-case 7: Sphere Dropping through a Steady Wind Field; See Discussion in Section D.1.7 (Cont'd)

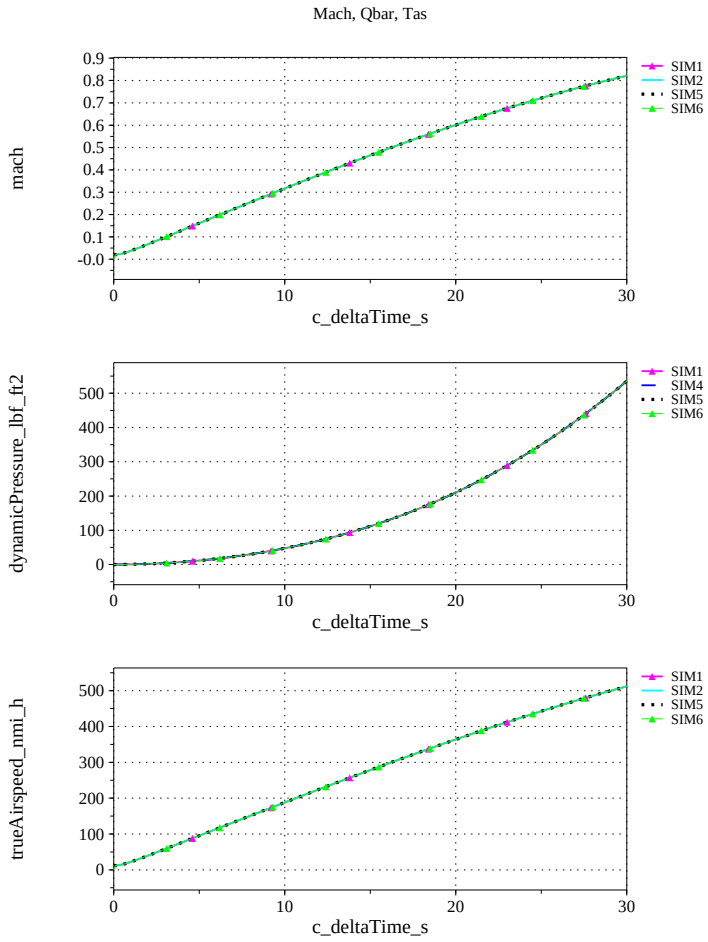

(k) Mach, Dynamic Pressure, and True Airspeed Compared

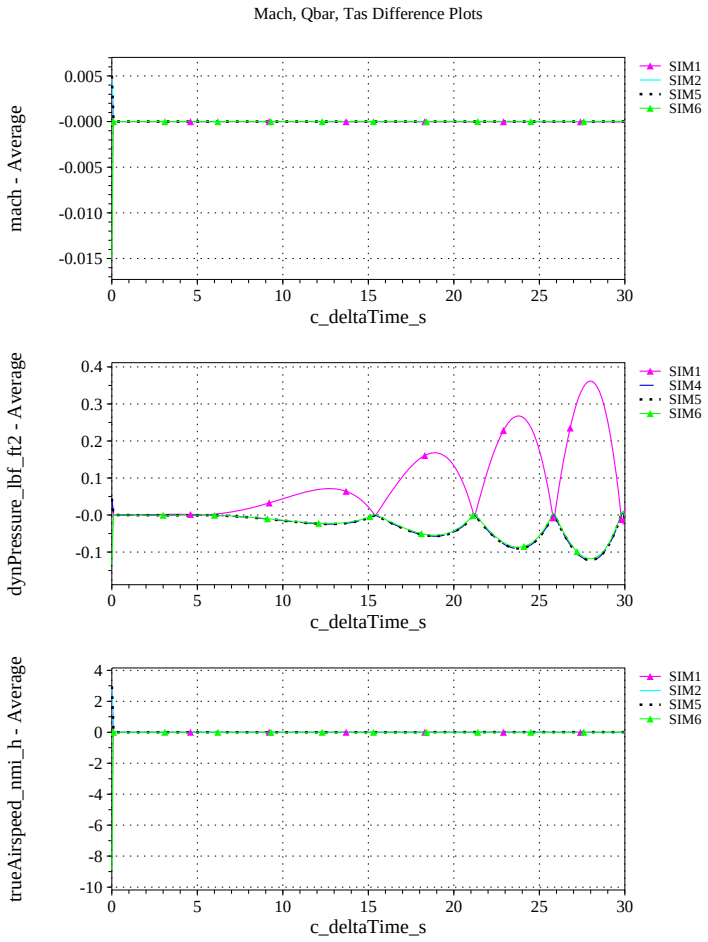

(l) Mach, Dynamic Pressure, and True Airspeed Differenced

Figure 22. Check-case 7: Sphere Dropping through a Steady Wind Field; See Discussion in Section D.1.7 (Cont'd)

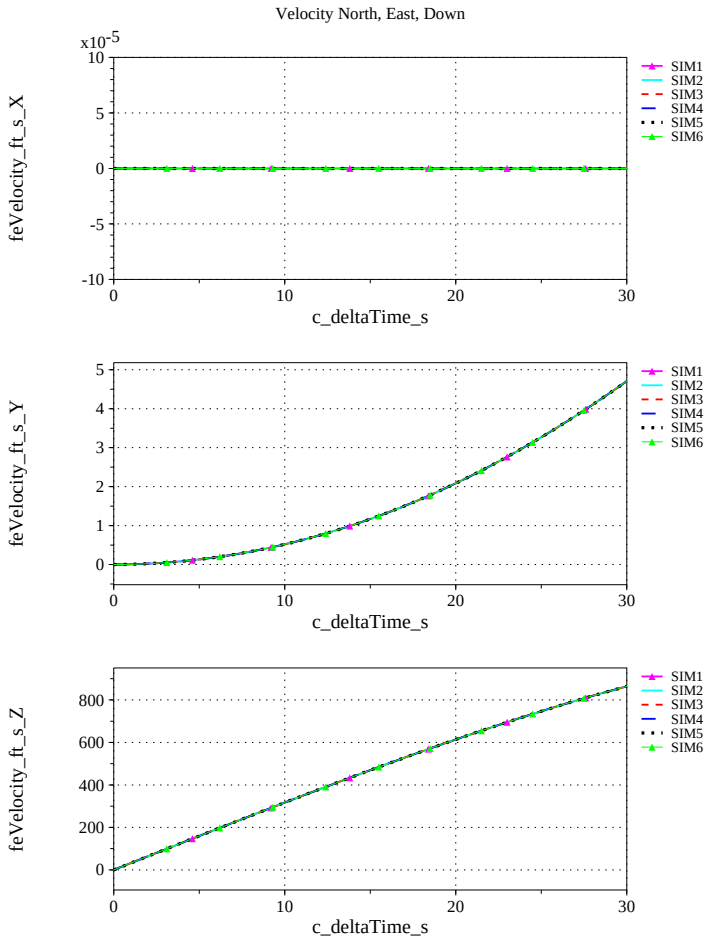

(m) NED Velocities Compared

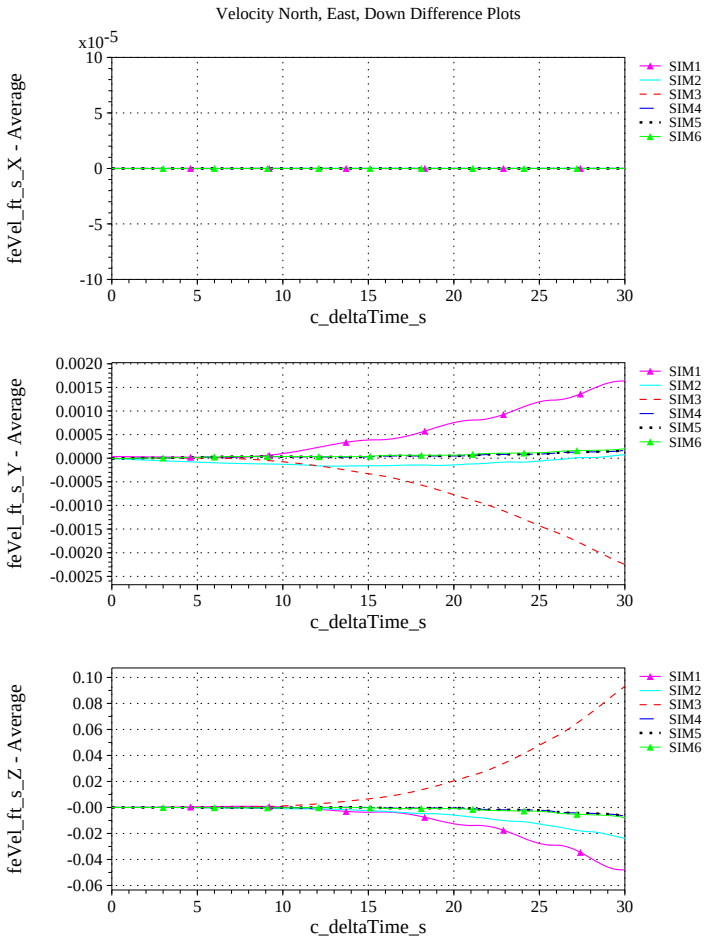

(n) NED Velocities Differenced

Figure 22. Check-case 7: Sphere Dropping through a Steady Wind Field; See Discussion in Section D.1.7 (Cont'd)

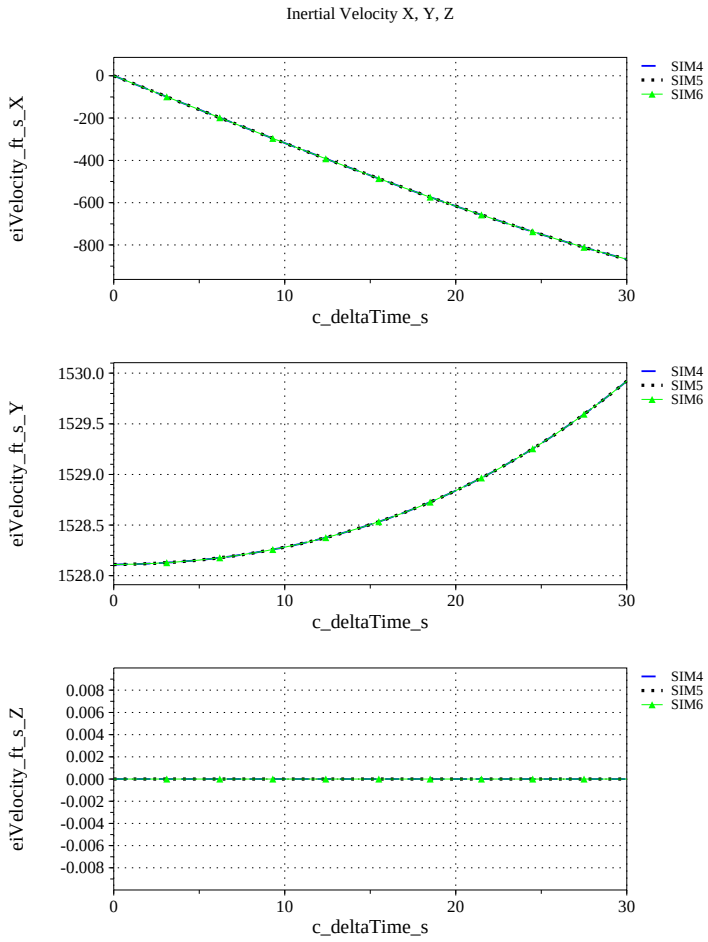

(o) Inertial Velocities Compared

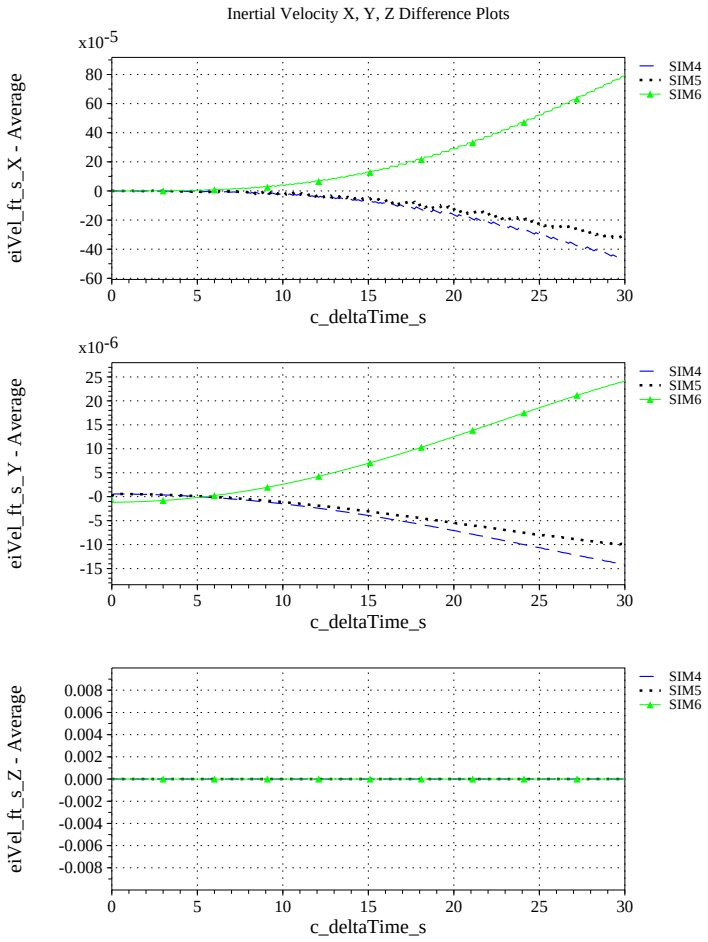

(p) Inertial Velocities Differenced

Figure 22. Check-case 7: Sphere Dropping through a Steady Wind Field; See Discussion in Section D.1.7 (Cont'd)

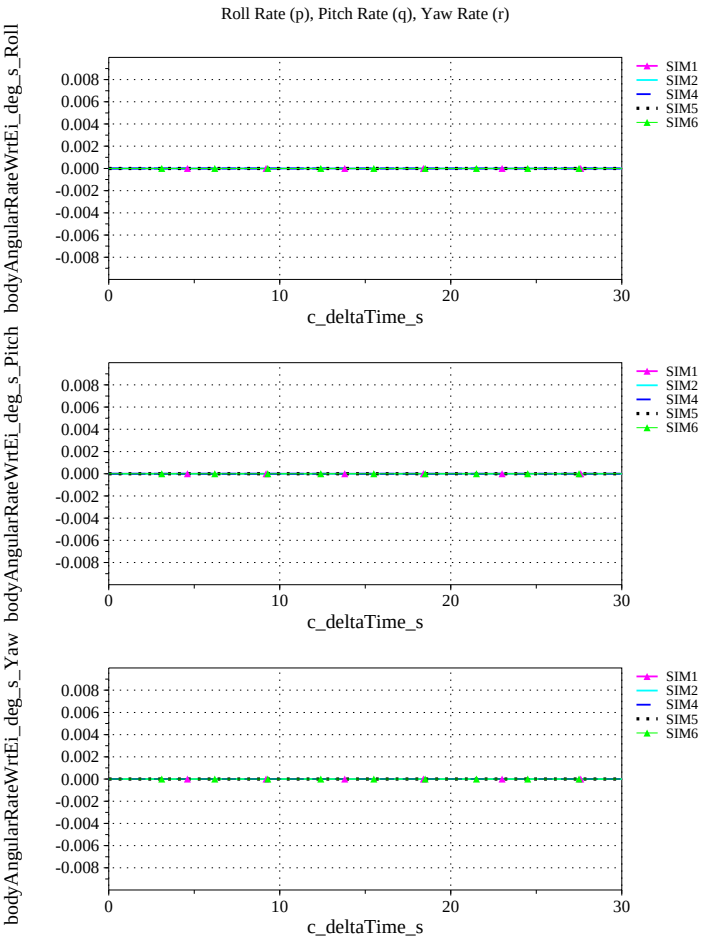

(q) Body-axis Angular Rates (w.r.t. NED Frame) Compared

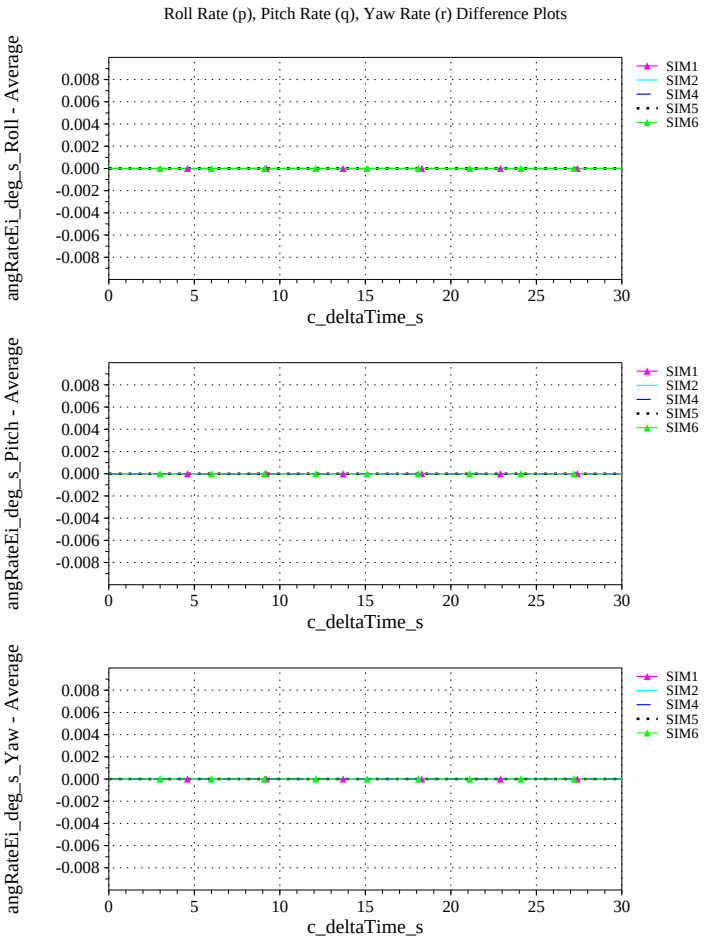

(r) Body-axis Angular Rates (w.r.t. NED Frame) Differenced

Figure 22. Check-case 7: Sphere Dropping through a Steady Wind Field; See Discussion in Section D.1.7 (Cont'd)

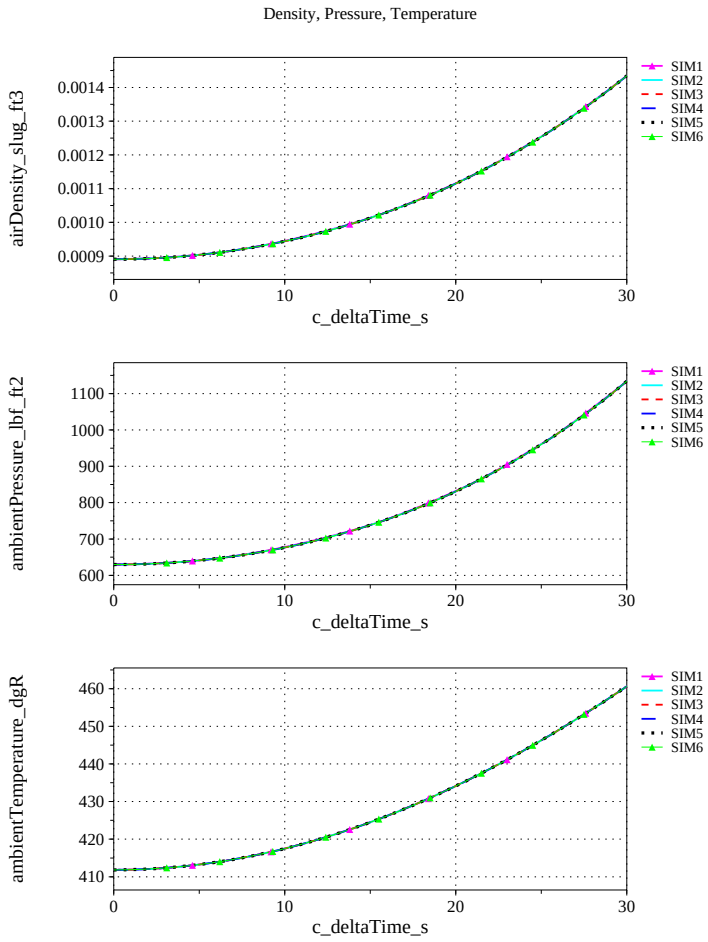

(s) Atmospheric Properties Compared

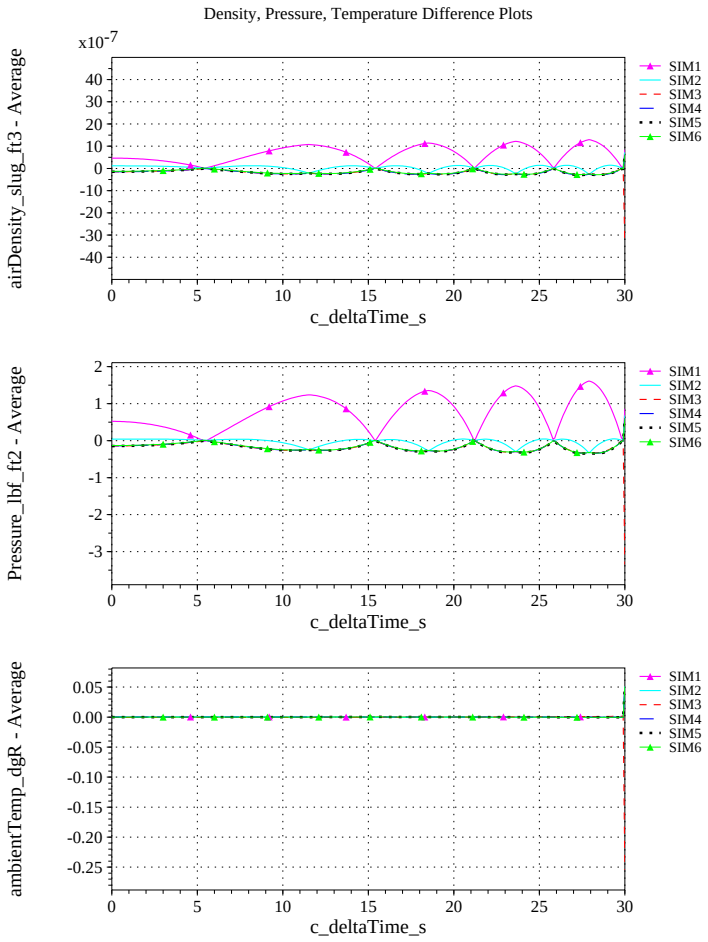

(t) Atmospheric Properties Differenced

Figure 22. Check-case 7: Sphere Dropping through a Steady Wind Field; See Discussion in Section D.1.7 (Cont'd)

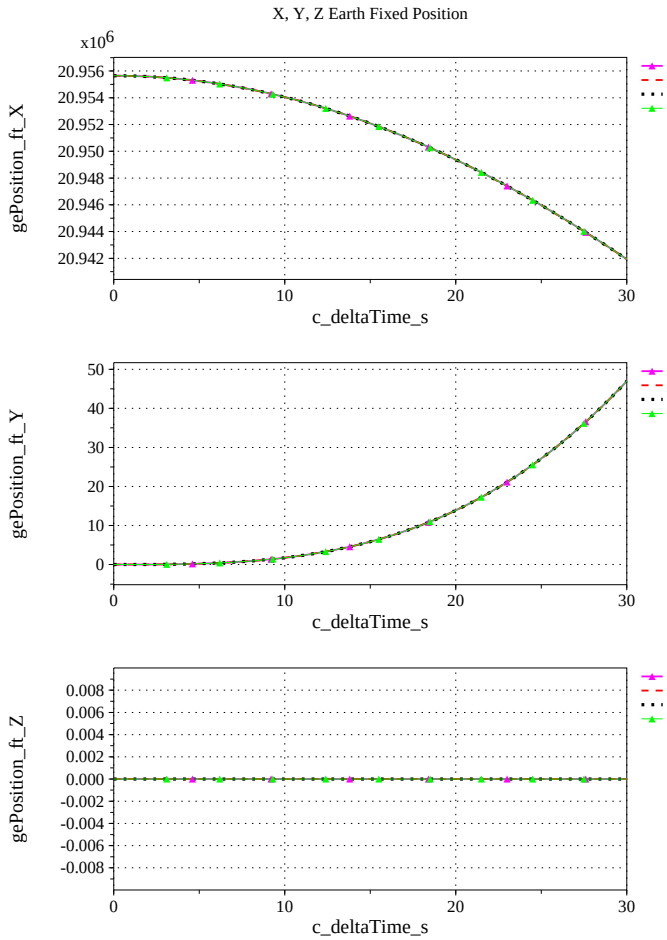

(u) Earth-centered, Earth-fixed Rectangular (X-Y-Z) Positions Compared

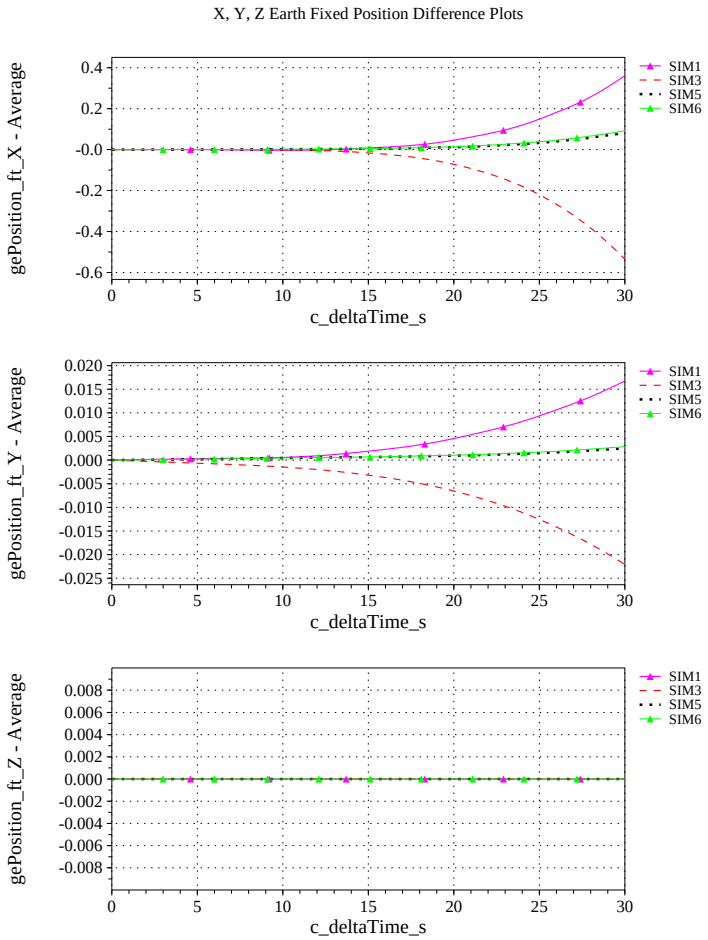

(v) Earth-centered, Earth-fixed Rectangular (X-Y-Z) Positions Differenced

Figure 22. Check-case 7: Sphere Dropping through a Steady Wind Field; See Discussion in Section D.1.7 (Cont'd)

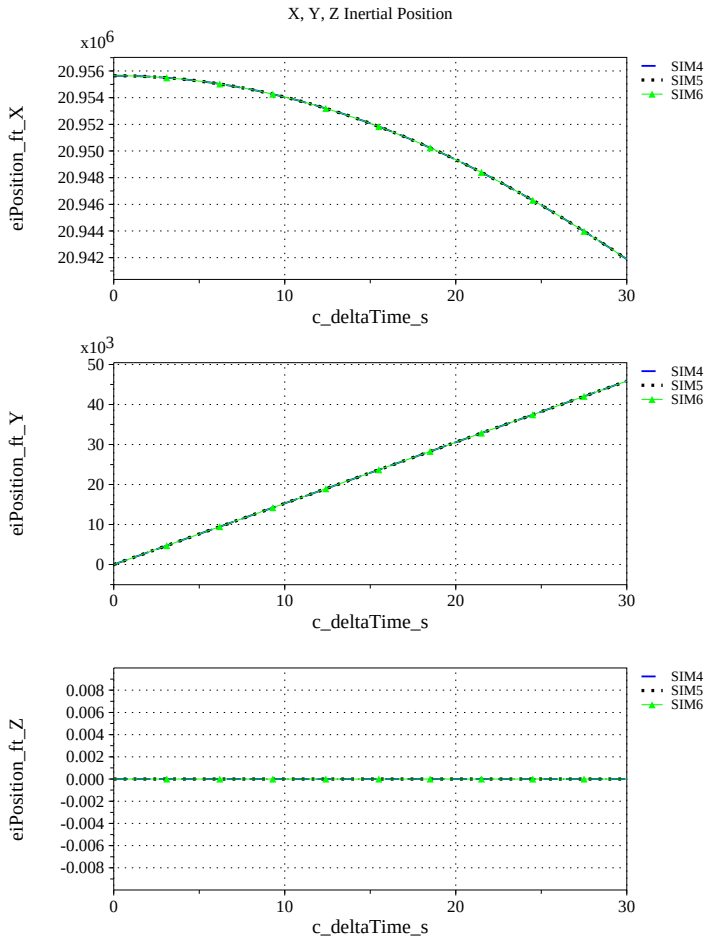

(w) Earth-centered Inertial Rectangular (x-y-z) Positions Compared

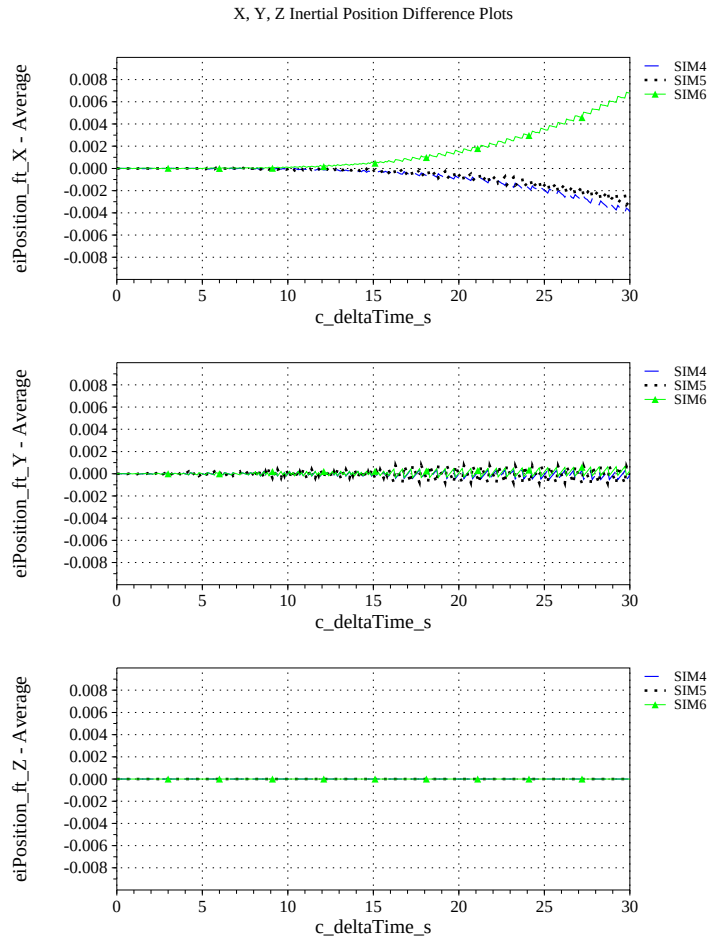

(x) Earth-centered Inertial Rectangular (x-y-z) Positions Differenced

Figure 22. Check-case 7: Sphere Dropping through a Steady Wind Field; See Discussion in Section D.1.7 (Concluded)

D.1.8 Check-case 8 – sphere dropping through a varying wind field

This section shows cross-plots for six of the selected simulation tools in modeling the dynamics of a sphere dropped with a fixed drag coefficient through an atmosphere with wind velocity as a function of altitude over an ellipsoidal rotating Earth with J_2 gravitational harmonics. This scenario is described in Section C.1.8. Figures 23a through 23x compare results between the six simulation tools, as well as the deviances of the outputs from each tool from the ensemble average value.

This check-case alters the previous case by modeling winds as varying linearly with altitude. Moreover, the initial winds were higher (70 ft/s versus 20 ft/s). Those higher winds exposed new contributors to differences in true airspeed, dynamic pressure, and aerodynamic forces that are largely hidden in the prior scenarios. As with the prior scenario, the initial winds were coming from the west. Given the initial vehicle velocity of zero relative to the Earth, the winds induced an initial drag eastward. In the chart for body y-axis aerodynamic force (Figure 23a), SIM 6 and SIM 3 recorded a value of zero at time zero. Furthermore, SIM 6 recorded a value of zero for true airspeed and dynamic pressure at $t = 0$ sec; SIM 3 did not record these values. In the case of SIM 6, the difference appeared to be a recording artifact only; SIM 6 maintained a close match in eastward velocity to other simulations at $t = 0.1$ sec. However, SIM 3 exhibited a difference in initial eastward velocity from $t = 0$ sec to $t = 0.1$ sec (Figure 23n) that is consistent with a starting aerodynamic y-axis force of zero. This initial jump in velocity difference, in turn, caused a growth in the difference for longitude (Figure 23f) and ECEF Y-axis position (Figure 23v) relative to the differences seen in the previous scenario (Check-case 7 – sphere dropping through a steady wind field).

Otherwise, differences visible in the plots appeared to be caused by the same contributors identified in prior check-cases.

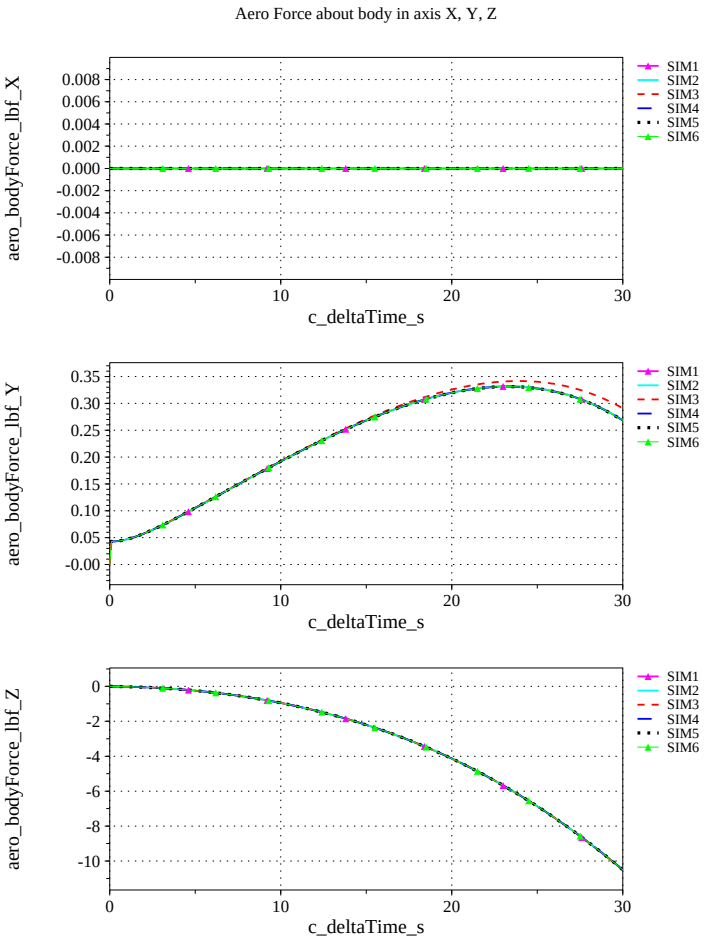

(a) Aerodynamic Forces Compared

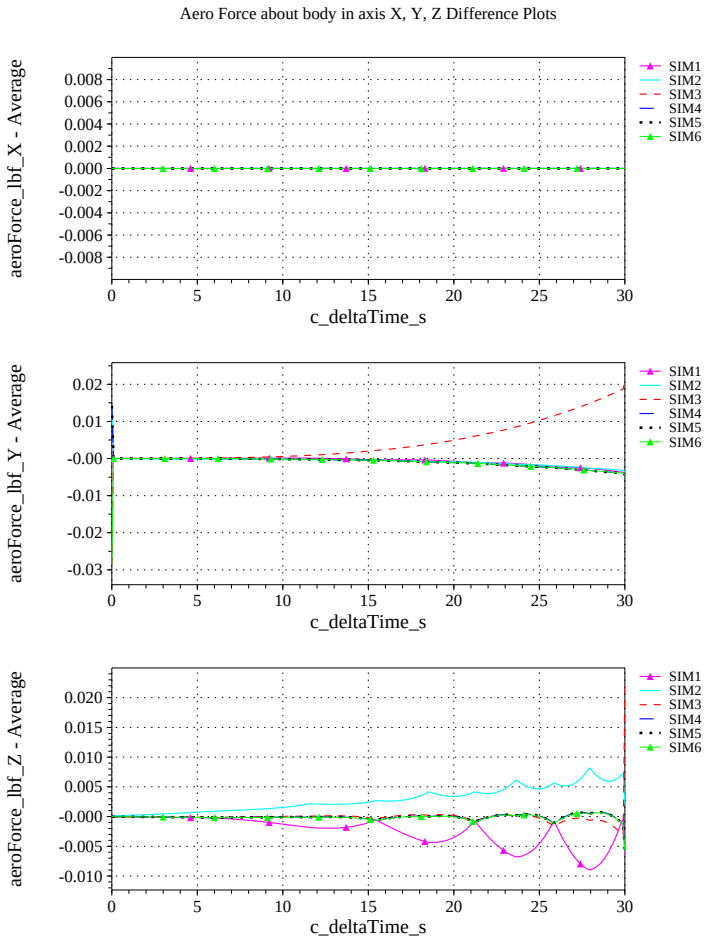

(b) Aerodynamic Forces Differenced

Figure 23. Check-case 8: Sphere Dropping through a Varying Wind Field; See Discussion in Section D.1.8

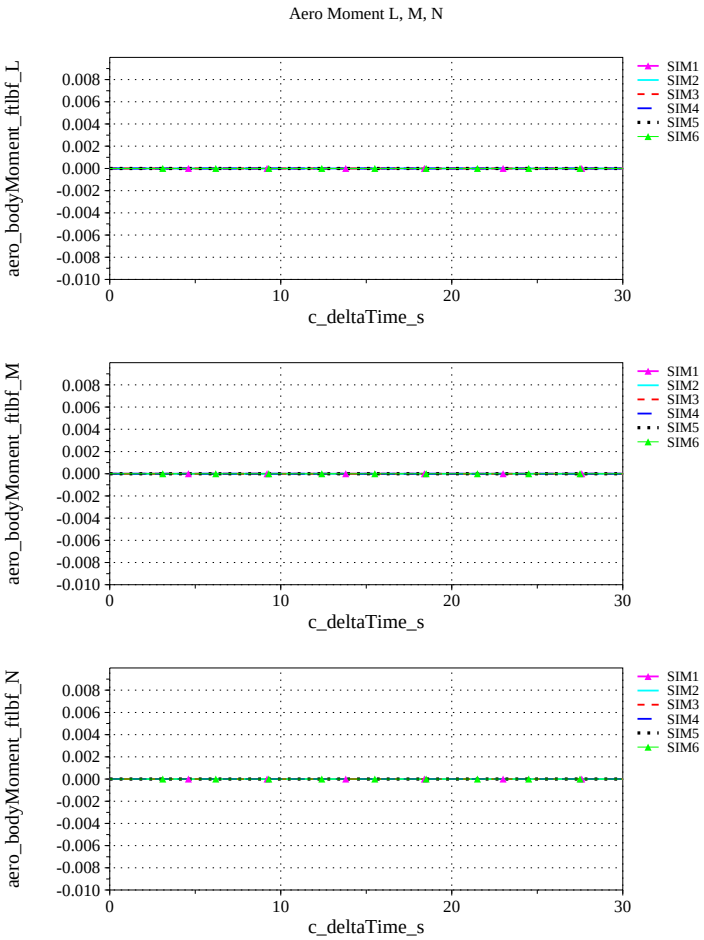

(c) Aerodynamic Moments Compared

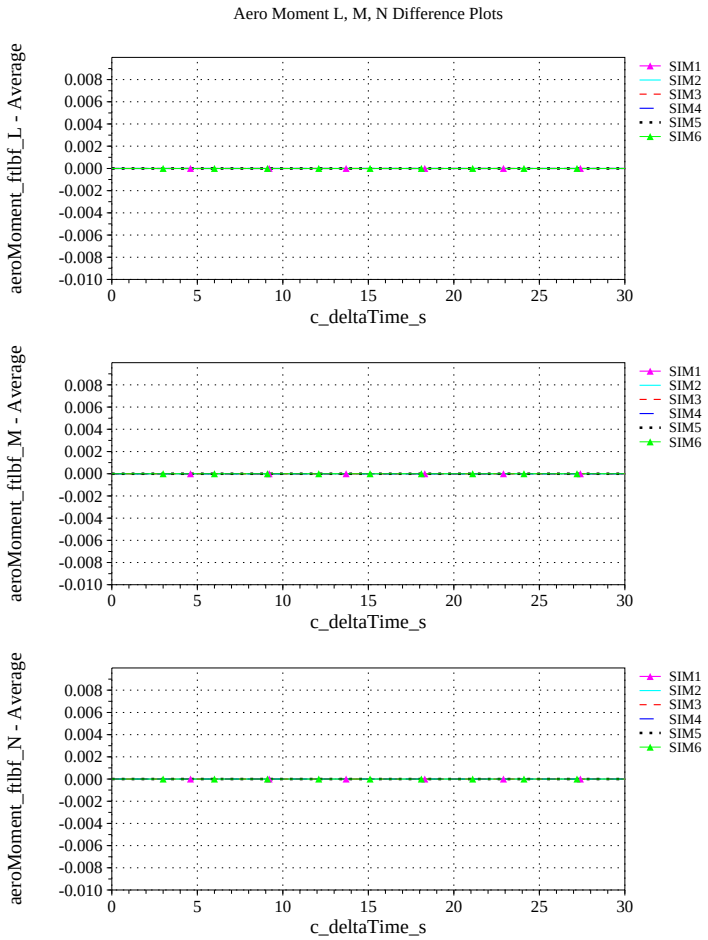

(d) Aerodynamic Moments Differenced

Figure 23. Check-case 8: Sphere Dropping through a Varying Wind Field; See Discussion in Section D.1.8 (Cont'd)

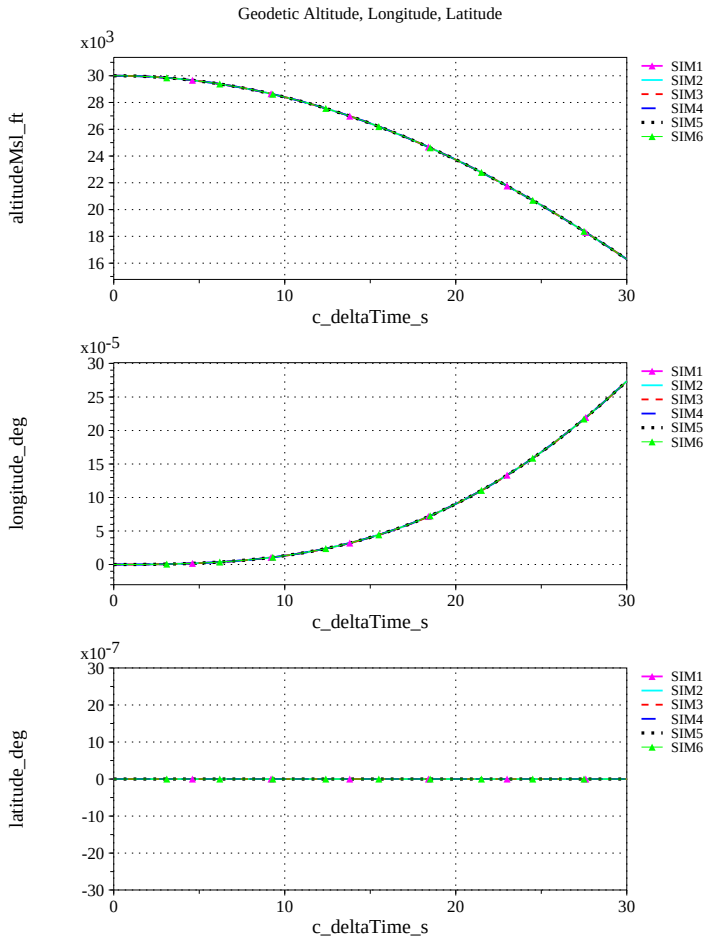

(e) Altitude, Geodetic Latitude and Longitude Compared

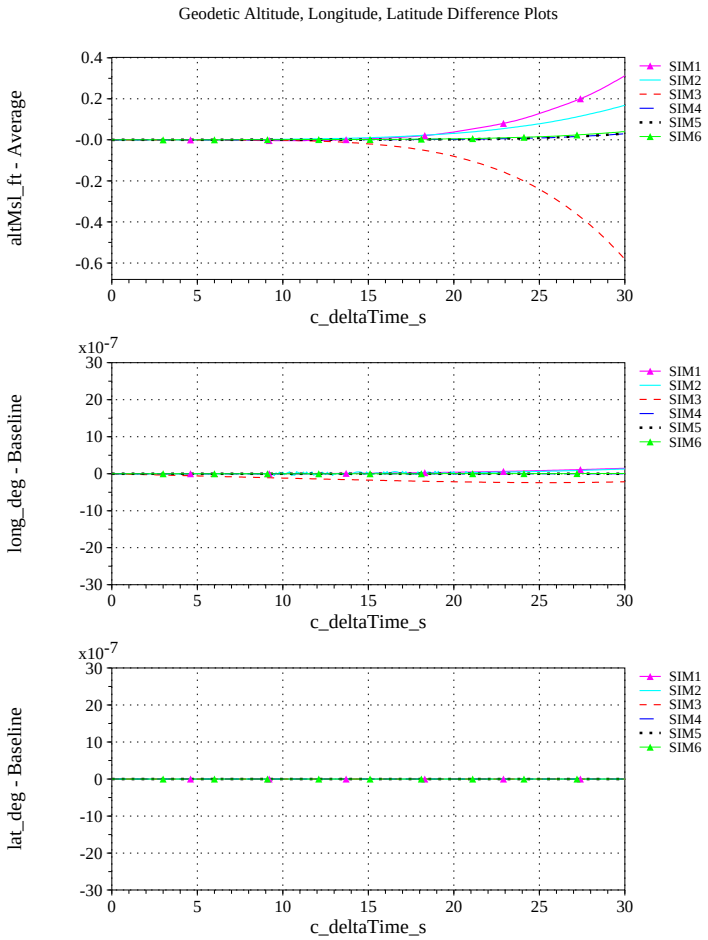

(f) Altitude, Geodetic Latitude and Longitude Differenced

Figure 23. Check-case 8: Sphere Dropping through a Varying Wind Field; See Discussion in Section D.1.8 (Cont'd)

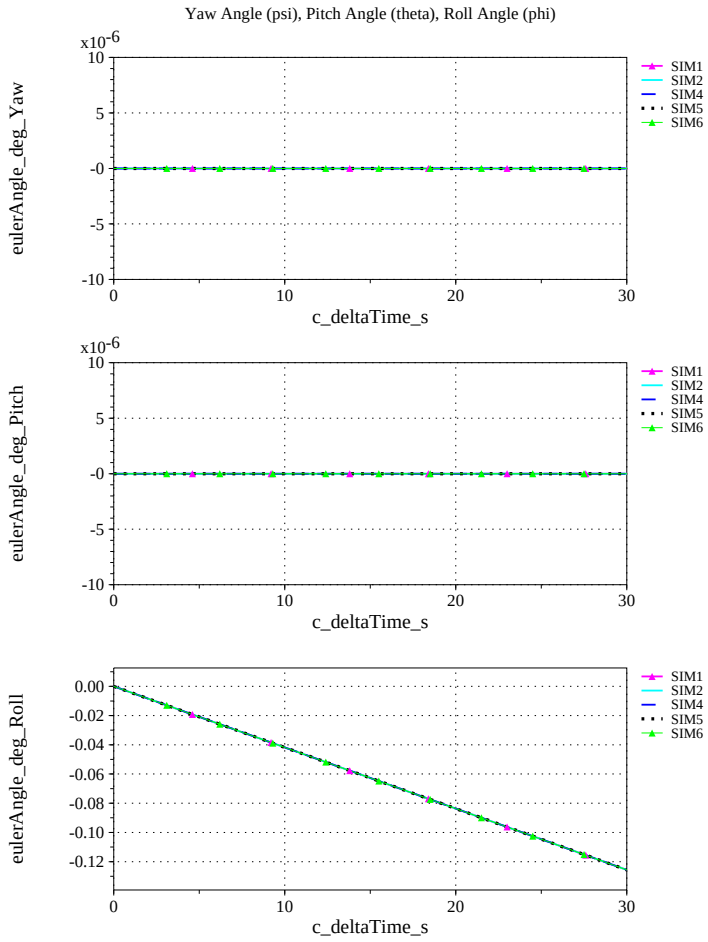

(g) Euler Angles (w.r.t. NED Frame) Compared

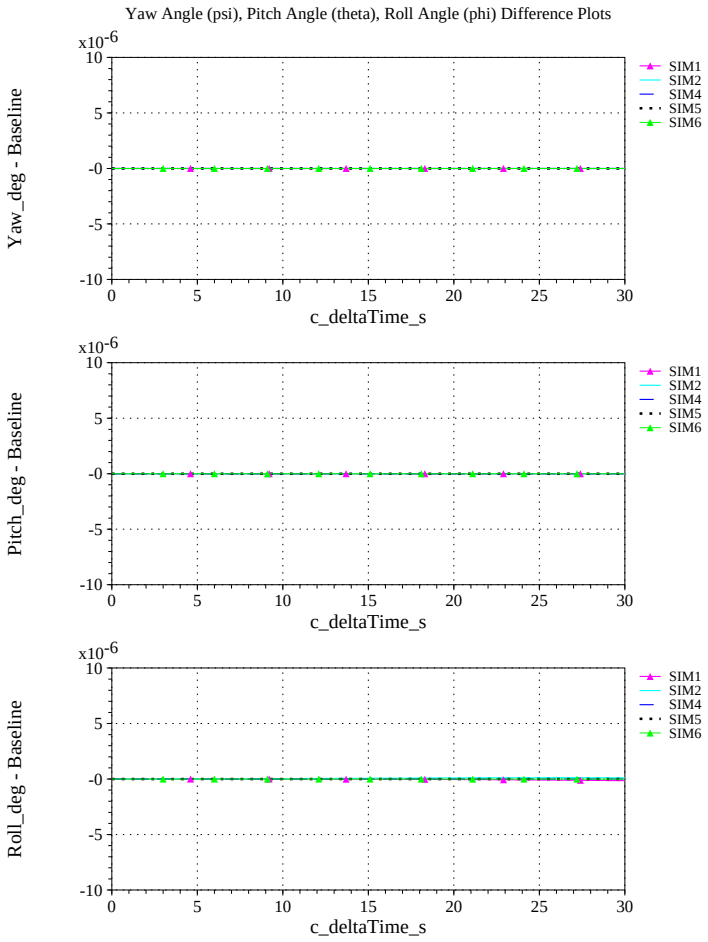

(h) Euler Angles (w.r.t. NED Frame) Differenced

Figure 23. Check-case 8: Sphere Dropping through a Varying Wind Field; See Discussion in Section D.1.8 (Cont'd)

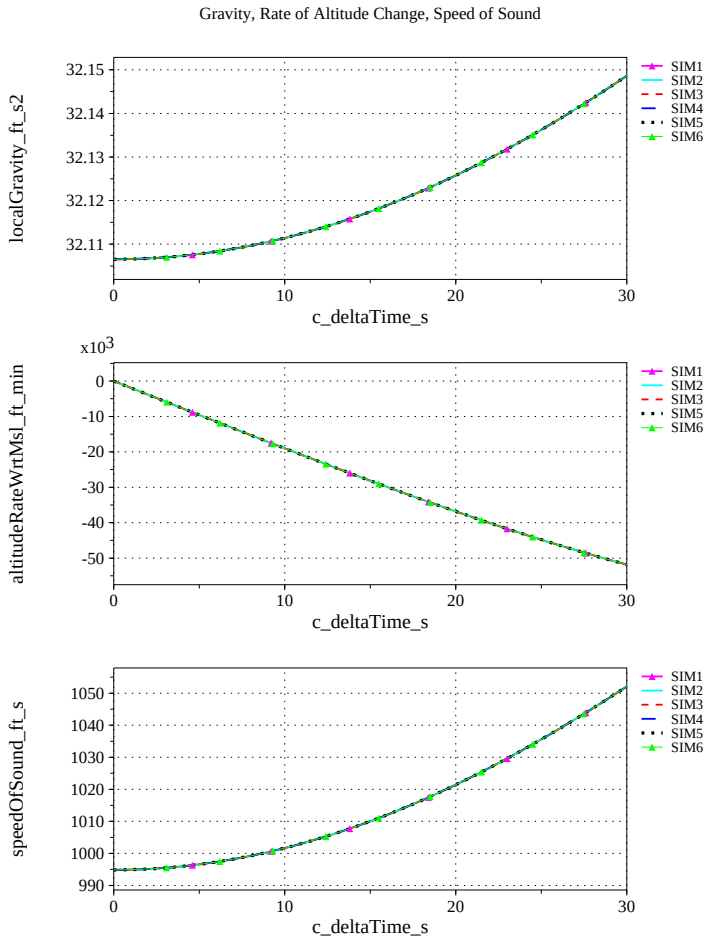

(i) Gravity, Climb Rate, and Speed-of-sound Compared

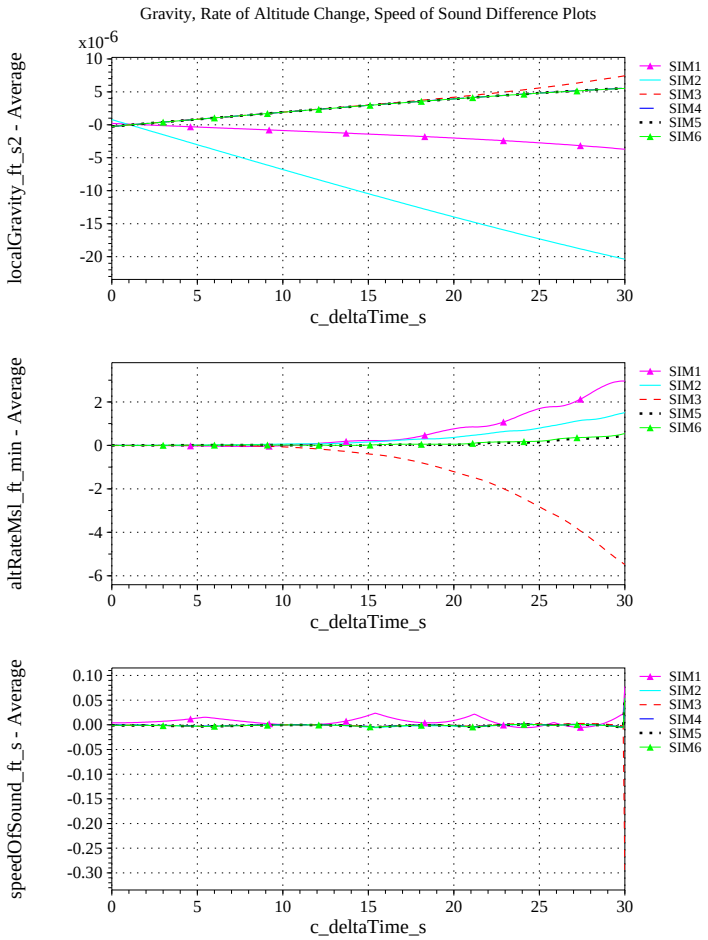

(j) Gravity, Climb Rate, and Speed-of-sound Differenced

Figure 23. Check-case 8: Sphere Dropping through a Varying Wind Field; See Discussion in Section D.1.8 (Cont'd)

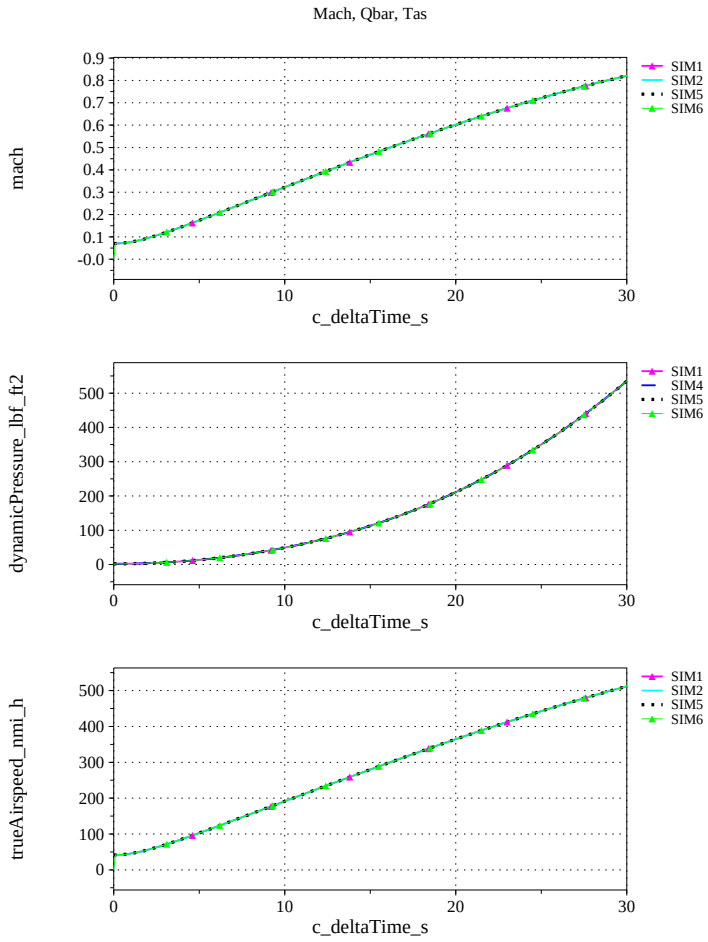

(k) Mach, Dynamic Pressure, and True Airspeed Compared

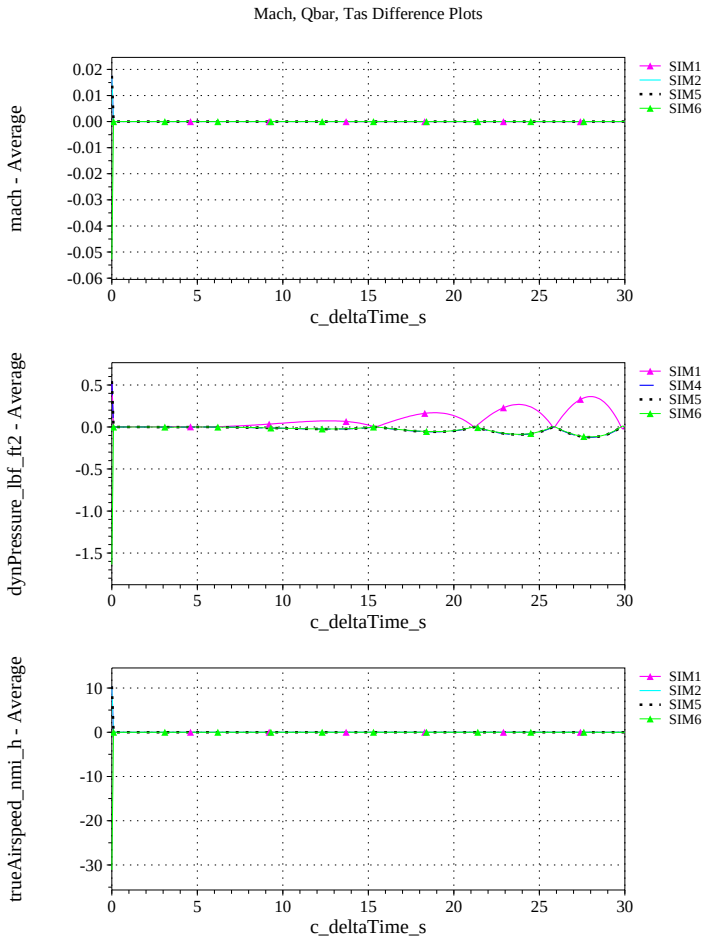

(l) Mach, Dynamic Pressure, and True Airspeed Differenced

Figure 23. Check-case 8: Sphere Dropping through a Varying Wind Field; See Discussion in Section D.1.8 (Cont'd)

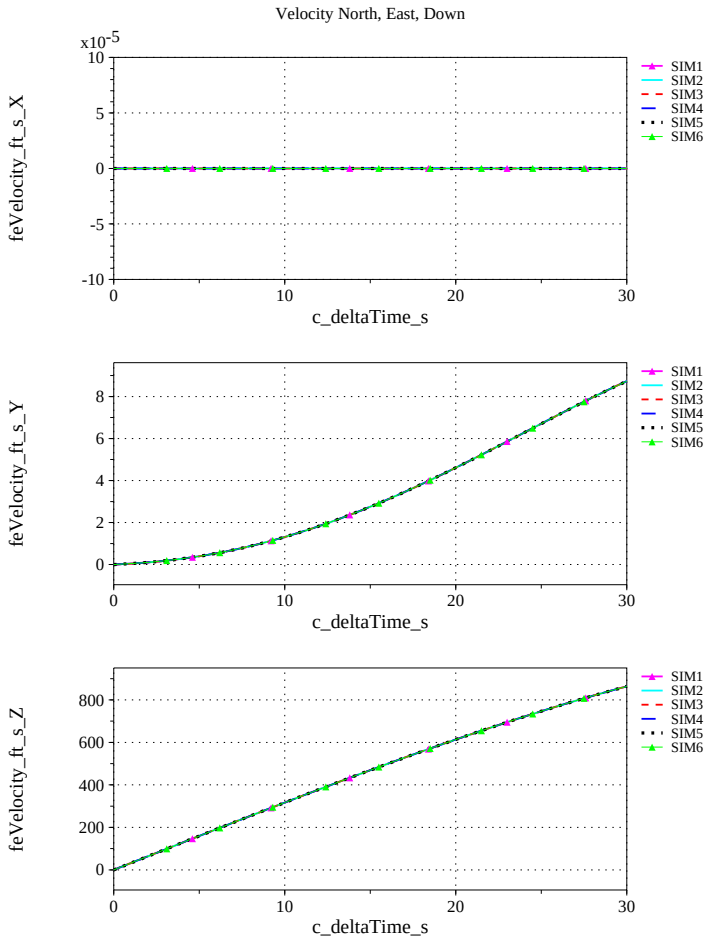

(m) NED Velocities Compared

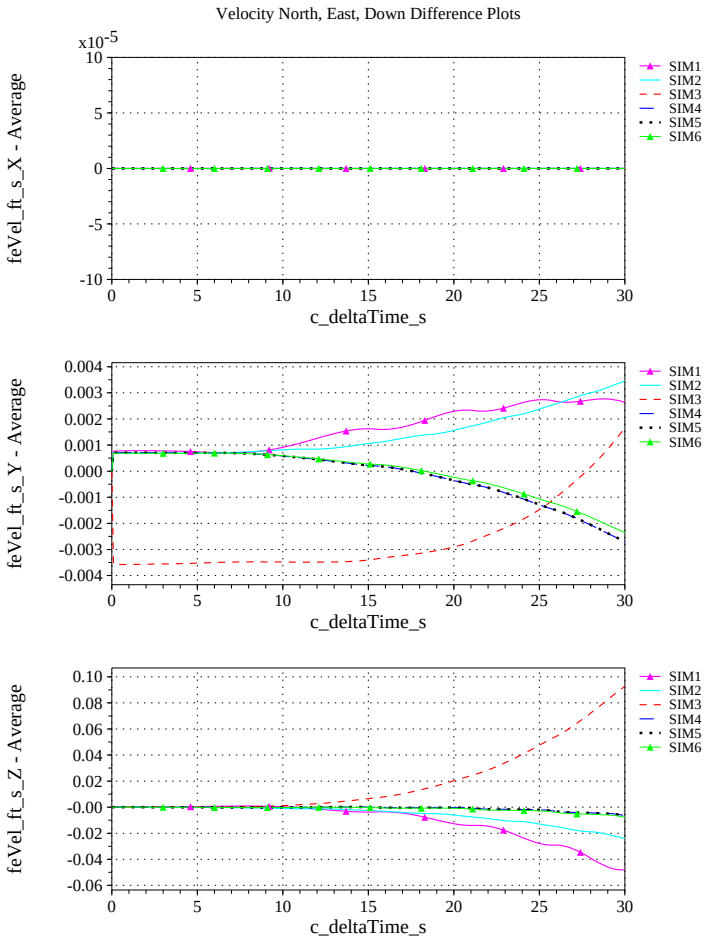

(n) NED Velocities Differenced

Figure 23. Check-case 8: Sphere Dropping through a Varying Wind Field; See Discussion in Section D.1.8 (Cont'd)

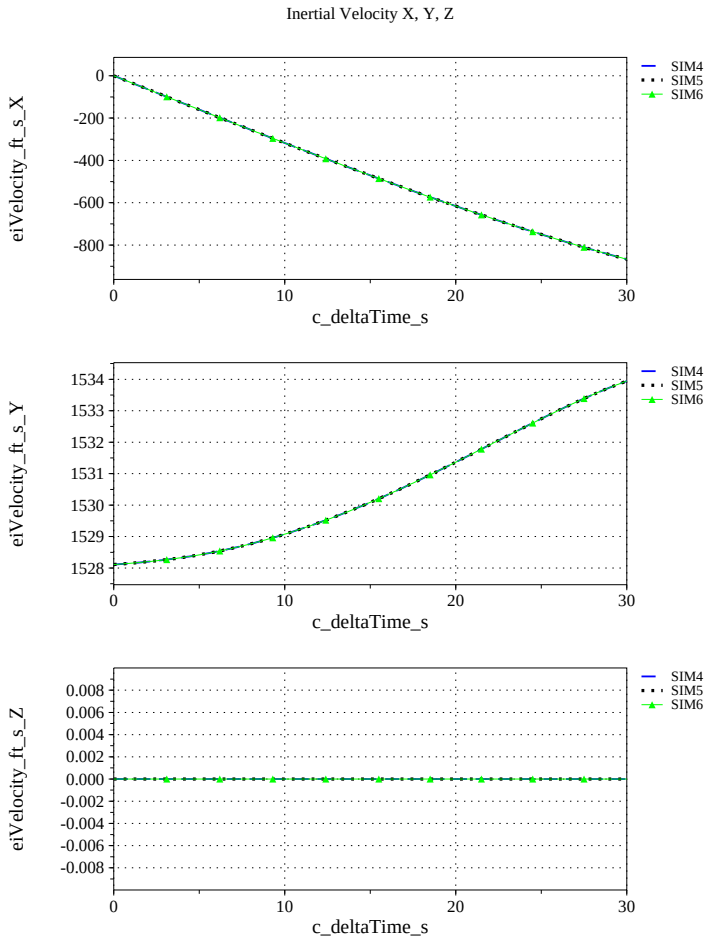

(o) Inertial Velocities Compared

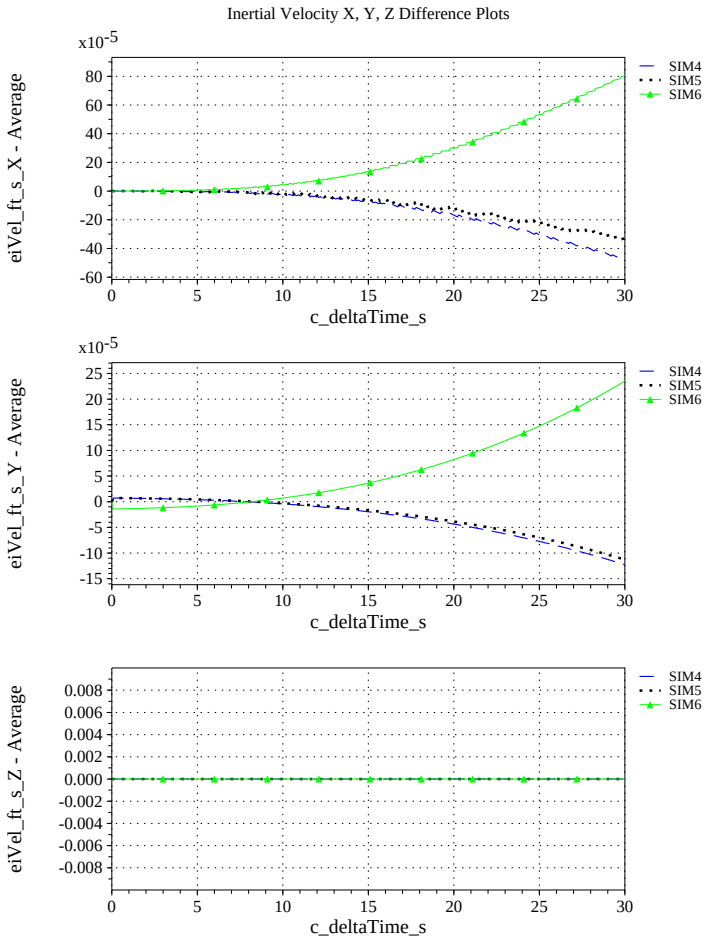

(p) Inertial Velocities Differenced

Figure 23. Check-case 8: Sphere Dropping through a Varying Wind Field; See Discussion in Section D.1.8 (Cont'd)

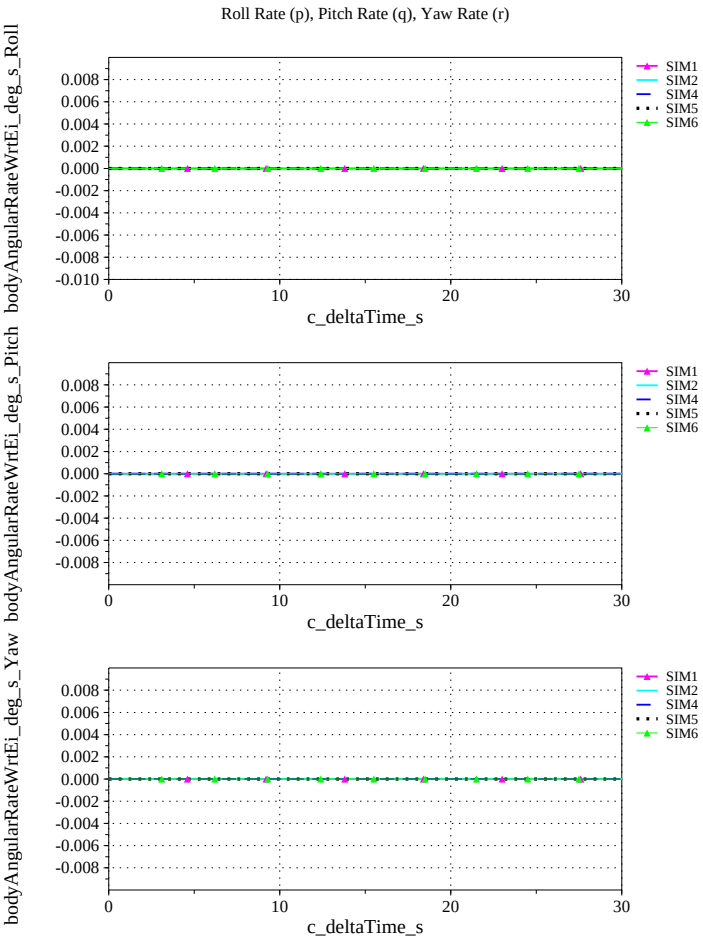

(q) Body-axis Angular Rates (w.r.t. NED Frame) Compared

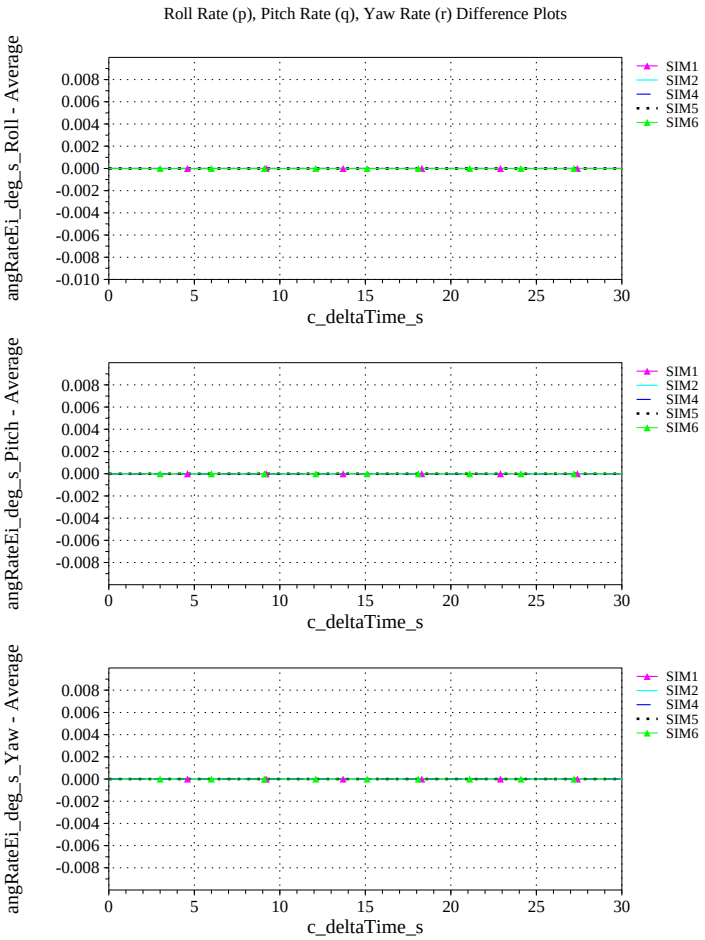

(r) Body-axis Angular Rates (w.r.t. NED Frame) Differenced

Figure 23. Check-case 8: Sphere Dropping through a Varying Wind Field; See Discussion in Section D.1.8 (Cont'd)

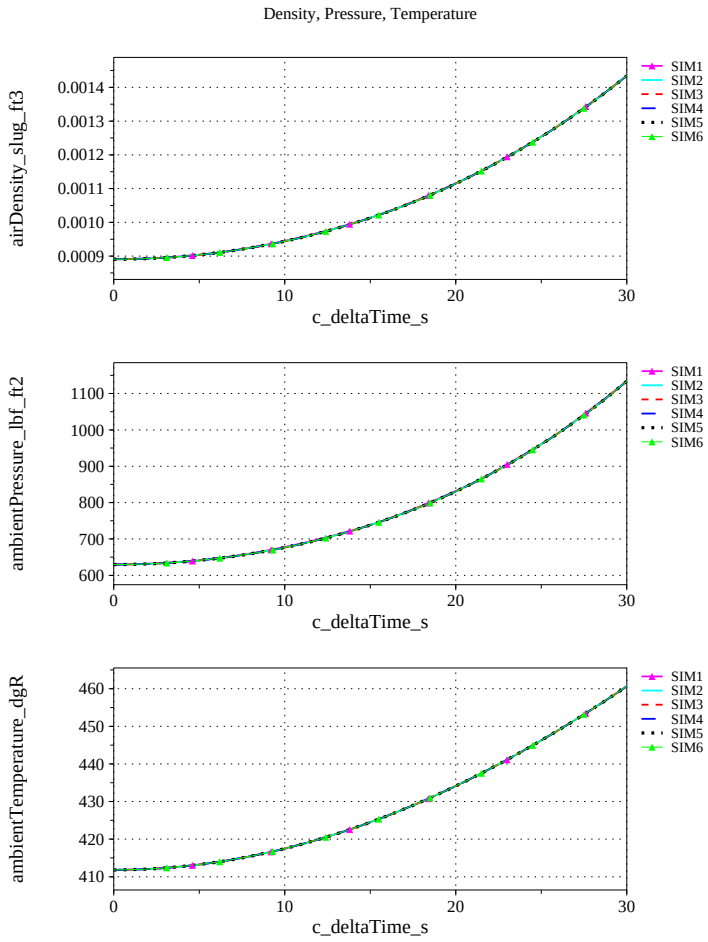

(s) Atmospheric Properties Compared

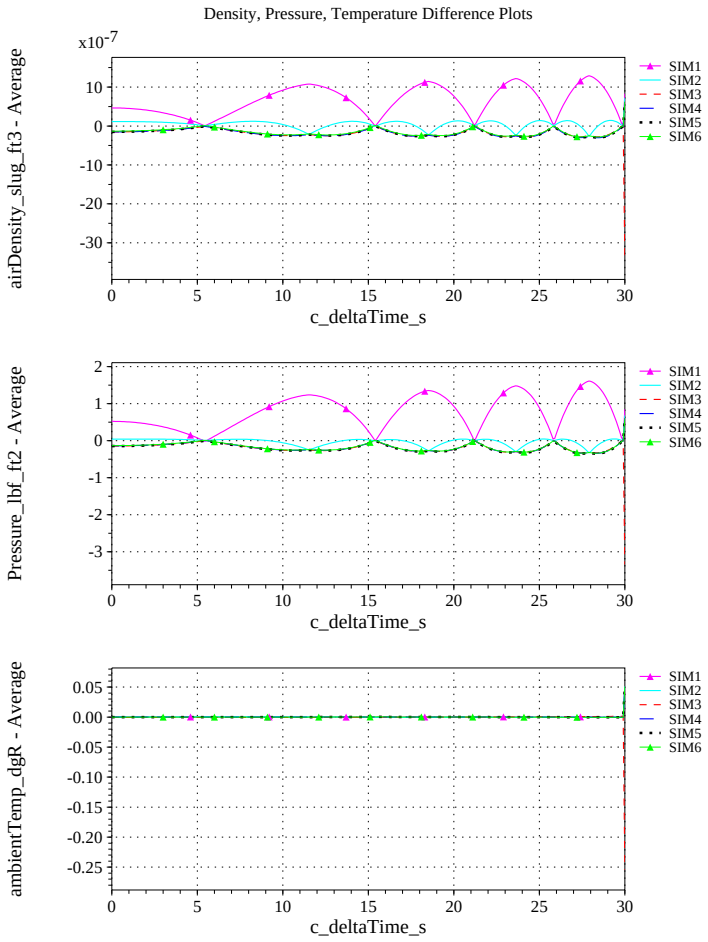

(t) Atmospheric Properties Differenced

Figure 23. Check-case 8: Sphere Dropping through a Varying Wind Field; See Discussion in Section D.1.8 (Cont'd)

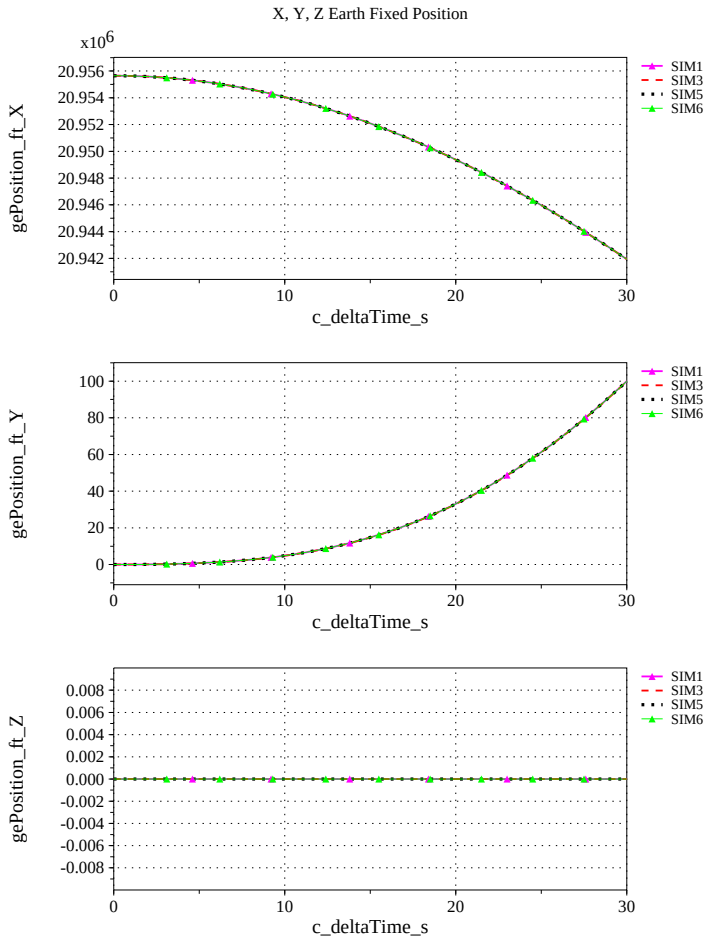

(u) Earth-centered, Earth-fixed Rectangular (X-Y-Z) Positions Compared

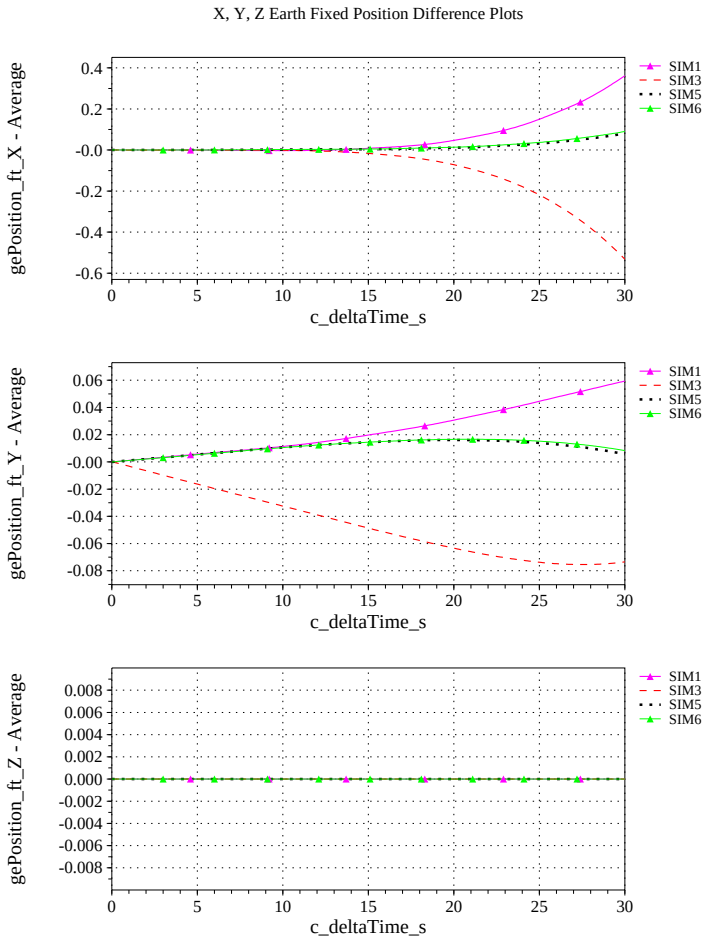

(v) Earth-centered, Earth-fixed Rectangular (X-Y-Z) Positions Differenced

Figure 23. Check-case 8: Sphere Dropping through a Varying Wind Field; See Discussion in Section D.1.8 (Cont'd)

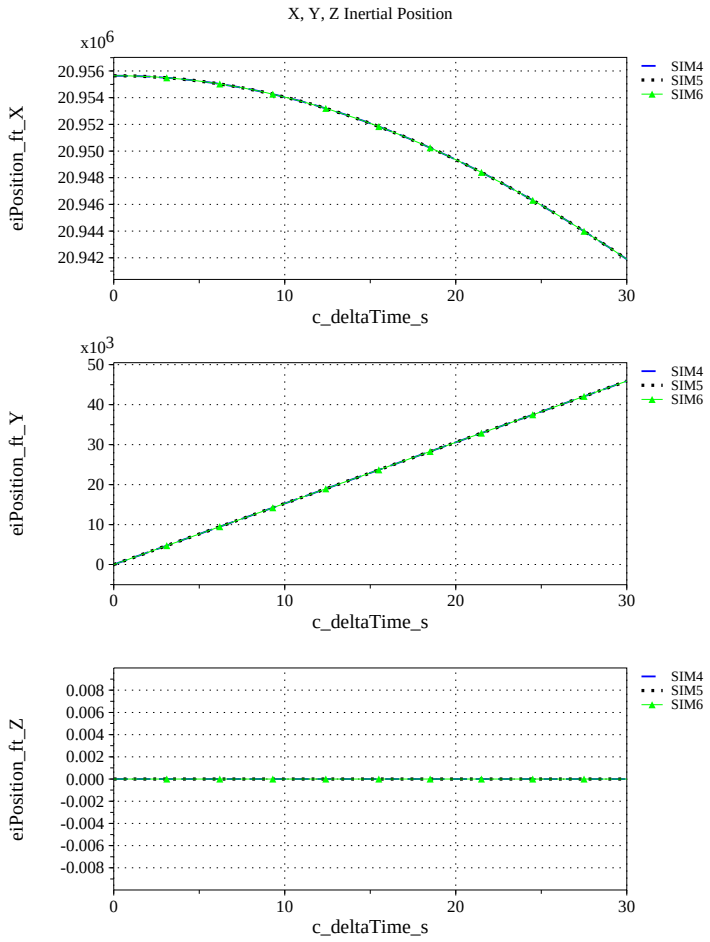

(w) Earth-centered Inertial Rectangular (x-y-z) Positions Compared

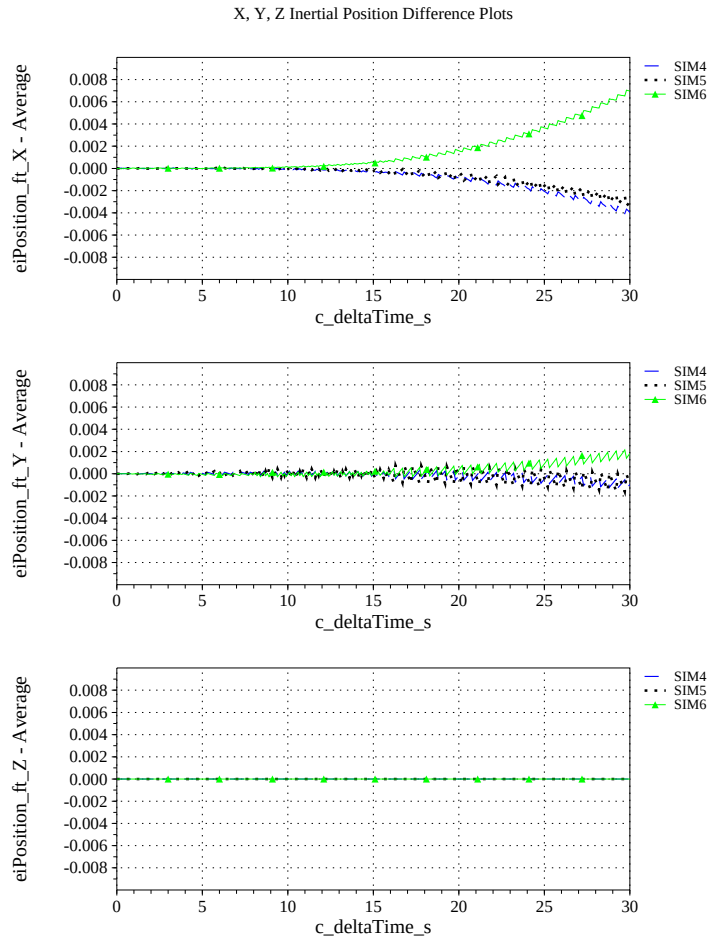

(x) Earth-centered Inertial Rectangular (x-y-z) Positions Differenced

Figure 23. Check-case 8: Sphere Dropping through a Varying Wind Field; See Discussion in Section D.1.8 (Concluded)

D.1.9 Check-case 9 – eastward ballistic flight of a sphere

This section shows cross-plots for six of the selected simulation tools in modeling the dynamics of a sphere launched eastward along the Equator of an ellipsoidal rotating Earth with J_2 gravitational harmonics. This scenario is described in Section C.1.9. Figures 24a through 24x compare results between the six simulation tools, as well as the deviances of the outputs from each tool from the ensemble average value.

This scenario launched the sphere on a ballistic trajectory to the east along the Equator. The sphere had zero initial Earth-relative velocity and angular rates. However, it developed a pitch relative to the Earth due to the eastward travel. In fact, the change in pitch angle should have been exactly equal to the change in longitude.

All the simulations showed this equivalence between longitude and pitch angle differences except for SIM 2. Given previous integration error differences for the Euler angles identified for SIM 2 in Section D.1.2, it was assumed that the pitch angle difference shown for SIM 2 were due to a combination of differences in integration methods and longitude traveled. In any case, the differences in pitch angle were not significant.

The differences in translational motion were larger. The simulations all agreed that no motion occurs to the north. But simulations differed on the amount of travel eastward and upward by nearly 5 ft at $t = 30$ sec. SIM 4, 5, and 6 closely agreed on gravitation, aerodynamic forces, translational velocity, and position; therefore, these simulations were used as a basis for evaluating differences among the remaining simulations. (This was not an endorsement that these simulations produce the "correct" result; this simply reduced the number of differences to analyze.)

First, the external forces were examined for the contributors to differences in translational motion. The difference plot for local gravity (Figure 24j) did portray a jump in the gravitational difference in SIM 1 and SIM 2 at $t = 0.1$ sec. However, these differences would correspond to altitude differences of about -10 and -3.5 ft respectively when compared to SIM 3, 4, 5, and 6. However, the altitude difference plot did not show any visible difference in altitude at $t = 0.1$ sec. An alternative explanation is an unknown delay in recording gravitation. This explanation matched well with the difference seen in SIM 2 if the recording delay was 0.01 sec. The initial upward velocity of the sphere was 1,000 ft/s; therefore, a delay of 0.01 sec in recording represented nearly a -10-ft altitude bias in the gravitation reported at simulation start. Moreover, since gravitation and aerodynamic drag would reduce the upwards velocity over time, the altitude bias in the reported gravity that was associated with a 0.01-sec lag should decline, at least until the sphere begins to accelerate back towards the Earth's surface. At $t = 30$ sec, the sphere had passed the apex in its trajectory but the downward velocity remained low. The altitude bias for a 0.01-sec delay would be $+1.8$ ft. However, at the same time, SIM 2 showed an altitude difference that had grown to approximately 1.4 ft, relative to the consensus group (SIM 4/5/6) (Figure 24f). The altitude difference, therefore, largely canceled the altitude bias from the recording lag and the difference in gravitation between SIM 2 and SIM 4/5/6 at $t = 30$ sec was reduced to nearly zero, as shown on the plots (Figure 24j). The "recording delay" also appeared to explain the gravitation differences in SIM 1 but the required delay would have needed to be about 0.004 sec. Furthermore, SIM 1 did not exhibit a steady decline in gravitation difference; instead, the gravitation difference exhibited a slight increase over time (Figure 24j). This likely occurred because the altitude difference between SIM 1 and SIM 4/5/6 was increasing in a direction that initially compensates for and then exceeded the decline in the lag-induced altitude bias.

Remaining differences in gravitation among the simulations were consistent with the plotted differences in altitude. In any case, even if the largest gravitation differences (which appeared to be due to recording delay) were applied to the EOM, they would account for differences in downward-axis velocity and altitude of less than 0.0005 ft/s and 0.009 ft, respectively, at $t = 30$ sec. Thus, gravitation differences were not a driving contributor to differences in translational motion.

Differences in aerodynamic forces were larger than those for gravitation. The differences in SIM 2 aerodynamic forces had two main contributors, a 0.01-sec delay in the recorded forces and a difference in atmospheric density. The delay was a recording artifact only and did not contribute to differences in velocity and position. The difference in atmospheric density, as discussed in previous check-cases, derived from implementing the atmosphere model using a lookup table. From the data, it appears that SIM 2 used 1,000 m for the first break-point but every break-point thereafter was at 500-m increments. Small aerodynamic force differences arising from differences in atmospheric density were the primary contributor for differences in translational motion between SIM 2 and SIM 4/5/6; they accounted for nearly all of the differences in velocity (Figure 24n) and position (Figure 24f) relative to SIM 4/5/6.

SIM 1 also used a lookup table to estimate atmospheric density; the lookup table has 1000-m breakpoints throughout the altitudes traversed in this case. The density difference was the primary contributor to the difference in aerodynamic forces between SIM 1 and SIM 4/5/6. The evolving difference in velocity was a secondary contributor. However, the aerodynamic force differences for SIM 1 would account for only 61% of the eastward velocity and longitude differences, 34% of the downward velocity difference, and 46% of the altitude difference.

The source of the remaining difference between SIM 1 and the SIM 4/5/6 group in translational motion could not be identified from the recorded data. The remaining contributor appeared to be an unknown difference in EOM implementation or configuration possibly including, but not limited to, differences in integration or other numerical methods.

Differences in aerodynamic forces (Figure 24b) in SIM 3 were largely a response to the growing differences in velocity and altitude, which determined atmospheric density. A small difference in orientation of SIM 3 relative to SIM 4/5/6 also contributed to the differences in aerodynamic forces. Although SIM 3 values for Euler angles are not plotted, the SIM 3 data file had a very small initial roll angle (-6.4×10^{-6} degrees). This small roll angle likely explained the difference of order 1×10^{-7} lbf seen in body y-axis aerodynamic force (Figure 24b). Nevertheless, the orientation difference did not contribute to differences in translational velocity and position. Relative to SIM 4/5/6, the expected contributions of the aerodynamic force differences to differences in translational motion at $t = 30$ sec were $+0.14$ ft/s in eastward velocity, $+6.4 \times 10^{-6}$ degrees in longitude, -0.098 ft/s in downward velocity, and $+1.8$ ft in altitude. However, the total differences were larger and in the opposite direction. They were -0.16 ft/s in eastward velocity, -1.4×10^{-5} degrees in longitude, $+0.14$ ft/s in downward velocity, and -4.3 ft in altitude. As with SIM 2, the additional contributor(s) to these small differences could not be identified using the recorded data; it is likely an unknown difference in EOM implementation or configuration including, but not limited to, differences in integration or other numerical methods.

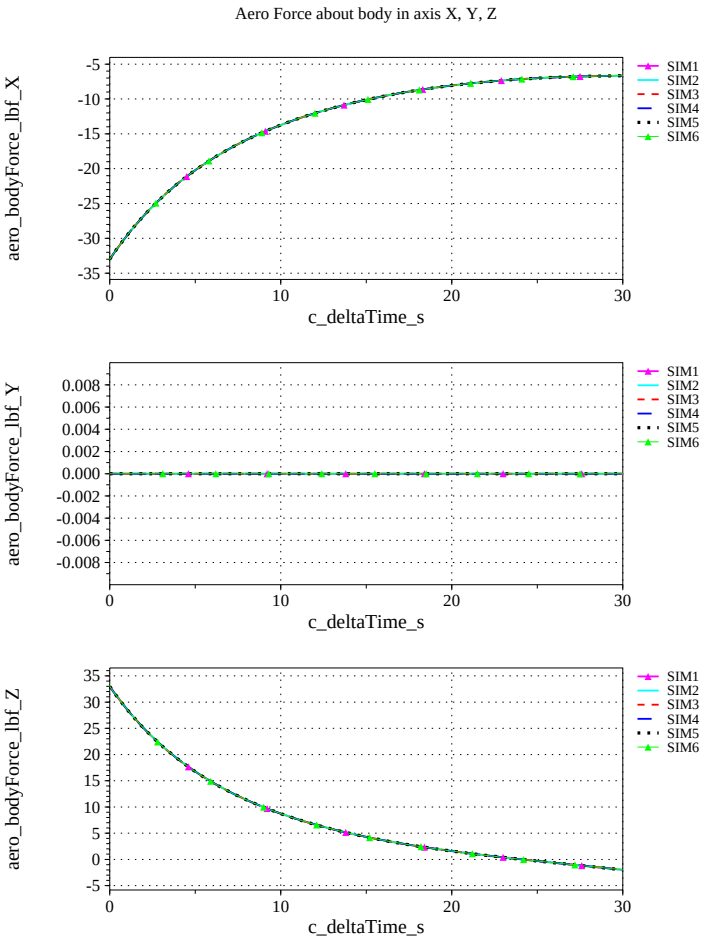

(a) Aerodynamic Forces Compared

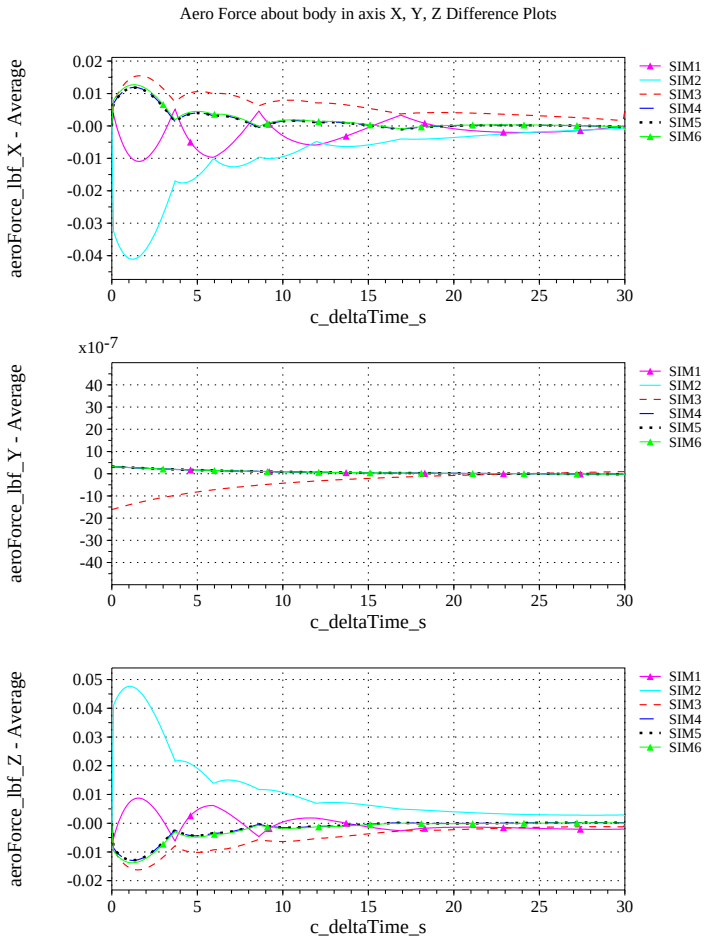

(b) Aerodynamic Forces Differenced

Figure 24. Check-case 9: Eastward Ballistic Flight of a Sphere; See Discussion in Section D.1.9

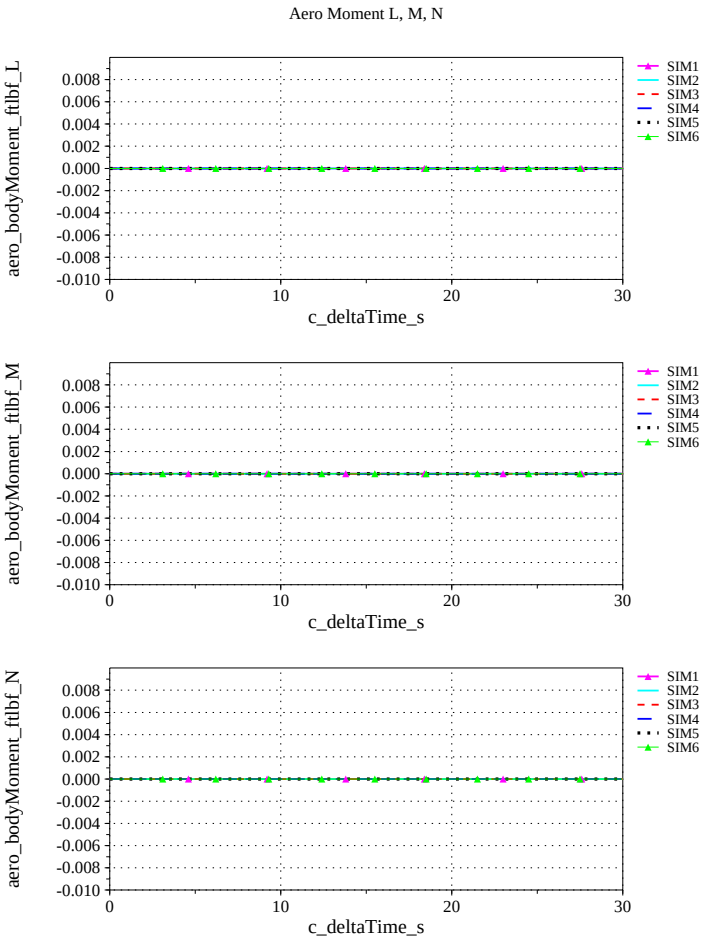

(c) Aerodynamic Moments Compared

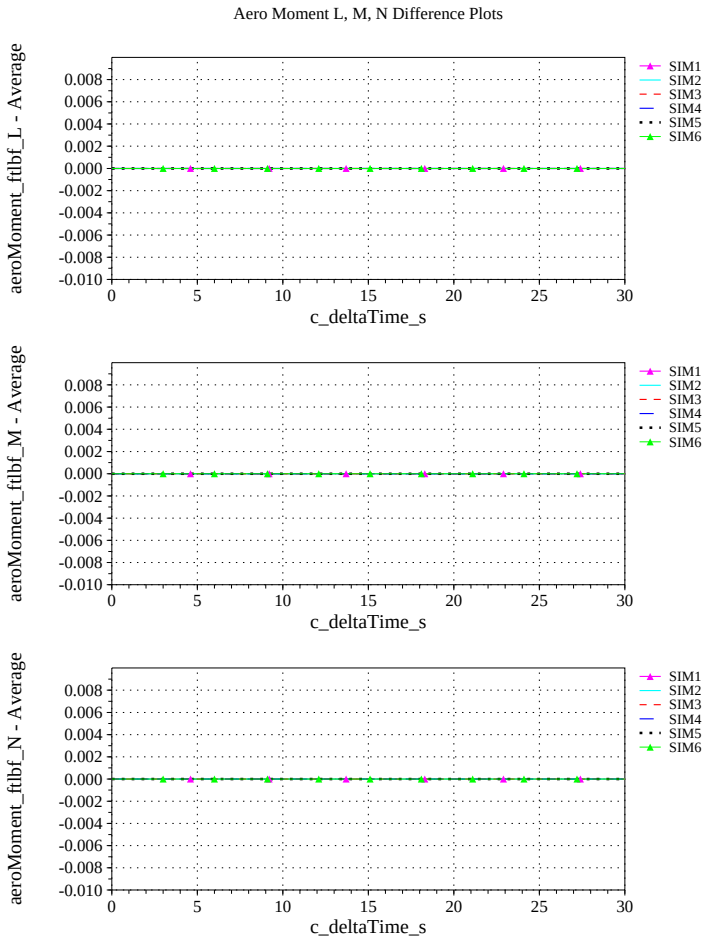

(d) Aerodynamic Moments Differenced

Figure 24. Check-case 9: Eastward Ballistic Flight of a Sphere; See Discussion in Section D.1.9 (Cont'd)

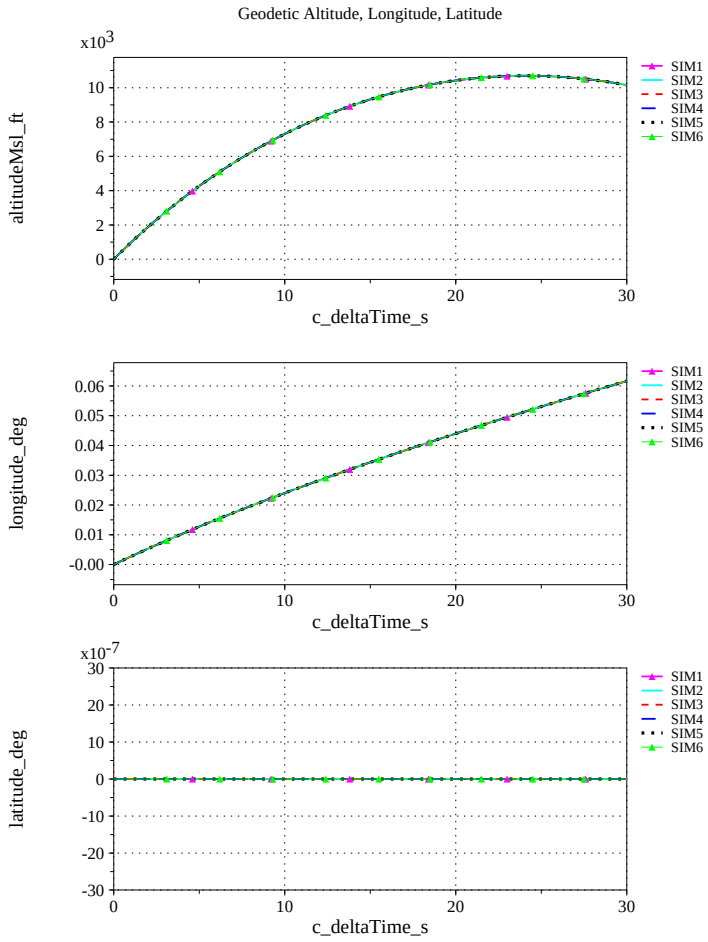

(e) Altitude, Geodetic Latitude and Longitude Compared

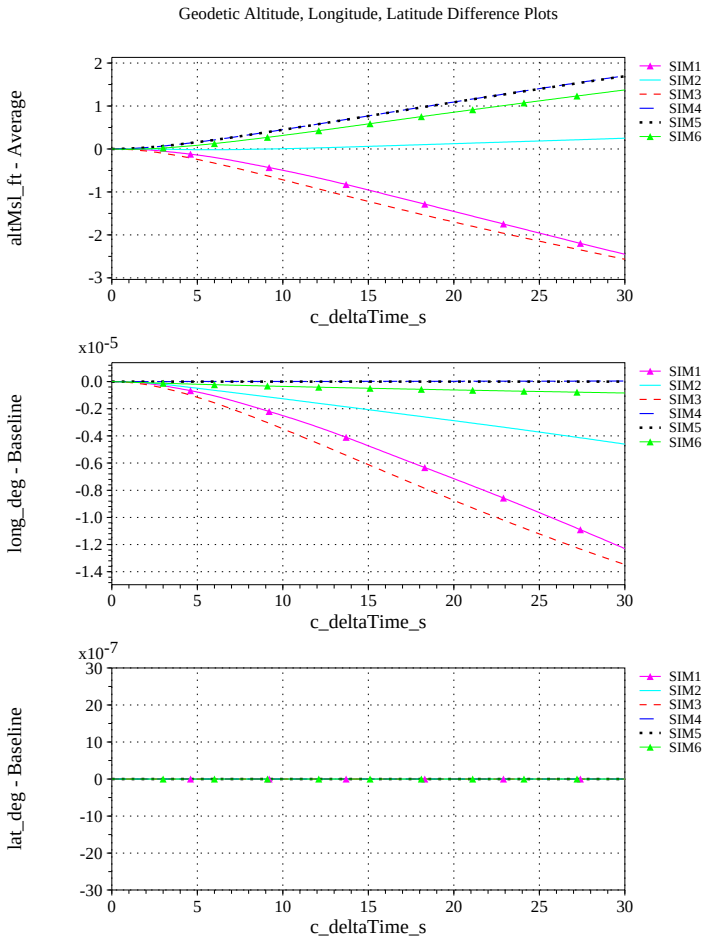

(f) Altitude, Geodetic Latitude and Longitude Differenced

Figure 24. Check-case 9: Eastward Ballistic Flight of a Sphere; See Discussion in Section D.1.9 (Cont'd)

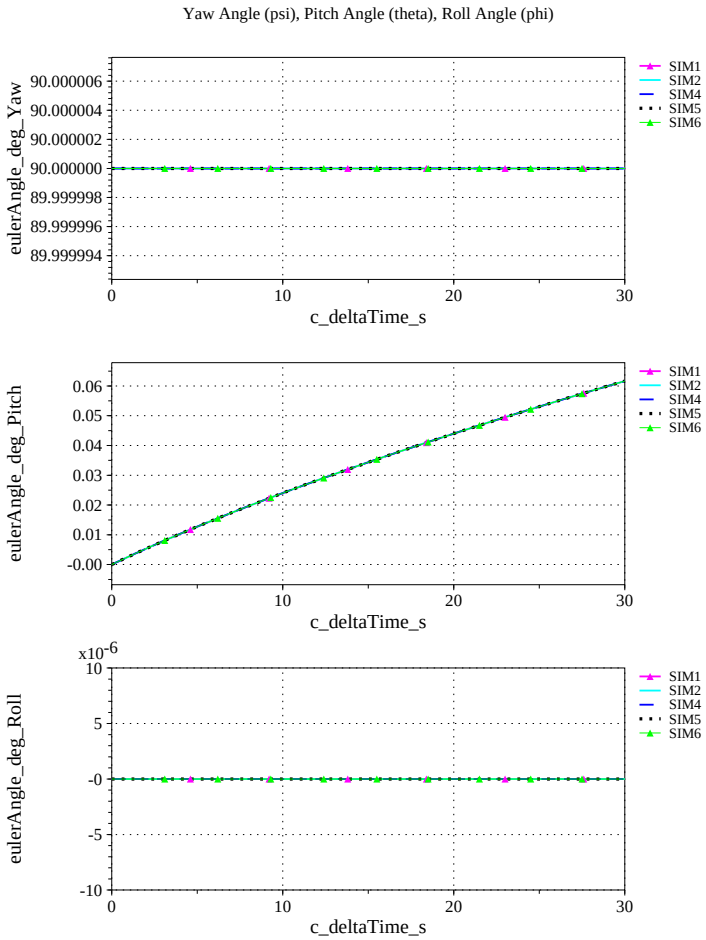

(g) Euler Angles (w.r.t. NED Frame) Compared

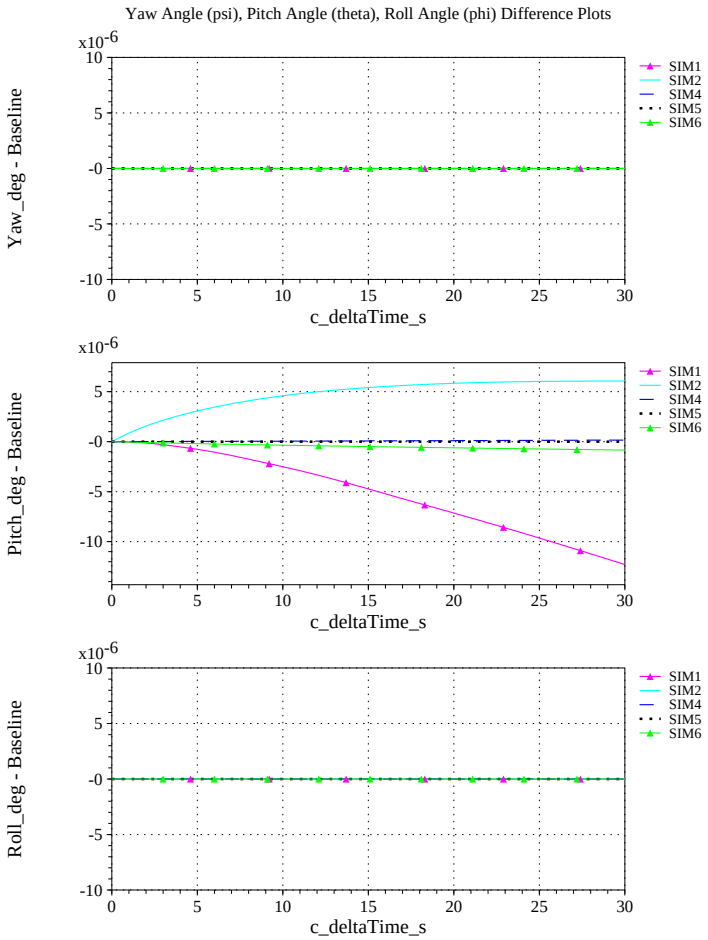

(h) Euler Angles (w.r.t. NED Frame) Differenced

Figure 24. Check-case 9: Eastward Ballistic Flight of a Sphere; See Discussion in Section D.1.9 (Cont'd)

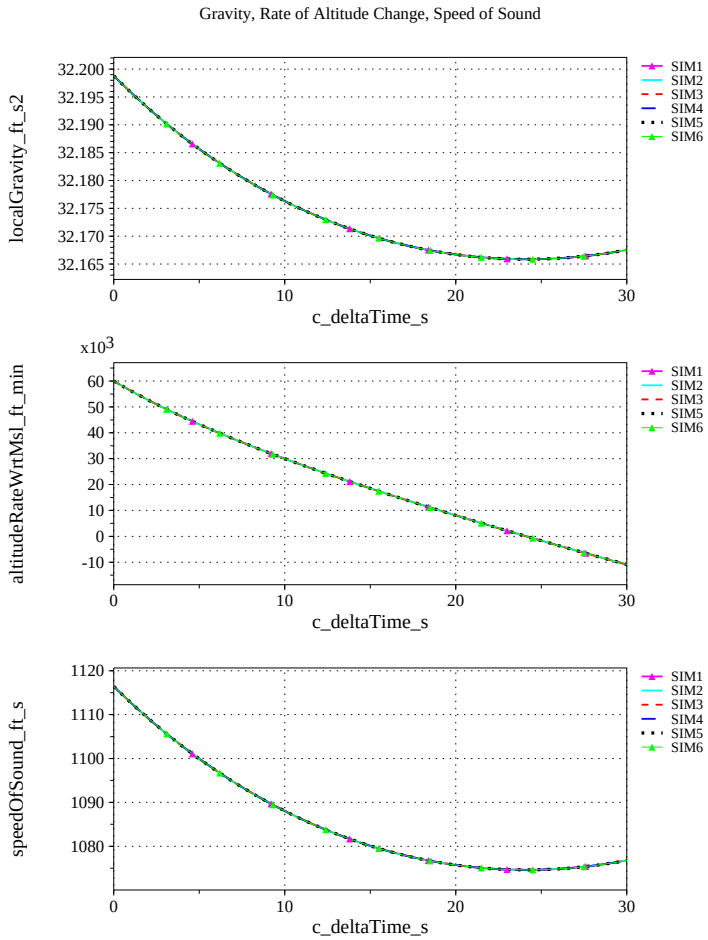

(i) Gravity, Climb Rate, and Speed-of-sound Compared

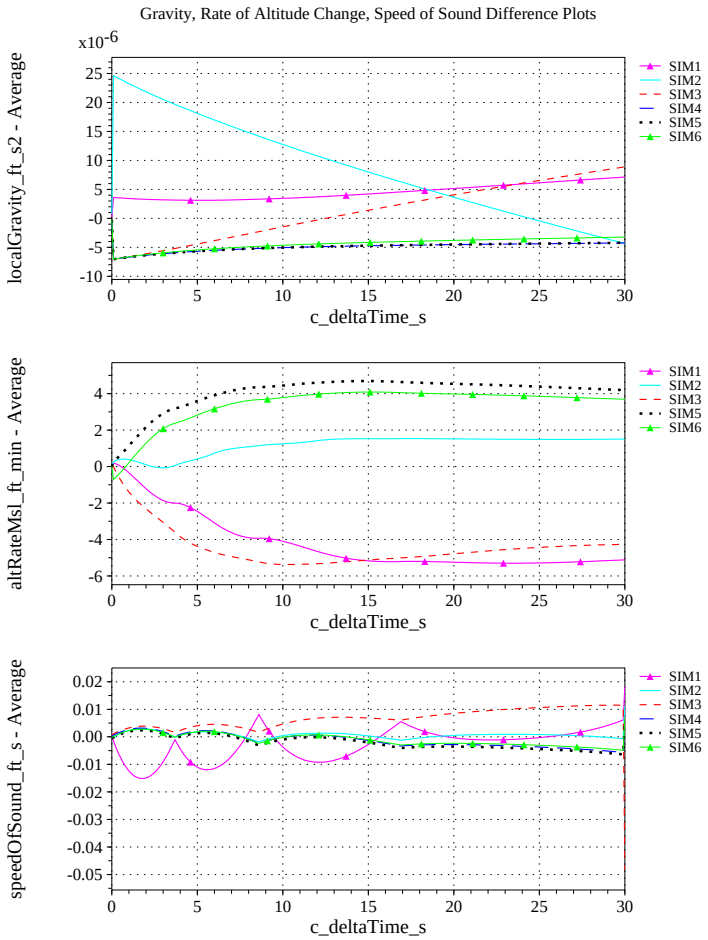

(j) Gravity, Climb Rate, and Speed-of-sound Differenced

Figure 24. Check-case 9: Eastward Ballistic Flight of a Sphere; See Discussion in Section D.1.9 (Cont'd)

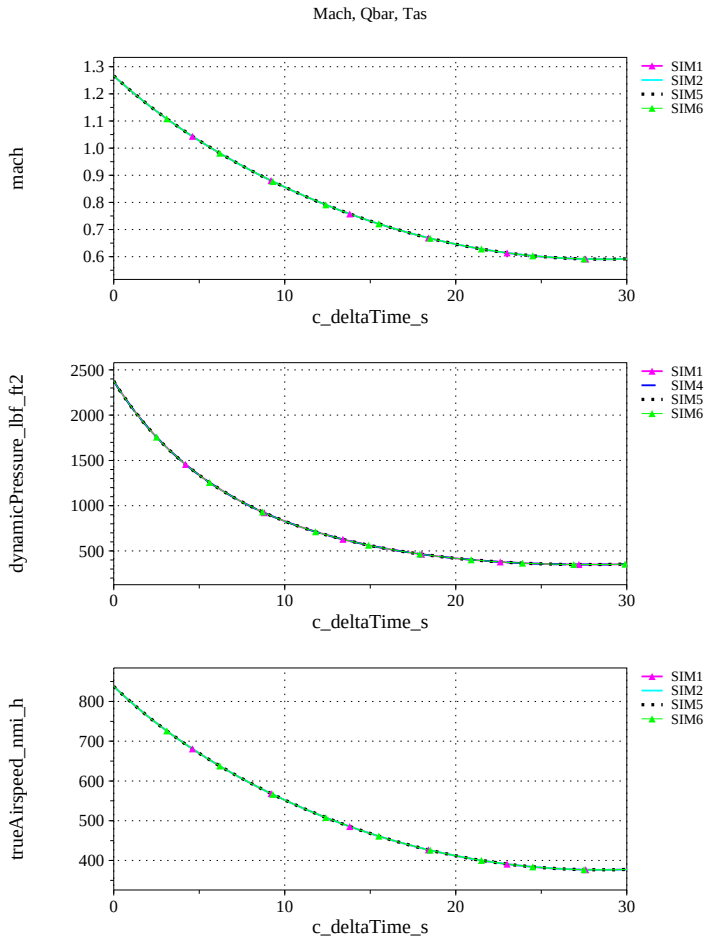

(k) Mach, Dynamic Pressure, and True Airspeed Compared

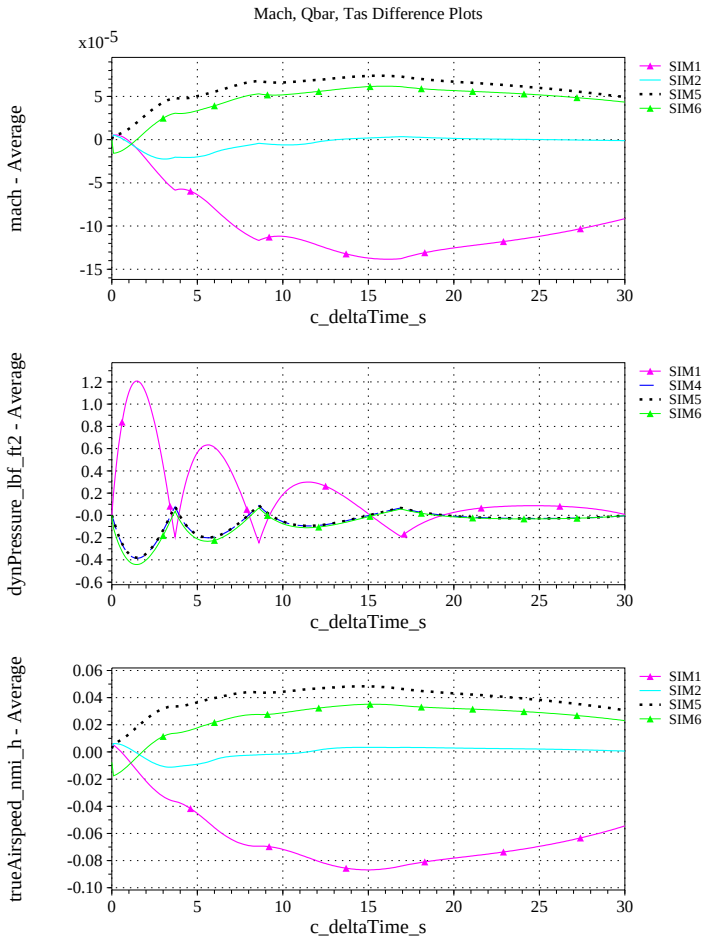

(l) Mach, Dynamic Pressure, and True Airspeed Differenced

Figure 24. Check-case 9: Eastward Ballistic Flight of a Sphere; See Discussion in Section D.1.9 (Cont'd)

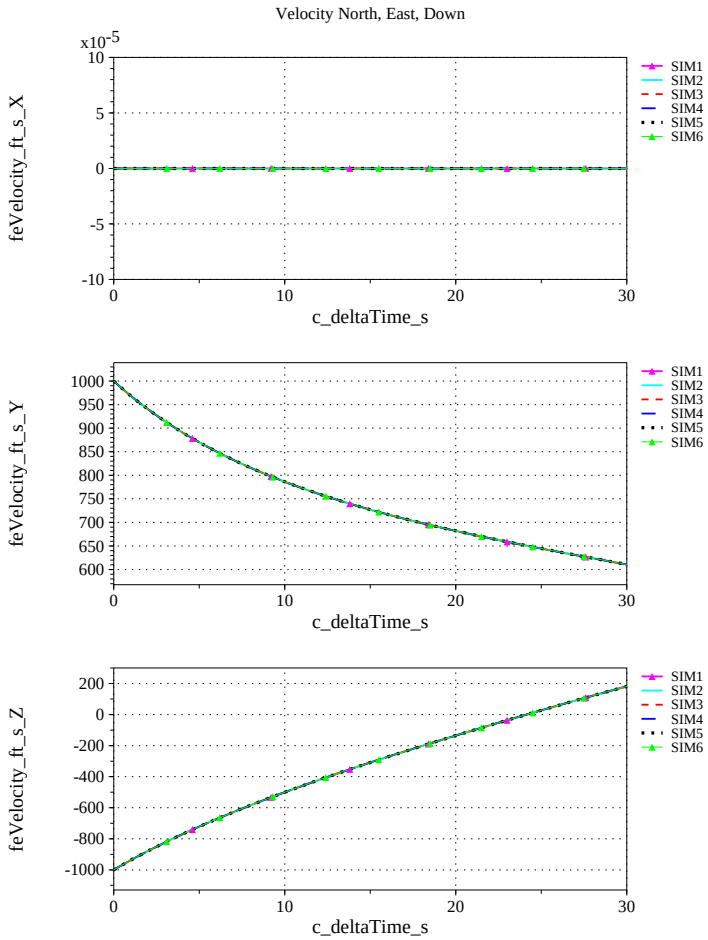

(m) NED Velocities Compared

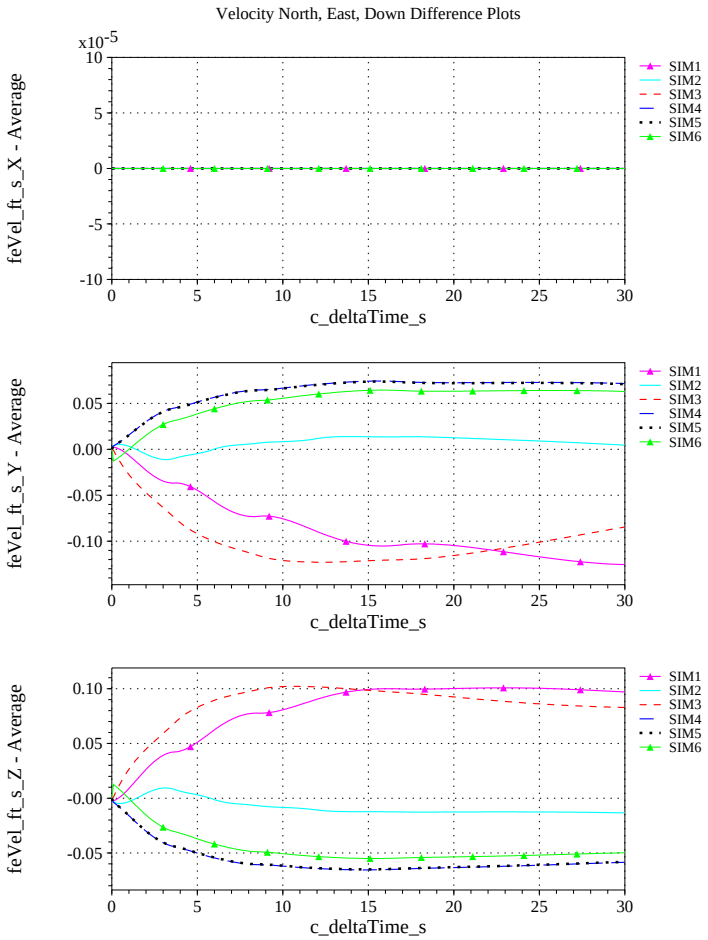

(n) NED Velocities Differenced

Figure 24. Check-case 9: Eastward Ballistic Flight of a Sphere; See Discussion in Section D.1.9 (Cont'd)

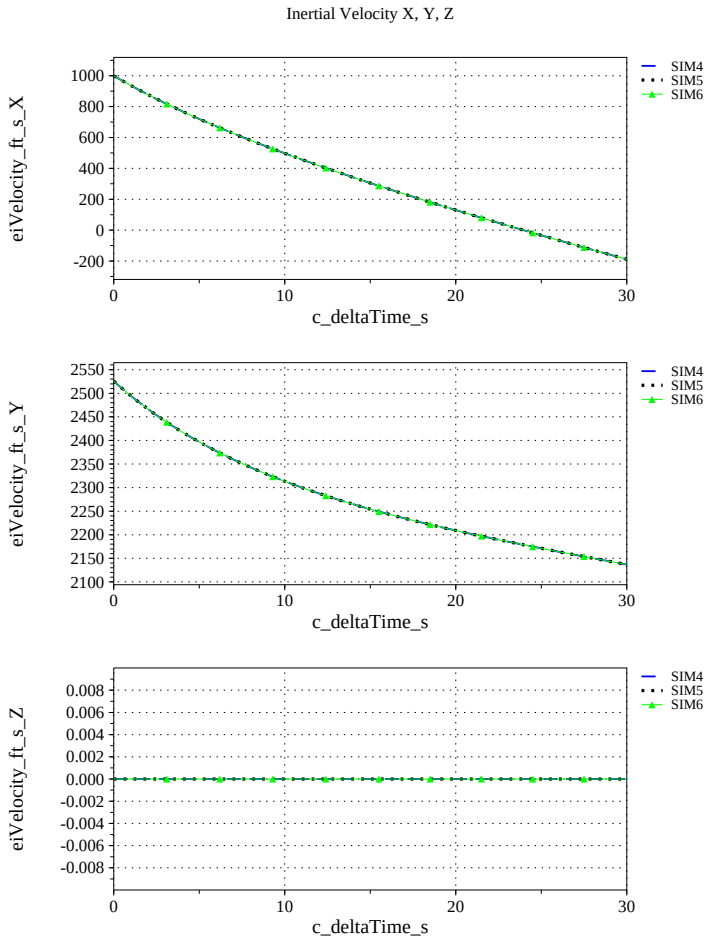

(o) Inertial Velocities Compared

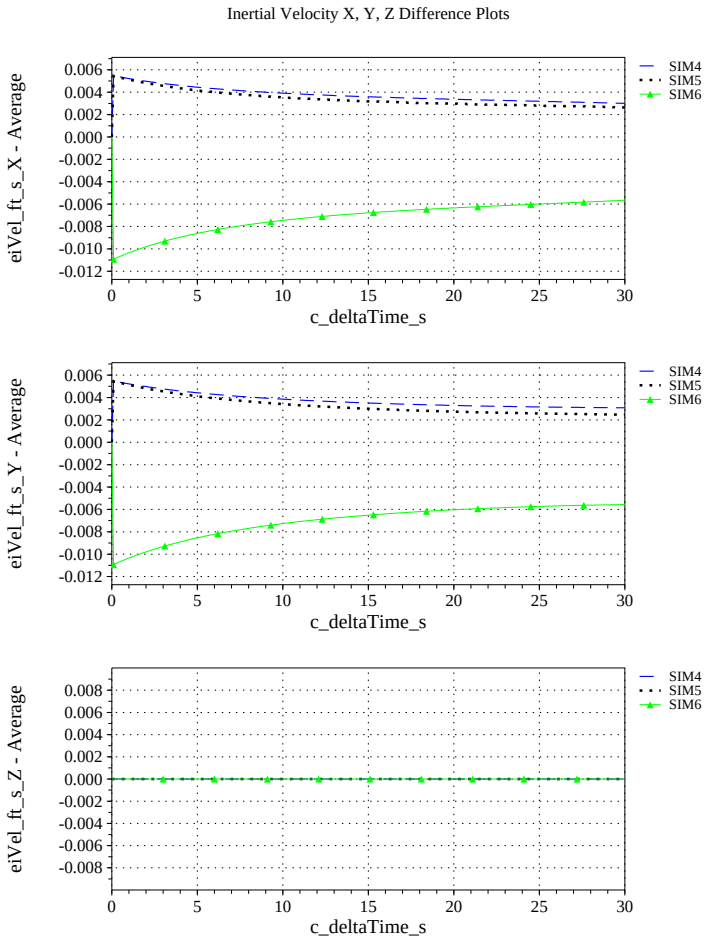

(p) Inertial Velocities Differenced

Figure 24. Check-case 9: Eastward Ballistic Flight of a Sphere; See Discussion in Section D.1.9 (Cont'd)

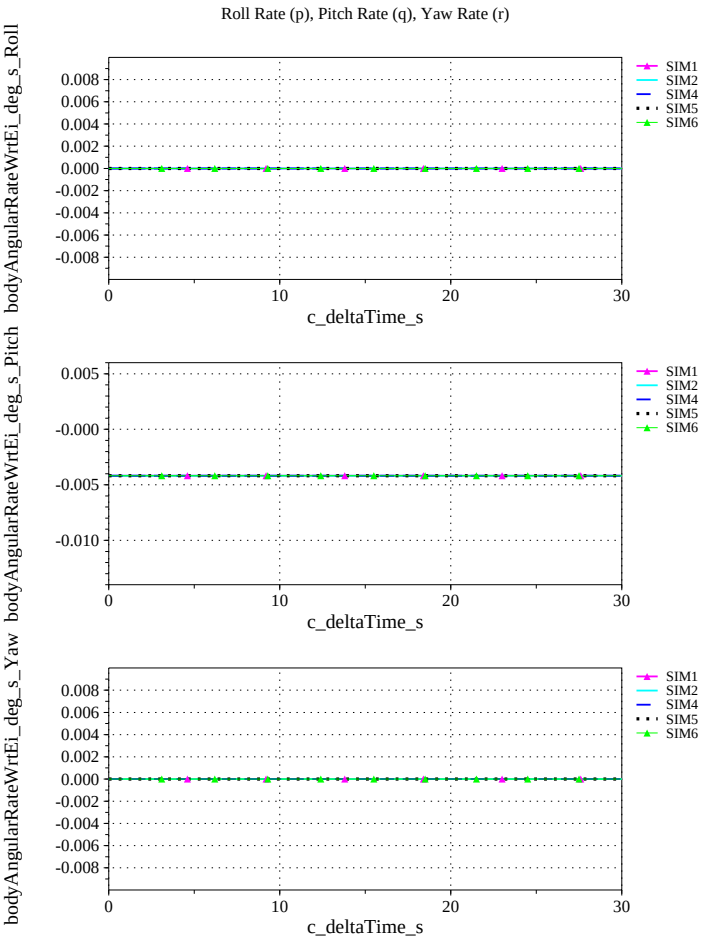

(q) Body-axis Angular Rates (w.r.t. NED Frame) Compared

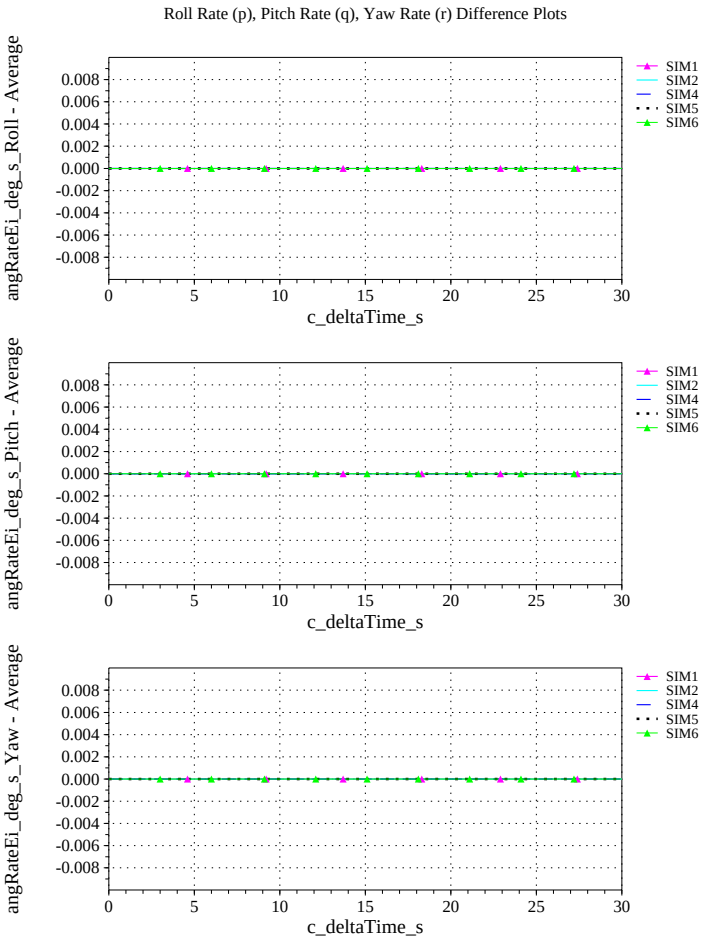

(r) Body-axis Angular Rates (w.r.t. NED Frame) Differenced

Figure 24. Check-case 9: Eastward Ballistic Flight of a Sphere; See Discussion in Section D.1.9 (Cont'd)

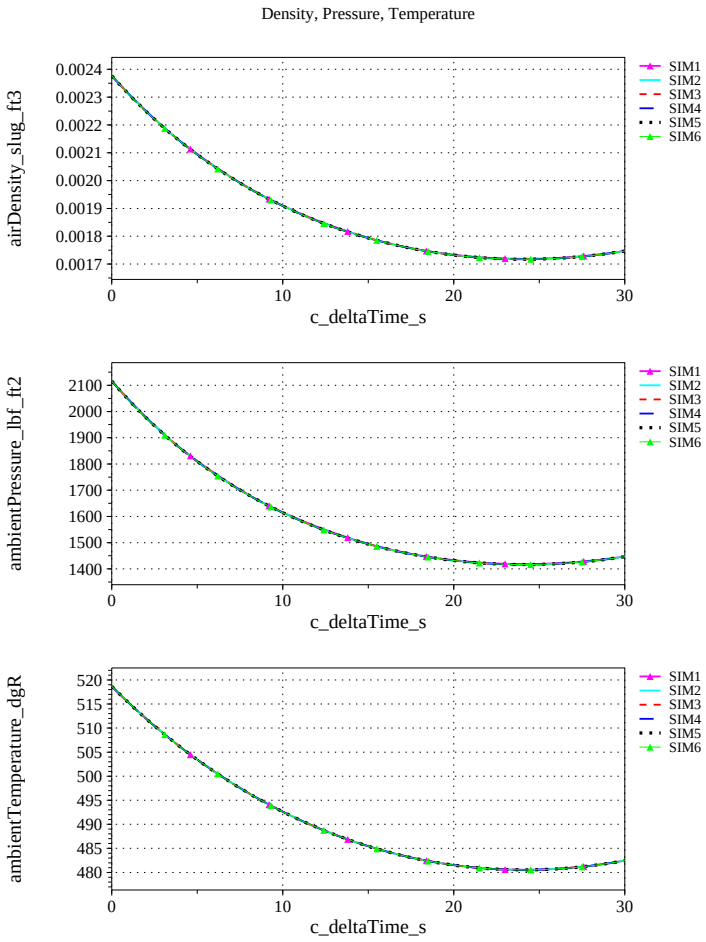

(s) Atmospheric Properties Compared

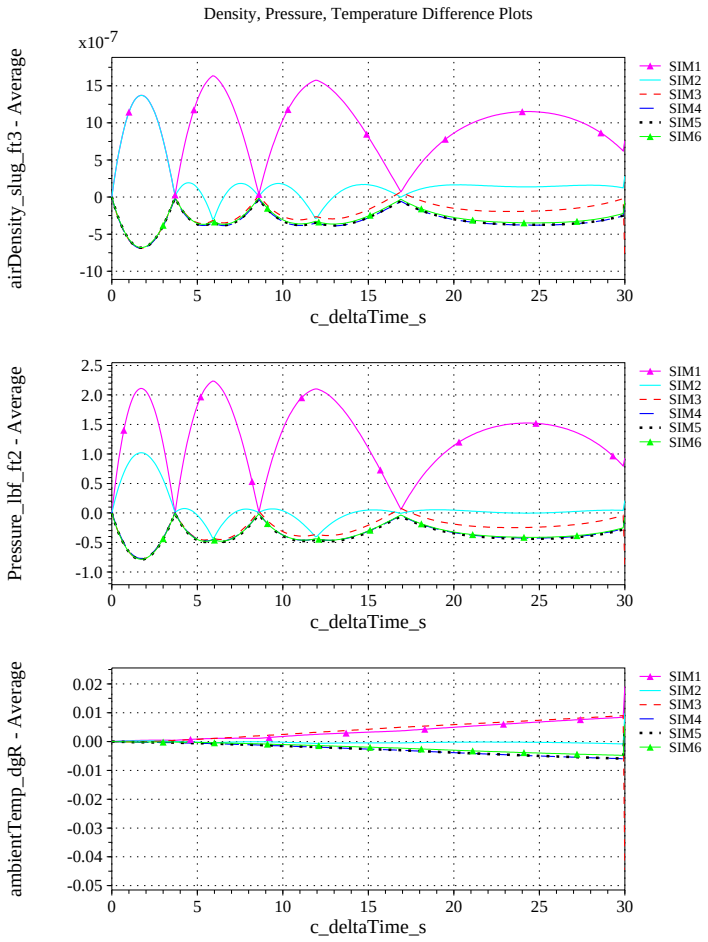

(t) Atmospheric Properties Differenced

Figure 24. Check-case 9: Eastward Ballistic Flight of a Sphere; See Discussion in Section D.1.9 (Cont'd)

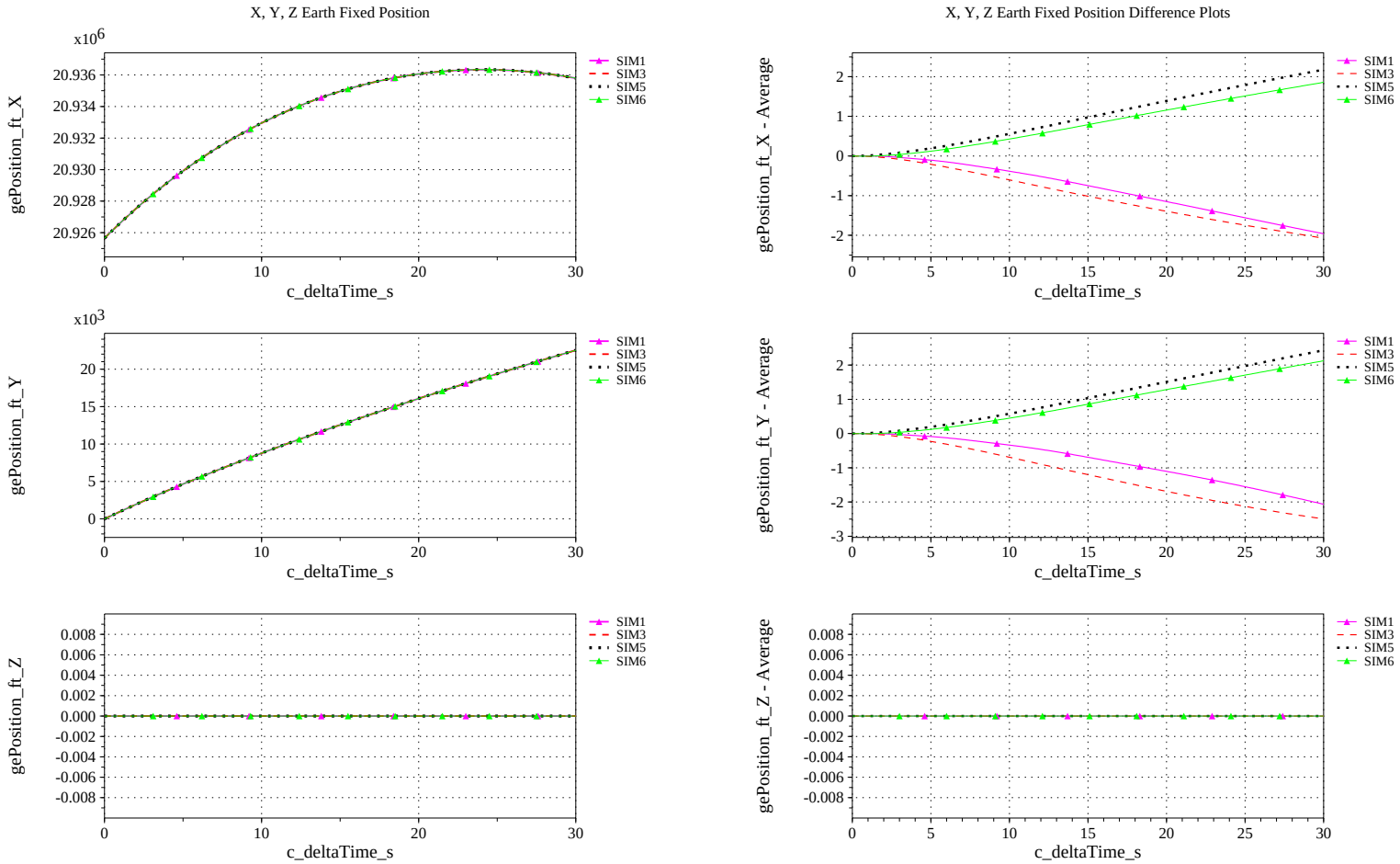

(u) Earth-centered, Earth-fixed Rectangular (X-Y-Z) Positions Compared (v) Earth-centered, Earth-fixed Rectangular (X-Y-Z) Positions Differenced

Figure 24. Check-case 9: Eastward Ballistic Flight of a Sphere; See Discussion in Section D.1.9 (Cont'd)

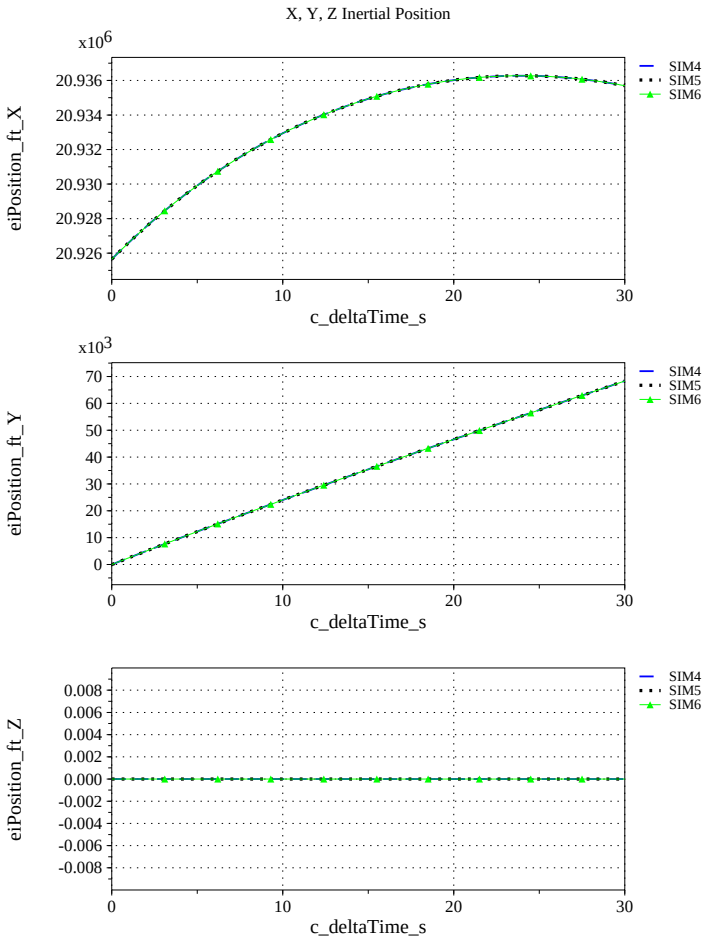

(w) Earth-centered Inertial Rectangular (x-y-z) Positions Compared

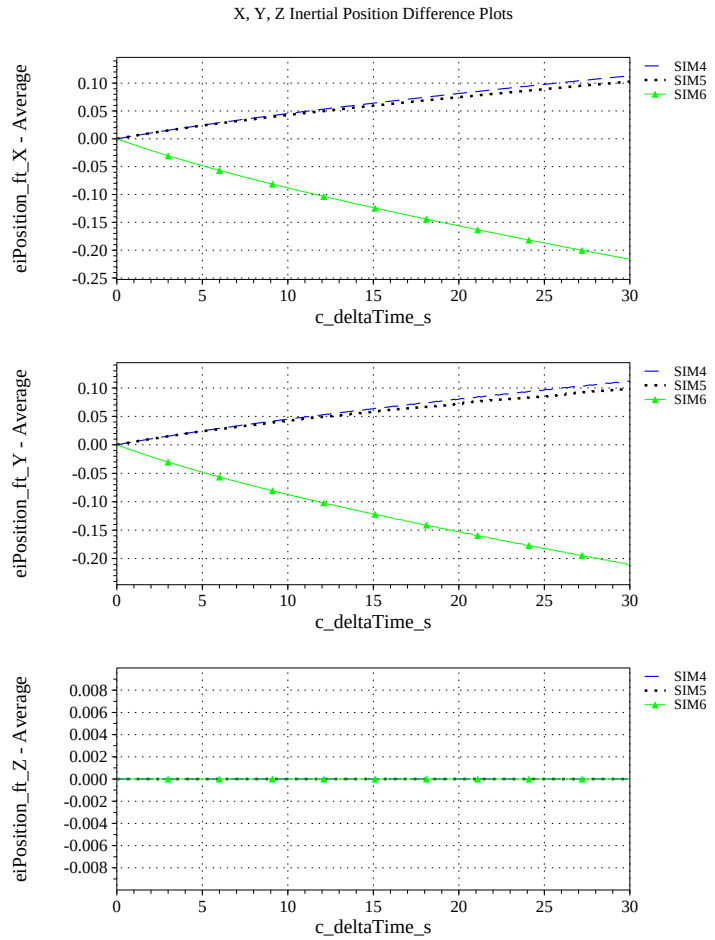

(x) Earth-centered Inertial Rectangular (x-y-z) Positions Differenced

Figure 24. Check-case 9: Eastward Ballistic Flight of a Sphere; See Discussion in Section D.1.9 (Concluded)

D.1.10 Check-case 10 – northward ballistic flight of a sphere

This section shows cross-plots for six of the selected simulation tools in modeling the dynamics of a sphere launched northward along the Equator of an ellipsoidal rotating Earth with J_2 gravitational harmonics. This scenario is described in Section C.1.10. Figures 25a through 25x compare results between the six simulation tools, as well as the deviances of the outputs from each tool from the ensemble average value.

This check-case scenario launched a sphere on a ballistic trajectory northward from the Equator. Due to Coriolis effects, the trajectory should have deflected slightly to the west. The sphere was initially oriented with its x-axis to the north and its z-axis pointing down; moreover, the sphere had an initial rotation rate, relative to the Earth, of zero. As a consequence, the pitch angle should have followed the change in latitude and the roll angle should have followed the change in longitude. All the simulations agreed on the angular rate. Consequently, differences in latitude and longitude should be the primary contributors to differences in pitch and roll angle. All simulations were in agreement for both longitude and roll angle. However, the differences in pitch angle (Figure 25h) did not match differences in latitude. In fact, the differences for pitch angle were larger than those for latitude and they divided the simulations into two camps. SIM 4 and SIM 5 agreed on one value. SIM 1, 2, and 6 agreed on another value that differed by up to 4.2×10^{-4} degrees at $t = 30$ sec.

Membership in two groupings were not coincidental. The difference in pitch angle between the two simulation groups was identical to the difference between geodetic and geocentric latitude. In other words, the pitch angles for SIM 4 and SIM 5 were relative to a NED frame where the downward axis was aligned with the geodetic normal, whereas the pitch angle for SIM 1, 2, and 6 is relative to a NED frame where the downward axis is aligned with the geocentric radial.

This difference in alignment of the NED frame, however, should have produced velocity differences in that frame an order of magnitude lower than the actual differences shown between simulations. The alignment differences should contribute to a difference of $+0.001$ ft/s in northward velocity and -0.004 ft/s in downward velocity at $t = 30$ sec. Instead, the differences in translational motion are nearly identical to those presented in "Check-case 9 – eastward ballistic flight of a sphere" if one where to swap the north and east variables. One exception is the SIM 2 difference in latitude, which will be discussed later. Otherwise, the same contributors summarized in results for atmospheric check-case 7 (Section D.1.7) were present in this check-case.

SIM 2 exhibited a difference in latitude relative to SIM 4/5, which was dissimilar to the difference in longitude exhibited between these simulations in the previous check-case (Check-case 9 – eastward ballistic flight of a sphere). Furthermore, this difference of -2.4×10^{-4} degrees was equivalent to a distance of almost -90 ft. The SIM 2 difference in latitude did not correlate with the difference in northward velocity which predicted a difference in distance of -1.7 ft. Furthermore, this difference of -1.7 ft could be reproduced by comparing geocentric latitude between SIM 2 and SIM 5. The SIM 2 data file recorded both geodetic and geocentric latitude. Geocentric latitude for SIM 5 was derived from its ECEF position. At $t = 30$ sec, geocentric latitude between the two simulations differed by -4.6×10^{-6} degrees which was equivalent to a distance of -1.7 ft at altitude. Therefore, the difference in geodetic latitude between SIM 2 and the other simulations was not a reflection of a difference in the predicted position of the vehicle. Instead, it appeared to be a difference in the accuracy of the method used to compute the geodetic coordinates.

In this check-case, the Coriolis effect introduces a drift westward which did not have a parallel in the previous check-case (i.e., there was no drift northward). As stated previously, the simulations appeared to agree on longitude. Moreover, the differences in eastward velocity and ECEF Y-axis position were not significant and were likely due to differences in integration methods.

All other differences between the simulations are derived from the contributors discussed previously.

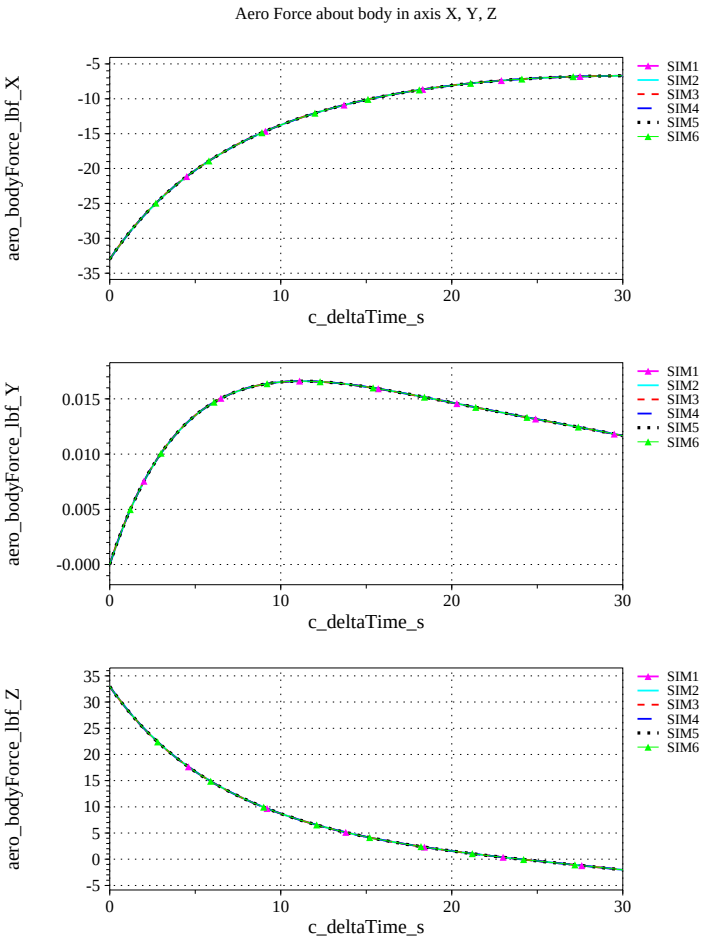

(a) Aerodynamic Forces Compared

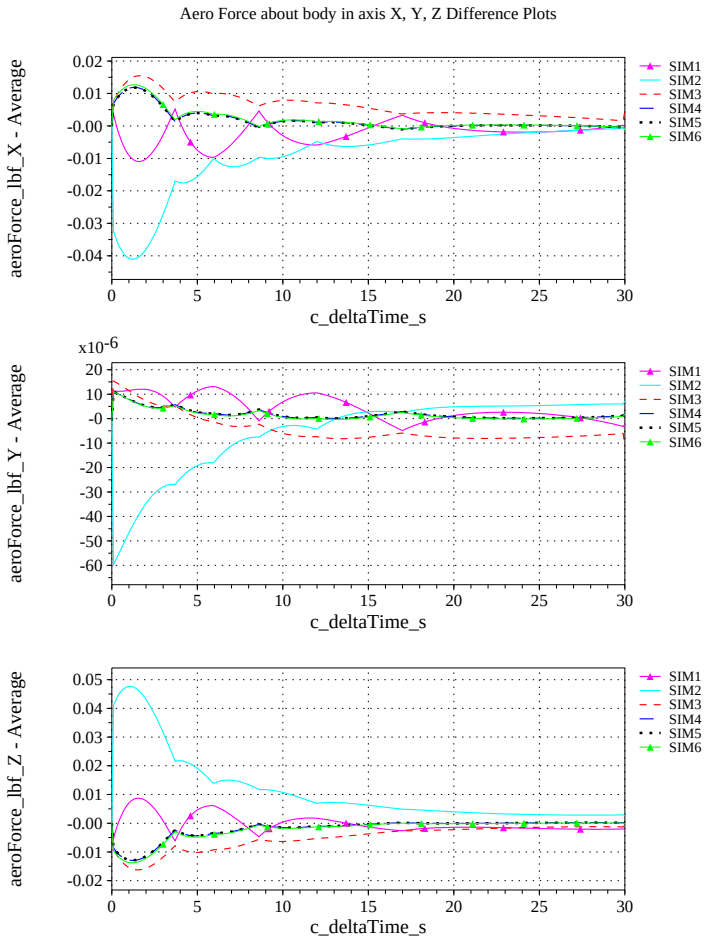

(b) Aerodynamic Forces Differenced

Figure 25. Check-case 10: Northward Ballistic Flight of a Sphere; See Discussion in Section D.1.10

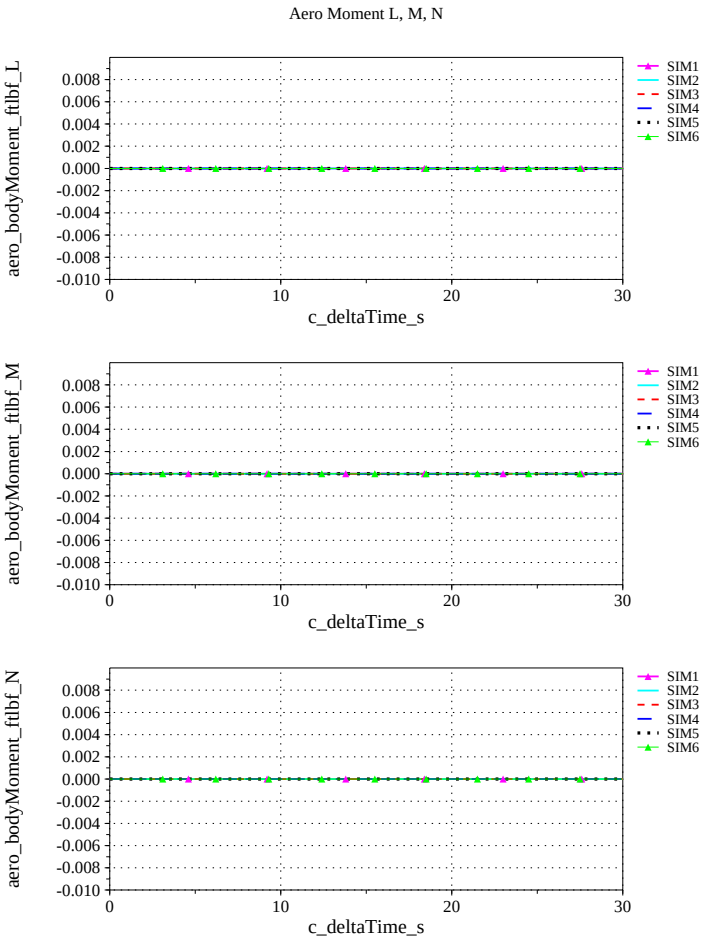

(c) Aerodynamic Moments Compared

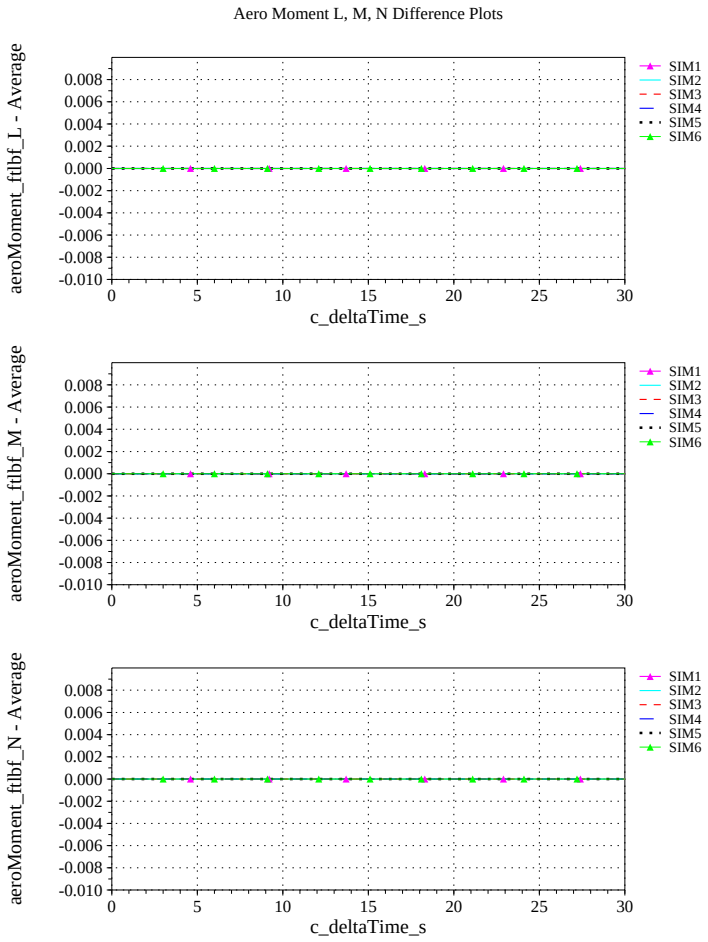

(d) Aerodynamic Moments Differenced

Figure 25. Check-case 10: Northward Ballistic Flight of a Sphere; See Discussion in Section D.1.10 (Cont'd)

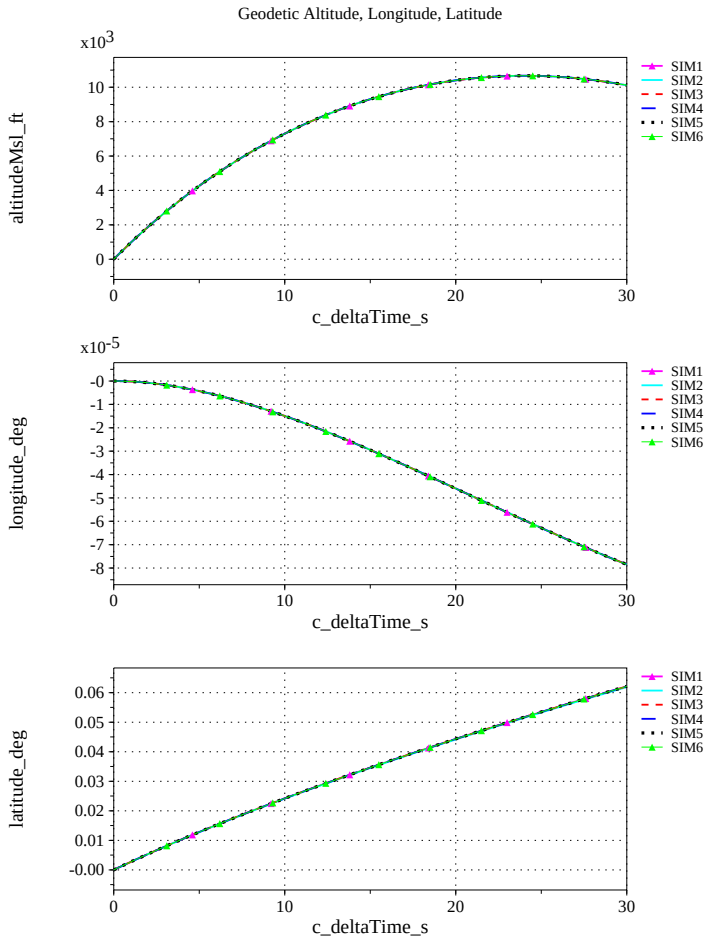

(e) Altitude, Geodetic Latitude and Longitude Compared

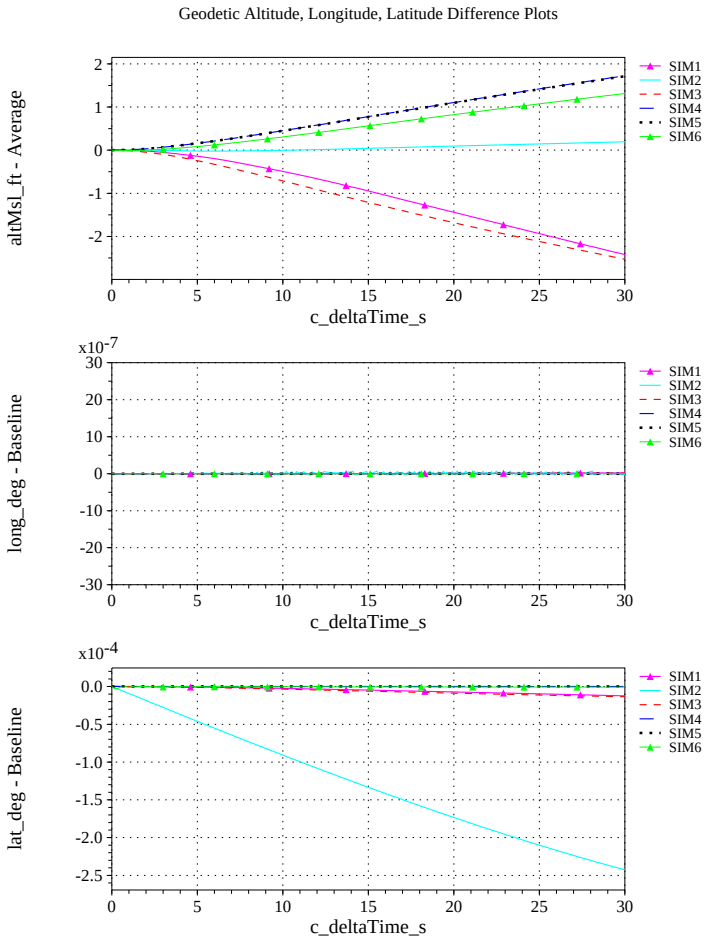

(f) Altitude, Geodetic Latitude and Longitude Differenced

Figure 25. Check-case 10: Northward Ballistic Flight of a Sphere; See Discussion in Section D.1.10 (Cont'd)

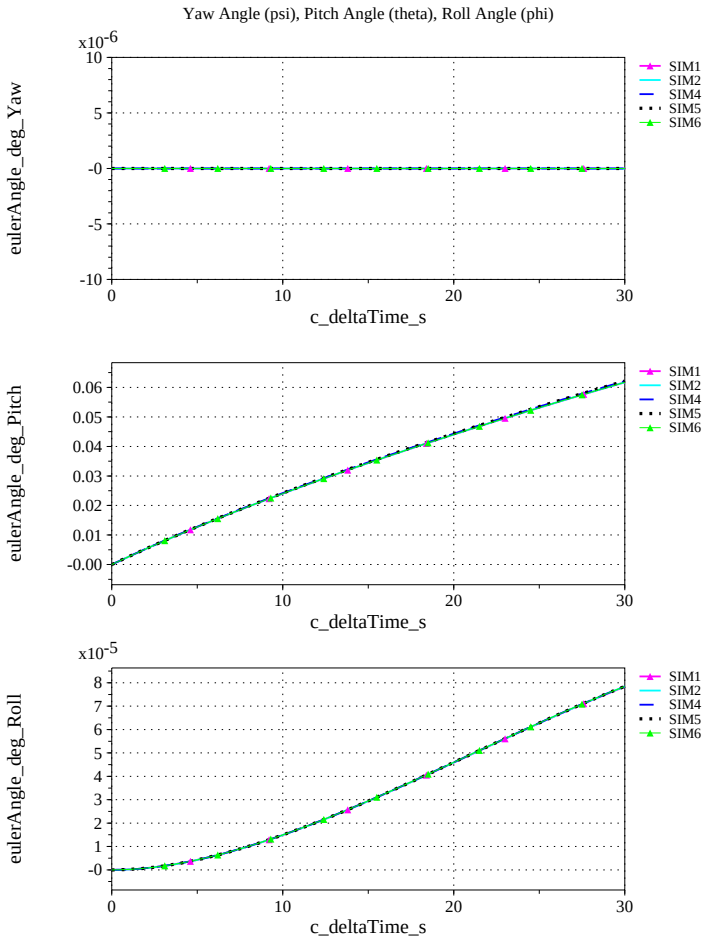

(g) Euler Angles (w.r.t. NED Frame) Compared

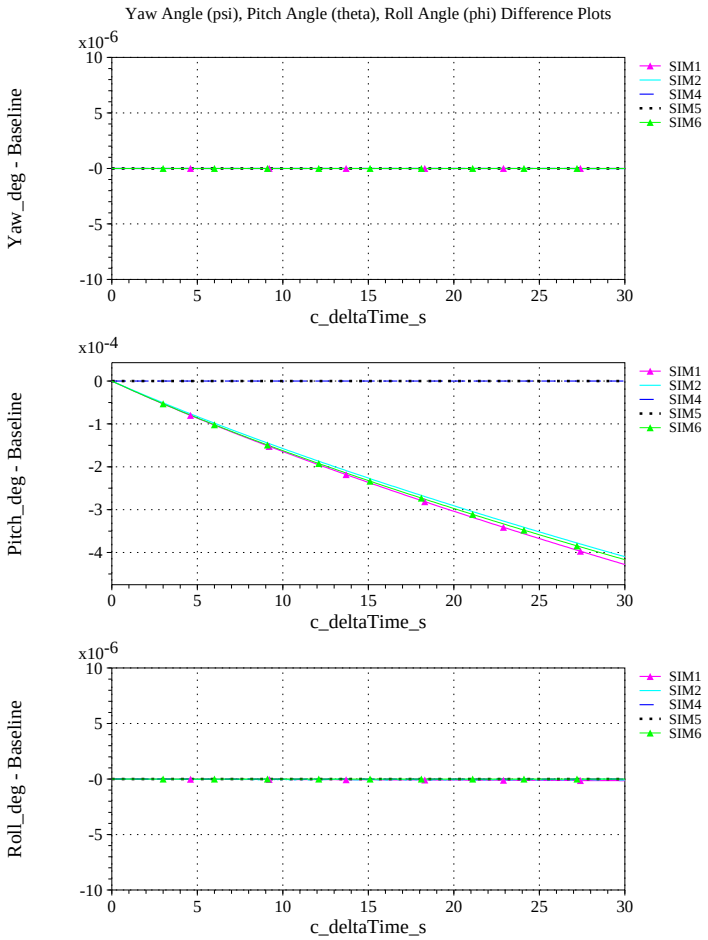

(h) Euler Angles (w.r.t. NED Frame) Differenced

Figure 25. Check-case 10: Northward Ballistic Flight of a Sphere; See Discussion in Section D.1.10 (Cont'd)

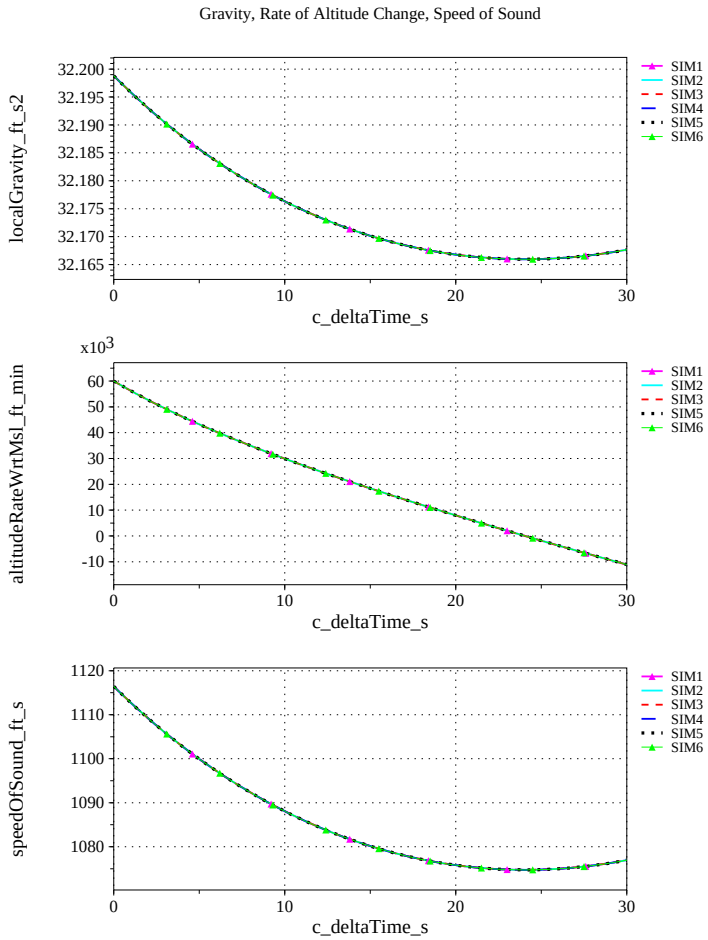

(i) Gravity, Climb Rate, and Speed-of-sound Compared

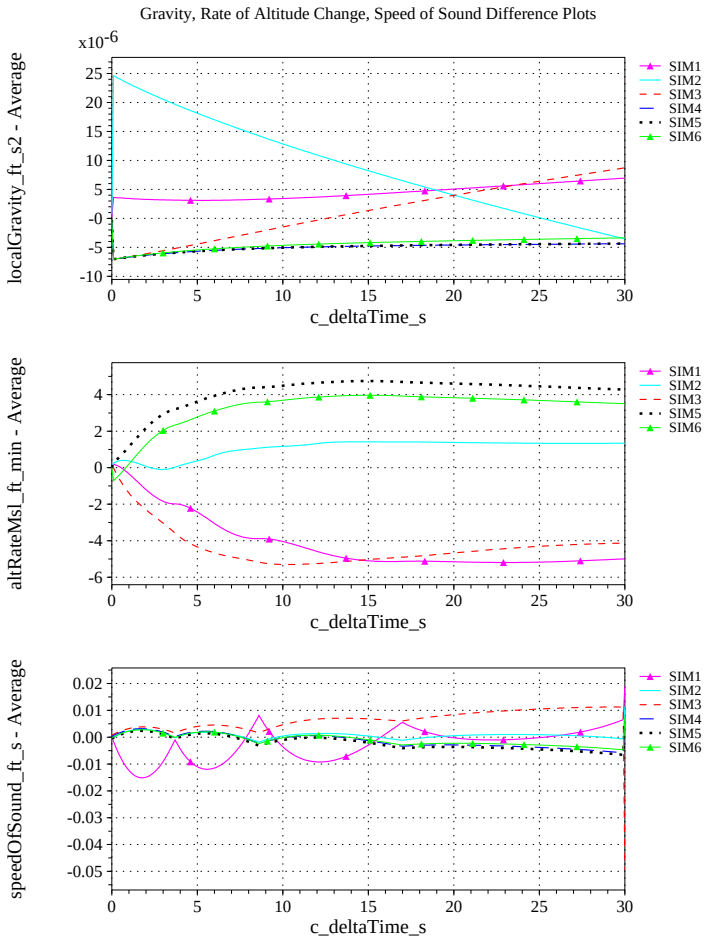

(j) Gravity, Climb Rate, and Speed-of-sound Differenced

Figure 25. Check-case 10: Northward Ballistic Flight of a Sphere; See Discussion in Section D.1.10 (Cont'd)

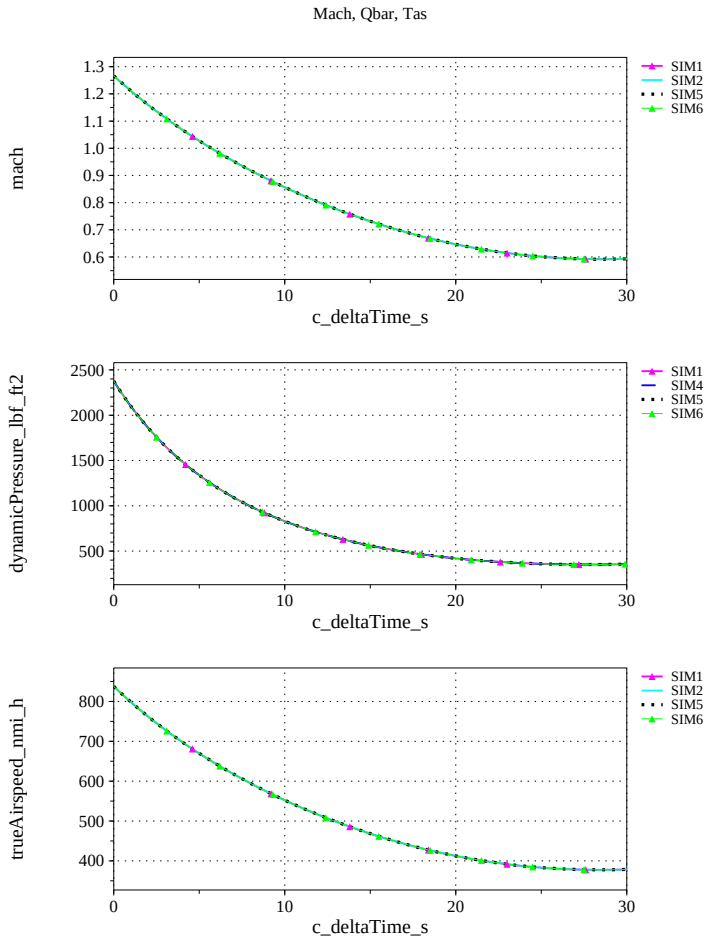

(k) Mach, Dynamic Pressure, and True Airspeed Compared

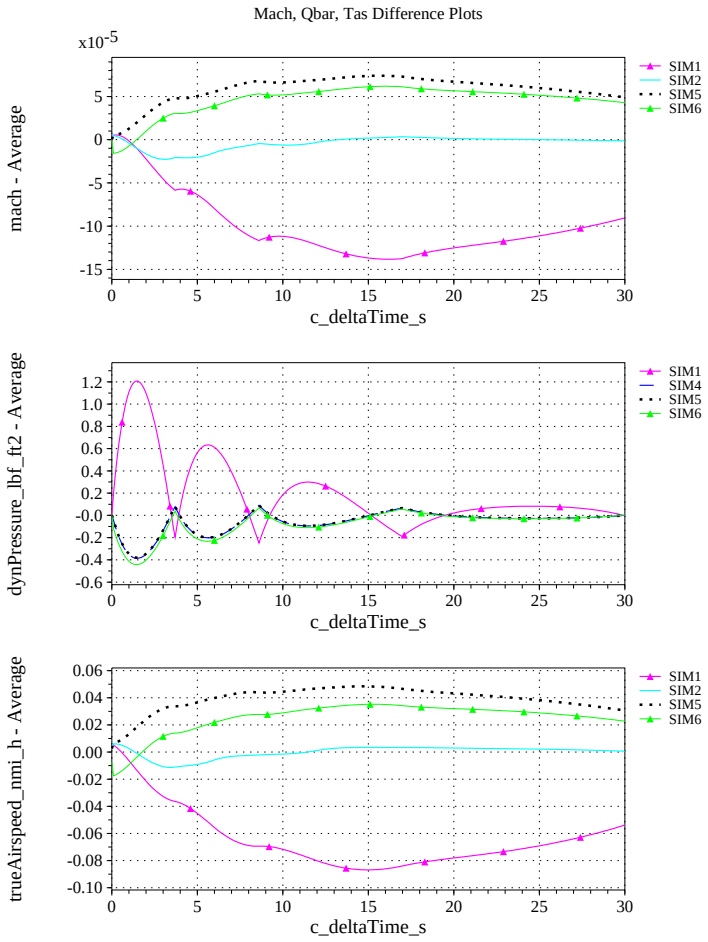

(l) Mach, Dynamic Pressure, and True Airspeed Differenced

Figure 25. Check-case 10: Northward Ballistic Flight of a Sphere; See Discussion in Section D.1.10 (Cont'd)

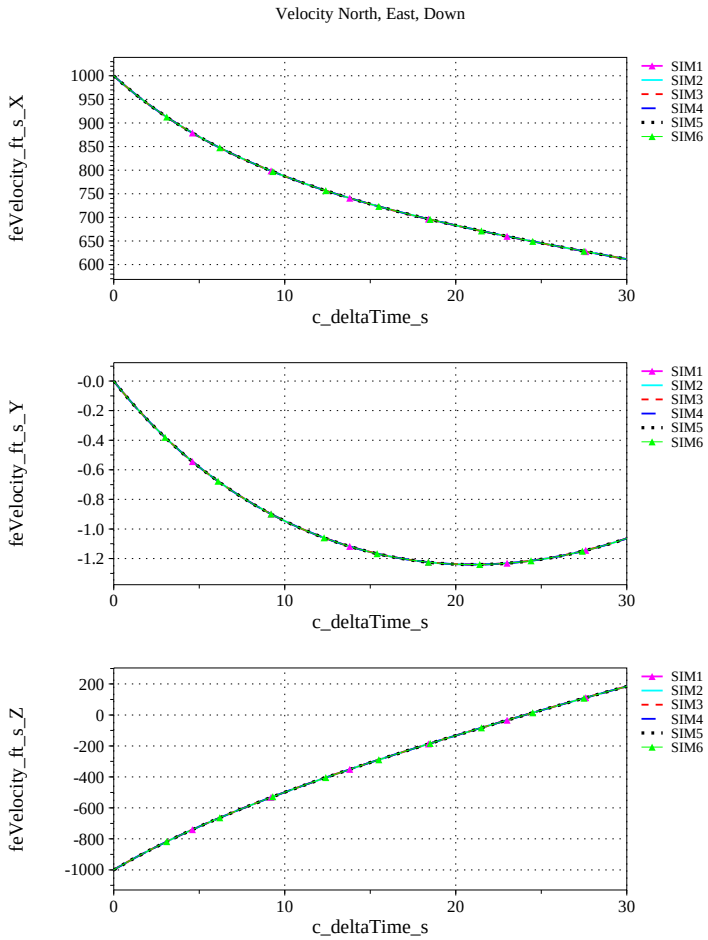

(m) NED Velocities Compared

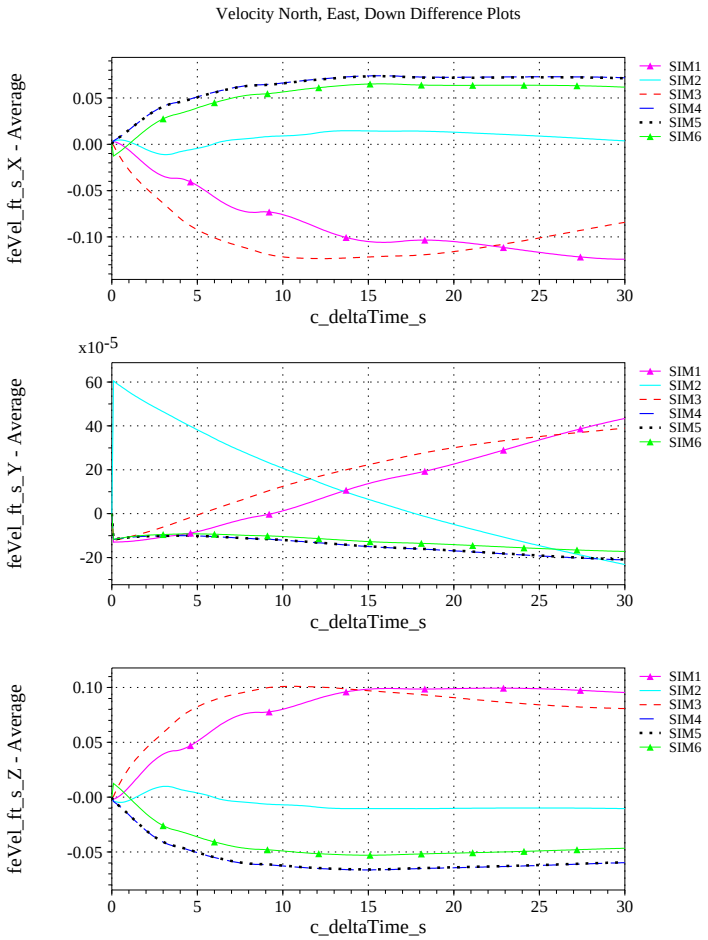

(n) NED Velocities Differenced

Figure 25. Check-case 10: Northward Ballistic Flight of a Sphere; See Discussion in Section D.1.10 (Cont'd)

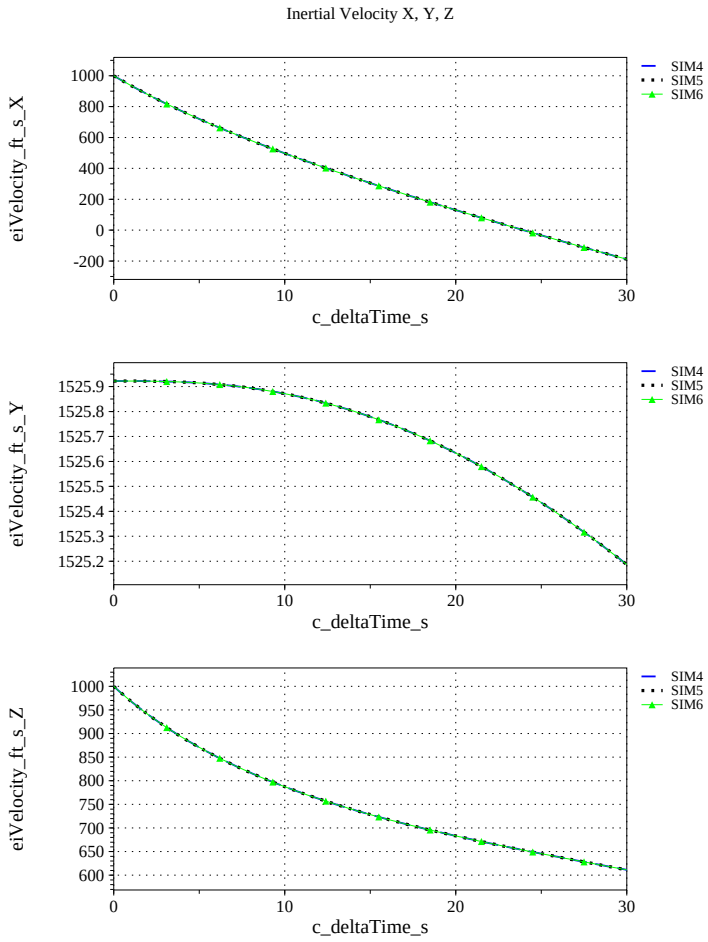

(o) Inertial Velocities Compared

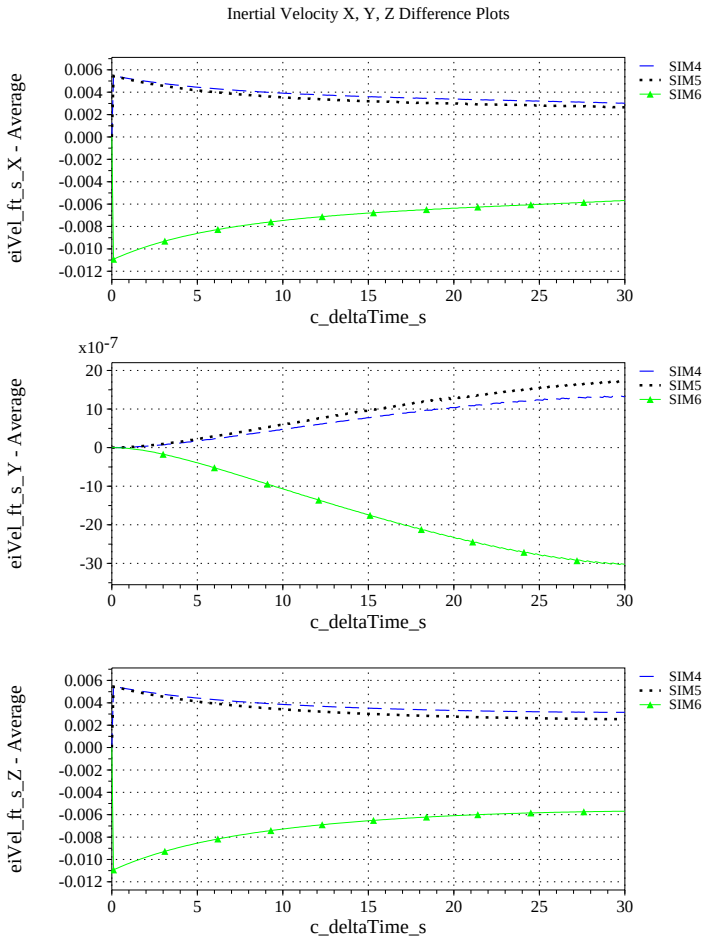

(p) Inertial Velocities Differenced

Figure 25. Check-case 10: Northward Ballistic Flight of a Sphere; See Discussion in Section D.1.10 (Cont'd)

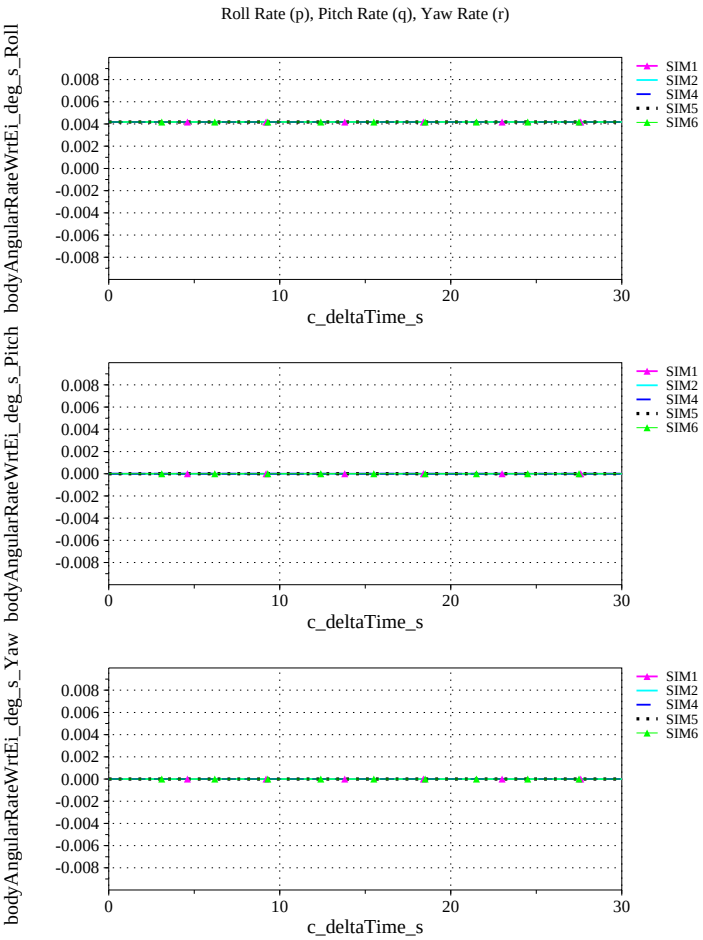

(q) Body-axis Angular Rates (w.r.t. NED Frame) Compared

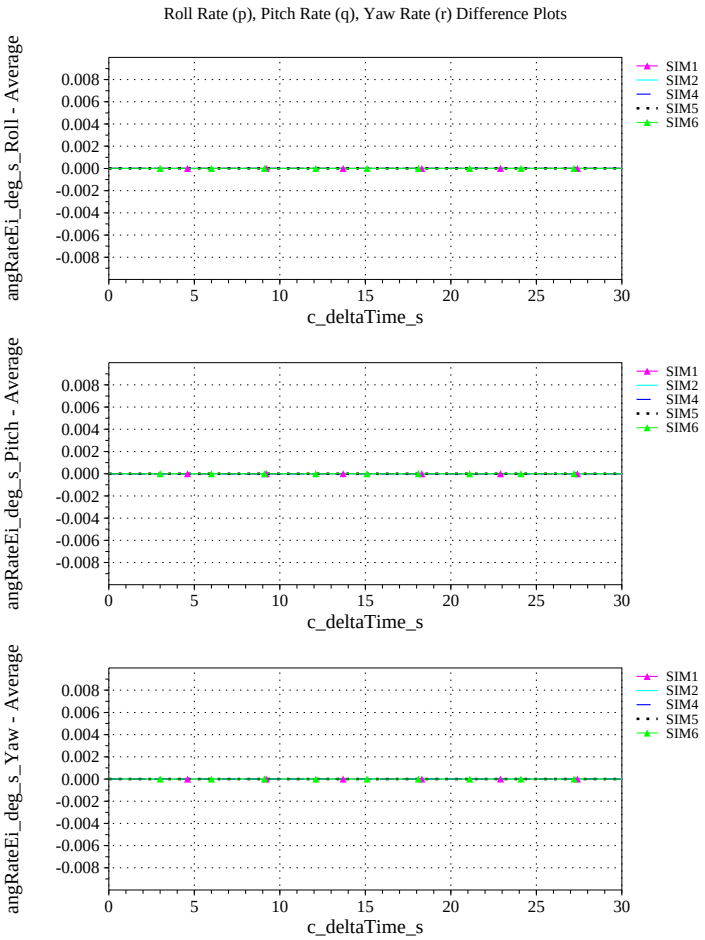

(r) Body-axis Angular Rates (w.r.t. NED Frame) Differenced

Figure 25. Check-case 10: Northward Ballistic Flight of a Sphere; See Discussion in Section D.1.10 (Cont'd)

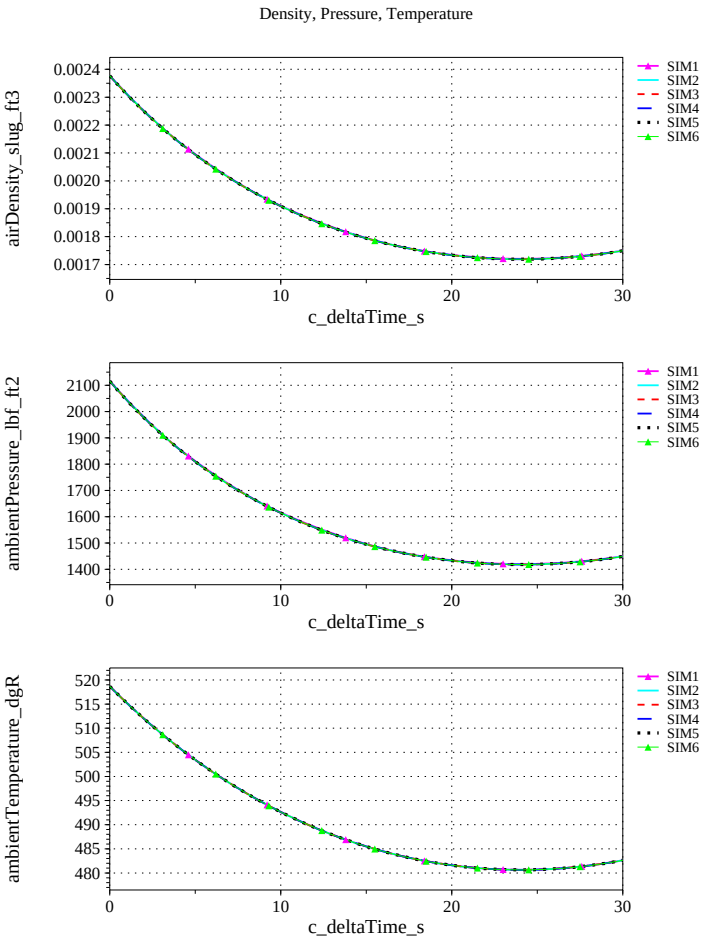

(s) Atmospheric Properties Compared

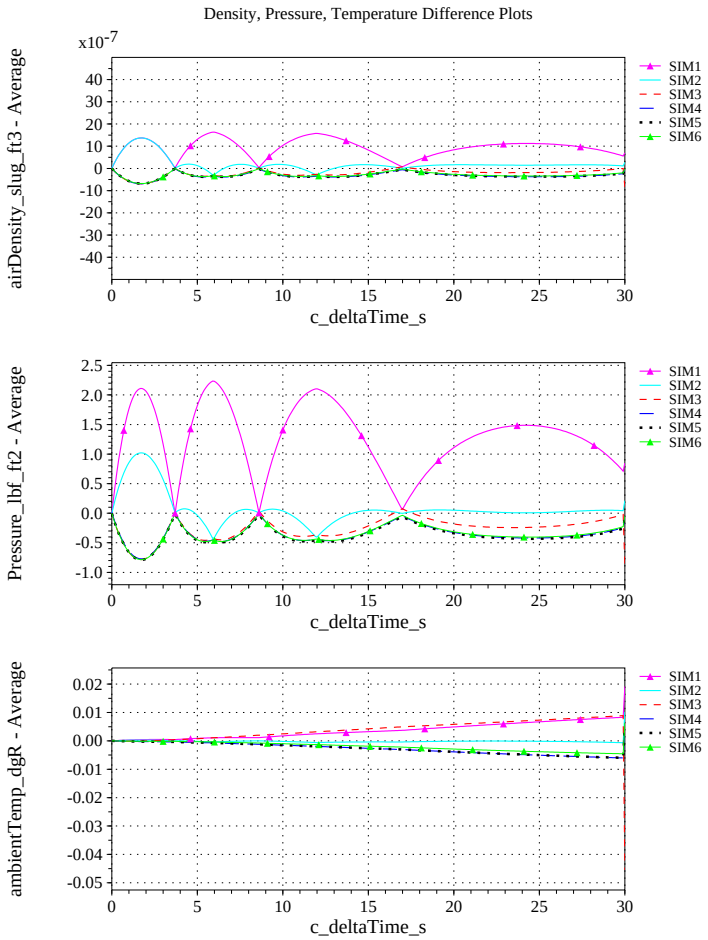

(t) Atmospheric Properties Differenced

Figure 25. Check-case 10: Northward Ballistic Flight of a Sphere; See Discussion in Section D.1.10 (Cont'd)

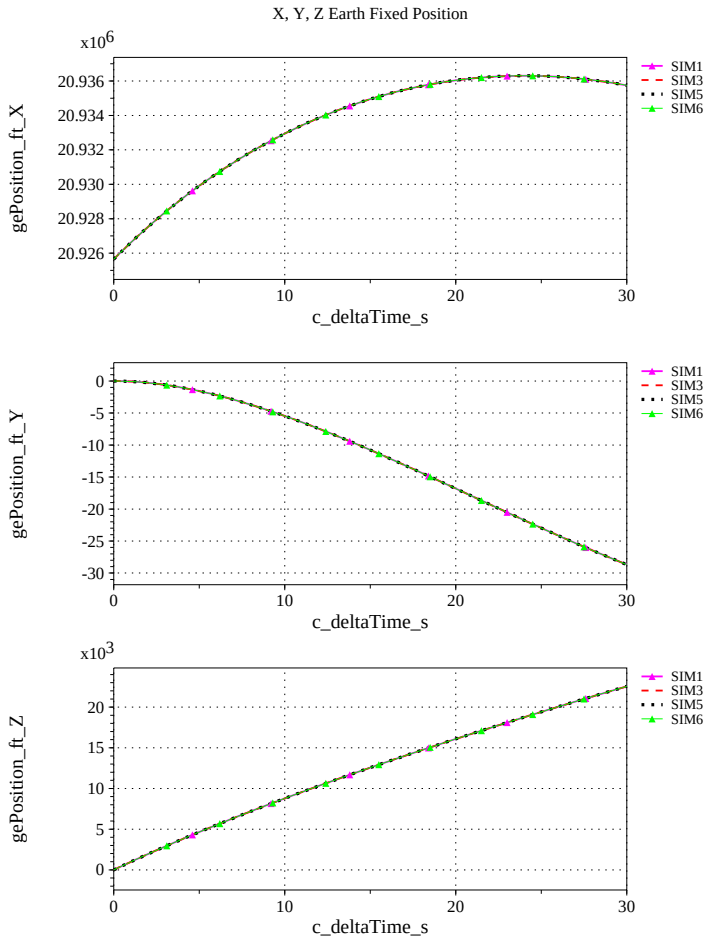

(u) Earth-centered, Earth-fixed Rectangular (X-Y-Z) Positions Compared

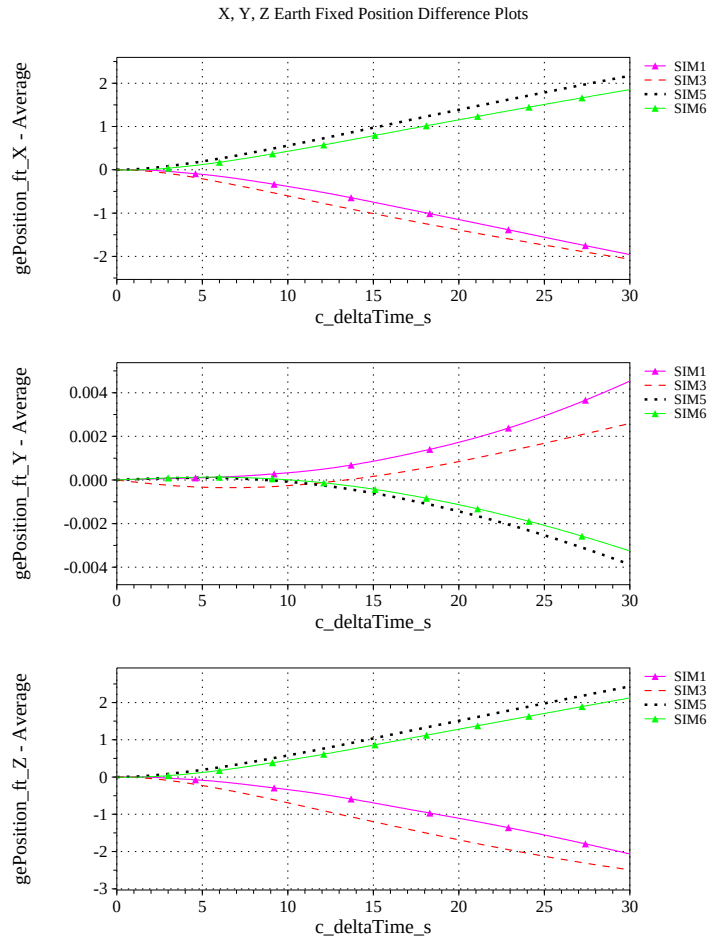

(v) Earth-centered, Earth-fixed Rectangular (X-Y-Z) Positions Differenced

Figure 25. Check-case 10: Northward Ballistic Flight of a Sphere; See Discussion in Section D.1.10 (Cont'd)

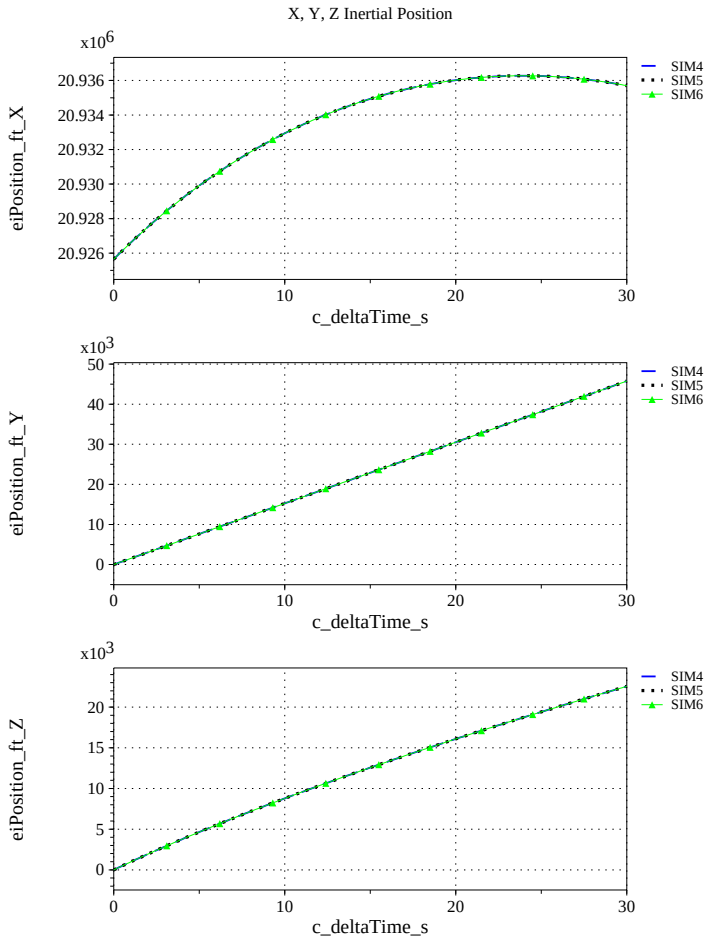

(w) Earth-centered Inertial Rectangular (x-y-z) Positions Compared

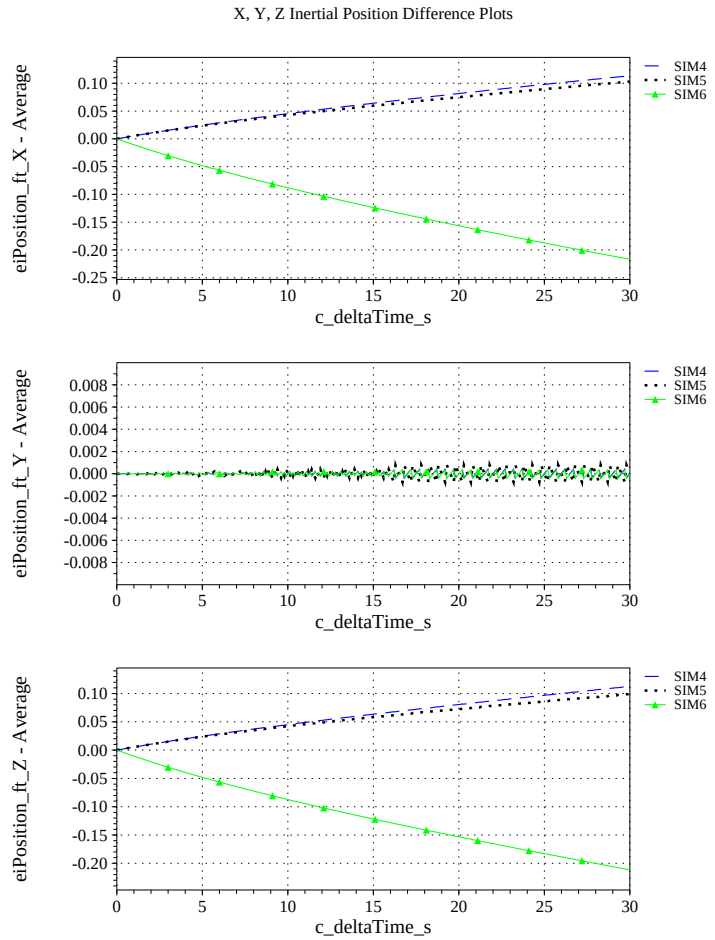

(x) Earth-centered Inertial Rectangular (x-y-z) Positions Differenced

Figure 25. Check-case 10: Northward Ballistic Flight of a Sphere; See Discussion in Section D.1.10 (Concluded)

D.1.11 Check-case 11 – steady flight of a subsonic aircraft

This section shows cross-plots for two of the selected simulation tools in modeling the dynamics of an aircraft in steady trimmed subsonic flight on an arbitrary heading. This scenario is described in Section C.1.11. Figures 26a through 26x compare results between the two simulation tools, as well as the deviances of the outputs from each tool from the ensemble average value.

This check-case was the first of a series utilizing the F-16 model. Unlike the first ten atmospheric scenarios, the F-16 scenarios required that the simulation tool generate an equilibrium ("trim") solution for the F-16 vehicle model so that its initial state, including control surface deflections and engine thrust, resulted in straight and level flight. This equilibrium solution requirement can introduce differences among the simulation implementations since different simulation tools may have different definitions for straight and level flight, especially over the curved surface of a round or ellipsoidal Earth reference. Simulation tools may also generate solutions with different tolerances for residual acceleration.

Such differences can be seen in the three simulations that provided data for this check-case (see, for example, Figure 26b). All three simulations used slightly different assumptions about the angular rate necessary for straight and level flight. SIM 2 constrained the angular rate to be zero in the inertial frame. SIM 4 solved for the pitch rate that maintained the pitch angle as the vehicle flew over the curved surface of the Earth. SIM 5 solved for the three-axis angular rate that maintained the vehicle orientation (i.e., all three Euler angles) relative to the local vertical frame as the vehicle flies over the curved surface of the Earth. Even so, the equilibrium roll and yaw rate computed by SIM 5 were very small, 3×10^{-5} and 8×10^{-4} deg/s respectively. Therefore, the equilibrium solutions for SIM 4 and SIM 5 were nearly identical. Nevertheless, each simulation exhibited an oscillation in angular rates during the first second of the simulation. Differences during the oscillation dwarfed the initial attitude differences. Once the oscillation settled, however, SIM 4 and SIM 5 were in near agreement on angular rate while the trajectory calculated by SIM 2 continued to differ from SIM 4/5.

The initial roll and pitch angle in SIM 2 also differed from SIM 4/5 (Figure 26g). The root cause was a difference in the simulated gravity vector. SIM 2 employed a simplification that creates a gravity vector that is slightly deflected from the surface normal. (As discussed in Section B.4, the terms gravitation and gravity have different meanings: gravitation is the force from the attraction of two masses; gravity is the sum of gravitation and the centrifugal acceleration due to the Earth's rotation. Gravity is the acceleration of a body in free fall measured by an observer stationed on the surface of the Earth.) All three simulations computed the geocentric gradient of the J_2 gravitation potential, which produced gravitation in the geocentric down direction and a much smaller contribution in the geocentric north direction. However, as first identified in atmospheric check-case 9 (Section D.1.9), SIM 2 approximated the geodetic NED frame as the geocentric frame to use the geocentric frame as the local vertical reference frame when computing gravity. SIM 4 and SIM 5 translated the geocentric gravitation vector into a geodetic gravitation vector. This rotation was necessary to produce a gravitation vector where the resulting small geodetic north-axis component of gravitation was canceled by the geodetic north-axis contribution of centrifugal acceleration due to the Earth's rotation. This resulted in a gravity vector whose direction matched the geodetic down-axis direction almost exactly. Without the rotational contribution, the gravitation and centrifugal acceleration combined to create a gravity vector slightly deflected from the geocentric downward direction. That deflection was equal to the difference between the geodetic and geocentric latitude since the true direction of the gravity vector is along the geodetic normal.

In the initial position specified by this check-case, the resulting gravity vector, in geocentric coordinates, is deflected 0.18 degrees southward of the radial vector. That deflection amount was approximately equal to the difference in roll angle between SIM 2 and SIM 4/5.

The equilibrium solver for SIM 2 appeared to roll the vehicle slightly so that its aerodynamic lift was more closely aligned with the slightly non-vertical gravity vector. The SIM 2 equilibrium solver also produced a slightly different pitch angle because the aerodynamic lift required for the trim solution differed slightly from those of SIM 4/5. With a non-zero roll angle, eliminating vertical acceleration in SIM 2 required balancing contributions from weight, thrust, lift, drag, and aerodynamic side force. When the roll angle was zero, as in SIM 4 and 5, no significant aerodynamic side force was generated.

Even if SIM 2 were modified to use a geodetic gravity vector, the difference plot for gravitation (Figure 26i) shows that there would remain a small difference in gravitation of 1.8×10^{-4} ft/s^2. There should be no difference in Earth parameters among the simulations given the match in J_2 gravitation for atmospheric case 1 (see Section D.1.1). What remains as a possible explanation of this difference in gravitation could be a difference in the conversion from the initial geodetic coordinates to an initial geocentric position. The difference could be significant. For example, a difference of -58 ft in the distance of the vehicle from Earth's center would produce the same change in magnitude. Nevertheless, the difference in magnitude should be a minor contributor to the vehicle dynamics as it adds only 0.11 lbf to the weight of the 20,500 lb F-16 example vehicle.

Differences in initial angular rates would induce differences in the aerodynamic forces and moments. However, those differences were very small and were dwarfed by other contributors including the contribution from the angular rate oscillation in the first second of the simulation.

A substantial difference in the plotted aerodynamic moments (26c) is the result of a difference in the reference location for recording aerodynamic moments. When recording the aerodynamic moments, SIM 2 recorded moments about the aerodynamic MRC; SIM 4 and 5 recorded the aerodynamic moment at the vehicle CM after these had been transferred from the MRC. This difference appears in the aerodynamic moment plots for all the F-16 cases hereafter; it just reflects a lack of agreement on which moment vector to record.

Even when the moments were adjusted for differences in the reference point, a difference in the initial aerodynamic yaw and pitching moments remained between SIM 2 and SIM 4/5 at the MRC; furthermore, SIM 2 also differed in the initial aerodynamic forces (Figures 26a). These differences resulted from the difference in the gravity vector as described in the previous paragraph. With the gravity vector deflected from the local vertical in SIM 2, SIM 2 required a trade-off in pitch angle and roll angle to create the right combination of angle of attack and sideslip such that the resulting aerodynamic lift and side force counteracted the gravity vector while leaving no residual force in the horizontal plane. As discussed above, the result is a roll angle that nearly aligned the body z-axis with the deflected gravity vector. The differing lift required a different aerodynamic pitching moment to counteract the lift-induced pitching moment at the CM. The resulting aerodynamic side force also induced a yawing moment at the CM and therefore required a counteracting aerodynamic yawing moment, which was not present in SIM 4 and SIM 5. That yawing moment was achieved, in SIM 2, by setting the rudder to a non-zero initial value.

The above differences, in general, set SIM 2 on a different trajectory from SIM 4 and SIM 5. After 180 sec, the difference in vehicle positions between SIM 2 and SIM 4/5 was approximately 666 ft according to the recorded values of latitude, longitude, and altitude. The position difference between SIM 4 and 5 at the end of the scenario was two orders of magnitude smaller, at approximately 4 ft.

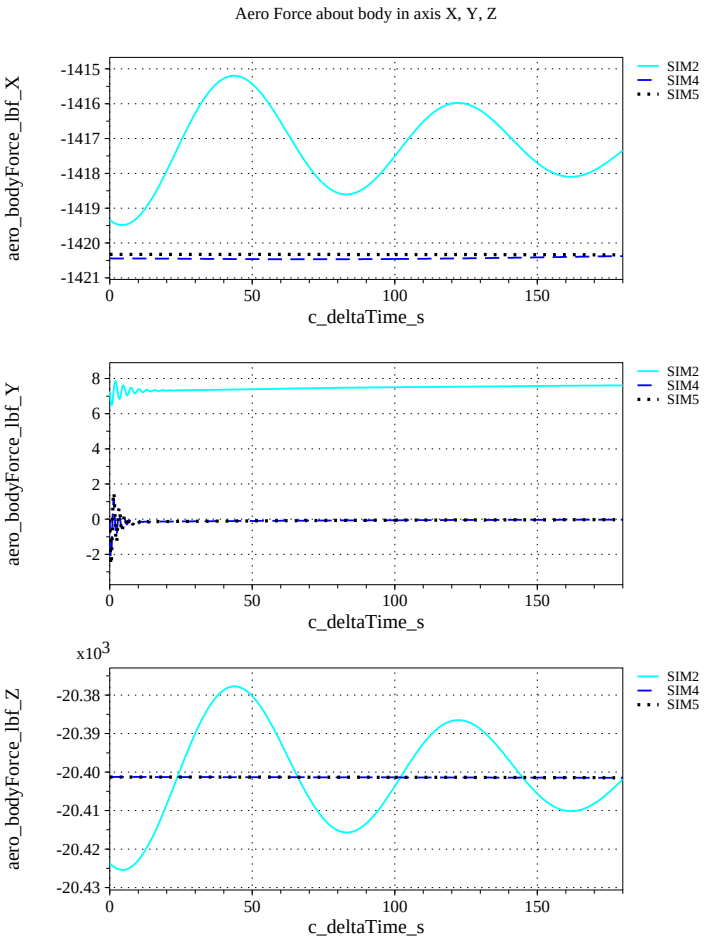

(a) Aerodynamic Forces Compared

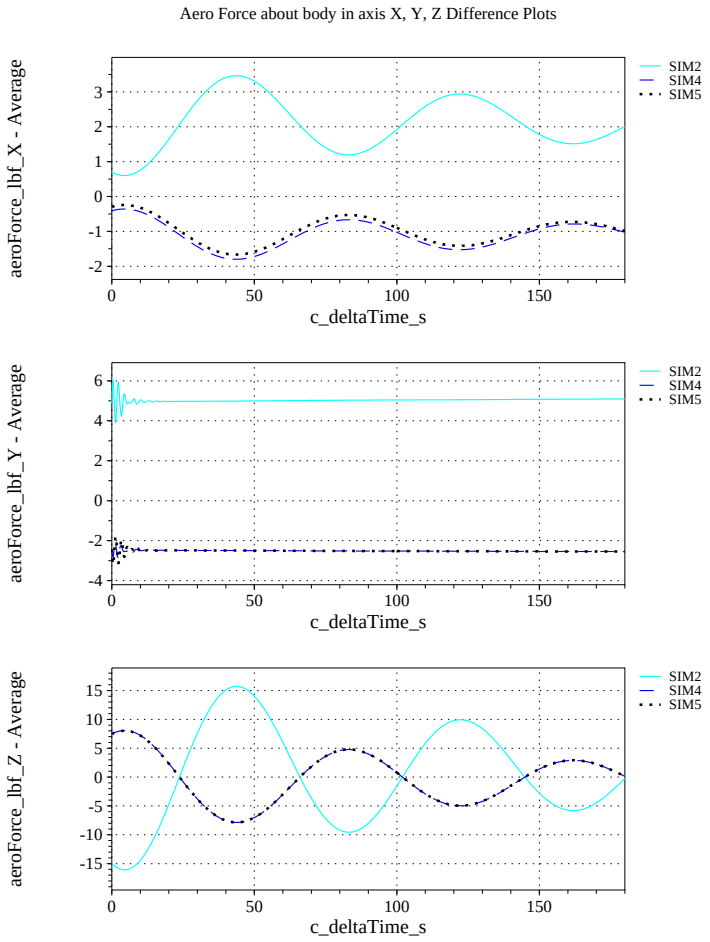

(b) Aerodynamic Forces Differenced

Figure 26. Check-case 11: Steady Flight of a Subsonic Aircraft; See Discussion in Section D.1.11

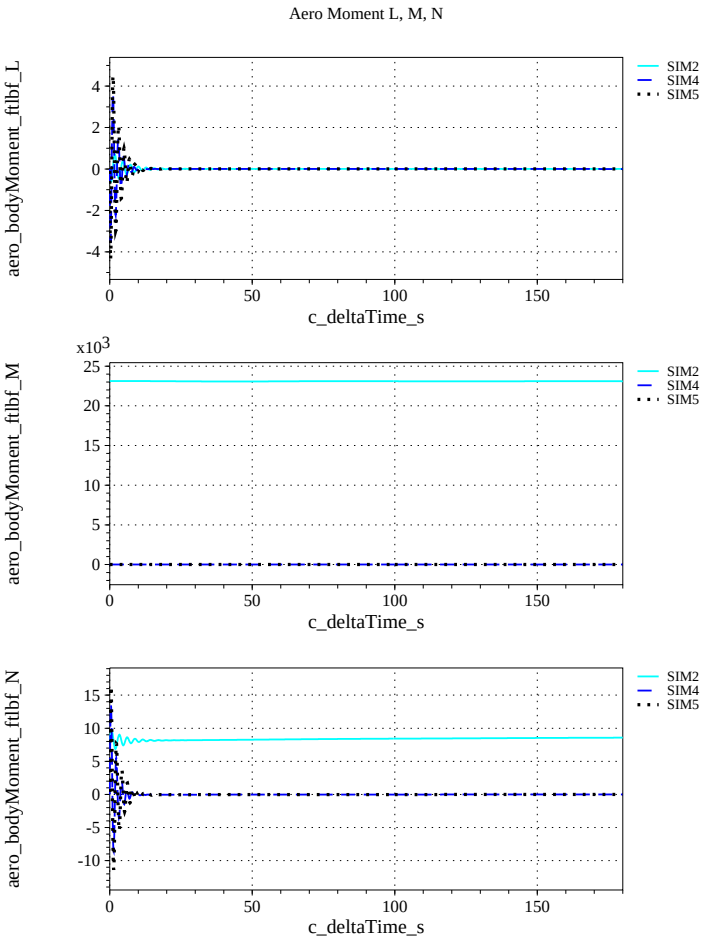

(c) Aerodynamic Moments Compared

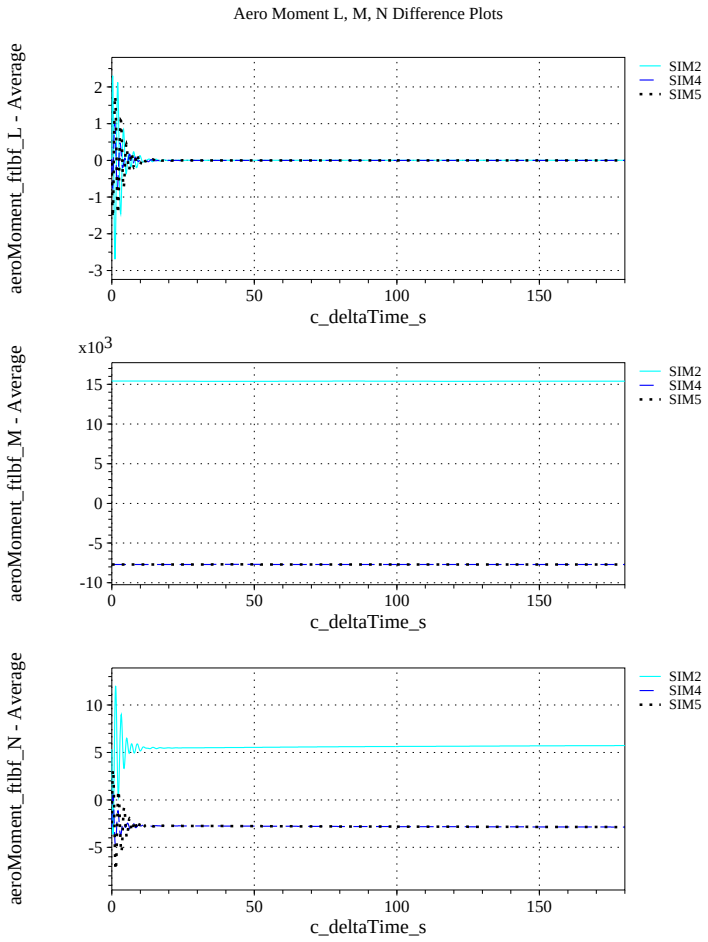

(d) Aerodynamic Moments Differenced

Figure 26. Check-case 11: Steady Flight of a Subsonic Aircraft; See Discussion in Section D.1.11 (Cont'd)

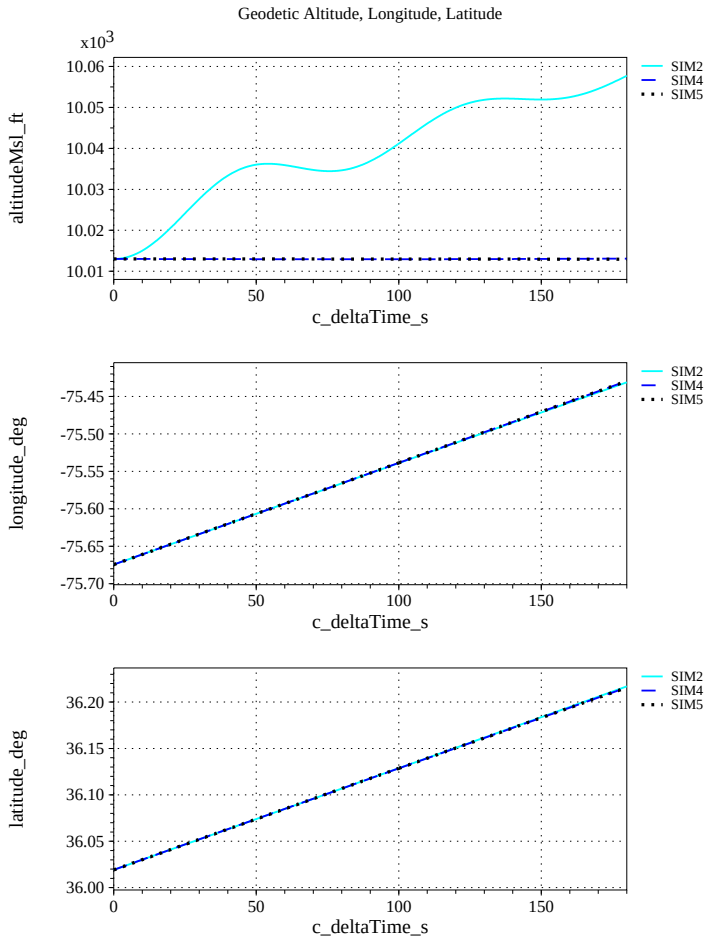

(e) Altitude, Geodetic Latitude and Longitude Compared

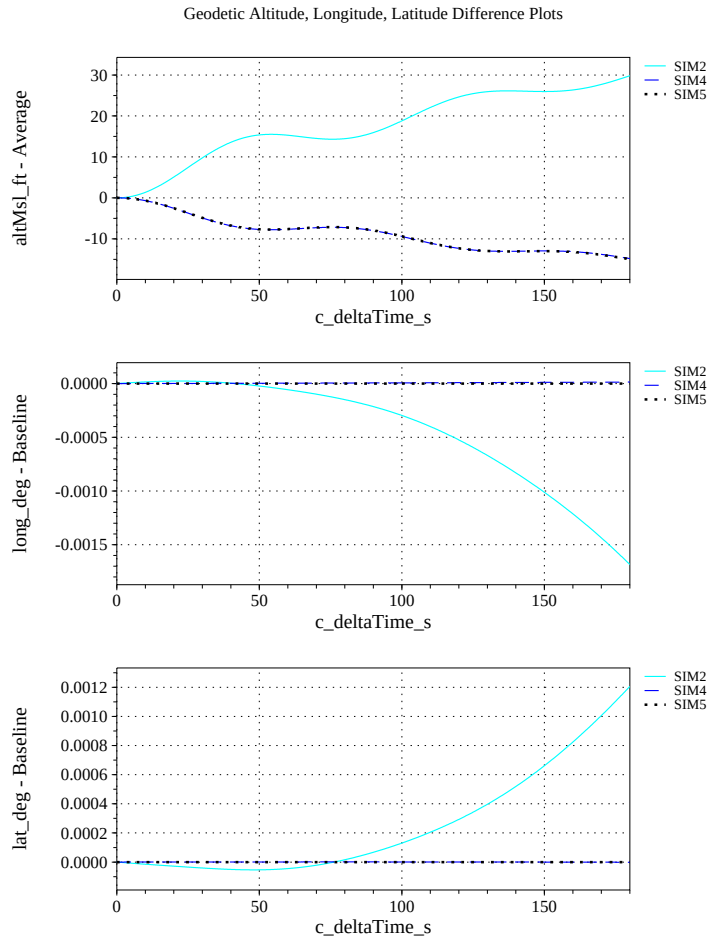

(f) Altitude, Geodetic Latitude and Longitude Differenced

Figure 26. Check-case 11: Steady Flight of a Subsonic Aircraft; See Discussion in Section D.1.11 (Cont'd)

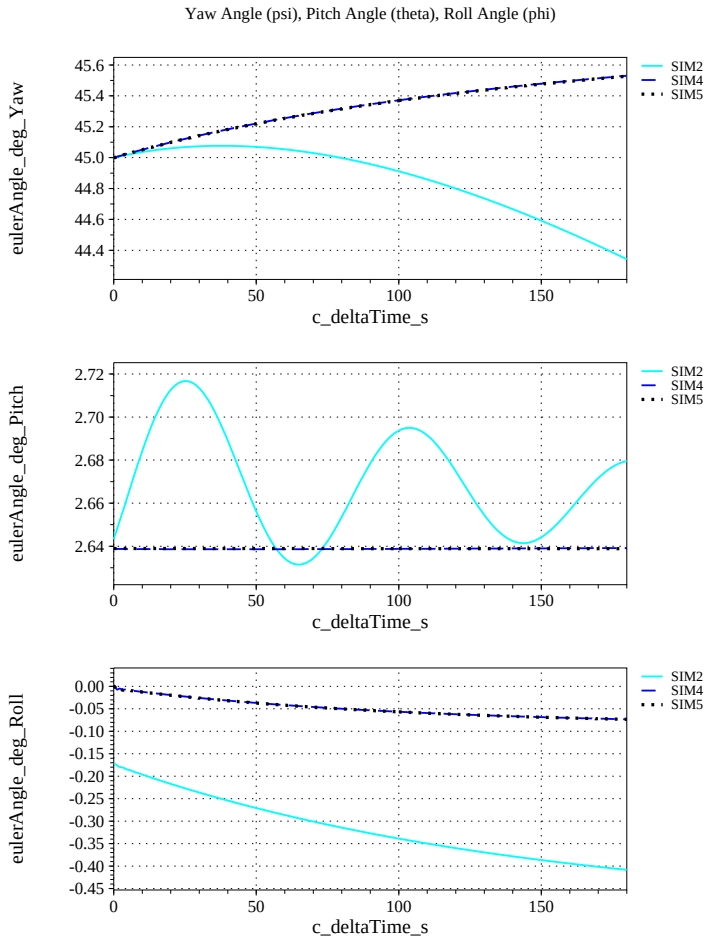

(g) Euler Angles (w.r.t. NED Frame) Compared

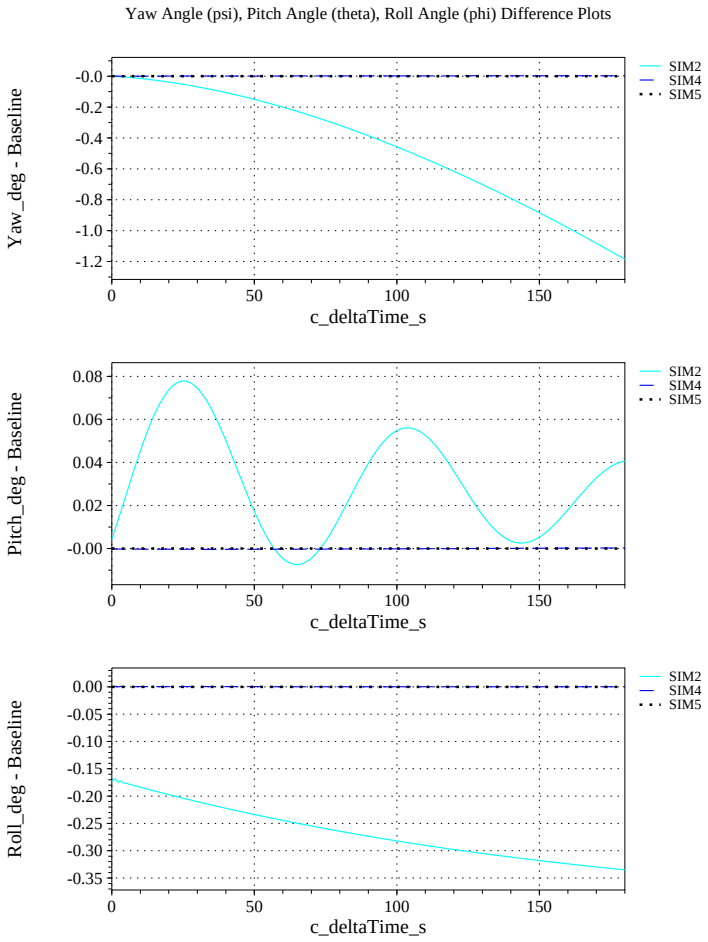

(h) Euler Angles (w.r.t. NED Frame) Differenced

Figure 26. Check-case 11: Steady Flight of a Subsonic Aircraft; See Discussion in Section D.1.11 (Cont'd)

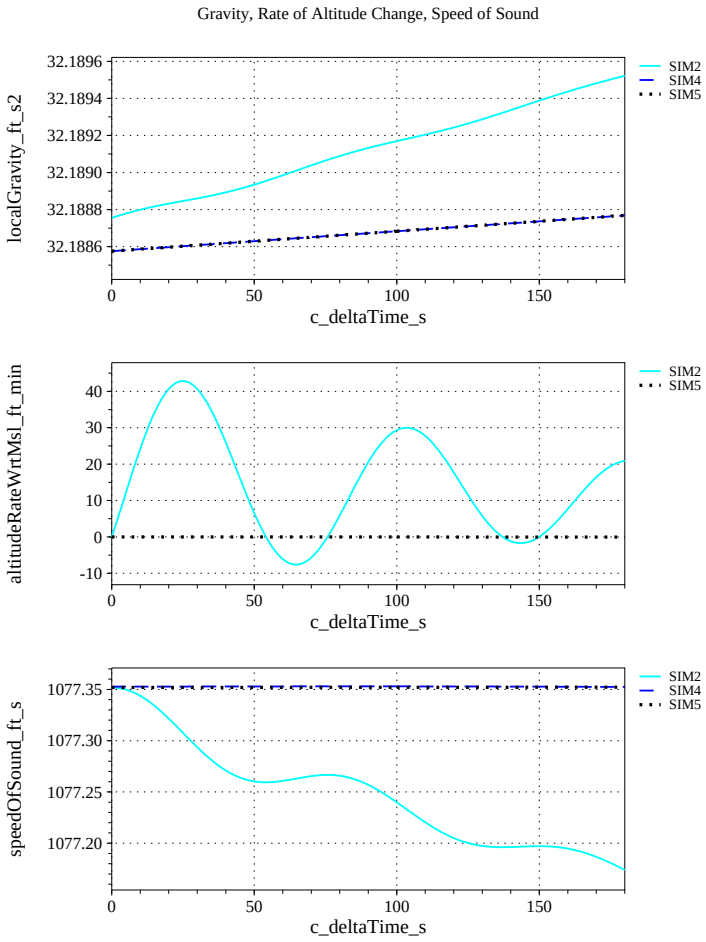

(i) Gravity, Climb Rate, and Speed-of-sound Compared

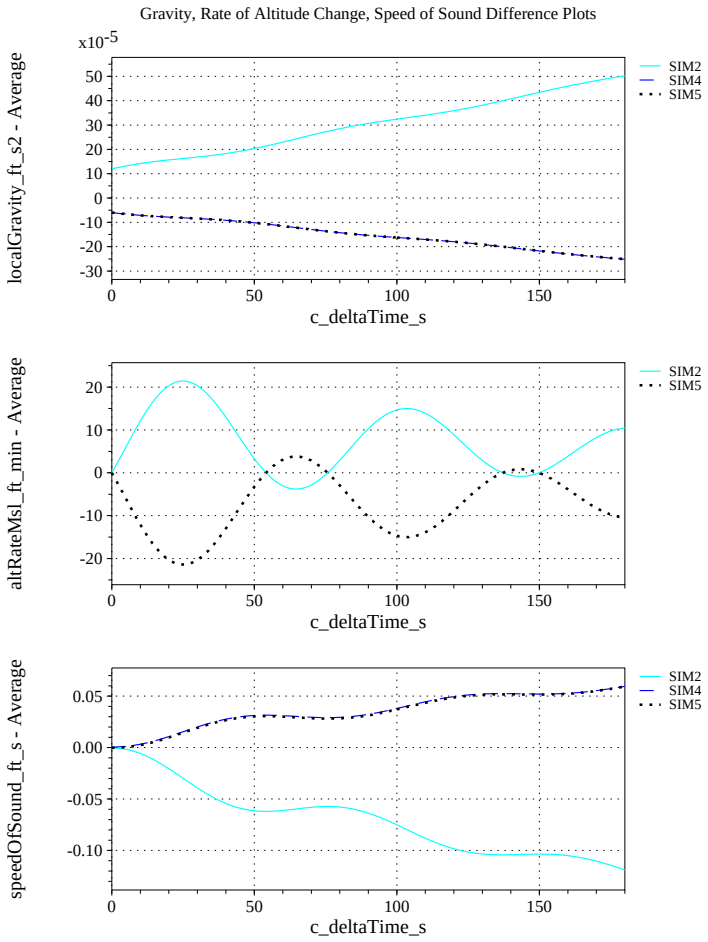

(j) Gravity, Climb Rate, and Speed-of-sound Differenced

Figure 26. Check-case 11: Steady Flight of a Subsonic Aircraft; See Discussion in Section D.1.11 (Cont'd)

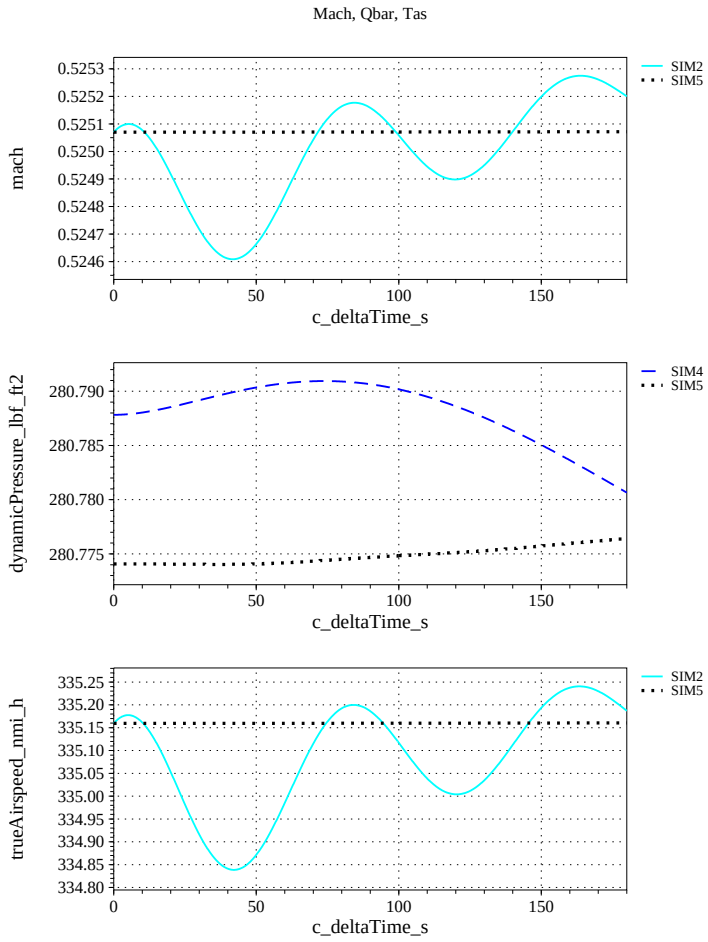

(k) Mach, Dynamic Pressure, and True Airspeed Compared

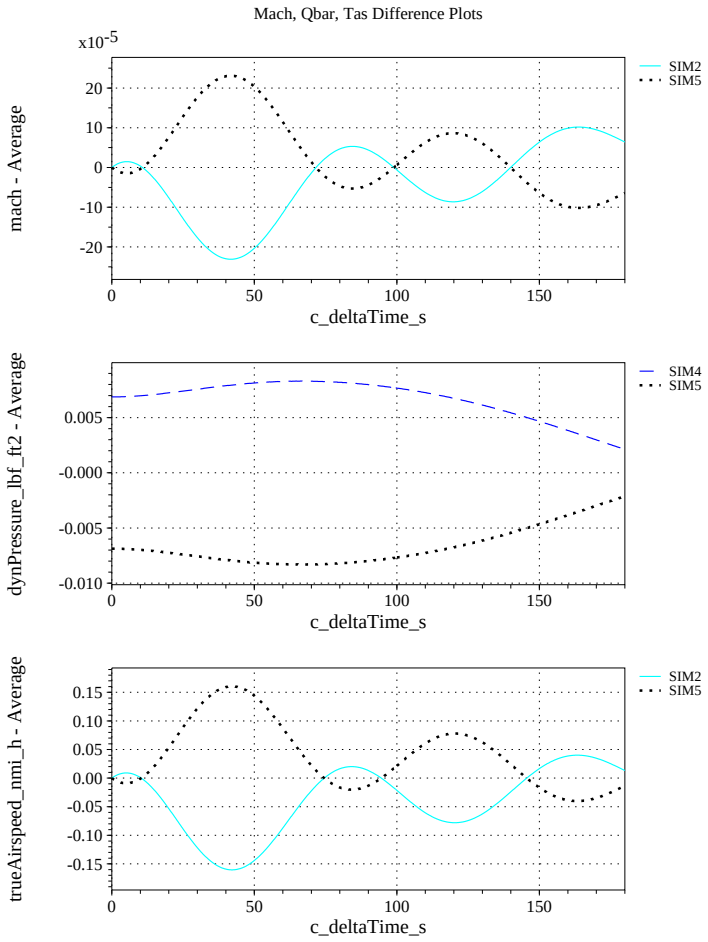

(l) Mach, Dynamic Pressure, and True Airspeed Differenced

Figure 26. Check-case 11: Steady Flight of a Subsonic Aircraft; See Discussion in Section D.1.11 (Cont'd)

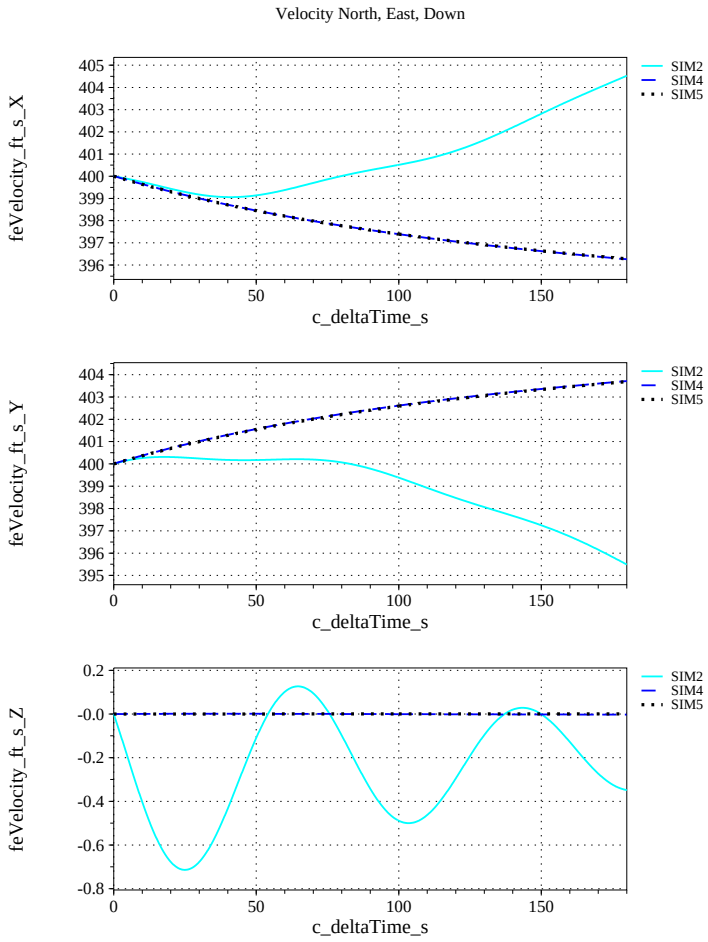

(m) NED Velocities Compared

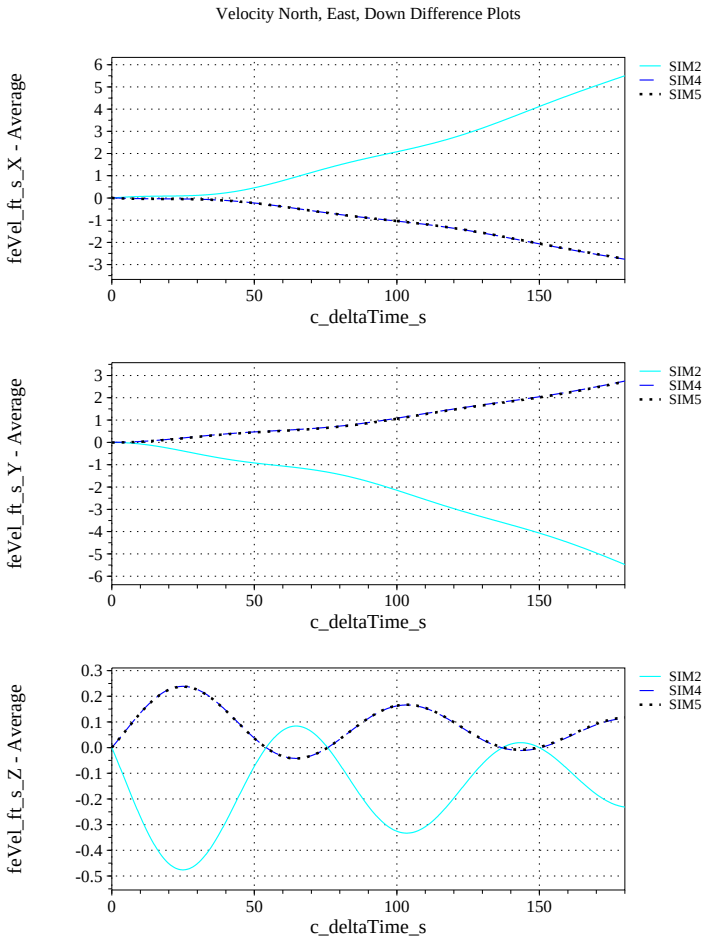

(n) NED Velocities Differenced

Figure 26. Check-case 11: Steady Flight of a Subsonic Aircraft; See Discussion in Section D.1.11 (Cont'd)

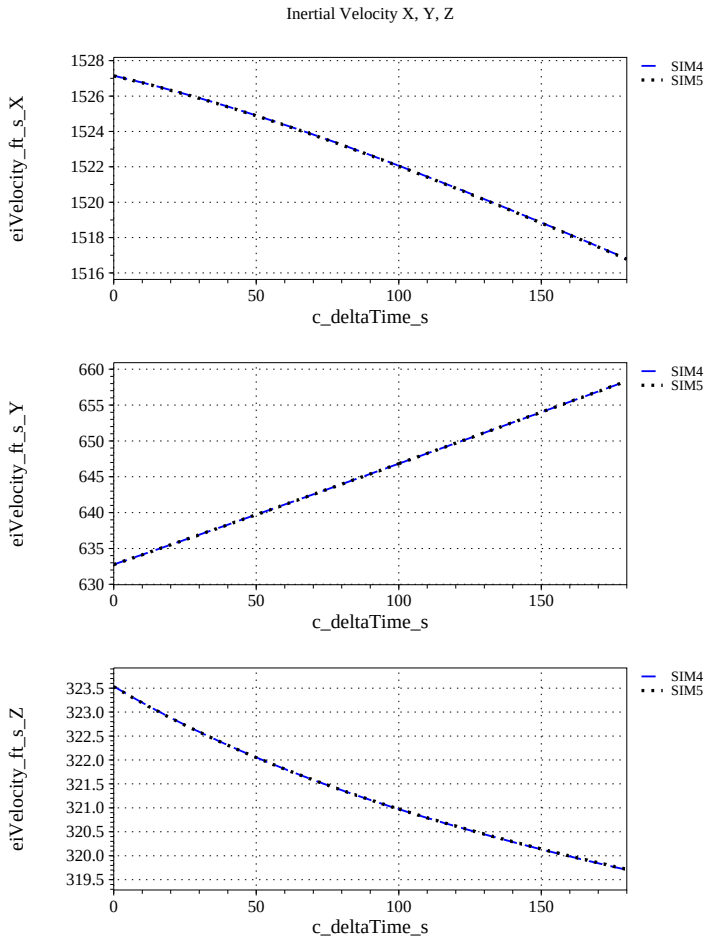

(o) Inertial Velocities Compared

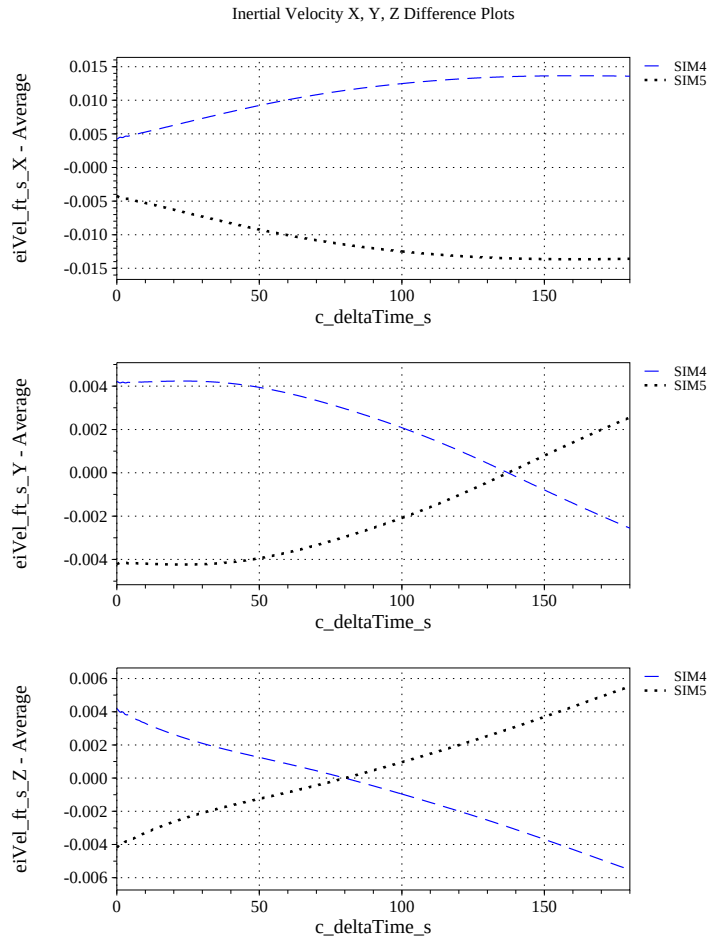

(p) Inertial Velocities Differenced

Figure 26. Check-case 11: Steady Flight of a Subsonic Aircraft; See Discussion in Section D.1.11 (Cont'd)

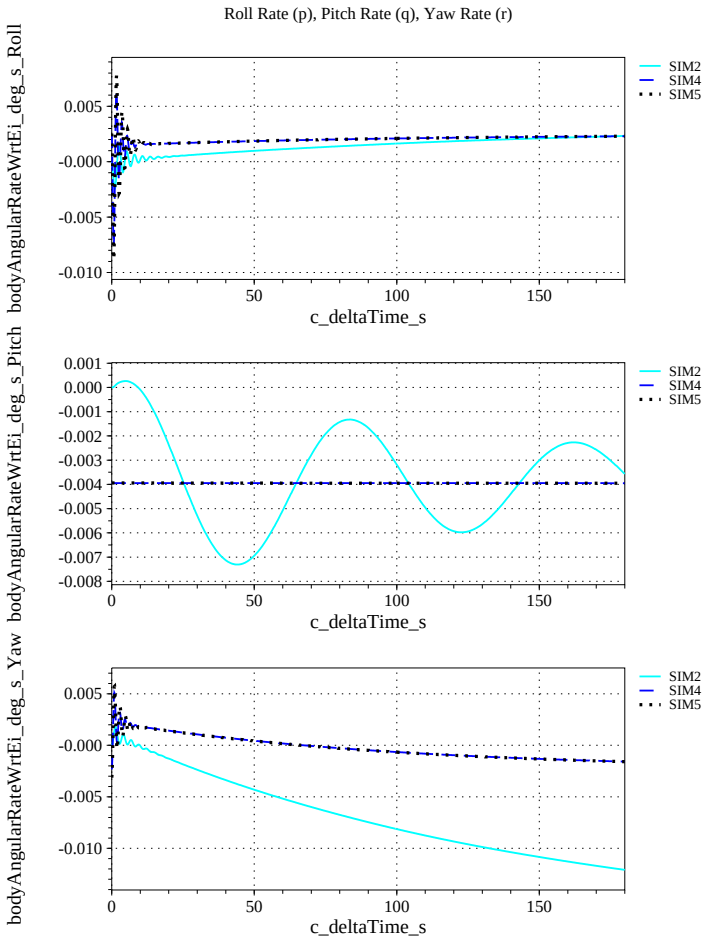

(q) Body-axis Angular Rates (w.r.t. NED Frame) Compared

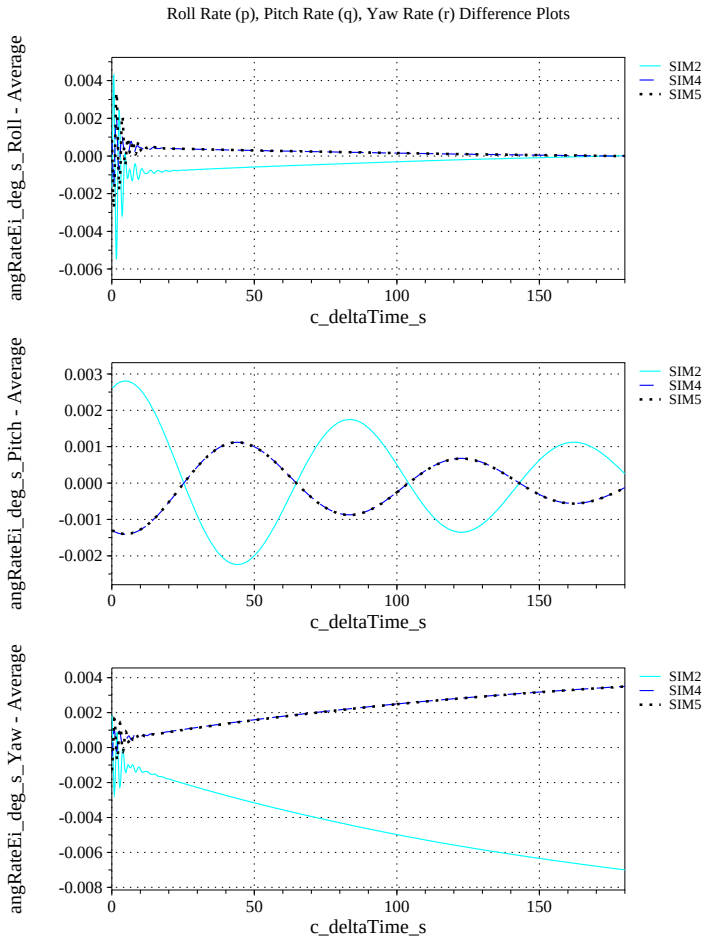

(r) Body-axis Angular Rates (w.r.t. NED Frame) Differenced

Figure 26. Check-case 11: Steady Flight of a Subsonic Aircraft; See Discussion in Section D.1.11 (Cont'd)

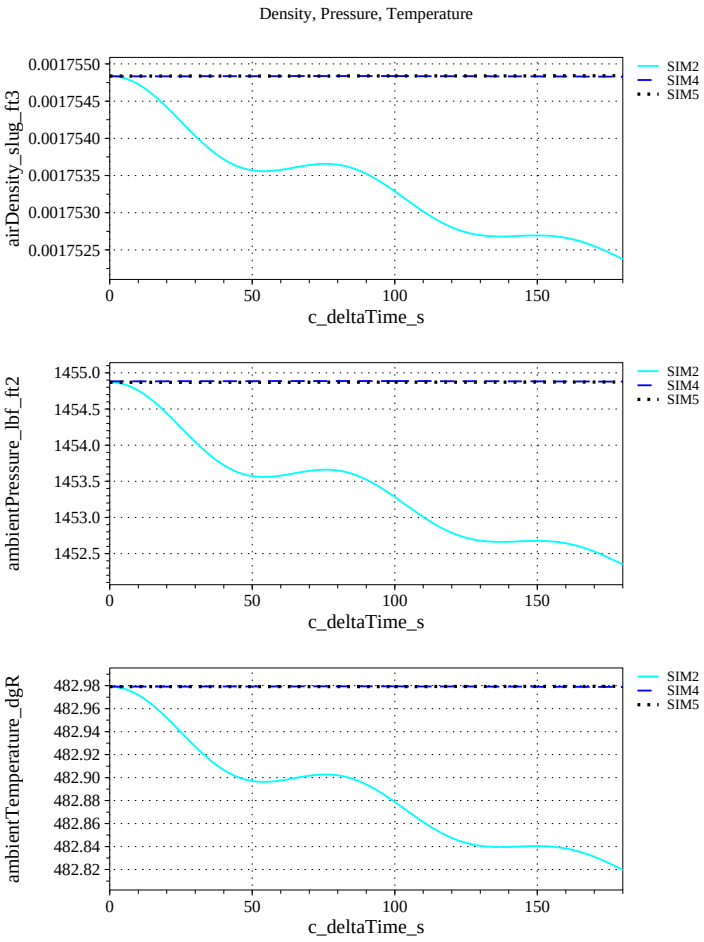

(s) Atmospheric Properties Compared

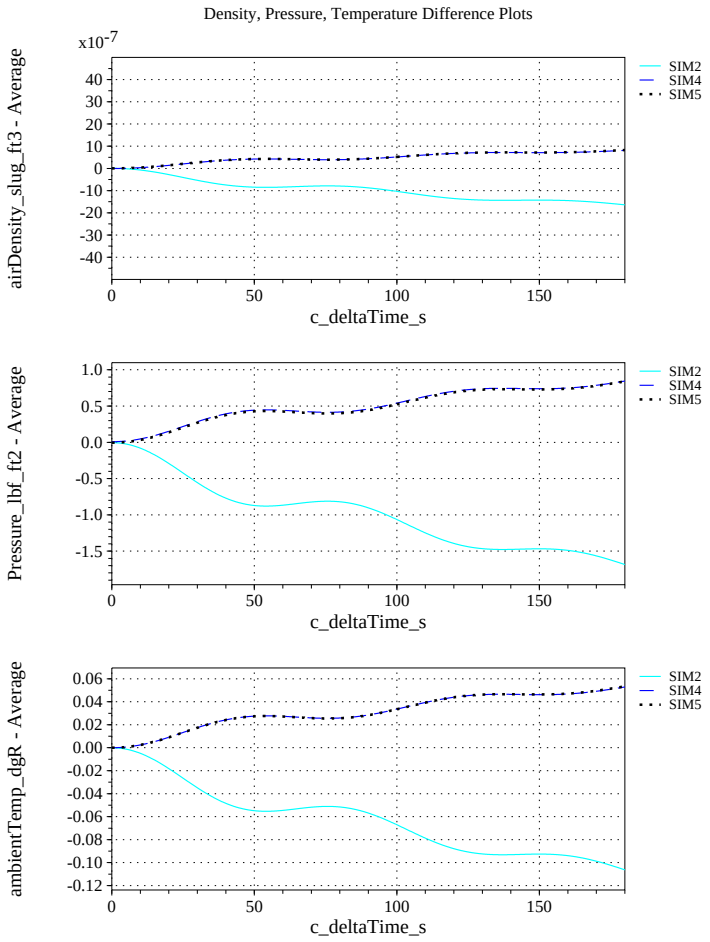

(t) Atmospheric Properties Differenced

Figure 26. Check-case 11: Steady Flight of a Subsonic Aircraft; See Discussion in Section D.1.11 (Cont'd)

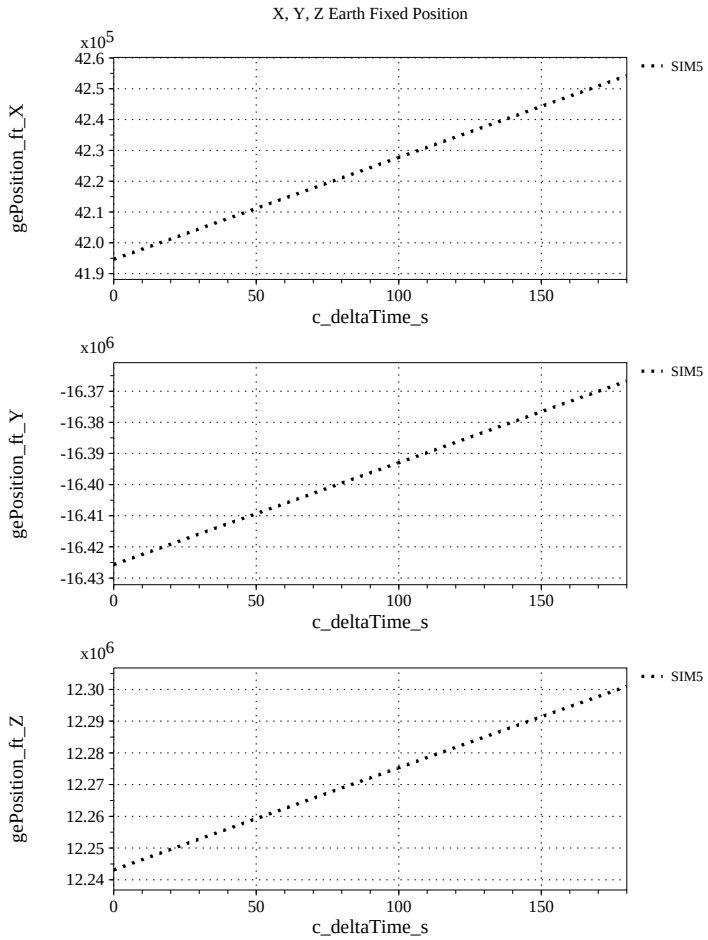

(u) Earth-centered, Earth-fixed Rectangular (X-Y-Z) Positions Compared

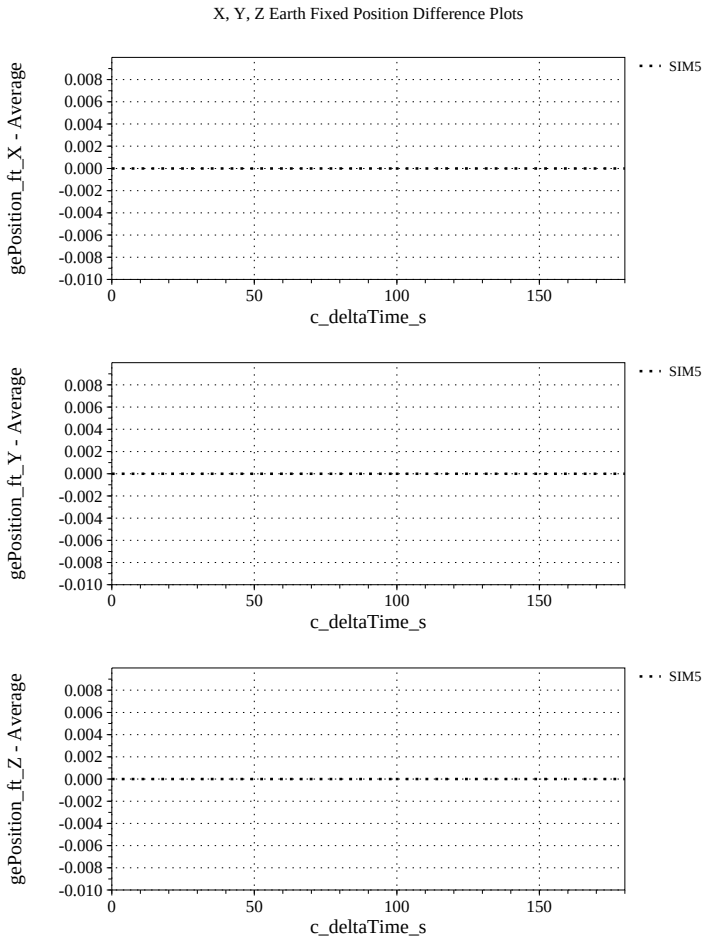

(v) Earth-centered, Earth-fixed Rectangular (X-Y-Z) Positions Differenced

Figure 26. Check-case 11: Steady Flight of a Subsonic Aircraft; See Discussion in Section D.1.11 (Cont'd)

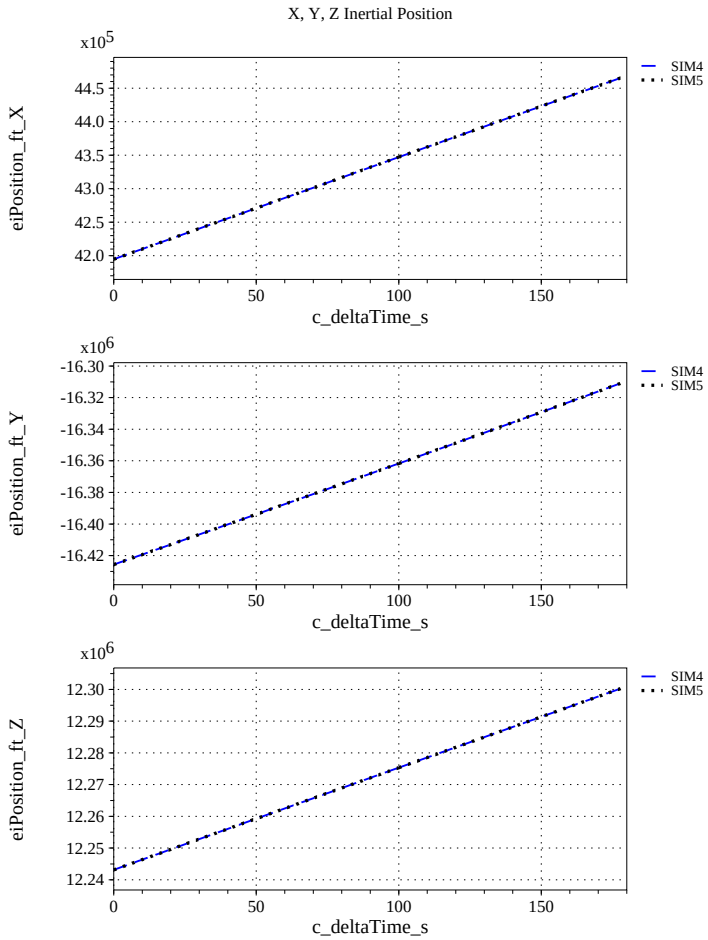

(w) Earth-centered Inertial Rectangular (x-y-z) Positions Compared

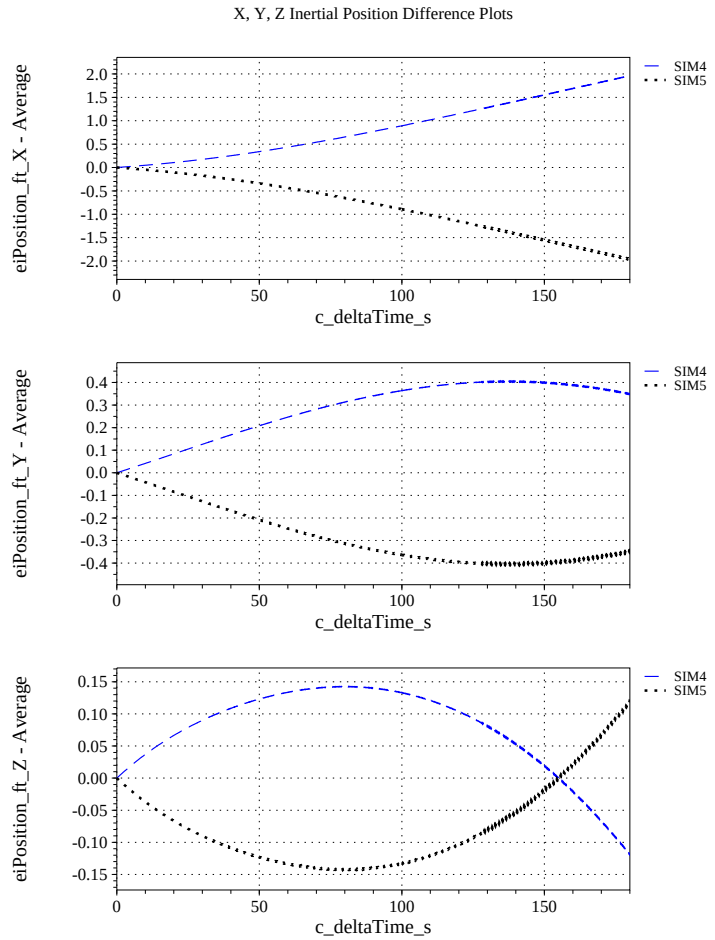

(x) Earth-centered Inertial Rectangular (x-y-z) Positions Differenced

Figure 26. Check-case 11: Steady Flight of a Subsonic Aircraft; See Discussion in Section D.1.11 (Concluded)

D.1.12 Check-case 12 – steady flight of a supersonic aircraft

This section shows cross-plots for two of the selected simulation tools in modeling the dynamics of an aircraft in steady trimmed supersonic flight on an arbitrary heading. This scenario is described in Section C.1.12. Figures 27a through 27x compare results between the two simulation tools, as well as the deviances of the outputs from each tool from the ensemble average value.

This check-case was the same as the previous check-case (Check-case 11 – steady flight of a subsonic aircraft) except that the F-16 was initialized with a supersonic initial velocity. The different initial conditions and trajectories visible in the plots were due to the same contributors discussed in atmospheric check-case 11:

- The simulations trimmed to different initial rotation rates (see Figure 27q). SIM 2 constrained the simulation to a zero inertial rotation rate. SIM 4 forced pitch rate to hold a constant pitch angle as the vehicle flew over the curved surface of the Earth. SIM 5 computed the three-axis rotation rate required to maintain three-axis orientation (roll, pitch, and yaw) as the aircraft flies over the curved surface of the Earth. In the subsonic check-case (Section D.1.11), the resulting roll and yaw rate for SIM 5 were near zero; thus, SIM 4 and SIM 5 could be said to have had a nearly equal initial angular rate. However, in the supersonic case, the roll rate computed by SIM 5 was of the same order as the pitch rate. Nevertheless, the first second of simulated flight continued to be marked by oscillations in the angular rates, indicating less than ideal trim, and, as Figure 27q shows, SIM 4 and SIM 5 settled to the same angular rates. Thus, the difference in initial roll rate did not substantially contribute to trajectory differences between SIM 4 and 5.

- SIM 2 recorded aerodynamic moments at the MRC. SIM 4 and SIM 5 recorded these at the vehicle CM (see Figure 27c).

- SIM 2 approximated the geocentric frame as being locally vertical. This resulted in a gravity vector that was deflected from local vertical by the difference between geocentric and geodetic latitude. This deflected gravity vector caused the SIM 2 equilibrium solver to roll the vehicle slightly so that lift was more closely aligned with the direction of gravity. The equilibrium solution also included an aerodynamic side force that generated a yawing moment at the CM. The equilibrium solution added rudder deflection to create a counter-acting aerodynamic yawing moment. The use of a non-vertical gravity vector in SIM 2 led to a difference in the initial values for roll angle, pitch angle, aerodynamic forces, aerodynamic pitching moment, and aerodynamic yawing moment.

- Even were SIM 2 modified to use the geodetic (instead of geodetic) gravitation vector, SIM 2 produced a J_2 gravitation vector that differed in magnitude from the other simulation results by 1.8×10^{-4} ft/s^2. The best explanation for this may have been a difference in the conversion of initial conditions from geodetic to geocentric coordinates. The difference in the geodetic coordinates would have to represent an altitude difference of 58 ft or greater. However, the difference in gravitation itself should have made a very small impact on vehicle dynamics as it added only 0.11 lbf to the weight of the vehicle.

Overall, the change from subsonic to supersonic speed did moderately increase the position difference between the simulations after 180 sec. SIM 4 and SIM 5 were separated by 7.5 ft. SIM 2 was separated from the other two simulations by 760 ft, based on the recorded differences in latitude, longitude, and altitude.

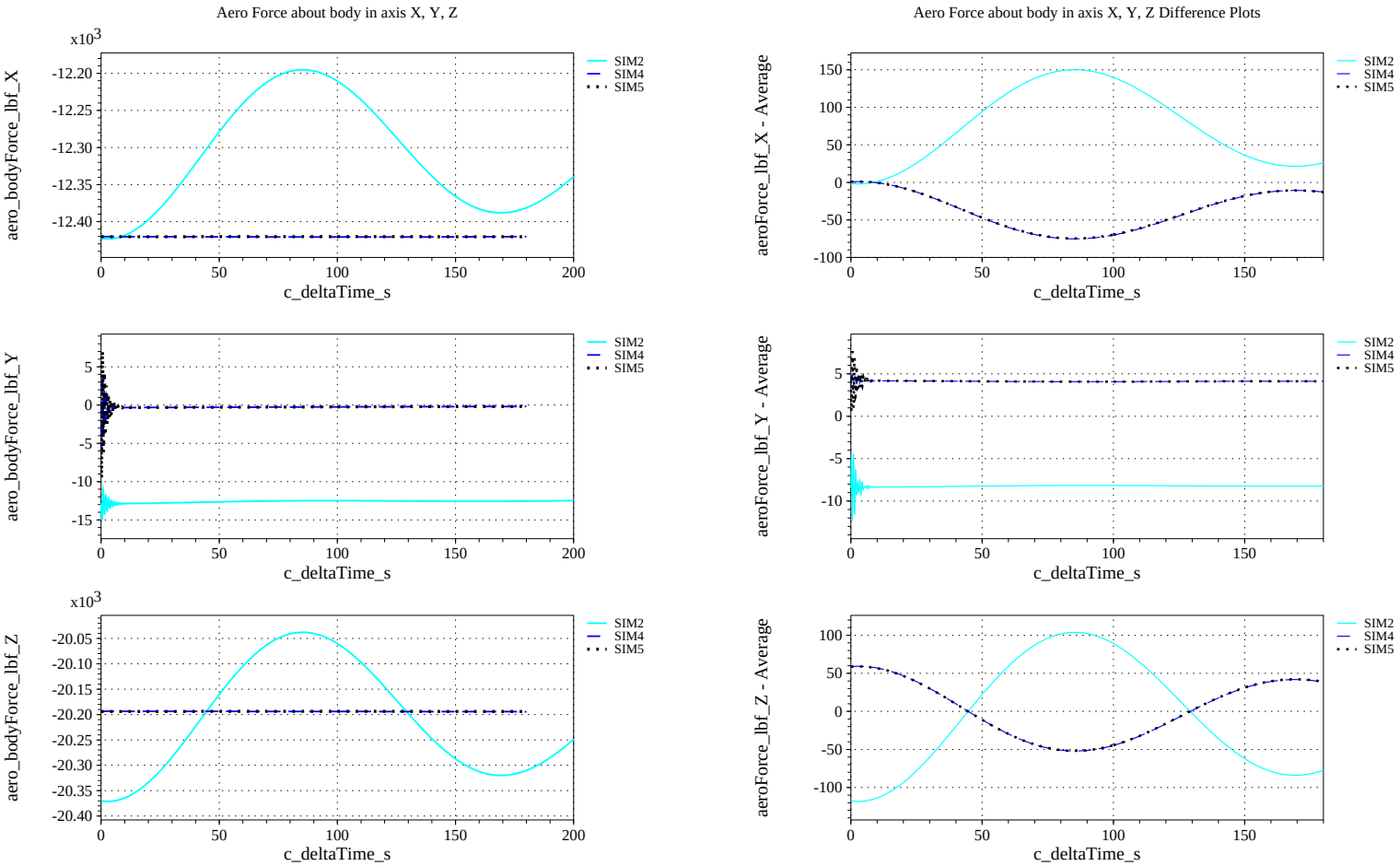

(a) Aerodynamic Forces Compared

(b) Aerodynamic Forces Differenced

Figure 27. Check-case 12: Steady Flight of a Supersonic Aircraft; See Discussion in Section D.1.12

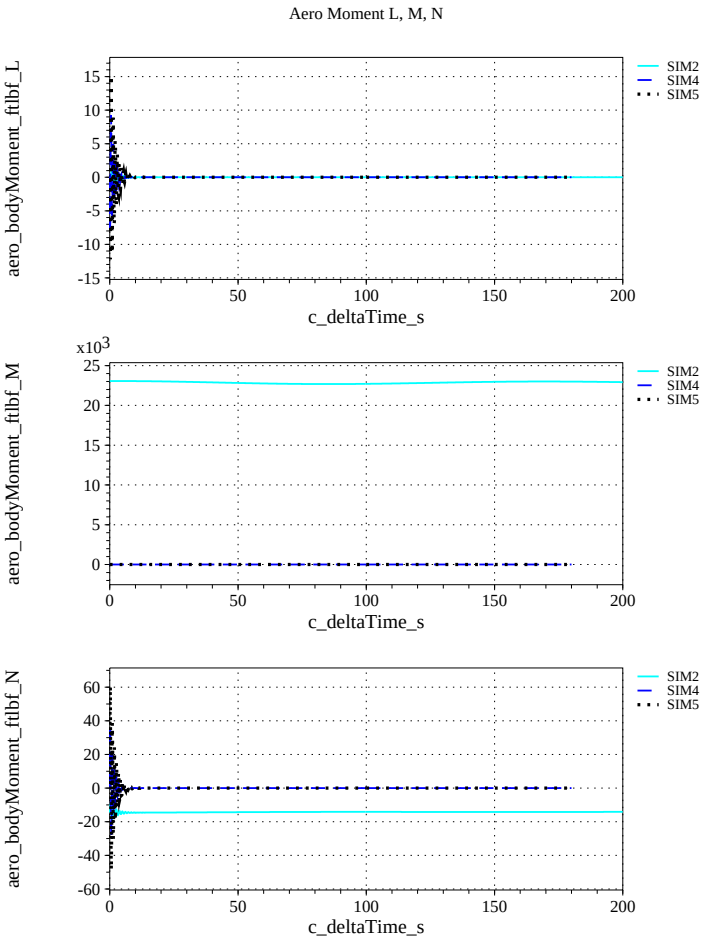

(c) Aerodynamic Moments Compared

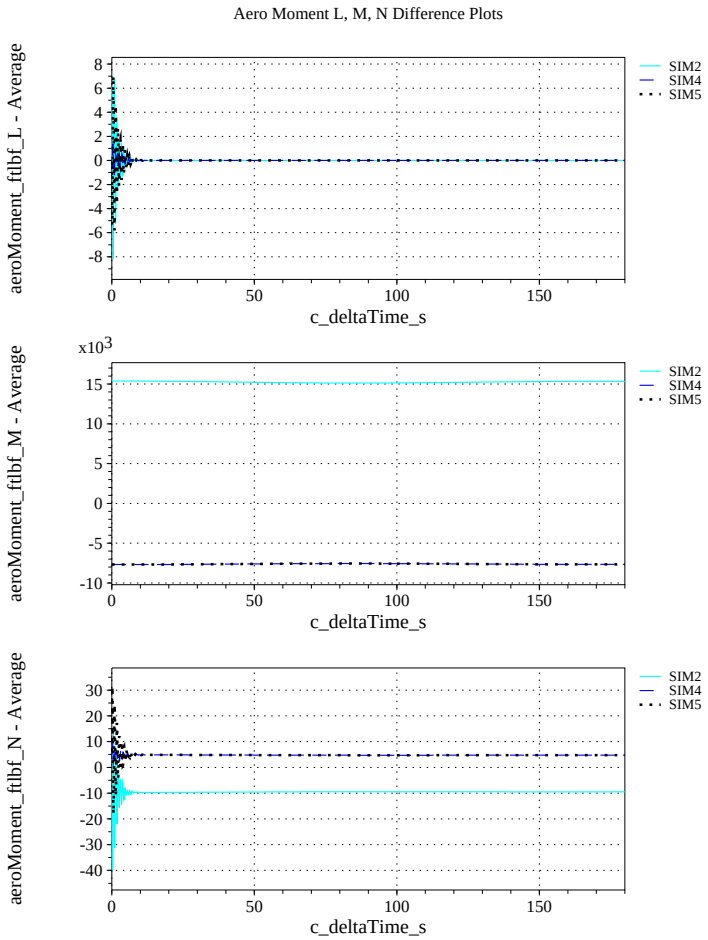

(d) Aerodynamic Moments Differenced

Figure 27. Check-case 12: Steady Flight of a Supersonic Aircraft; See Discussion in Section D.1.12 (Cont'd)

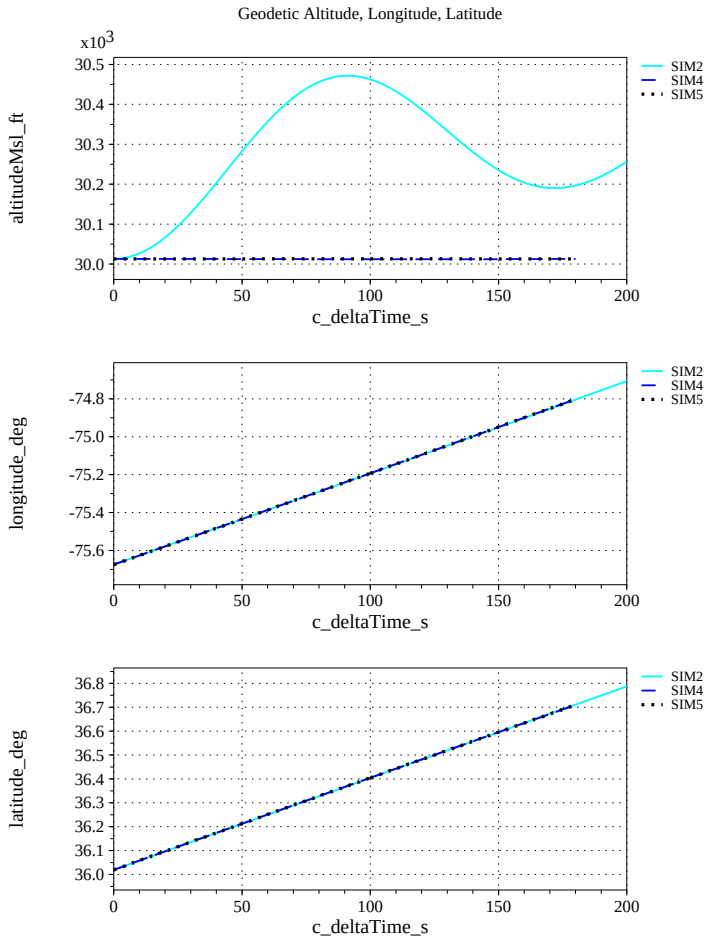

(e) Altitude, Geodetic Latitude and Longitude Compared

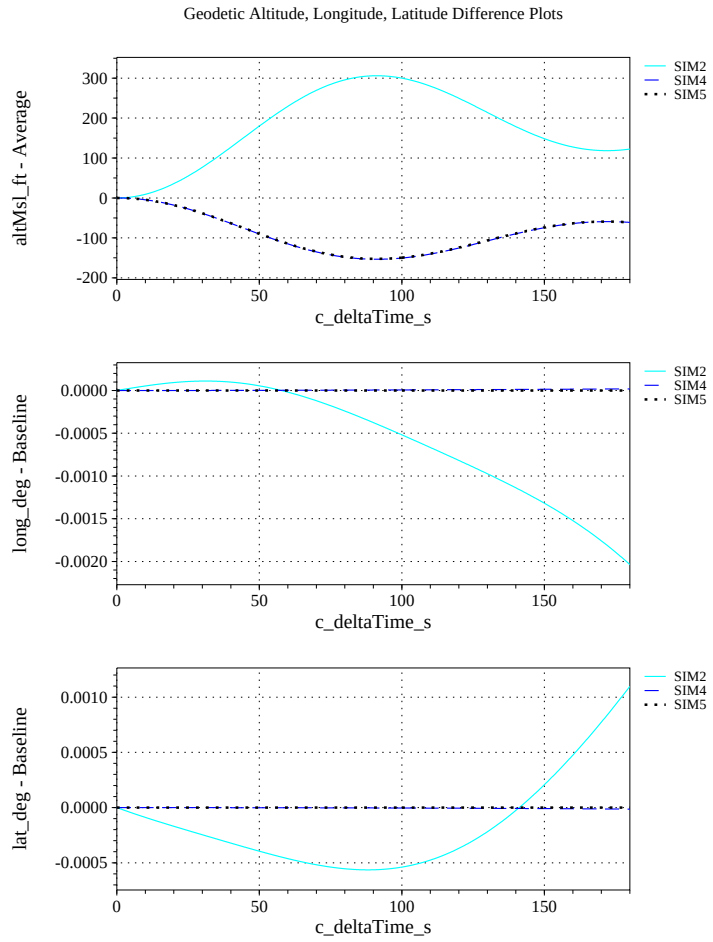

(f) Altitude, Geodetic Latitude and Longitude Differenced

Figure 27. Check-case 12: Steady Flight of a Supersonic Aircraft; See Discussion in Section D.1.12 (Cont'd)

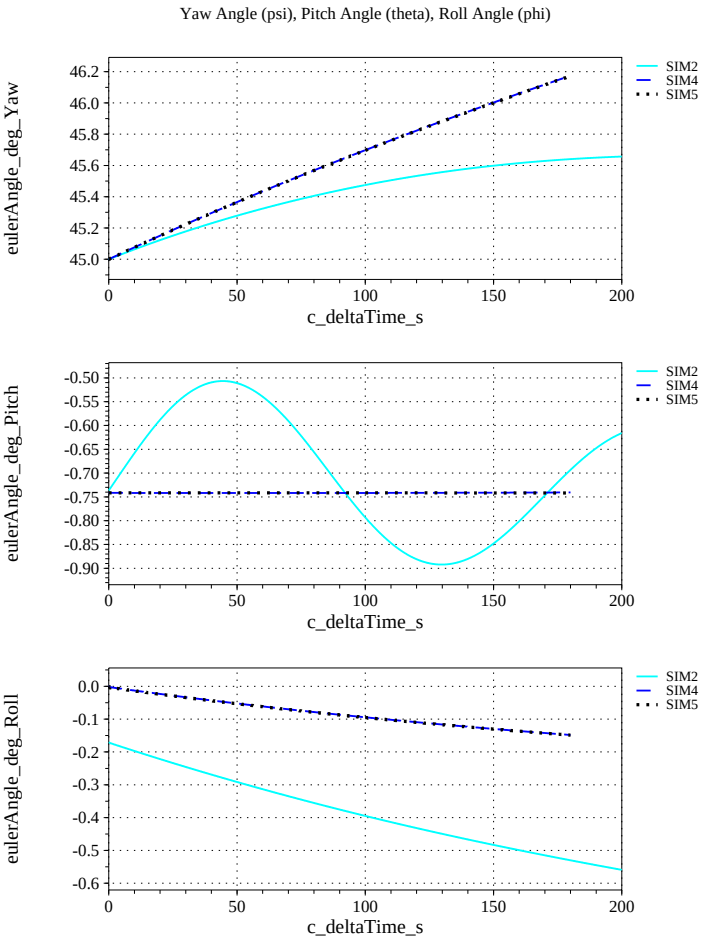

(g) Euler Angles (w.r.t. NED Frame) Compared

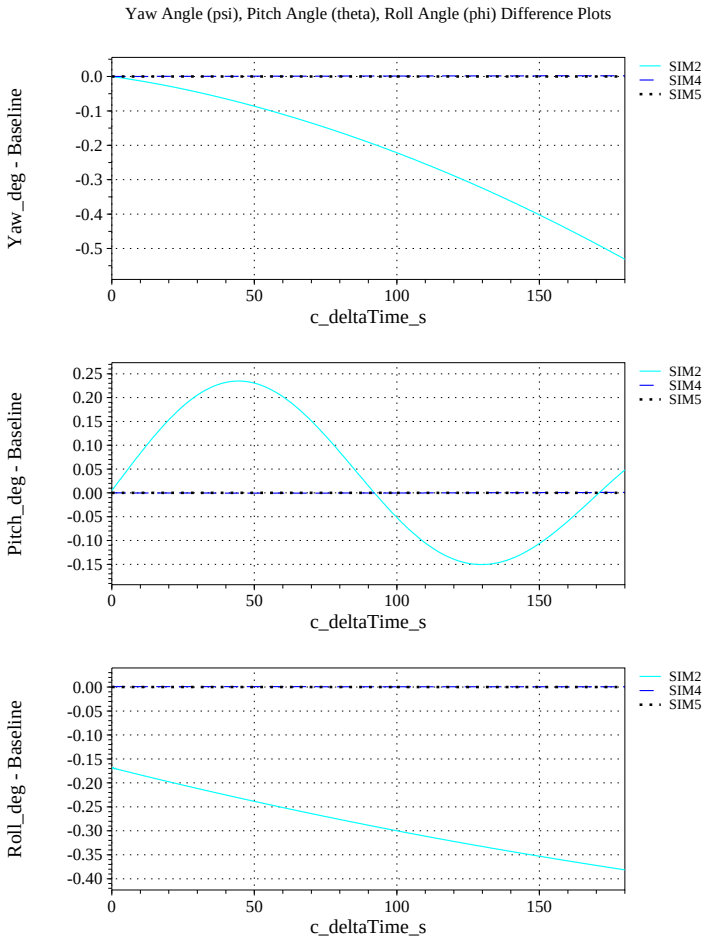

(h) Euler Angles (w.r.t. NED Frame) Differenced

Figure 27. Check-case 12: Steady Flight of a Supersonic Aircraft; See Discussion in Section D.1.12 (Cont'd)

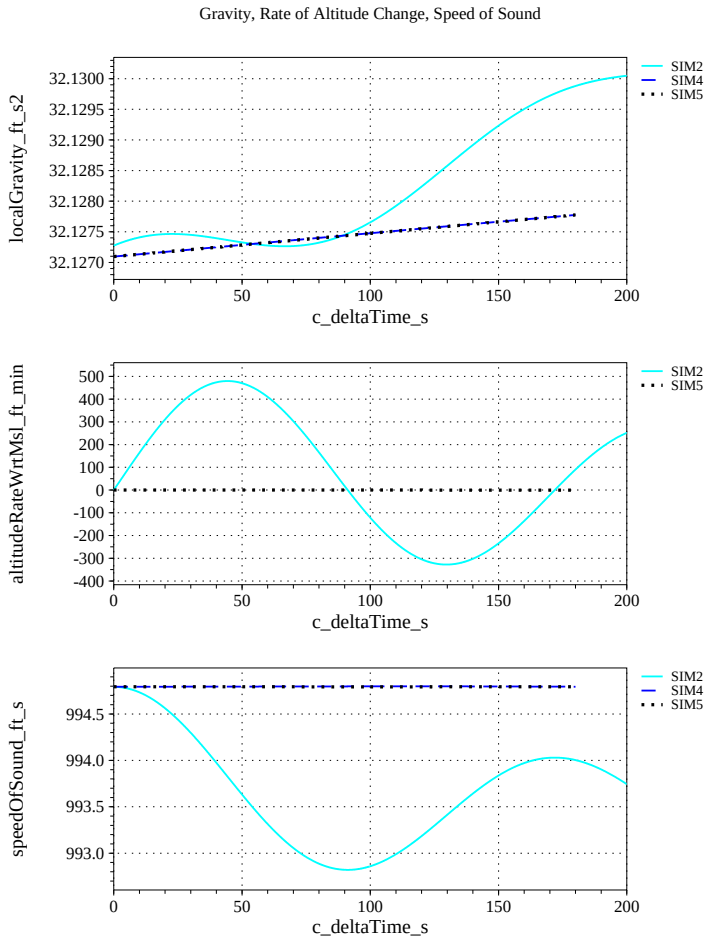

(i) Gravity, Climb Rate, and Speed-of-sound Compared

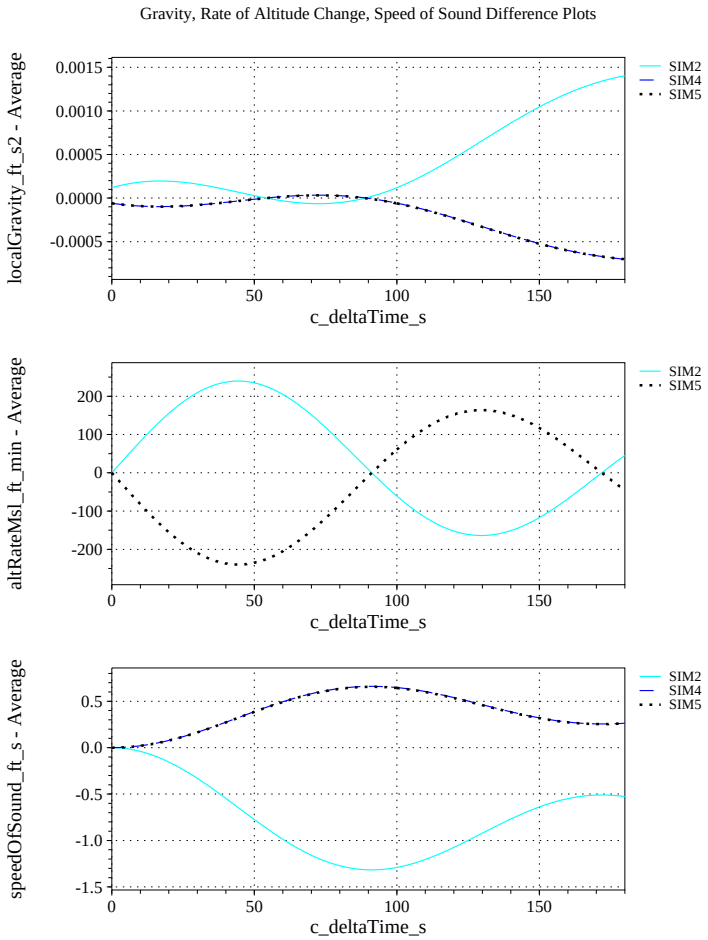

(j) Gravity, Climb Rate, and Speed-of-sound Differenced

Figure 27. Check-case 12: Steady Flight of a Supersonic Aircraft; See Discussion in Section D.1.12 (Cont'd)

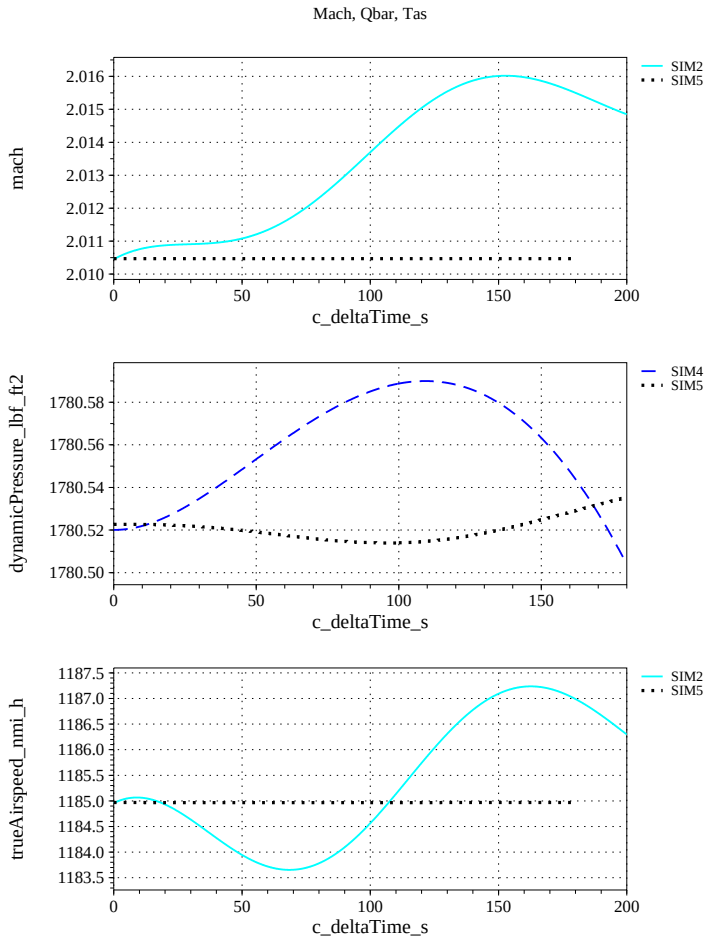

(k) Mach, Dynamic Pressure, and True Airspeed Compared

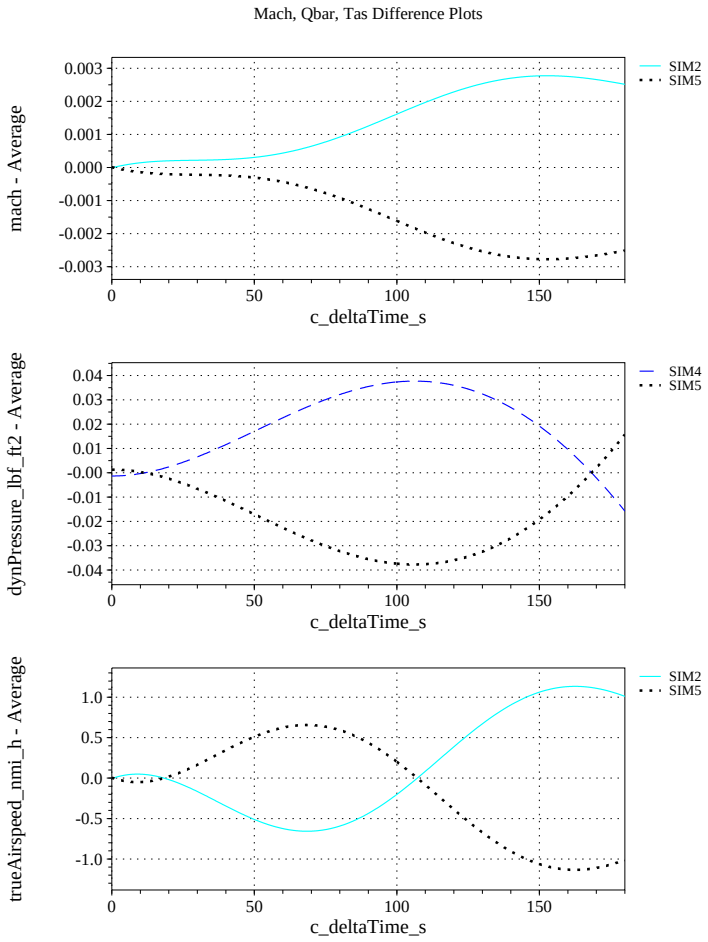

(l) Mach, Dynamic Pressure, and True Airspeed Differenced

Figure 27. Check-case 12: Steady Flight of a Supersonic Aircraft; See Discussion in Section D.1.12 (Cont'd)

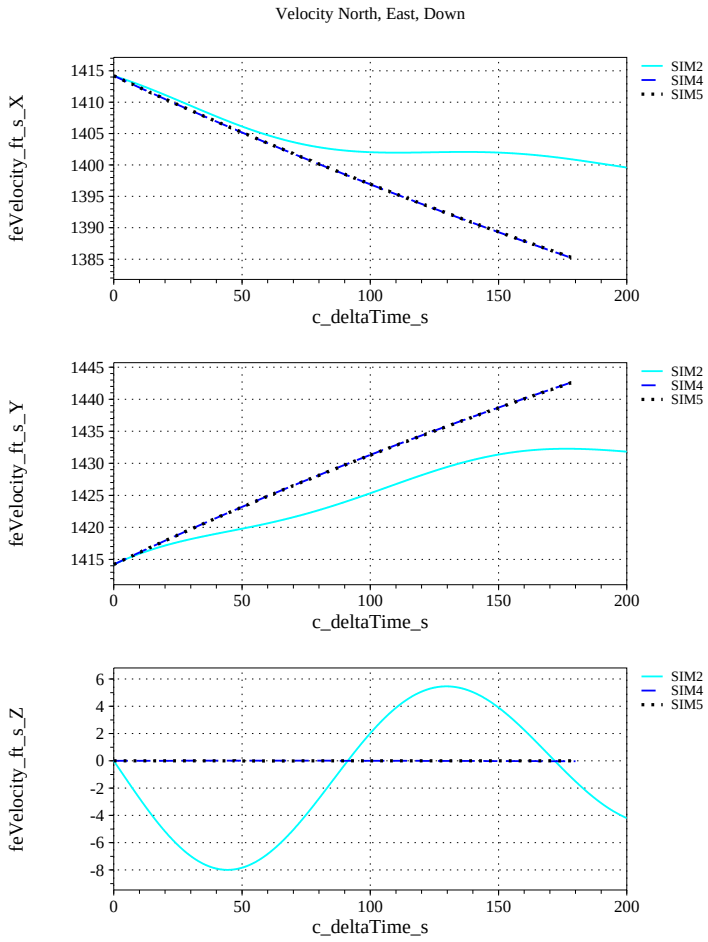

(m) NED Velocities Compared

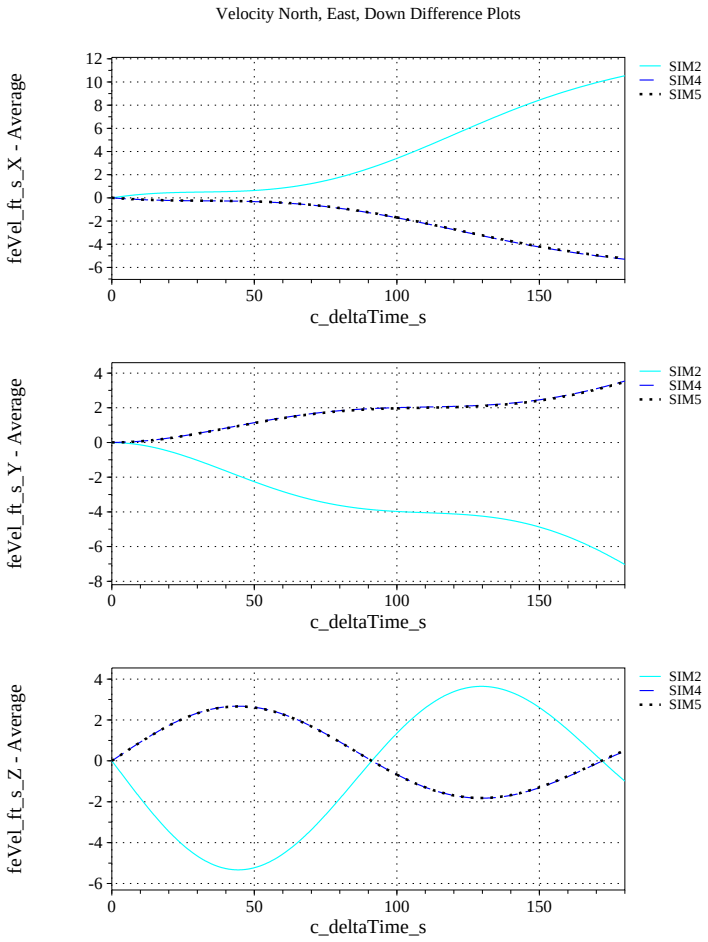

(n) NED Velocities Differenced

Figure 27. Check-case 12: Steady Flight of a Supersonic Aircraft; See Discussion in Section D.1.12 (Cont'd)

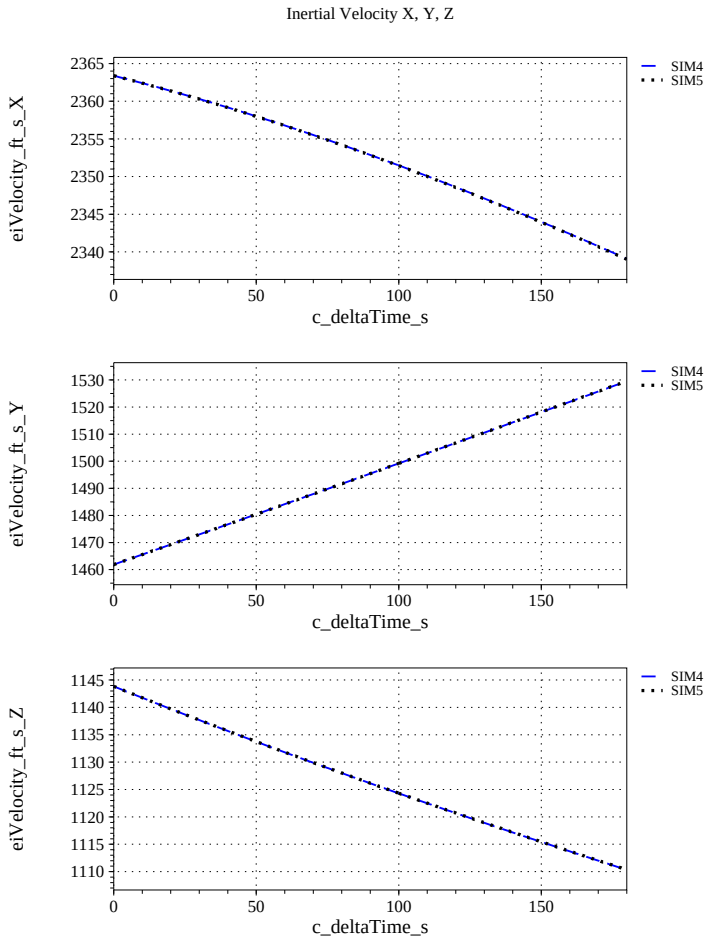

(o) Inertial Velocities Compared

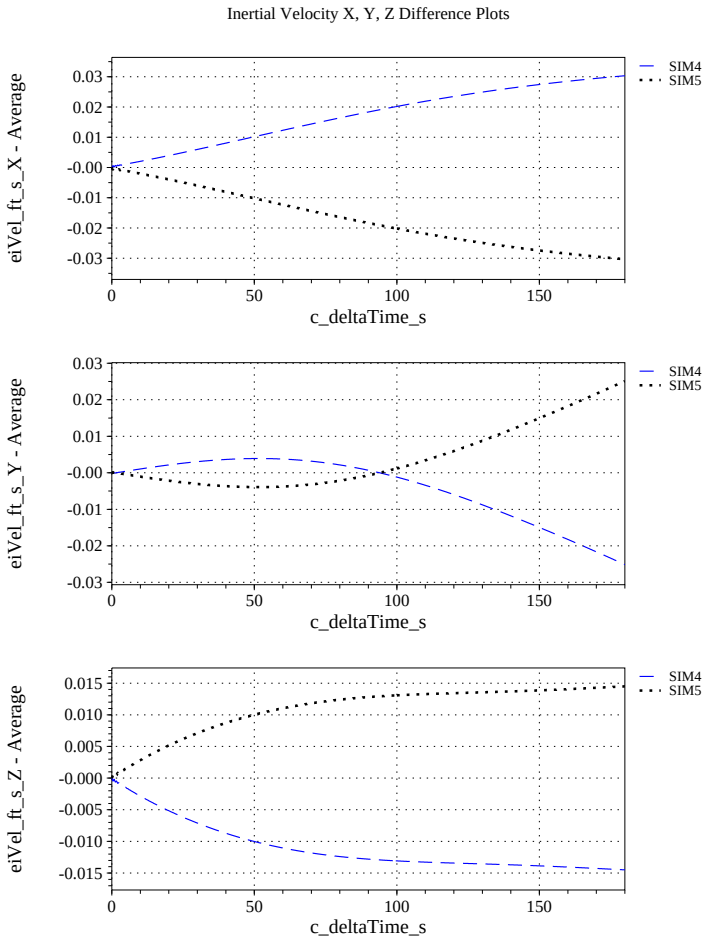

(p) Inertial Velocities Differenced

Figure 27. Check-case 12: Steady Flight of a Supersonic Aircraft; See Discussion in Section D.1.12 (Cont'd)

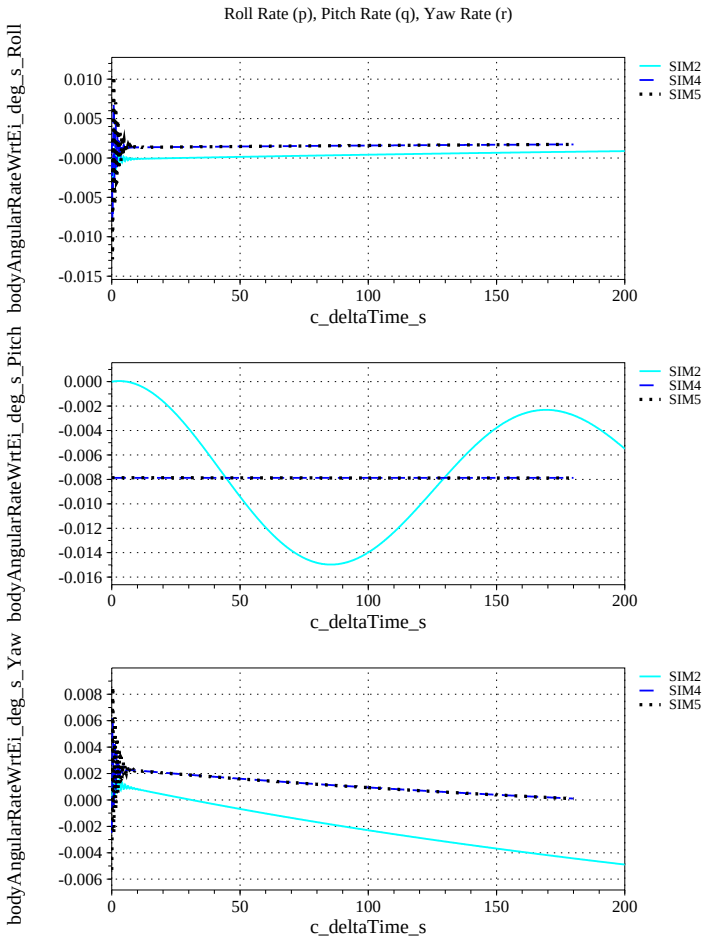

(q) Body-axis Angular Rates (w.r.t. NED Frame) Compared

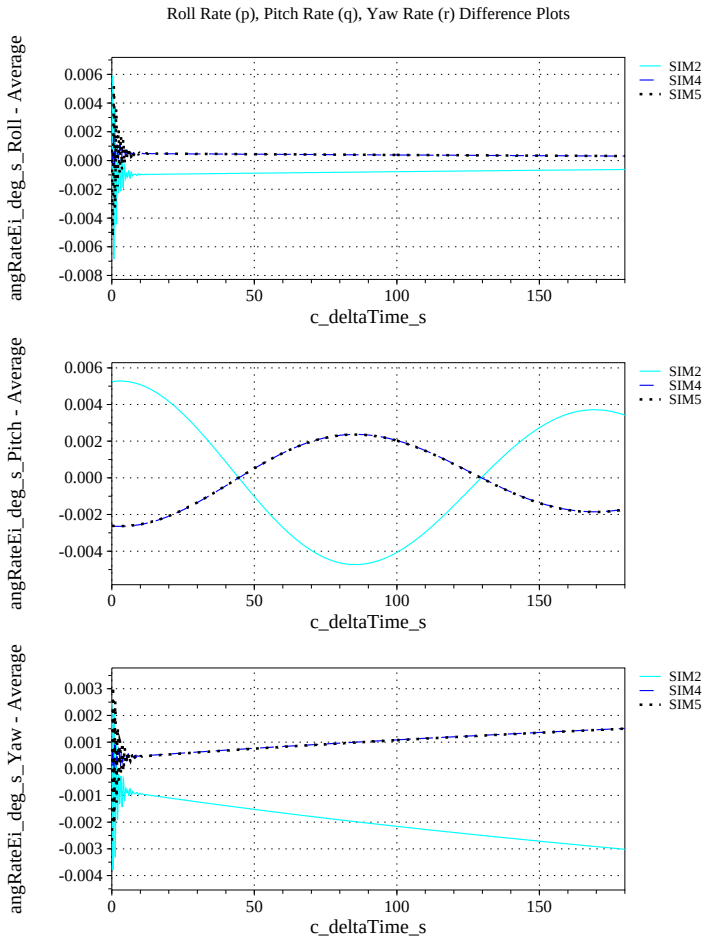

(r) Body-axis Angular Rates (w.r.t. NED Frame) Differenced

Figure 27. Check-case 12: Steady Flight of a Supersonic Aircraft; See Discussion in Section D.1.12 (Cont'd)

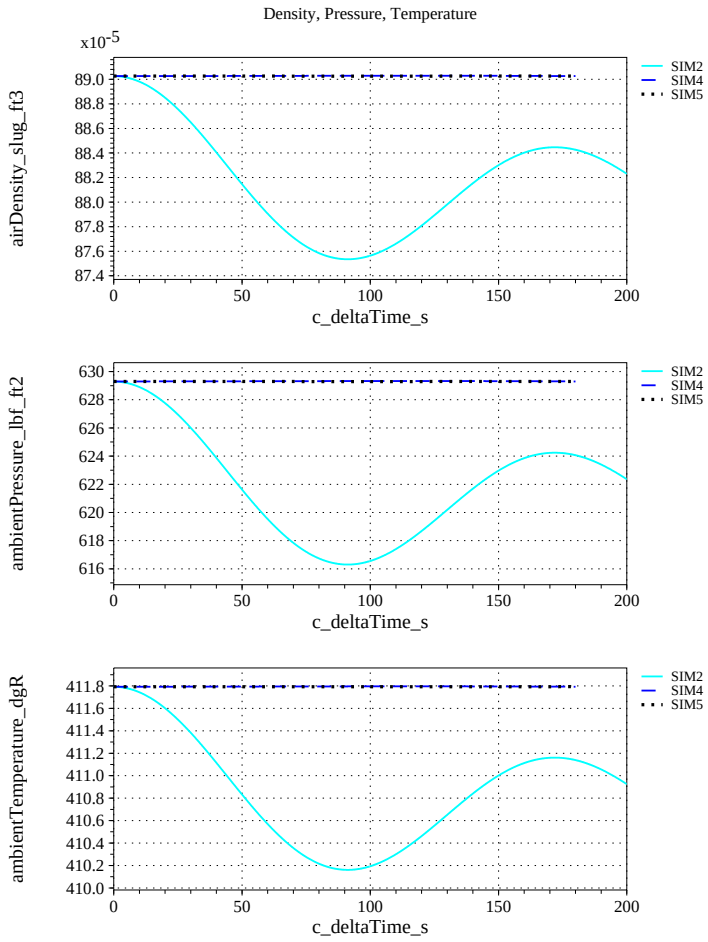

(s) Atmospheric Properties Compared

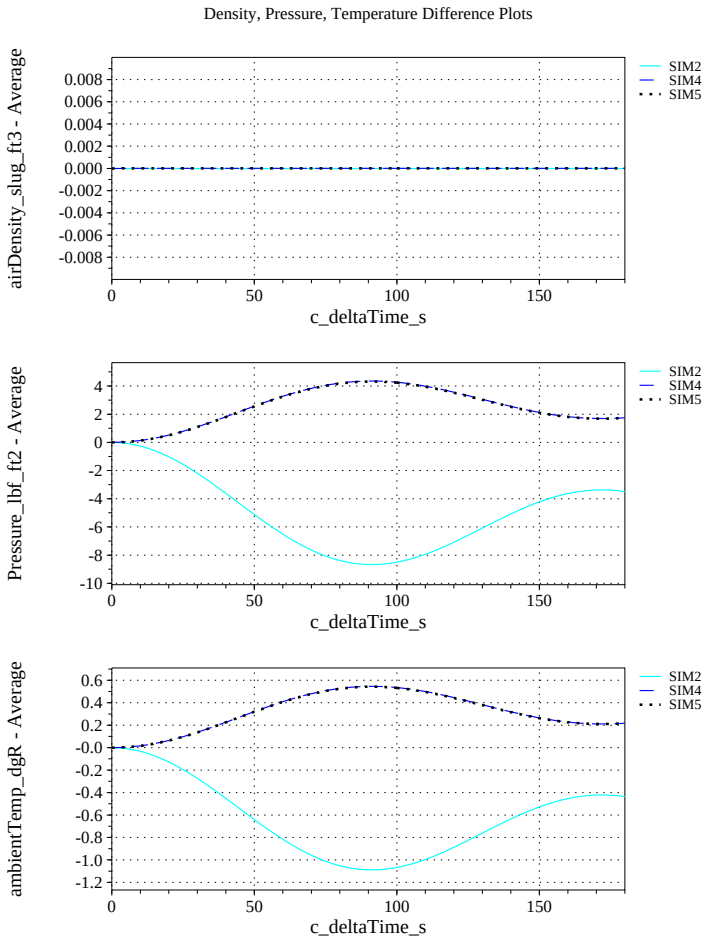

(t) Atmospheric Properties Differenced

Figure 27. Check-case 12: Steady Flight of a Supersonic Aircraft; See Discussion in Section D.1.12 (Cont'd)

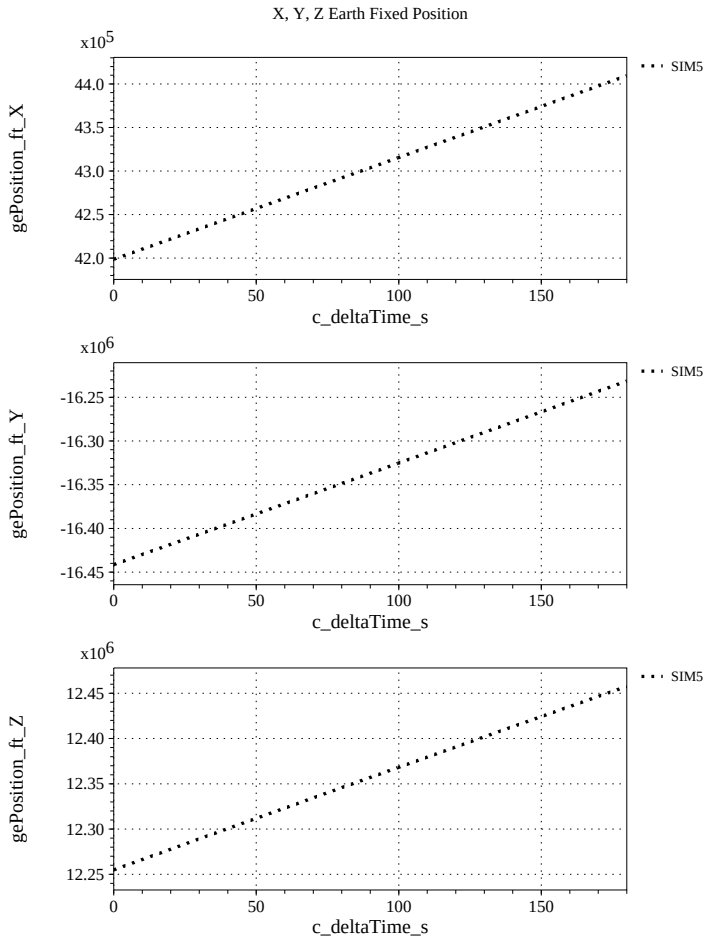

(u) Earth-centered, Earth-fixed Rectangular (X-Y-Z) Positions Compared

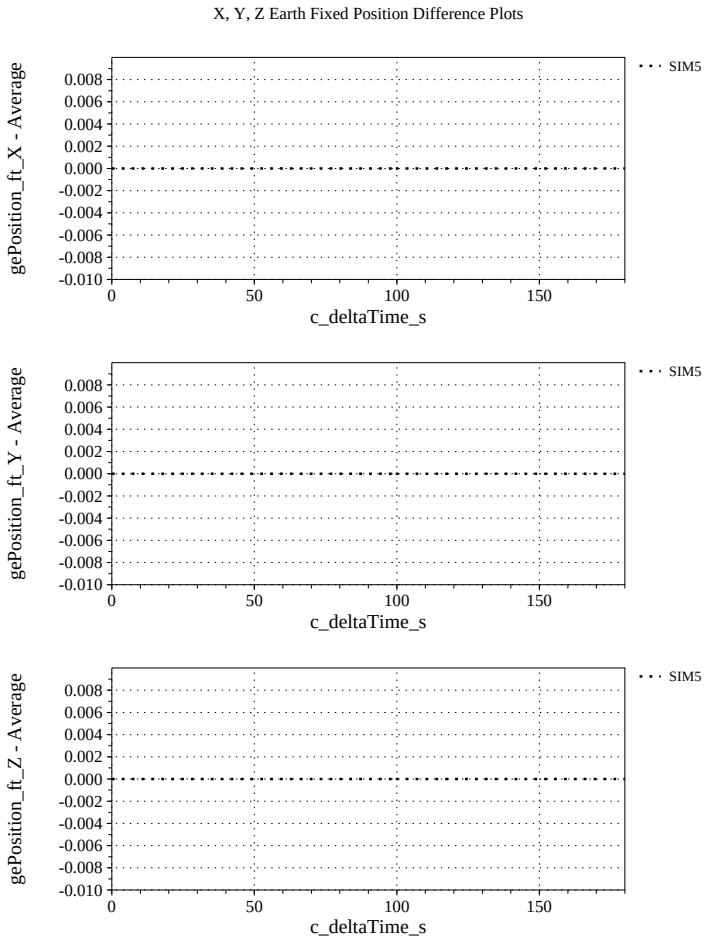

(v) Earth-centered, Earth-fixed Rectangular (X-Y-Z) Positions Differenced

Figure 27. Check-case 12: Steady Flight of a Supersonic Aircraft; See Discussion in Section D.1.12 (Cont'd)

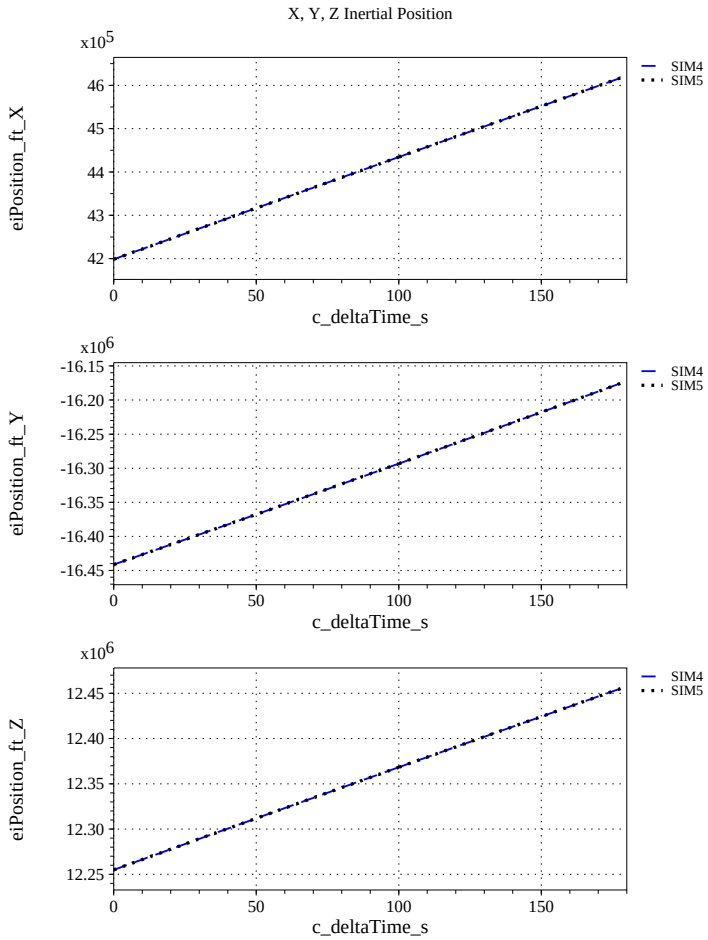

(w) Earth-centered Inertial Rectangular (x-y-z) Positions Compared

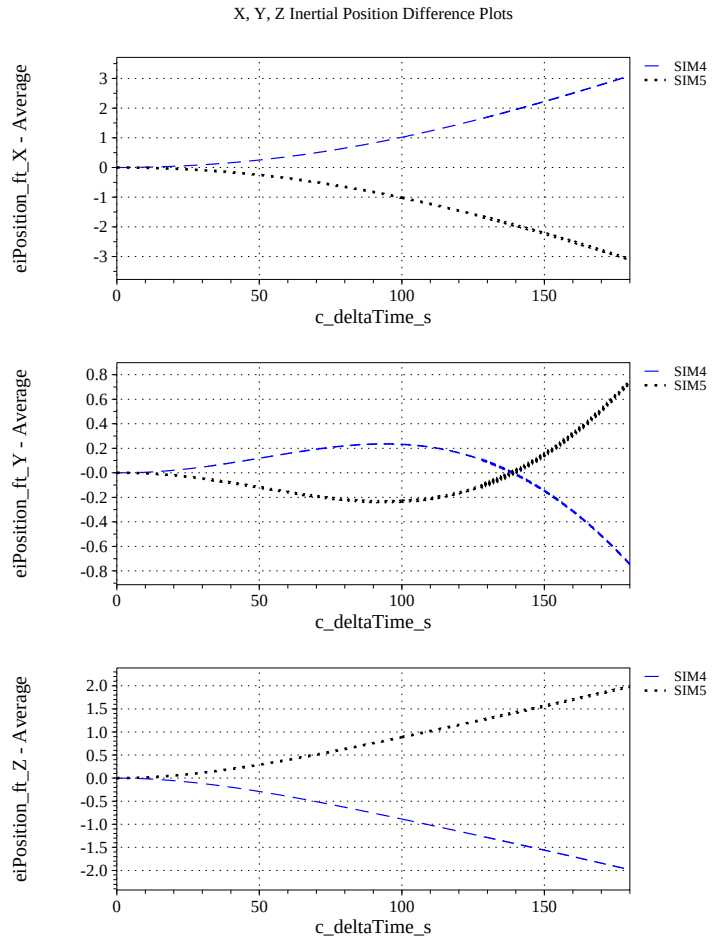

(x) Earth-centered Inertial Rectangular (x-y-z) Positions Differenced

Figure 27. Check-case 12: Steady Flight of a Supersonic Aircraft; See Discussion in Section D.1.12 (Concluded)

D.1.13 Check-case 13.1 – altitude change of a subsonic aircraft

This section shows cross-plots for three of the selected simulation tools in modeling the dynamics of a subsonic aircraft performing an altitude change. This scenario is described in Section C.1.13. Figures 28a through 28x compare results between the three simulation tools, as well as the deviances of the outputs from each tool from the ensemble average value.

This check-case used the same initial conditions as "Check-case 11 – steady flight of a subsonic aircraft" (Section D.1.11) but was flown with the simple F-16 autopilot (described in Section B.1.5) engaged and commanded to perform an altitude change of +100 ft at $t = 5$ sec. Furthermore, the simulation duration was shortened to 20 sec. The contributors to differences identified in atmospheric check-case 11 were also contributors to differences here. However, the autopilot quickly reduced their effect on differences in velocity and vehicle trajectory. Nevertheless, just as the equilibrium solvers resolved to different initial states due to these contributors, the autopilot arrived at different steady-state solutions among the simulations. Specifically, SIM 2 used the geocentric frame as the local vertical and, as a result, experienced a gravity vector that was deflected from the normal by the difference between geocentric and geodetic latitude, as described in check-case 11. In this scenario, the difference was 0.18 degrees. As a result, the steady-state conditions achieved with the autopilot engaged has the following differences between SIM 2 and SIM 4/5:

- SIM 2 settled to an orientation that differed slightly from that of SIM 4 and SIM 5 because a steady-state solution was required to partly align the body z-axis with the deflected gravity vector. Thus, the roll angle settled to a value different from SIM 4/5 by −0.14 degrees, but this was a slight improvement over the initial difference in roll angle of −0.17 degrees. The yaw angle settled to a smaller difference between simulations of 0.018 degrees. The pitch angle difference, however, was nearly zero at −0.003 degrees. (See Figure 28g.)
- The steady-state aerodynamic forces for SIM 2 included a small side force of 3.3 lbf and a reduced lift of −1.1 lbf in comparison to SIM 4 and 5. Furthermore, the steady-state solution created a small aerodynamic yawing moment at the MRC to counteract the moment at the CM induced by the aerodynamic side force.

As in atmospheric check-cases 11 (Section D.1.11) and 12 (Section D.1.12), the initial magnitude of the gravitation vector differed from the other two simulations by 1.8×10^{-4} ft/s^2, indicating a possible difference in the computation of the geocentric radial and geocentric latitude used to compute gravitation (see Figure 28i). However, no significant contribution to differences in the vehicle dynamics was expected from the difference in the magnitude of gravitation as it only added 0.11 lbf to the weight of the vehicle.

There are two reasons why the autopilot's steady-state solution differed in some respects from the equilibrium solution at $t = 0$. First, SIM 2 constrained the equilibrium solver to an inertial angular rate of zero. The autopilot solution is free to reach a solution where the Earth-relative angular rate is zero (instead of the equilibrium solver's apparent zero inertial rate constraint). In fact, the difference in angular rate between SIM 2 and SIM 5 at $t = 20$ sec was about one quarter of the Earth's rotation rate and that residual difference may be a consequence of SIM 2 having treated the geocentric frame as the local vertical. The second reason is that the SIM 2 equilibrium solver, like that for SIM 4 and SIM 5, constrained the heading to 45°, but the autopilot heading command actually attempted to maintain ground track at 45°. The autopilot is free to allow some variance in yaw angle while counterbalancing vehicle forces. Thus, the autopilot induced sideslip by both rolling and yawing the vehicle whereas the equilibrium solution induced sideslip through roll angle alone.

As in atmospheric check-cases 11 (Section D.1.11) and 12 (Section D.1.12), SIM 2 recorded aerodynamic moments at the MRC while the other two simulations recorded aerodynamic moments at the vehicle CM.

Therefore, Figure 28q shows positive aerodynamic pitching and yawing moments for SIM 2 while the moments for SIM 4 and 5 are nearly zero.

The introduction of the autopilot control generated some smaller contributions to the differences among simulations. In the control law implementation, the eventual steady-state of the vehicle was a balance achieved between the competing objectives of the autopilot and the LQR stability controller. The LQR stability controller attempted to keep the vehicle in the neighborhood of a trim state defined by predetermined values for unperturbed throttle, longitudinal stick, angle of attack, pitch attitude, and airspeed, while the autopilot outer-loop controller attempted to follow commands for altitude, airspeed, and ground track.

The F-16 control law documentation (Section B.1.5) included inputs to update the default trim values for the throttle and longitudinal stick with values computed by the simulation's equilibrium solver. But it was also possible to replace the hard-coded reference state values for angle of attack, pitch attitude, and airspeed with values calculated by the equilibrium solver in the LQR algorithm as well. All the simulations provided values for trimmed throttle and longitudinal stick. But, only SIM 5 replaced the hard-coded LQR reference state values for angle of attack, pitch attitude, and airspeed. Thus, small differences in autopilot results could arise with differences in the modification of the trim values used internally by the LQR controller.

One such difference was the difference in velocity predicted by SIM 4 and SIM 5 (see Figure 28l). Upon engaging the autopilot at the start of the simulation, SIM 4 exhibited an immediate reduction in airspeed of -0.11 ft/s. This reduction was caused by the difference between the internal LQR state reference value of 287.8 KEAS and the trim solver's speed of 287.98 KEAS, a difference of almost 0.30 ft/s. The combined inner- and outer-loop control law found a balance between the commanded airspeed and the internal reference value by approximately splitting the difference. This velocity difference persisted for the remainder of the run and accounted for nearly all of the 2.5-ft horizontal position difference between SIM 4 and SIM 5 at the end of the simulated maneuver ($t = 20$ sec).

The gravity and initial angular rate differences in SIM 2, described above, injected enough change into the autopilot solution that it is not possible to identify the contribution, if any, caused by differences between SIM 2 trimmed and LQR internal state values to differences in velocity and position. Nevertheless, under control of the autopilot, the difference in trajectory for SIM 2 shrank considerably compared to open-loop flight in atmospheric check-case 11 (Section D.1.11). The position difference between SIM 2 and SIM 5 after 20 sec is 19 ft based on the recorded differences in latitude, longitude, and altitude (Figure 28e). In any case, the autopilot succeeded in making the 100-ft altitude change under all the simulations while keeping the airspeed and track angle close to the commanded values.

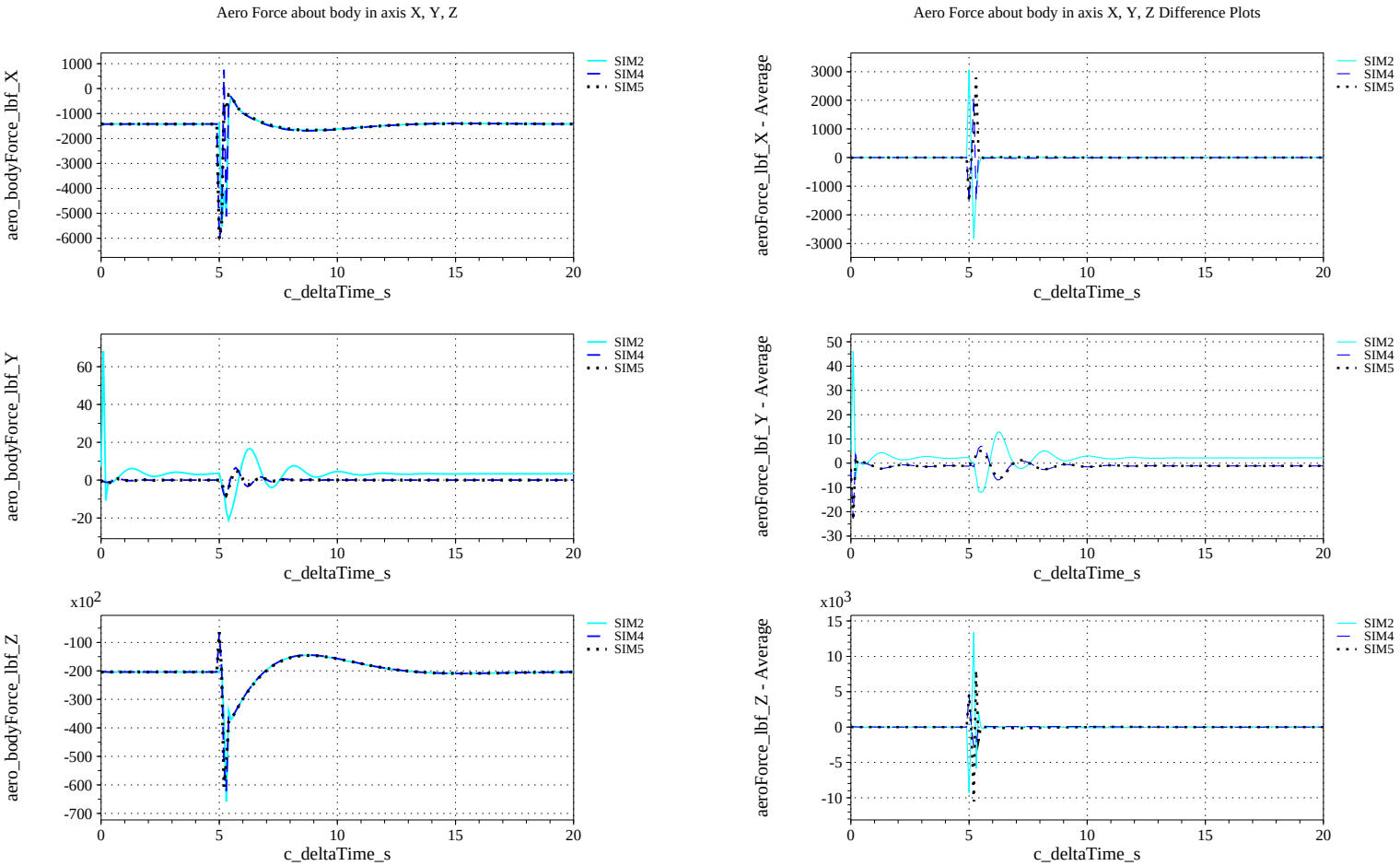

(a) Aerodynamic Forces Compared

(b) Aerodynamic Forces Differenced

Figure 28. Check-case 13.1: Altitude Change of a Subsonic Aircraft; See Discussion in Section D.1.13

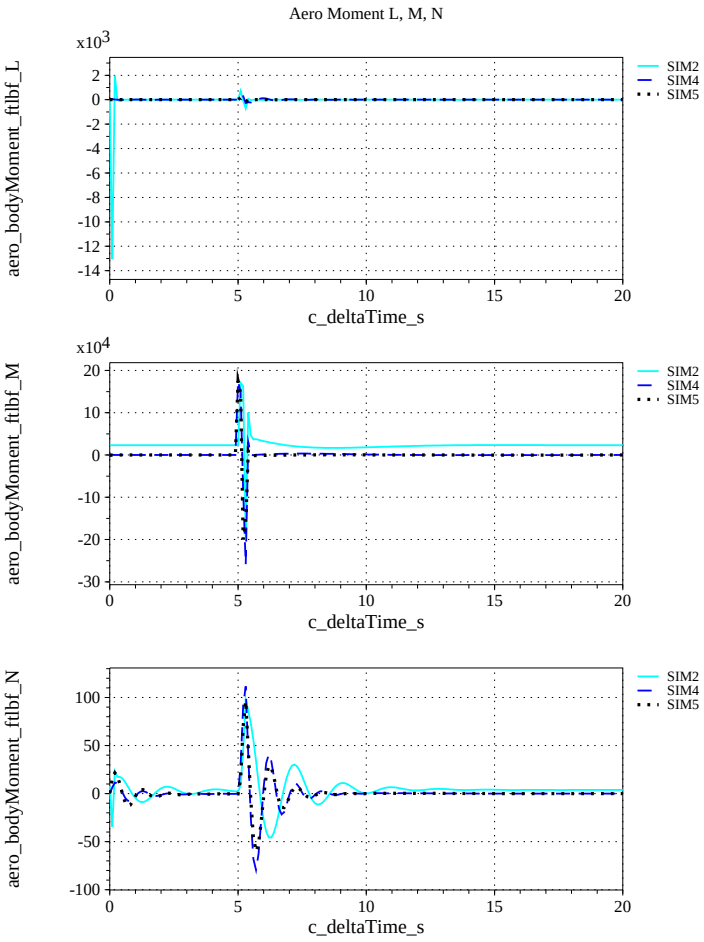

(c) Aerodynamic Moments Compared

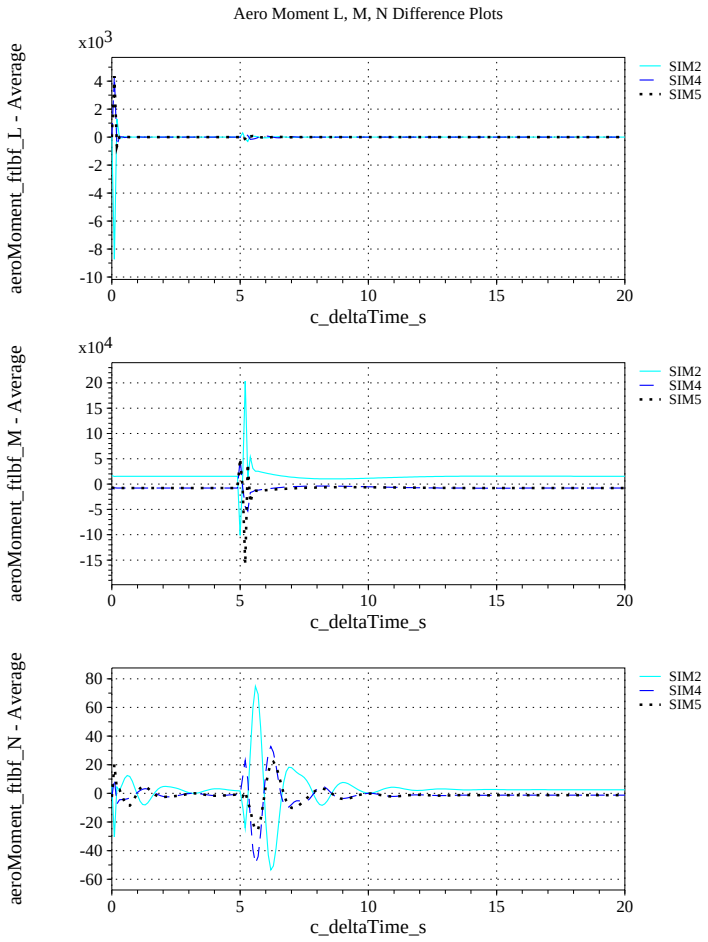

(d) Aerodynamic Moments Differenced

Figure 28. Check-case 13.1: Altitude Change of a Subsonic Aircraft; See Discussion in Section D.1.13 (Cont'd)

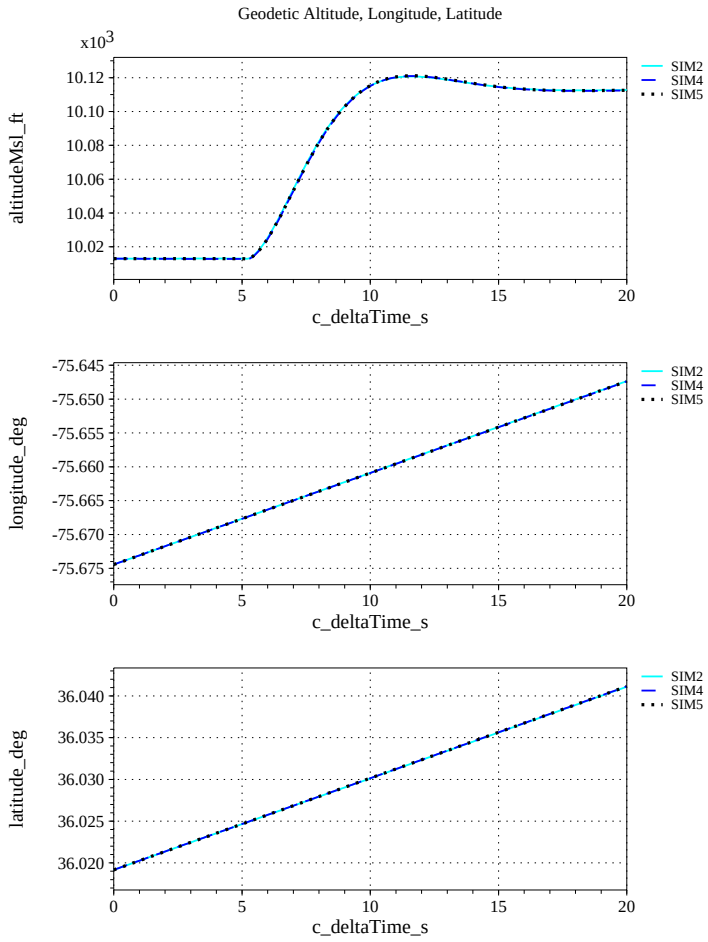

(e) Altitude, Geodetic Latitude and Longitude Compared

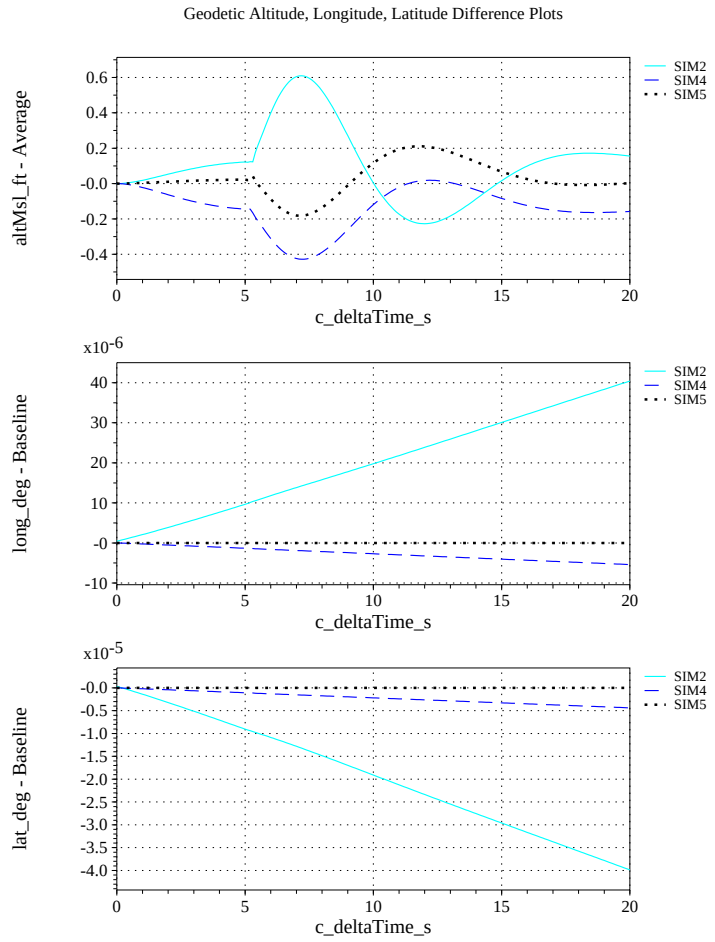

(f) Altitude, Geodetic Latitude and Longitude Differenced

Figure 28. Check-case 13.1: Altitude Change of a Subsonic Aircraft; See Discussion in Section D.1.13 (Cont'd)

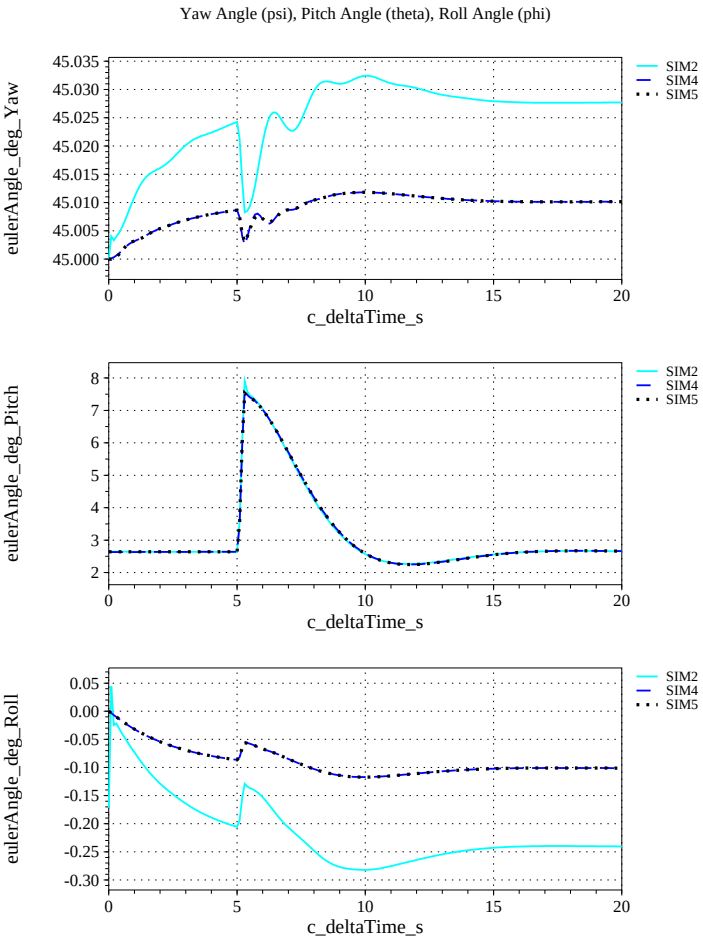

(g) Euler Angles (w.r.t. NED Frame) Compared

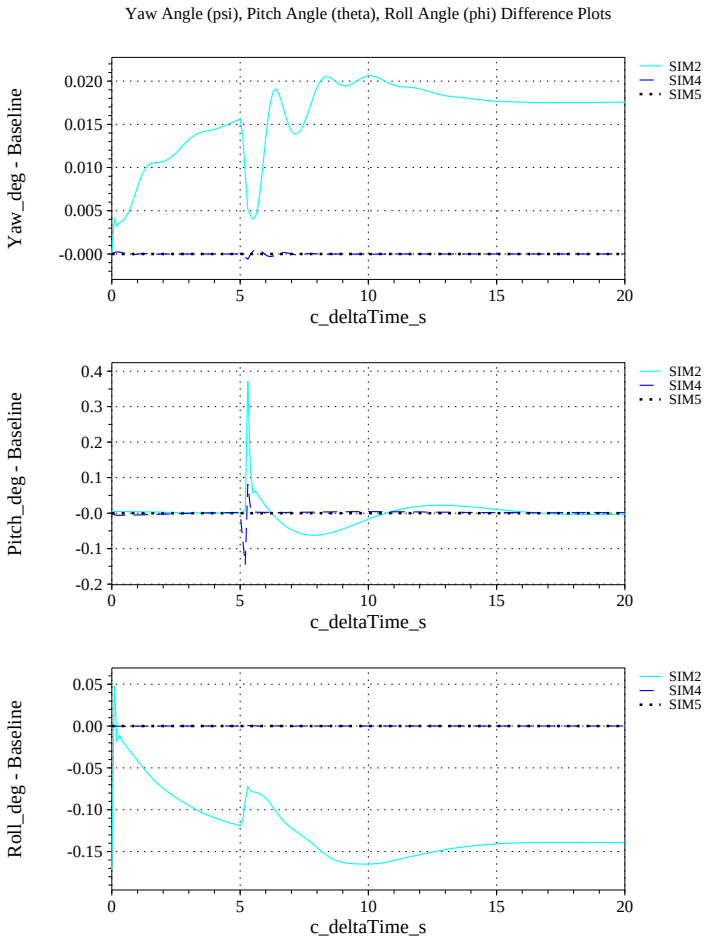

(h) Euler Angles (w.r.t. NED Frame) Differenced

Figure 28. Check-case 13.1: Altitude Change of a Subsonic Aircraft; See Discussion in Section D.1.13 (Cont'd)

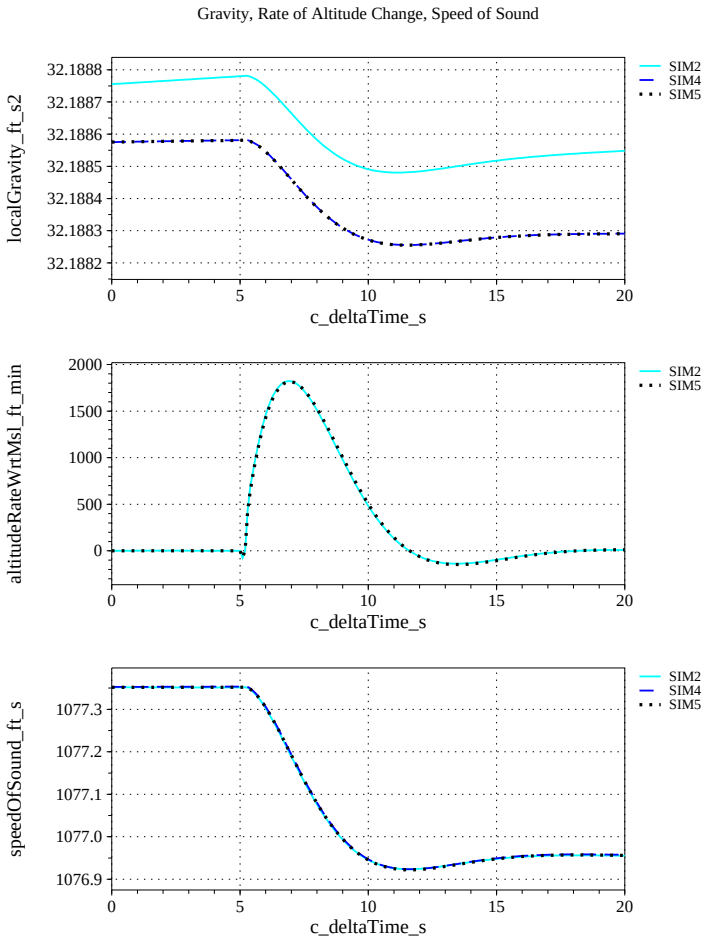

(i) Gravity, Climb Rate, and Speed-of-sound Compared

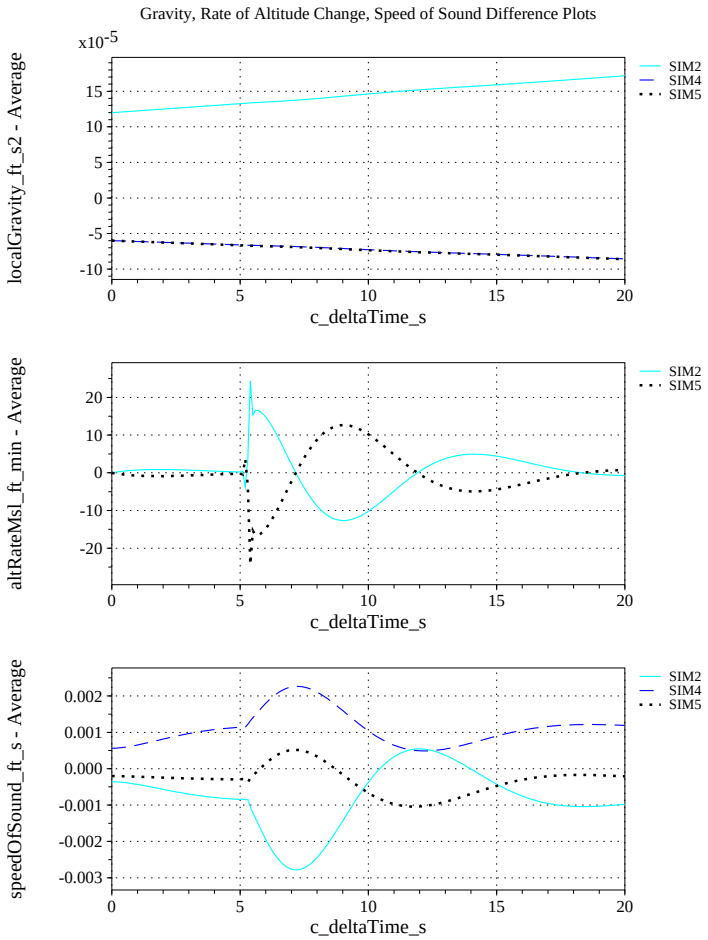

(j) Gravity, Climb Rate, and Speed-of-sound Differenced

Figure 28. Check-case 13.1: Altitude Change of a Subsonic Aircraft; See Discussion in Section D.1.13 (Cont'd)

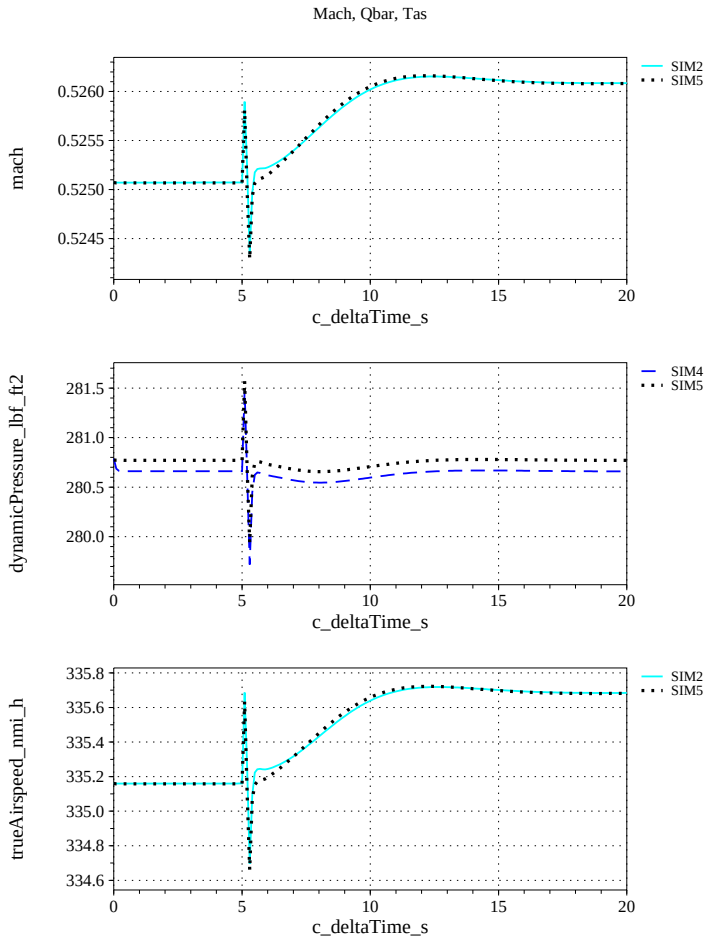

(k) Mach, Dynamic Pressure, and True Airspeed Compared

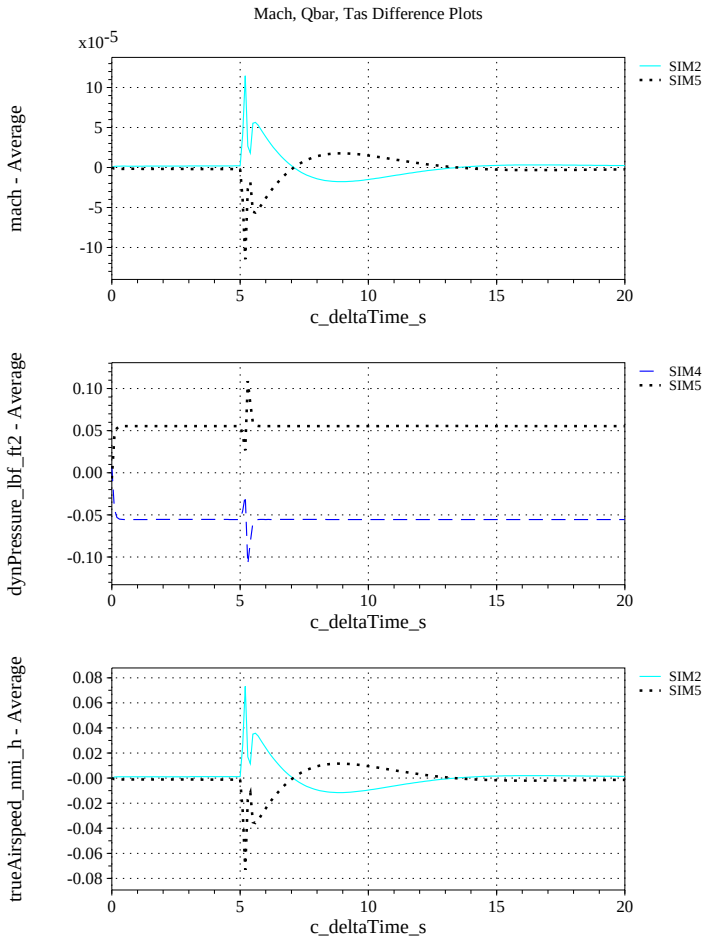

(l) Mach, Dynamic Pressure, and True Airspeed Differenced

Figure 28. Check-case 13.1: Altitude Change of a Subsonic Aircraft; See Discussion in Section D.1.13 (Cont'd)

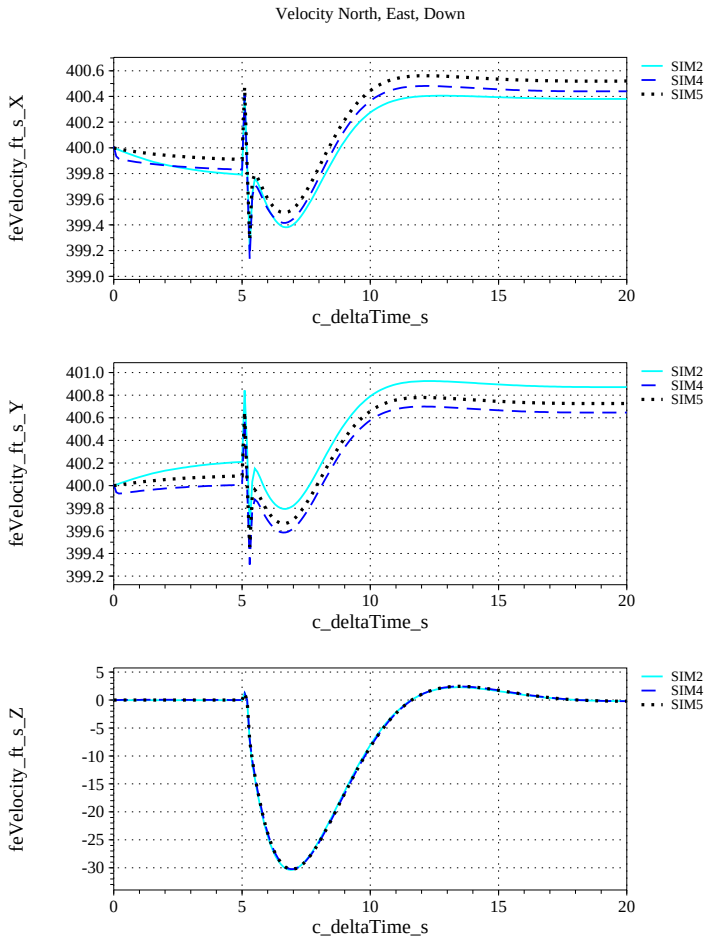

(m) NED Velocities Compared

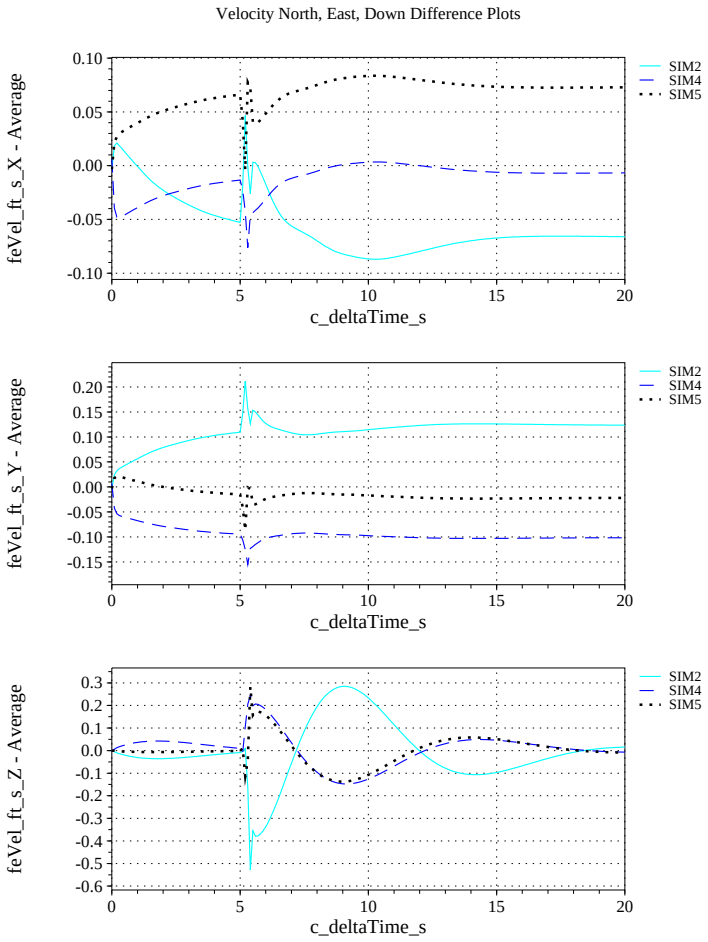

(n) NED Velocities Differenced

Figure 28. Check-case 13.1: Altitude Change of a Subsonic Aircraft; See Discussion in Section D.1.13 (Cont'd)

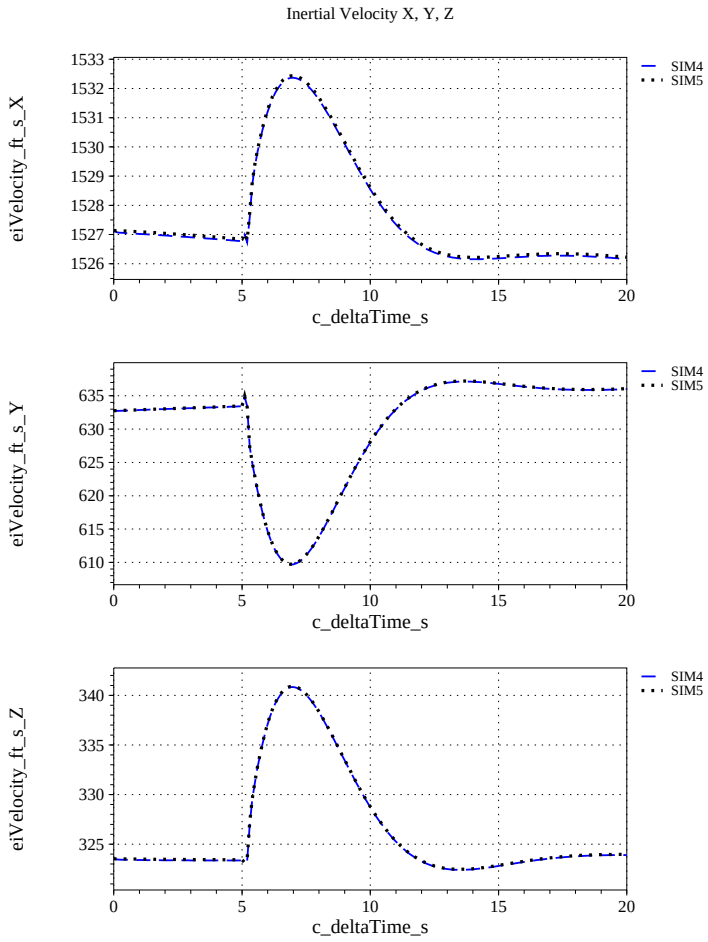

(o) Inertial Velocities Compared

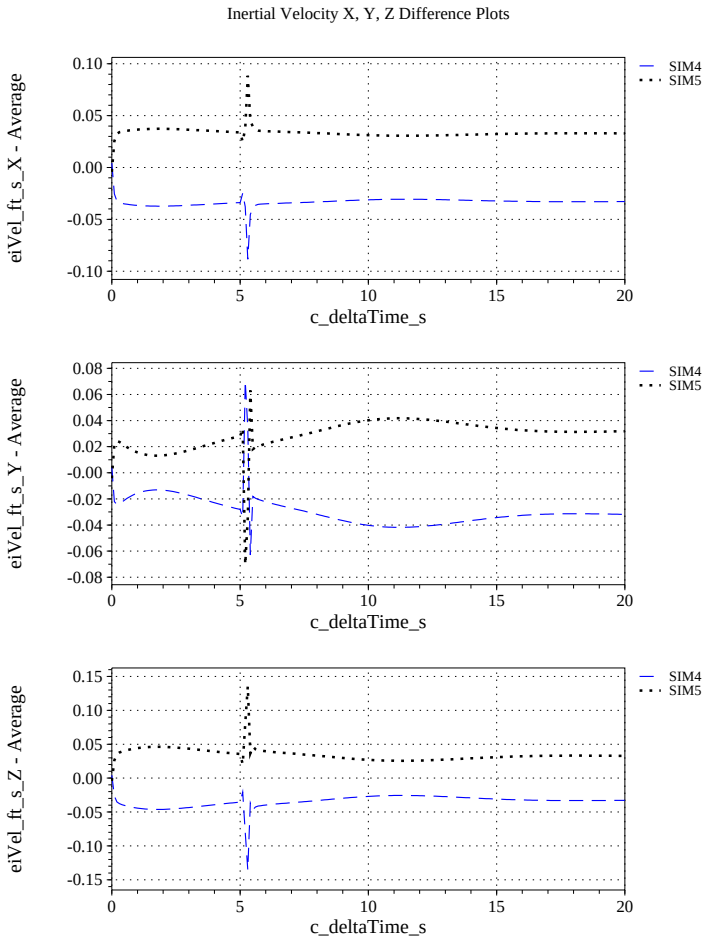

(p) Inertial Velocities Differenced

Figure 28. Check-case 13.1: Altitude Change of a Subsonic Aircraft; See Discussion in Section D.1.13 (Cont'd)

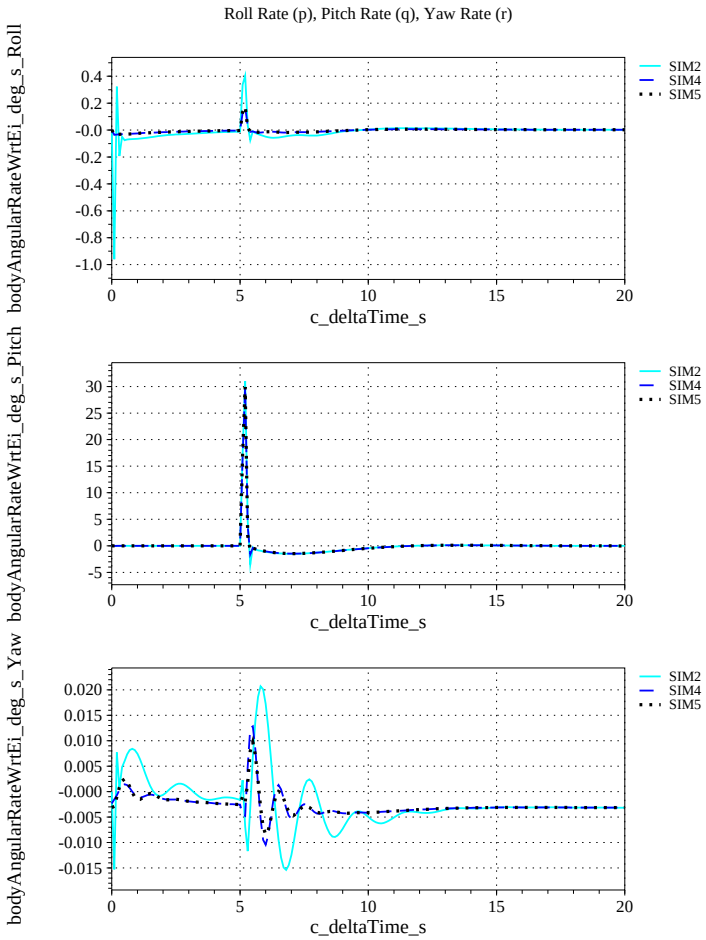

(q) Body-axis Angular Rates (w.r.t. NED Frame) Compared

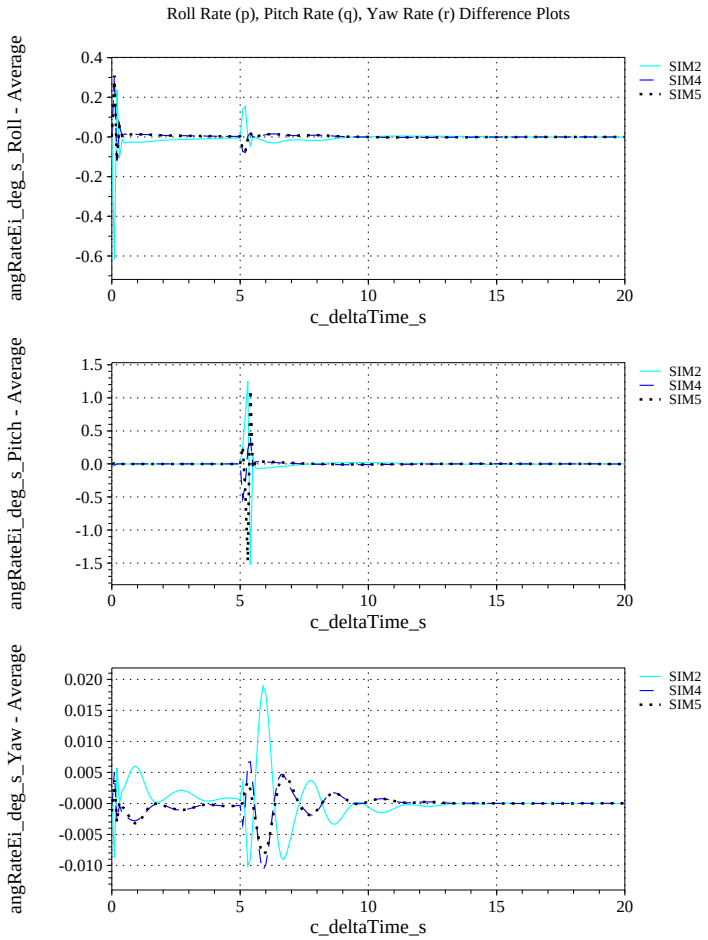

(r) Body-axis Angular Rates (w.r.t. NED Frame) Differenced

Figure 28. Check-case 13.1: Altitude Change of a Subsonic Aircraft; See Discussion in Section D.1.13 (Cont'd)

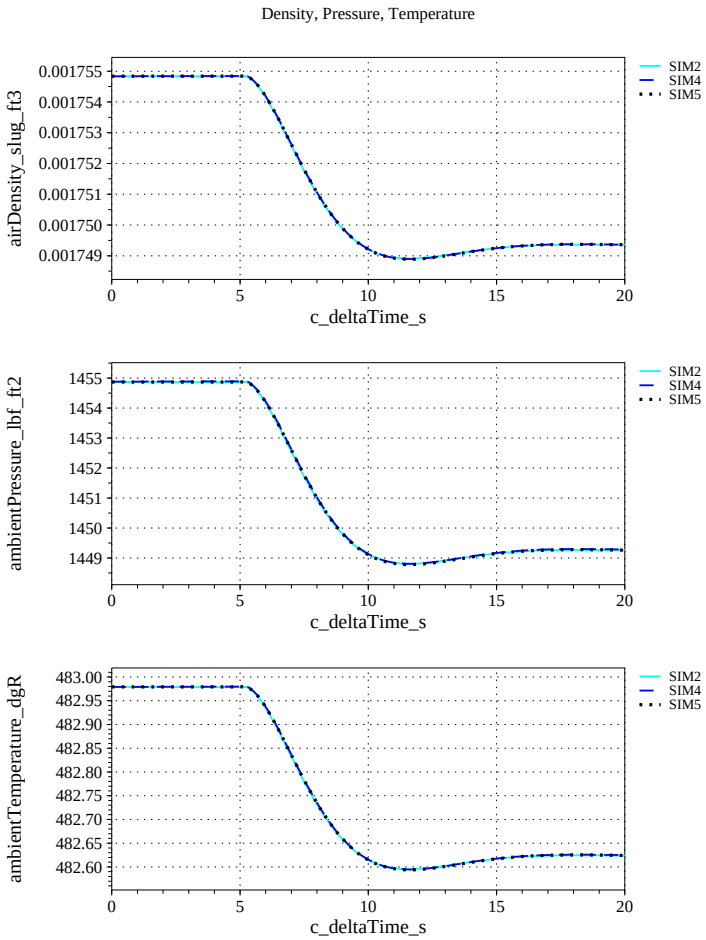

(s) Atmospheric Properties Compared

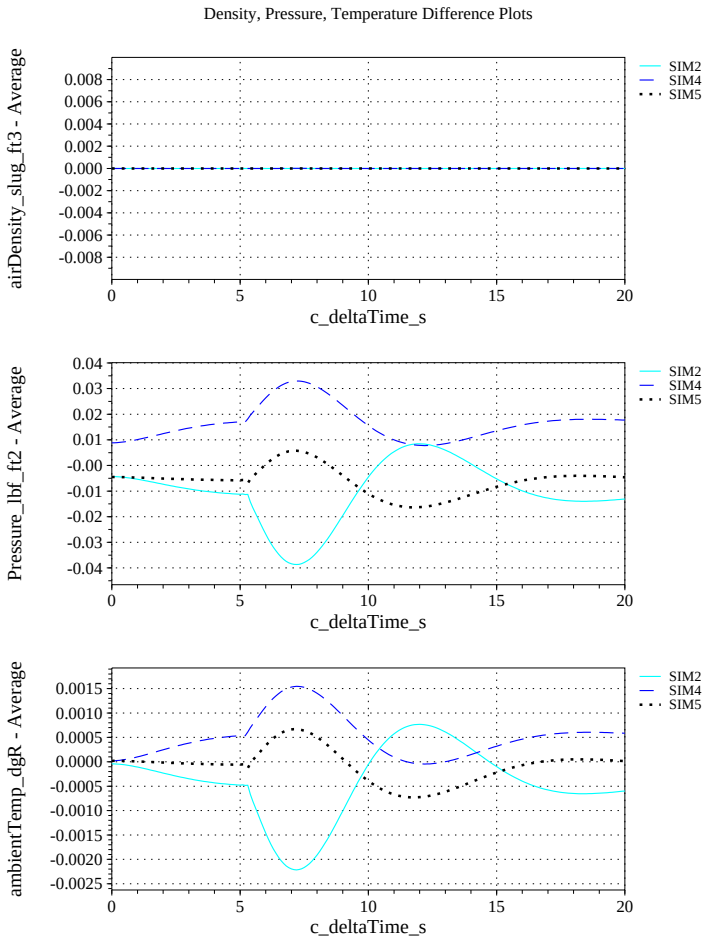

(t) Atmospheric Properties Differenced

Figure 28. Check-case 13.1: Altitude Change of a Subsonic Aircraft; See Discussion in Section D.1.13 (Cont'd)

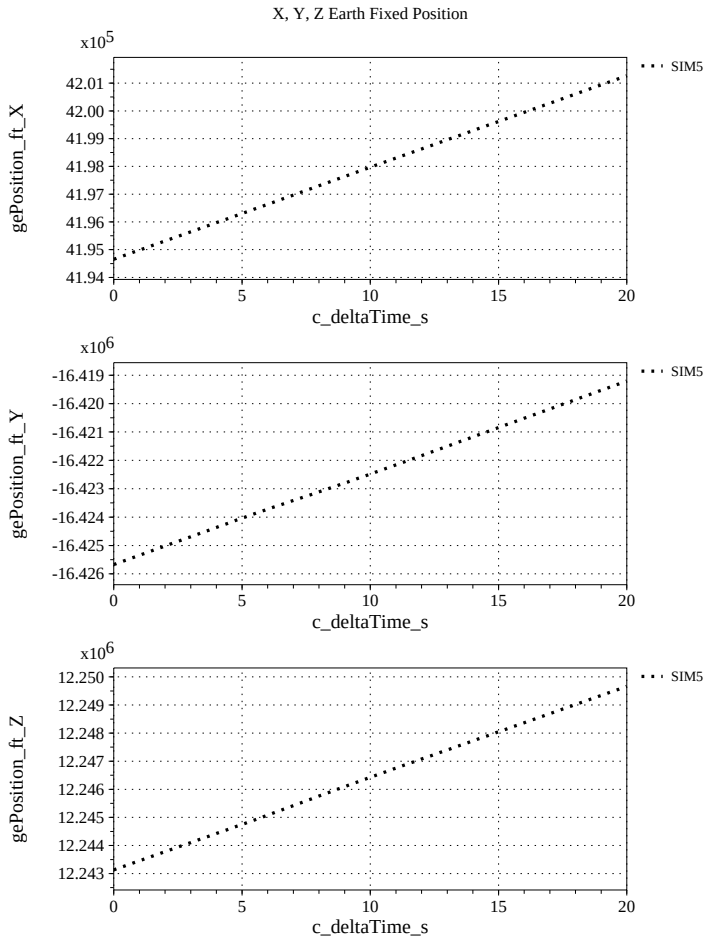

(u) Earth-centered, Earth-fixed Rectangular (X-Y-Z) Positions Compared

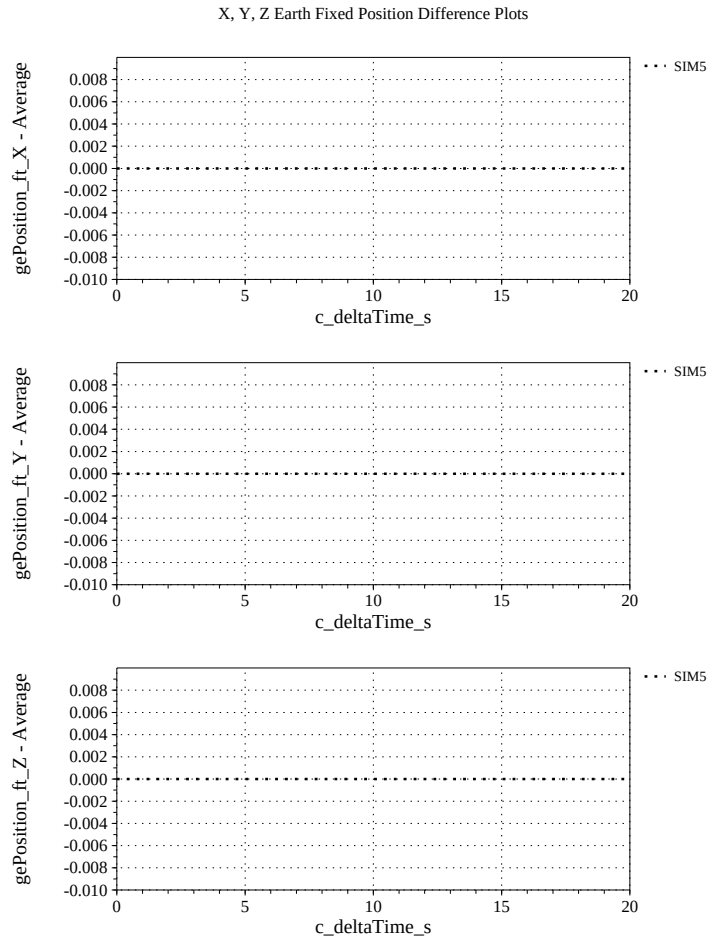

(v) Earth-centered, Earth-fixed Rectangular (X-Y-Z) Positions Differenced

Figure 28. Check-case 13.1: Altitude Change of a Subsonic Aircraft; See Discussion in Section D.1.13 (Cont'd)

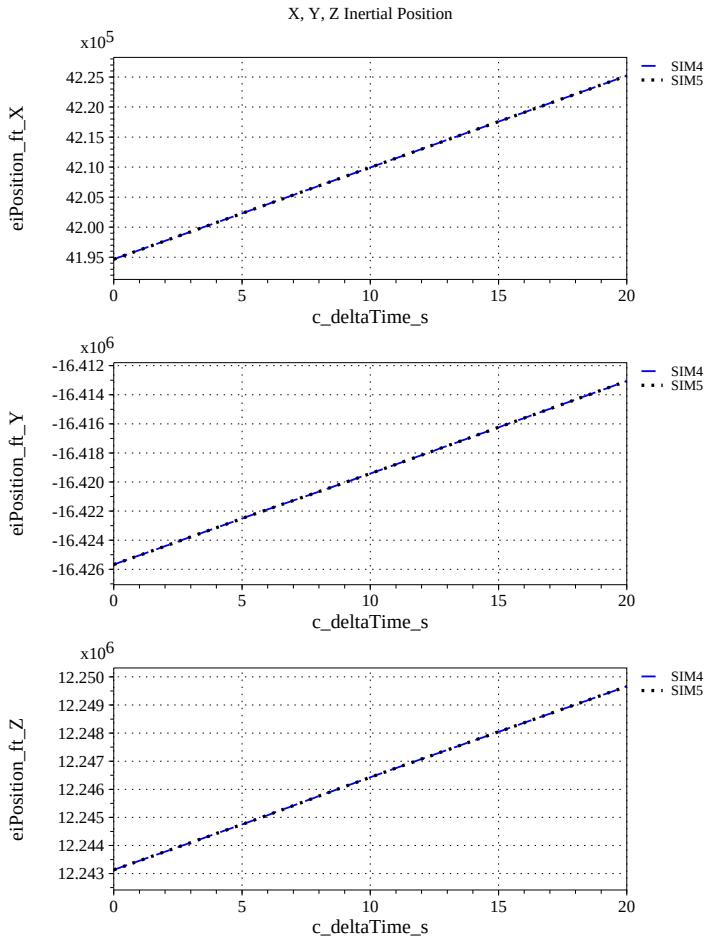

(w) Earth-centered Inertial Rectangular (x-y-z) Positions Compared

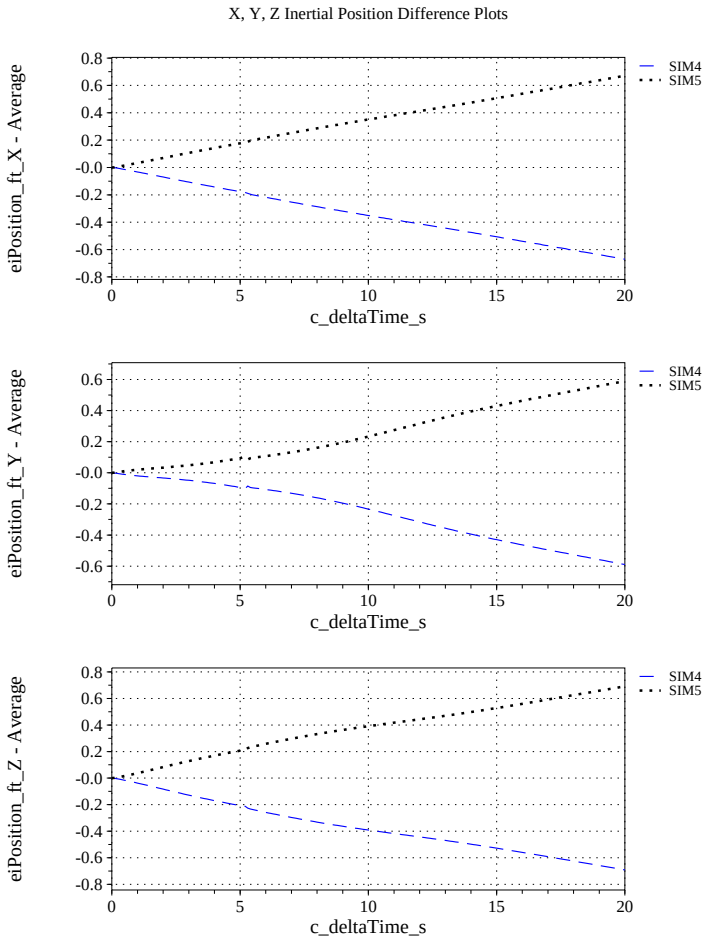

(x) Earth-centered Inertial Rectangular (x-y-z) Positions Differenced

Figure 28. Check-case 13.1: Altitude Change of a Subsonic Aircraft; See Discussion in Section D.1.13 (Concluded)

D.1.14 Check-case 13.2 – velocity change of a subsonic aircraft

This section shows cross-plots for three of the selected simulation tools in modeling the dynamics of a subsonic aircraft performing an airspeed change. This scenario is described in Section C.1.14. Figures 29a through 29x compare results between the three simulation tools, as well as the deviances of the outputs from each tool from the ensemble average value.

Atmospheric check-case 13.2 had the same starting condition as the previous check-case but replaced the altitude change maneuver with a command to decrease speed 5 kt to 282.98 KEAS at $t = 5$ sec. However, some early assessment plans conflicted with later versions on the magnitude of the change and, in initial runs, SIM 5 and SIM 2 performed speed changes twice as large. In the results presented, SIM 5 results were updated for a -5 kt speed change. But SIM 2 results have not been updated. This difference in commanded speed change is the dominant contributor to the difference in vehicle velocity and trajectory for SIM 2 after $t = 7.5$ sec. Differences among the simulations in the first few seconds were similar to those in atmospheric check-case 13.1 with the same set of contributors. Moreover, those contributors continue to explain the differences with SIM 4 and SIM 5 throughout the run:

- SIM 2 used the geocentric frame for the local vertical, leading to small non-zero values in the initial equilibrium condition in roll, angle of sideslip, and rudder deflection, as well as a slight difference in initial yaw angle.
- A different approach was taken in SIM 5 in the modification of the internal reference state values for the LQR controller for angle of attack, pitch attitude, and velocity states to match the values from the equilibrium solution for the initial conditions.
- SIM 2 recorded the aerodynamic moments at the MRC, versus at the CM for SIM 4 and 5, leading to the large differences shown in Figure 29c.
- SIM 2 differed from SIM 4 and 5 in the magnitude of the gravitation vector by 1.8×10^{-4} ft/s^2, possibly due to a different way to initialize the initial position from the specified geodetic coordinates; this is believed to have been only a minor contributor to differences in vehicle dynamics.

The larger commanded airspeed change used by SIM 2 affected more than just horizontal velocity and position. The lower speed required a larger angle of attack to maintain lift, and thus a larger pitch angle. This is likely the reason for an observed 0.185-degree difference in pitch angle for SIM 2 by the end of the run. The lower speed also induced a drop in altitude which may represent a change in the balance between the competing objectives of the autopilot and LQR controller. SIM 4 and SIM 5 lost approximately 3 ft of altitude in the course of the simulated run. SIM 2 lost about 6.6 ft of altitude (see Figure 29e).

At the end of the run, the simulated vehicles in SIM 4 and SIM 5 were separated by a distance of 2.2 ft. SIM 2's F-16 position was offset from those of SIM 4 and SIM 5 by distances of 135 ft and 137 ft, respectively.

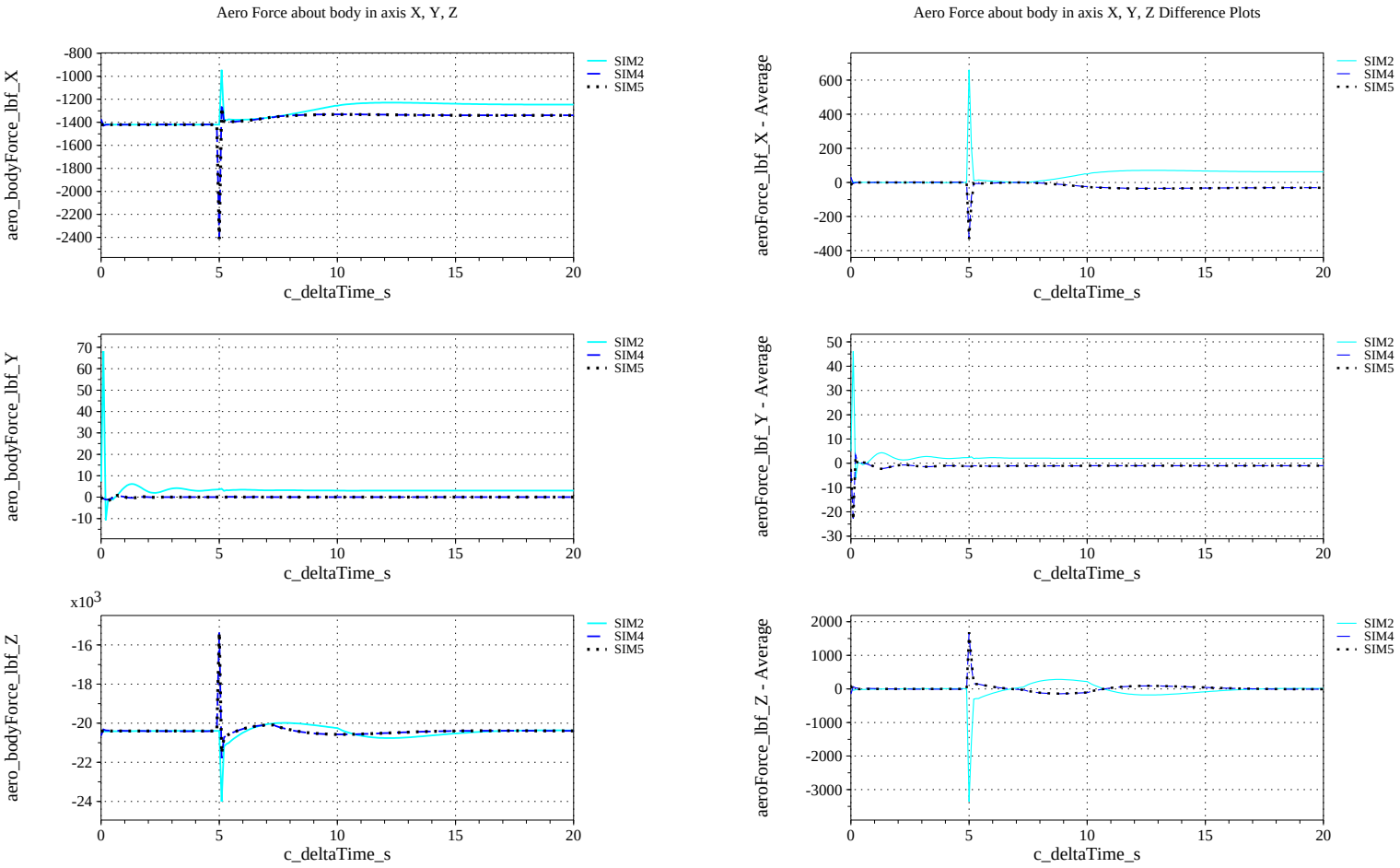

(a) Aerodynamic Forces Compared

(b) Aerodynamic Forces Differenced

Figure 29. Check-case 13.2: Velocity Change of a Subsonic Aircraft; See Discussion in Section D.1.14

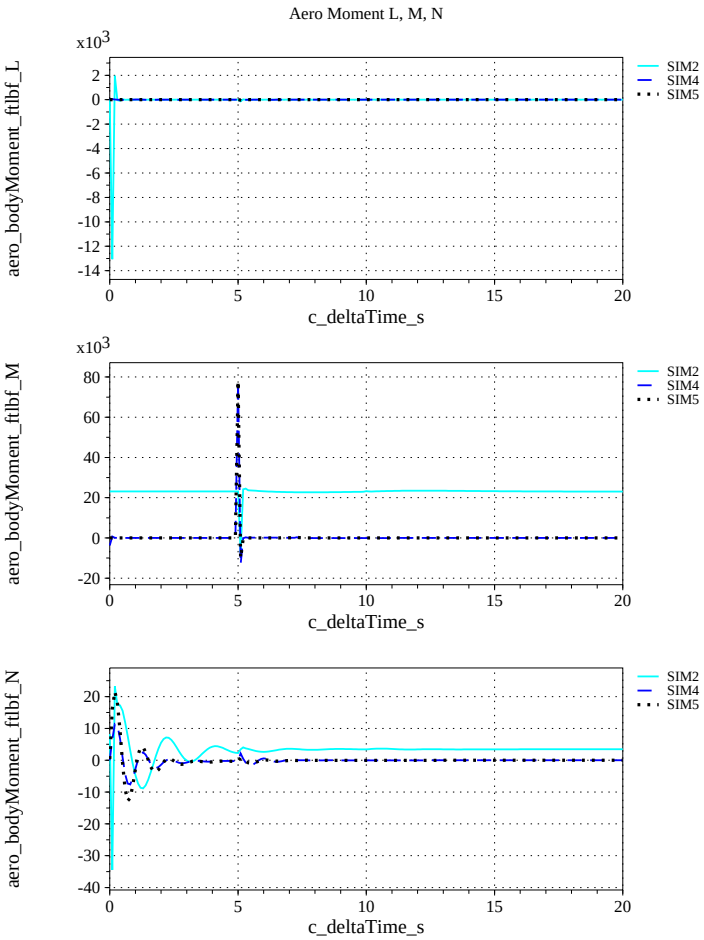

(c) Aerodynamic Moments Compared

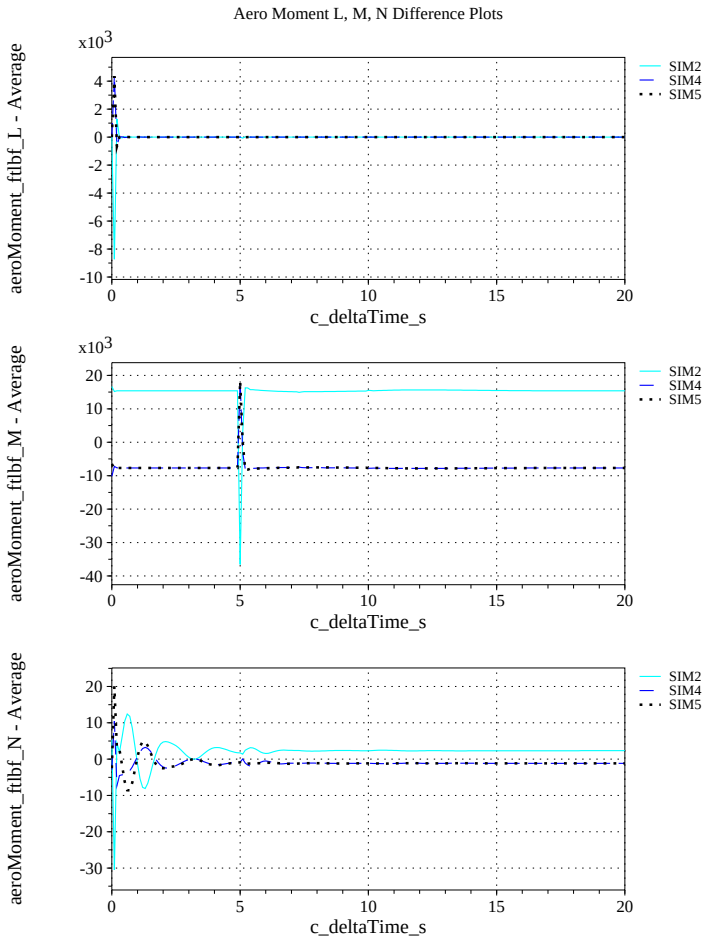

(d) Aerodynamic Moments Differenced

Figure 29. Check-case 13.2: Velocity Change of a Subsonic Aircraft; See Discussion in Section D.1.14 (Cont'd)

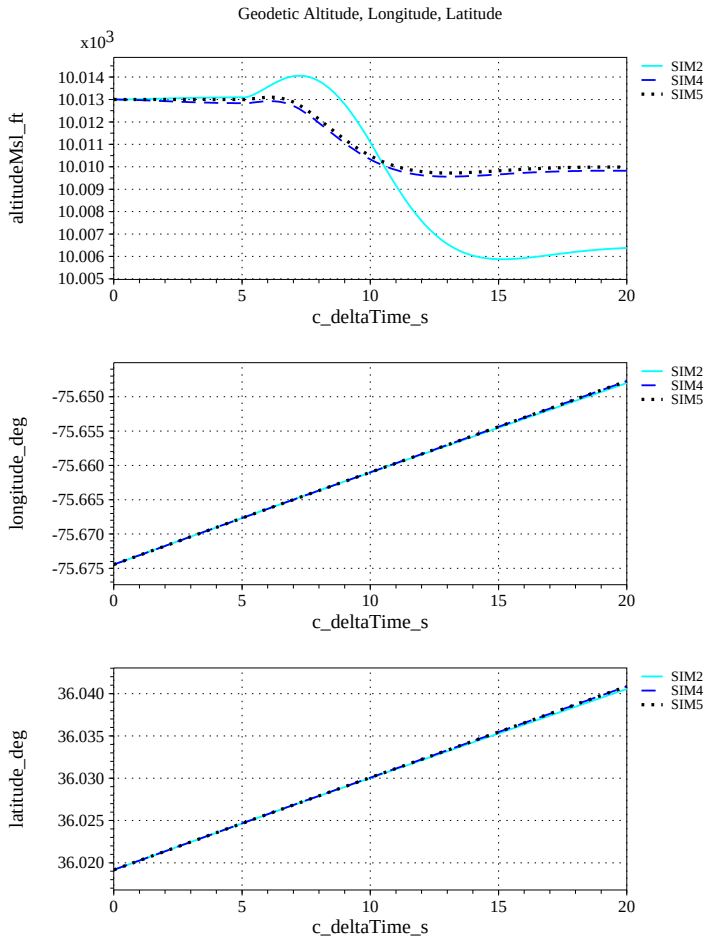

(e) Altitude, Geodetic Latitude and Longitude Compared

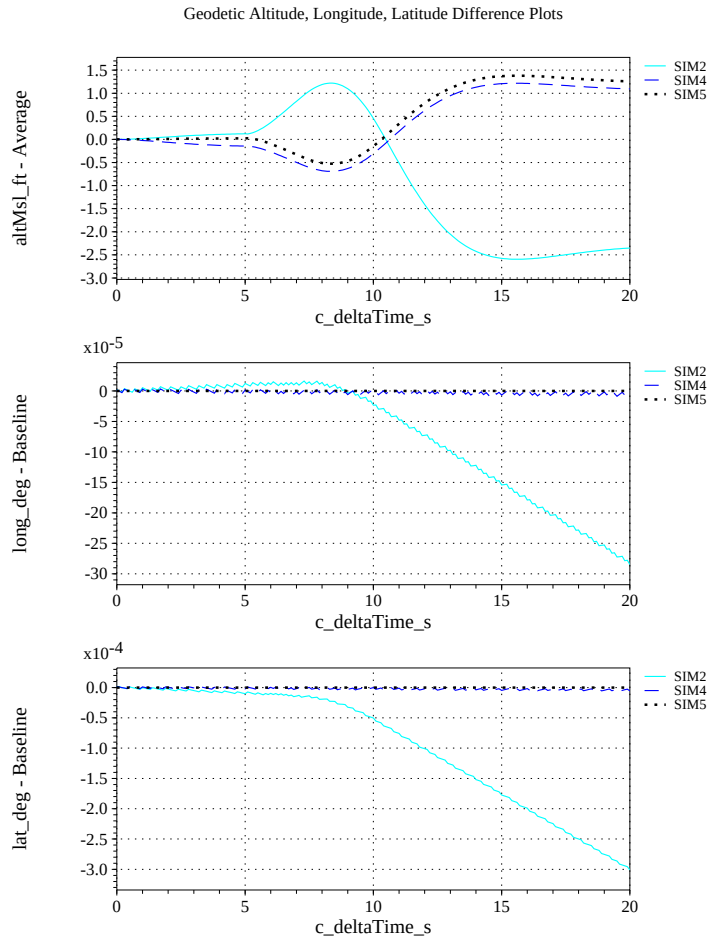

(f) Altitude, Geodetic Latitude and Longitude Differenced

Figure 29. Check-case 13.2: Velocity Change of a Subsonic Aircraft; See Discussion in Section D.1.14 (Cont'd)

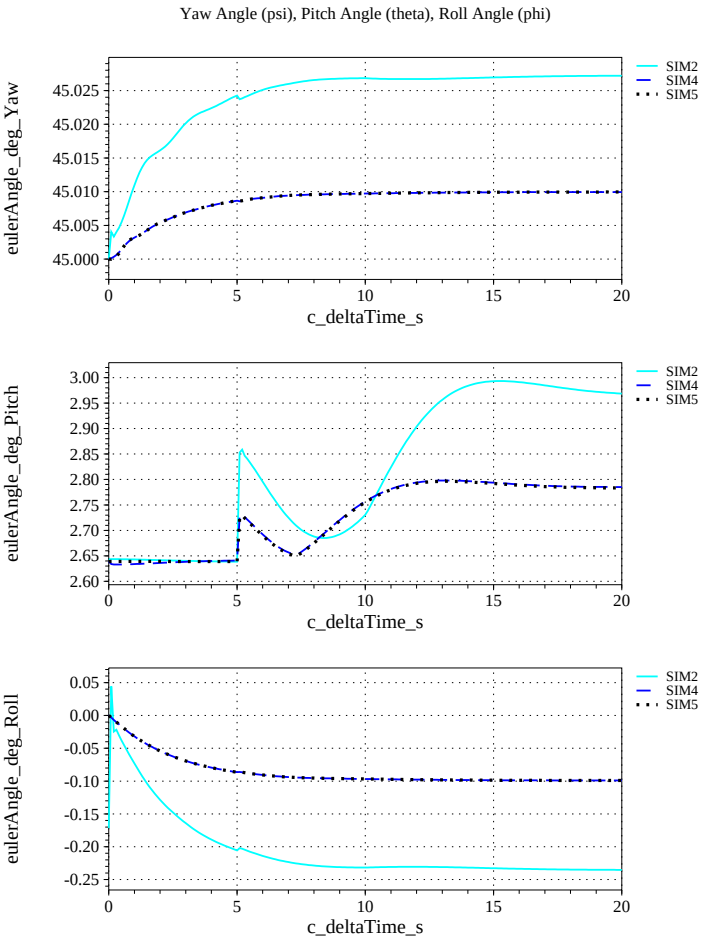

(g) Euler Angles (w.r.t. NED Frame) Compared

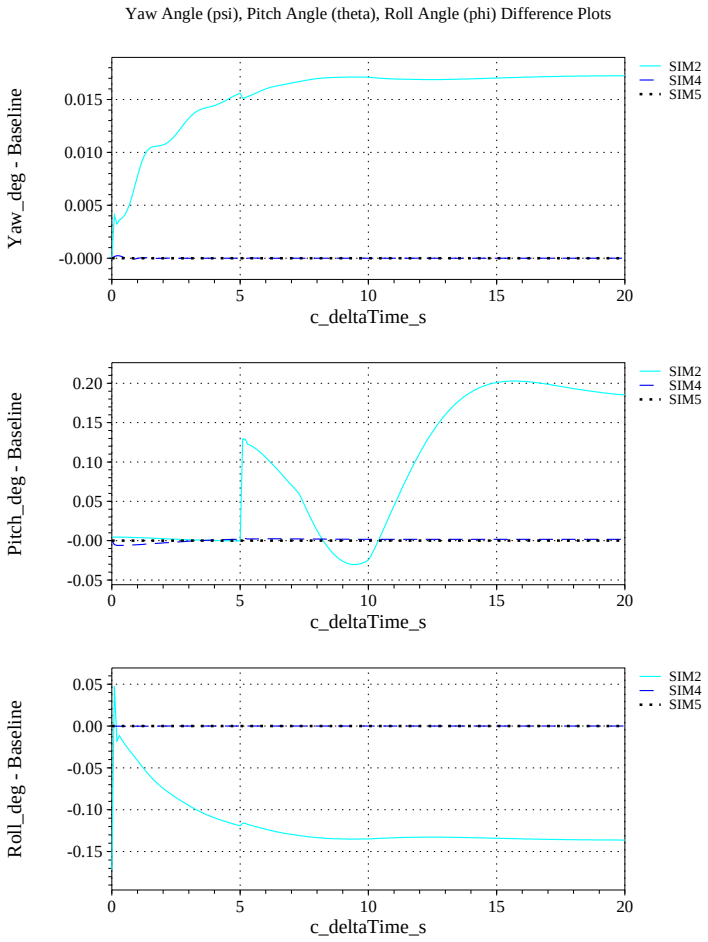

(h) Euler Angles (w.r.t. NED Frame) Differenced

Figure 29. Check-case 13.2: Velocity Change of a Subsonic Aircraft; See Discussion in Section D.1.14 (Cont'd)

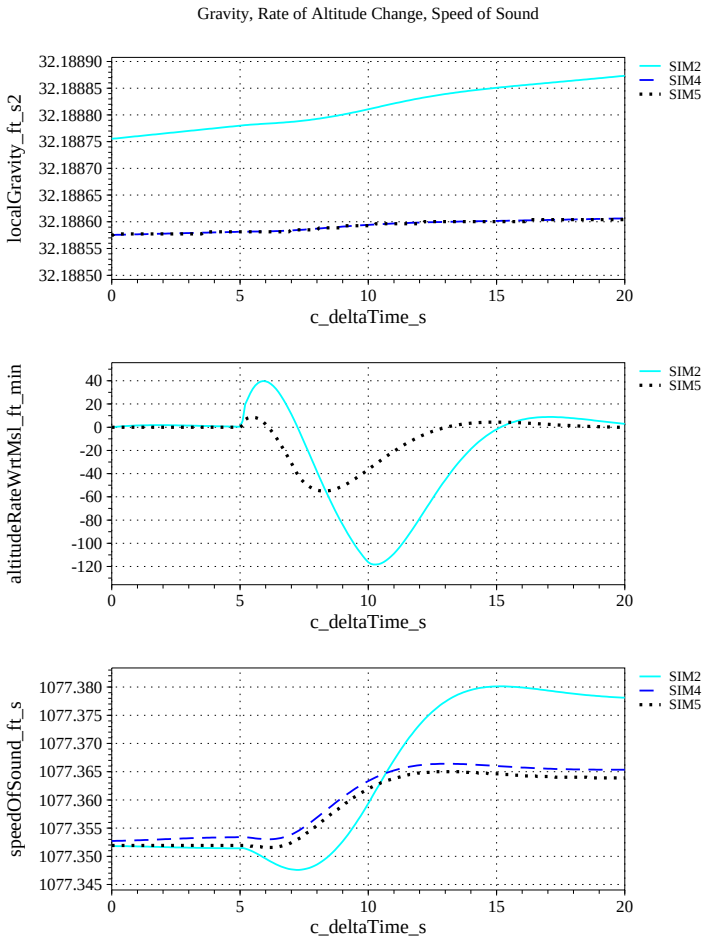

(i) Gravity, Climb Rate, and Speed-of-sound Compared

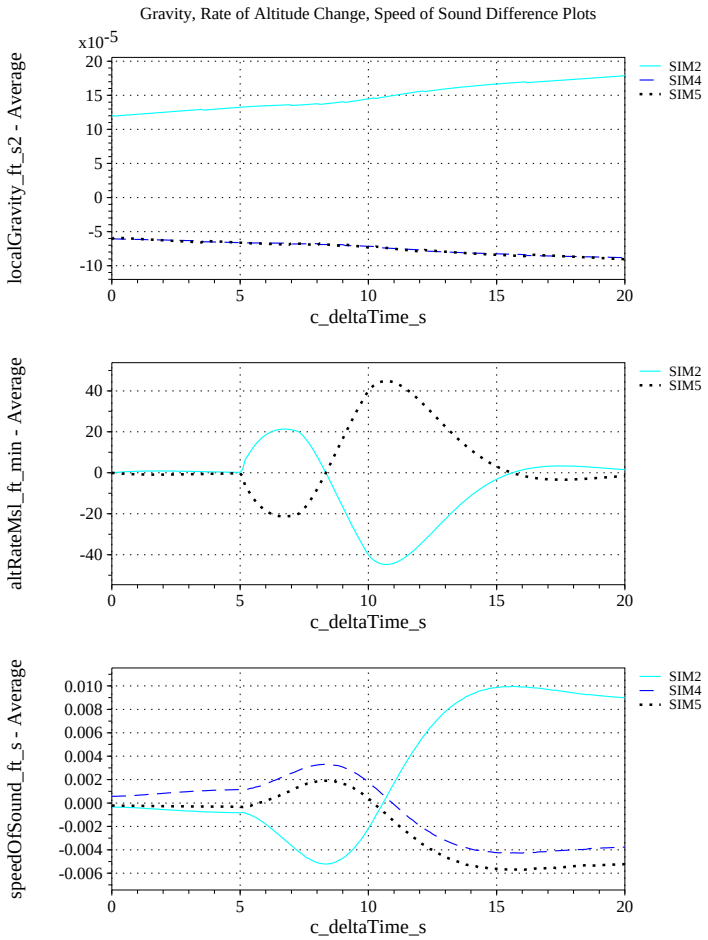

(j) Gravity, Climb Rate, and Speed-of-sound Differenced

Figure 29. Check-case 13.2: Velocity Change of a Subsonic Aircraft; See Discussion in Section D.1.14 (Cont'd)

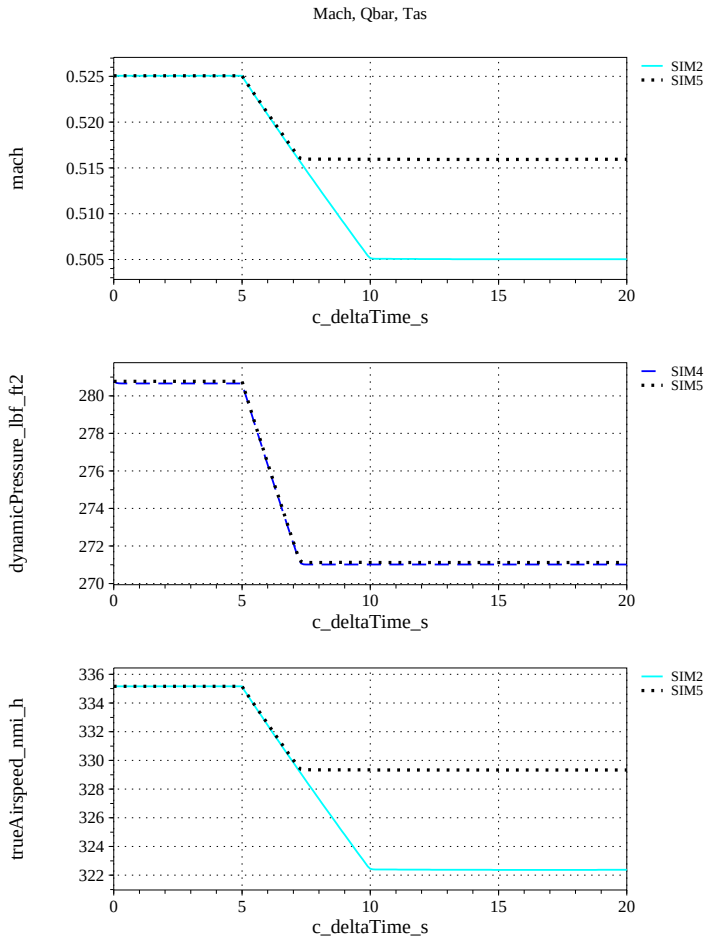

(k) Mach, Dynamic Pressure, and True Airspeed Compared

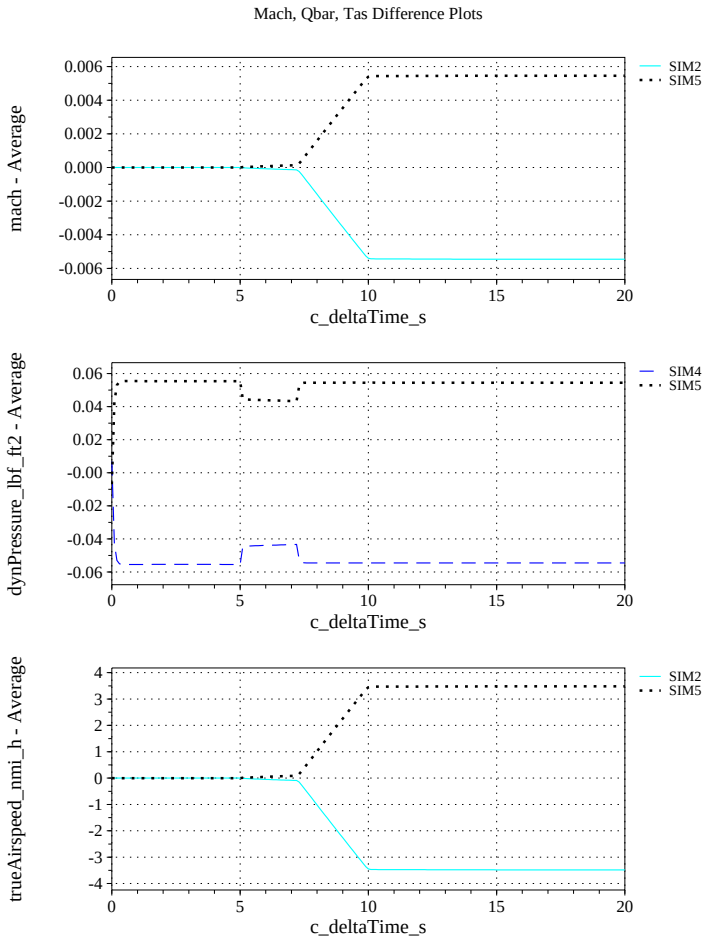

(l) Mach, Dynamic Pressure, and True Airspeed Differenced

Figure 29. Check-case 13.2: Velocity Change of a Subsonic Aircraft; See Discussion in Section D.1.14 (Cont'd)

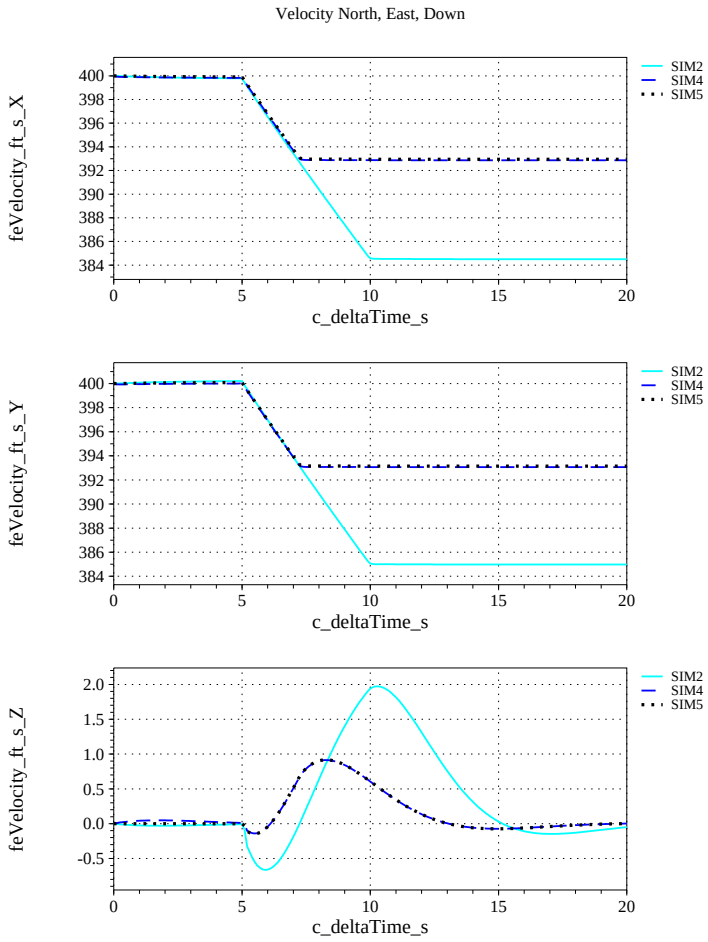

(m) NED Velocities Compared

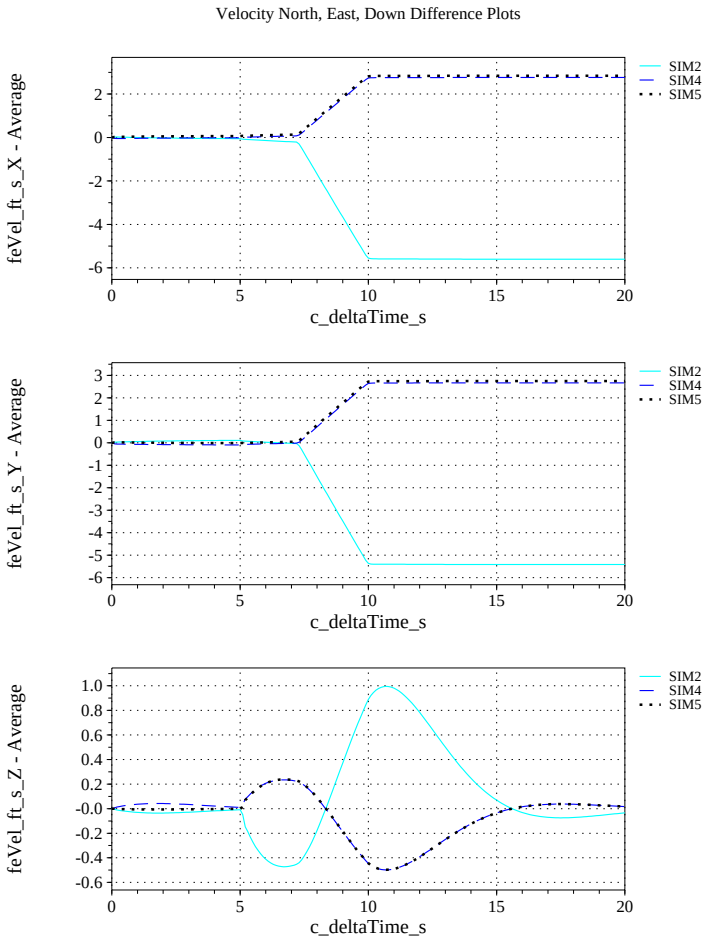

(n) NED Velocities Differenced

Figure 29. Check-case 13.2: Velocity Change of a Subsonic Aircraft; See Discussion in Section D.1.14 (Cont'd)

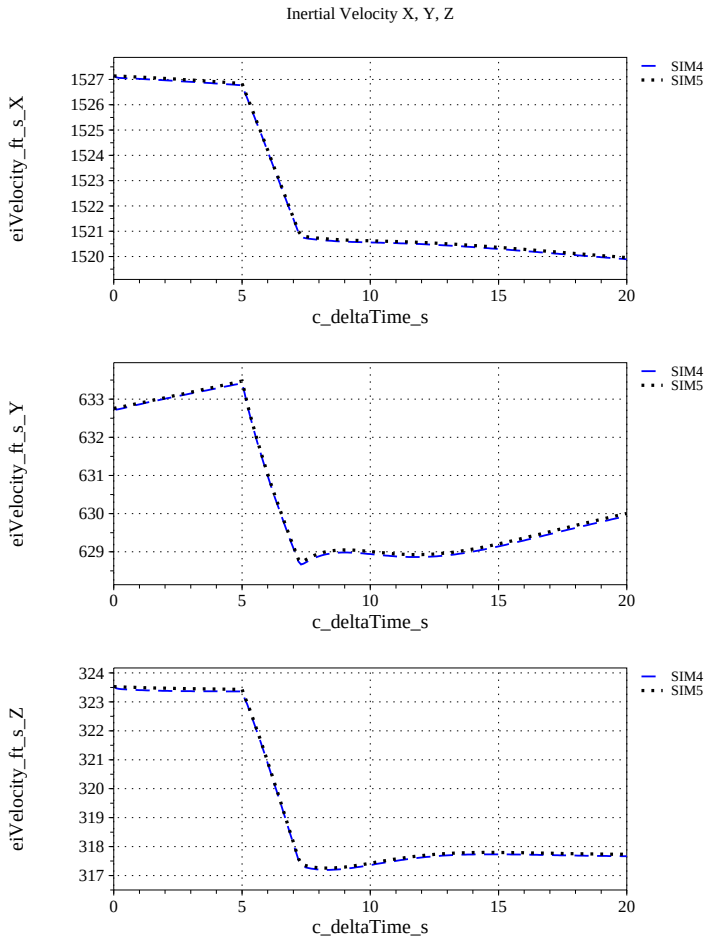

(o) Inertial Velocities Compared

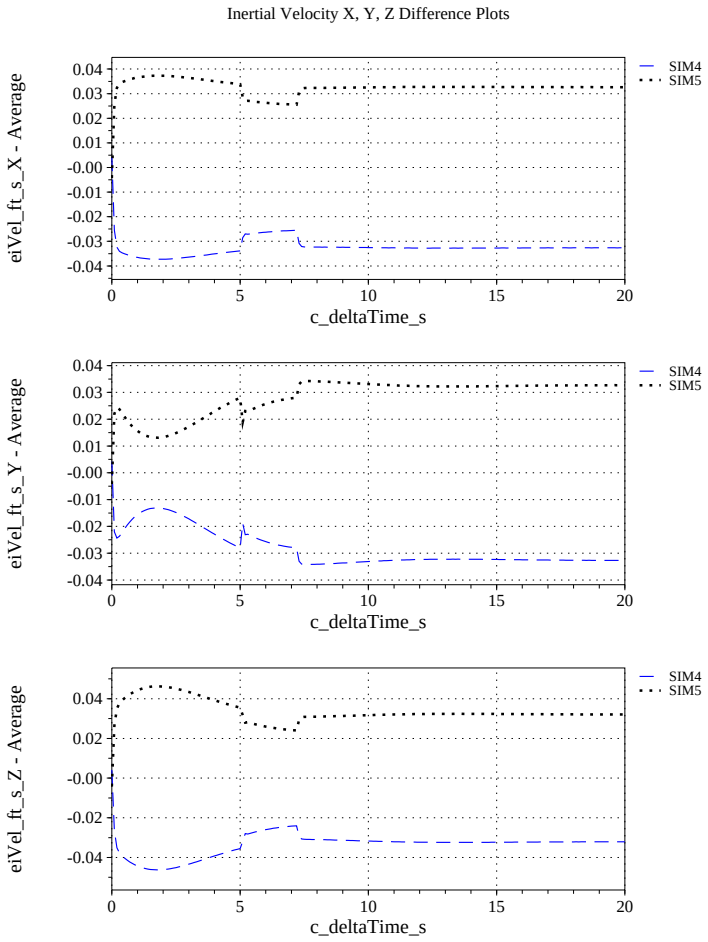

(p) Inertial Velocities Differenced

Figure 29. Check-case 13.2: Velocity Change of a Subsonic Aircraft; See Discussion in Section D.1.14 (Cont'd)

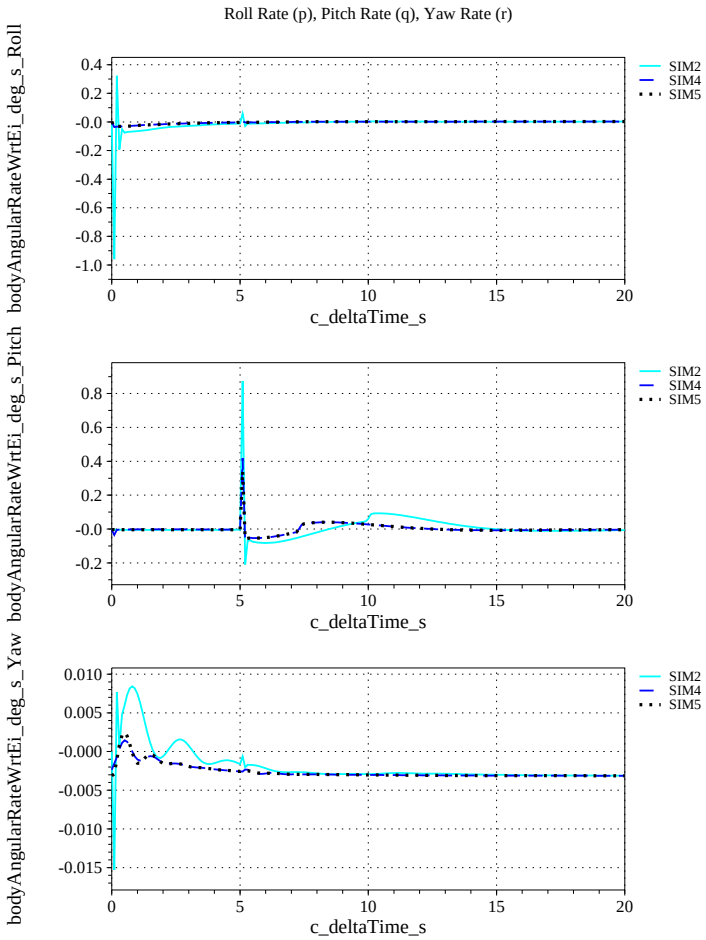

(q) Body-axis Angular Rates (w.r.t. NED Frame) Compared

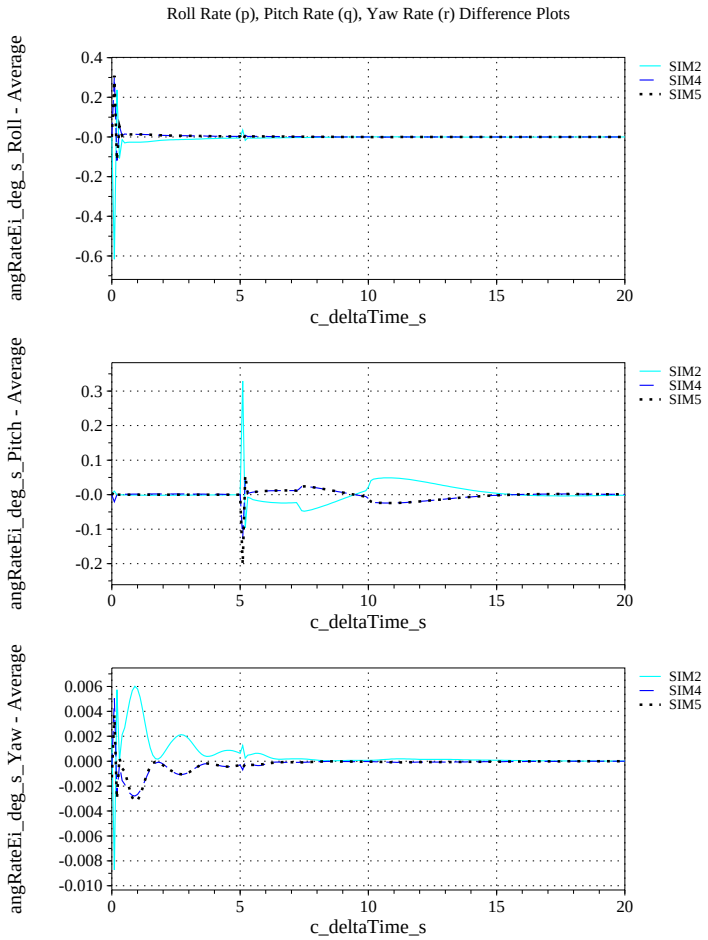

(r) Body-axis Angular Rates (w.r.t. NED Frame) Differenced

Figure 29. Check-case 13.2: Velocity Change of a Subsonic Aircraft; See Discussion in Section D.1.14 (Cont'd)

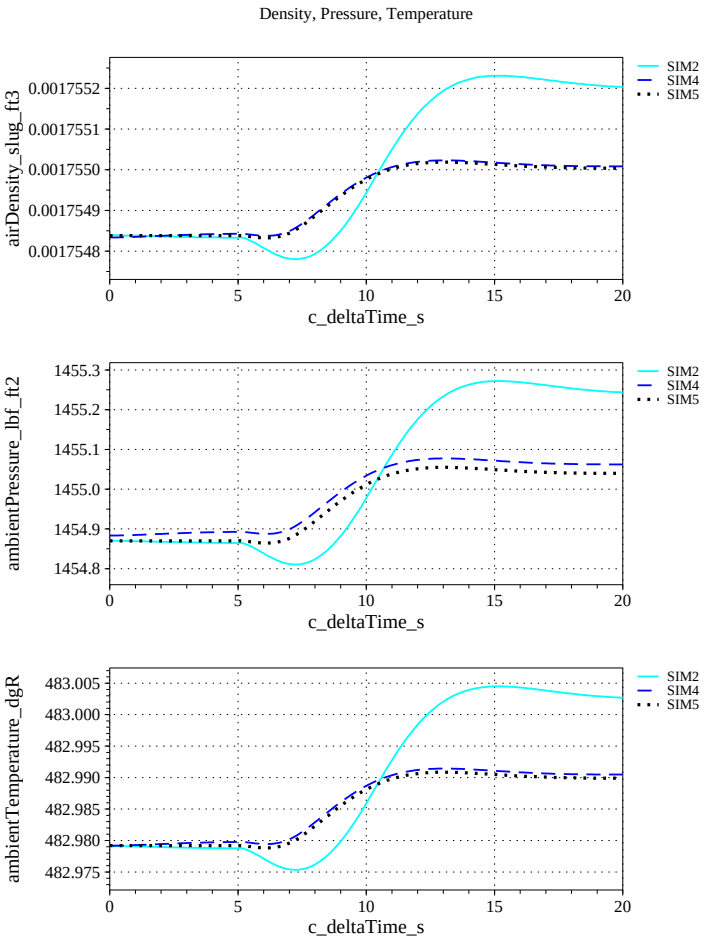

(s) Atmospheric Properties Compared

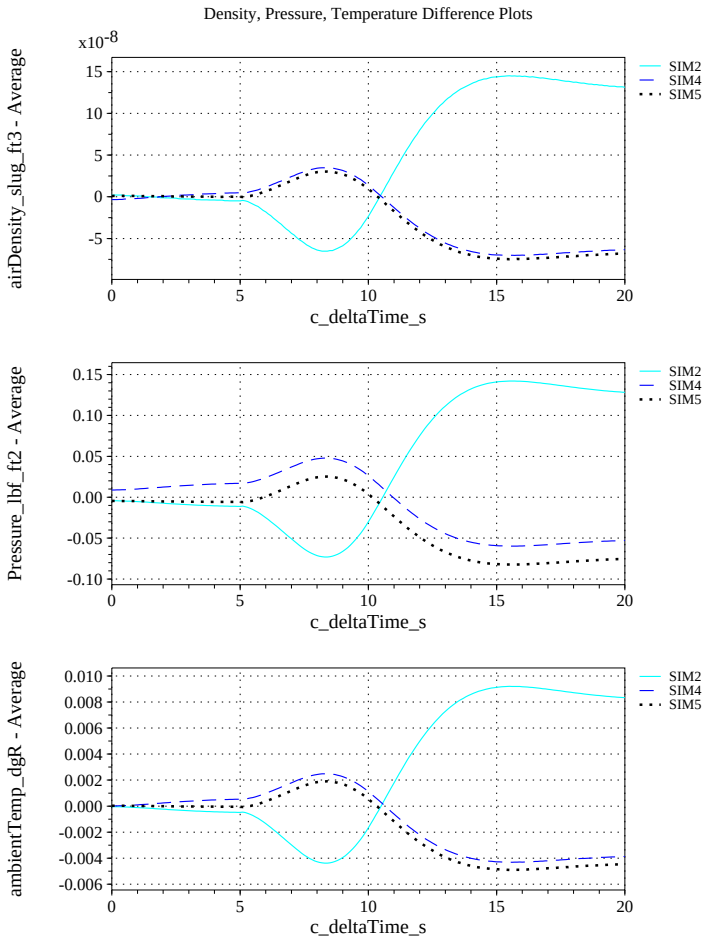

(t) Atmospheric Properties Differenced

Figure 29. Check-case 13.2: Velocity Change of a Subsonic Aircraft; See Discussion in Section D.1.14 (Cont'd)

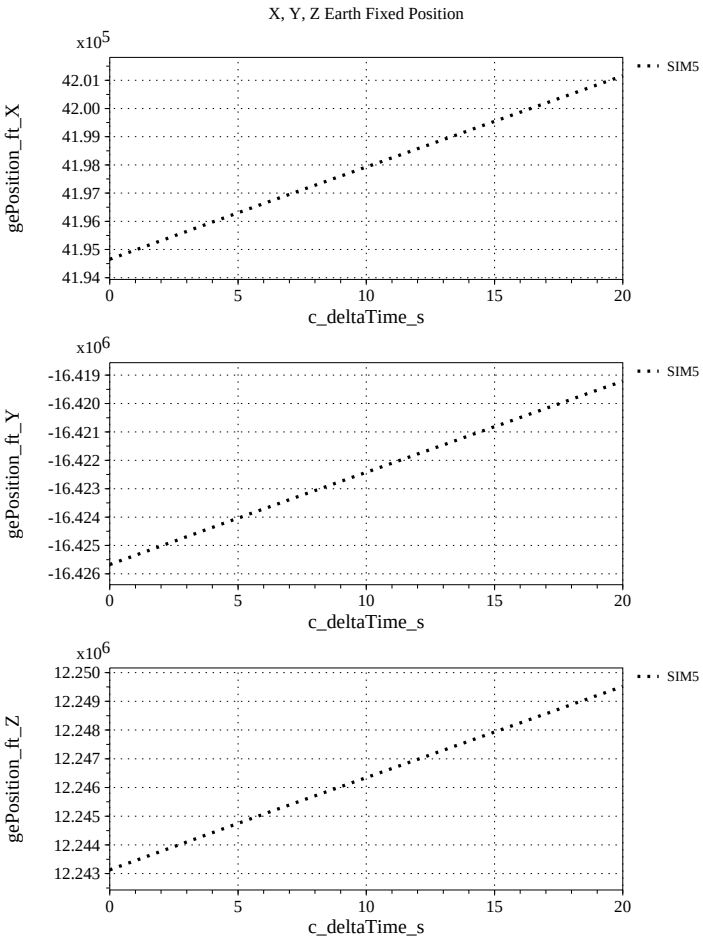

(u) Earth-centered, Earth-fixed Rectangular (X-Y-Z) Positions Compared

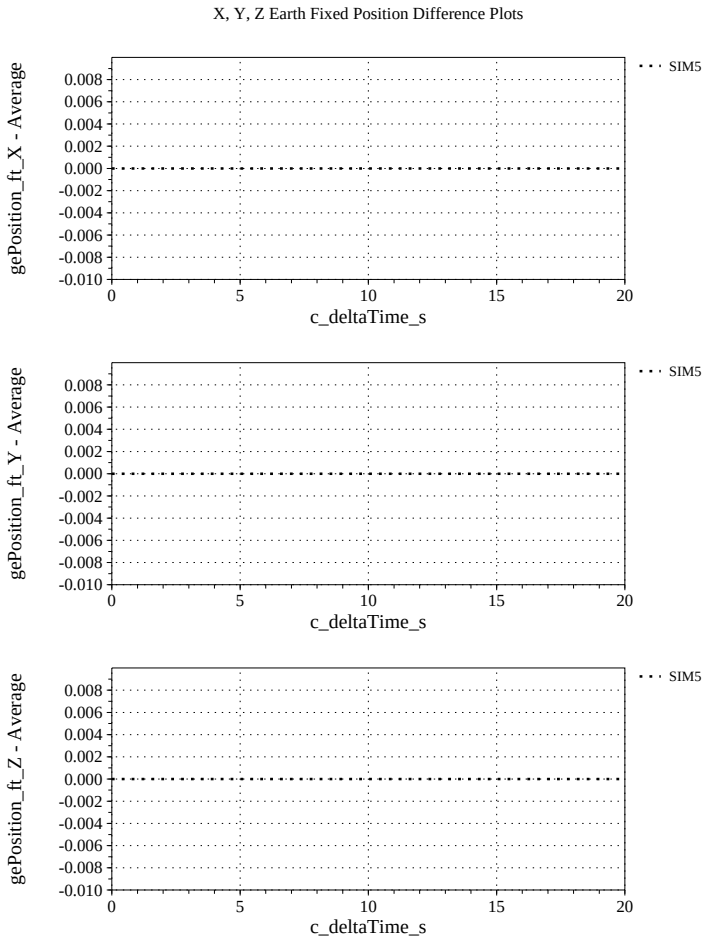

(v) Earth-centered, Earth-fixed Rectangular (X-Y-Z) Positions Differenced

Figure 29. Check-case 13.2: Velocity Change of a Subsonic Aircraft; See Discussion in Section D.1.14 (Cont'd)

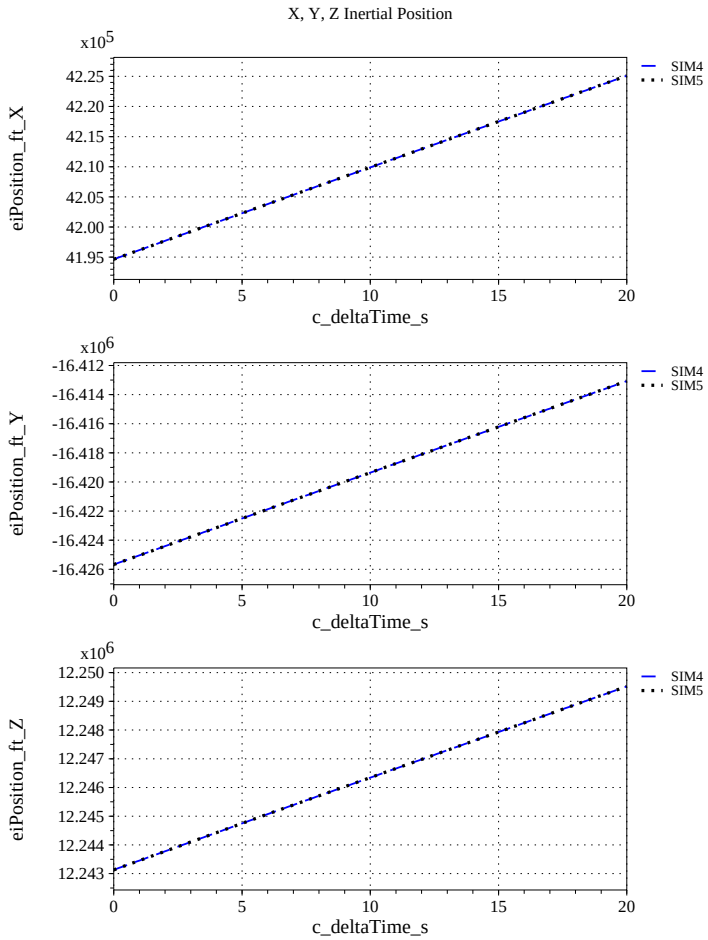

(w) Earth-centered Inertial Rectangular (x-y-z) Positions Compared

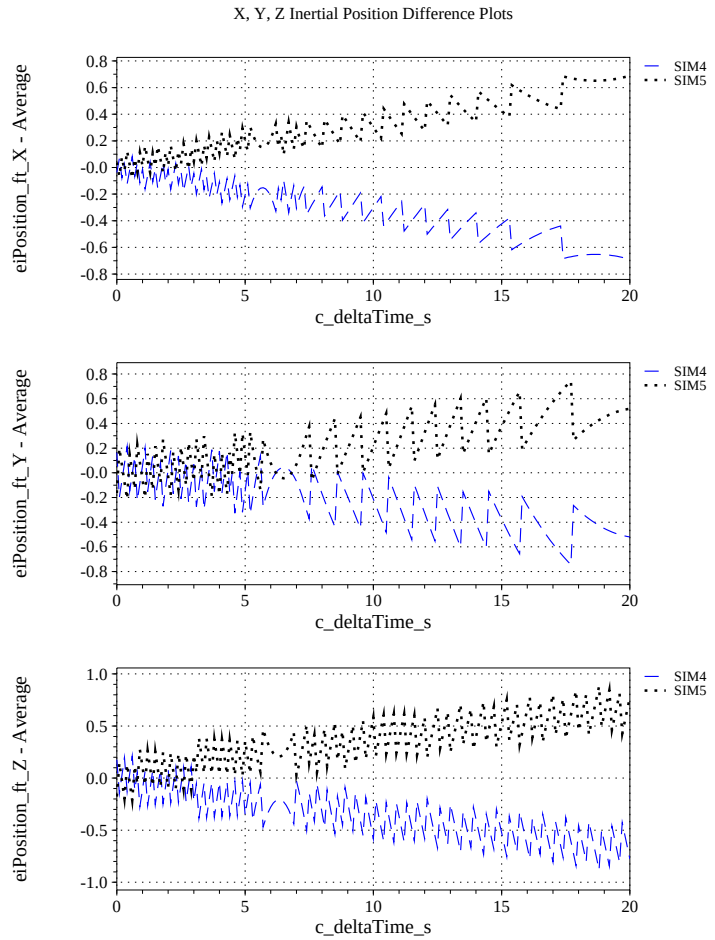

(x) Earth-centered Inertial Rectangular (x-y-z) Positions Differenced

Figure 29. Check-case 13.2: Velocity Change of a Subsonic Aircraft; See Discussion in Section D.1.14 (Concluded)

D.1.15 Check-case 13.3 – course change of a subsonic aircraft

This section shows cross-plots for three of the selected simulation tools in modeling the dynamics of a subsonic aircraft performing a heading change. This scenario is described in Section C.1.15. Figures 30a through 30x compare results between the three simulation tools, as well as the deviances of the outputs from each tool from the ensemble average value.

Atmospheric check-case 13.3 had the same starting condition as check-case 13.1 (Section D.1.13) but performed a heading change instead of an altitude change. The command to change heading 15° right from the initial heading occurs at $t = 15$ sec. All simulations accomplished the heading change while maintaining the commanded altitude and airspeed. The results exhibit differences similar to those in atmospheric case 13.1 with the same set of contributing causes:

- SIM 2 used the geocentric frame for the local vertical, leading to small non-zero values in the initial equilibrium condition in roll, angle of sideslip, and rudder deflection, as well as a slight difference in initial yaw angle.
- This steady-state roll angle and, under the command of the autopilot, the difference in yaw angle produced a small sideslip in SIM 2 that generated an aerodynamic side force of about 4 lbf. That aerodynamic side force induced a moment at the CM that required a counteracting aerodynamic yawing moment. In this scenario, however, all the simulations end the check-case with a negative yawing moment at the CM because they are still (asymptotically) completing the heading change. However, the difference in the aerodynamic yawing moment between SIM 2 and SIM 5 is approximately the additional yawing moment needed to counteract the moment induced by the aerodynamic side force.
- As noted previously, a different approach was taken in SIM 5 in the modification of the internal reference state values for the LQR controller for angle of attack, pitch attitude, and velocity states to match the values from the equilibrium solution for the initial conditions.
- As noted previously, SIM 2 recorded aerodynamic moments at the MRC, while SIM 4 and 5 recorded the aerodynamic moments at the vehicle center of gravity, leading to differences shown in Figure 30c.
- As noted previously, SIM 2 differs from SIM 4 and 5 in the magnitude of the gravitation vector for unexplained reasons, possibly due to a different way used to initialize the initial position from the specified geodetic coordinates, a non-trivial problem (see Section B.2.3).

A new difference emerged between SIM 4 and SIM 5 in the heading change scenario. After the change in heading is commanded, the track angle for SIM 5 quickly led that of SIM 4 by 0.114°; over the course of the turn the lead diminished to 0.002° at $t = 30$ sec. This lead might have been caused by the modification of the internal LQR reference state values or by a different execution rate for the control law. This lead in track angle accounted for a little more than half the position difference that developed between SIM 4 and SIM 5. On the other hand, SIM 2 fluctuated between a leading and lagging track angle relative to SIM 5 during the first 3 sec of the turn. The position difference slowly increased from a lag in the next 7 sec to a track angle lead for the last 5 sec of the run. At the end of run, the SIM 2 track angle had a lead of 0.023°. This behavior might have been caused by a combination of the deflected gravity vector, different internal LQR reference state values, and/or differences between simulations in the frame rate of the control law algorithm.

At the end of the run, SIM 4 and SIM 5 were separated by a distance of 5.4 ft. SIM 5 and SIM 2 were separated by a distance of 14.3 ft. SIM 2 and SIM 4 were separated by a distance of 19.1 ft.

At the end of the run, the simulated vehicles in SIM 4 and SIM 5 were separated by a distance of 5.4 ft, while the position of the F-16 in the trajectory generated by SIM 2 was offset from those of SIM 4 and SIM 5 by 135 ft and 137 ft, respectively.

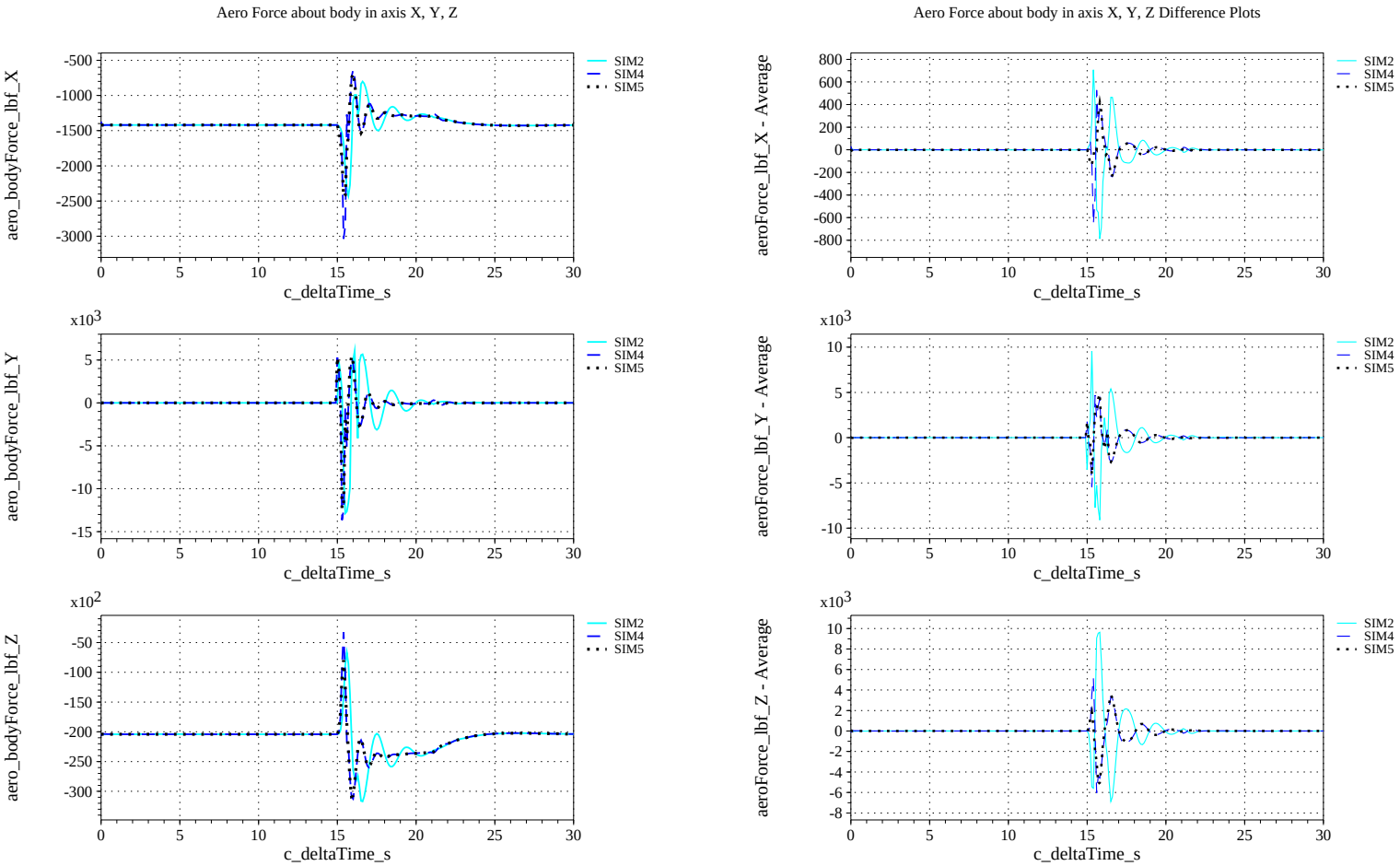

(a) Aerodynamic Forces Compared

(b) Aerodynamic Forces Differenced

Figure 30. Check-case 13.3: Course Change of a Subsonic Aircraft; See Discussion in Section D.1.15

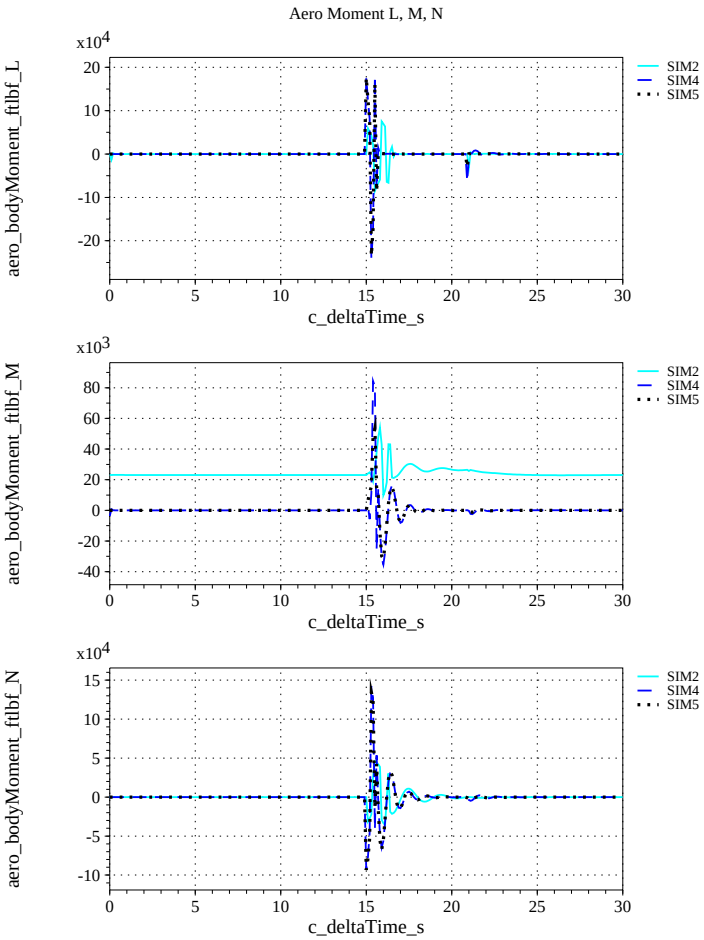

(c) Aerodynamic Moments Compared

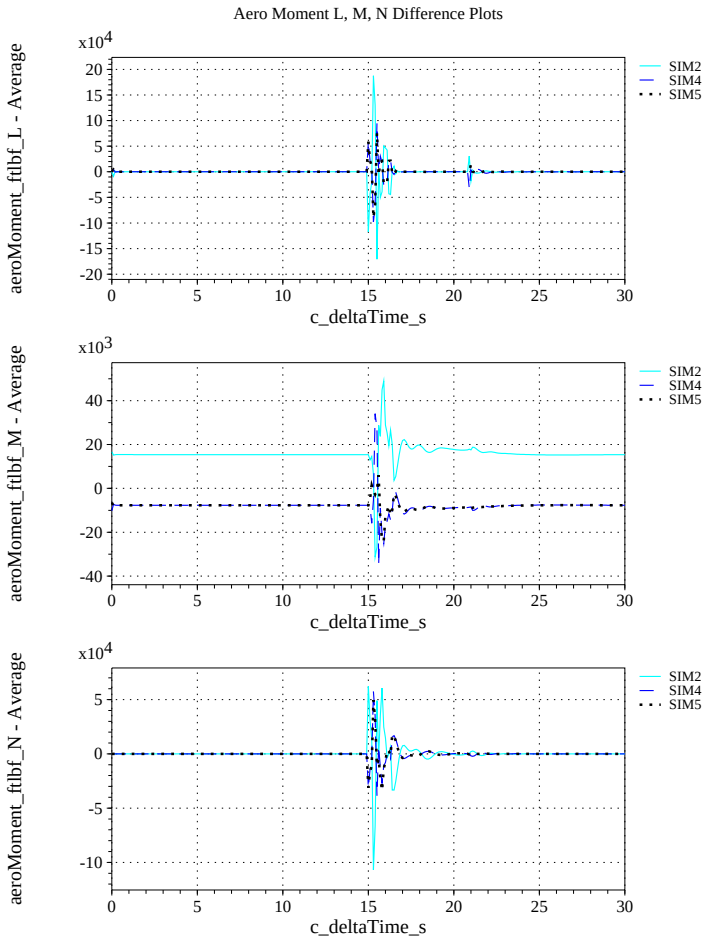

(d) Aerodynamic Moments Differenced

Figure 30. Check-case 13.3: Course Change of a Subsonic Aircraft; See Discussion in Section D.1.15 (Cont'd)

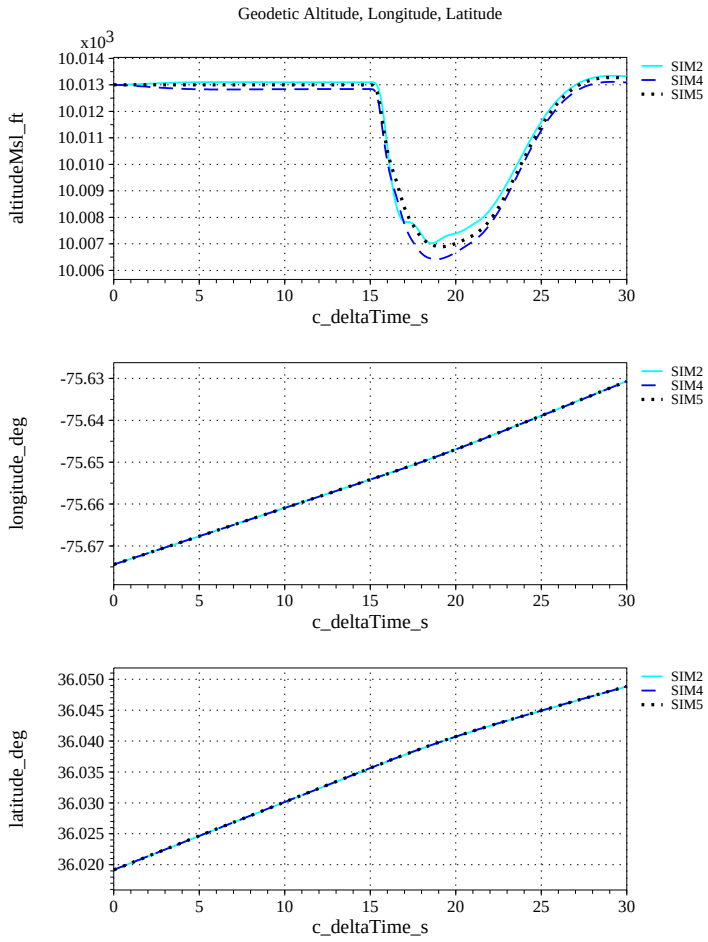

(e) Altitude, Geodetic Latitude and Longitude Compared

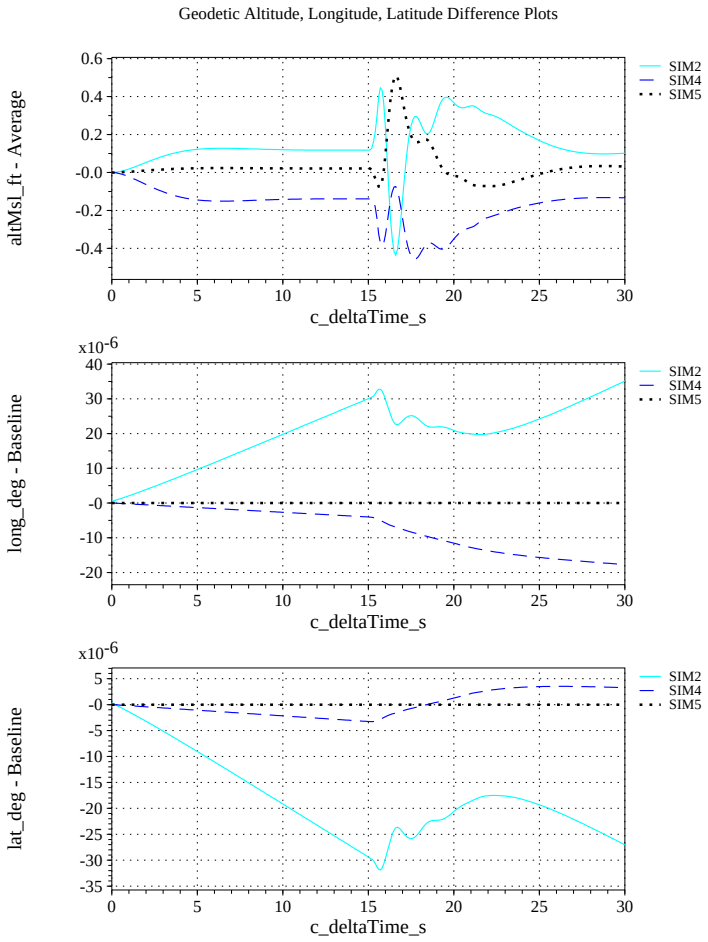

(f) Altitude, Geodetic Latitude and Longitude Differenced

Figure 30. Check-case 13.3: Course Change of a Subsonic Aircraft; See Discussion in Section D.1.15 (Cont'd)

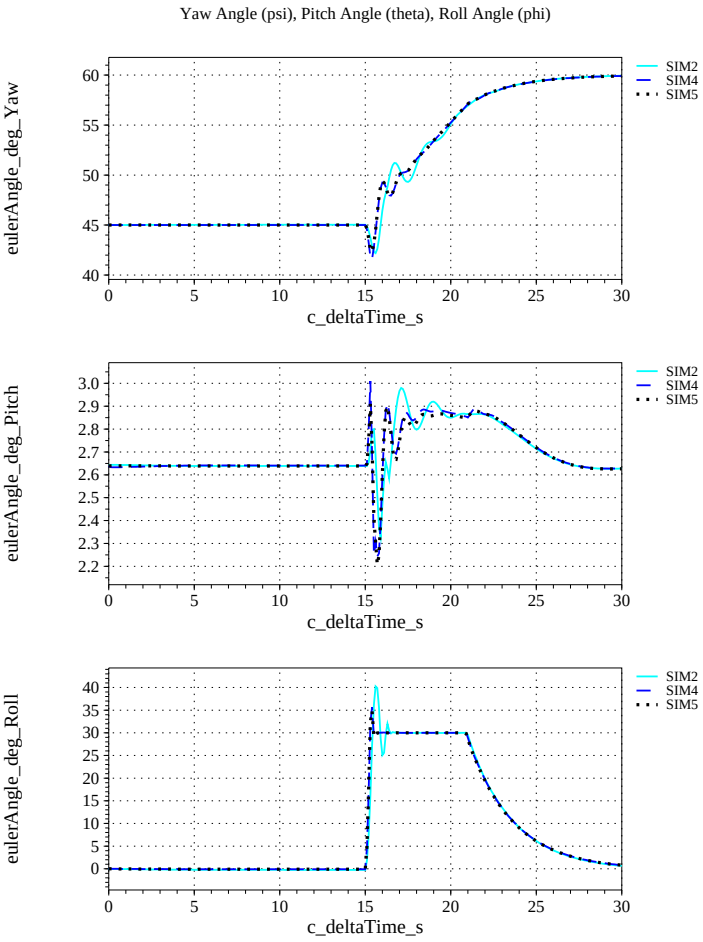

(g) Euler Angles (w.r.t. NED Frame) Compared

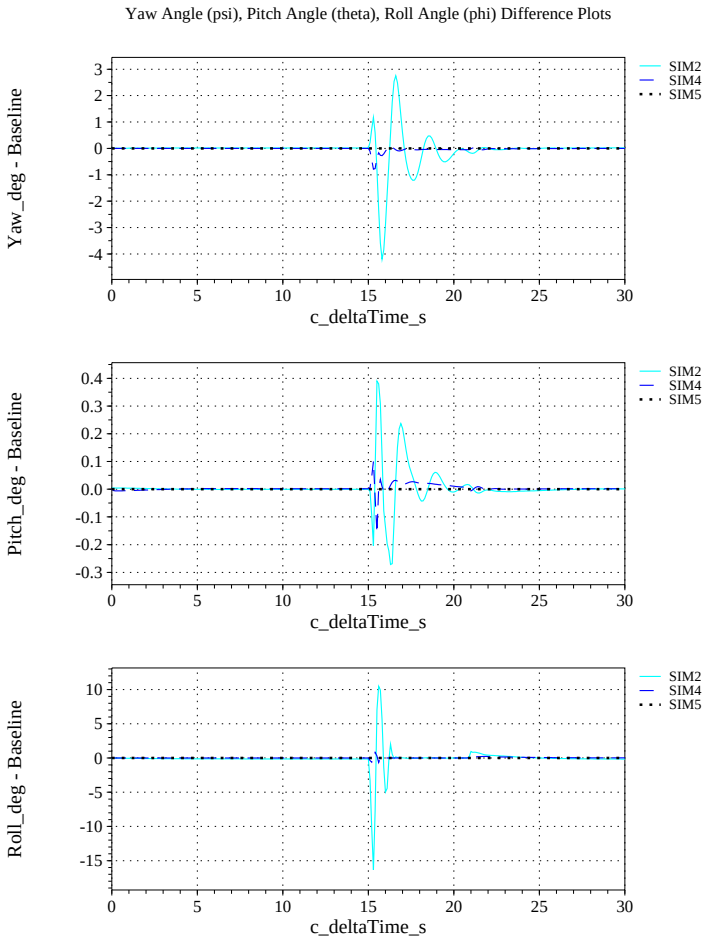

(h) Euler Angles (w.r.t. NED Frame) Differenced

Figure 30. Check-case 13.3: Course Change of a Subsonic Aircraft; See Discussion in Section D.1.15 (Cont'd)

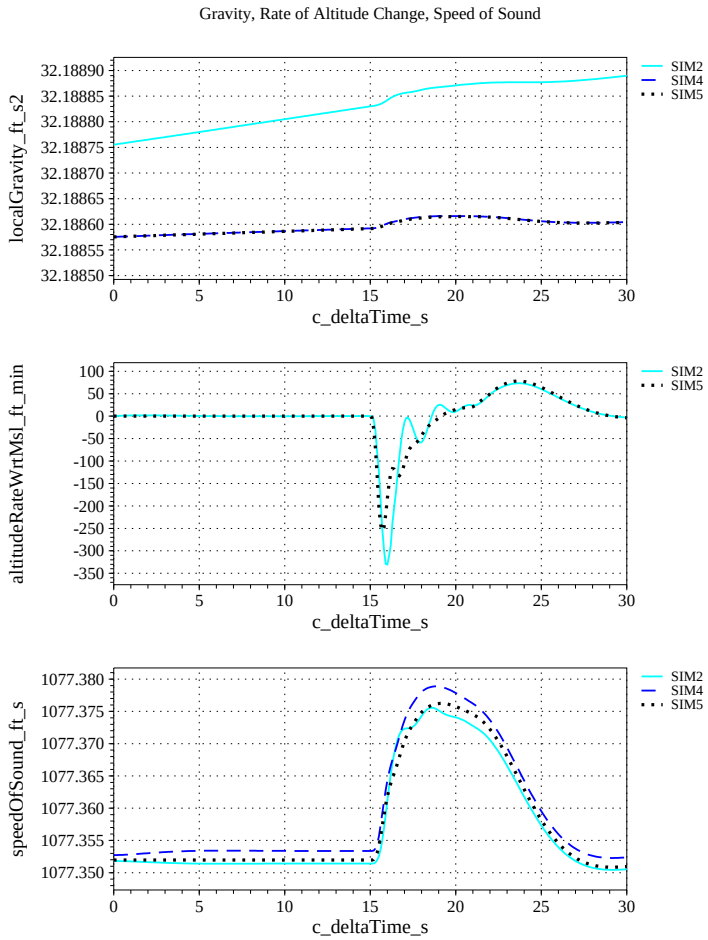

(i) Gravity, Climb Rate, and Speed-of-sound Compared

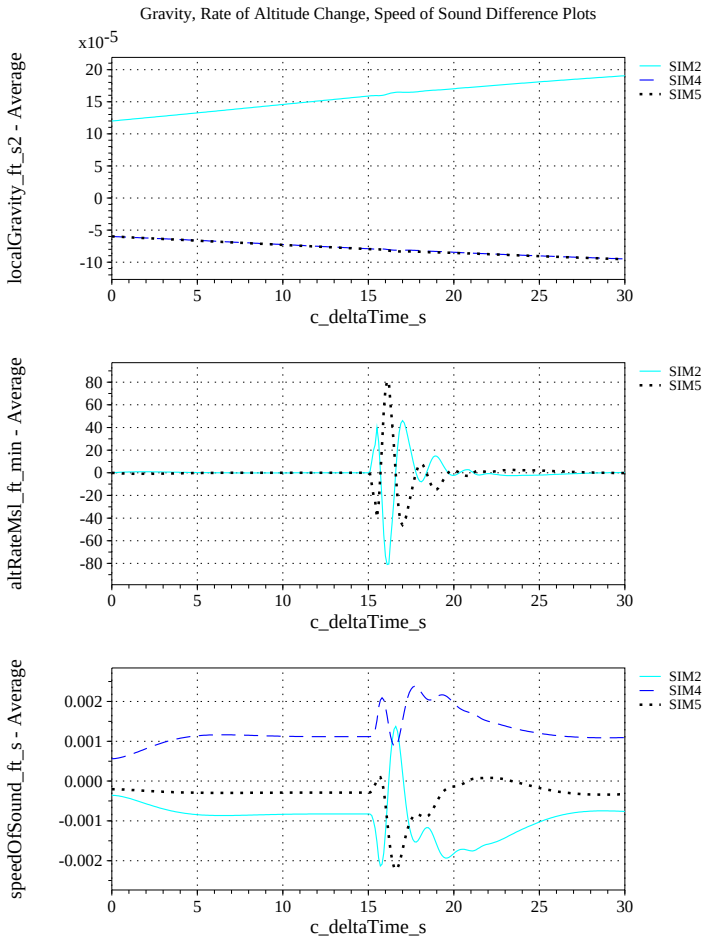

(j) Gravity, Climb Rate, and Speed-of-sound Differenced

Figure 30. Check-case 13.3: Course Change of a Subsonic Aircraft; See Discussion in Section D.1.15 (Cont'd)

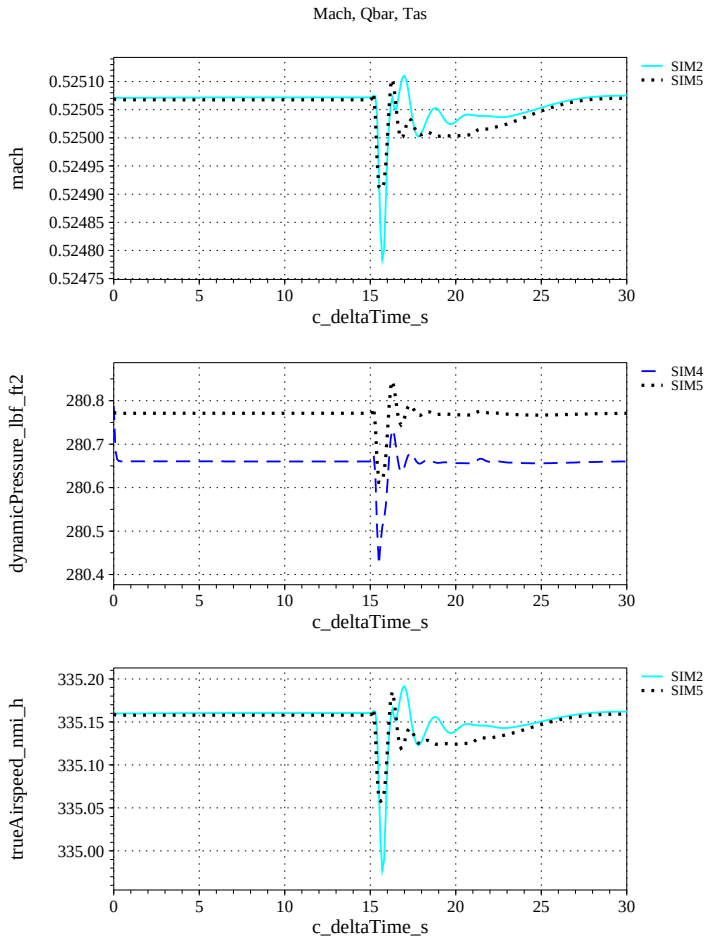

(k) Mach, Dynamic Pressure, and True Airspeed Compared

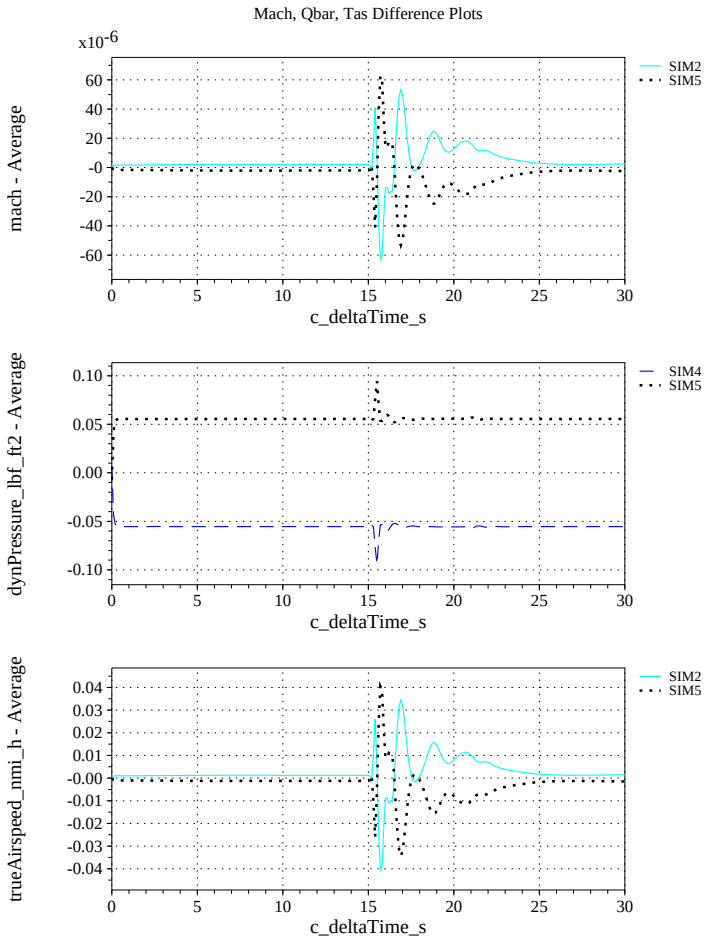

(l) Mach, Dynamic Pressure, and True Airspeed Differenced

Figure 30. Check-case 13.3: Course Change of a Subsonic Aircraft; See Discussion in Section D.1.15 (Cont'd)

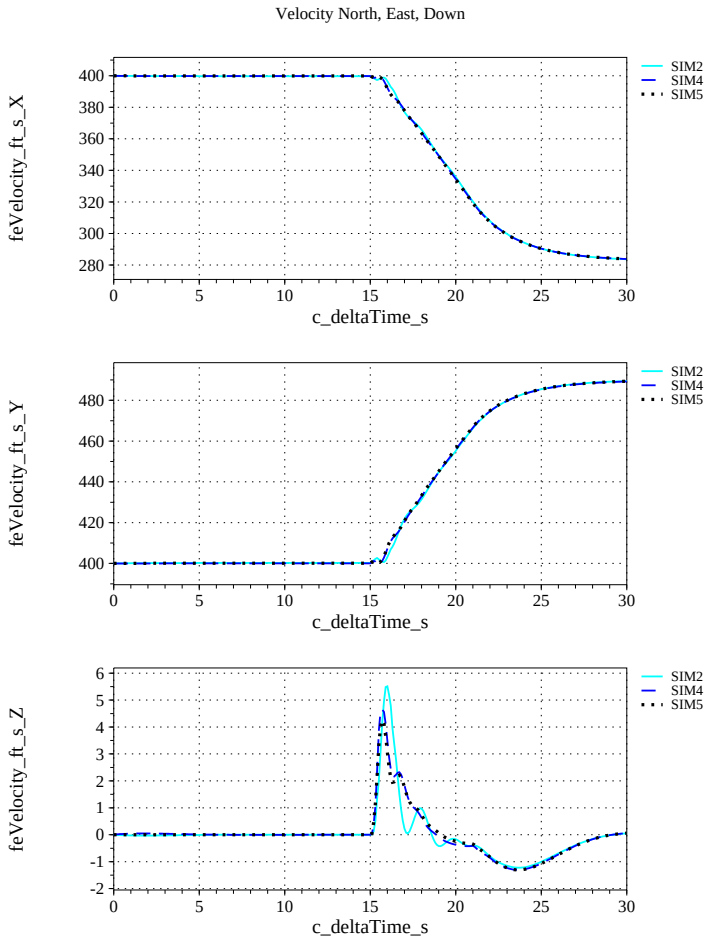

(m) NED Velocities Compared

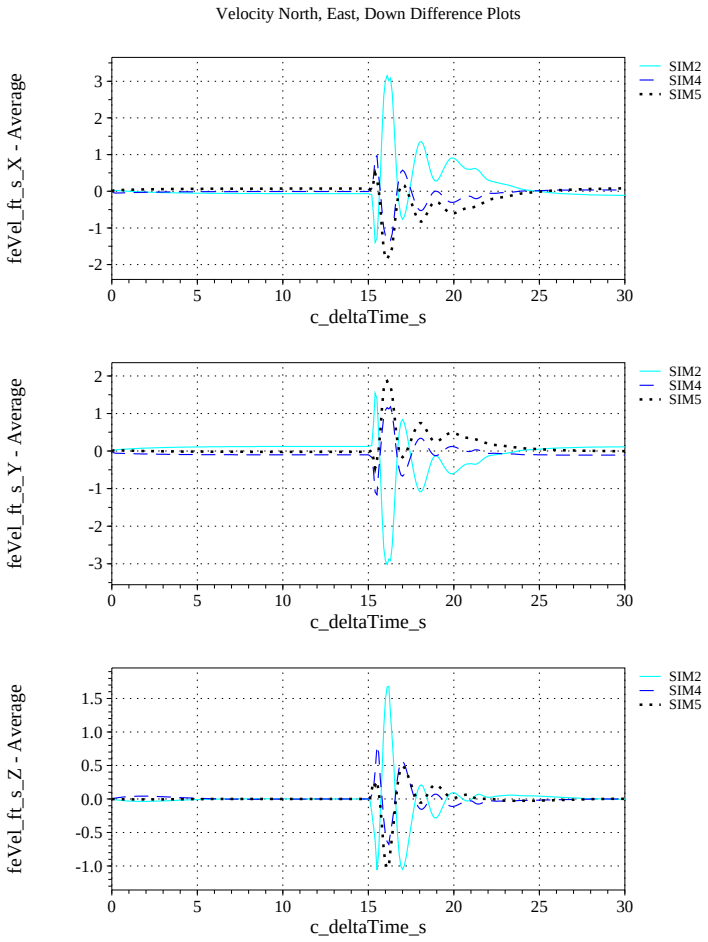

(n) NED Velocities Differenced

Figure 30. Check-case 13.3: Course Change of a Subsonic Aircraft; See Discussion in Section D.1.15 (Cont'd)

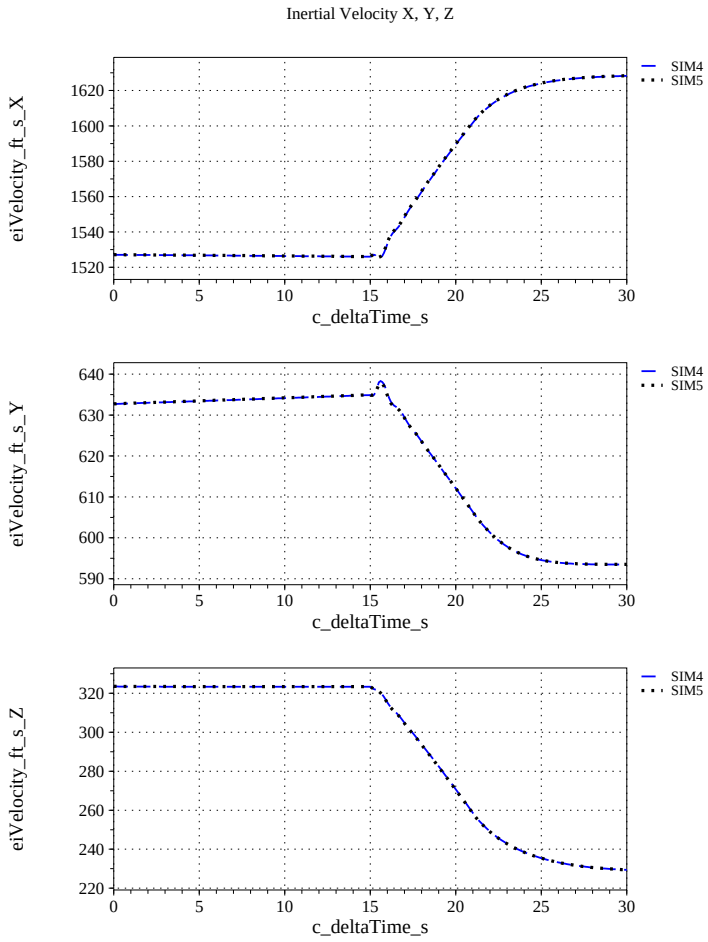

(o) Inertial Velocities Compared

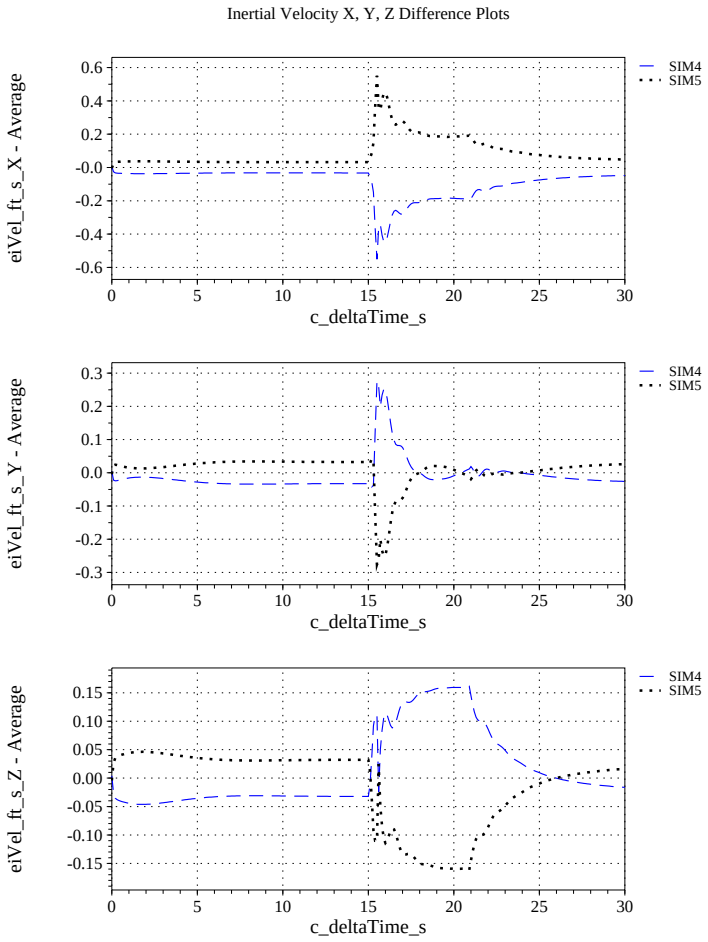

(p) Inertial Velocities Differenced

Figure 30. Check-case 13.3: Course Change of a Subsonic Aircraft; See Discussion in Section D.1.15 (Cont'd)

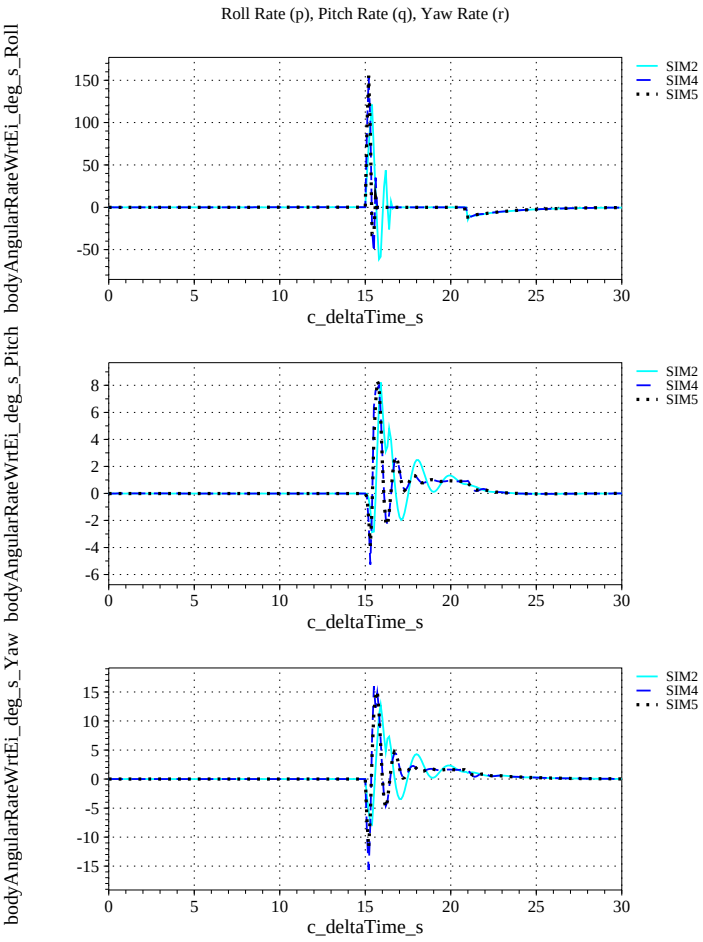

(q) Body-axis Angular Rates (w.r.t. NED Frame) Compared

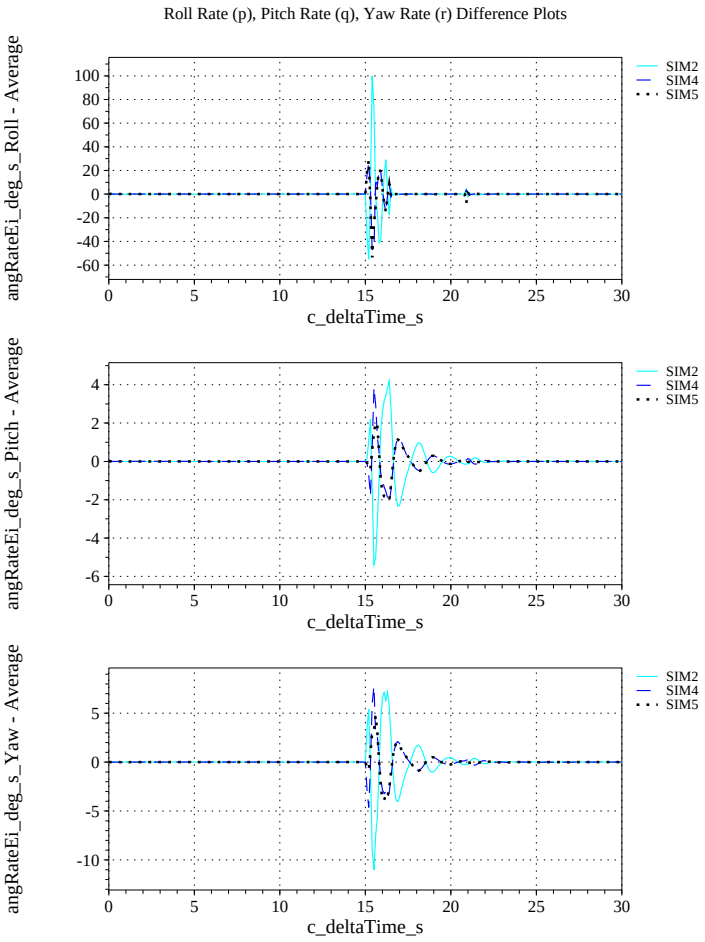

(r) Body-axis Angular Rates (w.r.t. NED Frame) Differenced

Figure 30. Check-case 13.3: Course Change of a Subsonic Aircraft; See Discussion in Section D.1.15 (Cont'd)

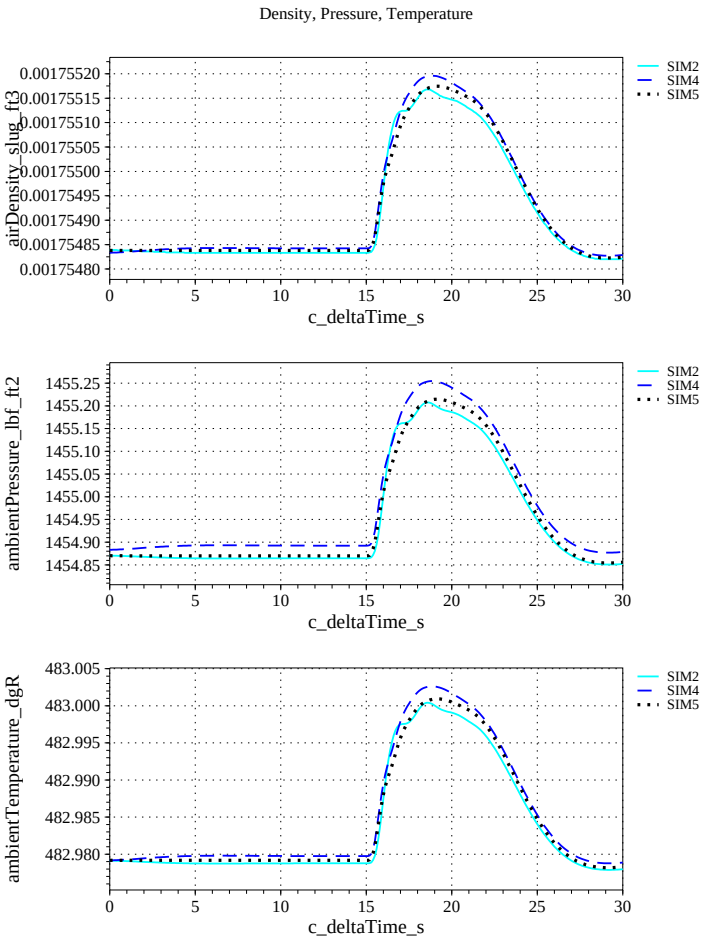

(s) Atmospheric Properties Compared

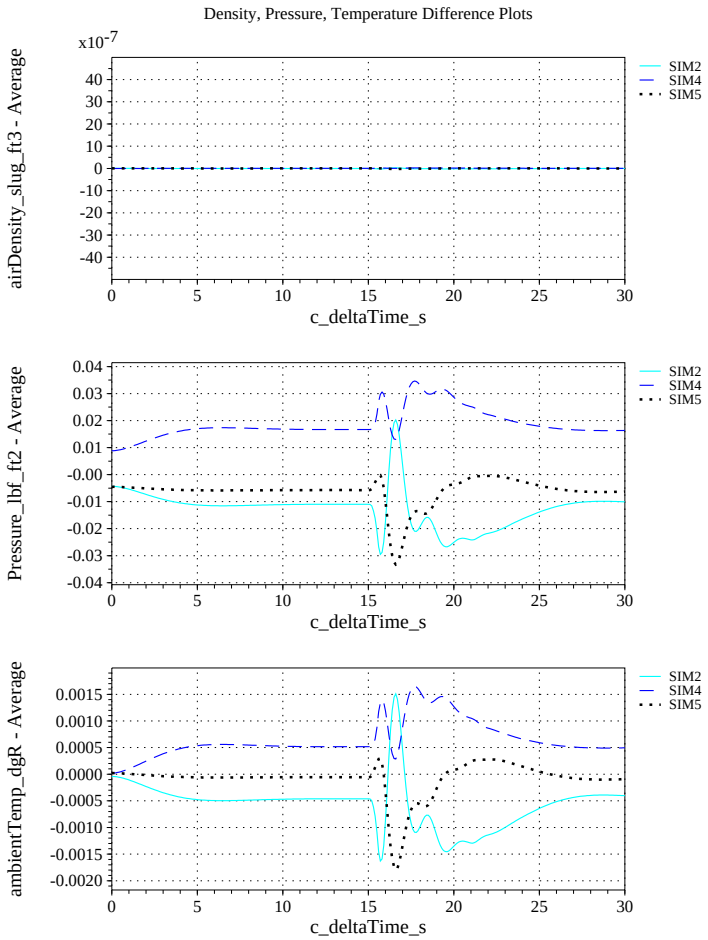

(t) Atmospheric Properties Differenced

Figure 30. Check-case 13.3: Course Change of a Subsonic Aircraft; See Discussion in Section D.1.15 (Cont'd)

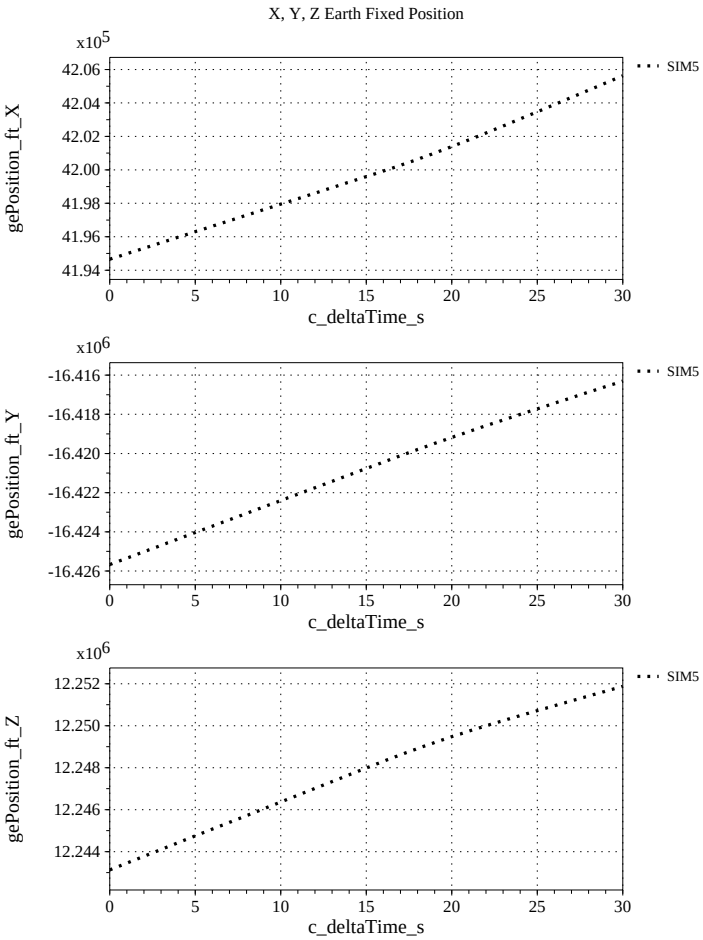

(u) Earth-centered, Earth-fixed Rectangular (X-Y-Z) Positions Compared

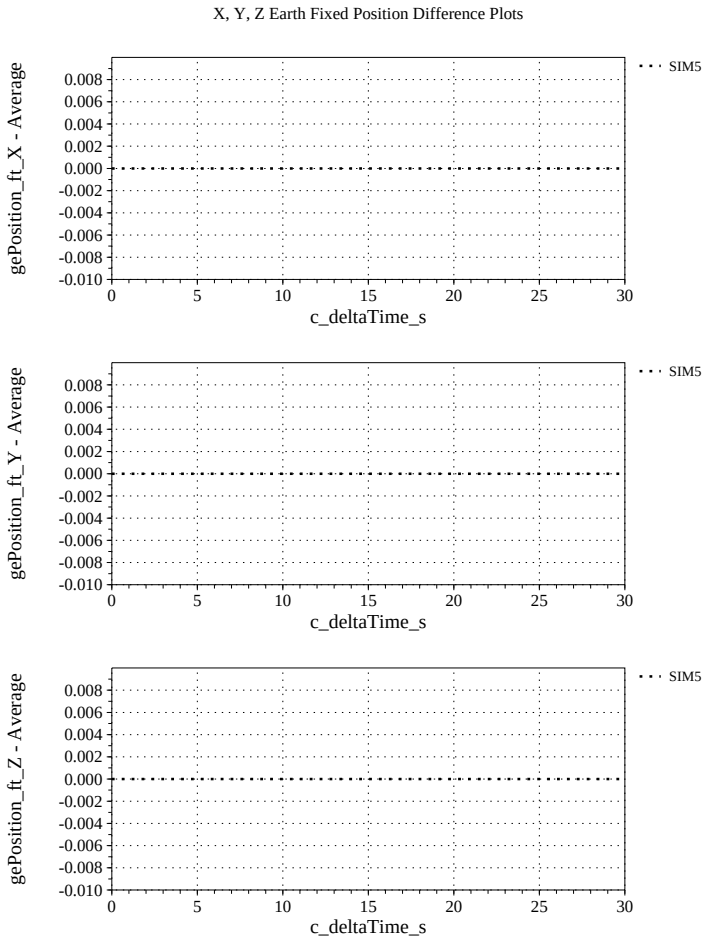

(v) Earth-centered, Earth-fixed Rectangular (X-Y-Z) Positions Differenced

Figure 30. Check-case 13.3: Course Change of a Subsonic Aircraft; See Discussion in Section D.1.15 (Cont'd)

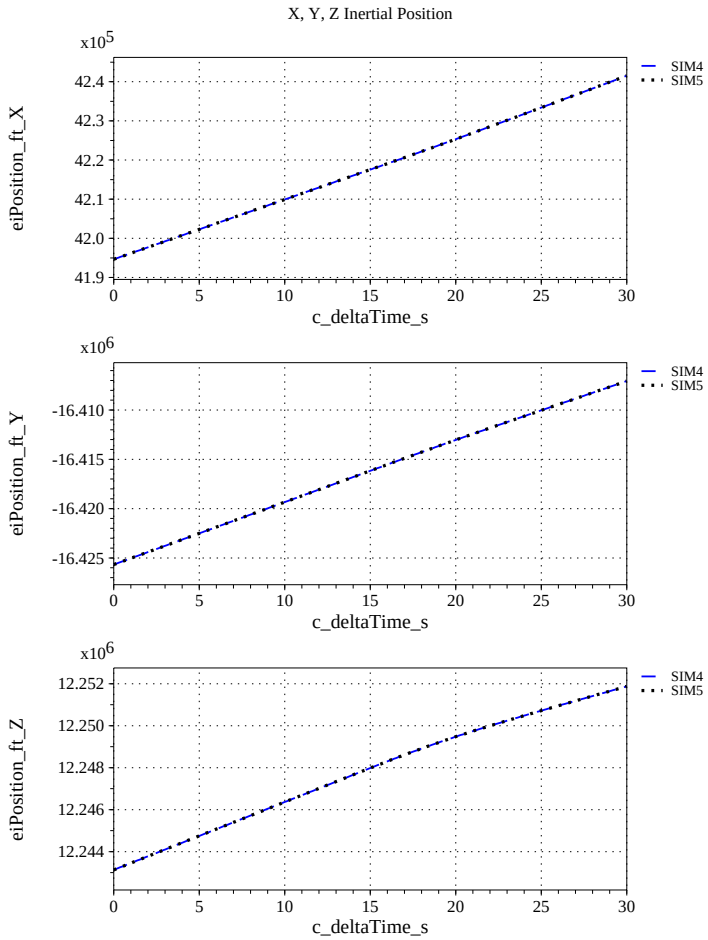

(w) Earth-centered Inertial Rectangular (x-y-z) Positions Compared

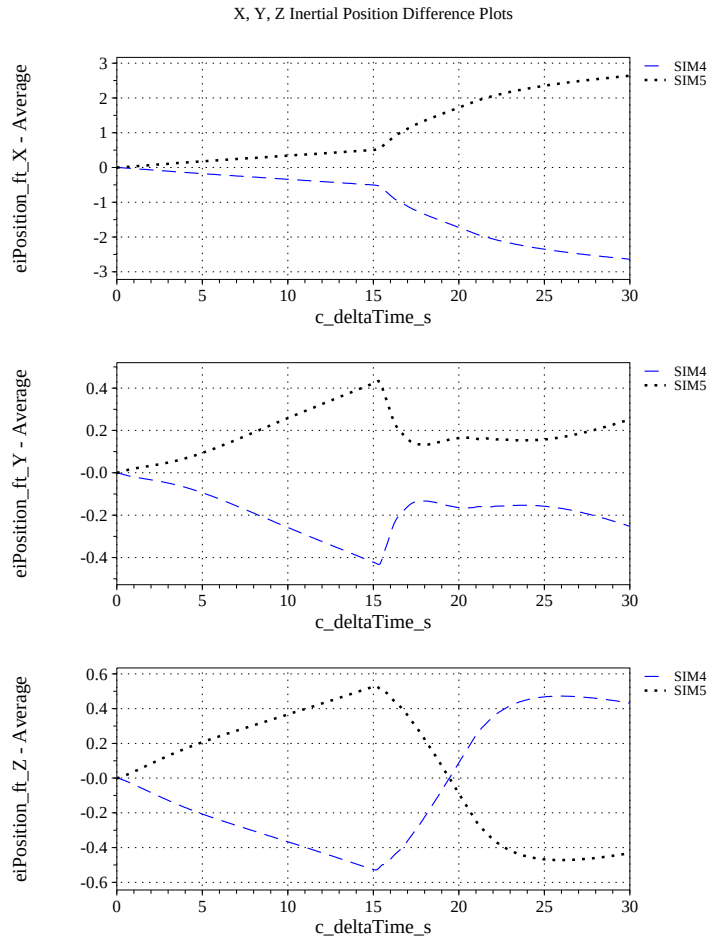

(x) Earth-centered Inertial Rectangular (x-y-z) Positions Differenced

Figure 30. Check-case 13.3: Course Change of a Subsonic Aircraft; See Discussion in Section D.1.15 (Concluded)

D.1.16 Check-case 13.4 – lateral offset maneuver of a subsonic aircraft

This section shows cross-plots for three of the selected simulation tools in modeling the dynamics of a subsonic aircraft performing a lateral offset. This scenario is described in Section C.1.16. Figures 31a through 31x compare results between the three simulation tools, as well as the deviances of the outputs from each tool from the ensemble average value.

This check-case has the same starting conditions as check-case 13.1 but replaced the command to change altitude with a command to execute a 2,000-ft lateral offset to the right of the initial path. The command took effect at $t = 20$ sec.

The predicted trajectories of all three tools are asymptotically approaching the commanded 2,000-ft offset at the end of the run ($t = 60$ sec). At this point, the simulations report a slight and decreasing deviation of between $+0.14°$ and $+0.21°$ from the commanded heading of 45° degrees. The simulations are also approximately maintaining the commanded altitude and airspeed during the run.

The following differences identified in atmospheric case 13.1 remain present in this case:

- SIM 2 used the geocentric frame for the local vertical. As a result, the gravity vector was deflected by the trim solver by the 0.18° difference between the geocentric and geodetic latitude. This caused the equilibrium solution for SIM 2 to roll the aircraft so that the body z-axis (and therefore the aerodynamic lift force) was nearly aligned with the deflected gravity vector. It also influenced the difference in roll angle between SIM 2 and the other simulations at the end of the run. Those differences are between $-0.14°$ and $-0.16°$. However, these differences are not visible in the charts due to the larger transient differences in roll angle that occur in the first few seconds after the simulations initiate the lateral offset. Those large transient differences are primarily driven by other causes.

- As in the prior autopilot check-cases, the initial roll angle of SIM 2 induced a small sideslip that generates an aerodynamic side force of about 7.2 lbf. That aerodynamic side force induced a moment at the CM that requires a counteracting aerodynamic yawing moment of 8.2 lbf-ft. For the other simulations, the side force and yawing moment at the MRC are nearly zero. However, these differences were again overshadowed by larger transient differences in aerodynamic forces and moments which occur in the first few seconds of executing the lateral offset.

- As in earlier check-cases, differences exist among the predicted trajectories due to treatment of the default, unperturbed, state reference values for the LQR controller. Specifically, the LQR state reference value for throttle and longitudinal stick may differ from the results of the equilibrium solver for each simulation. Moreover, only SIM 5 also replaced these LQR state reference values for α, θ, and V with its equilibrium solution. The final state of the vehicle under control of the autopilot is a balance between the autopilot and LQR commands. The default trim value for airspeed was 0.18 kt lower than the initial speed specified for the scenario. Because SIM 4 didn't replace the LQR trim value for airspeed, it experienced an immediate 0.11-ft/s decrease in speed when the autopilot was engaged. This drop in airspeed persisted for the remainder of the scenario and is a major contributor to the growing distance between SIM 4 and SIM 5. Differences in LQR trim values may also influence the results for SIM 2; however, such differences are overshadowed by other contributors.

- As in earlier check-cases, SIM 2 recorded the aerodynamic moments about the MRC; SIM 4 and 5 recorded the aerodynamic moments about the vehicle CM. Thus, SIM 4 and SIM 5 recorded pitching moments near zero when the vehicle is not maneuvering whereas SIM 2 recorded non-zero pitching moment throughout the run.

- As in earlier check-cases, SIM 2 differs from SIM 4 and 5 in the magnitude of the gravitation vector by 1.8×10^{-4} ft/s^2. A substantial difference in geocentric location would be necessary to cause this difference in gravitation. But, the gravitation difference itself would be a minor contributor to differences in vehicle dynamics since it adds only 0.11 lbf to the weight of the aircraft.

Unique to this check-case, the three participating simulation tools demonstrated large transient differences in Euler angles (Figure 31h), angular rates (Figure 31r), NED velocity (Figure 31n), and aerodynamic forces (Figure 31b) and moments (Figure 31d) in the first few seconds after commanding the lateral offset. These differences may have arisen from differences in the execution rate of the autopilot, differences in LQR state reference values, differences in the methods used by each simulation to estimate the current lateral offset, or from the influence of differences of the integration methods on the feedback response of the controller. The data sets do not provide sufficient information to further investigate these potential causes.

At the end of the run, SIM 4 and SIM 5 were separated by a distance of 11.6 ft. SIM 5 and SIM 2 were separated by a distance of 40.3 ft. SIM 2 and SIM 4 were separated by a distance of 31.8 ft. The distance between SIM 4 and SIM 5 is partly due to the difference in airspeed; the difference in airspeed alone would create a separation of 6.8 ft. The remaining difference is the result of differences in track over the course of the run. For the last 30 sec, the two simulations differ in heading by an average of 0.04°. Although that seems small, it would result in a separation of about 12 ft when flying at 566 ft/s for 30 sec. The track differences over the whole run would produce a separation of about 9.3 ft if the simulations were flying at the same speed. The root of the sum of the squares of the contributions from speed and track differences is approximately equal to the final distance between the two simulations. However, differences in speed and track cannot explain the separation distance between SIM 2 and the other simulations. Differences in speed between SIM 2 and SIM 5 are small and would produce an estimated separation between the simulations of only 0.5 ft. Likewise, differences in track produce a estimated separation of only 4.7 ft at the end of the run. The difference charts for longitude and latitude (Figure 31f) both show that the geodetic location of SIM 2 departs from the other simulations throughout the run. In fact, when the lateral offset is commanded at $t = 20$ sec, the reported geodetic position of SIM 2 is already 18.8 ft apart from SIM 5 and 18.6 ft away from SIM 4. Because these separations are not consistent with differences in speed or track, the likely cause is a difference in the methods employed to derive or propagate the geodetic position.

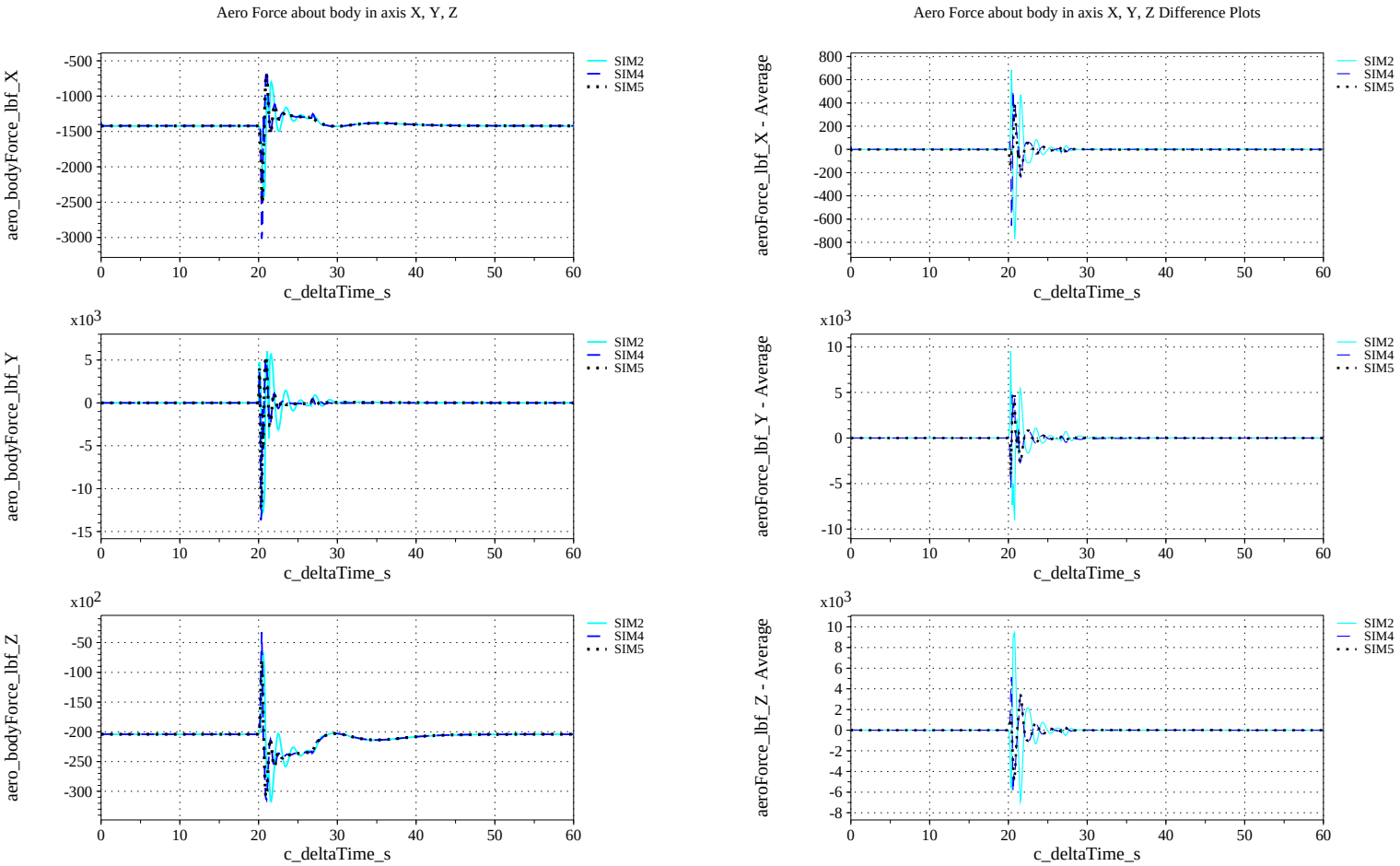

(a) Aerodynamic Forces Compared

(b) Aerodynamic Forces Differenced

Figure 31. Check-case 13.4: Lateral Offset Maneuver of a Subsonic Aircraft; See Discussion in Section D.1.16

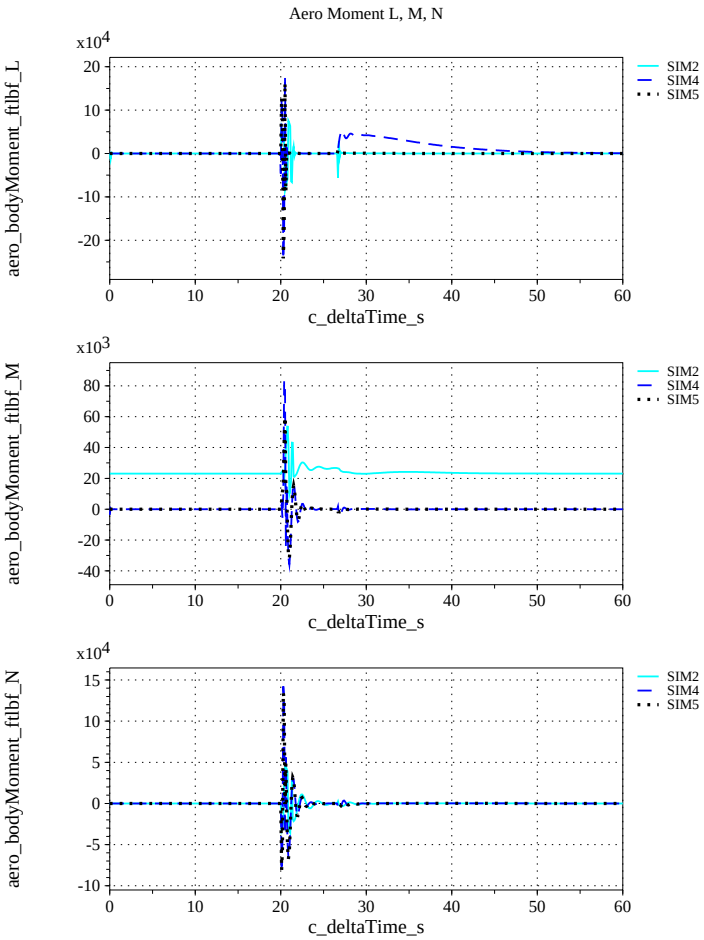

(c) Aerodynamic Moments Compared

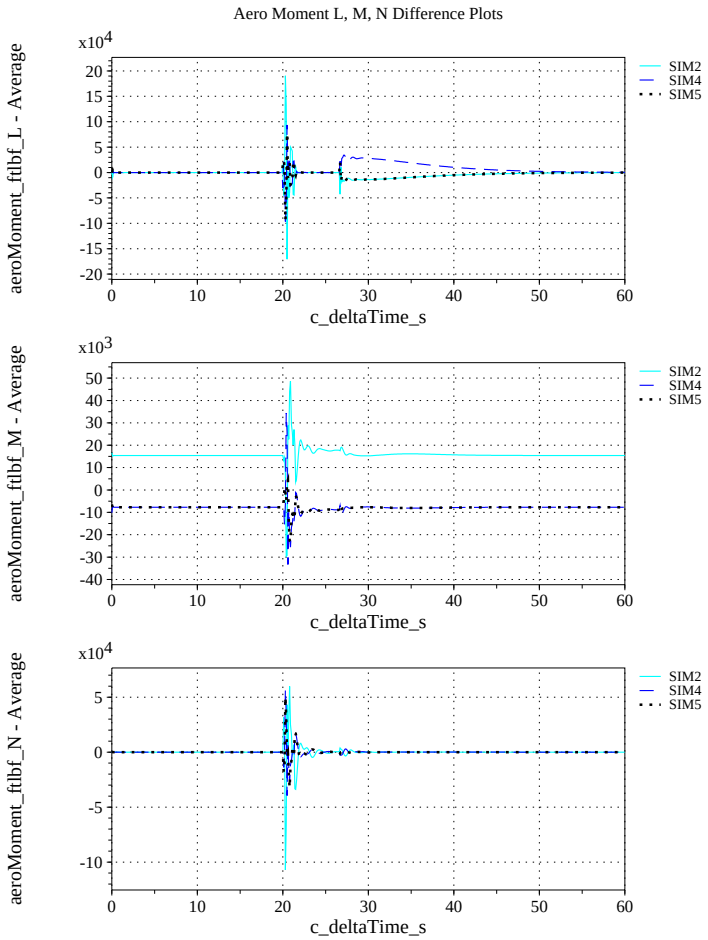

(d) Aerodynamic Moments Differenced

Figure 31. Check-case 13.4: Lateral Offset Maneuver of a Subsonic Aircraft; See Discussion in Section D.1.16 (Cont'd)

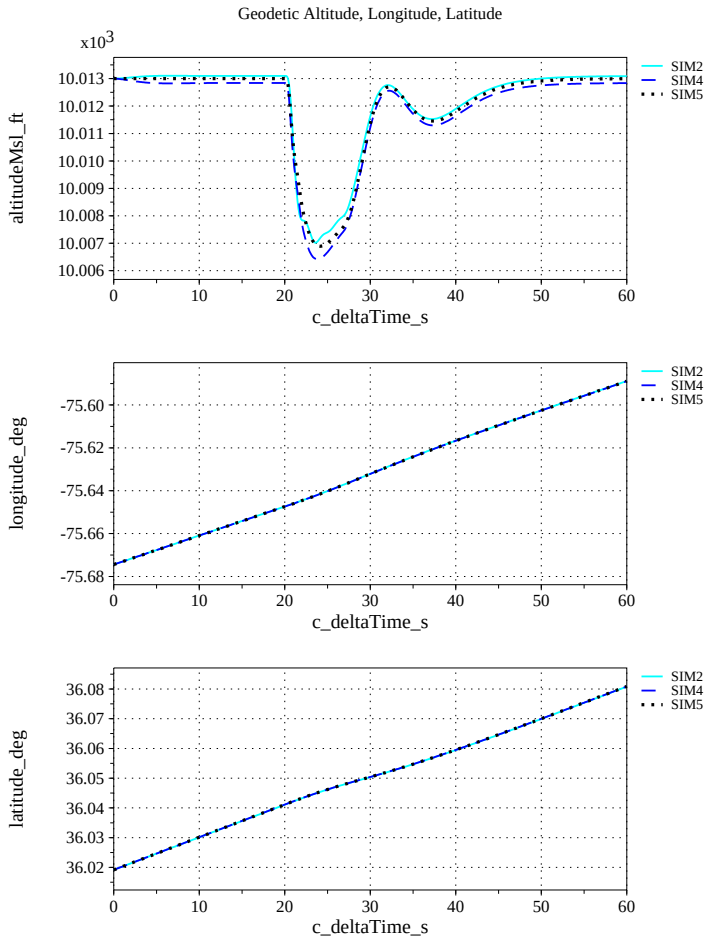

(e) Altitude, Geodetic Latitude and Longitude Compared

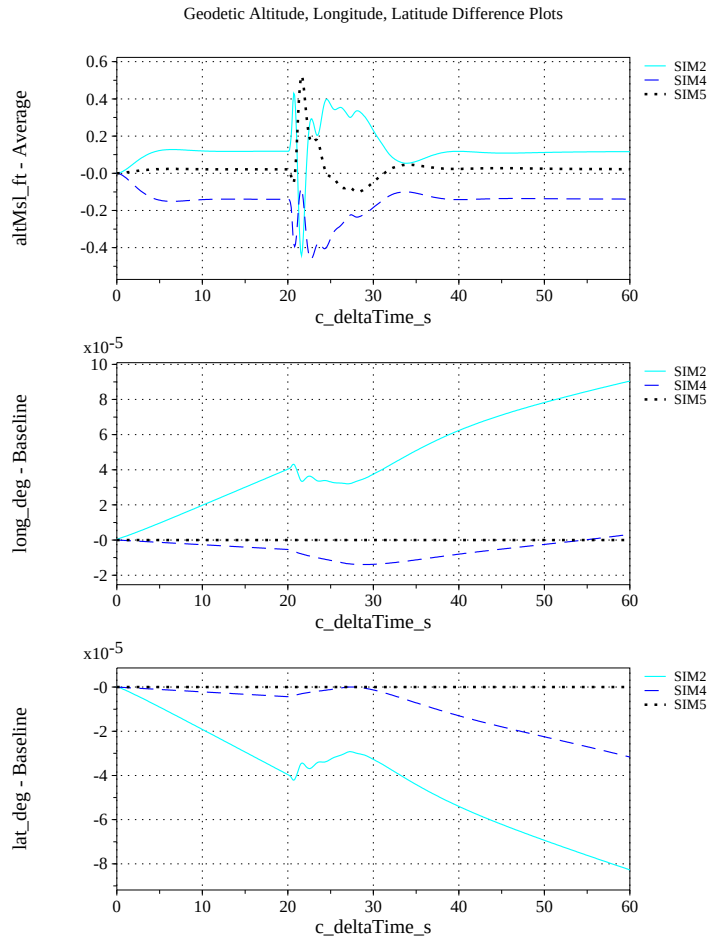

(f) Altitude, Geodetic Latitude and Longitude Differenced

Figure 31. Check-case 13.4: Lateral Offset Maneuver of a Subsonic Aircraft; See Discussion in Section D.1.16 (Cont'd)

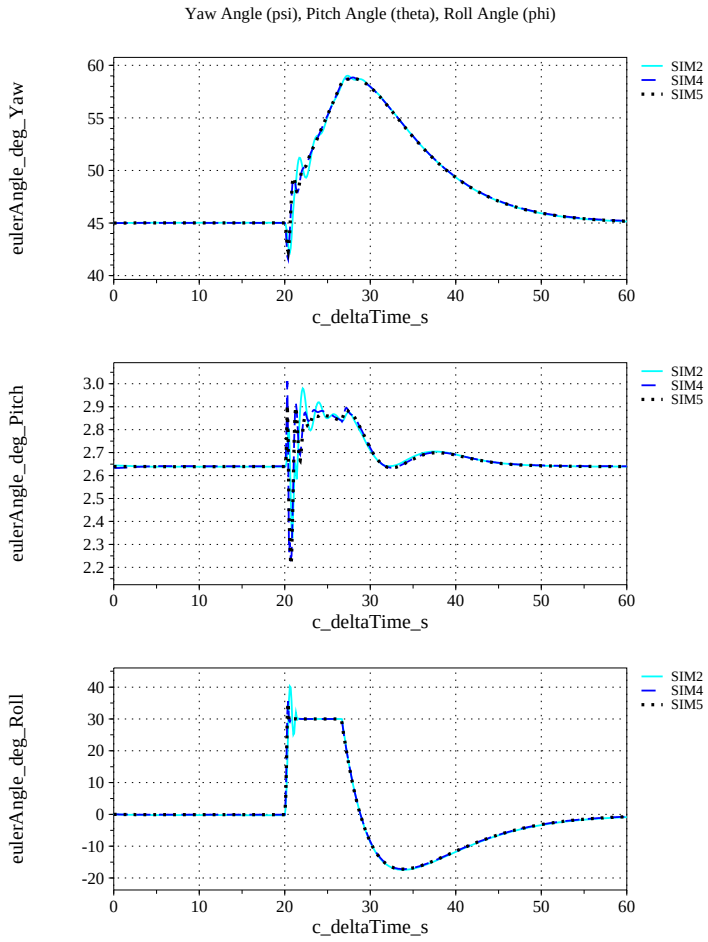

(g) Euler Angles (w.r.t. NED Frame) Compared

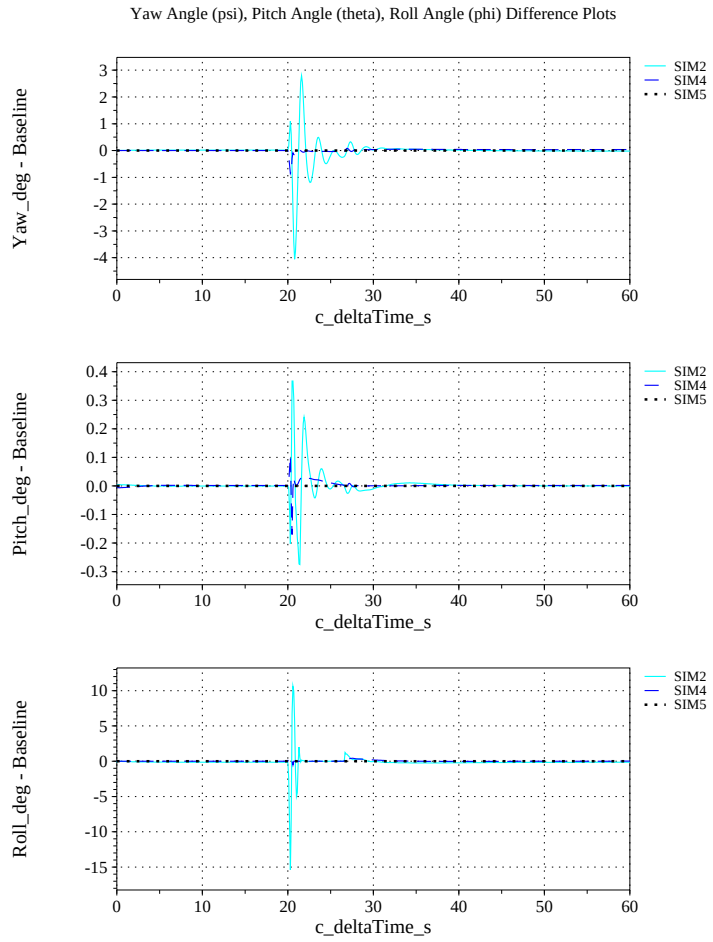

(h) Euler Angles (w.r.t. NED Frame) Differenced

Figure 31. Check-case 13.4: Lateral Offset Maneuver of a Subsonic Aircraft; See Discussion in Section D.1.16 (Cont'd)

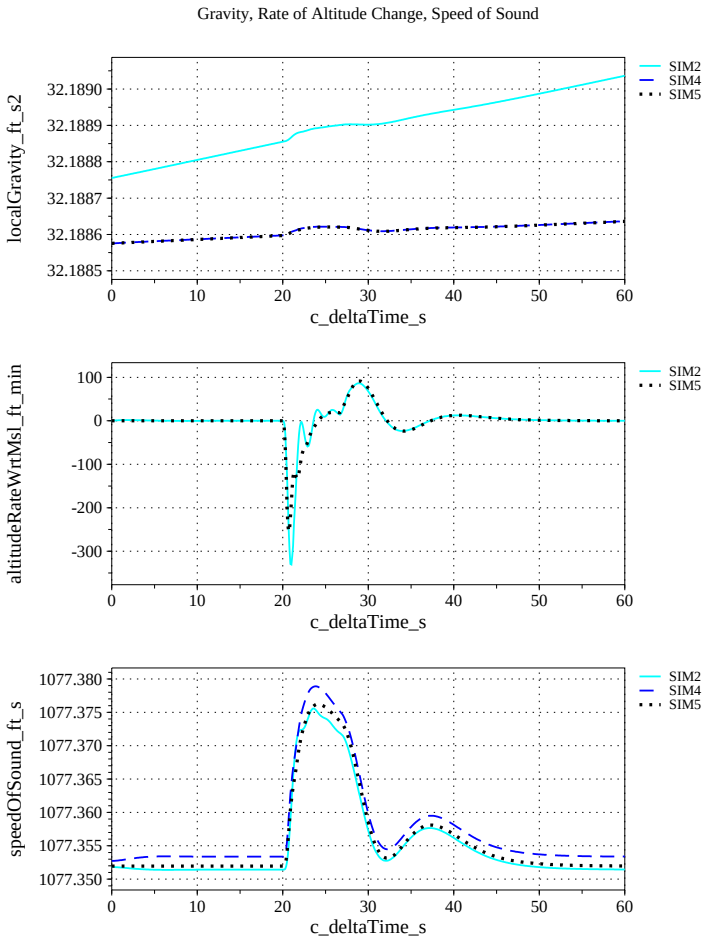

(i) Gravity, Climb Rate, and Speed-of-sound Compared

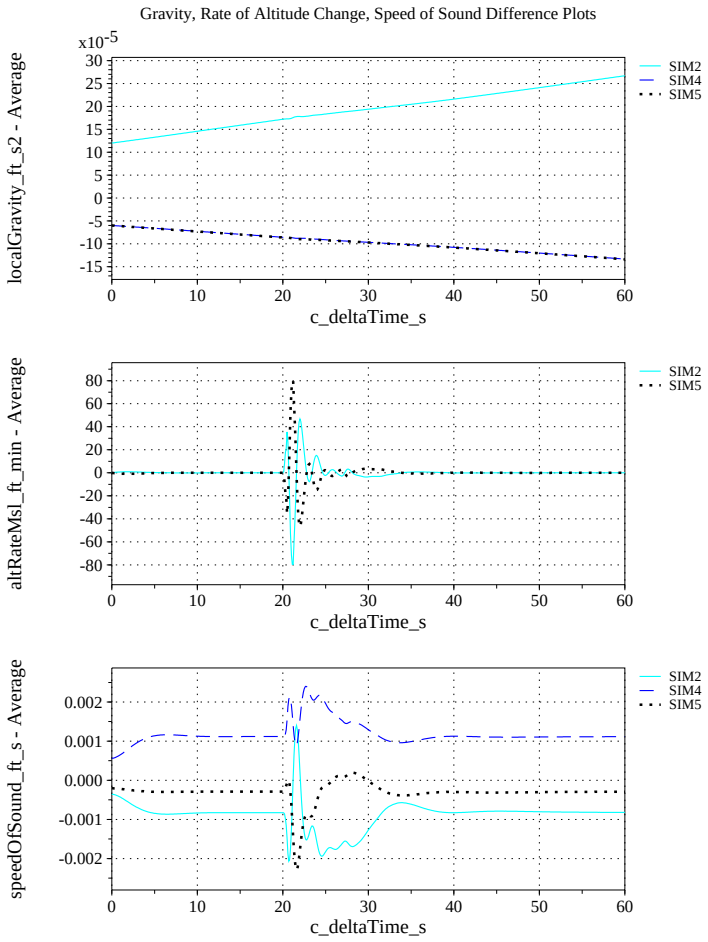

(j) Gravity, Climb Rate, and Speed-of-sound Differenced

Figure 31. Check-case 13.4: Lateral Offset Maneuver of a Subsonic Aircraft; See Discussion in Section D.1.16 (Cont'd)

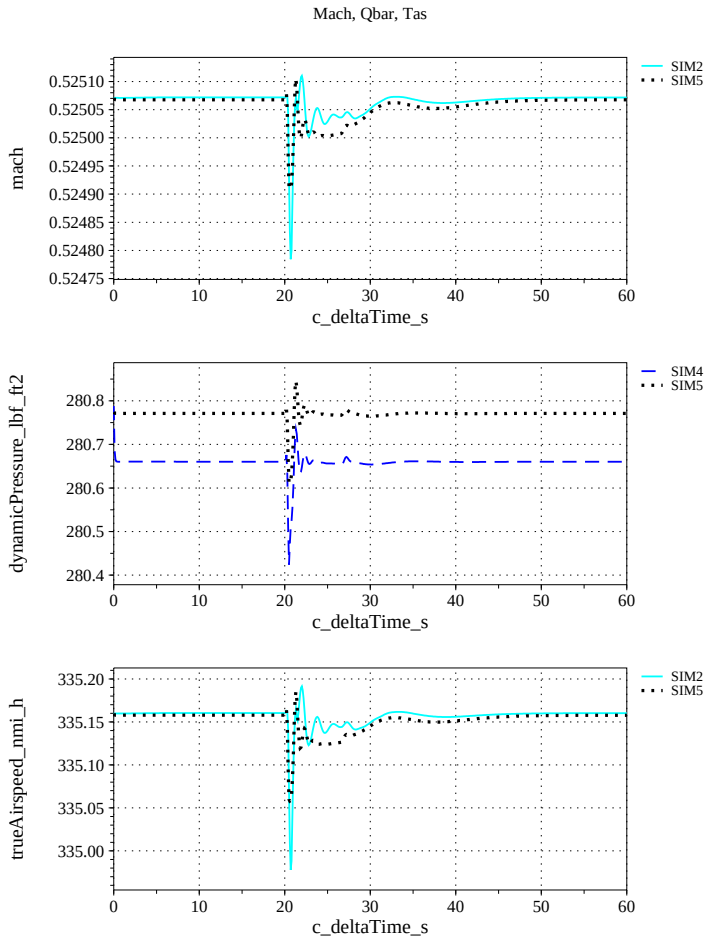

(k) Mach, Dynamic Pressure, and True Airspeed Compared

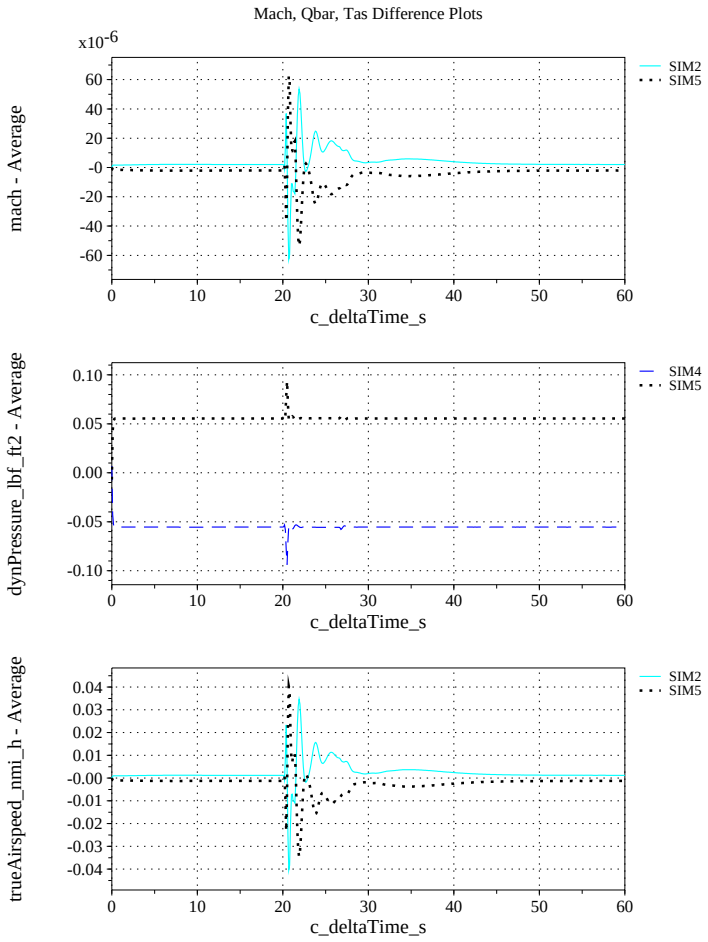

(l) Mach, Dynamic Pressure, and True Airspeed Differenced

Figure 31. Check-case 13.4: Lateral Offset Maneuver of a Subsonic Aircraft; See Discussion in Section D.1.16 (Cont'd)

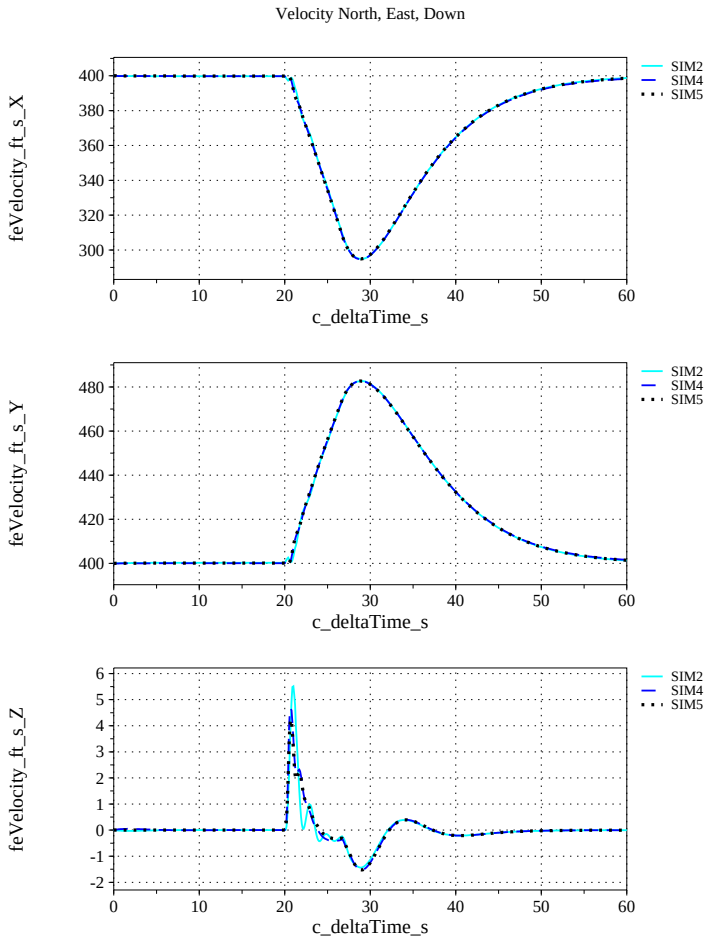

(m) NED Velocities Compared

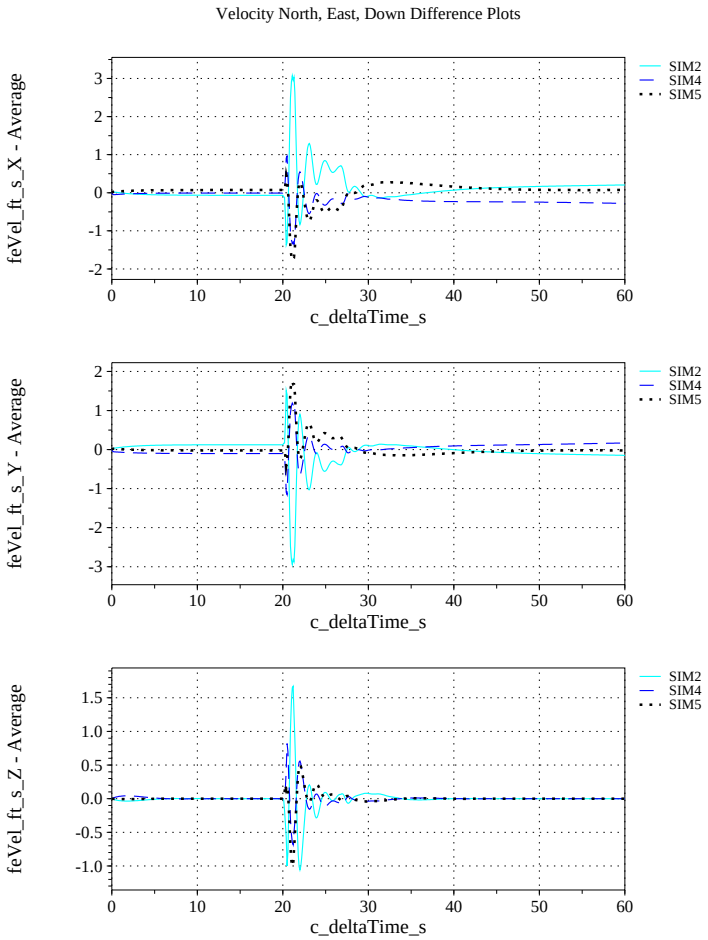

(n) NED Velocities Differenced

Figure 31. Check-case 13.4: Lateral Offset Maneuver of a Subsonic Aircraft; See Discussion in Section D.1.16 (Cont'd)

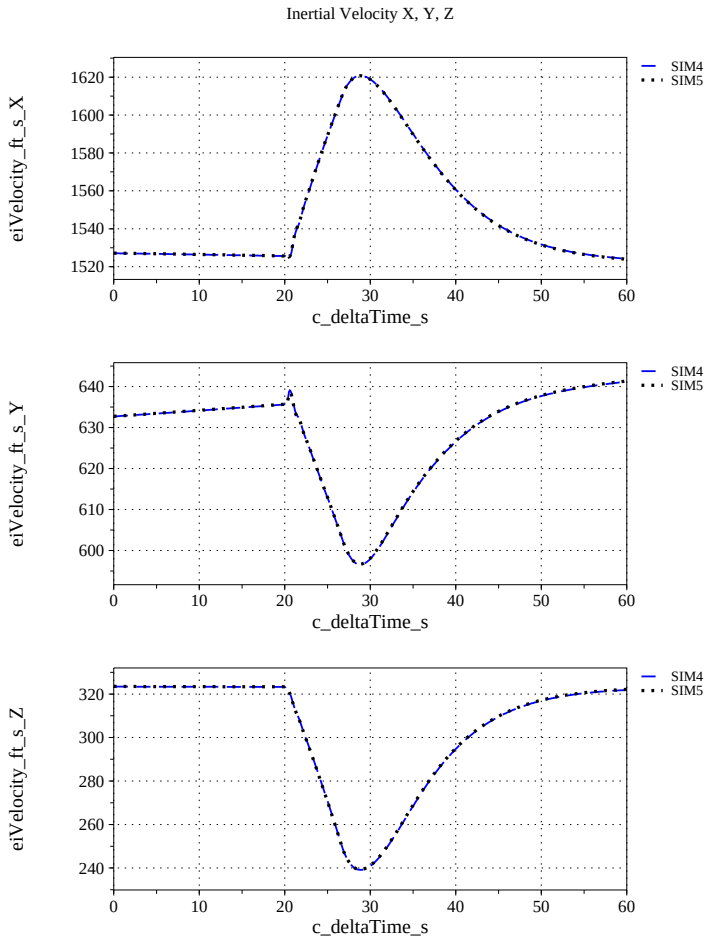

(o) Inertial Velocities Compared

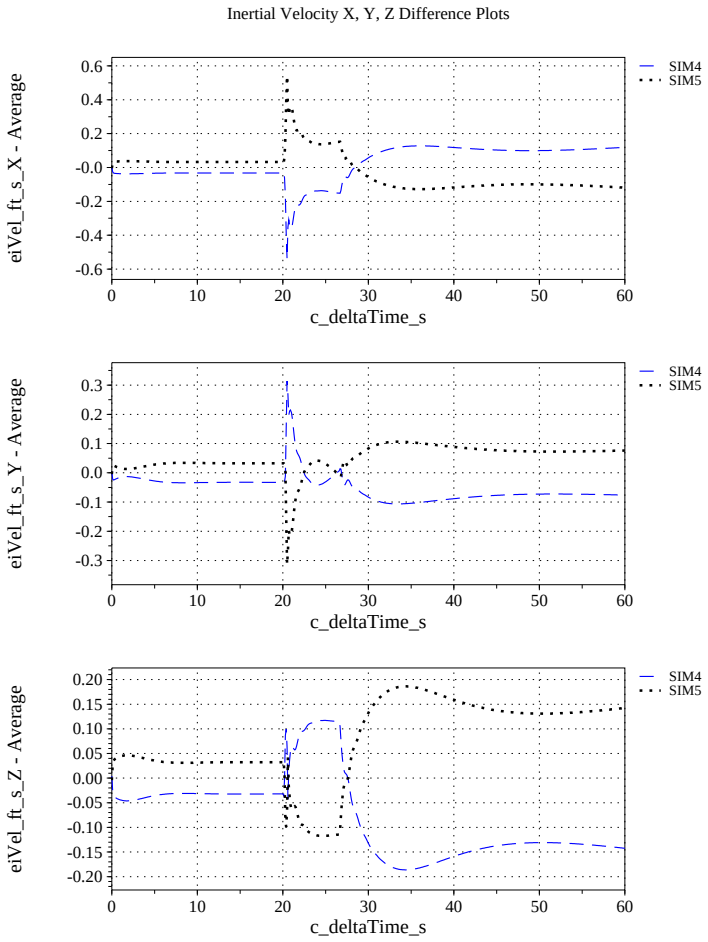

(p) Inertial Velocities Differenced

Figure 31. Check-case 13.4: Lateral Offset Maneuver of a Subsonic Aircraft; See Discussion in Section D.1.16 (Cont'd)

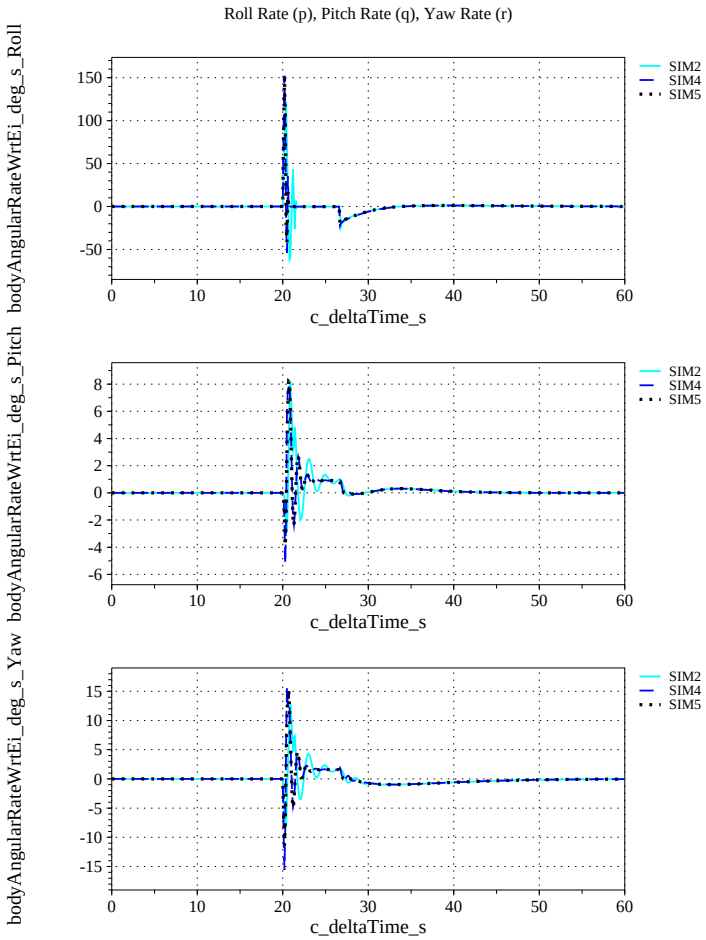

(q) Body-axis Angular Rates (w.r.t. NED Frame) Compared

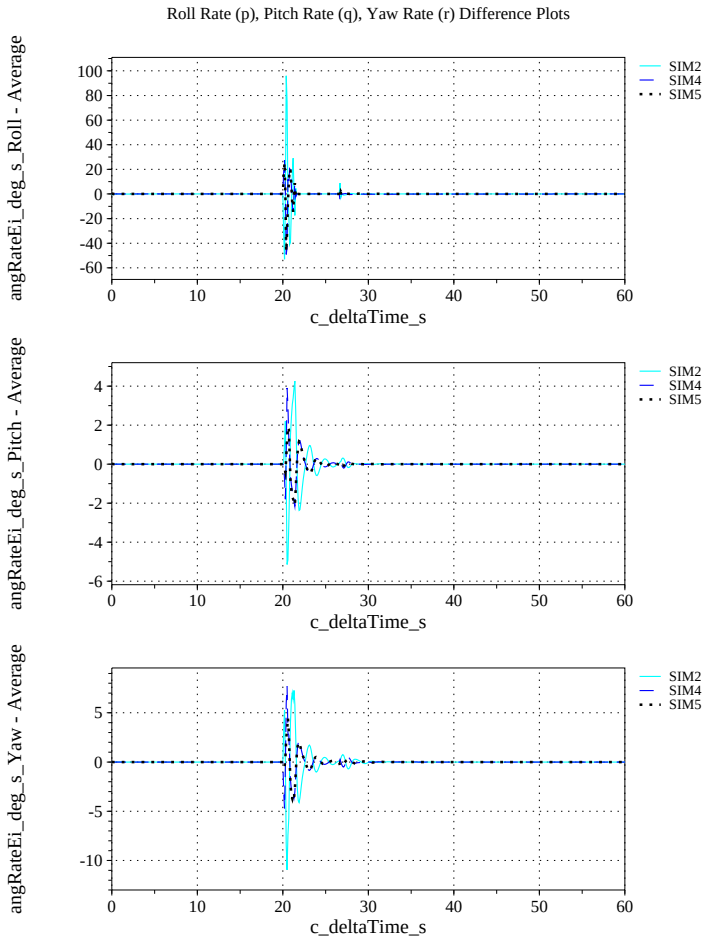

(r) Body-axis Angular Rates (w.r.t. NED Frame) Differenced

Figure 31. Check-case 13.4: Lateral Offset Maneuver of a Subsonic Aircraft; See Discussion in Section D.1.16 (Cont'd)

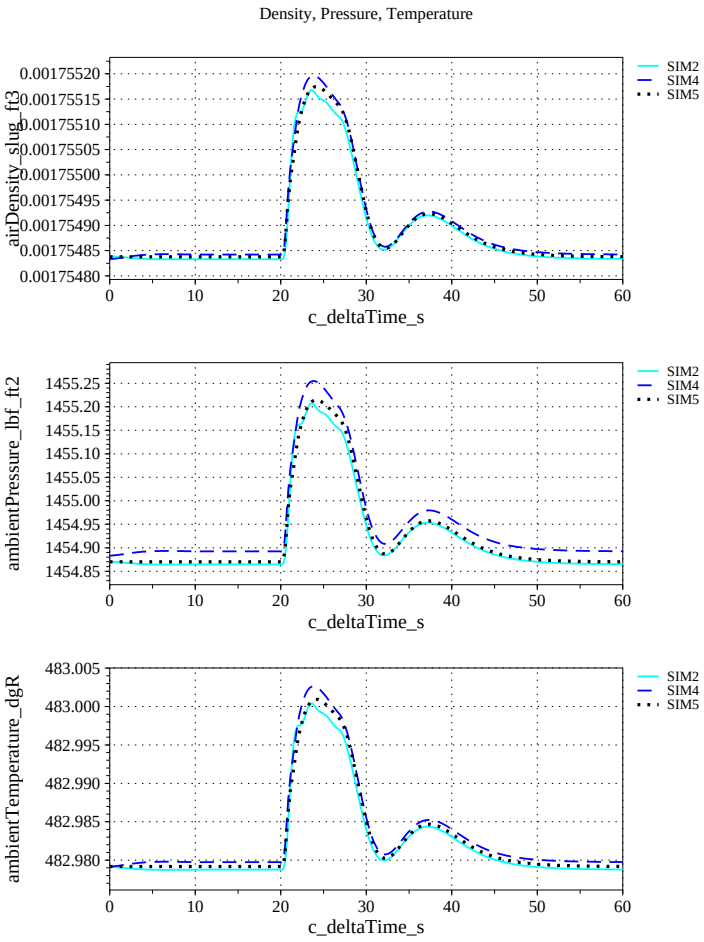

(s) Atmospheric Properties Compared

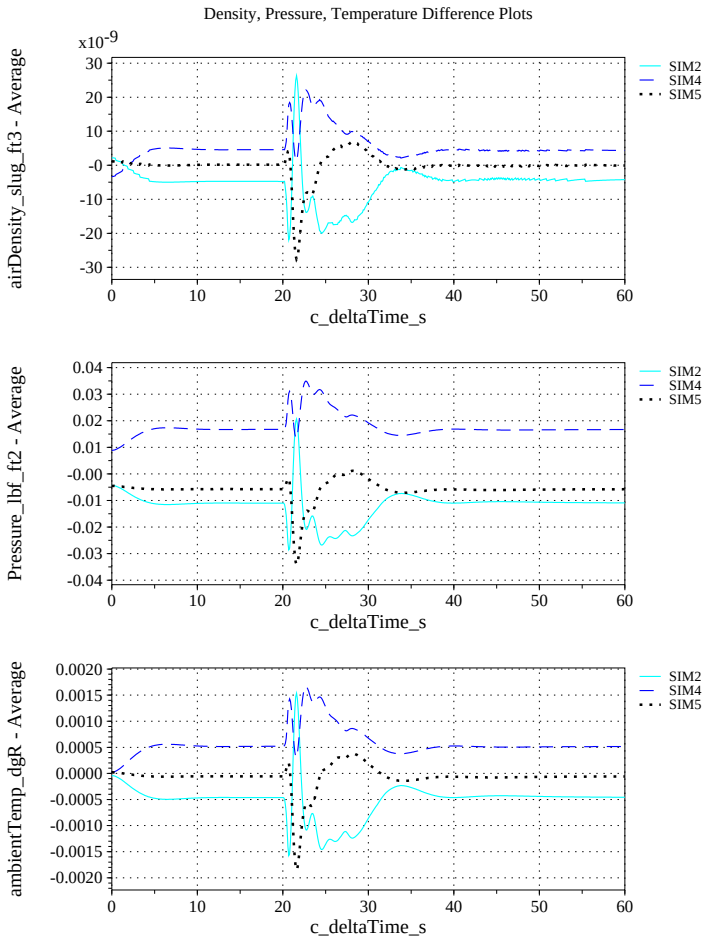

(t) Atmospheric Properties Differenced

Figure 31. Check-case 13.4: Lateral Offset Maneuver of a Subsonic Aircraft; See Discussion in Section D.1.16 (Cont'd)

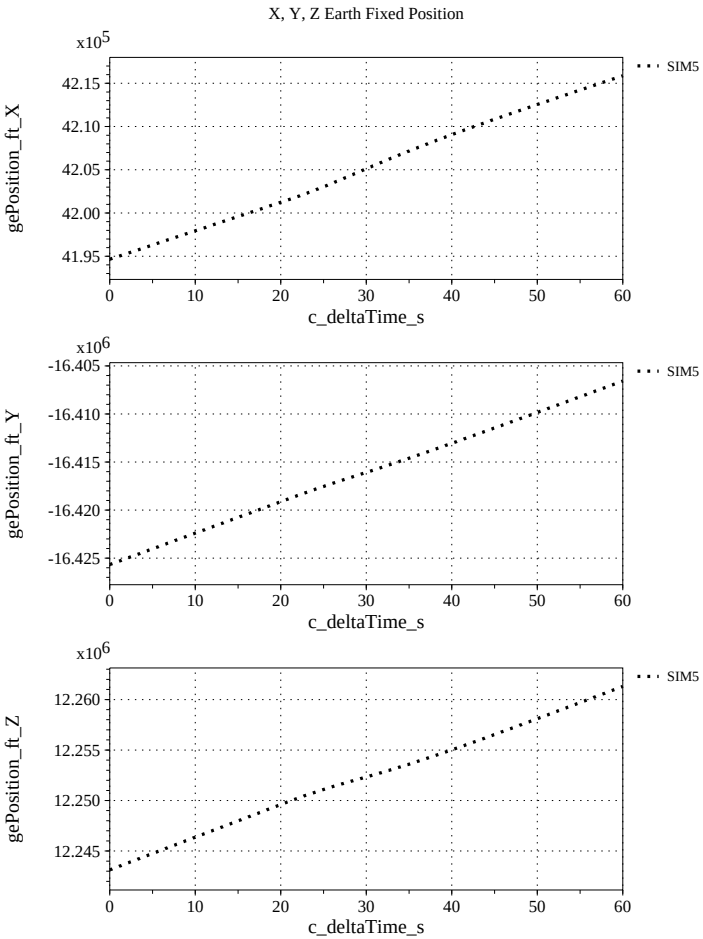

(u) Earth-centered, Earth-fixed Rectangular (X-Y-Z) Positions Compared

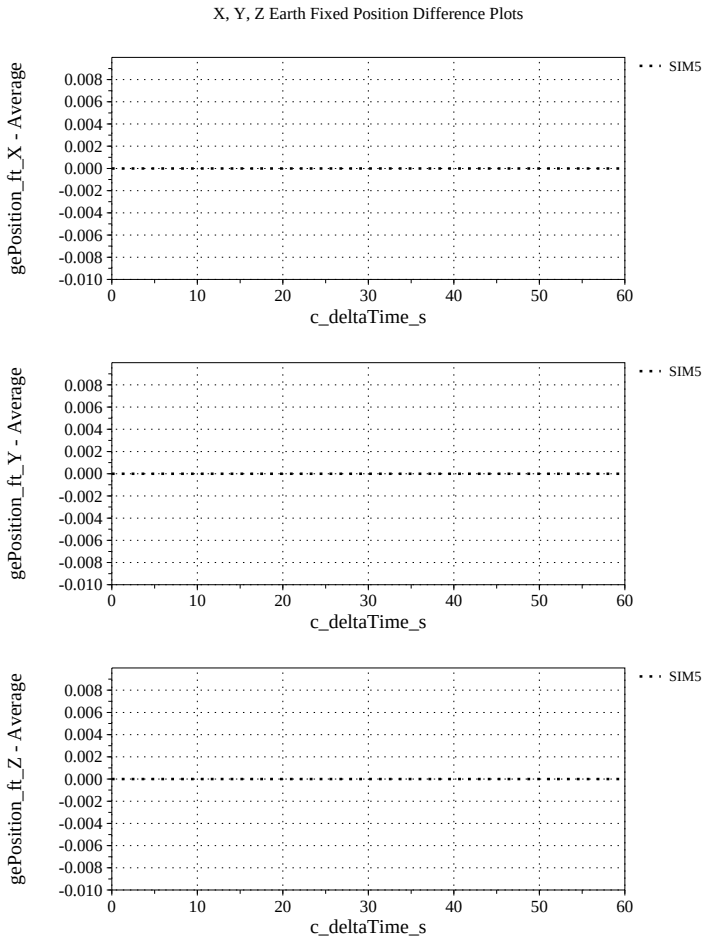

(v) Earth-centered, Earth-fixed Rectangular (X-Y-Z) Positions Differenced

Figure 31. Check-case 13.4: Lateral Offset Maneuver of a Subsonic Aircraft; See Discussion in Section D.1.16 (Cont'd)

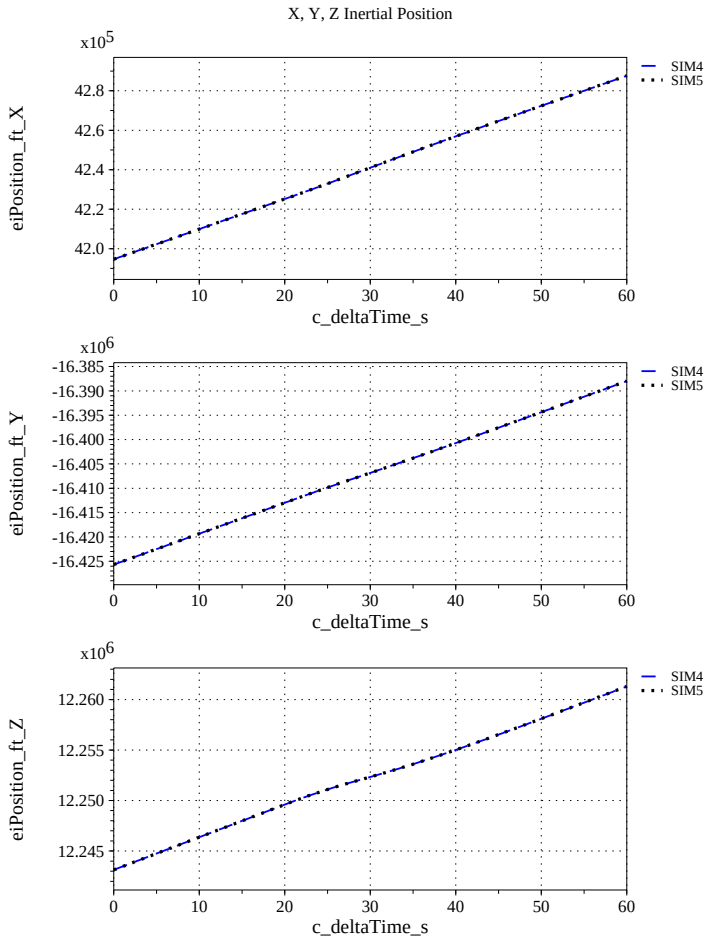

(w) Earth-centered Inertial Rectangular (x-y-z) Positions Compared

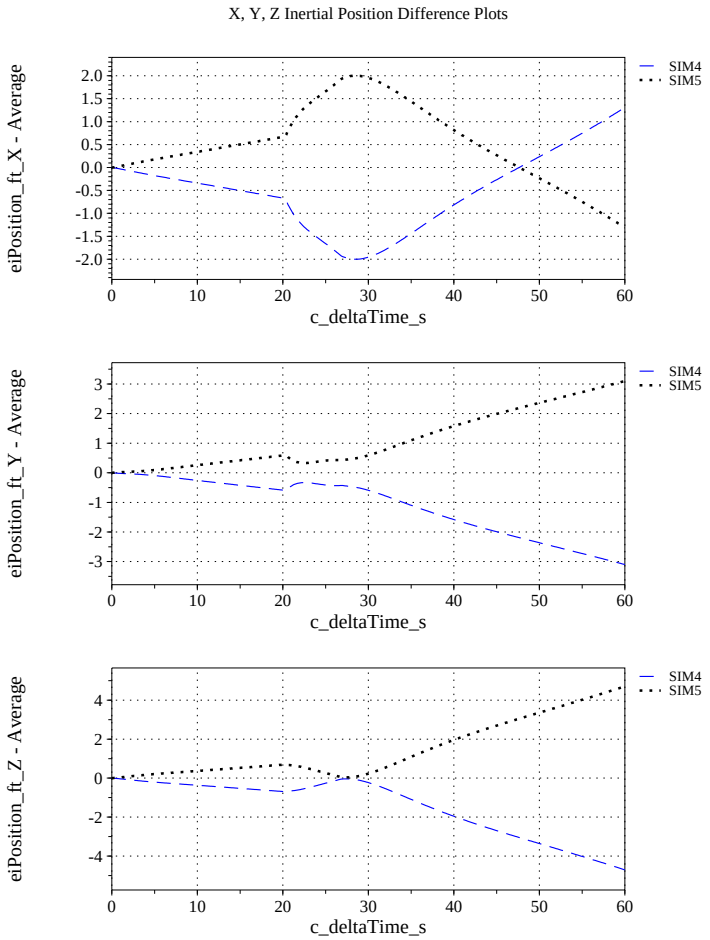

(x) Earth-centered Inertial Rectangular (x-y-z) Positions Differenced

Figure 31. Check-case 13.4: Lateral Offset Maneuver of a Subsonic Aircraft; See Discussion in Section D.1.16 (Concluded)

D.1.17 Check-case 15 – circumnavigation of the North Pole

This section shows cross-plots for two of the selected simulation tools in modeling the dynamics of a subsonic aircraft flying in a circle around the North Pole of a rotating, ellipsoidal (WGS-84) Earth with J_2 gravitational harmonics. This scenario is described in Section C.1.18. Figures 33a through 33x compare results between the two simulation tools, as well as the deviances of the outputs from each tool from the ensemble average value.

Atmospheric check-case 15 executed a circumnavigation of the North Pole as directed by a slightly more sophisticated autopilot. All participating simulation tools succeeded in establishing a steady-state circumnavigation of the pole; however, differences in both the initial state and the circumnavigation steady state values were observed.

Figure 32a shows a top-down view of the trajectory predicted by three simulation tools for this check-case. In the 180 sec of run-time, the three vehicles circumnavigate more than three-quarters of the way around a circle designed to have a radius of 3.0 nautical miles. Figure 32b shows a closer detail near the point where SIM 2's slightly larger circumnavigation ends, showing the location of the other two trajectories inside SIM 2's circle.

As with prior F-16 test cases, the simulations began with differences in their equilibrium solutions at the start of the scenario. In this scenario, all simulated trajectories began with distinctly different angular rates. As before, SIM 2 constrained the inertial angular rate of zero. SIM 4 appeared to have modified its equilibrium solution to target an angular rate of zero in the Earth-relative frame, while SIM 5 solved for the three-axis angular rate that maintained the vehicle orientation relative to the local vertical frame as the simulated vehicle flew over the curved surface of the Earth.

In SIM 4, the zero rotational rate relative to the Earth induced no aerodynamic side force, rolling moment, or yawing moment. In SIM 2, a zero inertial rate translated into an Earth-relative rate where much of the Earth's rotation rate appeared in body-axis yaw rate r_b with a small residual in body-axis roll rate p_b. The Earth-relative rate induced an aerodynamic side force, rolling moment, and yawing moment but these are small enough to be ignored: the induced side force was 0.14 lbf. On the other hand, SIM 5 initialized the vehicle at an Earth-relative roll, pitch, and yaw rate of 0.0828 deg/s, −0.0015 deg/s, and 1.7640 deg/s, respectively. These larger rates, especially in yaw, may seem excessive; however, the angular momentum represented by these rates is nearly identical to the angular momentum that the autopilot's control inputs generated for the circumnavigation flight.

The main difference in the starting and ending angular rates for SIM 5 was a result of the roll angle that the autopilot commands to establish the circumnavigation as a coordinated turn. That roll angle transfers some of the angular moment from the yaw rate to the pitch rate. The initial roll and yaw rates for SIM 5 do generate substantial lateral forces and moments. The initial aerodynamic side force, rolling moment, and yawing moment are −63 lbf, −226 lbf-ft, and 786 lbf-ft, respectively. The SIM 5 equilibrium solver forced rudder and ailerons to have zero deflection. Therefore, these rotation-induced forces and moments were not counterbalanced at the start of the simulation. Since the autopilot was engaged at the start of the scenario and would immediately command the vehicle into circumnavigation flight, the accelerations that would result from these induced forces and moments were quickly counterbalanced. Nevertheless, this led to differences in lateral forces and moments at the start of the run, compared to SIM 2 and SIM 4, before the autopilot achieved a steady-state circumnavigation configuration.

SIM 2 runs began with a non-zero aerodynamic side force and aerodynamic yawing moment that were larger than what would be induced by the initial non-zero angular rate relative to the Earth. Moreover, SIM 2 began with a small roll angle of −0.083 degrees. In previous cases, these differences were attributed to a gravity vector deflected from the local normal as a result of SIM 2 treating the geocentric frame as the

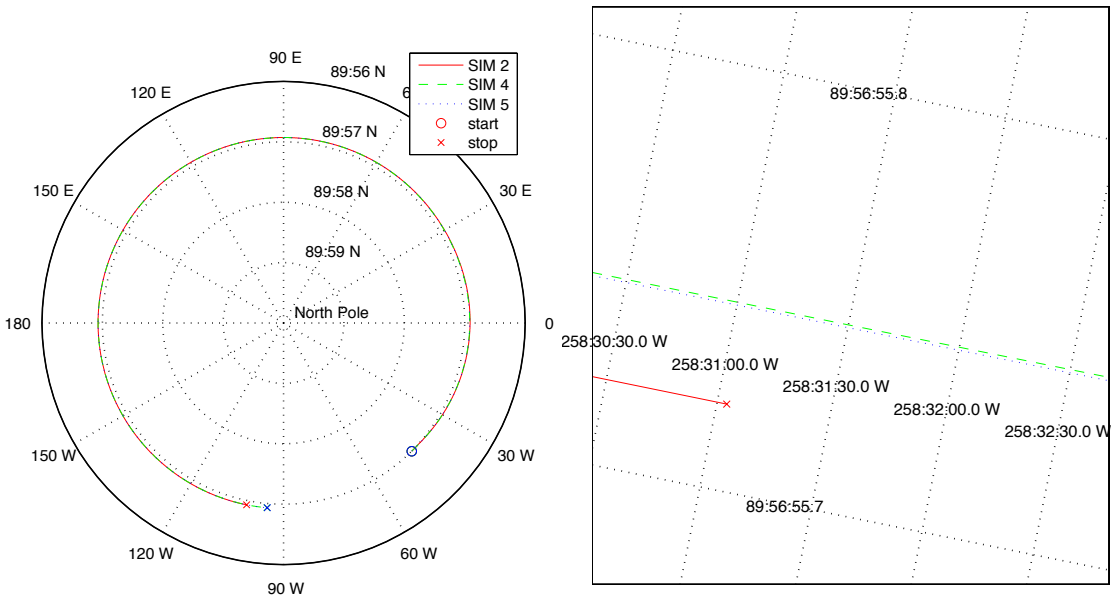

(a) View from above North Pole

(b) Detail near end of SIM 2

Figure 32. Trajectories of Simulated F-16 Circling the North Pole for Three Simulation Tools

local vertical. In the previous cases, the angle of deflection of SIM 2's gravity vector from a vector normal to the reference ellipsoid matched the difference between the geocentric and geodetic latitude. However, the geocentric and geodetic frames are nearly coincident for this check-case, as the scenario is performed close to the North Pole. At this initial location, the difference between the geodetic and geocentric "down" vector was only 0.00034 degrees. This is much smaller than the initial SIM 2 roll angle so the roll angle was not being driven into alignment with the gravity vector. The SIM 2 initial state showed that its rate of change for the air-relative velocity (i.e., $\dot{u}$, $\dot{v}$, and $\dot{w}$) was near zero. The rate-of-change for the air-relative velocity contains a term that is the cross product of the Earth-relative angular rate and the air-relative velocity. As discussed in the previous check-case, SIM 2 had an initial Earth-relative yaw rate equal to the Earth's rotation. The cross-product term would have contributed a value of -0.0411 ft/s^2 to $\dot{v}$. When this acceleration was combined with the gravity vector, the starting acceleration in the y-z plane that the equilibrium solver had to counter had a deflection of -0.07 degrees. This deflection is in the neighborhood of the initial SIM 2 roll angle; therefore, the initial roll angle and aerodynamic side force are driven by the angular-rate-induced $\dot{v}$. The initial aerodynamic yawing moment was needed to counteract the moment at the CM generated by the initial aerodynamic side force.

SIM 4's trajectory began with x and z (body axis) accelerations of -1.98 ft/s^2 and -4.32 ft/s^2, respectively. SIM 4 also had an initial pitch acceleration of -44 deg/s^2 which was the result of an untrimmed aerodynamic pitching moment of $-42,923$ lbf-ft at the CM. The non-zero body z-axis acceleration and aerodynamic pitching moment at the CM had the same root cause. The body z-axis acceleration arose from a lift vector that was larger than necessary for trim. The larger lift was not caused by a difference in dynamic pressure or angle of attack. Both values were nearly identical across the simulations. The cause of the larger lift appeared to be untrimmed elevator deflection. The initial elevator for SIM 4 was set at $+1.09$ degrees (trailing-edge

down). By comparison, the elevator deflection for SIM 5 was −3.26 degrees (trailing-edge up). This elevator deflection also resulted in a non-zero pitching moment at the CM. The initial elevator deflection for SIM 4 actually increased aerodynamic pitching moment at the CM.

The non-zero body x-axis acceleration in SIM 4 was caused by insufficient engine thrust. The initial thrust in SIM 4 of 845 lbf was less than half the thrust required to counter balance the aerodynamic drag and the component of weight in the x axis direction (due to pitch angle). In fact, the initial power level angle (PLA) of 6.32% for SIM 4 is less than half the initial PLA of 13.86% in SIM 5. It is unclear why SIM 4 failed to reduce these accelerations since it did this successfully in the previous F-16 cases, but it did not appear to have been trimmed at initialization. The autopilot quickly corrected these initial accelerations within the first tenth of a second. Therefore, the untrimmed initial conditions for SIM 5's solution did not contribute significantly to the outcome of the simulation.

As in the prior F-16 cases, SIM 2 recorded aerodynamic moments at the MRC, while SIM 4 and SIM 5 recorded aerodynamic moments at the vehicle CM. This led to the large differences shown in Figure 33d.

As with the prior autopilot check-cases 13.1 through 13.4, a different approach was taken in SIM 5 in the modification of the internal reference state values for the LQR controller for angle of attack, pitch attitude, and velocity states to match the values from the equilibrium solution for the initial conditions, which led to small differences in the steady-state circumnavigation conditions.

As in the prior autopilot check-cases, SIM 4 and SIM 5 ended with slightly different steady-state airspeeds. In this scenario the difference in true airspeed was 0.13 ft/s. The minute differences in final latitude and altitude indicated that the circumnavigation path for the two simulated trajectories is nearly identical. Thus the small difference in airspeed was the likely cause of small differences in roll angle and pitch angle, since velocity determines the necessary bank angle for coordinated flight at given turn radius as well as affecting the angle of attack necessary to maintain level flight. The difference in velocity was also the dominant contributor to the difference in longitude between the two simulations. The longitude difference of 0.0639 degrees after 180 sec represented a distance of 21 ft which was close to the distance of 23 ft that would occur with a 0.13 ft/s difference in airspeed for 180 sec.

SIM 2 followed a slightly larger circumnavigation radius than SIM 4 or SIM 5 (approximately 2.368 ft farther south) as shown in Figure 32b. However, such a small increase in circumnavigation radius was contradicted by the differences in longitude and roll angle, both of which should primarily depend on the differences in airspeed and circumnavigation radius. The airspeed difference between SIM 2 and SIM 5 was 0.02 ft/s and should have produced a lead for SIM 2 of 4 ft after $t = 180$ sec if the circumnavigation radii were equal. However, the larger radius circle flown by SIM 2 should have caused it to lag behind SIM 4 and 5 in longitude, despite having a slightly faster airspeed. The longitudinal difference at $t = 180$ sec should have been in the neighborhood of −0.03 degrees; thus SIM 2's simulated trajectory should have trailed behind those of SIM 4 and 5, ending with a distance of about 9 ft to the west. However, SIM 2 showed a lead in longitude of 0.93 degrees (300 ft east) at $t = 180$ sec. With identical airspeeds, this further distance flown in SIM 2's solution implied SIM 2's circumnavigation radius would need to be approximately 57 ft shorter. A steeper steady-state roll angle given by SIM 2's solution of 0.135 degrees also suggested a shorter navigation radius. To a first-order approximation, this increase would imply a reduction in circumnavigation radius of about 100 ft.

Assuming integrations were performed in inertial coordinates by all simulations and then positions were transferred to geodetic coordinates, it appears that there may be some difference between the simulation tools in the conversion from geodetic coordinates to geocentric coordinates that shortened the distance to the pole for a given geodetic latitude.

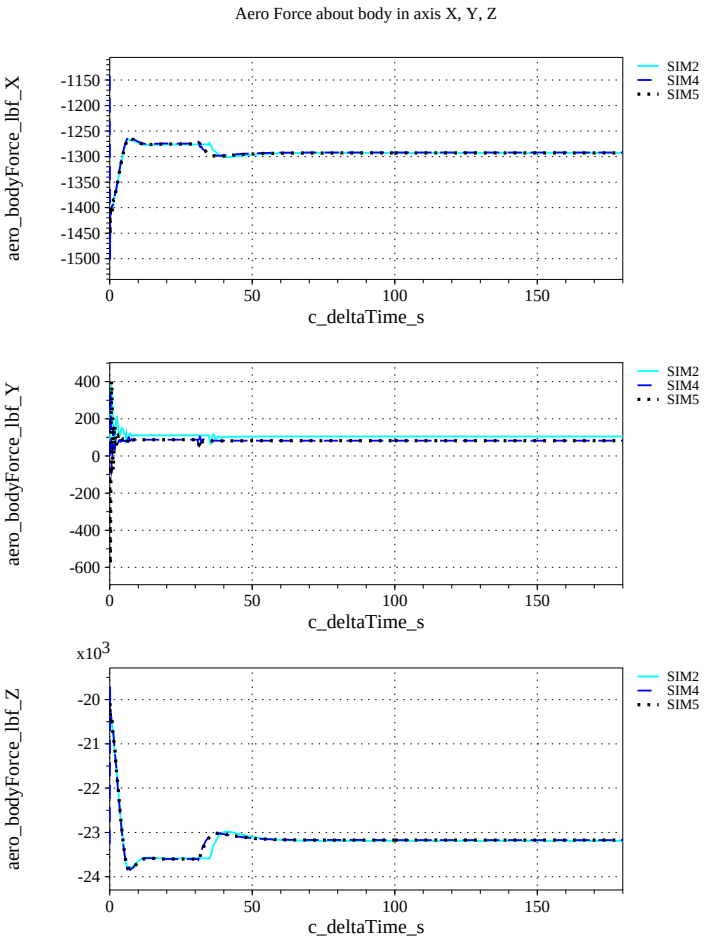

(a) Aerodynamic Forces Compared

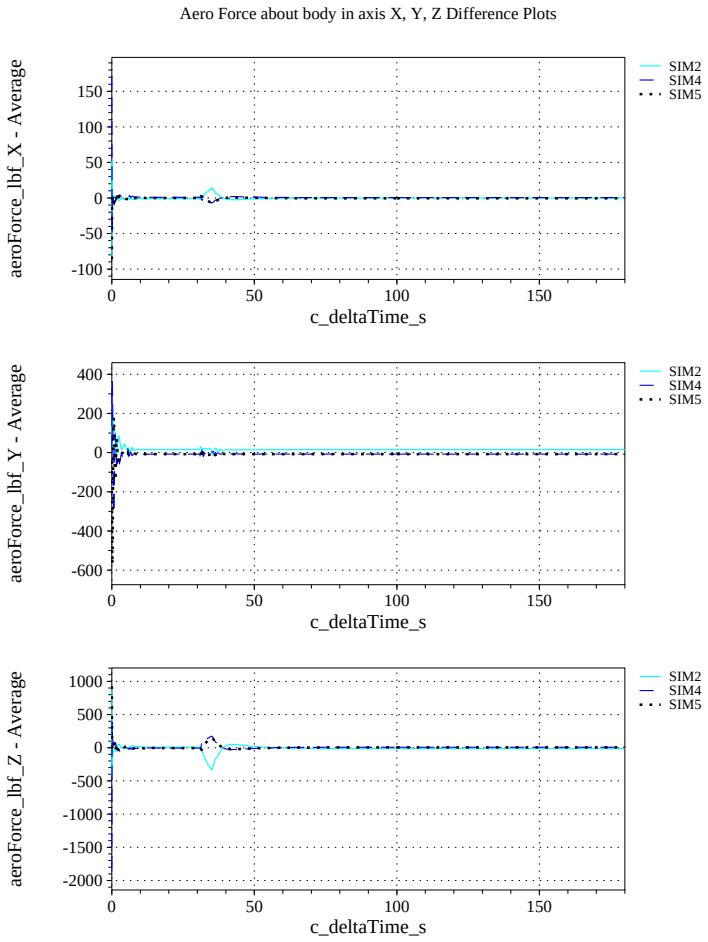

(b) Aerodynamic Forces Differenced

Figure 33. Check-case 15: Circumnavigation of the North Pole; See Discussion in Section D.1.17

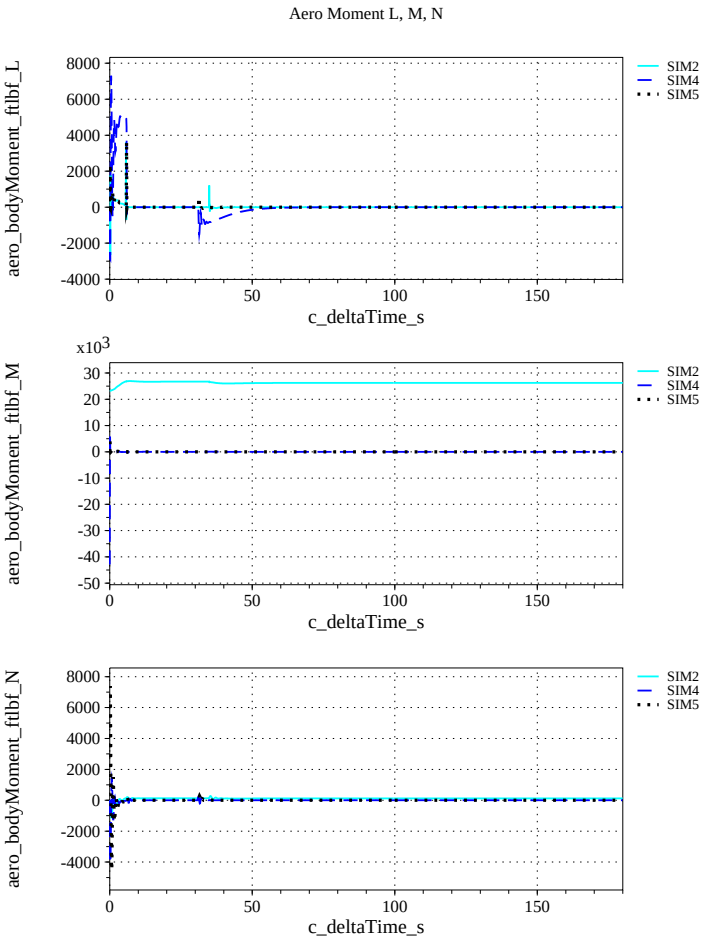

(c) Aerodynamic Moments Compared

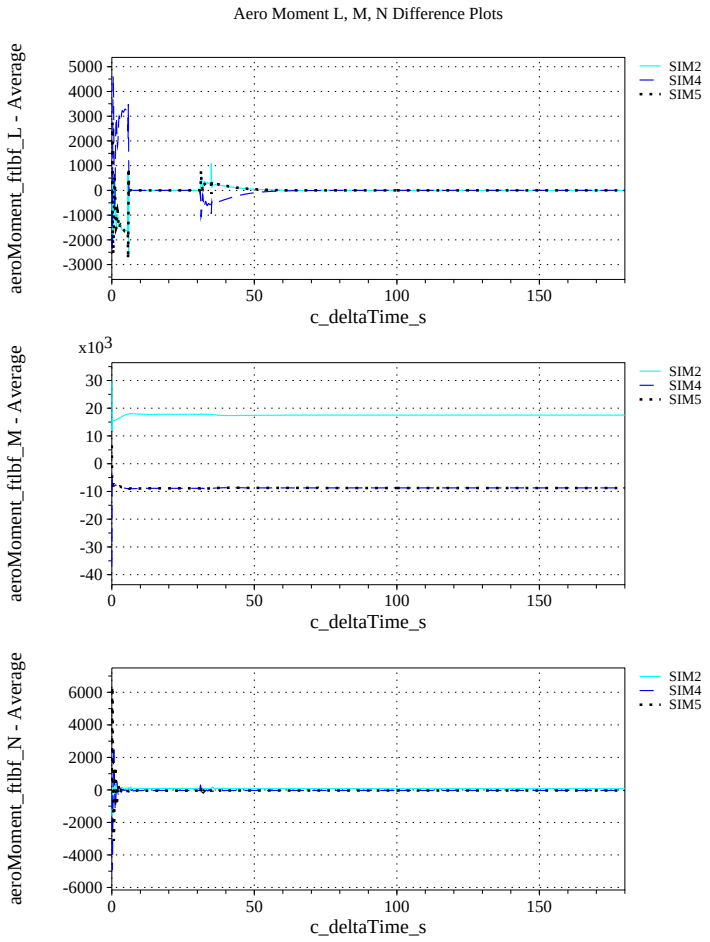

(d) Aerodynamic Moments Differenced

Figure 33. Check-case 15: Circumnavigation of the North Pole; See Discussion in Section D.1.17 (Cont'd)

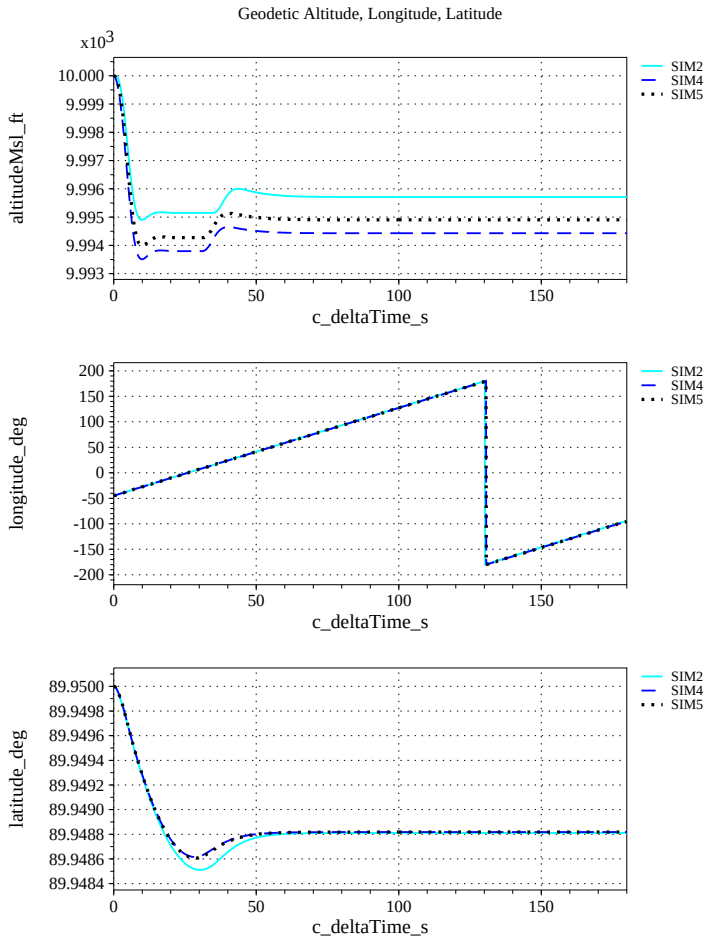

(e) Altitude, Geodetic Latitude and Longitude Compared

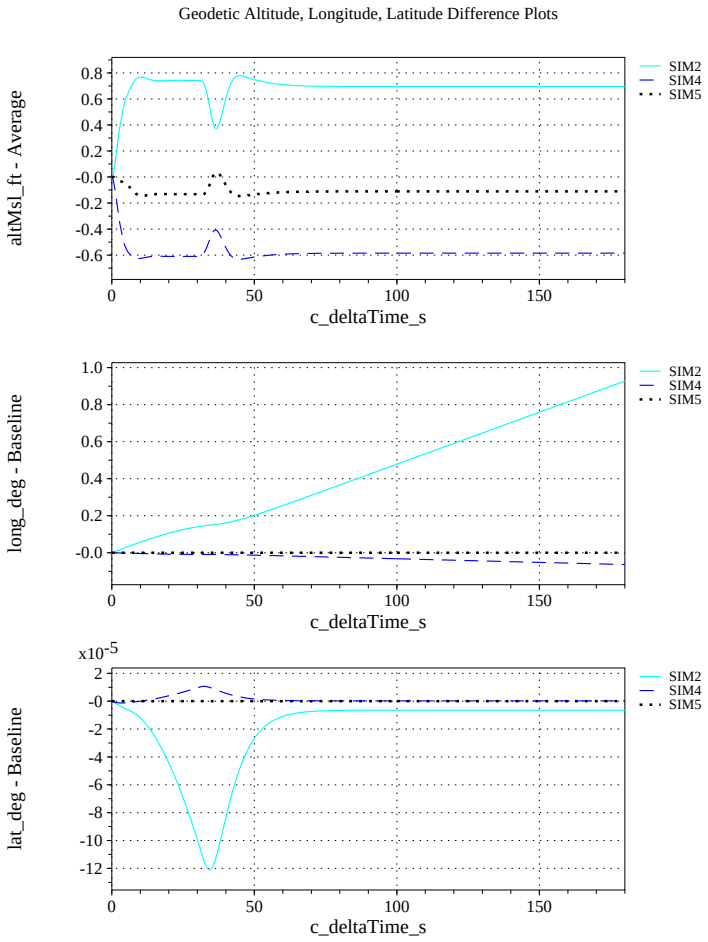

(f) Altitude, Geodetic Latitude and Longitude Differenced

Figure 33. Check-case 15: Circumnavigation of the North Pole; See Discussion in Section D.1.17 (Cont'd)

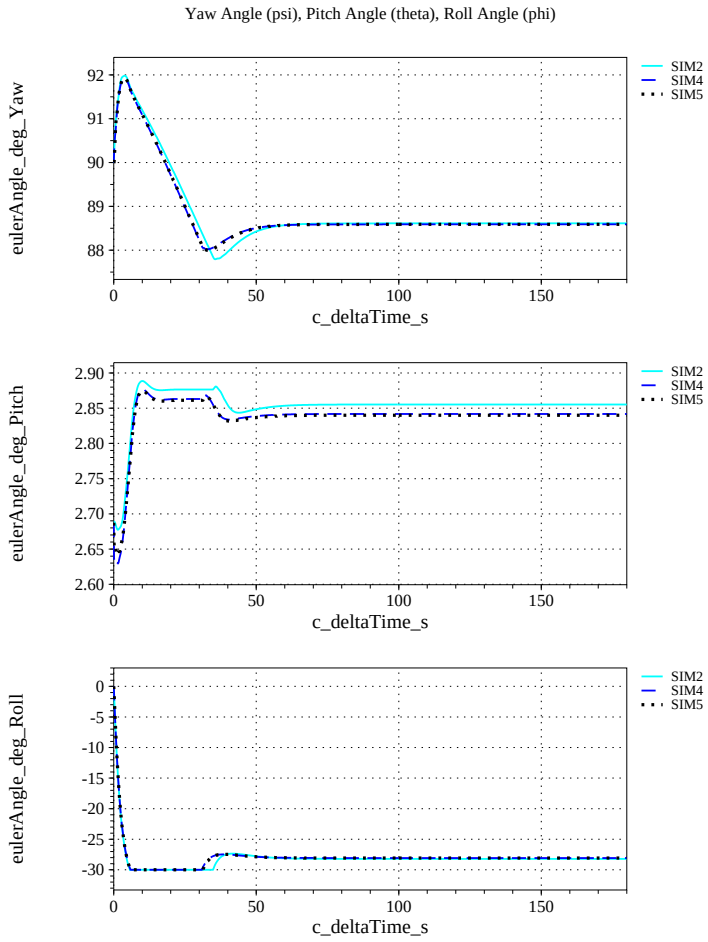

(g) Euler Angles (w.r.t. NED Frame) Compared

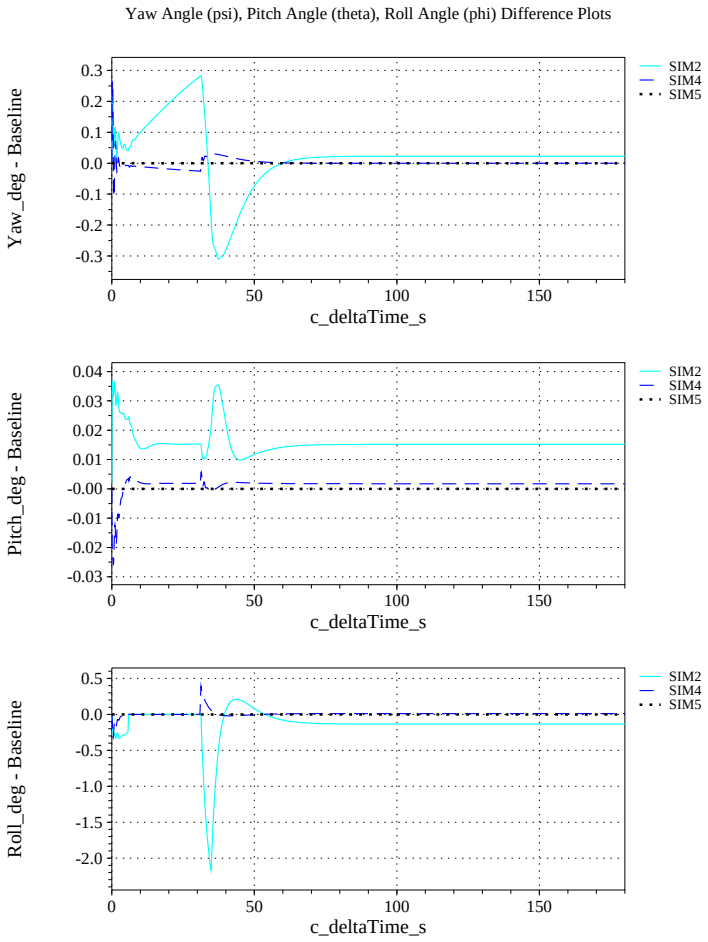

(h) Euler Angles (w.r.t. NED Frame) Differenced

Figure 33. Check-case 15: Circumnavigation of the North Pole; See Discussion in Section D.1.17 (Cont'd)

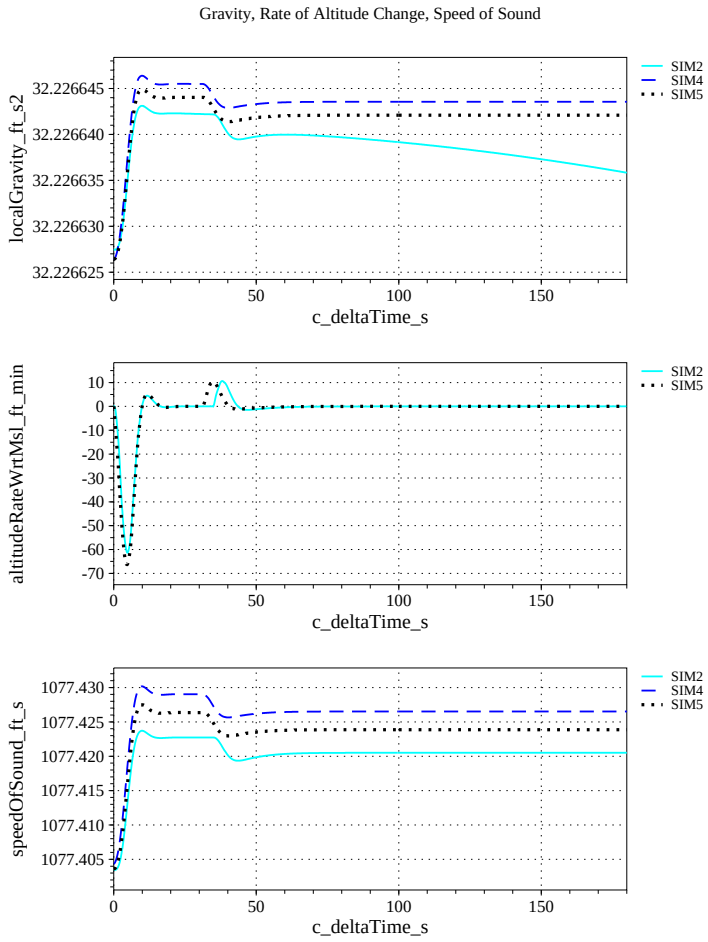

(i) Gravity, Climb Rate, and Speed-of-sound Compared

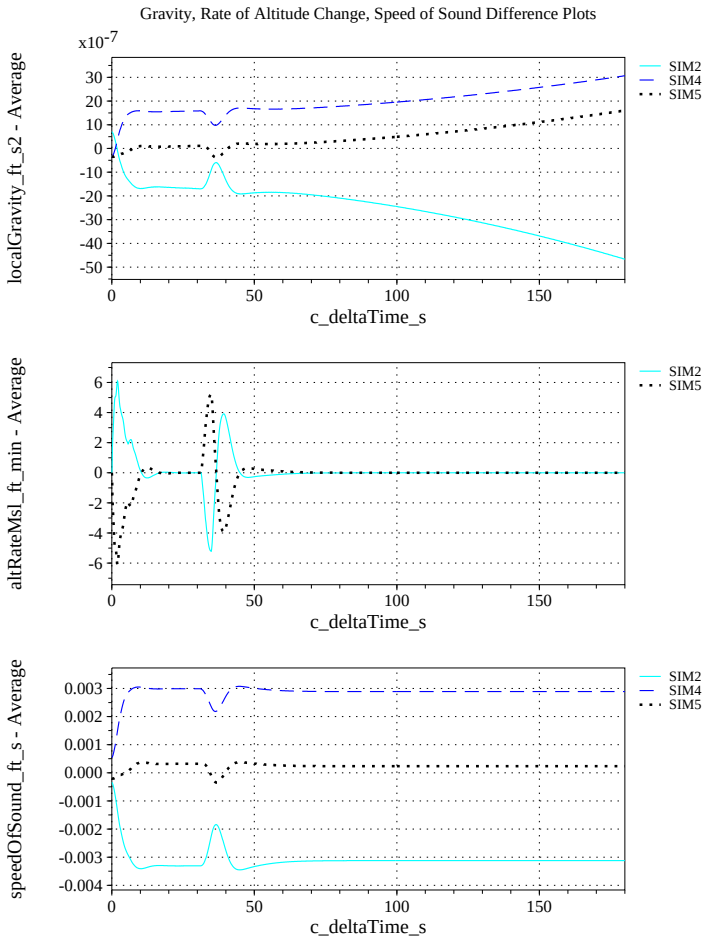

(j) Gravity, Climb Rate, and Speed-of-sound Differenced

Figure 33. Check-case 15: Circumnavigation of the North Pole; See Discussion in Section D.1.17 (Cont'd)

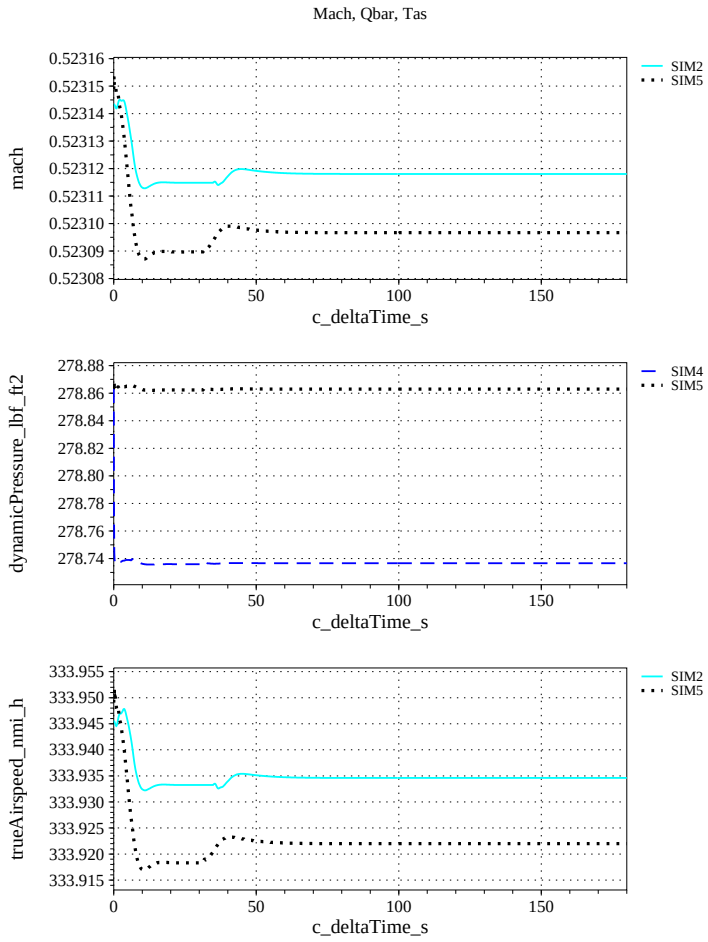

(k) Mach, Dynamic Pressure, and True Airspeed Compared

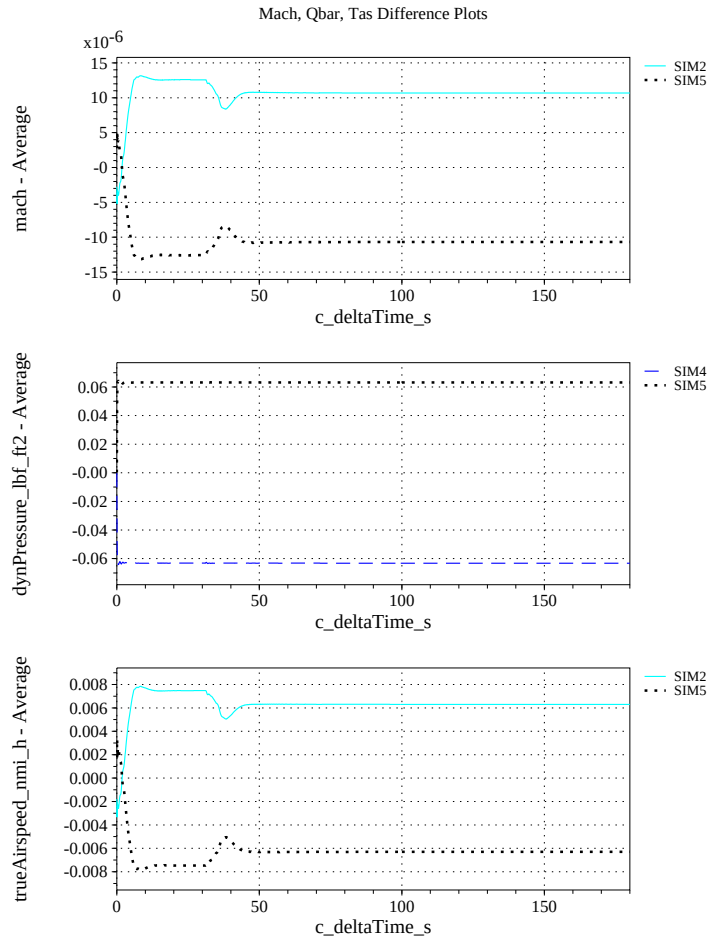

(l) Mach, Dynamic Pressure, and True Airspeed Differenced

Figure 33. Check-case 15: Circumnavigation of the North Pole; See Discussion in Section D.1.17 (Cont'd)

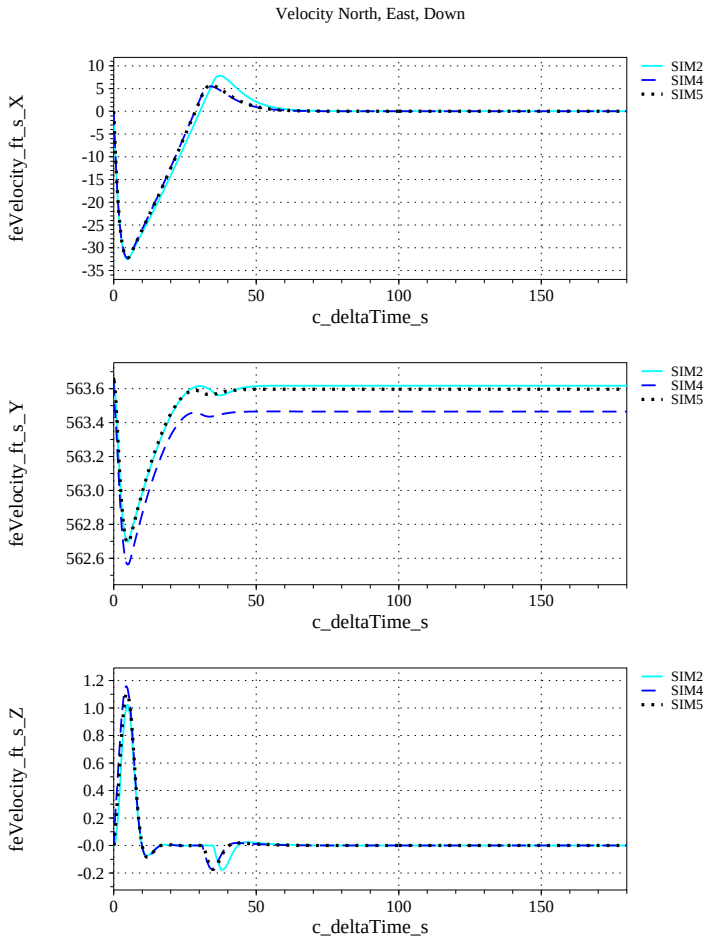

(m) NED Velocities Compared

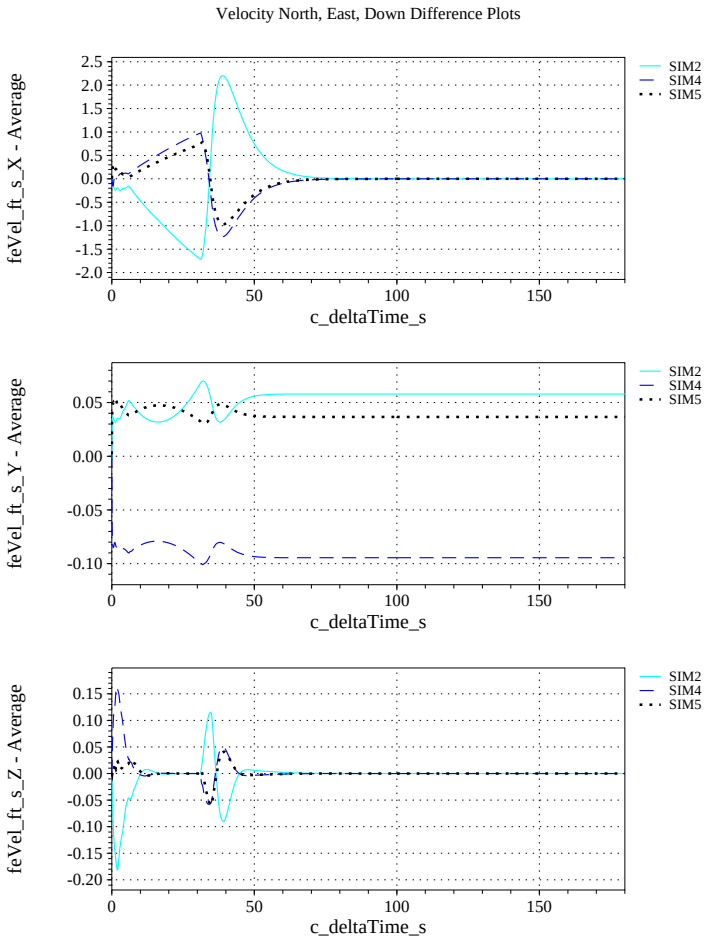

(n) NED Velocities Differenced

Figure 33. Check-case 15: Circumnavigation of the North Pole; See Discussion in Section D.1.17 (Cont'd)

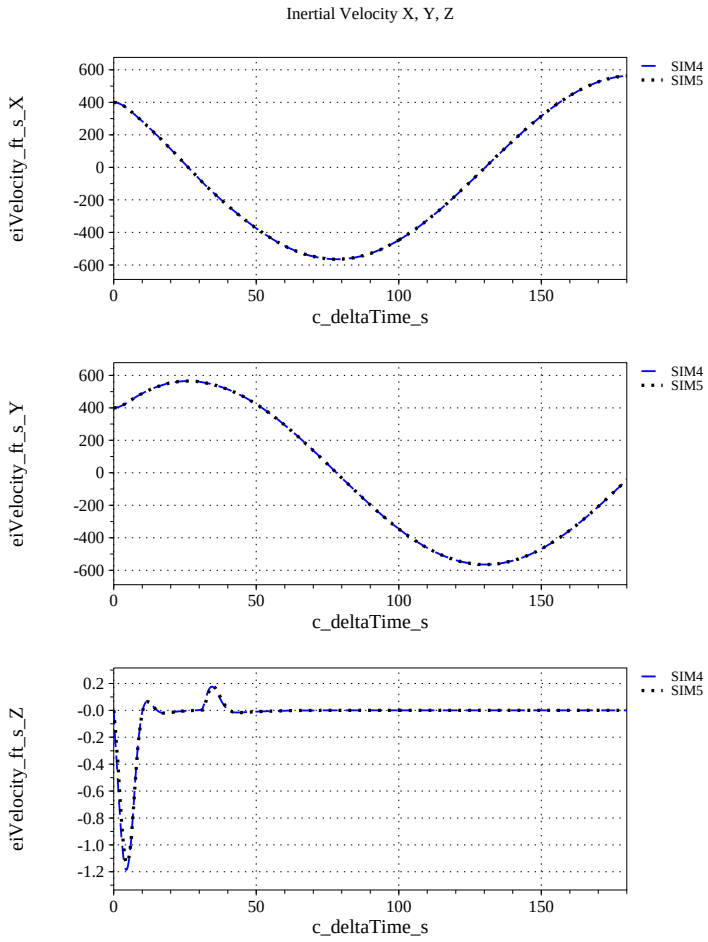

(o) Inertial Velocities Compared

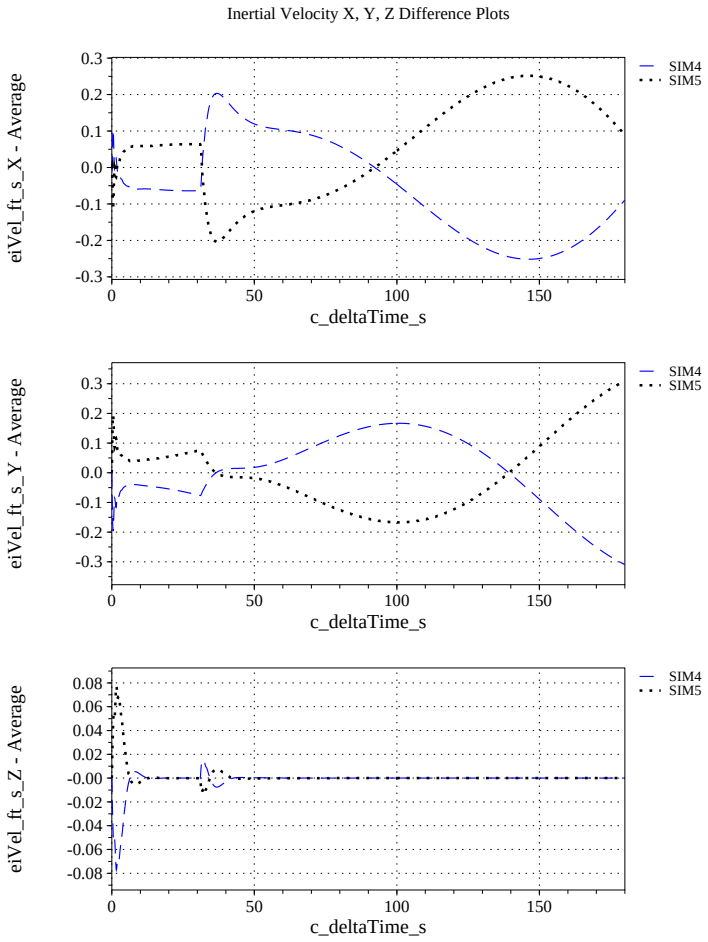

(p) Inertial Velocities Differenced

Figure 33. Check-case 15: Circumnavigation of the North Pole; See Discussion in Section D.1.17 (Cont'd)

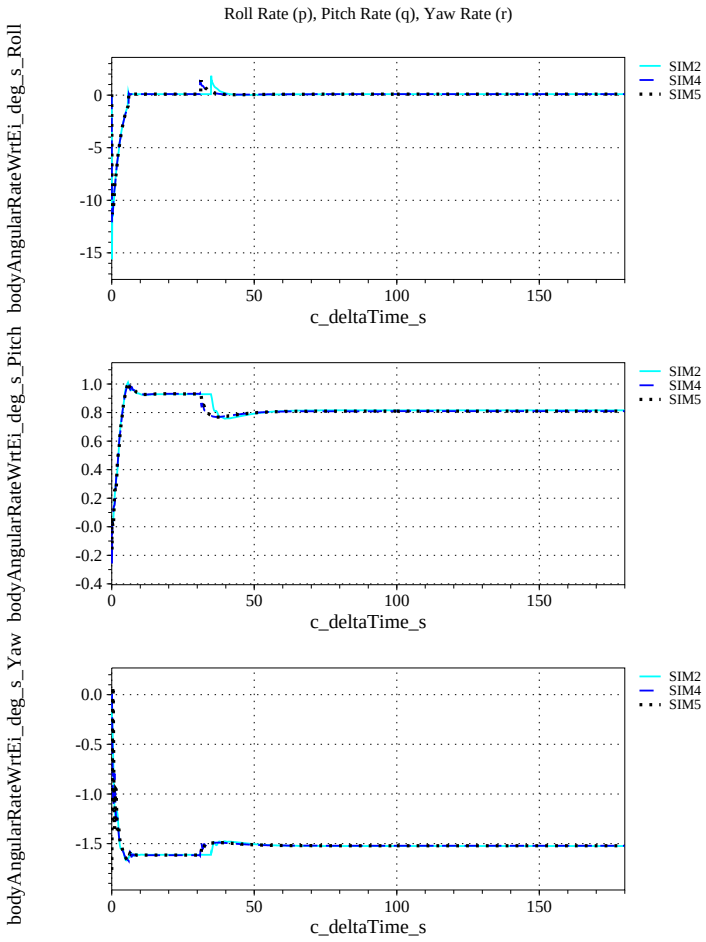

(q) Body-axis Angular Rates (w.r.t. NED Frame) Compared

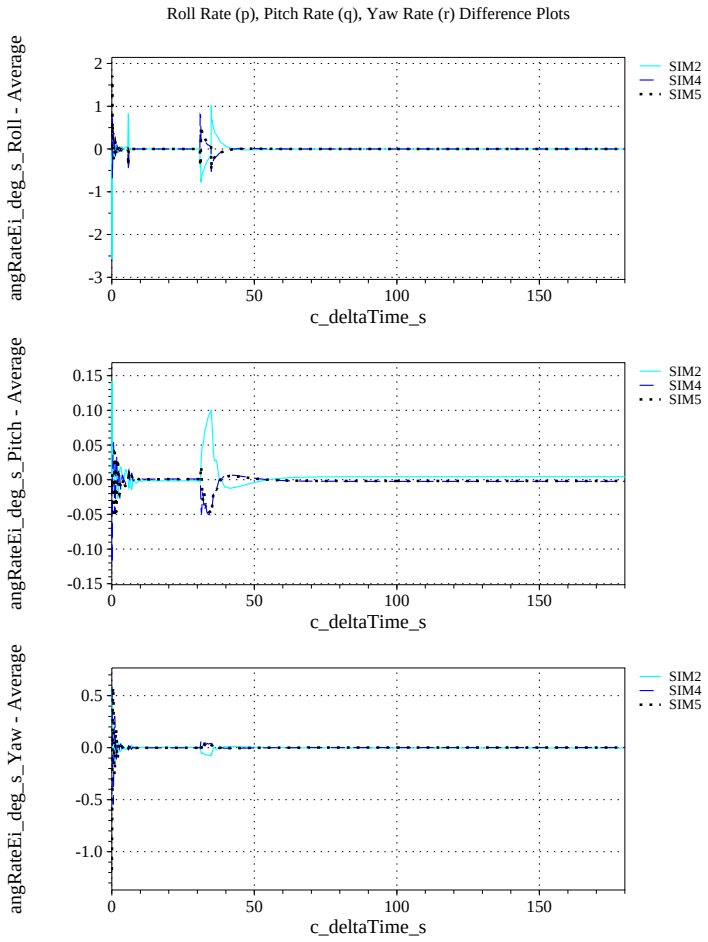

(r) Body-axis Angular Rates (w.r.t. NED Frame) Differenced

Figure 33. Check-case 15: Circumnavigation of the North Pole; See Discussion in Section D.1.17 (Cont'd)

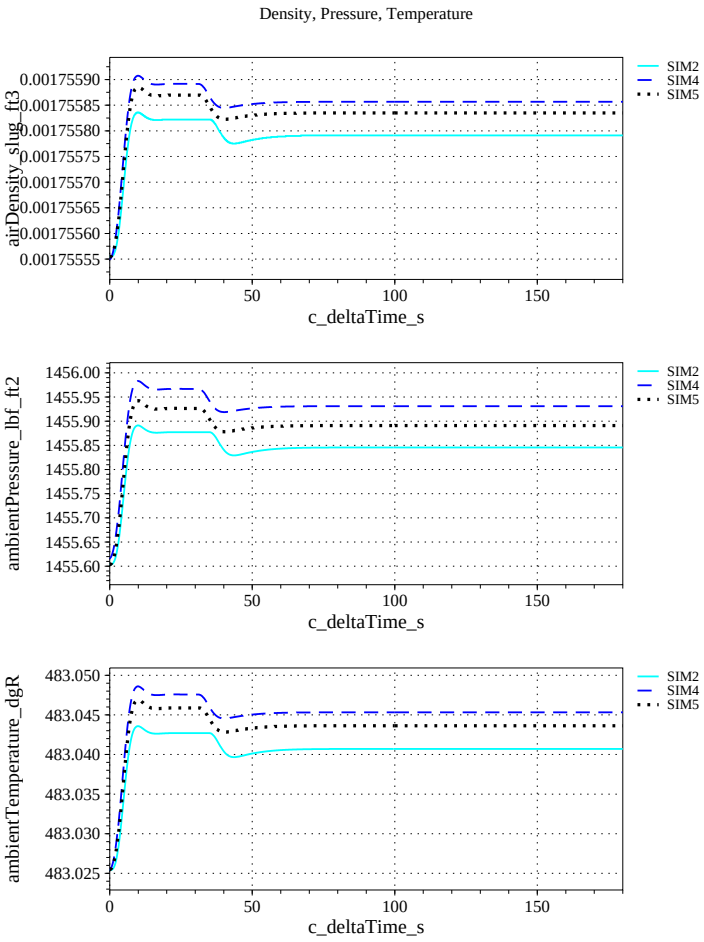

(s) Atmospheric Properties Compared

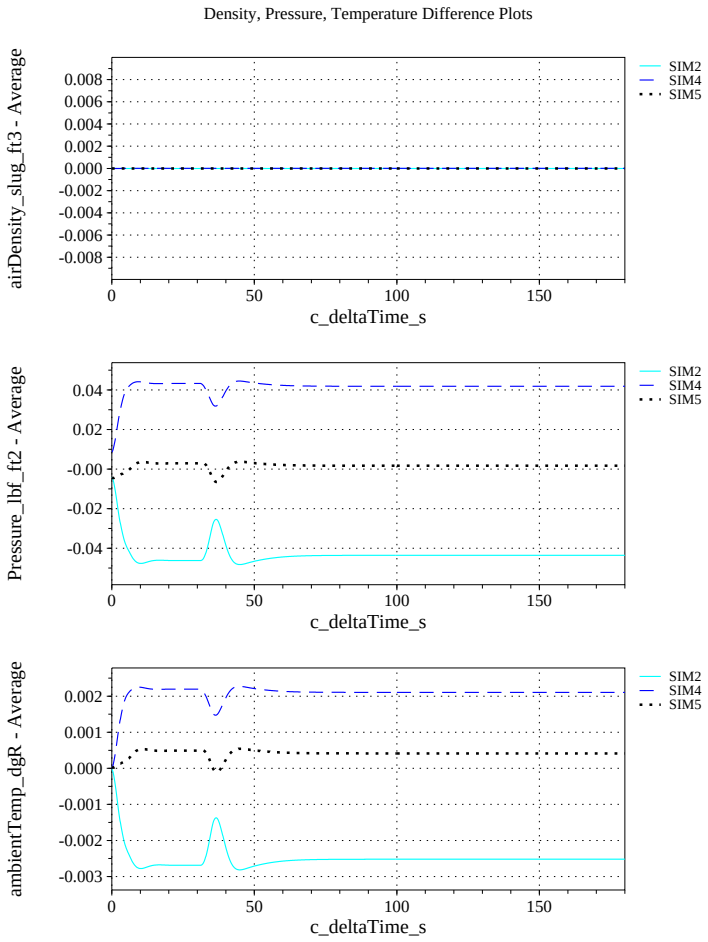

(t) Atmospheric Properties Differenced

Figure 33. Check-case 15: Circumnavigation of the North Pole; See Discussion in Section D.1.17 (Cont'd)

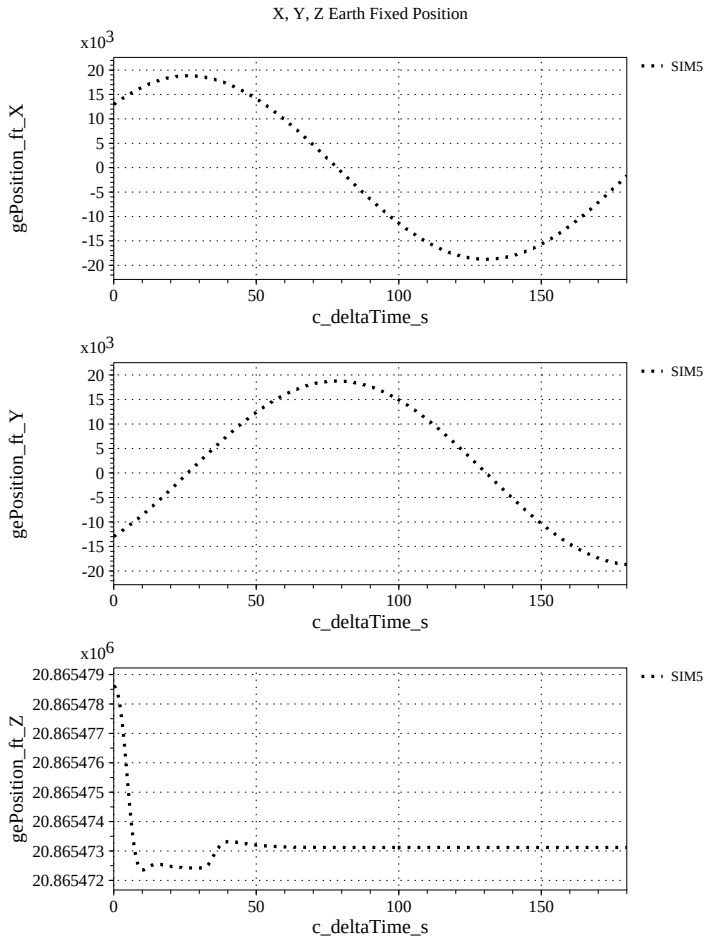

(u) Earth-centered, Earth-fixed Rectangular (X-Y-Z) Positions Compared

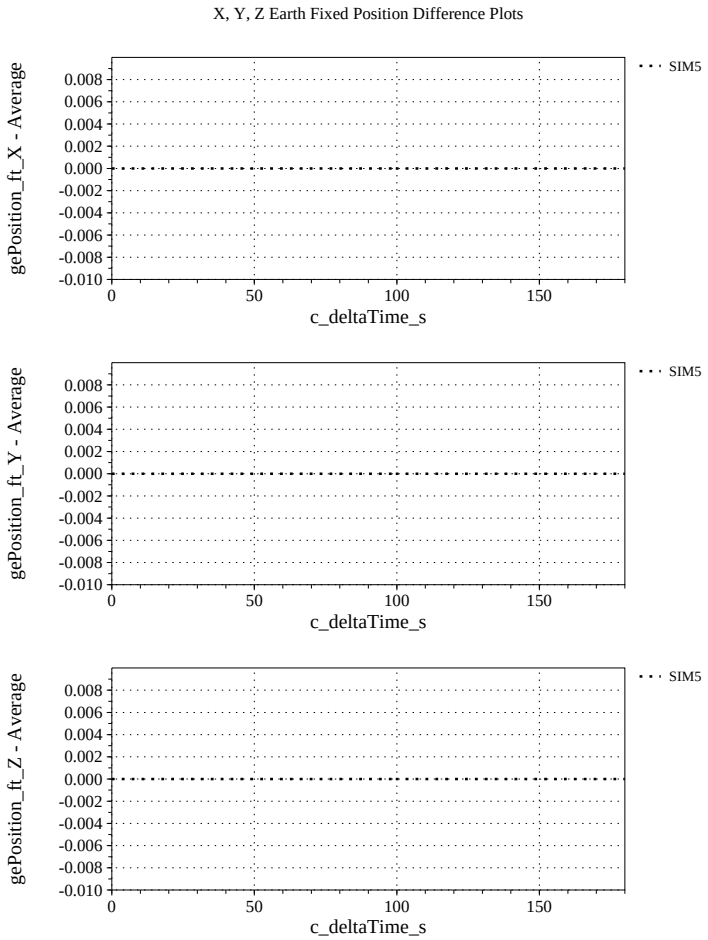

(v) Earth-centered, Earth-fixed Rectangular (X-Y-Z) Positions Differenced

Figure 33. Check-case 15: Circumnavigation of the North Pole; See Discussion in Section D.1.17 (Cont'd)

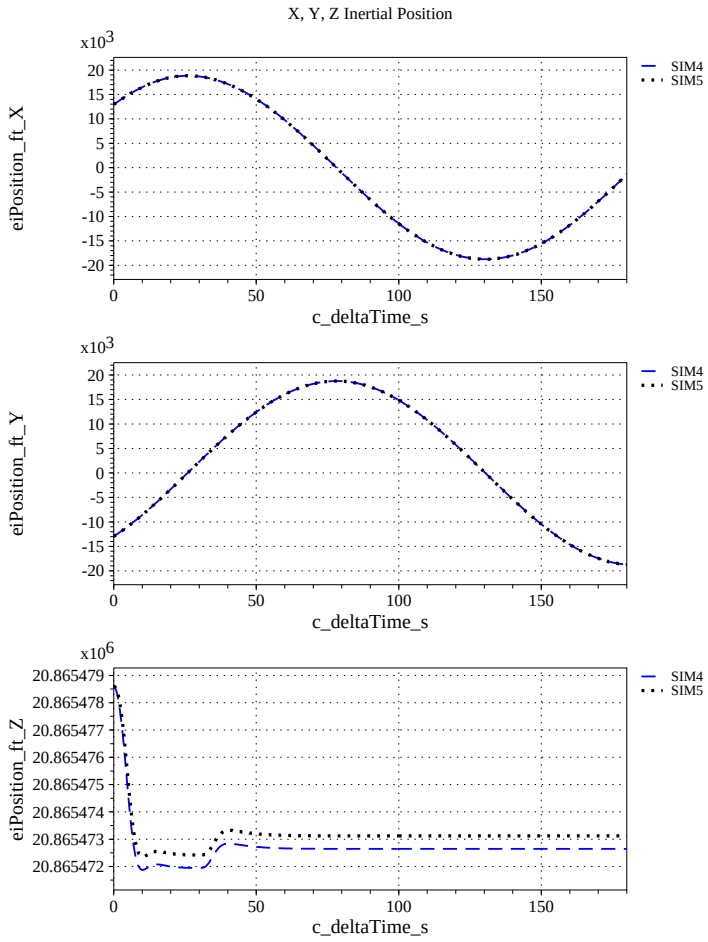

(w) Earth-centered Inertial Rectangular (x-y-z) Positions Compared

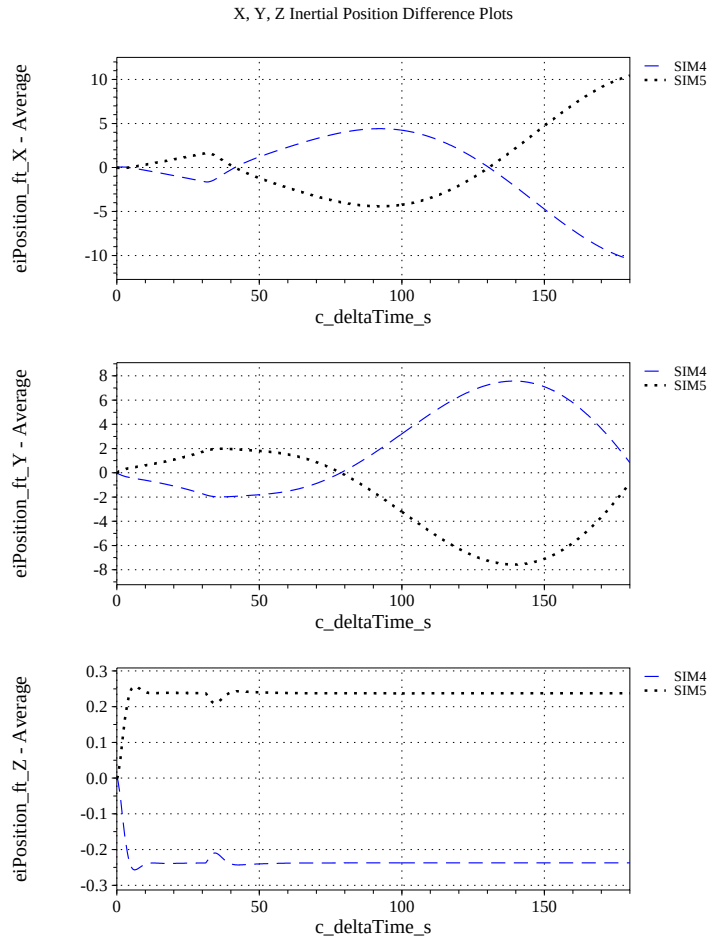

(x) Earth-centered Inertial Rectangular (x-y-z) Positions Differenced

Figure 33. Check-case 15: Circumnavigation of the North Pole; See Discussion in Section D.1.17 (Concluded)

D.1.18 Check-case 16 – circular flight around the equator-IDL intersection

This section shows cross-plots for three of the selected simulation tools in modeling the dynamics of a subsonic aircraft flying in a circle around the intersection of the Equator and ±180 deg longitude of the ellipsoidal Earth. This scenario is described in Section C.1.19. Figures 35a through 35x compare results between the three simulation tools, as well as the deviances of the outputs from each tool from the ensemble average value.

Atmospheric check-case 16 was similar to check-case 15 but instead of flying around the North Pole, it executed a circumnavigation about the intersection of the Equator and the International Date Line. This circumnavigation was controlled by the circumnavigating autopilot. All simulations do succeeded in establishing a steady-state circumnavigation; however, differences in initial state and the circumnavigation steady-state are noted.

The resulting trajectories from the three participating simulation tools are shown in Figure 34a. It shows that SIM 2 starts slightly inside the other two simulations, but finished slightly earlier and outside the path of the other two simulations.

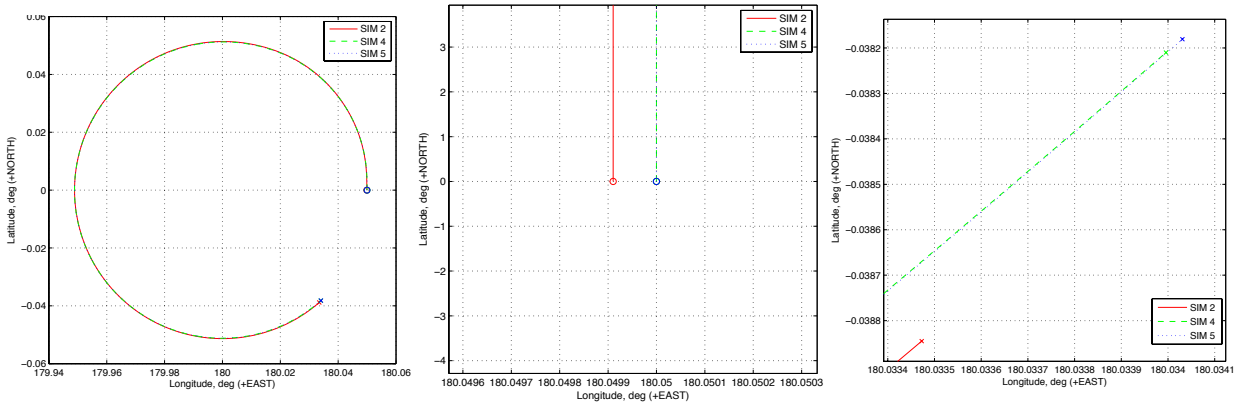

(a) Overview (b) Detail near start (c) Detail near end

Figure 34. Trajectories of Simulated F-16 Circling the Equator/IDL for Three Simulation Tools

A number of differences identified in previous F-16 check-cases persisted in this check-case:

- The simulations targeted different initial angular rates for straight and level flight. SIM 2 constrained the initial angular rate to be zero in the inertial frame. SIM 4 achieved an initial angular rate that was zero in the Earth-relative frame. SIM 5 targeted the three-axis Earth-relative angular rate that maintained the vehicle orientation as it traveled over the surface of the Earth. In this scenario, the resulting angular rate was zero in roll and yaw and was −0.00155 deg/s in pitch. Thus, it was most similar to the initial angular rate for SIM 4. Because the autopilot immediately caused a change in angular rates as it established circumnavigation, these differences did not have a significant impact on the steady state results.

- To some degree, the steady-state outcome under the autopilot was a balance achieved between the autopilot algorithm and the LQR stability algorithm. The LQR stability algorithm operated on perturbations of state variables (angle of attack, pitch rate, velocity and pitch attitude) from predetermined

reference values, resulting in delta commands to corresponding trimmed values for throttle and longitudinal stick. These internal referenced state values differed slightly from the trim values calculated by each simulation tool. All simulation tools were expected to replace the LQR trimmed values for throttle and longitudinal stick. SIM 2 and SIM 5 should have agreed on the LQR trim values for throttle and longitudinal stick based on similarities in other states. However, SIM 4 established initial throttle and longitudinal stick settings that differed substantially from SIM 2 and SIM 5. As explained below, those settings failed to reduce accelerations in the body x–z plane to zero. Additionally, SIM 5 replaced the LQR referenced state values for angle of attack, pitch angle, and airspeed (trimmed reference pitch rate was zero). The default trim values were about a degree higher for angle of attack and pitch angle and were about 0.8 kt higher for airspeed than the provided values in the F-16 autopilot DAVE-ML file. The difference between the default LQR trim values and the autopilot speed command was previously been identified as a possible source for the steady-state speed difference between SIM 4 and SIM 5. That trend continued here: the difference in steady-state speed between the two simulation tools was −0.13 ft/s and was established within the first second of the simulated maneuver. The steady-state speed difference between SIM 2 and SIM 5 was much smaller at 0.019 ft/s.

- SIM 4 did not begin the simulation in an equilibrium state for straight-and-level flight. Large accelerations remained in the body x- and z-axes and in pitch acceleration. The initial elevator deflection of −0.69 degrees did not generate sufficient aerodynamic pitching moment to counterbalance the pitching moment generated by the lift at the CM. The elevator deflection also did not reduce lift enough to counterbalance weight and left a net upward acceleration. The initial throttle setting did not generate enough thrust to counterbalance drag and the component of weight in the body x-axis due to the pitch angle.

- As before, SIM 2 recorded the aerodynamic moments at the MRC. SIM 4 and SIM 5 recorded aerodynamic moments at the vehicle CM. As a result, SIM 2 recorded non-zero aerodynamic pitching and yawing moments when the simulations achieve steady-state navigation.

In this scenario, it was more difficult to identify small differences in the steady-state circumnavigation radius among the simulations. Both latitude and longitude changed so the radius had to be estimated from both using the radii of curvature. The estimates used the last 100 sec of data in which all three simulations appeared to have achieved steady-state flight. The estimated radii indicate that the circumnavigation path was a slightly flattened circle for all simulations. For SIM 2, the circle had a major axis of 18,758 ft and a minor axis of 18,703 ft; the resultant flattening parameter was 0.0029. For SIM 4 and SIM 5, the circle had a major axis of about 18,721 ft and a minor axis of 18,685 ft; the resultant flattening parameter was 0.0019. The perimeters of the circles similarly differ. The circle for SIM 5 had a perimeter of 117,517.6 ft. The perimeter for SIM 2 differed from that of SIM 5 by +169 ft and the estimated perimeter for the SIM 4 circle differed by −3.23 ft. Due to its larger perimeter and near-equal speed, SIM 2 would be expected to lag SIM 5. Similarly, because of the near-equal perimeter but slower airspeed, SIM 4 would be expected to lag SIM 5. These expectations were confirmed by differencing the world-relative positions and taking the magnitude of the difference. Using this method, SIM 4 lagged SIM 5 by 16.8 ft and SIM 2 lagged SIM 5 by 320 ft.

The roll angle for each simulation varied with the circumnavigation radius; therefore, it fluctuated as the circumnavigation radius fluctuated. Even so, the average roll angle differed very little among the simulations and those differences could be predicted from the differences in the average circumnavigation radius and airspeed. The average roll angle for SIM 2 differed from SIM 5 by 0.0285 degrees and the SIM 4 roll angle differed from SIM 5 by 0.0122 degrees. Similarly, the average pitch angle differed among the simulations by less than 0.013 degrees. The yaw angle differed in accordance with the respective leading or lagging of

position of the simulated vehicles along the circumnavigation circle relative to the other simulation tools' predictions. At the end of the simulation, SIM 4 and SIM 5 differed in yaw angle by 0.05 degrees; SIM 2 and SIM 5 differ by 0.77 degrees. These values imply that SIM 4 lagged SIM 5 by around 16.6 ft and SIM 2 lagged SIM 5 by 251 ft, which are similar to the separations obtained by differencing the world-relative position vectors.

One unexplained result in this scenario was that SIM 4 quickly generated a large aerodynamic rolling moment of about 32,000 lbf-ft for about 5 sec. Then the moment went to zero. Then it returned to about 26,000 lbf-ft starting at 36.8 sec and for the remainder of the run. The roll acceleration ($\dot{p}$) responded to this aerodynamic rolling moment; however, the body-axis roll rate p did not react as if the vehicle were undergoing the recorded roll acceleration. The change of p from frame-to-frame is much smaller and often in the opposite direction to the recorded $\dot{p}$.

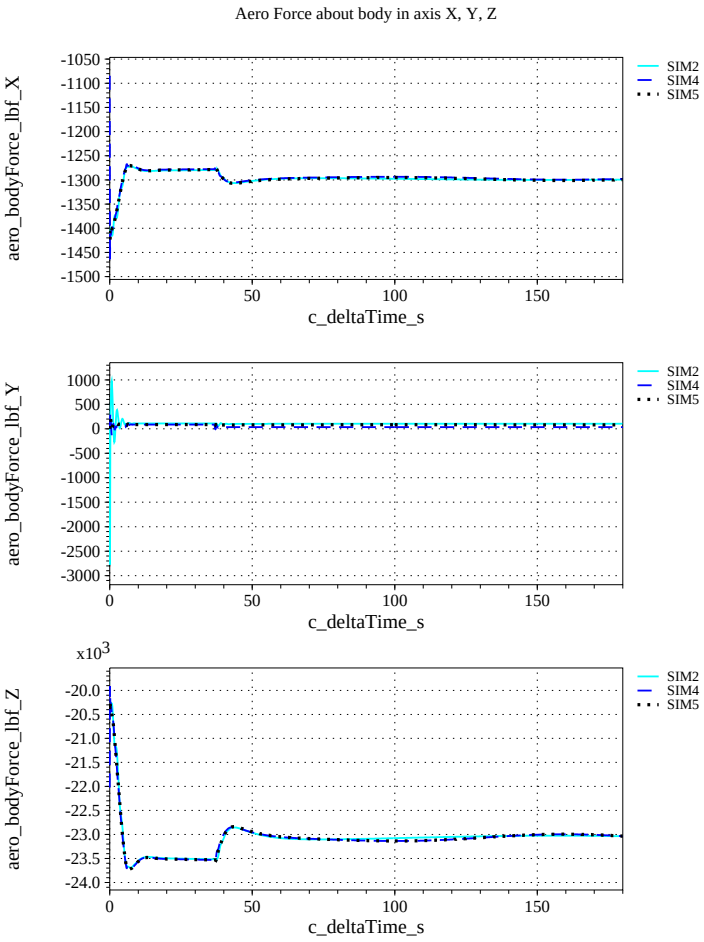

(a) Aerodynamic Forces Compared

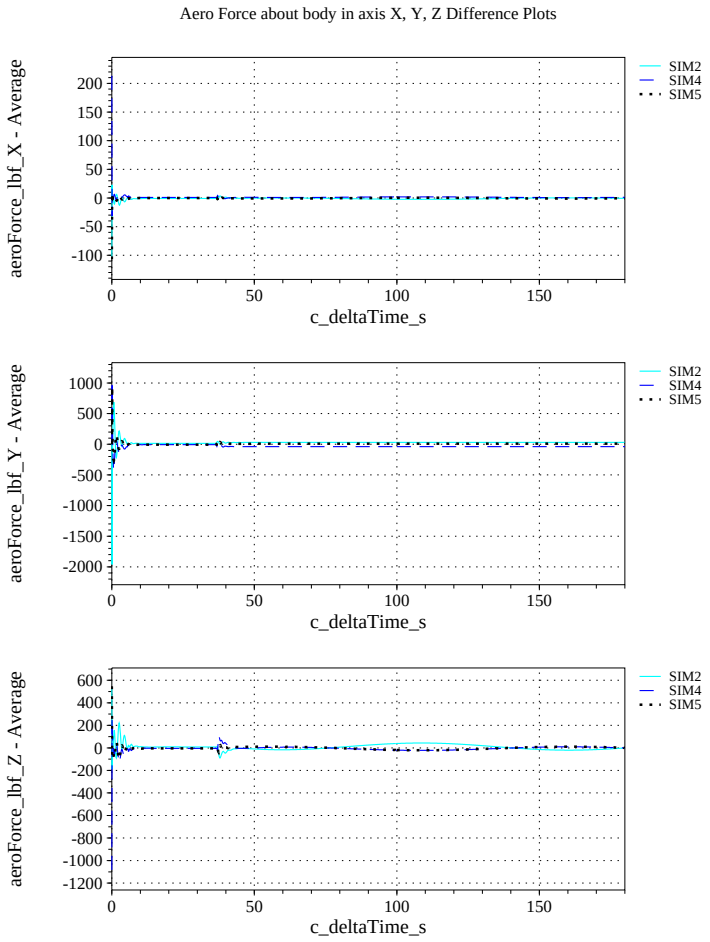

(b) Aerodynamic Forces Differenced

Figure 35. Check-case 16: Circular Flight around the Equator-IDL Intersection; See Discussion in Section D.1.18

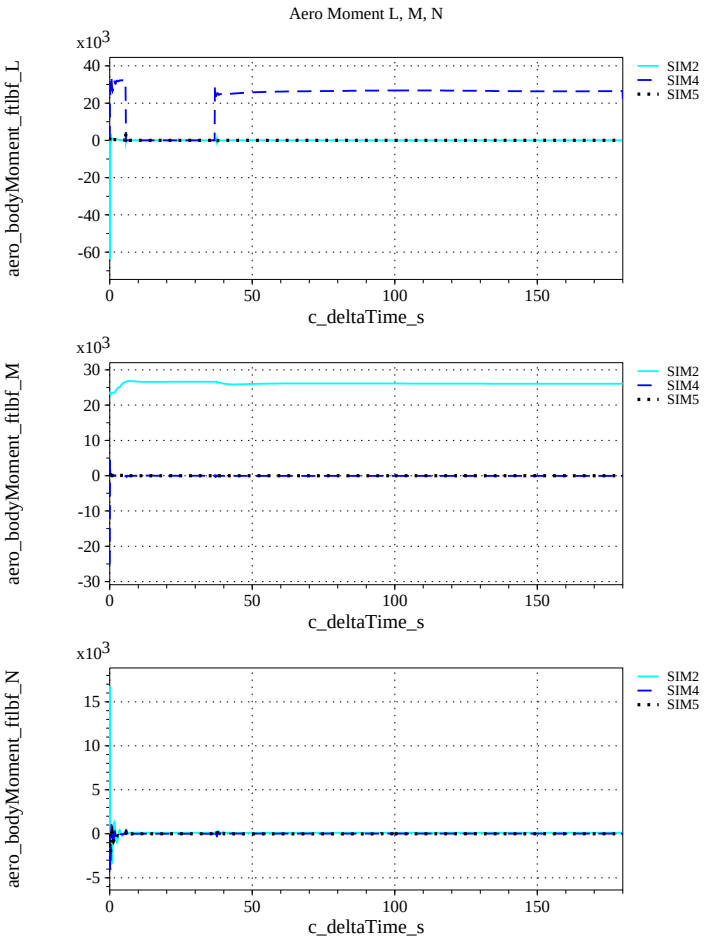

(c) Aerodynamic Moments Compared

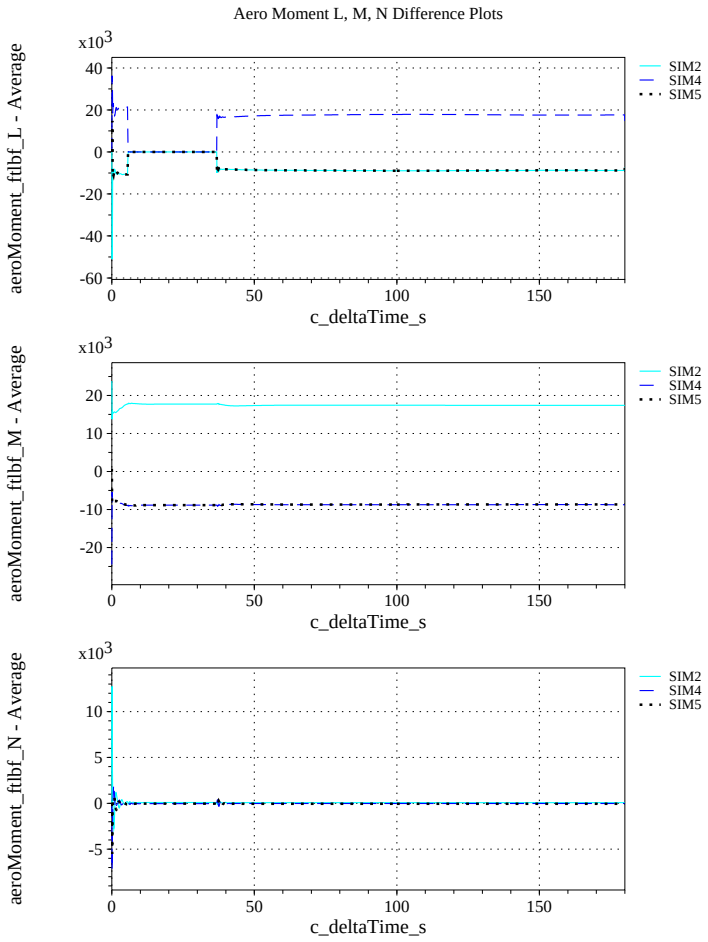

(d) Aerodynamic Moments Differenced

Figure 35. Check-case 16: Circular Flight around the Equator-IDL Intersection; See Discussion in Section D.1.18 (Cont'd)

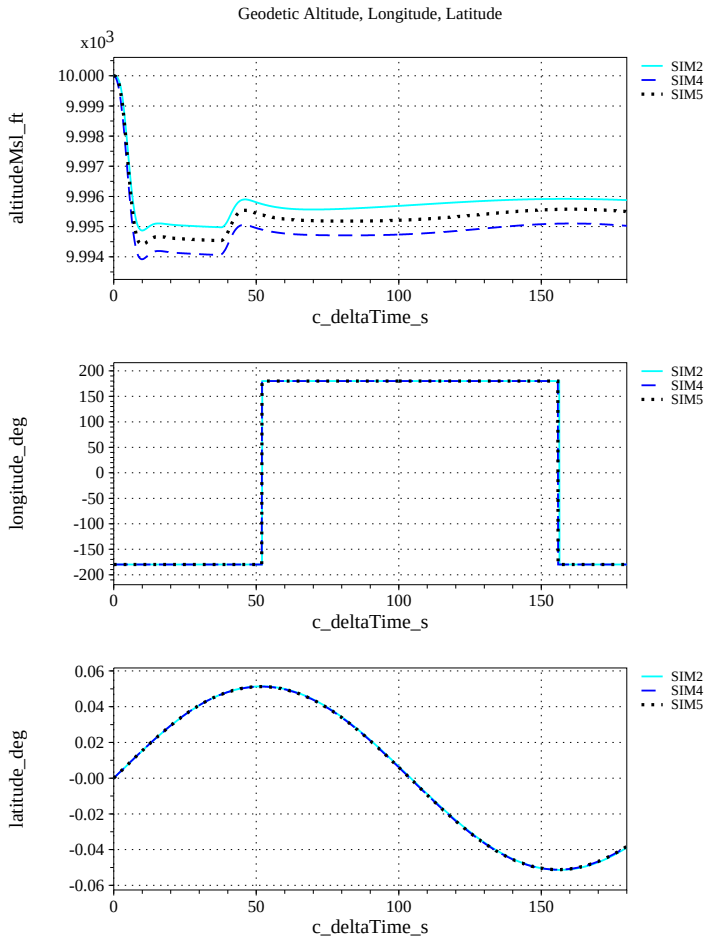

(e) Altitude, Geodetic Latitude and Longitude Compared

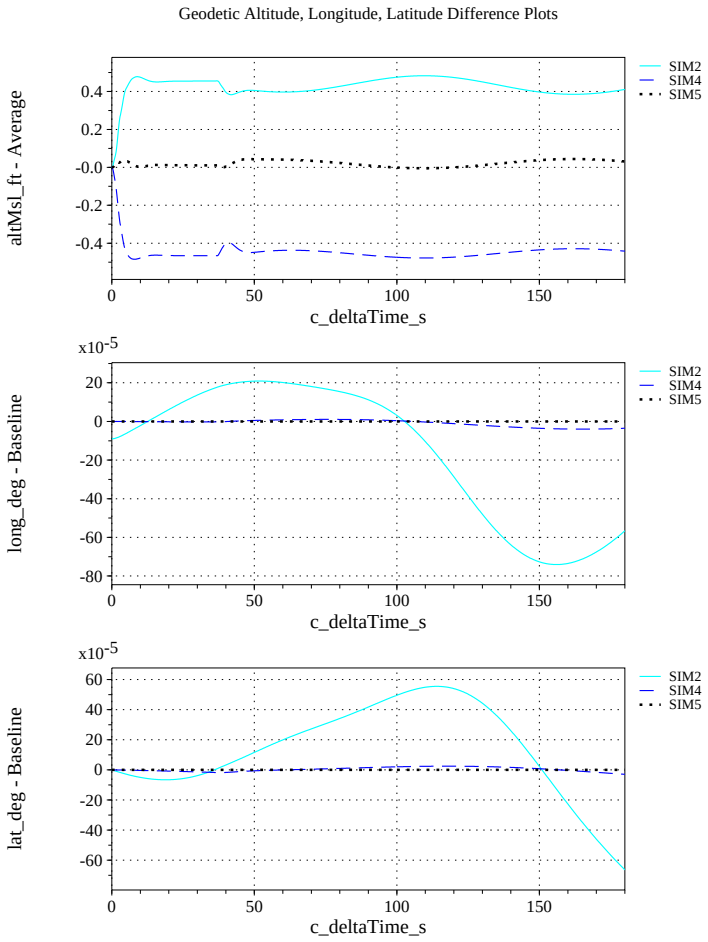

(f) Altitude, Geodetic Latitude and Longitude Differenced

Figure 35. Check-case 16: Circular Flight around the Equator-IDL Intersection; See Discussion in Section D.1.18 (Cont'd)

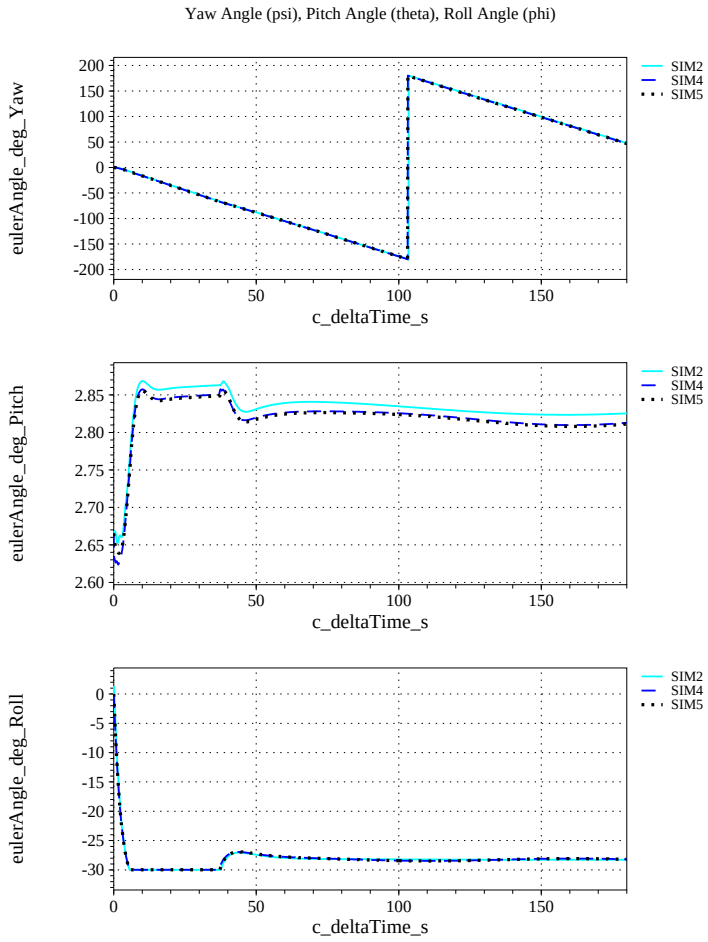

(g) Euler Angles (w.r.t. NED Frame) Compared

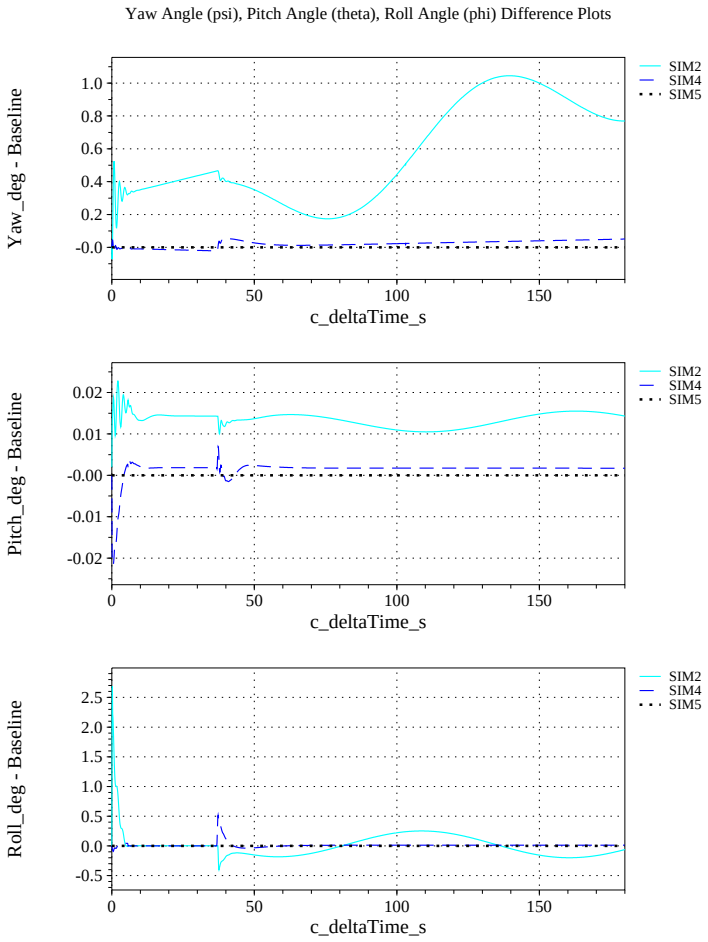

(h) Euler Angles (w.r.t. NED Frame) Differenced

Figure 35. Check-case 16: Circular Flight around the Equator-IDL Intersection; See Discussion in Section D.1.18 (Cont'd)

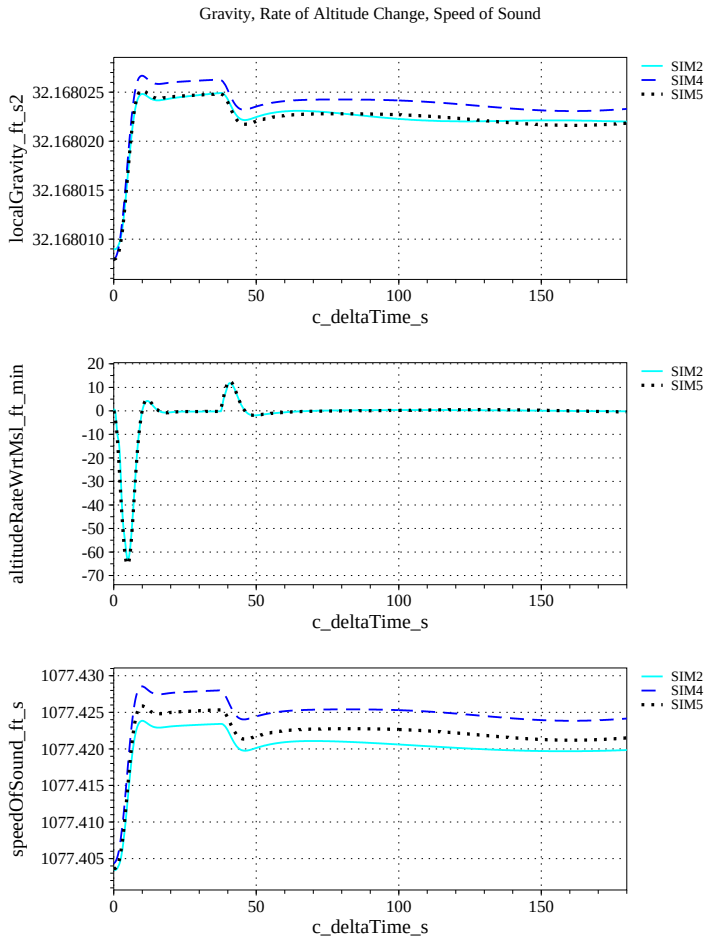

(i) Gravity, Climb Rate, and Speed-of-sound Compared

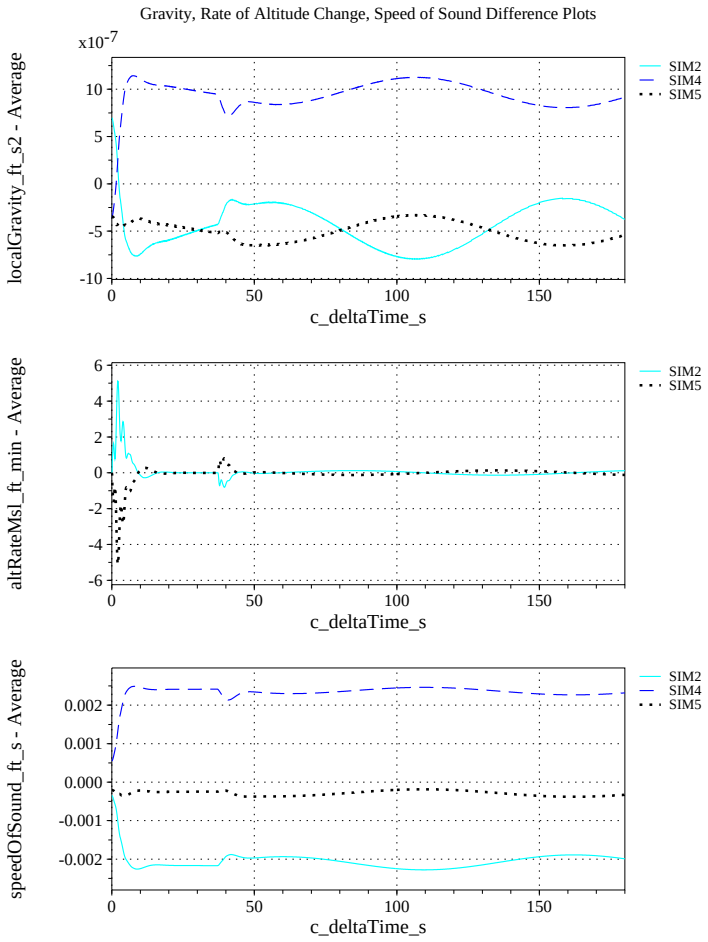

(j) Gravity, Climb Rate, and Speed-of-sound Differenced

Figure 35. Check-case 16: Circular Flight around the Equator-IDL Intersection; See Discussion in Section D.1.18 (Cont'd)

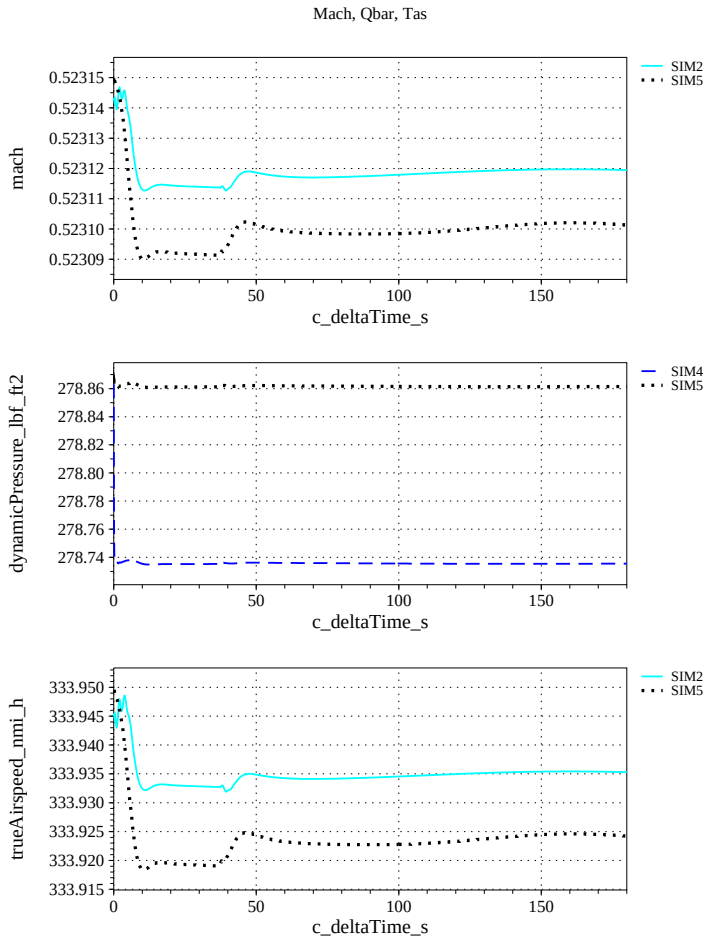

(k) Mach, Dynamic Pressure, and True Airspeed Compared

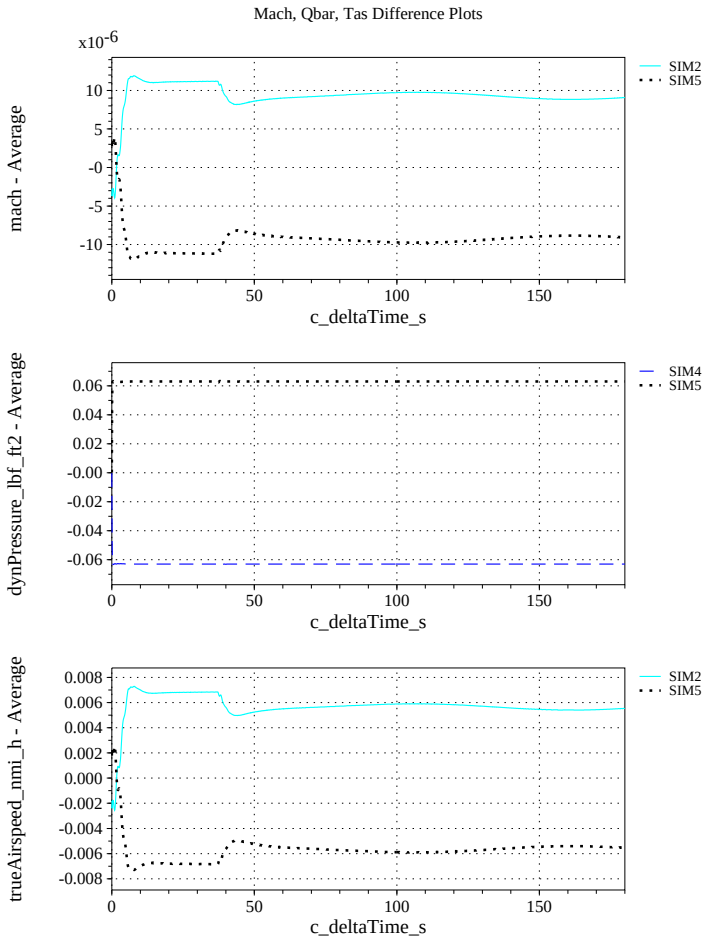

(l) Mach, Dynamic Pressure, and True Airspeed Differenced

Figure 35. Check-case 16: Circular Flight around the Equator-IDL Intersection; See Discussion in Section D.1.18 (Cont'd)

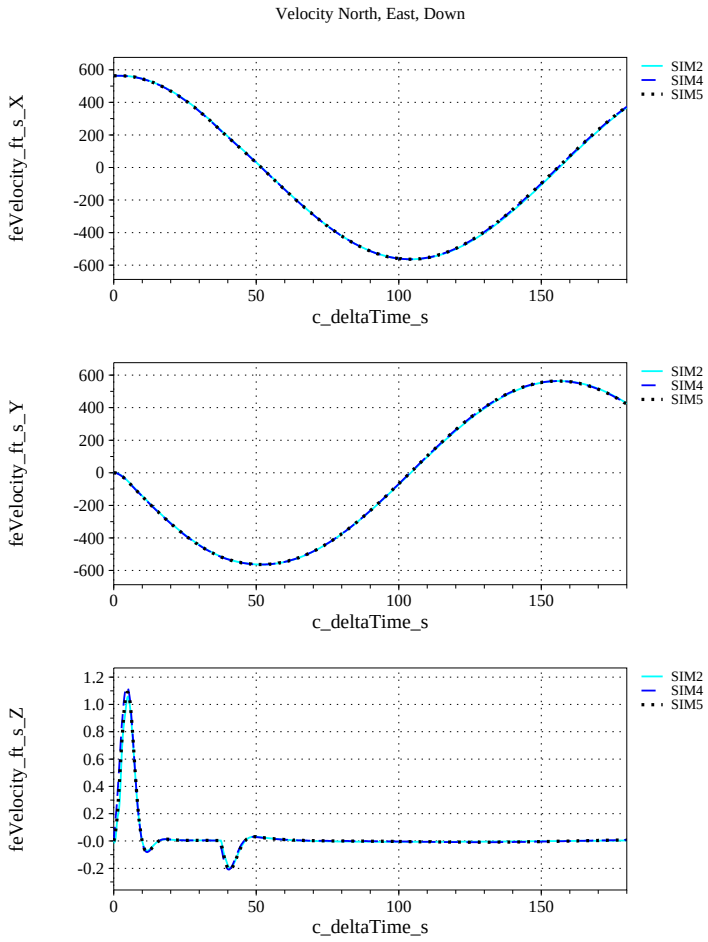

(m) NED Velocities Compared

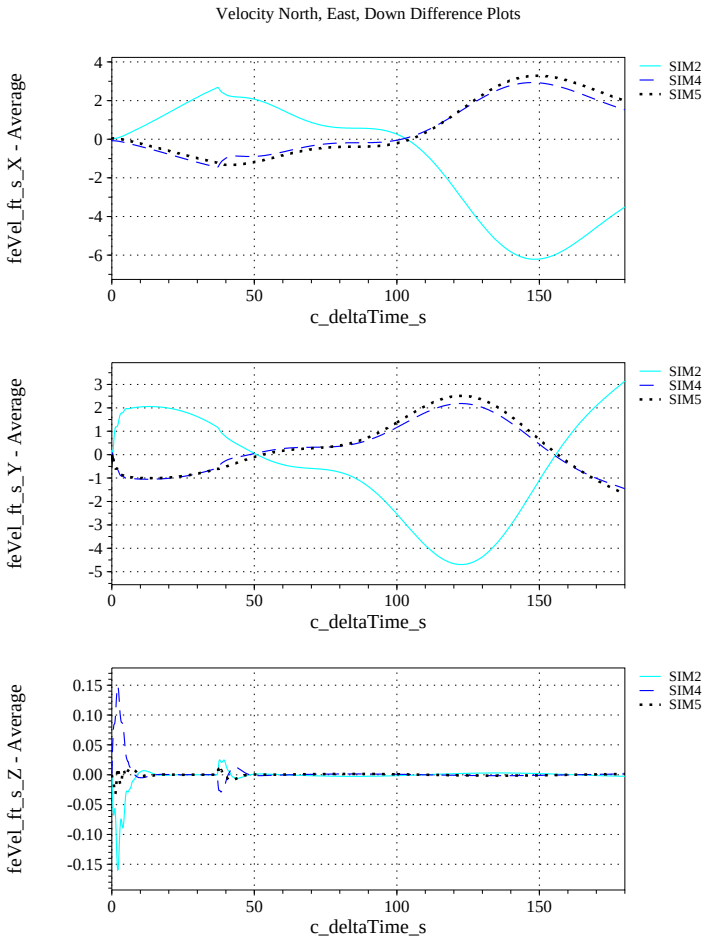

(n) NED Velocities Differenced

Figure 35. Check-case 16: Circular Flight around the Equator-IDL Intersection; See Discussion in Section D.1.18 (Cont'd)

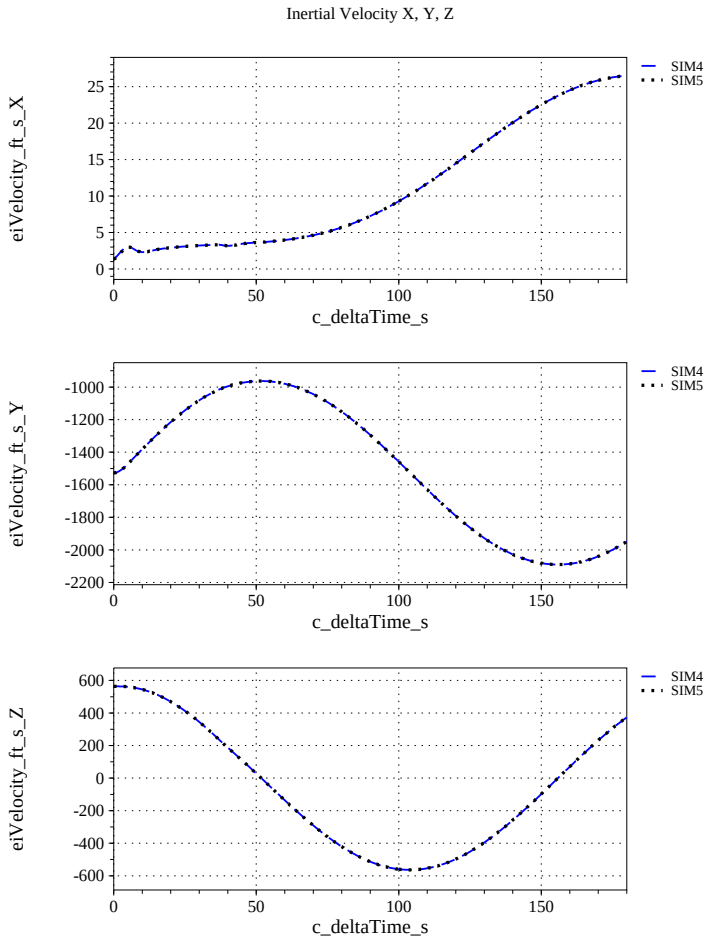

(o) Inertial Velocities Compared

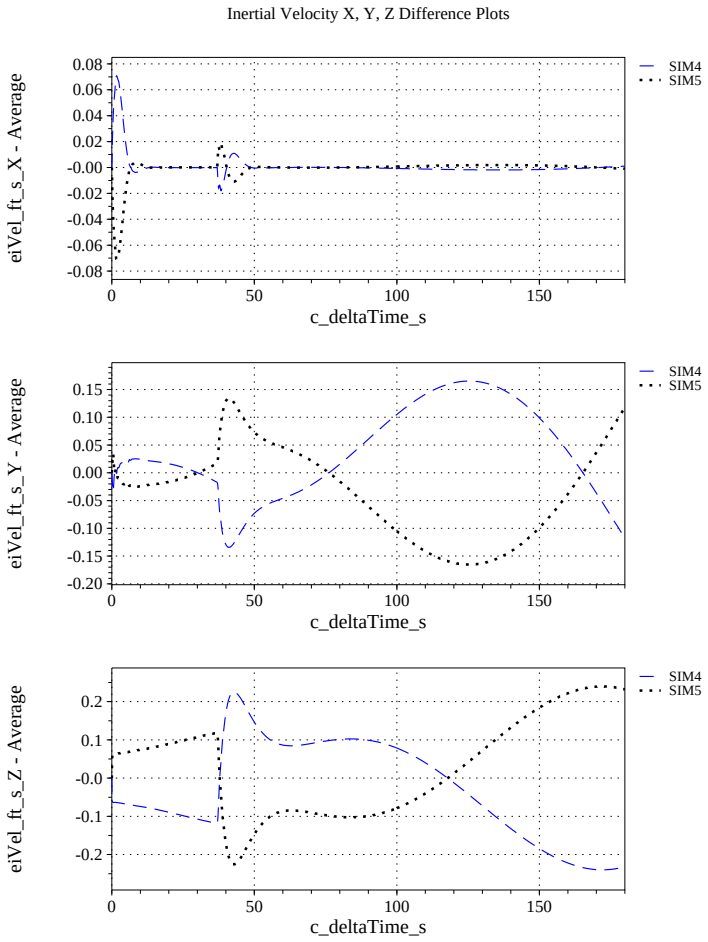

(p) Inertial Velocities Differenced

Figure 35. Check-case 16: Circular Flight around the Equator-IDL Intersection; See Discussion in Section D.1.18 (Cont'd)

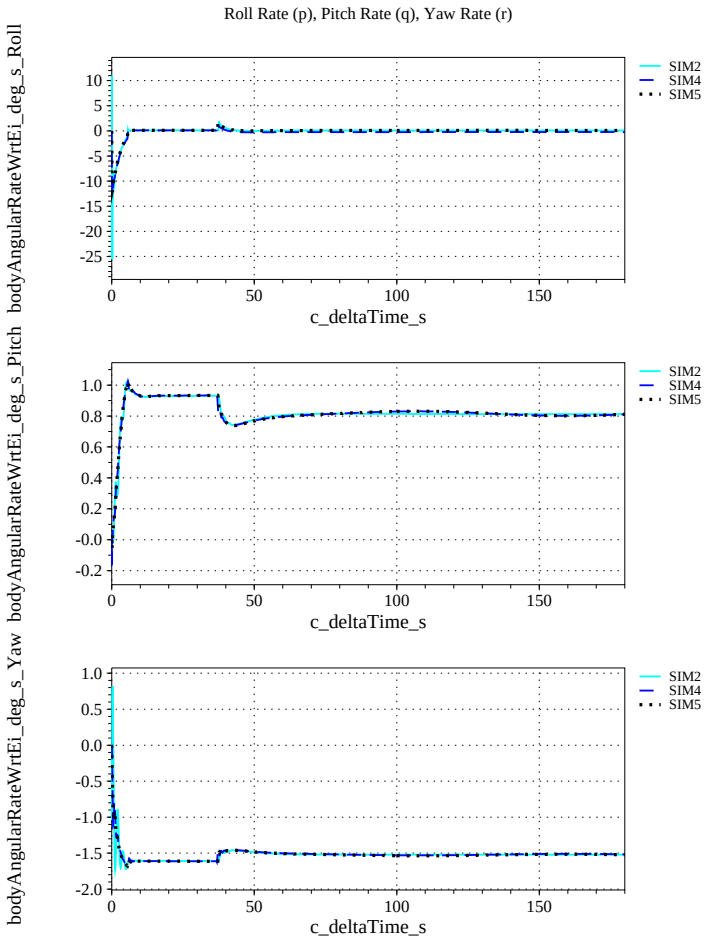

(q) Body-axis Angular Rates (w.r.t. NED Frame) Compared

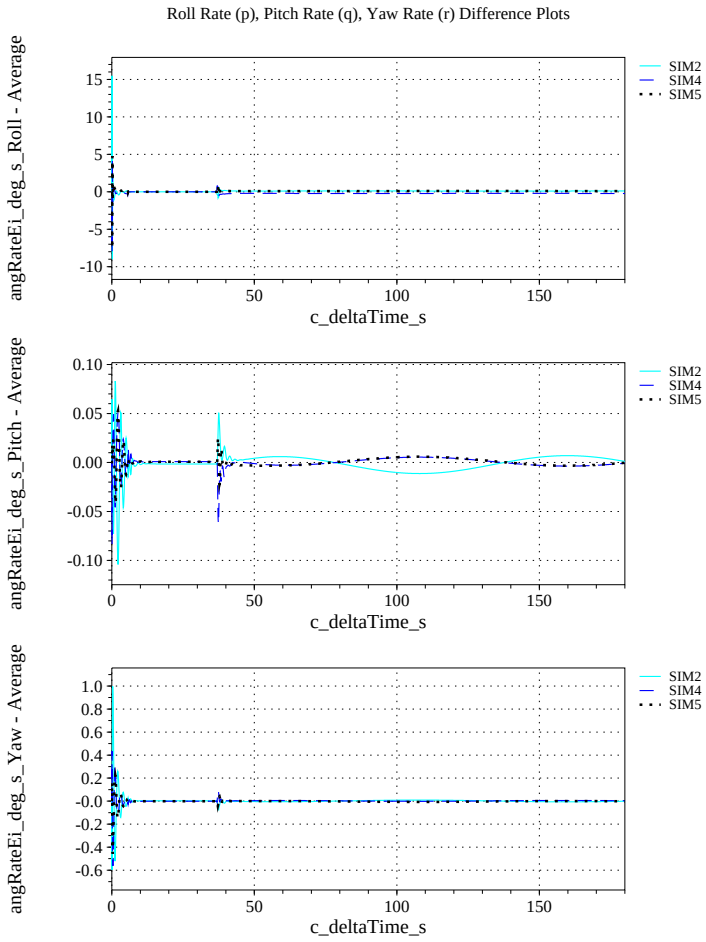

(r) Body-axis Angular Rates (w.r.t. NED Frame) Differenced

Figure 35. Check-case 16: Circular Flight around the Equator-IDL Intersection; See Discussion in Section D.1.18 (Cont'd)

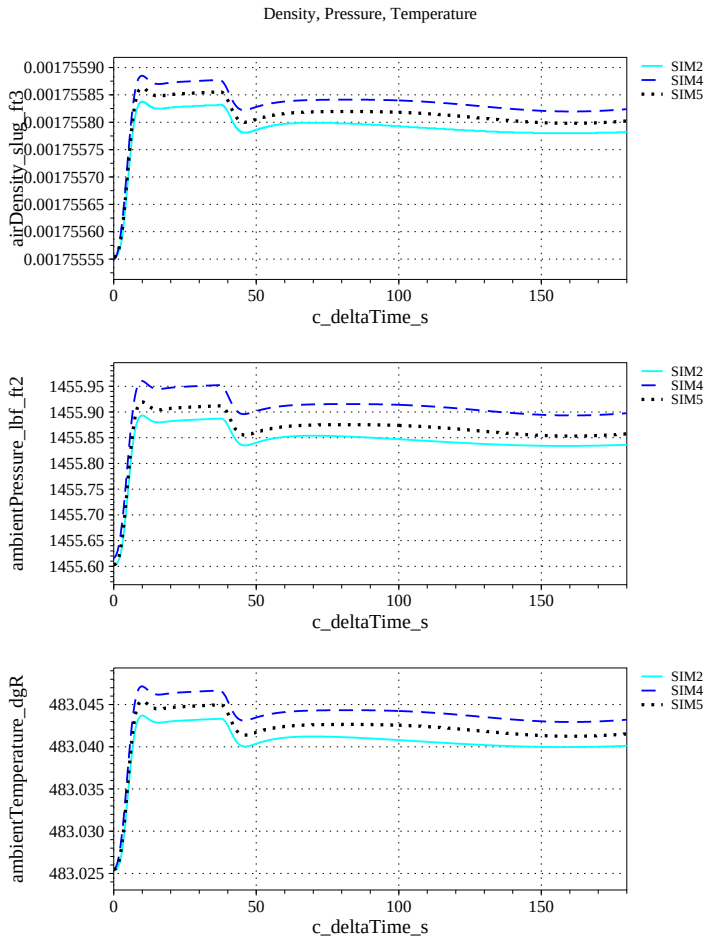

(s) Atmospheric Properties Compared

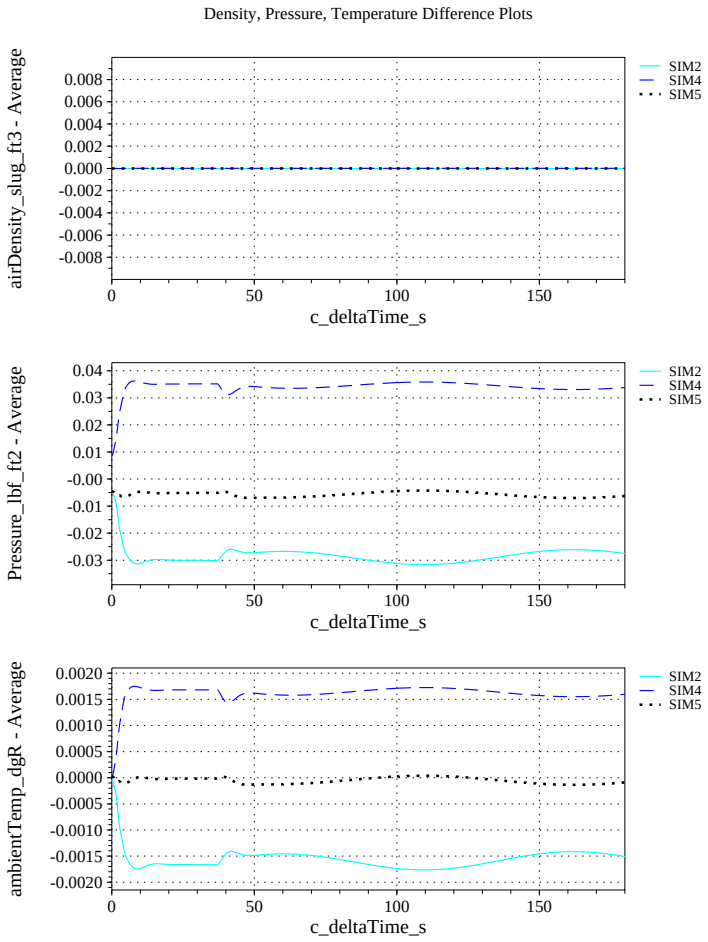

(t) Atmospheric Properties Differenced

Figure 35. Check-case 16: Circular Flight around the Equator-IDL Intersection; See Discussion in Section D.1.18 (Cont'd)

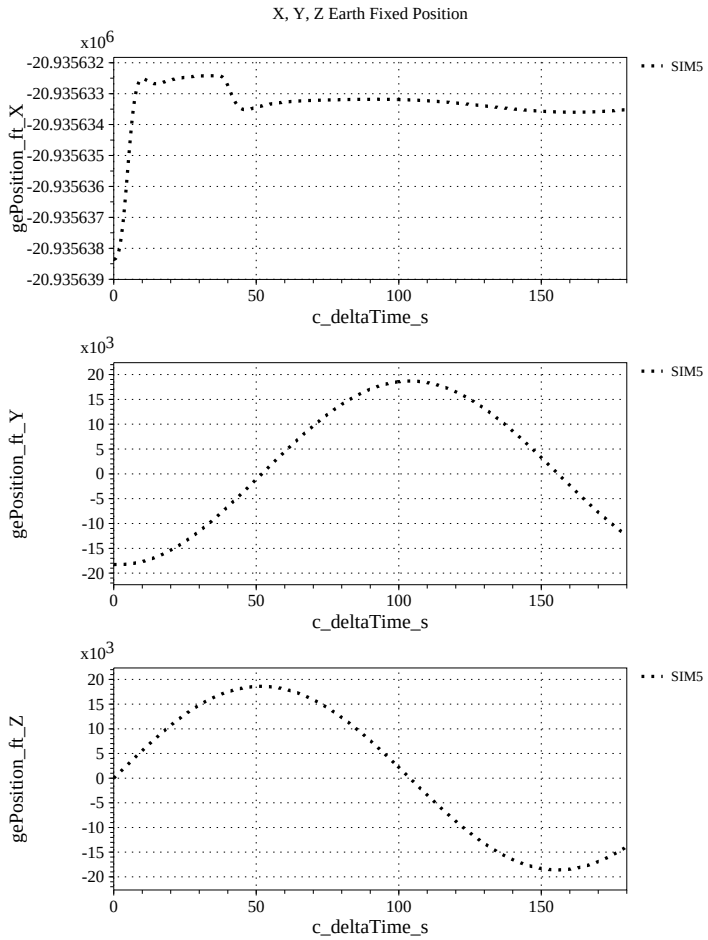

(u) Earth-centered, Earth-fixed Rectangular (X-Y-Z) Positions Compared

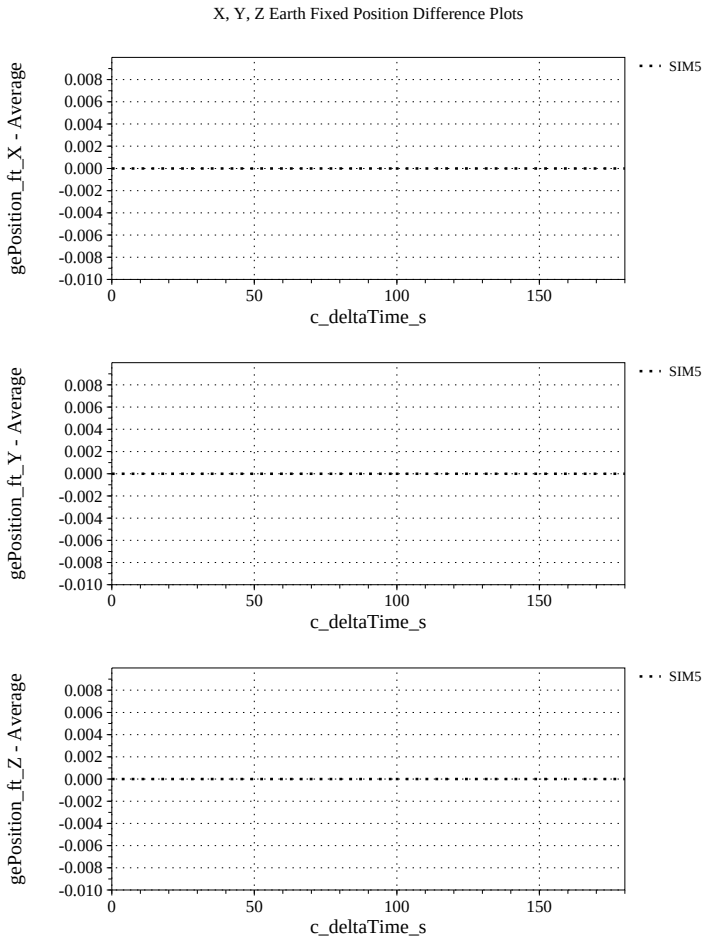

(v) Earth-centered, Earth-fixed Rectangular (X-Y-Z) Positions Differenced

Figure 35. Check-case 16: Circular Flight around the Equator-IDL Intersection; See Discussion in Section D.1.18 (Cont'd)

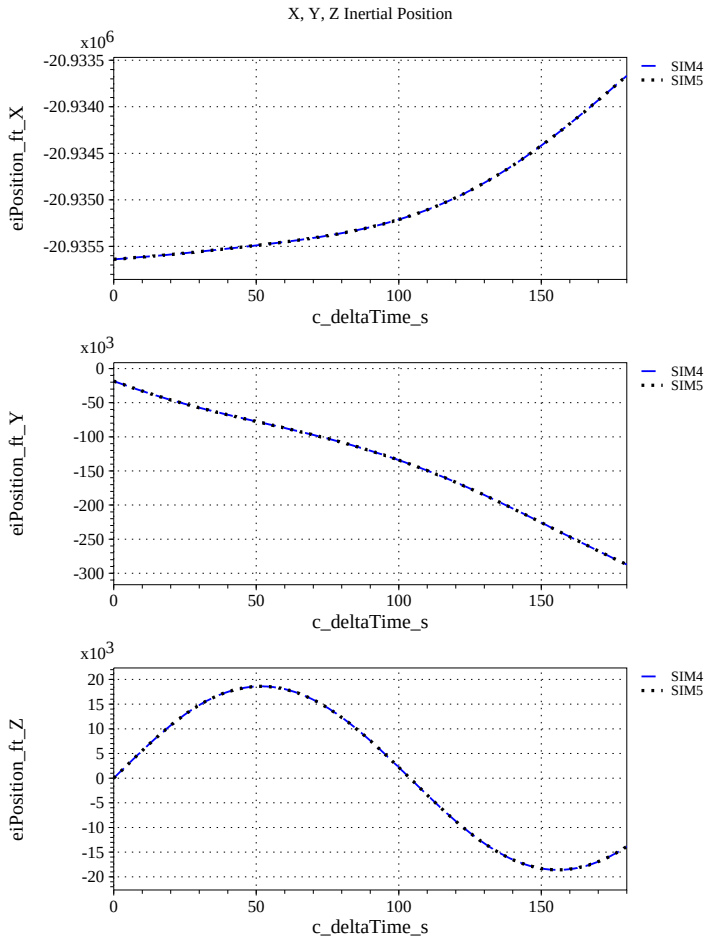

(w) Earth-centered Inertial Rectangular (x-y-z) Positions Compared

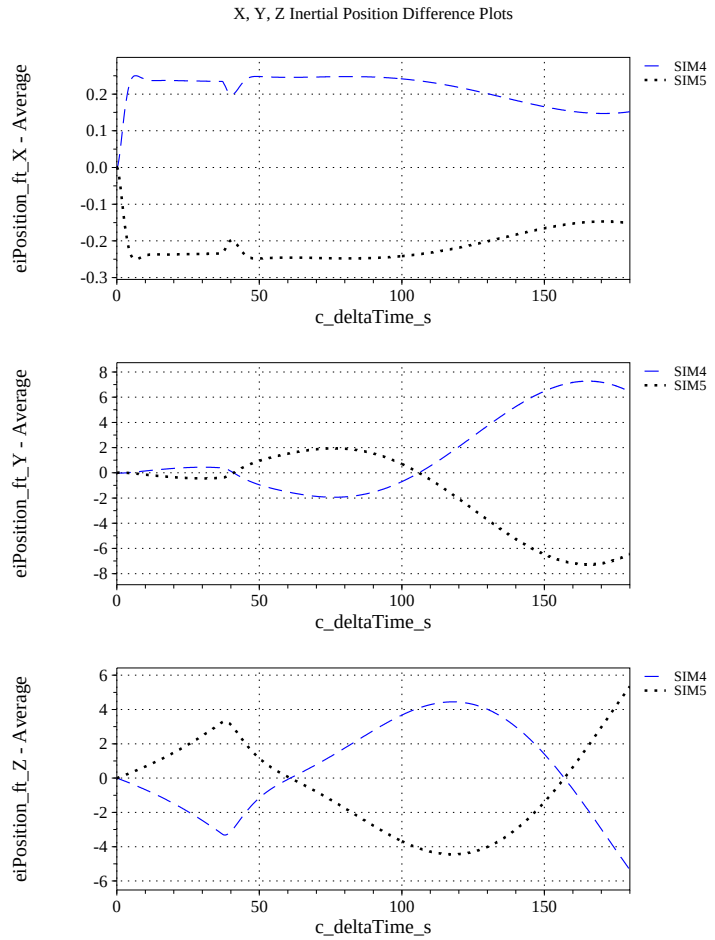

(x) Earth-centered Inertial Rectangular (x-y-z) Positions Differenced

Figure 35. Check-case 16: Circular Flight around the Equator-IDL Intersection; See Discussion in Section D.1.18 (Concluded)

D.1.19 Check-case 17 – flight of two-stage launch vehicle

This section shows cross-plots for three of the selected simulation tools in modeling the dynamics of an unguided two-stage rocket launched into a highly elliptical orbit. This scenario is described in Section C.1.20. Figures 36a through 36x compare results between the three simulation tools, as well as the deviances of the outputs from each tool from the ensemble average value.

This scenario simulated the ascent of a two-stage rocket. The translational and rotational dynamics were coupled in this check-case and the results were very sensitive to differences in the rotational dynamics since the attitude of the vehicle determined the direction of the thrust vector. The results were also sensitive to the exact timing of first-stage engine cutoff, first-stage jettison, second-stage ignition, and second-stage engine cutoff.

There were two main causes of the simulation differences in this scenario: First, the simulations differed on modeling the engine cutoff times. SIM 4 included the capability of modeling discrete events: it determined and modeled the exact moment of first-stage engine cutoff and second-stage engine firing. Moreover, the interstage coast time was specified to last a fixed amount of time from the exact moment of first-stage engine cutoff. However, SIM 5 and SIM 6 were both fixed-step simulations that did not model discrete events precisely. Thus, SIM 4 modeled first stage engine cutoff, second-stage engine ignition, and second-stage engine cutoff to occur at times that fell between the fixed time steps used by the other simulations. When SIM 5 was re-run with a faster frame rate, it better approximated the results of SIM 4 with the position differences at $t = 200$ sec showing a position difference of 2.4 ft (with a frame rate of 10,000 frames/s). Higher frame rates failed to improve results due to differences in integration error, the increasing magnitude of cumulative round-off error, and the cumulative effect of otherwise minute differences between the simulations. The SIM 5 results presented here were run at 1,000 frames/s and showed a position difference of 21.6 ft from SIM 4 at $t = 200$ sec.

The second cause of differences was a difference in modeling the change in the moments of inertia with fuel burn. The mass properties models in SIM 4 and SIM 5 were configured to execute or closely match a linear change in the moments of inertia with propellant burn. SIM 4 and SIM 5 agreed on moments of inertia to within 1 slug-ft^2. SIM 6, on the other hand, had a higher-fidelity mass properties model that could not easily be reconfigured to model a simple linear change in moments of inertia with fuel burn (but did provide a close approximation). Nevertheless, SIM 6 differed from SIM 4/5 in its moments of inertia by up to 1,400 slug-ft^2. This changed the rotational response of the vehicle enough that, at first-stage engine cutoff, the predicted attitude in SIM 6 differed from SIM 4/5 in pitch by 0.12 degrees and in pitch rate by 0.13 deg/s. As mentioned previously, attitude differences coupled strongly into subsequent thrust-induced linear acceleration, velocity and position differences, and since the vehicle model had no guidance or attitude control, small angular rate differences would integrate to become significant attitude differences.

The SIM 6 solution exhibited enough of difference in thrust vector pointing direction relative to SIM 4/5 that vehicle CM position differed by 46 ft at first-stage engine cutoff, and the direction of the velocity vector differed by 0.043 degrees. During the coast phase, the difference in pitch rate at engine cutoff between SIM 6 and SIM 4/5 was enough to increase the difference in pitch angle to 4 degrees when the second-stage engine fired. This essentially placed the rocket in SIM 6 on a different trajectory than the rocket in SIM 4/5 for the second-stage ignition. This is why the position difference increased to 61,000 ft (10 NM) by the end of the scenario.

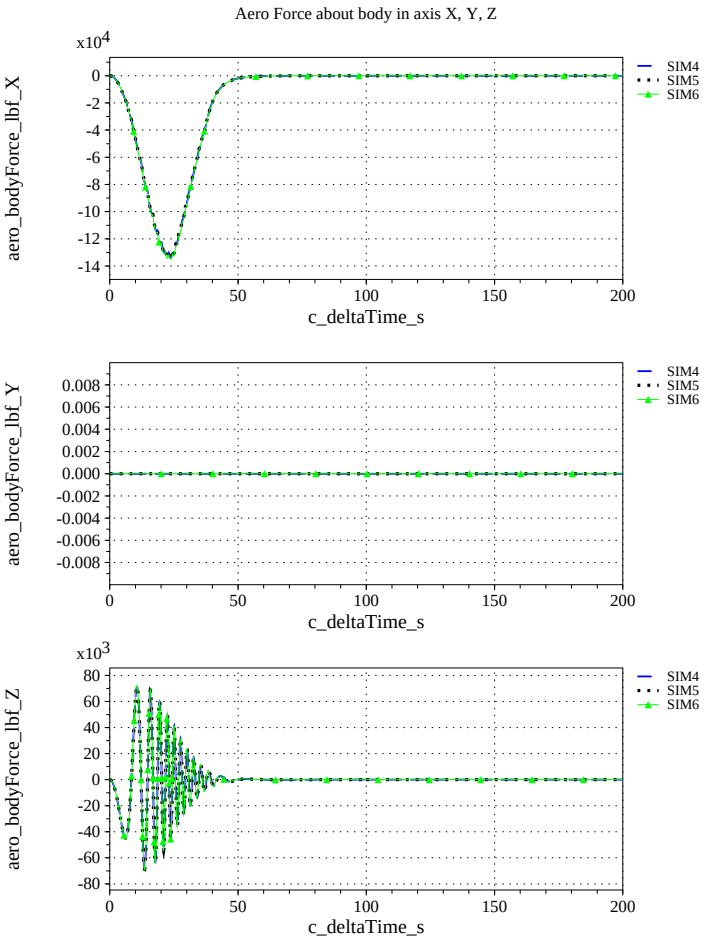

(a) Aerodynamic Forces Compared

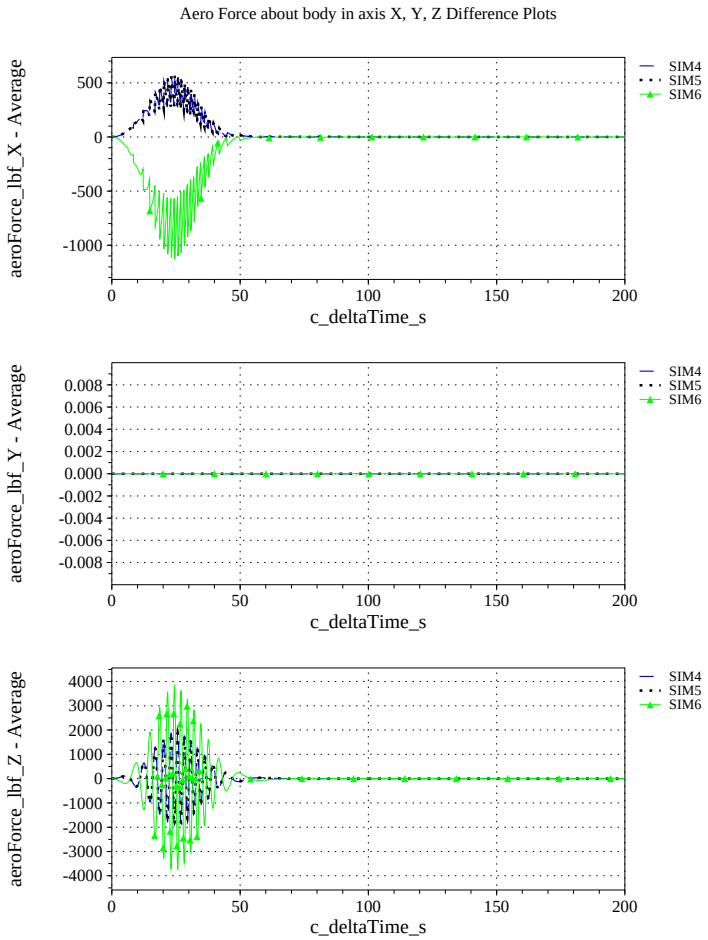

(b) Aerodynamic Forces Differenced

Figure 36. Check-case 17: Flight of Two-stage Launch Vehicle; See Discussion in Section D.1.19

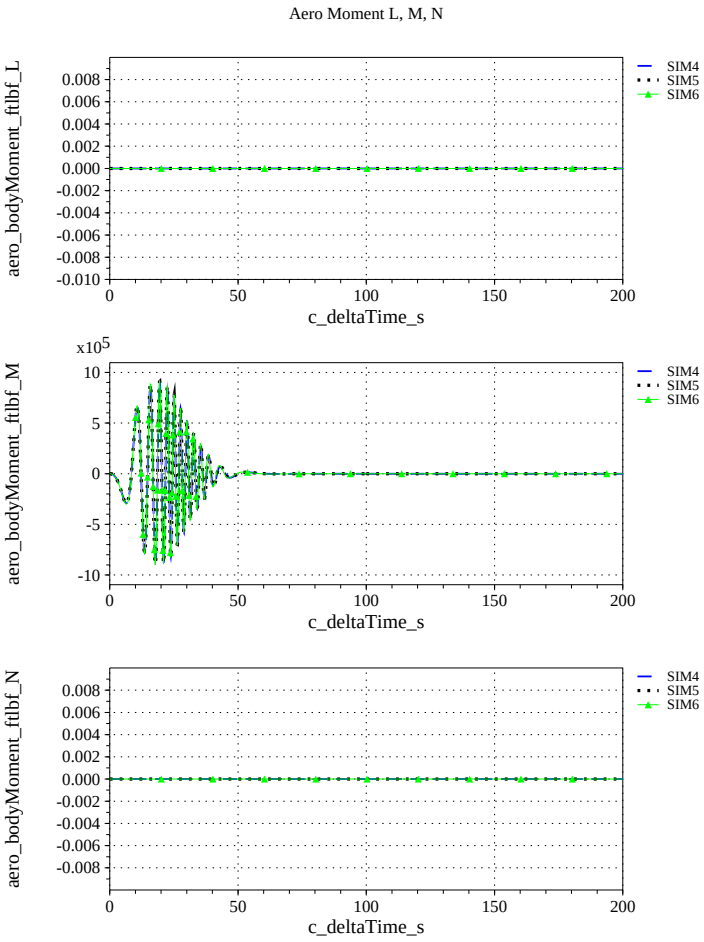

(c) Aerodynamic Moments Compared

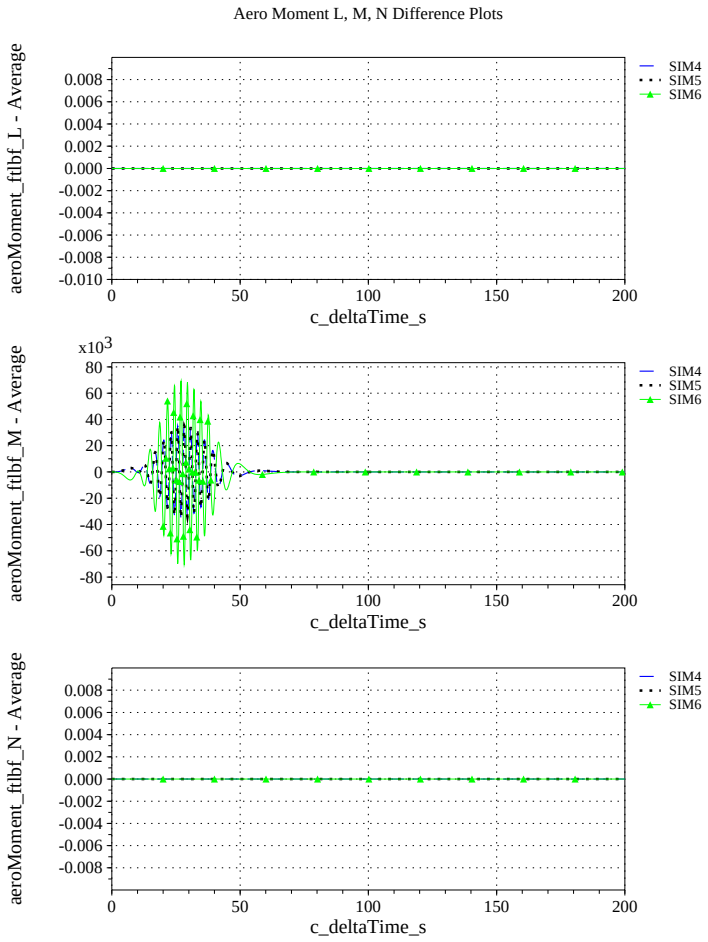

(d) Aerodynamic Moments Differenced

Figure 36. Check-case 17: Flight of Two-stage Launch Vehicle; See Discussion in Section D.1.19 (Cont'd)

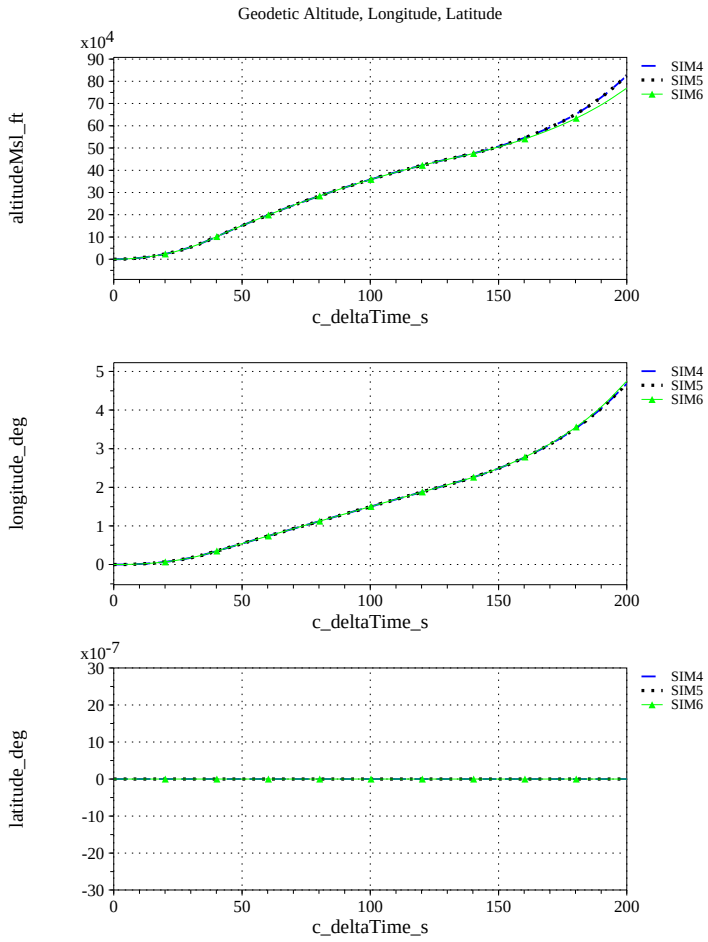

(e) Altitude, Geodetic Latitude and Longitude Compared

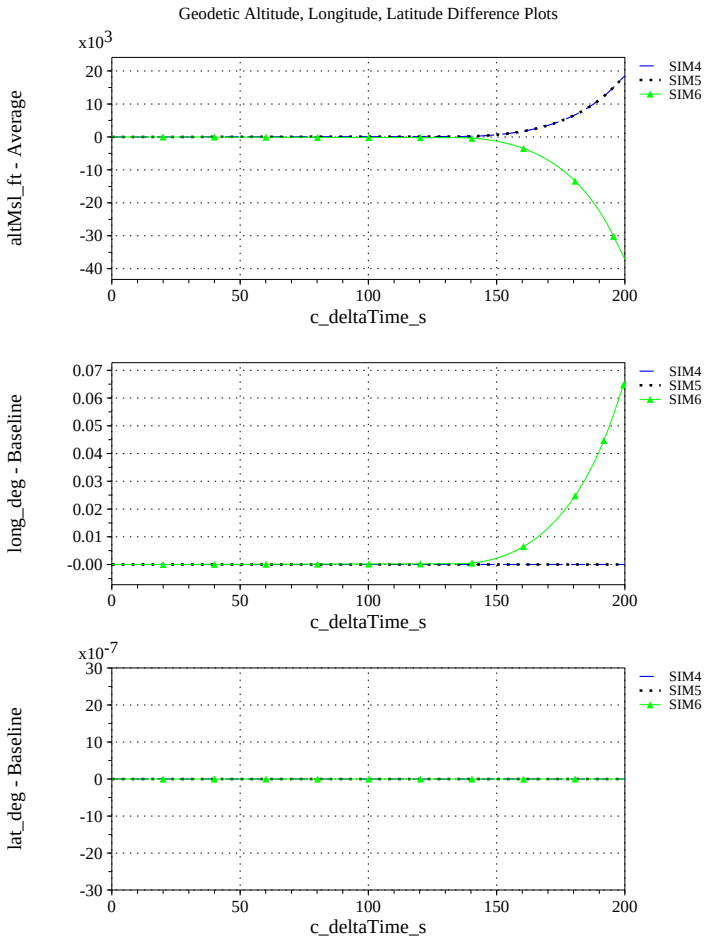

(f) Altitude, Geodetic Latitude and Longitude Differenced

Figure 36. Check-case 17: Flight of Two-stage Launch Vehicle; See Discussion in Section D.1.19 (Cont'd)

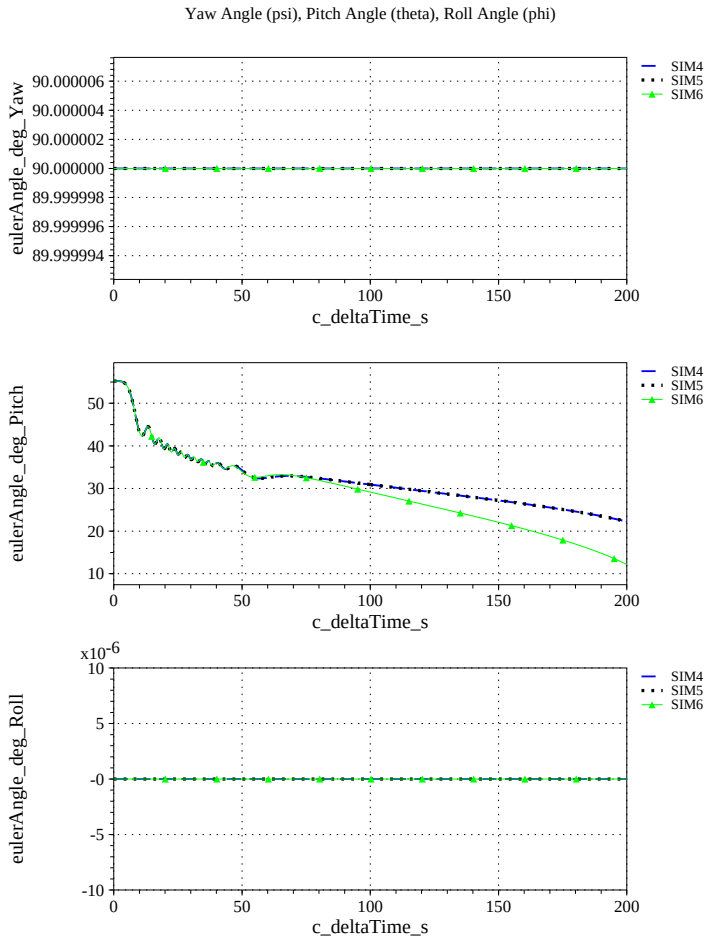

(g) Euler Angles (w.r.t. NED Frame) Compared

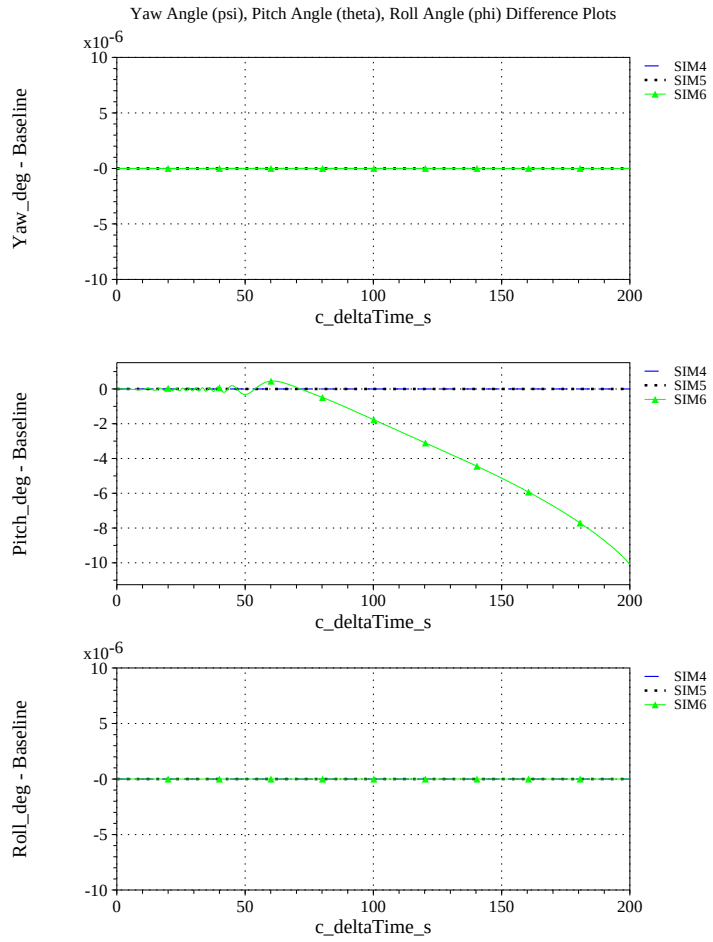

(h) Euler Angles (w.r.t. NED Frame) Differenced

Figure 36. Check-case 17: Flight of Two-stage Launch Vehicle; See Discussion in Section D.1.19 (Cont'd)

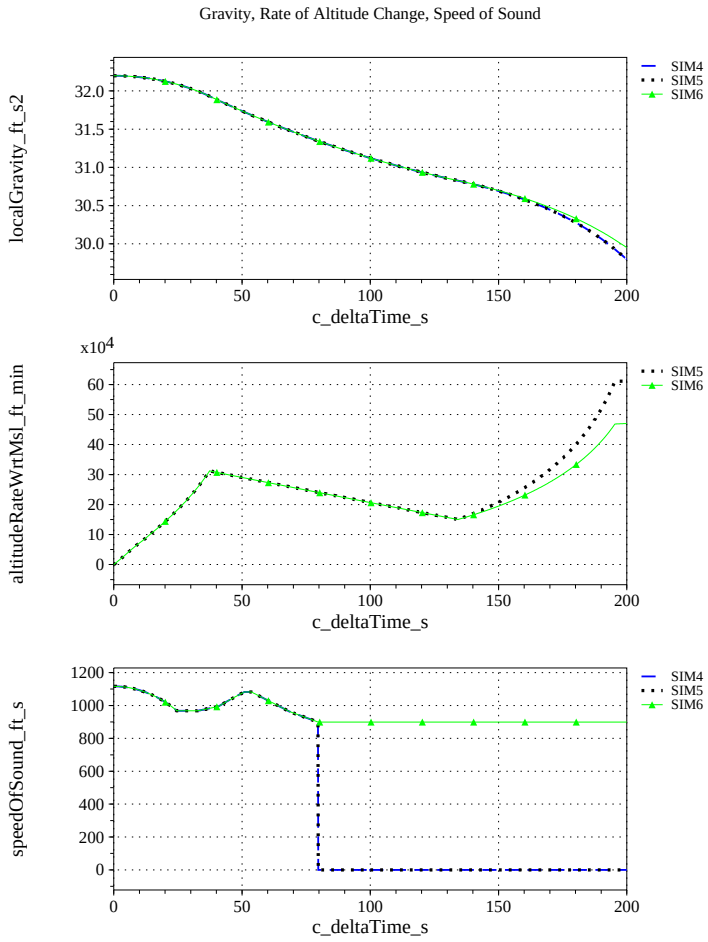

(i) Gravity, Climb Rate, and Speed-of-sound Compared

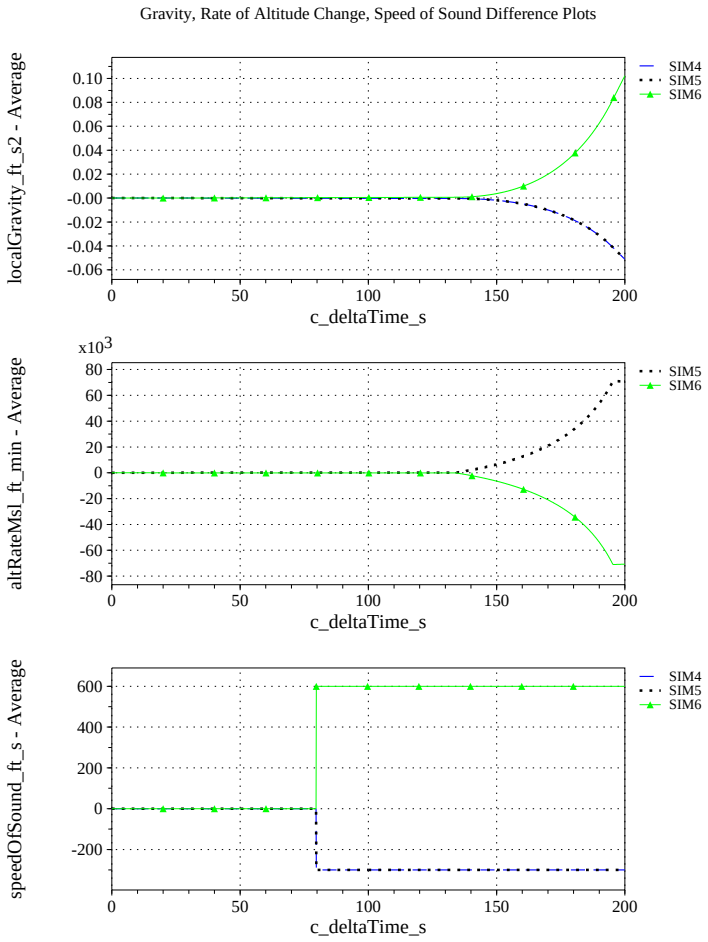

(j) Gravity, Climb Rate, and Speed-of-sound Differenced

Figure 36. Check-case 17: Flight of Two-stage Launch Vehicle; See Discussion in Section D.1.19 (Cont'd)

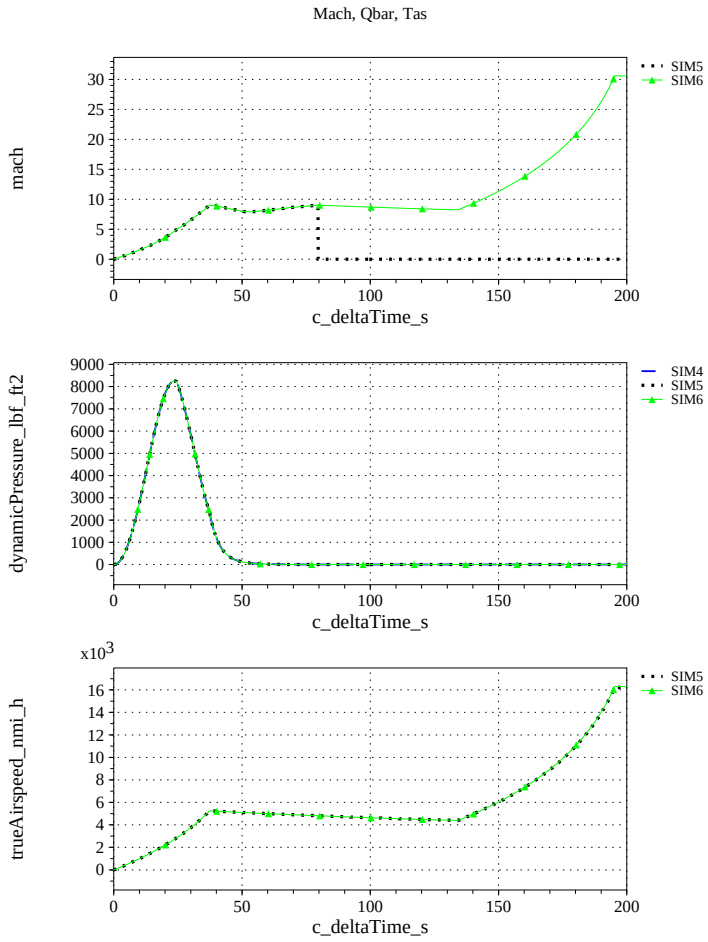

(k) Mach, Dynamic Pressure, and True Airspeed Compared

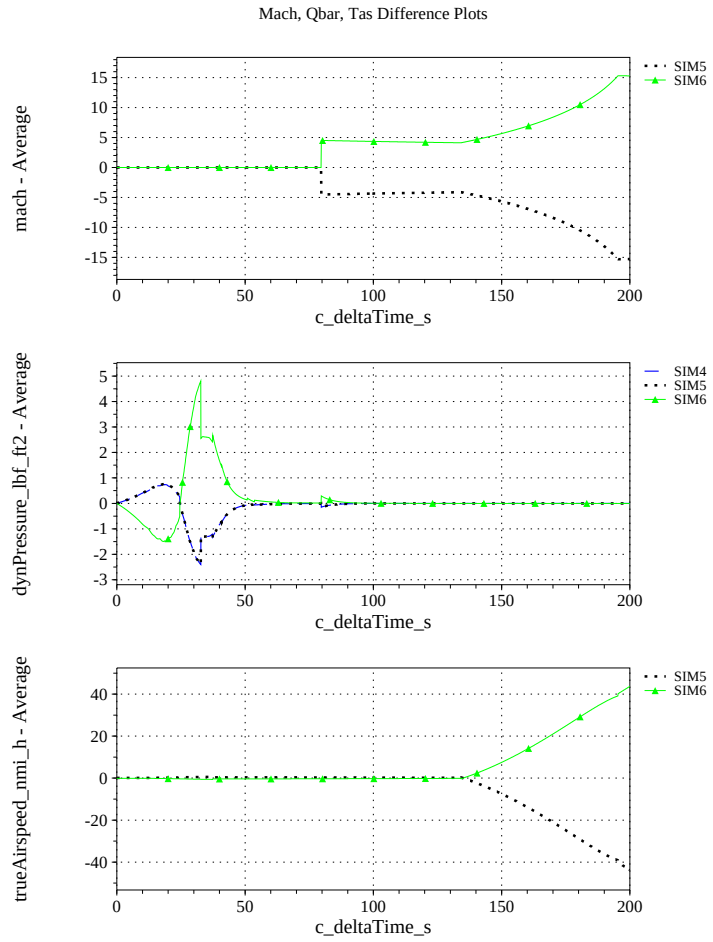

(l) Mach, Dynamic Pressure, and True Airspeed Differenced

Figure 36. Check-case 17: Flight of Two-stage Launch Vehicle; See Discussion in Section D.1.19 (Cont'd)

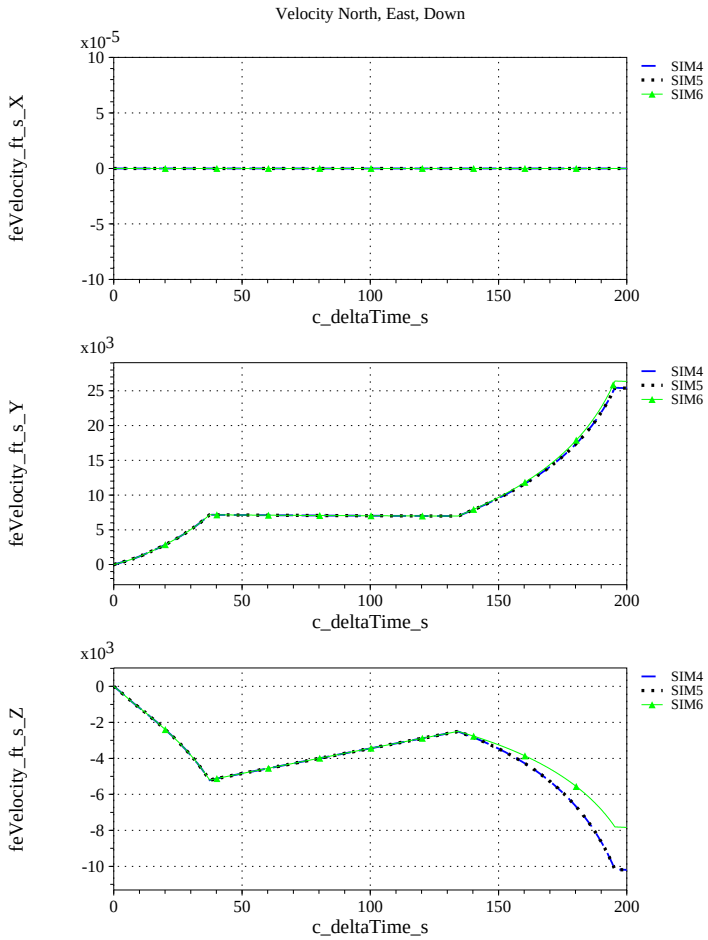

(m) NED Velocities Compared

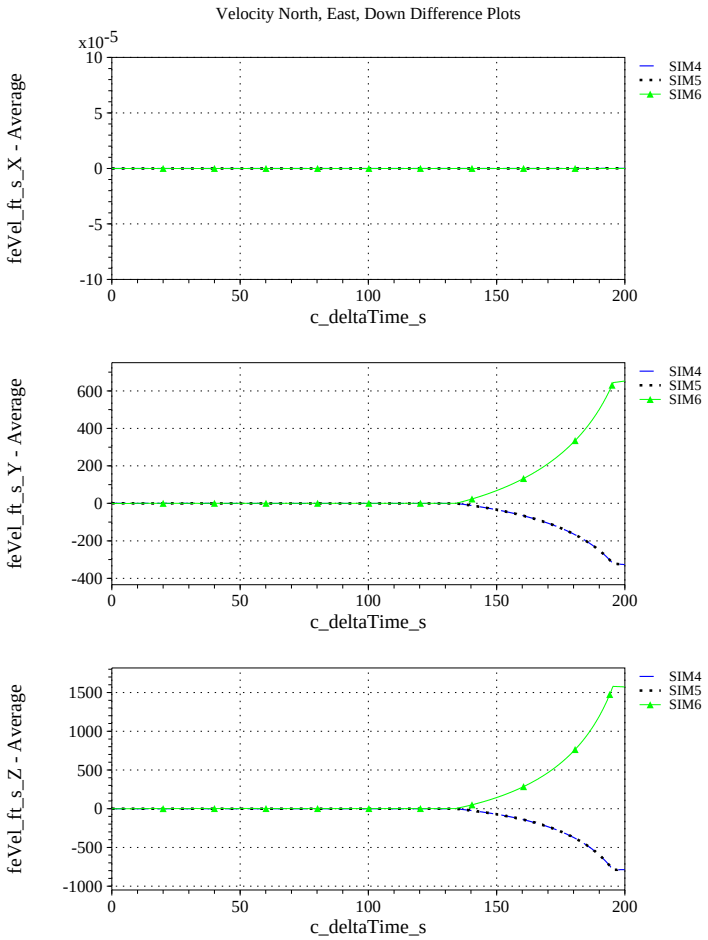

(n) NED Velocities Differenced

Figure 36. Check-case 17: Flight of Two-stage Launch Vehicle; See Discussion in Section D.1.19 (Cont'd)

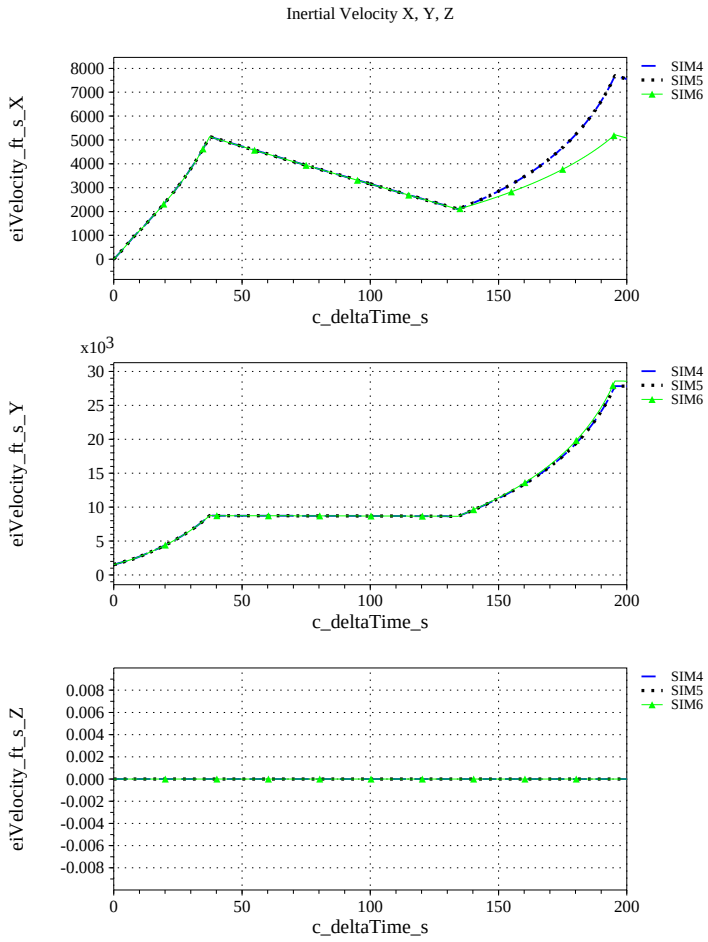

(o) Inertial Velocities Compared

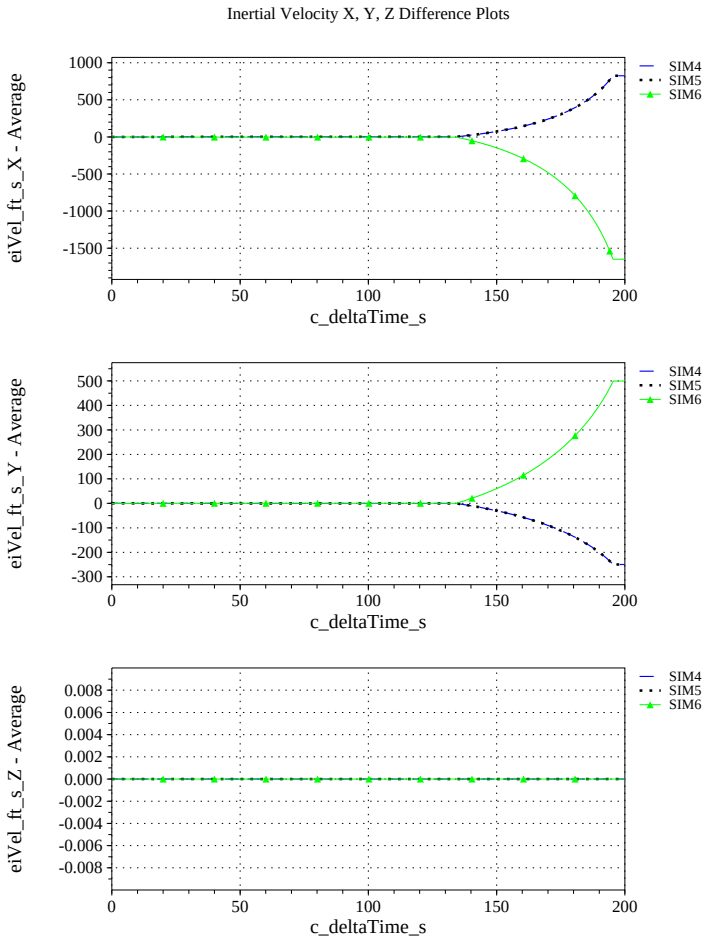

(p) Inertial Velocities Differenced

Figure 36. Check-case 17: Flight of Two-stage Launch Vehicle; See Discussion in Section D.1.19 (Cont'd)

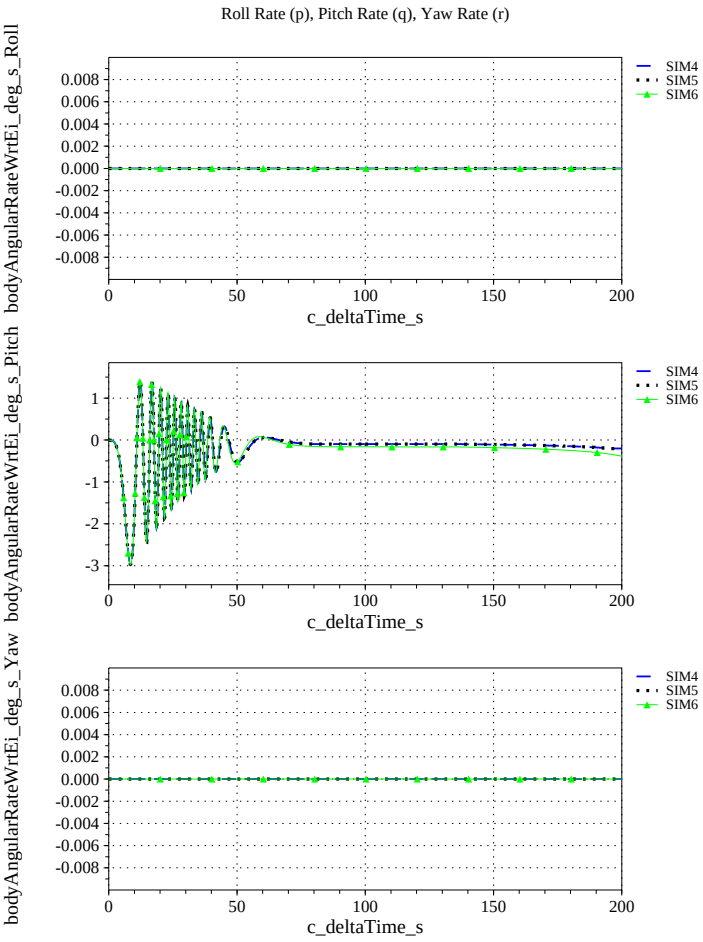

(q) Body-axis Angular Rates (w.r.t. NED Frame) Compared

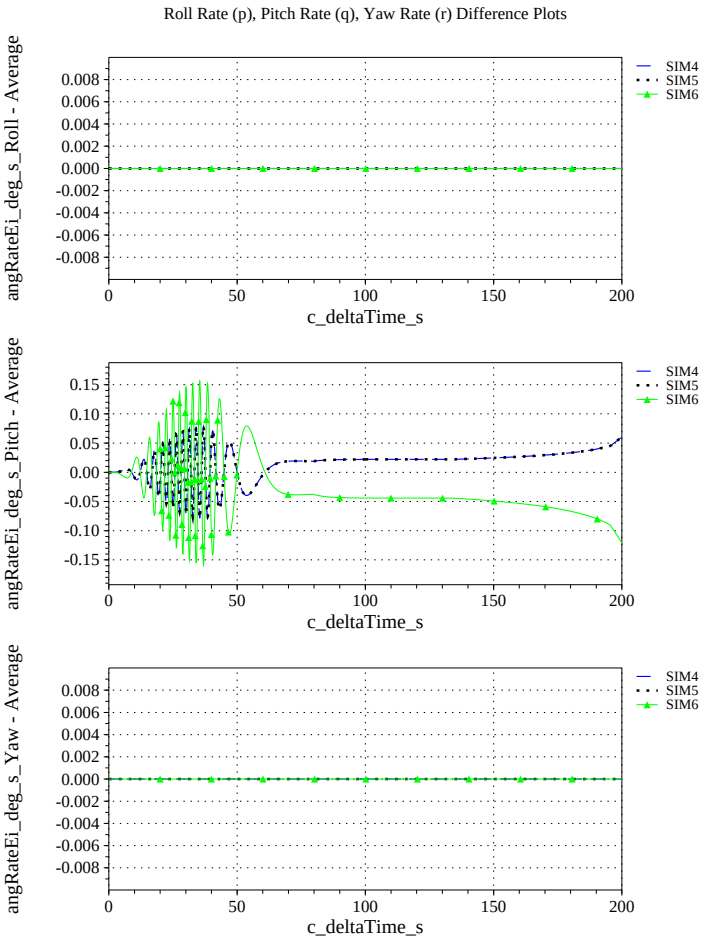

(r) Body-axis Angular Rates (w.r.t. NED Frame) Differenced

Figure 36. Check-case 17: Flight of Two-stage Launch Vehicle; See Discussion in Section D.1.19 (Cont'd)

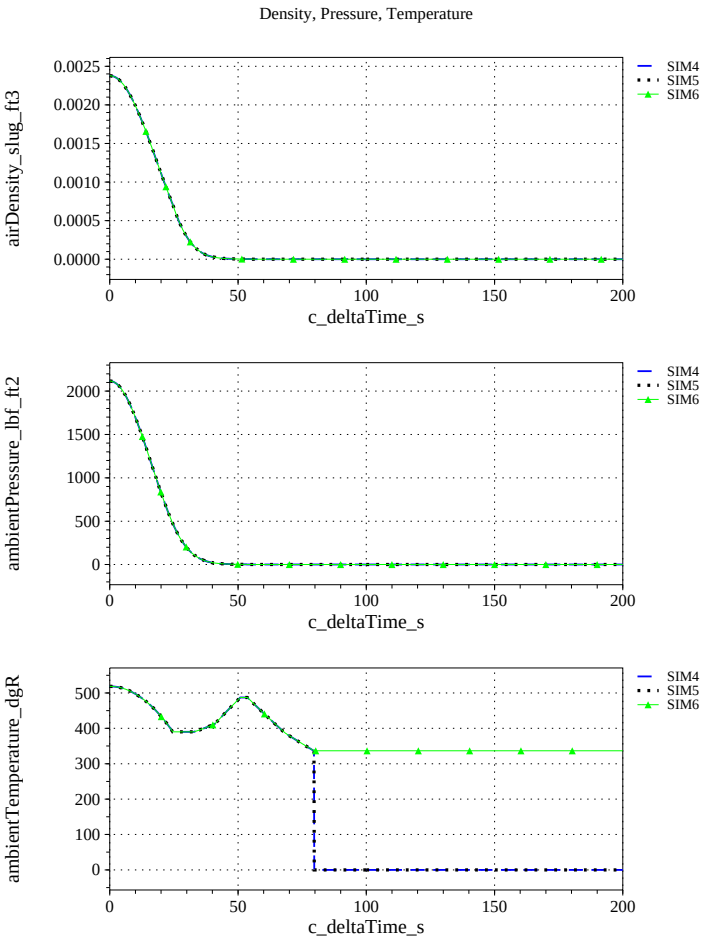

(s) Atmospheric Properties Compared

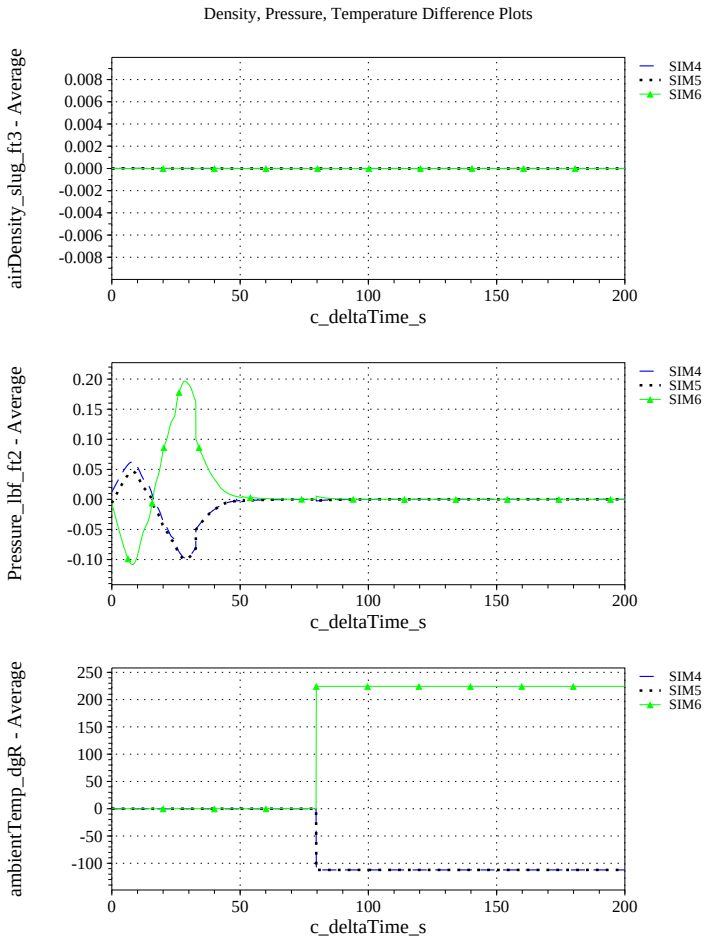

(t) Atmospheric Properties Differenced

Figure 36. Check-case 17: Flight of Two-stage Launch Vehicle; See Discussion in Section D.1.19 (Cont'd)

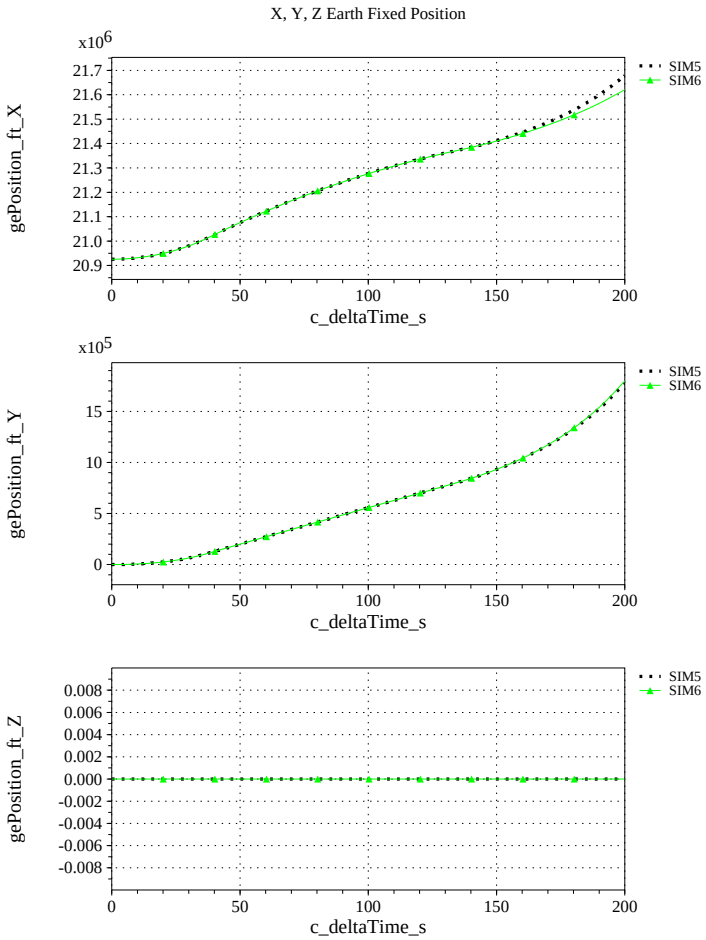

(u) Earth-centered, Earth-fixed Rectangular (X-Y-Z) Positions Compared

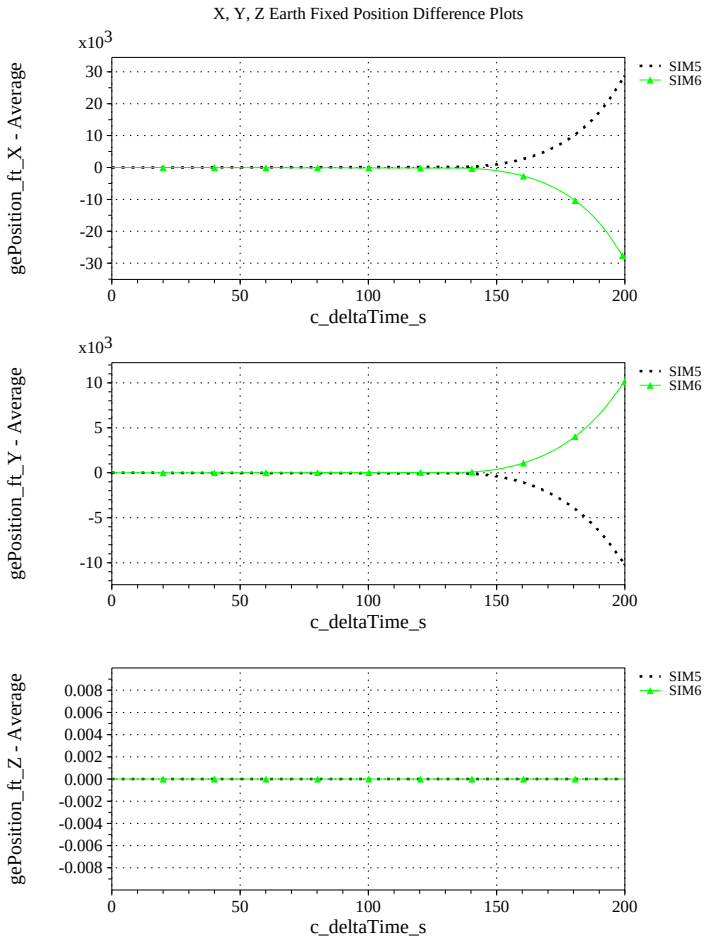

(v) Earth-centered, Earth-fixed Rectangular (X-Y-Z) Positions Differenced

Figure 36. Check-case 17: Flight of Two-stage Launch Vehicle; See Discussion in Section D.1.19 (Cont'd)

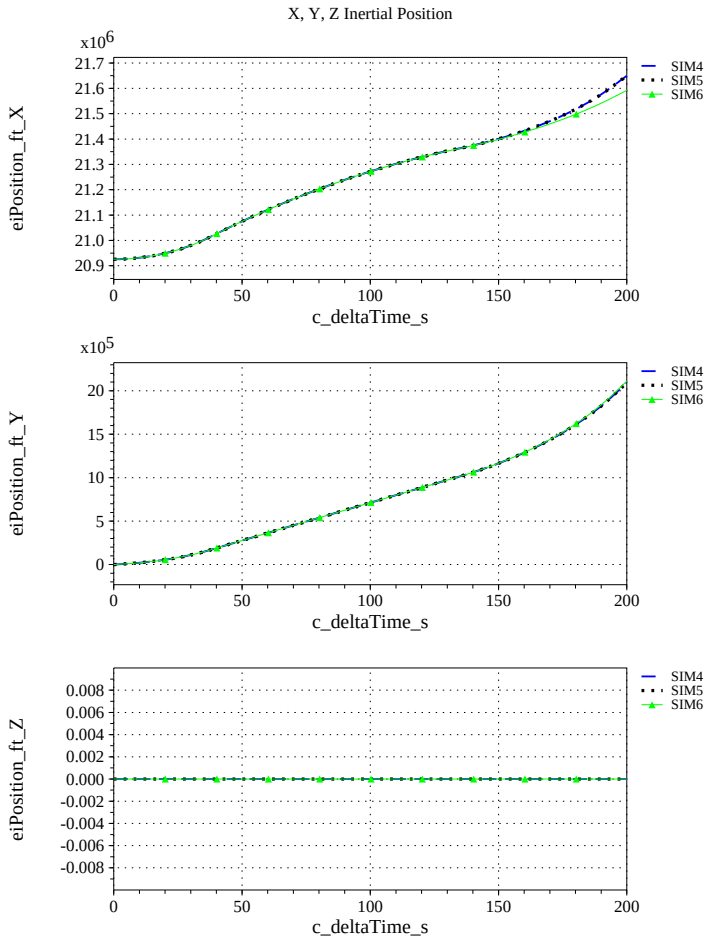

(w) Earth-centered Inertial Rectangular (x-y-z) Positions Compared

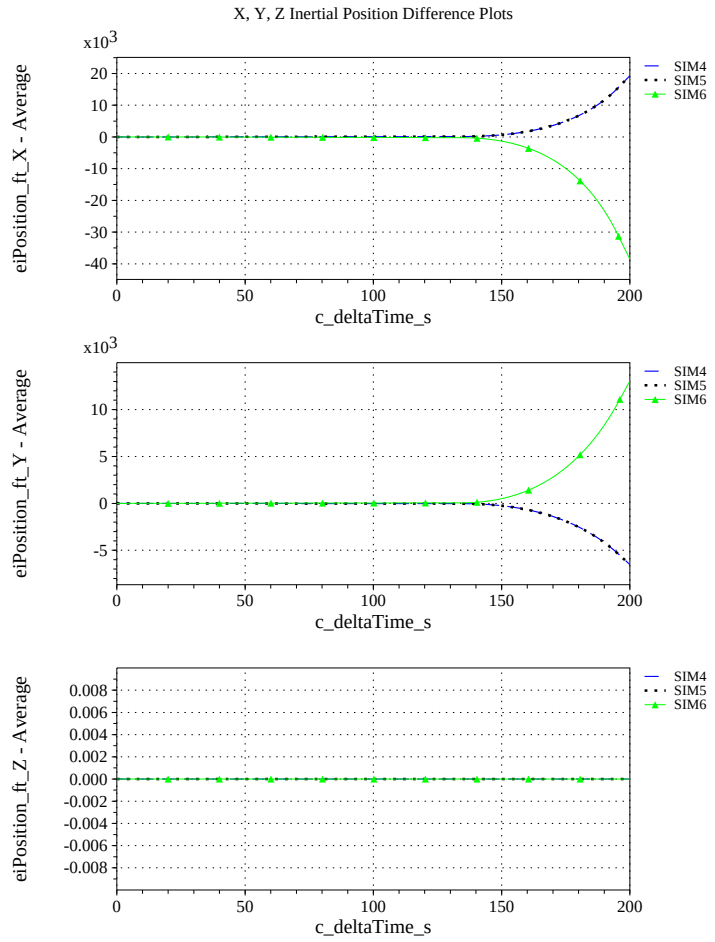

(x) Earth-centered Inertial Rectangular (x-y-z) Positions Differenced

Figure 36. Check-case 17: Flight of Two-stage Launch Vehicle; See Discussion in Section D.1.19 (Concluded)

D.2 Scenario comparisons – Orbital

D.2.1 Check-case 02 – ISS in spherical gravity

This section shows cross-plots for four of the selected simulation tools in modeling the dynamics of the ISS in orbit, propagating with spherical gravity model and no disturbances. This scenario is described in Section C.2.1. Figures 37a through 37p compare results between the four simulation tools, as well as the deviances of the outputs from each tool from the ensemble average value.

This check-case simulated an orbit where the Earth's gravitation is the only force acting on the vehicle. The Earth's gravitation is modeled using the assumption of a spherically symmetric mass. Thus, the Earth's gravitation is not dependent on Earth-relative position (aside from distance from the center of the Earth). This allowed independent comparison of the Earth-relative values reported by the simulations before applying gravitation and atmospheric models that are functions of the Earth-relative position.

The simulations agreed on inertial positions and inertial velocities. Differences plotted for velocity and position were likely due to varied integration methods and are negligible. Differences plotted for acceleration reflected the influence of position differences on the computed gravitation.

Since the simulations matched so closely in inertial coordinates, differences in Earth-fixed variables were due to differences in modeling the Earth. In propagated ECEF position, SIM B, C, and D agreed on the initial Earth-relative position vector. SIM A differed by a distance of less than 0.3 m; the difference vector was {-0.022, -0.231, 0.181} m. The SIM A position difference increased slightly reaching a maximum distance of 1 m and a vector difference of {-0.842, -0.413, 0.429} m. SIM B and SIM C remained in good agreement throughout the run. SIM D departed slightly from SIM B/C, reaching a maximum distance of 0.28 m where the vector difference was {-0.153, 0.103, 0.211} m. The differences in the position for SIM A arose from a difference in the international terrestrial reference frame (ITRF) realization used by the simulations. SIM A used ITRF93 (reference [29]). SIM B, C, and D use ITRF89 [30]. These models differed only in the definition of the reference figure of the Earth at epoch J2000; the methods for computing the change in RNP of the Earth at a given time were the same. Thus, the two ITRF realizations differed only by a constant rotation. SIM D began to depart from SIM B and C because SIM D used the RNP model to initialize the orientation of the Earth but assumed a constant Z-axis rotation afterward. SIM B and SIM C ran the full RNP model every frame.

On the altitude chart, the differences plot (Figure 37d) also segregated SIM A from the SIM B/C/D cluster. The differences were consistent given the ECEF differences. The difference in initial altitude was 4 parts per million whereas the difference in initial Earth position was 11 parts per million. There might also have been a minute difference in the accuracy of the method that SIM A used convert the Earth-relative position vector to altitude.

The difference plots for angular rate (Figure 37f) showed some small disparity between SIM A and the SIM B/C/D cluster. However, these differences were negligible and are likely caused by a difference in integration method. The differences in angular rate also contributed to the larger but still negligible differences in orientation (inertial and LVLH Euler angles). The difference in orientation was likely caused by both by the growing difference in angular rate and by a difference in integration method employed.

The simulations also showed differences in atmospheric properties (Figure 37d). These differences are explained in the discussion for orbital case 5A (see the discussion in Section D.2.5).

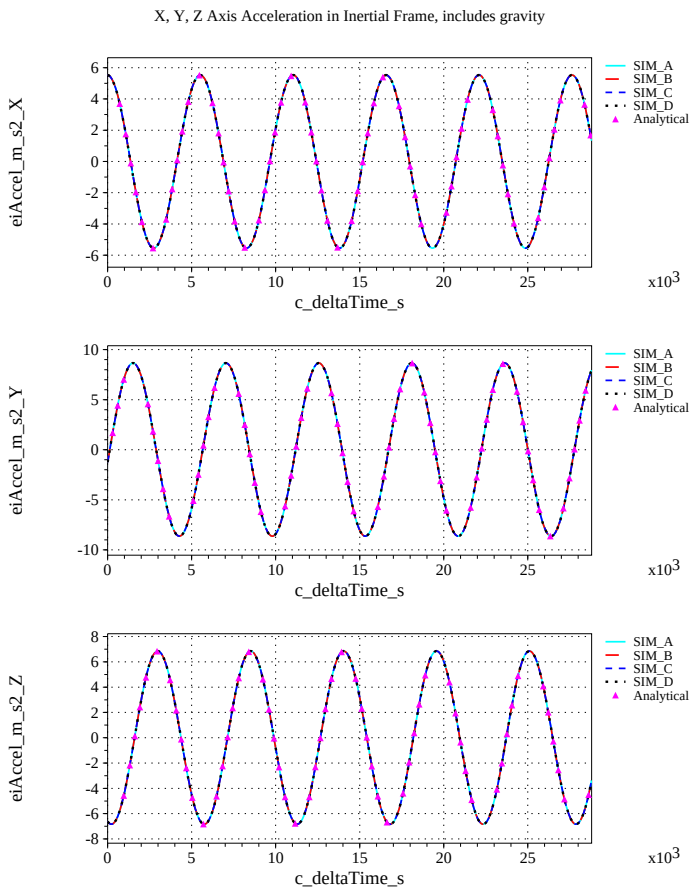

(a) Inertial Accelerations Compared

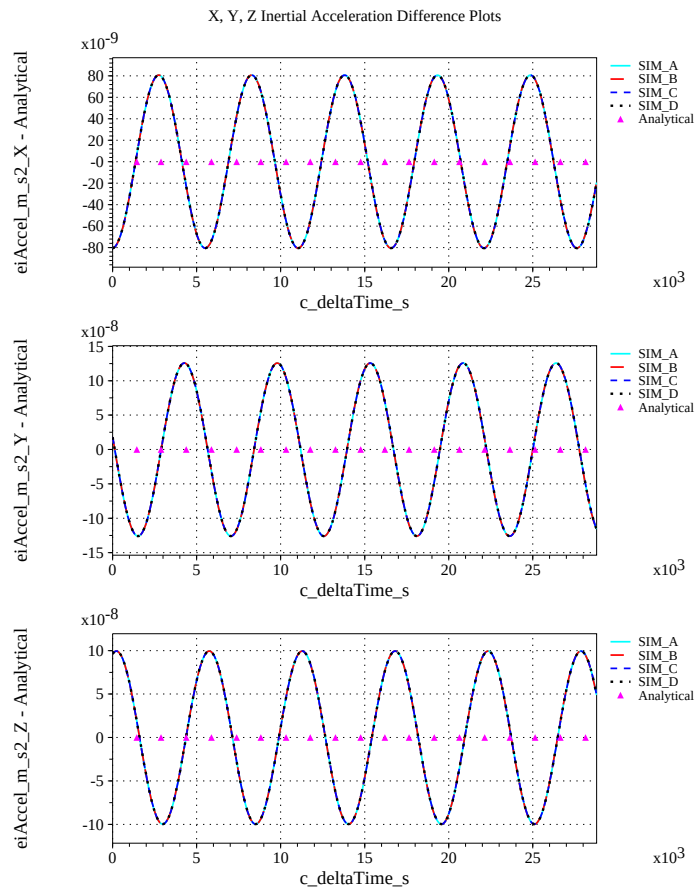

(b) Inertial Accelerations Differenced

Figure 37. Check-case 02: ISS in Spherical Gravity; See Discussion in Section D.2.1

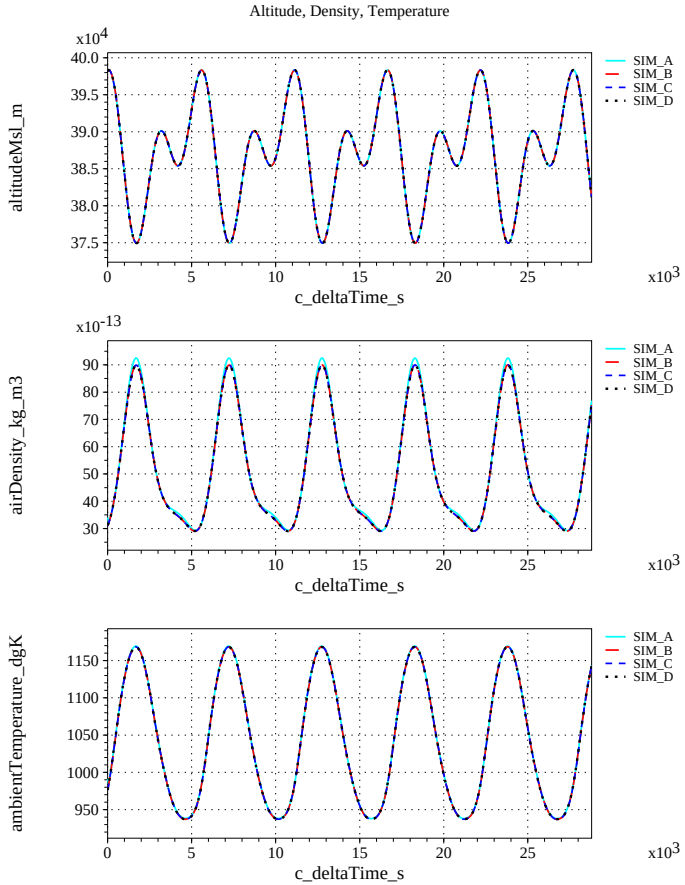

(c) Atmospheric Properties Compared

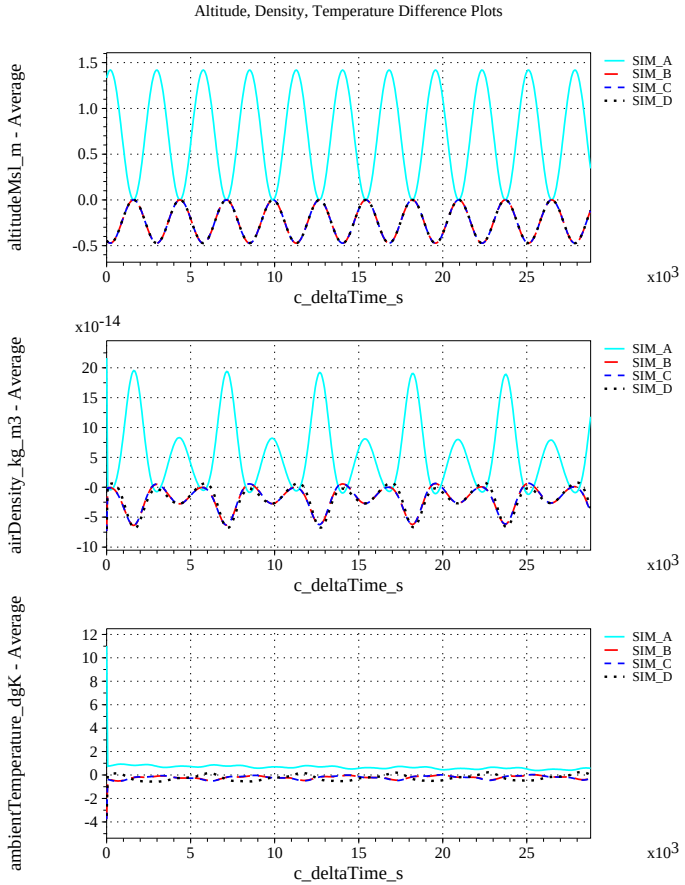

(d) Atmospheric Properties Differenced

Figure 37. Check-case 02: ISS in Spherical Gravity; See Discussion in Section D.2.1 (Cont'd)

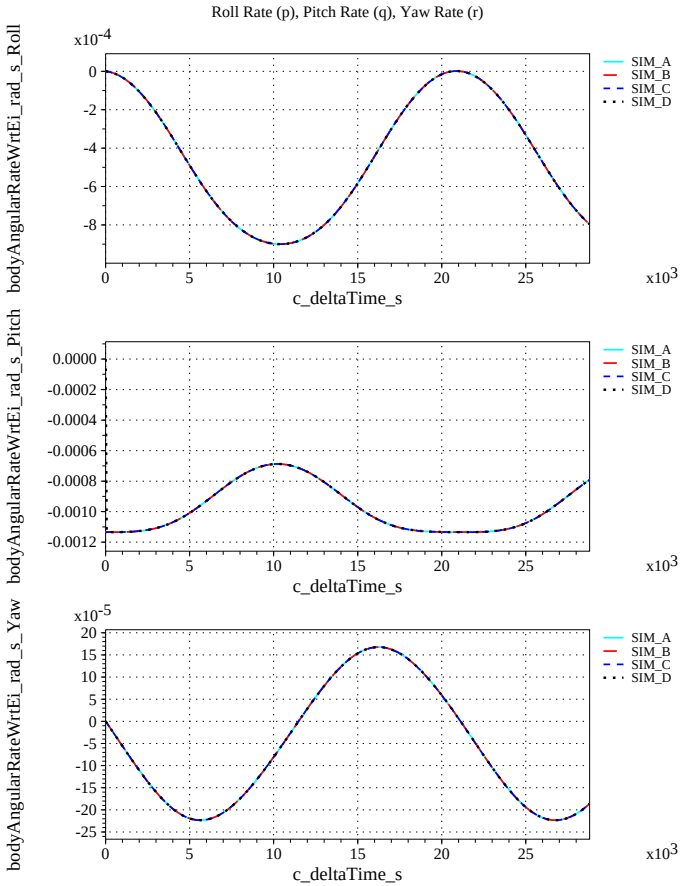

(e) Body-axis Angular Rates Compared

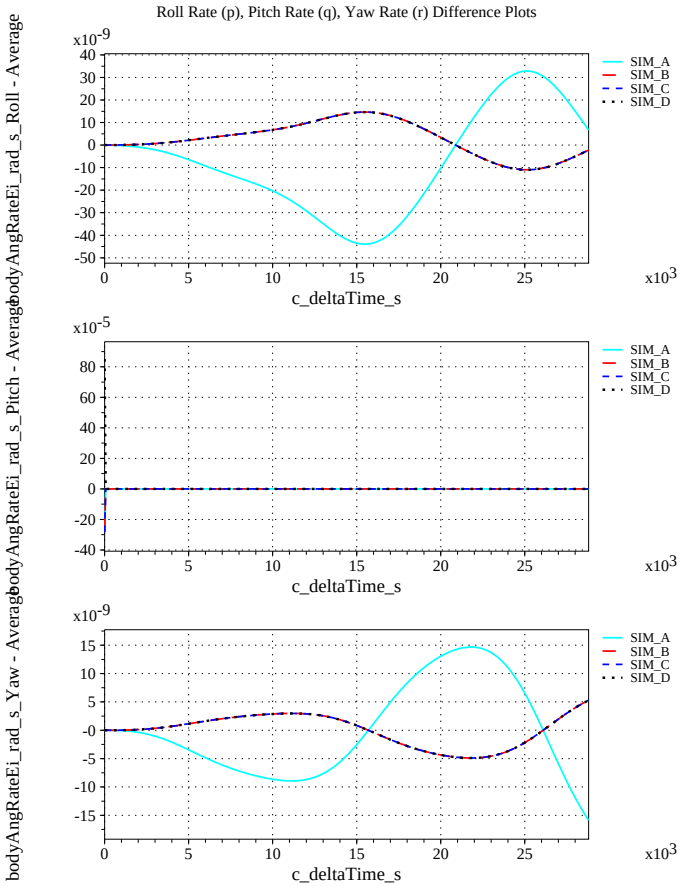

(f) Body-axis Angular Rates Differenced

Figure 37. Check-case 02: ISS in Spherical Gravity; See Discussion in Section D.2.1 (Cont'd)

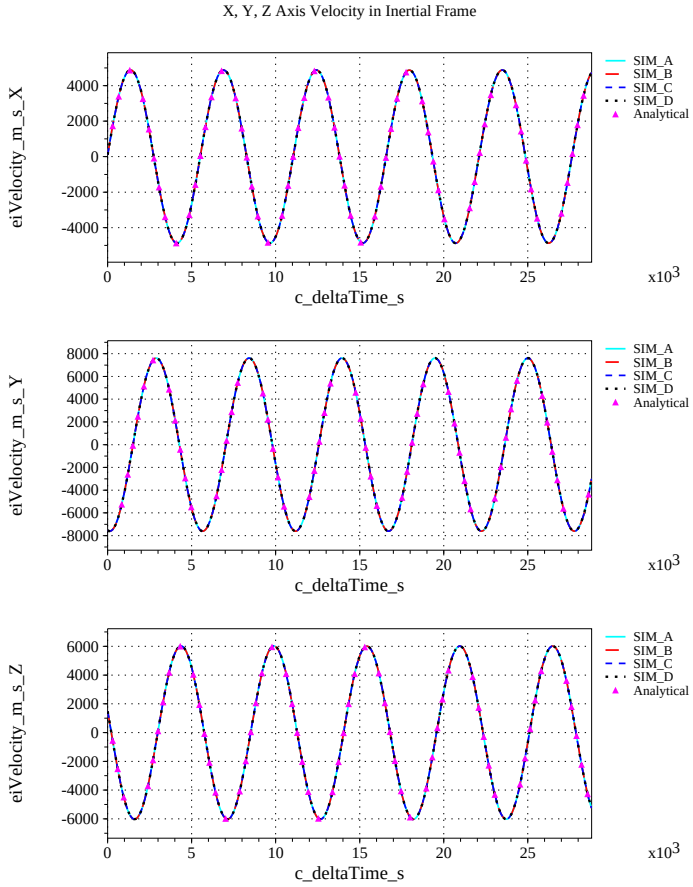

(g) Inertial Velocities Compared

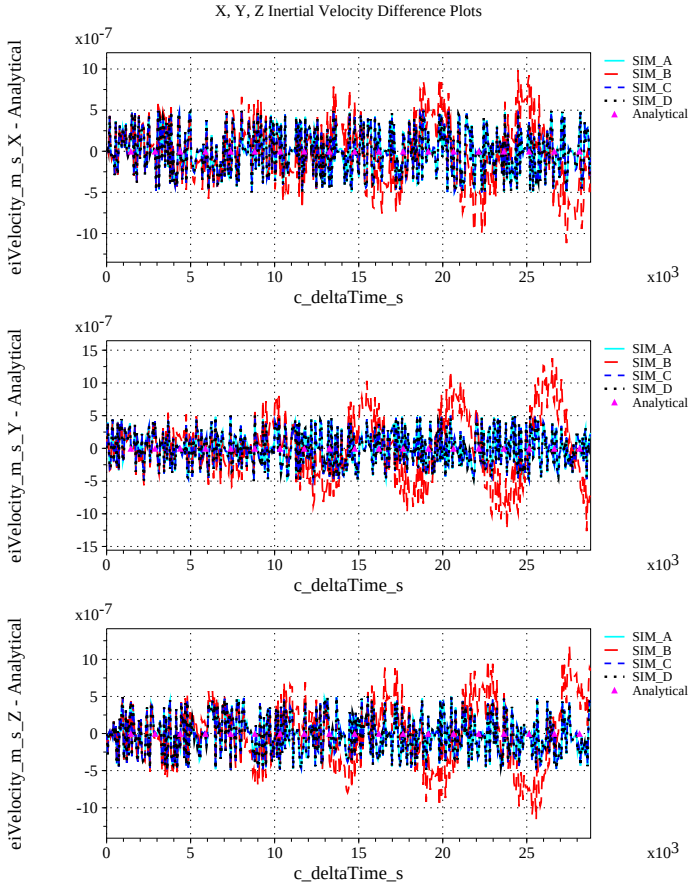

(h) Inertial Velocities Differenced

Figure 37. Check-case 02: ISS in Spherical Gravity; See Discussion in Section D.2.1 (Cont'd)

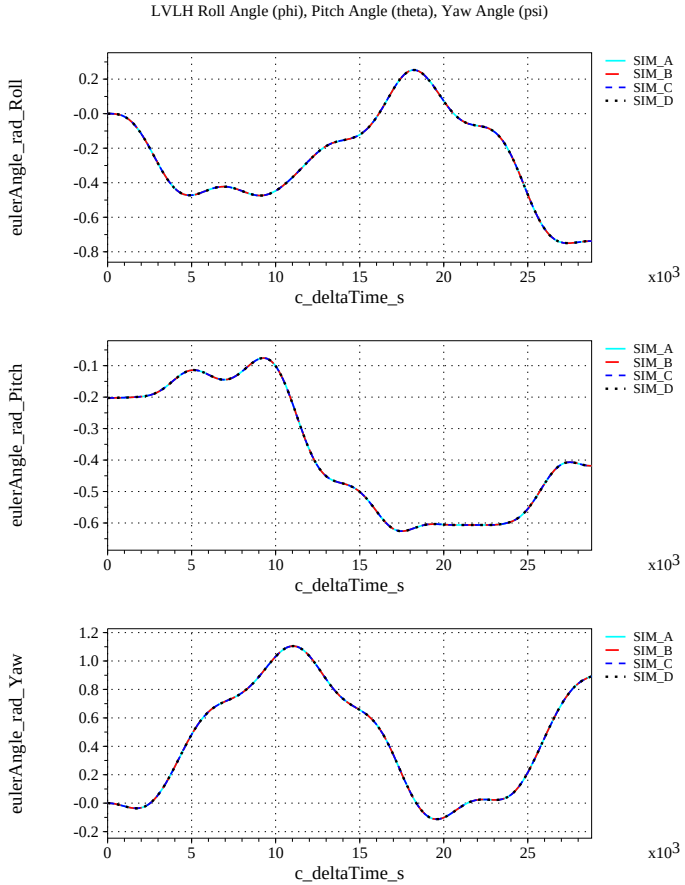

(i) Rotation Angles with Respect to LVLH Frame Compared

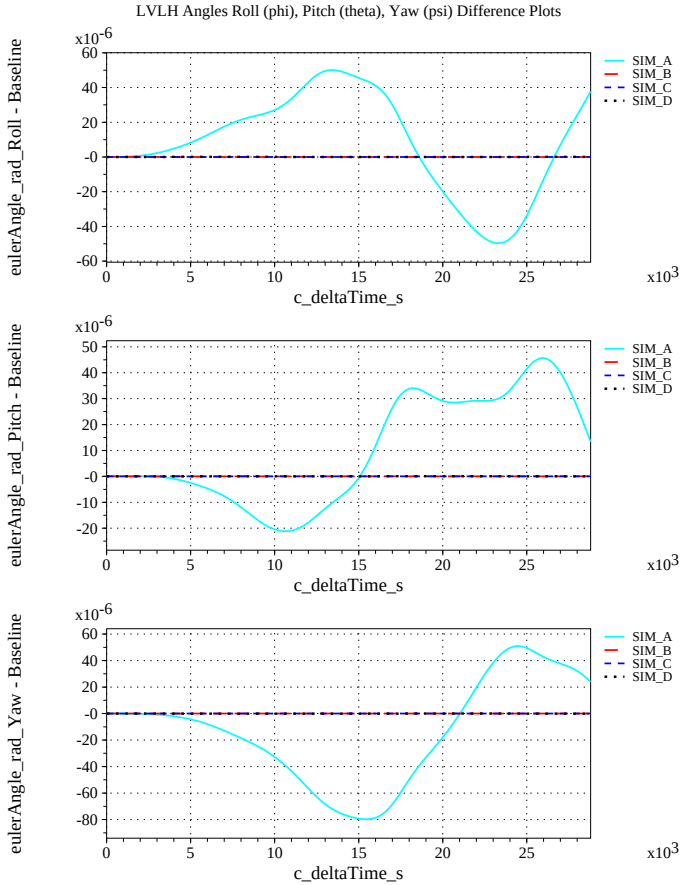

(j) Rotation Angles with Respect to LVLH Frame Differenced

Figure 37. Check-case 02: ISS in Spherical Gravity; See Discussion in Section D.2.1 (Cont'd)

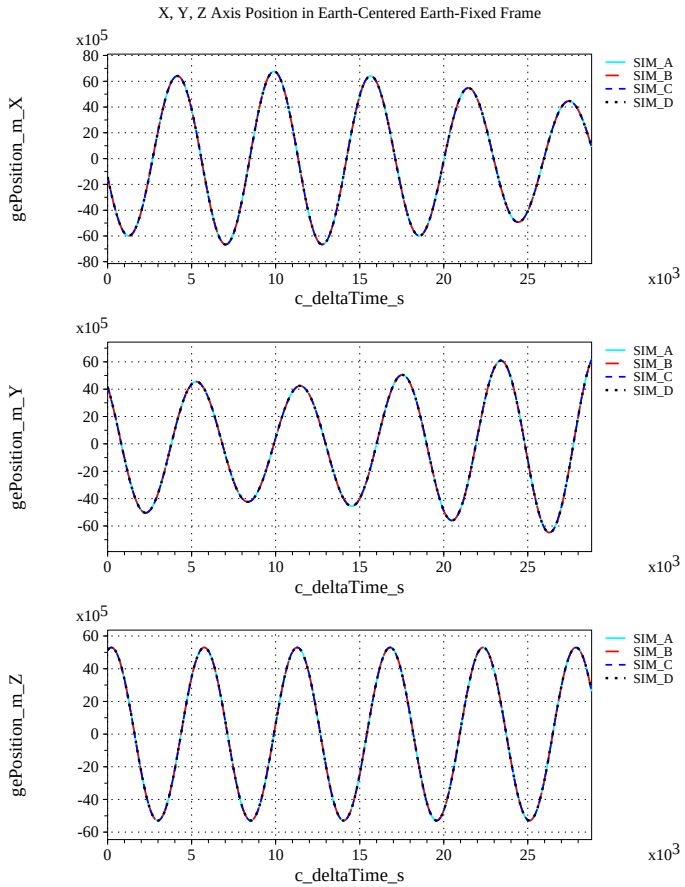

(k) Earth-centered, Earth-fixed Rectangular (X-Y-Z) Positions Compared

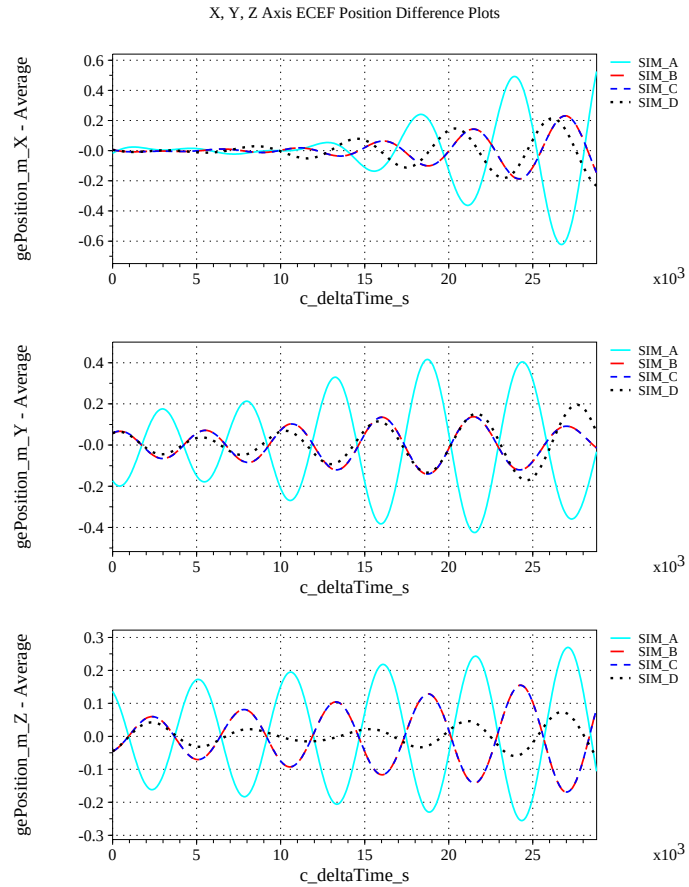

(l) Earth-centered, Earth-fixed Rectangular (X-Y-Z) Positions Differenced

Figure 37. Check-case 02: ISS in Spherical Gravity; See Discussion in Section D.2.1 (Cont'd)

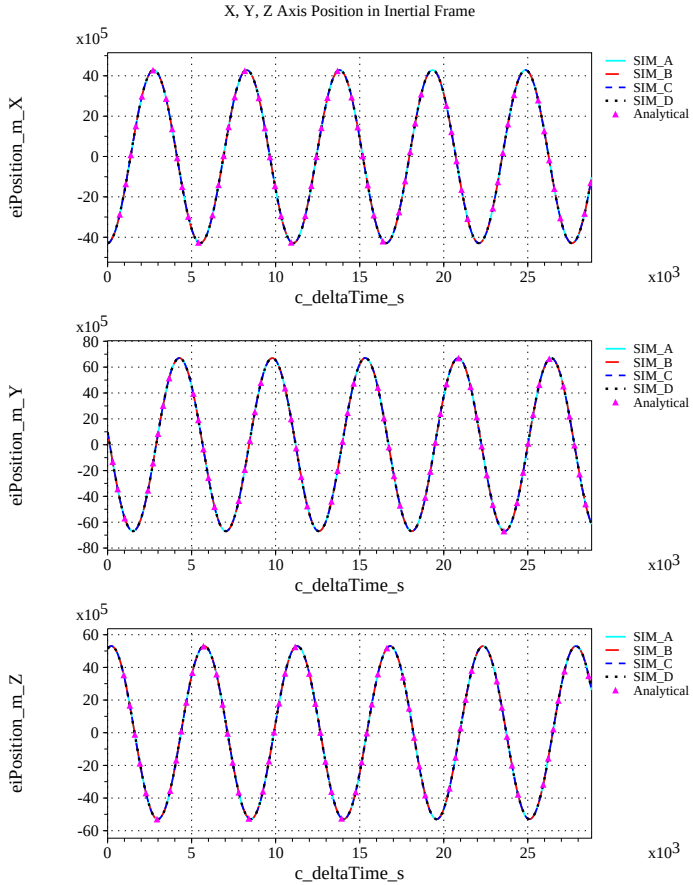

(m) Earth-centered Inertial Rectangular (x-y-z) Positions Compared

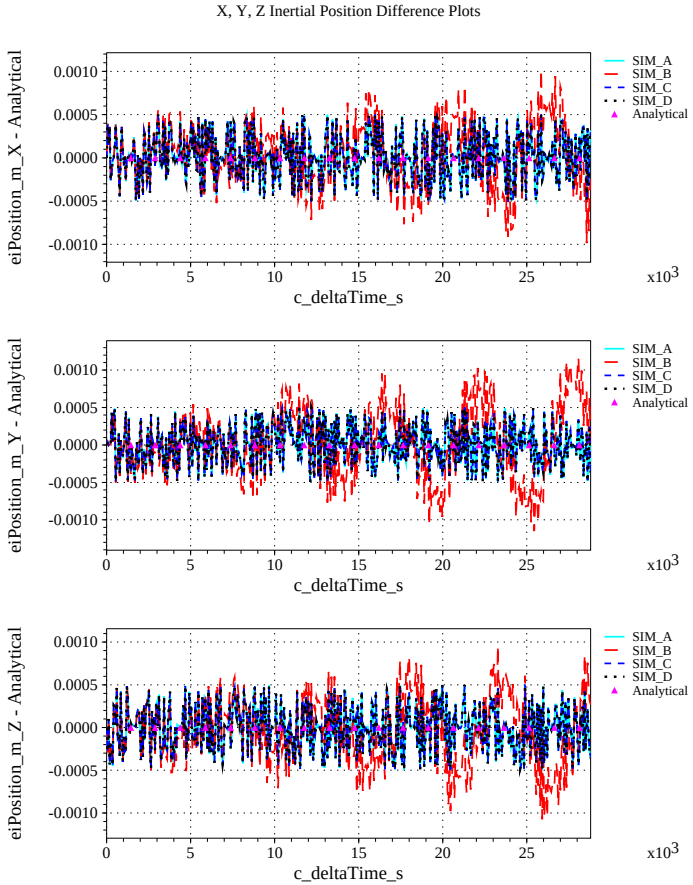

(n) Earth-centered Inertial Rectangular (x-y-z) Positions Differenced

Figure 37. Check-case 02: ISS in Spherical Gravity; See Discussion in Section D.2.1 (Cont'd)

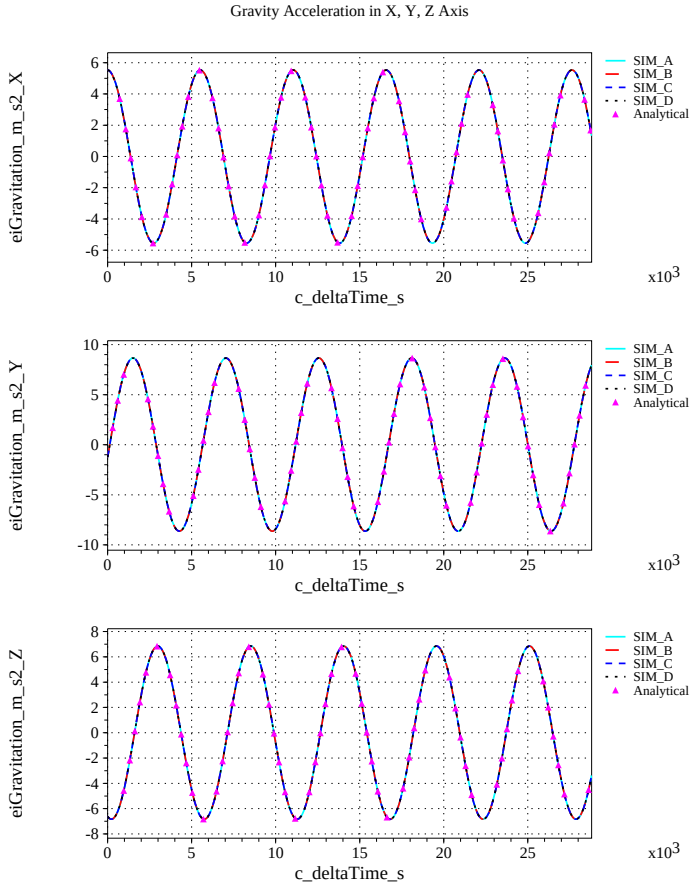

(o) Gravitational Components in Inertial (**X**-**Y**-**Z**) Directions Compared

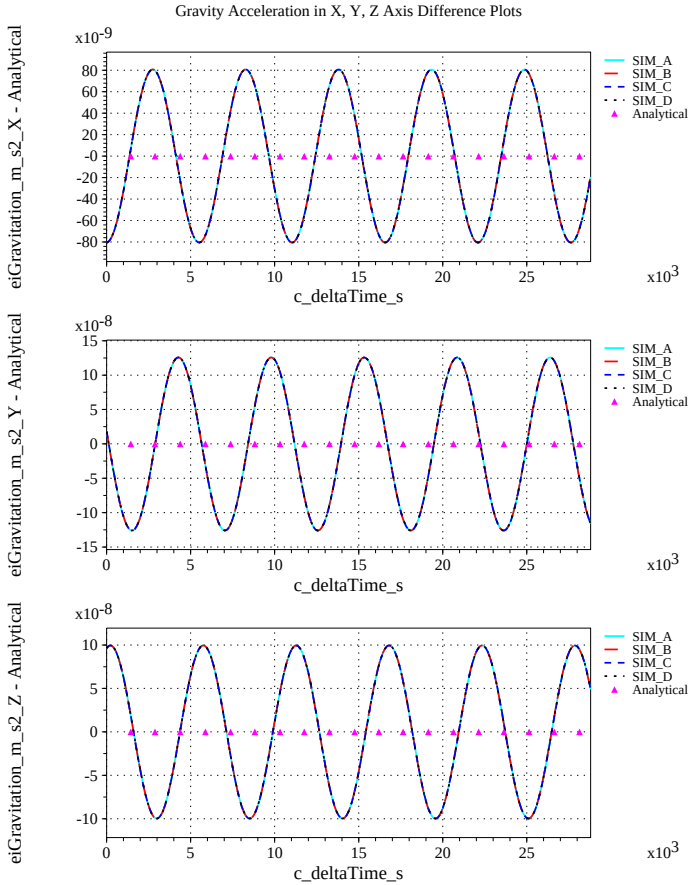

(p) Gravitational Components in Inertial (**X**-**Y**-**Z**) Directions Differenced

Figure 37. Check-case 02: ISS in Spherical Gravity; See Discussion in Section D.2.1 (Concluded)

D.2.2 Check-case 03A – ISS in 4×4 harmonic gravity

This section shows cross-plots for four of the selected simulation tools in modeling the dynamics of the ISS in orbit with a 4×4 harmonic gravity model and no disturbances. This scenario is described in Section C.2.2. Figures 38a through 38p compare results between the four simulation tools, as well as the deviances of the outputs from each tool from the ensemble average value.

This check-case modified orbital case 2 by replacing the gravitation model with a spherical harmonic geopotential model of degree four and order four. Gravitational attraction predicted by this model is a function of the geocentric position of the vehicle; therefore, differences in the Earth-relative position of the vehicle could produce small differences in the resultant gravitation vector. Orbital case 2 (section D.2.1) showed that differences in the modeling of the Earth RNP produced Earth-relative position differences among the simulations no greater than 1 m. Through their influence on the gravitation calculation, the Earth-relative position differences were expected to contribute to differences in inertial position. However, the difference plot for inertial position (Figure 38n) hints that differences in the gravitation model implementation were the dominant contributor to position differences. For example, SIM B and SIM C had the closest agreement on inertial and Earth-relative position in orbital case 2, yet, here they departed in inertial position by 1.77 m. On the other hand, SIM B and SIM D differed in inertial position by no more than 0.2 m even though, in orbital case 2, their Earth-relative position differed by up to 0.28 m.

Thus, more scrutiny was applied to the gravitation results. At the scenario start, SIM B, SIM C, and SIM D agreed on the Earth-relative position to within a millimeter. However, the SIM C gravitation vector differed in magnitude from the other two simulations by 5×10^{-8} m/s^2. While a small value, it was of the same order, or larger than, some of the terms in the spherical harmonic gravitation model. To objectively evaluate the gravitation results from each of the models, an independent model of the GEM-T1 spherical harmonic gravitation model was scripted in Mathematica®. The initial Earth-relative position reported by each simulation was fed into the calculation script, and the resultant gravitation vector was compared against the gravitation vector reported by the simulation. Table 76 shows the difference between the gravitation vector reported by the simulation and the results of the calculation script.

Table 76. Comparison of Simulation Gravitation Vectors to Calculation Script at $t = 0$ sec

Simulation Tool	Geocentric Gravitation Error, m/s^2 Up	North	East	Error Norm, m/s^2	Magnitude Error, m/s^2
SIM A					-2.73×10^{-07}
SIM B	2.66×10^{-14}	-4.56×10^{-15}	-1.17×10^{-14}	-1.60×10^{-14}	-1.60×10^{-14}
SIM C	-5.25×10^{-08}	-5.44×10^{-09}	-5.14×10^{-09}	5.25×10^{-08}	5.25×10^{-08}
SIM D	2.56×10^{-11}	-8.56×10^{-12}	1.36×10^{-12}	-2.62×10^{-11}	-2.62×10^{-11}

In the table, the "error norm" is the magnitude of the error vector and the "magnitude error" is the difference in the magnitude of the simulation gravitation vector compared to the calculation script output. In each case, the geocentric gravitation vector for the simulation was computed using the inertial gravitation vector, the RNP matrix (for inertial to ECEF transformation), and the ECEF position vector (to compute geocentric latitude and longitude for the ECEF-to-geocentric transformation). The ability to accurately reconstruct the geocentric gravitation vector was limited by the precision of these fields in the recorded data set. Also, it was assumed that no field leads or lags the others by a frame. SIM A does not report RNP in its data set so it was not possible to compute the geocentric gravitation vector; however, the magnitude of the gravitation vector

could still be compared. It is assumed that all the simulations were using GEM-T1 coefficients (ref [28]) and that those coefficients were the same. GEM-T1 coefficients were taken from SIM B.

The comparison revealed that:

- SIM B matched the Mathematica model to within machine precision.
- SIM D matched the Mathematica model to within the precision of its recorded output (the data set had ten digits of precision).
- SIM C showed differences larger than the precision of its output for all three geocentric axes. In fact, the differences were larger than the contributions of some of the degree-order pairs in the spherical harmonic series. Therefore, the accuracy of its results appeared to be slightly reduced from that of SIM B and SIM D.
- The magnitude error for SIM A suggests that it may be using an algorithm, like SIM C, that exhibited reduced accuracy for the initial condition.

Differences in inertial velocity followed the differences in gravitation. In turn, they drove the differences in inertial position. Differences in Earth-relative position were a combination of the differences in inertial position, the differences in the initial RNP orientation of the Earth, and differences in how the RNP transformation was updated during the simulation. As explained in orbital case 2 (Section D.2.1), SIM A differed in initial RNP orientation from the other simulations because it used ITRF93 instead of ITRF89 as the reference figure for the Earth. The Earth-relative position for SIM D diverged from SIM B and SIM C, in part, because SIM D updated the Earth RNP transformation matrix using a simple z-axis rotation; SIM B and SIM C updated the full RNP model each frame.

Differences in angular rates, inertial Euler angles, and LVLH Euler angles were identical to those seen in orbital case 2 and are attributed to differences in integration method. Though the orbits differed slightly due to the differences in the computed gravity vector, those differences were not large enough in this case to affect the orbit-relative LVLH Euler angles.

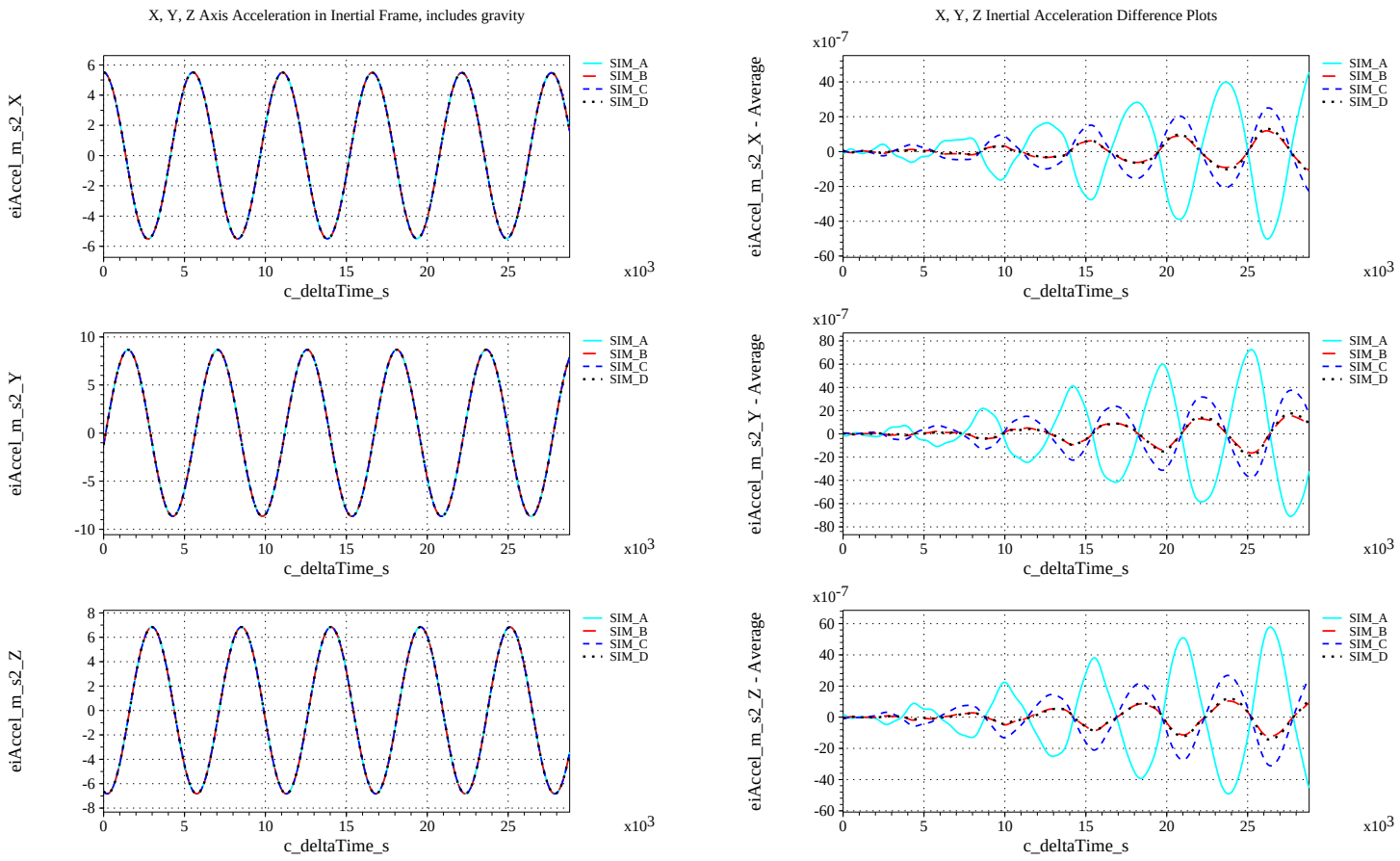

(a) Inertial Accelerations Compared

(b) Inertial Accelerations Differenced

Figure 38. Check-case 03A: ISS in 4×4 Harmonic Gravity; See Discussion in Section D.2.2

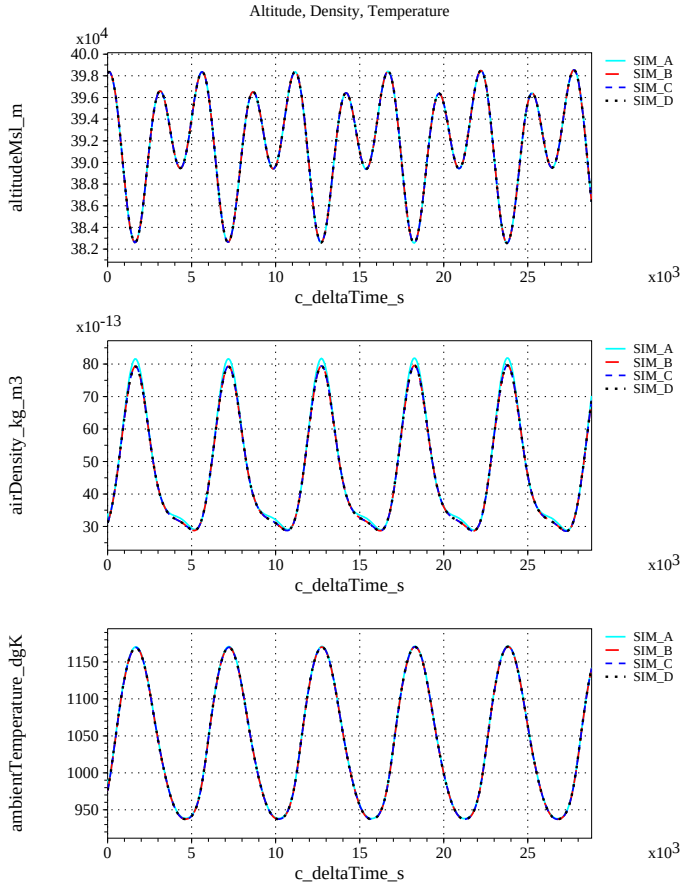

(c) Atmospheric Properties Compared

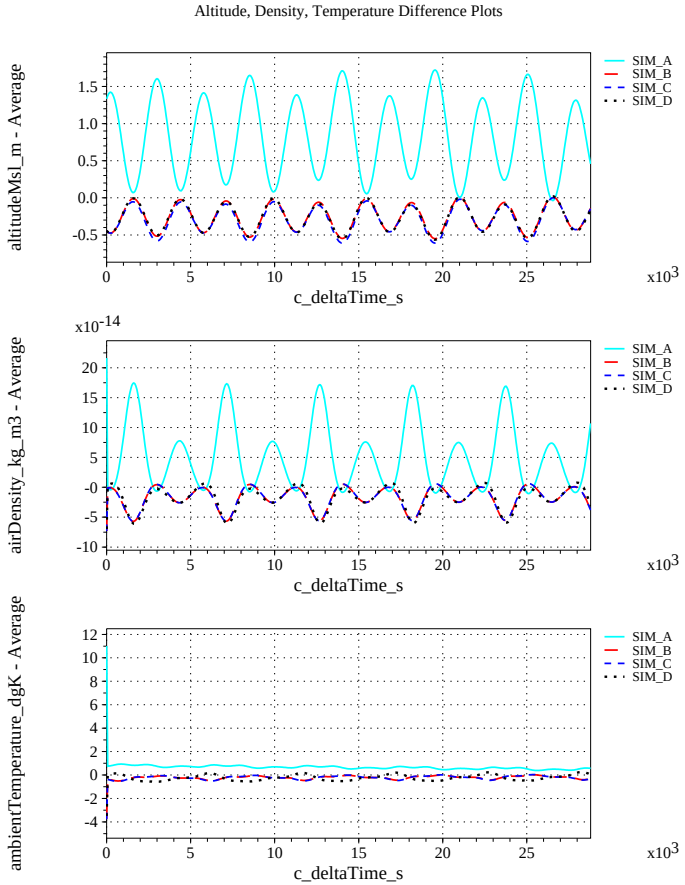

(d) Atmospheric Properties Differenced

Figure 38. Check-case 03A: ISS in 4×4 Harmonic Gravity; See Discussion in Section D.2.2 (Cont'd)

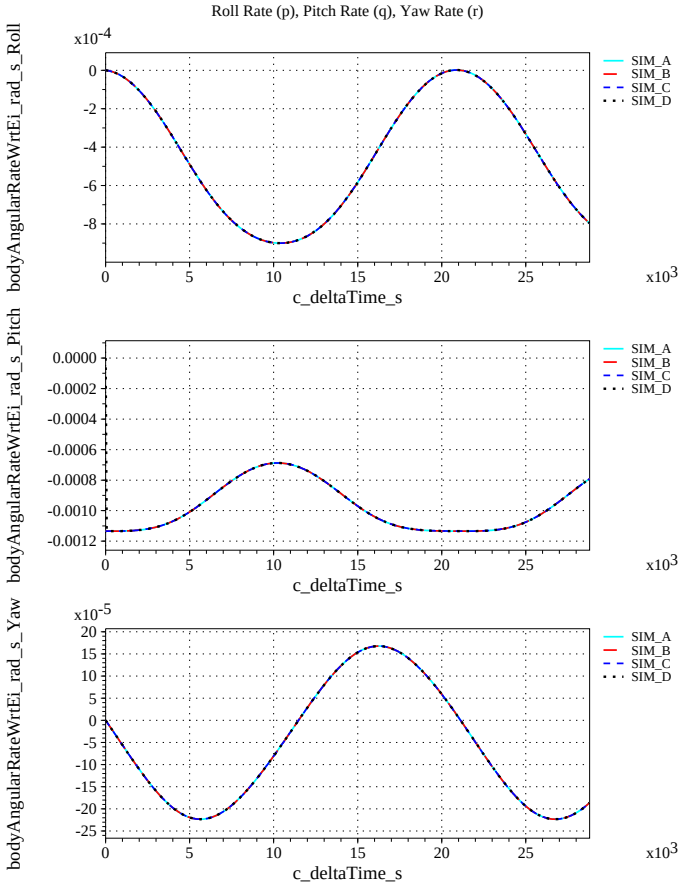

(e) Body-axis Angular Rates Compared

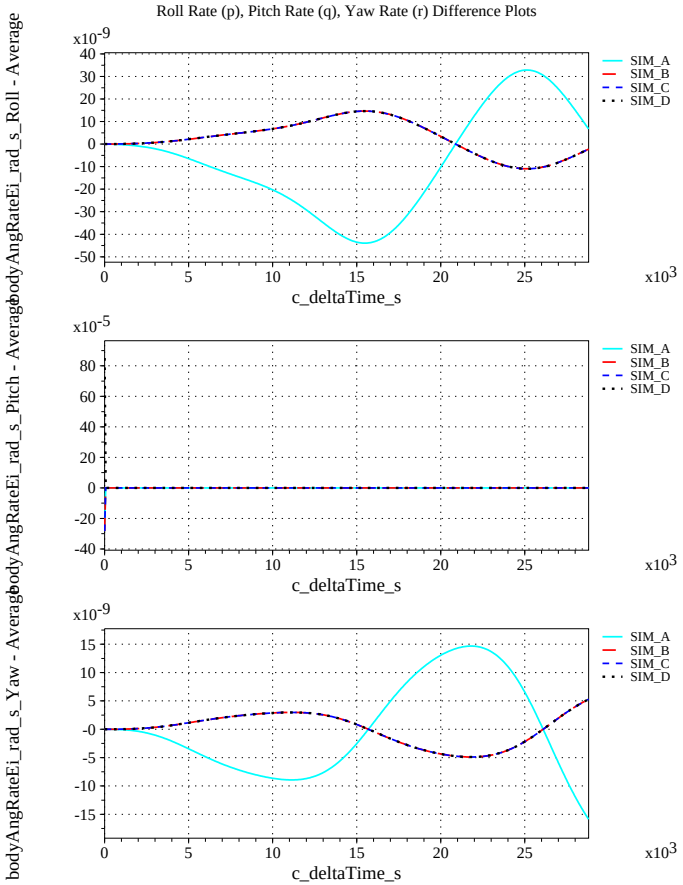

(f) Body-axis Angular Rates Differenced

Figure 38. Check-case 03A: ISS in 4×4 Harmonic Gravity; See Discussion in Section D.2.2 (Cont'd)

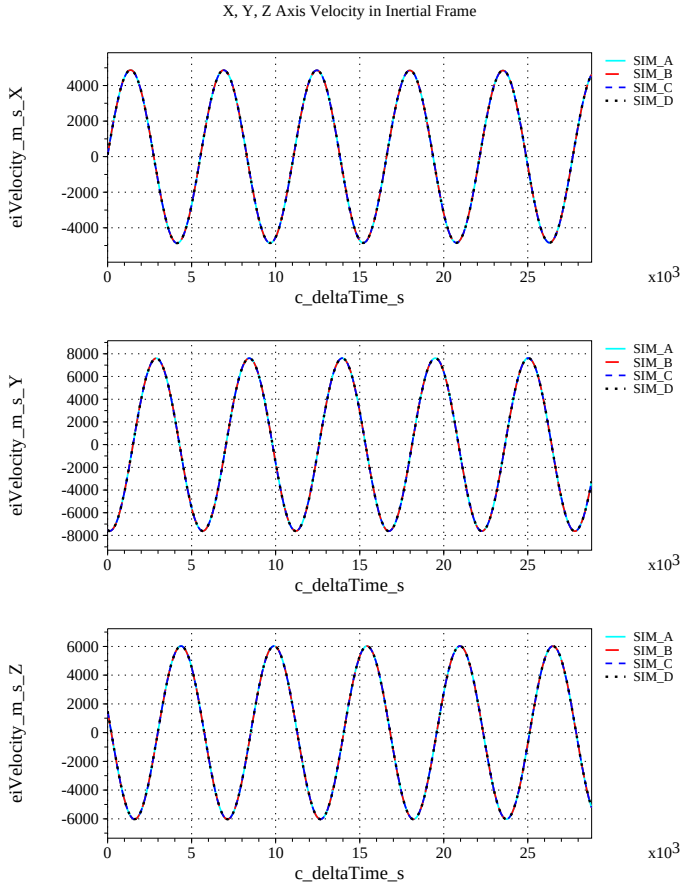

(g) Inertial Velocities Compared

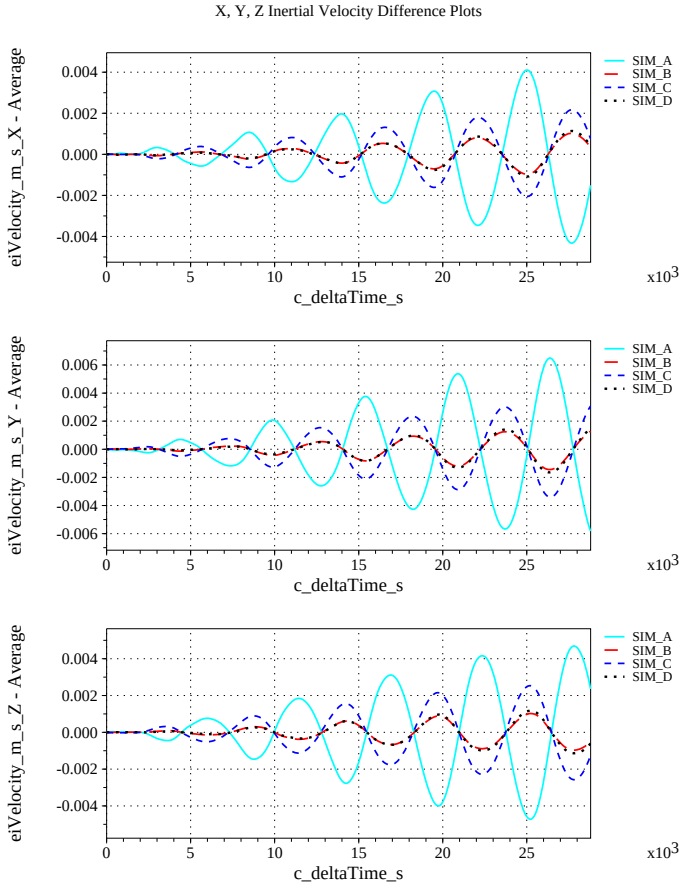

(h) Inertial Velocities Differenced

Figure 38. Check-case 03A: ISS in 4×4 Harmonic Gravity; See Discussion in Section D.2.2 (Cont'd)

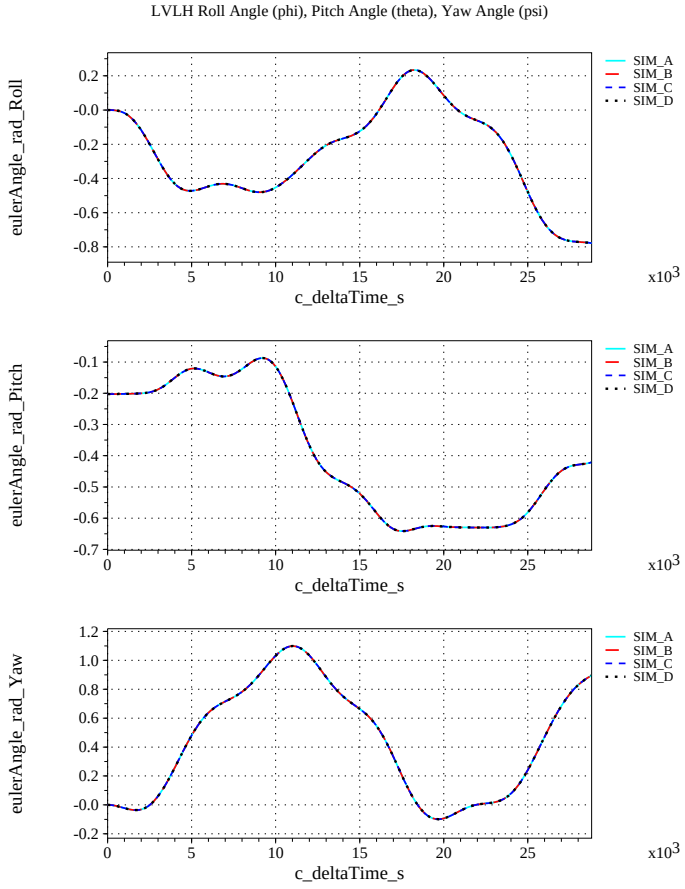

(i) Rotation Angles with Respect to LVLH Frame Compared

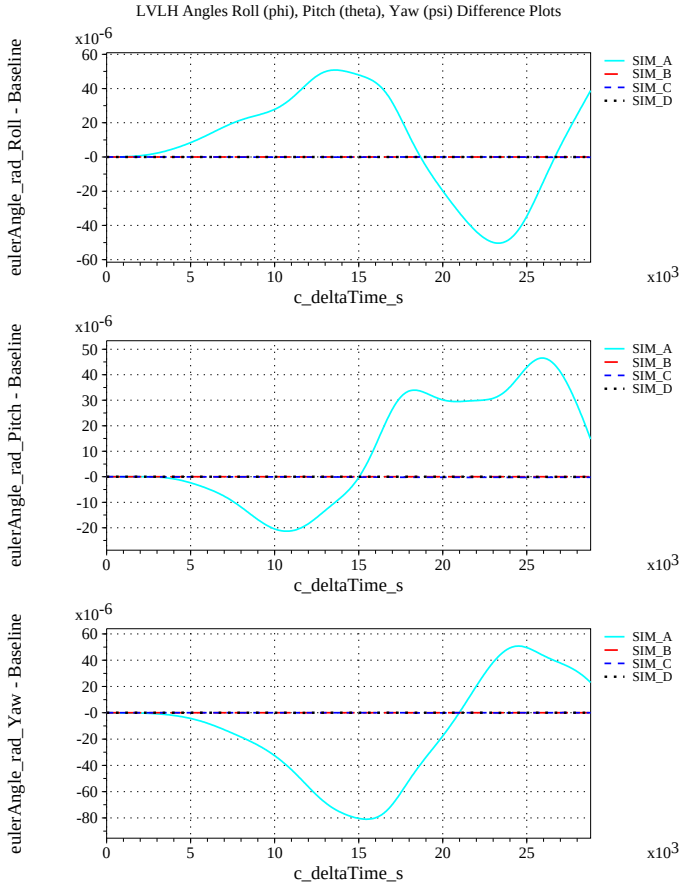

(j) Rotation Angles with Respect to LVLH Frame Differenced

Figure 38. Check-case 03A: ISS in 4×4 Harmonic Gravity; See Discussion in Section D.2.2 (Cont'd)

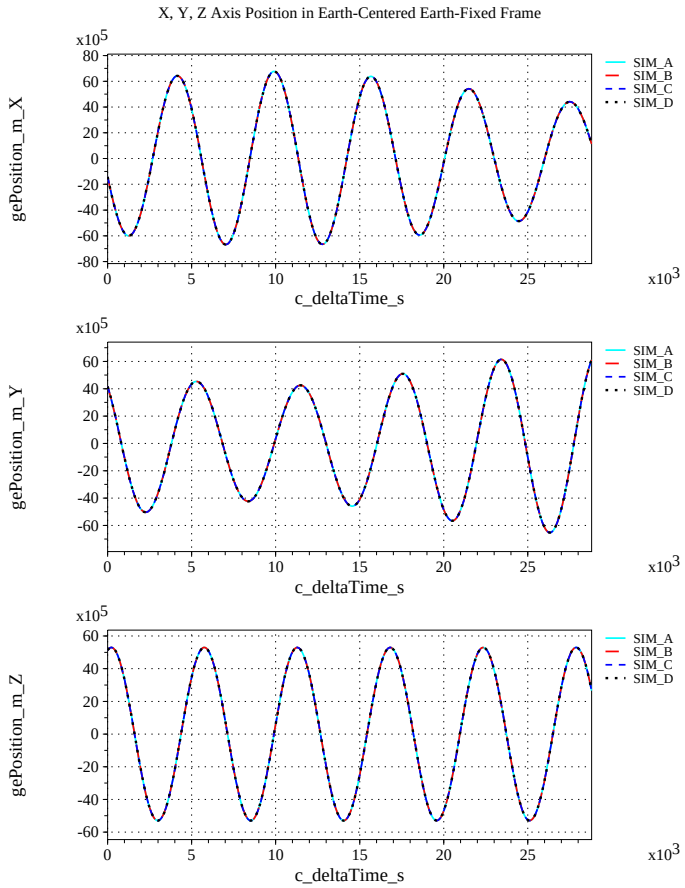

(k) Earth-centered, Earth-fixed Rectangular (X-Y-Z) Positions Compared

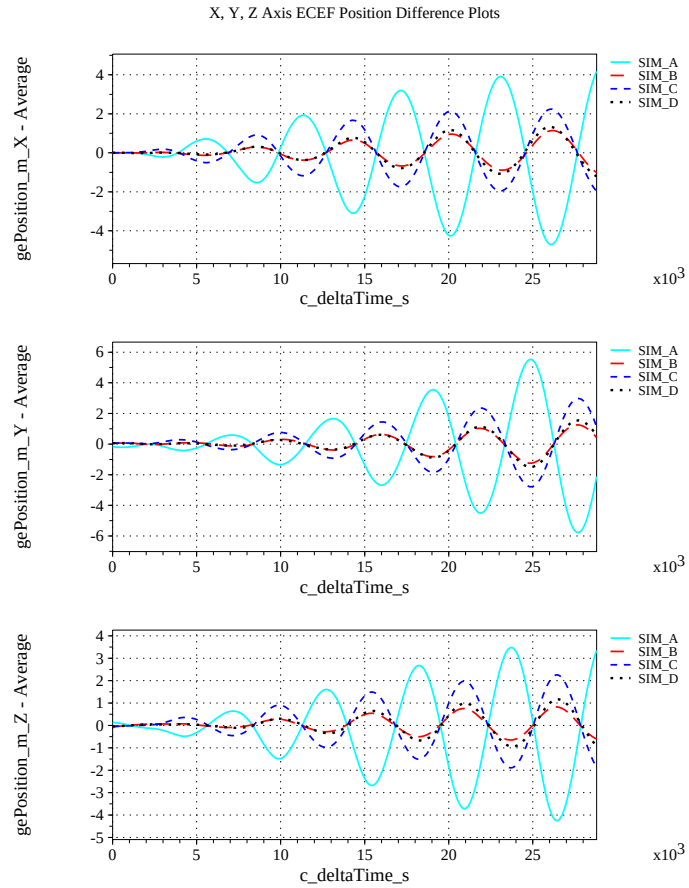

(l) Earth-centered, Earth-fixed Rectangular (X-Y-Z) Positions Differenced

Figure 38. Check-case 03A: ISS in 4×4 Harmonic Gravity; See Discussion in Section D.2.2 (Cont'd)

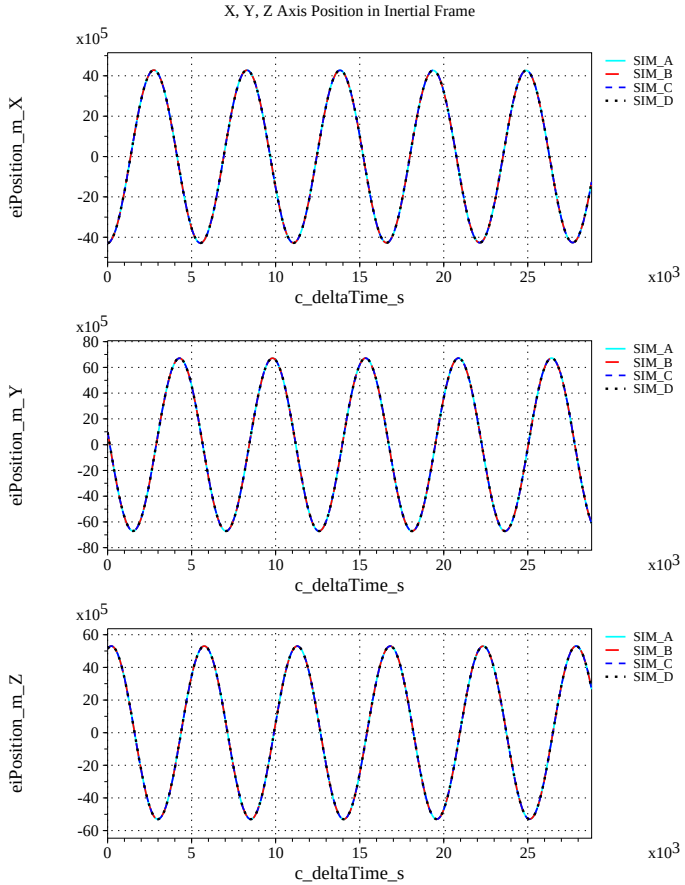

(m) Earth-centered Inertial Rectangular (x-y-z) Positions Compared

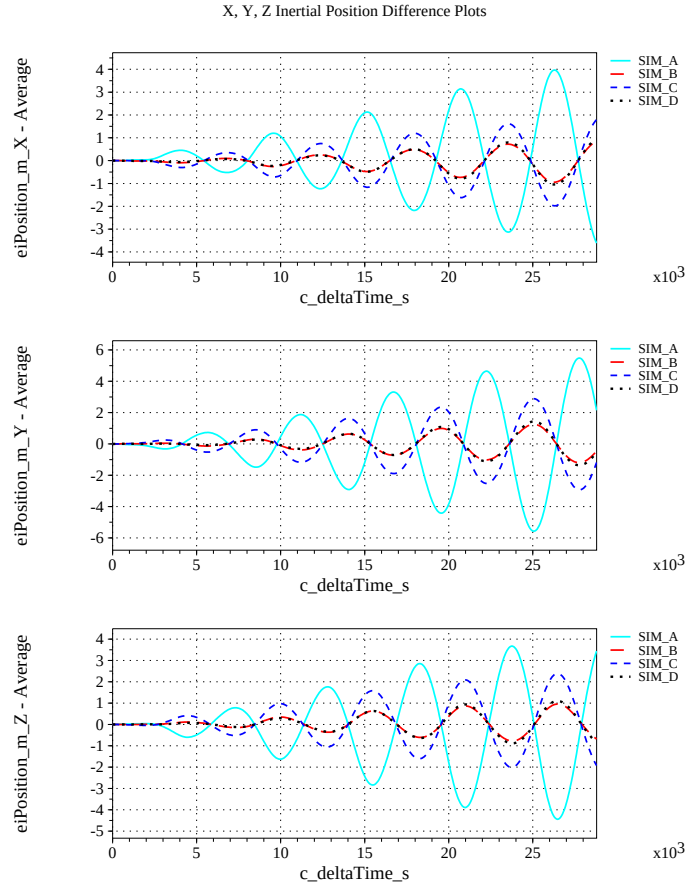

(n) Earth-centered Inertial Rectangular (x-y-z) Positions Differenced

Figure 38. Check-case 03A: ISS in 4×4 Harmonic Gravity; See Discussion in Section D.2.2 (Cont'd)

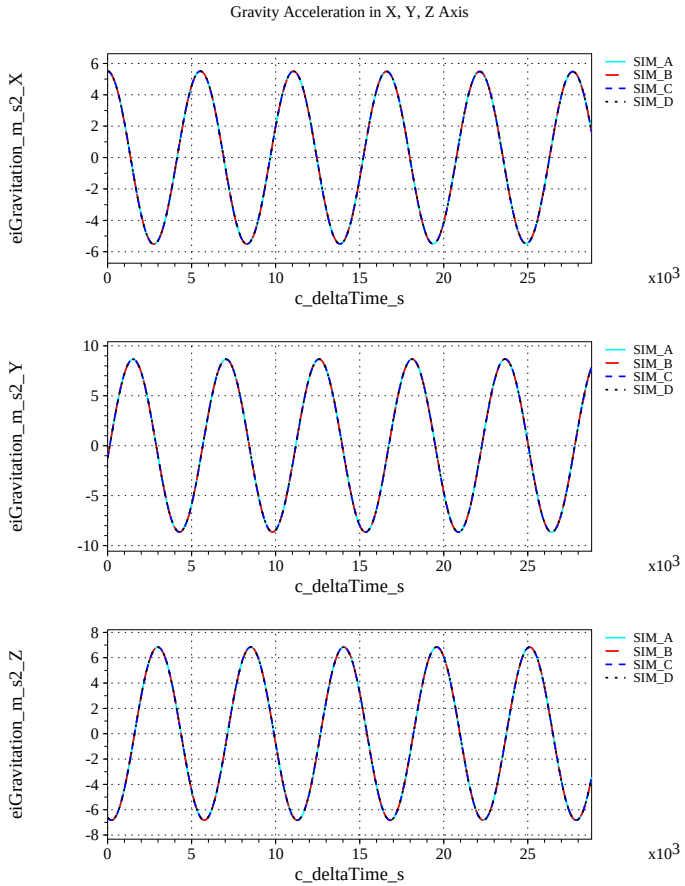

(o) Gravitational Components in Inertial (**X**-**Y**-**Z**) Directions Compared

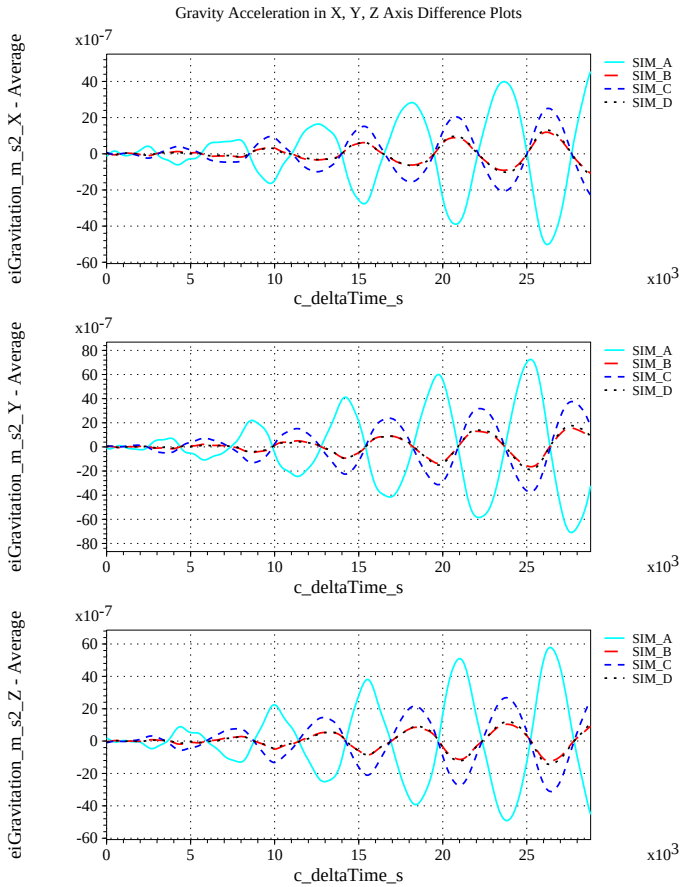

(p) Gravitational Components in Inertial (**X**-**Y**-**Z**) Directions Differenced

Figure 38. Check-case 03A: ISS in 4×4 Harmonic Gravity; See Discussion in Section D.2.2 (Concluded)

D.2.3 Check-case 03B – ISS in 8×8 harmonic gravity

This section shows cross-plots for four of the selected simulation tools in modeling the dynamics of the ISS in orbit with a 8×8 harmonic gravity model and no disturbances. This scenario is described in Section C.2.3. Figures 39a through 39p compare results between the four simulation tools, as well as the deviances of the outputs from each tool from the ensemble average value.

This check-case extended orbital check-case 3A by increasing the degree and order of the gravitation model to eight (8×8). The differences observed among the simulations were consistent with the differences in the accuracy of gravitation model implementations as described in orbital case 3A. Nevertheless, under the 8×8 gravitational configuration, the differences in translational states appeared more erratic but, in magnitude, was of the same order as the difference noted in orbital case 3A.

Rotational state differences were unchanged from orbital case 3A and are attributed to differences in integration methods.

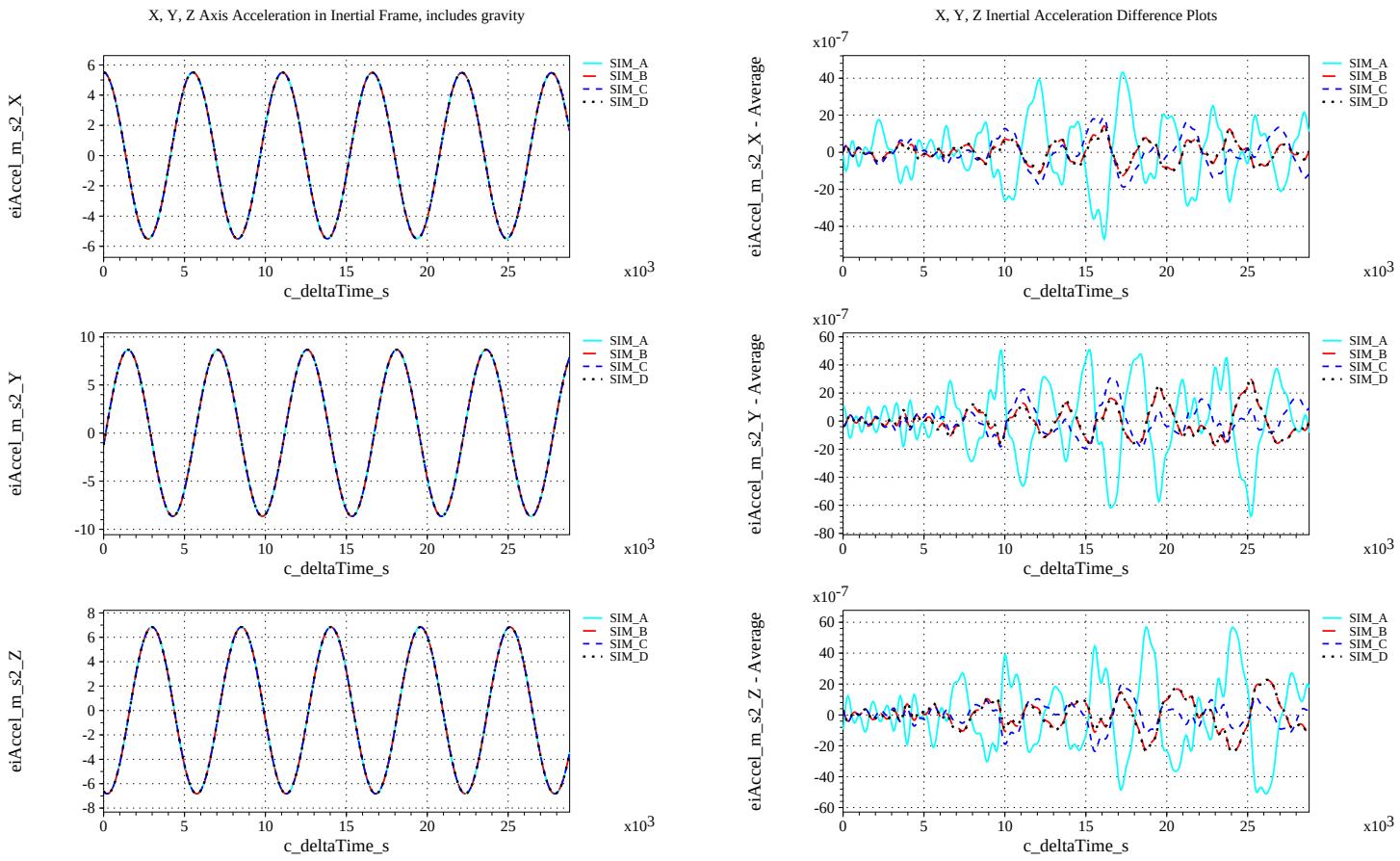

(a) Inertial Accelerations Compared

(b) Inertial Accelerations Differenced

Figure 39. Check-case 03B: ISS in 8×8 harmonic gravity; See Discussion in Section D.2.3

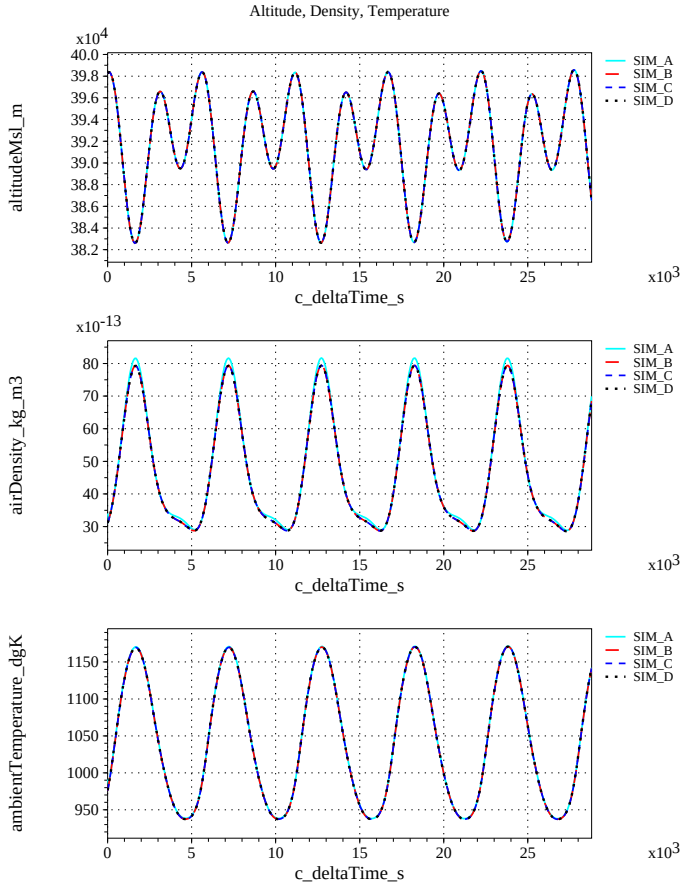

(c) Atmospheric Properties Compared

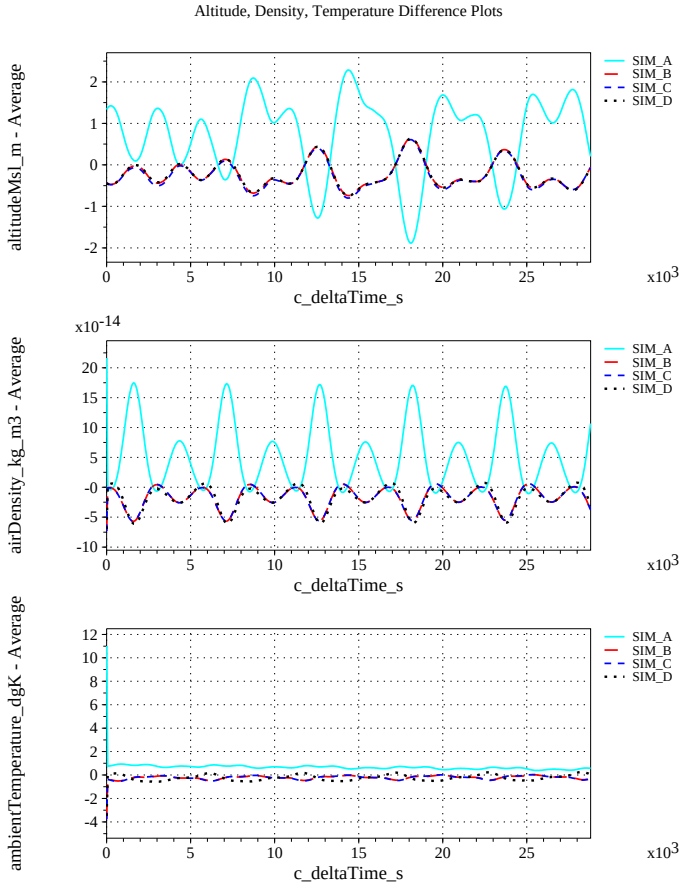

(d) Atmospheric Properties Differenced

Figure 39. Check-case 03B: ISS in 8×8 harmonic gravity; See Discussion in Section D.2.3 (Cont'd)

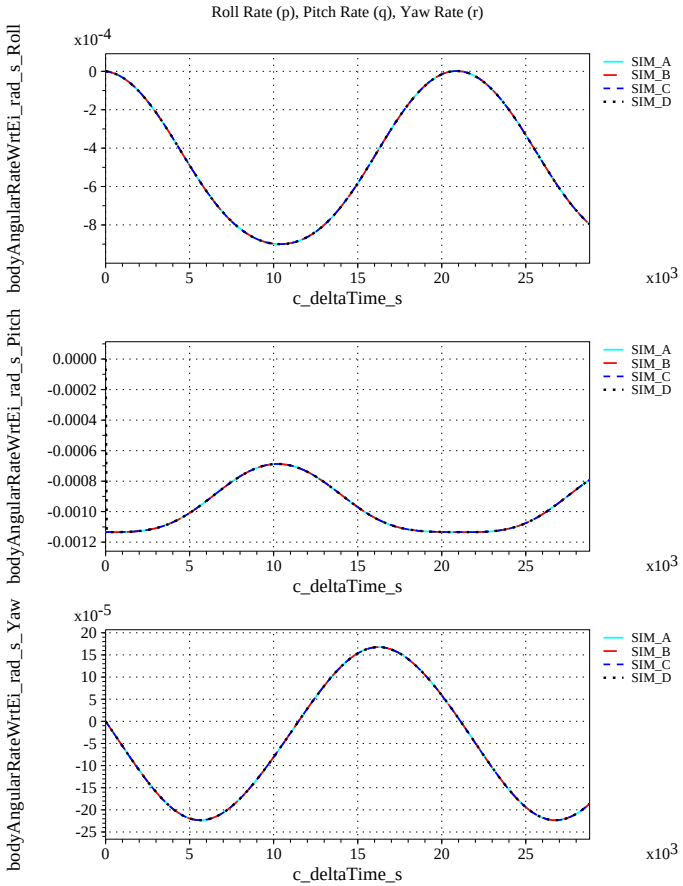

(e) Body-axis Angular Rates Compared

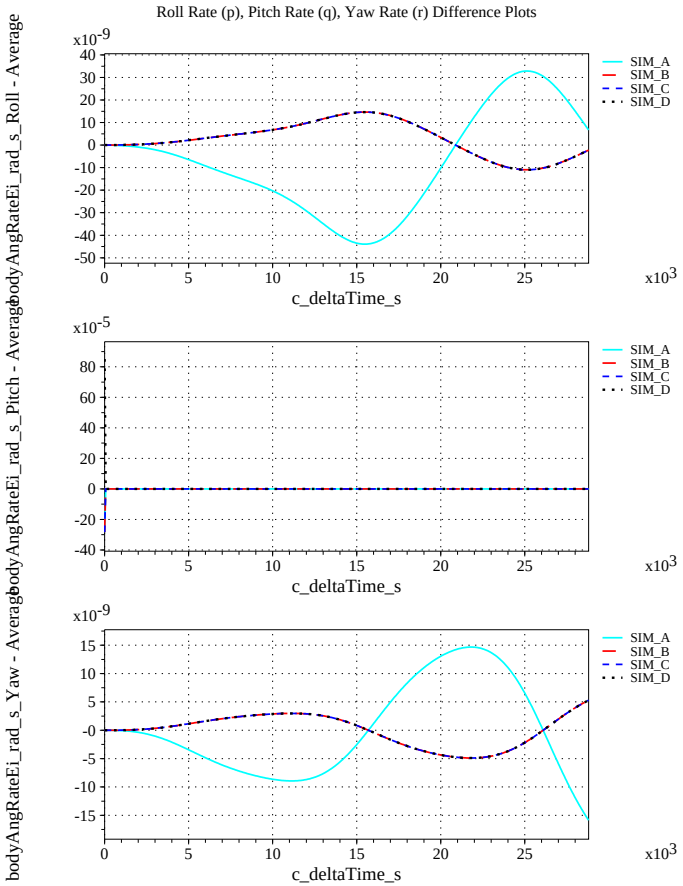

(f) Body-axis Angular Rates Differenced

Figure 39. Check-case 03B: ISS in 8×8 harmonic gravity; See Discussion in Section D.2.3 (Cont'd)

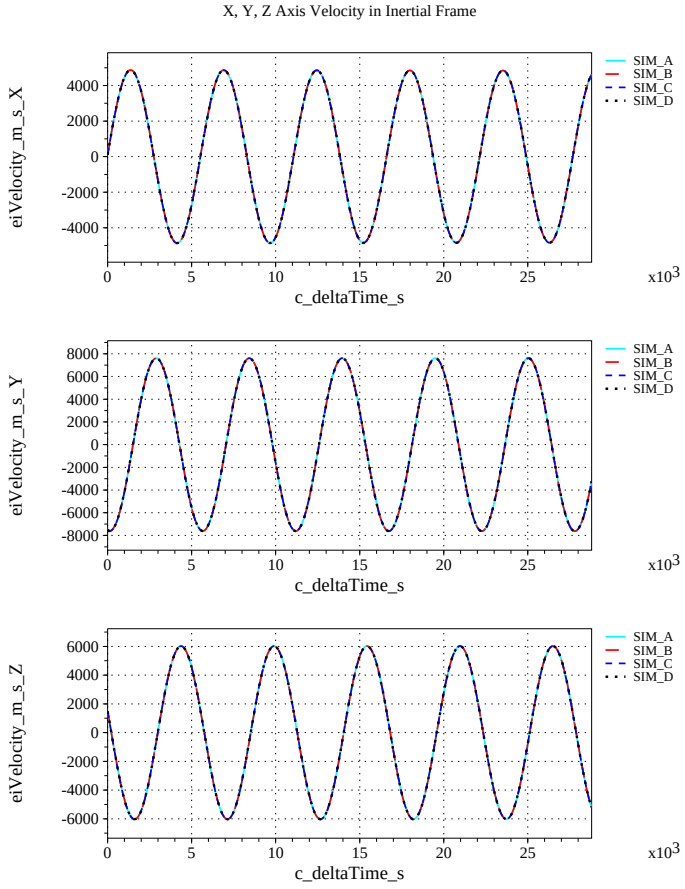

(g) Inertial Velocities Compared

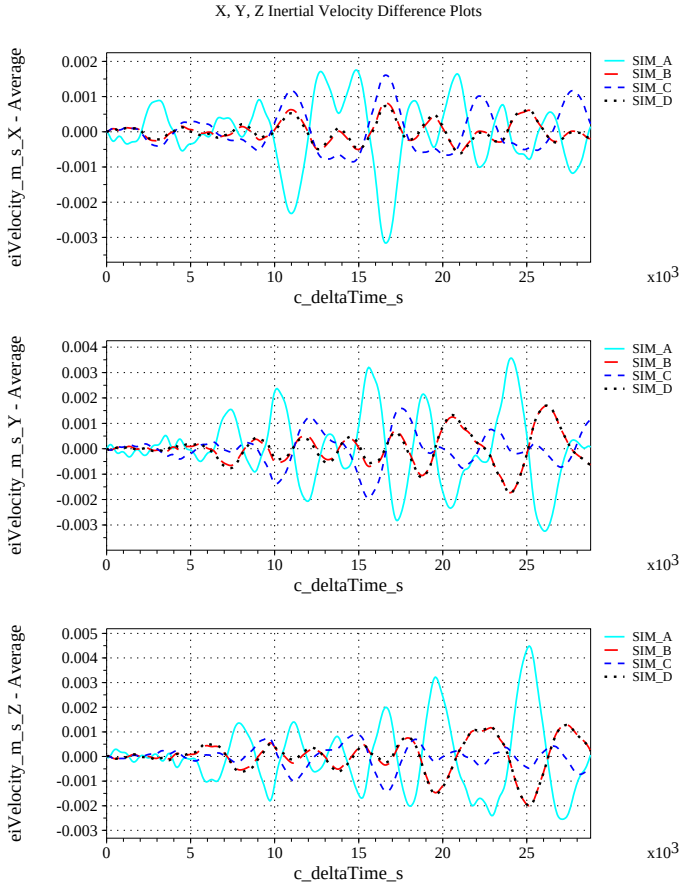

(h) Inertial Velocities Differenced

Figure 39. Check-case 03B: ISS in 8×8 harmonic gravity; See Discussion in Section D.2.3 (Cont'd)

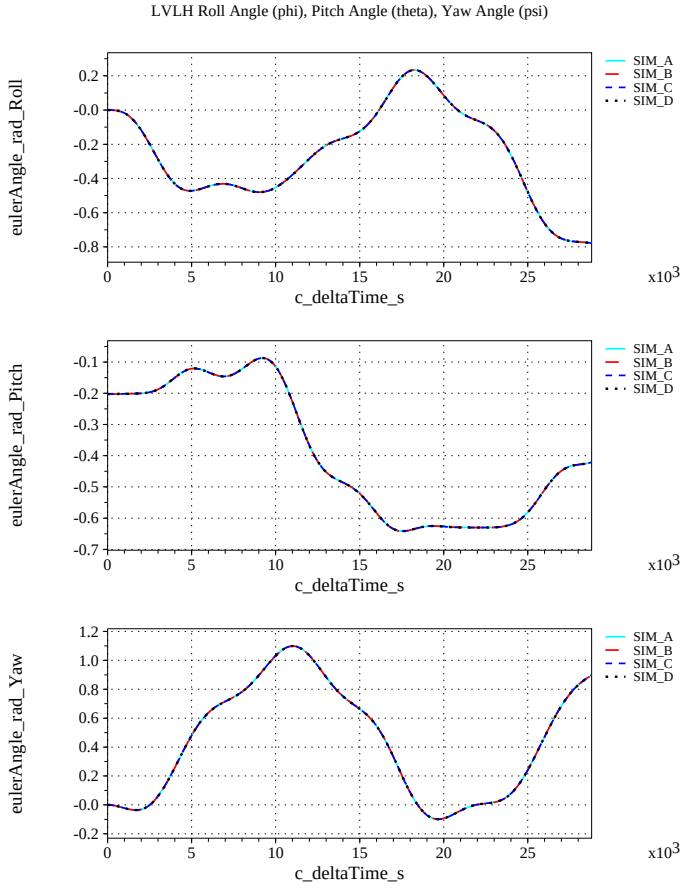

(i) Rotation Angles with Respect to LVLH Frame Compared

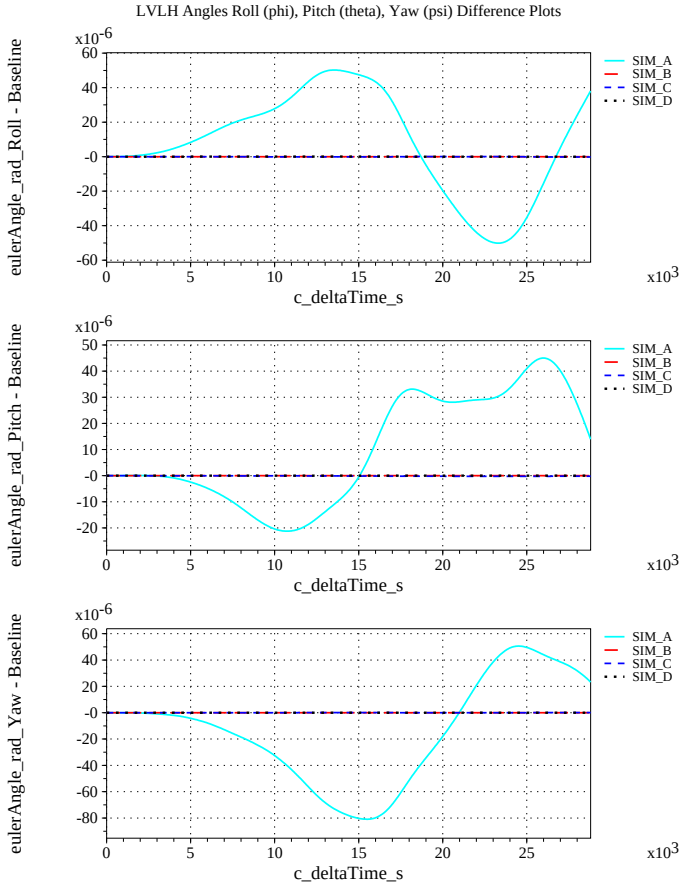

(j) Rotation Angles with Respect to LVLH Frame Differenced

Figure 39. Check-case 03B: ISS in 8×8 harmonic gravity; See Discussion in Section D.2.3 (Cont'd)

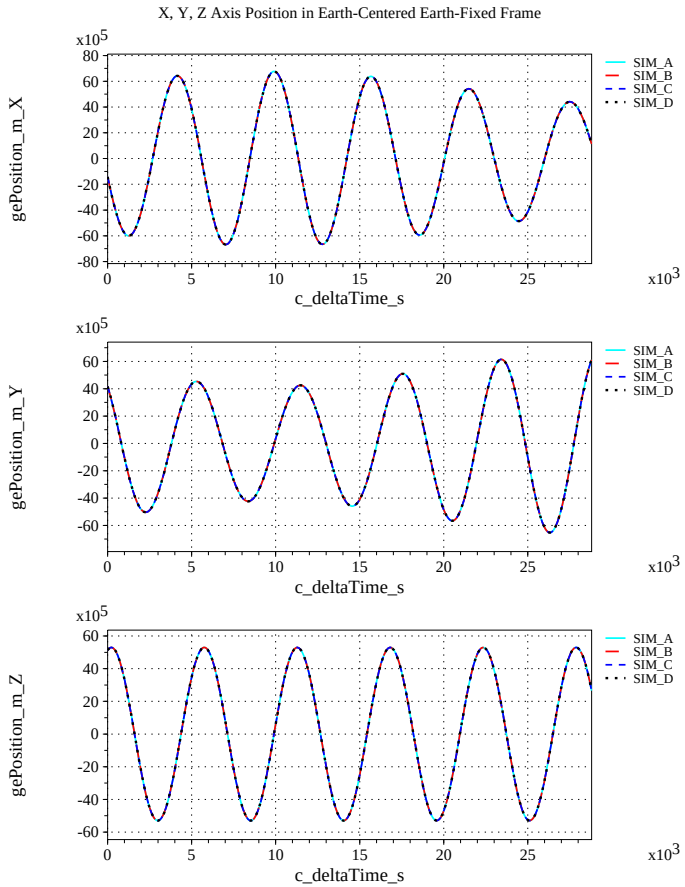

(k) Earth-centered, Earth-fixed Rectangular (X-Y-Z) Positions Compared

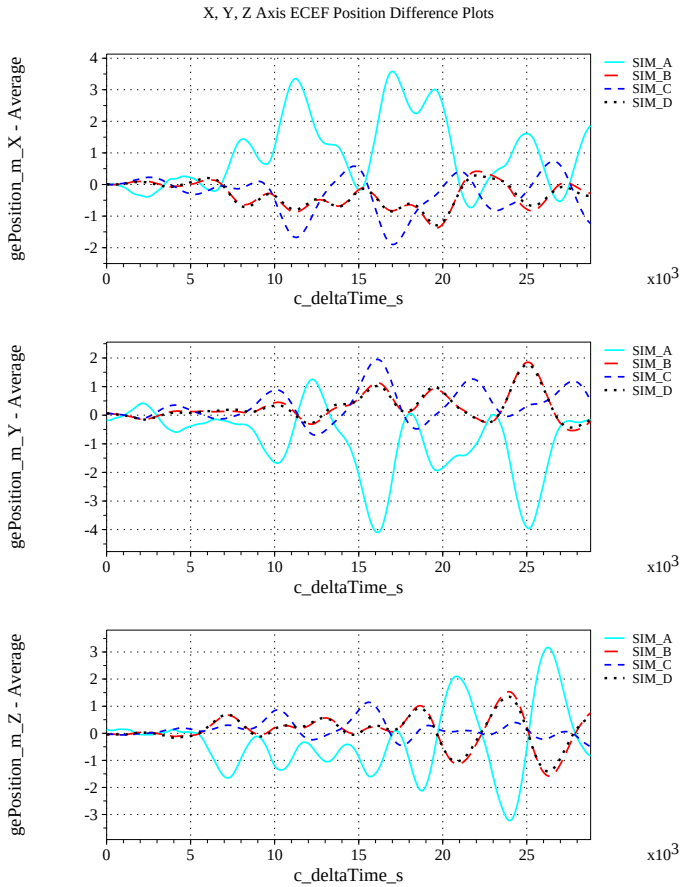

(l) Earth-centered, Earth-fixed Rectangular (X-Y-Z) Positions Differenced

Figure 39. Check-case 03B: ISS in 8×8 harmonic gravity; See Discussion in Section D.2.3 (Cont'd)

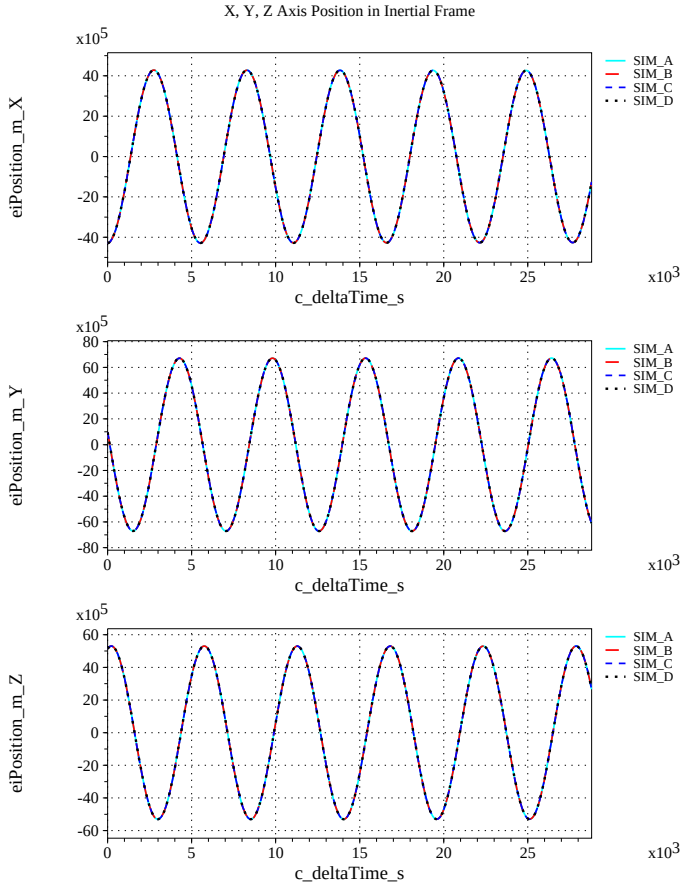

(m) Earth-centered Inertial Rectangular (x-y-z) Positions Compared

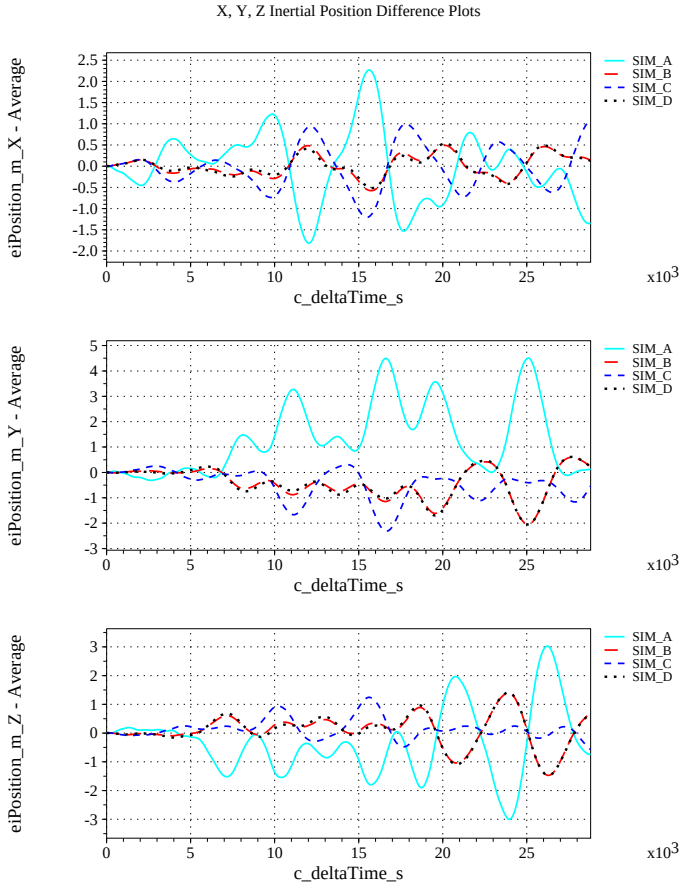

(n) Earth-centered Inertial Rectangular (x-y-z) Positions Differenced

Figure 39. Check-case 03B: ISS in 8×8 harmonic gravity; See Discussion in Section D.2.3 (Cont'd)

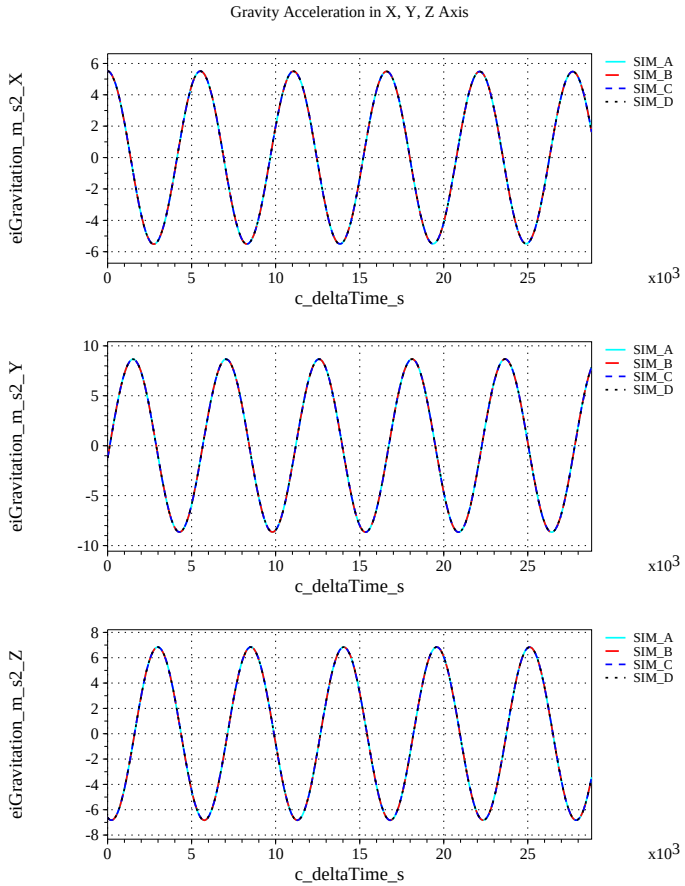

(o) Gravitational Components in Inertial (**X**-**Y**-**Z**) Directions Compared

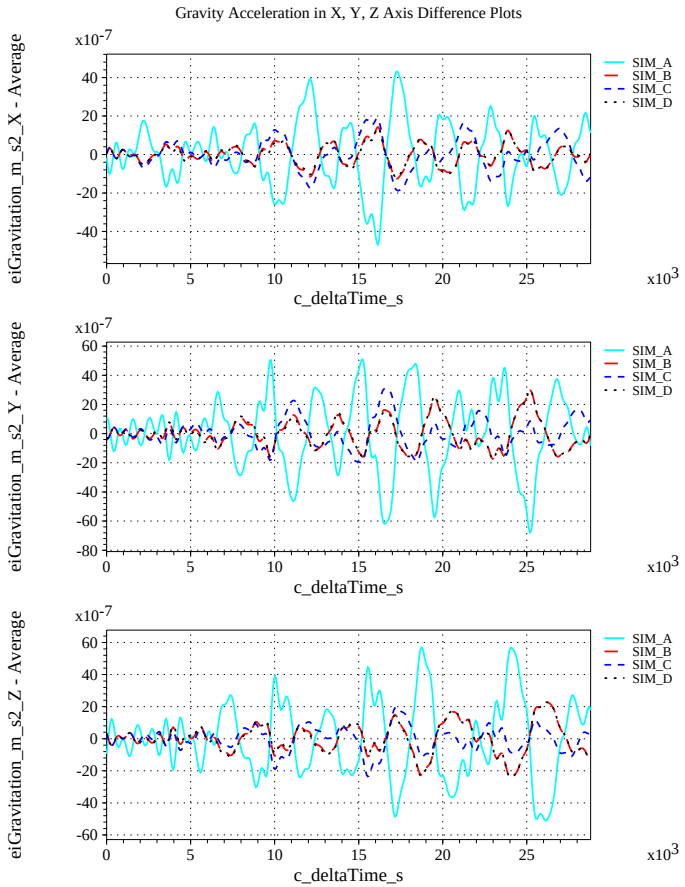

(p) Gravitational Components in Inertial (**X**-**Y**-**Z**) Directions Differenced

Figure 39. Check-case 03B: ISS in 8×8 harmonic gravity; See Discussion in Section D.2.3 (Concluded)

D.2.4 Check-case 04 – ISS with third-body disturbances

This section shows cross-plots for four of the selected simulation tools in modeling the dynamics of the ISS in orbit with Sun and Moon gravity perturbations. This scenario is described in Section C.2.4. Figures 40a through 40p compare results between the four simulation tools, as well as the deviances of the outputs from each tool from the ensemble average value.

This check-case applied gravitational forces from the Sun and Moon to the orbiting ISS. The ephemerides of the Sun and Moon were computed using the DE405 high-accuracy ephemeris data set published by the Jet Propulsion Laboratory [26]. To isolate differences due to ephemeris calculations, the gravitation of the Earth was modeled as a spherically symmetric mass.

In general, the translation states predicted by the simulations remained in agreement. The largest difference in inertial position among the simulations during the simulated 8-hour period were less than 2 cm. Differences in Earth-relative position were due to the same causes described in orbital check-case 2.

Rotational state differences were similar to those of the previous test cases and were attributed to differences in integration methods.

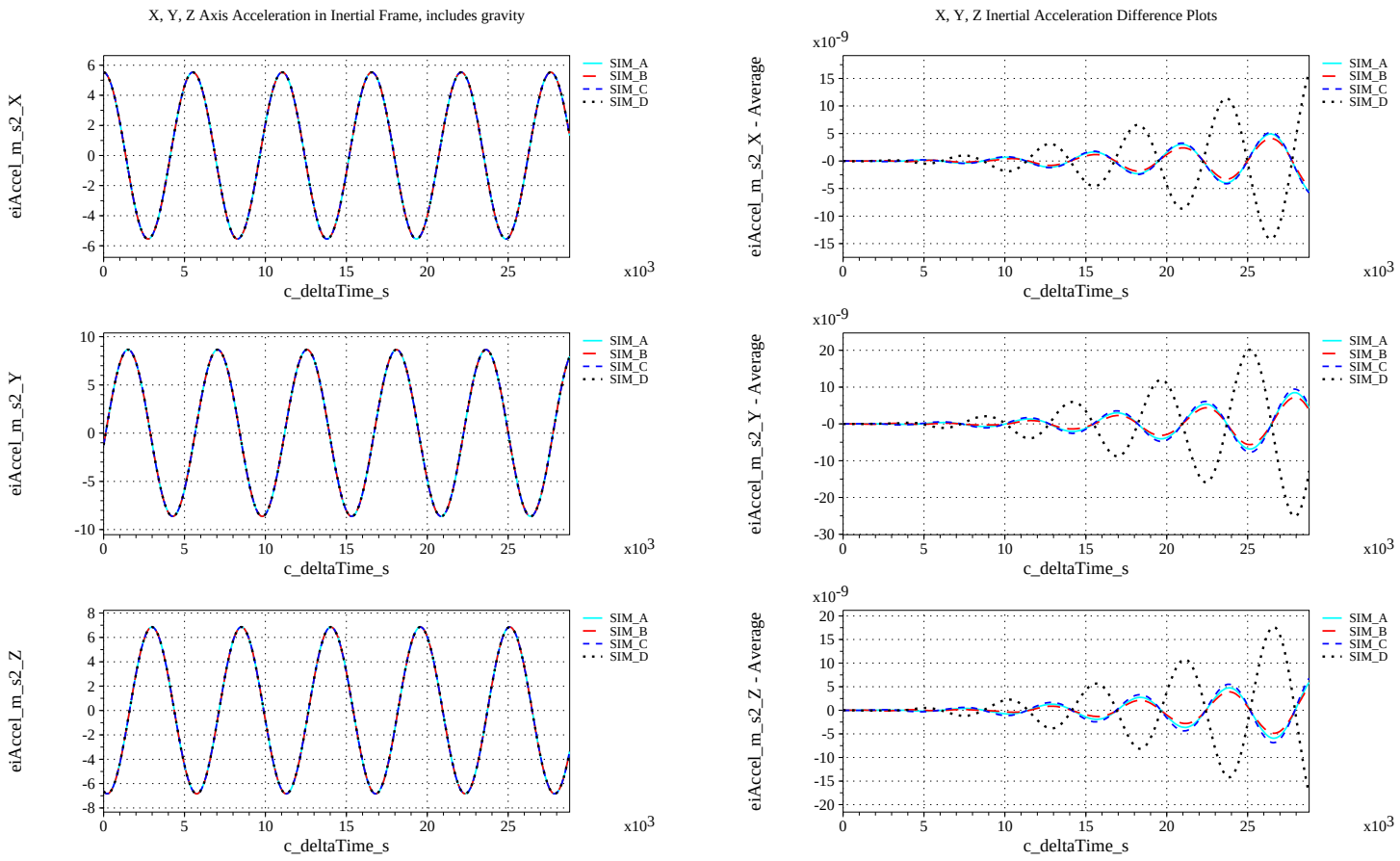

(a) Inertial Accelerations Compared

(b) Inertial Accelerations Differenced

Figure 40. Check-case 04: ISS with Third-body Disturbances; See Discussion in Section D.2.4

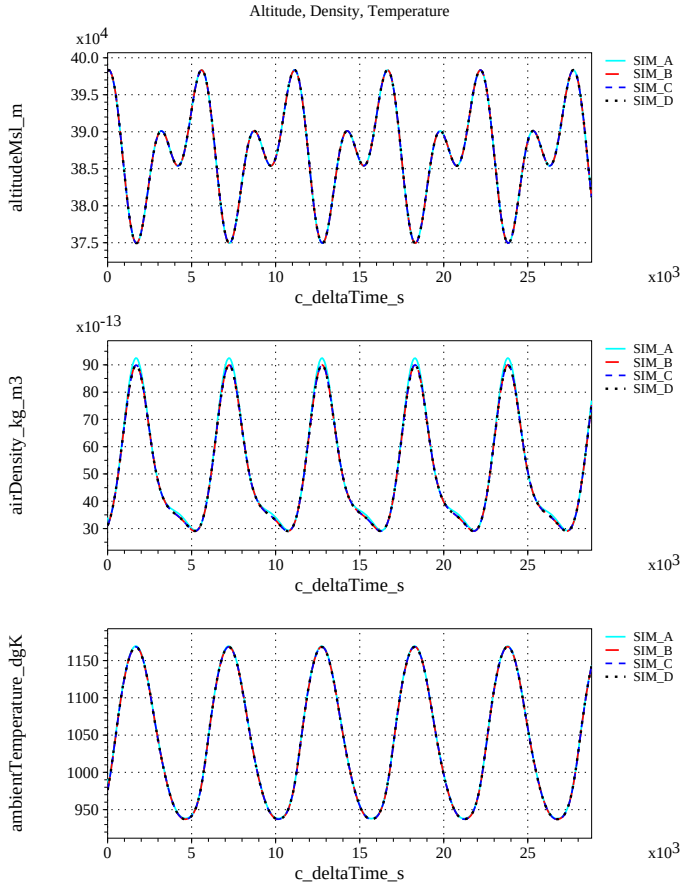

(c) Atmospheric Properties Compared

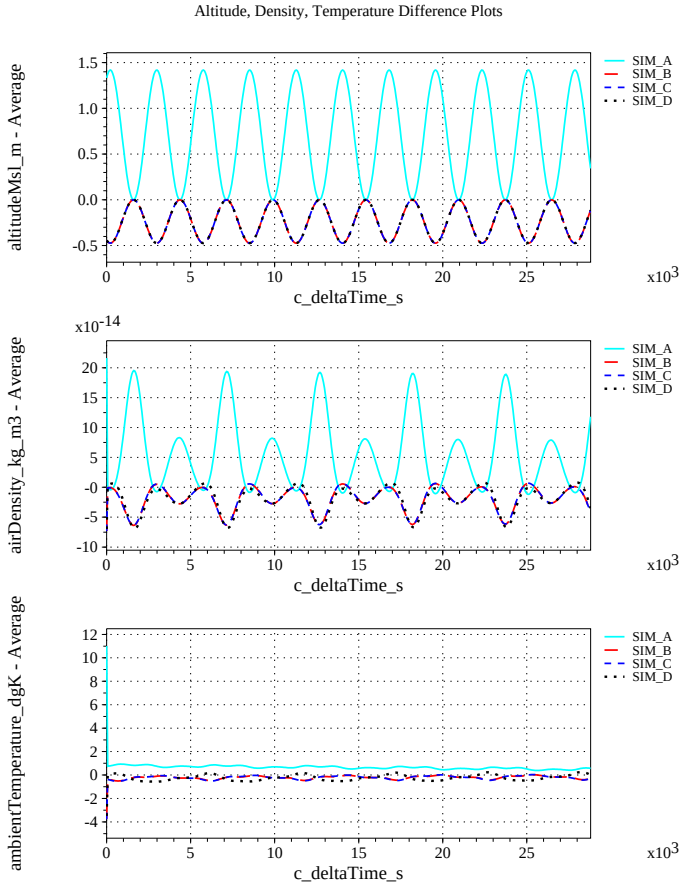

(d) Atmospheric Properties Differenced

Figure 40. Check-case 04: ISS with Third-body Disturbances; See Discussion in Section D.2.4 (Cont'd)

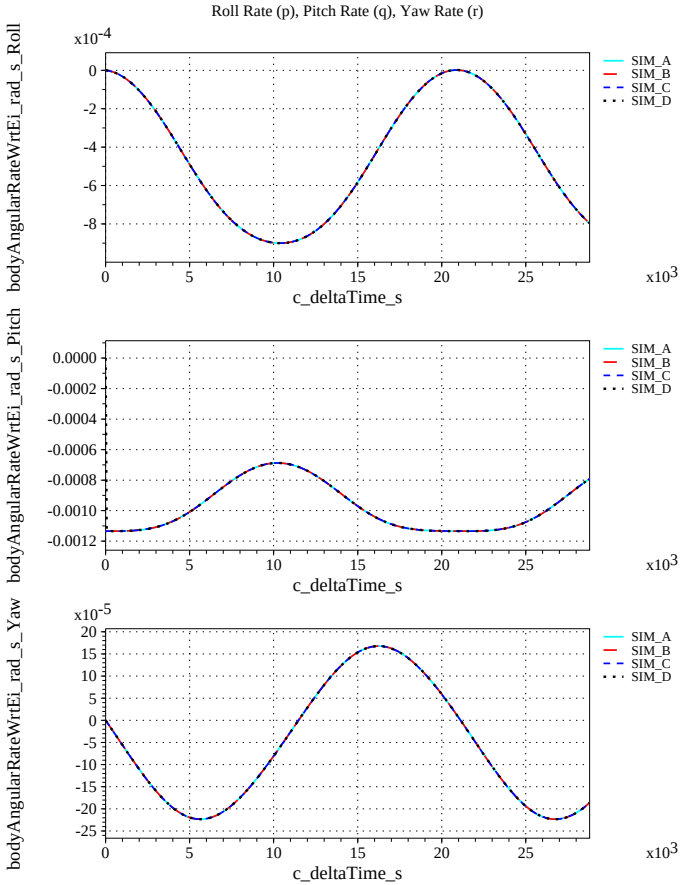

(e) Body-axis Angular Rates Compared

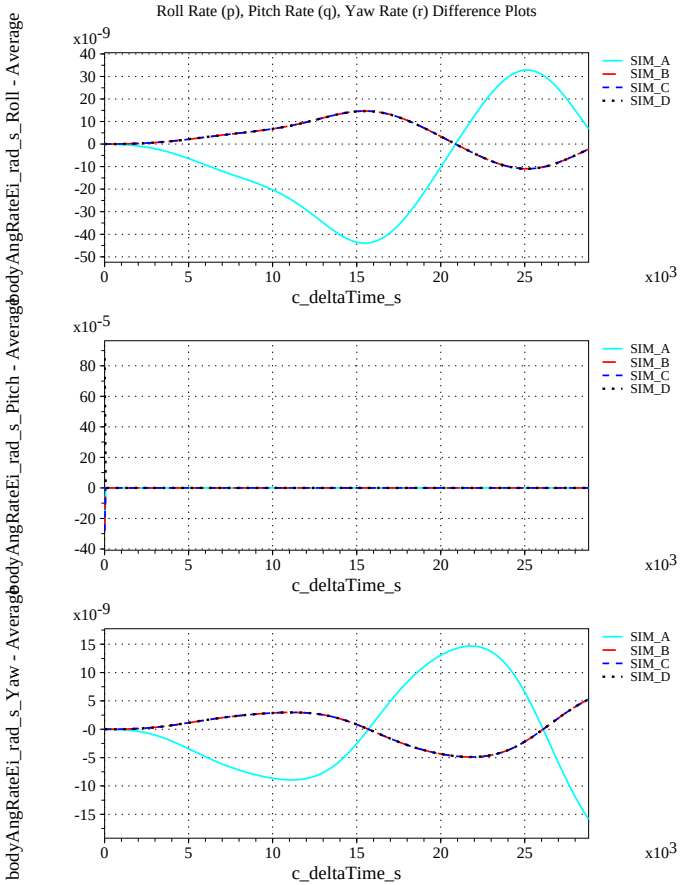

(f) Body-axis Angular Rates Differenced

Figure 40. Check-case 04: ISS with Third-body Disturbances; See Discussion in Section D.2.4 (Cont'd)

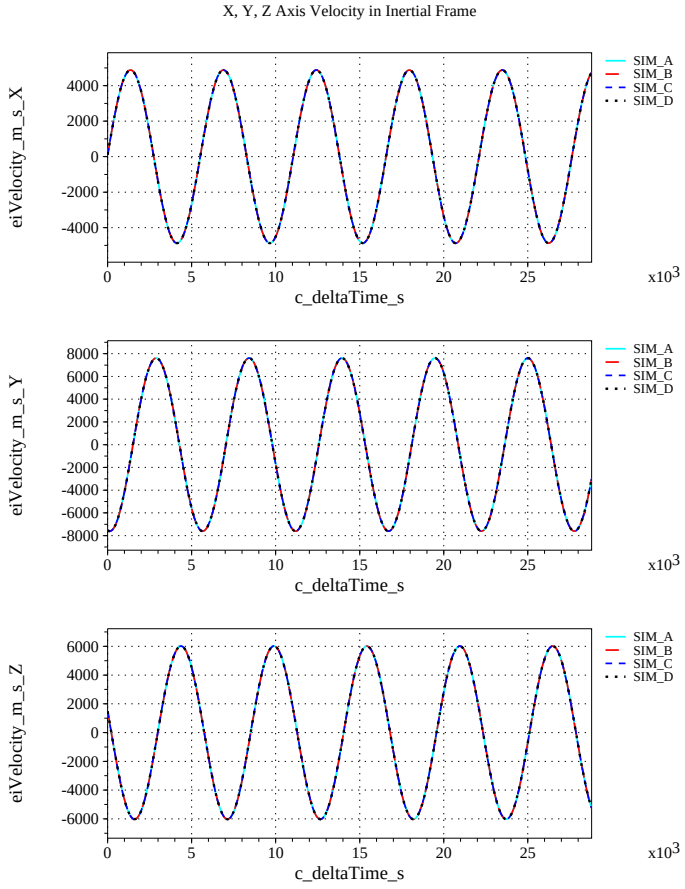

(g) Inertial Velocities Compared

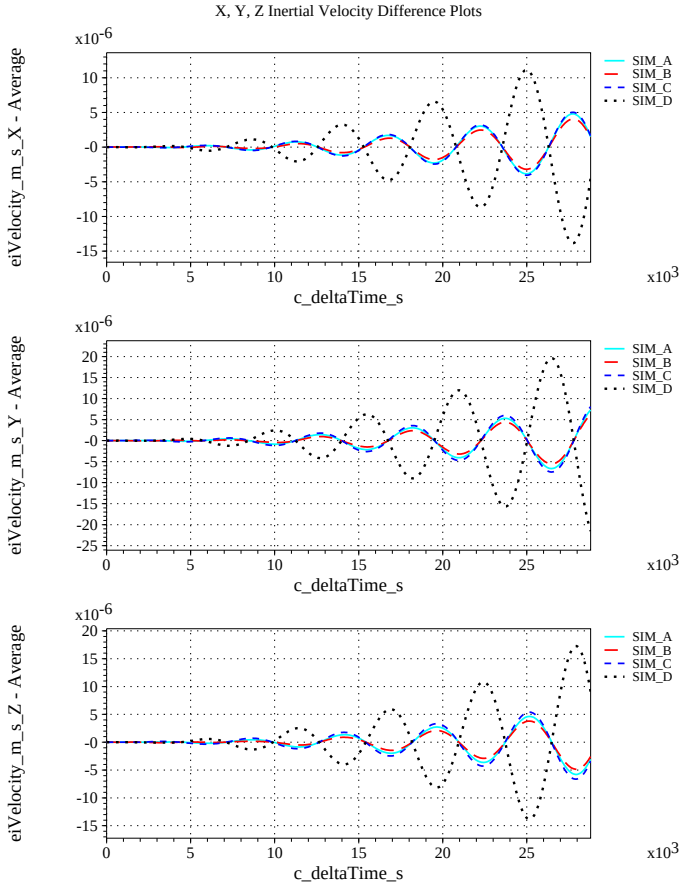

(h) Inertial Velocities Differenced

Figure 40. Check-case 04: ISS with Third-body Disturbances; See Discussion in Section D.2.4 (Cont'd)

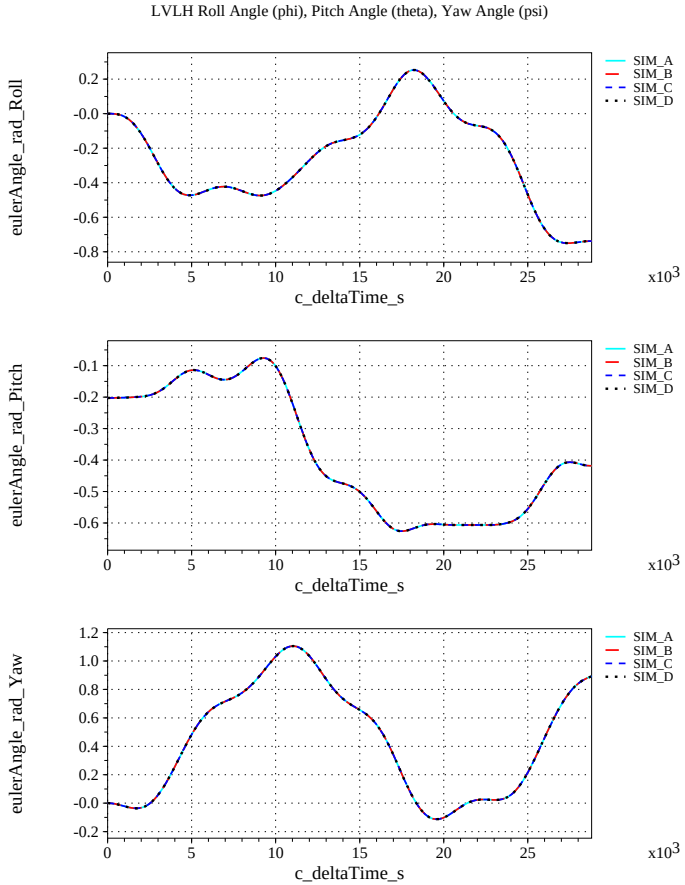

(i) Rotation Angles with Respect to LVLH Frame Compared

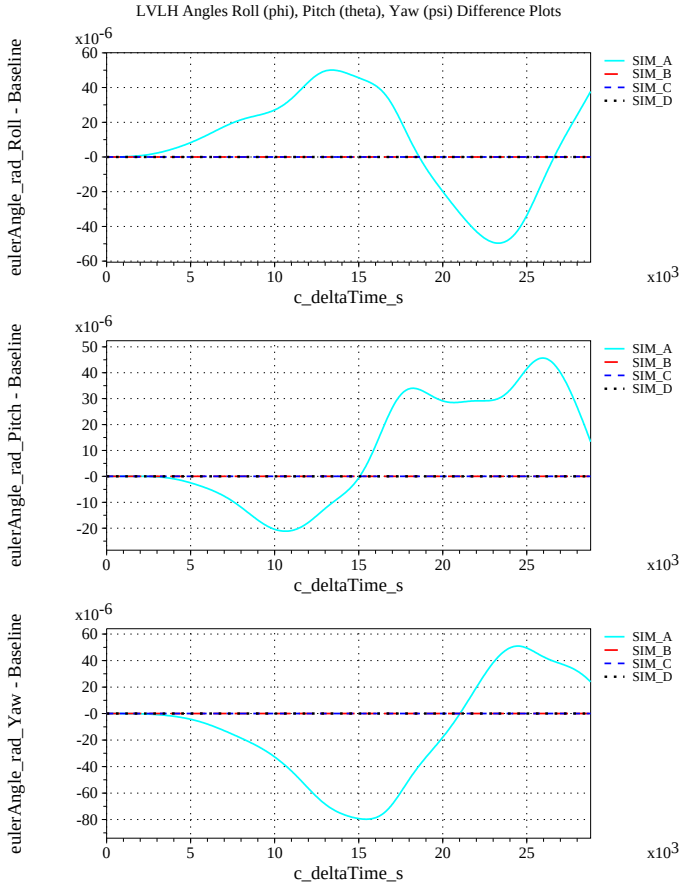

(j) Rotation Angles with Respect to LVLH Frame Differenced

Figure 40. Check-case 04: ISS with Third-body Disturbances; See Discussion in Section D.2.4 (Cont'd)

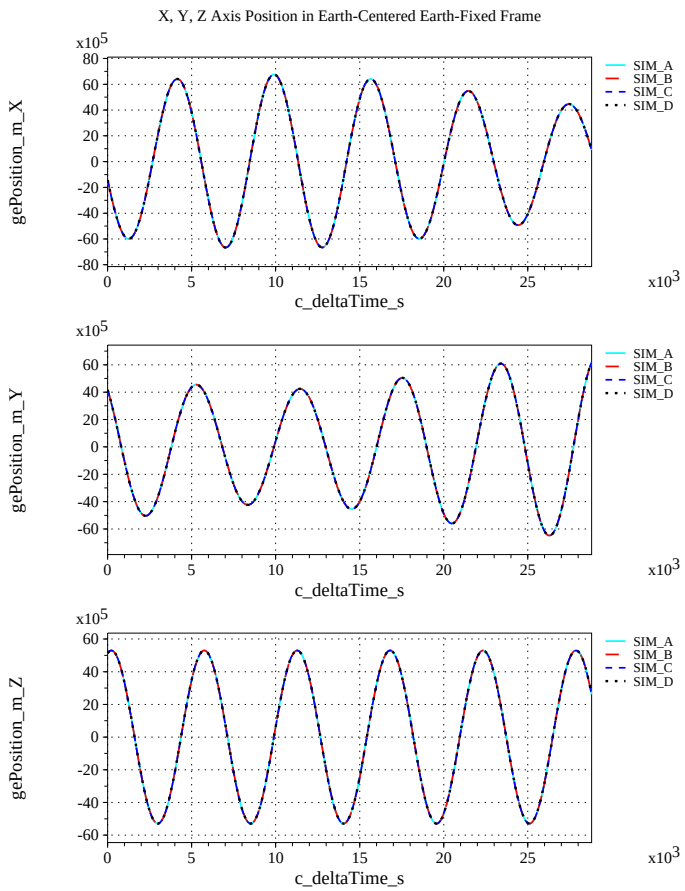

(k) Earth-centered, Earth-fixed Rectangular (X-Y-Z) Positions Compared

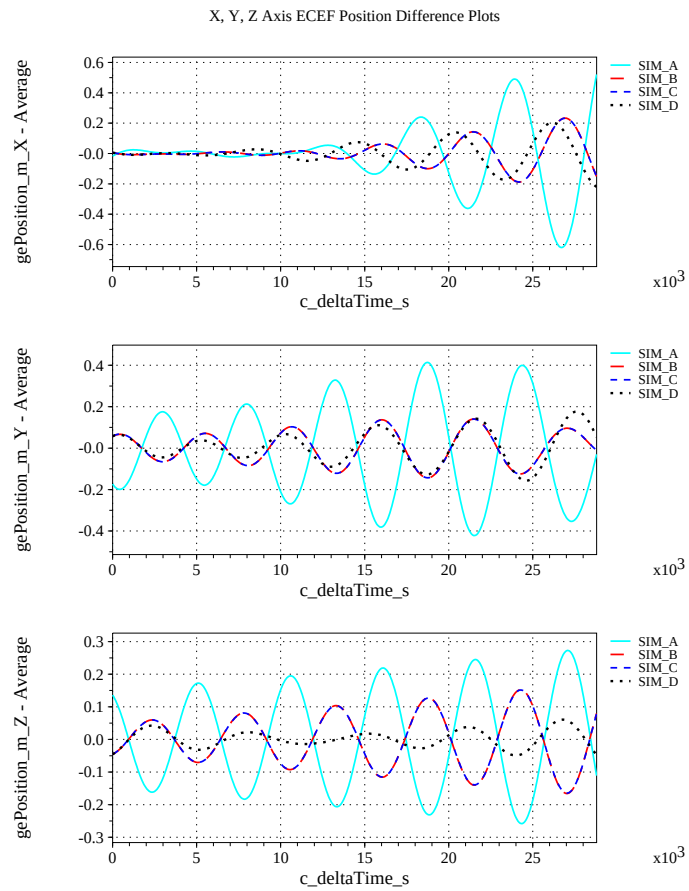

(l) Earth-centered, Earth-fixed Rectangular (X-Y-Z) Positions Differenced

Figure 40. Check-case 04: ISS with Third-body Disturbances; See Discussion in Section D.2.4 (Cont'd)

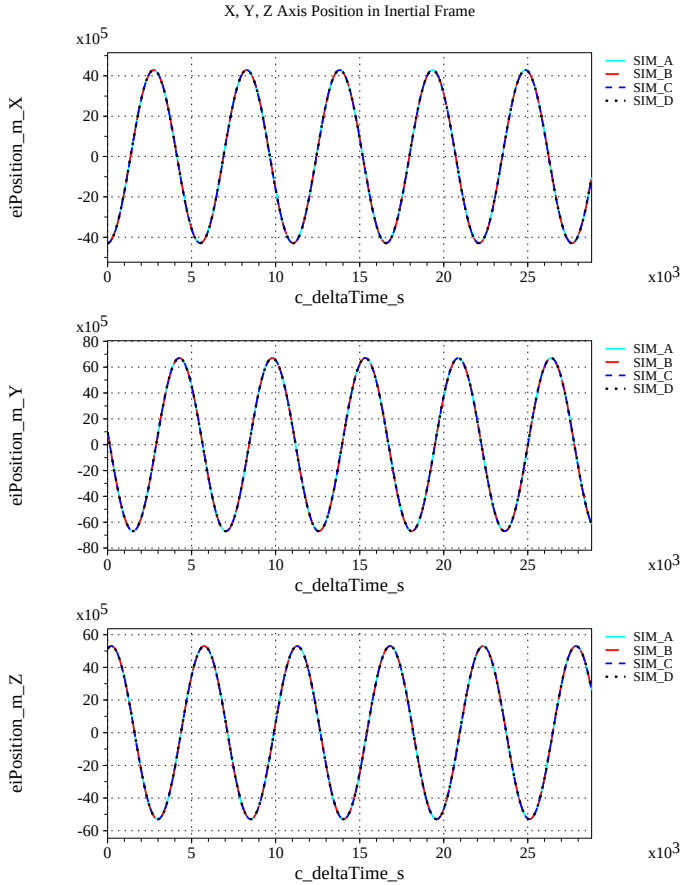

(m) Earth-centered Inertial Rectangular (x-y-z) Positions Compared

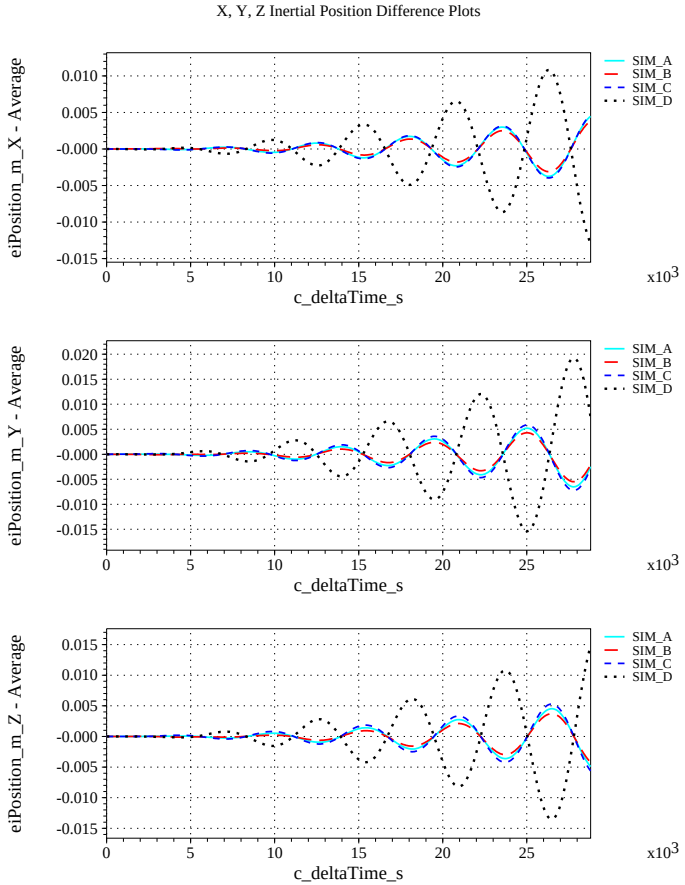

(n) Earth-centered Inertial Rectangular (x-y-z) Positions Differenced

Figure 40. Check-case 04: ISS with Third-body Disturbances; See Discussion in Section D.2.4 (Cont'd)

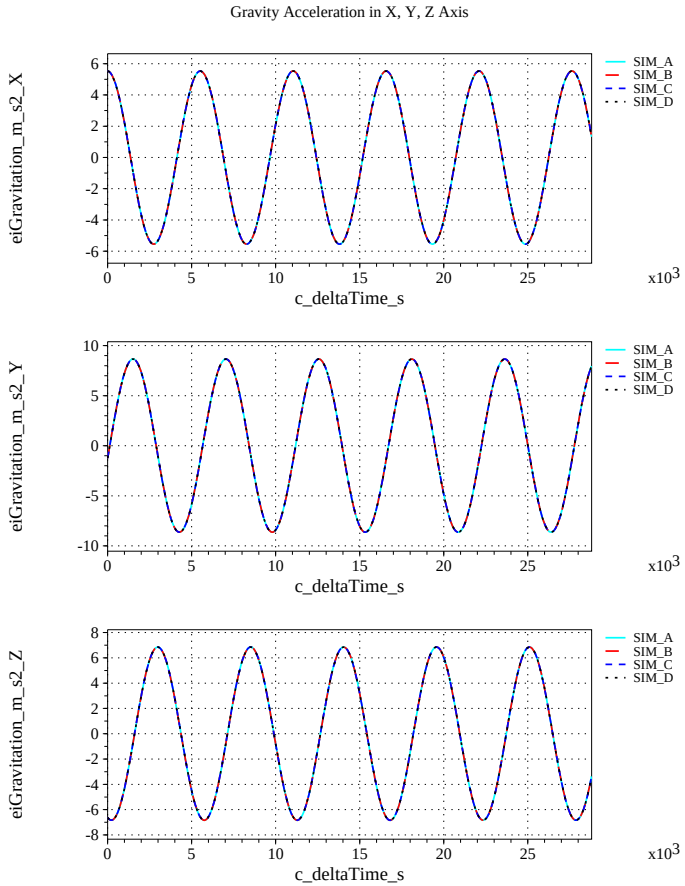

(o) Gravitational Components in Inertial (**X**-**Y**-**Z**) Directions Compared

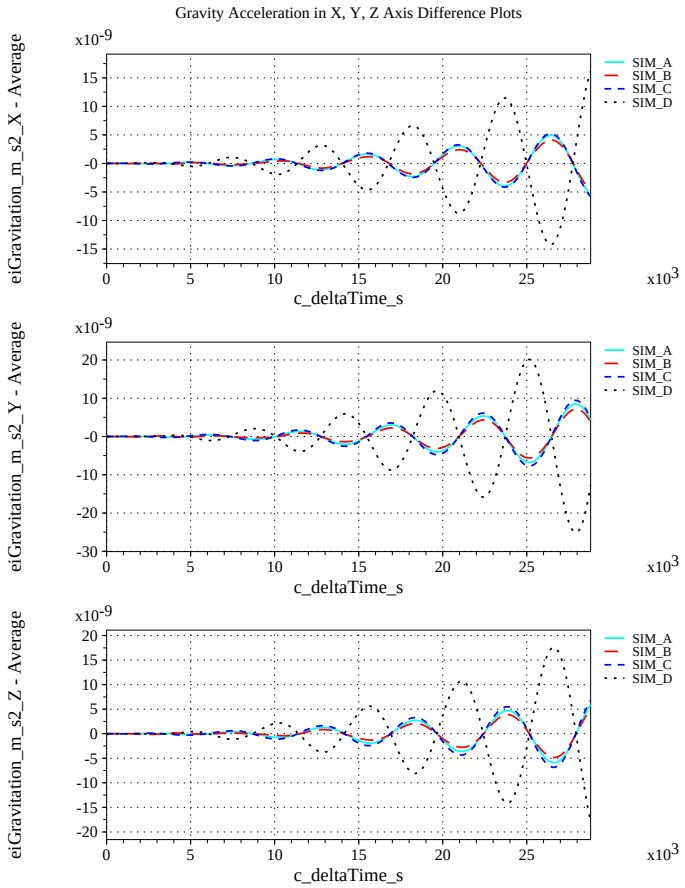

(p) Gravitational Components in Inertial (**X**-**Y**-**Z**) Directions Differenced

Figure 40. Check-case 04: ISS with Third-body Disturbances; See Discussion in Section D.2.4 (Concluded)

D.2.5 Check-case 05A – ISS (minimal solar activity)

This section shows cross-plots for four of the selected simulation tools in modeling the dynamics of the ISS in orbit with minimal solar activity disturbances. This scenario is described in Section C.2.5. Figures 41a through 41p compare results between the four simulation tools, as well as the deviances of the outputs from each tool from the ensemble average value.

Orbital test check-cases 5A through 5C compared the atmospheric properties predicted by the simulations. Simulations were asked to use the MET model [18] to predict the atmospheric temperature and density in the thermosphere. Atmospheric temperature and density are subject to the solar radiation flux; this case set the solar radiation flux for minimum solar activity. The MET model is a function of the geodetic position of the vehicle; therefore differences in the Earth-relative position of the vehicle can cause small differences in the predicted atmospheric properties. However, the dominant contributor to differences among the simulation tools' predicted orbits was the differing versions of MET used by different simulation tools. SIM A used MET07. SIM B and C used MET99. SIM D used MET95. (MET95 was the model provided as a reference to teams that did not have an existing implementation of the MET model.) As seen in plots of the atmospheric properties, MET95 and MET99 produced similar results. MET07 introduced a modeling improvement that differentiated it from MET95 and MET99. In computing the atmospheric properties, MET95 and MET99 used global, hard-coded values for surface gravity and effective radius for a spherical Earth. MET07 computed surface gravity and effective radius as a function of latitude using WGS-84 parameters (i.e., an ellipsoid Earth).

A secondary contributor to the differences in atmospheric properties between SIM A and the other simulations was the difference in computed altitude. The difference in altitude was greater than the difference in the ECEF position vector. This indicated a difference in the accuracy of the method used to convert ECEF position to geodetic position. SIM A also exhibited a spike in its temperature and density difference with the other simulations at $t = 0$. This was likely an artifact of the simulation's recording or initialization functions.

This check-case scenario first introduced the initial conditions for a highly elliptical orbit but modeled the Earth as a spherically symmetric mass in order to isolate differences in the atmospheric properties to the thermosphere model. Differences in translational states among the simulations were similar to orbital check-case 2. Differences in inertial states were attributed to differences in integration method. Differences in Earth-relative states were attributed to differences in the initial RNP matrix for the Earth and to differences in the propagation of RNP. See Section D.2.1 for more details. Differences in rotational state were also similar to orbital case 2 and were attributed to differences in integration methods.

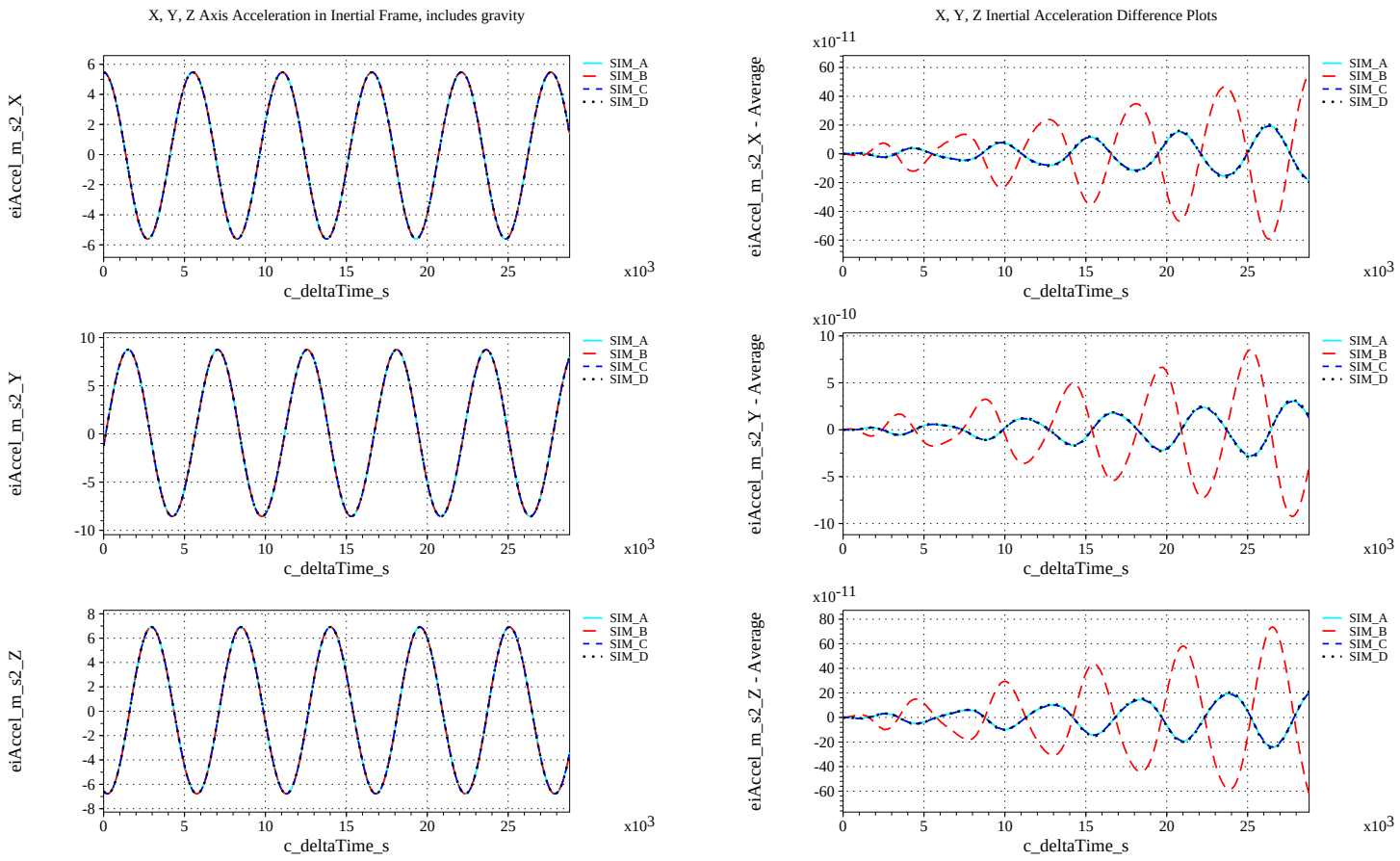

(a) Inertial Accelerations Compared

(b) Inertial Accelerations Differenced

Figure 41. Check-case 05A: ISS (Minimal Solar Activity); See Discussion in Section D.2.5

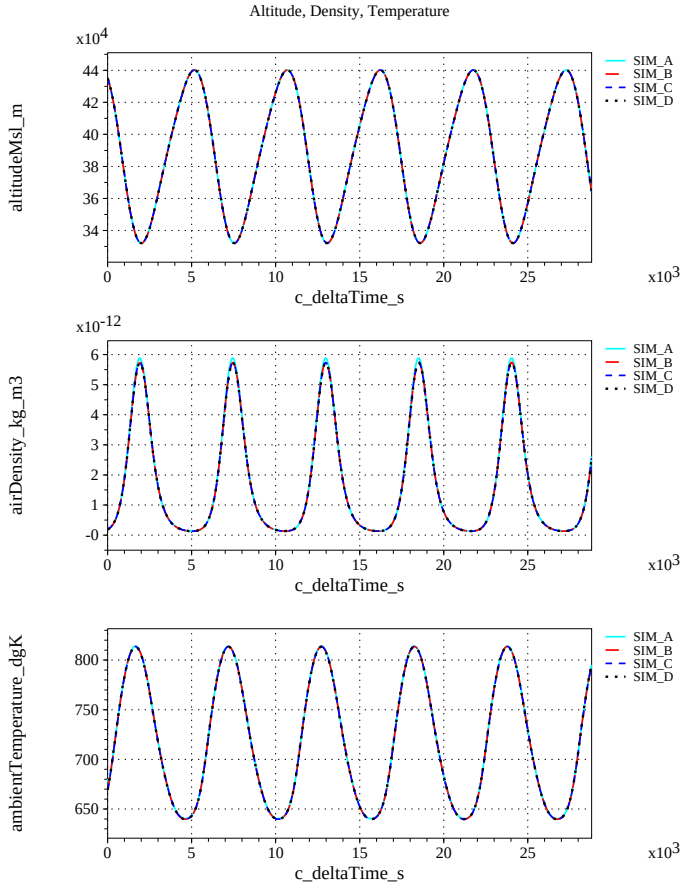

(c) Atmospheric Properties Compared

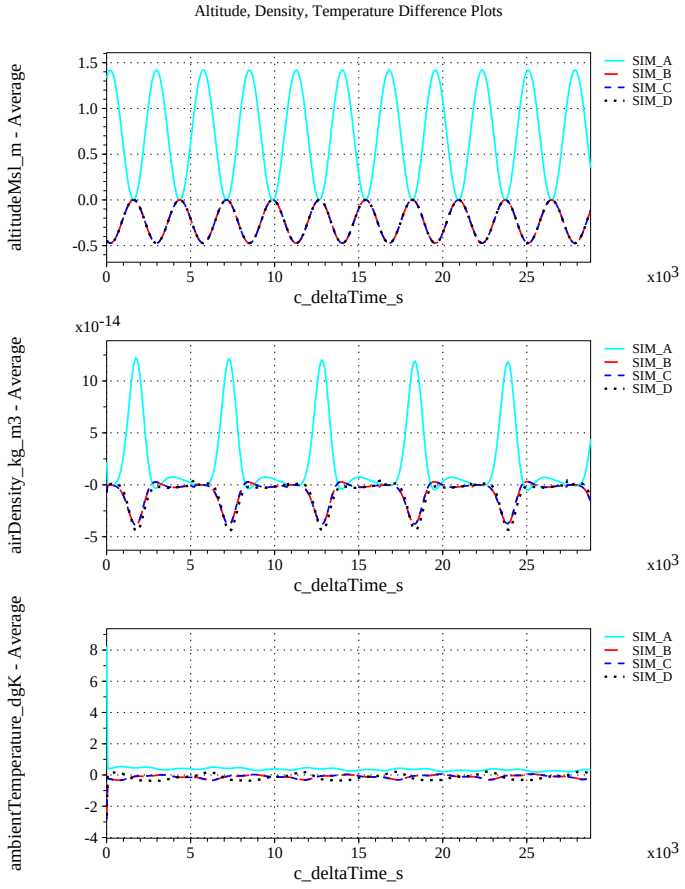

(d) Atmospheric Properties Differenced

Figure 41. Check-case 05A: ISS (Minimal Solar Activity); See Discussion in Section D.2.5 (Cont'd)

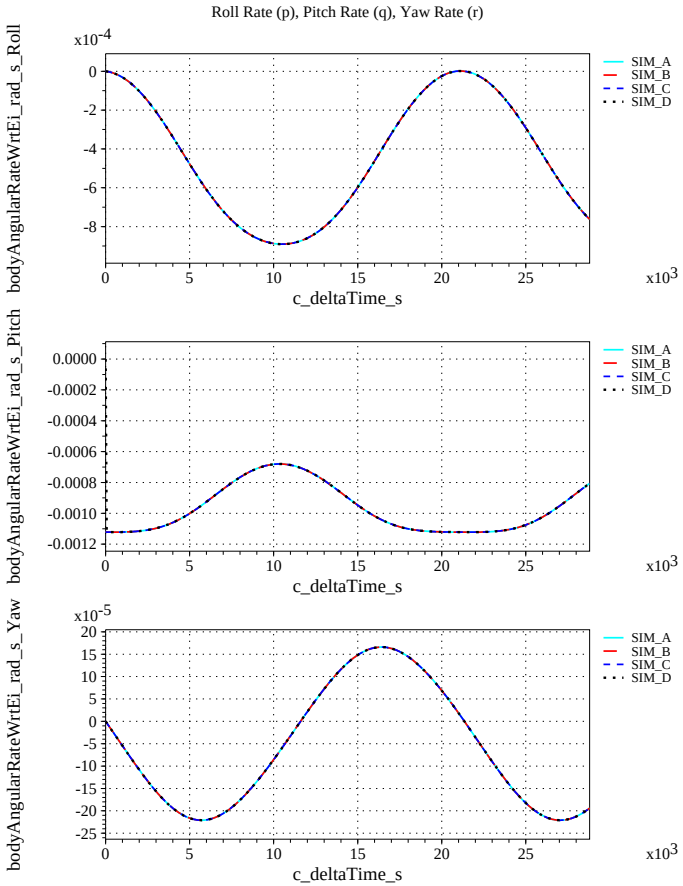

(e) Body-axis Angular Rates Compared

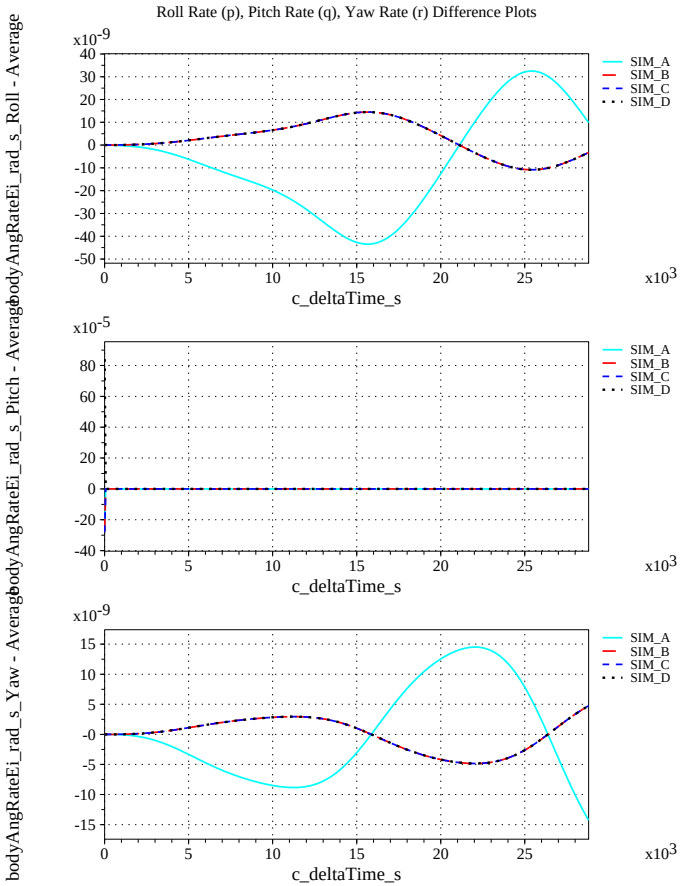

(f) Body-axis Angular Rates Differenced

Figure 41. Check-case 05A: ISS (Minimal Solar Activity); See Discussion in Section D.2.5 (Cont'd)

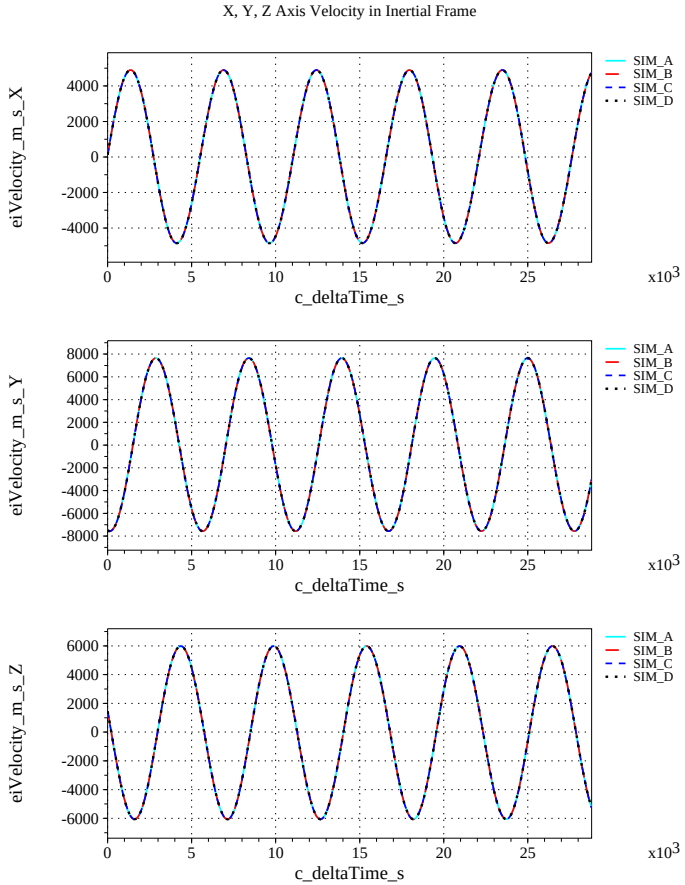

(g) Inertial Velocities Compared

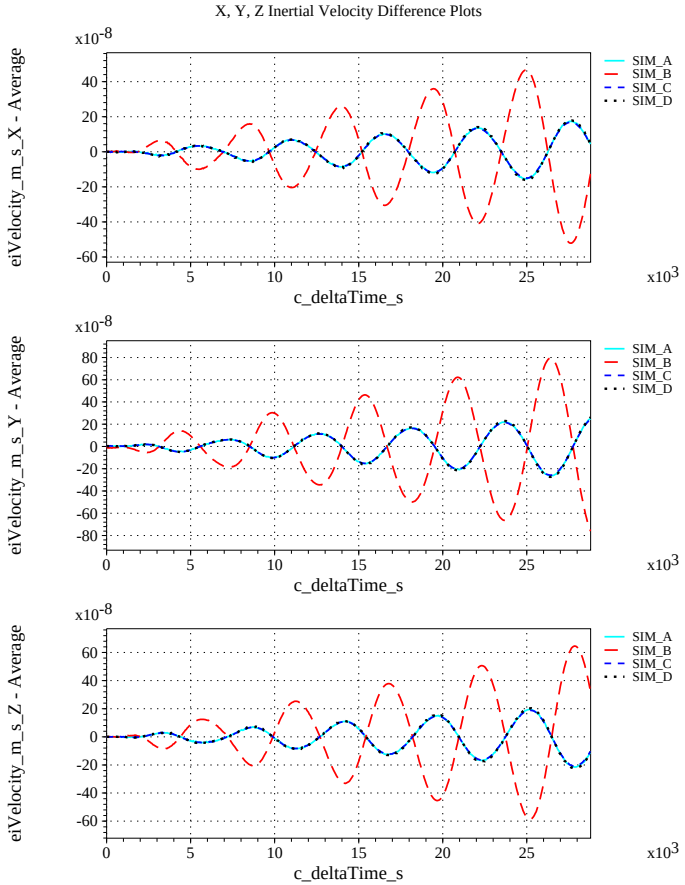

(h) Inertial Velocities Differenced

Figure 41. Check-case 05A: ISS (Minimal Solar Activity); See Discussion in Section D.2.5 (Cont'd)

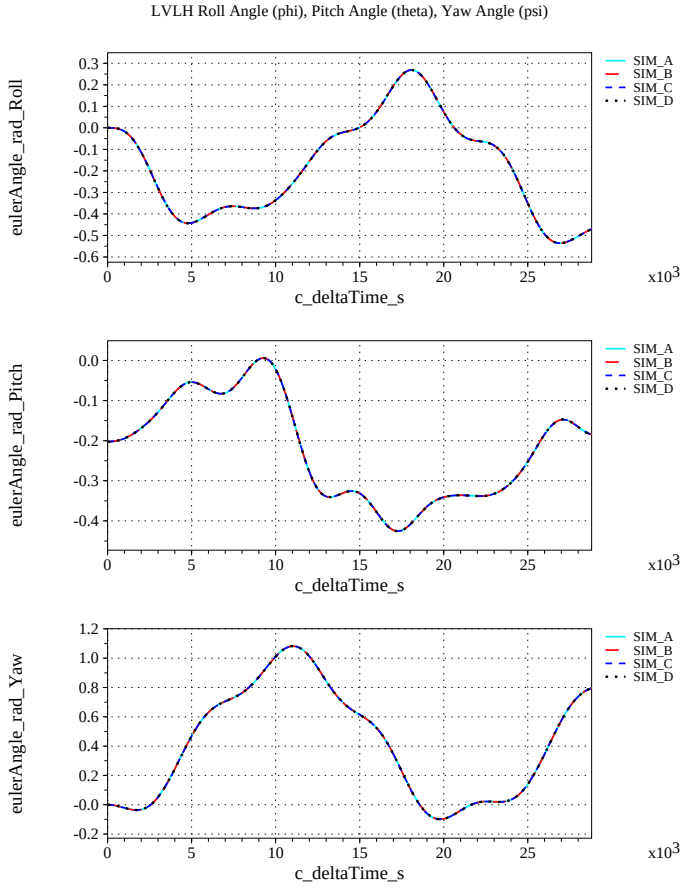

(i) Rotation Angles with Respect to LVLH Frame Compared

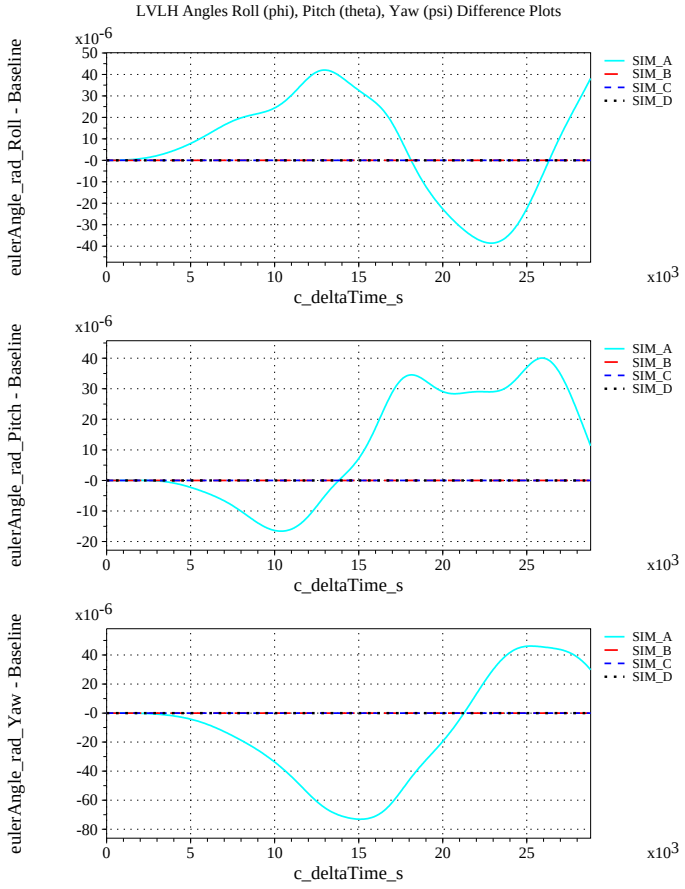

(j) Rotation Angles with Respect to LVLH Frame Differenced

Figure 41. Check-case 05A: ISS (Minimal Solar Activity); See Discussion in Section D.2.5 (Cont'd)

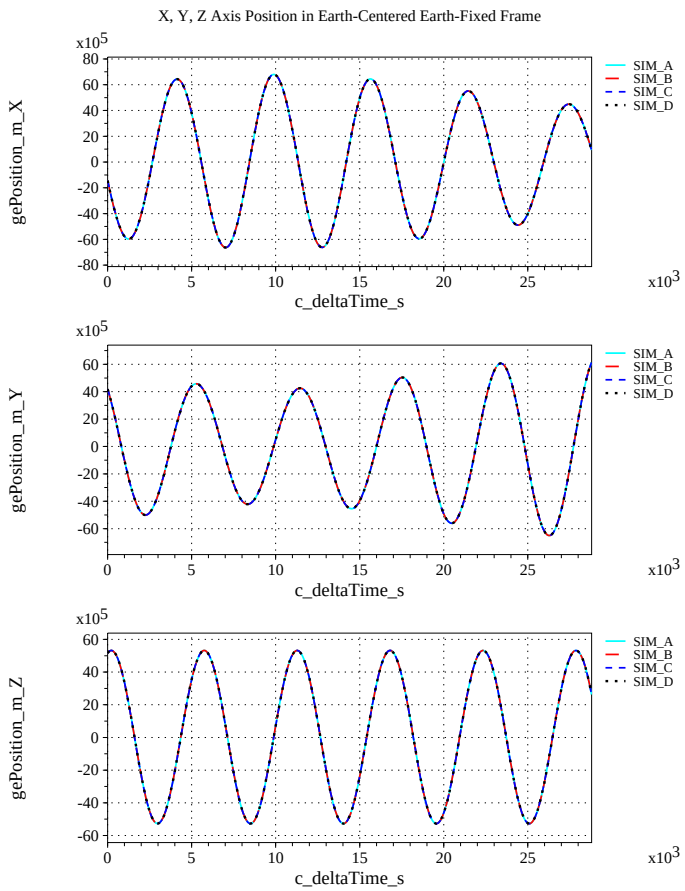

(k) Earth-centered, Earth-fixed Rectangular (X-Y-Z) Positions Compared

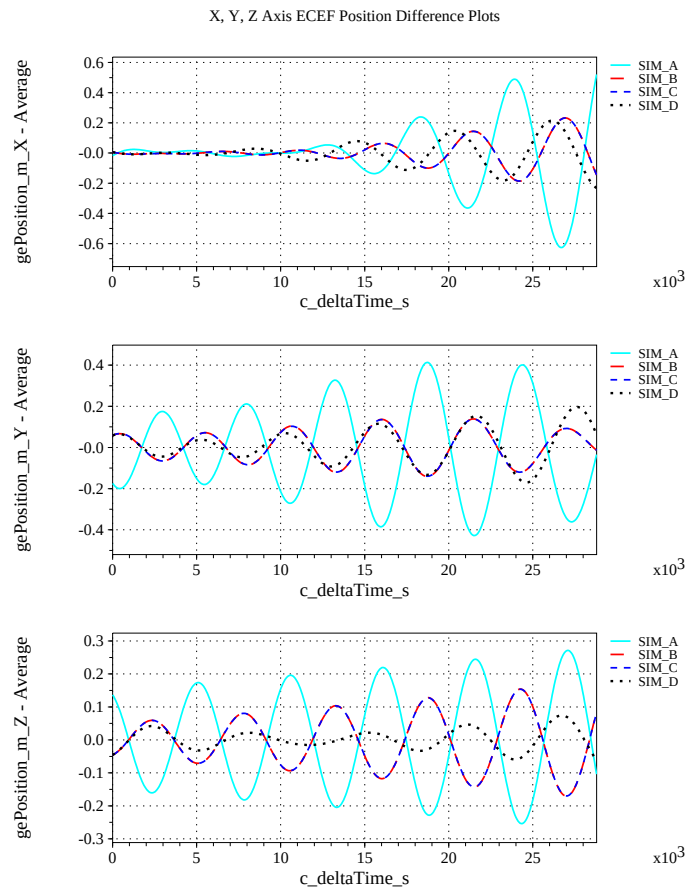

(l) Earth-centered, Earth-fixed Rectangular (X-Y-Z) Positions Differenced

Figure 41. Check-case 05A: ISS (Minimal Solar Activity); See Discussion in Section D.2.5 (Cont'd)

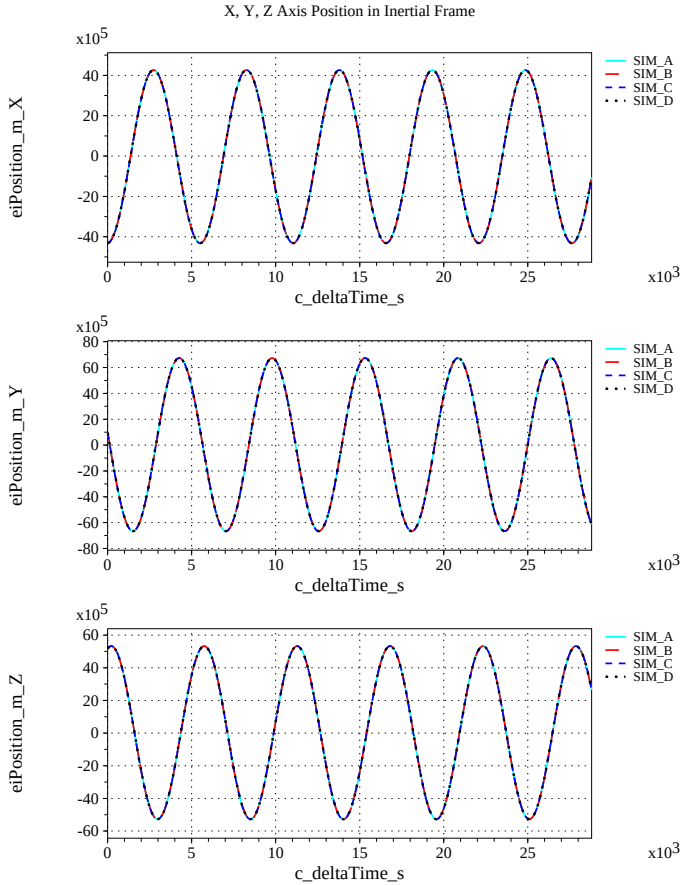

(m) Earth-centered Inertial Rectangular (x-y-z) Positions Compared

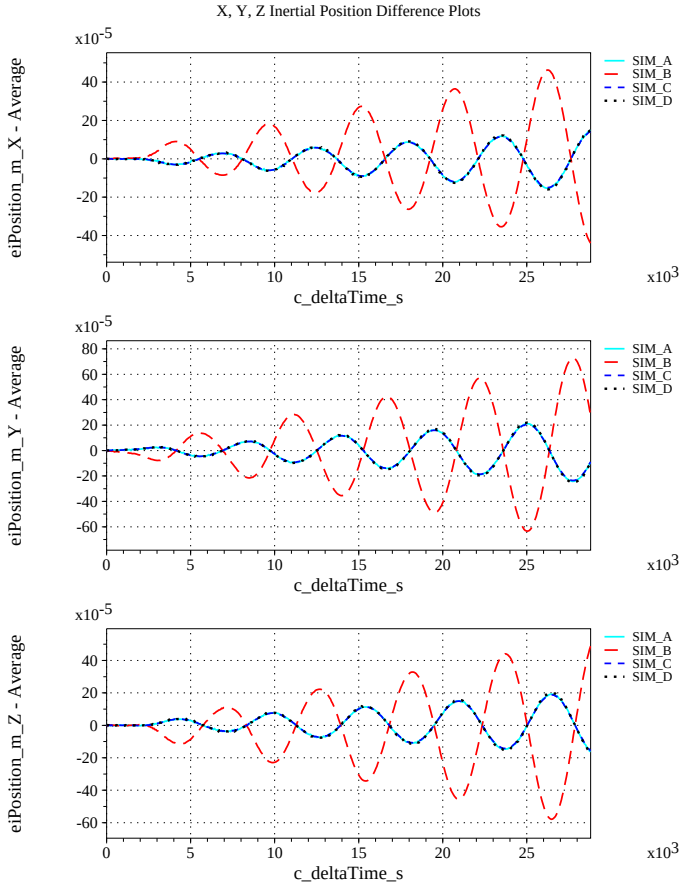

(n) Earth-centered Inertial Rectangular (x-y-z) Positions Differenced

Figure 41. Check-case 05A: ISS (Minimal Solar Activity); See Discussion in Section D.2.5 (Cont'd)

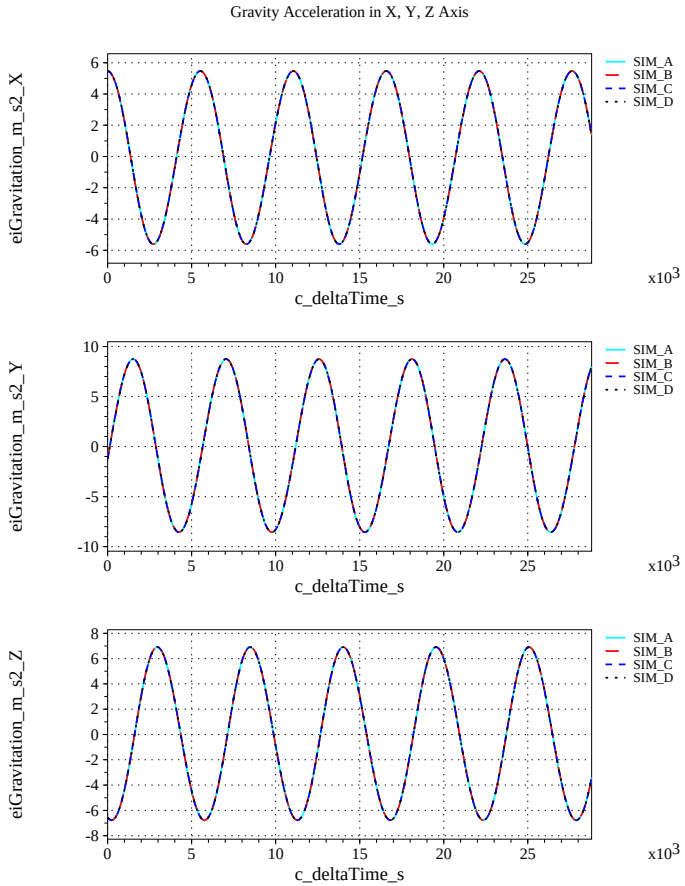

(o) Gravitational Components in Inertial (**X**-**Y**-**Z**) Directions Compared

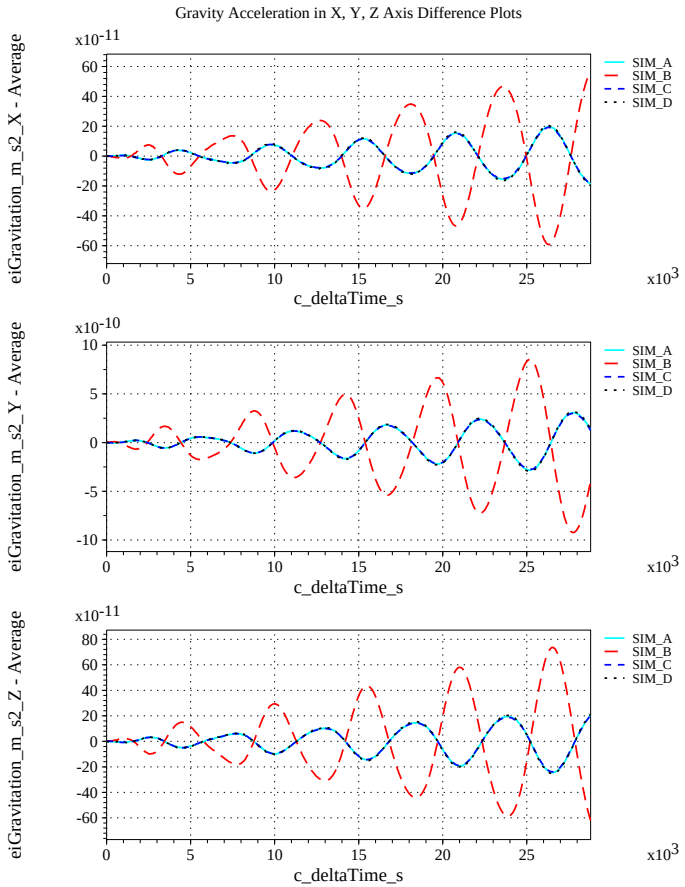

(p) Gravitational Components in Inertial (**X**-**Y**-**Z**) Directions Differenced

Figure 41. Check-case 05A: ISS (Minimal Solar Activity); See Discussion in Section D.2.5 (Concluded)

D.2.6 Check-case 05B – ISS (mean solar activity)

This section shows cross-plots for four of the selected simulation tools in modeling the dynamics of the ISS in orbit with mean solar activity disturbances. This scenario is described in Section C.2.6. Figures 42a through 42p compare results between the four simulation tools, as well as the deviances of the outputs from each tool from the ensemble average value.

Orbital check-cases 5A through 5C compared the atmospheric properties predicted by the simulations. Simulations were required to implement the MET model [18] to predict the atmospheric temperature and density in the thermosphere. Atmospheric temperature and density are subject to the solar radiation flux; this case set the solar radiation flux for mean solar activity. The MET model is a function of the geodetic position of the vehicle; therefore differences in the Earth-relative position of the vehicle can cause small differences in the predicted atmospheric properties. The differences in atmospheric properties among simulations B, C, and D were the result of using different versions of the MET model, as noted for check-case 5A. However, those differences were masked by the results of SIM A which appeared to have been somewhat misconfigured: the ECEF position, geodetic altitude and atmospheric temperature recorded for SIM A were a constant zero; the atmospheric density was a negative value. Likewise, SIM A produced a constant zero for inertial acceleration,velocity, and position. The same was true for the rotational states.

Agreement in translational and rotational states among SIM B, C, and D was unchanged from orbital case 5A (see Section D.2.5).

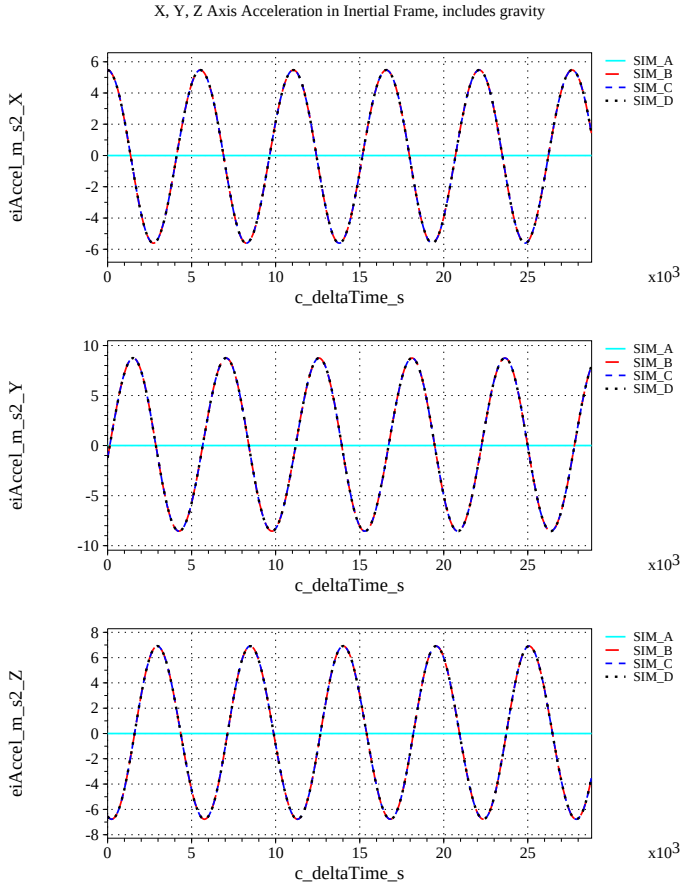

(a) Inertial Accelerations Compared

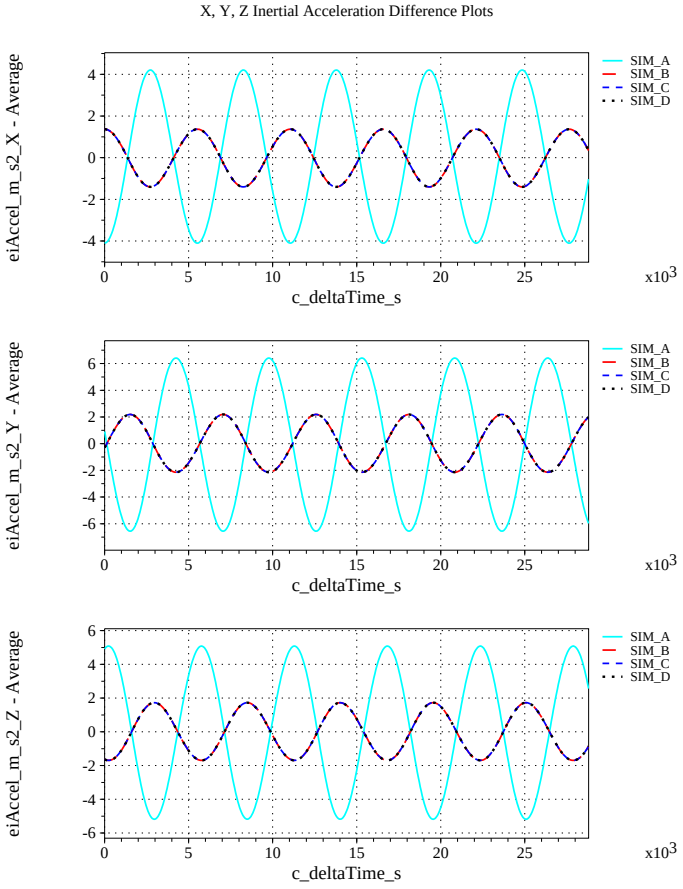

(b) Inertial Accelerations Differenced

Figure 42. Check-case 05B: ISS (Mean Solar Activity); See Discussion in Section D.2.6

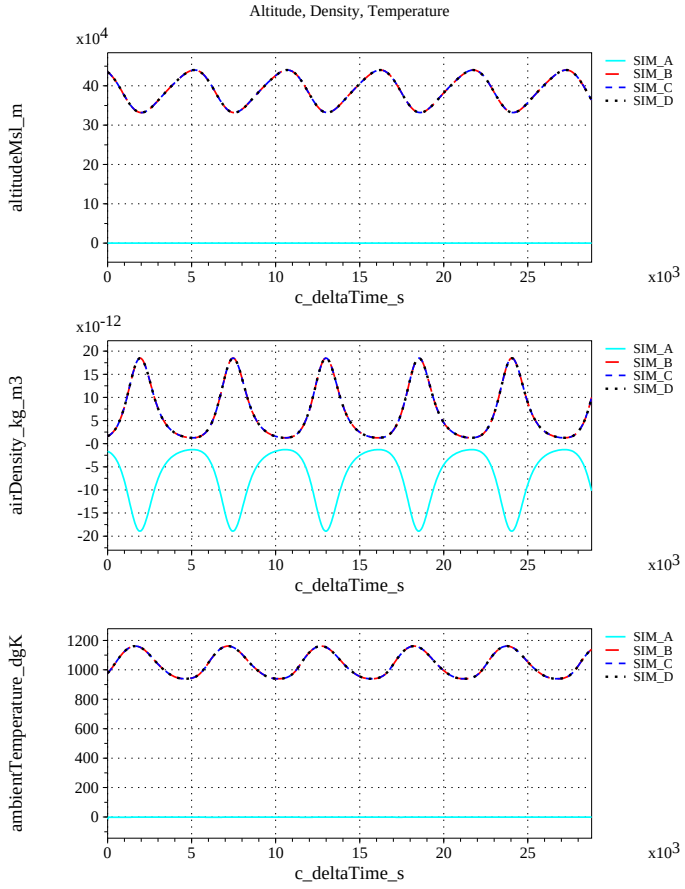

(c) Atmospheric Properties Compared

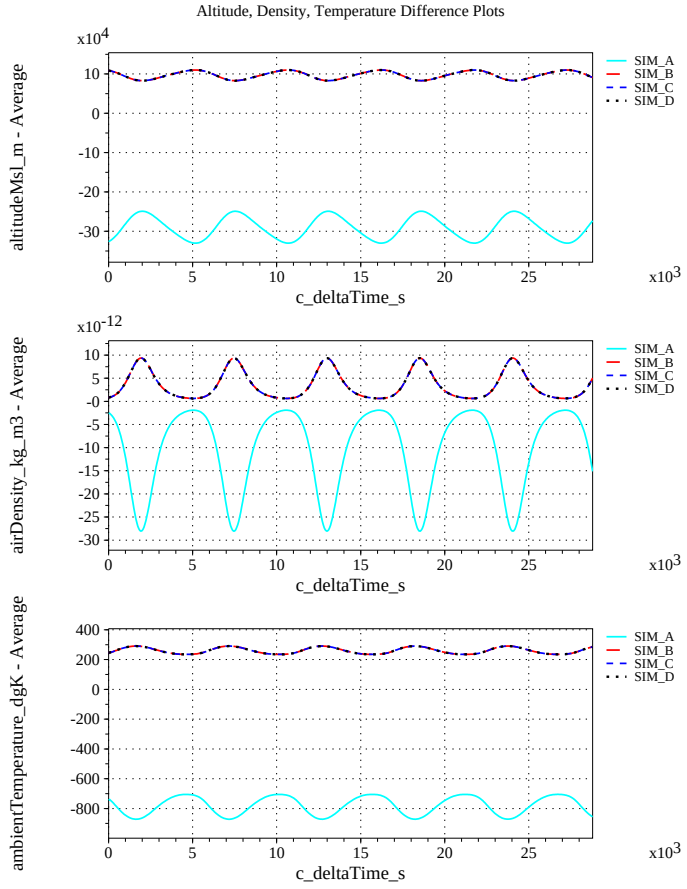

(d) Atmospheric Properties Differenced

Figure 42. Check-case 05B: ISS (Mean Solar Activity); See Discussion in Section D.2.6 (Cont'd)

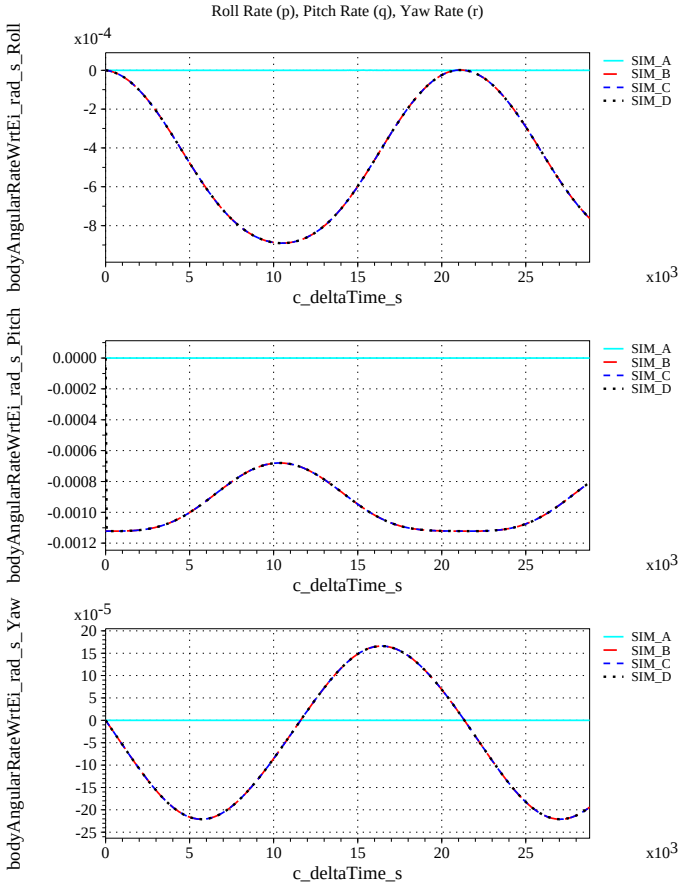

(e) Body-axis Angular Rates Compared

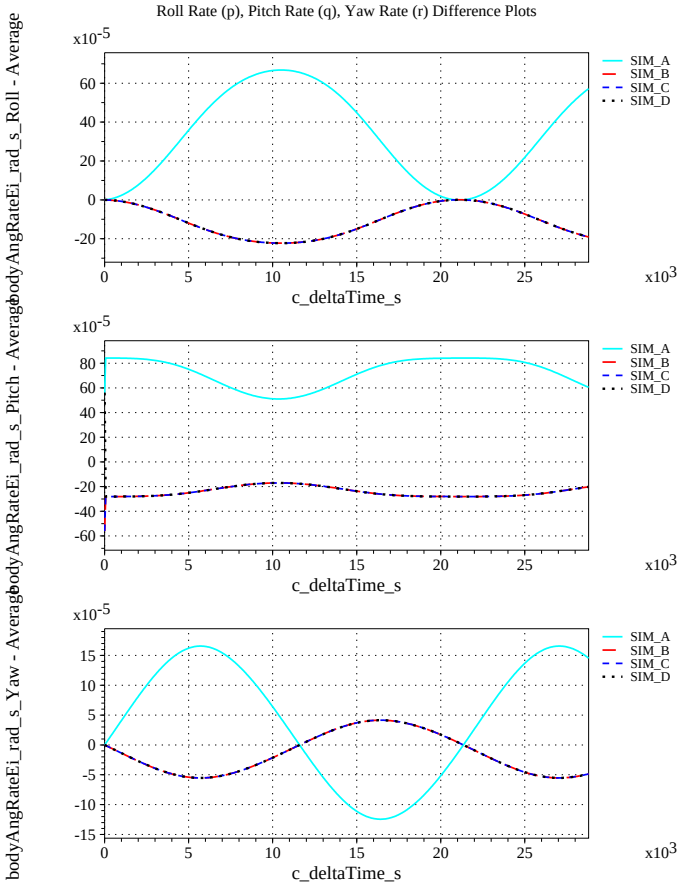

(f) Body-axis Angular Rates Differenced

Figure 42. Check-case 05B: ISS (Mean Solar Activity); See Discussion in Section D.2.6 (Cont'd)

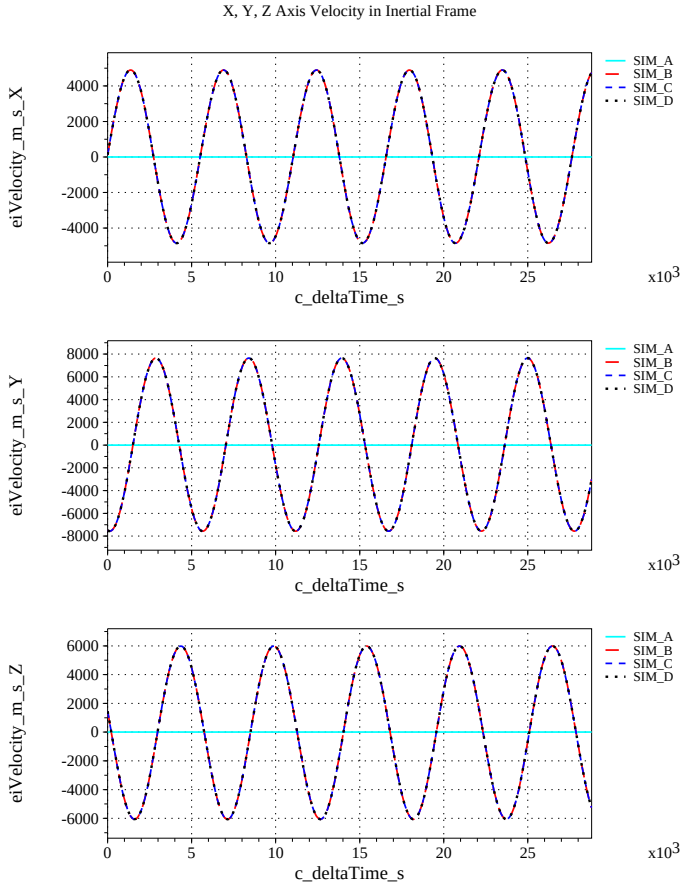

(g) Inertial Velocities Compared

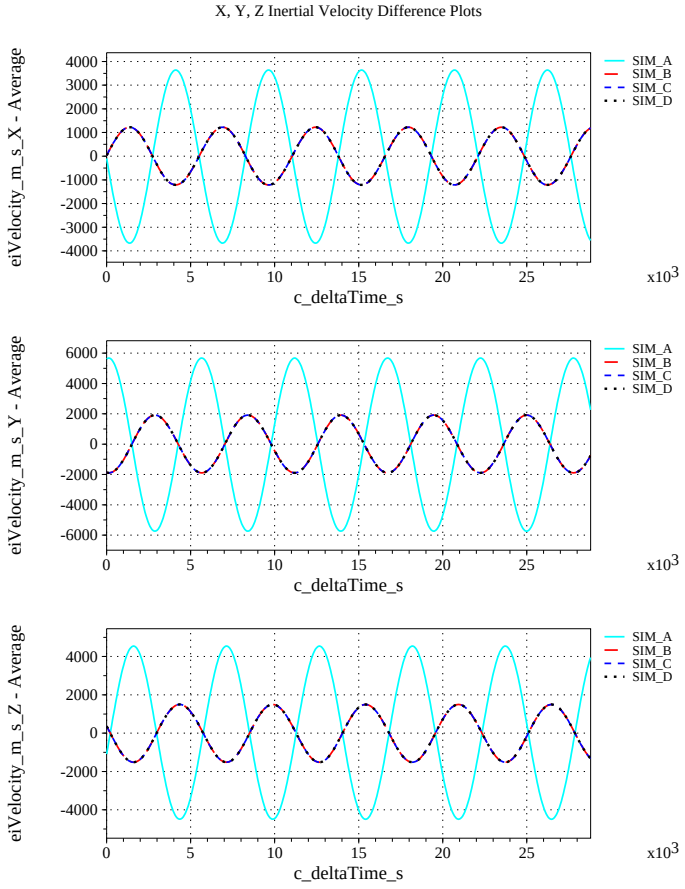

(h) Inertial Velocities Differenced

Figure 42. Check-case 05B: ISS (Mean Solar Activity); See Discussion in Section D.2.6 (Cont'd)

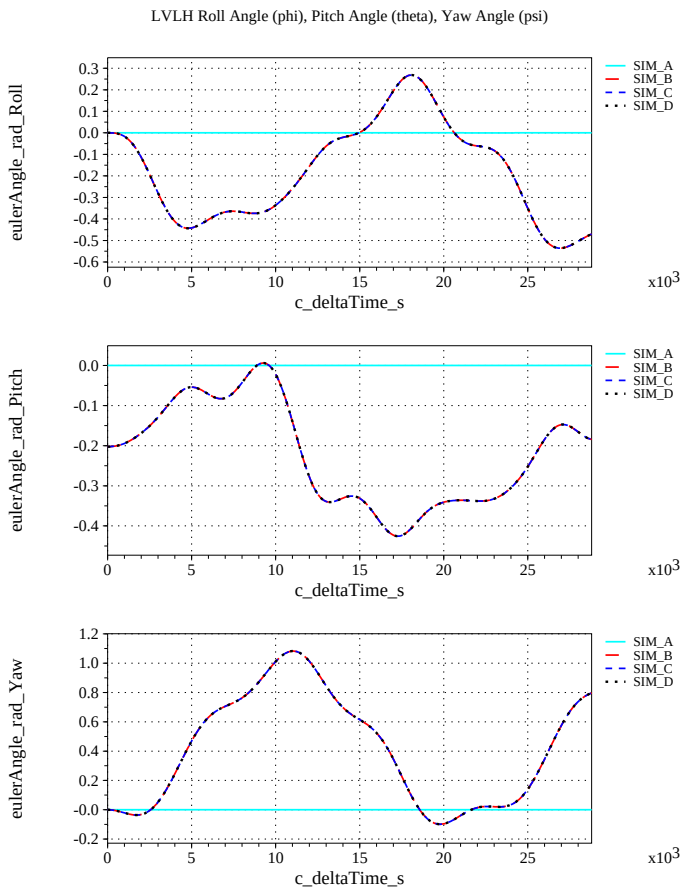

(i) Rotation Angles with Respect to LVLH Frame Compared

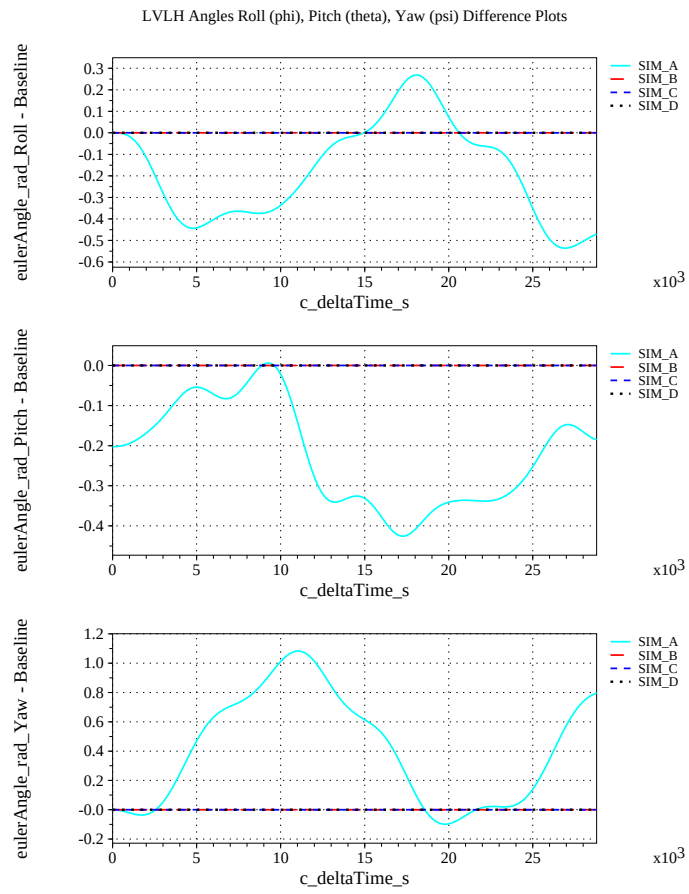

(j) Rotation Angles with Respect to LVLH Frame Differenced

Figure 42. Check-case 05B: ISS (Mean Solar Activity); See Discussion in Section D.2.6 (Cont'd)

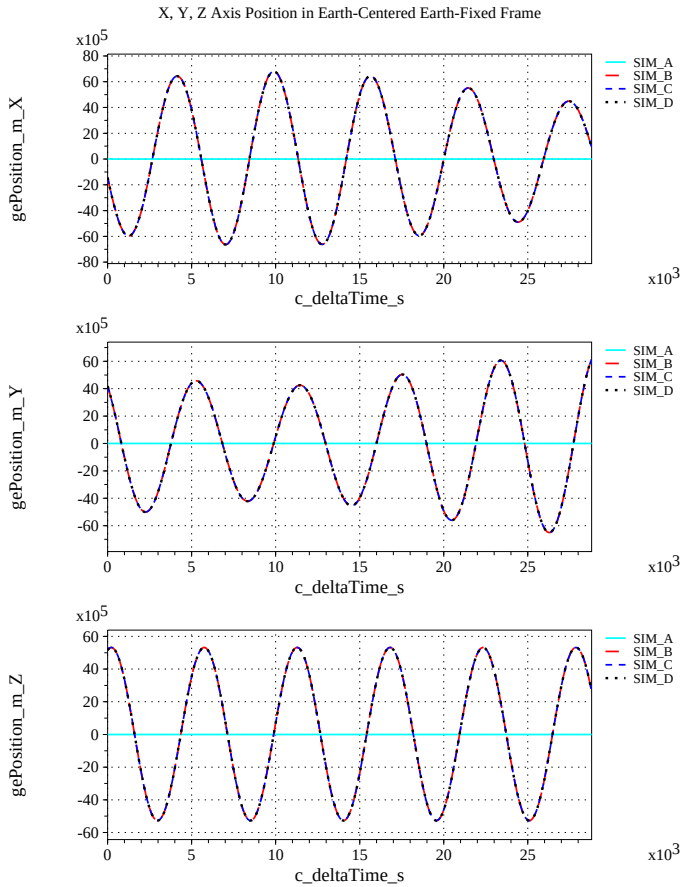

(k) Earth-centered, Earth-fixed Rectangular (X-Y-Z) Positions Compared

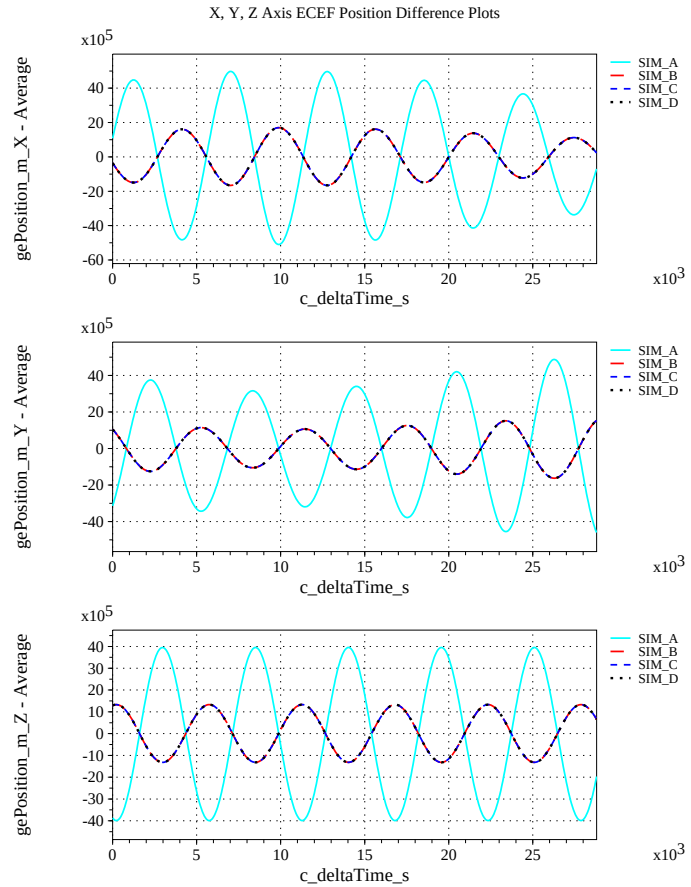

(l) Earth-centered, Earth-fixed Rectangular (X-Y-Z) Positions Differenced

Figure 42. Check-case 05B: ISS (Mean Solar Activity); See Discussion in Section D.2.6 (Cont'd)

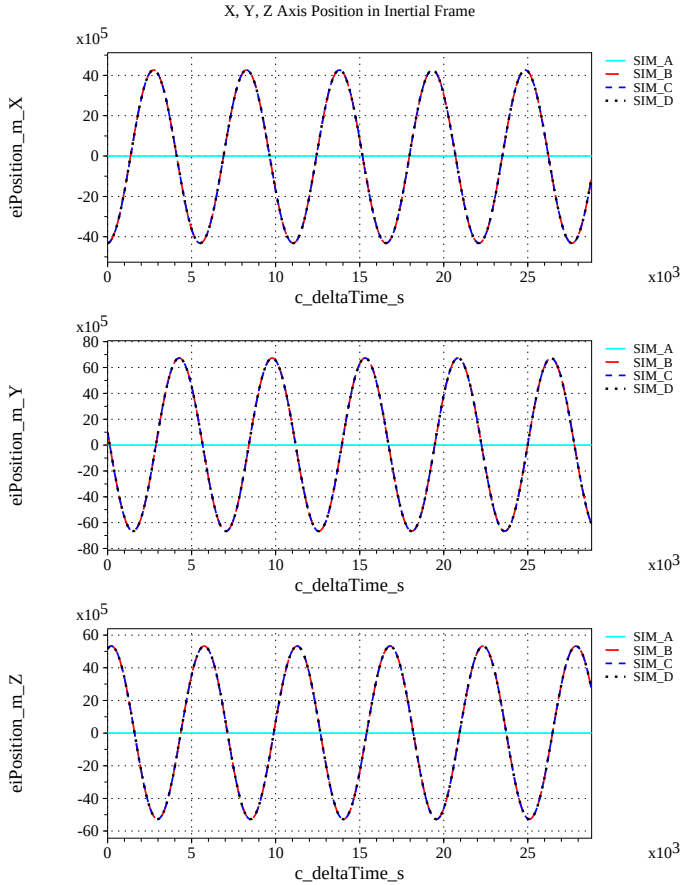

(m) Earth-centered Inertial Rectangular (x-y-z) Positions Compared

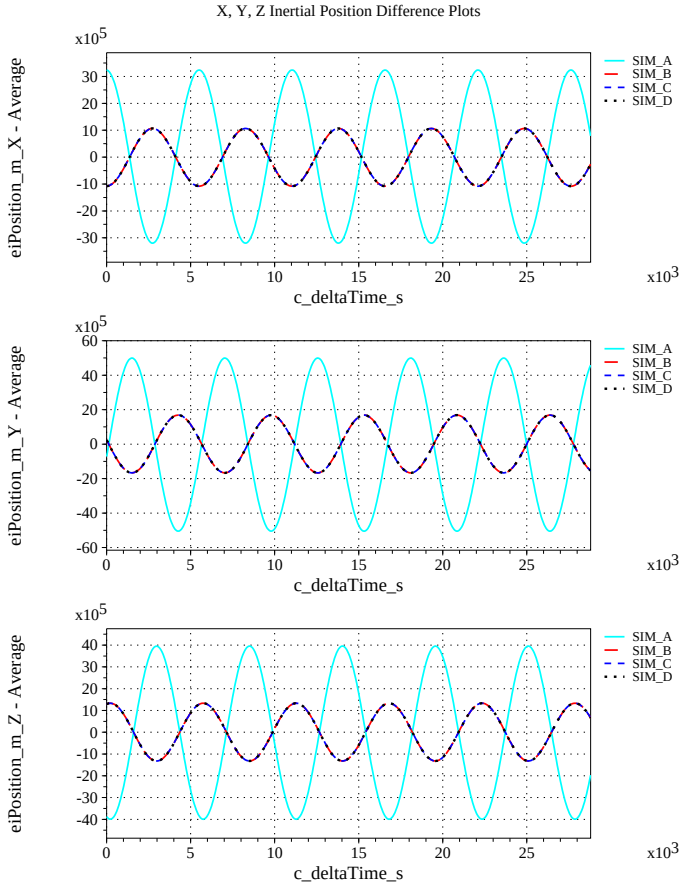

(n) Earth-centered Inertial Rectangular (x-y-z) Positions Differenced

Figure 42. Check-case 05B: ISS (Mean Solar Activity); See Discussion in Section D.2.6 (Cont'd)

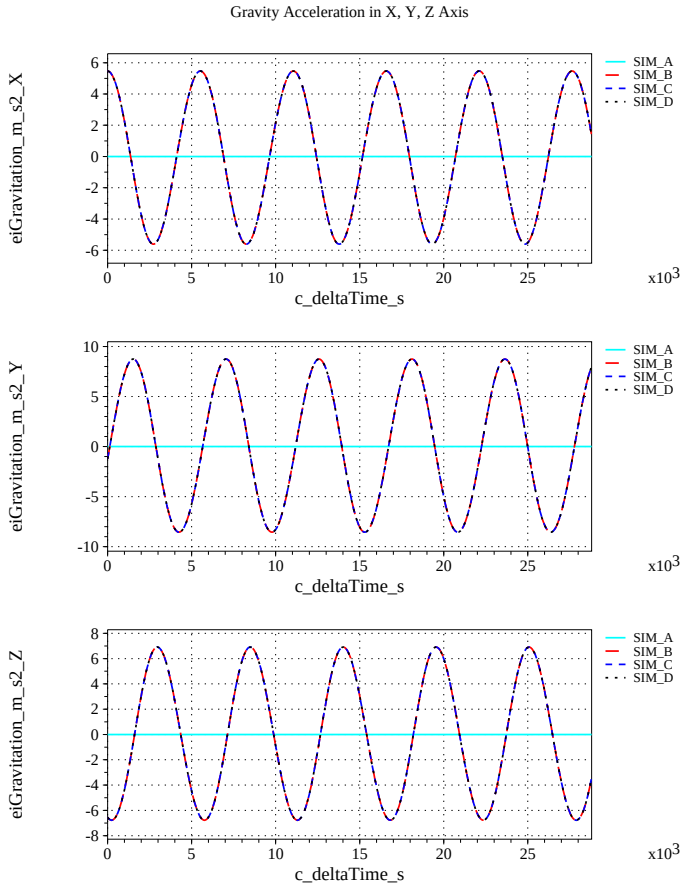

(o) Gravitational Components in Inertial (**X**-**Y**-**Z**) Directions Compared

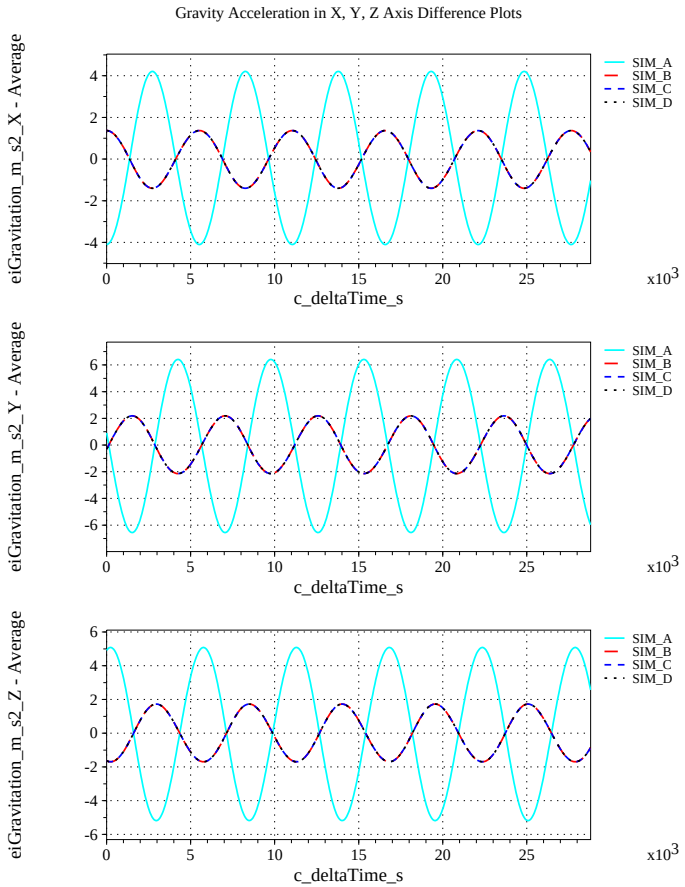

(p) Gravitational Components in Inertial (**X**-**Y**-**Z**) Directions Differenced

Figure 42. Check-case 05B: ISS (Mean Solar Activity); See Discussion in Section D.2.6 (Concluded)

D.2.7 Check-case 05C – ISS (maximal solar activity)

This section shows cross-plots for four of the selected simulation tools in modeling the dynamics of the ISS in orbit with maximal solar activity disturbances. This scenario is described in Section C.2.7. Figures 43a through 43p compare results between the four simulation tools, as well as the deviances of the outputs from each tool from the ensemble average value.

Orbital check-cases 5A through 5C compared the high-altitude atmospheric properties predicted by the simulations. Simulations were expected to the use the MET model [18] to predict the atmospheric temperature and density in the thermosphere. Atmospheric temperature and density are subject to the solar radiation flux; this check-case set the solar radiation flux for maximum solar activity. As explained in the discussion for orbital case 5A (see Section D.2.5), the differences in atmospheric properties among the simulations were primarily caused by differences in the version of the MET model used by each simulation. A secondary contributor to the differences in atmospheric properties between SIM A and the other simulations was a difference in computed altitude. The difference in altitude was attributed to a difference in the accuracy of the method used to convert ECEF position to geodetic position. As in orbital case 5A, SIM A also exhibited a spike in its temperature and density difference at $t = 0$. This difference appears to be an artifact of the simulation's recording or initialization function.

Differences in translational and rotational state were identical to the results of orbital case 5A.

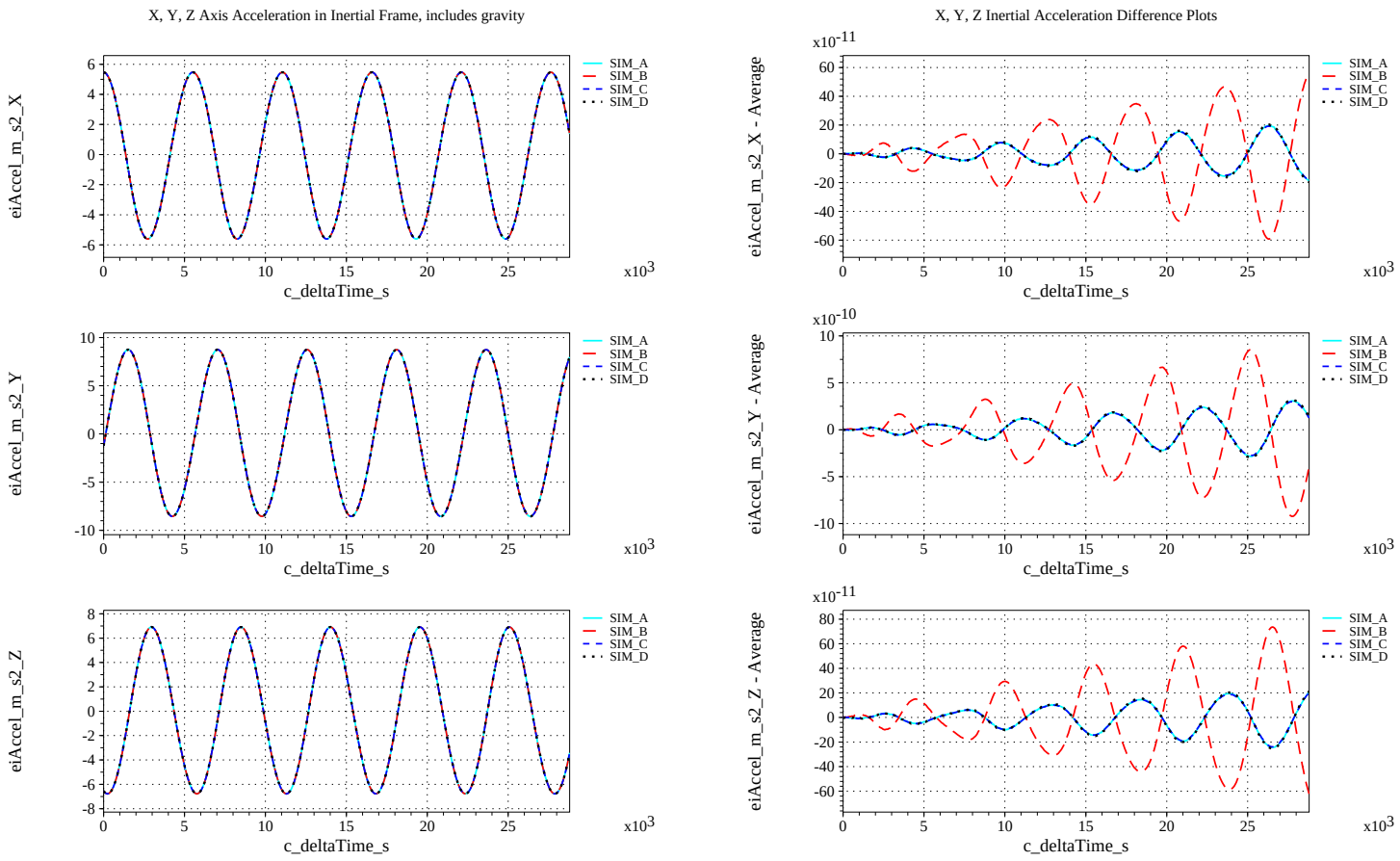

(a) Inertial Accelerations Compared

(b) Inertial Accelerations Differenced

Figure 43. Check-case 05C: ISS (Maximal Solar Activity); See Discussion in Section D.2.7

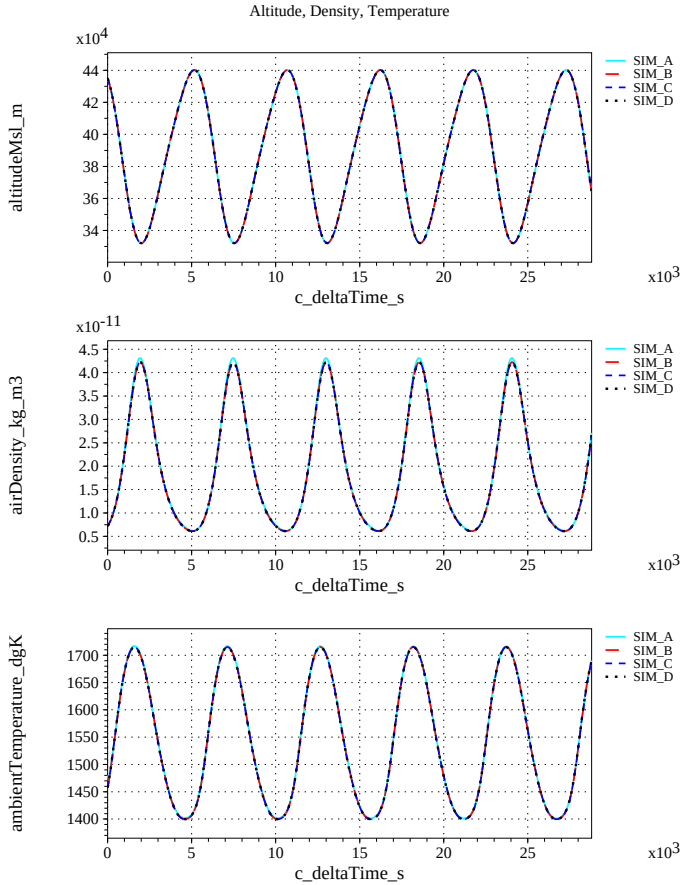

(c) Atmospheric Properties Compared

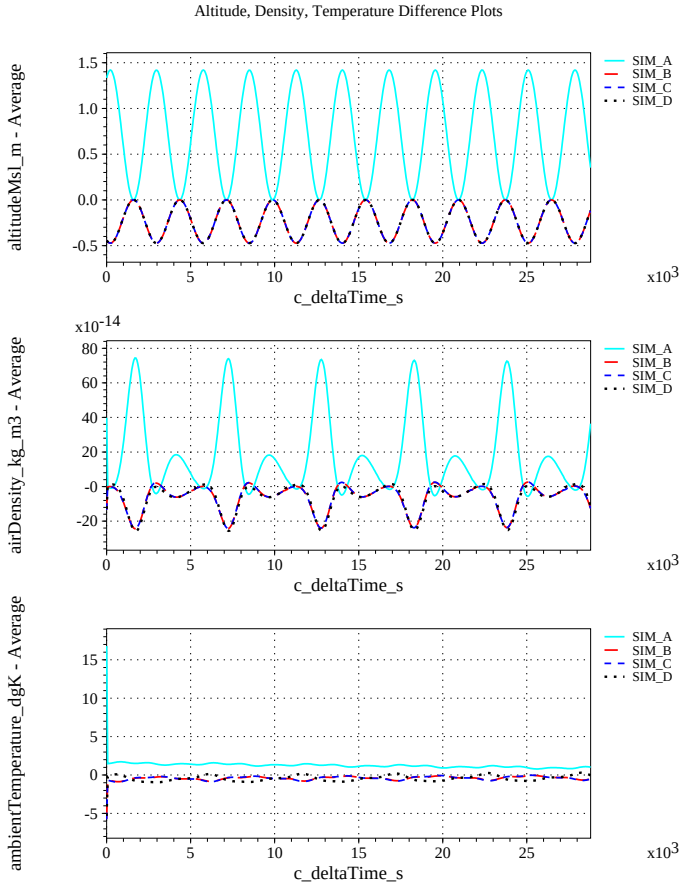

(d) Atmospheric Properties Differenced

Figure 43. Check-case 05C: ISS (Maximal Solar Activity); See Discussion in Section D.2.7 (Cont'd)

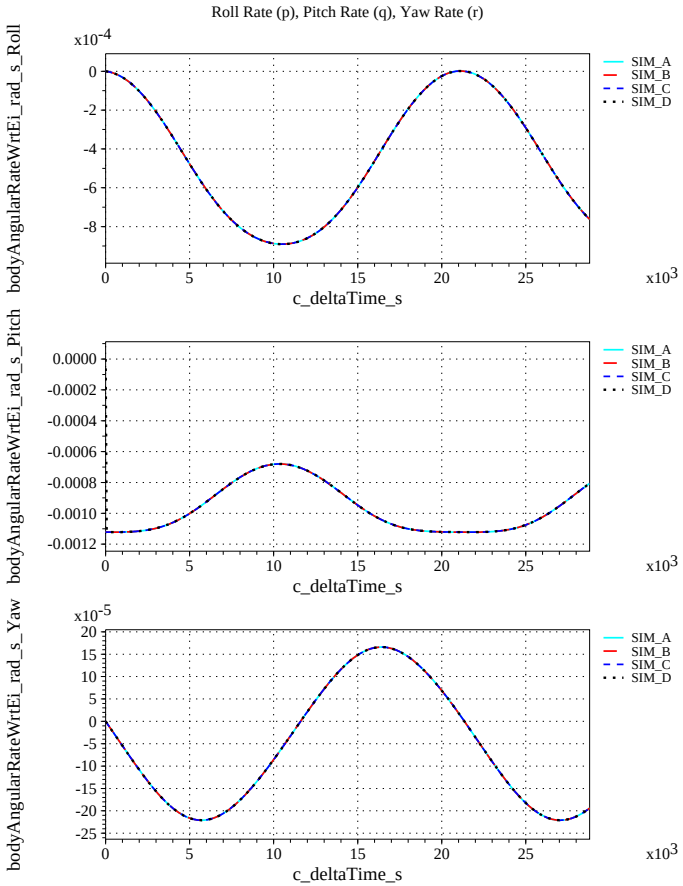

(e) Body-axis Angular Rates Compared

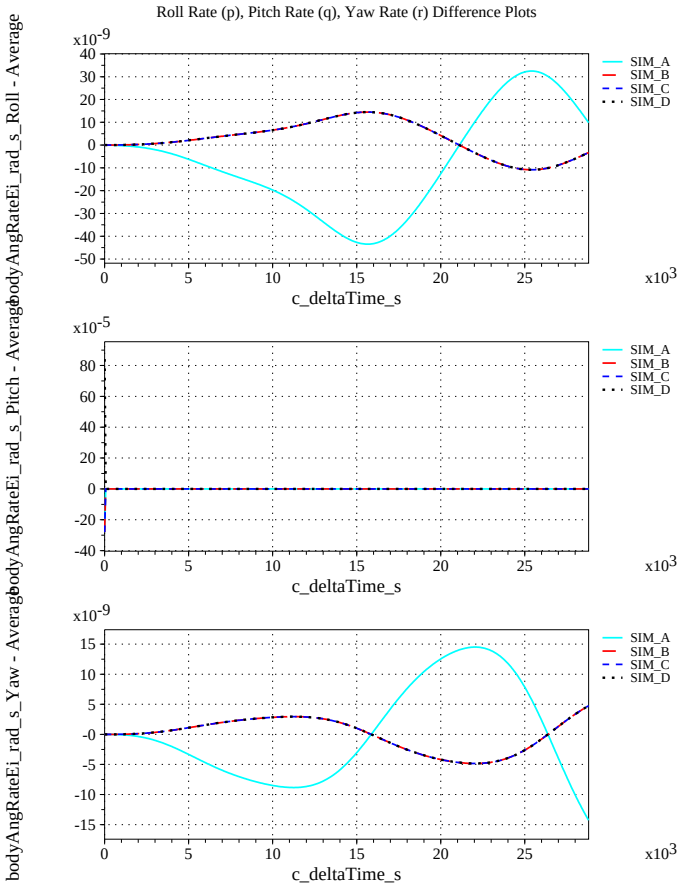

(f) Body-axis Angular Rates Differenced

Figure 43. Check-case 05C: ISS (Maximal Solar Activity); See Discussion in Section D.2.7 (Cont'd)

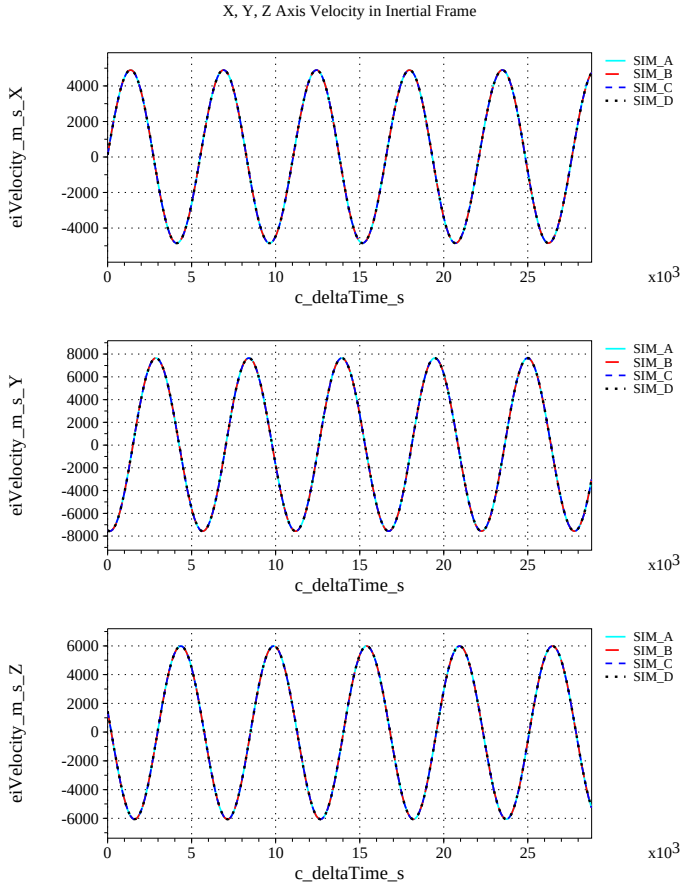

(g) Inertial Velocities Compared

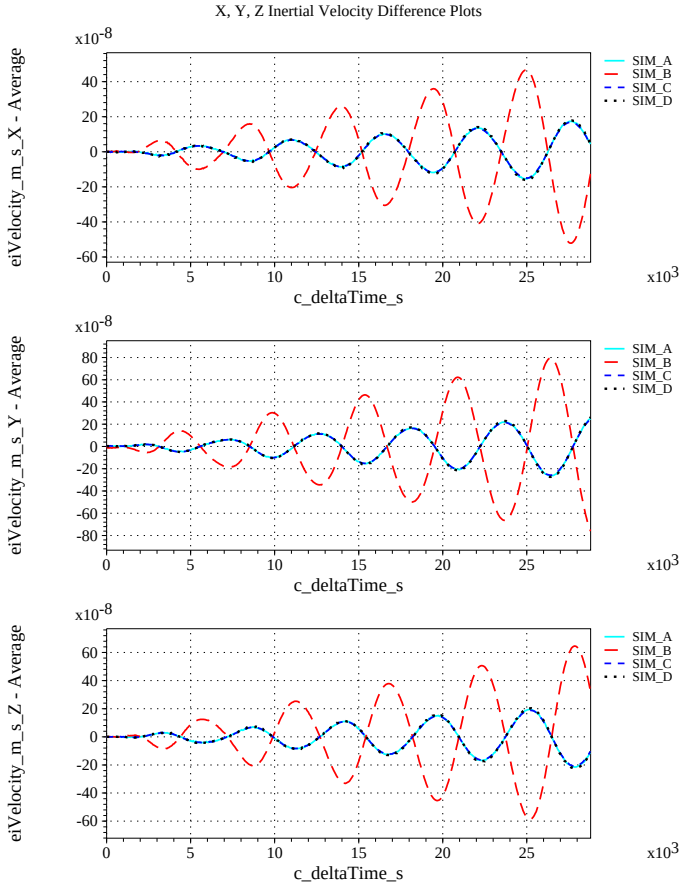

(h) Inertial Velocities Differenced

Figure 43. Check-case 05C: ISS (Maximal Solar Activity); See Discussion in Section D.2.7 (Cont'd)

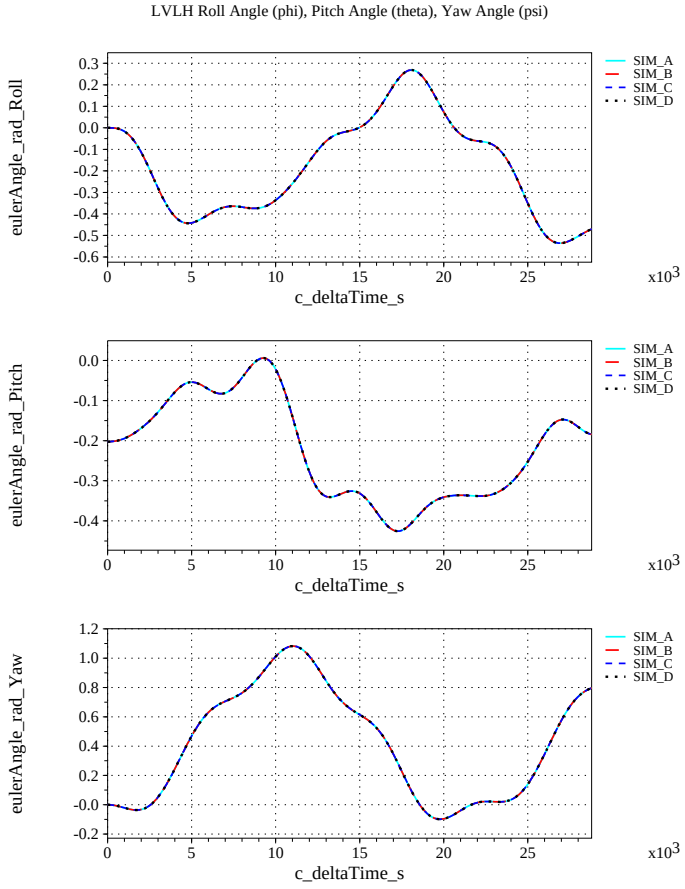

(i) Rotation Angles with Respect to LVLH Frame Compared

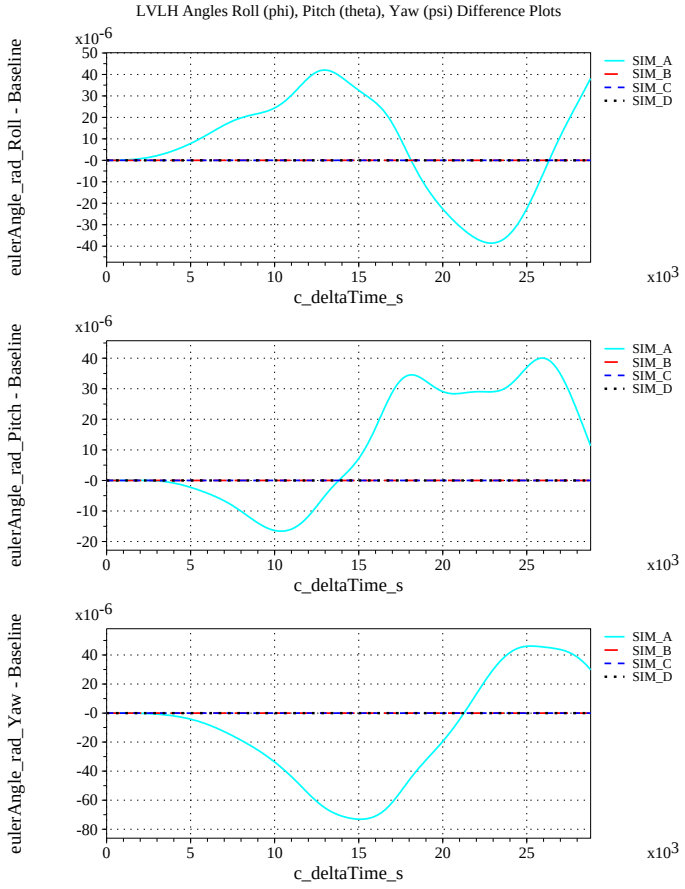

(j) Rotation Angles with Respect to LVLH Frame Differenced

Figure 43. Check-case 05C: ISS (Maximal Solar Activity); See Discussion in Section D.2.7 (Cont'd)

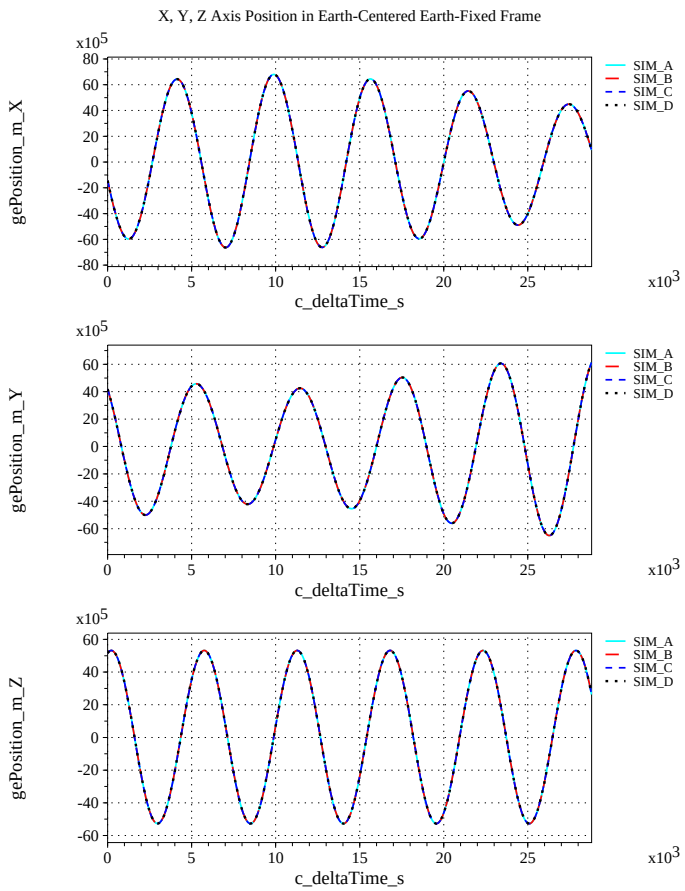

(k) Earth-centered, Earth-fixed Rectangular (X-Y-Z) Positions Compared

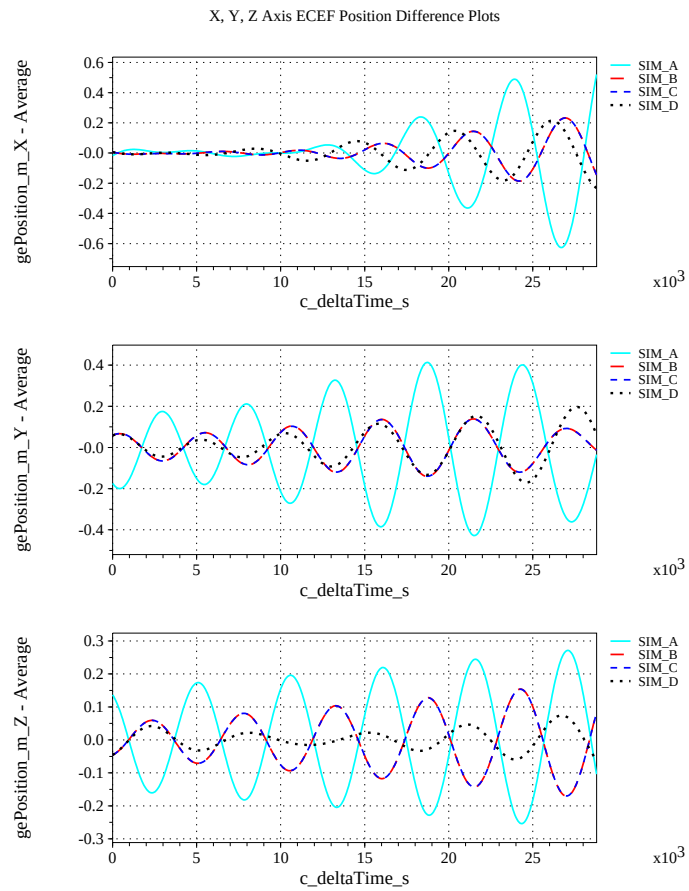

(l) Earth-centered, Earth-fixed Rectangular (X-Y-Z) Positions Differenced

Figure 43. Check-case 05C: ISS (Maximal Solar Activity); See Discussion in Section D.2.7 (Cont'd)

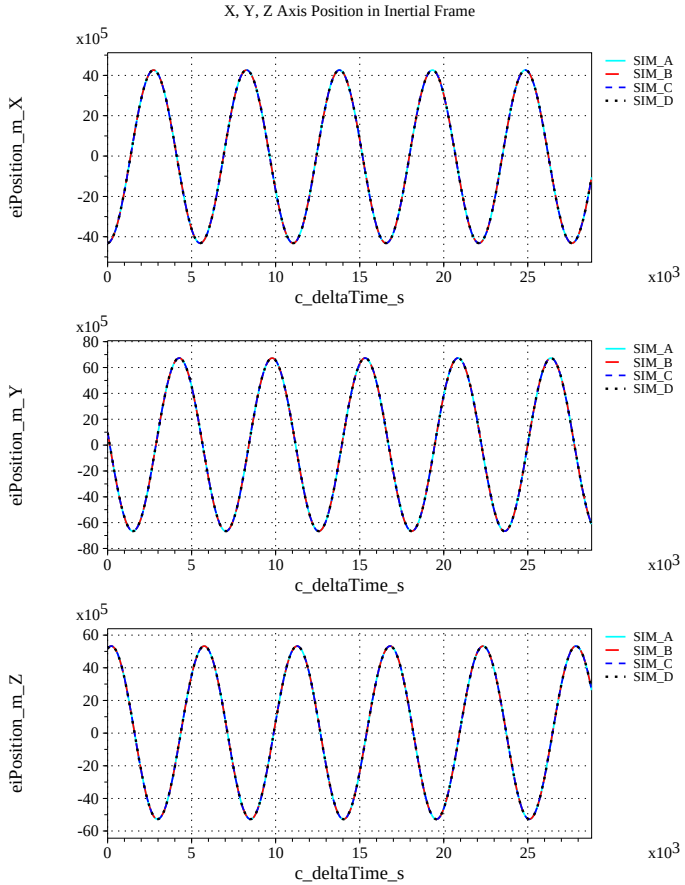

(m) Earth-centered Inertial Rectangular (x-y-z) Positions Compared

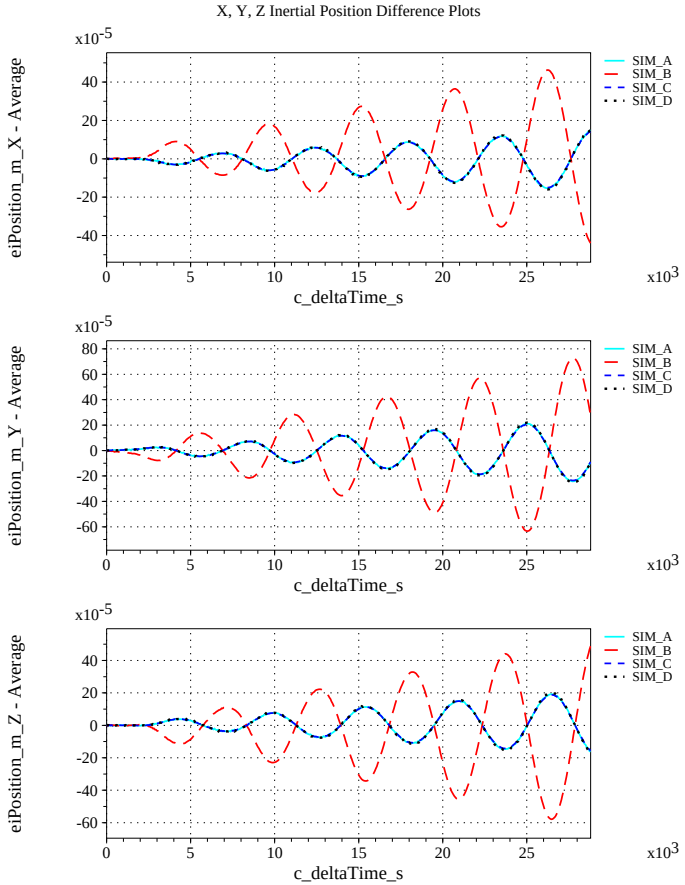

(n) Earth-centered Inertial Rectangular (x-y-z) Positions Differenced

Figure 43. Check-case 05C: ISS (Maximal Solar Activity); See Discussion in Section D.2.7 (Cont'd)

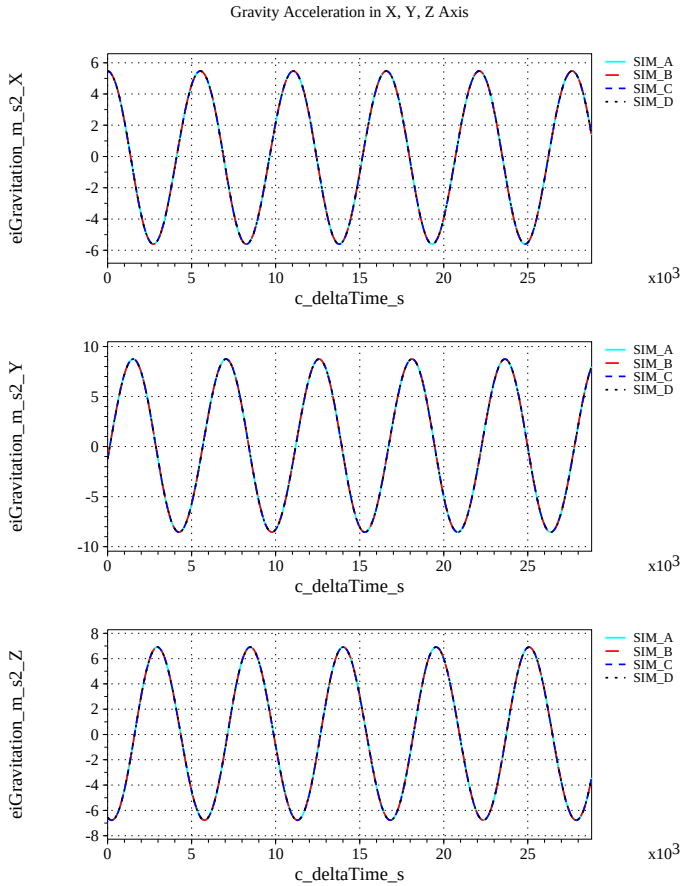

(o) Gravitational Components in Inertial (**X**-**Y**-**Z**) Directions Compared

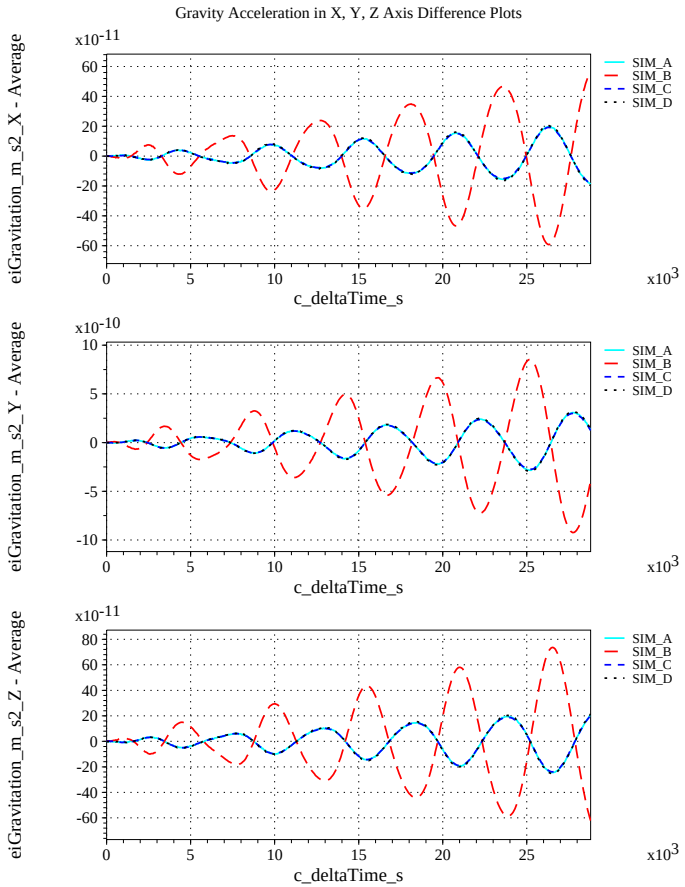

(p) Gravitational Components in Inertial (**X**-**Y**-**Z**) Directions Differenced

Figure 43. Check-case 05C: ISS (Maximal Solar Activity); See Discussion in Section D.2.7 (Concluded)

D.2.8 Check-case 06A – sphere with fixed drag

This section shows cross-plots for three of the selected simulation tools in modeling the dynamics of a sphere in orbit with fixed drag. This scenario is described in Section C.2.8. Figures 44a through 44p compare results between the three simulation tools, as well as the deviances of the outputs from each tool from the ensemble average value.

Orbital check-case 6A was the first of four test cases that applied external forces other than gravitation to the vehicle. This test case applied aerodynamic drag and used a constant density to isolate differences in the modeling or processing of aerodynamic effects. Among the simulations SIM B and SIM C showed agreement in translational and rotational states. SIM D departed from SIM B and C in the translational states and the orbit-relative LVLH orientation because the simulation had apparently not applied aerodynamic drag. SIM D's results were identical to its results for orbital case 2.

As shown on the plots for density (Figure 44d), SIM B and SIM C recorded density as calculated by the MET model. However, both simulations did appear to replace those values with a constant density term in computation of aerodynamic drag as requested.

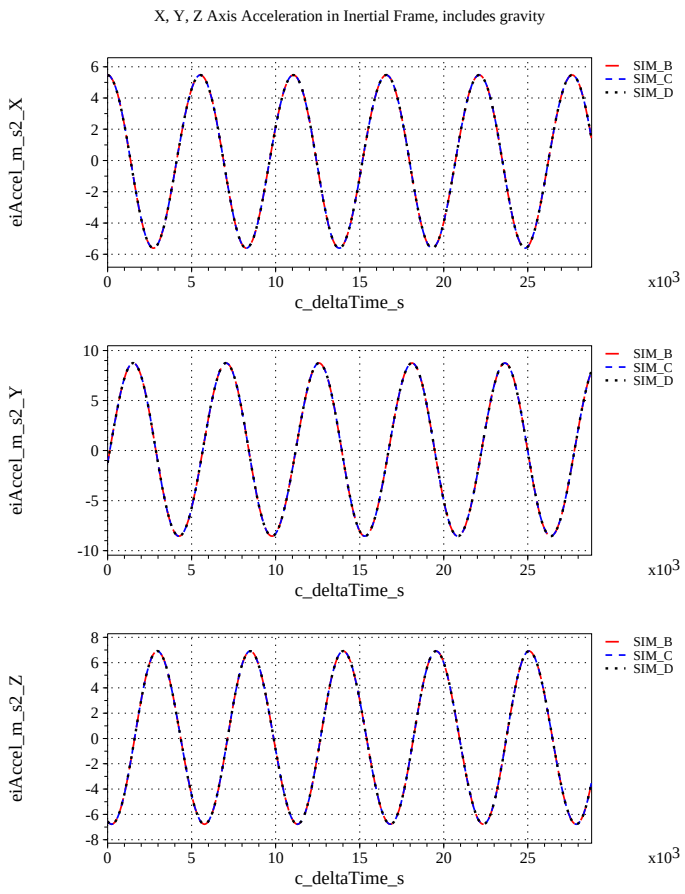

(a) Inertial Accelerations Compared

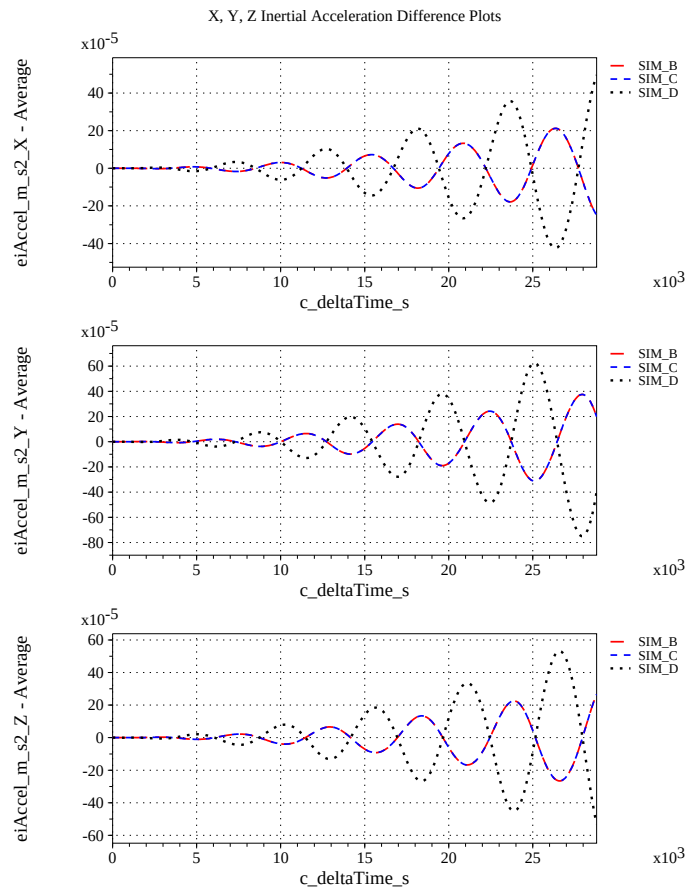

(b) Inertial Accelerations Differenced

Figure 44. Check-case 06A: Sphere with Fixed Drag; See Discussion in Section D.2.8

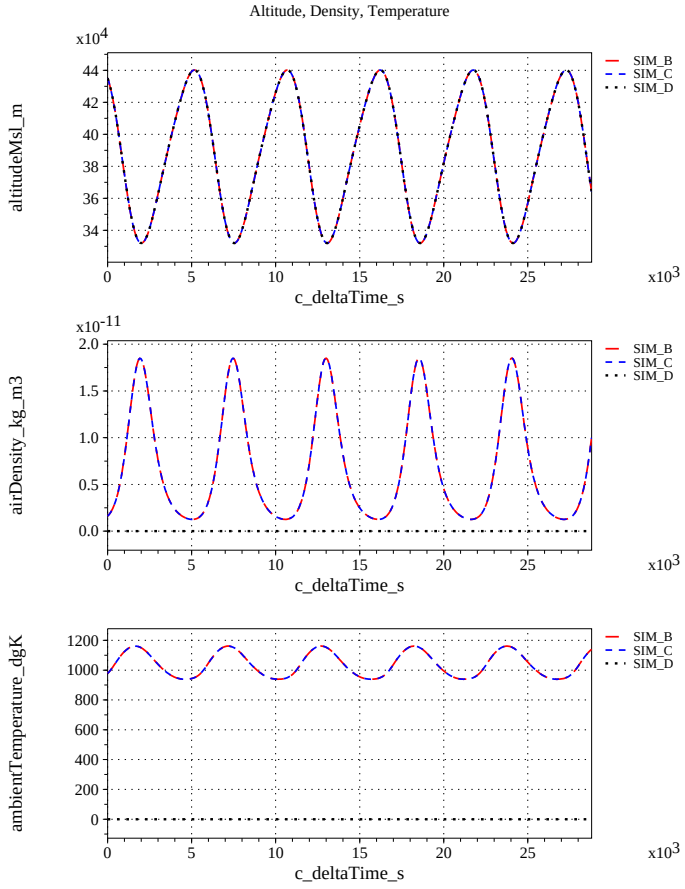

(c) Atmospheric Properties Compared

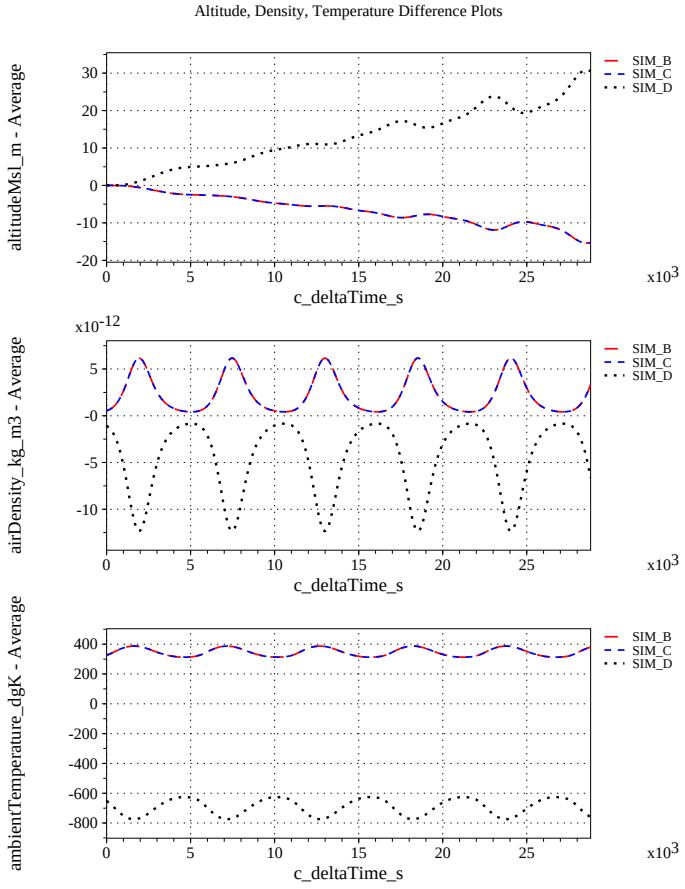

(d) Atmospheric Properties Differenced

Figure 44. Check-case 06A: Sphere with Fixed Drag; See Discussion in Section D.2.8 (Cont'd)

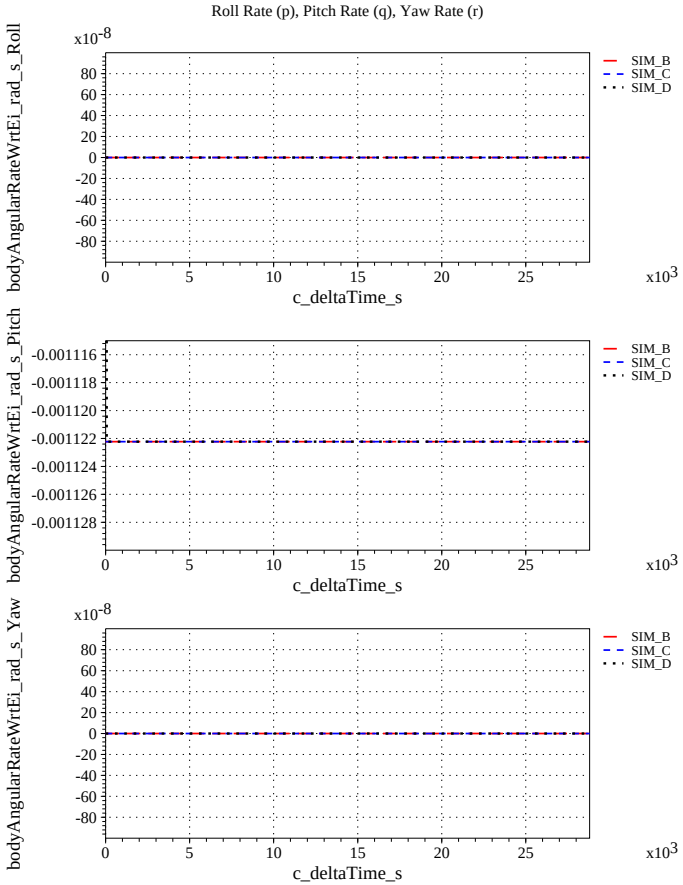

(e) Body-axis Angular Rates Compared

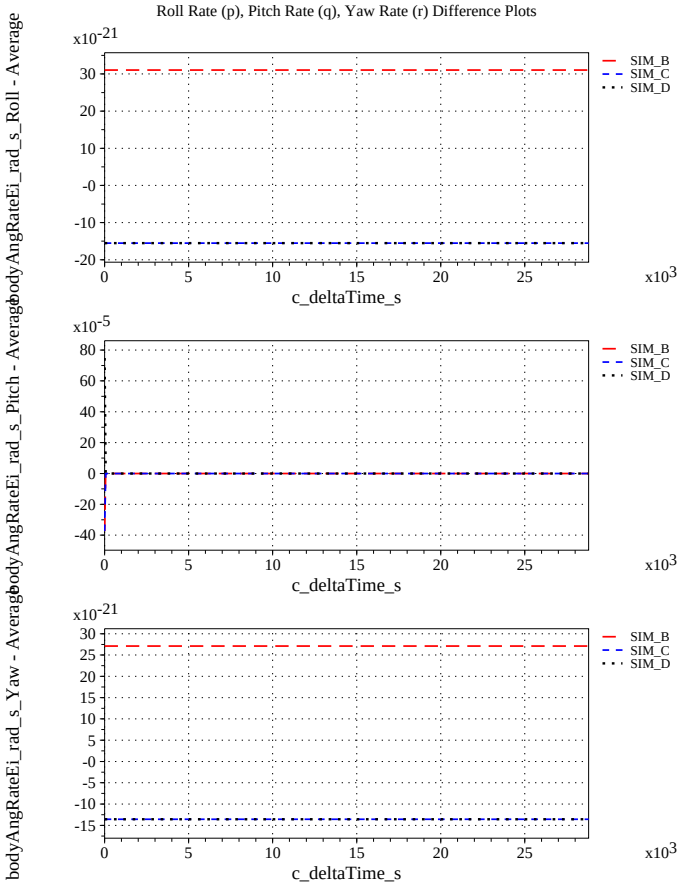

(f) Body-axis Angular Rates Differenced

Figure 44. Check-case 06A: Sphere with Fixed Drag; See Discussion in Section D.2.8 (Cont'd)

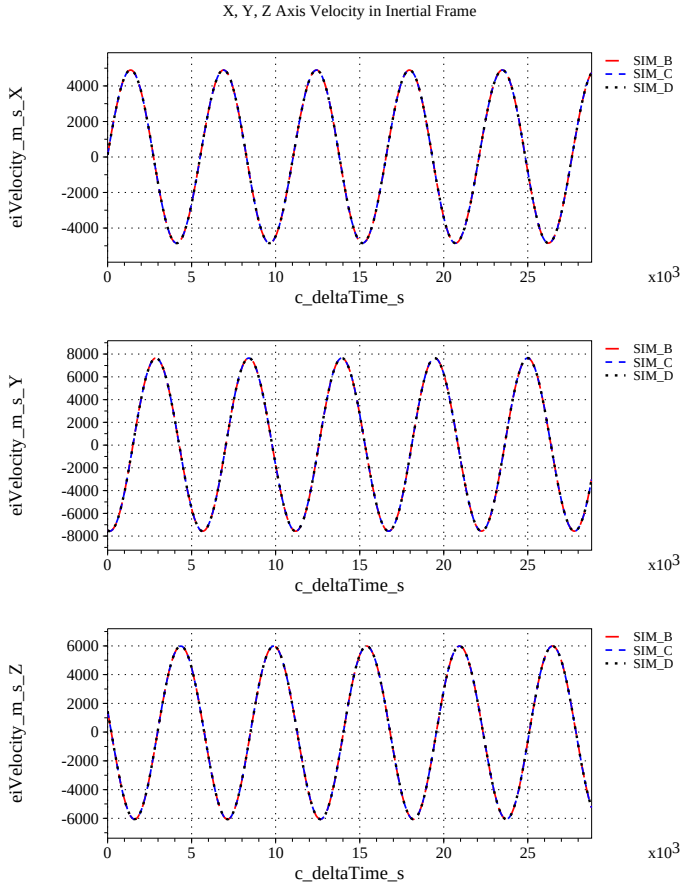

(g) Inertial Velocities Compared

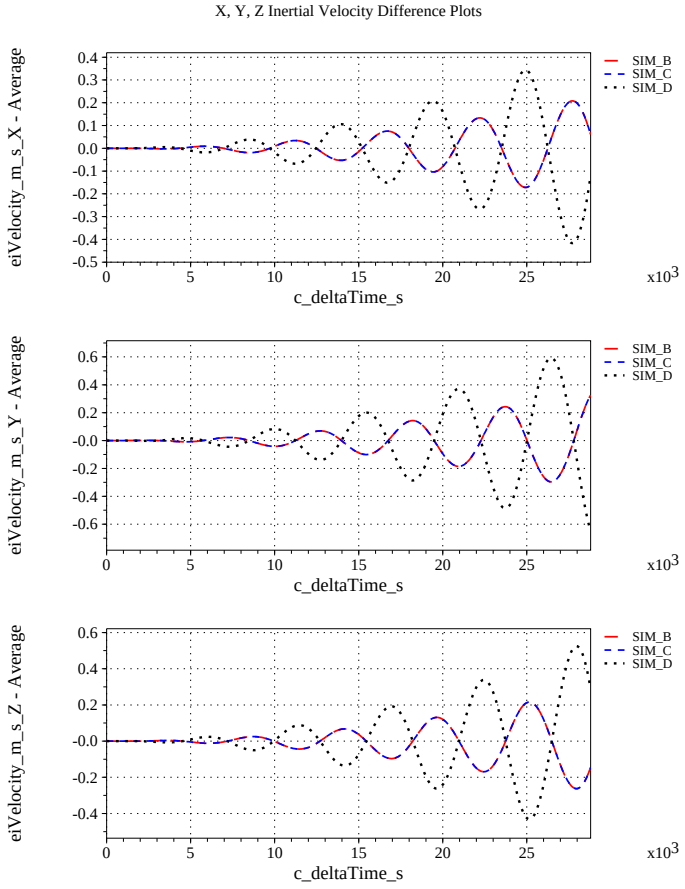

(h) Inertial Velocities Differenced

Figure 44. Check-case 06A: Sphere with Fixed Drag; See Discussion in Section D.2.8 (Cont'd)

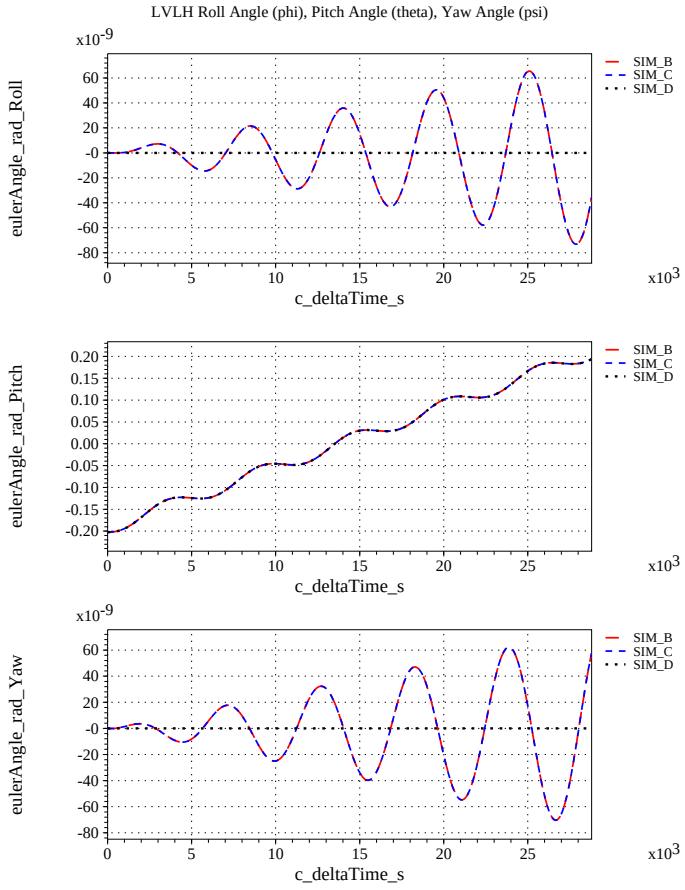

(i) Rotation Angles with Respect to LVLH Frame Compared

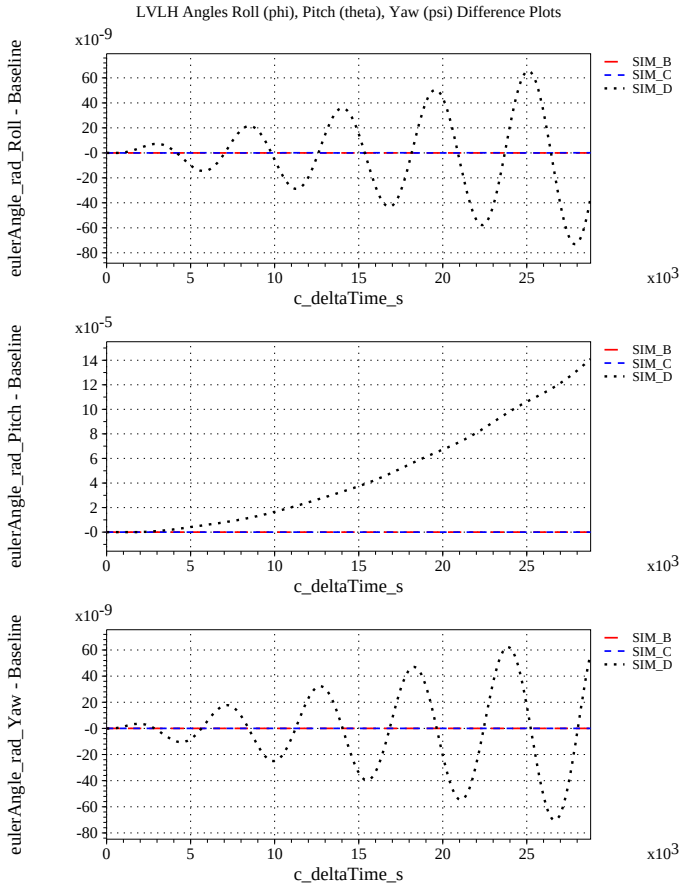

(j) Rotation Angles with Respect to LVLH Frame Differenced

Figure 44. Check-case 06A: Sphere with Fixed Drag; See Discussion in Section D.2.8 (Cont'd)

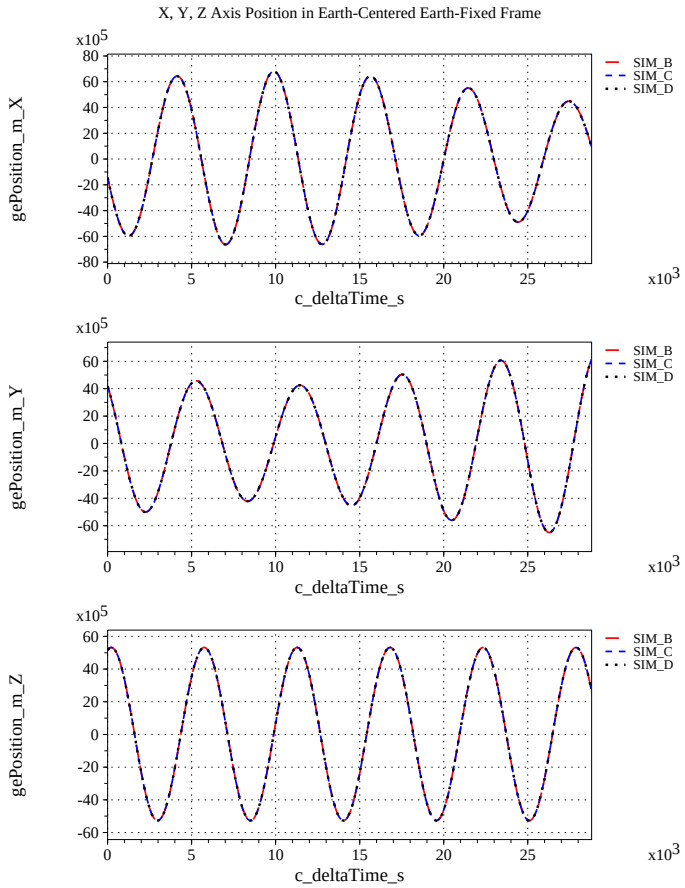

(k) Earth-centered, Earth-fixed Rectangular (X-Y-Z) Positions Compared

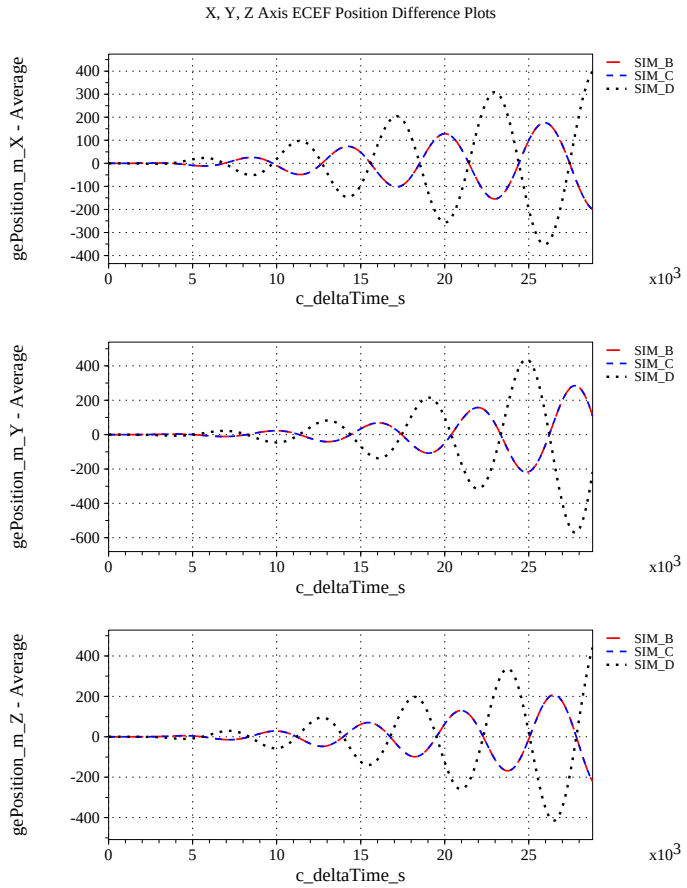

(l) Earth-centered, Earth-fixed Rectangular (X-Y-Z) Positions Differenced

Figure 44. Check-case 06A: Sphere with Fixed Drag; See Discussion in Section D.2.8 (Cont'd)

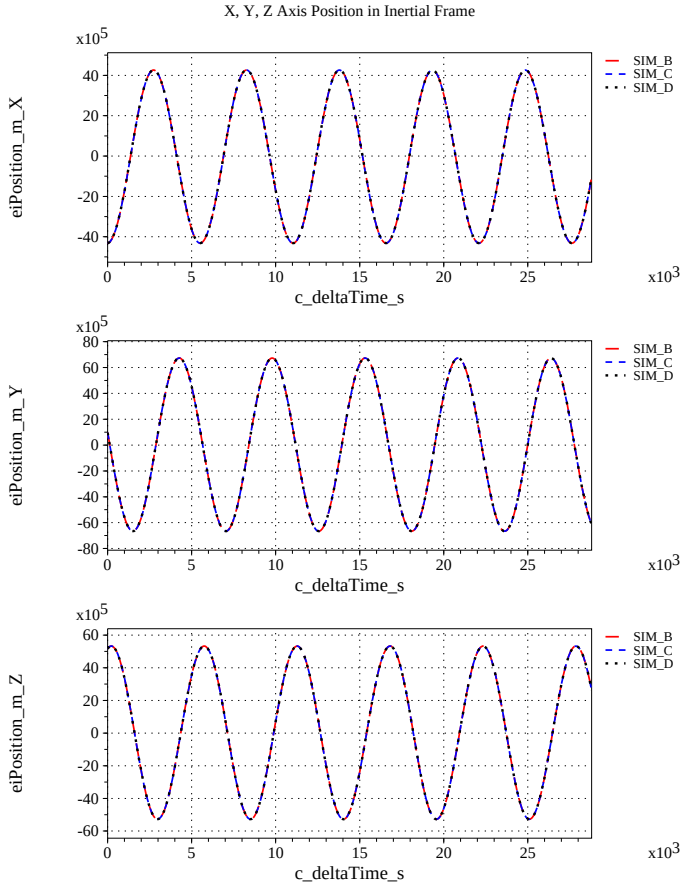

(m) Earth-centered Inertial Rectangular (x-y-z) Positions Compared

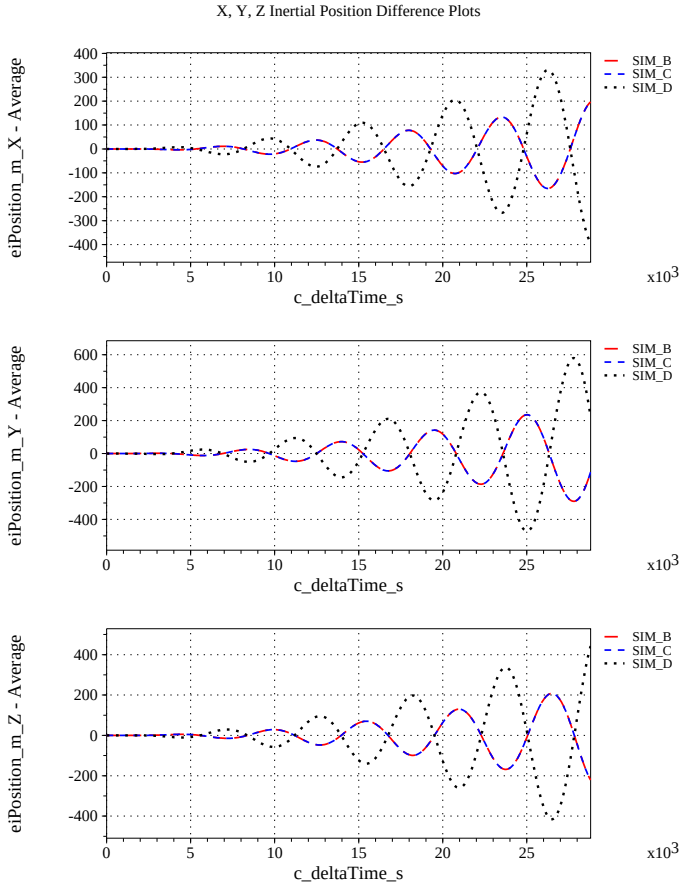

(n) Earth-centered Inertial Rectangular (x-y-z) Positions Differenced

Figure 44. Check-case 06A: Sphere with Fixed Drag; See Discussion in Section D.2.8 (Cont'd)

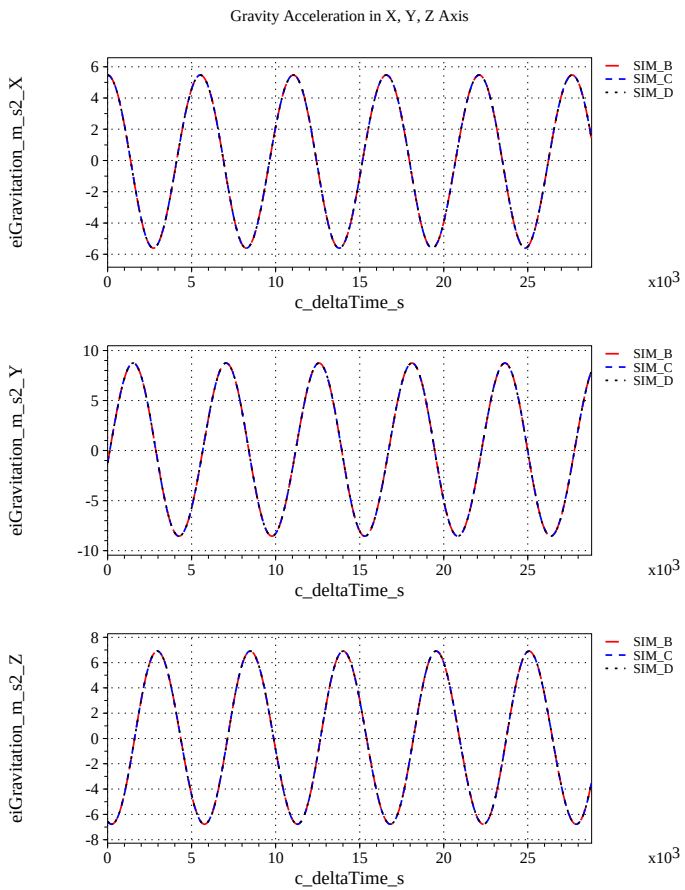

(o) Gravitational Components in Inertial (**X**-**Y**-**Z**) Directions Compared

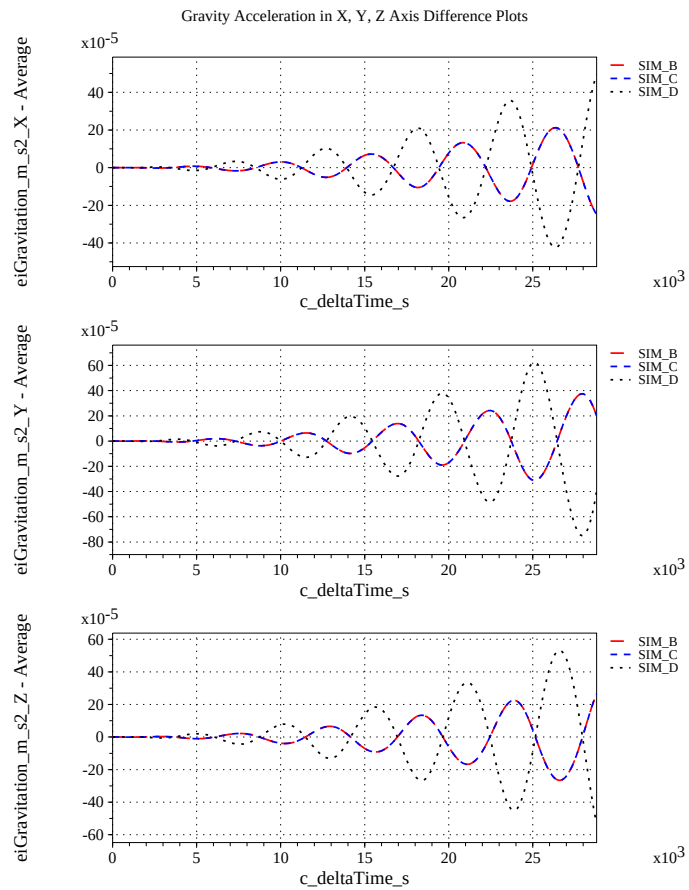

(p) Gravitational Components in Inertial (**X**-**Y**-**Z**) Directions Differenced

Figure 44. Check-case 06A: Sphere with Fixed Drag; See Discussion in Section D.2.8 (Concluded)

D.2.9 Check-case 06B – sphere with dynamic drag

This section shows cross-plots for four of the selected simulation tools in modeling the dynamics of a sphere in orbit with dynamically varying drag. This scenario is described in Section C.2.9. Figures 45a through 45p compare results between the four simulation tools, as well as the deviances of the outputs from each tool from the ensemble average value.

Orbital check-case 6B was the second of four test cases that applied external forces other than gravitation to the vehicle. This test case applied aerodynamic drag using the atmospheric density predicted by the MET model. Thus, differences in MET implementation or its Earth-relative inputs could affect results. Orbital cases 5A though 5C revealed that the simulations implemented different versions of the MET model and that the different versions were the primary cause of atmospheric density differences among the simulations. MET07 (used by SIM A) estimates of atmospheric density were up to 3% larger than MET99 and MET95. This difference in density was the major contributor, via aerodynamic drag, to the differences in the SIM A translational state and orbit-relative LVLH orientation. MET99 and MET95 models more closely agreed on estimated density and, therefore, generated smaller translational state differences between SIM B, SIM C, and SIM D.

The simulations showed agreement in inertial rotational states among the simulations. SIM A showed an improvement in differences over past check-cases, possibly indicating a change its integrator configuration. Overall, differences among the simulations were negligible.

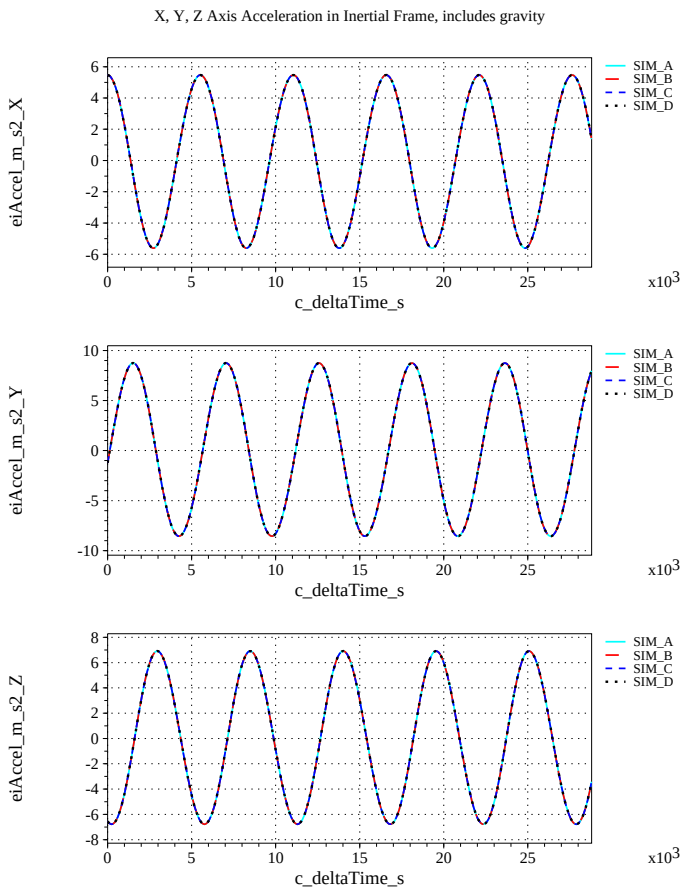

(a) Inertial Accelerations Compared

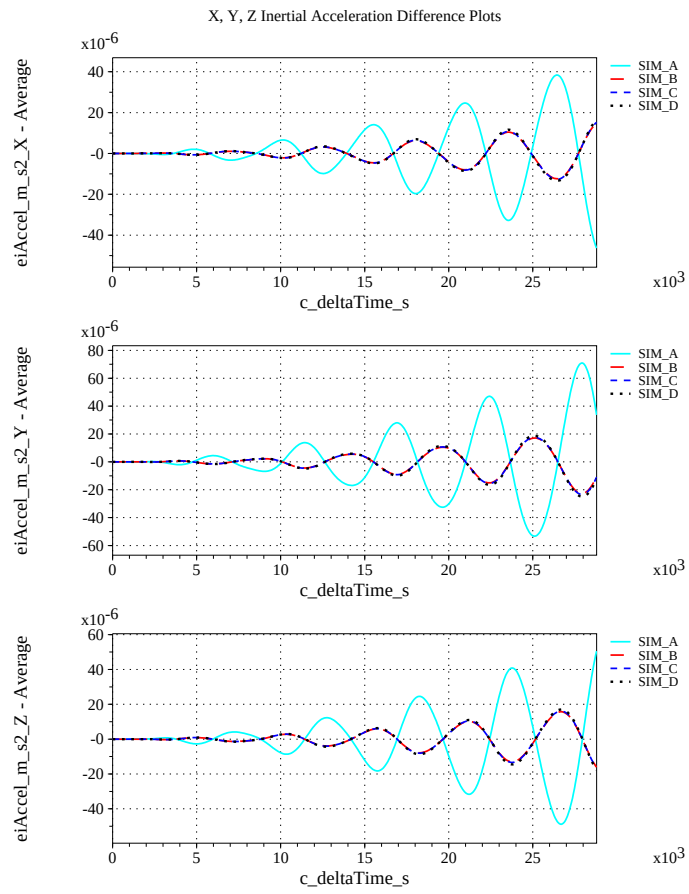

(b) Inertial Accelerations Differenced

Figure 45. Check-case 06B: Sphere with Dynamic Drag; See Discussion in Section D.2.9

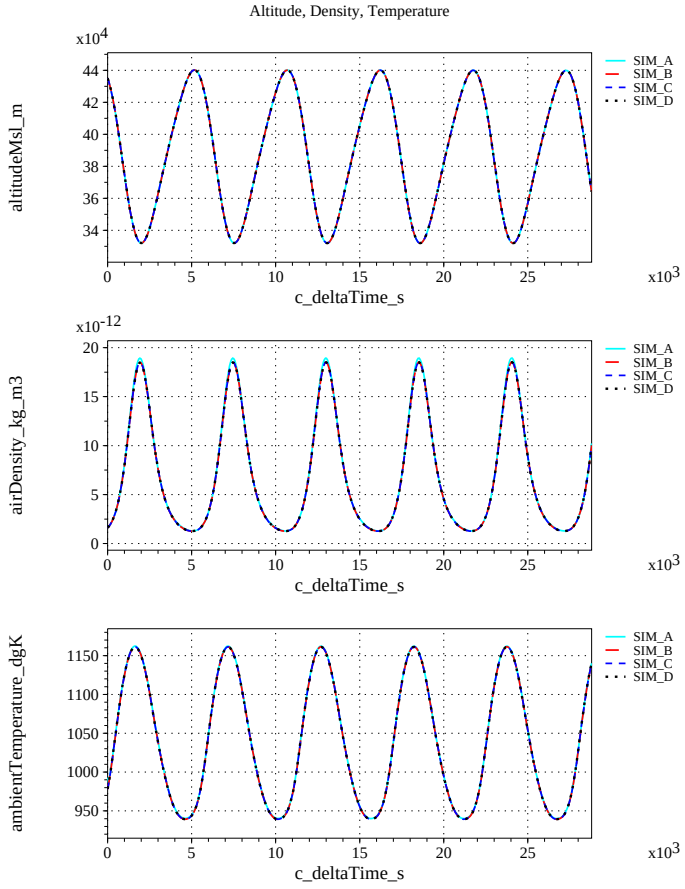

(c) Atmospheric Properties Compared

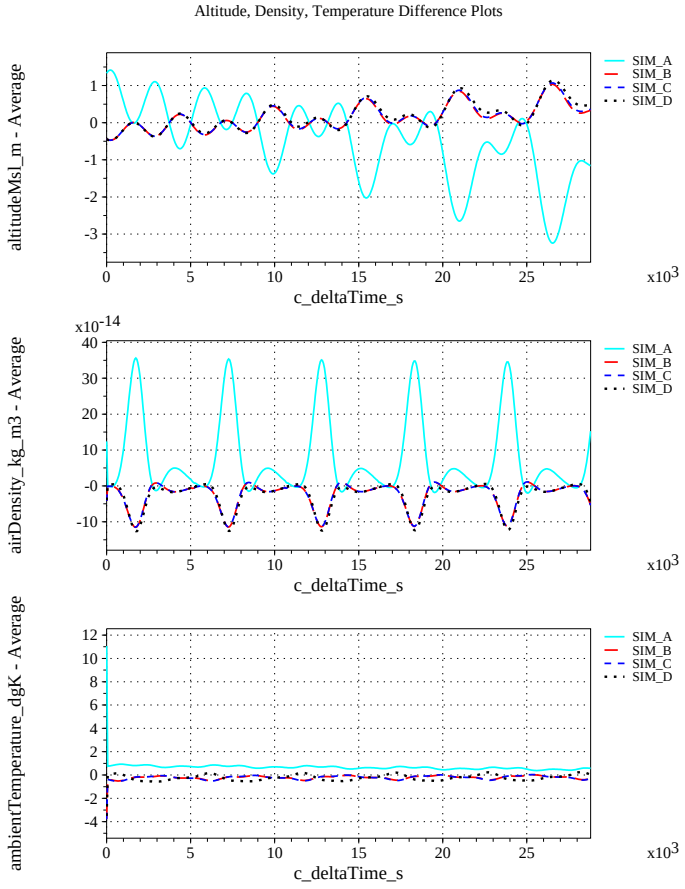

(d) Atmospheric Properties Differenced

Figure 45. Check-case 06B: Sphere with Dynamic Drag; See Discussion in Section D.2.9 (Cont'd)

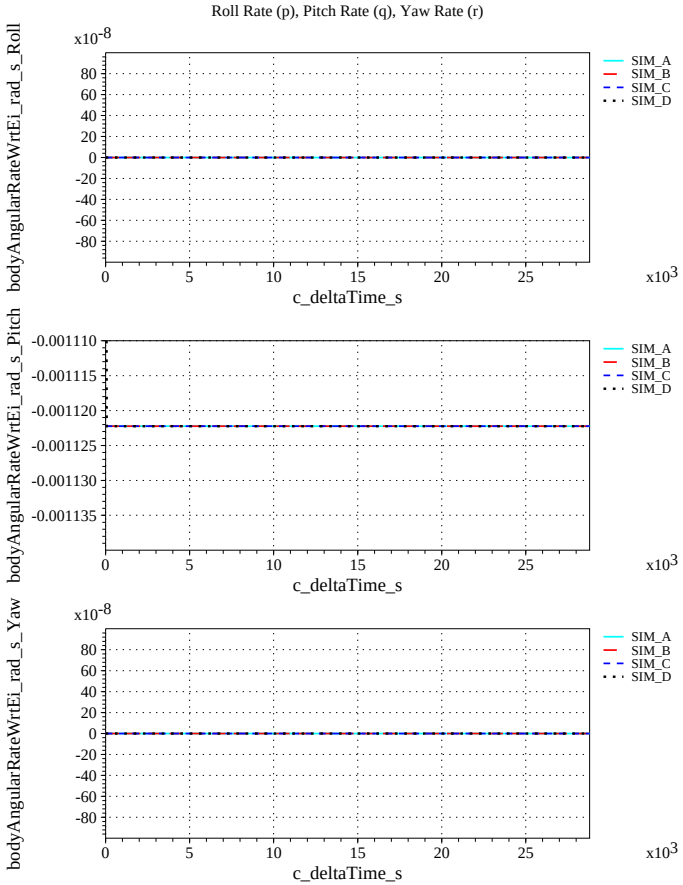

(e) Body-axis Angular Rates Compared

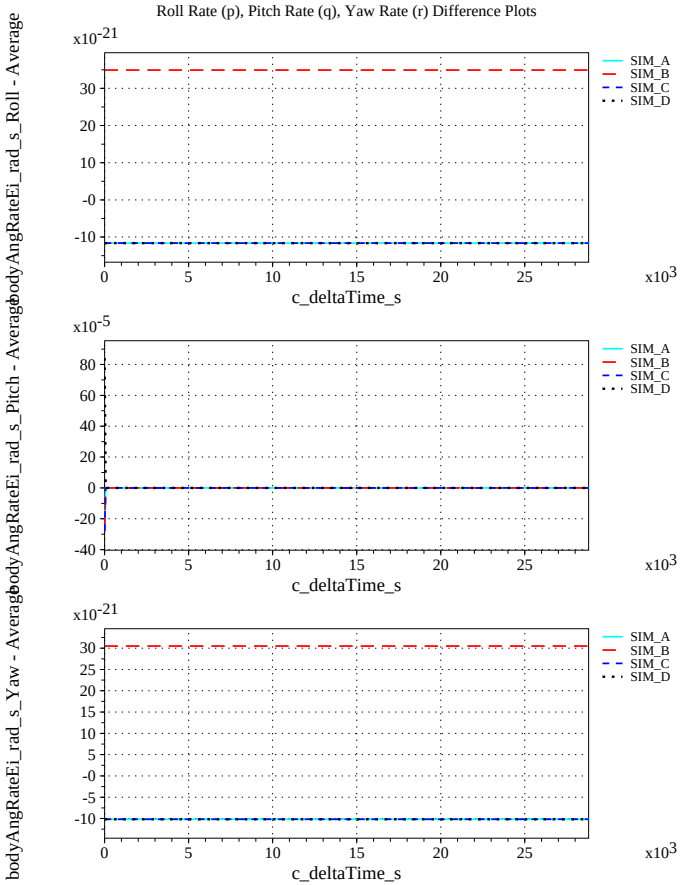

(f) Body-axis Angular Rates Differenced

Figure 45. Check-case 06B: Sphere with Dynamic Drag; See Discussion in Section D.2.9 (Cont'd)

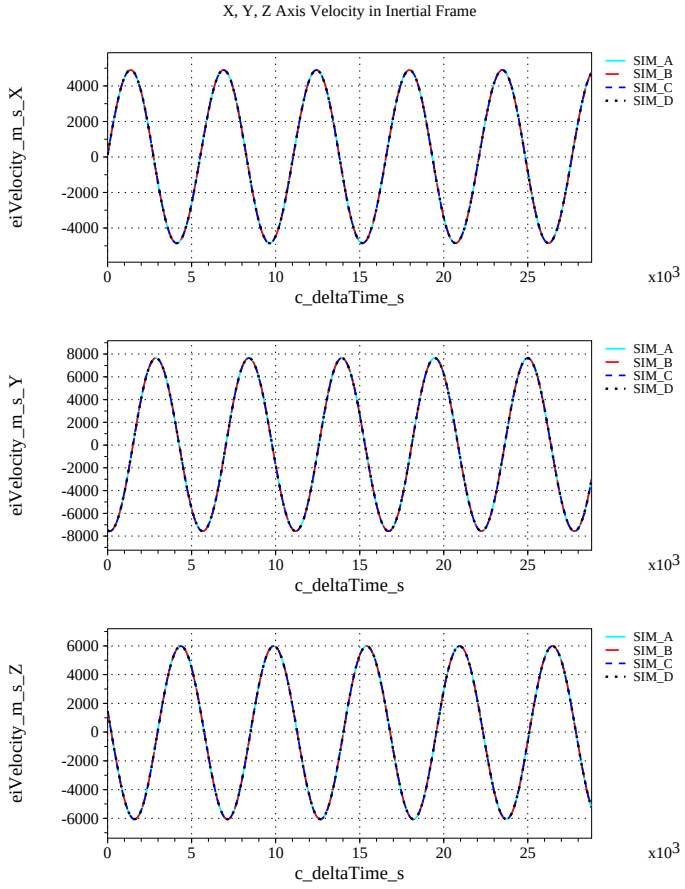

(g) Inertial Velocities Compared

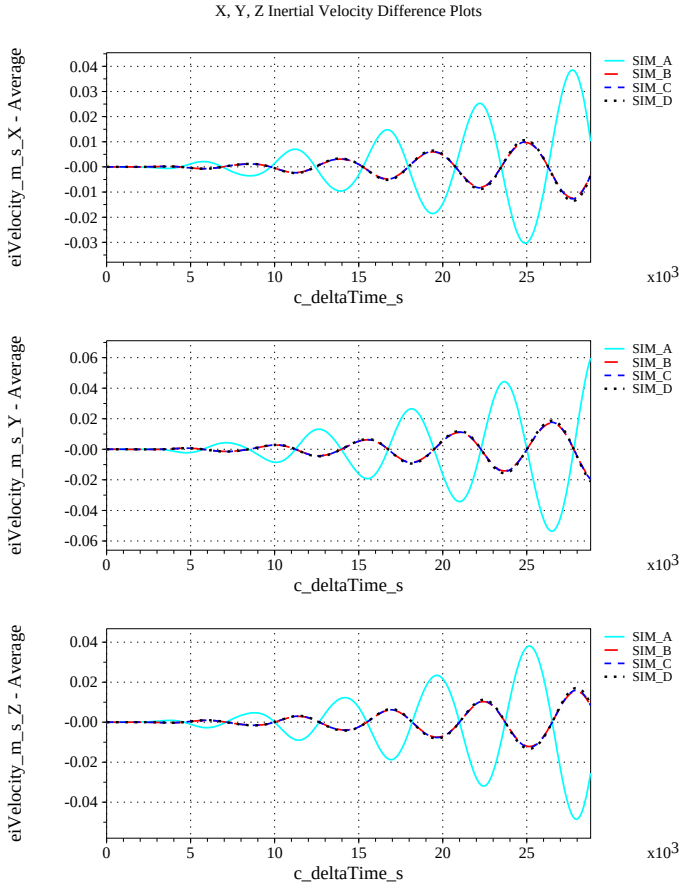

(h) Inertial Velocities Differenced

Figure 45. Check-case 06B: Sphere with Dynamic Drag; See Discussion in Section D.2.9 (Cont'd)

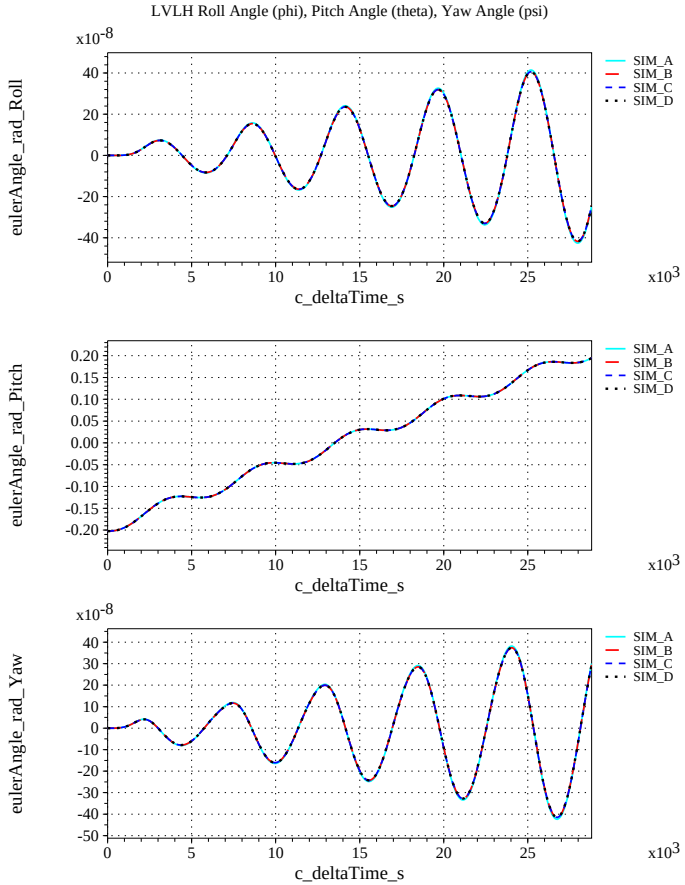

(i) Rotation Angles with Respect to LVLH Frame Compared

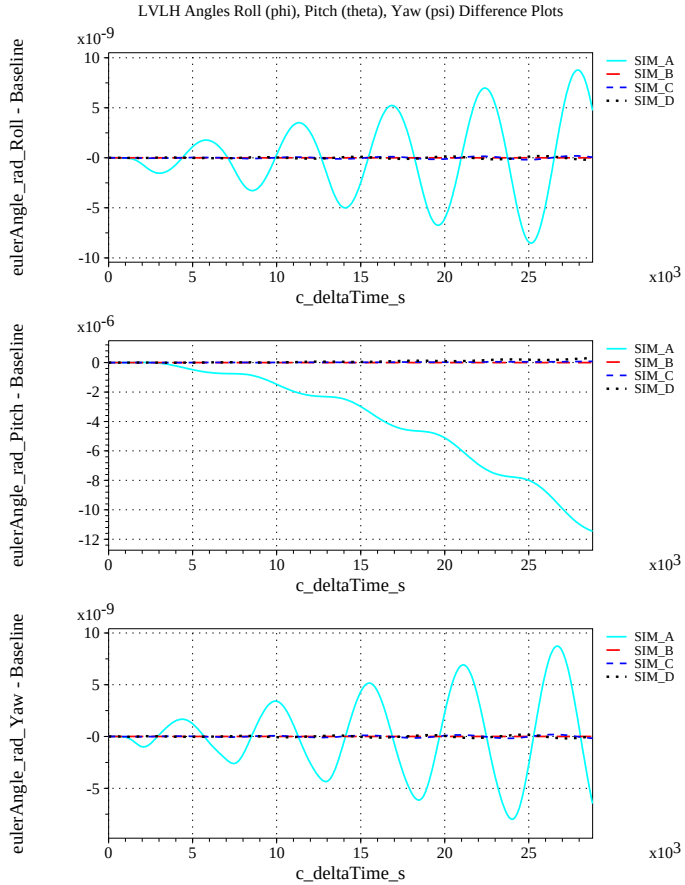

(j) Rotation Angles with Respect to LVLH Frame Differenced

Figure 45. Check-case 06B: Sphere with Dynamic Drag; See Discussion in Section D.2.9 (Cont'd)

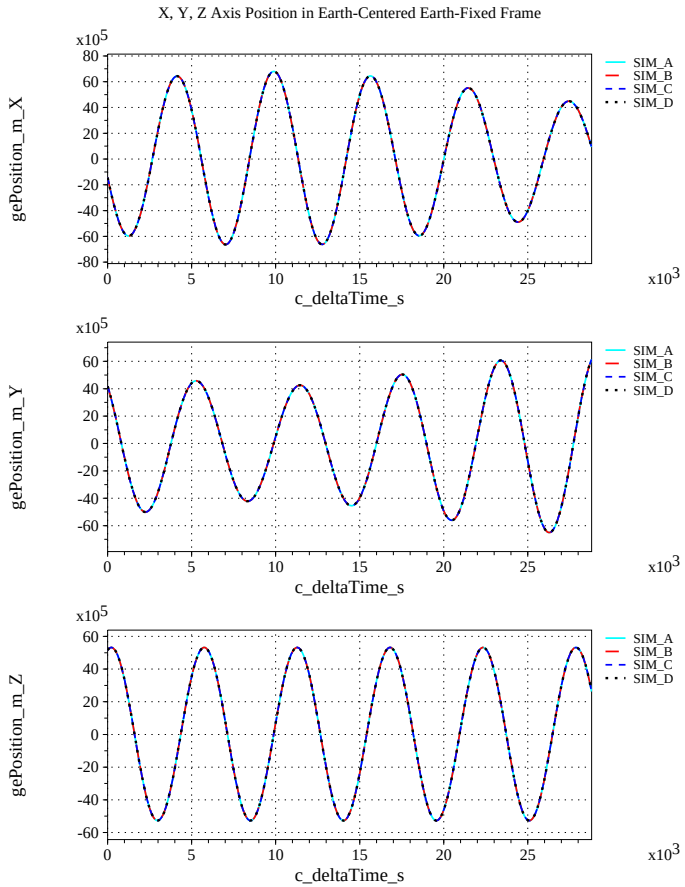

(k) Earth-centered, Earth-fixed Rectangular (X-Y-Z) Positions Compared

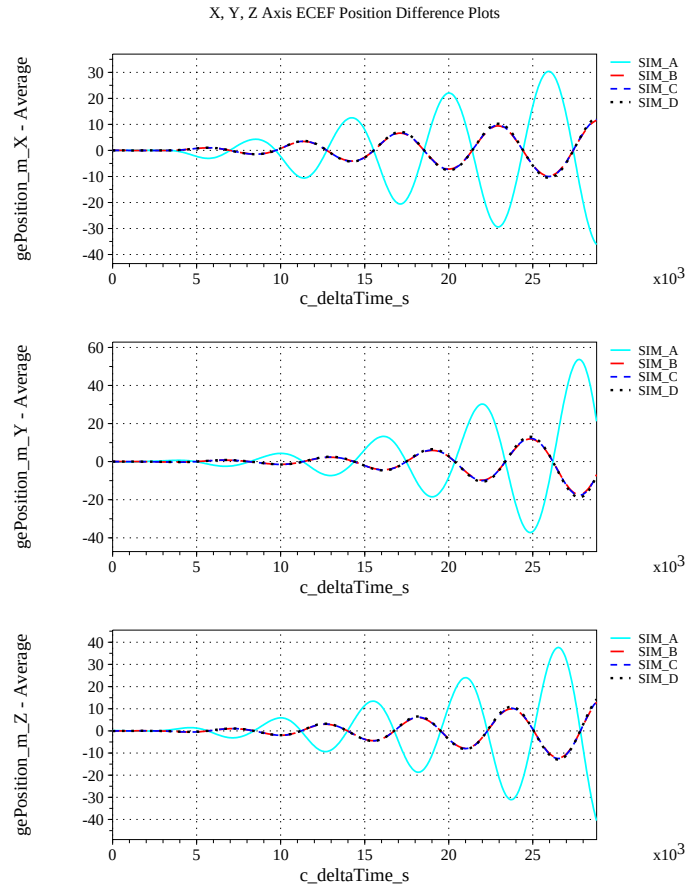

(l) Earth-centered, Earth-fixed Rectangular (X-Y-Z) Positions Differenced

Figure 45. Check-case 06B: Sphere with Dynamic Drag; See Discussion in Section D.2.9 (Cont'd)

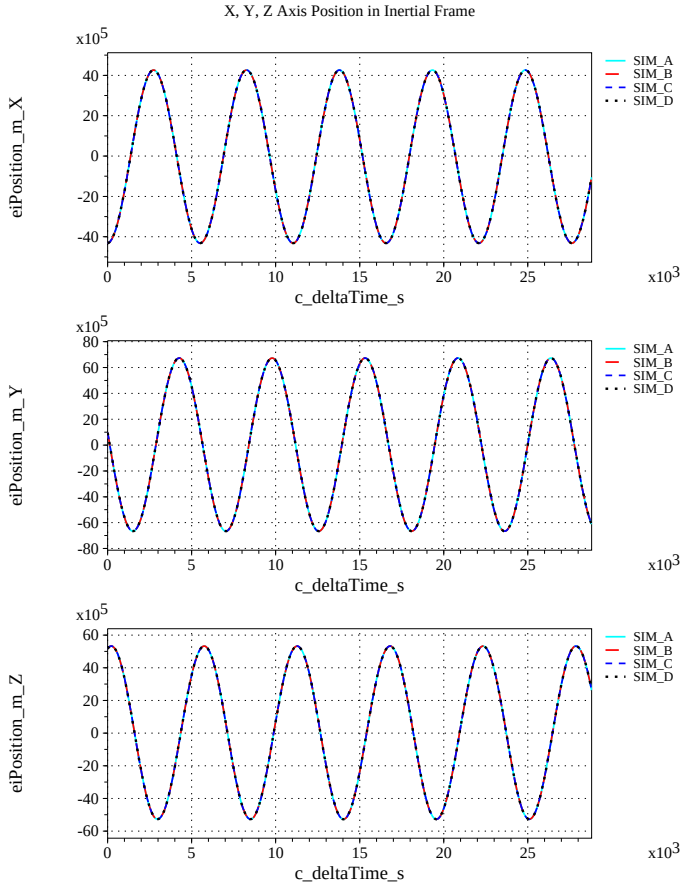

(m) Earth-centered Inertial Rectangular (x-y-z) Positions Compared

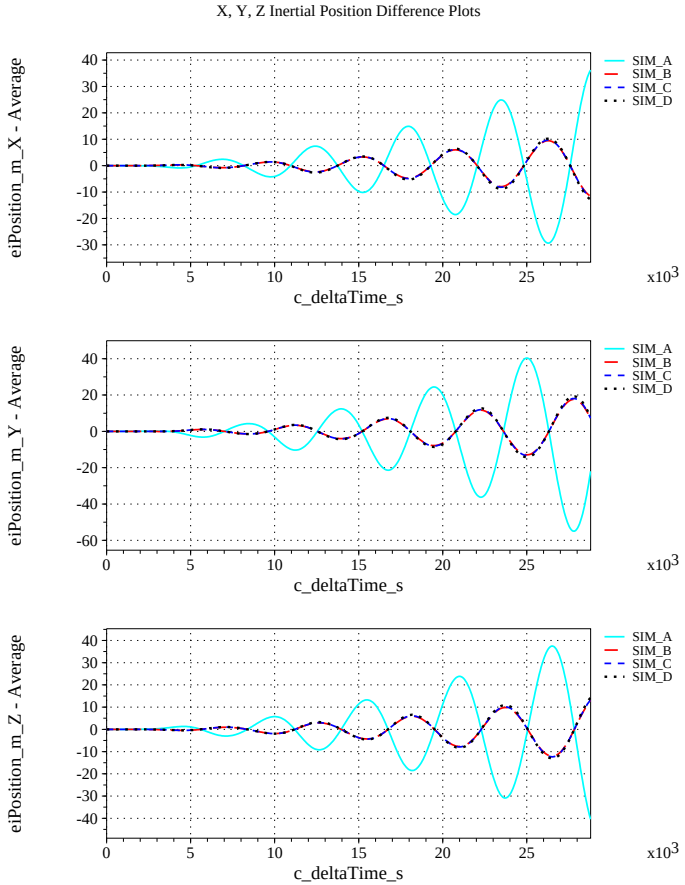

(n) Earth-centered Inertial Rectangular (x-y-z) Positions Differenced

Figure 45. Check-case 06B: Sphere with Dynamic Drag; See Discussion in Section D.2.9 (Cont'd)

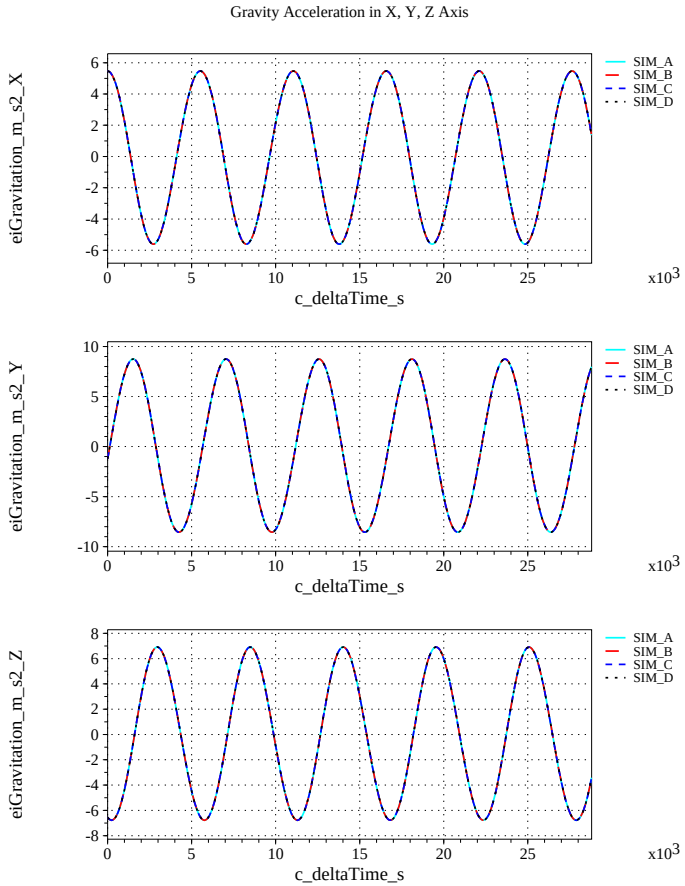

(o) Gravitational Components in Inertial (**X**-**Y**-**Z**) Directions Compared

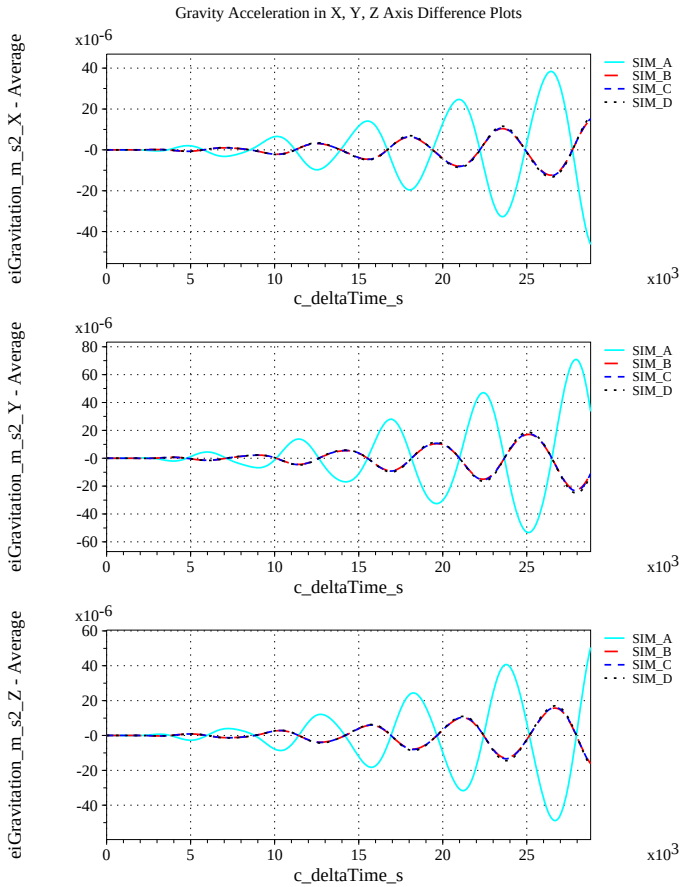

(p) Gravitational Components in Inertial (**X**-**Y**-**Z**) Directions Differenced

Figure 45. Check-case 06B: Sphere with Dynamic Drag; See Discussion in Section D.2.9 (Concluded)

D.2.10 Check-case 06C – cylinder undergoing plane change firing

This section shows cross-plots for four of the selected simulation tools in modeling the dynamics of a cylinder in orbit performing a plane change maneuver with intermittent propulsion. This scenario is described in Section C.2.10. Figures 46a through 46p compare results between the four simulation tools, as well as the deviances of the outputs from each tool from the ensemble average value.

Orbital check-case 6C was the third of four test cases that applied external forces other than gravitation to the vehicle. This test case applied engine thrust to execute an orbital-plane change maneuver. The engine thrust was modeled as a square pulse. A square acceleration can significantly increase the integration error for some numerical methods. Furthermore, a single frame difference in starting the pulse and/or ending it could have significant impact on velocity and position results over time, due to the single- and double-integration of a small error. Also, differences in vehicle orientation over the course of the burn could contribute to differences in velocity and position. The data recording rate was not fast enough to observe the start and end of the pulse in each simulation nor was it possible to identify the velocity that followed the starting and ending frames (which could have been analyzed for sudden jumps in integration error). Nevertheless, causes other than difference integration methods were ruled out. First, the differences in orientation between the simulations were insignificant and did not explain the observed differences in position and velocity. Next, SIM B was used to explore the effects of modifying start and end times of the pulse. Elongating the pulse by even 0.001 sec caused much larger differences in translational states than are shown in the plots. Adding a lead or lag to the pulse of up to 0.01 sec produced differences of similar magnitude but not similar behavior. Overall, the differences among the simulations in ΔV following the pulse were very small. The largest difference was approximately 0.001 m/s out of a total ΔV of about 2,700 m/s. However, these small differences contributed over time to differences in inertial position of up to 100 m after a simulated flight time of 8 hours.

The simulations agreed on inertial rotational states; differences in rates and attitudes among the simulations were negligible. Differences in the orbit-relative LVLH orientation were larger and caused by the small differences in the orbit defined by the translational states.

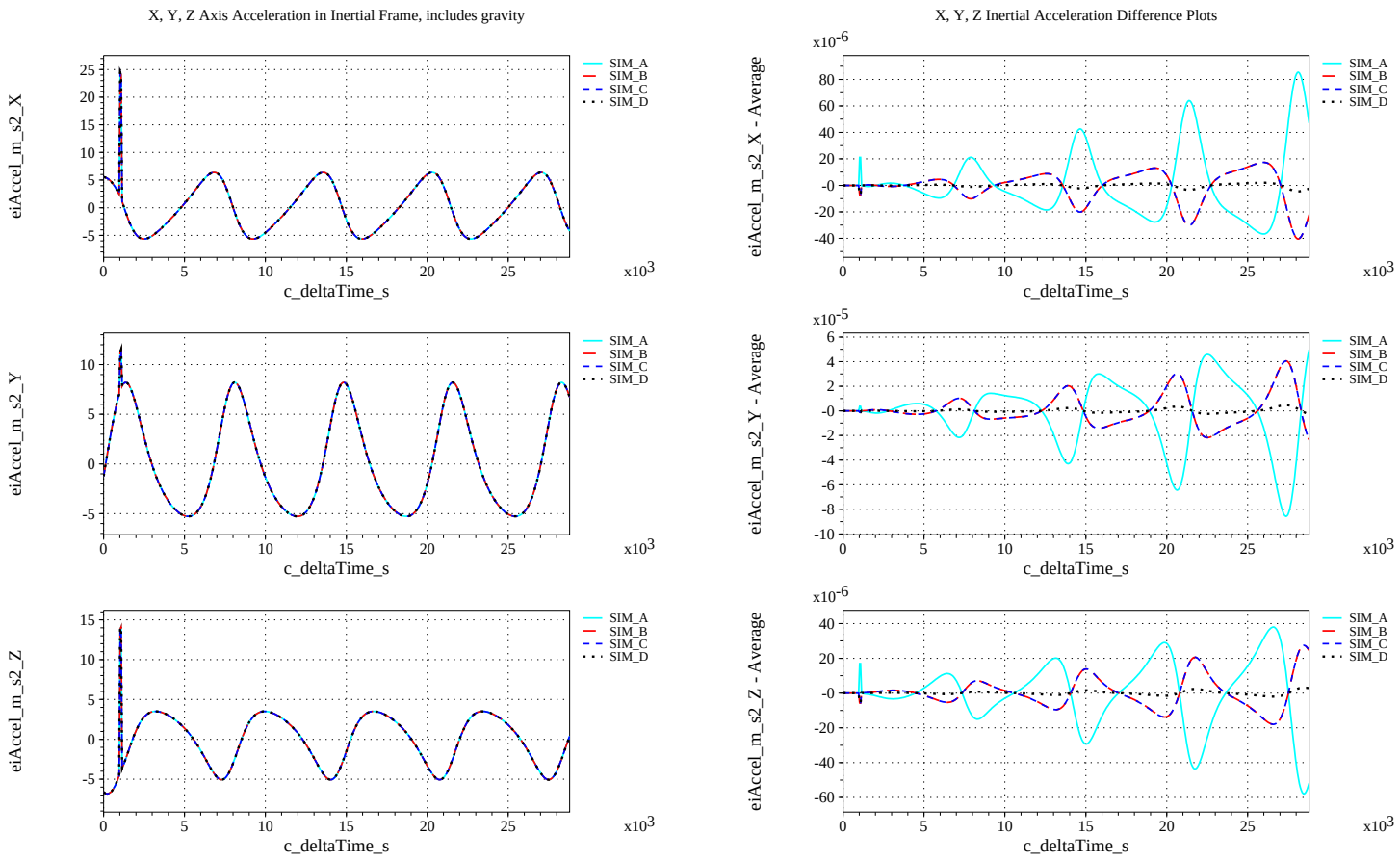

(a) Inertial Accelerations Compared

(b) Inertial Accelerations Differenced

Figure 46. Check-case 06C: Cylinder Undergoing Plane Change Firing; See Discussion in Section D.2.10

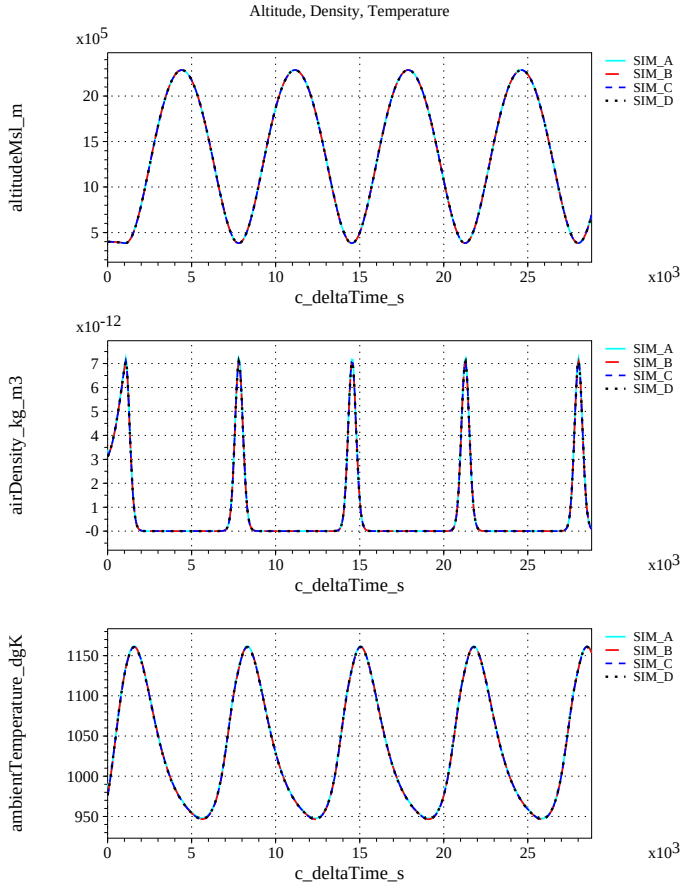

(c) Atmospheric Properties Compared

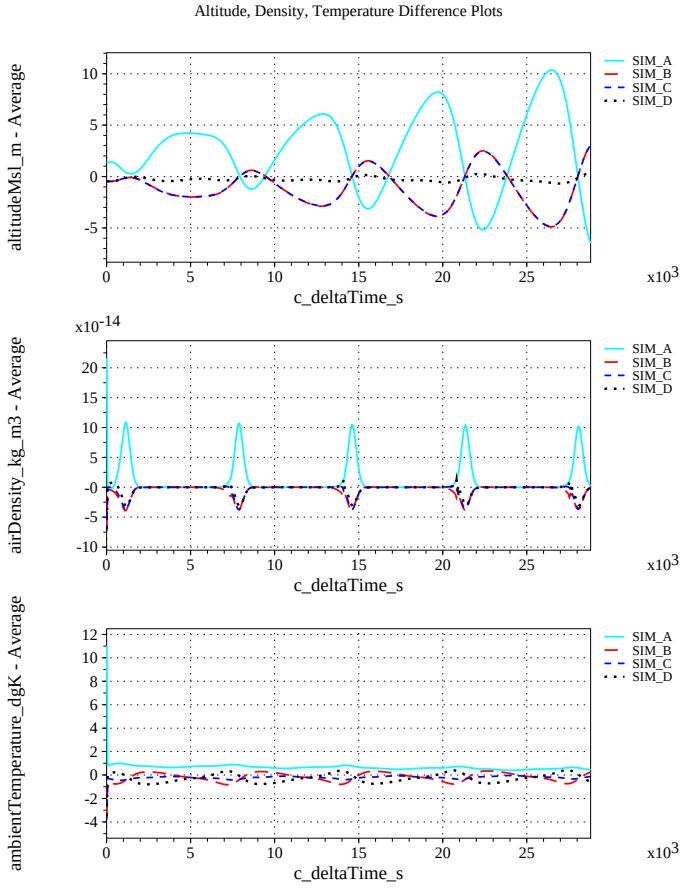

(d) Atmospheric Properties Differenced

Figure 46. Check-case 06C: Cylinder Undergoing Plane Change Firing; See Discussion in Section D.2.10 (Cont'd)

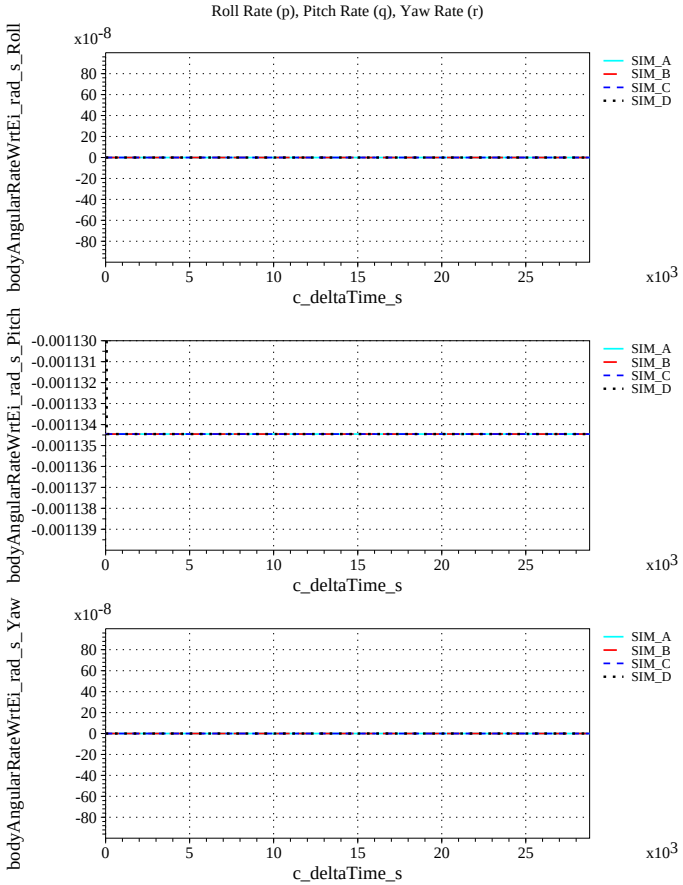

(e) Body-axis Angular Rates Compared

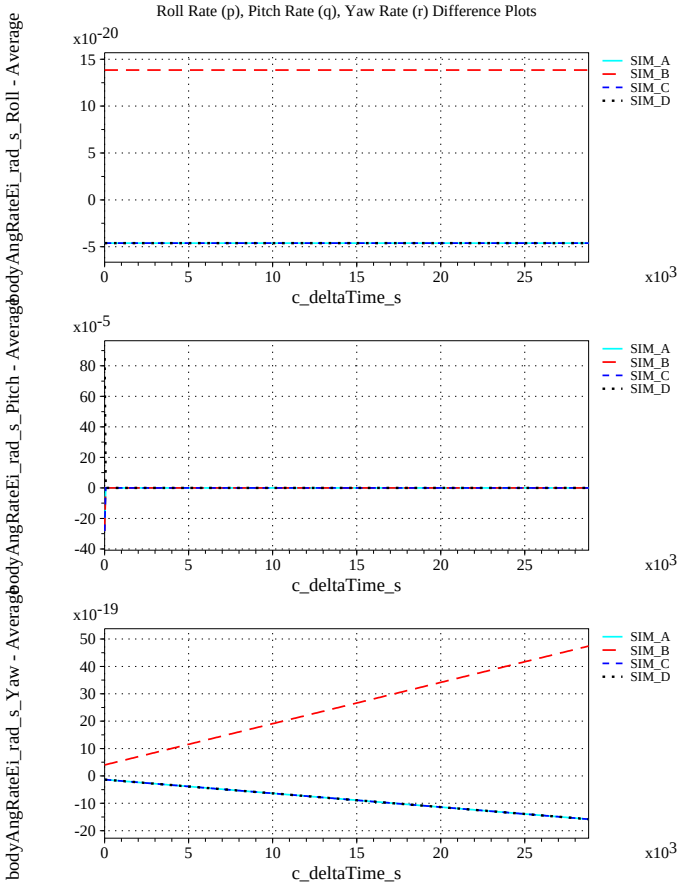

(f) Body-axis Angular Rates Differenced

Figure 46. Check-case 06C: Cylinder Undergoing Plane Change Firing; See Discussion in Section D.2.10 (Cont'd)

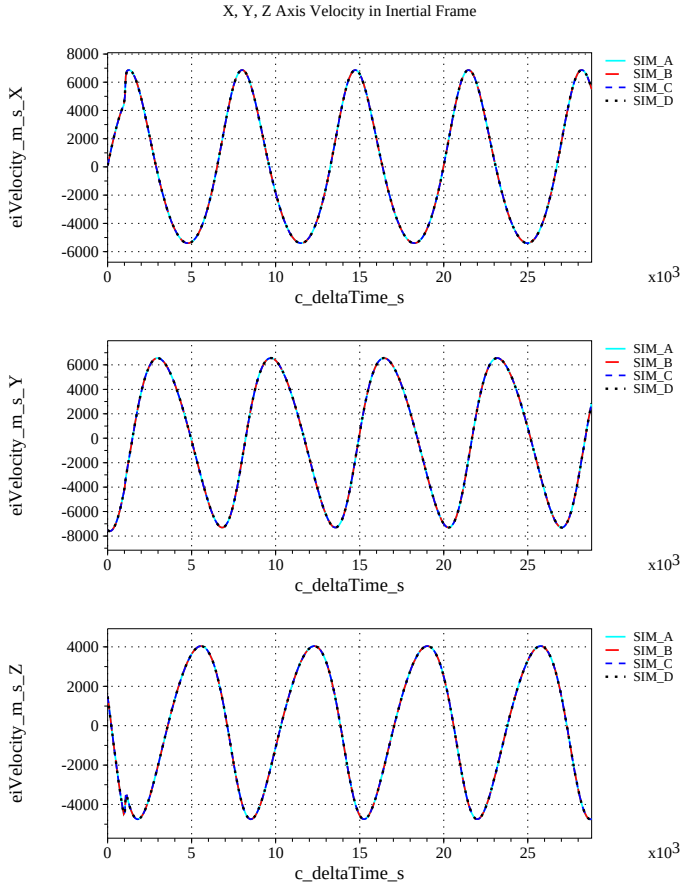

(g) Inertial Velocities Compared

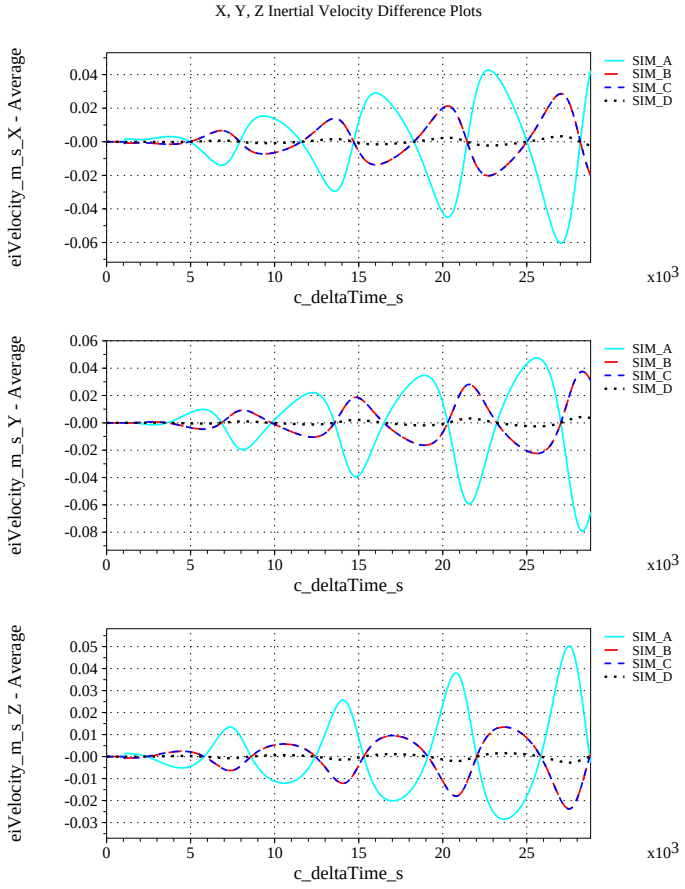

(h) Inertial Velocities Differenced

Figure 46. Check-case 06C: Cylinder Undergoing Plane Change Firing; See Discussion in Section D.2.10 (Cont'd)

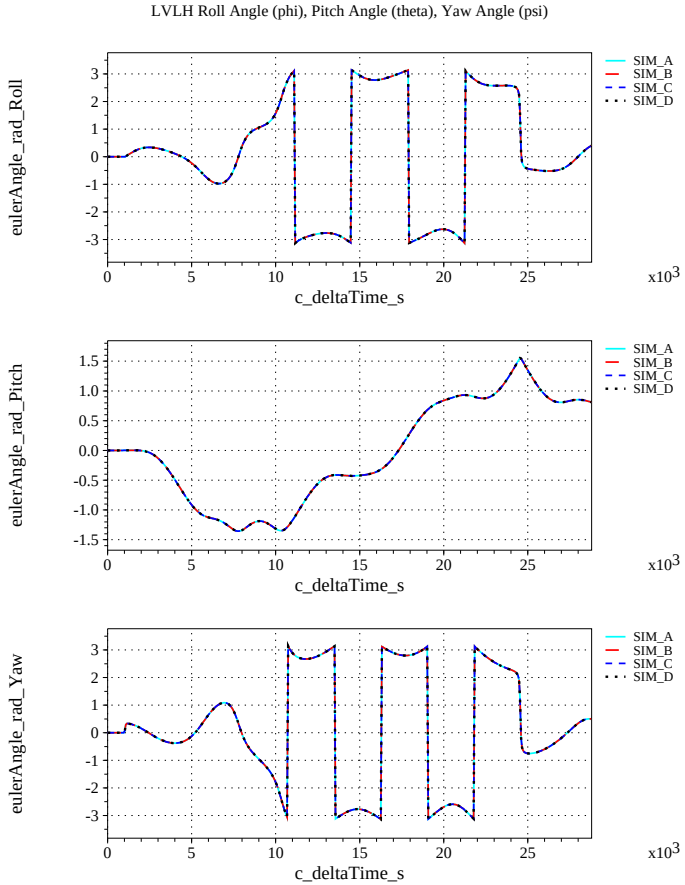

(i) Rotation Angles with Respect to LVLH Frame Compared

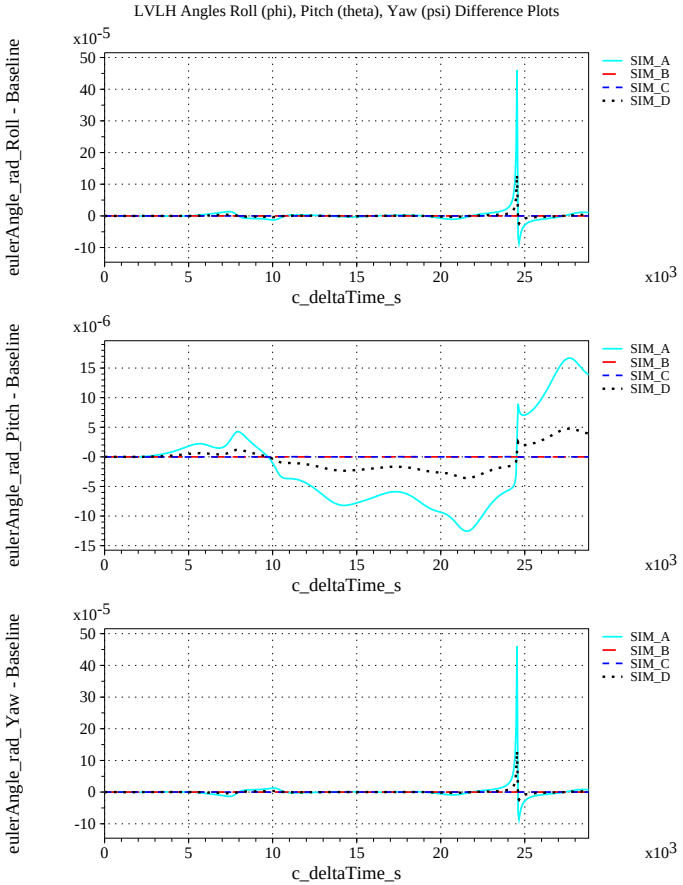

(j) Rotation Angles with Respect to LVLH Frame Differenced

Figure 46. Check-case 06C: Cylinder Undergoing Plane Change Firing; See Discussion in Section D.2.10 (Cont'd)

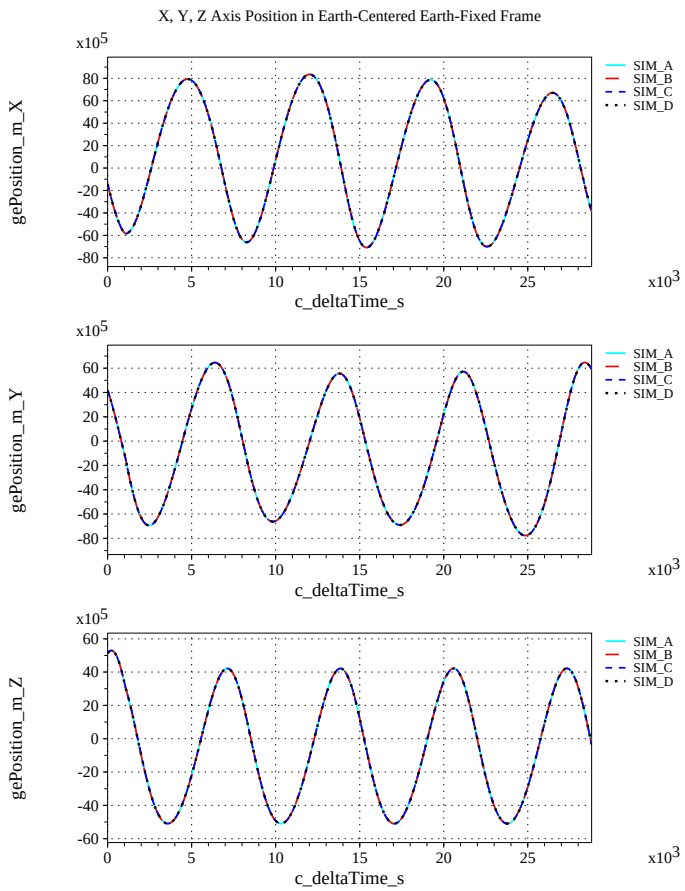

(k) Earth-centered, Earth-fixed Rectangular (X-Y-Z) Positions Compared

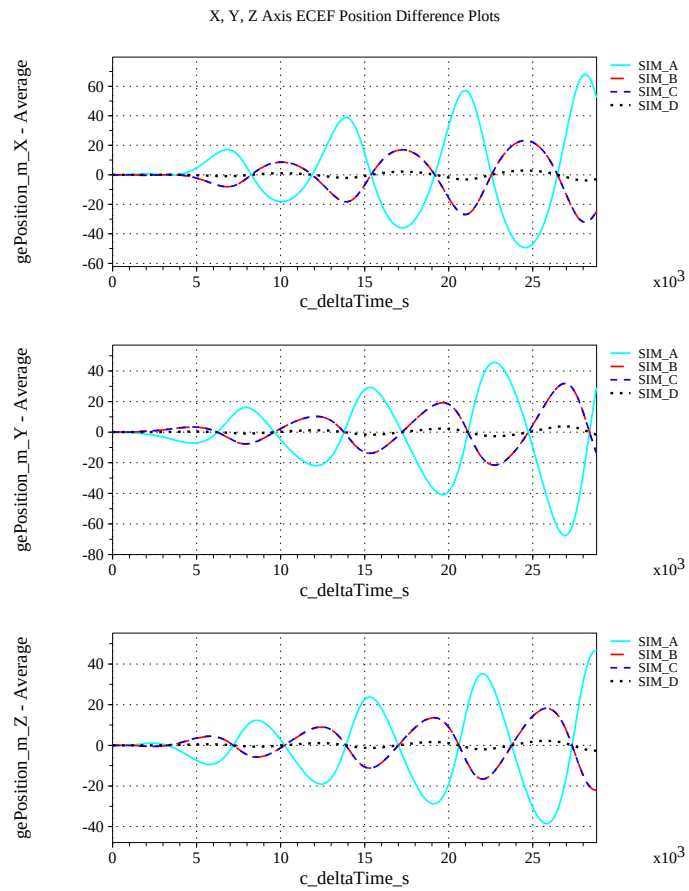

(l) Earth-centered, Earth-fixed Rectangular (X-Y-Z) Positions Differenced

Figure 46. Check-case 06C: Cylinder Undergoing Plane Change Firing; See Discussion in Section D.2.10 (Cont'd)

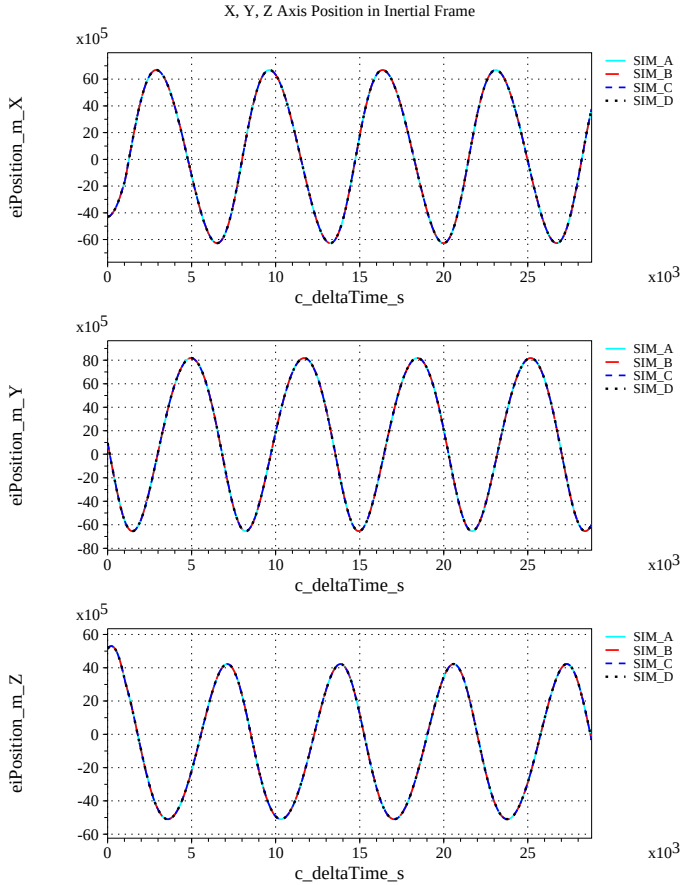

(m) Earth-centered Inertial Rectangular (x-y-z) Positions Compared

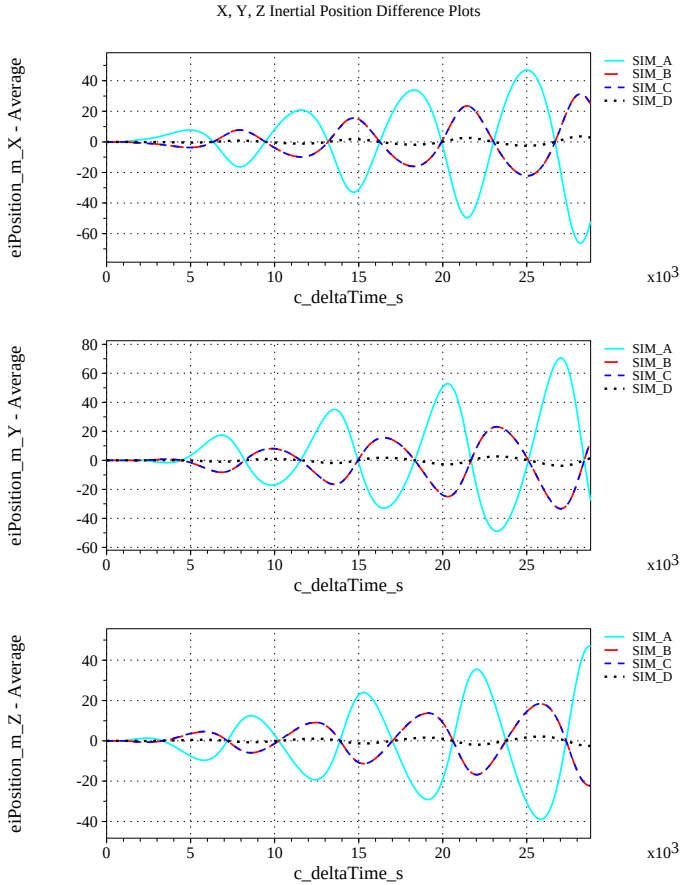

(n) Earth-centered Inertial Rectangular (x-y-z) Positions Differenced

Figure 46. Check-case 06C: Cylinder Undergoing Plane Change Firing; See Discussion in Section D.2.10 (Cont'd)

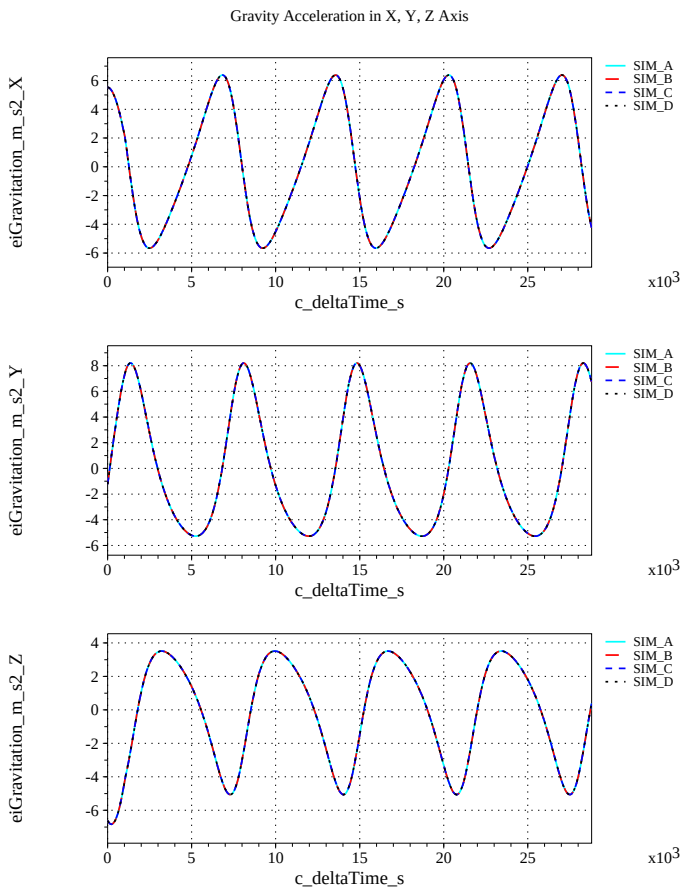

(o) Gravitational Components in Inertial (**X**-**Y**-**Z**) Directions Compared

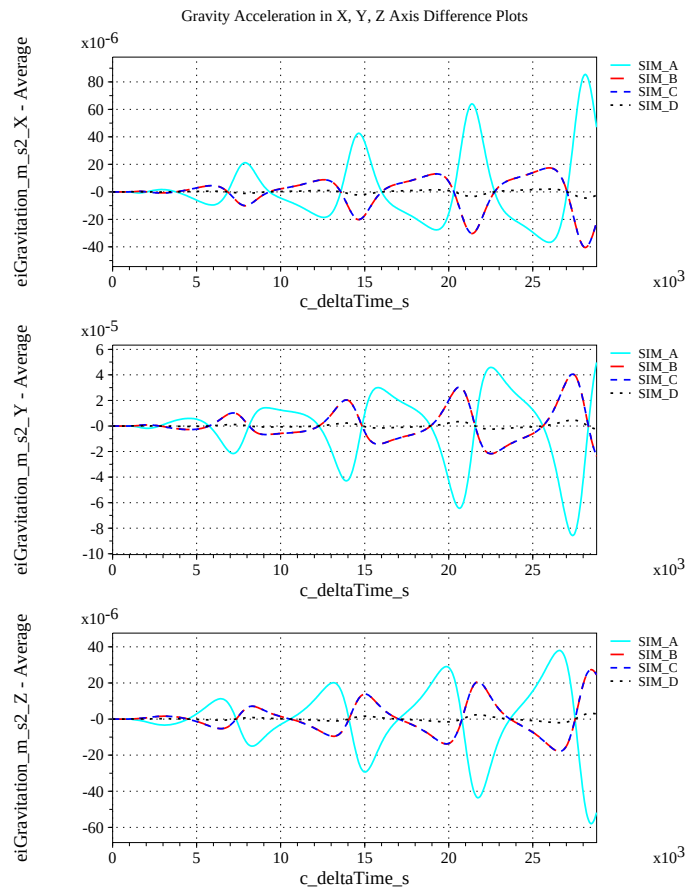

(p) Gravitational Components in Inertial (**X**-**Y**-**Z**) Directions Differenced

Figure 46. Check-case 06C: Cylinder Undergoing Plane Change Firing; See Discussion in Section D.2.10 (Concluded)

D.2.11 Check-case 06D – cylinder undergoing Earth departure firing

This section shows cross-plots for four of the selected simulation tools in modeling the dynamics of a cylinder in orbit performing an Earth departure maneuver with continuous propulsion. This scenario is described in Section C.2.11. Figures 47a through 47p compare results between the four simulation tools, as well as the deviances of the outputs from each tool from the ensemble average value.

Orbital test case 6D was the last of four test cases that applied external forces other than gravitation to the vehicle. This test case applies engine thrust to execute an Earth escape maneuver. The engine thrust was modeled as a square pulse. As discussed in orbital case 6C, a square pulse can significantly increase the integration error for some numerical methods. The growth in differences among the translational states was attributed to the differences in integration error caused by the square pulse.

The simulations agreed on inertial rotational states; differences among the simulations were negligible. Differences in the orbit-relative LVLH orientation were larger. These were caused primarily by the small differences in the vehicle trajectory among the simulations. Differences seen in the value plots for the LVLH angles demonstrated differences in how each simulation resolves roll and yaw angle under the Euler angle singularity that occurred after the vehicle trajectory becomes hyperbolic.

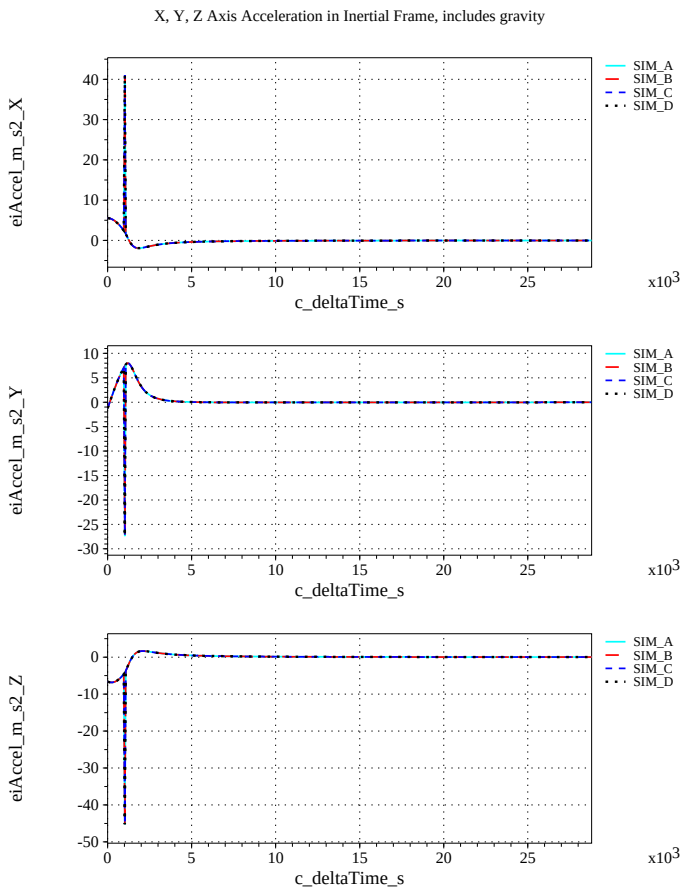

(a) Inertial Accelerations Compared

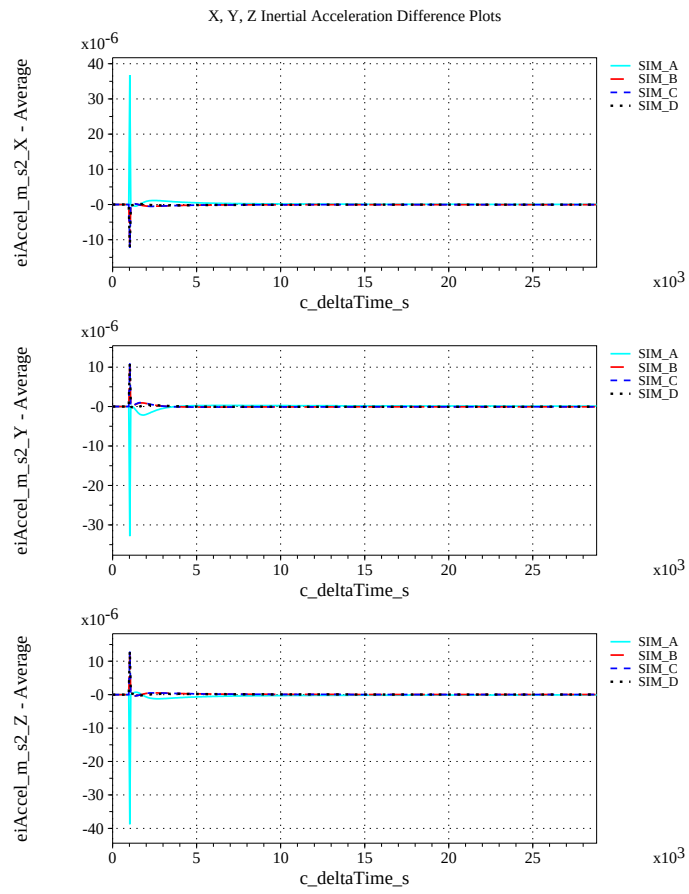

(b) Inertial Accelerations Differenced

Figure 47. Check-case 06D: Cylinder Undergoing Earth Departure Firing; See Discussion in Section D.2.11

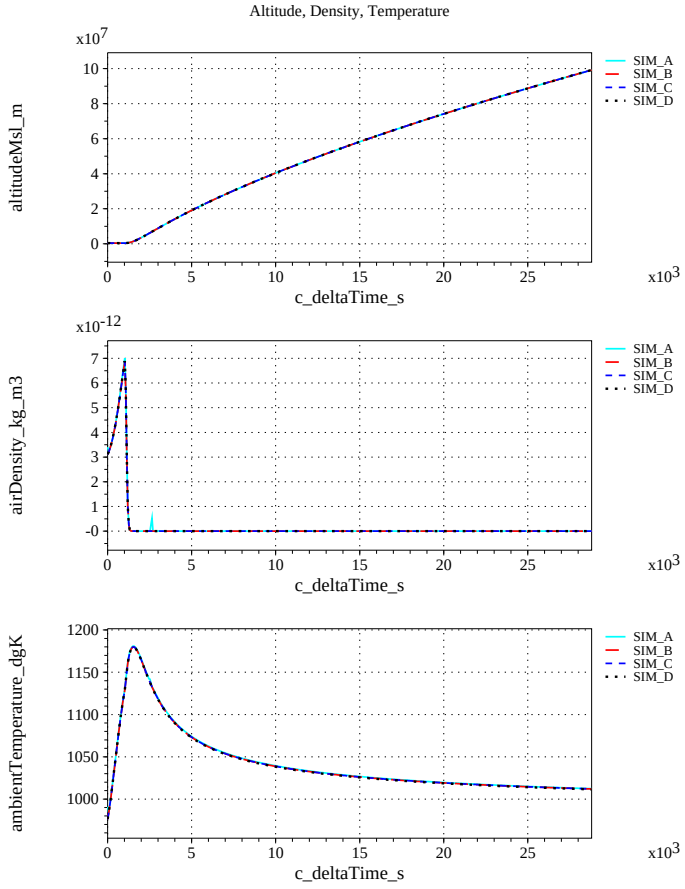

(c) Atmospheric Properties Compared

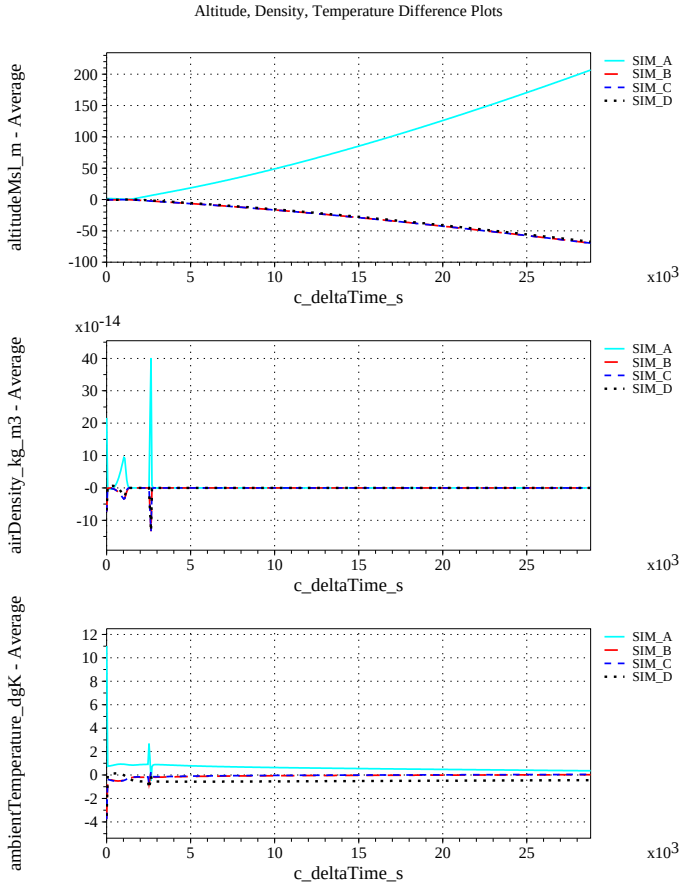

(d) Atmospheric Properties Differenced

Figure 47. Check-case 06D: Cylinder Undergoing Earth Departure Firing; See Discussion in Section D.2.11 (Cont'd)

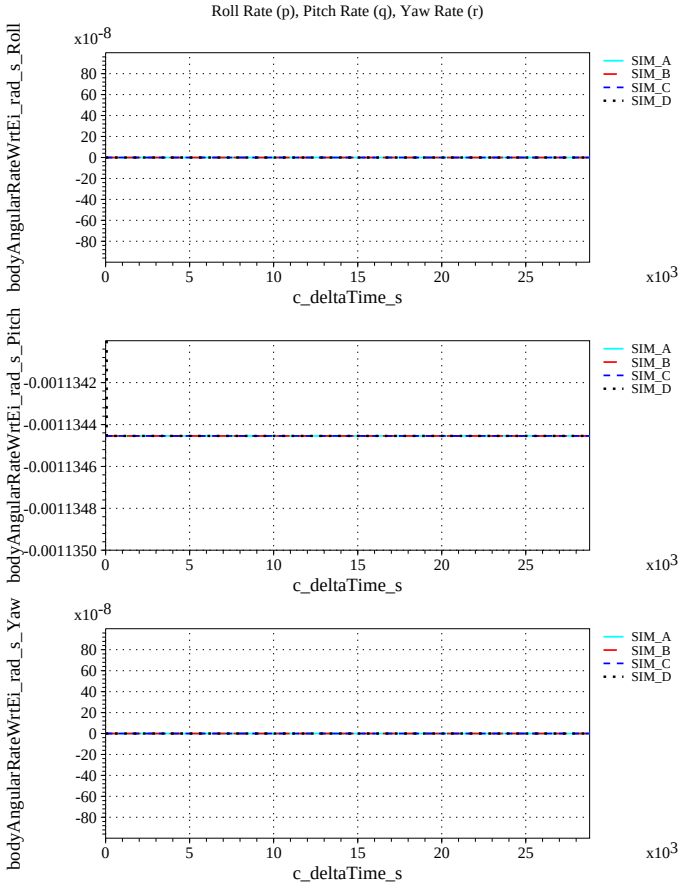

(e) Body-axis Angular Rates Compared

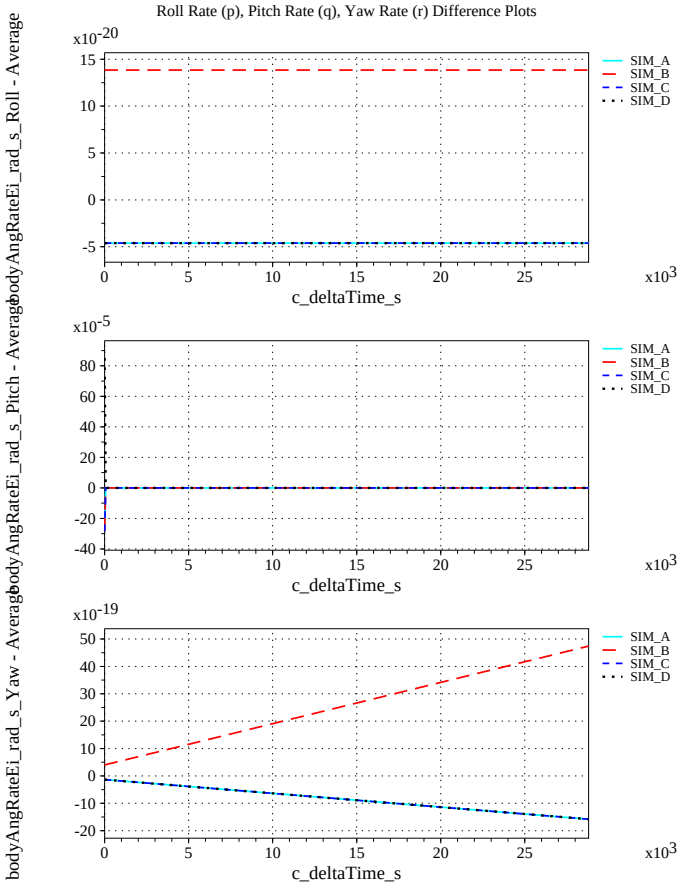

(f) Body-axis Angular Rates Differenced

Figure 47. Check-case 06D: Cylinder Undergoing Earth Departure Firing; See Discussion in Section D.2.11 (Cont'd)

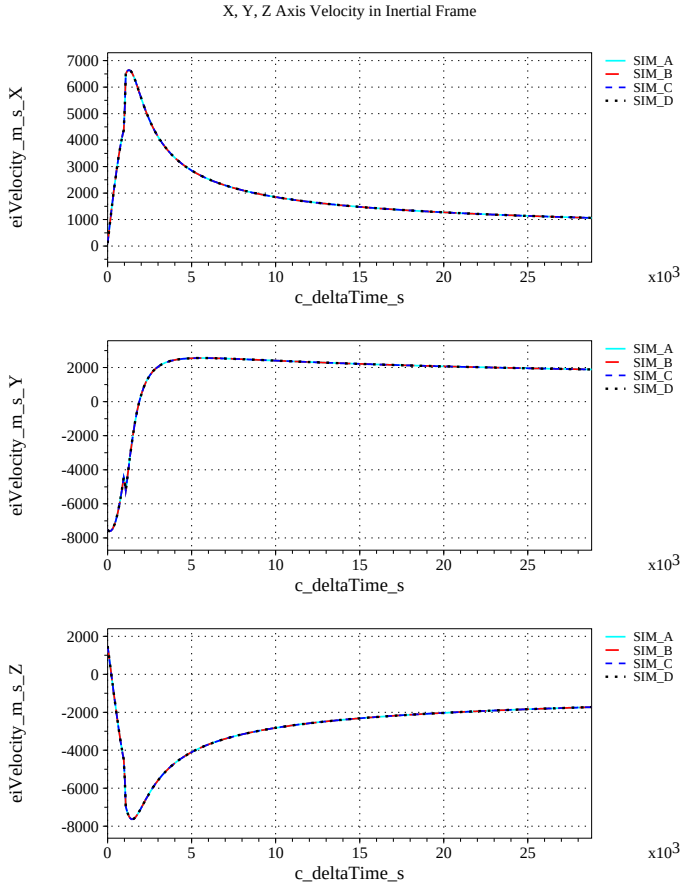

(g) Inertial Velocities Compared

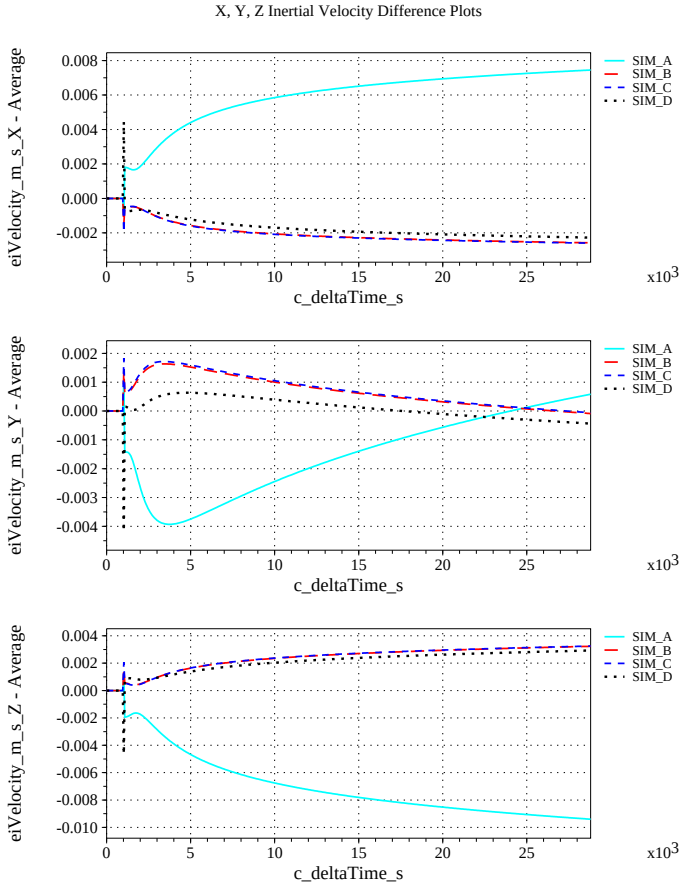

(h) Inertial Velocities Differenced

Figure 47. Check-case 06D: Cylinder Undergoing Earth Departure Firing; See Discussion in Section D.2.11 (Cont'd)

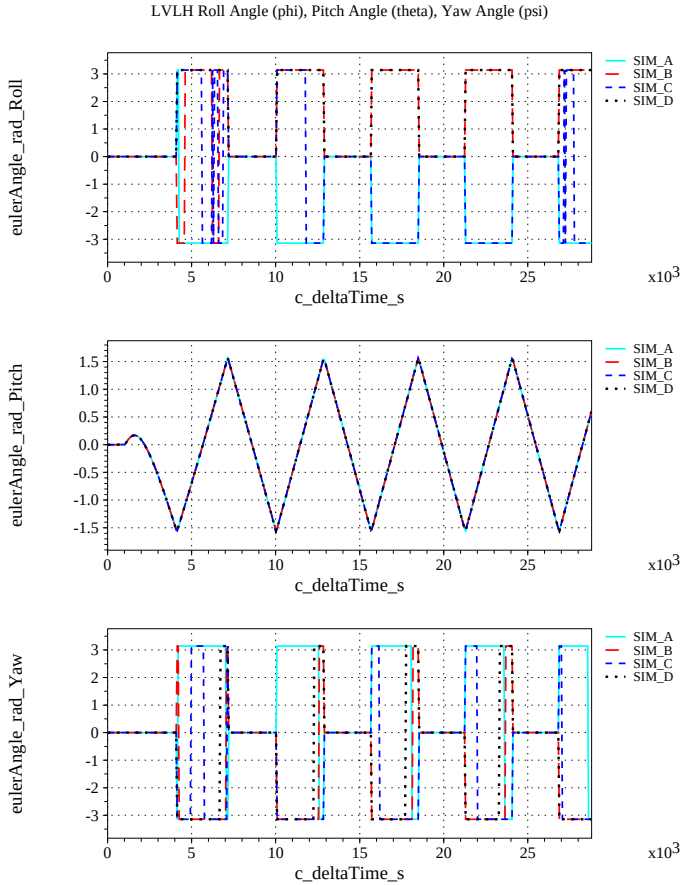

(i) Rotation Angles with Respect to LVLH Frame Compared

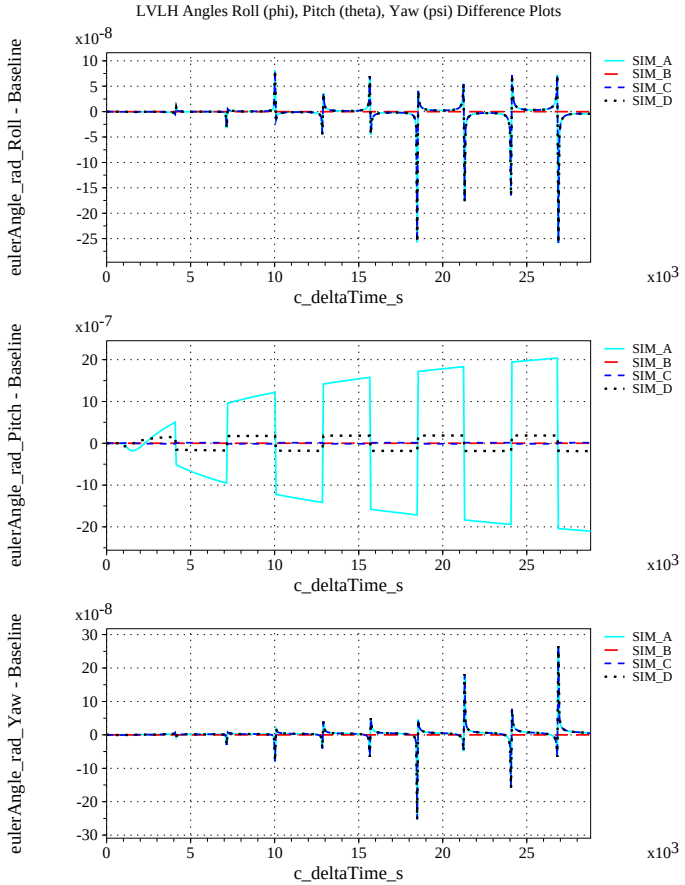

(j) Rotation Angles with Respect to LVLH Frame Differenced

Figure 47. Check-case 06D: Cylinder Undergoing Earth Departure Firing; See Discussion in Section D.2.11 (Cont'd)

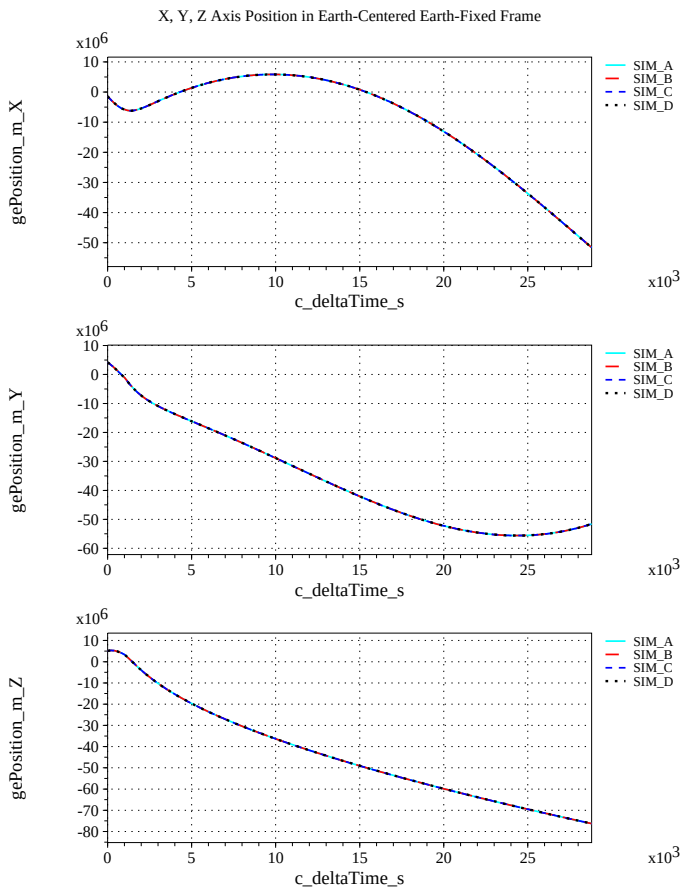

(k) Earth-centered, Earth-fixed Rectangular (X-Y-Z) Positions Compared

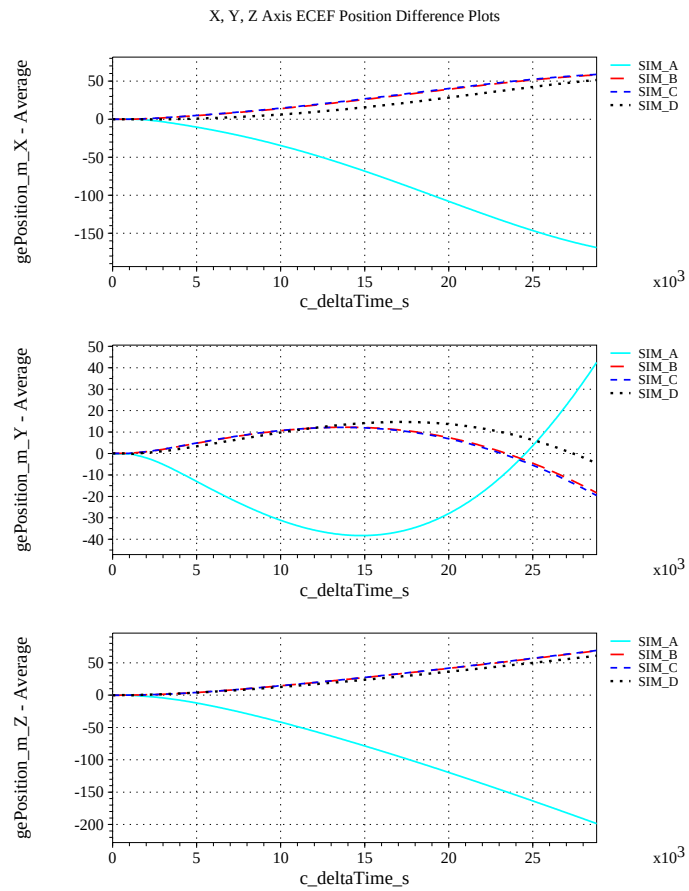

(l) Earth-centered, Earth-fixed Rectangular (X-Y-Z) Positions Differenced

Figure 47. Check-case 06D: Cylinder Undergoing Earth Departure Firing; See Discussion in Section D.2.11 (Cont'd)

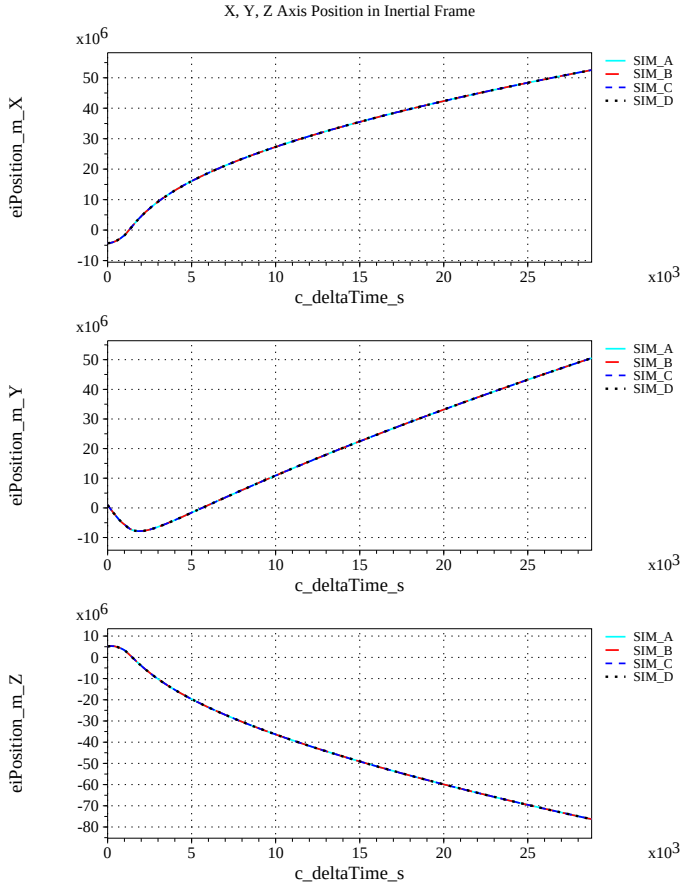

(m) Earth-centered Inertial Rectangular (x-y-z) Positions Compared

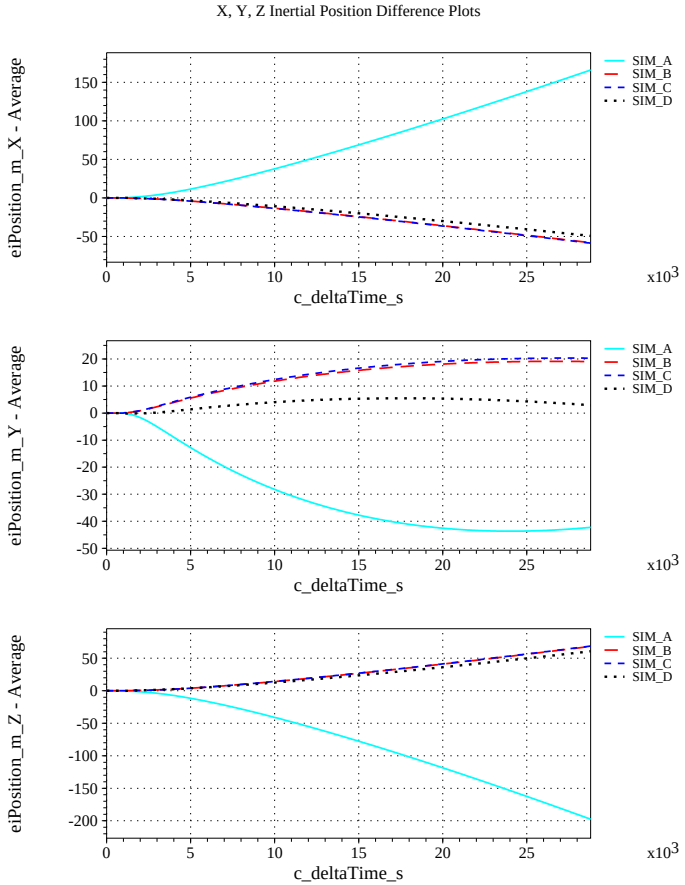

(n) Earth-centered Inertial Rectangular (x-y-z) Positions Differenced

Figure 47. Check-case 06D: Cylinder Undergoing Earth Departure Firing; See Discussion in Section D.2.11 (Cont'd)

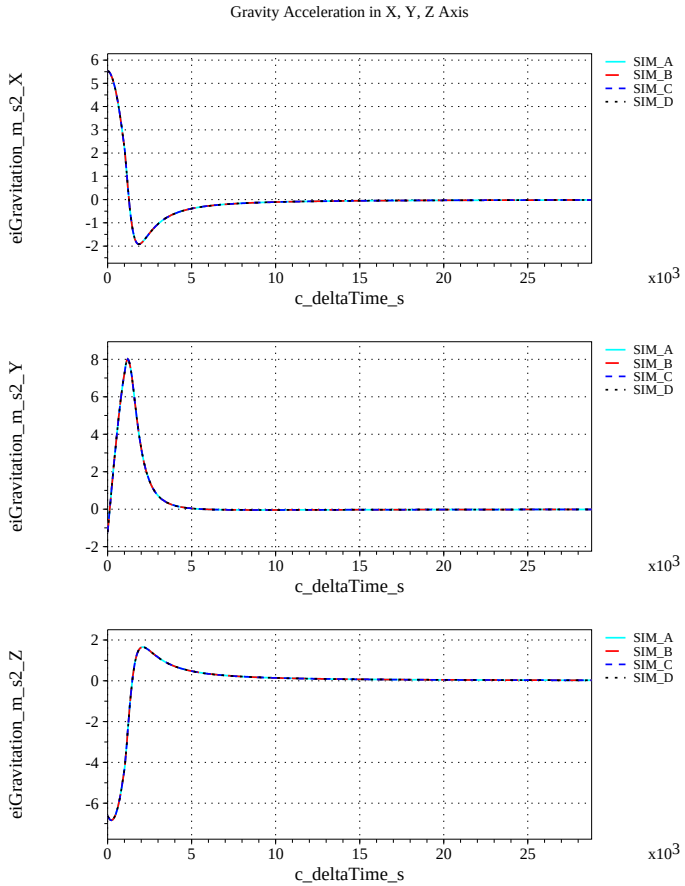

(o) Gravitational Components in Inertial (**X**-**Y**-**Z**) Directions Compared

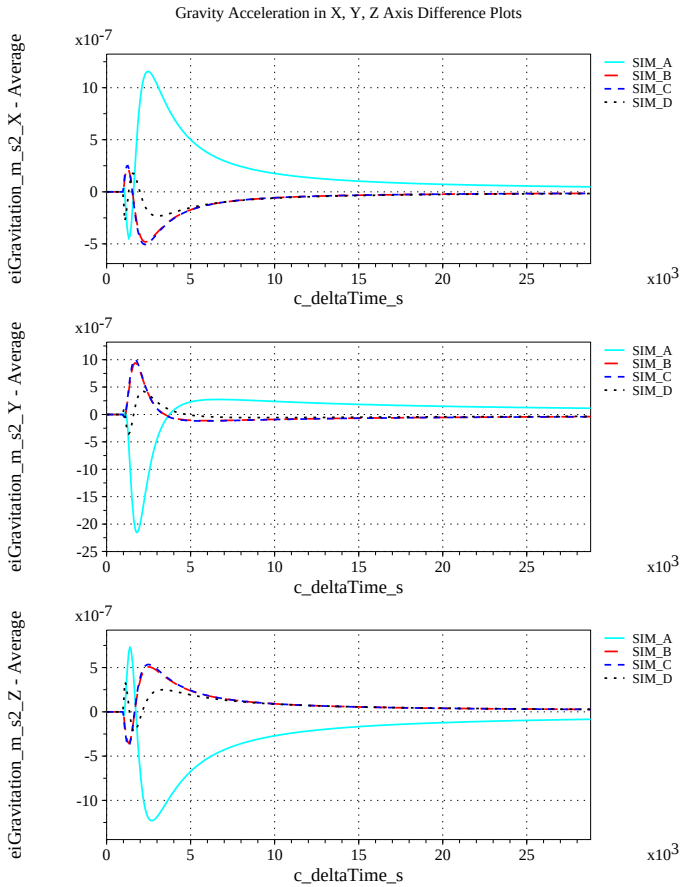

(p) Gravitational Components in Inertial (**X**-**Y**-**Z**) Directions Differenced

Figure 47. Check-case 06D: Cylinder Undergoing Earth Departure Firing; See Discussion in Section D.2.11 (Concluded)

D.2.12 Check-case 07A – sphere in 4×4 gravity and third-body perturbations

This section shows cross-plots for four of the selected simulation tools in modeling the dynamics of a sphere in orbit responding to a 4×4 gravity model, planetary ephemeris, and third-body perturbations. This scenario is described in Section C.2.12. Figures 48a through 48p compare results between the four simulation tools, as well as the deviances of the outputs from each tool from the ensemble average value.

Orbital check-case 7A was the first of four test cases that combined the geopotential gravitation perturbations of orbital check-case 3A and 3B, the Sun and Moon perturbations of orbital check-case 4, and the aerodynamic drag of orbital check-case 6B. This scenario used the geopotential model of order and degree four defined in orbital case 3A but disabled the aerodynamic drag.

The differences in translational states among the simulations was a combination of the differences appearing in orbital check-cases 3A and 4. Of these, the differences previously identified in orbital check-case 3A dominated. Those differences were primarily caused by apparent differences in the accuracy of the geopotential model implementations among the simulations. See the discussion of orbital check-case 3A difference (Section D.2.2) for more details.

The simulations agreed on the inertial rotational state. Differences among the simulations were negligible and were attributed to differences in integration methods. Differences in the orbit-relative LVLH orientation were larger as a result of the small differences in orbit parameters defined by the translational states.

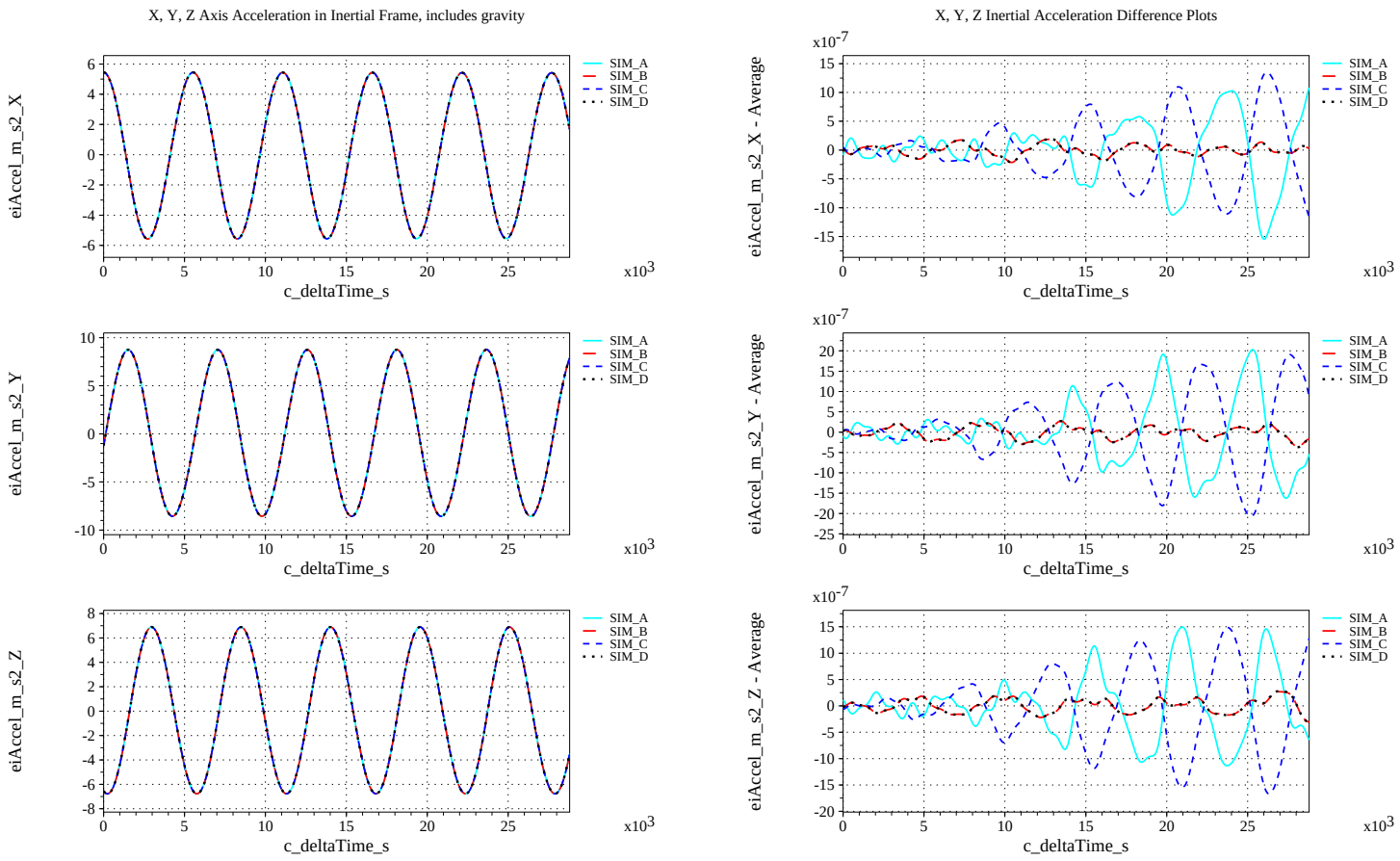

(a) Inertial Accelerations Compared

(b) Inertial Accelerations Differenced

Figure 48. Check-case 07A: Sphere in 4×4 Gravity and Third-body Perturbations; See Discussion in Section D.2.12

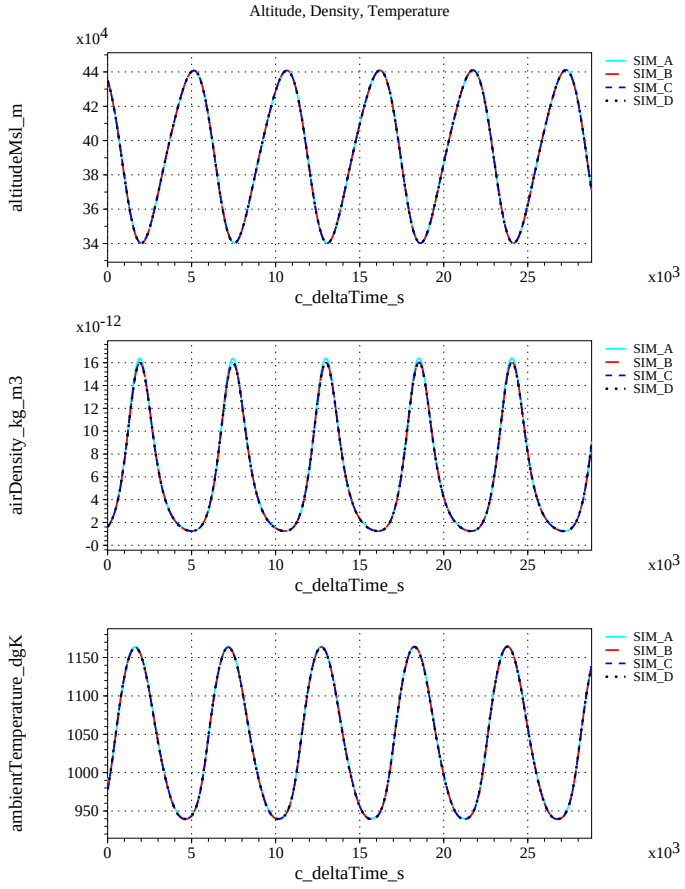

(c) Atmospheric Properties Compared

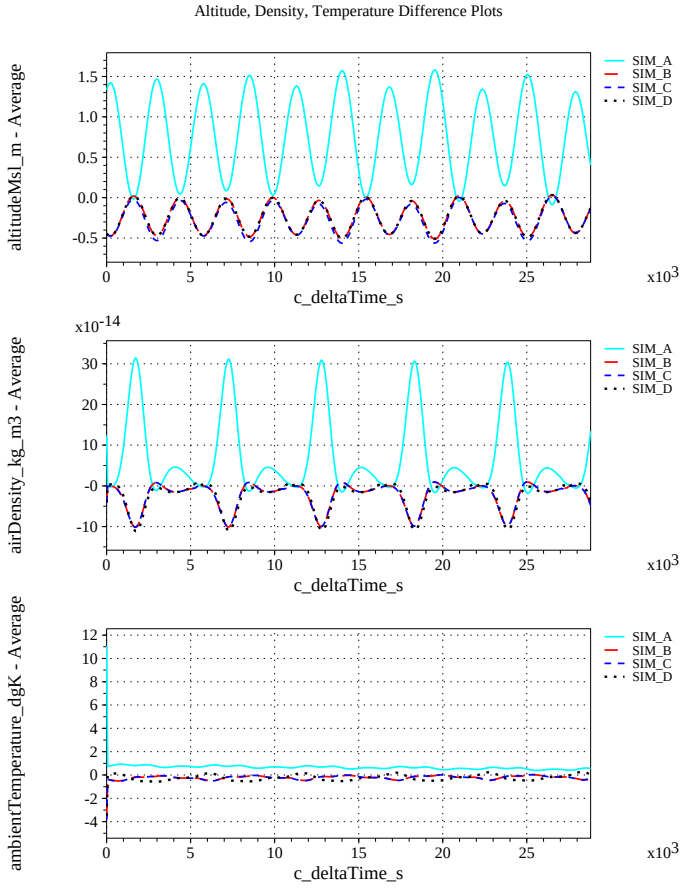

(d) Atmospheric Properties Differenced

Figure 48. Check-case 07A: Sphere in 4×4 Gravity and Third-body Perturbations; See Discussion in Section D.2.12 (Cont'd)

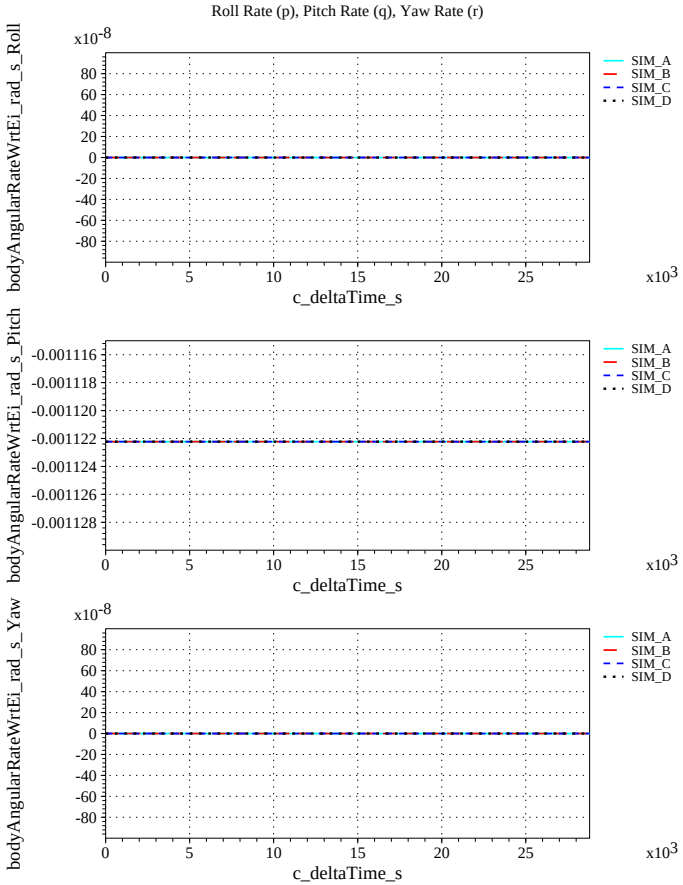

(e) Body-axis Angular Rates Compared

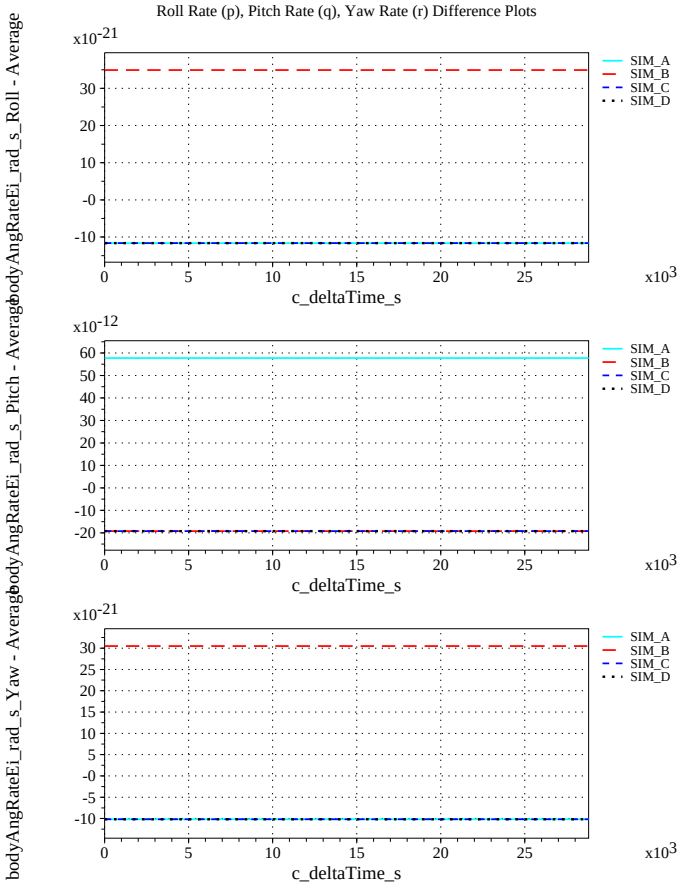

(f) Body-axis Angular Rates Differenced

Figure 48. Check-case 07A: Sphere in 4×4 Gravity and Third-body Perturbations; See Discussion in Section D.2.12 (Cont'd)

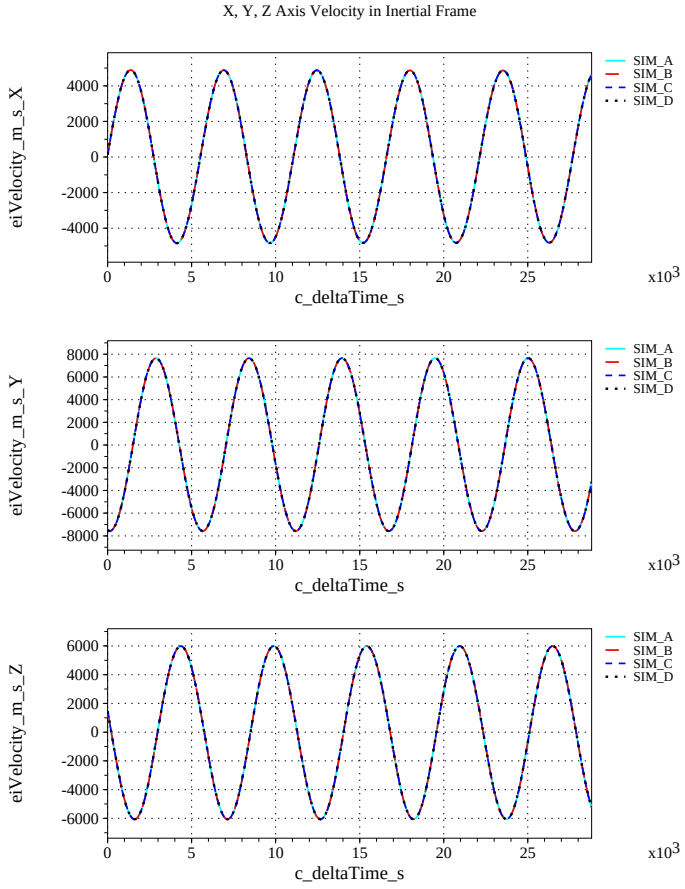

(g) Inertial Velocities Compared

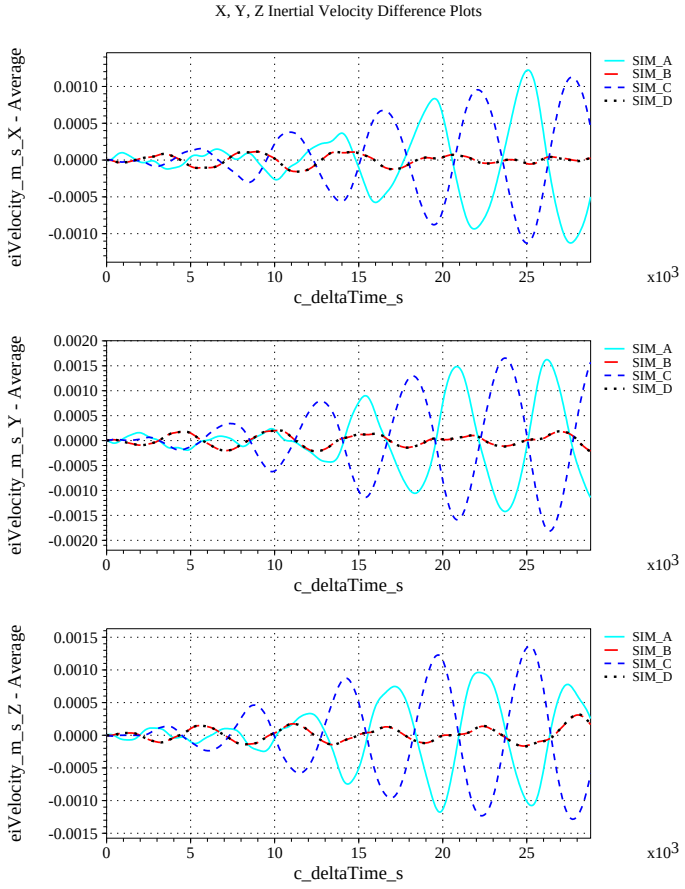

(h) Inertial Velocities Differenced

Figure 48. Check-case 07A: Sphere in 4×4 Gravity and Third-body Perturbations; See Discussion in Section D.2.12 (Cont'd)

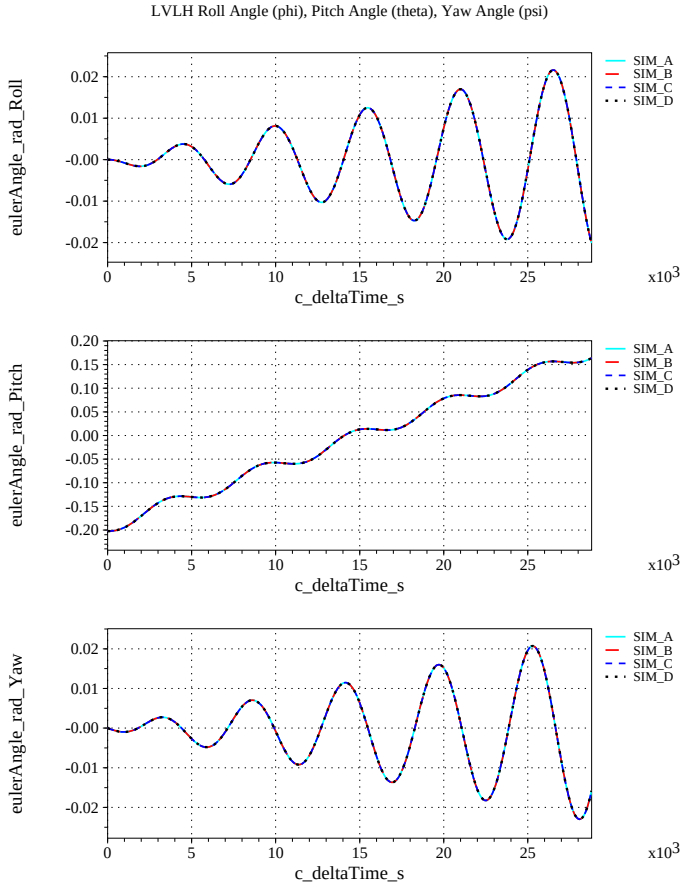

(i) Rotation Angles with Respect to LVLH Frame Compared

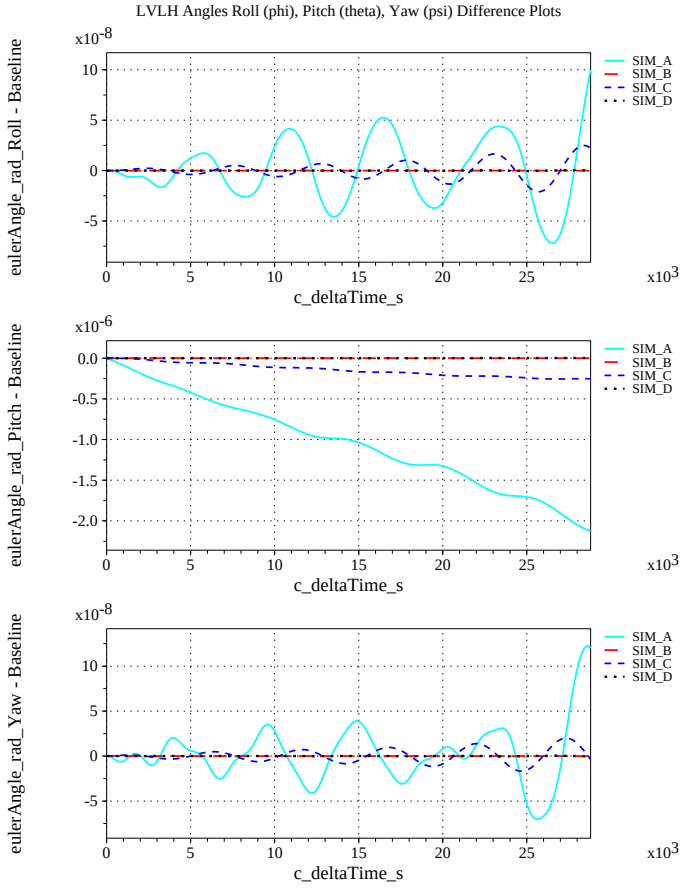

(j) Rotation Angles with Respect to LVLH Frame Differenced

Figure 48. Check-case 07A: Sphere in 4×4 Gravity and Third-body Perturbations; See Discussion in Section D.2.12 (Cont'd)

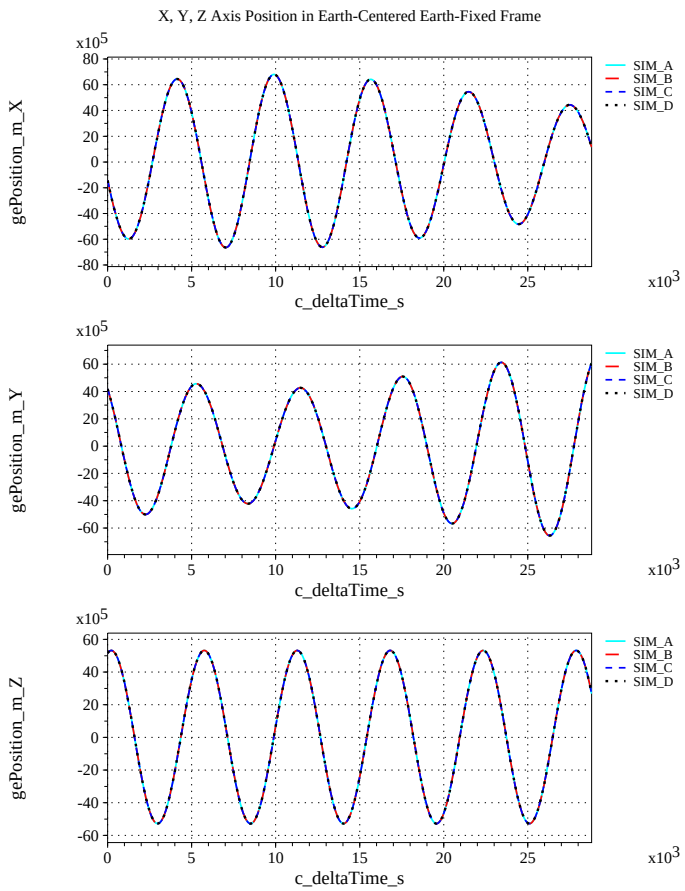

(k) Earth-centered, Earth-fixed Rectangular (X-Y-Z) Positions Compared

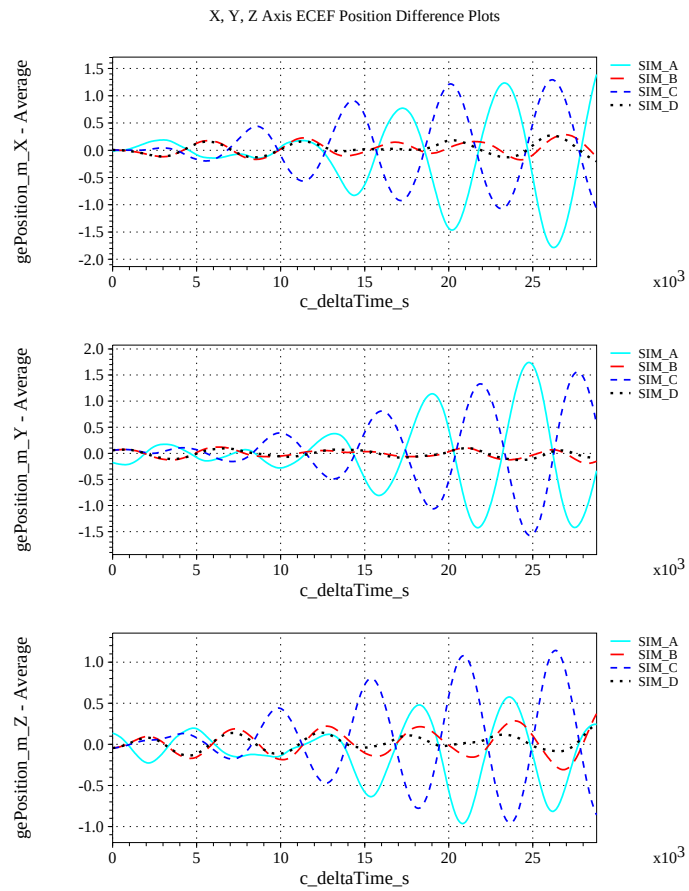

(l) Earth-centered, Earth-fixed Rectangular (X-Y-Z) Positions Differenced

Figure 48. Check-case 07A: Sphere in 4×4 Gravity and Third-body Perturbations; See Discussion in Section D.2.12 (Cont'd)

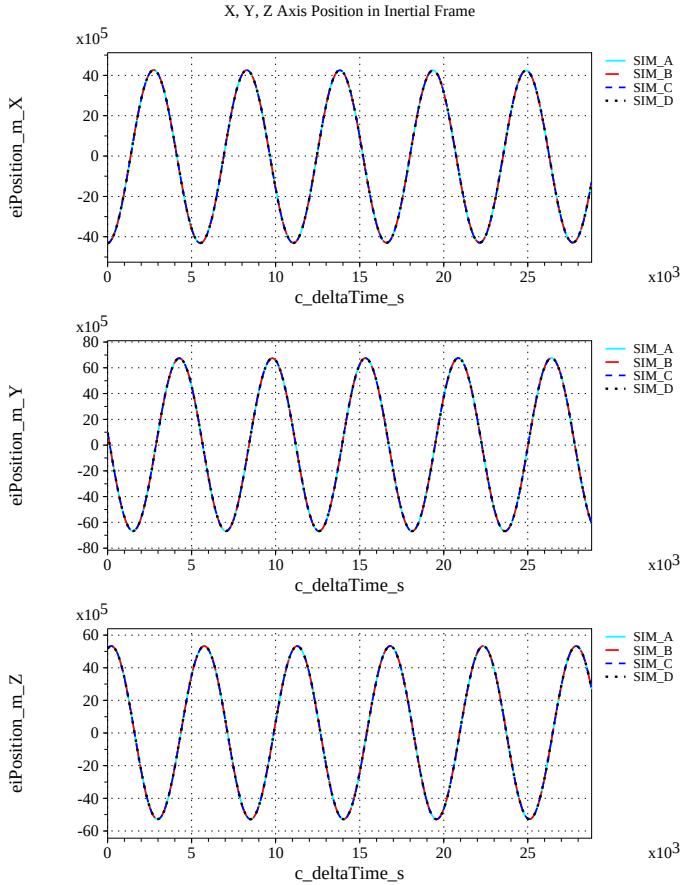

(m) Earth-centered Inertial Rectangular (x-y-z) Positions Compared

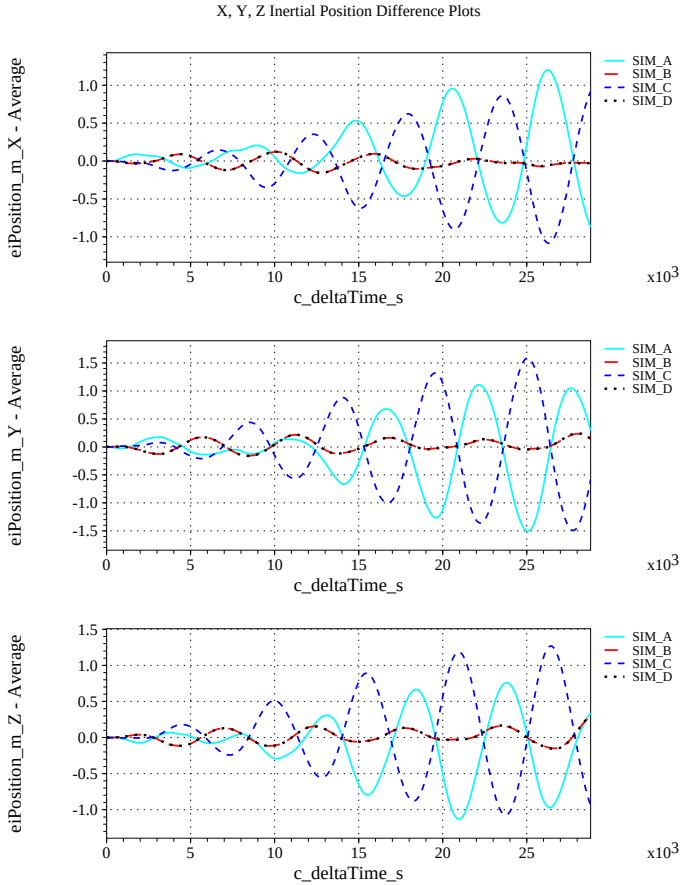

(n) Earth-centered Inertial Rectangular (x-y-z) Positions Differenced

Figure 48. Check-case 07A: Sphere in 4×4 Gravity and Third-body Perturbations; See Discussion in Section D.2.12 (Cont'd)

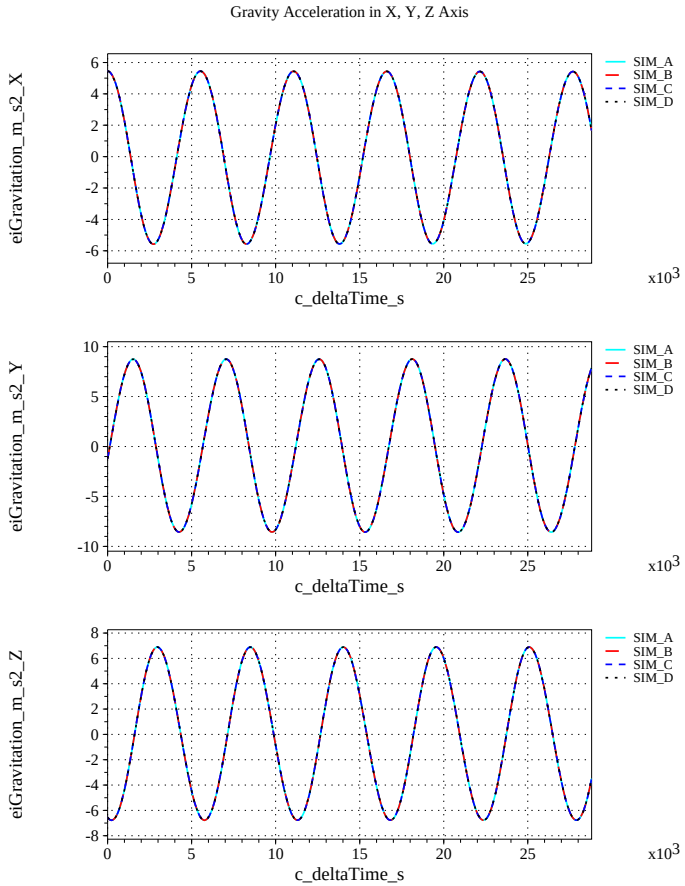

(o) Gravitational Components in Inertial (**X**-**Y**-**Z**) Directions Compared

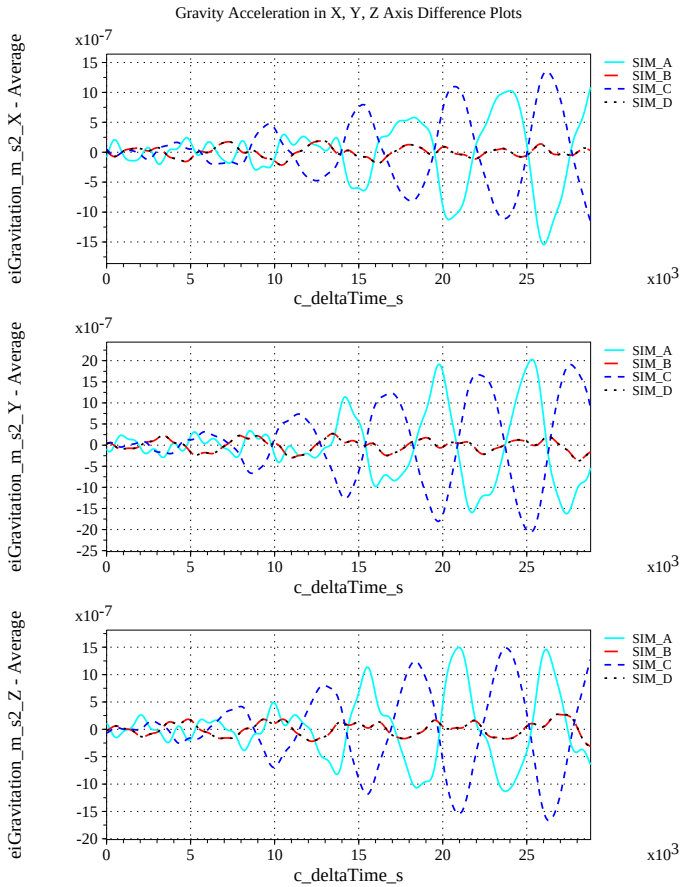

(p) Gravitational Components in Inertial (**X**-**Y**-**Z**) Directions Differenced

Figure 48. Check-case 07A: Sphere in 4×4 Gravity and Third-body Perturbations; See Discussion in Section D.2.12 (Concluded)

D.2.13 Check-case 07B – sphere in 8×8 gravity and third-body perturbations

This section shows cross-plots for four of the selected simulation tools in modeling the dynamics of a sphere in orbit responding to an 8×8 gravity model, planetary ephemeris, and third-body perturbations. This scenario is described in Section C.2.13. Figures 49a through 49p compare results between the four simulation tools, as well as the deviances of the outputs from each tool from the ensemble average value.

Orbital check-case 7B was the second of four test cases that combined the geopotential gravitation perturbations of orbital test case 3A and 3B, the Sun and Moon perturbations of orbital case 4, and the aerodynamic drag of orbital case 6B. This check-case used the geopotential model of order and degree eight defined in orbital case 3B but disabled aerodynamic drag.

The differences in translational states among the simulations was a combination of the differences appearing in orbital test check-cases 3B and 4. Of these, the differences from orbital test check-case 3B dominated. Those differences were primarily caused by apparent differences in the accuracy of the geopotential model implementations among the simulations. See the discussion of orbital check-case 3A difference (Section D.2.2) for more details.

The simulations agreed on the inertial rotational state. Differences among the simulations were negligible and were attributed to differences in integration methods. Differences in the orbit-relative LVLH orientation were larger as a result of the small differences in orbit parameters defined by the translational states.

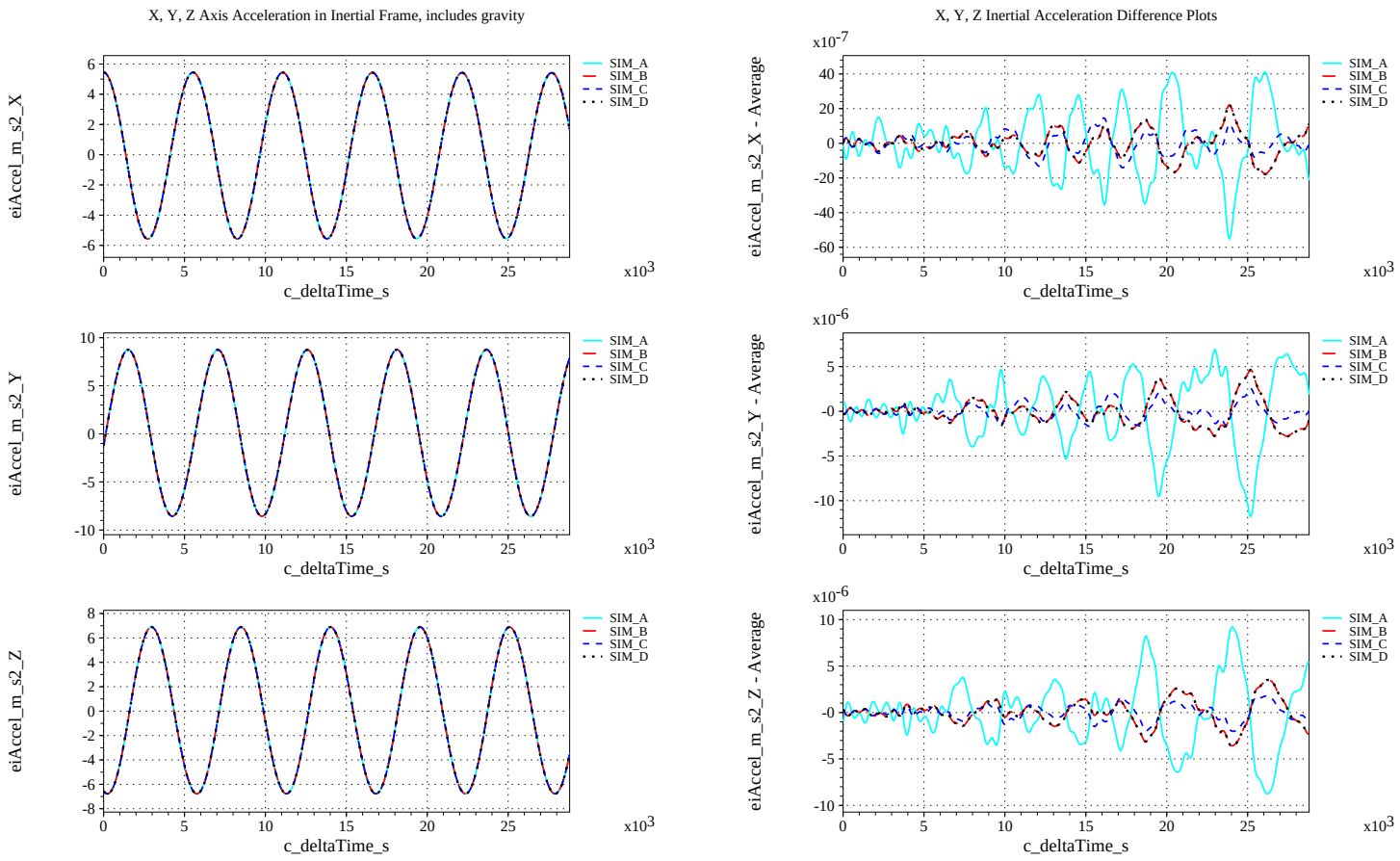

(a) Inertial Accelerations Compared

(b) Inertial Accelerations Differenced

Figure 49. Check-case 07B: Sphere in 8×8 Gravity and Third-body Perturbations; See Discussion in Section D.2.13

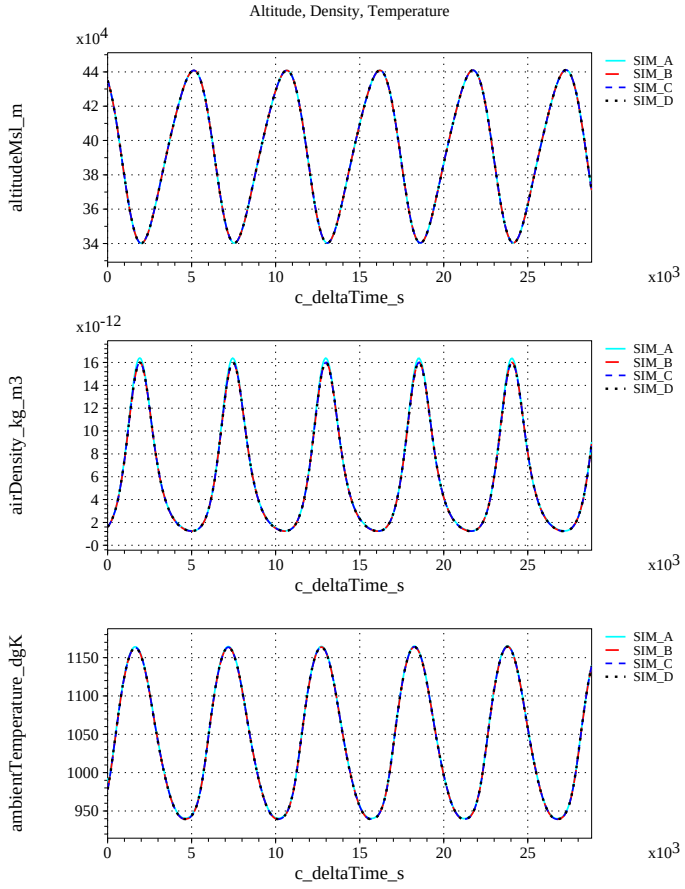

(c) Atmospheric Properties Compared

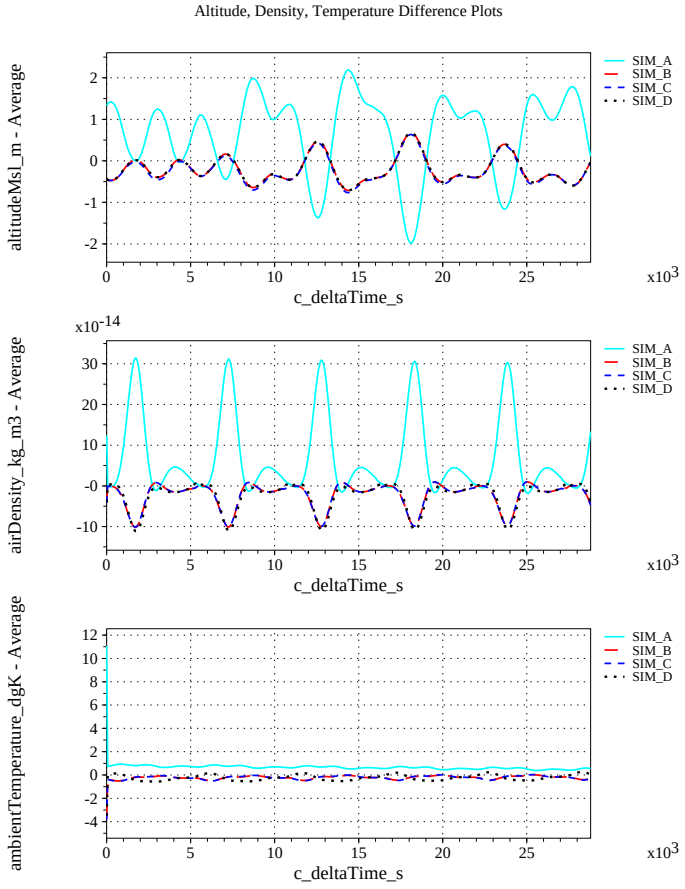

(d) Atmospheric Properties Differenced

Figure 49. Check-case 07B: Sphere in 8×8 Gravity and Third-body Perturbations; See Discussion in Section D.2.13 (Cont'd)

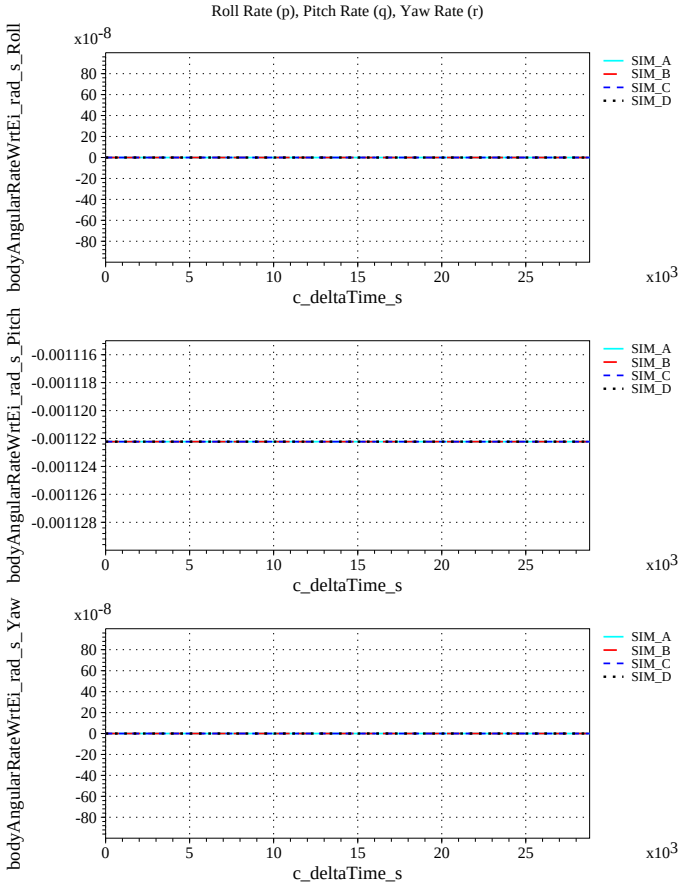

(e) Body-axis Angular Rates Compared

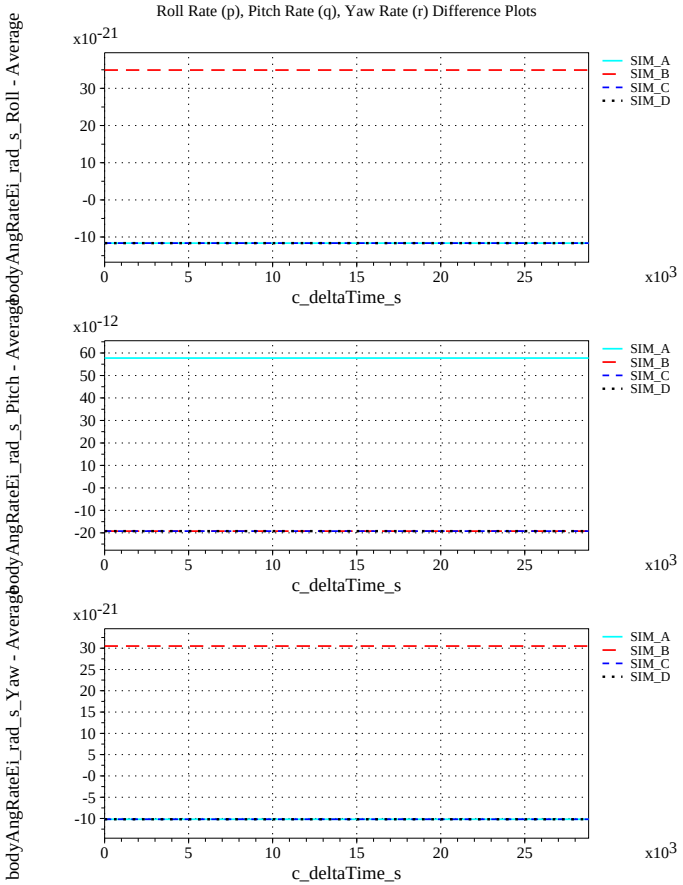

(f) Body-axis Angular Rates Differenced

Figure 49. Check-case 07B: Sphere in 8×8 Gravity and Third-body Perturbations; See Discussion in Section D.2.13 (Cont'd)

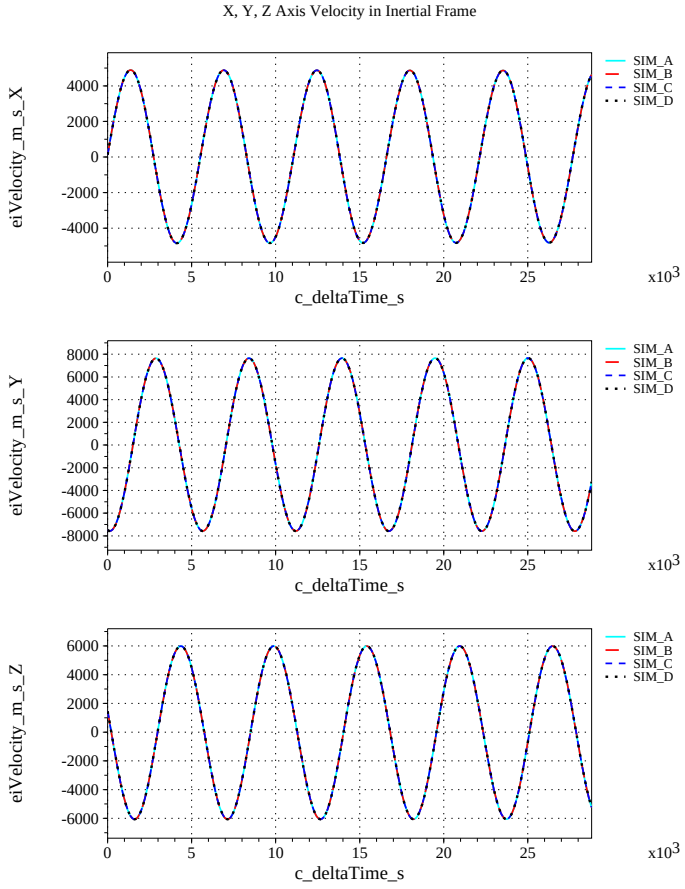

(g) Inertial Velocities Compared

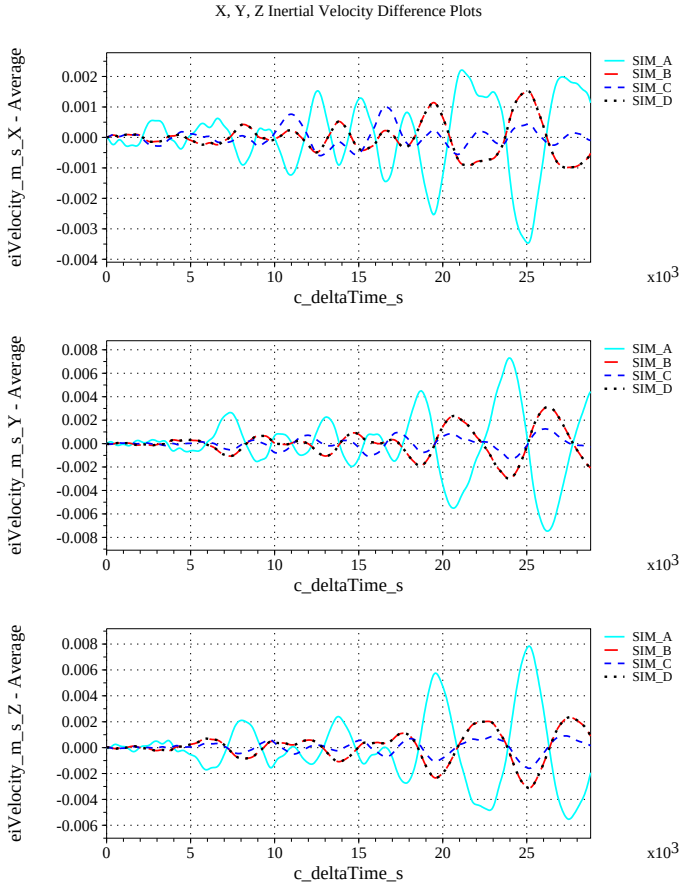

(h) Inertial Velocities Differenced

Figure 49. Check-case 07B: Sphere in 8×8 Gravity and Third-body Perturbations; See Discussion in Section D.2.13 (Cont'd)

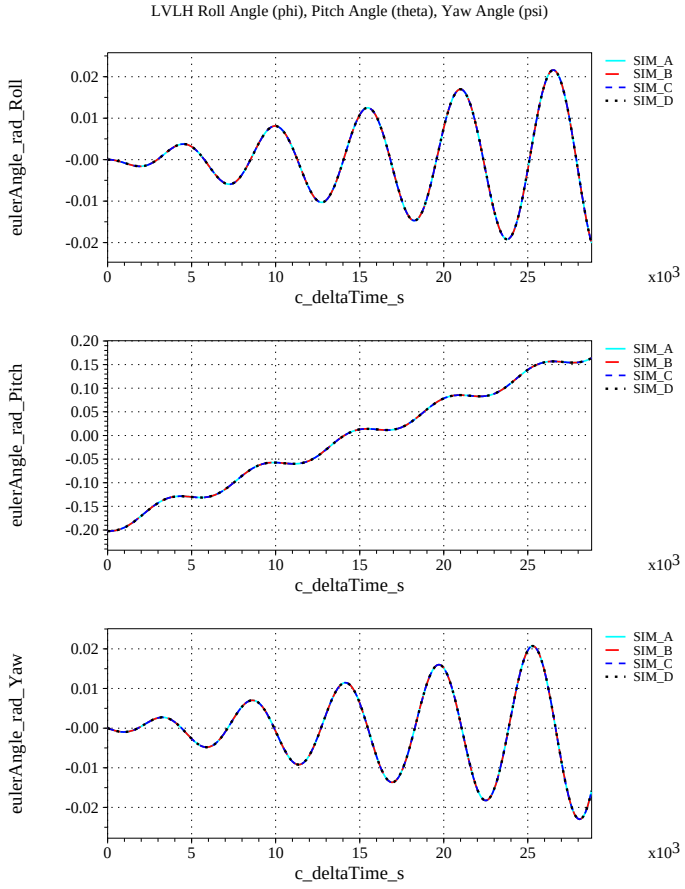

(i) Rotation Angles with Respect to LVLH Frame Compared

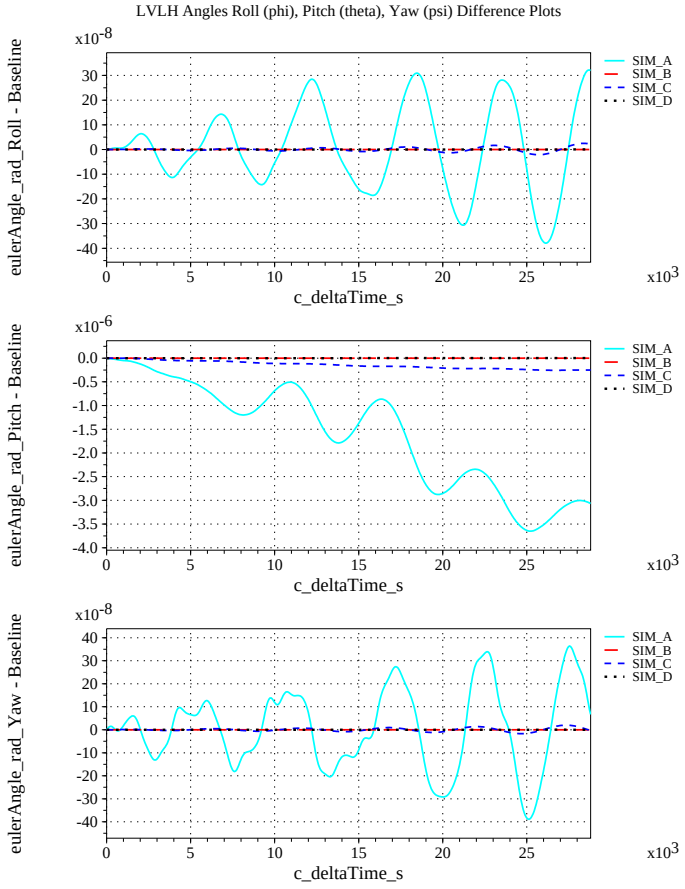

(j) Rotation Angles with Respect to LVLH Frame Differenced

Figure 49. Check-case 07B: Sphere in 8×8 Gravity and Third-body Perturbations; See Discussion in Section D.2.13 (Cont'd)

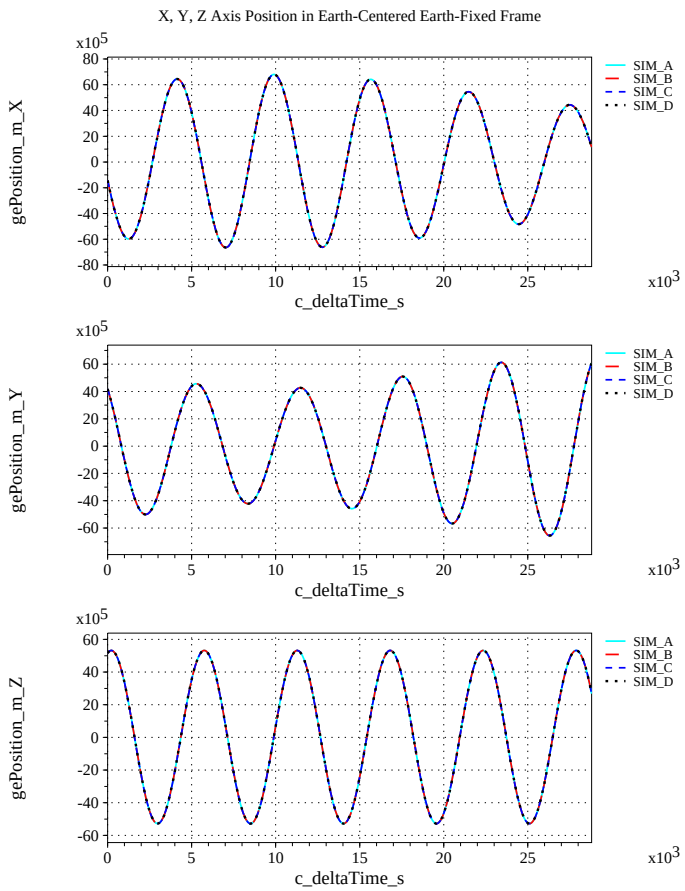

(k) Earth-centered, Earth-fixed Rectangular (X-Y-Z) Positions Compared

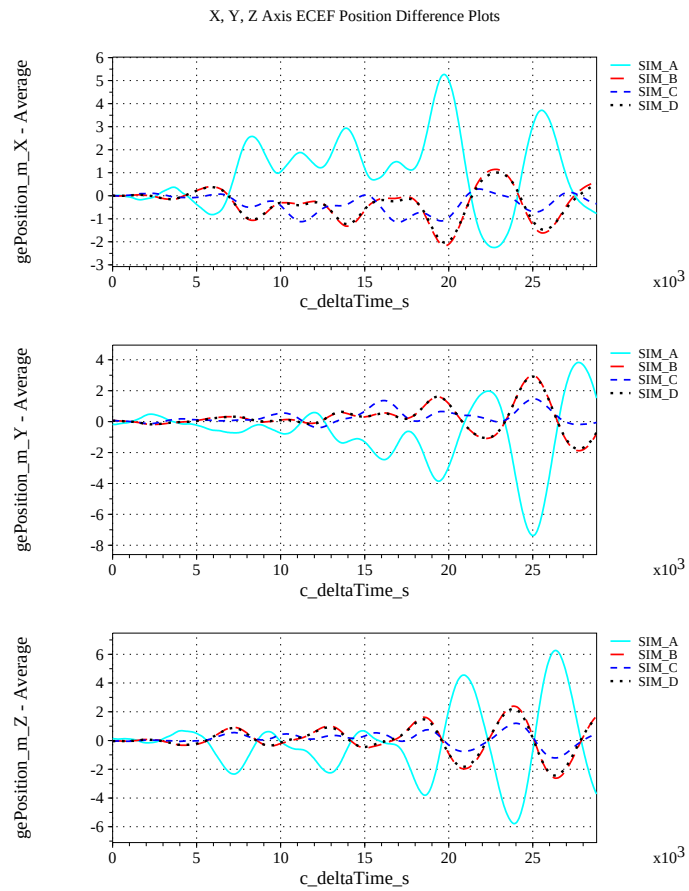

(l) Earth-centered, Earth-fixed Rectangular (X-Y-Z) Positions Differenced

Figure 49. Check-case 07B: Sphere in 8×8 Gravity and Third-body Perturbations; See Discussion in Section D.2.13 (Cont'd)

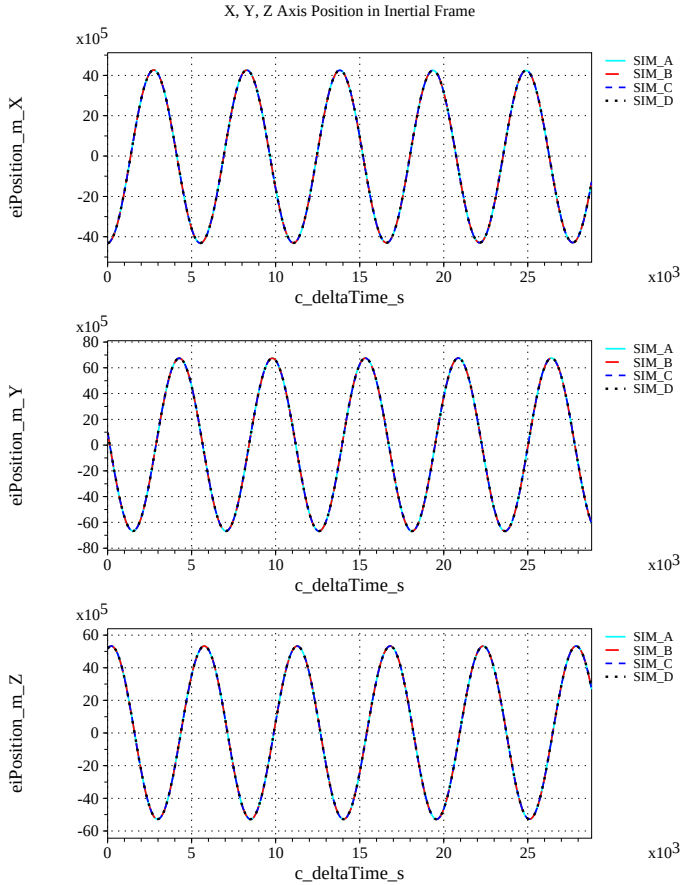

(m) Earth-centered Inertial Rectangular (x-y-z) Positions Compared

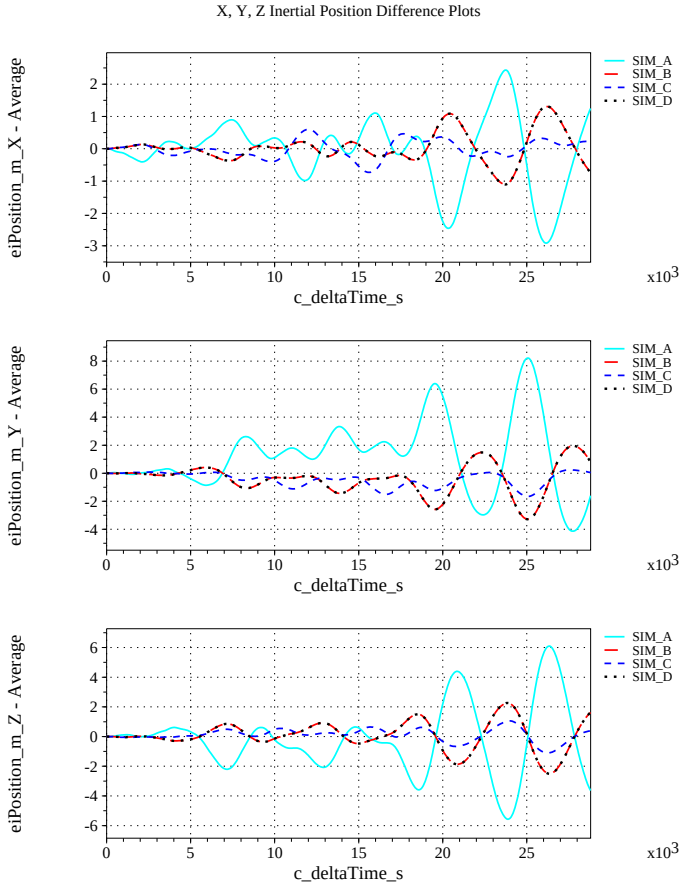

(n) Earth-centered Inertial Rectangular (x-y-z) Positions Differenced

Figure 49. Check-case 07B: Sphere in 8×8 Gravity and Third-body Perturbations; See Discussion in Section D.2.13 (Cont'd)

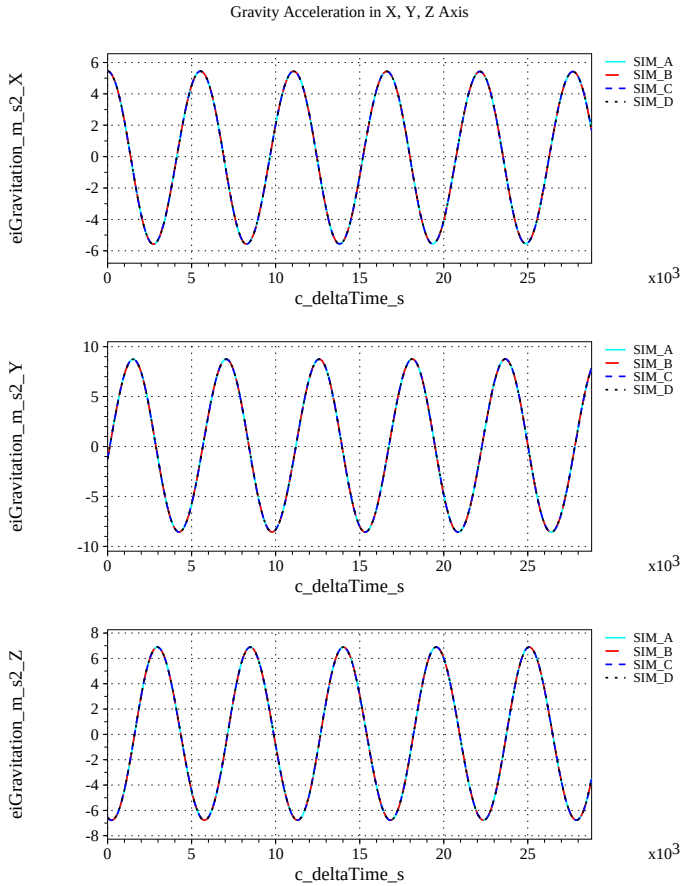

(o) Gravitational Components in Inertial (**X**-**Y**-**Z**) Directions Compared

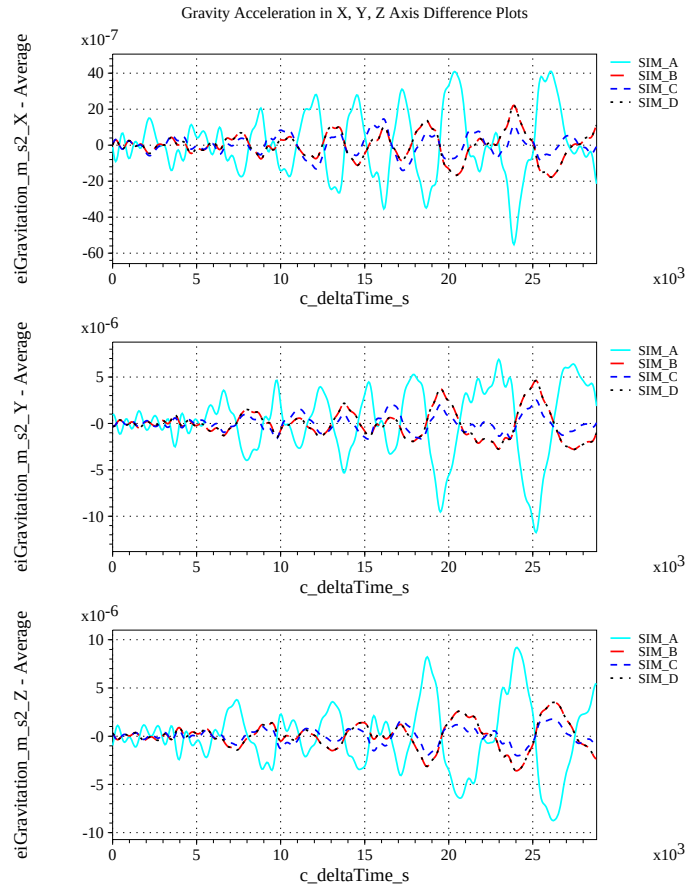

(p) Gravitational Components in Inertial (**X**-**Y**-**Z**) Directions Differenced

Figure 49. Check-case 07B: Sphere in 8×8 Gravity and Third-body Perturbations; See Discussion in Section D.2.13 (Concluded)

D.2.14 Check-case 07C – sphere in 4×4 gravity with drag and third-body perturbations

This section shows cross-plots for four of the selected simulation tools in modeling the dynamics of a sphere in orbit responding to a 4×4 gravity model, atmospheric drag, planetary ephemeris, and third-body perturbations. This scenario is described in Section C.2.14. Figures 50a through 50p compare results between the four simulation tools, as well as the deviances of the outputs from each tool from the ensemble average value.

Orbital check-case 7C was the third of four test cases that combined the geopotential gravitation perturbations of orbital test case 3A and 3B, the Sun and Moon perturbations of orbital case 4, and the aerodynamic drag of orbital case 6B. This check-case used the geopotential perturbations of order and degree four defined in orbital case 3A.

The differences in translational states among the simulations was a combination of the differences appearing in orbital check-cases 3A, 4, and 6B. Differences for the translation states in SIM A were primarily caused its unique use of the MET07 model to predict the atmospheric density input to the aerodynamic drag. By comparison, differences among the other simulations barely registered on the plots. These differences were likely caused by apparent differences in accuracy of the geopotential gravitation implementation and differences in atmospheric density predicted by the MET95 and MET99 models. See orbital case 3A (Section D.2.2) for more details on the apparent accuracy differences in geopotential gravitation implementation and see orbital case 5A (Section D.2.5) for more details on the differences among the MET model versions in predicting atmospheric density.

The simulations agreed on the inertial rotational state. Differences among the simulations were negligible and were attributed to differences in integration error. Differences in the orbit-relative LVLH orientation were larger as a result of the small differences in orbit parameters defined by the translational states.

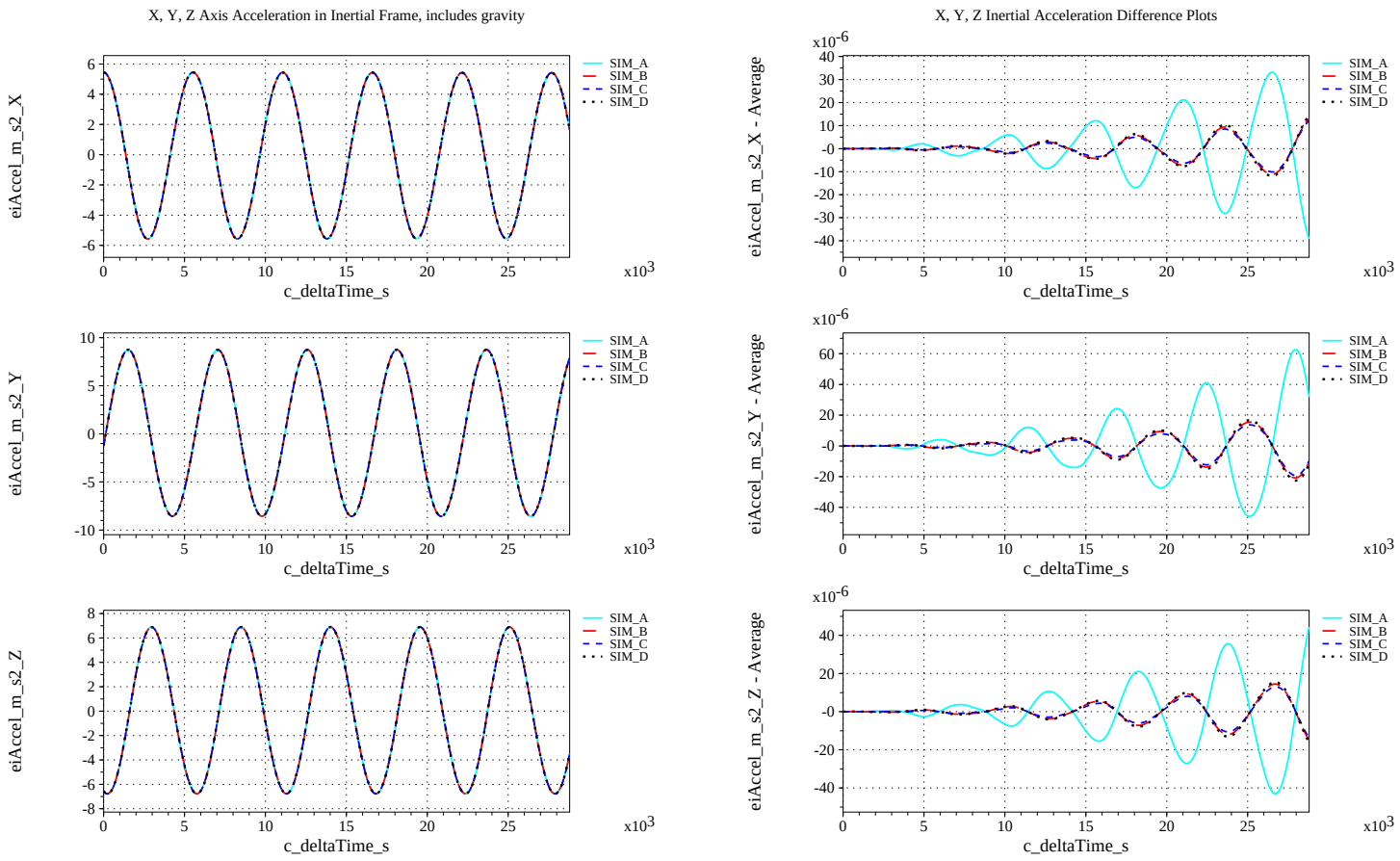

(a) Inertial Accelerations Compared

(b) Inertial Accelerations Differenced

Figure 50. Check-case 07C: Sphere in 4×4 Gravity with Drag and Third-body Perturbations; See Discussion in Section D.2.14

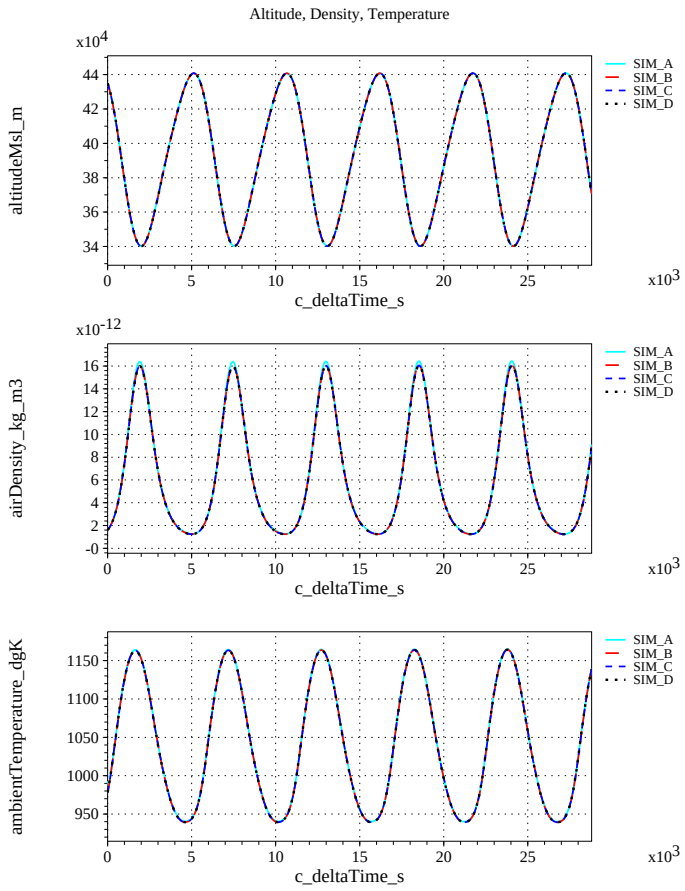

(c) Atmospheric Properties Compared

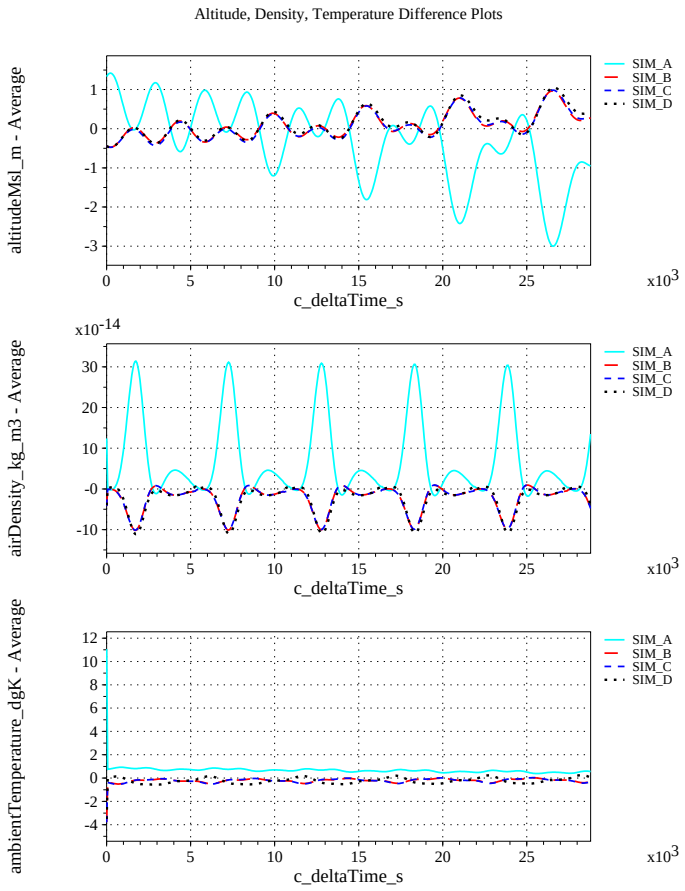

(d) Atmospheric Properties Differenced

Figure 50. Check-case 07C: Sphere in 4×4 Gravity with Drag and Third-body Perturbations; See Discussion in Section D.2.14 (Cont'd)

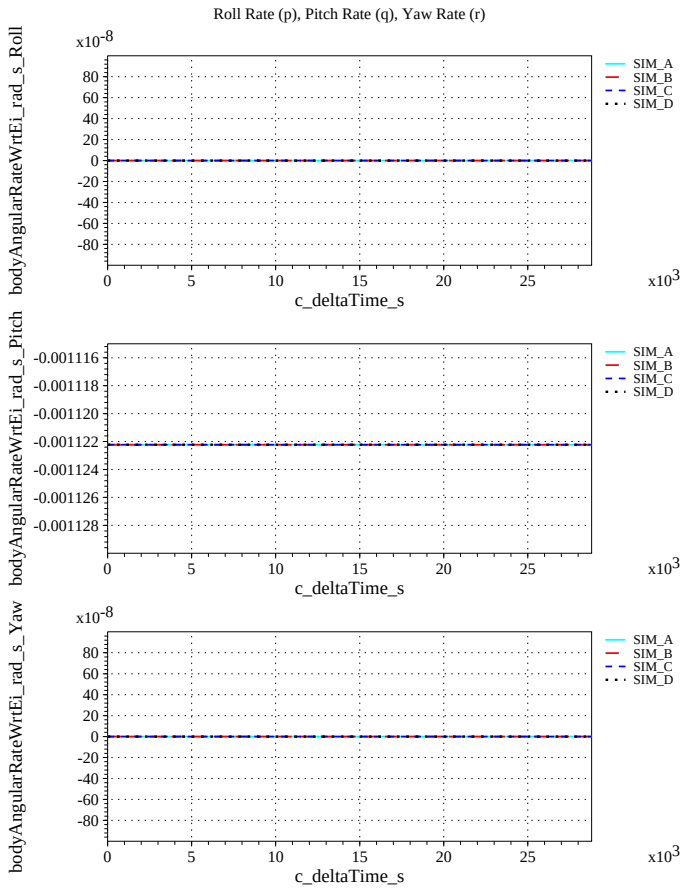

(e) Body-axis Angular Rates Compared

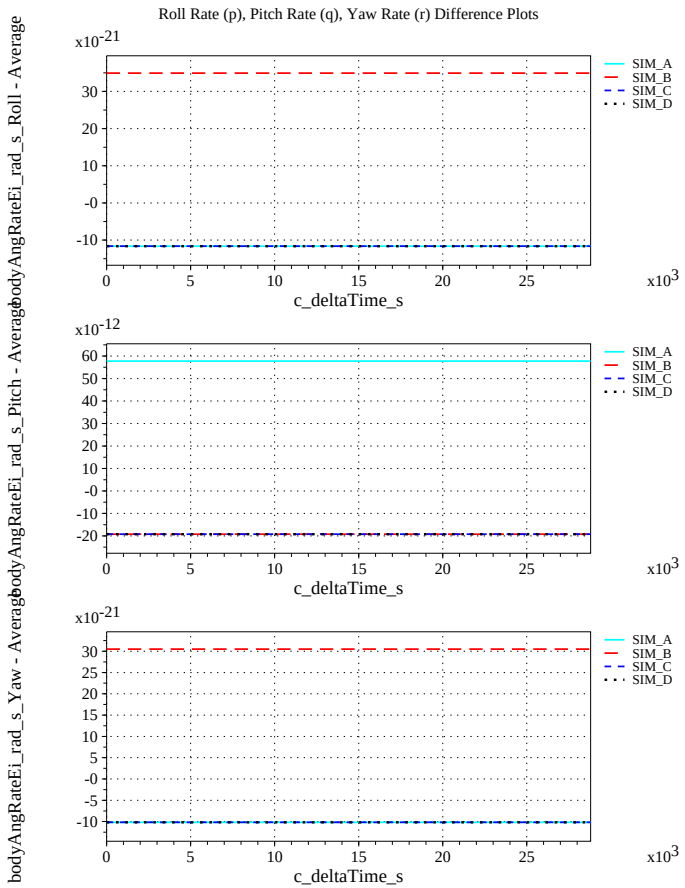

(f) Body-axis Angular Rates Differenced

Figure 50. Check-case 07C: Sphere in 4×4 Gravity with Drag and Third-body Perturbations; See Discussion in Section D.2.14 (Cont'd)

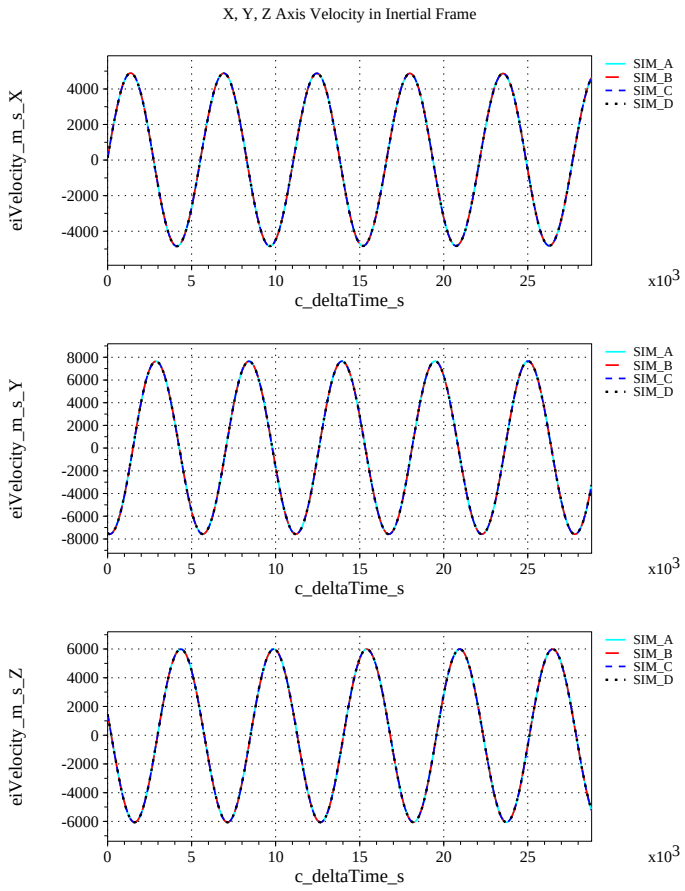

(g) Inertial Velocities Compared

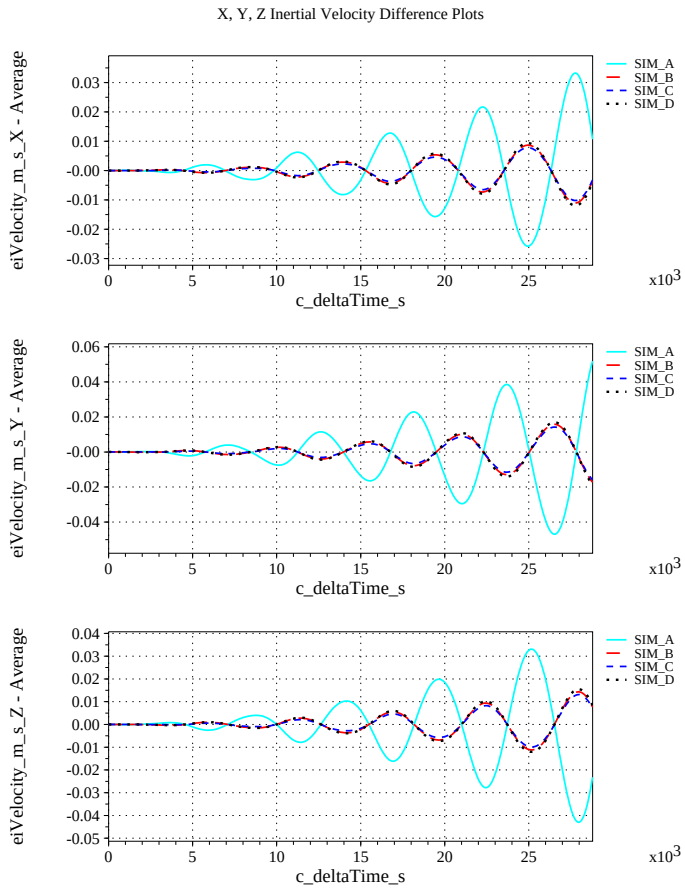

(h) Inertial Velocities Differenced

Figure 50. Check-case 07C: Sphere in 4×4 Gravity with Drag and Third-body Perturbations; See Discussion in Section D.2.14 (Cont'd)

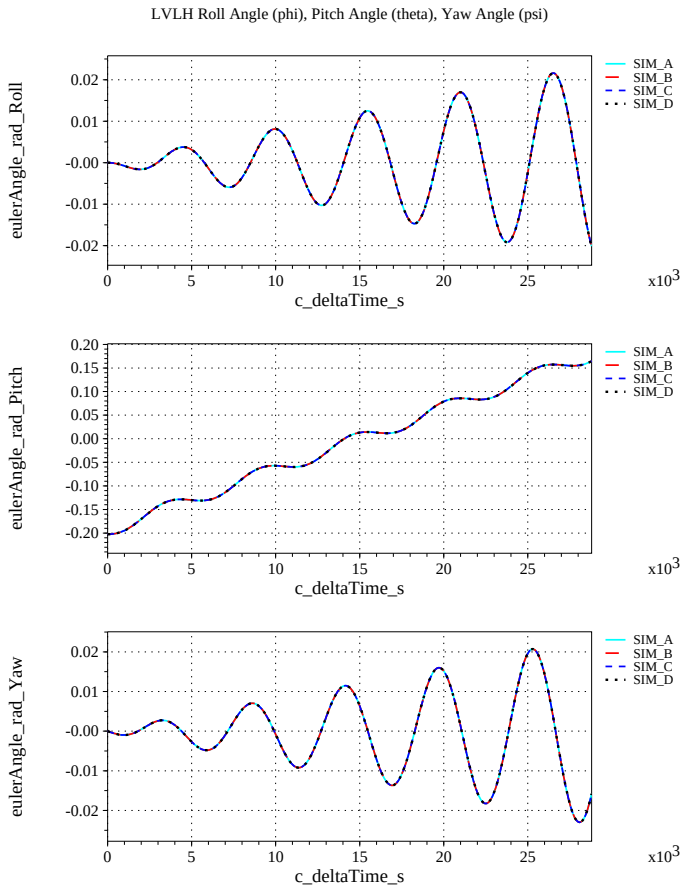

(i) Rotation Angles with Respect to LVLH Frame Compared

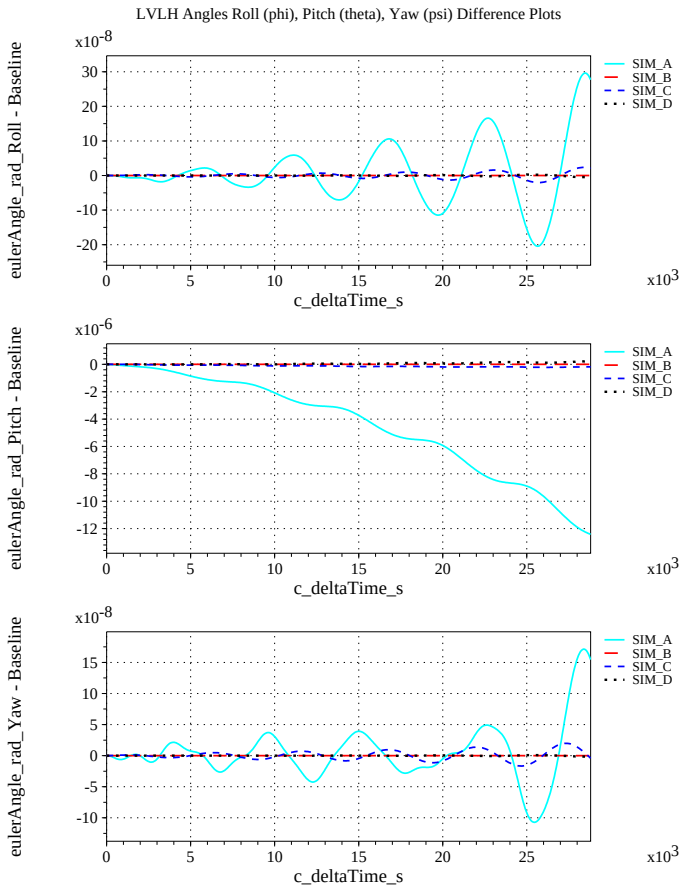

(j) Rotation Angles with Respect to LVLH Frame Differenced

Figure 50. Check-case 07C: Sphere in 4×4 Gravity with Drag and Third-body Perturbations; See Discussion in Section D.2.14 (Cont'd)

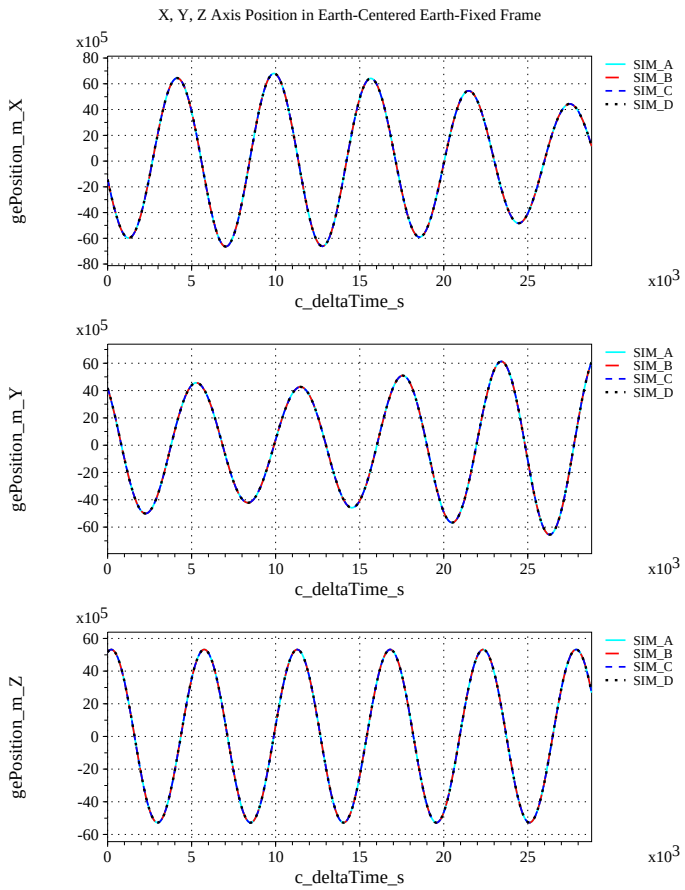

(k) Earth-centered, Earth-fixed Rectangular (X-Y-Z) Positions Compared

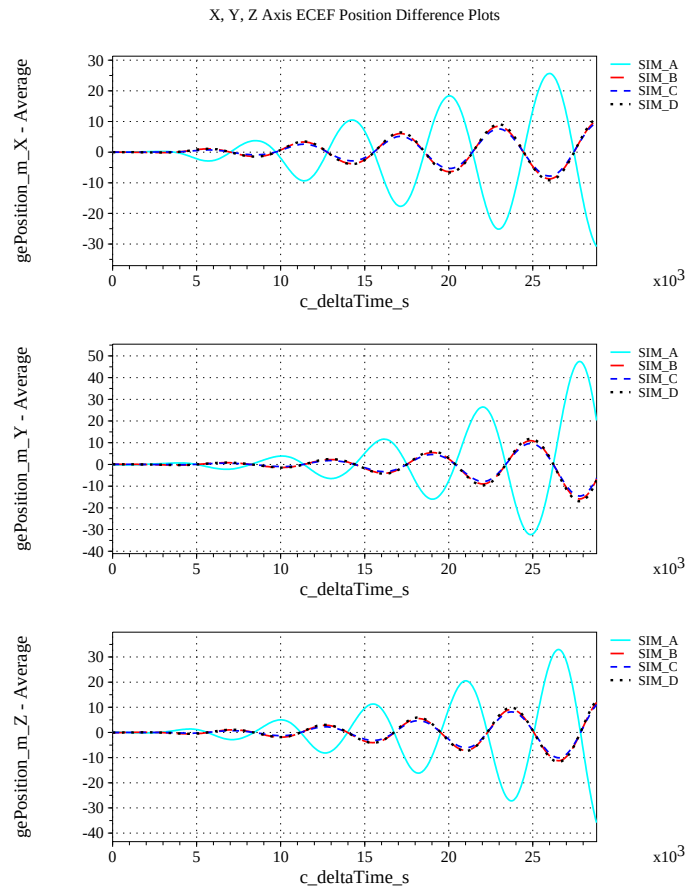

(l) Earth-centered, Earth-fixed Rectangular (X-Y-Z) Positions Differenced

Figure 50. Check-case 07C: Sphere in 4×4 Gravity with Drag and Third-body Perturbations; See Discussion in Section D.2.14 (Cont'd)

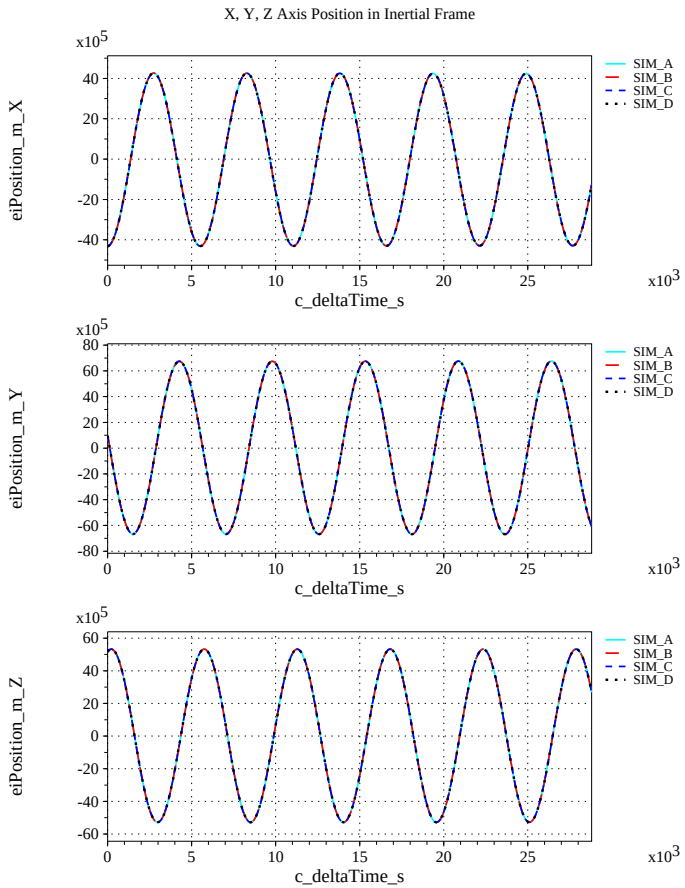

(m) Earth-centered Inertial Rectangular (x-y-z) Positions Compared

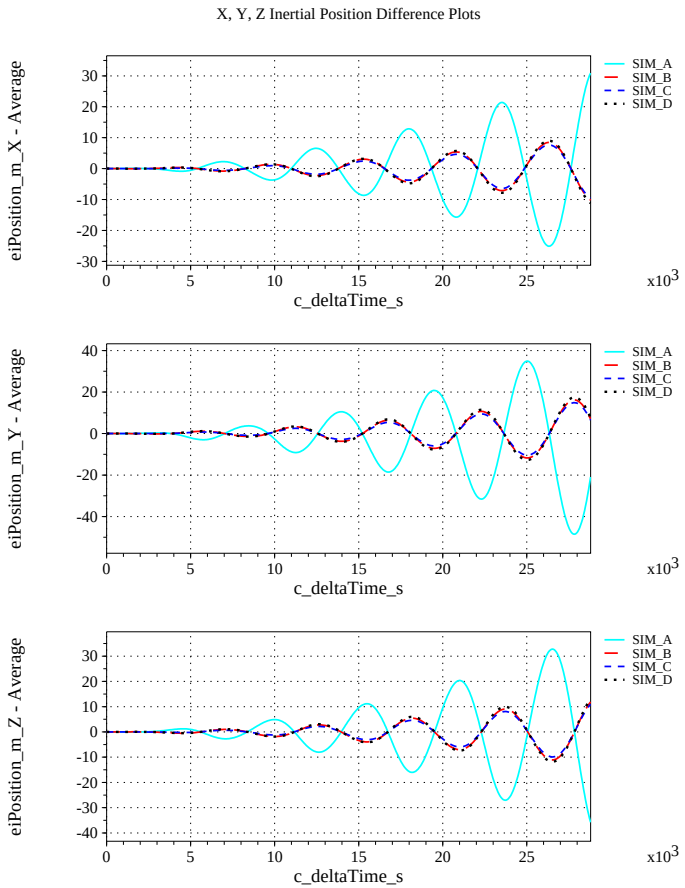

(n) Earth-centered Inertial Rectangular (x-y-z) Positions Differenced

Figure 50. Check-case 07C: Sphere in 4×4 Gravity with Drag and Third-body Perturbations; See Discussion in Section D.2.14 (Cont'd)

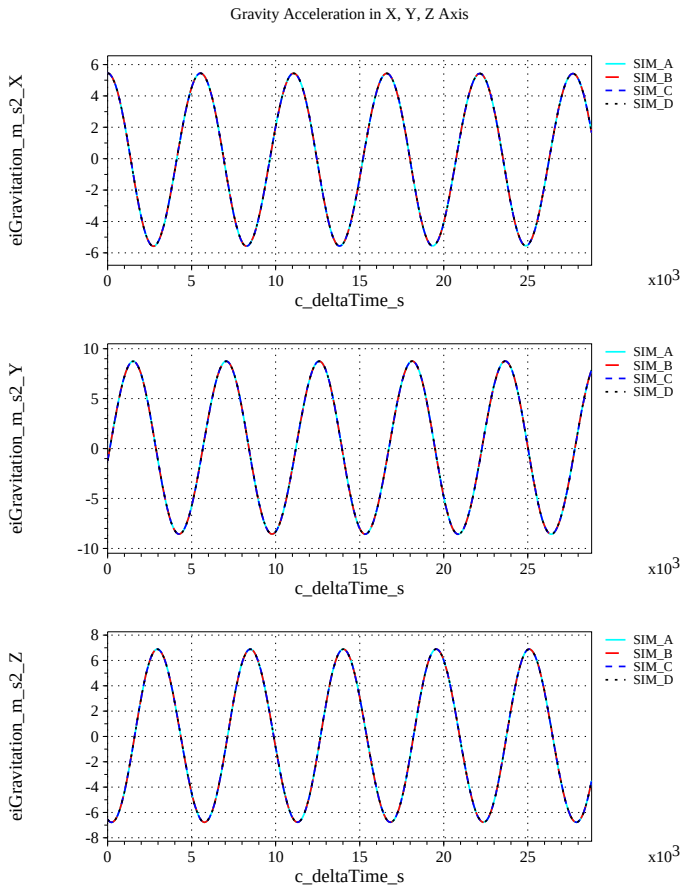

(o) Gravitational Components in Inertial (**X**-**Y**-**Z**) Directions Compared

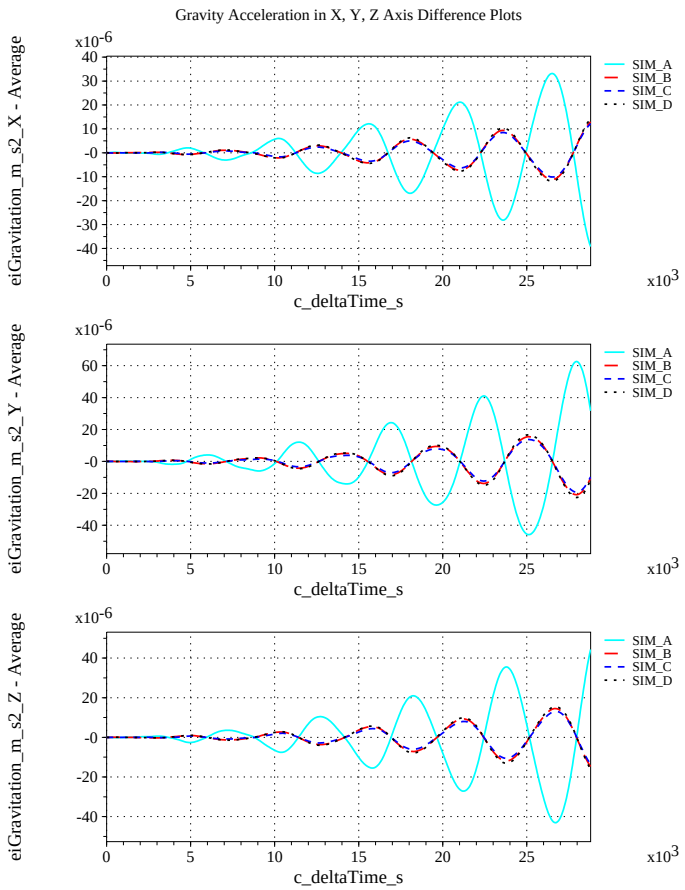

(p) Gravitational Components in Inertial (**X**-**Y**-**Z**) Directions Differenced

Figure 50. Check-case 07C: Sphere in 4×4 Gravity with Drag and Third-body Perturbations; See Discussion in Section D.2.14 (Concluded)

D.2.15 Check-case 07D – sphere in 8×8 gravity with drag and third-body perturbations

This section shows cross-plots for four of the selected simulation tools in modeling the dynamics of a sphere in orbit responding to an 8×8 gravity model, atmospheric drag, planetary ephemeris, and third-body perturbations. This scenario is described in Section C.2.15. Figures 51a through 51p compare results between the four simulation tools, as well as the deviances of the outputs from each tool from the ensemble average value.

Orbital check-case 7D was the last of four test cases that combined the geopotential gravitation perturbations of orbital test case 3A and 3B, the Sun and Moon perturbations of orbital case 4, and the aerodynamic drag of orbital case 6B. This check-case used the geopotential perturbations of order and degree eight defined in orbital case 3B.

The differences in translational states among the simulations was a combination of the differences appearing in orbital test cases 3A, 4, and 6B. Differences for the translation states in SIM A were primarily caused its unique use of the MET07 model to predict the atmospheric density input to the aerodynamic drag. By comparison, differences among the other simulations barely registered on the plots. These differences were probably caused by apparent differences in accuracy of the geopotential gravitation implementation and differences in atmospheric density predicted by the MET95 and MET99 models. See orbital case 3A (Section D.2.2) for more details on the apparent accuracy differences in geopotential gravitation implementation and see orbital case 5A (Section D.2.5) for more details on the differences among the MET model versions in predicting atmospheric density.

The simulations agreed on the inertial rotational state. Differences among the simulations were negligible and were attributed to differences in integration error. Differences in the orbit-relative LVLH orientation were larger as a result of the small differences in orbit parameters defined by the translational states.

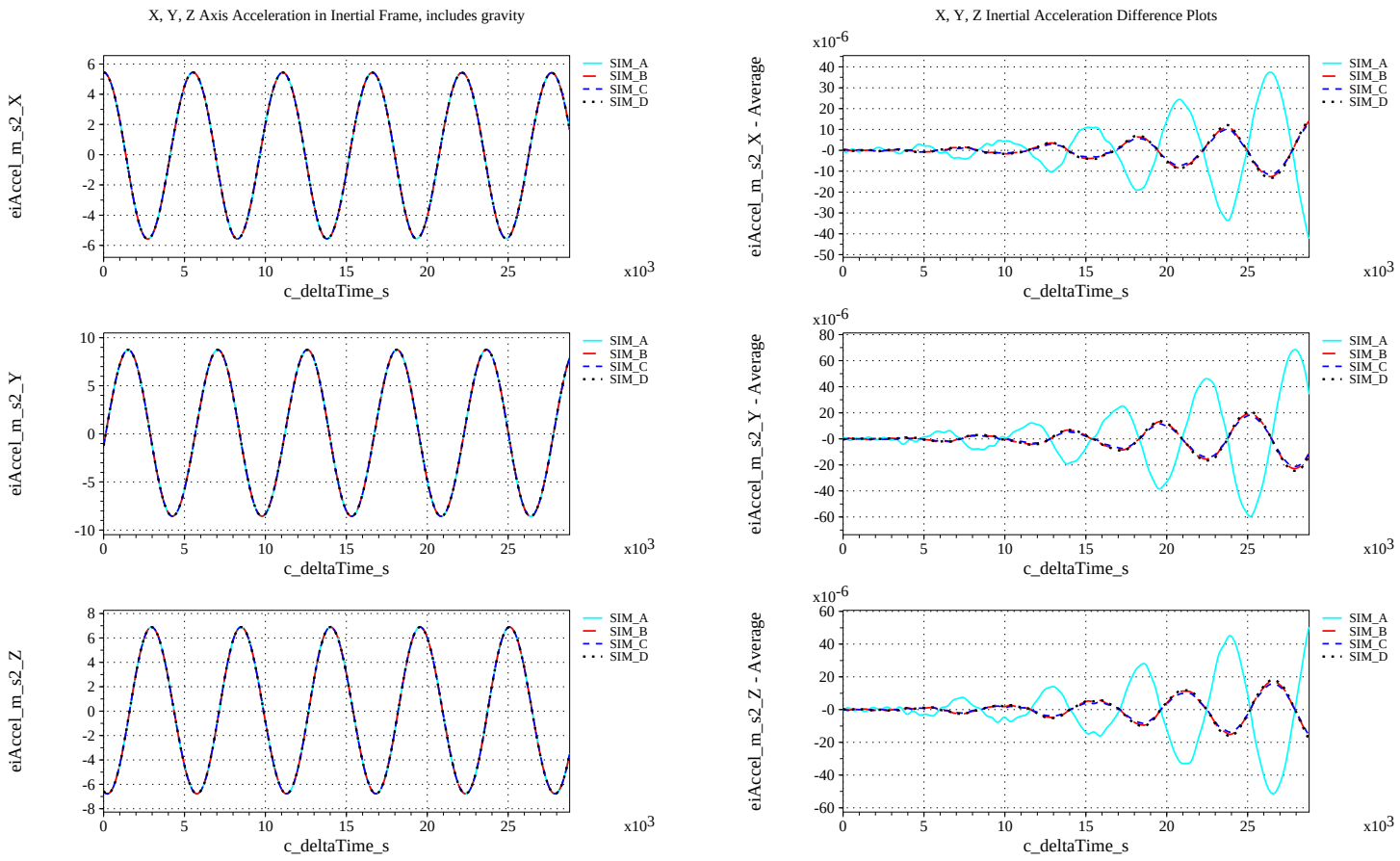

(a) Inertial Accelerations Compared

(b) Inertial Accelerations Differenced

Figure 51. Check-case 07D: Sphere in 8×8 Gravity with Drag and Third-body Perturbations; See Discussion in Section D.2.15

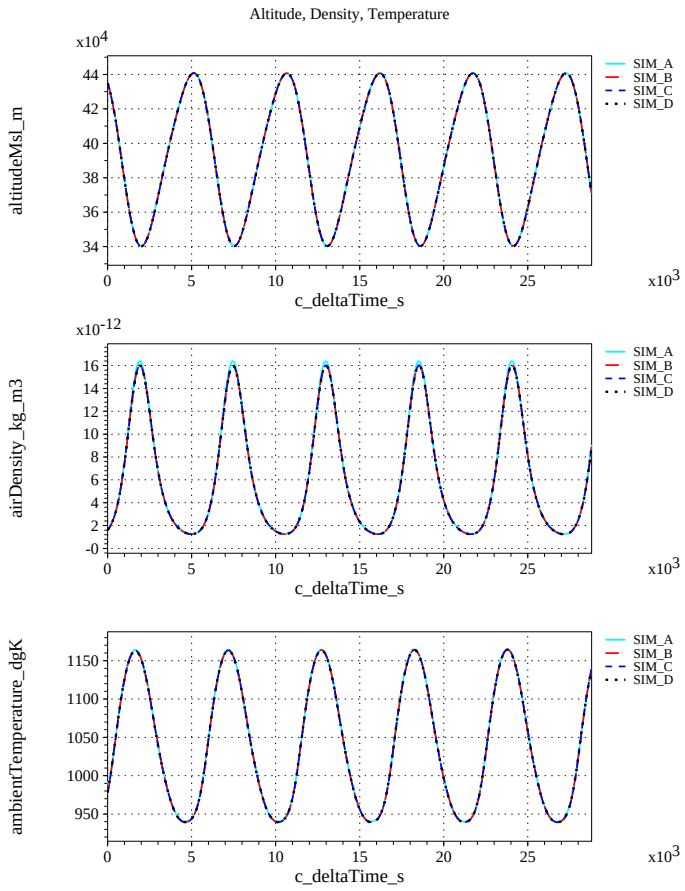

(c) Atmospheric Properties Compared

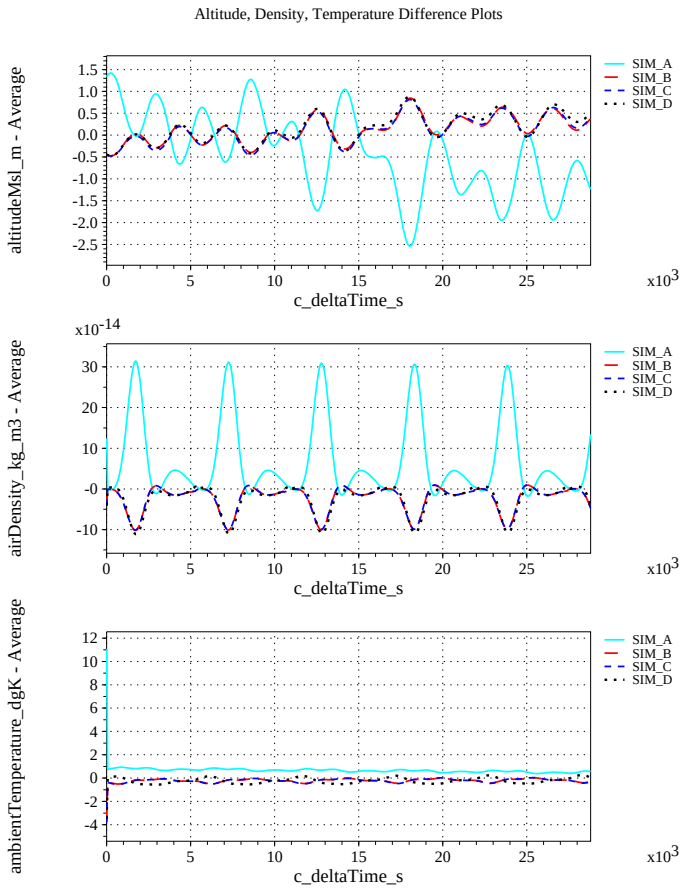

(d) Atmospheric Properties Differenced

Figure 51. Check-case 07D: Sphere in 8×8 Gravity with Drag and Third-body Perturbations; See Discussion in Section D.2.15 (Cont'd)

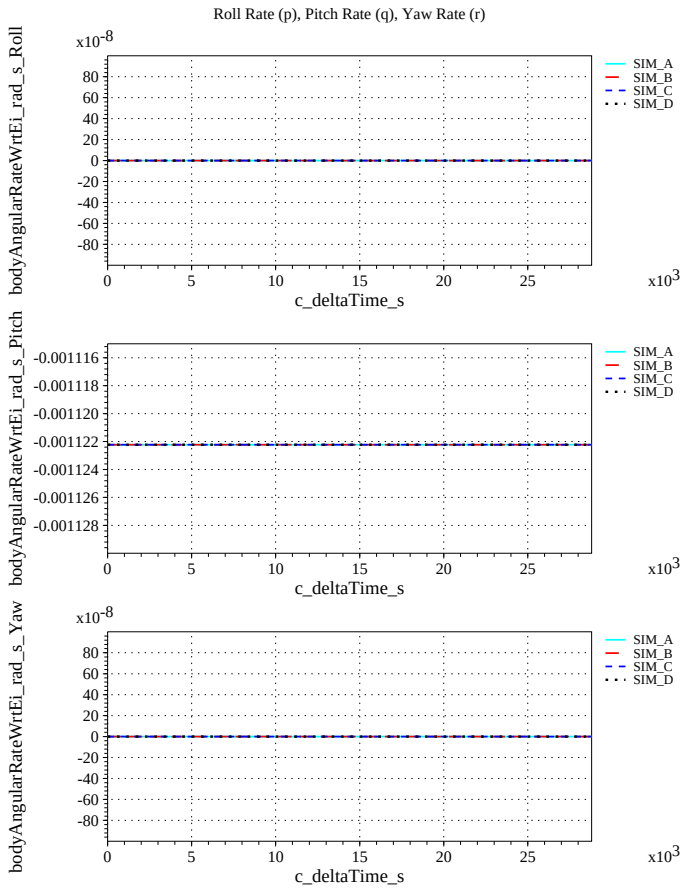

(e) Body-axis Angular Rates Compared

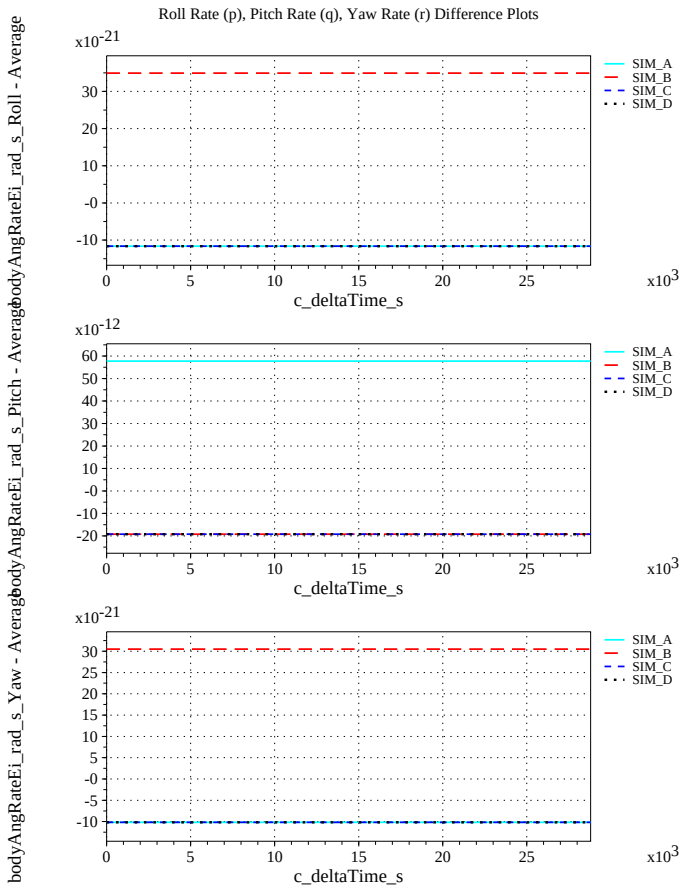

(f) Body-axis Angular Rates Differenced

Figure 51. Check-case 07D: Sphere in 8×8 Gravity with Drag and Third-body Perturbations; See Discussion in Section D.2.15 (Cont'd)

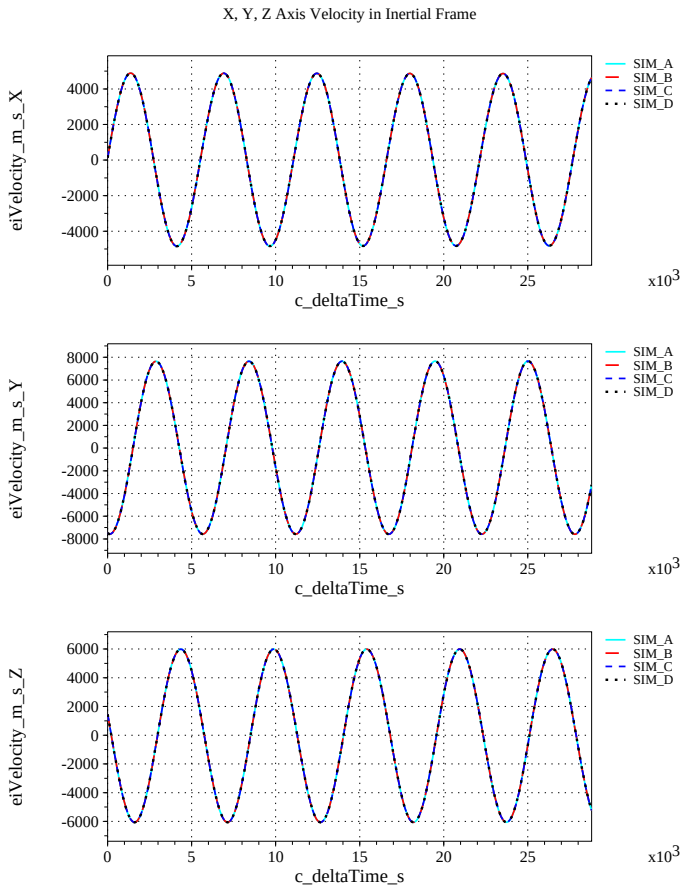

(g) Inertial Velocities Compared

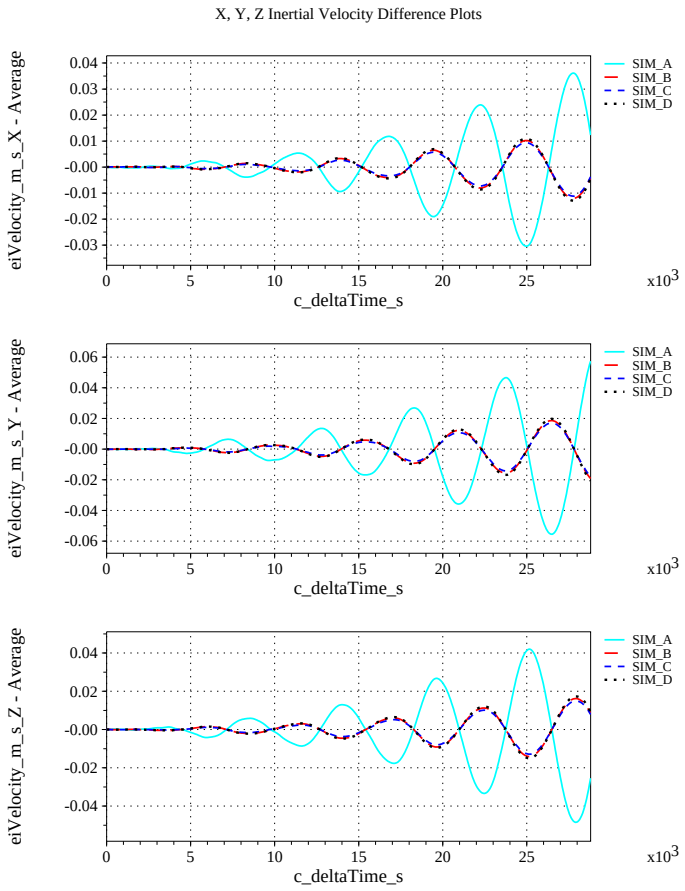

(h) Inertial Velocities Differenced

Figure 51. Check-case 07D: Sphere in 8×8 Gravity with Drag and Third-body Perturbations; See Discussion in Section D.2.15 (Cont'd)

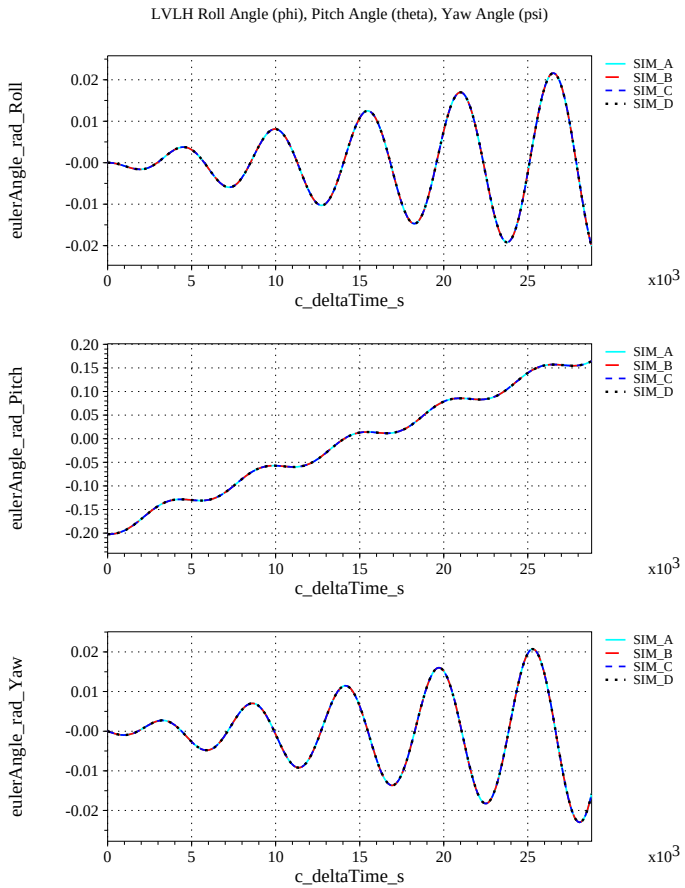

(i) Rotation Angles with Respect to LVLH Frame Compared

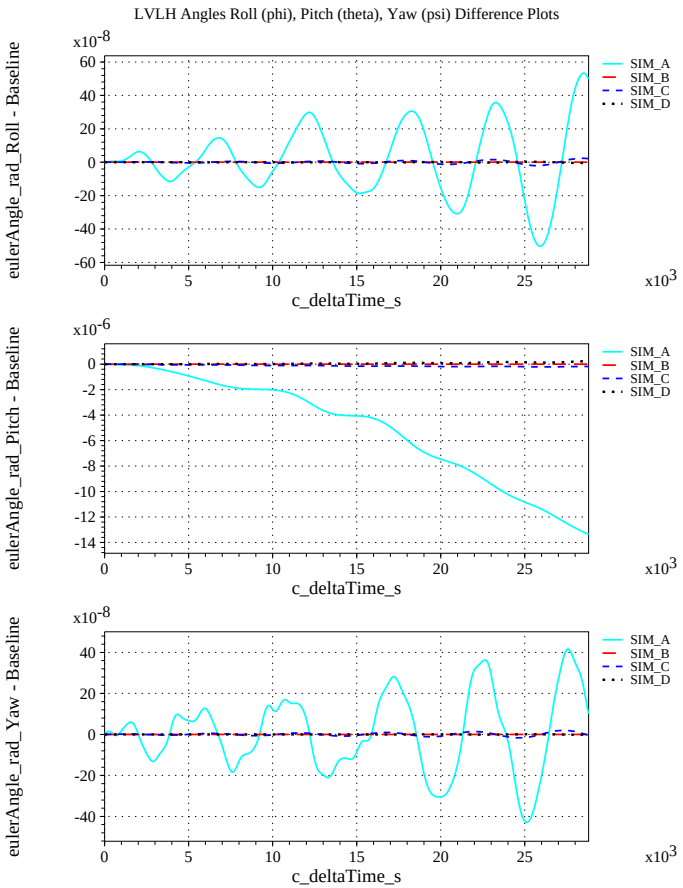

(j) Rotation Angles with Respect to LVLH Frame Differenced

Figure 51. Check-case 07D: Sphere in 8×8 Gravity with Drag and Third-body Perturbations; See Discussion in Section D.2.15 (Cont'd)

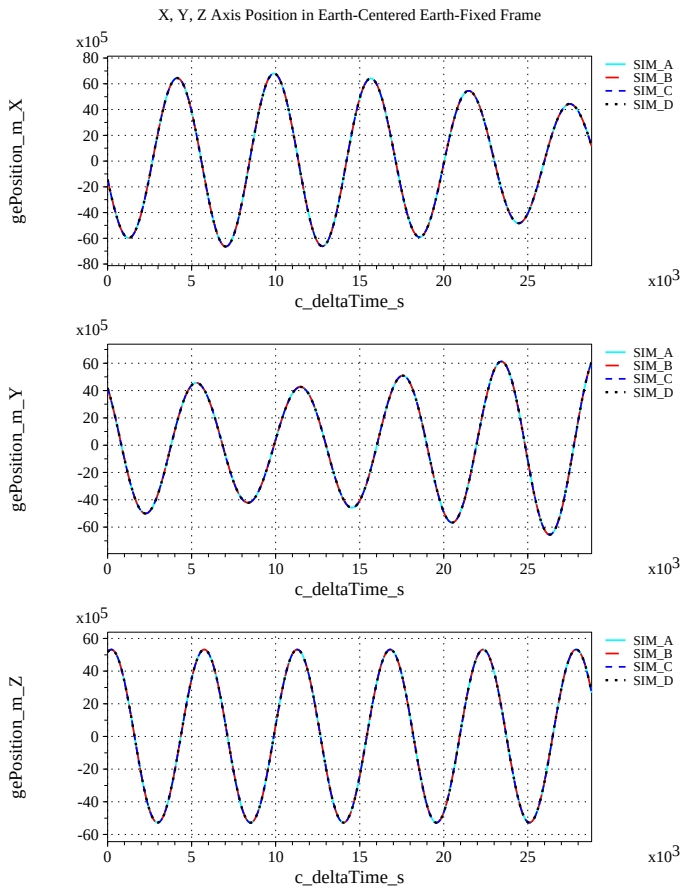

(k) Earth-centered, Earth-fixed Rectangular (X-Y-Z) Positions Compared

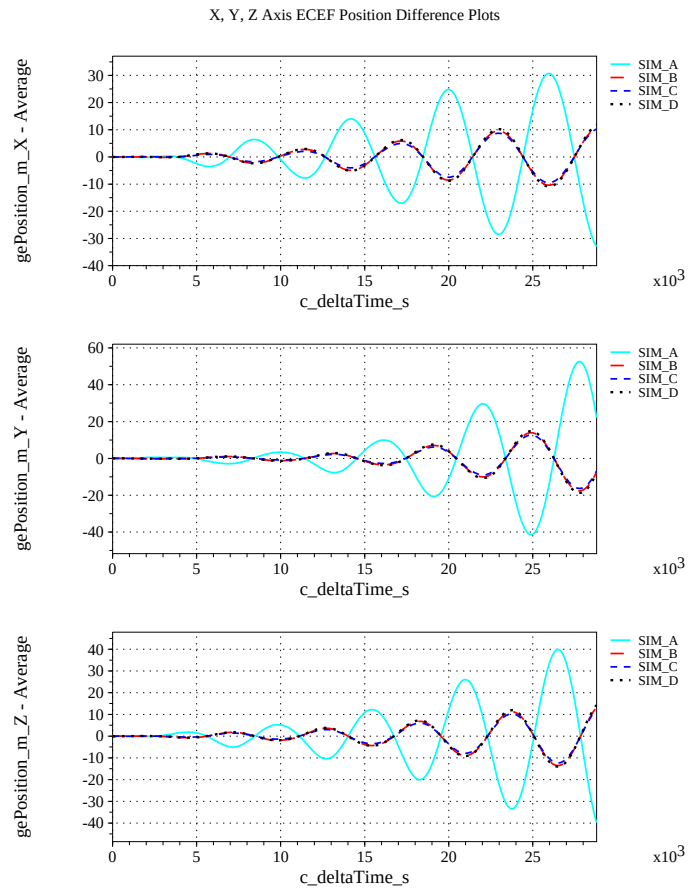

(l) Earth-centered, Earth-fixed Rectangular (X-Y-Z) Positions Differenced

Figure 51. Check-case 07D: Sphere in 8×8 Gravity with Drag and Third-body Perturbations; See Discussion in Section D.2.15 (Cont'd)

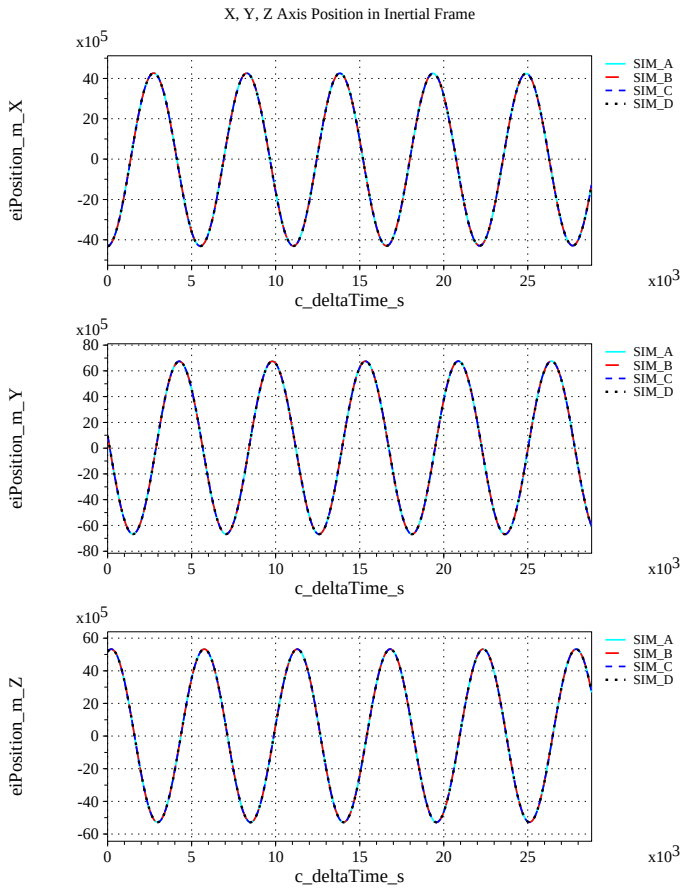

(m) Earth-centered Inertial Rectangular (x-y-z) Positions Compared

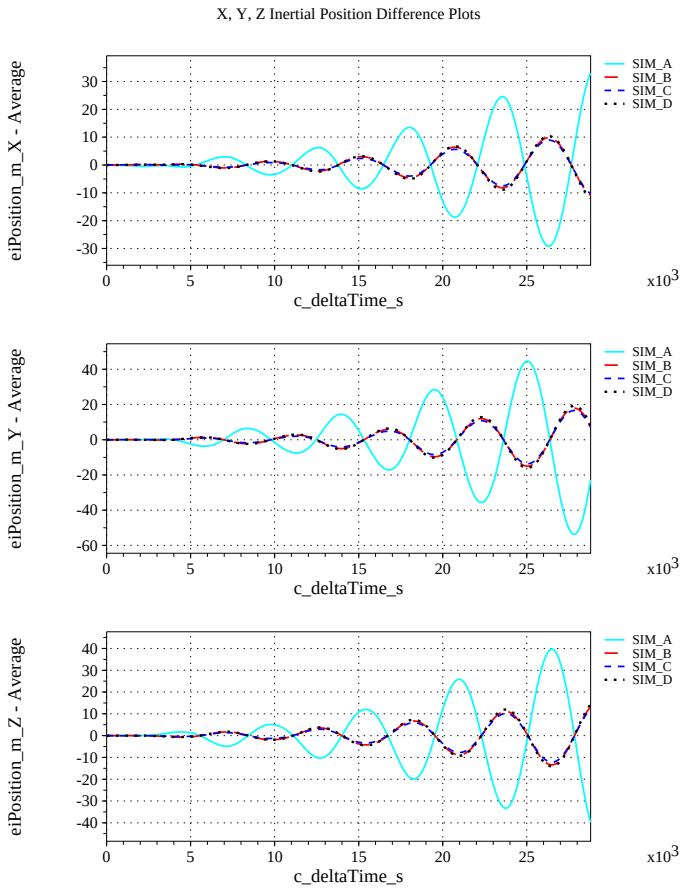

(n) Earth-centered Inertial Rectangular (x-y-z) Positions Differenced

Figure 51. Check-case 07D: Sphere in 8×8 Gravity with Drag and Third-body Perturbations; See Discussion in Section D.2.15 (Cont'd)

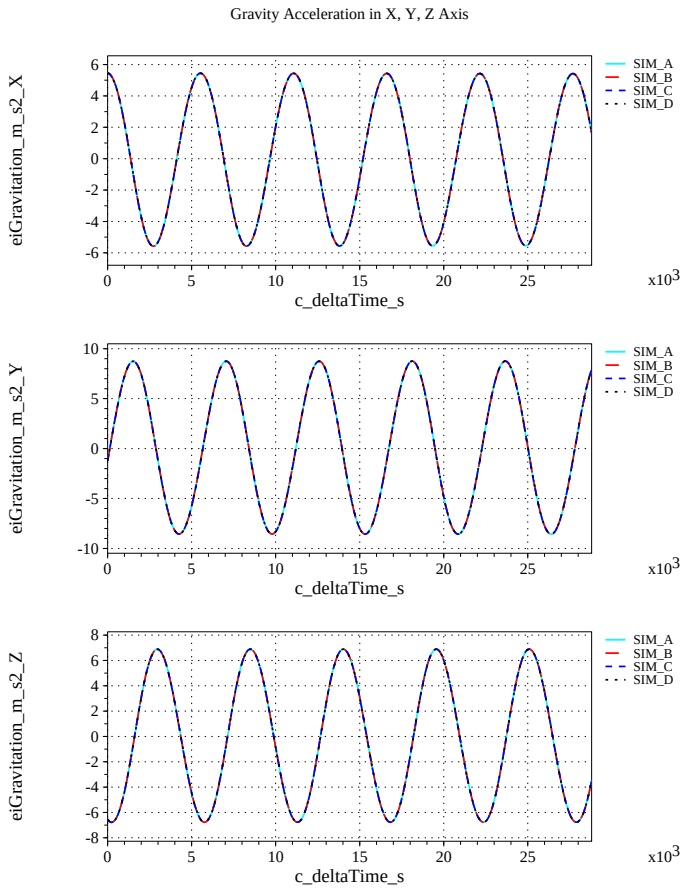

(o) Gravitational Components in Inertial (**X**-**Y**-**Z**) Directions Compared

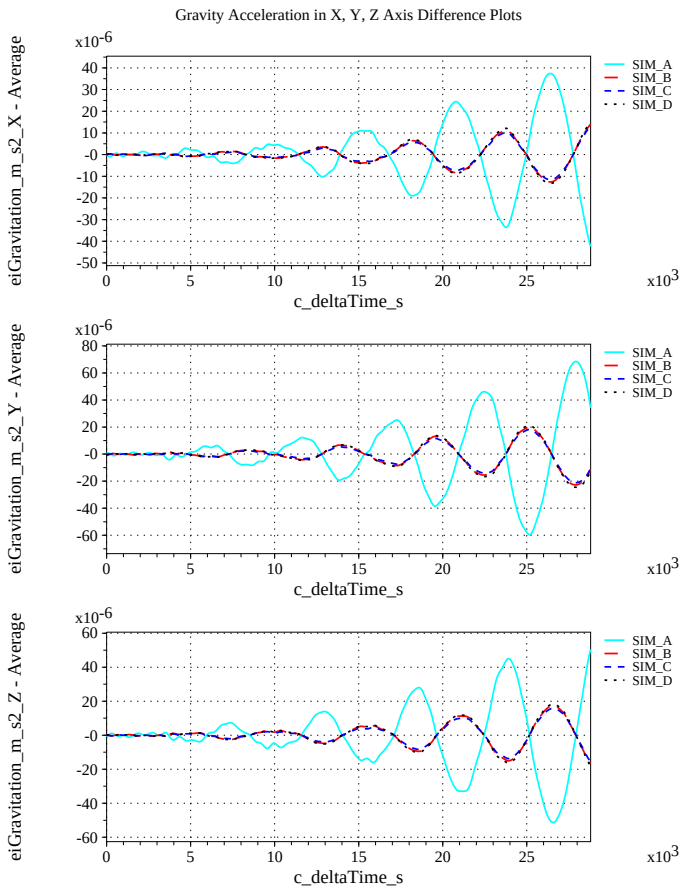

(p) Gravitational Components in Inertial (**X**-**Y**-**Z**) Directions Differenced

Figure 51. Check-case 07D: Sphere in 8×8 Gravity with Drag and Third-body Perturbations; See Discussion in Section D.2.15 (Concluded)

D.2.16 Check-case 08A – ISS free rotation with zero rates

This section shows cross-plots for four of the selected simulation tools in modeling the dynamics of the ISS in torque-free rotation starting with zero inertial rate. This scenario is described in Section C.2.16. Figures 52a through 52p compare results between the four simulation tools, as well as the deviances of the outputs from each tool from the ensemble average value.

Orbital check-case 8A was the first of two orbital cases to focus on torque-free rotation. This case defined an initial rotation rate of zero relative to the inertial frame. Differences in rotational states between the simulations were negligible and were attributed to differences in integration error or differences in the precision of the recorded data.

Differences in translational states among the simulations were nearly identical to orbital case 2 (see Section D.2.1).

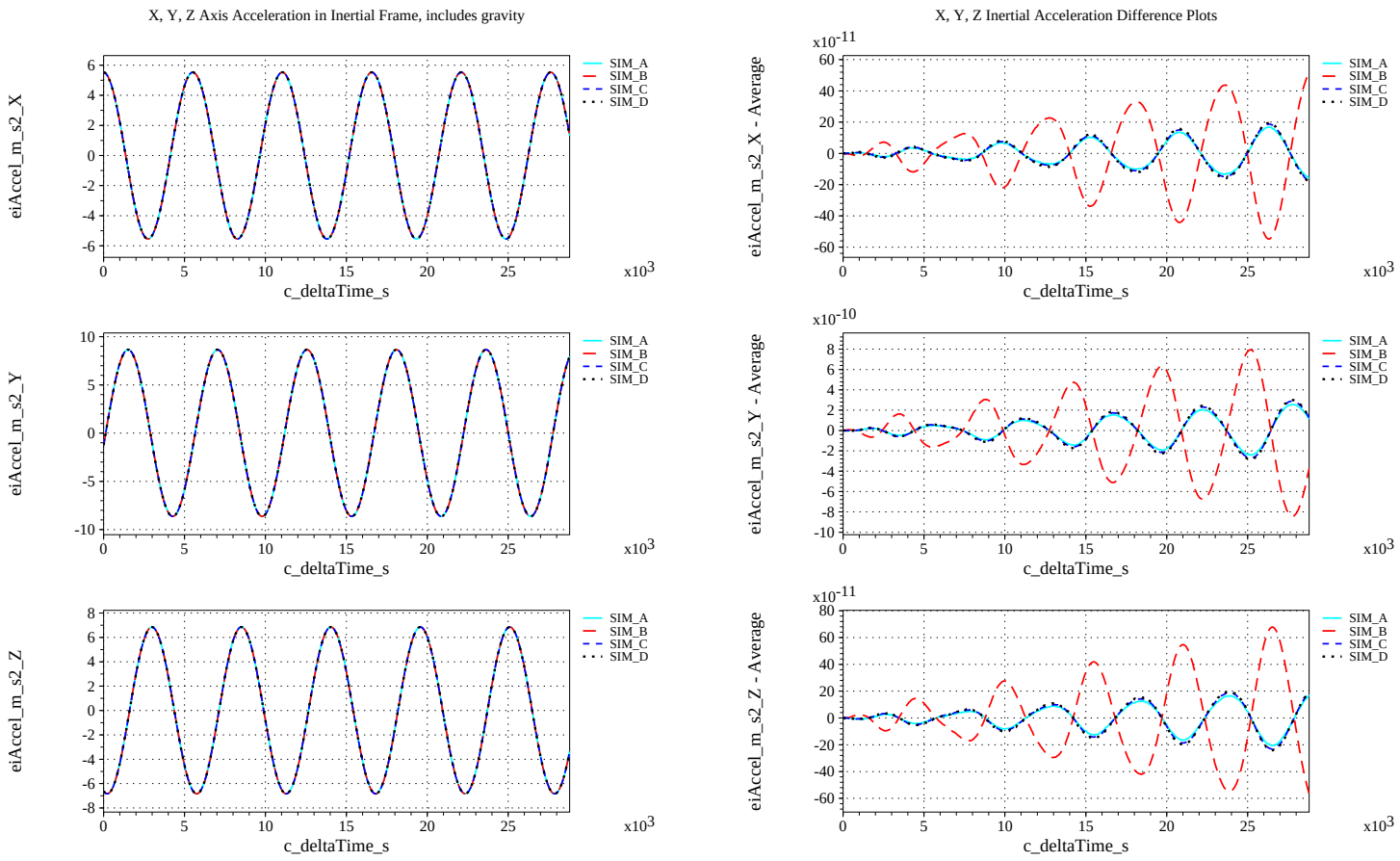

(a) Inertial Accelerations Compared

(b) Inertial Accelerations Differenced

Figure 52. Check-case 08A: ISS Free Rotation with Zero Rates; See Discussion in Section D.2.16

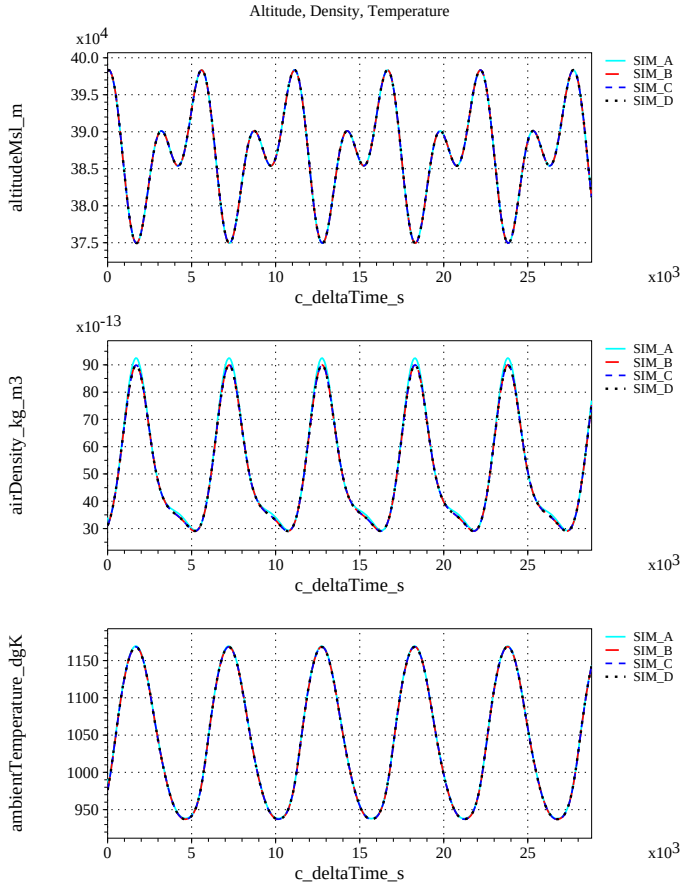

(c) Atmospheric Properties Compared

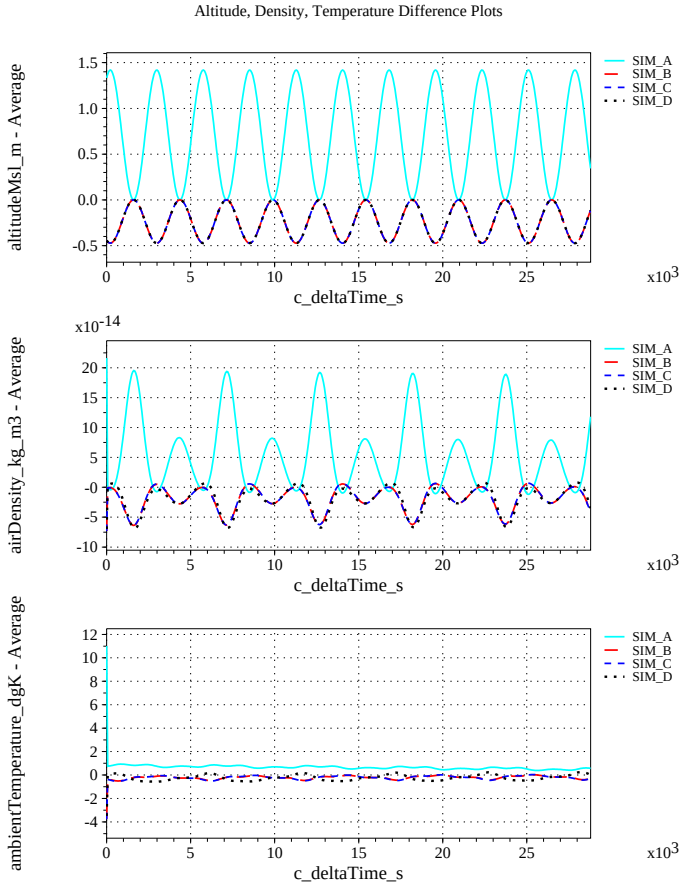

(d) Atmospheric Properties Differenced

Figure 52. Check-case 08A: ISS Free Rotation with Zero Rates; See Discussion in Section D.2.16 (Cont'd)

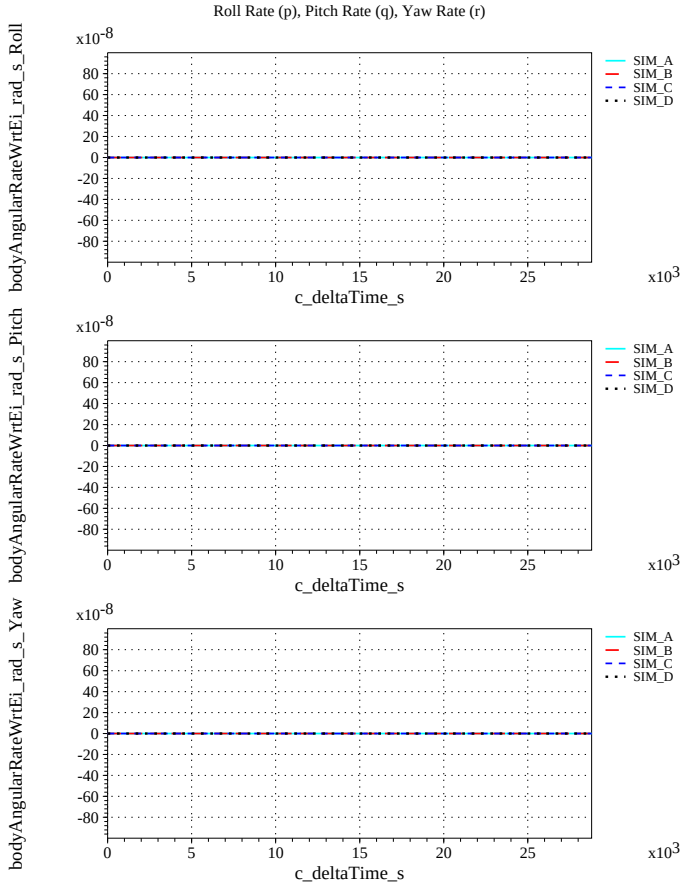

(e) Body-axis Angular Rates Compared

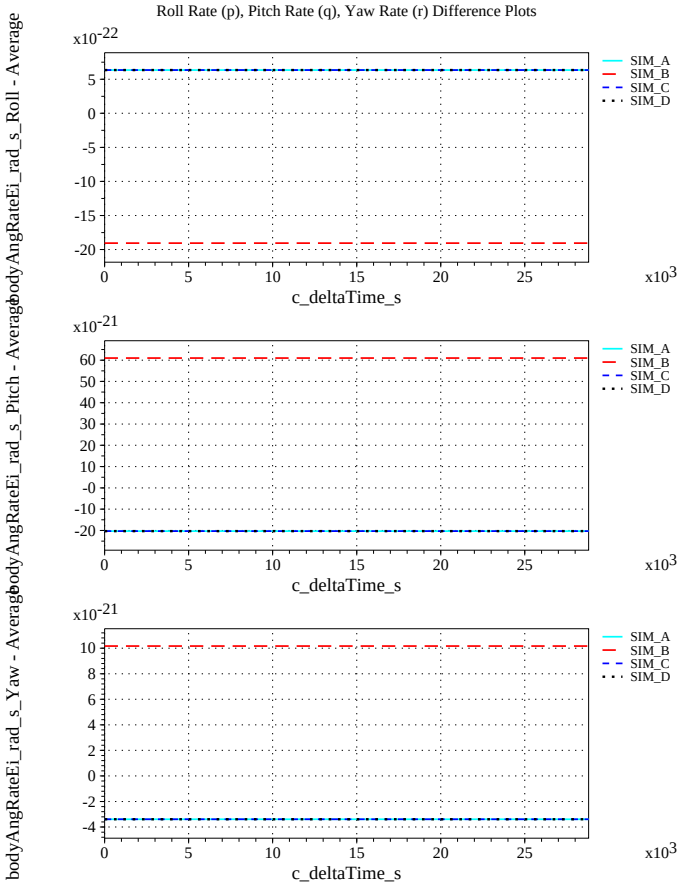

(f) Body-axis Angular Rates Differenced

Figure 52. Check-case 08A: ISS Free Rotation with Zero Rates; See Discussion in Section D.2.16 (Cont'd)

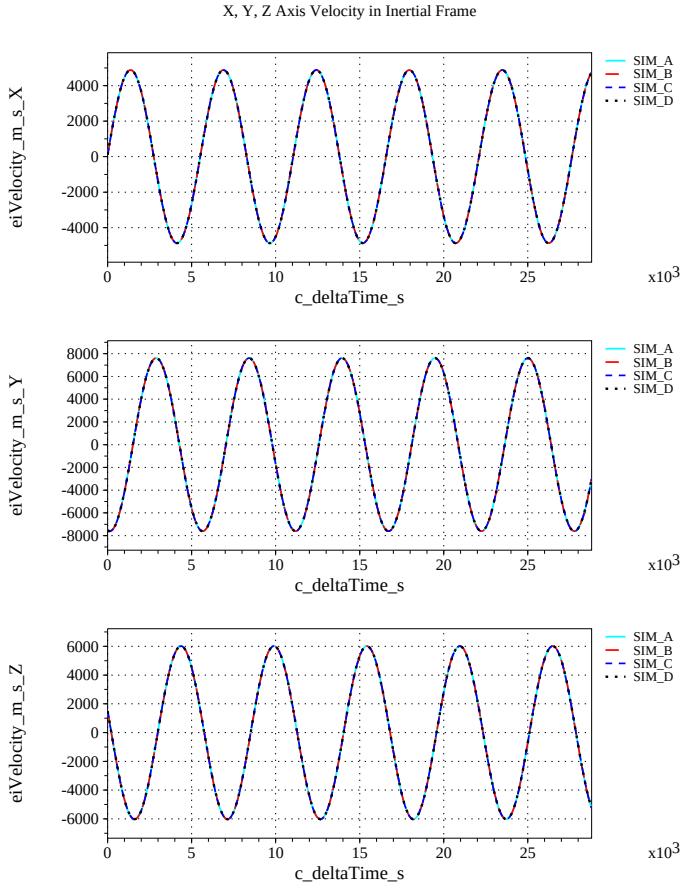

(g) Inertial Velocities Compared

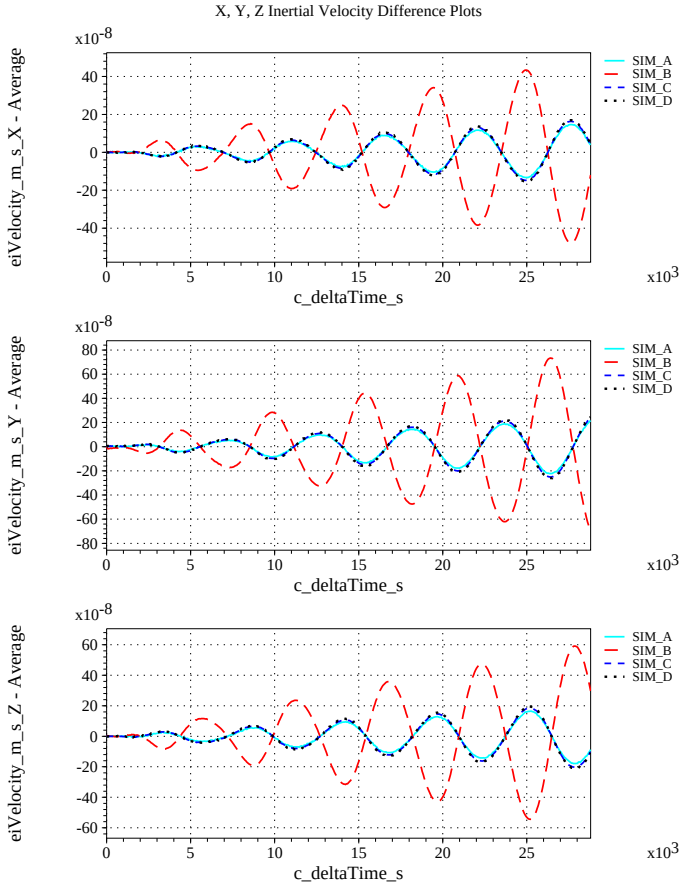

(h) Inertial Velocities Differenced

Figure 52. Check-case 08A: ISS Free Rotation with Zero Rates; See Discussion in Section D.2.16 (Cont'd)

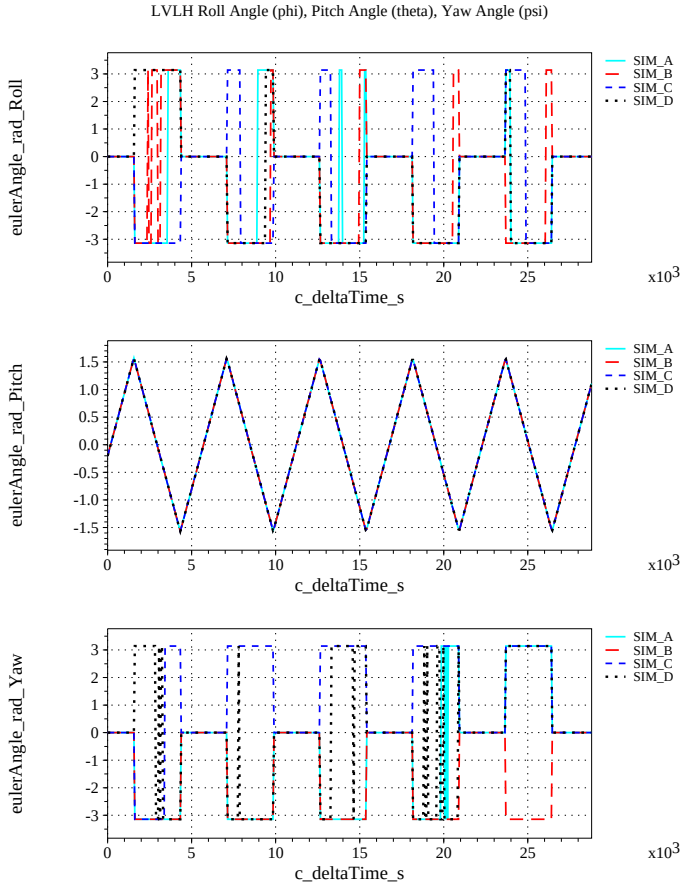

(i) Rotation Angles with Respect to LVLH Frame Compared

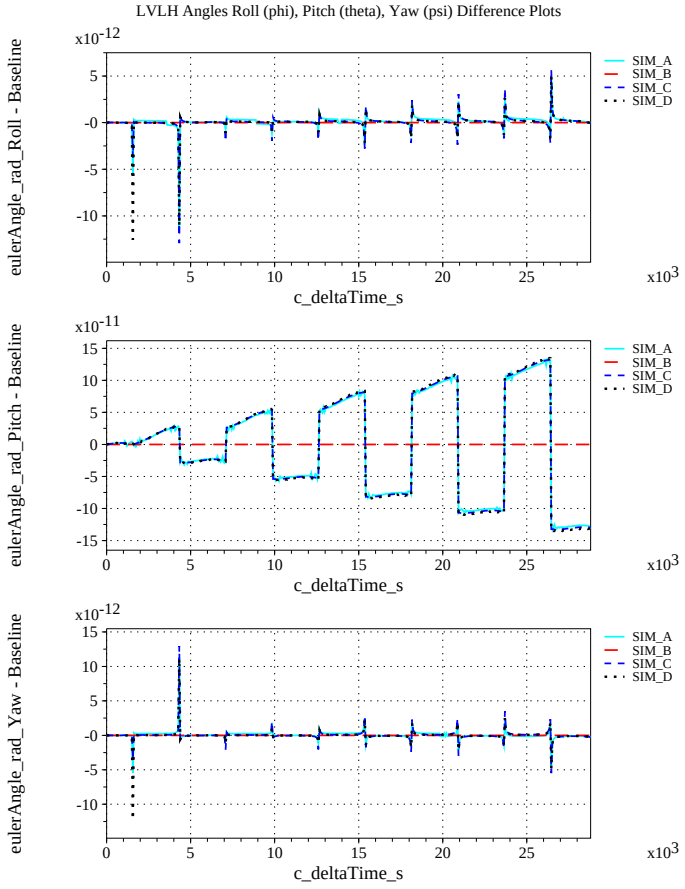

(j) Rotation Angles with Respect to LVLH Frame Differenced

Figure 52. Check-case 08A: ISS Free Rotation with Zero Rates; See Discussion in Section D.2.16 (Cont'd)

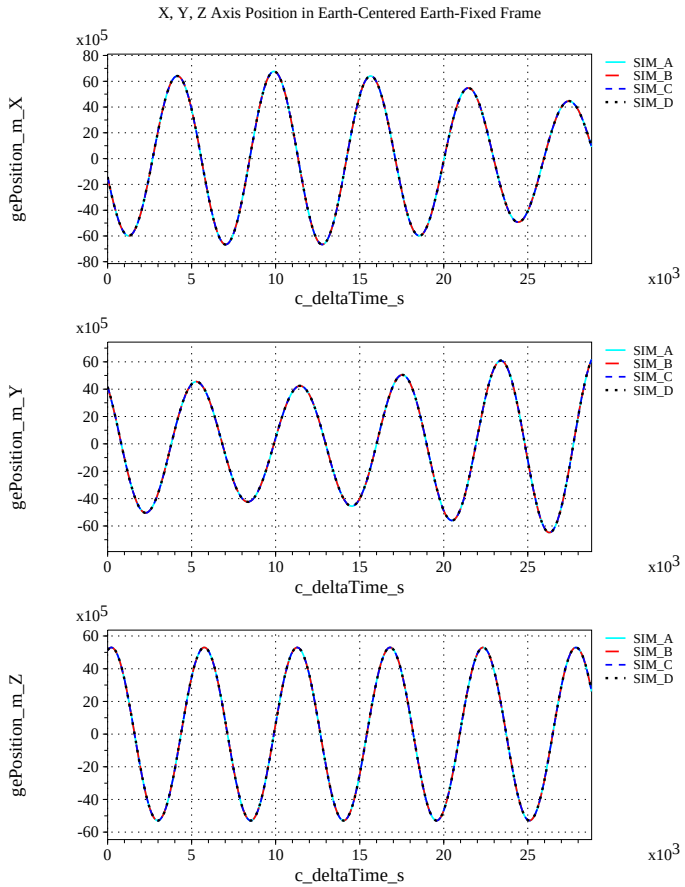

(k) Earth-centered, Earth-fixed Rectangular (X-Y-Z) Positions Compared

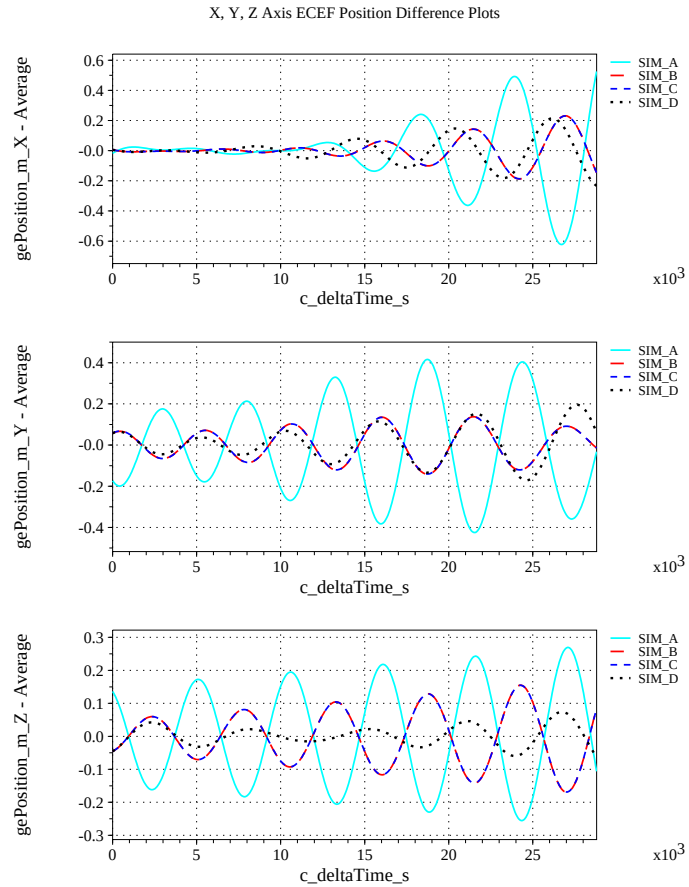

(l) Earth-centered, Earth-fixed Rectangular (X-Y-Z) Positions Differenced

Figure 52. Check-case 08A: ISS Free Rotation with Zero Rates; See Discussion in Section D.2.16 (Cont'd)

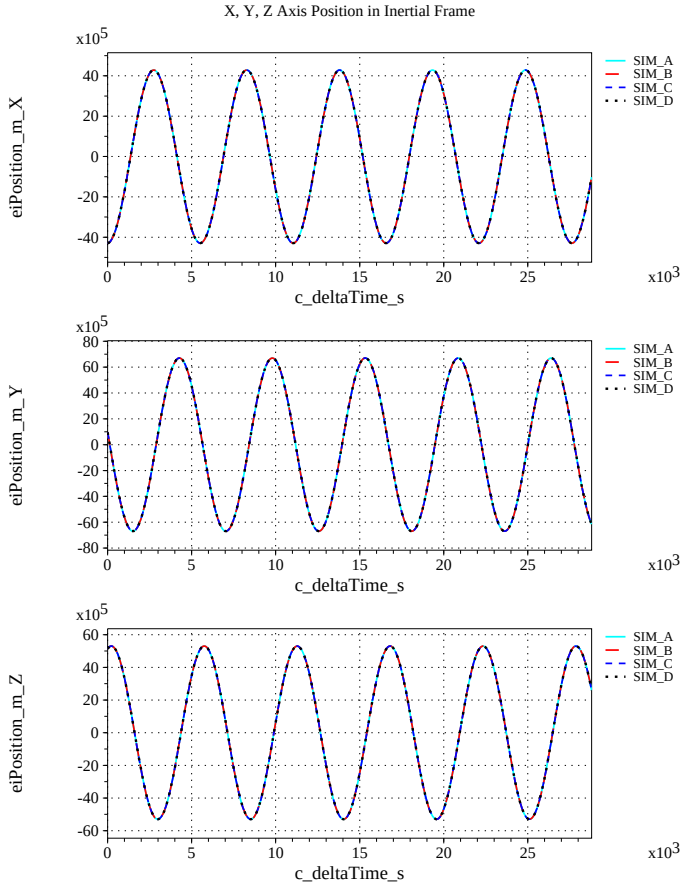

(m) Earth-centered Inertial Rectangular (x-y-z) Positions Compared

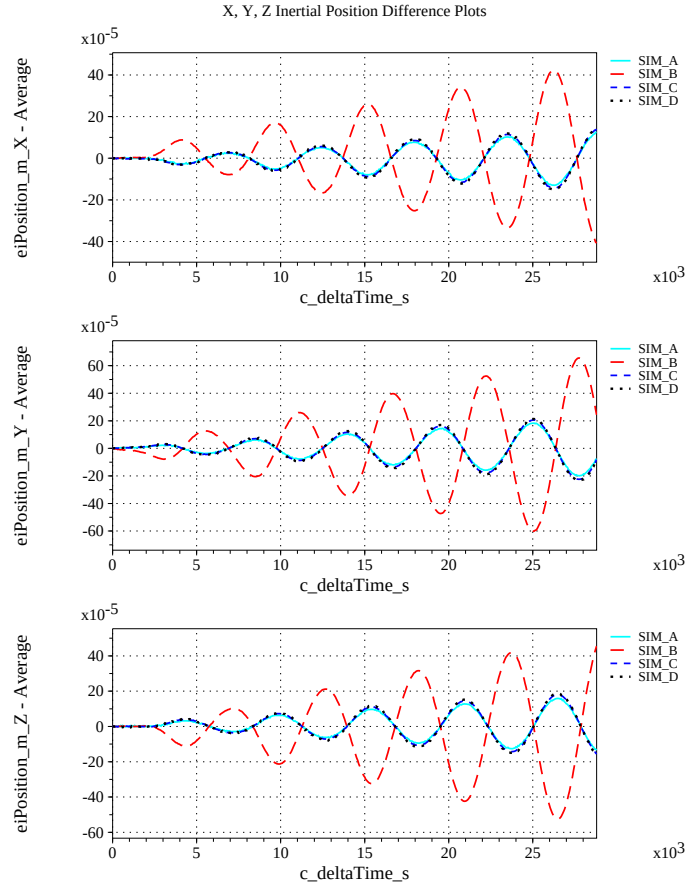

(n) Earth-centered Inertial Rectangular (x-y-z) Positions Differenced

Figure 52. Check-case 08A: ISS Free Rotation with Zero Rates; See Discussion in Section D.2.16 (Cont'd)

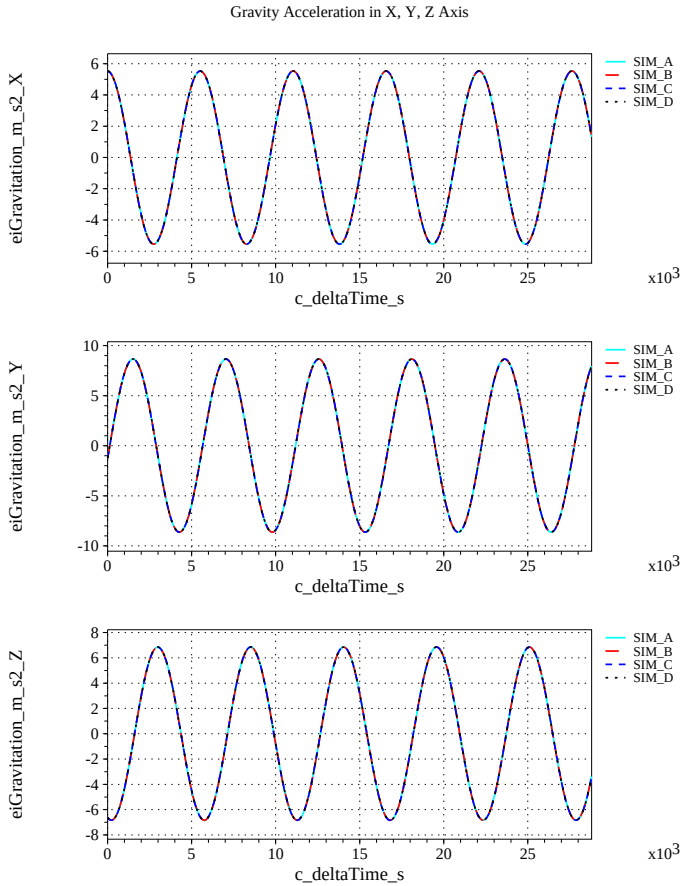

(o) Gravitational Components in Inertial (**X**-**Y**-**Z**) Directions Compared

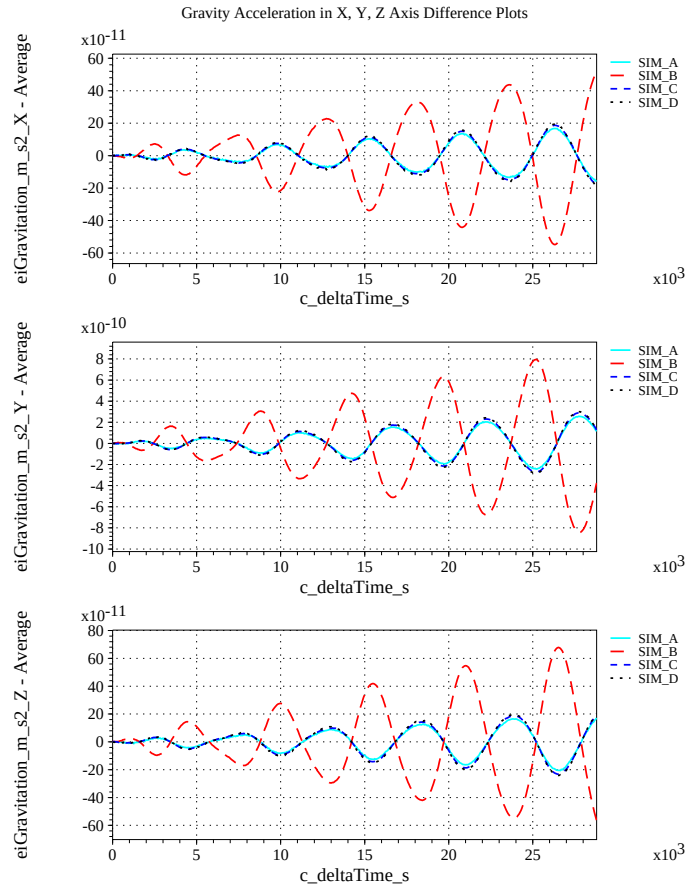

(p) Gravitational Components in Inertial (**X**-**Y**-**Z**) Directions Differenced

Figure 52. Check-case 08A: ISS Free Rotation with Zero Rates; See Discussion in Section D.2.16 (Concluded)

D.2.17 Check-case 08B – ISS free rotation with non-zero rates

This section shows cross-plots for four of the selected simulation tools in modeling the dynamics of the ISS in torque-free rotation starting with a non-zero inertial rate. This scenario is described in Section C.2.17. Figures 53a through 53p compare results between the four simulation tools, as well as the deviances of the outputs from each tool from the ensemble average value.

Orbital check-case 8B was the second of two orbital cases to focus on torque-free rotation. This case defined an initial rotation rate of zero relative to the LVLH frame, i.e. an inertial rate that was not zero.

Differences in rotational states between the simulations were negligible and were attributed to differences in integration method or differences in the precision of the recorded data. The one exception was the difference in the initial inertial pitch rate for SIM D (see Figure 53f).

Although hard to see in the plots, SIM D recorded a sudden jump in pitch rate from 0 rad/s at $t = 0$ to 0.0011 rad/s at $t = 60$ sec (the next recorded frame). However, this jump appeared to be an artifact of the data recording as the Euler angles showed no response to this jump. Nevertheless, this jump was sufficiently large to require the comparison plots to use a range that was too large to display the differences between the simulations in the rest of the maneuver. Even so, those differences were similar in magnitude to the differences seen in the roll and yaw rates.

Differences in translational states among the simulations were nearly identical to orbital check-case 2 (see Section D.2.1).

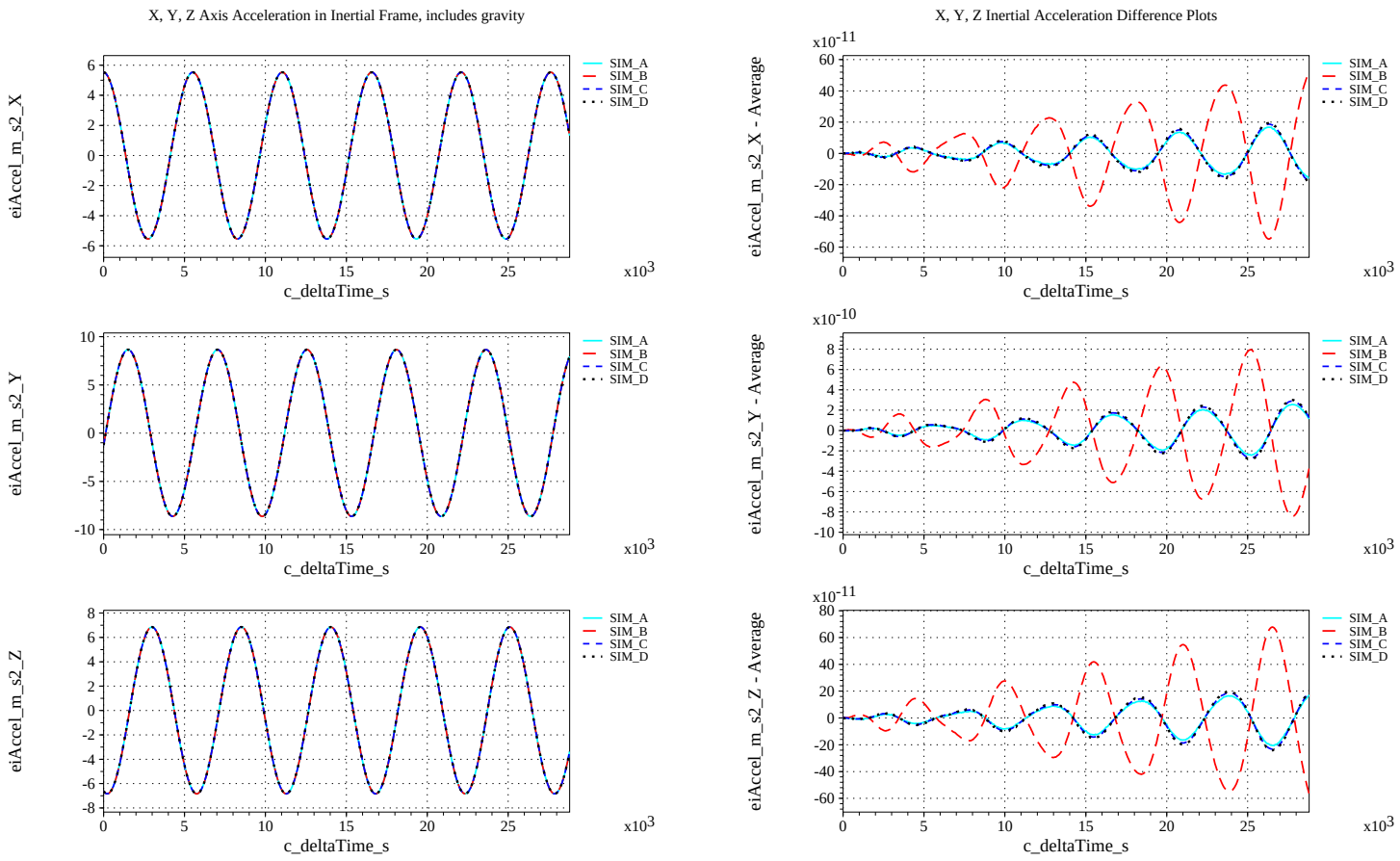

(a) Inertial Accelerations Compared

(b) Inertial Accelerations Differenced

Figure 53. Check-case 08B: ISS Free Rotation with Non-zero Rates; See Discussion in Section D.2.17

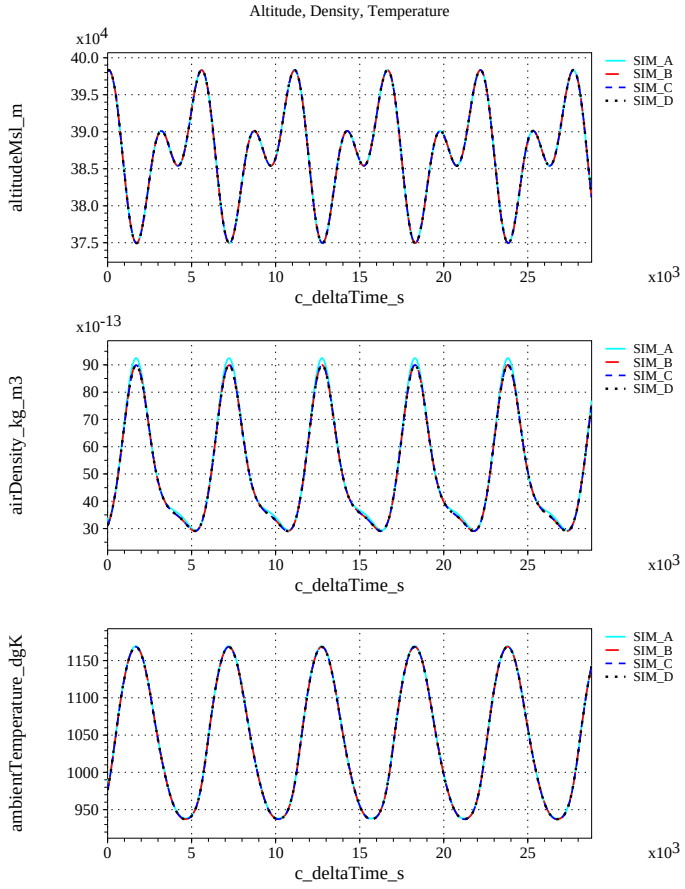

(c) Atmospheric Properties Compared

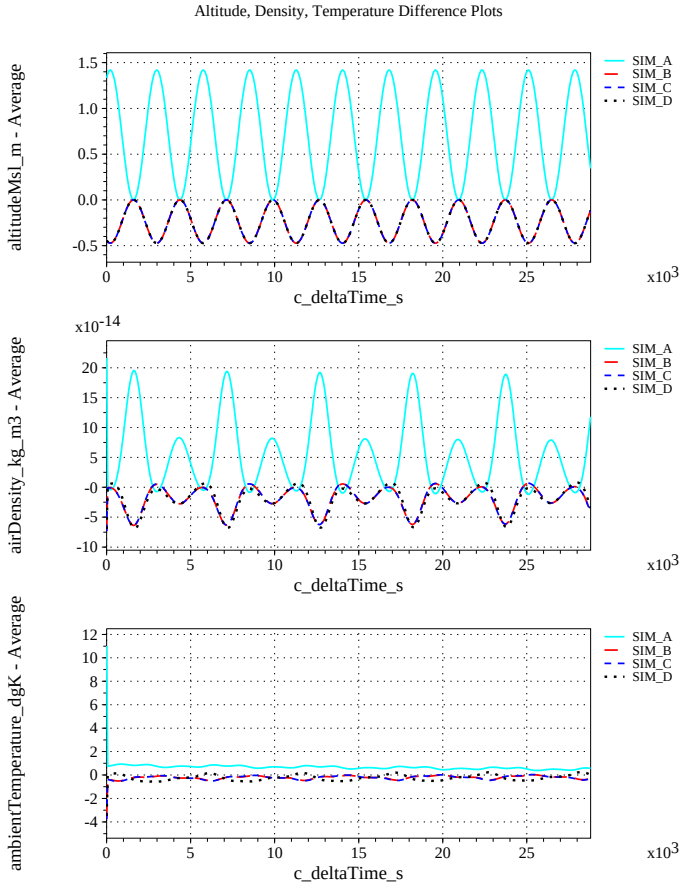

(d) Atmospheric Properties Differenced

Figure 53. Check-case 08B: ISS Free Rotation with Non-zero Rates; See Discussion in Section D.2.17 (Cont'd)

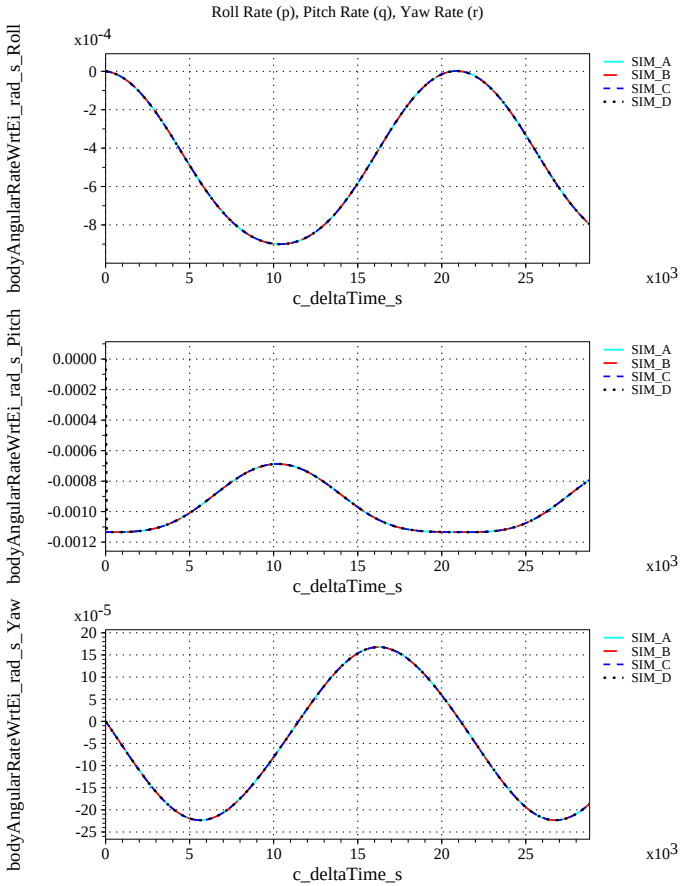

(e) Body-axis Angular Rates Compared

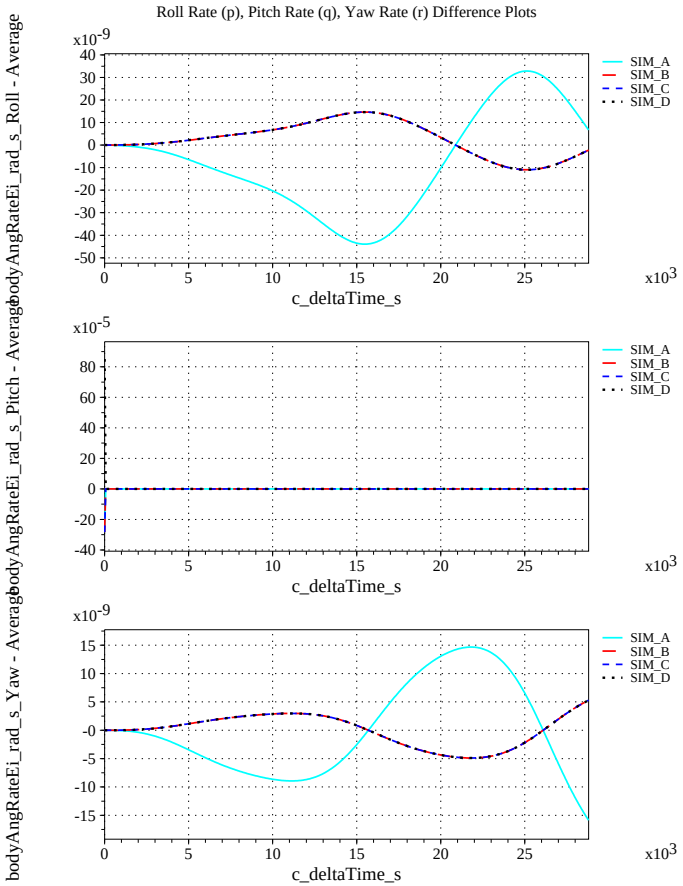

(f) Body-axis Angular Rates Differenced

Figure 53. Check-case 08B: ISS Free Rotation with Non-zero Rates; See Discussion in Section D.2.17 (Cont'd)

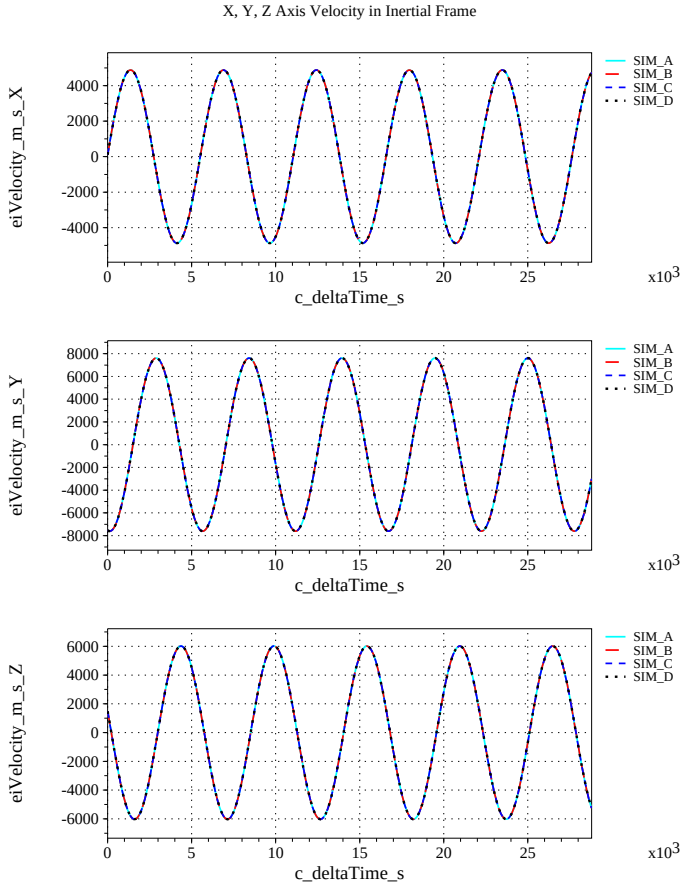

(g) Inertial Velocities Compared

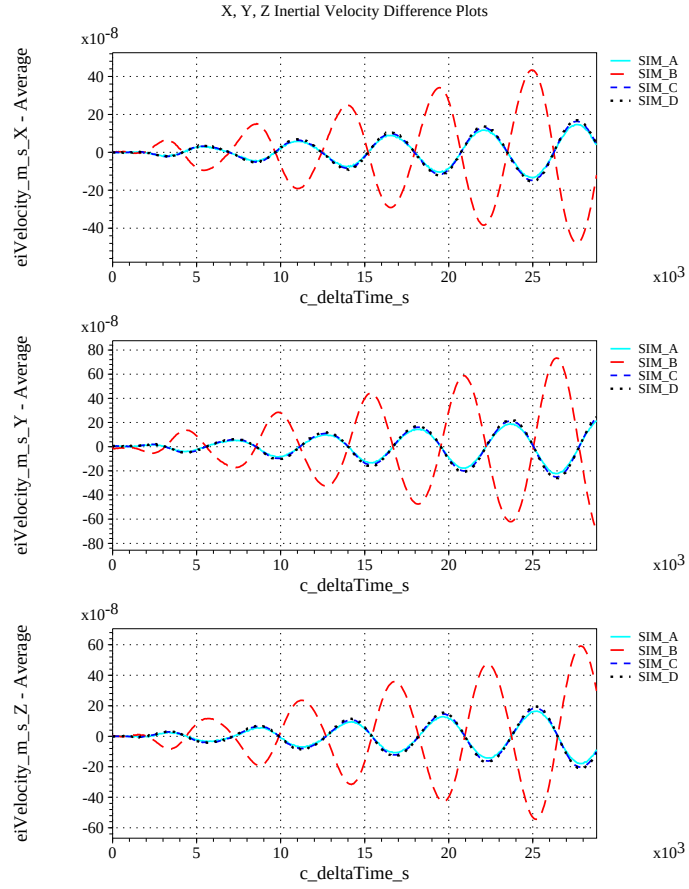

(h) Inertial Velocities Differenced

Figure 53. Check-case 08B: ISS Free Rotation with Non-zero Rates; See Discussion in Section D.2.17 (Cont'd)

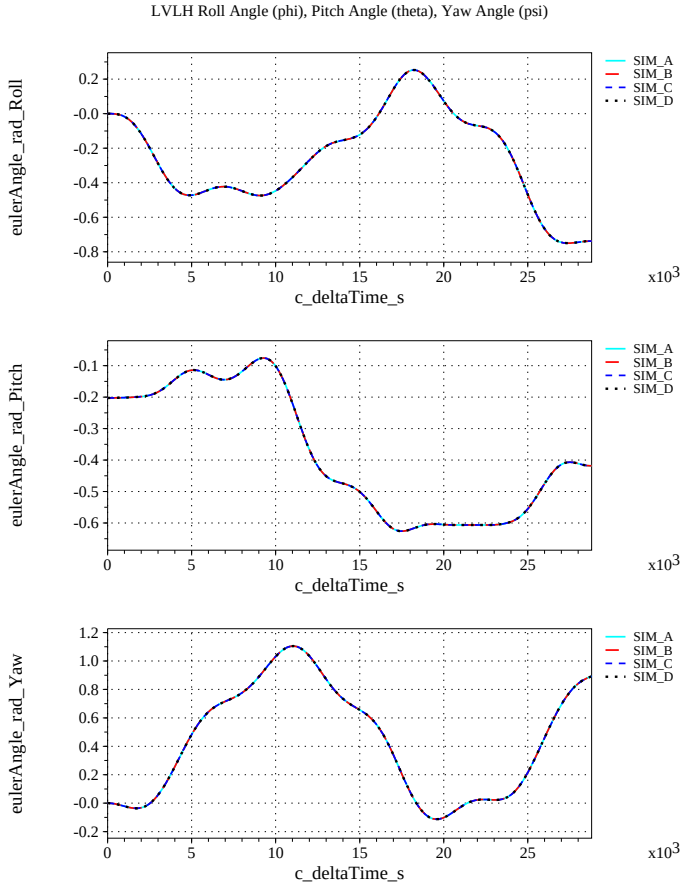

(i) Rotation Angles with Respect to LVLH Frame Compared

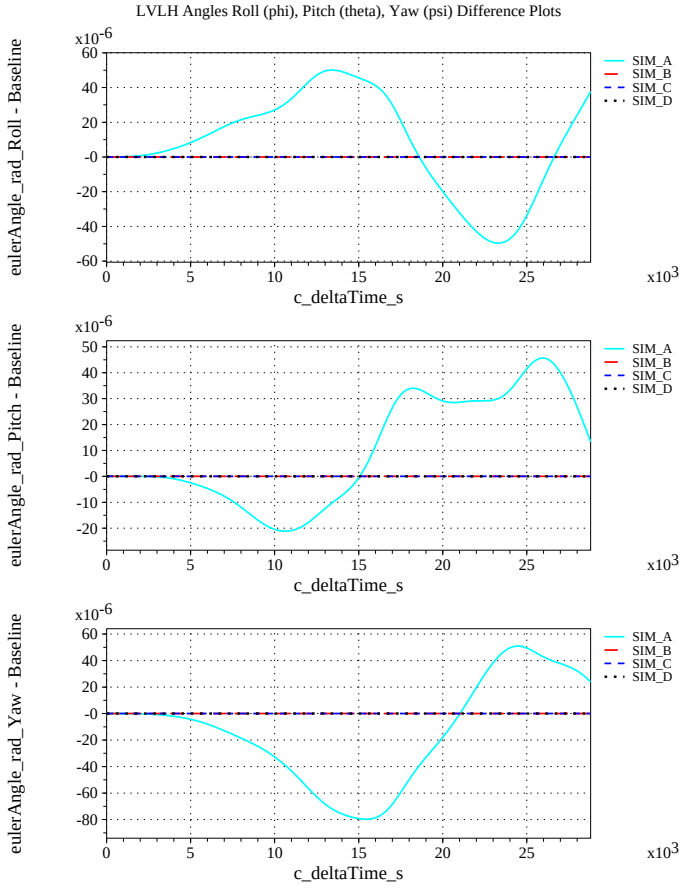

(j) Rotation Angles with Respect to LVLH Frame Differenced

Figure 53. Check-case 08B: ISS Free Rotation with Non-zero Rates; See Discussion in Section D.2.17 (Cont'd)

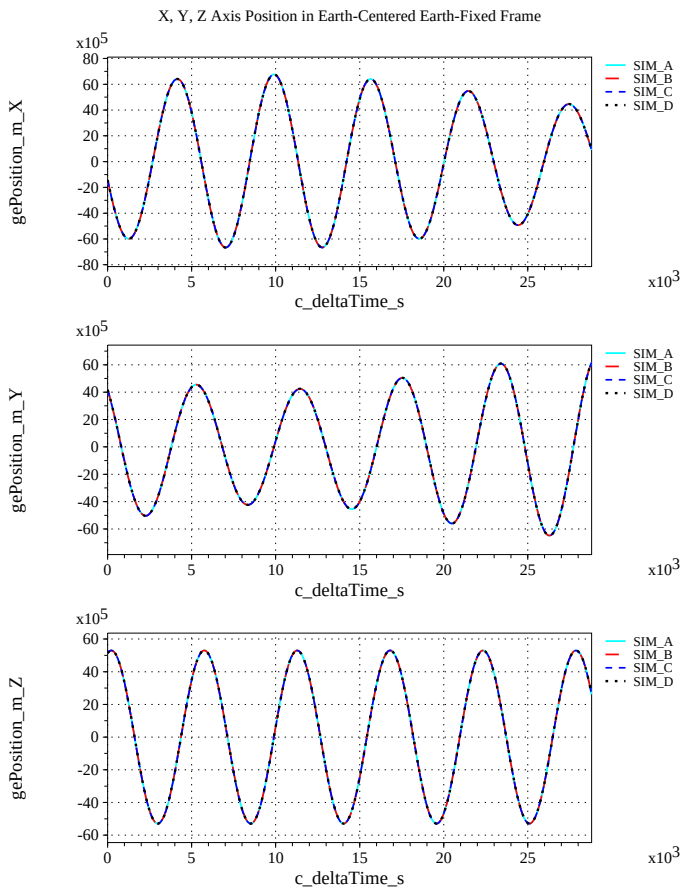

(k) Earth-centered, Earth-fixed Rectangular (X-Y-Z) Positions Compared

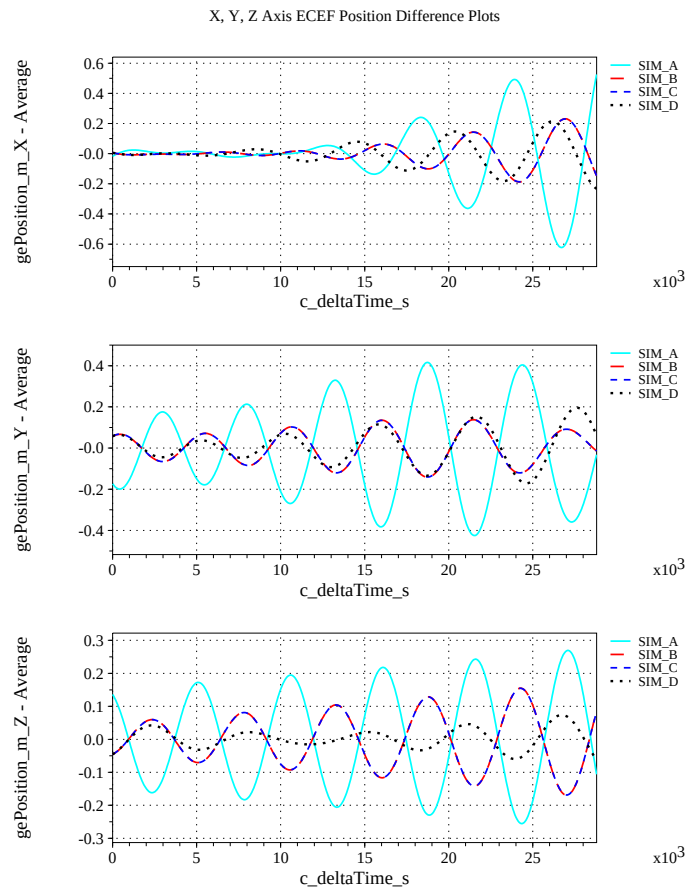

(l) Earth-centered, Earth-fixed Rectangular (X-Y-Z) Positions Differenced

Figure 53. Check-case 08B: ISS Free Rotation with Non-zero Rates; See Discussion in Section D.2.17 (Cont'd)

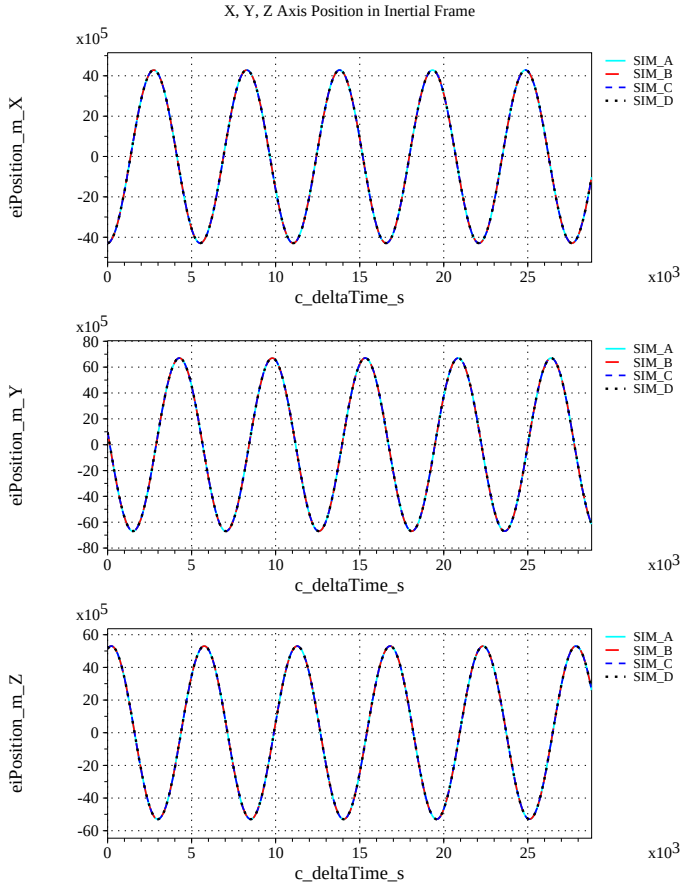

(m) Earth-centered Inertial Rectangular (x-y-z) Positions Compared

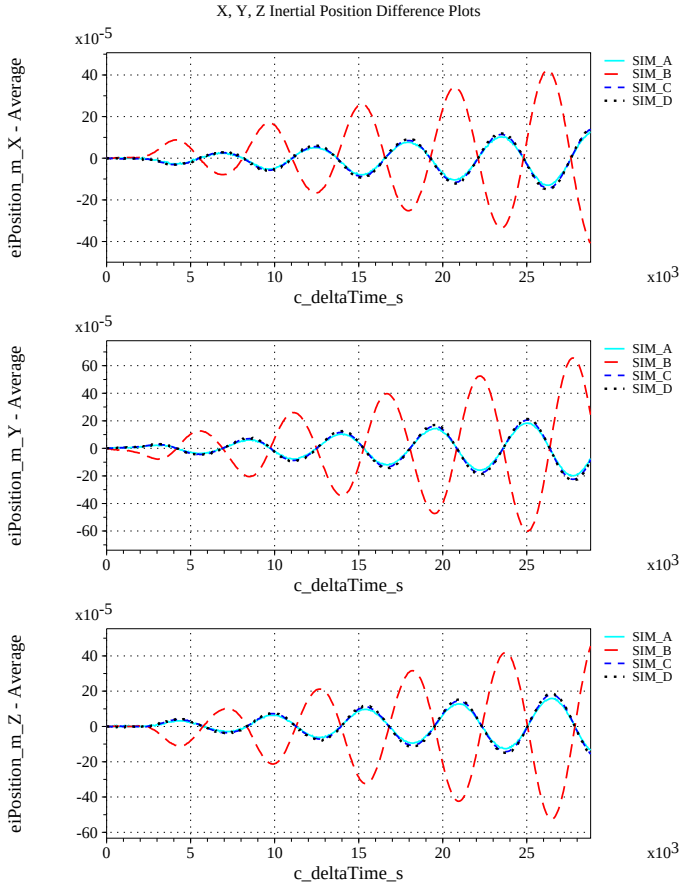

(n) Earth-centered Inertial Rectangular (x-y-z) Positions Differenced

Figure 53. Check-case 08B: ISS Free Rotation with Non-zero Rates; See Discussion in Section D.2.17 (Cont'd)

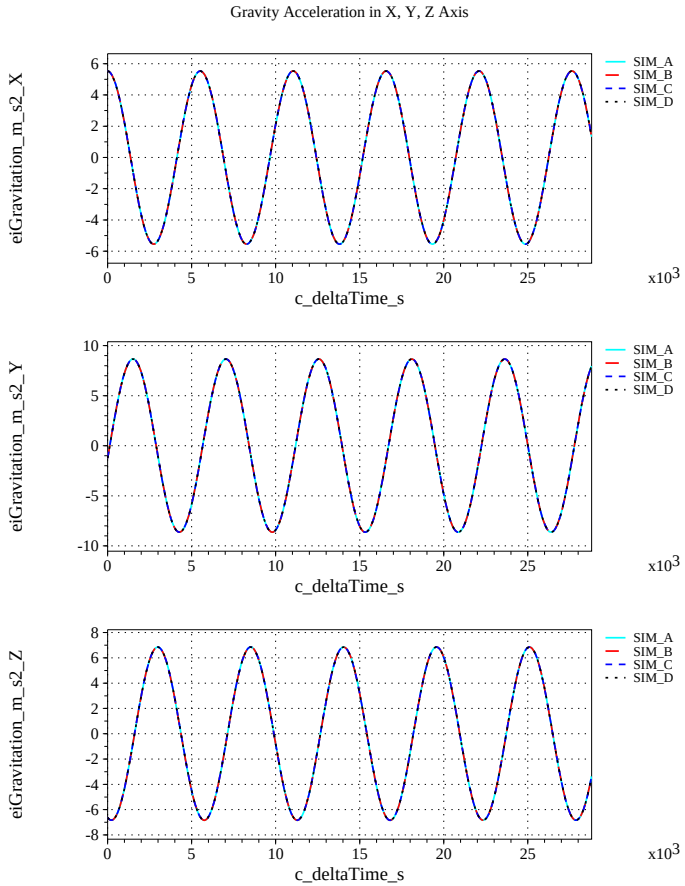

(o) Gravitational Components in Inertial (**X**-**Y**-**Z**) Directions Compared

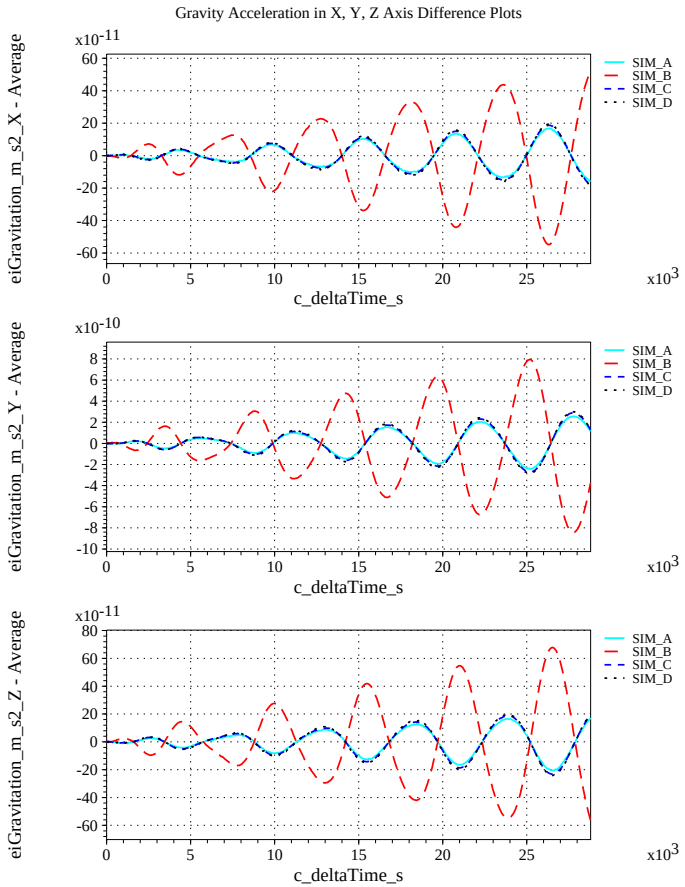

(p) Gravitational Components in Inertial (**X**-**Y**-**Z**) Directions Differenced

Figure 53. Check-case 08B: ISS Free Rotation with Non-zero Rates; See Discussion in Section D.2.17 (Concluded)

D.2.18 Check-case 09A – ISS being torqued with zero initial rates

This section shows cross-plots for four of the selected simulation tools in modeling the dynamics of the ISS in responding to an external torque starting with zero inertial rate. This scenario is described in Section C.2.18. Figures 54a through 54p compare results between the four simulation tools, as well as the deviances of the outputs from each tool from the ensemble average value.

Orbital check-case 9A was the first of two cases that applied a torque to the simulated ISS spacecraft. In this case, the vehicle began with a zero rotation rate in the inertial frame. The torque was applied as a square pulse. As initially discussed in orbital check-case 6C, a square pulse force or torque can induce an increase in the integration error for some integration methods.

SIM B and SIM C agreed on the rotational states; differences between them were negligible. In comparison to SIM B and C, SIM D exhibited a minute difference in angular momentum on the leading edge of the torque pulse but returns to near agreement with SIM B and SIM C on the trailing edge of the pulse, as shown in Figure 54f. This is one effect that a square input can have on integration error. (Throughout this assessment, we are making relative comparisons; it is certainly possible that SIM B and SIM C experienced an equal jump in integration error of opposite sign, relative to SIM D.) The amplitude and duration of the difference in angular momentum caused the momentary spike in difference for the LVLH and inertial Euler angles, but the long-term increase in difference was very modest. Moreover, these differences were considered insignificant.

Also shown in Figure 54f, SIM A shows a minute difference in angular momentum, relative to the other simulations, following the torque pulse that is likely caused by a difference in integration method. This minute difference in angular momentum caused the increasing difference in LVLH and inertial Euler angles over time. Overall, the differences were not considered significant.

Differences in translational states were similar to the differences reported for orbital check-case 2 (see Section D.2.1). However, the differences for SIM B decreased significantly in this case because SIM B was executed at a higher frame rate to reduce integration error on the leading and trailing edge of the square pulse torque.

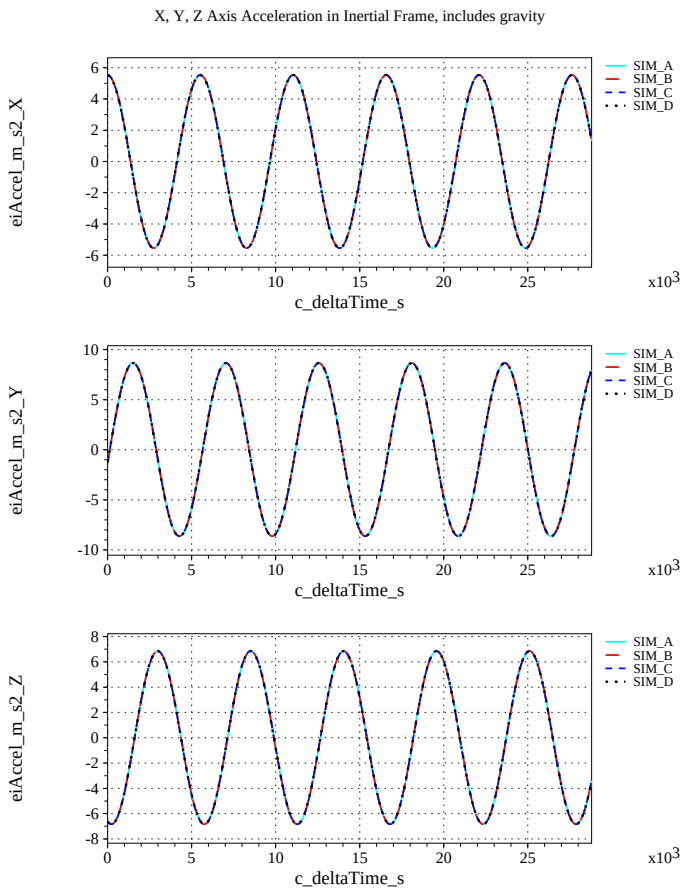

(a) Inertial Accelerations Compared

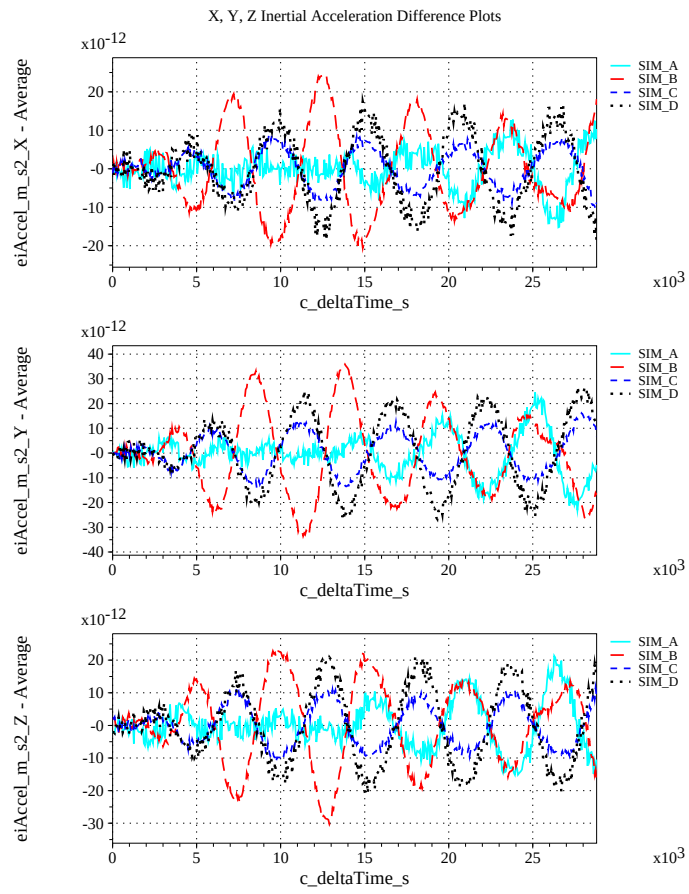

(b) Inertial Accelerations Differenced

Figure 54. Check-case 09A: ISS Being Torqued with Zero Initial Rates; See Discussion in Section D.2.18

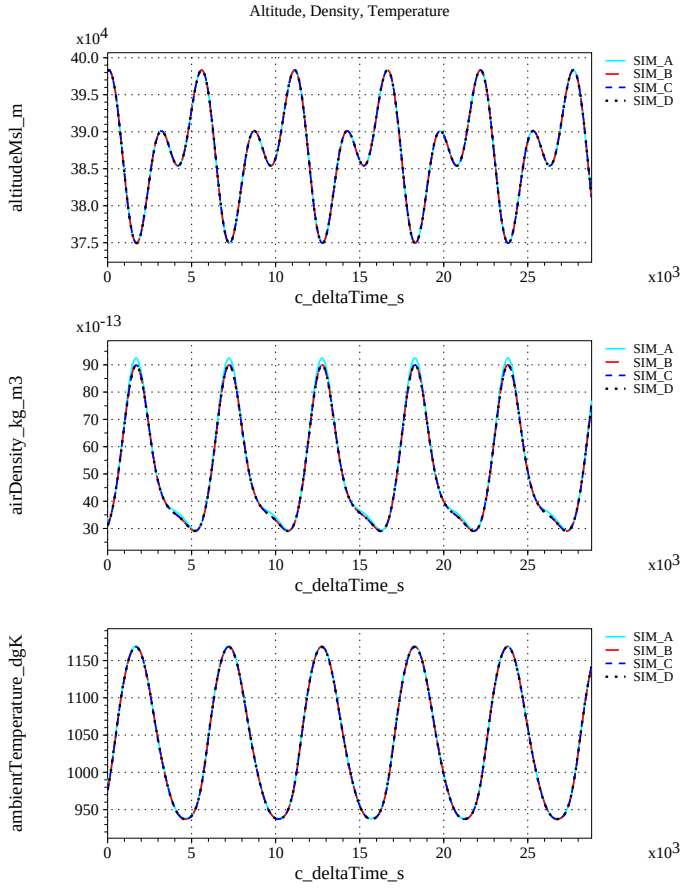

(c) Atmospheric Properties Compared

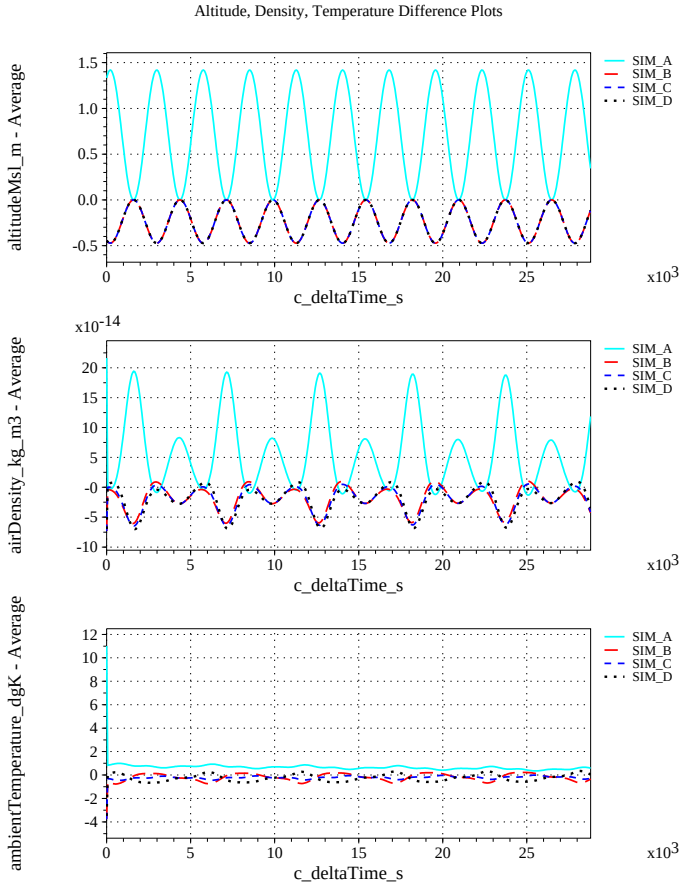

(d) Atmospheric Properties Differenced

Figure 54. Check-case 09A: ISS Being Torqued with Zero Initial Rates; See Discussion in Section D.2.18 (Cont'd)

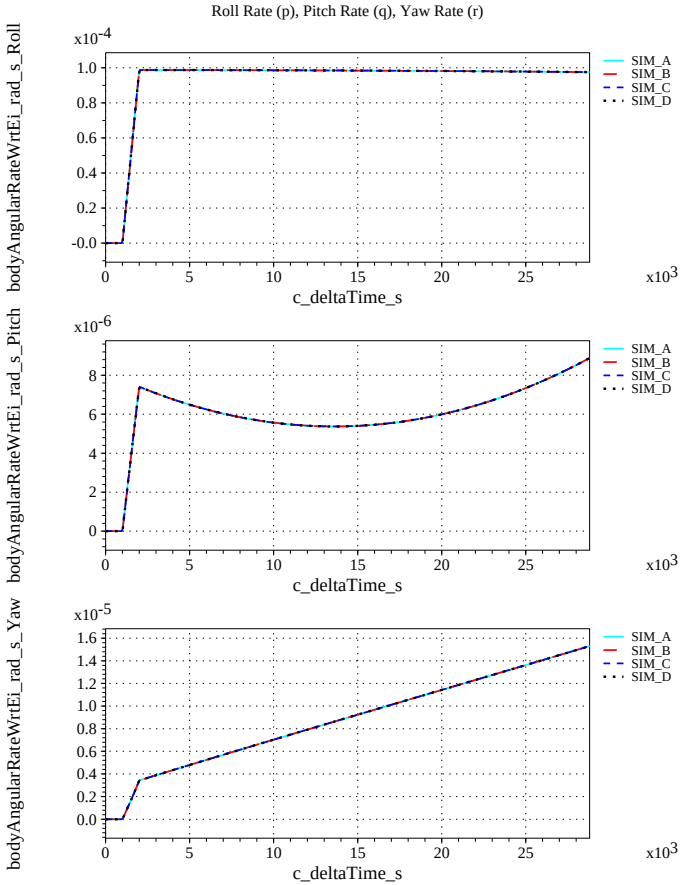

(e) Body-axis Angular Rates Compared

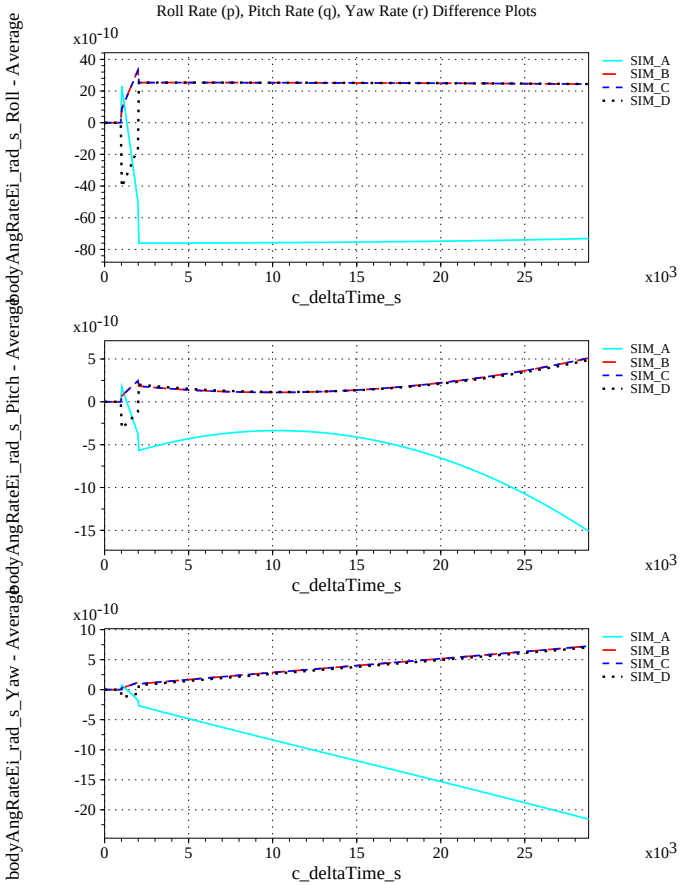

(f) Body-axis Angular Rates Differenced

Figure 54. Check-case 09A: ISS Being Torqued with Zero Initial Rates; See Discussion in Section D.2.18 (Cont'd)

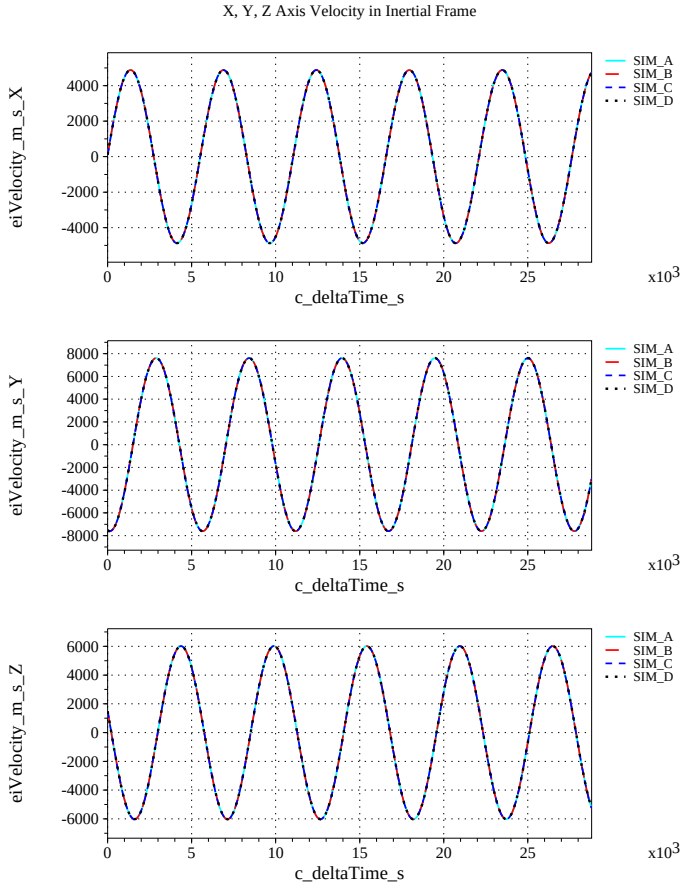

(g) Inertial Velocities Compared

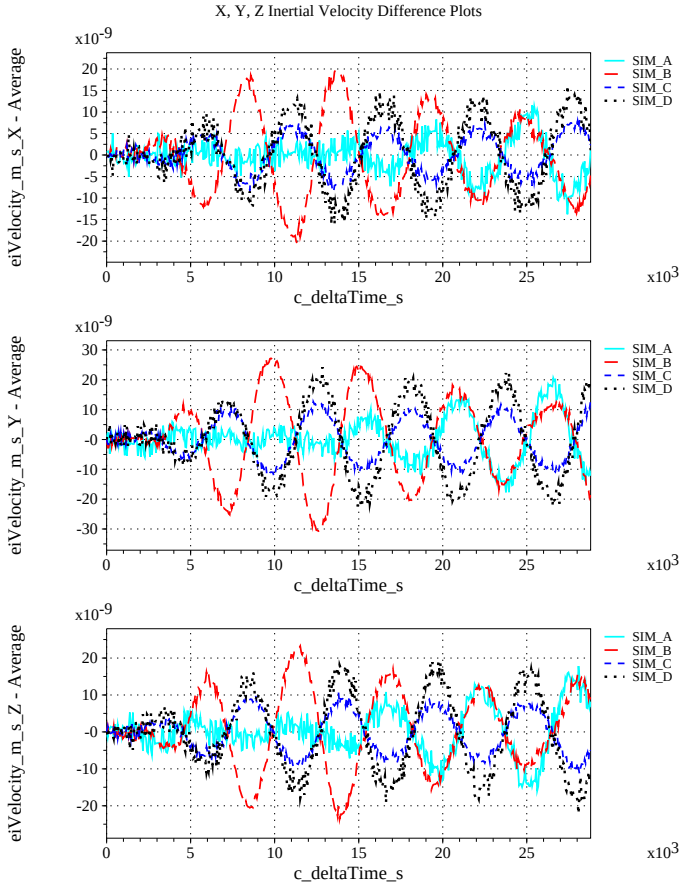

(h) Inertial Velocities Differenced

Figure 54. Check-case 09A: ISS Being Torqued with Zero Initial Rates; See Discussion in Section D.2.18 (Cont'd)

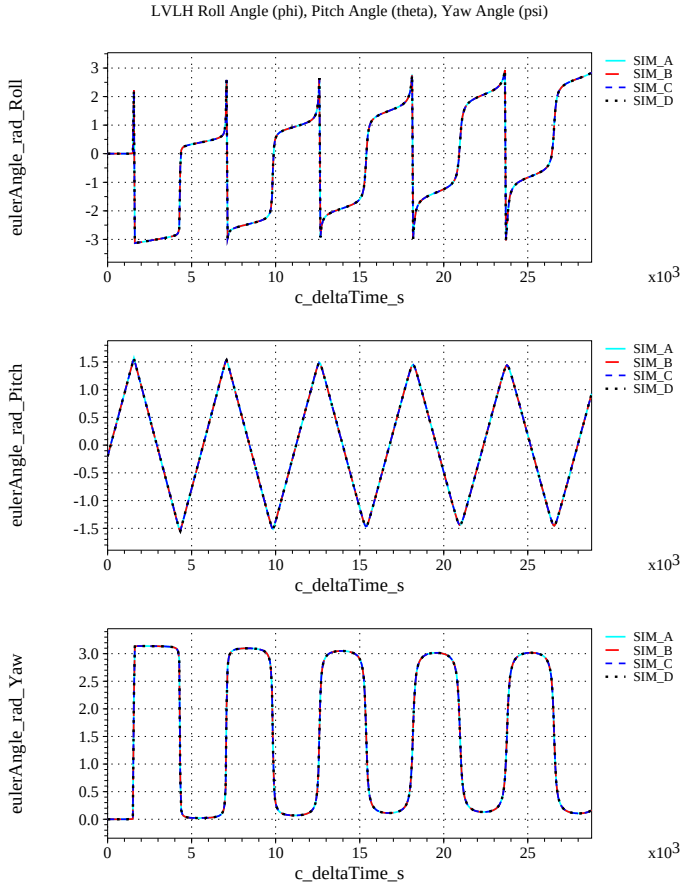

(i) Rotation Angles with Respect to LVLH Frame Compared

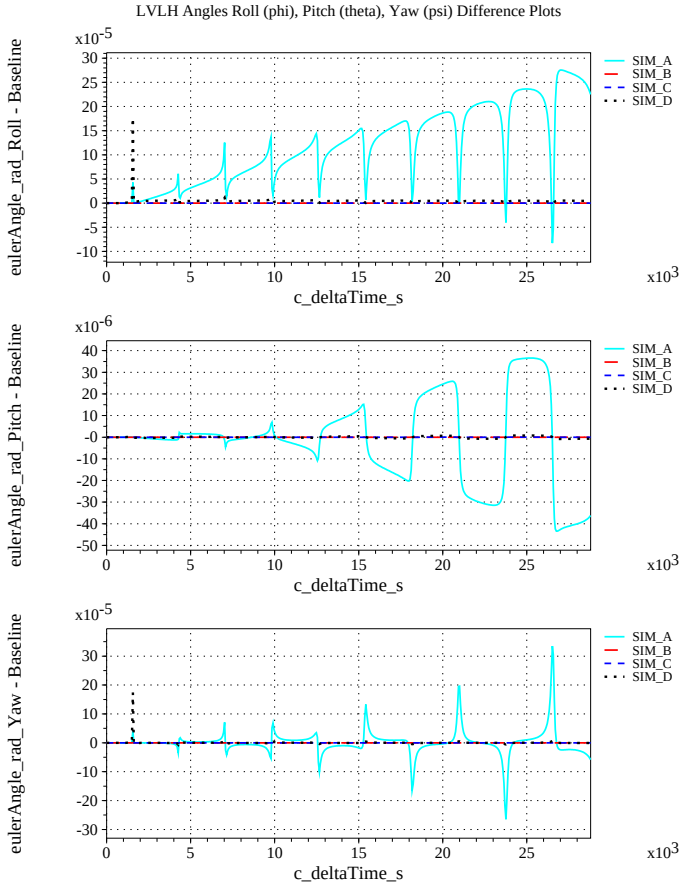

(j) Rotation Angles with Respect to LVLH Frame Differenced

Figure 54. Check-case 09A: ISS Being Torqued with Zero Initial Rates; See Discussion in Section D.2.18 (Cont'd)

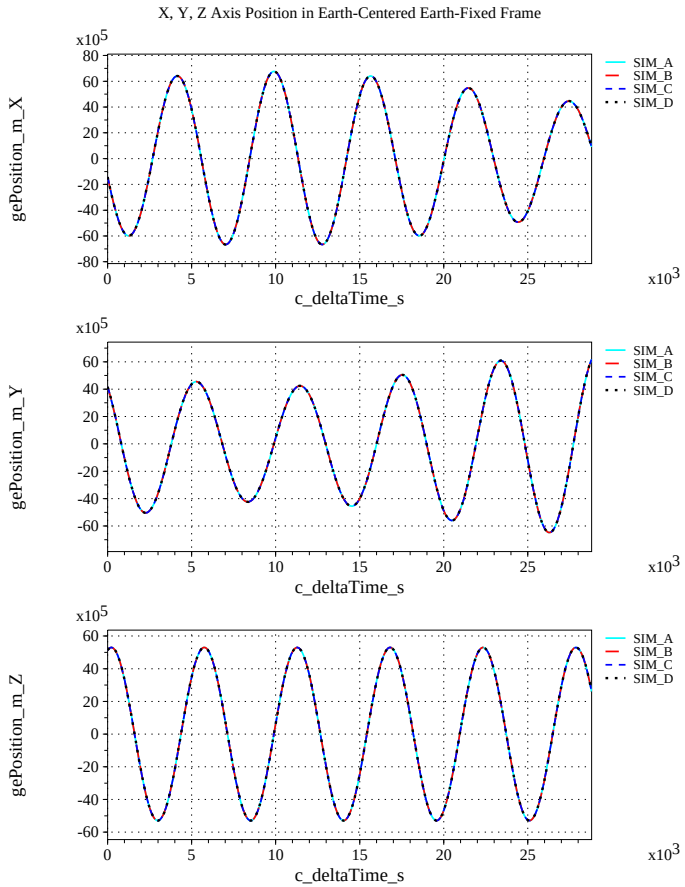

(k) Earth-centered, Earth-fixed Rectangular (X-Y-Z) Positions Compared

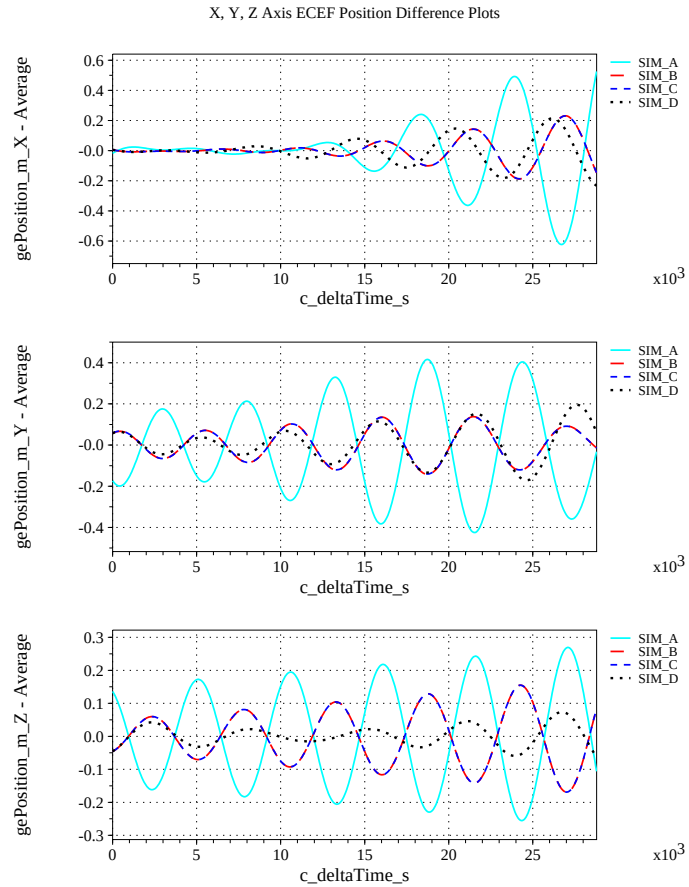

(l) Earth-centered, Earth-fixed Rectangular (X-Y-Z) Positions Differenced

Figure 54. Check-case 09A: ISS Being Torqued with Zero Initial Rates; See Discussion in Section D.2.18 (Cont'd)

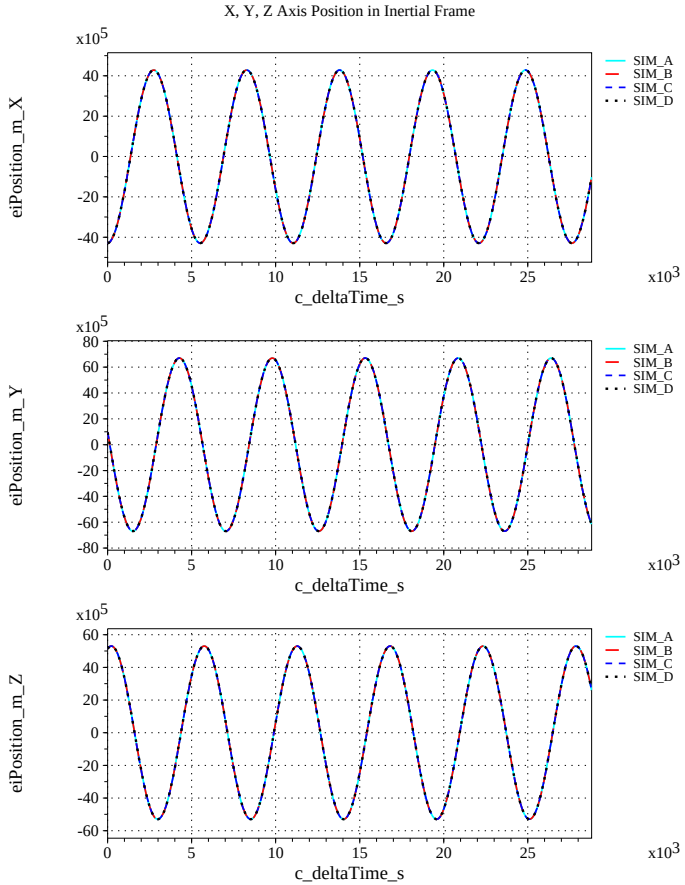

(m) Earth-centered Inertial Rectangular (x-y-z) Positions Compared

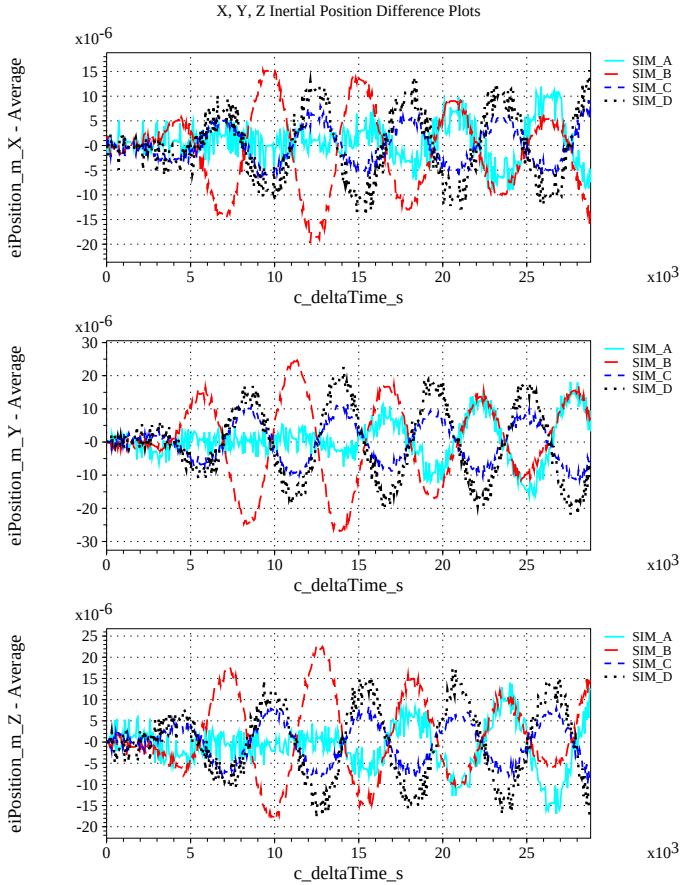

(n) Earth-centered Inertial Rectangular (x-y-z) Positions Differenced

Figure 54. Check-case 09A: ISS Being Torqued with Zero Initial Rates; See Discussion in Section D.2.18 (Cont'd)

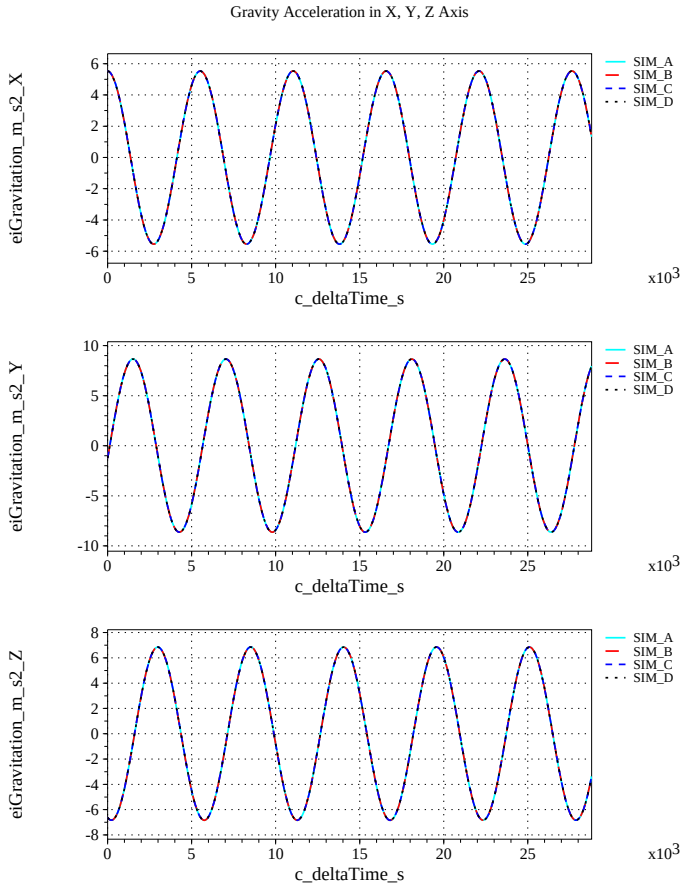

(o) Gravitational Components in Inertial (**X**-**Y**-**Z**) Directions Compared

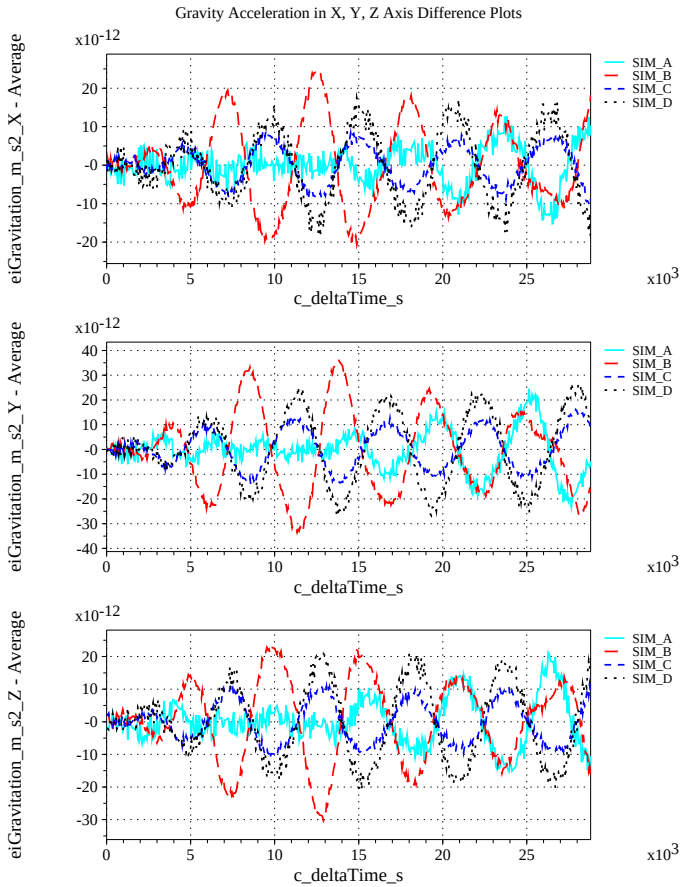

(p) Gravitational Components in Inertial (**X**-**Y**-**Z**) Directions Differenced

Figure 54. Check-case 09A: ISS Being Torqued with Zero Initial Rates; See Discussion in Section D.2.18 (Concluded)

D.2.19 Check-case 09B – ISS being torqued with non-zero initial rates

This section shows cross-plots for four of the selected simulation tools in modeling the dynamics of the ISS in responding to an external torque starting with a non-zero inertial rate. This scenario is described in Section C.2.19. Figures 55a through 55p compare results between the four simulation tools, as well as the deviances of the outputs from each tool from the ensemble average value.

Orbital check-case 9B was the second of two cases that applied a torque to the simplified ISS. In this case, the vehicle began with a zero rotation rate in the LVLH frame, i.e. a non-zero rate relative to the inertial frame. As with orbital check-case 9A, the torque was applied as a square pulse. As initially discussed in orbital check-case 6C, a square pulse force or torque can induce an increase in the integration error for some integration methods (see Section D.2.10).

Starting with a non-zero inertial rotation did not qualitatively change the outcome of the simulation comparisons as discussed in orbital case 9A. As shown in Figure 55f, SIM B and SIM C agreed on the value of rotational states; differences between them were negligible. Compared to SIM B and C, SIM D exhibited a minute difference in angular momentum at the leading edge of the torque pulse but returns to near agreement with SIM B and SIM C at the trailing edge of the input. The amplitude and duration of the difference in angular momentum caused the momentary spike in difference for the LVLH (Figure 55j) and inertial Euler angles, but the long-term increase in difference was very modest. Moreover, these differences were considered insignificant. SIM A shows a minute difference in angular momentum, relative to the other simulations, following the torque pulse that is likely caused by a difference in integration method (see Figure 55f). This minute difference in angular momentum caused the increasing difference in LVLH and inertial Euler angles over time. Previously-identified differences in integration methods for torque-free rotation in orbital case 8B also contributed to the differences in Euler angles. Overall, the differences were not considered significant.

Body pitch rate exhibited an anomaly previously noted in orbital check-case 8B (Section D.2.17) for SIM D; this is not considered significant.

Differences in translational states were similar to the differences in orbital check-case 2 (Section D.2.1). However, the differences for SIM B decreased significantly in this case because SIM B was executed at a higher frame rate to reduce integration error on the leading and trailing edge of the square pulse torque.

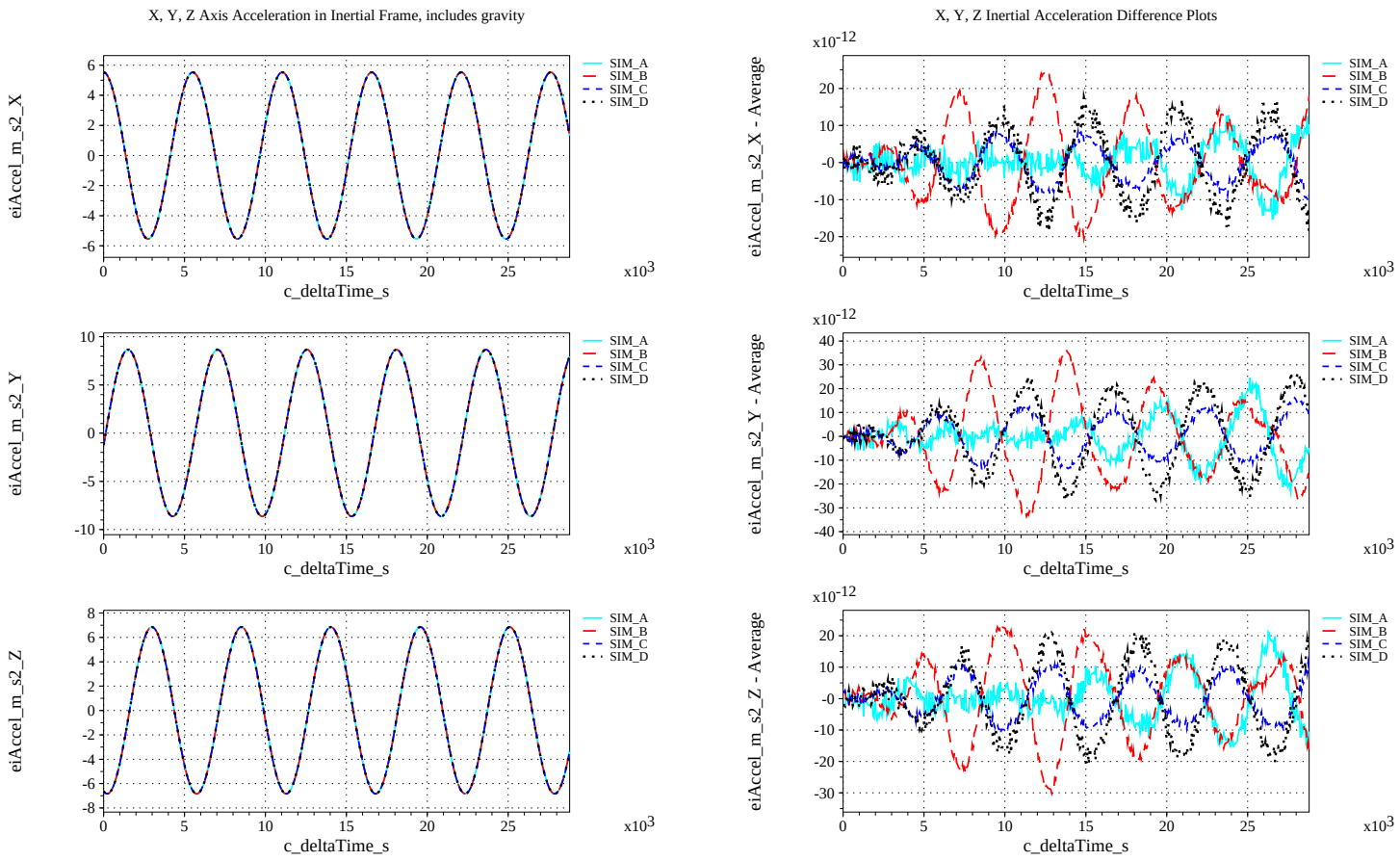

(a) Inertial Accelerations Compared

(b) Inertial Accelerations Differenced

Figure 55. Check-case 09B: ISS Being Torqued with Non-zero Initial Rates; See Discussion in Section D.2.19

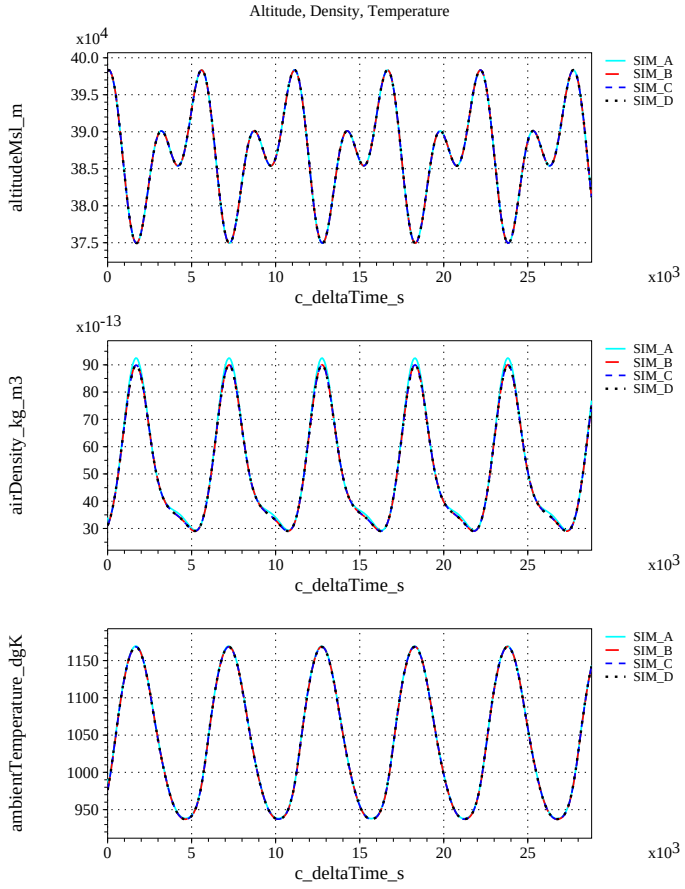

(c) Atmospheric Properties Compared

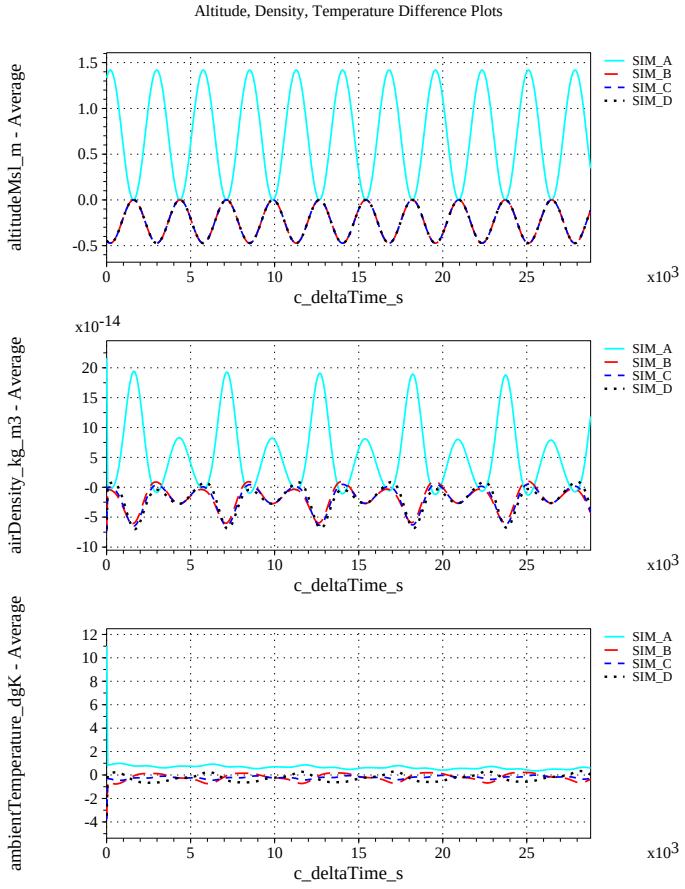

(d) Atmospheric Properties Differenced

Figure 55. Check-case 09B: ISS Being Torqued with Non-zero Initial Rates; See Discussion in Section D.2.19 (Cont'd)

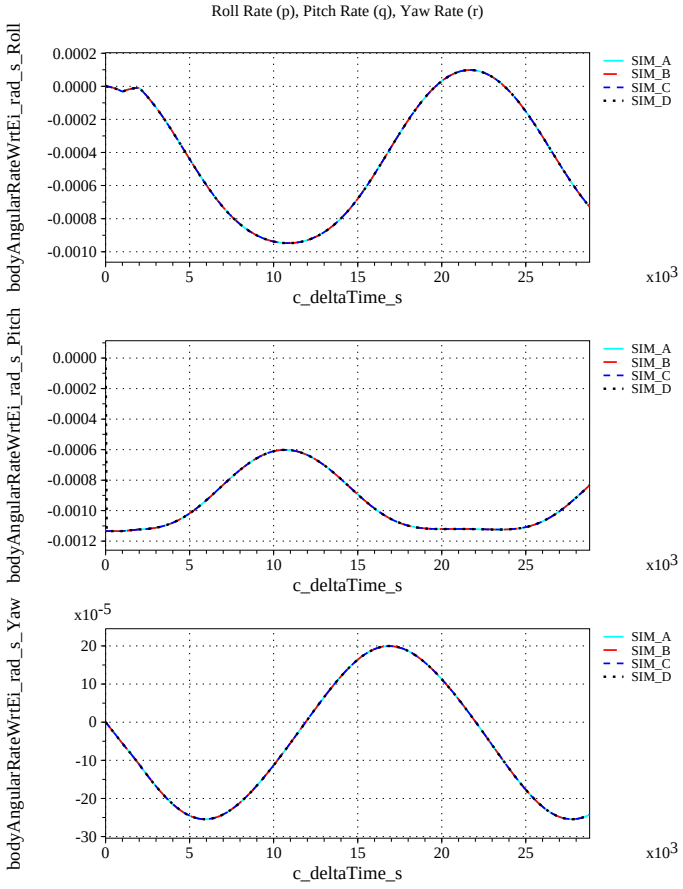

(e) Body-axis Angular Rates Compared

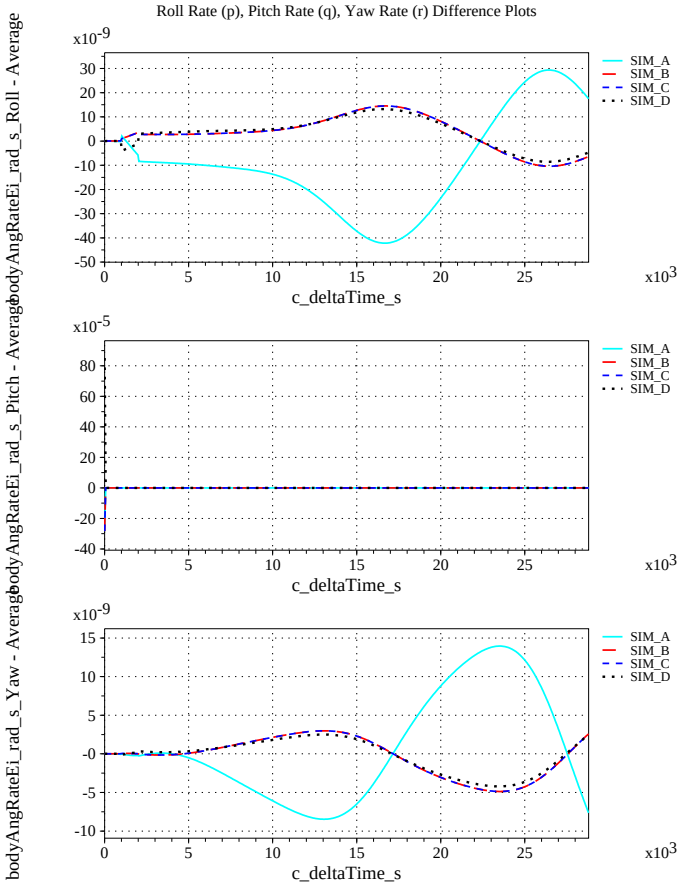

(f) Body-axis Angular Rates Differenced

Figure 55. Check-case 09B: ISS Being Torqued with Non-zero Initial Rates; See Discussion in Section D.2.19 (Cont'd)

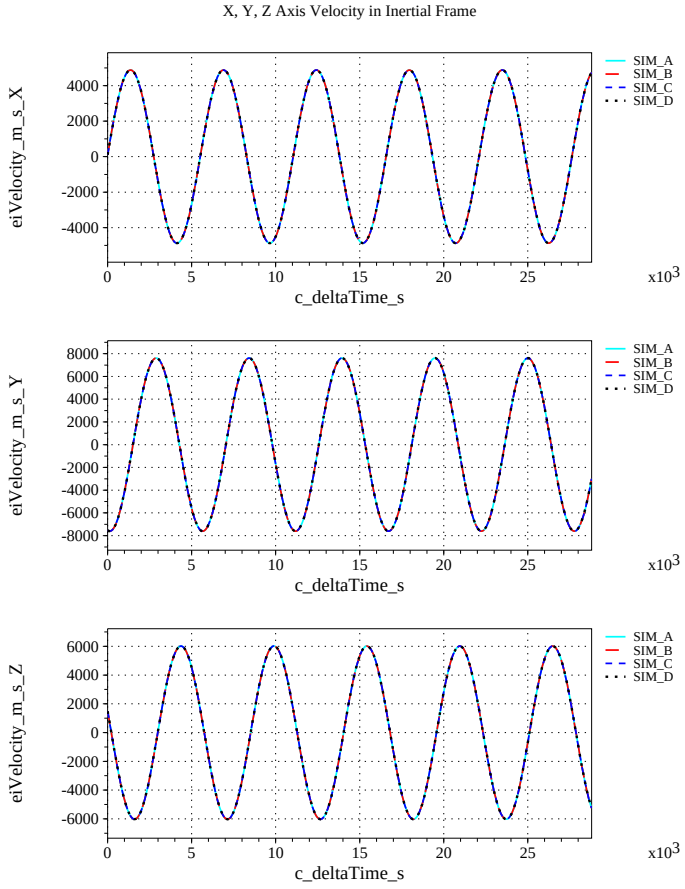

(g) Inertial Velocities Compared

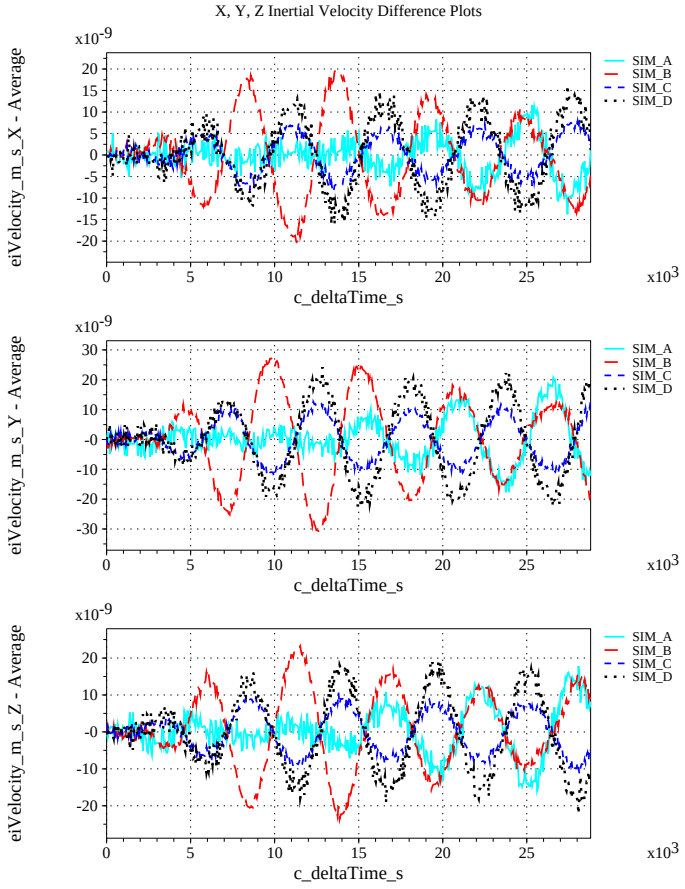

(h) Inertial Velocities Differenced

Figure 55. Check-case 09B: ISS Being Torqued with Non-zero Initial Rates; See Discussion in Section D.2.19 (Cont'd)

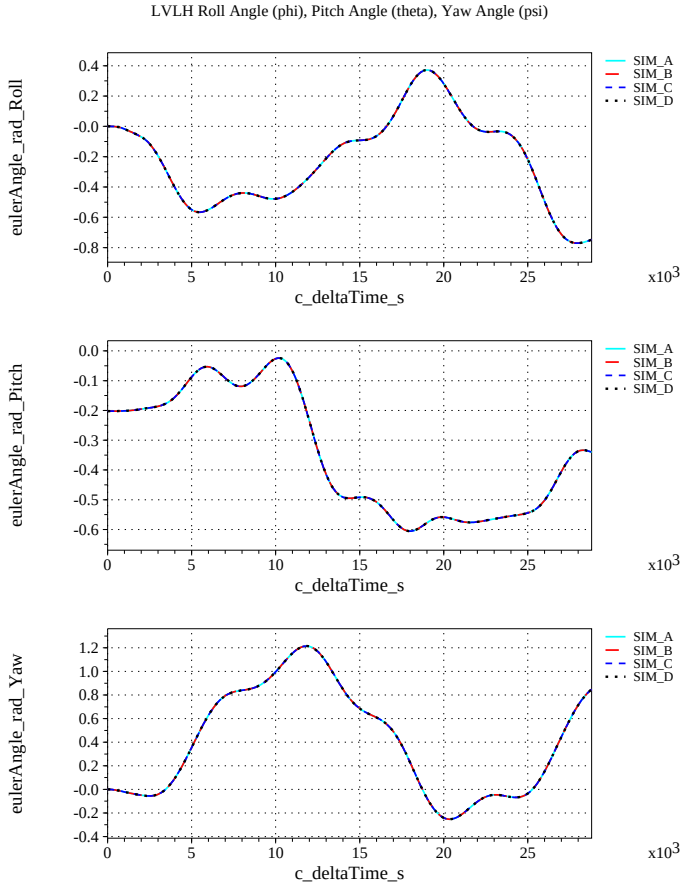

(i) Rotation Angles with Respect to LVLH Frame Compared

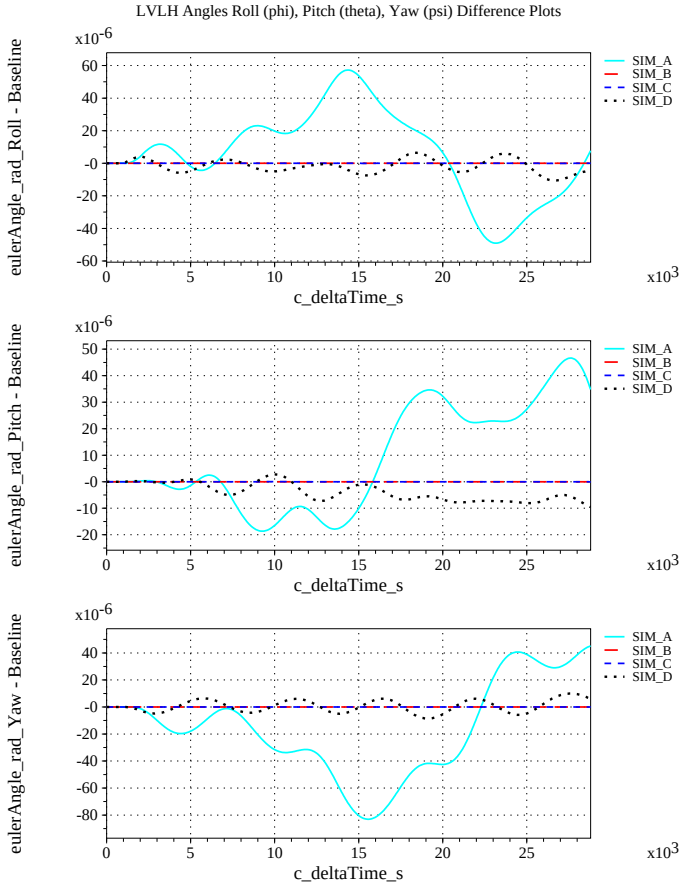

(j) Rotation Angles with Respect to LVLH Frame Differenced

Figure 55. Check-case 09B: ISS Being Torqued with Non-zero Initial Rates; See Discussion in Section D.2.19 (Cont'd)

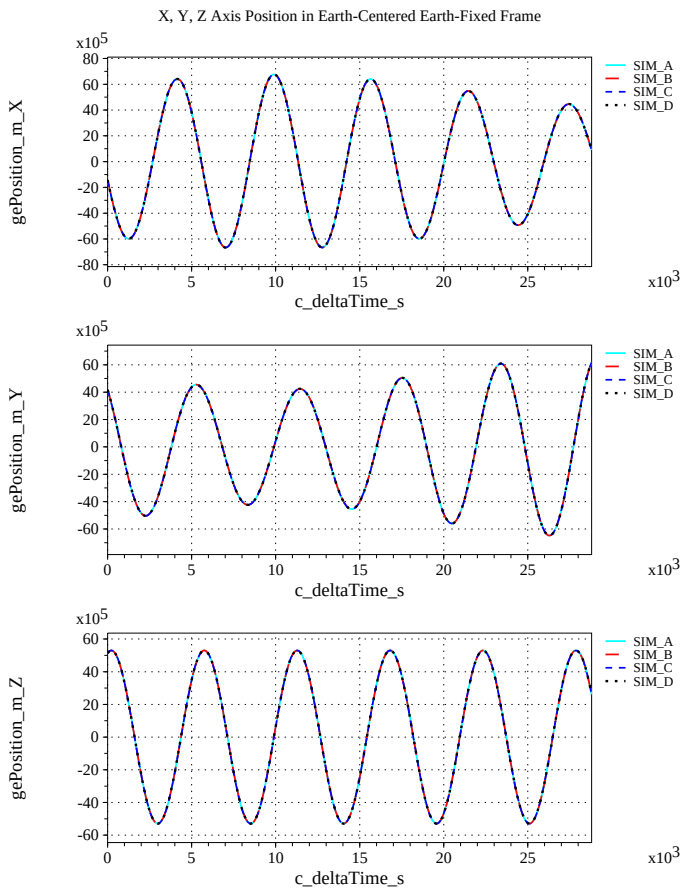

(k) Earth-centered, Earth-fixed Rectangular (X-Y-Z) Positions Compared

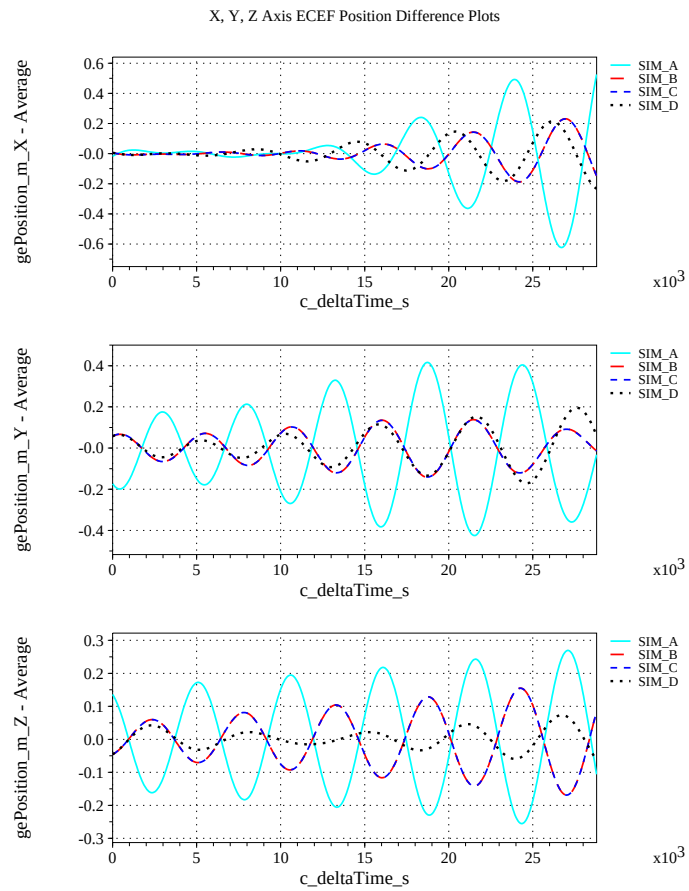

(l) Earth-centered, Earth-fixed Rectangular (X-Y-Z) Positions Differenced

Figure 55. Check-case 09B: ISS Being Torqued with Non-zero Initial Rates; See Discussion in Section D.2.19 (Cont'd)

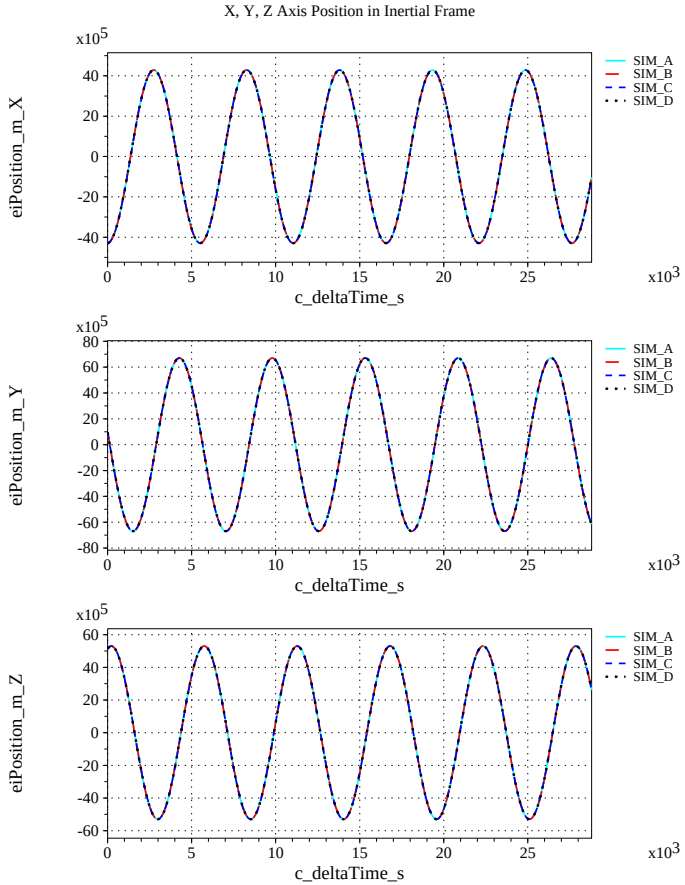

(m) Earth-centered Inertial Rectangular (x-y-z) Positions Compared

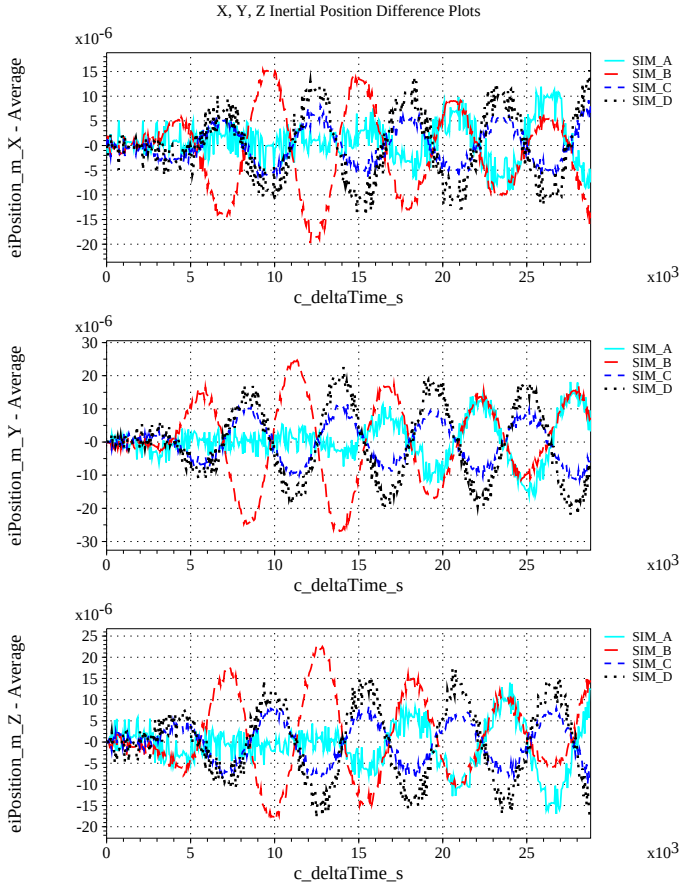

(n) Earth-centered Inertial Rectangular (x-y-z) Positions Differenced

Figure 55. Check-case 09B: ISS Being Torqued with Non-zero Initial Rates; See Discussion in Section D.2.19 (Cont'd)

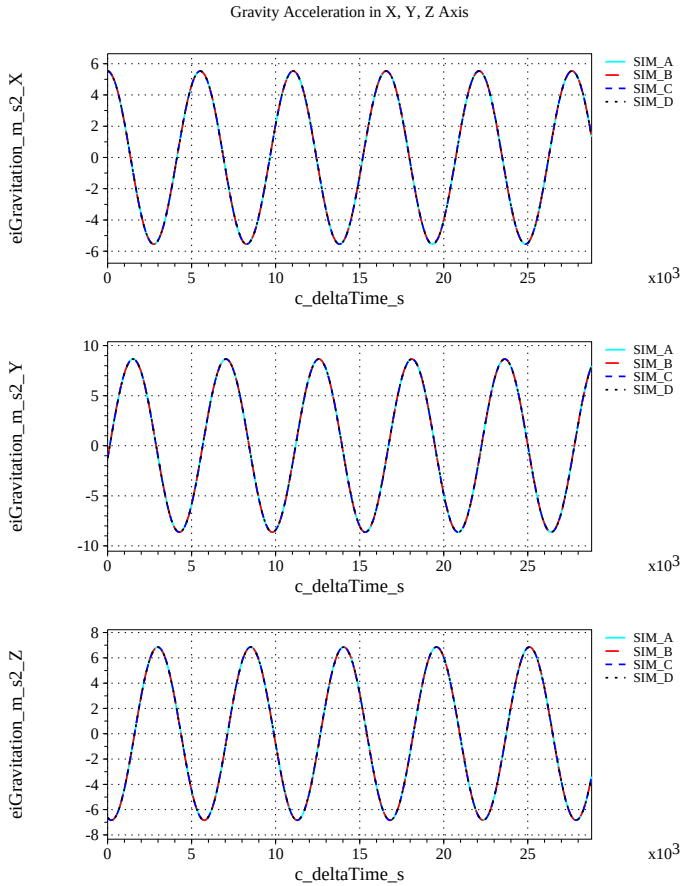

(o) Gravitational Components in Inertial (**X**-**Y**-**Z**) Directions Compared

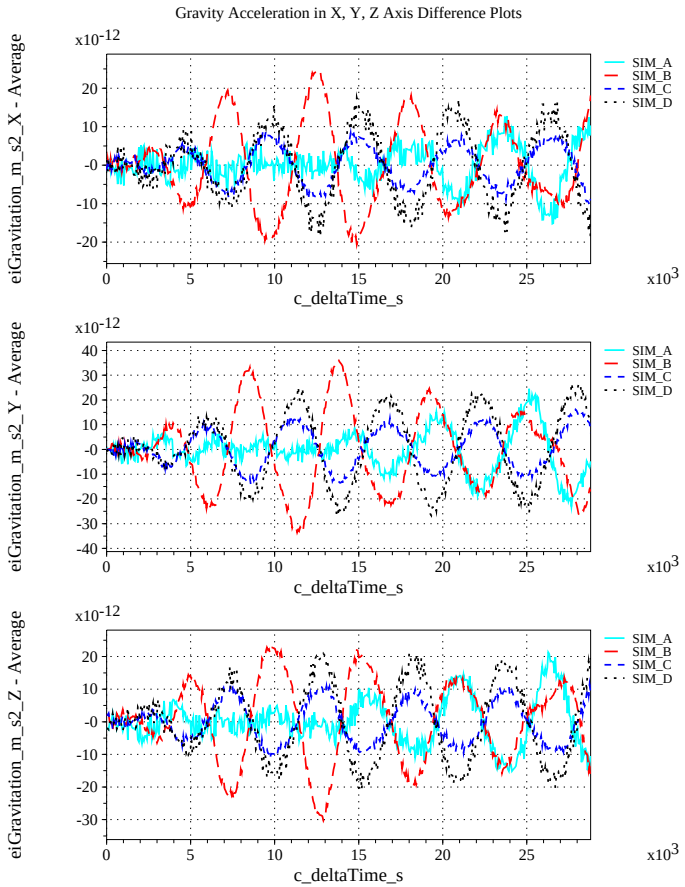

(p) Gravitational Components in Inertial (**X**-**Y**-**Z**) Directions Differenced

Figure 55. Check-case 09B: ISS Being Torqued with Non-zero Initial Rates; See Discussion in Section D.2.19 (Concluded)

D.2.20 Check-case 09C – ISS under torque and force with zero initial rates

This section shows cross-plots for four of the selected simulation tools in modeling the dynamics of the ISS in responding to external torque and force starting with zero inertial rate. This scenario is described in Section C.2.20. Figures 56a through 56p compare results between the four simulation tools, as well as the deviances of the outputs from each tool from the ensemble average value.

Orbital check-case 9C was the first of two cases that apply a simultaneous torque and force to the simulated ISS spacecraft. These scenarios examined the coupling of translational and rotational motion via a body-fixed thrust vector on a rotating body. In this case, the vehicle began with a zero rotation rate in the inertial frame. The torque and force were both modeled as a square pulse. As initially discussed in orbital case 6C (Section D.2.10), this could have presented a problem for some integration methods.

SIM B and SIM C showed agreement on both translational and rotational states. SIM A showed the same differences in rotational states seen in orbital check-case 9A. However, those differences were demonstrated to be insignificant given their negligible impact via the direction of thrust on translational states. SIM A showed close agreement on translational states with SIM B and C. SIM A also demonstrated the same differences in rotational state as orbital case 9A. Those rotational state differences had a more noticeable impact on the translational states via their impact on the direction of the thrust vector. However, the difference in position remained below a decimeter, a value not considered significant.

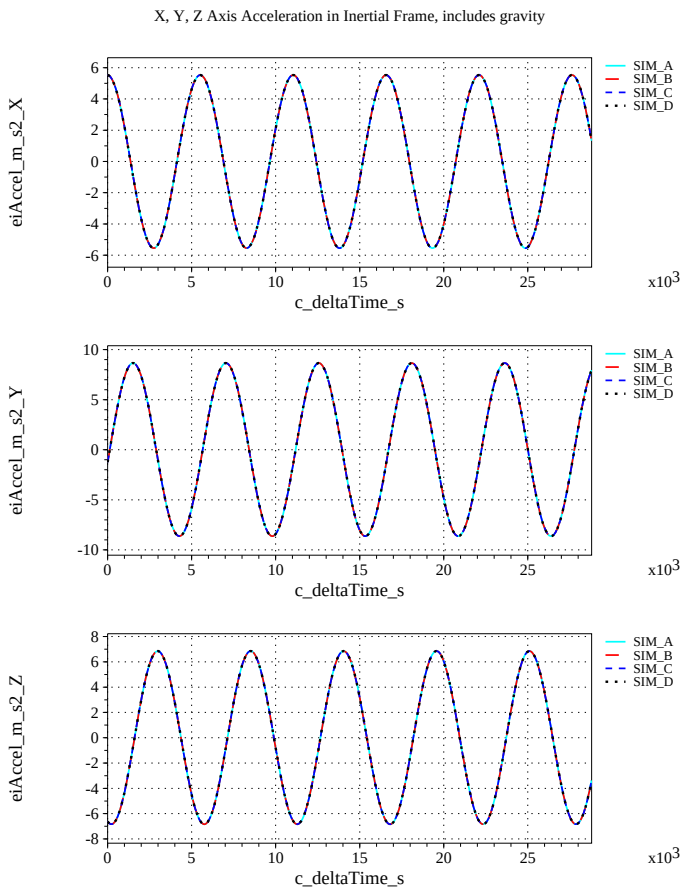

(a) Inertial Accelerations Compared

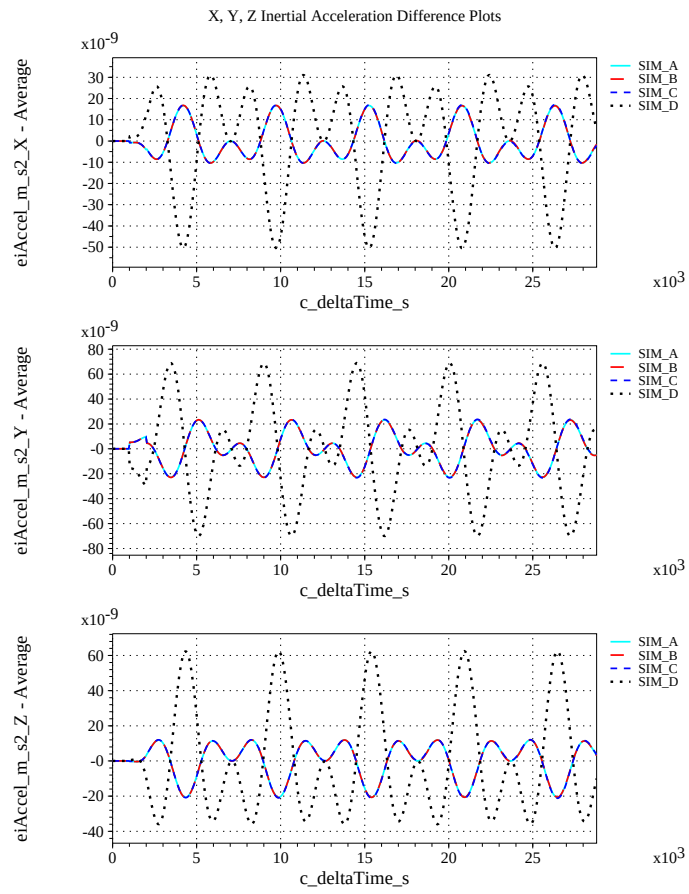

(b) Inertial Accelerations Differenced

Figure 56. Check-case 09C: ISS Under Torque and Force with Zero Initial Rates; See Discussion in Section D.2.20

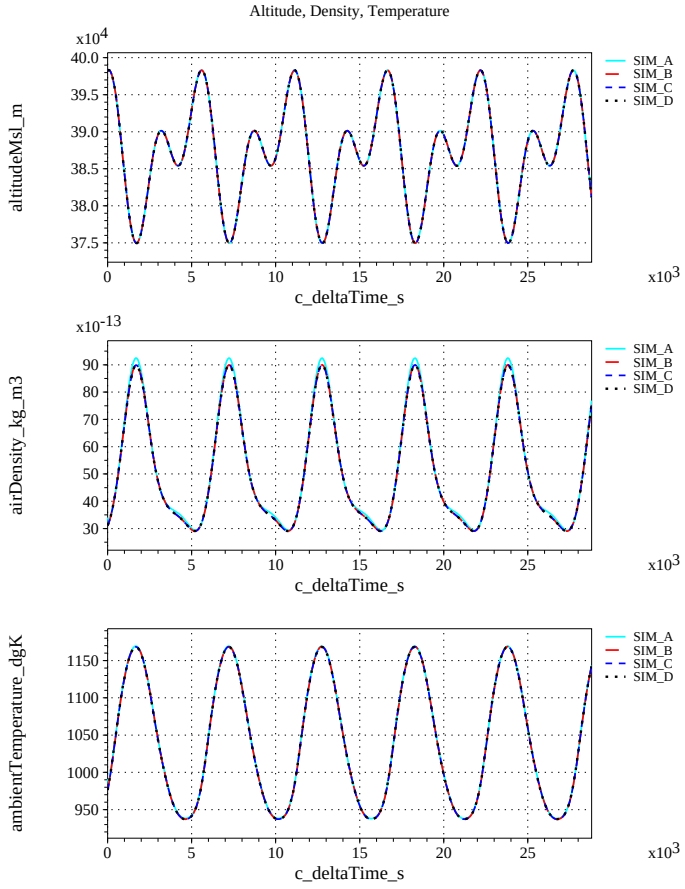

(c) Atmospheric Properties Compared

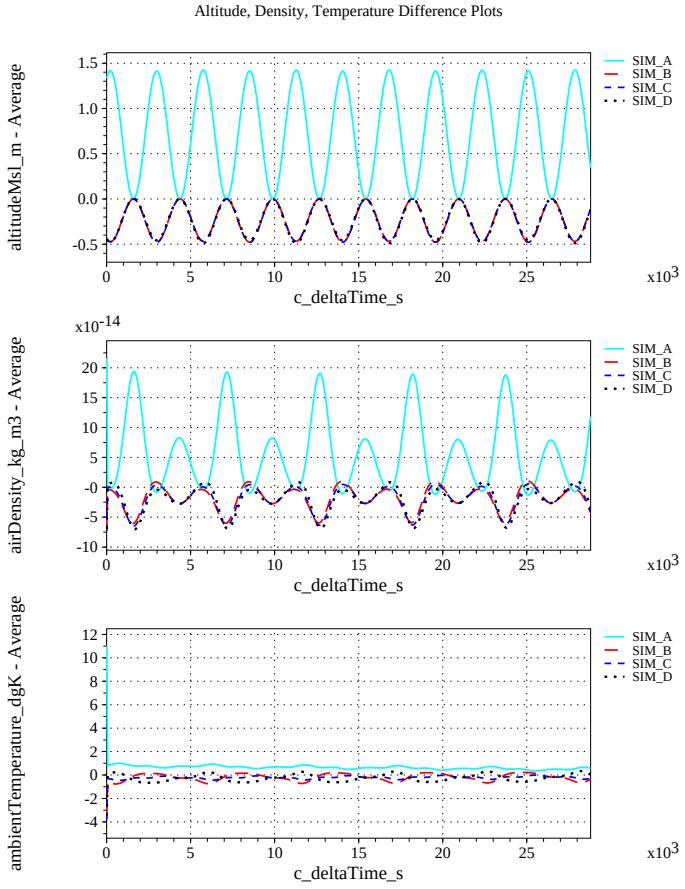

(d) Atmospheric Properties Differenced

Figure 56. Check-case 09C: ISS Under Torque and Force with Zero Initial Rates; See Discussion in Section D.2.20 (Cont'd)

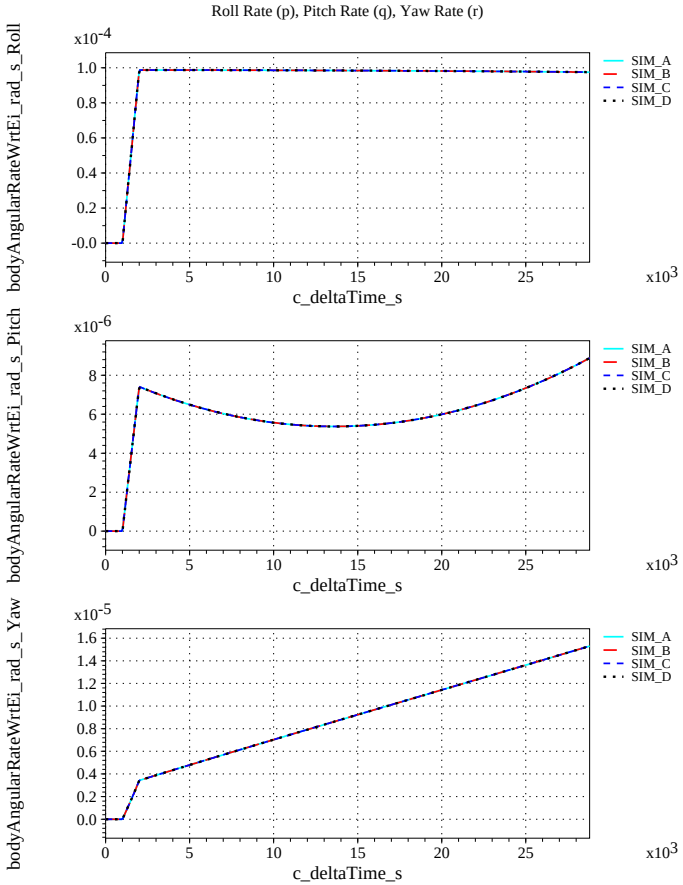

(e) Body-axis Angular Rates Compared

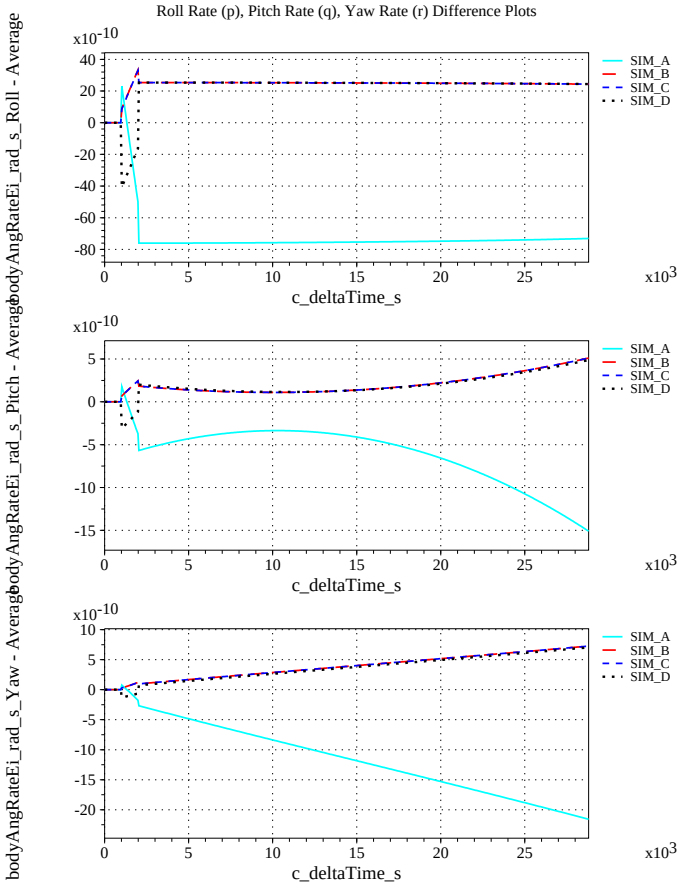

(f) Body-axis Angular Rates Differenced

Figure 56. Check-case 09C: ISS Under Torque and Force with Zero Initial Rates; See Discussion in Section D.2.20 (Cont'd)

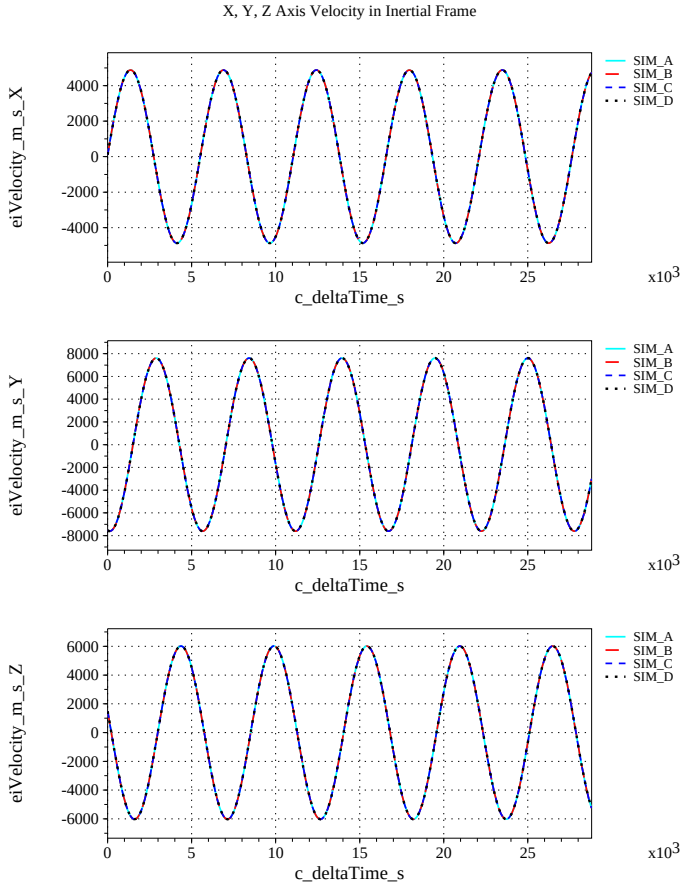

(g) Inertial Velocities Compared

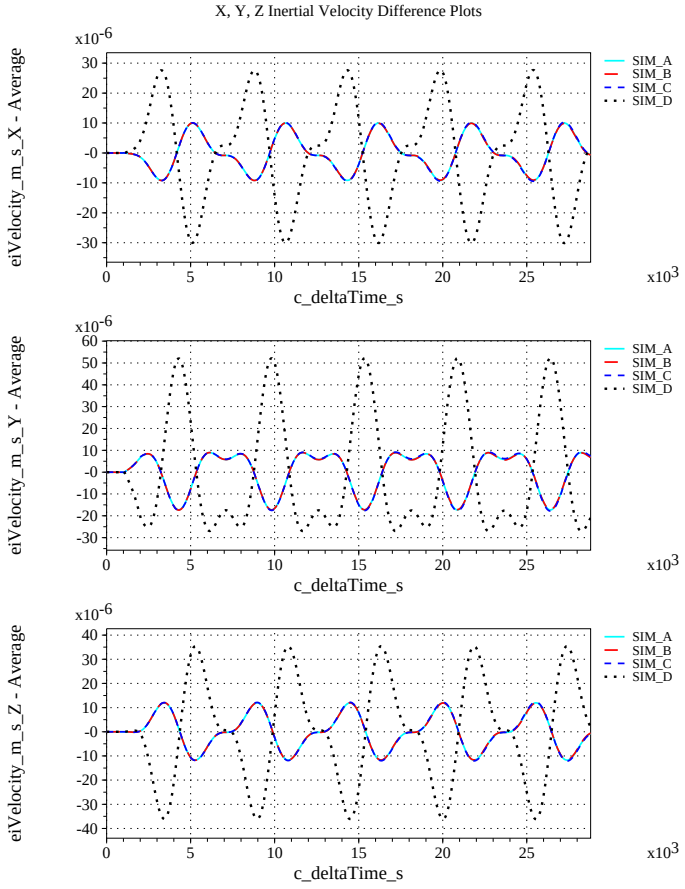

(h) Inertial Velocities Differenced

Figure 56. Check-case 09C: ISS Under Torque and Force with Zero Initial Rates; See Discussion in Section D.2.20 (Cont'd)

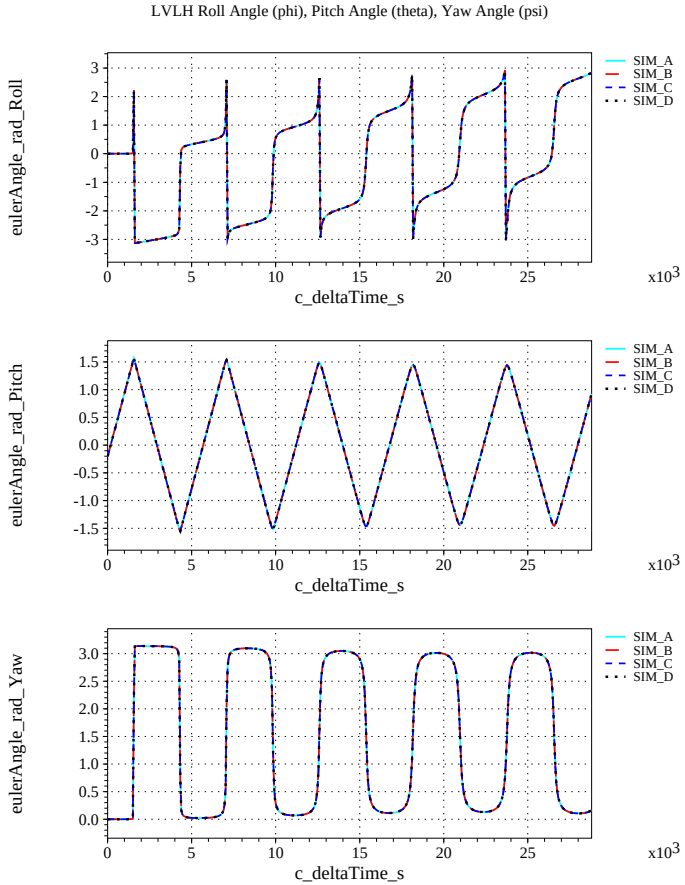

(i) Rotation Angles with Respect to LVLH Frame Compared

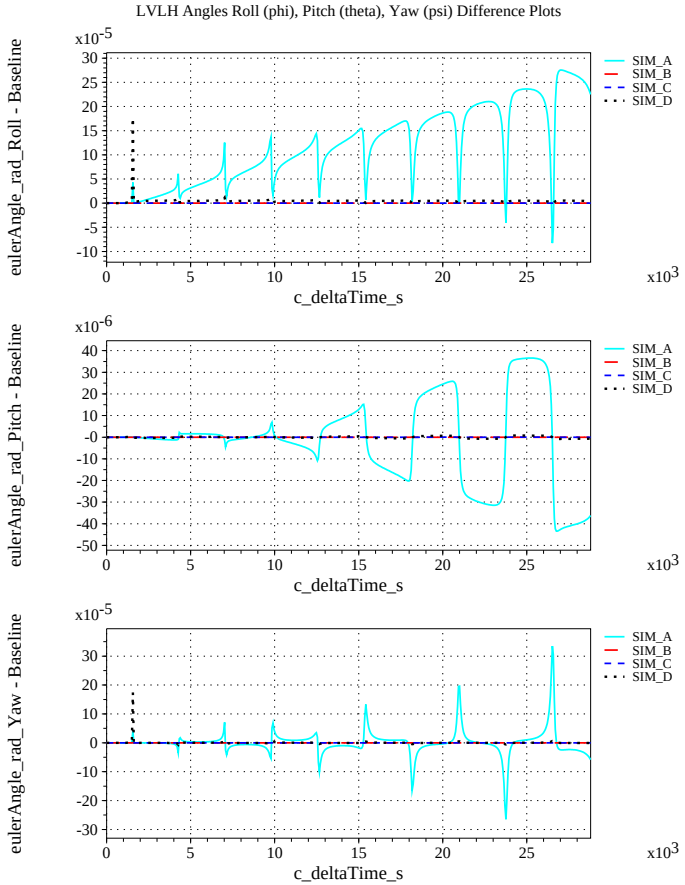

(j) Rotation Angles with Respect to LVLH Frame Differenced

Figure 56. Check-case 09C: ISS Under Torque and Force with Zero Initial Rates; See Discussion in Section D.2.20 (Cont'd)

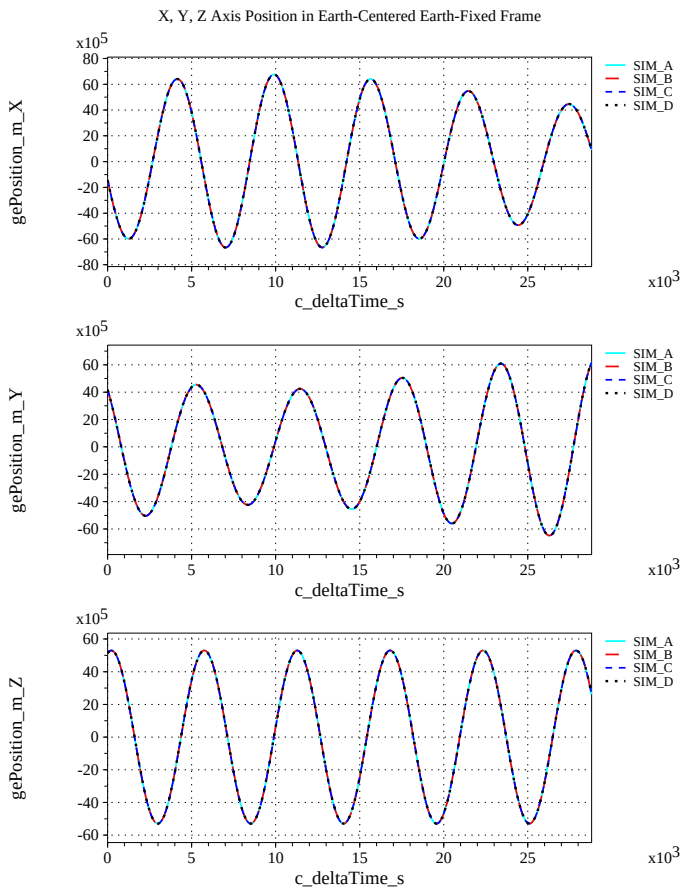

(k) Earth-centered, Earth-fixed Rectangular (X-Y-Z) Positions Compared

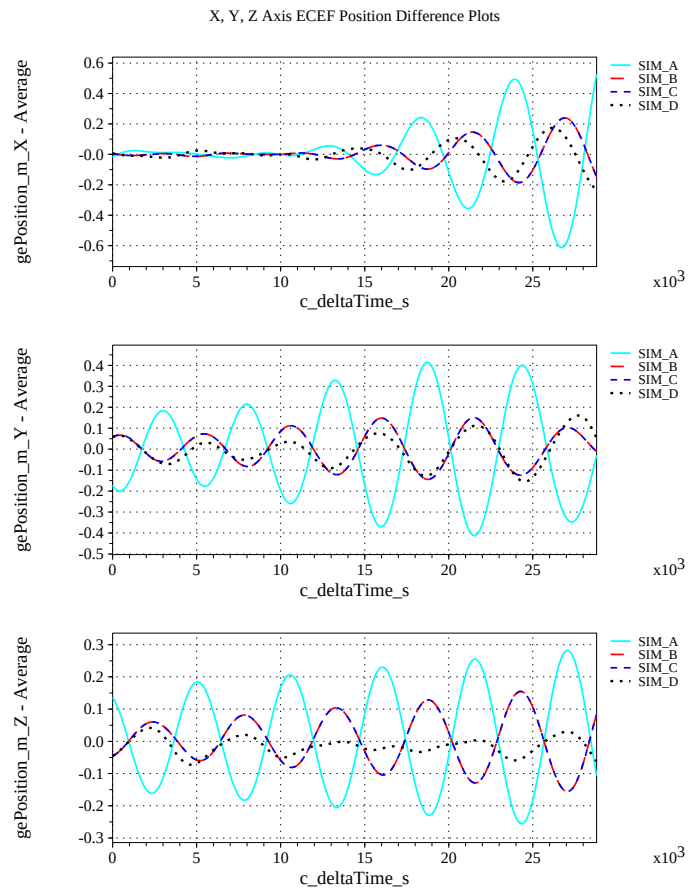

(l) Earth-centered, Earth-fixed Rectangular (X-Y-Z) Positions Differenced

Figure 56. Check-case 09C: ISS Under Torque and Force with Zero Initial Rates; See Discussion in Section D.2.20 (Cont'd)

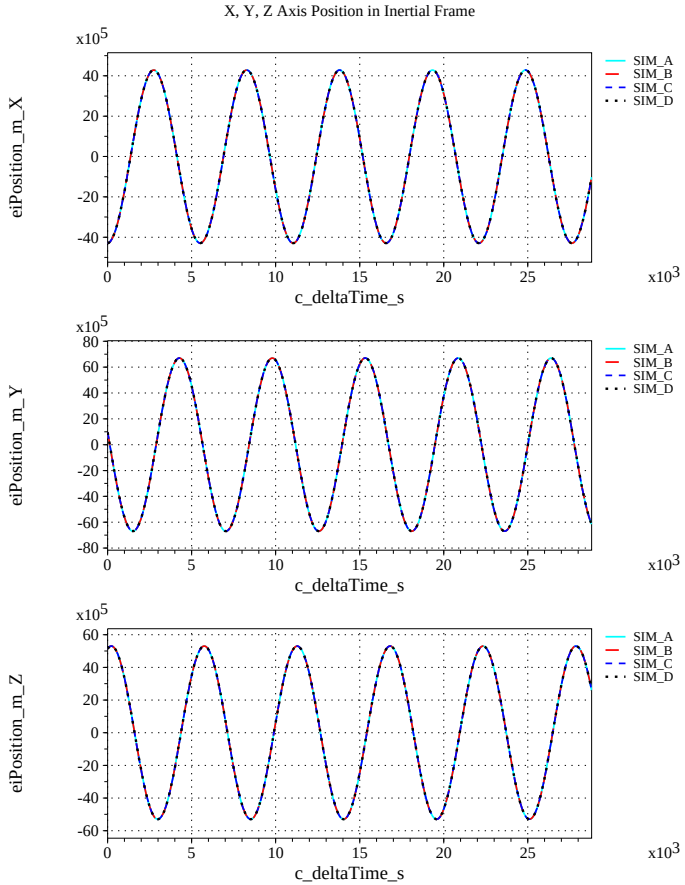

(m) Earth-centered Inertial Rectangular (x-y-z) Positions Compared

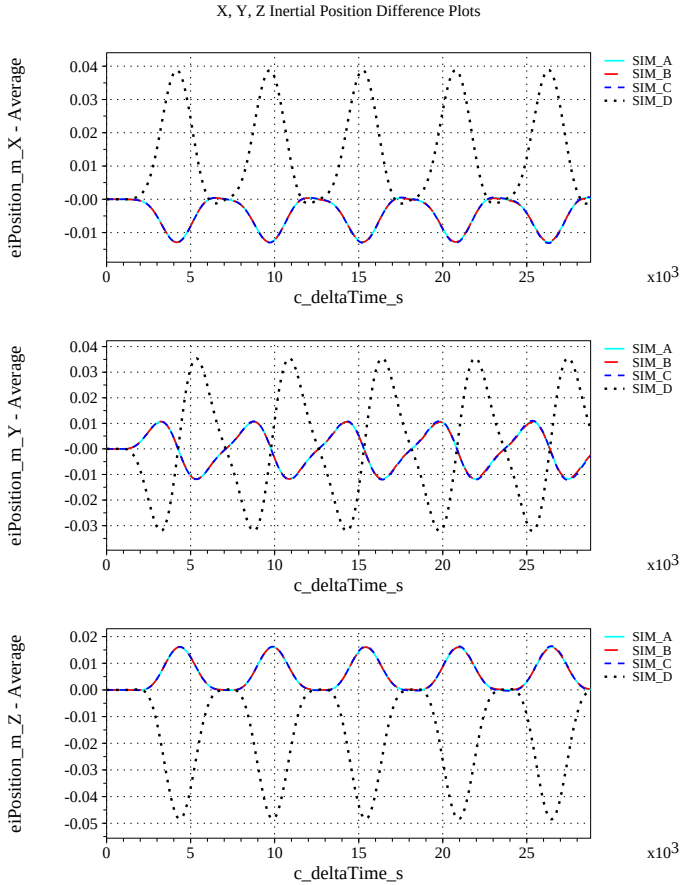

(n) Earth-centered Inertial Rectangular (x-y-z) Positions Differenced

Figure 56. Check-case 09C: ISS Under Torque and Force with Zero Initial Rates; See Discussion in Section D.2.20 (Cont'd)

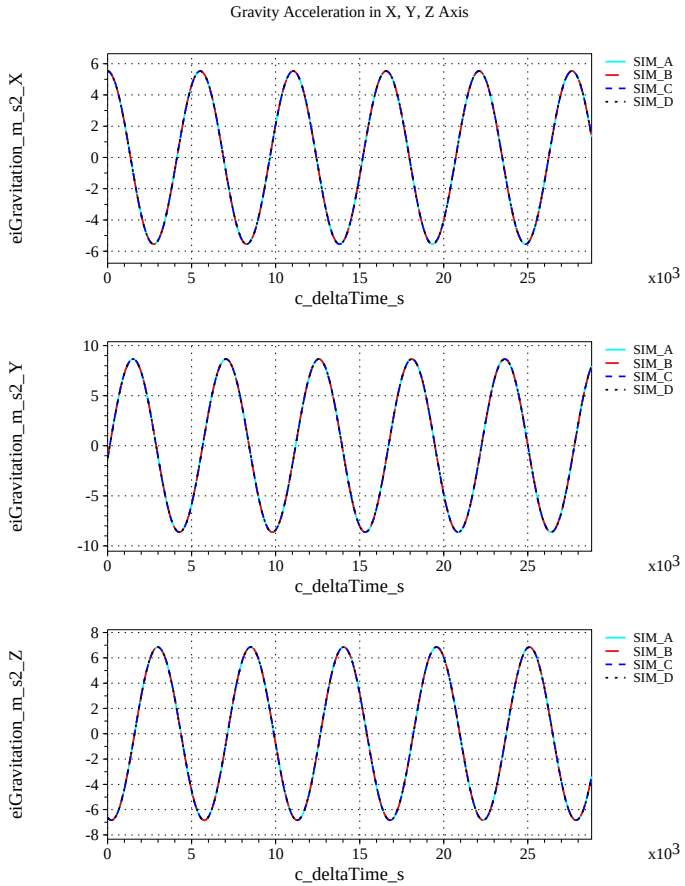

(o) Gravitational Components in Inertial (**X**-**Y**-**Z**) Directions Compared

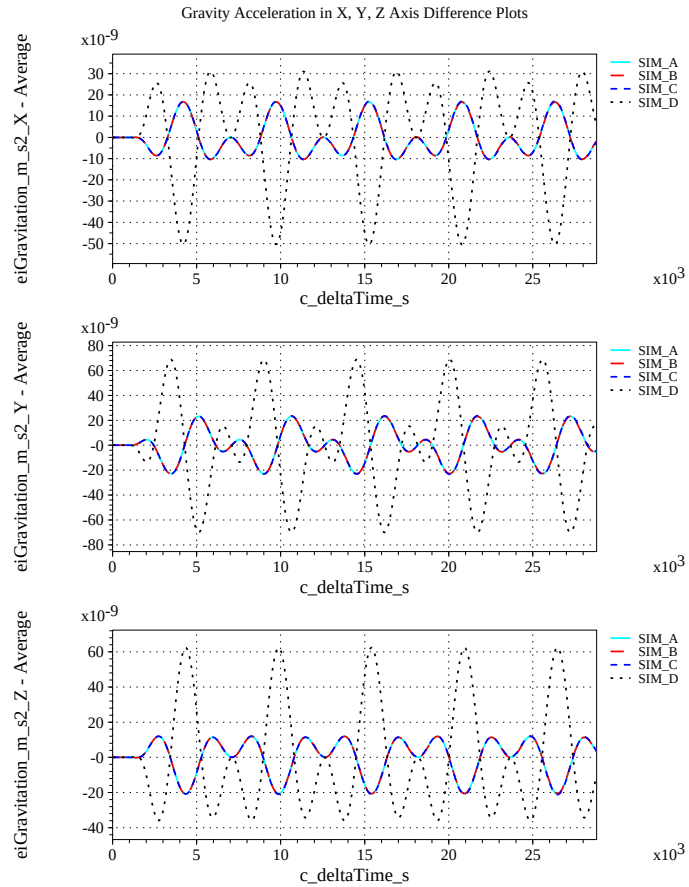

(p) Gravitational Components in Inertial (**X**-**Y**-**Z**) Directions Differenced

Figure 56. Check-case 09C: ISS Under Torque and Force with Zero Initial Rates; See Discussion in Section D.2.20 (Concluded)

D.2.21 Check-case 09D – ISS under torque and force with non-zero initial rates

This section shows cross-plots for four of the selected simulation tools in modeling the dynamics of the ISS in responding to external torque and force starting with a non-zero inertial rate. This scenario is described in Section C.2.21. Figures 57a through 57p compare results between the four simulation tools, as well as the deviances of the outputs from each tool from the ensemble average value.

Orbital check-case 9D was the second of two cases that applied a simultaneous torque and force to the ISS spacecraft. These scenarios examined the coupling of translational and rotational motion via a body-fixed thrust vector on a rotating body. In this case, the vehicle began with a zero rotation rate in the LVLH frame, i.e. a non-zero rotation rate in the inertial frame. The torque and force were both applied as a square pulse. As initial discussed in orbital case 6C, a square pulse force or torque can induce an increase in the integration error for some integration methods.

The differences in rotational state were identical to the differences for the previous scenario (orbital case 9B). For SIM A, SIM B, and SIM C, those rotational state differences did not contribute significantly to the differences in translational state, as a result of influencing the direction of the thrust vector. The differences in translational state were negligible.

SIM D, however, exhibited Euler angle differences due to differences in integration residues for both the initial rotation rate and the applied torque. Those integration differences combined to increase the translational-state differences similar to the differences SIM D exhibited in orbital check-case 9C. The difference in inertial position increased from less than 1 decimeter to less than 2 m at the end of the simulated eight hour flight. However, the differences are entirely attributed to combined differences in integration method and not to any differences in modeling or equations of motion. Thus, whether it was SIM D or the other three simulations exhibiting increased integration residue, the integrators could likely be reconfigured to reduce the residue in position if an application required greater accuracy in results.

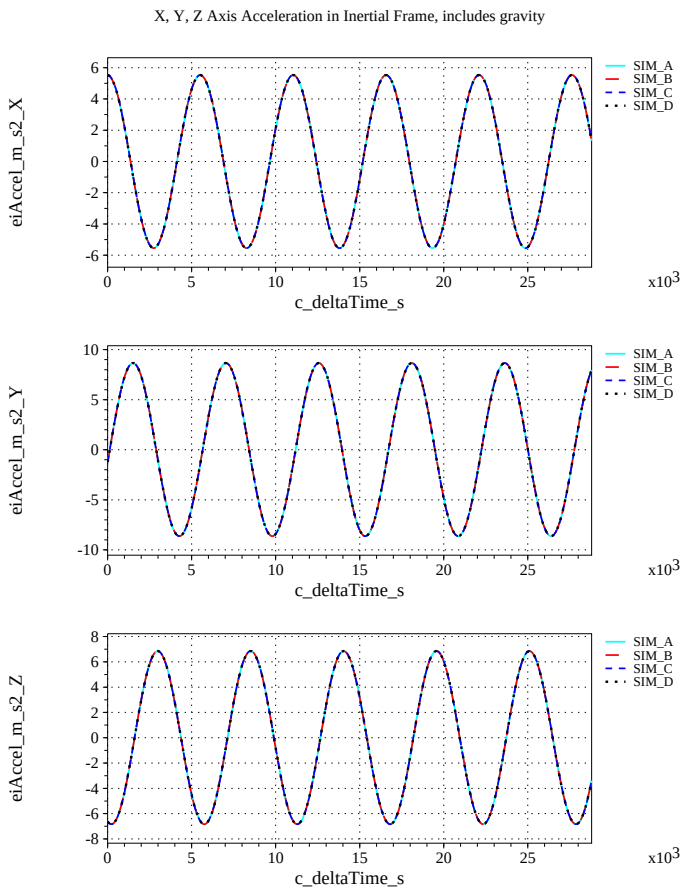

(a) Inertial Accelerations Compared

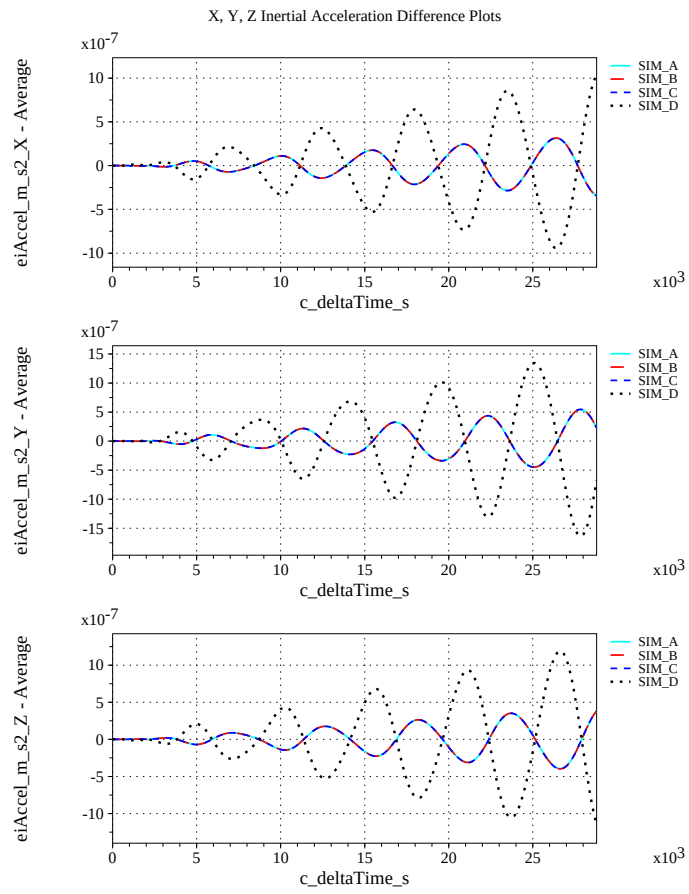

(b) Inertial Accelerations Differenced

Figure 57. Check-case 09D: ISS Under Torque and Force with Non-zero Initial Rates; See Discussion in Section D.2.21

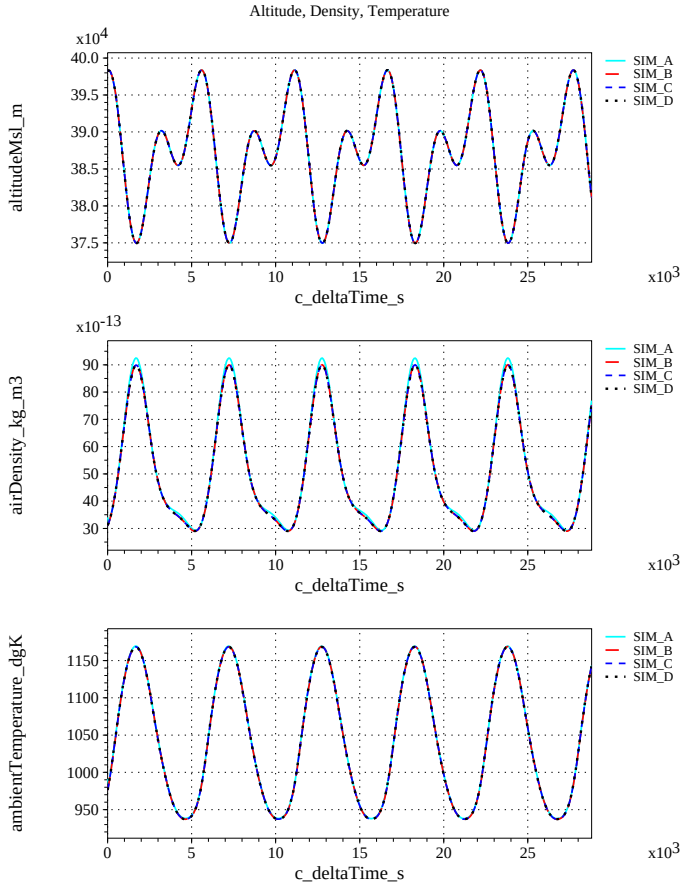

(c) Atmospheric Properties Compared

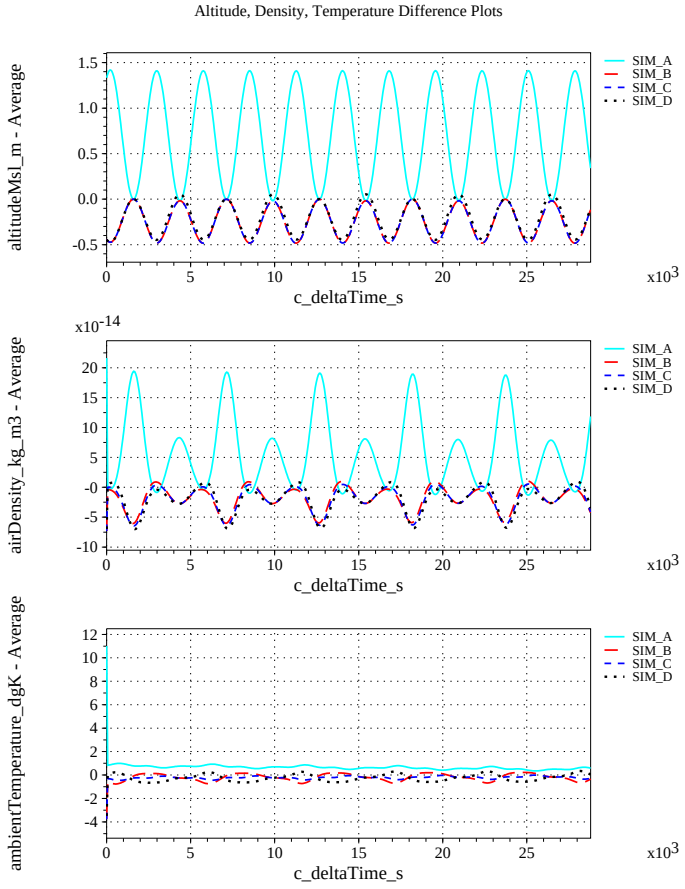

(d) Atmospheric Properties Differenced

Figure 57. Check-case 09D: ISS Under Torque and Force with Non-zero Initial Rates; See Discussion in Section D.2.21 (Cont'd)

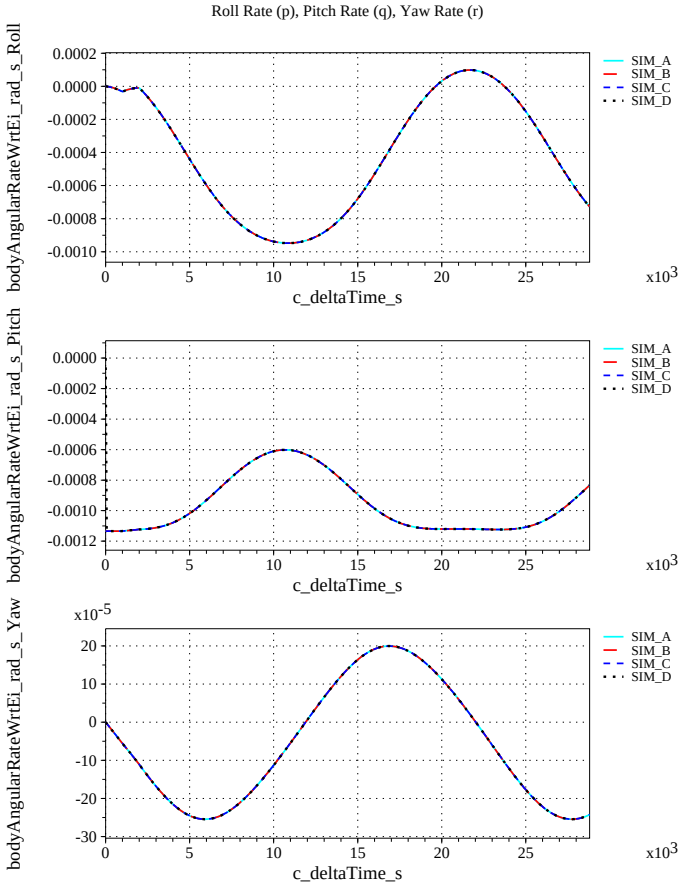

(e) Body-axis Angular Rates Compared

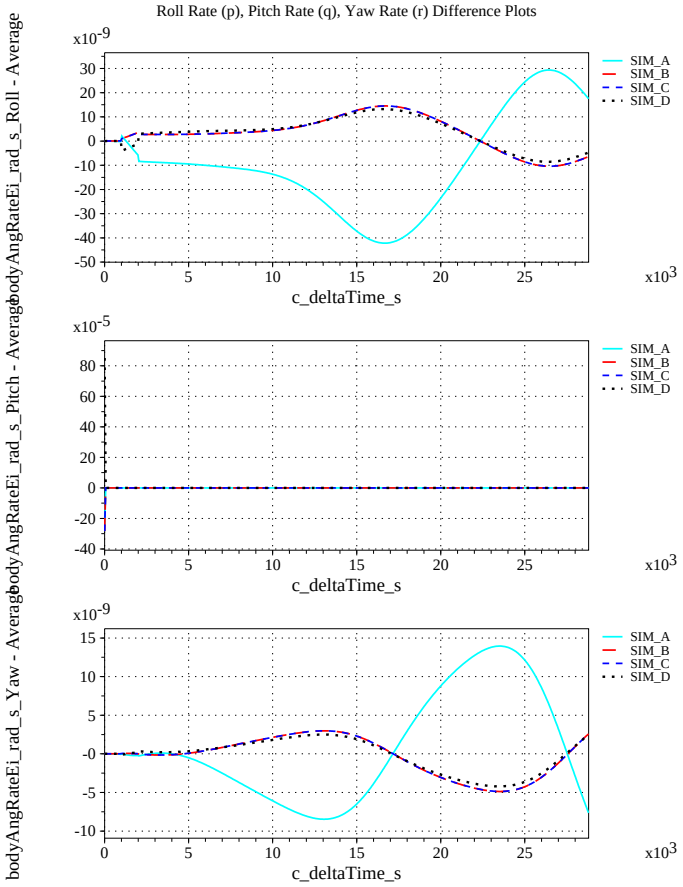

(f) Body-axis Angular Rates Differenced

Figure 57. Check-case 09D: ISS Under Torque and Force with Non-zero Initial Rates; See Discussion in Section D.2.21 (Cont'd)

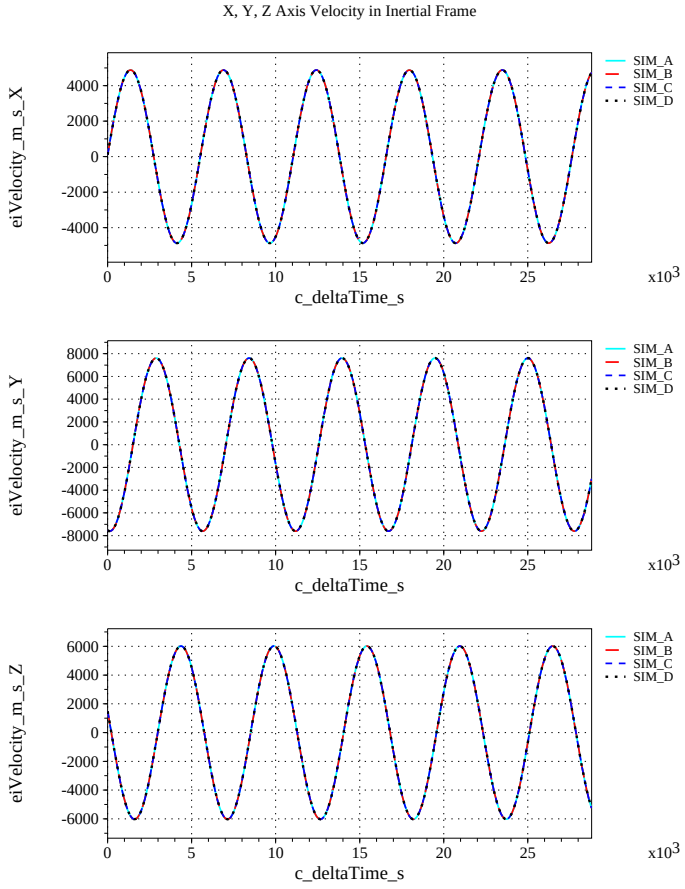

(g) Inertial Velocities Compared

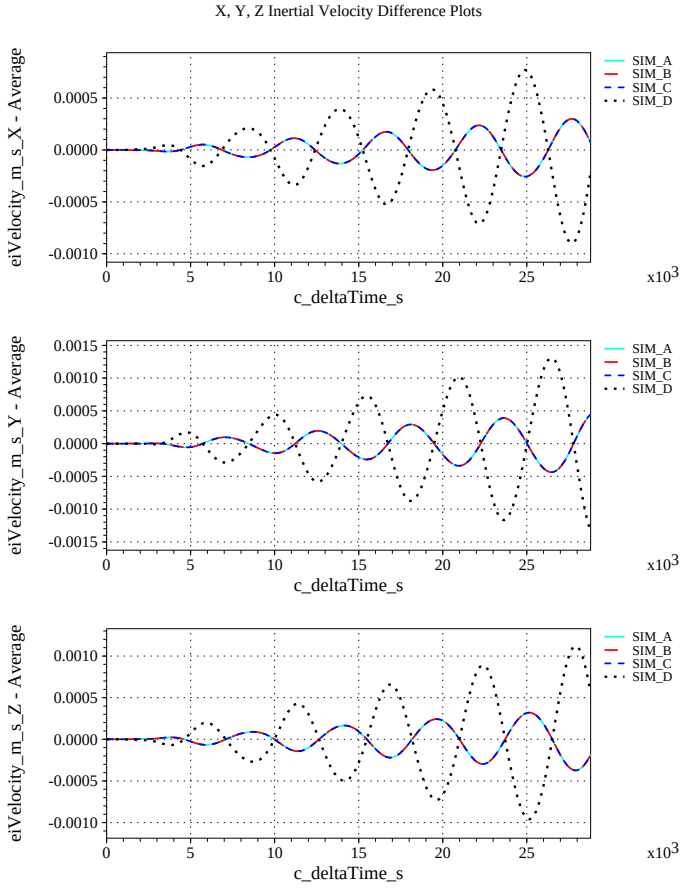

(h) Inertial Velocities Differenced

Figure 57. Check-case 09D: ISS Under Torque and Force with Non-zero Initial Rates; See Discussion in Section D.2.21 (Cont'd)

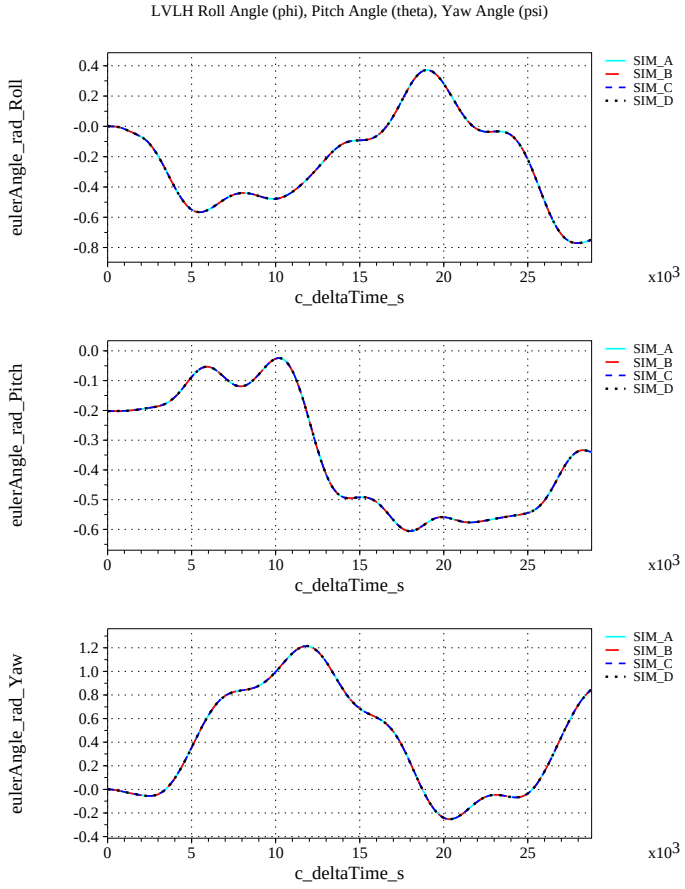

(i) Rotation Angles with Respect to LVLH Frame Compared

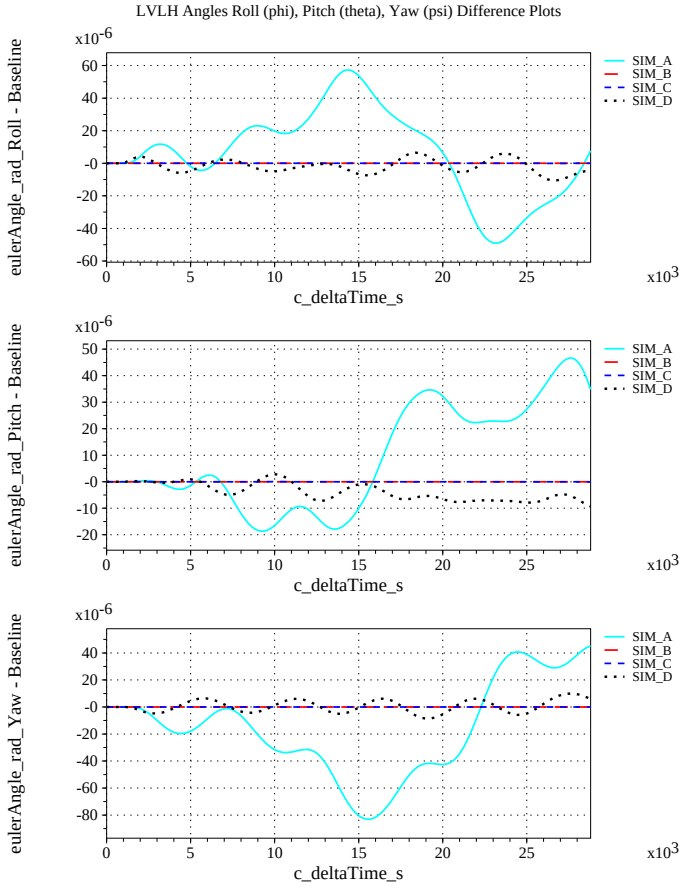

(j) Rotation Angles with Respect to LVLH Frame Differenced

Figure 57. Check-case 09D: ISS Under Torque and Force with Non-zero Initial Rates; See Discussion in Section D.2.21 (Cont'd)

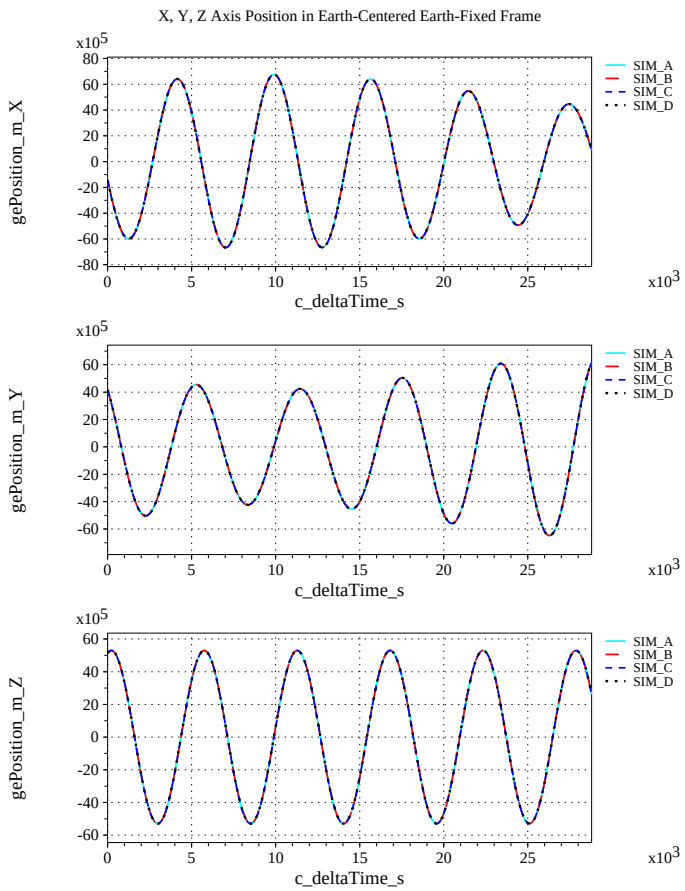

(k) Earth-centered, Earth-fixed Rectangular (X-Y-Z) Positions Compared

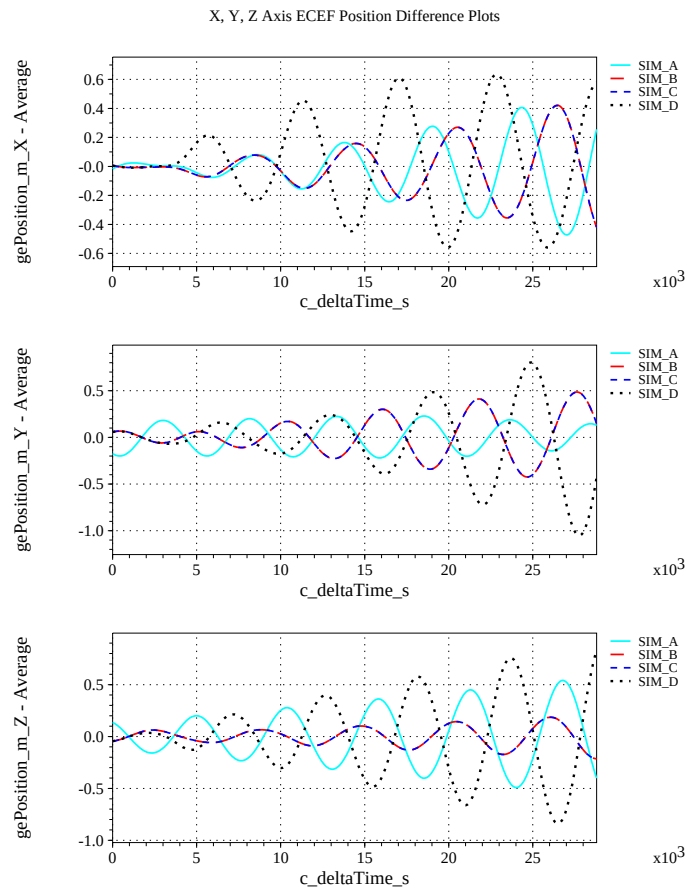

(l) Earth-centered, Earth-fixed Rectangular (X-Y-Z) Positions Differenced

Figure 57. Check-case 09D: ISS Under Torque and Force with Non-zero Initial Rates; See Discussion in Section D.2.21 (Cont'd)

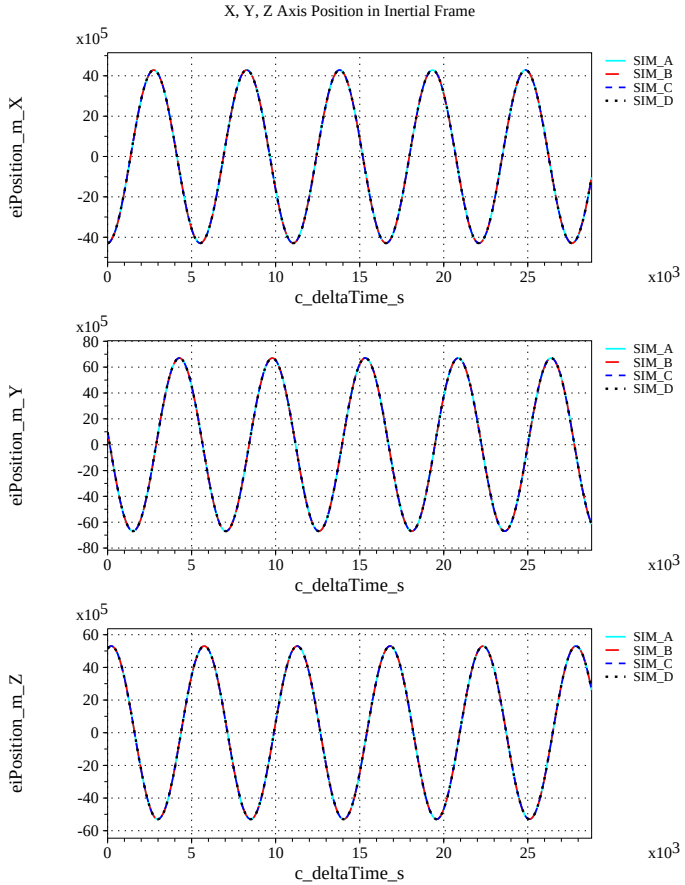

(m) Earth-centered Inertial Rectangular (x-y-z) Positions Compared

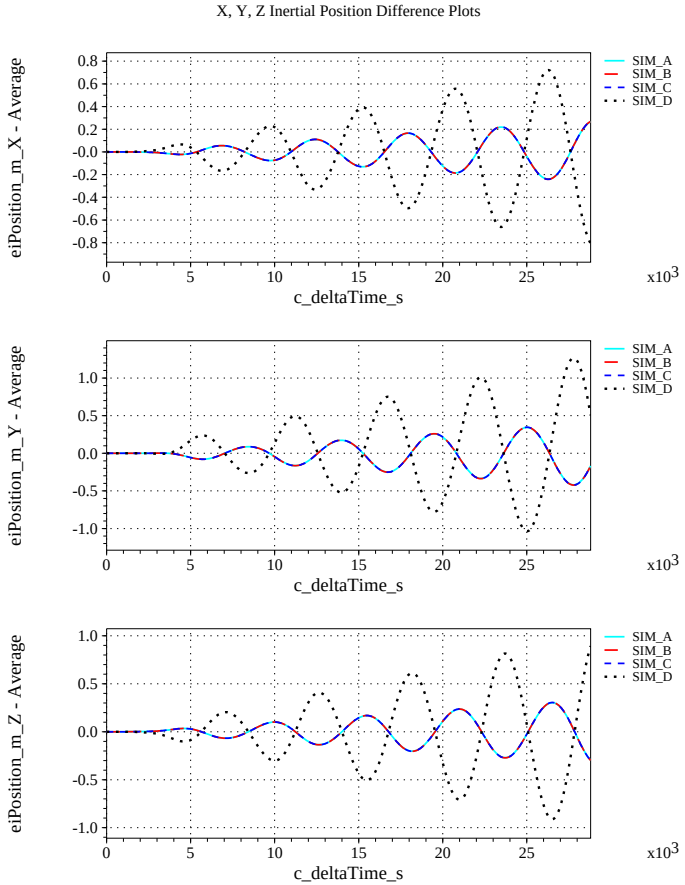

(n) Earth-centered Inertial Rectangular (x-y-z) Positions Differenced

Figure 57. Check-case 09D: ISS Under Torque and Force with Non-zero Initial Rates; See Discussion in Section D.2.21 (Cont'd)

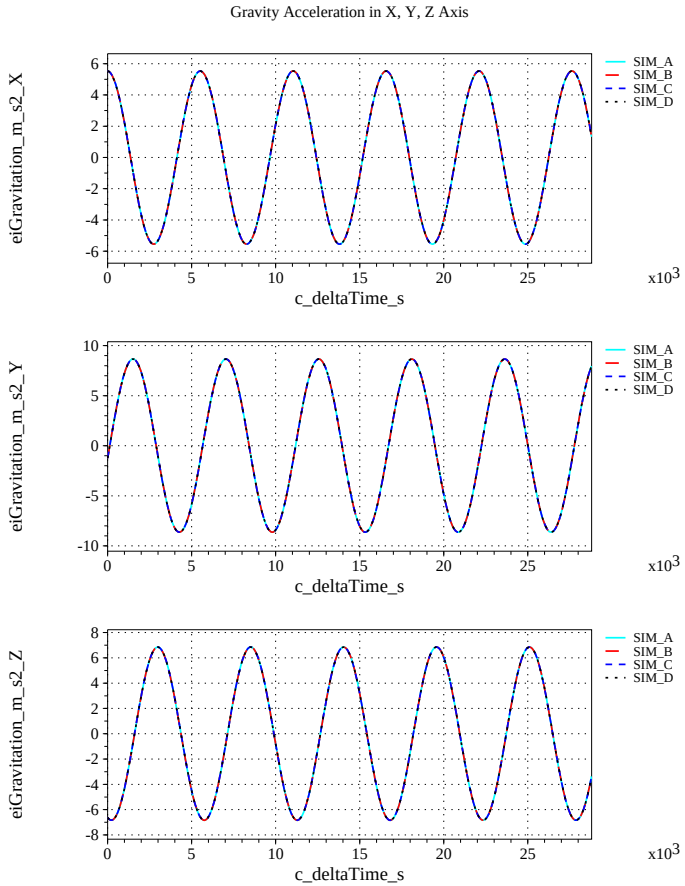

(o) Gravitational Components in Inertial (**X**-**Y**-**Z**) Directions Compared

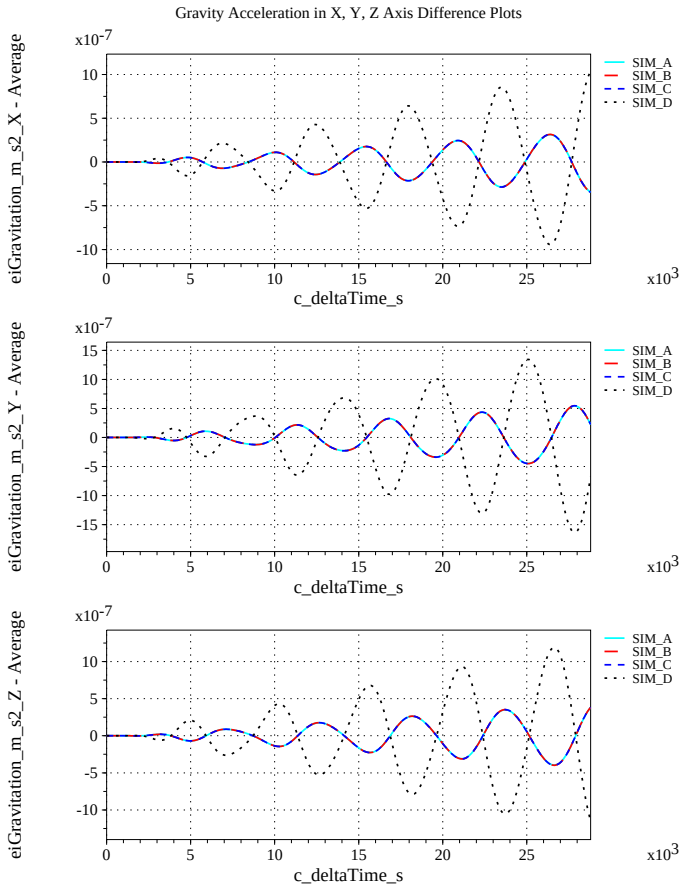

(p) Gravitational Components in Inertial (**X**-**Y**-**Z**) Directions Differenced

Figure 57. Check-case 09D: ISS Under Torque and Force with Non-zero Initial Rates; See Discussion in Section D.2.21 (Concluded)

D.2.22 Check-case 10A – cylinder in circular orbit with gravity gradient with zero initial rates

This section shows cross-plots for four of the selected simulation tools in modeling the dynamics of a cylinder in low Earth orbit responding to the gravity gradient starting with zero inertial rate. This scenario is described in Section C.2.22. Figures 58a through 58p compare results between the four simulation tools, as well as the deviances of the outputs from each tool from the ensemble average value.

Orbital check-case 10A was the first of four scenarios to assess the modeling and application of gravity gradient torque among the simulations. This test case initialized the cylindrical vehicle to a near circular orbit with a initial rate of zero relative to the LVLH frame.

The simulations demonstrated close agreement on the inertial rotational states. The negligible differences that remained were attributed to differences in integration method or differences in the precision of recorded outputs. Likewise, the simulations showed close agreement on the inertial translational states. Despite this agreement on inertial orientation and orbit, SIM C reported LVLH Euler angles that differ substantially from the other simulations (see Figure 58j). Such differences were not exhibited in prior test cases. Thus, it appears that SIM C may have been configured with a different Euler angle convention or different LVLH definition for these check-cases.

The differences in ECEF position among the simulations were identical to orbital case 2 with the simulations differing by less than 0.3 m after a simulated 8-hour flight. However, the difference in altitude of up to 33 m exhibited by SIM A in this case were much larger than the approximately 2 m difference seen in orbital case 2 (Section D.2.1). Thus, it appeared that SIM A may have been configured with a different set of Earth surface modeling parameters for this check-case.

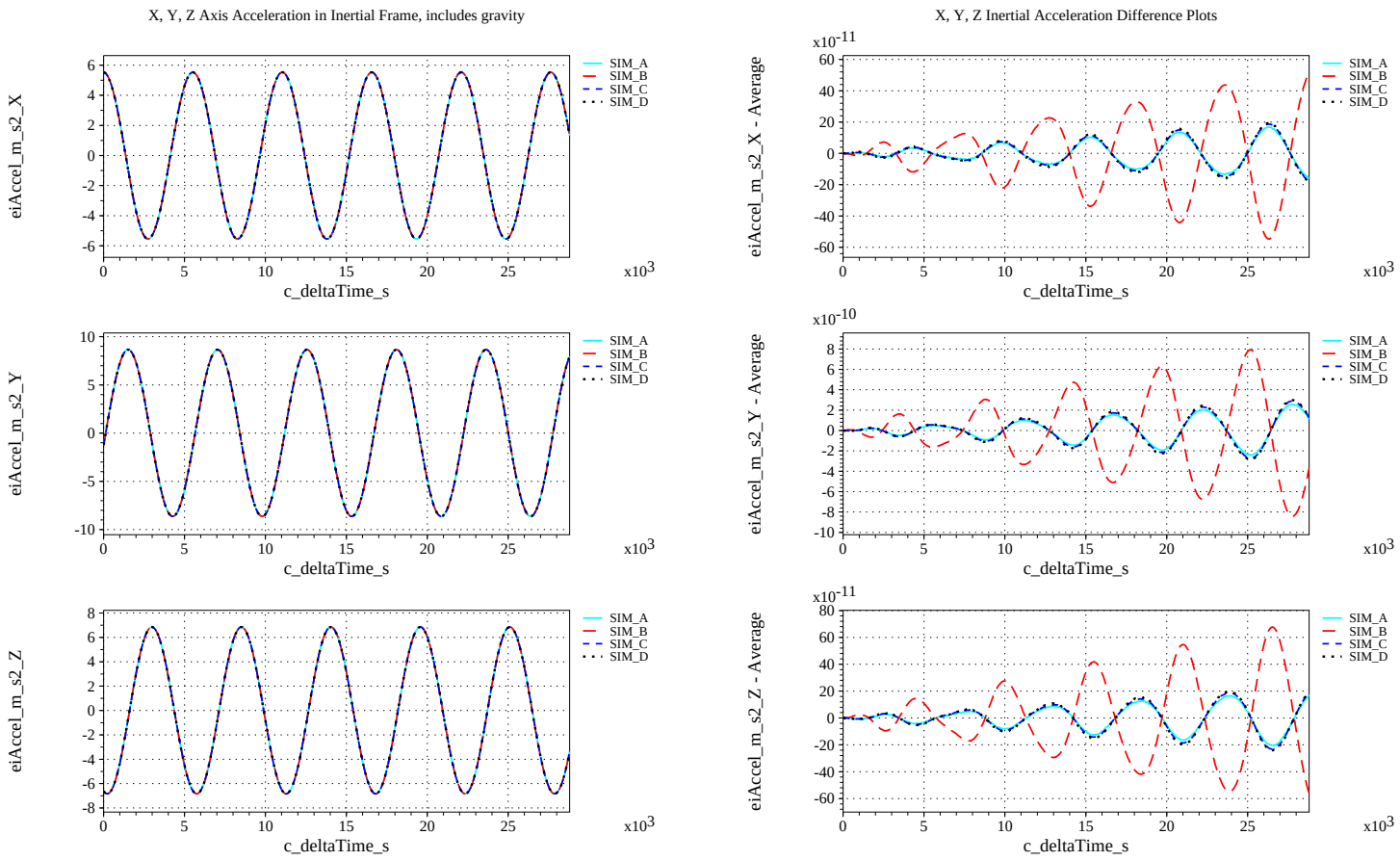

(a) Inertial Accelerations Compared

(b) Inertial Accelerations Differenced

Figure 58. Check-case 10A: Cylinder in Circular Orbit with Gravity Gradient with Zero Initial Rates; See Discussion in Section D.2.22

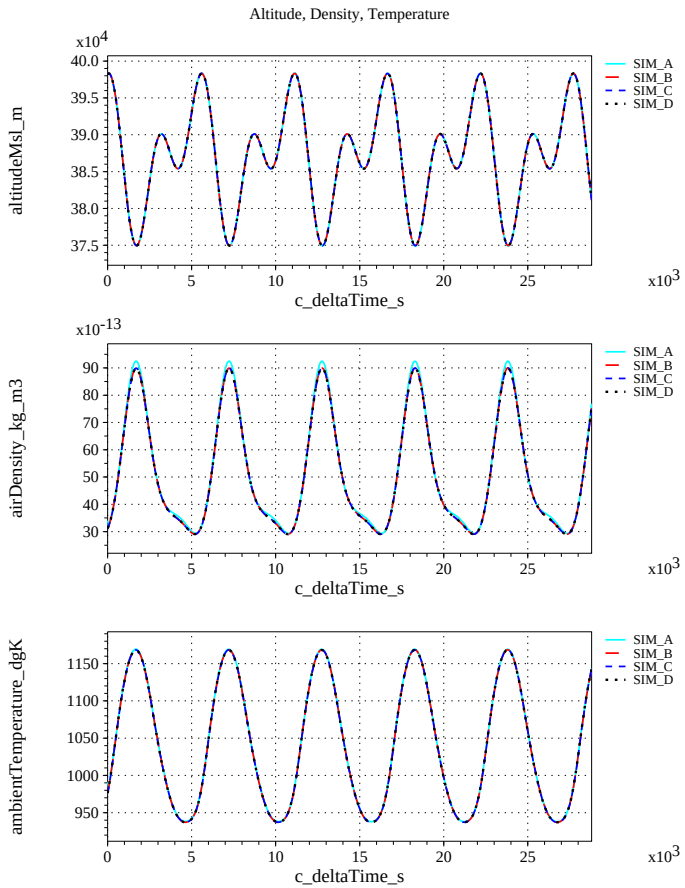

(c) Atmospheric Properties Compared

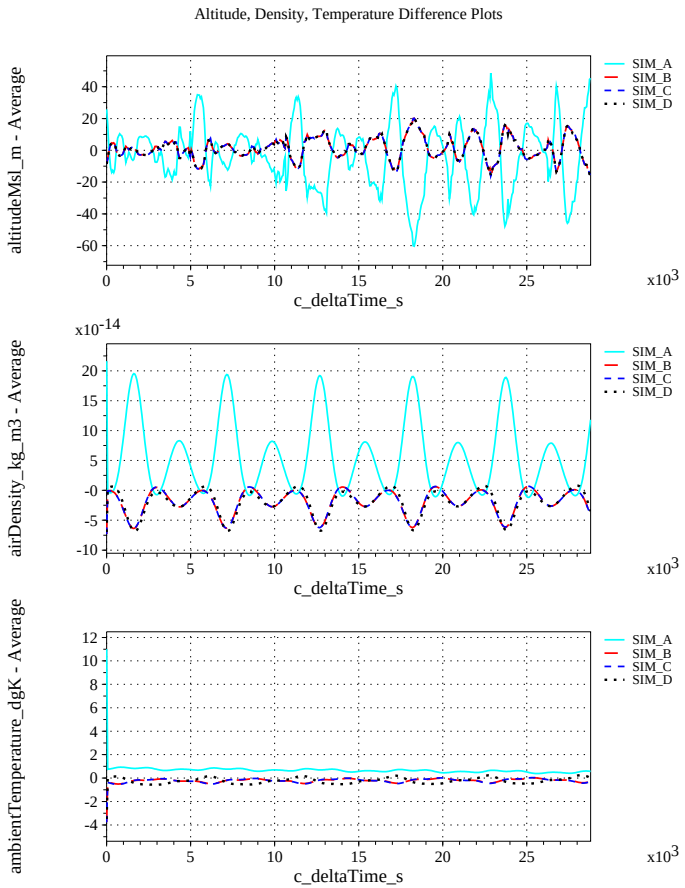

(d) Atmospheric Properties Differenced

Figure 58. Check-case 10A: Cylinder in Circular Orbit with Gravity Gradient with Zero Initial Rates; See Discussion in Section D.2.22 (Cont'd)

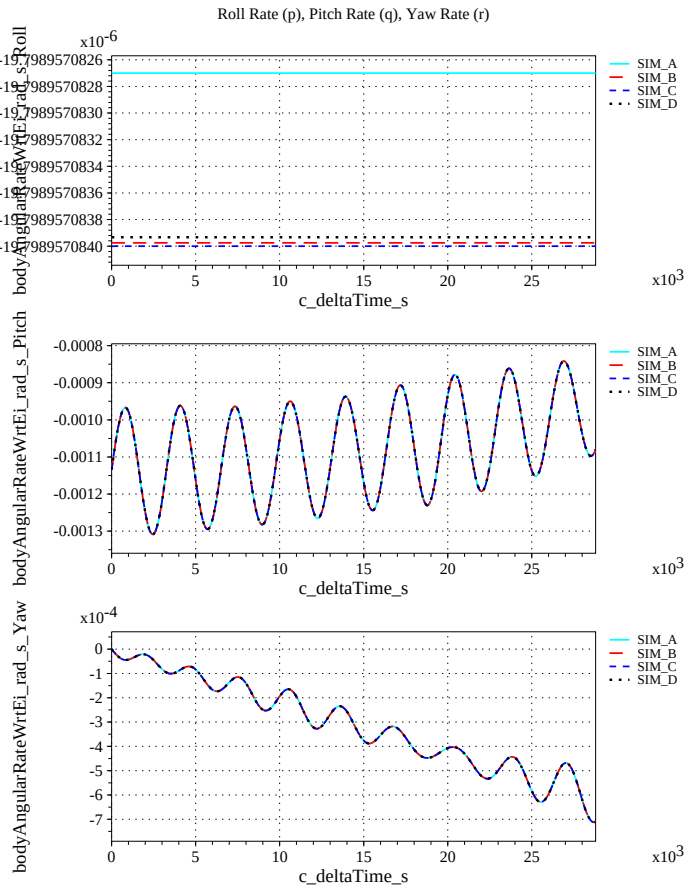

(e) Body-axis Angular Rates Compared

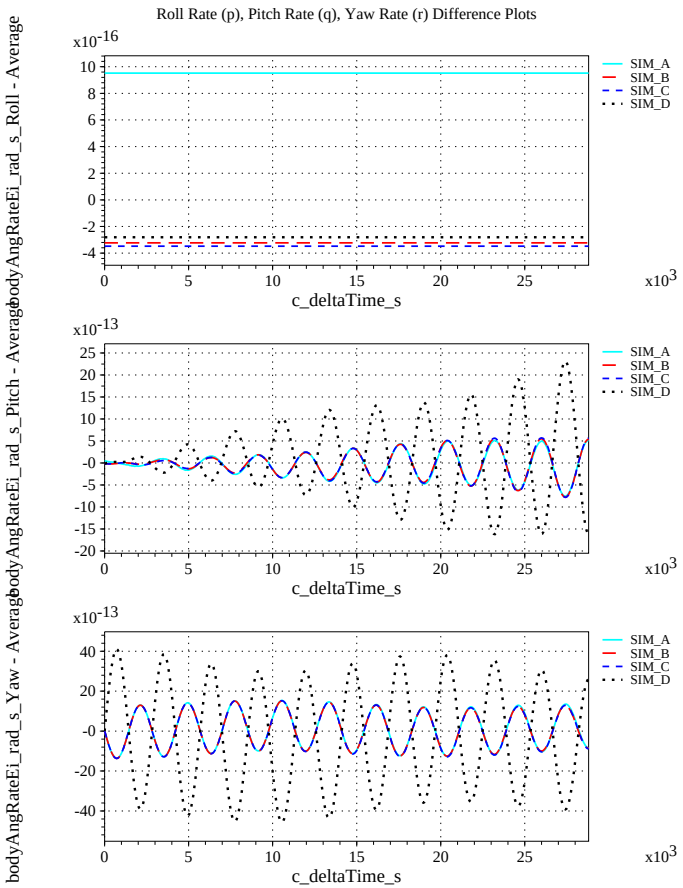

(f) Body-axis Angular Rates Differenced

Figure 58. Check-case 10A: Cylinder in Circular Orbit with Gravity Gradient with Zero Initial Rates; See Discussion in Section D.2.22 (Cont'd)

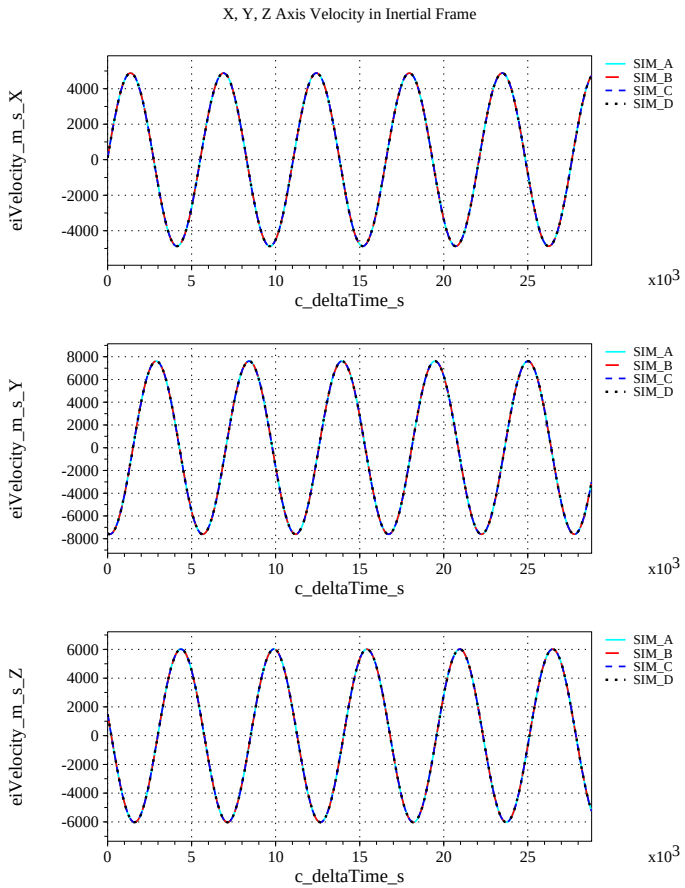

(g) Inertial Velocities Compared

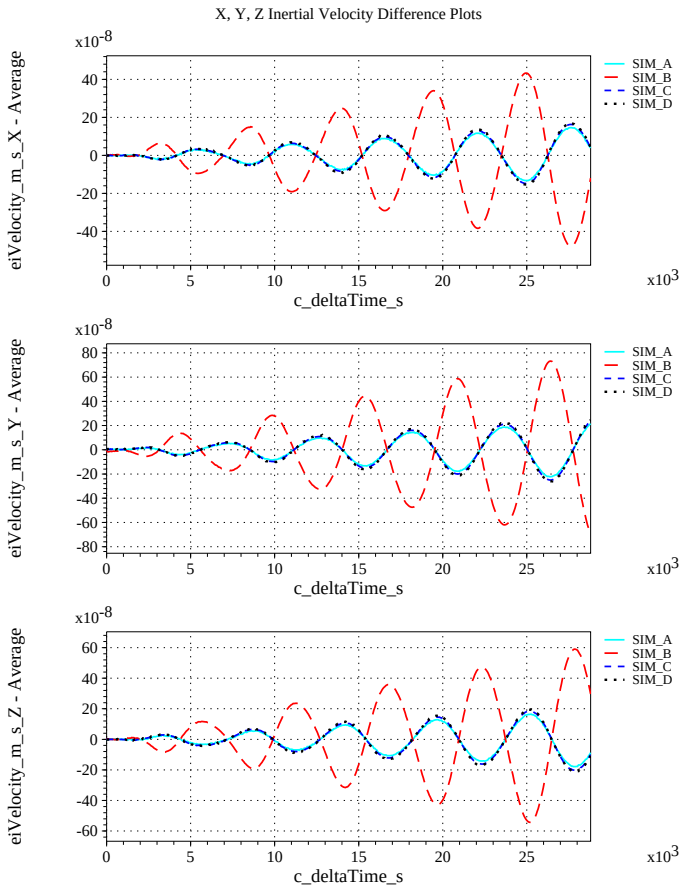

(h) Inertial Velocities Differenced

Figure 58. Check-case 10A: Cylinder in Circular Orbit with Gravity Gradient with Zero Initial Rates; See Discussion in Section D.2.22 (Cont'd)

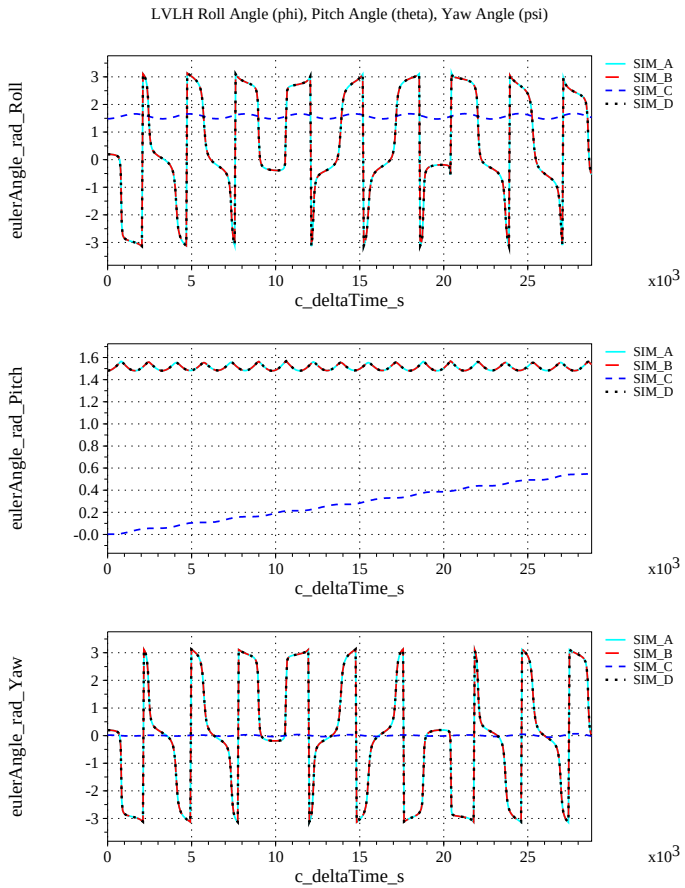

(i) Rotation Angles with Respect to LVLH Frame Compared

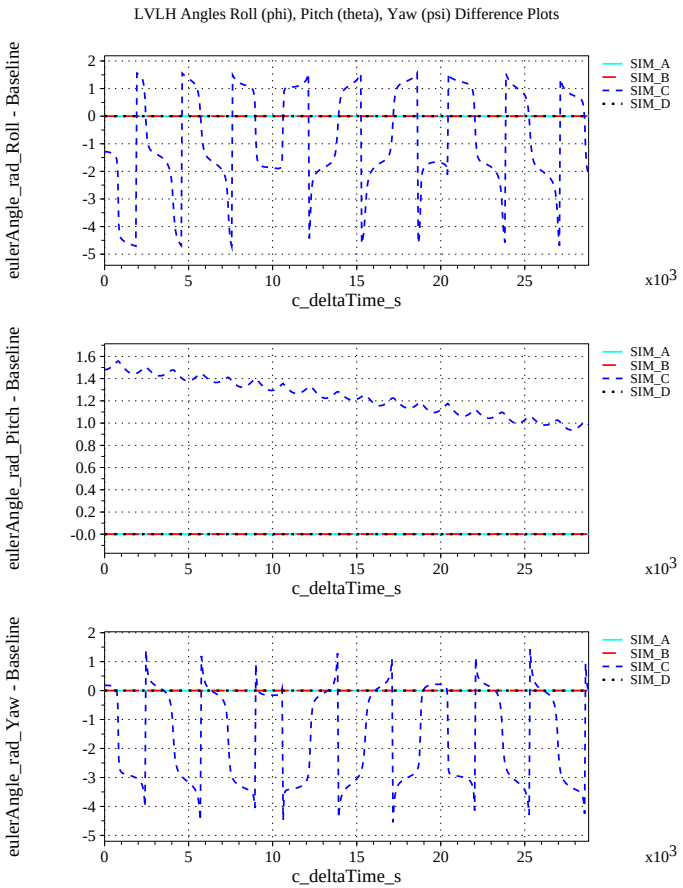

(j) Rotation Angles with Respect to LVLH Frame Differenced

Figure 58. Check-case 10A: Cylinder in Circular Orbit with Gravity Gradient with Zero Initial Rates; See Discussion in Section D.2.22 (Cont'd)

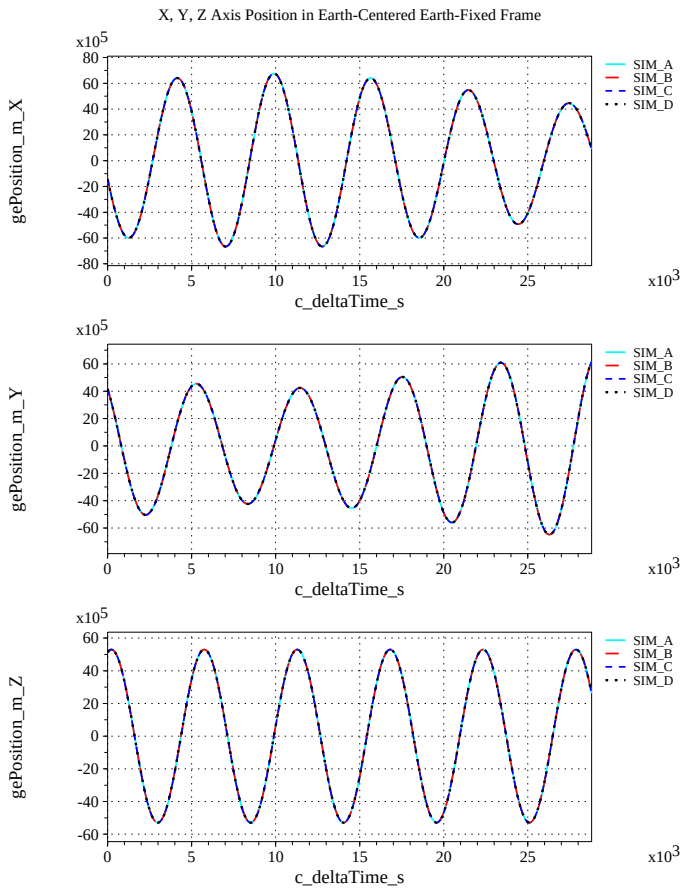

(k) Earth-centered, Earth-fixed Rectangular (X-Y-Z) Positions Compared

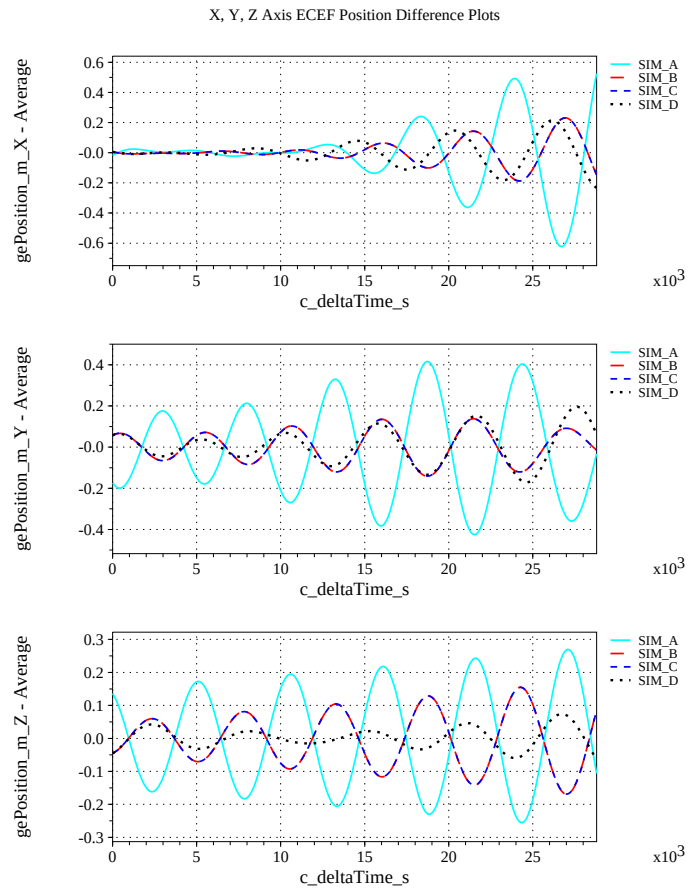

(l) Earth-centered, Earth-fixed Rectangular (X-Y-Z) Positions Differenced

Figure 58. Check-case 10A: Cylinder in Circular Orbit with Gravity Gradient with Zero Initial Rates; See Discussion in Section D.2.22 (Cont'd)

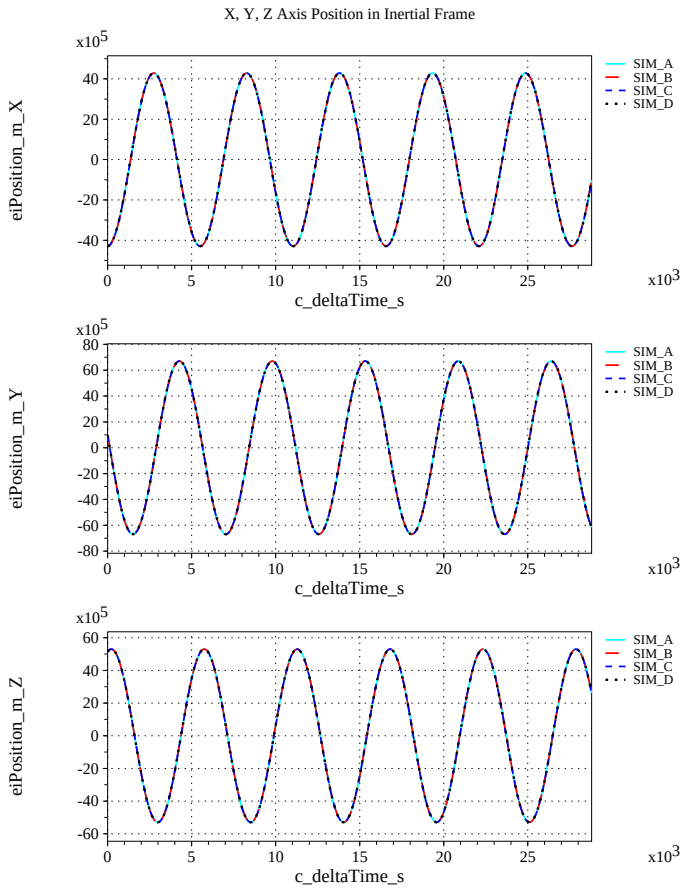

(m) Earth-centered Inertial Rectangular (x-y-z) Positions Compared

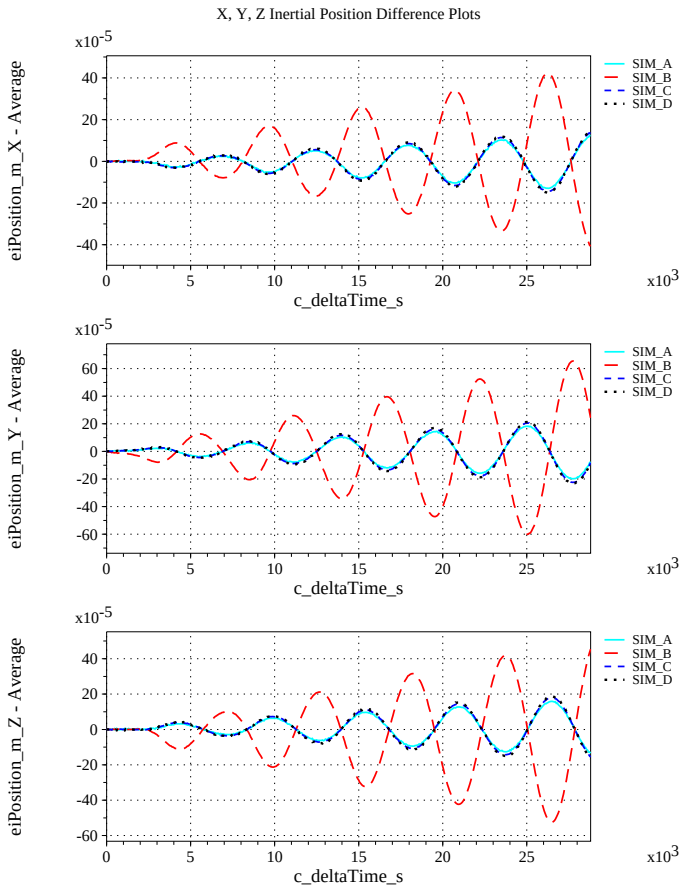

(n) Earth-centered Inertial Rectangular (x-y-z) Positions Differenced

Figure 58. Check-case 10A: Cylinder in Circular Orbit with Gravity Gradient with Zero Initial Rates; See Discussion in Section D.2.22 (Cont'd)

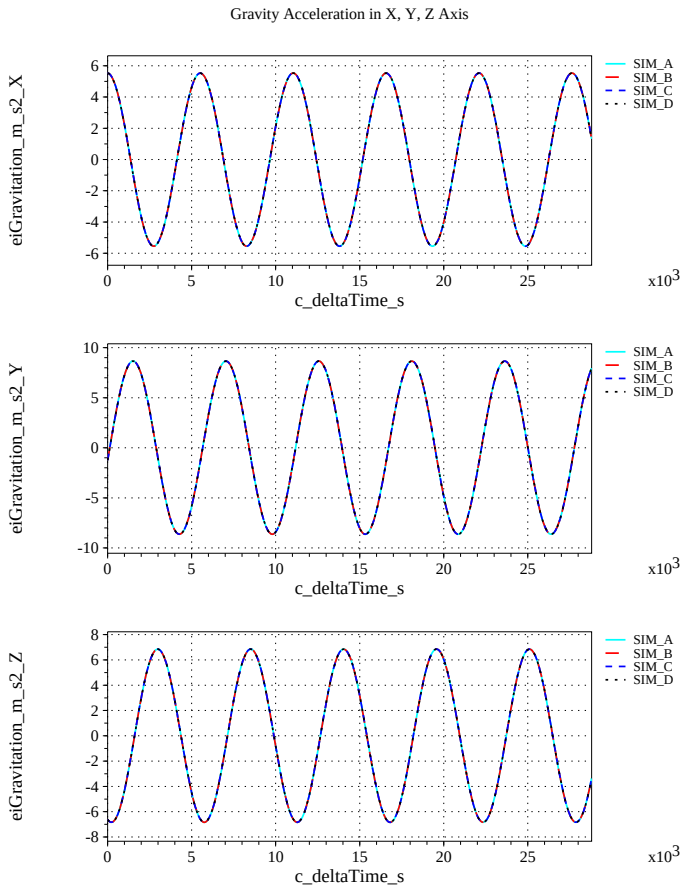

(o) Gravitational Components in Inertial (**X**-**Y**-**Z**) Directions Compared

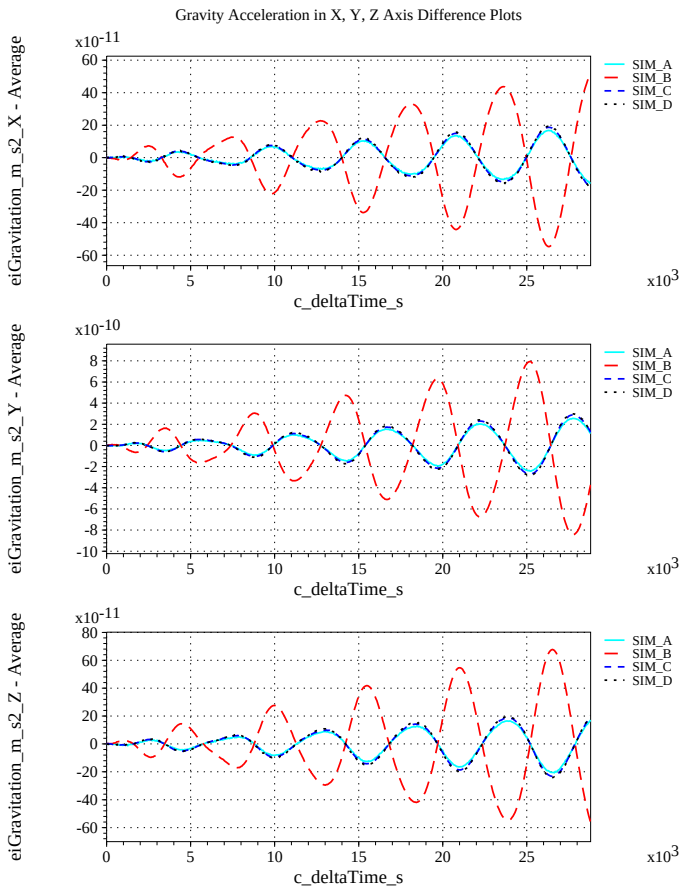

(p) Gravitational Components in Inertial (**X**-**Y**-**Z**) Directions Differenced

Figure 58. Check-case 10A: Cylinder in Circular Orbit with Gravity Gradient with Zero Initial Rates; See Discussion in Section D.2.22 (Concluded)

D.2.23 Check-case 10B – cylinder in circular orbit with gravity gradient with non-zero initial rates

This section shows cross-plots for four of the selected simulation tools in modeling the dynamics of a cylinder in low Earth orbit responding to the gravity gradient starting with a non-zero inertial rate. This scenario is described in Section C.2.23. Figures 59a through 59p compare results between the four simulation tools, as well as the deviances of the outputs from each tool from the ensemble average value.

Orbital check-case 10B was the second of four scenarios to assess the modeling and application of gravity gradient torque among the simulations. This test case initialized the cylindrical spacecraft to a near circular orbit with a initial pitch rate of 0.01 deg/s relative to the LVLH frame.

The introduction of an initial pitch rate in the LVLH frame did not qualitatively change the simulation comparison as described in orbital check-case 10A. The simulations demonstrated close agreement on the inertial rotational states. The negligible differences that remained were attributed to differences in integration method or differences in the precision of recorded outputs. Likewise, the simulations showed close agreement on the inertial translational states. Despite this agreement on inertial orientation and orbit, SIM C reported LVLH Euler angles that differ substantially from the other simulations, as shown in Figure 59j. Such differences were not exhibited in test cases prior to check-case 10A. Thus, it appears that SIM C may have been configured with a different Euler angle convention or different LVLH definition for these check-cases.

The differences in ECEF position among the simulations were identical to orbital case 2 with the simulations differing by less than 0.3 m after 8 hours, with the exception of SIM A as noted in the previous check-case.

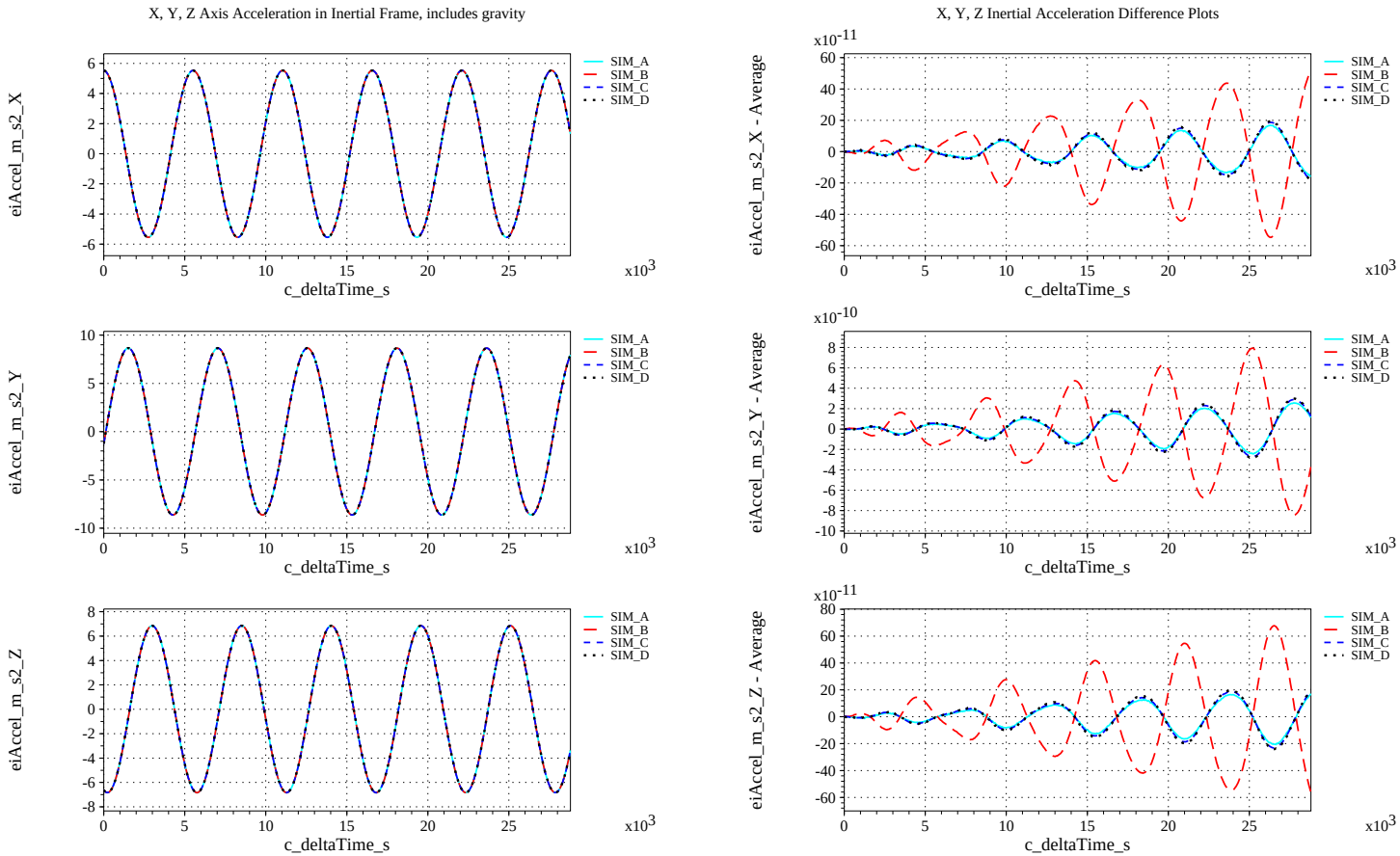

(a) Inertial Accelerations Compared

(b) Inertial Accelerations Differenced

Figure 59. Check-case 10B: Cylinder in Circular Orbit with Gravity Gradient with Non-zero Initial Rates; See Discussion in Section D.2.23

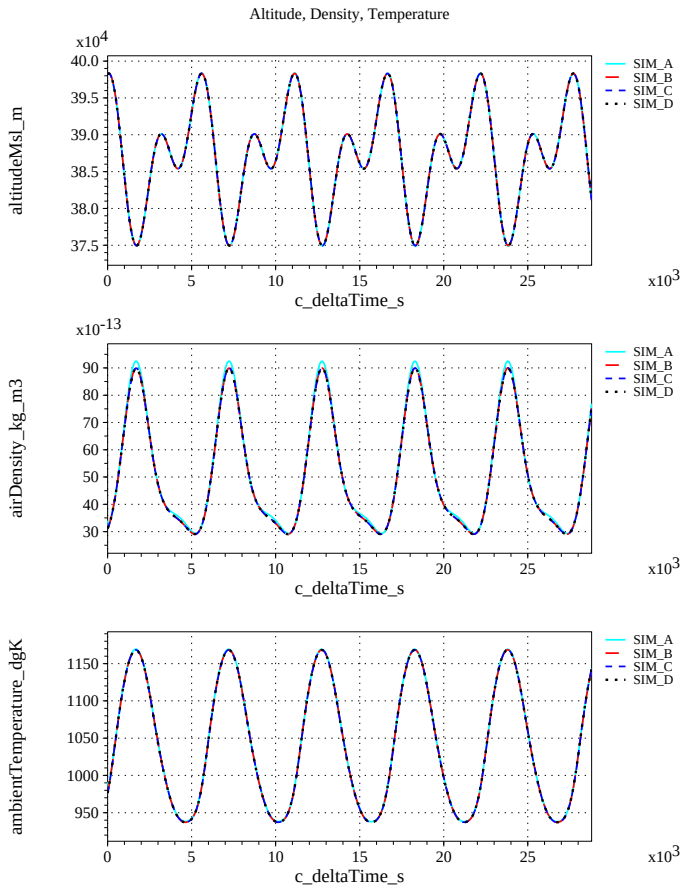

(c) Atmospheric Properties Compared

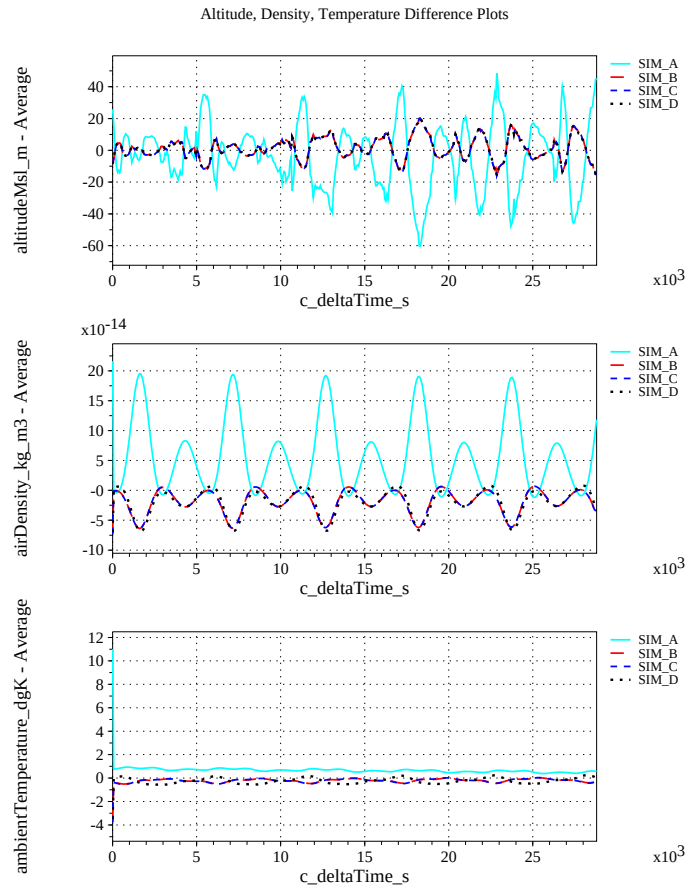

(d) Atmospheric Properties Differenced

Figure 59. Check-case 10B: Cylinder in Circular Orbit with Gravity Gradient with Non-zero Initial Rates; See Discussion in Section D.2.23 (Cont'd)

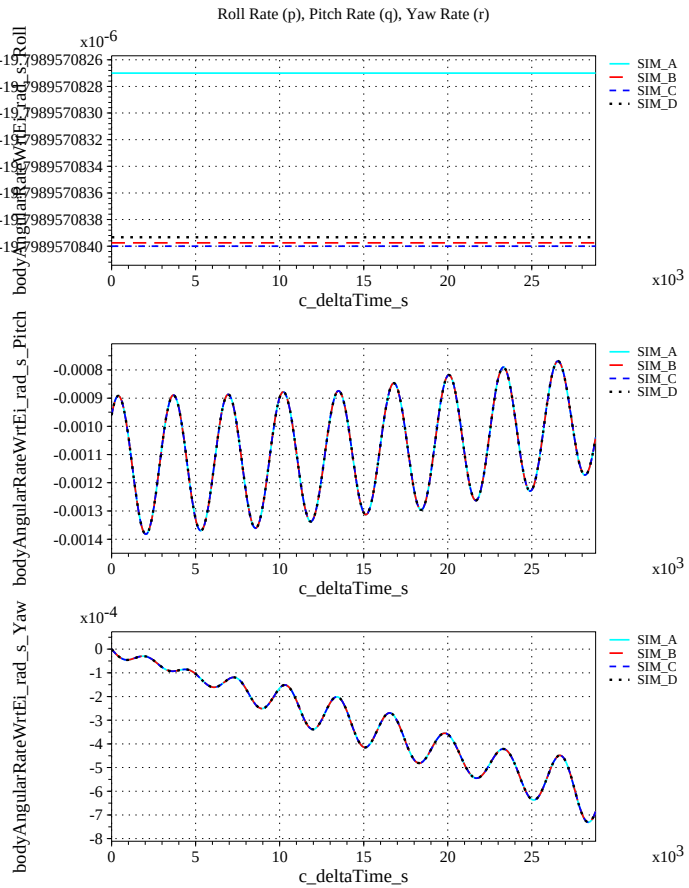

(e) Body-axis Angular Rates Compared

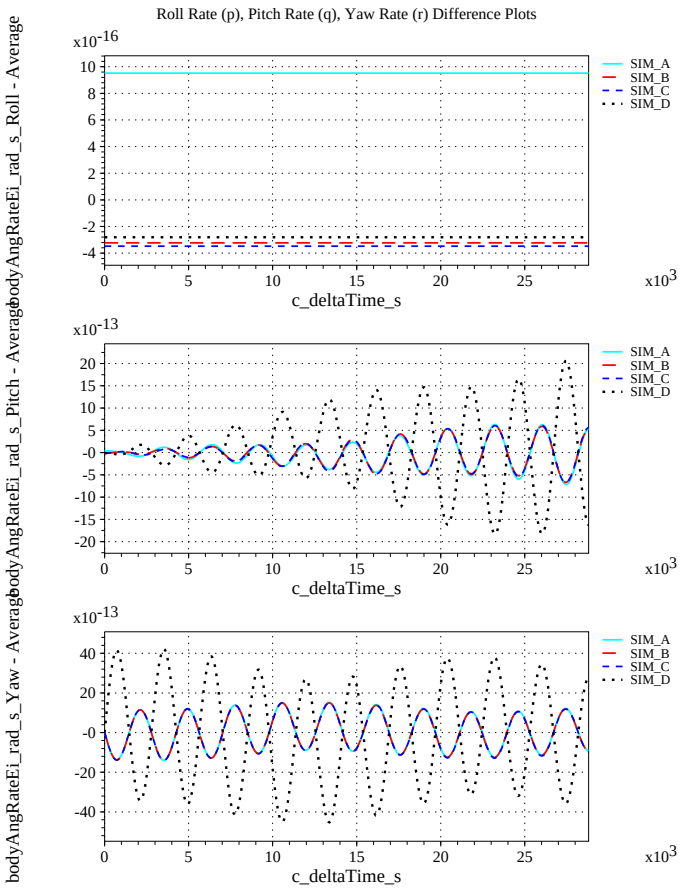

(f) Body-axis Angular Rates Differenced

Figure 59. Check-case 10B: Cylinder in Circular Orbit with Gravity Gradient with Non-zero Initial Rates; See Discussion in Section D.2.23 (Cont'd)

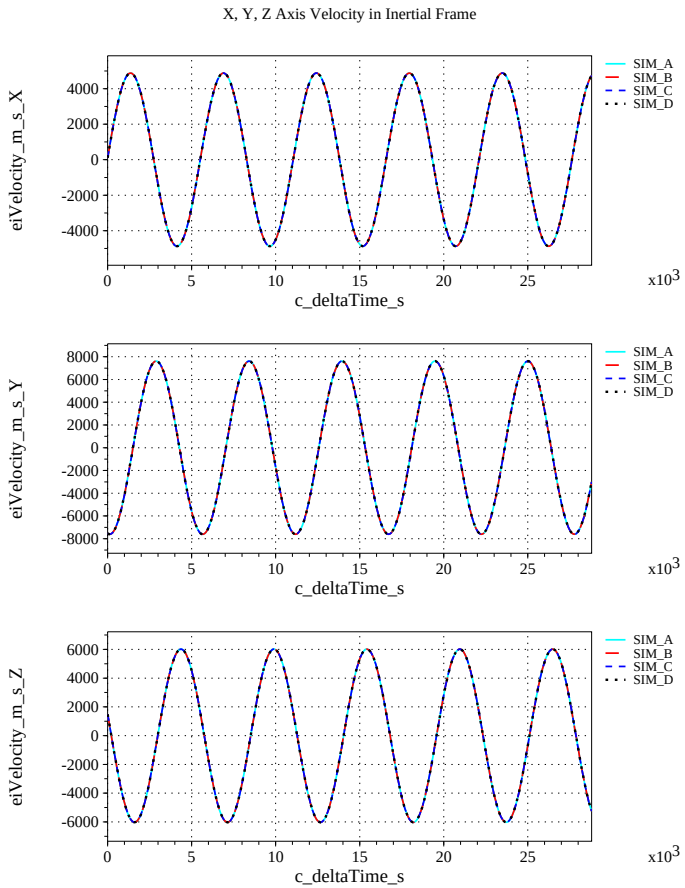

(g) Inertial Velocities Compared

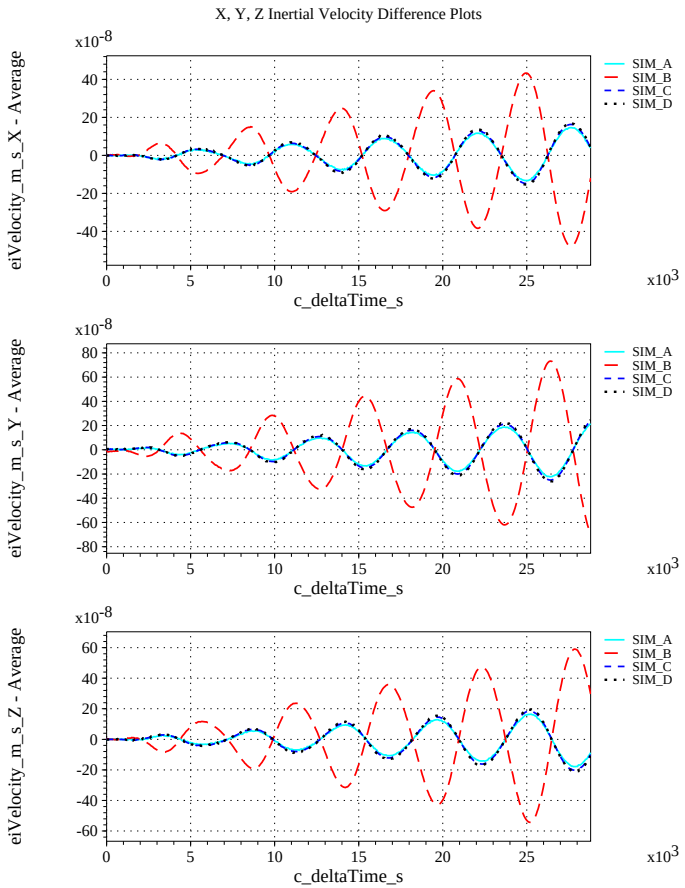

(h) Inertial Velocities Differenced

Figure 59. Check-case 10B: Cylinder in Circular Orbit with Gravity Gradient with Non-zero Initial Rates; See Discussion in Section D.2.23 (Cont'd)

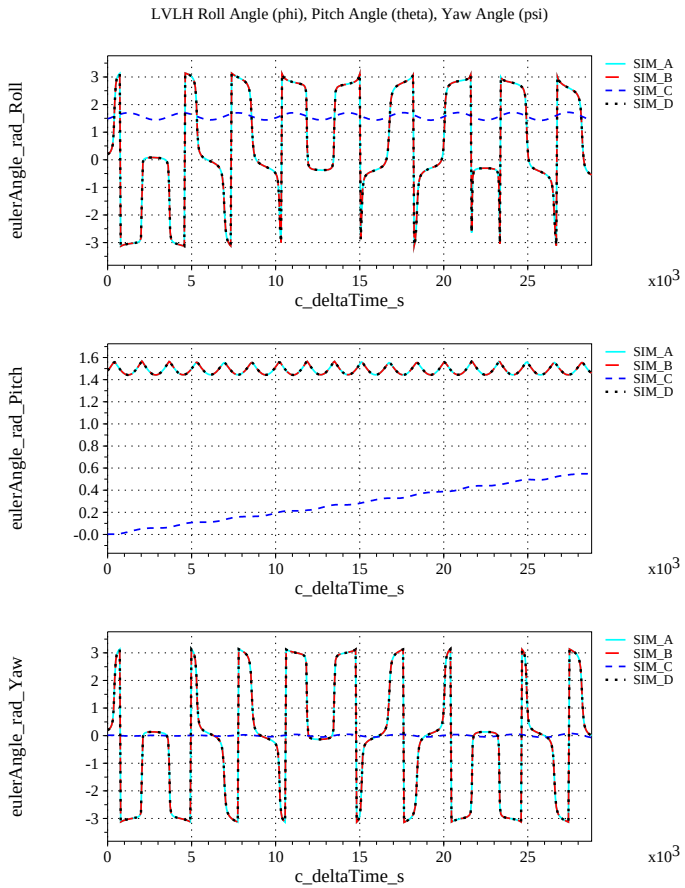

(i) Rotation Angles with Respect to LVLH Frame Compared

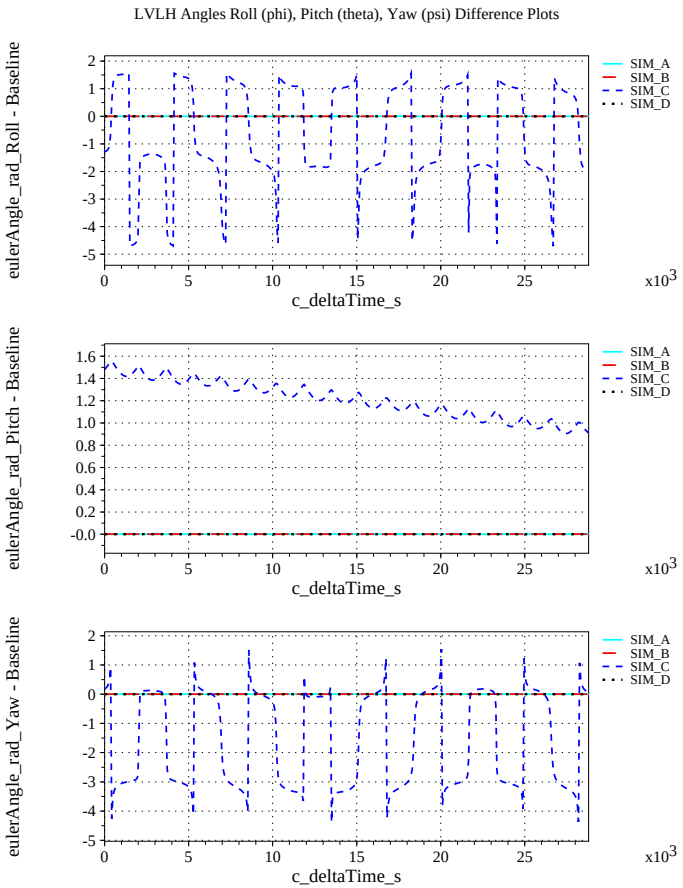

(j) Rotation Angles with Respect to LVLH Frame Differenced

Figure 59. Check-case 10B: Cylinder in Circular Orbit with Gravity Gradient with Non-zero Initial Rates; See Discussion in Section D.2.23 (Cont'd)

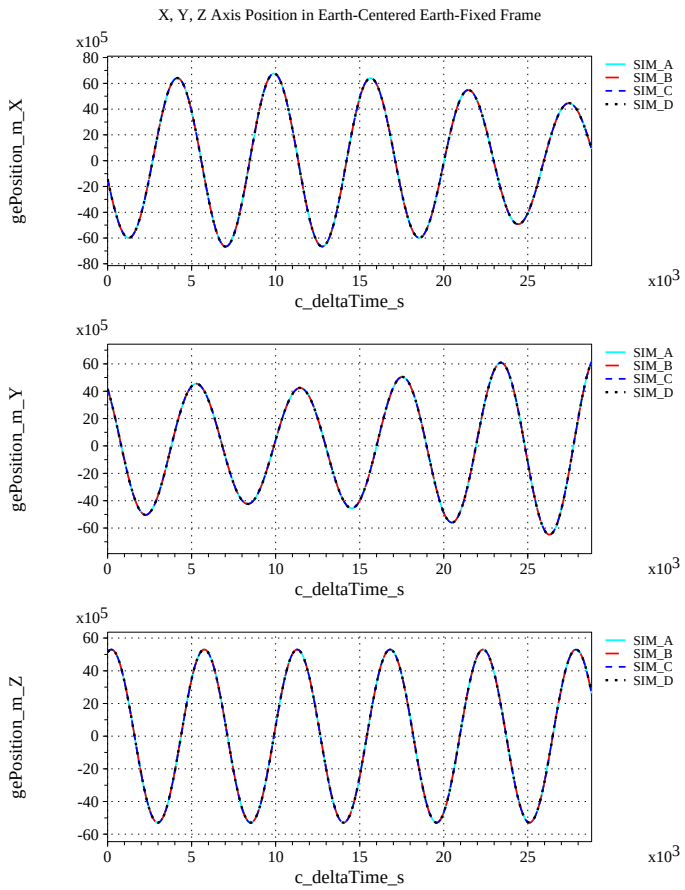

(k) Earth-centered, Earth-fixed Rectangular (X-Y-Z) Positions Compared

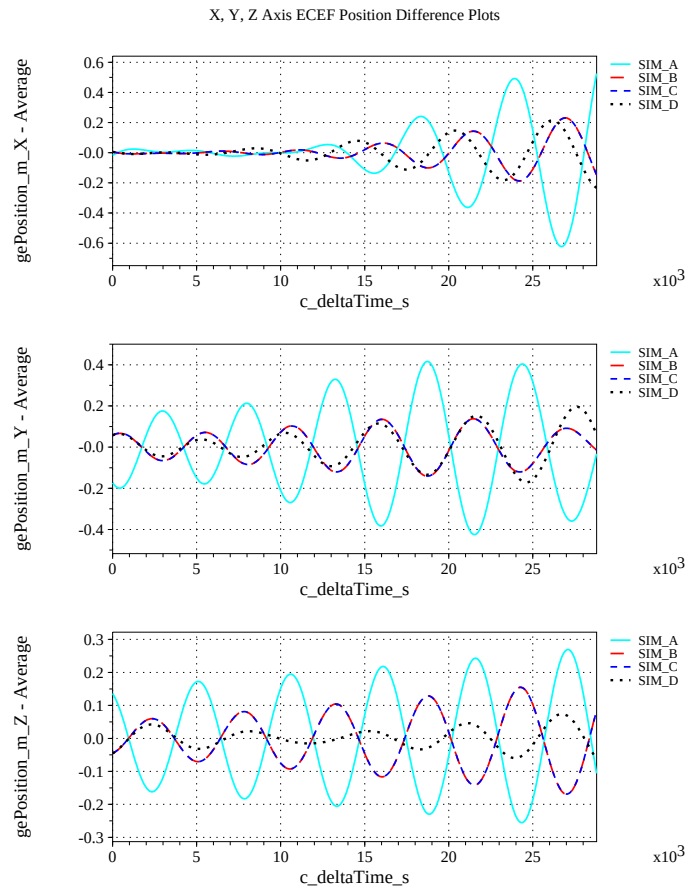

(l) Earth-centered, Earth-fixed Rectangular (X-Y-Z) Positions Differenced

Figure 59. Check-case 10B: Cylinder in Circular Orbit with Gravity Gradient with Non-zero Initial Rates; See Discussion in Section D.2.23 (Cont'd)

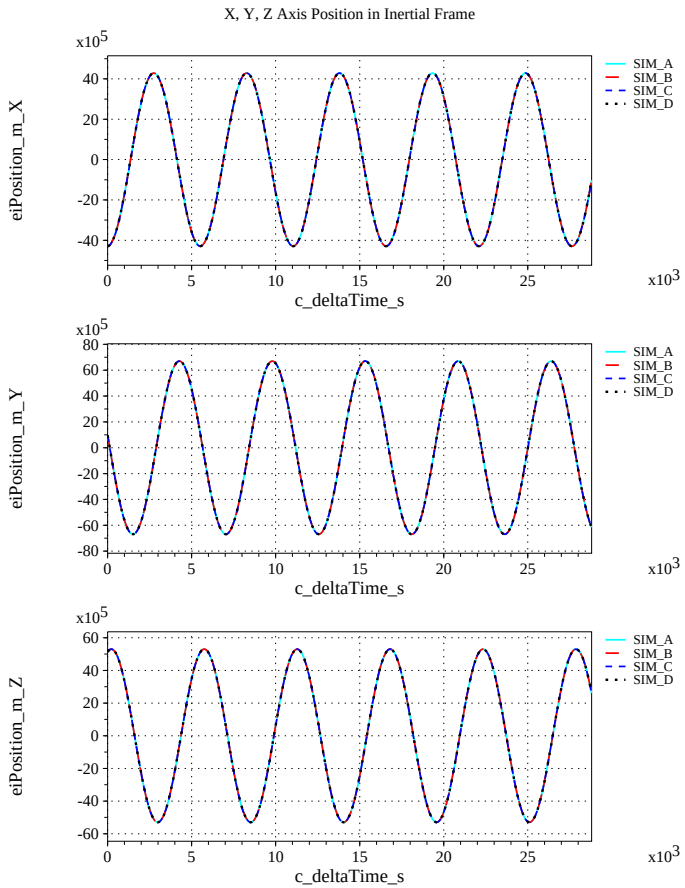

(m) Earth-centered Inertial Rectangular (x-y-z) Positions Compared

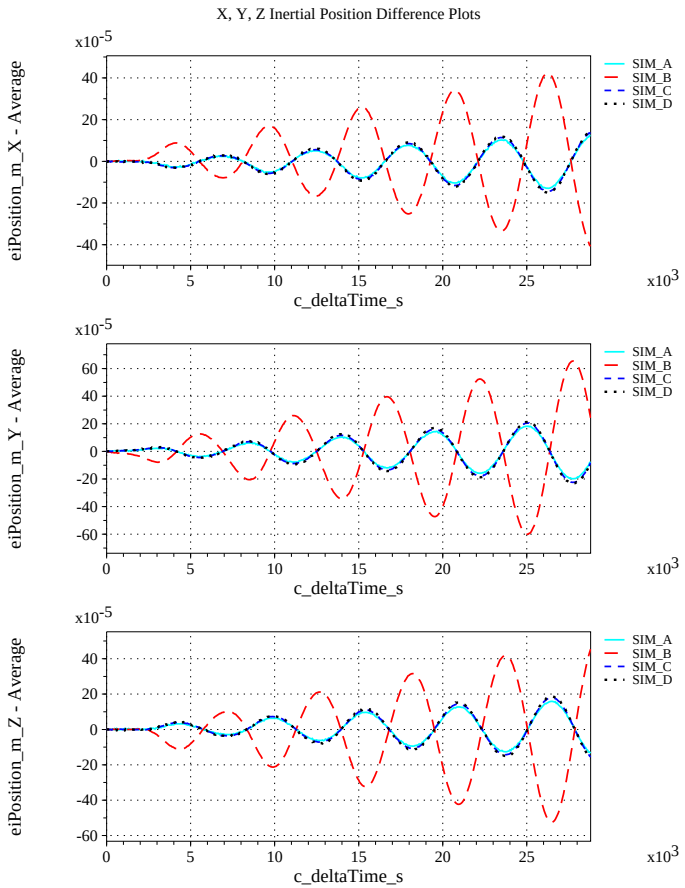

(n) Earth-centered Inertial Rectangular (x-y-z) Positions Differenced

Figure 59. Check-case 10B: Cylinder in Circular Orbit with Gravity Gradient with Non-zero Initial Rates; See Discussion in Section D.2.23 (Cont'd)

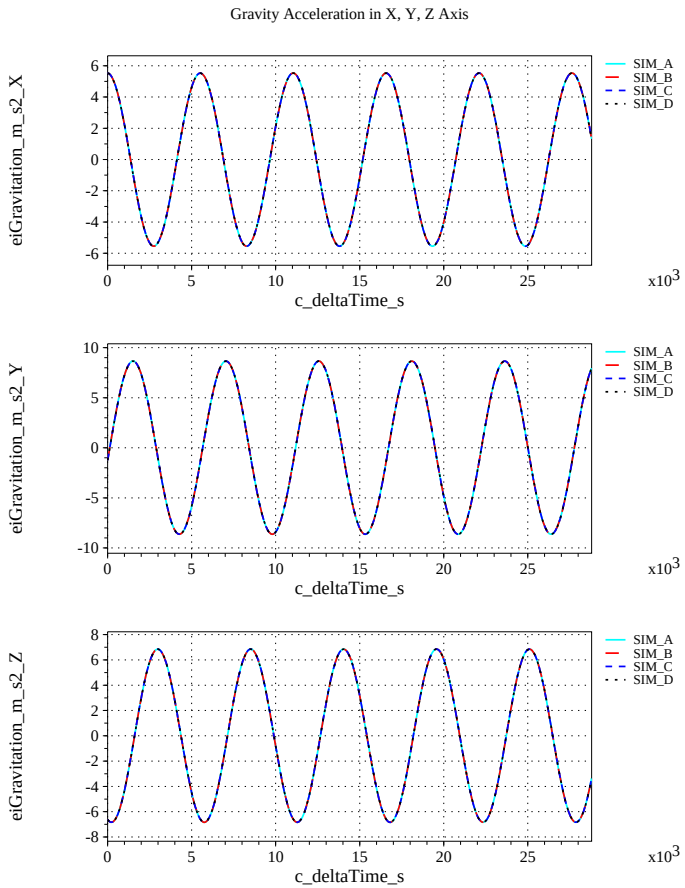

(o) Gravitational Components in Inertial (**X**-**Y**-**Z**) Directions Compared

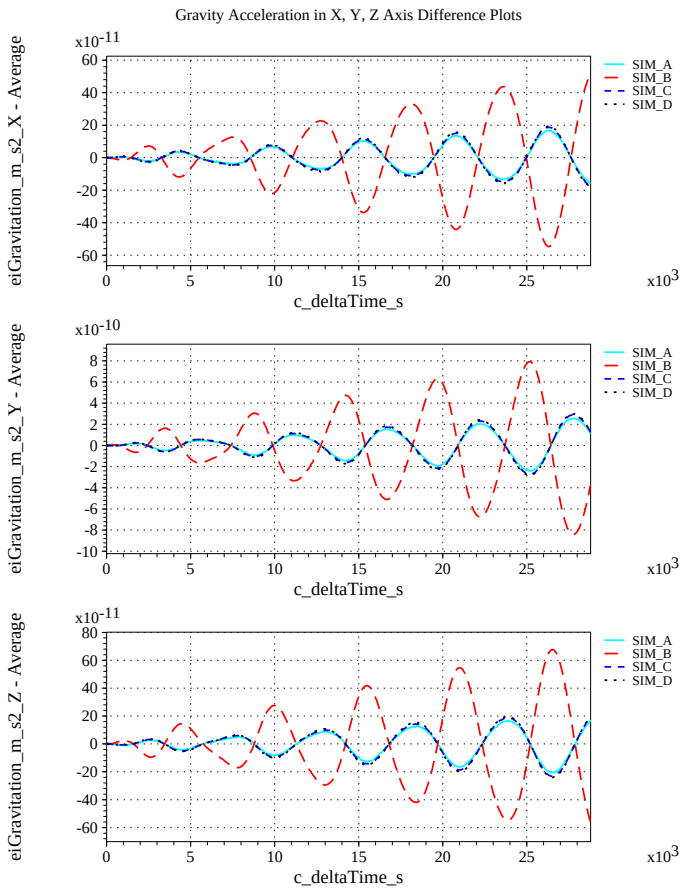

(p) Gravitational Components in Inertial (**X**-**Y**-**Z**) Directions Differenced

Figure 59. Check-case 10B: Cylinder in Circular Orbit with Gravity Gradient with Non-zero Initial Rates; See Discussion in Section D.2.23 (Concluded)

D.2.24 Check-case 10C – cylinder in elliptical orbit with gravity gradient with zero initial rates

This section shows cross-plots for four of the selected simulation tools in modeling the dynamics of a cylinder in an elliptical orbit responding to the gravity gradient starting with zero inertial rate. This scenario is described in Section C.2.24. Figures 60a through 60p compare results between the four simulation tools, as well as the deviances of the outputs from each tool from the ensemble average value.

Orbital check-case 10C was the third of four scenarios to assess the modeling and application of gravity gradient torque among the simulations. This test case initialized the vehicle to a highly elliptical orbit with a initial rate of zero relative to the LVLH frame.

The change to a highly elliptical orbit did not qualitatively change the simulation comparison as described in orbital case 10A. The simulations demonstrated close agreement on the inertial rotational states. The negligible differences that remained were attributed to differences in integration methods or differences in the precision of recorded outputs. Likewise, the simulations showed close agreement on the inertial translational states. Despite this agreement on inertial orientation and orbit, SIM C reported LVLH Euler angles that differ substantially from the other simulations. Such differences were not exhibited in check-cases prior to check-case 10A. Thus, it appears that SIM C may have been configured with a different Euler angle convention or different LVLH definition for these check-cases.

The differences in ECEF position among the simulations were identical to orbital check-case 5A with the simulations differing by less than 1 m after 8 hours of simulated flight. However, the difference in altitude of up to 60 m exhibited by SIM A in this case was much larger than the 2-m difference seen in orbital case 5A. Thus, it appeared that SIM A may have been configured with a different set of Earth surface modeling parameters for this run.

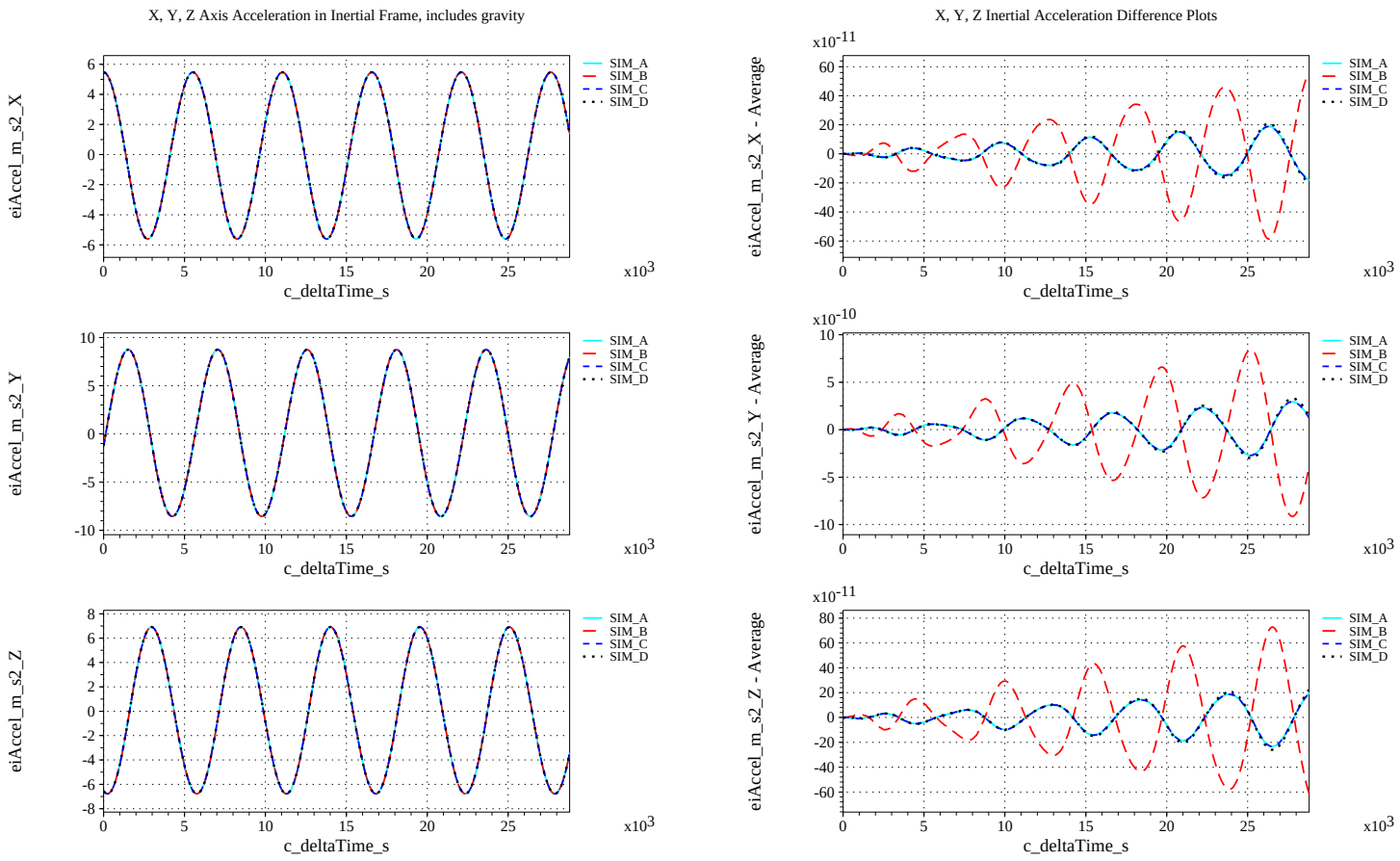

(a) Inertial Accelerations Compared

(b) Inertial Accelerations Differenced

Figure 60. Check-case 10C: Cylinder in Elliptical Orbit with Gravity Gradient with Zero Initial Rates; See Discussion in Section D.2.24

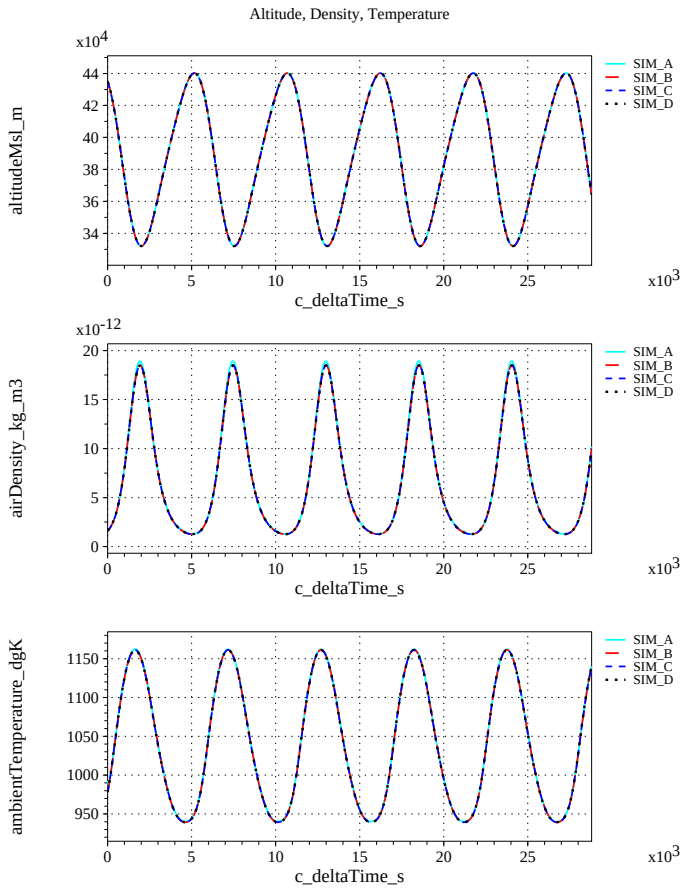

(c) Atmospheric Properties Compared

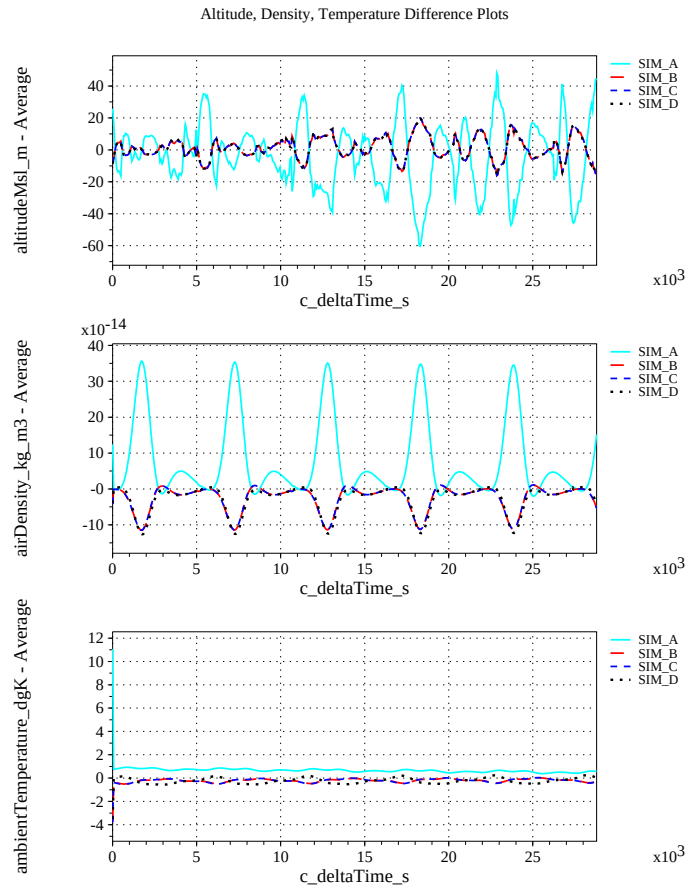

(d) Atmospheric Properties Differenced

Figure 60. Check-case 10C: Cylinder in Elliptical Orbit with Gravity Gradient with Zero Initial Rates; See Discussion in Section D.2.24 (Cont'd)

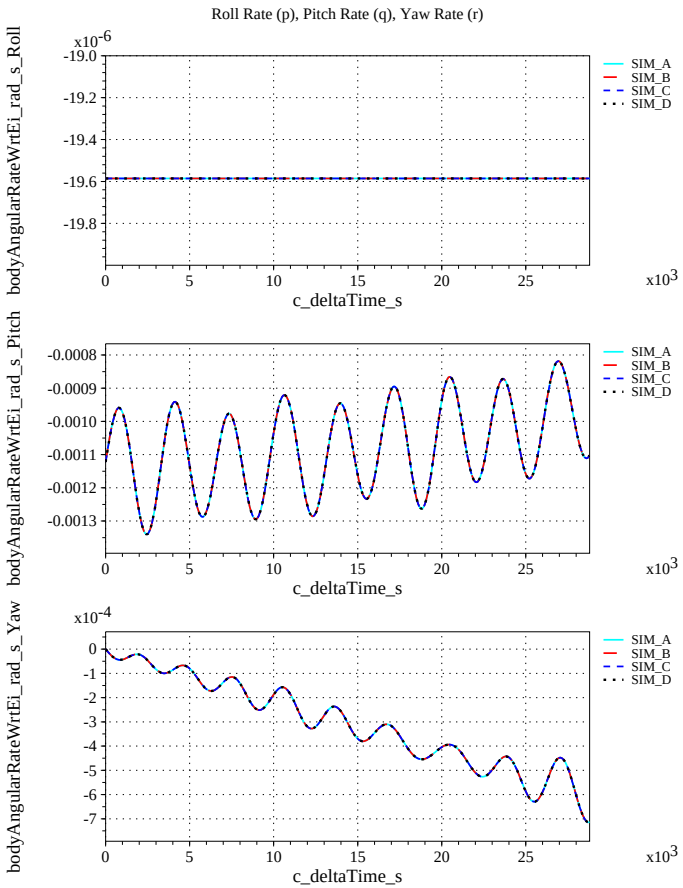

(e) Body-axis Angular Rates Compared

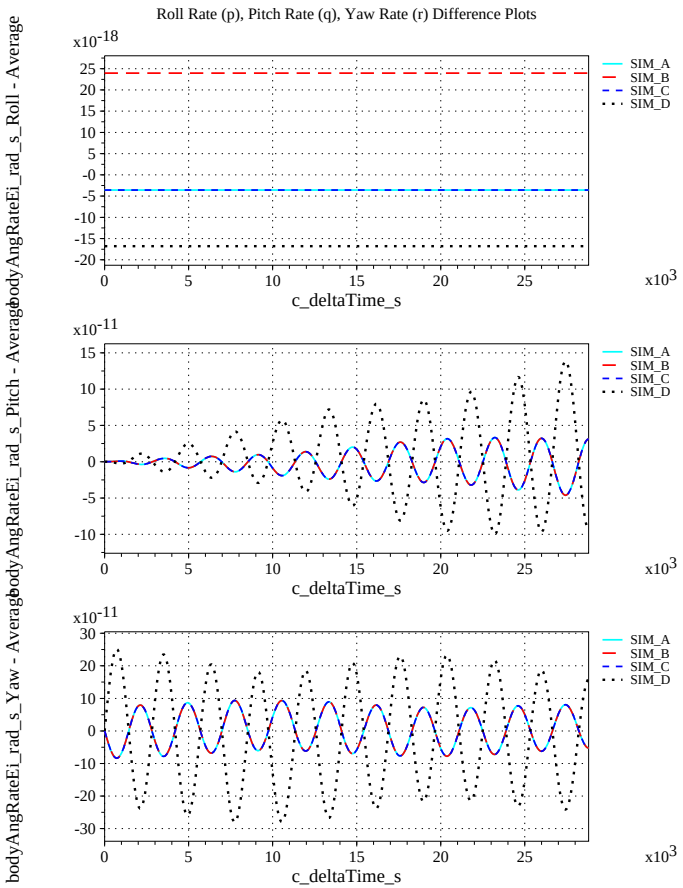

(f) Body-axis Angular Rates Differenced

Figure 60. Check-case 10C: Cylinder in Elliptical Orbit with Gravity Gradient with Zero Initial Rates; See Discussion in Section D.2.24 (Cont'd)

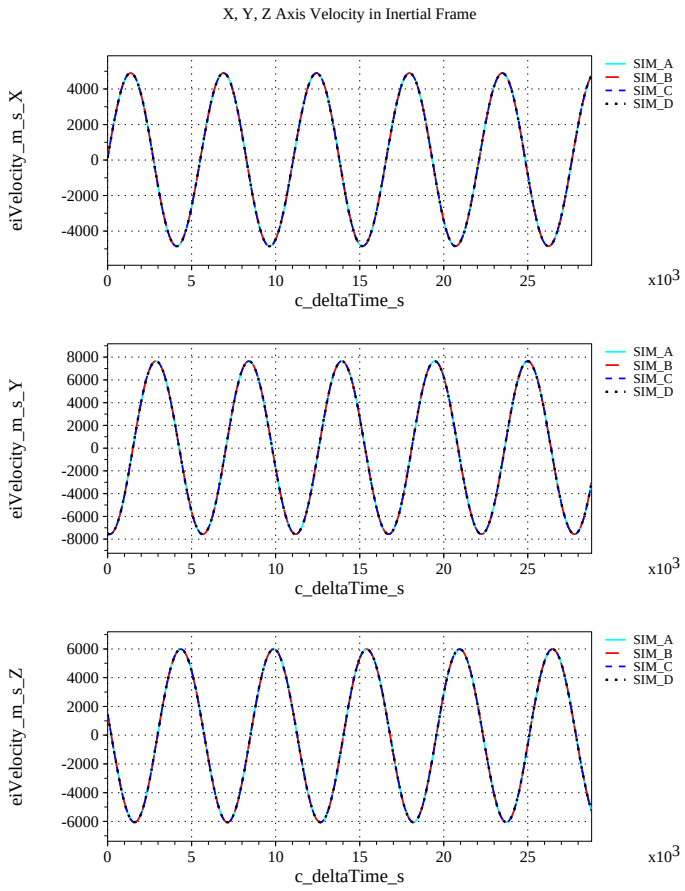

(g) Inertial Velocities Compared

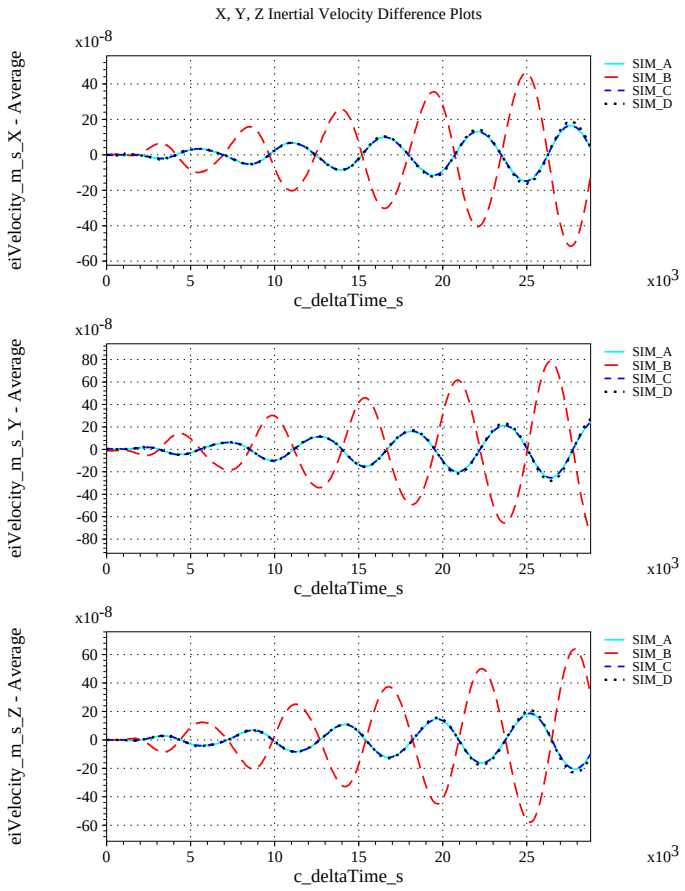

(h) Inertial Velocities Differenced

Figure 60. Check-case 10C: Cylinder in Elliptical Orbit with Gravity Gradient with Zero Initial Rates; See Discussion in Section D.2.24 (Cont'd)

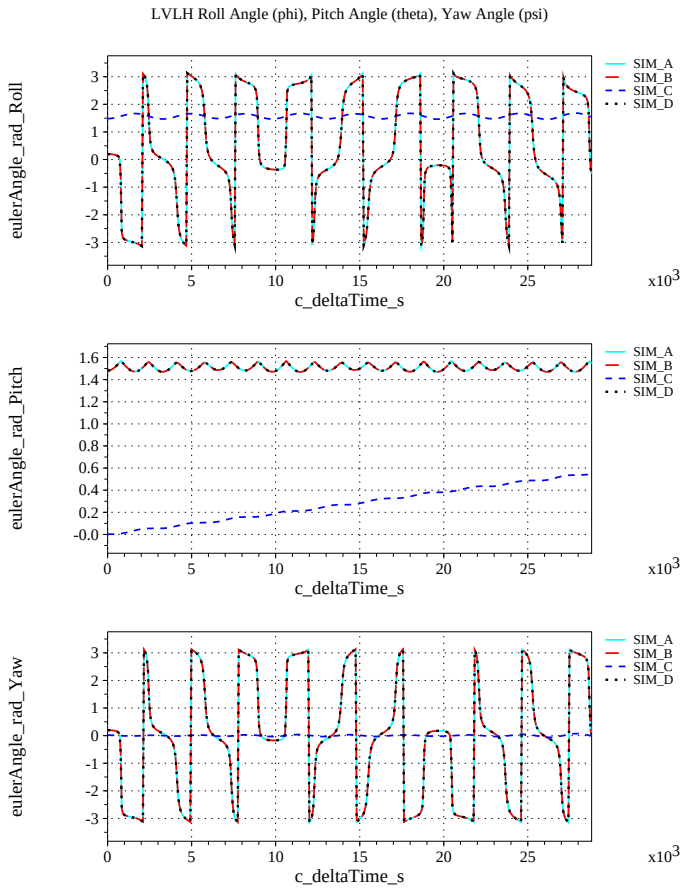

(i) Rotation Angles with Respect to LVLH Frame Compared

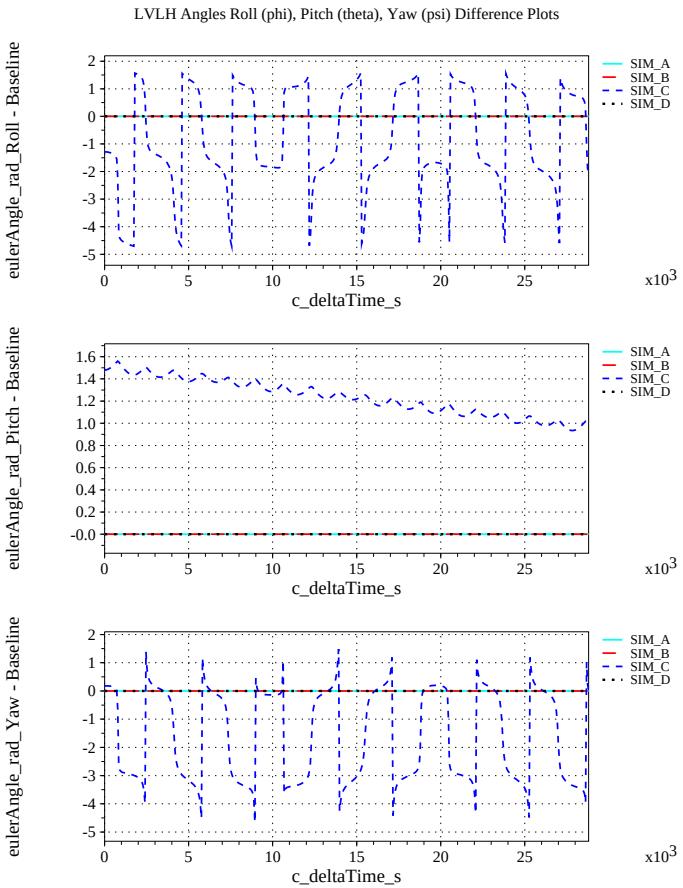

(j) Rotation Angles with Respect to LVLH Frame Differenced

Figure 60. Check-case 10C: Cylinder in Elliptical Orbit with Gravity Gradient with Zero Initial Rates; See Discussion in Section D.2.24 (Cont'd)

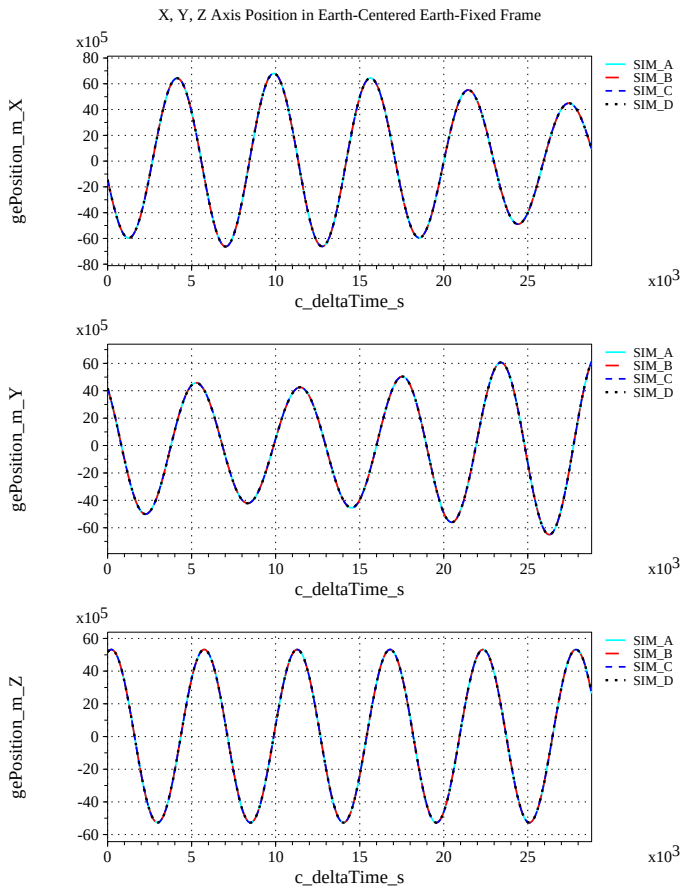

(k) Earth-centered, Earth-fixed Rectangular (X-Y-Z) Positions Compared

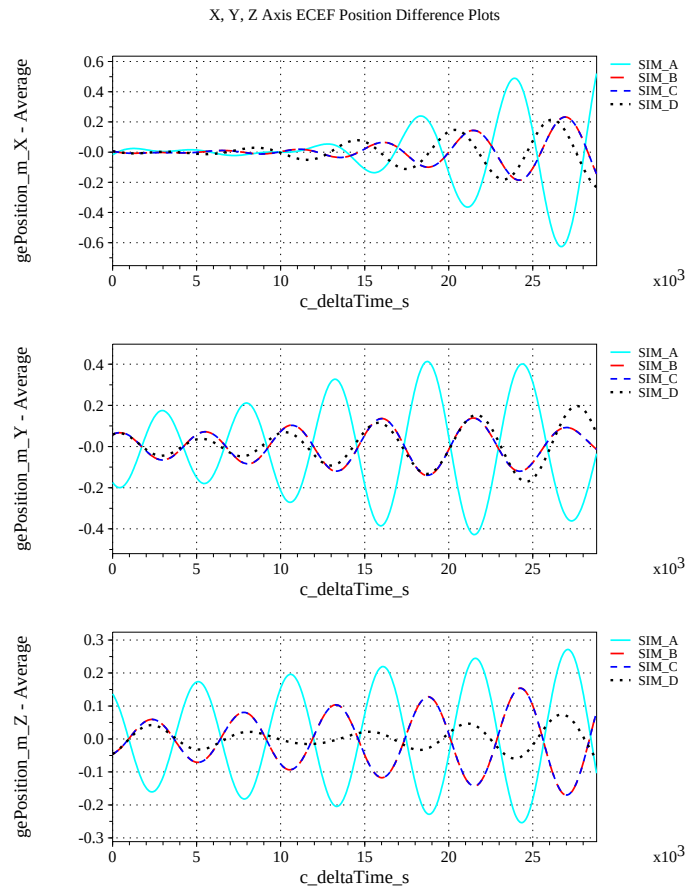

(l) Earth-centered, Earth-fixed Rectangular (X-Y-Z) Positions Differenced

Figure 60. Check-case 10C: Cylinder in Elliptical Orbit with Gravity Gradient with Zero Initial Rates; See Discussion in Section D.2.24 (Cont'd)

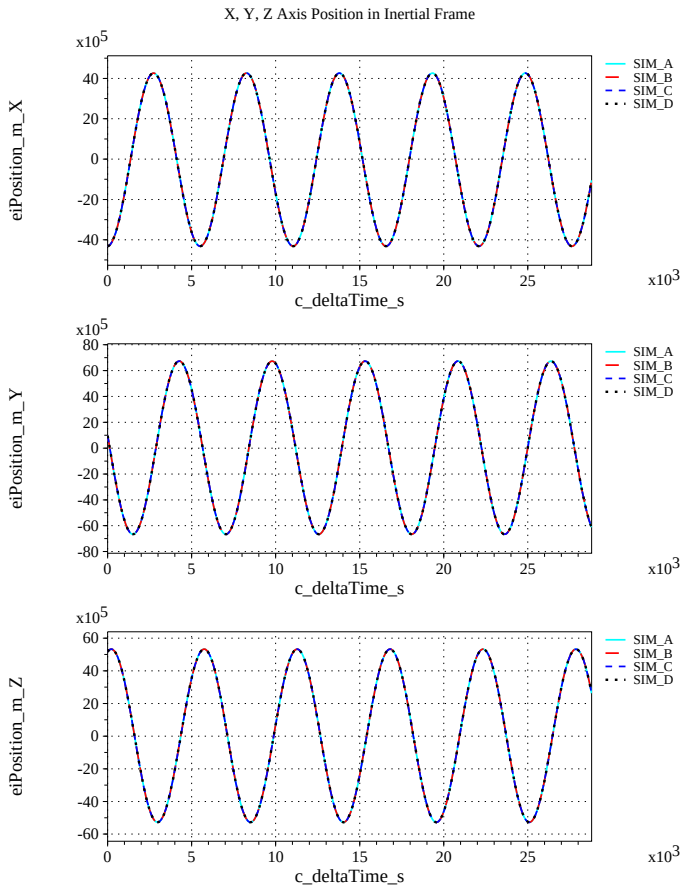

(m) Earth-centered Inertial Rectangular (x-y-z) Positions Compared

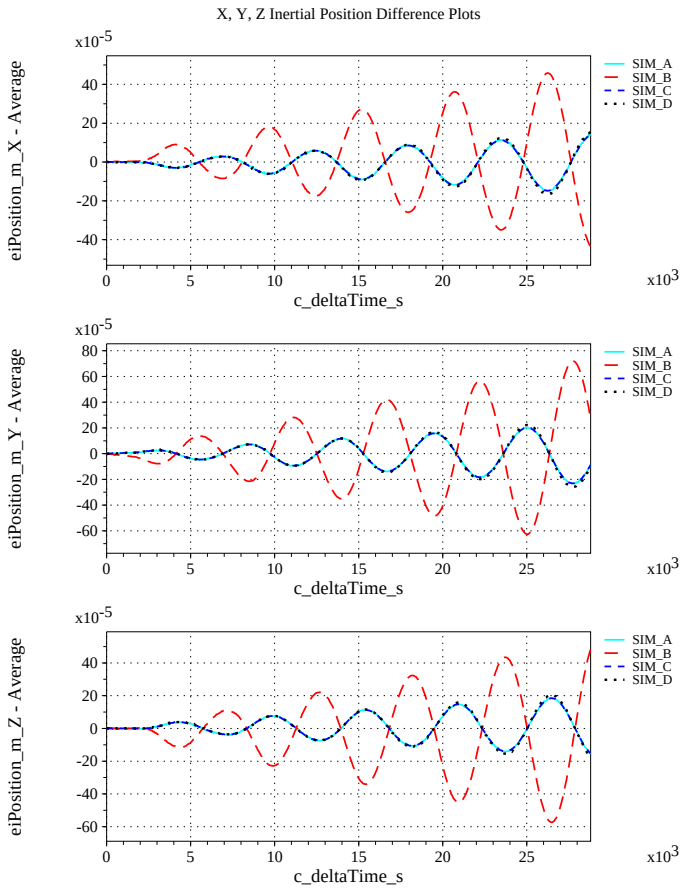

(n) Earth-centered Inertial Rectangular (x-y-z) Positions Differenced

Figure 60. Check-case 10C: Cylinder in Elliptical Orbit with Gravity Gradient with Zero Initial Rates; See Discussion in Section D.2.24 (Cont'd)

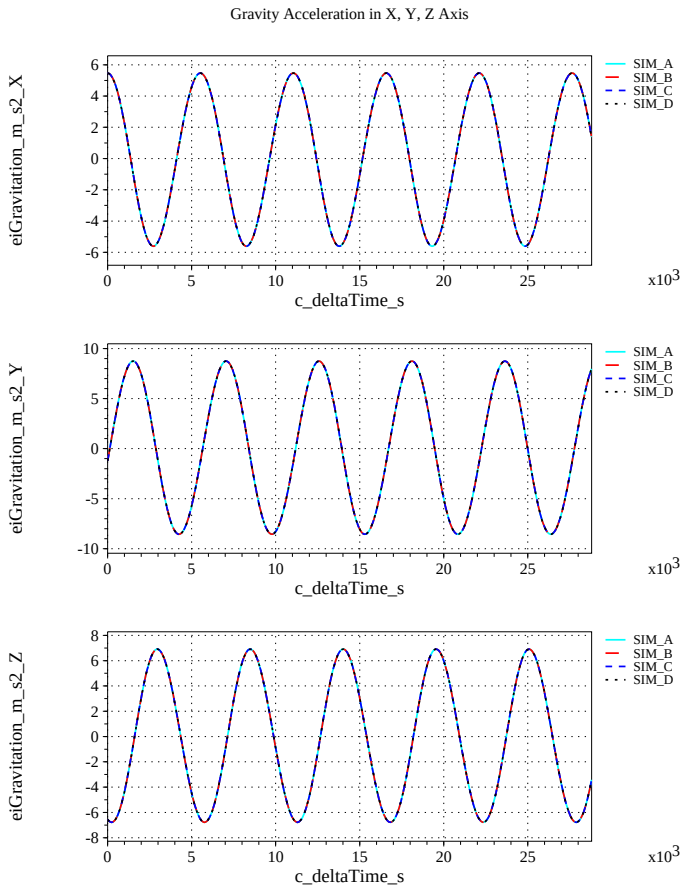

(o) Gravitational Components in Inertial (**X**-**Y**-**Z**) Directions Compared

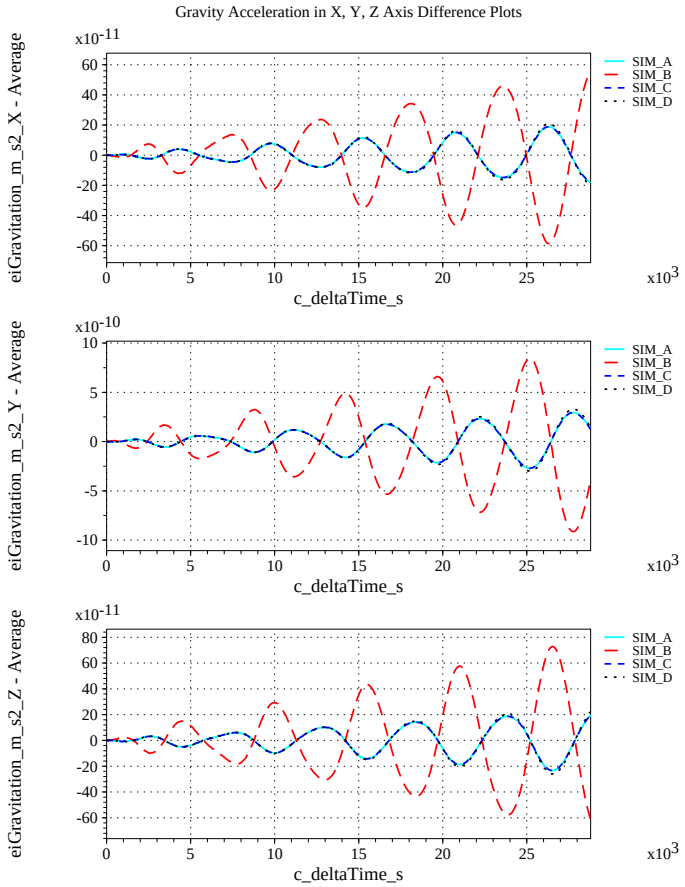

(p) Gravitational Components in Inertial (**X**-**Y**-**Z**) Directions Differenced

Figure 60. Check-case 10C: Cylinder in Elliptical Orbit with Gravity Gradient with Zero Initial Rates; See Discussion in Section D.2.24 (Concluded)

D.2.25 Check-case 10D – cylinder in elliptical orbit with gravity gradient with non-zero initial rates

This section shows cross-plots for four of the selected simulation tools in modeling the dynamics of a cylinder in an elliptical orbit responding to the gravity gradient starting with a non-zero inertial rate. This scenario is described in Section C.2.25. Figures 61a through 61p compare results between the four simulation tools, as well as the deviances of the outputs from each tool from the ensemble average value.

Orbital check-case 10D was the last of four scenarios to assess the modeling and application of gravity gradient torque among the simulations. This test case initialized the cylindrical vehicle in a highly elliptical orbit with a initial pitch rate of 0.01 deg/s relative to the LVLH frame.

The change in initial rotation did not qualitatively change the simulation comparison as described in orbital case 10C. The simulations demonstrated close agreement on the inertial rotational states. The negligible differences that remained were attributed to differences in integration methods or differences in the precision of recorded outputs. Likewise, the simulations showed close agreement on the inertial translational states. Despite this agreement on inertial orientation and orbit, SIM C recorded LVLH Euler angles that differed substantially from the other simulations. Such differences were not exhibited in check-cases prior to check-case 10A. Thus, it appears that SIM C may have been configured with a different Euler angle convention or different LVLH definition for these check-cases.

The differences in ECEF position among the simulations were identical to orbital check-case 5A with the simulations differing by less than 1 m after 8 hours of simulated flight. However, the difference in altitude of up to 60 m exhibited by SIM A in this case was much larger than the nearly 2-m difference seen in orbital check-case 5A. Thus, it appeared that SIM A may have been configured with a different set of Earth surface modeling parameters for this run.

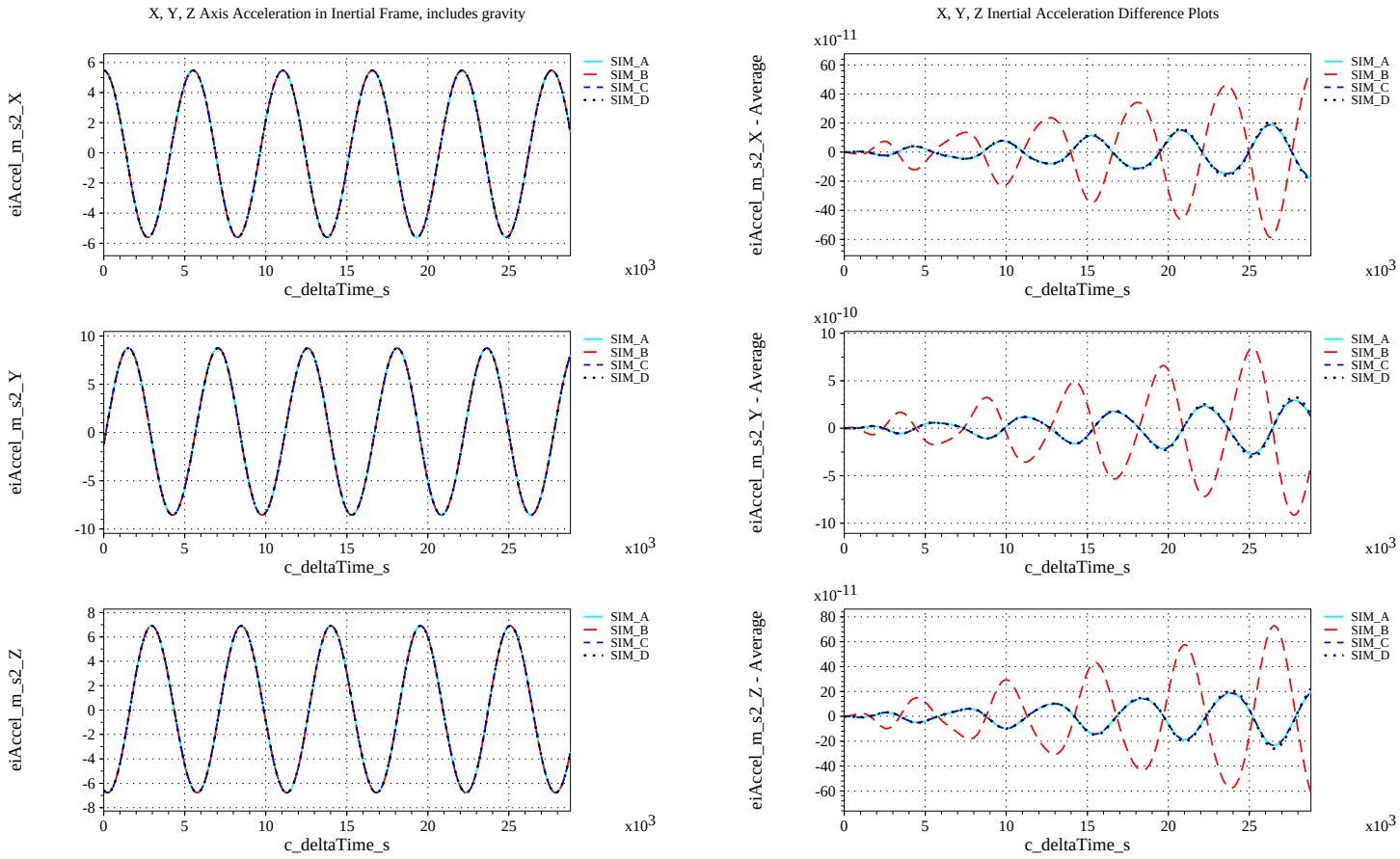

(a) Inertial Accelerations Compared

(b) Inertial Accelerations Differenced

Figure 61. Check-case 10D: Cylinder in Elliptical Orbit with Gravity Gradient with Non-zero Initial Rates; See Discussion in Section D.2.25

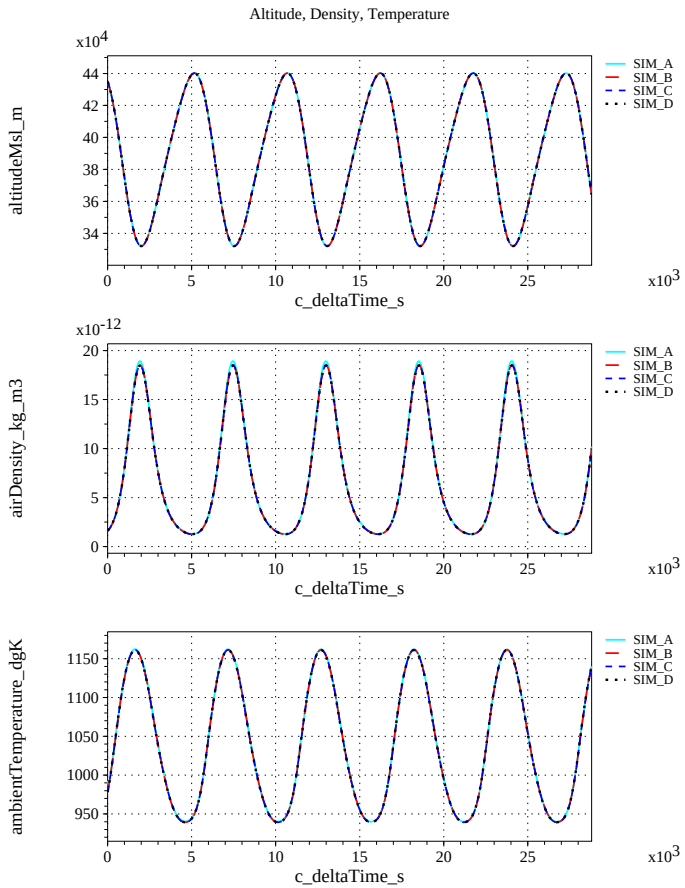

(c) Atmospheric Properties Compared

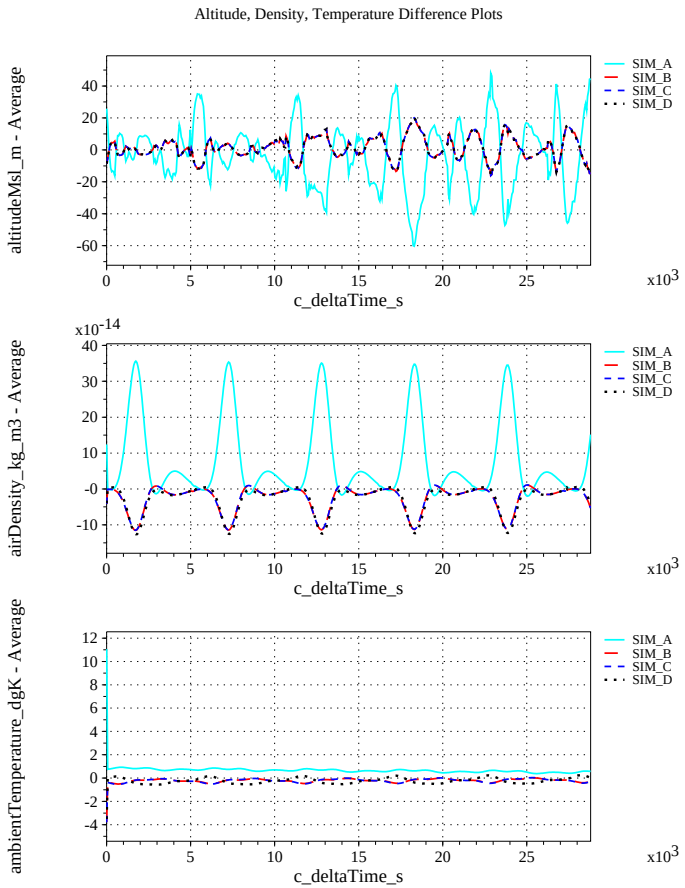

(d) Atmospheric Properties Differenced

Figure 61. Check-case 10D: Cylinder in Elliptical Orbit with Gravity Gradient with Non-zero Initial Rates; See Discussion in Section D.2.25 (Cont'd)

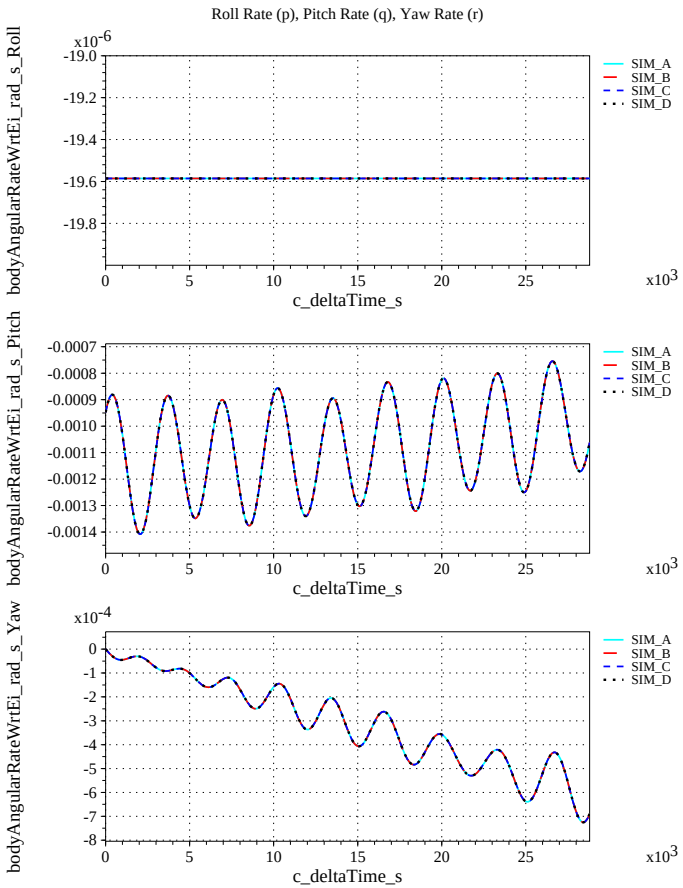

(e) Body-axis Angular Rates Compared

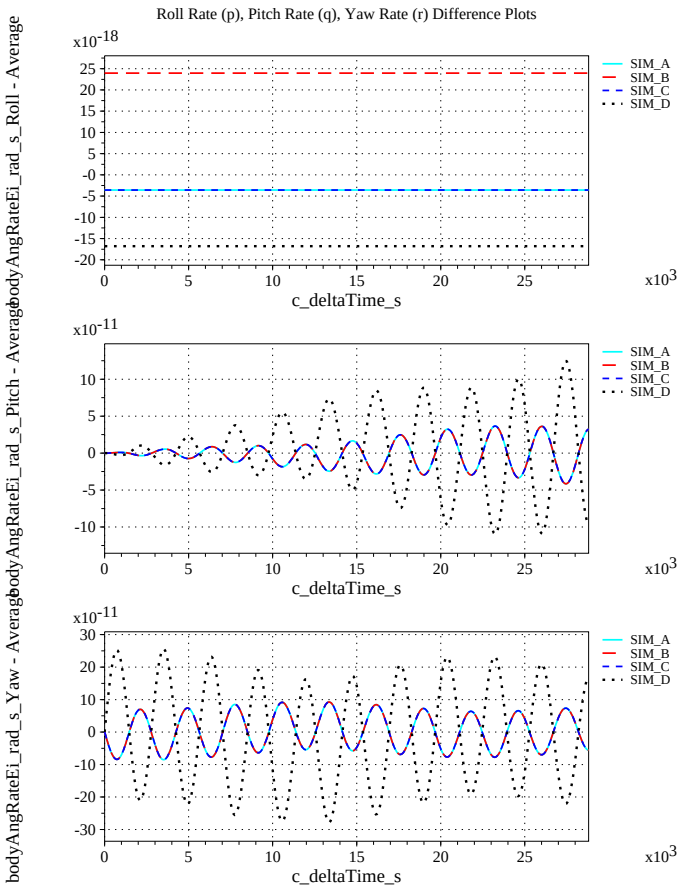

(f) Body-axis Angular Rates Differenced

Figure 61. Check-case 10D: Cylinder in Elliptical Orbit with Gravity Gradient with Non-zero Initial Rates; See Discussion in Section D.2.25 (Cont'd)

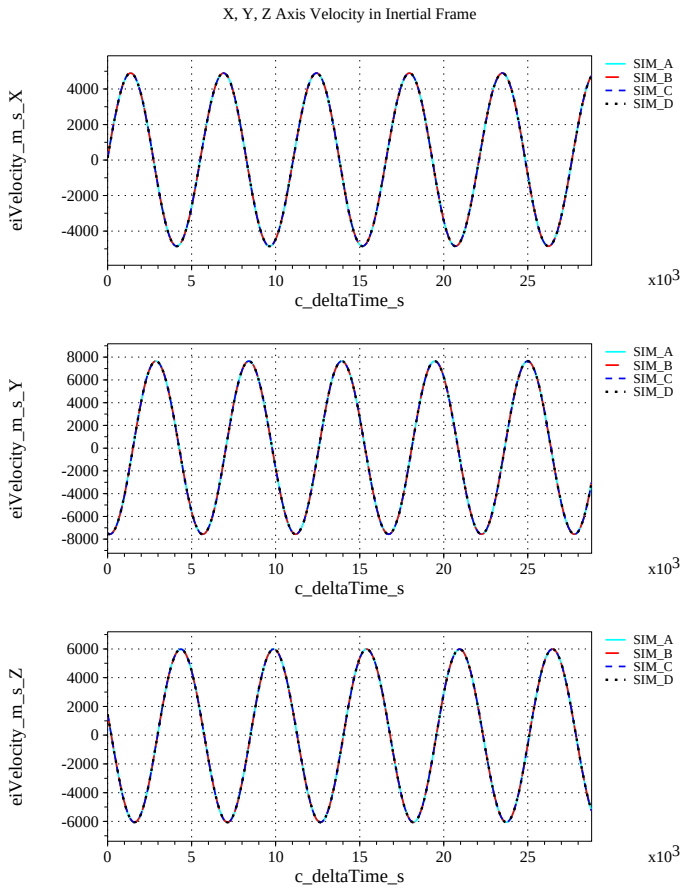

(g) Inertial Velocities Compared

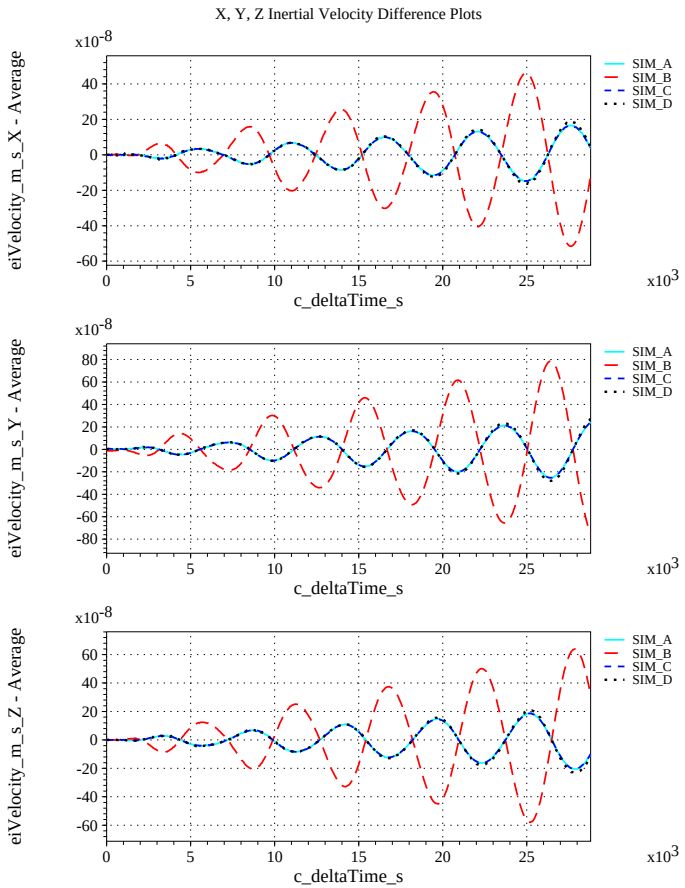

(h) Inertial Velocities Differenced

Figure 61. Check-case 10D: Cylinder in Elliptical Orbit with Gravity Gradient with Non-zero Initial Rates; See Discussion in Section D.2.25 (Cont'd)

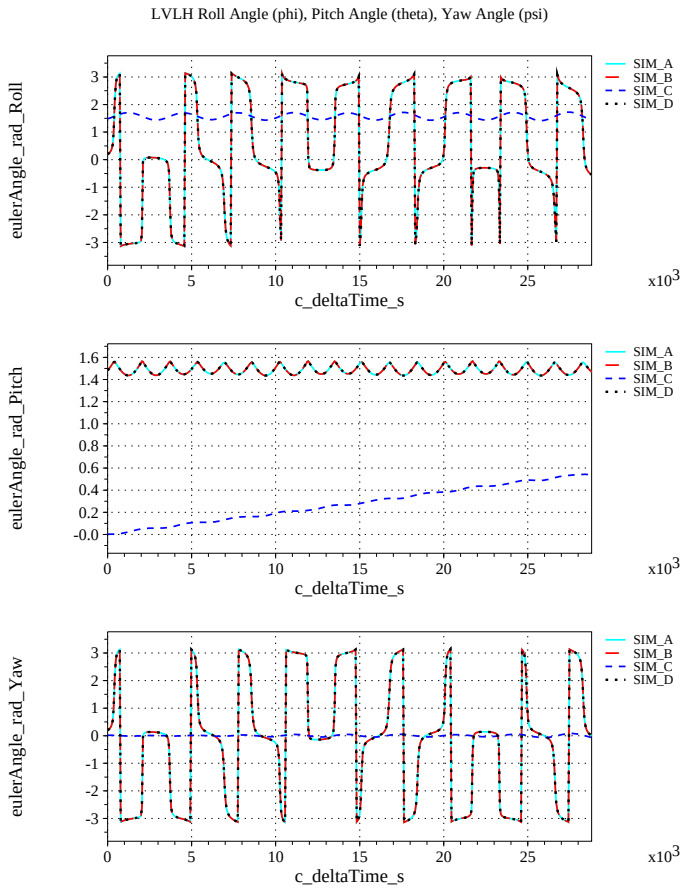

(i) Rotation Angles with Respect to LVLH Frame Compared

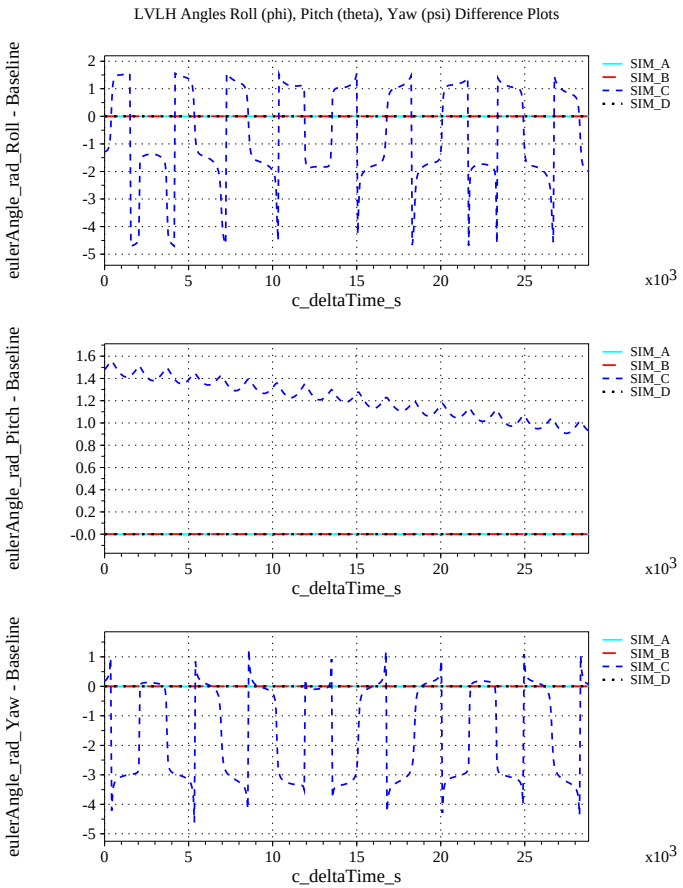

(j) Rotation Angles with Respect to LVLH Frame Differenced

Figure 61. Check-case 10D: Cylinder in Elliptical Orbit with Gravity Gradient with Non-zero Initial Rates; See Discussion in Section D.2.25 (Cont'd)

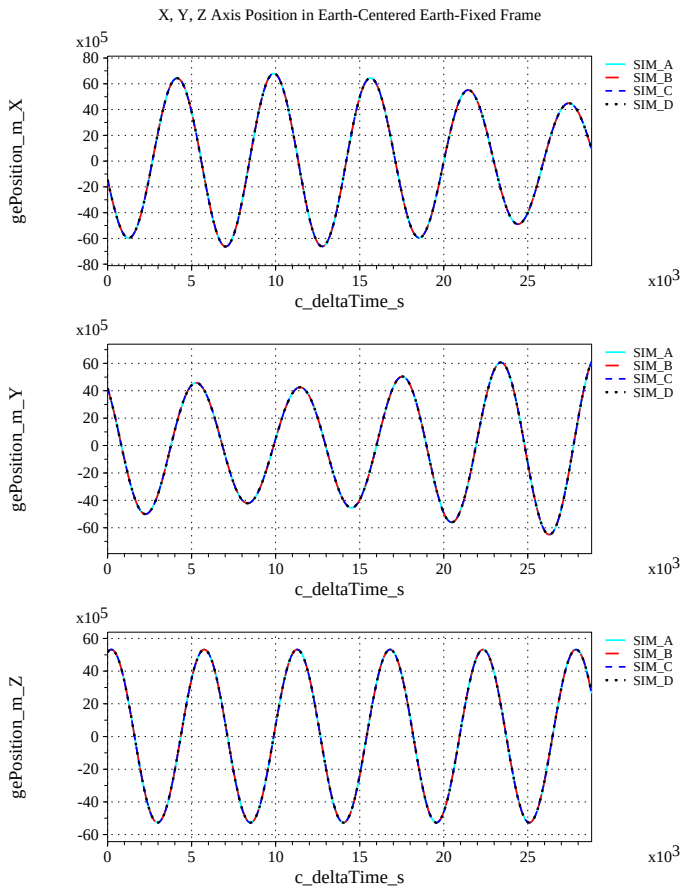

(k) Earth-centered, Earth-fixed Rectangular (X-Y-Z) Positions Compared

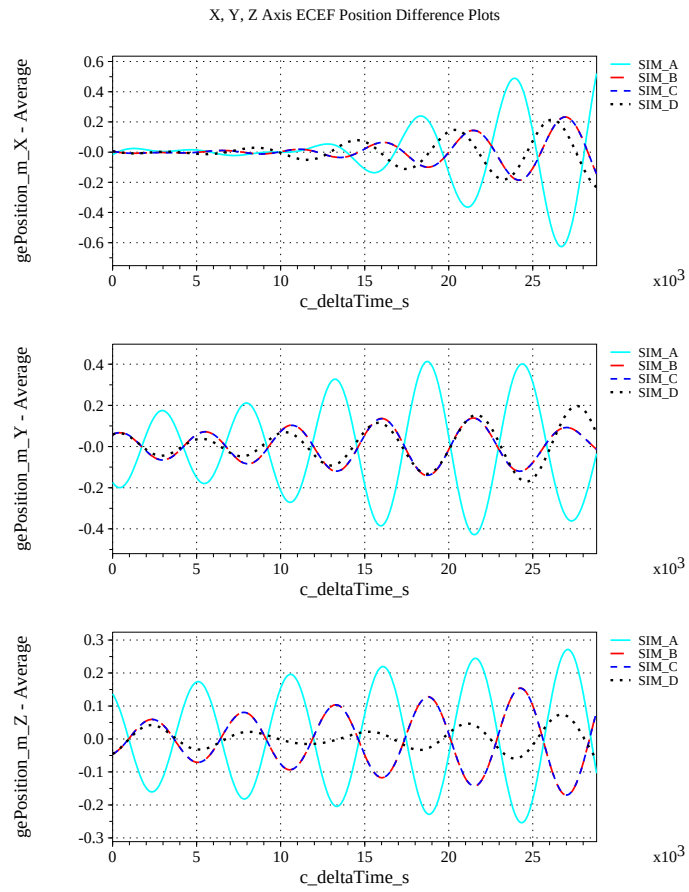

(l) Earth-centered, Earth-fixed Rectangular (X-Y-Z) Positions Differenced

Figure 61. Check-case 10D: Cylinder in Elliptical Orbit with Gravity Gradient with Non-zero Initial Rates; See Discussion in Section D.2.25 (Cont'd)

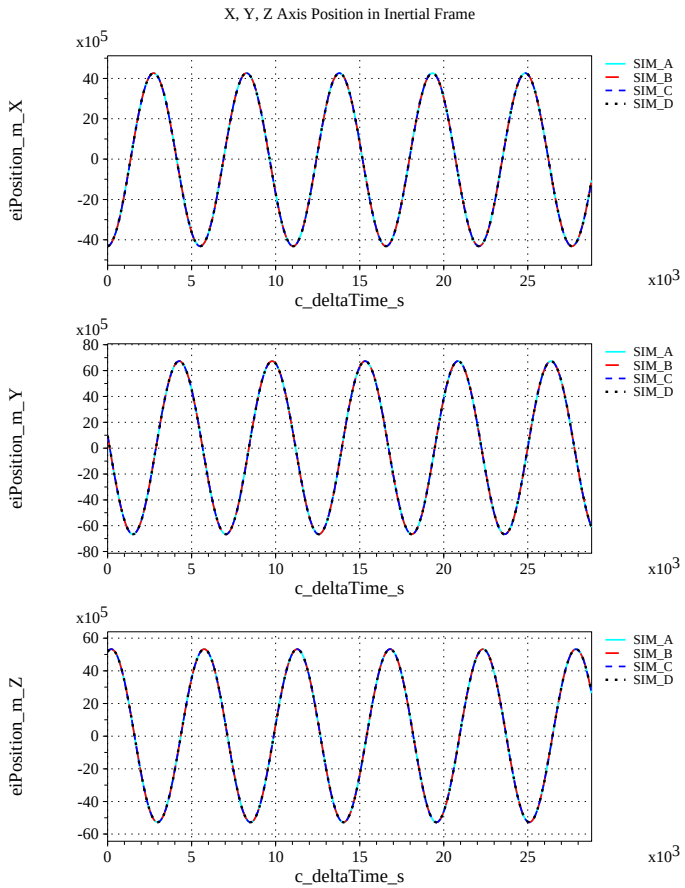

(m) Earth-centered Inertial Rectangular (x-y-z) Positions Compared

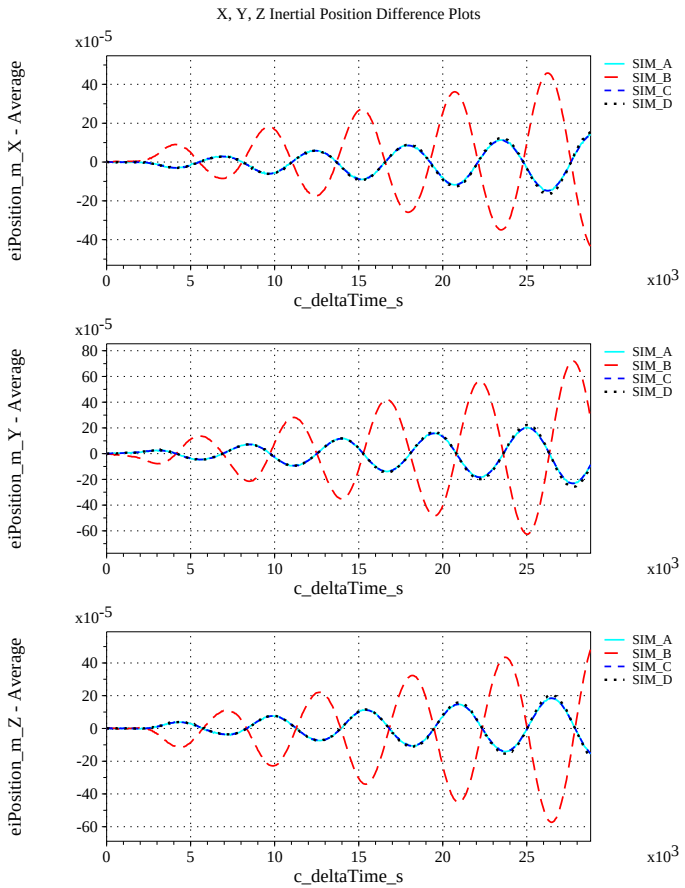

(n) Earth-centered Inertial Rectangular (x-y-z) Positions Differenced

Figure 61. Check-case 10D: Cylinder in Elliptical Orbit with Gravity Gradient with Non-zero Initial Rates; See Discussion in Section D.2.25 (Cont'd)

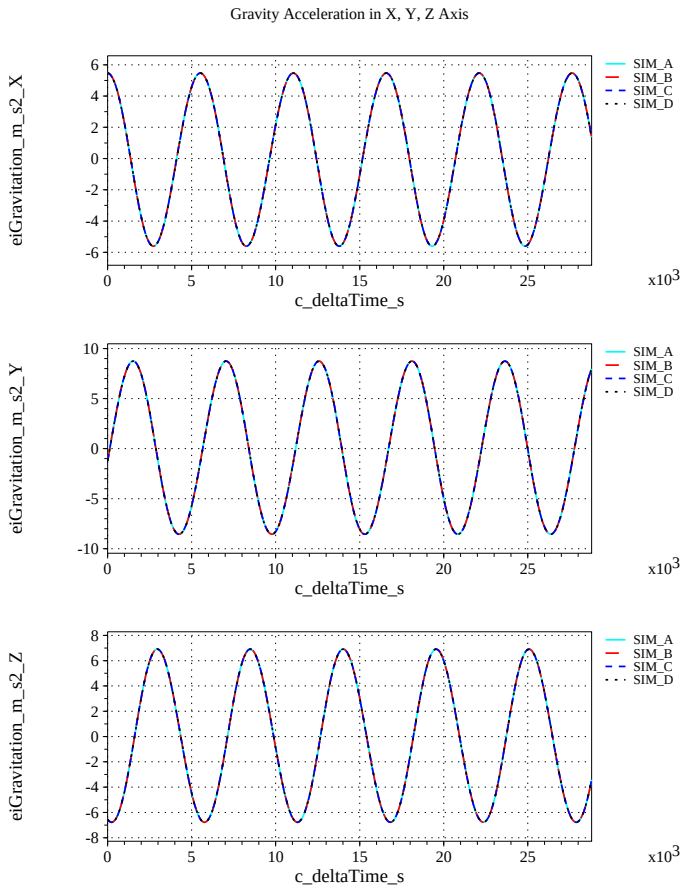

(o) Gravitational Components in Inertial (**X**-**Y**-**Z**) Directions Compared

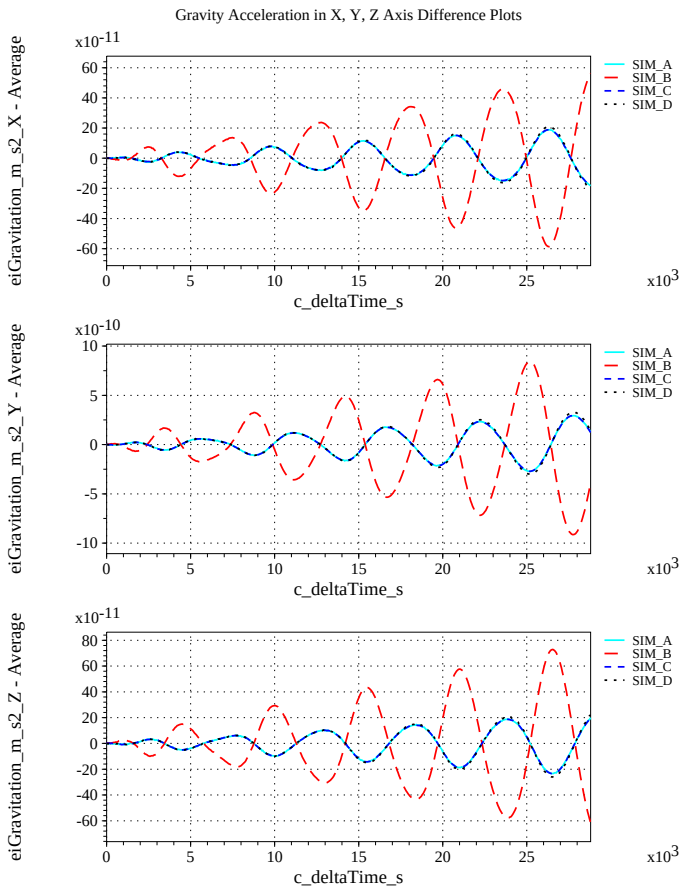

(p) Gravitational Components in Inertial (**X**-**Y**-**Z**) Directions Differenced

Figure 61. Check-case 10D: Cylinder in Elliptical Orbit with Gravity Gradient with Non-zero Initial Rates; See Discussion in Section D.2.25 (Concluded)

D.2.26 Check-case Full – ISS responding to all effects

This section shows cross-plots for four of the selected simulation tools in modeling the dynamics of the ISS responding to all effects previously tested. This scenario is described in Section C.2.26. Figures 62a through 62p compare results between the four simulation tools, as well as the deviances of the outputs from each tool from the ensemble average value.

Orbital check-case "Full" applied all the environmental affects that were tested in isolation in prior check-cases. This included geopotential gravitation perturbations, Sun and Moon gravitation perturbations, gravity gradient torque, and aerodynamic drag.

In the inertial translational states, SIM A exhibited the largest differences in position, velocity, and acceleration. These differences were primarily caused by the effect of differences in the atmospheric density contribution to aerodynamic drag. As explained in orbital check-case 5A, the atmospheric density predicted by SIM A differed by up to 3% from the other simulations because it was the sole simulation to run MET07 as the thermosphere model. The other simulations ran older versions (MET99 and MET95).

The translational differences seen in this scenario were consistent with those seen for orbital check-case 6B (aerodynamic drag) after recognizing that the differences between vehicles in those two scenarios led to an aerodynamic deceleration in this case that is about one-third of that modeled in case 6B. The aerodynamic drag differences did not, however, directly drive the differences in acceleration. Instead, the slight increase in deceleration it produced created a feedback through the gravitation model and caused the gravitation differences to increase over time.

Smaller differences in inertial velocity and position appeared among SIM B, SIM C, and SIM D. These differences appeared to be caused by differences in the accuracy of the geopotential gravitation implementations as described in orbital case 3A as well as the difference in atmospheric density predicted by MET95 and MET99 as described in orbital case 5A.

The differences in inertial position among the simulations drove the differences in ECEF position. However, SIM A presented differences in altitude much larger than suggested by the differences in ECEF position. These differences, however, were consistent with the differences seen in orbital check-cases 10A through 10D. These differences were attributed to a likely change in the configuration of the Earth surface parameters since orbital check-cases 2 through 9D showed much lower differences in altitude.

For the rotational states, SIM D no longer matched the other simulations after about an hour of simulated flight. Differences in the modeling of the gravity gradient were ruled out: the gravity gradient from SIM D was reconstructed using the recorded inertial position and inertial attitude from the SIM D data file and comparing it to the gravity gradient recorded in the data file; the reconstructed gravity gradient matched the recorded gravity gradient to less than 1×10^{-9} N-m in 41 frame samples examined.

Differences in initial orientation and angular velocity were also negligible. However, the difference in initial angular acceleration was unexpected, given the close match in initial angular rate and gravity gradient. In fact, when the gravity gradient (which was the only external torque in this scenario) was reconstructed from the SIM D data file using the scenario-defined inertia matrix, the recorded angular velocity, and the recorded angular acceleration, the resultant torque differed (in all three components) from the recorded gravity gradient by up to 5.4 N-m in the 81 samples tested.

When this same reconstruction was performed for check-case 10A, the gravity gradient was reproduced to the precision of the recorded data. One difference between case 10A and case FULL was that the ISS vehicle has non-zero off-diagonal terms in the inertia matrix. A difference in treating the sign of the off-diagonal terms, a common simulation implementation difference, was ruled out using the reconstruction; changing signs produced an even larger difference with the recorded gravity gradient.

The other possible explanations were either 1) a transcription error in configuring the inertia matrix or 2) a simplifying assumption or an error in applying the off-diagonal terms to the computation of the angular accelerations. Nevertheless, the root cause for the difference between SIM D and the other simulations could not be identified.

The SIM D differences in rotational states dwarfed the differences that appeared between SIM A, SIM B, and SIM C. These simulations displayed close agreement in the difference charts for angular rate, inertial Euler angles, and LVLH Euler angles.

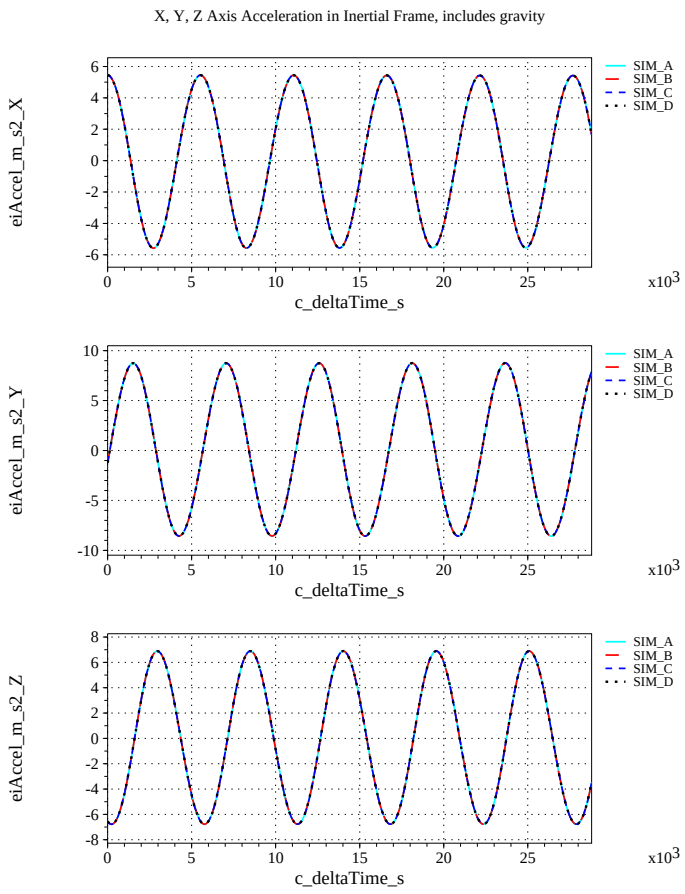

(a) Inertial Accelerations Compared

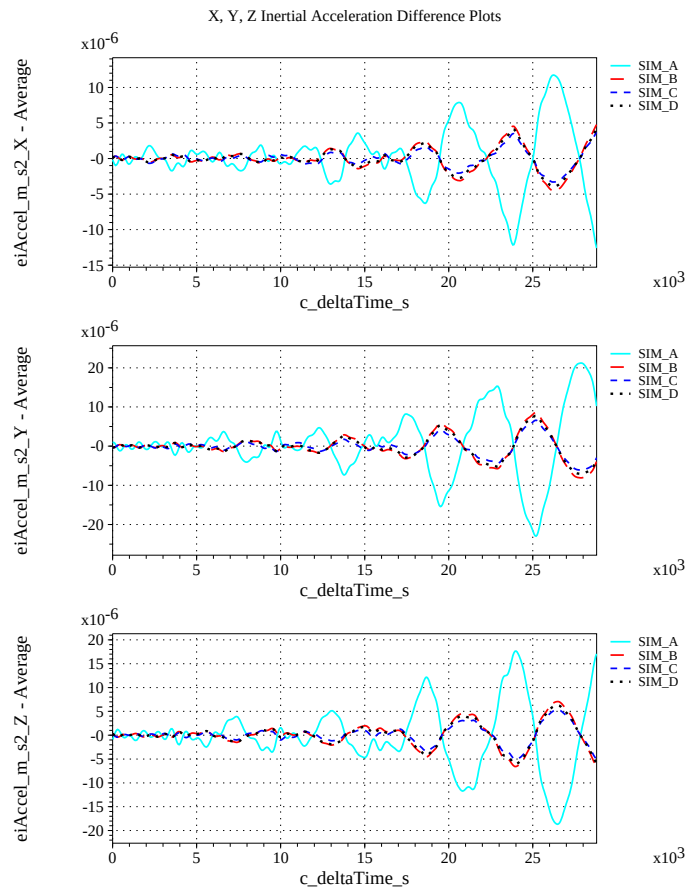

(b) Inertial Accelerations Differenced

Figure 62. Check-case Full: ISS Responding to All Effects; See Discussion in Section D.2.26

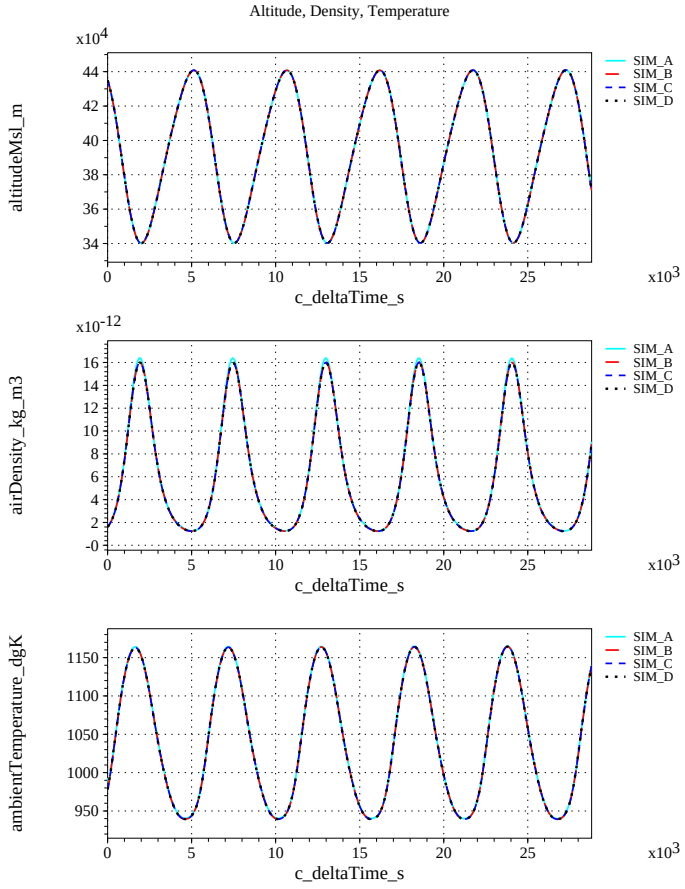

(c) Atmospheric Properties Compared

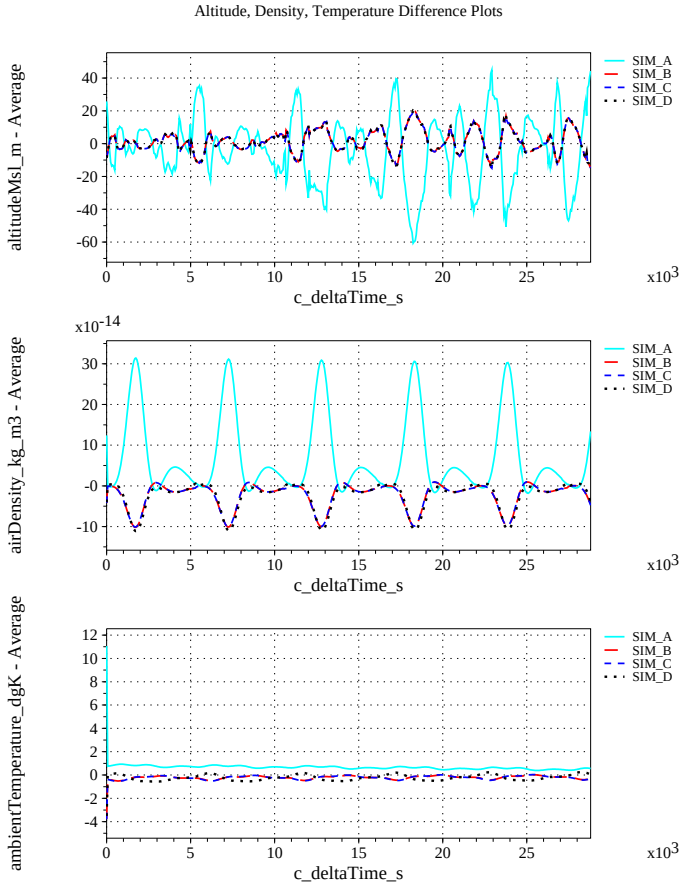

(d) Atmospheric Properties Differenced

Figure 62. Check-case Full: ISS Responding to All Effects; See Discussion in Section D.2.26 (Cont'd)

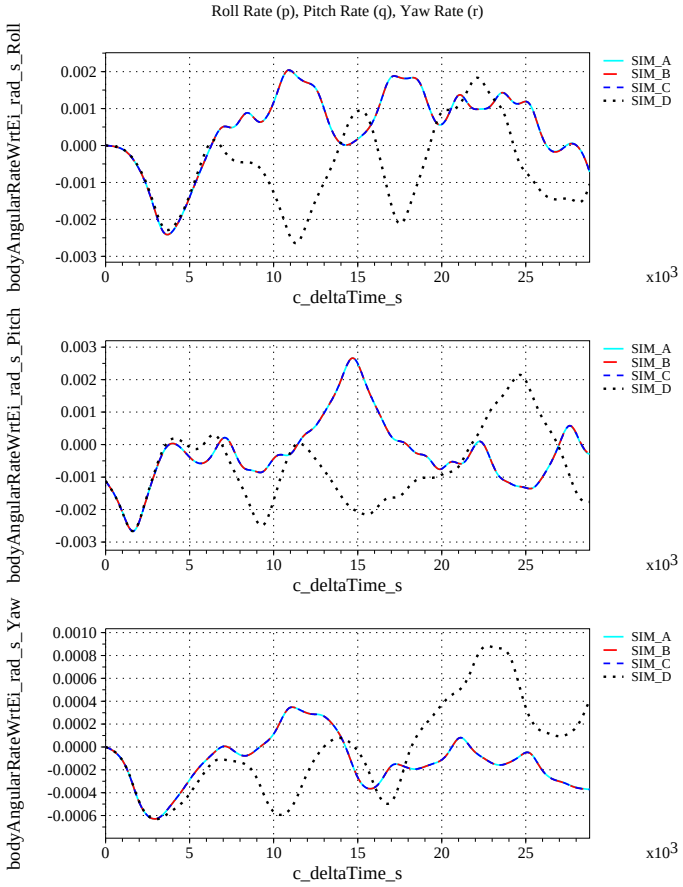

(e) Body-axis Angular Rates Compared

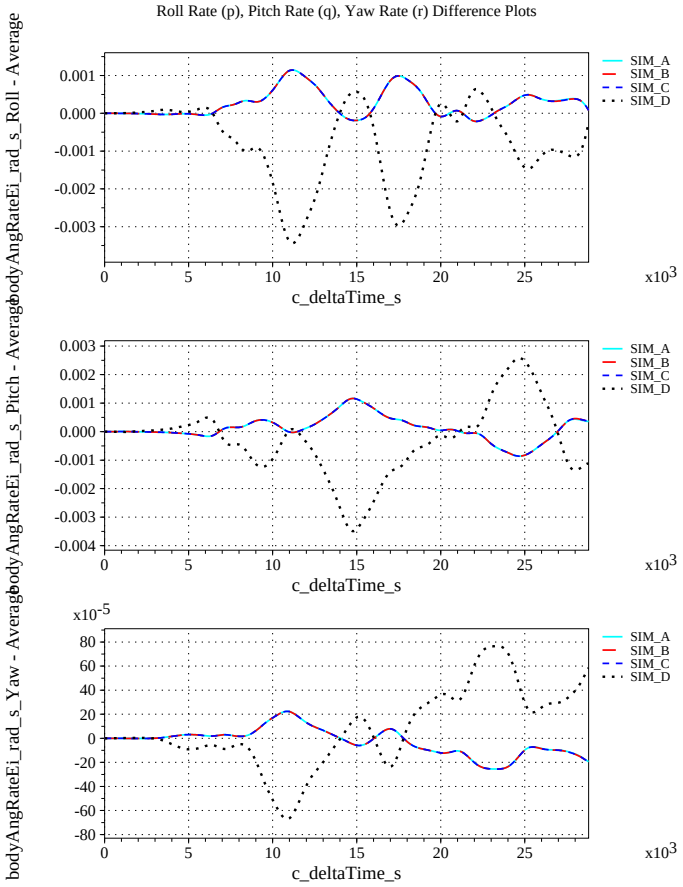

(f) Body-axis Angular Rates Differenced

Figure 62. Check-case Full: ISS Responding to All Effects; See Discussion in Section D.2.26 (Cont'd)

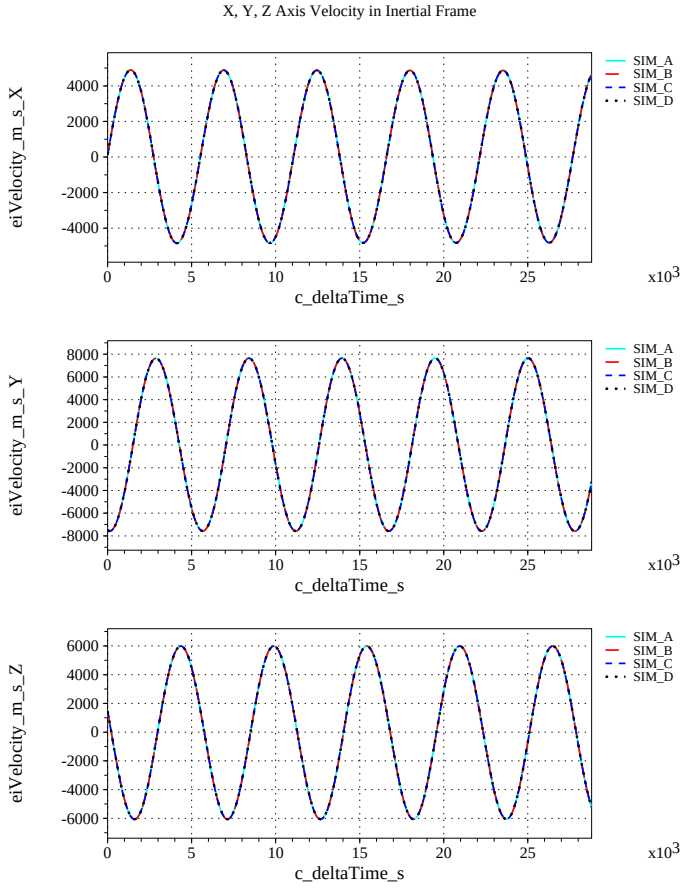

(g) Inertial Velocities Compared

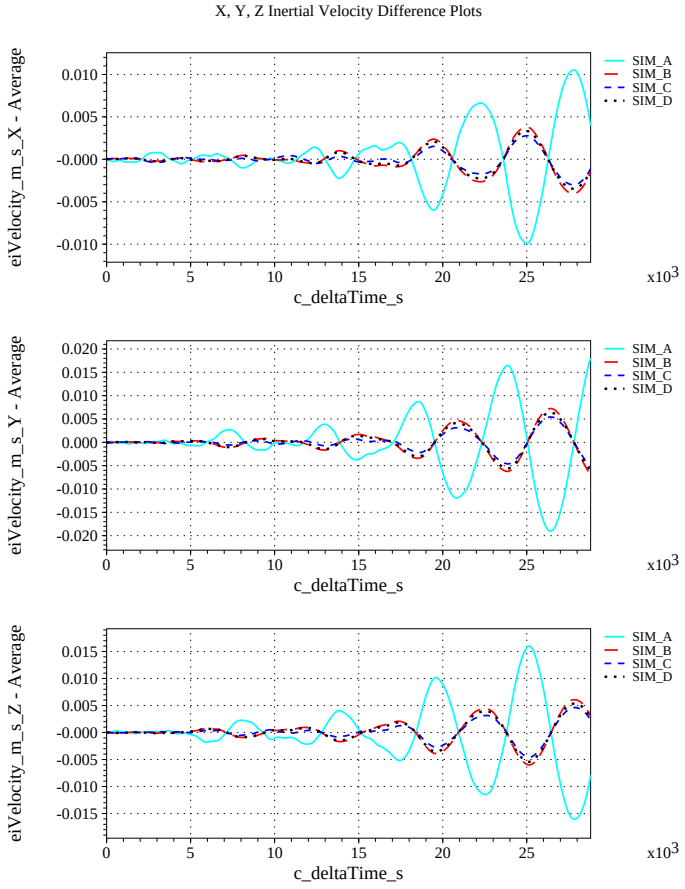

(h) Inertial Velocities Differenced

Figure 62. Check-case Full: ISS Responding to All Effects; See Discussion in Section D.2.26 (Cont'd)

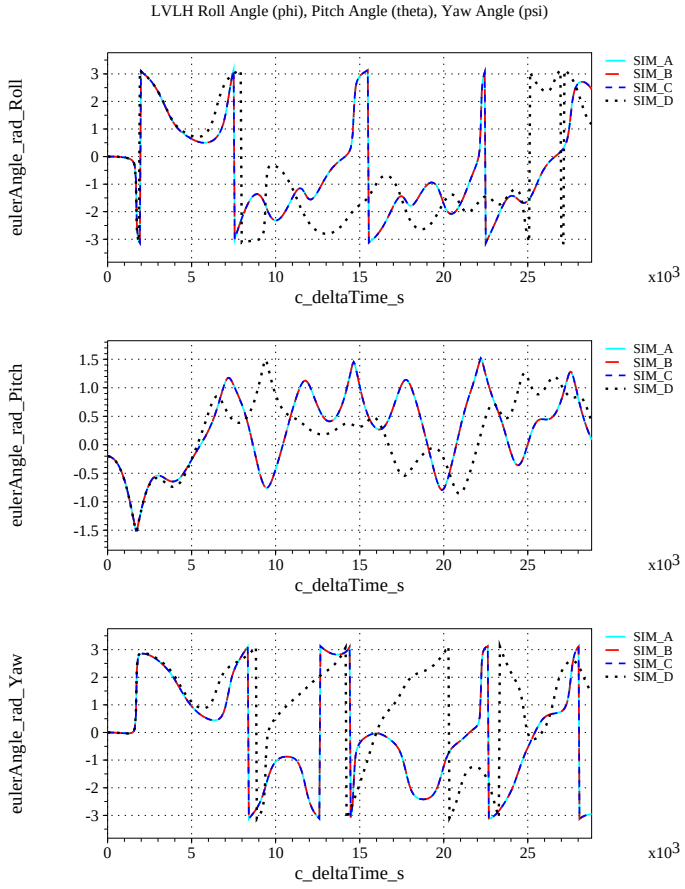

(i) Rotation Angles with Respect to LVLH Frame Compared

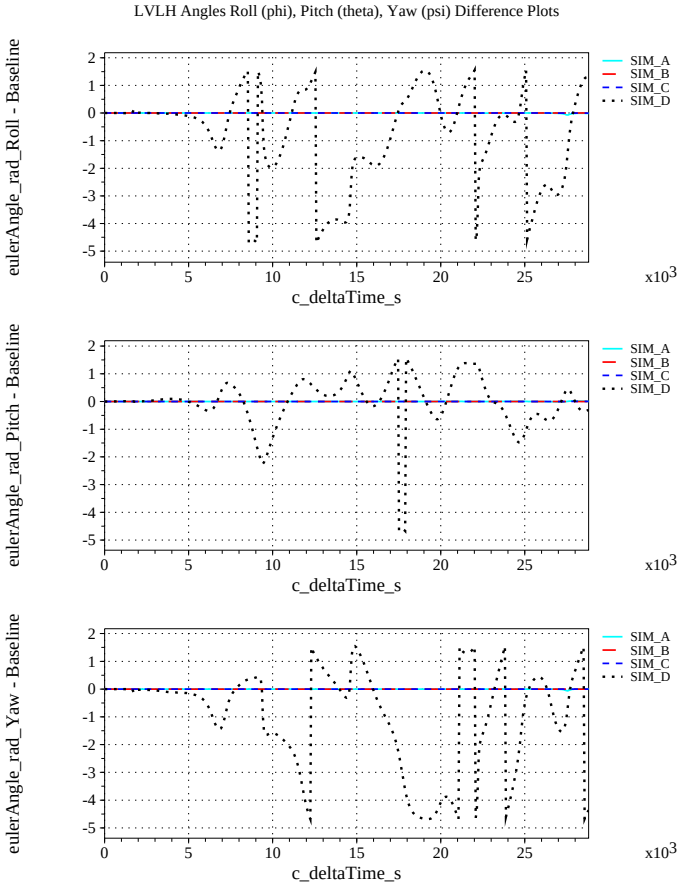

(j) Rotation Angles with Respect to LVLH Frame Differenced

Figure 62. Check-case Full: ISS Responding to All Effects; See Discussion in Section D.2.26 (Cont'd)

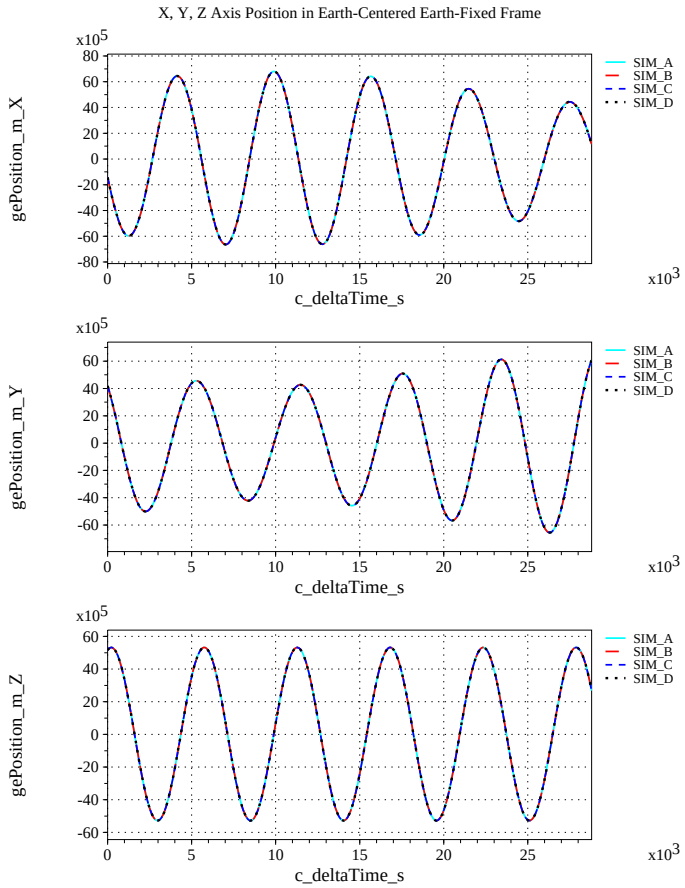

(k) Earth-centered, Earth-fixed Rectangular (X-Y-Z) Positions Compared

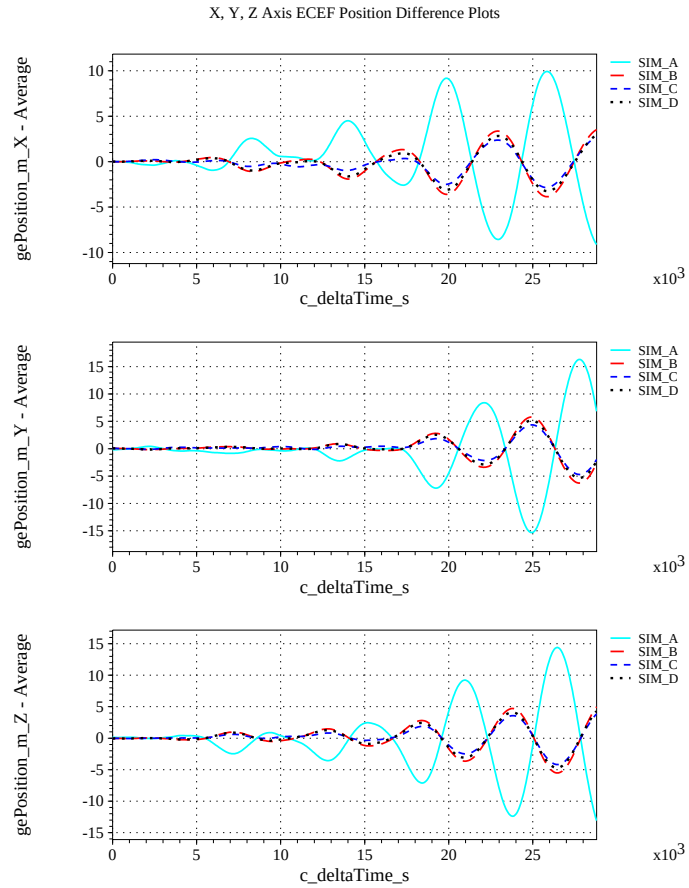

(l) Earth-centered, Earth-fixed Rectangular (X-Y-Z) Positions Differenced

Figure 62. Check-case Full: ISS Responding to All Effects; See Discussion in Section D.2.26 (Cont'd)

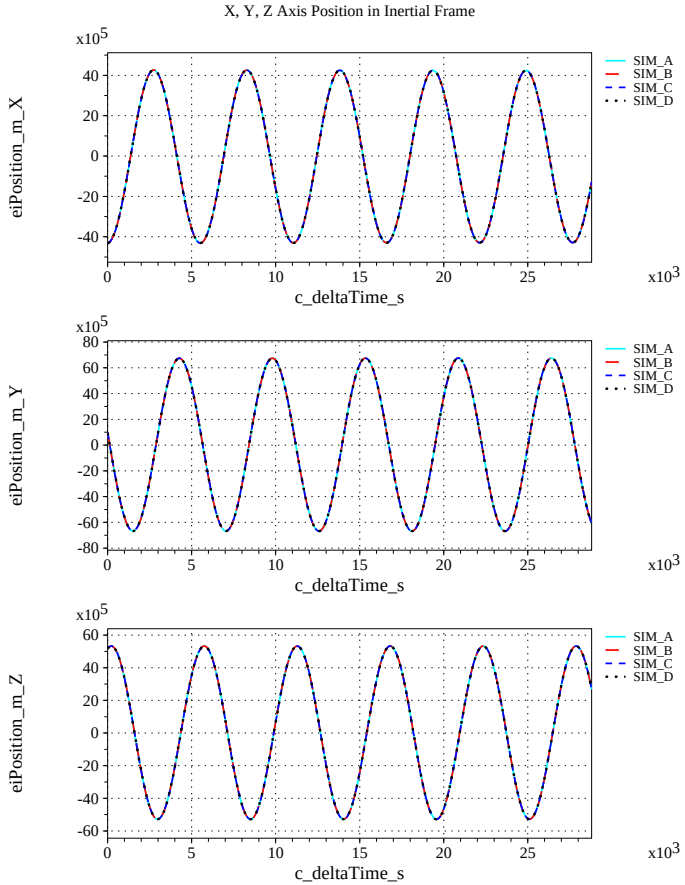

(m) Earth-centered Inertial Rectangular (x-y-z) Positions Compared

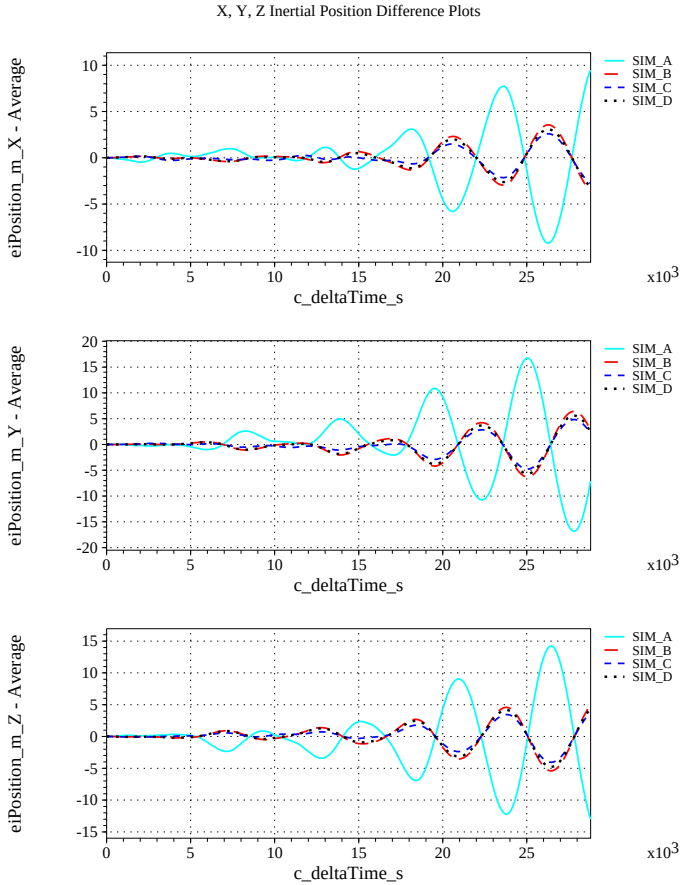

(n) Earth-centered Inertial Rectangular (x-y-z) Positions Differenced

Figure 62. Check-case Full: ISS Responding to All Effects; See Discussion in Section D.2.26 (Cont'd)

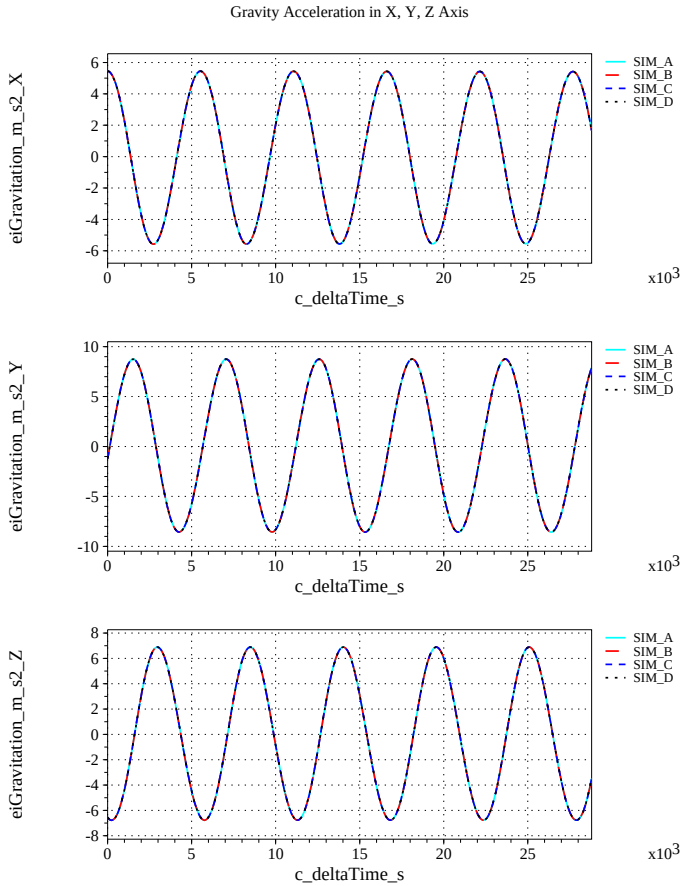

(o) Gravitational Components in Inertial (**X**-**Y**-**Z**) Directions Compared

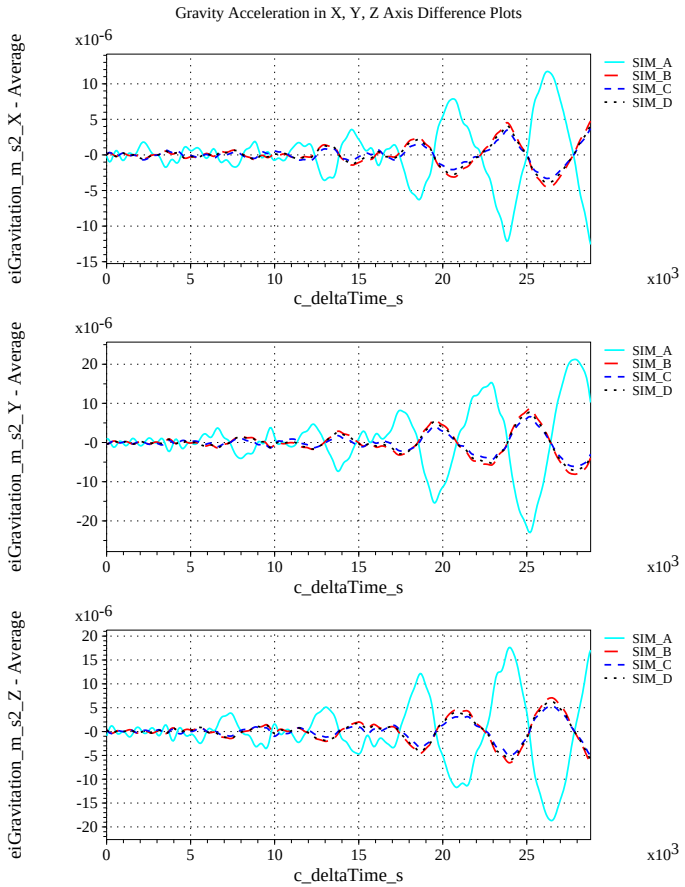

(p) Gravitational Components in Inertial (**X**-**Y**-**Z**) Directions Differenced

Figure 62. Check-case Full: ISS Responding to All Effects; See Discussion in Section D.2.26 (Concluded)

E Discussion of results

E.1 Quality of matches

Each realm of check-cases had its own peculiarities and recurring differences between simulation tools. Some of these differences can be explained fairly easily; some are as yet unexplained. Of the differences with apparent explanations, only a few trace back to a conscious decision to make a simplifying assumption or a difference in engineering judgment; most could be improved with additional effort.

Only a few of these differences raised objectionable matches between a majority of at least three simulated trajectories, as shown in the plots accompanying the Results section.

E.1.1 Quantitative match of parameters

Percent variation. A quantitative measure can be obtained by calculating the numerical difference between each simulation tool's parameter value and a reference value (either the average of the ensemble, or the analytical solution) at each point of time along the trajectory of a simulated maneuver, and dividing that difference by the maximum absolute value of that reference over the entire maneuver, expressed as a percentage:

$$\delta u_{\text{pct}} = 100 \frac{\max\left(|u(t) - u_{\text{ref}}(t)|\right)}{\max_{0 \le t \le t_{\text{end}}} |u_{\text{ref}}|)} \tag{38}$$

where $u(t)$ represents each parameter in the comparison set, and $u_{\text{ref}}(t)$ is the ensemble average or analytical solution at time t.

As mentioned in Section D, angular measurement variables with limited ranges that wrapped, such as Euler angle and spherical coordinates for latitude and longitude, had to be compared in a special way using the angular difference equations from trigonometry. It was not meaningful to create an ensemble average from which to measure variation, so instead the values from SIM 5 for the atmospheric cases and SIM D for the orbital cases were used as benchmarks.

This treatment may give an unfair advantage to SIM 5 and SIM D, as its angular differences must necessarily be zero. However, it seemed the most tractable solution since the results indicate the differences between the ensemble of simulation tools.

In formulating an overall percentage match for the check-cases, allowances were made for the identified differences and the unidentified differences that appeared to be incorrect. The allowance was to not include the incorrect parameter, or in some cases, the whole trajectory, in calculating the percent error between either the ensemble average, the truth solution if available, or SIM 5 or SIM D for Euler angles.

A second allowance was to ignore very small parameter values, where no simulation calculated a value over 0.001 (larger than the largest value of atmospheric density) as even small variations could generate large percentage errors.

E.1.2 Atmospheric scenarios

This section summarizes the principal causes for disparities that remain in the set of trajectories generated by the simulation tools that participated in the atmospheric check-cases.

Identified differences in atmospheric check-cases.

- Differences in numerical integration methods.
- Use of tabular vs. smooth atmospheric properties models.
- SIM 2 used an incorrect initial value for velocity in some cases.
- SIM 2 appears to have used a truncated gravitational constant in its inverse-square gravitation model.
- SIM 2 appears to have recorded aerodynamic force and gravitational acceleration values one frame later than calculated.
- SIM 3 appears to have interpreted the initial rotation rates as Earth-relative rather than inertial as specified.
- Each sim used a different interpretation of trimmed flight, and ended up starting the F-16 scenarios from slightly different initial conditions.
- SIM 3 incorrectly reported zero aerodynamic force reactions in first frame.
- A small difference in initial rotation rate appears in case 9 from the results from SIM 3.
- Case 10 highlights a disagreement over the alignment of local vertical (geocentric instead of geodetic).
- Case 10 shows a likely Incorrect geodetic conversion by SIM 2.
- Different tools used a different implementation of LQR autopilot reference state vector (cases 13.1-13.4, 15, and 16).
- Slight differences in timing of discrete events in fixed-step tools in cases 13-17.
- SIM 6 was unable to implement the simplified linear interpolation of mass properties called for in case 17.

Unidentified differences in atmospheric check-cases.

- An anomaly appears in rolling moment for case 16 results recorded by SIM 4.
- An unidentified bias appears in translational forces for case 9 in data recorded from SIM 1.

Atmospheric mismatch percentages. The maximum variation of each parameter reported by each simulation tool that participated in the atmospheric check-cases was calculated, using the equation given in Section E.1.1. Not all reported values were included in this analysis however. The following signals were ignored while identifying the worst percentage mismatches:

- Euler angle calculations in SIM 2 (all cases), likely due to integration method differences.
- Unexplained X-body force and local gravity difference in SIM 2 (cases 4 & 5).
- Unexplained non-zero value in Y-body force in SIM 3 (cases 6, 7, & 8).
- F-16 test cases (11 through 16, 18 and 19) for SIM 2 due to large trim differences.

- Ignored first 8 sec for all F-16 test cases due to initial transients (all simulation tools).
- Aerodynamic moments in all cases for SIM 2 since they appear to be reported at the MRC, not the CM as in other simulation tools.
- Mismatched timing of pitching and rolling moment and X-body force transients during altitude change test (check-case 13.1) for SIM 4 and 5.
- Mismatched timing of pitching moment transients during heading change and course side-step maneuvers (check-cases 13.3 and 13.4) for SIM 4 and 5.
- Mismatched timing of rolling moment and X-body force transients during North Pole circumnavigation test (check-case 15) for SIM 4 and 5.
- Tiny differences in vertical velocity for supersonic trim fly-out case 12 that led to large percentage errors (all simulation tools).
- For two-stage rocket (case 17), only one simulation tool included MET atmosphere model at higher altitudes, leading to large mismatches in atmospheric properties, so density, temperature, pressures (both static and dynamic), speed of sound, and Mach were ignored. Also, due to the large effect of the timing of stage firing/shutdown, pitch angle, flight path angle, and vertical velocities were considerably different in flight of the second stage, so differences in pitch angle, altitude rate, and true airspeed were ignored.

The remaining signals were compared and worst-case percentage differences between them and the reference value over the course of each check-case duration were computed for each case, as given in Tables 77, 79, and 81 for the simple, fixed-wing, and two-stage rocket check-cases, respectively.

A summary by signal name for all atmospheric check-cases is given in Tables 78, 80, and 82 for the simple, fixed-wing, and two-stage rocket check-cases, respectively.

As can be seen in Tables 79 and 81, the subsonic maneuvering (cases 13.x) and two-stage rocket (case 17) were the cases with the largest mismatch between one simulation tool and the ensemble average. These poor matches were caused by the timing of sharp-edged inputs occurring at slightly different times in various tools, as discussed for each check-case previously. As listed in Tables 79 and 80, the largest difference (19.5%) was between SIM 5 and 6 in the aerodynamic sideforce calculation for flight around the Equator/IDL intersection. This difference was caused by a 0.4-sec difference in the time at which the two simulations predicted the vehicle would intercept the desired circular track around the Equator/IDL intersection and would then be commanded, by the autopilot, to roll out slightly from the 30-degree limited bank angle held while intercepting the desired circular track from inside the circle.

The second-largest magnitude difference of 16.8%, listed in Tables 81 and 82 occurred in vertical velocity at the end of the two-stage rocket scenario, where SIM 6 diverged in trajectory from SIM 4 and 5 as shown in Figures 36m and 36n, for reasons discussed in Section D.1.19.

Other sizable differences appeared during the F-16 maneuvering check-cases and most can be attributed to slight timing differences of discrete events such as when a control surface came off a limit in position.

Table 77. Largest Differences for the Simple Atmospheric Check-cases, By Check-case (Percent of Largest Reference Value)

#	Check-case name	See Section	SIM 1	SIM 2[ad]	SIM 3	SIM 4	SIM 5	SIM 6	Largest diff. (%)
1	Dragless sphere	D.1.1	0.139	0.027	0.030	0.029	0.030	0.029	0.139
2	Dragless tumbling brick	D.1.2	0.133	0.033	- -	0.035	0.036	0.035	0.133
3	Dragless tumbling brick with damping	D.1.3	0.972	0.065	- -	0.264	0.067	0.072	0.972
4	Ball drop (round non-rotating Earth)[b]	D.1.4	- -	9.998	- -	3.333	3.333	3.333	9.998
5	Ball drop (round rotating Earth)[b]	D.1.5	- -	10.011	- -	3.337	3.337	3.337	10.011
6	Ball drop (WGS-84 Earth)[c]	D.1.6	0.142	0.080	0.029	0.030	0.031	0.030	0.142
7	Ball drop (steady wind)[c]	D.1.7	0.142	0.079	0.044	0.030	0.031	0.030	0.142
8	Ball drop (wind shear)[c]	D.1.8	0.142	0.153	0.076	0.077	0.076	0.068	0.153
9	Eastward ballistic shot	D.1.9	0.106	0.144	0.049	0.039	0.039	0.042	0.144
10	Northward ballistic shot	D.1.10	0.106	0.281	0.069	0.048	0.048	0.047	0.281
Largest % difference for each simulation tool			0.972	10.011	0.076	3.337	3.337	3.337	10.011

Key: - - – no data provided

[a]SIM 2 Euler angles exhibit large integration errors and were not included in any check-cases.

[b]Unexplained X-body force and local gravity differences appeared in SIM 2 results for check-cases 4 & 5 and were not included.

[c]Unexplained non-zero values in Y-body force in SIM 3 (cases 6, 7, & 8) were not included.

[d]Aerodynamic moments in all cases for SIM 2 were not included since they appear to be reported at the MRC, not the CM as in other simulation tools.

Table 78. Largest Differences across the Simple Atmospheric Check-cases (1–10), By Signal (Percent of Largest Reference Value)

Parameter name (S-119)	SIM 1	SIM 2	SIM 3	SIM 4	SIM 5	SIM 6	Largest (%)
gePosition_ft_X	0.000	- -	0.000	- -	0.000	0.000	0.000
gePosition_ft_Y	0.057	- -	0.076	- -	0.016	0.017	0.076
gePosition_ft_Z	0.009	- -	0.011	- -	0.010	0.009	0.011
feVelocity_ft_s_X	0.012	0.001	0.012	0.007	0.007	0.007	0.012
feVelocity_ft_s_Y	0.034	0.109	0.044	0.036	0.036	0.036	0.109
feVelocity_ft_s_Z	0.010	0.091	0.010	0.030	0.030	0.030	0.091
altitudeMsl_ft	0.022	0.043	0.023	0.016	0.015	0.014	0.043
longitude_deg	0.000	0.000	0.000	0.000	0.000	0.000	0.000
latitude_deg	0.000	0.000	0.000	0.000	0.000	0.000	0.000
localGravity_ft_s2[b]	0.000	0.000	0.000	0.000	0.000	0.000	0.000
eulerAngle_deg_Yaw[a]	0.972	*0.000*	- -	0.083	0.000	0.043	0.972
eulerAngle_deg_Pitch[a]	0.249	*0.000*	- -	0.264	0.000	0.016	0.264
eulerAngle_deg_Roll[a]	0.241	*0.000*	- -	0.174	0.000	0.032	0.241
bodyAngularRateWrtEi_deg_s_Roll	0.247	0.049	- -	0.061	0.067	0.072	0.247
bodyAngularRateWrtEi_deg_s_Pitch	0.266	0.065	- -	0.073	0.067	0.062	0.266
bodyAngularRateWrtEi_deg_s_Yaw	0.043	0.006	- -	0.011	0.012	0.013	0.043
altitudeRateWrtMsl_ft_min	0.009	0.081	0.009	- -	0.041	0.041	0.081
speedOfSound_ft_s	0.002	0.005	0.001	0.002	0.002	0.002	0.005
airDensity_slug_ft3	0.090	0.058	0.029	0.029	0.029	0.029	0.090
ambientPressure_lbf_ft2	0.142	0.048	0.037	0.036	0.037	0.037	0.142
ambientTemperature_dgR	0.002	0.010	0.002	0.003	0.003	0.003	0.010
aero_bodyForce_lbf_X[b]	0.033	3.999	0.047	1.333	1.333	1.333	3.999
aero_bodyForce_lbf_Y[c]	0.110	10.011	0.069	3.337	3.337	3.337	10.011
aero_bodyForce_lbf_Z	0.086	3.337	0.049	1.112	1.112	1.113	3.337
aero_bodyMoment_ftlbf_L	0.000	0.000	0.000	0.000	0.000	0.000	0.000
aero_bodyMoment_ftlbf_M[d]	0.000	*0.000*	0.000	0.000	0.000	0.000	0.000
aero_bodyMoment_ftlbf_N[d]	0.000	*0.000*	0.000	0.000	0.000	0.000	0.000
mach	0.012	0.087	- -	0.029	0.029	0.029	0.087
dynamicPressure_lbf_ft2	0.068	- -	- -	0.023	0.023	0.022	0.068
trueAirspeed_nmi_h	0.010	0.081	- -	- -	0.041	0.040	0.081
Largest % diff. for each sim. tool	0.972	10.011	0.076	3.337	3.337	3.337	10.011

Key: - - – no data provided
0.000 – data provided but not included in calculation

[a]SIM 2 Euler angles exhibit large integration errors and were not included in any check-cases.
[b]Unexplained X-body force and local gravity differences appeared in SIM 2 results for check-cases 4 & 5 and were not included.
[c]Unexplained non-zero values in Y-body force in SIM 3 (cases 6, 7, & 8) were not included.
[d]Aerodynamic moments in all cases for SIM 2 were not included since they appear to be reported at the MRC, not the CM as in other simulation tools.

Table 79. Largest Differences for the Fixed-wing Aircraft Check-cases, by Check-case (Percent of Largest Reference Value)

#	Check-case name[a]	See Section	SIM 2[b]	SIM 4	SIM 5	Largest diff. (%)
11	Subsonic aircraft (trimmed)	D.1.11	*0.000*	2.786	2.786	2.786
12	Supersonic aircraft (trimmed)[c]	D.1.12	*0.000*	0.631	0.631	0.631
13.1	Subsonic aircraft (altitude change)[d]	D.1.13	*0.000*	1.080	1.080	1.080
13.2	Subsonic aircraft (velocity change)	D.1.14	*0.000*	0.218	0.218	0.218
13.3	Subsonic aircraft (heading change)[e]	D.1.15	*0.000*	14.947	14.947	14.947
13.4	Subsonic aircraft (course offset)[e]	D.1.16	*0.000*	16.312	16.312	16.312
15	Subsonic aircraft (North Pole)[f]	D.1.17	*0.000*	11.845	11.845	11.845
16	Subsonic aircraft (intersection)	D.1.18	*0.000*	19.513	19.513	19.513
Largest % difference for each simulation tool			*0.000*	19.513	19.513	19.513

Key: *0.000* – data provided but not included in calculation

[a]The first 8 sec for all F-16 test cases due to initial transients (all simulation tools) were not included.

[b]SIM 2 results are ignored for all F-16 check-cases (11 through 16, 18 and 19) due to large trim differences.

[c]Tiny differences in vertical velocity for supersonic trim fly-out case 12 that led to large percentage errors (all simulation tools).

[d]Mismatched timing of pitching and rolling moment and X-body force transients during altitude change test (check-case 13.1) for SIM 4 and 5.

[e]Mismatched timing of pitching moment transients during heading change and course side-step maneuvers (check-cases 13.3 and 13.4) for SIM 4 and 5.

[f]Mismatched timing of rolling moment and X-body force transients during North Pole circumnavigation test (check-case 15) for SIM 4 and 5.

Table 80. Largest Differences across the Fixed-wing Aircraft Check-cases (11-16), By Signal (Percent of Largest Reference Value)

Parameter name (S-119)[a]	SIM 2[b]	SIM 4	SIM 5	Largest (%)
gePosition_ft_X	- -	- -	0.000	0.000
gePosition_ft_Y	- -	- -	0.000	0.000
gePosition_ft_Z	- -	- -	0.000	0.000
feVelocity_ft_s_X	*0.000*	0.451	0.451	0.451
feVelocity_ft_s_Y	*0.000*	0.095	0.095	0.095
feVelocity_ft_s_Z[c]	*0.000*	7.142	7.142	7.142
altitudeMsl_ft	*0.000*	0.003	0.003	0.003
longitude_deg	*0.000*	0.001	0.000	0.001
latitude_deg	*0.000*	0.000	0.000	0.000
localGravity_ft_s2	*0.000*	0.000	0.000	0.000
eulerAngle_deg_Yaw	*0.000*	2.660	0.000	2.660
eulerAngle_deg_Pitch	*0.000*	0.528	0.000	0.528
eulerAngle_deg_Roll	*0.000*	2.519	0.000	2.519
bodyAngularRateWrtEi_deg_s_Roll	*0.000*	7.703	7.703	7.703
bodyAngularRateWrtEi_deg_s_Pitch	*0.000*	16.312	16.312	16.312
bodyAngularRateWrtEi_deg_s_Yaw	*0.000*	14.947	14.947	14.947
altitudeRateWrtMsl_ft_min	*0.000*	- -	0.000	0.000
speedOfSound_ft_s	*0.000*	0.000	0.000	0.000
airDensity_slug_ft3	*0.000*	0.001	0.001	0.001
ambientPressure_lbf_ft2	*0.000*	0.003	0.003	0.003
ambientTemperature_dgR	*0.000*	0.000	0.000	0.000
aero_bodyForce_lbf_X[d]	*0.000*	11.619	11.619	11.619
aero_bodyForce_lbf_Y	*0.000*	19.513	19.513	19.513
aero_bodyForce_lbf_Z	*0.000*	7.567	7.567	7.567
aero_bodyMoment_ftlbf_L[d]	*0.000*	10.549	10.549	10.549
aero_bodyMoment_ftlbf_M[e]	*0.000*	1.562	1.562	1.562
aero_bodyMoment_ftlbf_N	*0.000*	12.969	12.969	12.969
mach	*0.000*	0.017	0.017	0.017
dynamicPressure_lbf_ft2	- -	0.034	0.034	0.034
trueAirspeed_nmi_h	*0.000*	- -	0.000	0.000
Largest % diff. for each sim. tool	*0.000*	19.513	19.513	19.513

Key: - - – no data provided
0.000 – data provided but not included in calculation

[a]The first 8 sec for all F-16 test cases due to initial transients (all simulation tools) were not included.
[b]SIM 2 results are ignored for all F-16 check-cases (11 through 16, 18 and 19) due to large trim differences.
[c]Tiny differences in vertical velocity for supersonic trim fly-out case 12 that led to large percentage errors (all simulation tools).
[d]Mismatched timing of pitching and rolling moment and X-body force transients during altitude change test (check-case 13.1) for SIM 4 and 5.
[e]Mismatched timing of pitching moment transients during heading change and course side-step maneuvers (check-cases 13.3 and 13.4) for SIM 4 and 5.
[f]Mismatched timing of rolling moment and X-body force transients during North Pole circumnavigation test (check-case 15) for SIM 4 and 5.

Table 81. Largest Differences for the Two-stage Rocket Check-case (Case 17) (Percent of Largest Reference Value)

#	Check-case name	See Section	SIM 4	SIM 5	SIM 6	Largest diff. (%)
17	Two-stage rocket[a]	D.1.19	8.398	8.391	16.790	16.790
Largest % difference for each simulation tool			8.398	8.391	16.790	16.790

[a]One simulation tool included the MET atmosphere model while the other two did not, so density, temperature, pressures (both static and dynamic), speed of sound, and Mach were not numerically compared. Also, due to the large effect of the timing of stage firing/shutdown, pitch angle, flight path angle and vertical velocities were considerably different in flight of the second stage, so differences in pitch angle, altitude rate, and true airspeed were not compared.

Table 82. Largest Differences across the Two-stage Rocket Check-case (Case 17), by Signal (Percent of Largest Reference Value)

Parameter name (S-119)[a]	SIM 4	SIM 5	SIM 6	Largest (%)
gePosition_ft_X	- -	0.127	0.127	0.127
gePosition_ft_Y	- -	0.547	0.547	0.547
feVelocity_ft_s_X	0.000	0.000	0.000	0.000
feVelocity_ft_s_Y	1.263	1.262	2.525	2.525
feVelocity_ft_s_Z	8.398	8.391	16.790	16.790
altitudeMsl_ft	2.198	2.195	4.394	4.394
longitude_deg	0.000	0.000	0.000	0.000
latitude_deg	0.000	0.000	0.000	0.000
localGravity_ft_s2	0.152	0.151	0.303	0.303
eulerAngle_deg_Yaw	0.000	0.000	0.000	0.000
eulerAngle_deg_Roll	0.000	0.000	0.000	0.000
bodyAngularRateWrtEi_deg_s_Roll	0.000	0.000	0.000	0.000
bodyAngularRateWrtEi_deg_s_Pitch	2.663	2.661	5.324	5.324
bodyAngularRateWrtEi_deg_s_Yaw	0.000	0.000	0.000	0.000
altitudeRateWrtMsl_ft_min	- -	0.000	0.000	0.000
aero_bodyForce_lbf_X	0.421	0.421	0.842	0.842
aero_bodyForce_lbf_Y	0.000	0.000	0.000	0.000
aero_bodyForce_lbf_Z	2.662	2.659	5.322	5.322
aero_bodyMoment_ftlbf_L	0.000	0.000	0.000	0.000
aero_bodyMoment_ftlbf_M	3.875	3.871	7.746	7.746
aero_bodyMoment_ftlbf_N	0.000	0.000	0.000	0.000
Largest % diff. for each sim. tool	8.398	8.391	16.790	16.790

Key: - - – no data provided

[a]One simulation tool included the MET atmosphere model while the other two did not, so density, temperature, pressures (both static and dynamic), speed of sound, and Mach were not numerically compared. Also, due to the large effect of the timing of stage firing/shutdown, pitch angle, flight path angle and vertical velocities were considerably different in flight of the second stage, so differences in pitch angle, altitude rate, and true airspeed were not compared.

E.1.3 Orbital scenarios

This section summarizes the principal causes for disparities that remain in the set of trajectories generated by the simulation tools that participated in the orbital check-cases.

Identified differences in orbital check-cases.

- Differences in integration method employed by each simulation tool.
- Disagreement on precise RNP rotations (Earth attitude with respect to J2000 inertial frame).
- Different versions of MET model were employed by various tools.
- A substantial gravitational magnitude difference appeared in the results for case 3A recorded by SIM C.
- Atmospheric drag was not computed for case 6A by SIM D.

Unidentified differences in orbital check-cases.

- Constant zero values were recorded for some parameters in case 5B by SIM A.
- SIM A has a consistent difference in altitude in all check-cases.

Orbital mismatch percentages. The maximum variation of each parameter reported by each simulation tool that participated in the orbital check-cases was calculated, using the equation given in Section E.1.1. Not all reported values were included in this analysis however. The following signals were ignored while identifying the worst percentage mismatches:

- SIM A values for case 5B appear corrupted.
- SIM D values for atmospheric density and ambient temperature are clearly incorrect.
- Semi-major axis length calculations are widely different in case 6D.
- Euler angles are significantly different for SIM C in the 10A-10D check-cases.
- Euler angles and body angular rates are significantly different for SIM D in the Full Effects checkcase.

The remaining signals were compared and worst-case percentage differences between them and the reference value over the course of each check-case were computed for each case, as given in Table 83.

A summary by signal name for all orbital check-cases is given in Table 84.

As listed in Table 83, the worst mismatches between the signals that remain viable occur in the most complex scenario, the Full Effects check-case described in Section C.2.26 and discussed in Section D.2.26. The mismatches are in Euler angles for roll and yaw, as given in Table 84 for large values of pitch attitude; this is due to the singularity that exists in the Euler 3-2-1 rotation sequence when close to $\pm\frac{\pi}{2}$ radians in pitch angle, as discussed in Section E.2.2 in the **Conventions for representing attitude** discussion.

Aside from the mismatches caused by proximity to the Euler 'gimbal lock' singularity, all signals matched within 0.54 % over the typical 28,800 s simulated orbital time-frames, a remarkable result.

Table 83. Largest Differences for All Orbital Check-cases, by Check-case (Percent of Largest Reference Value)

#	Check-case name	See Section	SIM A	SIM B	SIM C	SIM D	Largest diff. (%)
2	ISS in spherical gravity	D.2.1	0.080	0.043	0.046	0.048	0.080
3A	ISS in 4×4 harmonic gravity	D.2.2	0.079	0.043	0.046	0.048	0.079
3B	ISS in 8×8 harmonic gravity	D.2.3	0.079	0.043	0.046	0.048	0.079
4	ISS with third-body disturbances	D.2.4	0.080	0.043	0.046	0.048	0.080
5A	ISS (minimal solar activity)	D.2.5	0.066	0.041	0.043	0.046	0.066
5B	ISS (mean solar activity)[1]	D.2.6	- -	0.018	0.020	0.038	0.038
5C	ISS (maximal solar activity)	D.2.7	0.100	0.051	0.053	0.055	0.100
6A	Sphere with fixed drag[2]	D.2.8	- -	0.004	0.004	0.009	0.009
6B	Sphere with dynamic drag	D.2.9	0.080	0.044	0.046	0.048	0.080
6C	Cylinder undergoing plane change firing	D.2.10	0.086	0.071	0.040	0.069	0.086
6D	Cylinder undergoing Earth departure firing[3]	D.2.11	0.226	0.066	0.063	0.097	0.226
7A	Sphere in 4×4 gravity and third-body perturbations	D.2.12	0.080	0.044	0.046	0.048	0.080
7B	Sphere in 8×8 gravity and third-body perturbations	D.2.13	0.080	0.044	0.046	0.048	0.080
7C	Sphere in 4×4 gravity with drag and third-body perturbations	D.2.14	0.080	0.044	0.046	0.048	0.080
7D	Sphere in 8×8 gravity with drag and third-body perturbations	D.2.15	0.080	0.044	0.046	0.048	0.080
8A	ISS free rotation with zero rates	D.2.16	0.080	0.043	0.046	0.048	0.080
8B	ISS free rotation with a non-zero rates	D.2.17	0.080	0.043	0.046	0.048	0.080
9A	ISS being torqued with zero initial rates	D.2.18	0.085	0.066	0.040	0.056	0.085
9B	ISS being torqued with non-zero initial rates	D.2.19	0.085	0.066	0.040	0.056	0.085
9C	ISS under torque and force with zero initial rates	D.2.20	0.085	0.066	0.040	0.056	0.085
9D	ISS under torque and force with a non-zero initial rates	D.2.21	0.085	0.066	0.040	0.056	0.085
10A	Cylinder in circular orbit with gravity gradient with zero initial rates[4]	D.2.22	0.080	0.043	0.046	0.048	0.080
10B	Cylinder in circular orbit with gravity gradient with non-zero initial rates[4]	D.2.23	0.080	0.043	0.046	0.048	0.080
10C	Cylinder in elliptical orbit with gravity gradient with zero initial rates[4]	D.2.24	0.080	0.044	0.046	0.048	0.080
10D	Cylinder in elliptical orbit with gravity gradient with a non-zero initial rates[4]	D.2.25	0.080	0.044	0.046	0.048	0.080
Full	ISS responding to all effects[5]	D.2.26	2.256	0.322	0.281	0.048	2.256
Largest % difference for each simulation tool			2.256	0.322	0.281	0.097	2.256

Key: - - – no data provided

[a]SIM A values for case 5B appear to be corrupted and were not included.
[b]SIM D values for atmospheric density and ambient temperature in case 6A are clearly incorrect and were not included.
[c]Semi-major axis length calculations are widely different in case 6D and were not included.
[d]Euler angles are significantly different for SIM C in the 10A-10D check-cases and were not included.
[e]Euler angles and body angular rates are significantly different for SIM D in the Full Effects checkcase and were not included.

Table 84. Largest Differences for All Orbital Check-cases, by Signal (Percent of Largest Reference Value)

Parameter name (S-119)	SIM A[a]	SIM B	SIM C	SIM D	Largest (%)
gePosition_m_X	0.001	0.003	0.003	0.006	0.006
gePosition_m_Y	0.001	0.004	0.004	0.009	0.009
gePosition_m_Z	0.001	0.004	0.004	0.008	0.008
eiPosition_m_X	0.001	0.004	0.004	0.009	0.009
eiPosition_m_Y	0.001	0.004	0.004	0.009	0.009
eiPosition_m_Z	0.001	0.004	0.004	0.008	0.008
eiVelocity_m_s_X	0.001	0.004	0.004	0.009	0.009
eiVelocity_m_s_Y	0.001	0.004	0.004	0.008	0.008
eiVelocity_m_s_Z	0.001	0.004	0.004	0.009	0.009
eiAccel_m_s2_X	0.001	0.004	0.004	0.009	0.009
eiAccel_m_s2_Y	0.001	0.004	0.004	0.009	0.009
eiAccel_m_s2_Z	0.001	0.004	0.004	0.008	0.008
semiMajorAxis_m[b]	0.000	0.000	0.000	0.000	0.000
gast_rad	0.000	0.000	0.000	0.001	0.001
eulerAngle_rad_Roll[cd]	2.256	0.000	0.281	0.006	2.256
eulerAngle_rad_Pitch[cd]	0.516	0.000	0.064	0.004	0.516
eulerAngle_rad_Yaw[cd]	1.967	0.000	0.245	0.006	1.967
eulerAngleWrtEi_rad_Roll[d]	0.737	0.000	0.092	0.003	0.737
eulerAngleWrtEi_rad_Pitch[d]	0.334	0.000	0.042	0.000	0.334
eulerAngleWrtEi_rad_Yaw[d]	0.674	0.000	0.084	0.003	0.674
bodyAngularRateWrtEi_rad_s_Roll[d]	0.383	0.229	0.153	0.000	0.383
bodyAngularRateWrtEi_rad_s_Pitch[d]	0.537	0.322	0.215	0.001	0.537
bodyAngularRateWrtEi_rad_s_Yaw[d]	0.000	0.000	0.000	0.000	0.000
altitudeMsl_m[e]	0.015	0.005	0.005	0.007	0.015
airDensity_kg_m3[e]	0.000	0.000	0.000	0.000	0.000
ambientTemperature_dgK	0.226	0.071	0.063	0.097	0.226
eiGravitation_m_s2_X	0.001	0.004	0.004	0.009	0.009
eiGravitation_m_s2_Y	0.001	0.004	0.004	0.009	0.009
eiGravitation_m_s2_Z	0.001	0.004	0.004	0.008	0.008
Largest % diff. for each sim. tool	2.256	0.322	0.281	0.097	2.256

[a]SIM A values for case 5B appear to be corrupted and were not included.
[b]Semi-major axis length calculations are widely different in case 6D and were not included.
[c]Euler angles are significantly different for SIM C in the 10A-10D check-cases and were not included.
[d]Euler angles and body angular rates are significantly different for SIM D in the Full Effects checkcase and were not included.
[e]SIM D values for atmospheric density and ambient temperature in case 6A are clearly incorrect and were not included.

E.2 Corrections to improve matching

The assessment team went through several comparison cycles to produce the results presented in the report. Initial comparisons showed much larger differences. In some cases, simulations were effectively executing scenarios that differed in small ways from each other and from the scenario that was intended.

The goal was to present a family of simulation solutions (time histories of state and output variables) whose differences were traceable only to engineering choices in the modeling and implementation of the equations of motion, implementation of the environment models, selection of time step, or selection of integration method. Therefore, analysis of early comparison cycles attempted to identify and correct other sources of output variation including initial conditions, simulation parameters (physical constants and unit conversions), simulation conventions, output recording, and defects.

These corrections were intended to ensure that the simulations were accurately executing the same scenario and faithfully reporting the same quantities at the same time step while avoiding any suggestion that any one simulation tool should modify its implementation to conform to other tools. Not all variations due to simulation tool configuration, recording, or possible defects were eliminated in the results presented in this report. Some are still identified in the discussion of the results in Volume 1 of this report. This section describes the most prevalent corrections that were made prior to the runs presented here. These corrections should inform attempts to match the results presented here.

E.2.1 Simulation parameters

For this discussion, the term "simulation parameters" is restricted to physical constants and unit conversions. At the start of this assessment, not all simulation tools were using the same values for physical constants and unit conversions. Either the value used came from a different source or the value was not carried to the same digits of precision. Sometimes this issue was compounded when a source document presented different units for a physical constant than the native units of the simulation tool. If so, a truncated unit conversion could lead to real physical differences between simulations using SI units and those using English units. For example, in one of the early runs of atmospheric check-case 1, the initial ECEF X-axis coordinate of the sphere differed by up to 0.7 ft due to a truncation of the meter-to-foot conversion for the Earth's equatorial radius.

Eventually all tools used the parameters presented in Tables 73 and 74, which improved matching.

E.2.2 Simulation conventions

Simulation tools were found to have different conventions for defining or naming quantities. These differences could cause confusion in establishing scenario consistency and comparing results. Among the simulation tools participating in this assessment, the conventions for representing attitude, the conventions for naming output variables, the conventions for the LVLH frame, and conventions for products of inertia caused issues in establishing good comparisons.

Conventions for representing attitude. Attitude can be represented using Euler angles, quaternions, or direction cosine matrices (DCMs). Of these, Euler angles tend to be the most intuitive to visualize and are favored for defining the initial state and analyzing results. However, there exist twelve different conventions for Euler angles. Use of a 3-2-1 (yaw-pitch-roll) rotation convention has long been common practice for aircraft simulations. But spacecraft simulations may support differing conventions with 3-1-3 being a popular choice for orbital mechanics. There was not a common convention among the participating

simulation tools for this rotation sequence for either initialization or recording and, in the case of at least one of the tools, different outputs used more than one Euler angle convention by default. Simulation runs could, therefore, err in the Euler angle convention used for either initialization or output. A second alternative but redundant representation could catch such errors.

Of the remaining two attitude representations, quaternions are more compact since they are defined by four scalar values. However, there exist in practice differing conventions for the definition of quaternions since quaternions are not unique: quaternion values of opposite sign define the same attitude. Not all the simulation tools participating in the atmospheric cases employed quaternions to represent attitude. When quaternions were compared among participating tools for the orbital cases, it was revealed that the tools did not share the same quaternion convention. In fact, one of the tools used a convention that always kept the scalar component of the quaternion positive. Thus, it was not possible to compare quaternions in post-processing by simply changing quaternion sign of one or more simulation data sets. Thus, comparison of quaternions was abandoned.

Direct comparison of nine-element DCMs as a representation of attitude was briefly entertained since the DCM has a uniform definition among the simulation tools. However, this idea was also abandoned because using a DCM for input and/or output would require code changes to some simulation tools, including all nine scalars comprising the DCM at each time step would increase the size of the data files, and the difficulty posed in extracting physical meaning from any DCM differences.

This led to a final decision to standardize on a 3-2-1 Euler angle convention for attitude representation for both atmospheric and orbital check-cases. Both initial conditions and simulation outputs used this convention.

This decision required special treatment when comparing these angles, since each Euler angle is typically limited to a range of values which must necessarily "wrap" from one limit to another as the vehicle rotates. Comparing attitudes that are close but are separated by one of these wrappings was avoided by use of equation 37 discussed in Section D.

Use of the 3-2-1 sequence of Euler angles to compare attitudes led to another consequence: an ambiguity in roll and yaw angles when pitch angle approaches $\pm\frac{\pi}{2}$ radians, i.e., vertical in either sense. As will be shown in the "(Quality of matches" section, some significant numerical mis-matches resulted.

Conventions for naming output variables. The naming convention for output variables was unique to each simulation tool. Those names often did not unambiguously define the variable. In fact, there were a few instances were similar variables names between two tools referred to different quantities. The best examples of this were variables usually named "P," "Q," or "R." In some simulation tools, these variables represented inertial-relative rotation rates presented in body coordinates; in other simulations, these variables represented Earth-relative rotation rates in body coordinates. Similar names for dissimilar quantities did lead to some dissimilar quantities being compared by co-plotting. Also, it led to some confusion over initial conditions when one simulation team tried using the outputs of another simulation team to match initial conditions.

Two steps were taken to resolve this issue. First, the variable naming convention of the ANSI/AIAA S-119 standard [5] was adopted for labeling the plots. The S-119 standard provides unambiguous names for states. Second, each simulation team was asked to produce a dictionary for the parameters in their data files. Ultimately, each simulation team was responsible for ensuring that the output variable used on each plot was the best match to the S-119 name on the plot.

Conventions for the Local Horizontal Local Vertical (LVLH) frame. The LVLH frame, used as the basis for vehicle attitude relative to the Earth's surface, often has a different definition in atmospheric check-

cases than in orbital check-cases. The different definitions reflect different preferences of locally horizontal and vertical directions in the aircraft and spacecraft communities.

In the atmospheric flight community, the local vertical is defined as perpendicular to the surface of the Earth and the local horizontal is tangent to the surface of the Earth. In the space flight community, the local vertical is usually parallel to the geocentric radial and the local horizontal is perpendicular to the orbit plane. With the few simulation tools that could attempt both the atmospheric and orbital cases, early atmospheric case comparisons included a mixture of Euler angles defined using the orbital and atmospheric LVLH conventions. All but one of the simulations participating in the atmospheric cases could provide Euler angles using the atmospheric LVLH convention. In cases where the simulation could provide Euler angles under either convention, those simulations often used a different name for the atmospheric LVLH frame.

Convention for the products-of-inertia. When the products-of-inertia (I_{xy}, I_{xz}, and I_{yz}) appear in the mass tensor, they usually have a negative sign (i.e., $-I_{xy}$, $-I_{xz}$, and $-I_{yz}$). Simulation tools can differ in whether they expect input values for the products-of-inertia to include the negating operand. Therefore, for those check-cases where the products-of-inertia were not zero, initial comparisons showed differences in rotational dynamics attributed to differences in the sign of the products-of-inertia between the simulation tools. These differences were easily confirmed by changing the sign of the products-of-inertia in one of the tools that differed and running a new set of results. In some cases, the sign confusion lay with the published scenario and clarifying text was added to the scenario description. In other cases, the sign confusion resulted from user oversight in changing sign as needed to match the product-of-inertia convention for the simulation tool.

E.2.3 Initial conditions

The team attempted to define the initial condition for each check-case unambiguously. Nevertheless, early comparisons demonstrated differences in interpretation or application of initial conditions. There were a number of contributors to this confusion:

- Initial states had to be defined using multiple reference frames and coordinate systems to accommodate the variety of practices represented by the simulation tools. Managing and maintaining a consistent set of multiple state definitions was difficult and subject to errors.
- A simulation team might interpret a published state defined for one pair of reference frame and coordinate system as if it were defined for the simulation tool's preferred pair of reference frame and coordinate system.
- Problems with configuration file management: a simulation team occasionally neglected to update some aspect of the configuration file when setting up the next scenario. Likewise, a simulation team occasionally made a correction to one set of configuration files but failed to recognize that other configuration files suffered from the same issue.
- Differences and limits in defining initial ECEF orientation relative to ECI.
- There was confusion over the definition of the initial altitude, whether it was geometric, MSL, or above ground level and whether sea-level or ground-level were different from the reference ellipsoid surface.
- Errors in implementing the scenarios caused some simulation tools to ignore certain non-zero initial conditions at $t = 0$.

- Confusion over initial center-of-mass location for F-16 model.
- Due to the separation between orbital and atmospheric simulation communities, no single document existed that listed the initial conditions; there were at least two sources given initial values and, when a better initial conditions document was developed, there were three source documents.

Using multiple reference frames and coordinate systems to specify initial conditions. Most initial states (position, velocity, etc.) are vector quantities. A vector quantity is not only expressed in a given coordinate system but it may have a different value depending on the reference frame in which it is observed. For example, the vehicle velocity has a different measured value when observed in the inertial frame than when observed in an Earth-fixed frame due to the rotation of the Earth-fixed frame relative to the inertial frame. Then, the measured velocity vector can have different component values depending on the coordinate system in which it is expressed. An Earth-relative vehicle velocity expressed in NED coordinates necessarily had different component values than when the vector was expressed in body coordinates. Thus, the least ambiguous manner to express a set of initial vector quantities was to measure and express them in the same frame. An initial attempt was made to define all the initial states using ECI as the normative frame.

However, few of the simulation tools were designed to accept an initial condition specification in ECI coordinates. Often the reference frames and coordinate systems that a simulation tool accepted for defining the vehicle initial condition were based on the native frame(s) for its EOM (e.g., ECI, ECEF, reference-point Cartesian) and the tool's previous history. The simulation tools simply reflected the variety of practices common in the aerospace community for defining scenarios.

This was especially true for the atmospheric check-cases. Atmospheric simulation tools might accept a position measured in the Earth-fixed frame and expressed as either geodetic coordinates (latitude, longitude, and altitude) or reference-point relative Cartesian coordinates (e.g., runway-relative coordinates). Initial velocity was often measured in the Earth-fixed frame and expressed in either NED or body coordinates. Initial attitude was universally measured in the Earth-fixed frame and expressed as 3-2-1 Euler angles relative to NED coordinates. Initial rotational rate may be relative to the inertial frame, the Earth-fixed frame, or the atmospheric LVLH frame and expressed in body coordinates.

Use of multiple reference frames and coordinates systems was less prevalent in the orbital simulation community. Initial position and velocity vectors were acceptable when given relative to and expressed in ECI. Initial attitude was defined as Euler angles representing the 3-2-1 rotation from orbital LVLH coordinates to body coordinates. Only initial rotation rate switched between inertial and LVLH reference frames and was represented in body coordinates.

To solve the initial condition incompatibility problem, scenario definitions were expanded to include the variety of reference frame/coordinate system pairs that each of the simulation tools used as inputs. Initially, this was done in a Microsoft® PowerPoint document that published the original scenario definitions. However, as more simulation teams joined the assessment, the PowerPoint document became unsuitable to publish and maintain the growing list of reference frame/coordinate system pairs and a Microsoft® Excel spreadsheet was created. The new spreadsheet inadvertently introduced discrepancies in the initial conditions between the existing simulation implementations. First, some teams originally working from the PowerPoint document continued to use the PowerPoint document as the source for initial conditions. Some initial condition adjustments made to the spreadsheet were not updated in the PowerPoint document and vice-versa. Second, the precision of physical parameters and unit conversions used the construction of the spreadsheet differed for some states from those used in the PowerPoint document. This caused a difference in the accuracy of initial condition representations between the documents and these differences manifested in some of the simulation runs. Reconciling the two documents improved comparisons.

Misinterpreting an initial condition. Before documentation of the initial conditions was expanded to address the variety of reference frames and coordinates systems used by the simulation tools, simulation teams showed a tendency to interpret the documented initial conditions in the context of the scenario definitions, to which they were accustomed. In essence, some initial condition values were shoehorned into the preferred reference frame/coordinate system pair of the simulation tool. This was most prevalent for the initial angular rate under the atmospheric check cases. The initial angular rate that was first published for the atmospheric cases was measured in and represented in ECI coordinates. Some simulation teams took these values and input them directly into their tool when their tool expected inertial angular rate represented in body coordinates, Earth-relative angular rate represented in body coordinates, or atmospheric LVLH-relative angular rate represented in body coordinates, leading to poor matches.

In the next couple of comparison cycles, simulations attempted to improve comparisons by matching the initial angular rate reported by the other simulations. However, due to differences in defining variables angular rate variables (usually labeled "P", "Q", and "R", see Section E.2.2), the result was a consolidation into two camps. One camp initialized their angular rates as intended (i.e., consistent with the published initial state), and the other camp presented an initial Earth-relative rate that matched the inertial rate of the first camp. In some simulations, outputs labeled P, Q, or R were inertial-relative and in others they were Earth-relative. Most of these misinterpretations have been reconciled through discussion and updates to the scenario definitions.

Issues managing configuration files. This assessment addressed a set of 17 atmospheric check-cases and 26 orbital check-cases. This number of cases is just large enough to increase the chance of errors during construction and maintenance of configuration files.

Because the check-cases are designed to incrementally progress from simpler to more complex scenarios, simulation teams often started the next scenario by copying and tailoring the configuration file for a prior scenario. Sometimes, the simulation team would overlook a difference between the current and previous scenario. Common oversights included:

- Failing to recognize that the Spherical Earth check-cases (Atmospheric Check-cases 4 and 5) use a different radius than the equatorial radius defined for the WGS-84 Earth.
- Failing to recognize when the gravitation model changed.
- Failing to recognize when the initial attitude changed.
- Failing to recognize when the initial rotation rate changed.

Furthermore, when a simulation team made a correction to one or more configuration files in response to differences in early comparison cycles, the team sometimes failed to recognize all of the configuration files that required the same change. The simulation results would then show sudden improvement or sudden decline in the state comparisons of later scenarios relative to earlier scenarios.

Initial ECEF orientation relative to ECI. For the atmospheric cases, published initial conditions for the ECI frame assumed that the ECEF and ECI coordinate systems were coincident at $t = 0$. First, not all of the simulation tools participating in the atmospheric cases calculated states in the ECI frame. Therefore, the initial conditions specified in the ECI frame had to be converted into the ECEF frame, as well as any ECEF-referenced state outputs. Second, one of the simulation tools wasn't designed to arbitrarily define the attitude of the ECEF frame relative to the nECI frame. That tool used an ITRF model and an initial

date and time to establish the initial orientation of the ECEF to the ECI frame. This team made a valiant attempt to find a date and time where the frames were coincident. The team was able to get very close, reducing the difference to micro-arcseconds, but an exact alignment was elusive. Thus, this team worked to assure that its initial ECEF state matched the published initial condition and allowed the ECI-to-ECEF error to affect the initial inertial state. Nevertheless, the inertial state data remained useful when analyzing the ECEF state differences in that simulation relative to other simulations that also were able to report ECI state. If the differences were not consistent between the two reference frames, then the differences in one or the other frame likely had contributors other than differences in integration methods.

Definition of initial altitude. In the atmospheric check-cases, initial position in the Earth-fixed frame was specified using geodetic coordinates: latitude, longitude, and altitude. The intended initial altitude was defined as geometric, i.e. height above the reference ellipsoid or sphere. However, some simulation tools needed altitude to be expressed above ground level or above MSL as an initial condition. Between PowerPoint and spreadsheet documentation of the environment models, atmospheric check-cases, and initial conditions, there were more than one presentation of the Earth's radius in English units; each version presented a value that differed by digits of precision or by the precision of the meter-to-foot conversion for the WGS-84 published value in meters, leading to poor initial matches, as some teams interpreted the different altitude values as the difference between MSL and reference surface or elevation and reference surface. This was clarified through discussion.

Initial states not realized at $t = 0$. Some of the check-cases required the implementation of an external force model, e.g., aerodynamic drag. Furthermore, some simulation tools did not initially have, and needed to implement, new gravitation models (e.g., J_2). Some simulation tools also implemented code for accepting initial conditions under references frames and coordinates systems not previously supported by the simulation.

In some instances, the initial implementation failed to execute the new code during initialization and the associated initial values remained at a default value of zero. The new code did not operate until the first time step. If the associated state was an integrand or an integrand was derived from than state, the initial default value of zero would induce a jump in integration error that would propagate a growing state divergence relative to other simulations. This problem was most prevalent for atmospheric cases 7 and 8 that introduced winds. The winds had a non-zero initial magnitude. Therefore, the wind would induce an initial aerodynamic drag at $t = 0$ even though the initial world-relative velocity of the sphere was zero. More than one simulation tool recorded a non-zero aerodynamic drag at $t = 0$ when they first ran this scenario.

Confusion over initial center-of-mass location for F-16 model. Initially, the intended initial CM location for the F-16 model was not published with the scenario description. The DAVE-ML model for the F-16 contained a default CM location of 35% mean aerodynamic chord (MAC). However, the README.html file for the model contained a trim solution for CM at 25% MAC. Thus, first comparisons of the F-16 cases included a mix of simulations initializing the CM to 35% MAC or 25% MAC. After some discussion, consensus was reached on fixing the CM at 25% MAC.

E.2.4 Output data recording differences

Some differences between the simulation tools in earlier comparisons were not indicative of differences in dynamics or modeling but were artifacts of the data output (recording) function. The following aspects of data recording contributed to apparent initial differences between the simulations:

- Insufficient output precision.
- A persistent one frame lag in recording an output variable.
- Issues with capturing the correct time-correlated value in the first or last recording frame.
- Range of angle quantities.
- No common coordinate system among the data files for the state being compared.

Insufficient precision in output fields. The initial requirement for output data was to provide at least six digits of precision. Some simulation teams configured recording output for six significant digits and other simulation teams configured recording output for six decimal places. Six decimal places would not be adequate for some output variables; for example, atmospheric density in slug/ft^3 is $O(10^{-3})$ and would, at most, present three significant digits with six decimal digit output. However, even six significant digits would often prove inadequate to capture differences between simulations that were traceable to causes other than differences in integration methods. For example, capturing longitude to six significant digits at the Equator cannot show position differences smaller than 20 ft in most of the atmospheric cases.

The orbital cases were even more sensitive to differences in modeling perturbations and these differences could only be uncovered by analyzing data with at least 10 to 12 significant digits. As simulation teams increased the significant digits of displayed for data fields, a new issue emerged. To save space, some simulations were storing variables with four-byte data types. Increasing output precision simply added random numbers or zeros to those digits of precision that could not be retained in four-byte data types. In other words, the accuracy of the output data was smaller than its precision. Those simulations then increased storage to eight-byte data types. It took a few cycles for all simulations to produce output with sufficient accuracy and precision to meaningfully analyze the data sets for modeling or implementation differences.

Persistent lag in output variable. The output variable of a simulation would occasionally lag in value by one computational frame when compared to the other simulations. A recording rate was agreed to for each check-case. However, simulation teams were free to run at whatever rate they determined produces adequate results.

In most cases, simulation tools were executed at a faster rate than the data was recorded. Therefore, detecting a lag in an output value was often difficult. In some cases, the simulation team would record at the execution rate and see if a better match were obtained if the data were shifted forward by a frame. In other cases, another simulation team would record at the execution rate and test whether a better match was obtained using a value delayed one frame.

Another means of detecting potential lags in the recording was to estimate the time history of next computation frame values from the reported time history of the values. Estimation techniques included linear interpolation, integration of the variables reported derivatives, or partial application of kinematic relationships using output variables that did not appear to lag by a computational frame.

Uncorrelated values in the first or last recording frame. An output variable in one simulation occasionally exhibited a sudden decrease in difference relative to other simulations from the first to second frame. Similarly, an output variable in one simulation sometimes exhibited a sudden increase in difference relative to the other simulations in the last frame.

There were a number of potential causes for the first case. The output variable may not have been updated with a complete set of input values correlated at $t = 0$. Alternatively, the recording function may capture

the output variable at a point in the execution sequence that is incomplete prior to the execution of first frame, or the recording function may capture a value in the first frame that leads the other simulations by one computational frame because the output value is not computed prior to the first frame.

For the case where differences suddenly change in the last frame, the recording function may be forced to capture a value that leads or lags the other simulations by a computational frame because the simulation shutdown changes the sequence of operations in the last frame. It is also possible that the plotting software causes these artifacts when processing data files with different recording rates or different recording lengths.

Range for angles. The simulations maintained different ranges for the angle outputs. For example, initial comparisons showed three different ranges for yaw angle exhibited by the simulations. One set of simulations used the range $[0, 360)$, another set used $(-180, 180]$, and a third set used $[0, \text{inf})$.

Furthermore, when a scenario neared the wrap-around point for the range, it was possible for two simulations to cross the wrap-around point at different but adjacent recording frames; this would produce an apparent difference near the full range and hide the real angular difference between the simulations.

Differences in angle range were handled during comparison plotting by reducing all simulation data to the same range and using one simulation as the basis of comparison rather than attempting to compute an ensemble average.

No common coordinate system for a quantity. Sometimes, there was no common coordinate system among the simulation data files. For example, in the atmospheric cases, output data files presented the gravitation vector in body coordinates, NED coordinates, or ECI coordinates. Some simulation teams were able to implement a new coordinate system in order to establish commonality. In other situations, post-processing might be used to generate a common item for comparison. In the example of the gravitation vector, the early atmospheric cases generated no north or east components of gravitation. Thus, the Down component of gravitation was compared to the magnitude of the gravitation vector in simulations using body or ECI coordinates. However, this post-processing would generate apparent differences in later scenarios where a north component of gravitation emerged.

To improve comparisons, the post-processing was then updated to compare gravitation magnitudes across all simulations.

E.2.5 Timing of external forces and torques

Atmospheric check-case 17 and orbital check-cases 6C, 6D, and 9A through 9D specified an input shaped like a square pulse in force or torque with a start time and duration. During initial comparisons, there was some ambiguity over the exact times at which the leading- and trailing-edge of the square occurred. Both the leading- and trailing-edge of the square pulse occurred in-between recording steps for the simulations. To clarify agreement on the leading- and trailing-edge of the pulse, simulation teams exchanged partial runs where the recording rate was increased to capture the exact time for both edges of the square pulse.

E.3 Suggestions for future work

This report documents the results of a 6-DOF flight simulation comparison study running a specified set of models and flight maneuvers in specified check-cases. This effort was intended to aid the aerospace community in resolving differences in its simulation tool-sets, but it is hoped an additional benefit will be

to provide confidence in other industry-developed simulation tools if they show similar results for the same check-cases.

Ongoing work is to resolve as many differences in flight simulation tools as possible. The supersonic maneuvering flight check-case (case 14) was not satisfactorily completed; although three simulation tools provided trajectories, the timing and amplitude of input sequences were different due to a change in specification that occurred mid-assessment. An additional atmospheric check-case involving a Apollo-like capsule during atmospheric reentry was proposed, but was not evaluated by any simulation tool due to resource limitations.

The authors welcome participation by other simulation tool developers who might wish to perform the same simulated flight trajectory comparisons.

References

[1] Crues, Edwin Z.; Jackson, A. A.; and Morris, J. C.: A Process for Comparing Dynamics of Distributed Space Systems Simulations. *Joint 2009 Simulation Interoperability Workshop*, San Diego, CA, 2009.

[2] Stevens, B. L.; and Lewis, F. L.: *Aircraft Control and Simulation*. John Wiley & Sons, Hoboken, NJ, second ed., 2003.

[3] Garza, F. R.; and Morelli, E. A.: A Collection of Nonlinear Aircraft Simulations in MATLAB. NASA TM-2003-212145, National Aeronautics and Space Administration, Hampton, VA, 2003.

[4] Nguyen, L. T.; Ogburn, M. E.; Gilbert, W. P.; Kibler, K. S.; Brown, P. W.; and Deal, P. L.: Simulator Study of Stall/Post-Stall Characteristics of a Fighter Airplane with Relaxed Longitudinal Static Stability. NASA TP-1538, National Aeronautics and Space Administration, Hampton, VA, 1979.

[5] Anon.: Flight Dynamics Model Exchange Standard. ANSI/AIAA S-119-2011, American National Standard, Washington, DC, March 2011.

[6] Anon.: US Standard Atmosphere 1976. NASA-TM-X-74335, Joint NOAA, NASA, and USAF publication, Washington, DC, 1976.

[7] Anon.: Department of Defense World Geodetic System 1984. NIMA TR8350.2, National Imagery and Mapping Agency, Washington, DC, 2000.

[8] Borkowski, K. M.: Transformation of Geocentric to Geodetic Coordinates Without Approximations. *Bulletin Geodesique 63*, vol. 139, December 1987, pp. 1–4.

[9] Beaty, J. R.: *Fundamentals of Geodetic Kinematics, Part 1 of 2*. May 2014. URL `http://nescacademy.nasa.gov/video_catalog.php?catid=3&subcatid=6`.

[10] Montenbruck, O.; and Gill, E.: *Satellite Orbits: Models, Methods, and Applications*. Springer-Verlag, Berlin, 2000.

[11] Vallado, D.: *Fundamentals of Astrodynamics and Applications*. Microcosm Press, El Segundo, CA, second ed., 2001.

[12] Kaula, W.: *Theory of Geodesy: Applications of Satellites to Geodesy*. Blaisdell Publishing Company, Waltham, Massachusetts, 1966.

[13] Torge, W.: *Geodesy*. Walter de Gruyter, Berlin, third ed., 2001.

[14] Madden, M. M.: Gravity Modeling for Variable Fidelity Environments. *2006 AIAA Modeling and Simulation Technologies Conference*, NASA Langley Research Center, Aug. 2006.

[15] Jacchia, L. G.: New Static Models of the Thermosphere and Exosphere with Empirical Temperature Profiles. SAO Special Report No. 313, Smithsonian Institution Astrophysical Observatory, Cambridge, MA, 1970.

[16] Jacchia, L. G.: Revised Static Models of the Thermosphere and Exosphere with Empirical Temperature Profiles. SAO Special Report No. 322, Smithsonian Institution Astrophysical Observatory, Cambridge, MA, 1971.

[17] Hedin, A.: Extension of the MSIS Thermosphere Model into the Middle and Lower Atmosphere. *Journal of Geophysical Research*, vol. 96, 1991, p. 1159.

[18] Hickey, M. P.: The NASA Marshall Engineering Thermosphere Model. NASA CR-179359, National Aeronautics and Space Administration, Washington, D.C., July 1988.

[19] Hickey, M. P.: An Improvement in the Integration Procedure Used in the Marshall Engineering Thermosphere Model. NASA CR-179389, National Aeronautics and Space Administration, Washington, D.C., 1988.

[20] Owens, J.: NASA Marshall Engineering Thermosphere Model-Version 2.0. NASA/TM-2002-211786, NASA, June 2002.

[21] Leslie, R. A.; Geyer, D. W.; Cunningham, K.; Glaab, P. C.; Kenney, P. S.; and Madden, M. M.: LaSRS++: An Object-Oriented Framework for Real-Time Simulation of Aircraft. *1998 AIAA Modeling and Simulation Technologies Conference*, NASA Langley Research Center, Aug. 1998.

[22] Barker, L. E. J.: Development and application of a local linearization algorithm for the integration of quaternion rate equations in real-time flight simulation problems. NASA-TN-D-7347, NASA, 1973.

[23] McFarland, R. E.: *Stability of Discrete Integration Algorithms for a Real-Time, Second-Order System*. Oct. 1997. URL `http://www.aviationasystemsdivision.arc.nasa.gov/publications/hitl/rtsim/Stab.pdf`.

[24] Newman, D. M.: *The Janus C++ Library: An Interface Class for DAVE-ML Compliant XML-Based Flight Model Datasets*. Air Vehicles Division, Defence Science and Technology Organisation, July 2005. URL `http://www.dsto.defence.gov.au/opportunity/janus-dynamic-aerospace-vehicle-exchange-mark-language-dave-ml-c-interpreter`.

[25] Crues, E. Z.: Distributed Space Exploration Simulation Space Environment and Dynamics Comparison Phase 2 Test Plan. Revision 0.5 (unpublished), Simulation and Graphics Branch (ER7), NASA Johnson Space Center, May 2006.

[26] Anonymous: JPL Planetary and Lunar Ephemerides, DE450/LE450. DE405, Jet Propulsion Laboratory, May 1997.

[27] Seidelmann, P. K.: *Explanatory Supplement to the Astronomical Almanac*. University Science Books, revised ed., Aug 2005.

[28] Marsh, J. G.; Lerch, F. J.; Putney, B. H.; Christodoulidis, D. C.; Smith, D. E.; Felsentreger, T. L.; Sanchez, B. V.; Klosko, S. M.; Pavlis, E. C.; Martin, T. V.; Robbins, J. W.; Williamson, R. G.; Colombo, O. L.; Rowlands, D. D.; Eddy, W. F.; Chander, N. L.; Rachlin, K. E.; Patel, G. B.; Bhati, S.; and Chinn,

D. S.: A New Gravitational Model for the Earth from Satellite Tracking Data: GEM-T1. *Journal of Geophysical Research*, vol. 93, 1999, p. 6169.

[29] Boucher, C.; Altamimi, Z.; and Duhem, L.: Results and analysis of the ITRF93. IERS Technical Note 18, Institut Géographicque National, October 1994.

[30] Boucher, C.; and Altamimi, Z.: The initial IERS Terrestrial Reference Frame. IERS Technical Note 1, Institut Géographicque National, June 1989.

REPORT DOCUMENTATION PAGE

Form Approved
OMB No. 0704-0188

The public reporting burden for this collection of information is estimated to average 1 hour per response, including the time for reviewing instructions, searching existing data sources, gathering and maintaining the data needed, and completing and reviewing the collection of information. Send comments regarding this burden estimate or any other aspect of this collection of information, including suggestions for reducing this burden, to Department of Defense, Washington Headquarters Services, Directorate for Information Operations and Reports (0704-0188), 1215 Jefferson Davis Highway, Suite 1204, Arlington, VA 22202-4302. Respondents should be aware that notwithstanding any other provision of law, no person shall be subject to any penalty for failing to comply with a collection of information if it does not display a currently valid OMB control number.
PLEASE DO NOT RETURN YOUR FORM TO THE ABOVE ADDRESS.

1. REPORT DATE *(DD-MM-YYYY)*	2. REPORT TYPE	3. DATES COVERED *(From - To)*
01- 01 - 2015	Technical Memorandum	April 2012 - October 2014

4. TITLE AND SUBTITLE
Check-Cases for Verification of 6-Degree-of-Freedom Flight Vehicle Simulations
Appendices

5a. CONTRACT NUMBER

5b. GRANT NUMBER

5c. PROGRAM ELEMENT NUMBER

6. AUTHOR(S)
Murri, Daniel G.; Jackson, E. Bruce; Shelton, Robert O.

5d. PROJECT NUMBER

5e. TASK NUMBER

5f. WORK UNIT NUMBER
869021.05.07.01.17

7. PERFORMING ORGANIZATION NAME(S) AND ADDRESS(ES)
NASA Langley Research Center
Hampton, VA 23681-2199

8. PERFORMING ORGANIZATION REPORT NUMBER
L-20519 NESC-RP-12-00770

9. SPONSORING/MONITORING AGENCY NAME(S) AND ADDRESS(ES)
National Aeronautics and Space Administration
Washington, DC 20546-0001

10. SPONSOR/MONITOR'S ACRONYM(S)
NASA

11. SPONSOR/MONITOR'S REPORT NUMBER(S)
NASA/TM-2015-218675/Volume II

12. DISTRIBUTION/AVAILABILITY STATEMENT
Unclassified - Unlimited
Subject Category 61 Computer Programming and Software
Availability: NASA CASI (443) 757-5802

13. SUPPLEMENTARY NOTES

14. ABSTRACT
This NASA Engineering and Safety Center (NESC) assessment was established to develop a set of time histories for the flight behavior of increasingly complex example aerospacecraft that could be used to partially validate various simulation frameworks. The assessment was conducted by representatives from several NASA Centers and an open-source simulation project. This document contains details on models, implementation, and results.

15. SUBJECT TERMS
Check-case; Simulation and Analysis Tools; 6-degree-of-freedom Flight Simulation Tool; NASA Engineering and Safety Center

16. SECURITY CLASSIFICATION OF:			17. LIMITATION OF ABSTRACT	18. NUMBER OF PAGES	19a. NAME OF RESPONSIBLE PERSON
a. REPORT	b. ABSTRACT	c. THIS PAGE			STI Help Desk (email: help@sti.nasa.gov)
U	U	U	UU	614	19b. TELEPHONE NUMBER *(Include area code)* (443) 757-5802

Standard Form 298 (Rev. 8-98)
Prescribed by ANSI Std. Z39.18